

Notes on Numerical Fluid Mechanics  
and Multidisciplinary Design 139

David Anderson · Pierre-Etienne Gautier  
Masanobu Iida · James T. Nelson  
David J. Thompson · Thorsten Tielkes  
David A. Towers · Paul de Vos  
Jens C. O. Nielsen *Editors*

# Noise and Vibration Mitigation for Rail Transportation Systems

Proceedings of the 12th International  
Workshop on Railway Noise, 12–16  
September 2016, Terrigal, Australia

# Notes on Numerical Fluid Mechanics and Multidisciplinary Design

Volume 139

## Series editors

Wolfgang Schröder, Lehrstuhl für Strömungslehre und Aerodynamisches Institut,  
Aachen, Germany  
e-mail: office@aia.rwth-aachen.de

Bendiks Jan Boersma, Delft University of Technology, CA Delft, The Netherlands  
e-mail: b.j.boersma@tudelft.nl

Kozo Fujii, The Institute of Space and Astronautical Science, Kanagawa, Japan  
e-mail: fujii@flab.eng.isas.jaxa.jp

Werner Haase, Neubiberg, Germany  
e-mail: whac@haa.se

Ernst Heinrich Hirschel, Zorneding, Germany  
e-mail: e.h.hirschel@t-online.de

Michael A. Leschziner, Imperial College of Science Technology and Medicine,  
London, UK  
e-mail: mike.leschziner@imperial.ac.uk

Jacques Periaux, Paris, France  
e-mail: jperiaux@free.fr

Sergio Pirozzoli, Università di Roma "La Sapienza", Roma, Italy  
e-mail: sergio.pirozzoli@uniroma1.it

Arthur Rizzi, KTH Royal Institute of Technology, Stockholm, Sweden  
e-mail: rizzi@aero.kth.se

Bernard Roux, Technopole de Chateau-Gombert, Marseille Cedex, France  
e-mail: broux@13m.univ-mrs.fr

Yurii I. Shokin, Siberian Branch of the Russian Academy of Sciences,  
Novosibirsk, Russia  
e-mail: shokin@ict.nsc.ru

*Notes on Numerical Fluid Mechanics and Multidisciplinary Design* publishes state-of-art methods (including high performance methods) for numerical fluid mechanics, numerical simulation and multidisciplinary design optimization. The series includes proceedings of specialized conferences and workshops, as well as relevant project reports and monographs.

More information about this series at <http://www.springer.com/series/4629>

David Anderson · Pierre-Etienne Gautier  
Masanobu Iida · James T. Nelson  
David J. Thompson · Thorsten Tielkes  
David A. Towers · Paul de Vos  
Jens C. O. Nielsen  
Editors

# Noise and Vibration Mitigation for Rail Transportation Systems

Proceedings of the 12th International  
Workshop on Railway Noise, 12–16  
September 2016, Terrigal, Australia

 Springer

*Editors*

David Anderson  
Acoustic Studio  
Stanmore, NSW  
Australia

Thorsten Tielkes  
DB Systemtechnik GmbH  
Munich  
Germany

Pierre-Etienne Gautier  
SYSTRA  
Paris  
France

David A. Towers  
Harris Miller Miller & Hanson Inc  
Burlington, MA  
USA

Masanobu Iida  
Environmental Engineering Division  
Railway Technical Research Institute  
Tokyo  
Japan

Paul de Vos  
SATIS  
Weesp  
The Netherlands

James T. Nelson  
Wilson Ihrig & Associates  
Emeryville, CA  
USA

Jens C. O. Nielsen  
Department of Applied  
Mechanics/CHARMEC  
Chalmers University of Technology  
Gothenburg  
Sweden

David J. Thompson  
Institute of Sound and Vibration Research,  
University of Southampton  
Southampton  
UK

ISSN 1612-2909

ISSN 1860-0824 (electronic)

Notes on Numerical Fluid Mechanics and Multidisciplinary Design

ISBN 978-3-319-73410-1

ISBN 978-3-319-73411-8 (eBook)

<https://doi.org/10.1007/978-3-319-73411-8>

Library of Congress Control Number: 2018933008

© Springer International Publishing AG, part of Springer Nature 2018

This work is subject to copyright. All rights are reserved by the Publisher, whether the whole or part of the material is concerned, specifically the rights of translation, reprinting, reuse of illustrations, recitation, broadcasting, reproduction on microfilms or in any other physical way, and transmission or information storage and retrieval, electronic adaptation, computer software, or by similar or dissimilar methodology now known or hereafter developed.

The use of general descriptive names, registered names, trademarks, service marks, etc. in this publication does not imply, even in the absence of a specific statement, that such names are exempt from the relevant protective laws and regulations and therefore free for general use.

The publisher, the authors and the editors are safe to assume that the advice and information in this book are believed to be true and accurate at the date of publication. Neither the publisher nor the authors or the editors give a warranty, express or implied, with respect to the material contained herein or for any errors or omissions that may have been made. The publisher remains neutral with regard to jurisdictional claims in published maps and institutional affiliations.

Printed on acid-free paper

This Springer imprint is published by the registered company Springer International Publishing AG part of Springer Nature

The registered company address is: Gewerbestrasse 11, 6330 Cham, Switzerland

# Preface

This volume contains the peer-reviewed contributions to the 12th International Workshop on Railway Noise (IWRN12), which took place in Terrigal, Australia, on 12–16 September 2016. The workshop was hosted by the Australian Acoustical Society (AAS, the Australian professional body for those working in acoustics) in partnership with the Asset Standards Authority (ASA, the design and standards authority within Transport for NSW).

IWRN12 was also made possible by the support of the primary sponsors for the event: Pandrol Track Systems (Gold sponsor), Delkor Rail (Silver sponsor) and Vossloh Fastening Systems (Bronze sponsor).

The workshop was attended by 135 delegates and 11 accompanying persons from 16 countries: Australia (53), China (19), UK (11), Japan (11), Belgium (6), USA (5), Singapore (5), Germany (5), France (5), Sweden (4), Canada (3), Austria (2), Switzerland (1), Spain (1), South Africa (1) and the Netherlands (1).

In comparison with other modes of transportation, rail transport is safe and environmentally friendly and is generally described as the most sustainable mode for regional and international transport. However, it is also recognised that the environmental impact of railway noise and vibration needs to be further reduced. Since the first IWRN in 1976, held in Derby (UK) with 35 delegates, the workshop series has been established as a regular event (held every three years) that brings together the leading researchers and engineers in all fields related to railway noise and vibration. The IWRN workshops have contributed significantly to the understanding and solution of many problems in railway noise and vibration, building a scientific foundation for reducing environmental impact by air-borne, ground-borne and structure-borne noise and vibration.

Following the tradition from previous workshops, the scientific programme of IWRN12 was held as a single-session event (no parallel sessions) over three and a half days. The programme contained 54 oral presentations and 25 poster presentations. The poster sessions commenced with a series of two-minute oral presentations to introduce each paper, and these sessions were very well attended.

This volume contains the peer-reviewed papers from 61 of these presentations, including two state-of-the-art papers on curve noise and on policy, regulation and perception. IWRN12 covered eight different themes: High-Speed Rail and Aerodynamic Noise; Interior Noise; Policy, Regulation and Perception; Predictions, Measurements and Modelling; Rail Roughness, Corrugation and Grinding; Squeal Noise; Structure-Borne Noise, Ground-Borne Vibration and Resilient Track Forms; and Wheel and Rail Noise.

In parallel with the scientific programme, 11 companies gathered at IWRN12 to display their technology and services in the area of railway noise and vibration: Pandrol Track Systems; Delkor Rail; Brüel & Kjær; ETMC Technologies; JSG Industrial Systems; Marshall Day Acoustics; LB Foster/Airlube Australasia; Pyrotek; Schrey & Veit; SoundScience and Wilson Acoustics.

There is no formal organisation behind the IWRN but rather an informal, committed International Committee. It supports the chairman during the preparation process with the experience and expertise of its members. Assistance is given to formulate the scientific programme by reviewing the submitted abstracts, to act as session chairmen and to act as peer review group and editors of the IWRN proceedings published in this volume.

The International Committee is grateful to David Hanson for his diligent work in organising the scientific programme and to Kym Burgemeister, Tom Cockings, Peter Karantonis, Serge Vegh and Conrad Weber of the local committee for their great commitment and care in organising the workshop.

The editors of this volume are grateful to Professor Wolfgang Schröder as the general editor of the “Notes on Numerical Fluid Mechanics and Multidisciplinary Design” and also to the staff of the Springer Verlag (in particular, Dr. Leontina Di Cecco) for the opportunity to publish the proceedings of the IWRN12 workshop in this series. Note that previous workshop proceedings have also been published in this series (IWRN9 in volume 99, IWRN10 in volume 118 and IWRN11 in volume 126).

We hope that this volume will be used as a “state-of-the-art” reference by scientists and engineers involved in solving noise and vibration problems related to railway traffic.

Stanmore, Australia  
 Paris, France  
 Tokyo, Japan  
 Emeryville, USA  
 Southampton, UK  
 Munich, Germany  
 Burlington, USA  
 Weesp, The Netherlands  
 Gothenburg, Sweden  
 June 2017

David Anderson  
 Pierre-Etienne Gautier  
 Masanobu Iida  
 James T. Nelson  
 David J. Thompson  
 Thorsten Tielkes  
 David A. Towers  
 Paul de Vos  
 Jens C. O. Nielsen

# Contents

## Part I Squeal Noise

<b>A State-of-the-Art Review of Curve Squeal Noise: Phenomena, Mechanisms, Modelling and Mitigation</b> . . . . .	3
David J. Thompson, G. Squicciarini, B. Ding and L. Baeza	
<b>Wheel Squeal: Insights from Wayside Condition Monitoring</b> . . . . .	43
J. Jiang, D. Hanson and B. Dowdell	
<b>Analysis of Railway Wheel-Squeal Due to Unsteady Longitudinal Creepage Using the Complex Eigenvalue Method</b> . . . . .	57
D. J. Fourie, P. J. Gräbe, P. S. Heyns and R. D. Fröhling	
<b>Prediction of Wheel Squeal Amplitude</b> . . . . .	71
Paul A. Meehan and Xiaogang Liu	
<b>Investigation of Railway Curve Squeal Using a Combination of Frequency- and Time-Domain Models</b> . . . . .	83
A. Pieringer, P. T. Torstensson, J. Giner and L. Baeza	

## Part II Policy, Regulation and Perception

<b>State of the Art Review of Rail Noise Policy</b> . . . . .	99
B. E. Croft and B. Hemsworth	
<b>Supporting Decision Making and Management of Freight Rail Noise Using GIS</b> . . . . .	121
L. Basutu and K. Sharpe	
<b>Between the Wheel and the Track: A Regulator’s Reflections on Rail Noise Regulation in NSW</b> . . . . .	131
J. M. Hanemann and P. Maddock	
<b>Abatement of Railway Noise in Germany</b> . . . . .	143
R. Weinandy, P. Appel and T. Myck	



### **Part III Predictions, Measurements and Modelling**

<b>Quantifying Uncertainties in Measurements of Railway Vibration . . . . .</b>	<b>155</b>
K. A. Kuo, G. Lombaert and G. Degrande	
<b>Reproducibility of Railway Noise Measurements—Influence of Weather and Test Site Conditions . . . . .</b>	<b>167</b>
Jens C. O. Nielsen, E. Augis and F. Biebl	
<b>Train Speed Estimations from Ground Vibration Measurements Using a Simple Rail Deflection Model Mask . . . . .</b>	<b>181</b>
V. Jurdic, O. Bewes, K. Burgemeister and David J. Thompson	
<b>Groundborne Railway Noise and Vibration in Buildings: Results of a Structural and Acoustic Parametric Study . . . . .</b>	<b>193</b>
D. E. J. Lurcock, David J. Thompson and O. G. Bewes	
<b>Identifying Noise Levels of Individual Rail Pass by Events . . . . .</b>	<b>205</b>
Matthew Ottley, Alex Stoker, Stephen Dobson and Nicholas Lynar	
<b>A Modified Turnout Noise Model and Field Validation . . . . .</b>	<b>215</b>
W. Ho, B. Wong and T. Cai	
<b>Railway Noise: A New Paradigm for SNCF Acousticians . . . . .</b>	<b>227</b>
F. Poisson, D. Laousse, F. Dubois, B. Faure and E. Bongini	
<b>Ageing Cuts Down the Track Homogeneity Causing Differences Between Calculations and Measurements of Railway Noise . . . . .</b>	<b>239</b>
H. Venghaus	
<b>Track Condition Assessment Using Primary Suspension Data . . . . .</b>	<b>251</b>
Y. K. Siow, D. Y. Foo, T. N. Nguyen and W. L. Chia	
<b>Modelling Framework for Electromagnetic Noise Generation from Traction Motors . . . . .</b>	<b>263</b>
F. Botling, I. Lopez Arteaga and S. Leth	
<b>Design and Performance of a Permanent Vibration Monitoring System with Exceedance Alarms in Train Tunnels . . . . .</b>	<b>279</b>
S. Rajaram, James T. Nelson and H. J. Saurenman	
<b>The Uncertainty Associated with Short-Term Noise Measurements of Passenger and Freight Trains . . . . .</b>	<b>293</b>
C. Weber and L. Zoontjens	
<b>Rail Ground-Borne Noise and Vibration Prediction Uncertainties . . . . .</b>	<b>307</b>
C. Weber and P. Karantonis	
<b>Genset Locomotives: Implications for Type Testing in NSW . . . . .</b>	<b>319</b>
D. R. McGregor	

**Part IV Rail Roughness, Corrugation and Grinding**

**Routine Measurement of Long Wavelength Irregularities from Vehicle-Based Equipment** . . . . . 333  
 Stuart L. Grassie

**Noise Reduction Measure for Trussed Non-slab Bridges** . . . . . 343  
 Shinji Mori, Minoru Kobayashi and Junichiro Osawa

**Effects of Rail Lateral Dynamic Deflection and Vibration Level on Rail Corrugation Development** . . . . . 355  
 A. Wang, Z. Wang, Z. Zhang, N. Xu, X. Qiao and M. Du

**Impact of Rail Dampers on the Mainline Rail Roughness Development** . . . . . 367  
 Christoph Gramowski and Patrick Suppin

**Part V High Speed Rail Noise**

**Estimation of Aerodynamic Bogie Noise Through Field and Wind Tunnel Tests** . . . . . 377  
 T. Uda, N. Yamazaki, T. Kitagawa, K. Nagakura and Y. Wakabayashi

**Aerodynamic Noise Reduction of Brake Disc for High-Speed Trains** . . . . . 389  
 N. Shiraishi, Y. Wakabayashi, T. Kurita, T. Fujimoto and Y. Ichikawa

**Development of New Noise Reduction Equipment for the Slits on Tunnel Hoods** . . . . . 401  
 Masaaki Matsunuma and Nobuyuki Kimura

**Reduction of Aerodynamic Noise Emitted from Pantograph by Appropriate Aerodynamic Interference Around Pantograph Head Support** . . . . . 411  
 T. Mitsumoji, Y. Sato, N. Yamazaki, T. Uda, T. Usuda and Y. Wakabayashi

**Application Effect of Chinese High-Speed Railway Noise Barriers** . . . . . 423  
 Yanliang Li and Zhiqiang Li

**Experimental Research on the Characteristics of the Noise Source of the Chinese High-Speed Railway** . . . . . 431  
 Lanhua Liu and Zhiqiang Li

**Psychoacoustic Evaluation of Noises Generated by Passenger Seats for High Speed Trains** . . . . . 439  
 J. Sapena and R. Caminal

<b>Active Noise Control of Interior Noise of a High-Speed Train Carriage</b> . . . . .	451
Yanju Zhao, Renzhong Shuai, Leiwei Zhu, Peng Lin and Zongcai Liu	
<b>Development of a Suspended Floor Structure for a Railway Vehicle</b> . . . . .	461
K. Yamamoto, T. Goto, M. Asahina, Y. Akiyama and N. Imaoka	
<b>Study on Sound Absorption Seats in High Speed Trains</b> . . . . .	473
Xiaojun Deng, Yanju Zhao, Haijin Zhang and Peng Lin	
<b>Part VI Structure-Borne Noise and Ground-Borne Noise</b>	
<b>On the Propagation and Prediction of Rail-Induced Ground-Borne Vibration Within Sandy Soils</b> . . . . .	485
Binghui Li and Luke Zoontjens	
<b>Modelling of Ground-Borne Vibration When the Train Speed Approaches the Critical Speed</b> . . . . .	497
J. Y. Shih, David J. Thompson and A. Zervos	
<b>Influence of Soil Properties and Model Parameters on Vibrations Induced by Underground Railways for Deep Stratified Alluvial Deposits</b> . . . . .	509
Hailing Xing, Tong Jiang, Jiahua Liu and Tianxing Wu	
<b>Attenuation Properties of Ground Vibration Propagated from Subway Tunnels in Soft Ground</b> . . . . .	521
K. Tsuno and M. Furuta	
<b>Effects of Tuned Slab Damper on Low Frequency Ground Vibration Levels on Metro Systems</b> . . . . .	533
G. Xu, A. Wang, Y. Li, Y. Fan, Z. Zhang, Z. Wang, G. Dong and J. Liu	
<b>Optimal Design of Wave Barriers for the Reduction of Vibration Levels</b> . . . . .	547
C. Van hoorickx, M. Schevenels and G. Lombaert	
<b>Vibration Reduction with Installation of Rail Dampers—A Case Study</b> . . . . .	557
B. E. Croft and C. M. Weber	
<b>Computation of Ground Vibration Around Pier by Using Axisymmetric Finite Element Method</b> . . . . .	571
Jun Kaneda, Hirofumi Ikemoto, Takeshi Ishii and Kunio Saitoh	
<b>Development of Orthogonal Resilient Materials for Tuned Mass Dampers</b> . . . . .	585
Po-lai Tam, Chi-wah Leung, Chee-leung Mak, Wilson Ho and Ting Cai	

**Reduction of Vibration Emissions and Secondary Airborne Noise with Under-Sleeper Pads—Effectiveness and Experiences** . . . . . 595  
 Harald Loy, Andreas Augustin and Lukas Tschann

**Sound Transit Prototype High Performance Low Frequency Floating Slab Testing and Evaluation** . . . . . 607  
 James T. Nelson, Derek L. Watry, Michael A. Amato, Patrick G. Faner, Sarah E. Kaddatz and Thomas F. Bergen

**Development of a Test Procedure for Stiffness Measurements Appropriate to Ground-Borne Noise Modelling** . . . . . 619  
 D. Herron, E. Bongini, B. Faure, R. Potvin and S. Cox

**A Comprehensive Review of Force Density Levels from Sound Transit’s Light Rail Transit Fleet** . . . . . 633  
 S. Rajaram, James T. Nelson and H. J. Saurenman

**Estimating Adjustment Factors to Predict Vibration at Research Facilities Based on Measurements in a Subway Tunnel** . . . . . 645  
 A. L. Evans, C. G. Ono and H. J. Saurenman

**Mechanism and Reduction Countermeasure of Structure Borne Sound of Reinforced Concrete Viaducts** . . . . . 659  
 T. Watanabe, K. Matsuoka and S. Fuchigami

**The Factors Associated with the Management of Combined Rail/Wheel Roughness to Control Groundborne Noise and Vibration from the UK’s Crossrail Project** . . . . . 671  
 R. H. Method, C. J. C. Jones, C. Cobbing and J. Cronje

**Verification of the Effectiveness of a Floating Track Slab System After 20 Years of Service** . . . . . 683  
 Hanno Töll, Günther Achs, Christoph Kuttelwascher, Michael Mach and Mirko Dold

**Part VII Wheel and Rail Noise**

**Low Cost Noise Barriers for Mitigation of Rail Noise** . . . . . 697  
 L. Basutu, W. Chan, D. Hanson, B. Dowdell and C. Weber

**A New Model for the Prediction of Track Sound Radiation** . . . . . 709  
 Xianying Zhang, David J. Thompson and Giacomo Squicciarini

**Friction Management as a Sustainable Solution for Controlling Noise at the Wheel-Rail Interface** . . . . . 723  
 R. Stock, M. Santoro, T. Makowsky, D. Elvidge and P. Xia

**Development of Supported Rail Vibration Models** . . . . . 735  
 W. Li and R. A. Dwight

**Characterization of Train Fleet Wheel Condition in a Metro** . . . . . 747  
K. G. Albindo, C. J. Ng, T. P. Ng and W. L. Chia

**Hybrid Model for Prediction of Impact Noise Generated  
at Railway Crossings** . . . . . 759  
P. T. Torstensson, G. Squicciarini, M. Krüger, Jens C. O. Nielsen  
and David J. Thompson

**Classification of Impact Signals from Insulated Rail Joints Using  
Spectral Analysis** . . . . . 771  
Andrew Yuen, Dingyang Zheng, Peter Mutton and Wenyi Yan

**Part I**  
**Squeal Noise**

# A State-of-the-Art Review of Curve Squeal Noise: Phenomena, Mechanisms, Modelling and Mitigation



David J. Thompson, G. Squicciarini, B. Ding and L. Baeza

**Abstract** Curve squeal is an intense tonal noise occurring when a rail vehicle negotiates a sharp curve. The phenomenon can be considered to be chaotic, with a widely differing likelihood of occurrence on different days or even times of day. The term curve squeal may include several different phenomena with a wide range of dominant frequencies and potentially different excitation mechanisms. This review addresses the different squeal phenomena and the approaches used to model squeal noise; both time-domain and frequency-domain approaches are discussed and compared. Supporting measurements using test rigs and field tests are also summarised. A particular aspect that is addressed is the excitation mechanism. Two mechanisms have mainly been considered in previous publications. In many early papers the squeal was supposed to be generated by the so-called falling friction characteristic in which the friction coefficient reduces with increasing sliding velocity. More recently the mode coupling mechanism has been raised as an alternative. These two mechanisms are explained and compared and the evidence for each is discussed. Finally, a short review is given of mitigation measures and some suggestions are offered for why these are not always successful.

## 1 Introduction

Curve squeal is an intense tonal noise produced when railway vehicles negotiate sharp curves. It is probably the most annoying type of noise produced by the railway system due to its tonal nature and its high noise levels. It is also highly unpredictable, with a widely differing likelihood of occurrence for nominally identical vehicles, or for same vehicles on different days or even times of day and might be considered to be chaotic rather than deterministic. Anderson et al. [1] indicate that curve squeal is one of the Australian rail industry's top noise miti-

---

D. J. Thompson (✉) · G. Squicciarini · B. Ding · L. Baeza  
Institute of Sound and Vibration Research, University of Southampton,  
Southampton SO17 1BJ, UK  
e-mail: djt@isvr.soton.ac.uk

© Springer International Publishing AG, part of Springer Nature 2018  
D. Anderson et al. (eds.), *Noise and Vibration Mitigation for Rail Transportation Systems*, Notes on Numerical Fluid Mechanics and Multidisciplinary Design 139,  
[https://doi.org/10.1007/978-3-319-73411-8\\_1](https://doi.org/10.1007/978-3-319-73411-8_1)

gation priorities. Moreover, Hanson et al. [2] point out that squeal noise can be seen as a symptom of the deterioration of some aspect of the maintenance or operation of the railway system: insufficient lubrication leading to wear as well as noise; poor rail profiles leading to high stresses; or poorly steering rolling stock leading to increased wear and fuel consumption.

This paper provides a review of curving noise phenomena, mechanisms, models and mitigation measures. The term curve squeal (or screech) may be used to include several different phenomena with a wide range of dominant frequencies and potentially with different excitation mechanisms. Some authors have made a distinction between ‘curve squeal’, in which the noise is strongly tonal, and the more intermittent, higher frequency noise that is sometimes called ‘flanging noise’. Despite this naming convention there is little conclusive evidence that the latter is actually associated with contact at the wheel flange. Rail corrugation can also occur in curves and lead to high noise levels which may be mistaken for curving noise.

Curve squeal is usually associated with the wider field of friction-induced vibration, a field that includes the classic example of the excitation of the violin string by the bow, some forms of tyre/road noise and brake squeal. Rudd [3] described three alternative mechanisms but concluded that the unsteady lateral creepage at the wheel/rail contact is the most likely reason to induce squeal noise. According to Rudd, the falling friction mechanism (described in Sect. 2) leads to unstable vibration of a mode of the wheel; this will grow in amplitude until the non-linearities in the creep forces result in a limit cycle. He also suggested that rail vibration can be neglected in comparison with the vibration of wheel. Rudd’s model was also described by Remington at IWRN4 in a review that covered squeal and impact noise [4] as well as rolling noise [5].

The model of Rudd [3], based on the concept of ‘falling friction’, has formed the basis of many subsequent and more detailed models of curve squeal. However, more recently a number of authors have proposed an alternative mechanism based on ‘mode coupling’. The purpose of this paper is to explain these two mechanisms, to review experimental and theoretical work in the field of curve squeal and to discuss mitigation measures in terms of these two mechanisms. The mechanisms are introduced and compared in Sect. 2 on the basis of simple models. Models of curve squeal are reviewed in Sect. 3, measurements on test rigs and in the field are described in Sect. 4 and mitigation measures are discussed in Sect. 5.

## 2 Frictional Excitation

### 2.1 *Curving Behaviour*

Curve squeal can be attributed to ‘imperfect’ curving behaviour of railway vehicles. The coned wheelset naturally steers around a curve by aligning itself radially to the curve and moving outwards so that the rolling radius difference between the wheels



compensates for the different distances travelled. However, for a bogie (or a two-axle vehicle) the yaw stiffness between the axles and the frame, required to ensure stable running at high speed, prevents the axles from orientating themselves fully radially [6]. Consequently, the wheelsets have a non-zero angle of attack. On sharp curves the leading wheelset of a bogie tends to run in flange contact at the outer wheel whereas the trailing wheelset may run in flange contact at the inner wheel; at higher speeds it moves outwards. The angle of attack is greatest at the leading wheelset, as shown schematically in Fig. 1a.

Due to the non-zero angle of attack, there is a small lateral relative velocity between the wheel and the rail, see Fig. 1b. The relative velocity normalised by the rolling velocity is known as the creepage; components in the longitudinal and spin (rotation about the normal) directions also exist. The lateral creepage is approximately equal to the angle of attack. The creepages give rise to reaction forces known as creep forces. At low values of creepage, the creep force increases linearly with increasing creepage [8]. However, at large values of creepage, such as occurring in sharp curves, the creep force ‘saturates’ and takes the value of the Coulomb friction coefficient multiplied by the normal load. The ratio of the creep force to the normal load will be referred to here as the adhesion coefficient; in the saturated region it is identical to the friction coefficient. Models for the creep behaviour have been developed by Kalker [8] including the approximate method FASTSIM and the fuller method CONTACT. Vermeulen and Johnson [9] and Shen et al. [10] also give approximate methods.

The importance of friction behaviour on the excitation of squeal noise is widely recognised. To illustrate this, and the basic mechanisms behind it, simple systems are considered in the next sections consisting of a single mode of vibration or a pair of modes.

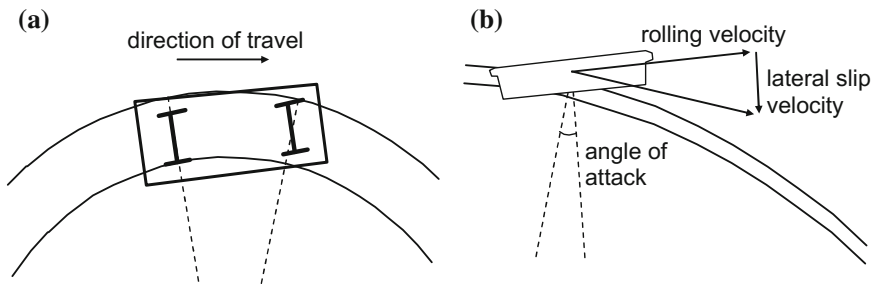
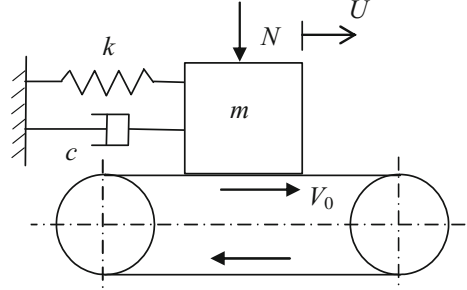


**Fig. 1** a Typical curving behaviour for small radius curve showing that the leading wheelset has a large angle of attack; b generation of lateral creepage by a non-zero angle of attack [7]

**Fig. 2** Schematic view of a restrained mass on a moving belt



## 2.2 Simple Models of Oscillators with Friction

A simple model that can be used to illustrate stick-slip mechanisms is a mass on a belt moving at velocity  $V_0$ , as shown in Fig. 2. The mass  $m$  is restrained by a spring of stiffness  $k$  and damper  $c$  and held against the belt by a constant normal load  $N$ . This model can be used to represent a wheel vibrating in a single natural mode (although a wheel has many modes, the squeal response is usually dominated by a single mode). The sliding velocity between the mass and the belt represents the lateral creep velocity (not the rolling velocity), which has a steady-state value of  $V_0$ .

In this section we consider friction to be represented by a static coefficient  $\mu_s$  (when there is no relative motion) and a dynamic coefficient  $\mu_d$  (when there is slip), with  $\mu_s > \mu_d$ . In the stick phase the mass moves at the same velocity as the belt and the friction force  $F$  satisfies  $|F| < \mu_s N$ . As the mass moves, the spring is extended until the spring force exceeds the friction limit and sliding commences. The equation of motion for this system satisfies two different conditions, one for the stick phase of the mechanism and one for the slip phase:

$$m\ddot{U} + c\dot{U} + kU = F \quad \text{with} \quad \begin{cases} \dot{U} = V_0, & |F| \leq \mu_s N \\ \dot{U} \neq V_0, & |F| = \mu_d N \end{cases} \quad (2.1)$$

where  $U$  represents the vibration displacement. During sliding, according to the second equation, the mass undergoes harmonic motion at the natural frequency  $\omega_0 = \sqrt{k/m}$ . However, due to the existence of the stick phase, the period of oscillation is longer than the natural period associated with the mass-spring system. As shown in [7] the relative importance of the stick and slip phases depends on a non-dimensional parameter

$$\beta = (\mu_s - \mu_d) \frac{N}{V_0 m \omega_0} \quad (2.2)$$

For curve squeal situations the value of  $\beta$  is usually in the range 0.1–1 [7]. Figure 3a shows examples of the stick-slip motion for three values of  $\beta$ . These are shown in the ‘phase plane’ in which the velocity is plotted against the displacement.

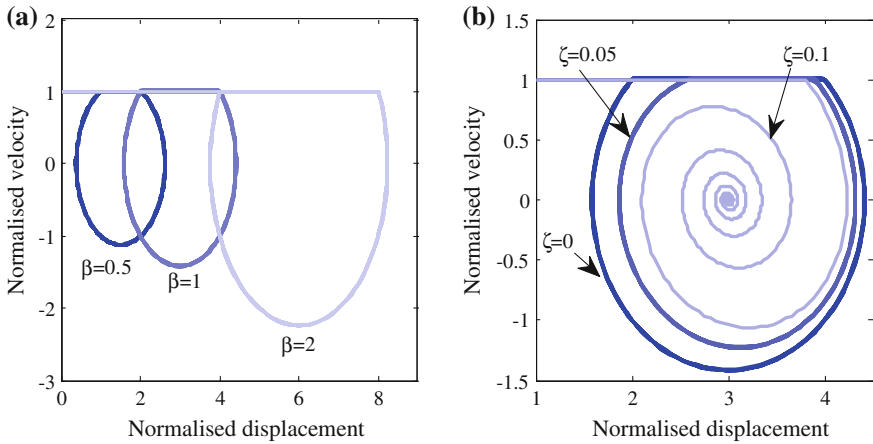


**Fig. 3** Normalised displacement versus non-dimensional velocity of a simplified stick-slip mechanism:  $\mu_s = 0.4$ ,  $\mu_d = 0.3$ . **a** Without damping; **b** for different damping levels ( $\beta = 1$ )

Here, the velocity is normalised by the belt velocity  $V_0$  whereas the displacement is normalised by  $V_0/\omega_0$ . These results illustrate the formation of a ‘limit cycle’: a stable periodic motion that is reached from a variety of initial conditions. It is found that, for small values of  $\beta$  the slip phase predominates, the motion is close to elliptical on the phase plane and the oscillation frequency is close to the natural frequency, whereas for large values of  $\beta$  the stick phase predominates and the oscillation frequency is lower than the natural frequency [7]. Moreover, as the motion is not purely sinusoidal due to the nonlinearity of the friction model, its spectrum will contain higher harmonics in addition to the fundamental frequency, a feature often seen in squeal measurements.

Using this simple model also allows the effect of damping to be assessed. Figure 3b shows results for  $\beta = 1$  for three values of damping ratio. As the damping is increased, this has only a small effect on the amplitude of the limit cycle until the damping reaches a value where the oscillations are suppressed; in this case for  $\zeta = 0.1$  the damping exceeds the limiting value and the oscillations decay. The limiting value of damping ratio can be approximated as  $\zeta > \beta^2/4\pi$  [7].

### 2.3 Negative Friction Slope Model

As will be seen, the friction coefficient is often found to fall with increasing sliding velocity. The slope of the relation between force and velocity corresponds to a damper (the force due to a damper is proportional to the relative velocity) so a force which falls in magnitude with increasing relative velocity corresponds to a negative damper. If there is a greater negative damping than the positive damping inherent in

the oscillator, unstable self-excited vibration occurs [3], the amplitude of which grows exponentially. In reality, the amplitude is then limited by non-linear effects in the creep force, as there is a region with positive slope close to the origin of the force-creepage relation; see Fig. 4a.

To illustrate this, the single-degree-of-freedom system of the mass on a moving belt can still be adopted to simulate the self-excited vibration of a single wheel mode. Eliminating the steady-state component of the displacement and force, the equation of motion of the system takes the form:

$$\ddot{u} + 2\zeta\omega_0\dot{u} + \omega_0^2u = -\frac{N}{m}\left(\mu|_{\gamma_0+\gamma} - \mu|_{\gamma_0}\right) \quad (2.3)$$

where  $u = U - U_0$  is the dynamic component of the vibration displacement ( $U_0$  is the displacement of the belt moving at speed  $V_0$ ),  $\zeta$  is the damping ratio,  $\omega_0$  is the natural frequency,  $N$  is the load normal to the contact plane,  $m$  is the mass,  $\mu$  is the adhesion coefficient (creep force normalised by the normal load),  $\gamma_0$  is the lateral creepage at steady state and  $\gamma = \dot{u}/V$  is its dynamic component. The right-hand side represents the dynamic component of creep force (normalised by the mass).

For small variations in creepage, the right-hand side of Eq. (2.3) can be linearized:

$$\ddot{u} + 2\zeta\omega_0\dot{u} + \omega_0^2u = -\frac{N}{mV}\frac{d\mu}{d\gamma}\Big|_{\gamma_0}\dot{u} \quad (2.4)$$

This can be identified as a damping term corresponding to the creep force, which can be compared with the structural damping as a check for stability. Thus if the damping ratio is smaller than

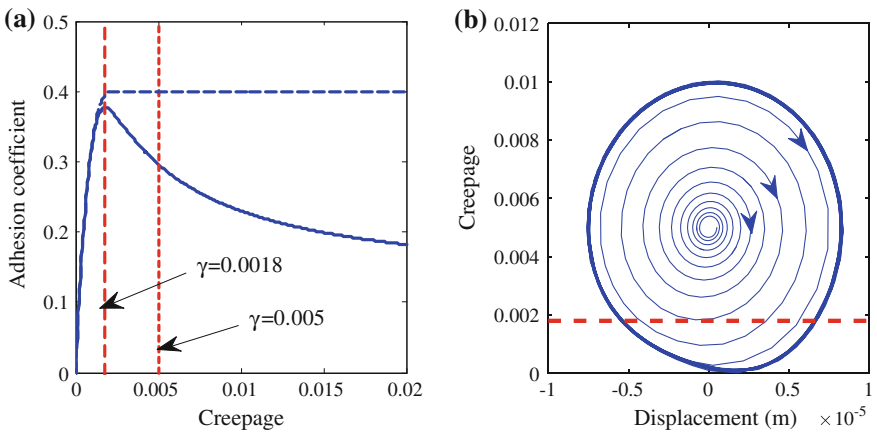


**Fig. 4** **a** Normalized creep force from Vermeulen-Johnson [9] (dashed line) and combined with falling part from Huang [11] (solid line); **b** simulation results for a case without damping

$$\zeta_{\text{lim}} = - \left. \frac{N}{2m\omega_0 V} \frac{d\mu}{d\gamma} \right|_{\gamma_0} \quad (2.5)$$

the system will be unstable and the vibration will grow, whereas for larger values of damping the oscillation will decay. Meanwhile, the solution of the non-linear Eq. (2.3) gives the limit cycle.

The parameters given in Table 1 are adopted in an illustrative simulation and, although arbitrary, they are plausible for a railway wheel. The simplified creep force model proposed by Vermeulen and Johnson [9] is adopted with a falling part as proposed by Huang [11] (see also Sect. 4.1.2). Figure 4a shows the creep force normalised by the normal load (referred to as the adhesion coefficient). Also shown is the corresponding curve obtained with a constant friction coefficient of 0.4. The steady-state creepage is chosen as 0.005. The solution for the undamped system with falling friction is shown in Fig. 4b; the solution grows exponentially until the creepage falls below 0.0018, which corresponds to the value where the slope in Fig. 4a changes sign. For values below this (indicated by the horizontal line in Fig. 4b) the creep force tends to stabilise the system. The limit cycle is reached when the energy fed into the system during the portion of the period corresponding to a falling creep force (overall negative damping) equals the energy dissipated during the time spent in the region with force increasing with creepage (overall positive damping). Clearly, in a situation like this, instability can be avoided by increasing the structural damping above the limit value given in Eq. (2.5). For constant friction there is no instability of this system. According to this model the instability is also independent of the level of static friction.

## 2.4 Mode Coupling Mechanisms

In addressing curve squeal there is an increase of interest in the direction of mode-coupling phenomena, which have been explained in a simplified form by Hoffmann et al. [12, 13], see also [14]. This type of instability arises from non-conservative displacement-dependent forces and often goes under the name of “flutter”. It also occurs in the absence of falling friction. Figure 5a shows the typical system adopted to illustrate this mechanism. Here the mass has two degrees of freedom and two springs. As the mass vibrates, variations in the normal load occur, leading to variations in the friction force. This is also equivalent to the system

**Table 1** Parameters of a single mode of the wheel

Modal mass	156 kg	Steady-state creepage, $\gamma_0$	0.005
Natural frequency, $\omega_0/2\pi$	1003 Hz	Rolling velocity, $V$	10 m/s
Normal contact force, $N$	42 kN	Damping ratio	0

shown in Fig. 5b in which the modes of the wheel may have both vertical and lateral components and the contact angle  $\alpha$  of the wheel with the rail may vary.

By considering small oscillations around the equilibrium of steady-state sliding, the system in Fig. 5 can be mathematically described as

$$\begin{bmatrix} m & 0 \\ 0 & m \end{bmatrix} \begin{Bmatrix} \ddot{x} \\ \ddot{y} \end{Bmatrix} + \begin{bmatrix} k_{11} & k_{12} - \mu k_H \\ k_{12} & k_{22} \end{bmatrix} \begin{Bmatrix} x \\ y \end{Bmatrix} = \begin{Bmatrix} 0 \\ 0 \end{Bmatrix} \quad (2.6)$$

where the terms  $k_{ij}$  in the stiffness matrix depend on the orientation and stiffness of the springs [12]:

$$\begin{aligned} k_{11} &= k_1 \cos^2 \alpha_1 + k_2 \cos^2 \alpha_2 \\ k_{12} &= k_1 \cos \alpha_1 \sin \alpha_1 + k_2 \cos \alpha_2 \sin \alpha_2 \\ k_{22} &= k_1 \sin^2 \alpha_1 + k_2 \sin^2 \alpha_2 + k_H \end{aligned} \quad (2.7)$$

$k_H$  represents the linearized Hertzian contact stiffness [15];  $x$  and  $y$  are the vibration displacements in tangential and normal directions. The effect of damping in this system has been studied in [13, 14] and will be briefly discussed below. The most important feature of Eq. (2.6) is that the stiffness matrix is non-symmetric. It can be shown [12] that if the upper diagonal term of the stiffness matrix  $k_{12} - \mu k_H \leq 0$ , due to the value of friction coefficient  $\mu$ , the system can become unstable.

To illustrate the mode-coupling mechanism in curve squeal it is convenient to use a modal approach to describe the dynamic properties of the wheel and rail; often modal properties of the wheels are known from finite element (FE) modelling or from modal tests. At least two modes are necessary to initiate this mechanism. Following this idea, as an example Eq. (2.6) has been adopted to represent the two wheel modes summarised in Table 2. These are arbitrarily chosen but represent possible modes encountered in railway wheels. An extensive parameter study is beyond the scope of this review paper but some examples are shown to illustrate some typical features.

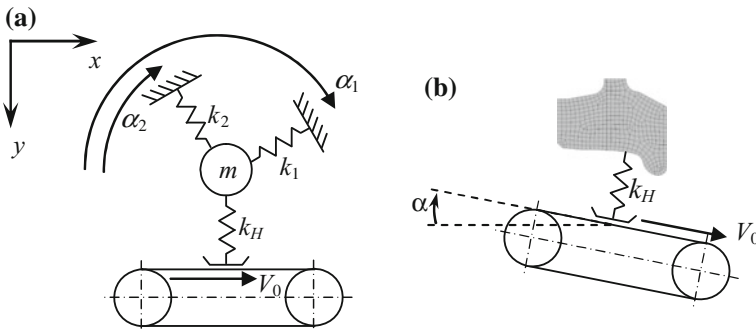


**Fig. 5** Two-degree-of-freedom system on moving belt

**Table 2** Parameters of a two-modes model of the wheel

	Lowest mode	Highest mode
Natural frequency (Hz)	1983	1993
Modal mass (kg)	0.5	0.5
Mode shape at nominal contact point Normal direction (m)	$5.5 \times 10^{-2}$	$2.7 \times 10^{-2}$
Mode shape at nominal contact point Axial direction (m)	$2.1 \times 10^{-2}$	$3.5 \times 10^{-1}$
Damping ratio	$1 \times 10^{-4}$	$1 \times 10^{-2}$
Rolling velocity (m/s)	2.78	

This approach allows investigation of the effect of the lateral position of the contact point (by adjusting the mode shape parameters) or of the inclination of the contact plane (i.e. the contact angle) between wheel and rail ( $\alpha$  in Fig. 5b). Figure 6 shows stability maps obtained for this example by analyzing the real part of the eigenvalues of the system [12]. Results are shown in Fig. 6a for contact on the wheel tread for different values of contact position typical of the leading inner wheel. In this example instability is found for contact positions above 2 mm towards the flange side. Figure 6b shows results for a contact position typical of flange contact for a range of contact angles (40 mm from the nominal position). Here, instability is found for contact angles between  $48^\circ$  and  $65^\circ$  for a friction coefficient of at least 0.4. Although this example is not exhaustive and is given solely for illustrative purposes, it shows that, for these two modes, mode coupling can occur under certain contact conditions and not others.

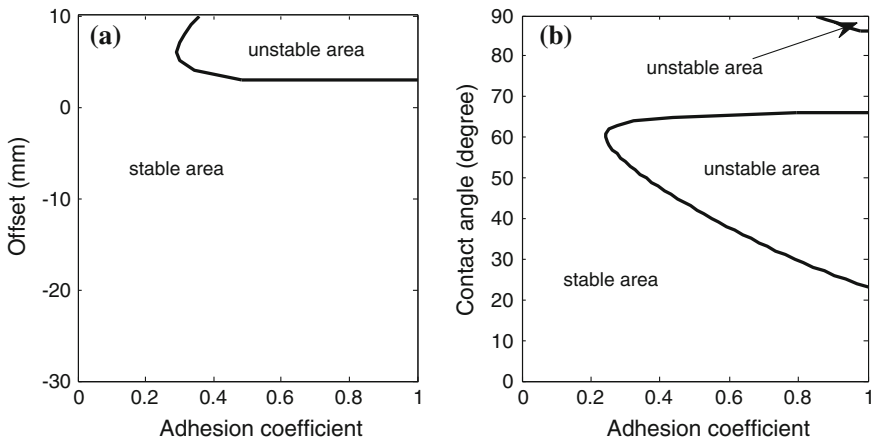


**Fig. 6** Stability map for two-mode system with parameters in Table 2: **a** for varying lateral position of the contact and contact angle of  $2^\circ$ ; **b** for varying contact angle with a contact position at the wheel flange (40 mm)

Numerical integration of the equations of motion allows the time domain response of the nonlinear system to be obtained. Figure 7a shows the corresponding results obtained with the same two wheel modes. Again the simplified creep force model proposed by Vermeulen and Johnson [9] is adopted, see Fig. 4a, but no negative slope is introduced here. A particular combination of friction coefficient and contact angle in the unstable region is chosen according to the stability map in Fig. 6b, with a value of  $50^\circ$  for the contact angle and 0.6 for the friction coefficient.

An interesting feature of the response due to mode coupling is that both vertical and lateral vibration can increase to a limit cycle and there is a phase lag between the two directions (see Fig. 7b). This phase lag is necessary to transfer the energy from one direction to the other one and generate the instability [12].

The effect of damping in the case of mode coupling is not straightforward [13, 14]; in fact an increase in damping can favour instability in some situations or can improve stability in others. This can be illustrated using the linearized system, again with values from Table 2. Figure 8a shows the stability map for varying friction coefficient when the damping ratio of only the second mode is varied, while the damping ratio of the first mode is kept at  $10^{-4}$ . The system is stable for low values of damping and becomes more unstable when the damping of the second mode is between about  $2 \times 10^{-3}$  and  $10^{-1}$ . Figure 8b shows the stability map when the damping ratios of both modes are increased together while keeping their ratio fixed. In this case changing damping has no effect on the stability up to about  $10^{-2}$ , while the system is quickly stabilised above this value.

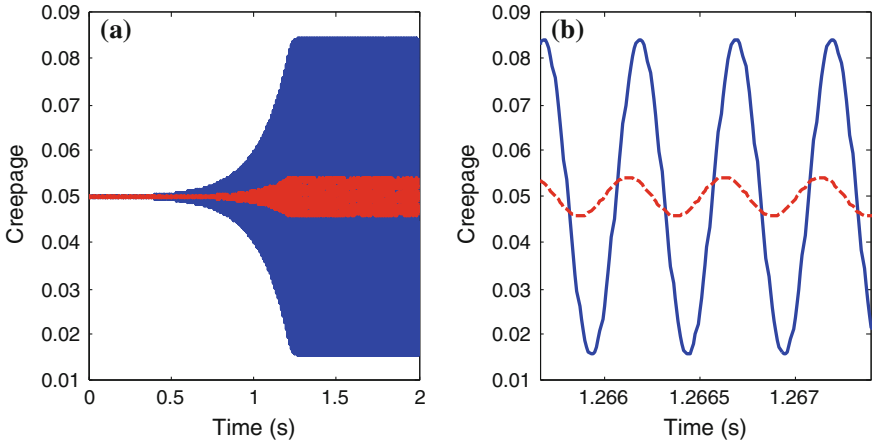


**Fig. 7** Time domain solution for a two-mode wheel. **a** Complete solution; **b** close-up in the limit cycle. Red: normal vibration; blue: tangential vibration (shown as creepage or non-dimensional velocity)



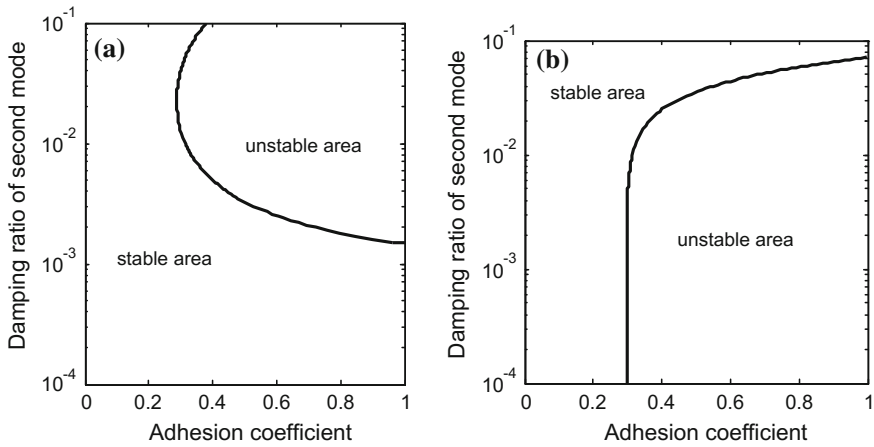


**Fig. 8** Stability maps for two-mode system for contact angle  $3^\circ$  and lateral contact position of 8 mm showing effect of damping ratio. **a** Damping ratio of second mode only is varied; **b** damping ratio of both modes is varied, keeping the ratio between them fixed

## 2.5 Brake Squeal

A related field which has been widely investigated is automotive brake squeal. Kinkaid et al. [16] gave a thorough review of research in this field, and identify a number of potential mechanisms. These were also reviewed by Ghazaly et al. [17]. Stick-slip due to the negative slope of the friction characteristic (see Sect. 2.3) was considered for many years to be an essential ingredient of the brake squeal mechanism but more recent work tends to consider it less important. Other mechanisms discussed include ‘sprag-slip’ due to geometrically-induced variations in normal force, self-excited vibration under a constant friction coefficient involving mode coupling (as described in Sect. 2.4) and hammering—excitation of disc natural frequencies by impacts between pad and disc. The mode coupling mechanism, in particular between modes of the pad and the disc, is currently the most popular mechanism in brake squeal [17]. Nevertheless it is pointed out that a single mechanism cannot explain all phenomena. Although there are lessons to be learnt from this field for curve squeal, a major difference is that in railway curving the sliding velocities are much smaller than in brake squeal.

Brake squeal modelling often makes use of numerical modelling techniques, representing the disc and pad with finite element models. Ouyang et al. [18] give a review of this approach.

### 3 Modelling

#### 3.1 *Modelling Approaches*

There are two main modelling approaches that can be used for curve squeal. In the first, based in the frequency domain, the system is linearized for small fluctuations in friction force about the steady state values and the stability of the linearized system is studied to determine potential unstable frequencies. In the second, the nonlinear equations are solved directly in the time domain.

In curve squeal studies the two most widely used frequency domain methods used to study the stability of the linearized system are complex eigenvalue analysis and the Nyquist criterion. According to the first method the eigenvalues of the system are first calculated and instability is identified when the real part of at least one eigenvalue becomes positive. The growth rate can be identified from the real part of the eigenvalue. In the second case the system is described by a feedback loop with positive feedback and the Nyquist criterion [19] is applied to the open loop transfer function. The open loop transfer function is plotted on the complex plane and if it encloses the point (+1,0) the system is unstable. In addition, by plotting the magnitude of the open loop transfer function against frequency, the frequencies associated with these unstable points can be identified as likely squeal frequencies. The two methods essentially give similar information: the growth rate is proportional to the ratio of the loop gain to the modal mass of the corresponding mode [20]. Both can give multiple unstable frequencies; the one which will dominate the squeal response depends on the initial conditions as well as the respective growth rates and cannot be determined using these frequency domain methods.

Time domain methods allow the evolution of the response to be determined and the limit cycle amplitude to be obtained taking full account of the system nonlinearities. The calculation effort is much greater, especially for a detailed model of the wheel and track, and this method is therefore more difficult to use in parametric investigations. Nevertheless, with the improvement in computational speed these methods are being used more widely.

#### 3.2 *Wheel Dynamic Behaviour*

The wheel dynamic behaviour is an important component of curve squeal. In particular, squeal is usually associated with lightly damped modes of vibration of the wheel. Each mode has a harmonic variation in amplitude around the circumferential direction, which can be categorized according to the number of nodal diameters,  $n$  [7]. Example modeshapes are shown in Fig. 9 for a wheel with diameter 0.84 m. These modes are for  $n = 2$ , but for other values of  $n$  the cross-section of the modeshape is similar. Axial modes can be identified according

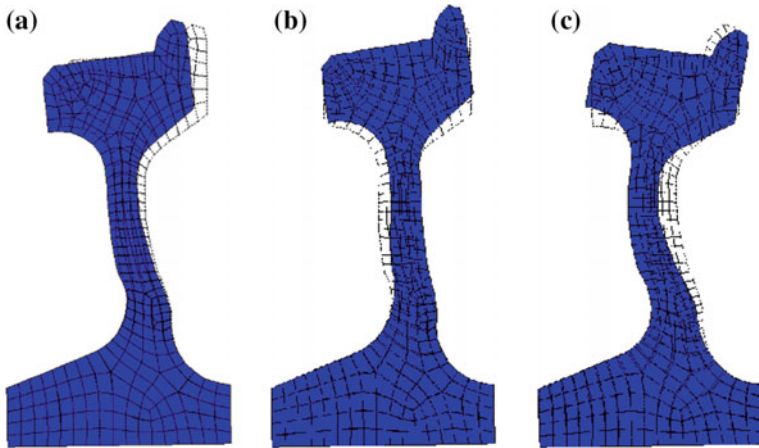


**Fig. 9** Examples of mode shapes of Class 15x wheel with  $n = 2$ . **a** 0-nodal-circle axial mode (2,0), 463.0 Hz; **b** radial mode (2,R), 2220 Hz; **c** 1-nodal-circle mode (2,1), 2901 Hz

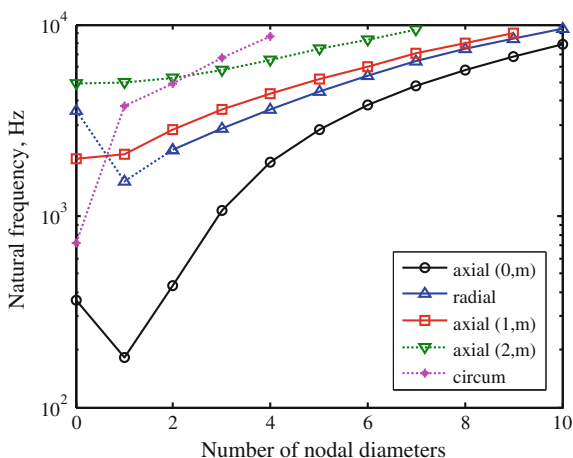
to the number of nodal circles  $m$  and will be identified as mode  $(n,m)$ . Additionally radial ( $n,R$ ) and circumferential ( $n,C$ ) modes occur [7].

The natural frequencies of the various mode types of this wheel are plotted in Fig. 10 against the number of nodal diameters,  $n$ . Measured values are plotted using a solid line and, where these could not be identified, corresponding results from finite element calculations are supplied using a dotted line. Generally curve squeal occurs most often in one of the 0-nodal-circle axial modes which have a large axial component at the wheel/rail contact point and small radial component but, as will be seen, in some situations other mode types are excited. For a monobloc steel wheel, the damping ratio of these axial modes is of the order of  $10^{-4}$  for  $n \geq 2$ . For  $n = 1$  the modes are strongly coupled with the axle bending and are therefore much more strongly damped due to the bearings. Similarly for  $n = 0$  the modes are coupled with axle extension or torsion.

### 3.3 Models Based on Falling Friction

Rudd [3] developed an early model of curve squeal, based on excitation by lateral creepage at the wheel/rail contact with instability induced by falling friction in the saturated region, a mechanism first suggested by von Stappenbeck [21]. Rudd's approach was based on the concept of negative damping introduced by the falling friction characteristic; the wheel was represented by a single mode. Rudd's model was also adopted by van Ruiten [22] in an investigation of the squeal noise of trams.

**Fig. 10** Natural frequencies of Class 15x wheel, diameter 0.84 m. Solid line measured; dotted line calculated



Nakai et al. [23–25] developed a model in which a stationary steel disc (representing the wheel) is rubbed by a moving rod (representing the rail). This theoretical study shows that squeal noise frequency usually relates to one wheel axial mode with a small damping value. Contact load and contact position were found to have an effect on the occurrence of squeal noise.

Schneider et al. [26] modelled the wheel analytically as a disc and its sound radiation using a Rayleigh integral. They used Kraft’s friction model [27] (see Sect. 4.1.1) and solved the non-linear equations of motion in the time domain. Only the axial 0-nodal-circle modes were included in the calculation; the response was found to contain multiple modes. Fingberg [28] extended the model of Schneider et al. [26] to use a finite element model of the wheel, a dynamic model of the track and a boundary element model for the sound radiation. This was again solved in the time domain. The dominant frequency was found to vary with the rolling velocity. This work has been extended further by Périard [29] who also included the vehicle curving behaviour in the same time-stepping calculation procedure as the squeal model.

Heckl and Abrahams [30] presented a simple time-domain model based on the impulse response of a disc, representing the wheel. The lateral friction force was considered as a piecewise linear function with a falling region at large relative velocities and a rising region at small creepages. They showed that the non-linear friction force leads to a limit cycle response, and this limit cycle frequency is determined by one unstable mode of the wheel. Axial modes (2,0) and (3,0) were both unstable but the limit cycle consists of one of these modes, depending on the conditions. Heckl [31, 32] also presented a frequency-domain model of the same disc which allowed the growth rate and frequency of the squeal to be determined and its dependence on the damping loss factor of the disc to be determined. Measurements were presented of the squeal of this simple disc running on a rotating turntable.

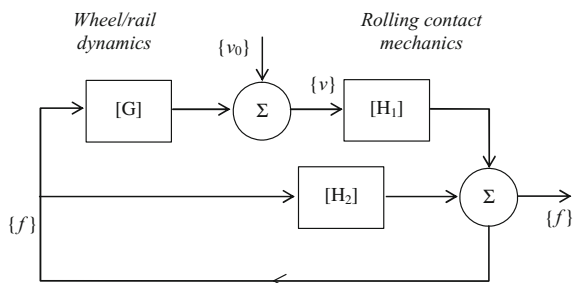
Liu and Meehan [33, 34] recently developed a simple single-degree-of-freedom model for curve squeal which neglects vertical dynamics (so no mode coupling is possible) and relies on the negative slope of the friction curve as the source of instability. This is used to explain the increase in sound level with rolling speed and with angle of attack found in a test rig. In their tests, peaks were found corresponding to the axial modes with  $n = 3, 4, 5$  and  $6$ .

### 3.4 Inclusion of Vertical Dynamics

De Beer et al. [20, 35, 36] developed a model for squeal noise in the frequency domain, which combines models of wheel dynamics, rail dynamics and contact dynamics in the vertical and lateral directions. For wheel and rail dynamics, mobilities obtained from the TWINS software [37] were used. For the contact dynamics in the vertical direction, a contact spring mobility was adopted, while for the lateral contact dynamics the creepage at low sliding velocities was calculated using the model of Shen et al. [10] and a falling region was introduced using the model of Kraft [27]. The Nyquist criterion was used to assess the stability of the system in the frequency domain. Unstable frequencies were found corresponding to 0-nodal-circle axial modes with between 2 and 6 nodal diameters. This model appears to be the first in which the variation of the normal contact force was included in a curve squeal model. Although this will potentially introduce mode-coupling phenomena, this possibility was not considered explicitly in this paper and from measurements the presence of squeal was associated with a falling friction curve. The model showed the importance of the lateral position of the contact point on the wheel.

Monk-Steel and Thompson [38] extended de Beer’s model to include varying longitudinal and spin creepage as well as lateral creepage and normal load variations. Again only the falling friction aspect was considered. The model was presented in the form of a flow diagram as shown in Fig. 11. The upper part represents the excitation due to falling friction, where  $[G]$  contains the mobilities of the wheel and rail system and  $[H_1]$  contains terms from the contact mechanics including the slope of the adhesion coefficient. The term  $[H_2]$  represents the influence of the

**Fig. 11** Feedback loop for squeal model [38]



normal load variations on the transverse forces. The open loop transfer function is given by  $H_1G + H_2$  [11]. In the case where longitudinal and spin creepage are included this feedback loop involves matrices and the generalised Nyquist criterion is used based on the eigenvalues of the open loop transfer function matrix [39]. For a contact point on the wheel tread, squeal was predicted to occur in the 0-nodal-circle axial modes with various numbers of nodal diameters.

Huang [11, 40] also used this approach to extend de Beer's model to include all possible degrees of freedom in the wheel/rail contact and compared results with measurements obtained on a test rig [41]. A heuristic formula for falling friction at large creepages was introduced and combined with the FASTSIM model for rolling contact [8]. Both frequency-domain and time-domain approaches were considered and compared. A parametric study was carried out, which included changing the steady-state creepages, contact position and contact angle. An extension of this model to include the effect of a second contact point was developed following this approach by Squicciarini et al. [42]. They also considered a statistical approach in which the model was run for a large number of cases in which various parameters were selected from a statistical distribution.

Xie et al. [43] introduced into SIMPACK a modified version of FASTSIM including falling friction as developed by Giménez et al. [44] so that the curving analysis would be consistent with the squeal model.

Chiello et al. [45] developed a squeal model that considered normal contact dynamics. The wheel dynamics was derived from a modal basis. The friction force used included a falling part, linearly decreasing with speed after saturation, which can induce instability. It was pointed out that the asymmetry of the stiffness matrix, leading to mode coupling, can be another possible source of instability but this was believed not to be important by the authors in this particular case and was found to occur only with large lateral offset of the contact point. The modal growth rate was obtained as a measure of stability, which showed that the model could only be destabilised by negative damping. Squeal was predominantly found in the (3,0) axial mode at around 1.1 kHz. However, it was found that the dominant mode can be different if different initial conditions are considered, and if harmonically-related modes are present they can coexist in the limit cycle. Collette [46] investigated the influence of vertical dynamics and showed that, even with a constant friction coefficient, this could lead to unstable vibration.

Brunel et al. [47] performed a transient analysis of a wheel using an axi-harmonic finite element model. Two friction laws were considered based on measurements from Kooijman et al. [35], one with a falling characteristic and one with an increasing friction force. It was found that even the positive friction law could lead to a limit cycle solution, which the authors identified with the coupling of the normal and lateral dynamics of the wheel (which they misleadingly refer to as sprag-slip). Nevertheless, it was found that the falling friction characteristic led to much higher levels of squeal. Squeal was found to occur in axial modes with  $n = 3, 4$  and  $5$  between 1 and 3 kHz.

### 3.5 Mode Coupling

More recently a number of authors have focussed on the mode coupling mechanism. Glocker et al. [48] stated that the model should be insensitive to the slope of the friction characteristic, and proposed instead an approach based on a constant friction coefficient. They developed an FE model of the wheel and assumed a rigid rail. The mass and stiffness matrices were extracted from the FE model and combined with the contact forces. Friction was included at the contact point. A qualitative comparison was also made with measurements, showing that the squeal frequency of 4.1 kHz was also found in the simulations. They found that three closely-spaced modes were necessary for squeal to occur; of these the mode at 4.1 kHz is the 0-nodal-circle axial mode with  $n = 6$ , while the other two were a radial mode with  $n = 4$  and a 2-nodal-circle axial mode with  $n = 2$ .

Pieringer [49] also demonstrated that a model with a constant friction coefficient can show squeal at relevant frequencies. The model was based on pre-calculated impulse response functions of the wheel and rail [50], accounting for the lateral and vertical directions. The model includes an implementation of Kalker's more complete CONTACT method [8]. The value of lateral creepage, the friction coefficient and the lateral contact position on the wheel tread have a strong influence on the occurrence and amplitude of the stick/slip oscillations. Depending on the conditions, squeal occurred at the axial modes (2,0), (3,0) and (7,0), the latter mode at 5.2 kHz being close to the circumferential mode with  $n = 2$ . This work has been extended in [51–54].

Chen et al. [55] used commercial software to perform Finite Element complex eigenvalue analysis of a wheel in contact with a rail. The rail was only 5 m long and included springs at the locations of the railpads; it may be remarked that such a rail model will not adequately represent the behaviour of an infinite track. A Coulomb friction model was adopted with a constant friction coefficient, assuming that the lateral creep force has reached saturation. Several wheel modes appeared to be unstable as a result of mode coupling. In one example it was shown that the friction required for instability increases from 0.1 to 0.4 when the railpad stiffness is increased by 50%. Complex eigenvalue analysis has also been used by Fourie et al. [56] and Wang et al. [57].

### 3.6 Other Questions

#### 3.6.1 Should the Rail Be Included?

Ding et al. [58] used the curve squeal model from Huang [11] in both the frequency domain and time domain to consider the effect of including or neglecting the rail dynamics. Additionally, the effect of including or neglecting the falling friction characteristic was also considered. Huang's time-domain model was updated to

include the rail dynamics in terms of an equivalent state space representation in various directions. Thus, although the track dynamic behaviour is not modal, it can be represented by equivalent modes. The results showed that, although more wheel modes are potentially unstable in the presence of falling friction, this is not the only reason for squeal in Huang's model, mode coupling also being present for some modes. Moreover, rail dynamics can play an important role, especially under constant friction conditions, modifying the unstable frequency from 2 kHz without the rail to 1.1 kHz when it is included. In the presence of the rail, the mode coupling can occur between a lightly damped wheel mode and a highly damped equivalent rail mode as well as between pairs of wheel modes. For example, Pieringer et al. [54] have shown unstable coupled wheel-rail eigenmodes that include a significant contribution from the rail.

### 3.6.2 Is the Effect of Wheel Rotation Important?

In [51] Pieringer et al. extended the model of [49] to include the effects of wheelset rotation. Three models were compared: stationary wheel, stationary wheel with rotating force and full model of wheel rotation including gyroscopic effects and centrifugal stiffening. At the speed considered, 50 km/h, no difference was found between the rotating force and the rotating wheel models. Moreover, the stationary wheel model was found to be sufficient to capture the tendency to squeal, although the rotation of the wheel delays the build-up of the stick-slip oscillation.

### 3.6.3 What Is the Effect of Flange Contact?

Remington [4] reported results from Bleedorn and Johnstone [59] taken on a test rig that showed that flange contact led to noise reductions of over 10 dB. Moreover, it was reported that flange contact alone did not produce squeal. Koch et al. [60] observed on a 1/4 scale rig that for a high angle of attack squeal stopped when flange contact occurred.

Monk-Steel and Thompson [38] presented prediction results for flange contact on the outer wheel as well as for lateral creepage on the inner wheel. These results indicated that flange contact could lead to squeal in radial modes of the wheel rather than axial modes, suggesting that it would have higher frequency content. Squicciarini et al. [42] showed through measurements and modelling that squeal can occur with flange contact and with two-point contact, in this case for a tram system with resilient wheels.

### 3.6.4 Contact Model

The model used for the wheel/rail contact dynamics is important in the representation of squeal. Although the steady-state creepage and contact stiffness can be



obtained using simplified contact models, more detailed models including transient effects may be needed for a correct representation of the squeal mechanisms. Further study is needed to clarify the differences caused by using different contact models.

### **3.6.5 Consideration of the Vehicle Curving in the Model**

Most squeal models assume a constant value of steady creepage as an input. The value of creepage, the contact position on the wheel running surface and the normal load can be obtained from standard vehicle dynamics calculations using commercial or dedicated software. Glocker et al. [48], for example, used commercial software whereas Huang [11] used his own software for steady-state curving in a pre-processing step. Périard [29] used his own model in the same calculation steps as the curve squeal calculation, which leads to unnecessarily small time steps.

## **4 Measurements**

### ***4.1 Laboratory Measurements for Friction Coefficients and Squeal Noise***

This section provides an historical review on laboratory measurements aimed at measuring rolling friction or adhesion coefficients in both lateral and longitudinal directions and at characterizing curve squeal. Particular attention is given to the presence (or absence) of falling friction as this is becoming a controversial feature in modelling curve squeal.

#### **4.1.1 Longitudinal Creep**

There are many reported results of longitudinal creep force—creepage relations, particularly from the area of locomotive traction; the results summarised here represent a selection but it is by no means exhaustive.

Kraft [27] gave an extensive theoretical investigation of the adhesion between wheel and rail. He reported previous results of field tests by Metzkwow and Curtius & Kniffler; as sliding begins, friction falls rapidly at first and then more slowly. In the case of wet rails the adhesion is reduced further. As used by Schneider et al. [26], Fingberg [28] and de Beer et al. [36], Kraft's formula for the friction coefficient can be written as

$$\mu = \mu_0 \left[ 1 - \frac{1}{2} \exp(-a/|V_0|) - \frac{1}{2} \exp(-50a/|V_0|) \right] \quad (4.1)$$

with  $\mu_0$  the static friction coefficient, and  $a$  chosen as 0.138 m/s;  $V_0$  is the sliding velocity.

Logston and Itami [61] present falling friction curves from locomotive traction tests carried out by General Motors. Falling friction was found for dry contact above a creepage of 10%. When a third body is introduced between the surfaces (dry sand, wet sand or oil) the curve starts to fall above 3–5% creepage.

Ertz [62] reported previous field-test measurements by Lang and Roth [63] where falling friction was observed above about 2% creepage. In this paper Ertz also focuses on the importance of temperature as well as micro-roughness in explaining the slope found in the range of full sliding. Polach [64] studied adhesion limits and reported five sets of measurements from locomotives under traction which showed falling friction above a creepage of 0.3%. These measurements included those of Lang and Roth [63] reported by Ertz [62] and of Logston and Itami [61]. The negative slope was steeper at higher speeds. He also developed a model to represent the traction behaviour.

Zhang et al. [65] performed extensive measurements of adhesion coefficient on full scale roller rig. Only the longitudinal direction was considered and various contact conditions were investigated. The adhesion coefficient was measured to decrease above 2–3% creepage and the slope was steeper with higher rolling speeds.

Conversely, Harrison et al. [66] did not detect any presence of falling friction while measuring on a real track with a measurement vehicle and with a hand-pushed tribometer.

Gallardo-Hernandez and Lewis [67] performed roller rig measurements to quantify longitudinal friction with different contaminating materials (particularly leaves). In the case of dry friction a negative slope is found above 1–2% creepage. A possible explanation for the existence of the falling region was given as an increase in temperature due to sliding which can form oxides. Similarly Fletcher and Lewis [68] and Fletcher [69] showed that, for longitudinal friction measurements, the presence of lubricating material removes the negative slope found in dry condition and makes it positive for a wide range of creepage.

Matsumoto et al. [70] presented test rig results for both longitudinal and lateral creepage. They found falling friction for dry contact but in the presence of friction modifiers the force became a rising function of creep velocity.

Results for longitudinal creepage are summarized in the upper part of Table 3. Eight datasets from full scale tests and results from two test rigs all confirm the existence of falling friction; only Harrison et al. [66] reported a constant slope and this was obtained with a hand-push tribometer.

**Table 3** Summary of rolling friction measurements

		With falling friction	No falling friction
Longitudinal creep	Full scale	Kraft [27] (Metzkow/Curtius and Kniffler) Logston and Itami [61] Ertz [62] (Lang and Roth [63]) Polach [64] (five datasets including Logston and Itami [61] and Lang and Roth [63]) Zhang et al. [65]	Harrison et al. [66] <sup>a</sup>
Longitudinal creep	Reduced scale	Matsumoto et al. [70] Gallardo-Hernandez and Lewis [67], Fletcher and Lewis [68], Fletcher [69]	
Lateral creep	Full scale	Harrison et al. [66] <sup>a</sup>	
Lateral creep	Reduced scale	Matsumoto et al. [70] Remington [4]	
Lateral creep with curve squeal	Reduced scale	De Beer et al. [20, 36], Monk-Steel et al. [72] Hsu et al. [41], Huang [11] Liu and Meehan [31, 73] Jie et al. [76]	Koch et al. [60], Collette [46]

<sup>a</sup>Tribometers

### 4.1.2 Lateral Creep

Harrison et al. [66] also presented results from TriboRailer equipment which measured lateral creepage. Some evidence of falling friction was observed, unlike the hand-pushed tribometer based on longitudinal creepage.

Apart from this, the only measurement results available for lateral creepage are from small scale test rigs. Again the results are summarised in Table 3. Although not supported by measurements Rudd’s model [3] introduced friction characteristics which fall with increasing sliding velocity above saturation. However Remington [4] compared some results measured on a twin roller rig with Rudd’s assumed curve showing broad agreement despite wide variation being found in the results; nevertheless they indicate falling friction above a lateral creepage of 0.9%.

De Beer et al. [20, 36, 71] used a 1:3 scale model of a wheel on a roller to measure friction coefficient and assess the presence of squeal. A clear relation between measured falling friction and the presence of squeal was observed with this rig: a negative slope was found for angles of attack above 0.3° (creepage of 0.5%) and squeal was detected above 0.4° (creepage of 0.7%), clearly in a region where friction was decreasing with sliding velocity. The average creep forces measured in the presence of squeal were lower than without.

Monk-Steel et al. [72] measured curve squeal noise and friction coefficients on the same 1:3 scale roller rig. The main outcomes are similar to those reported in [36] as curve squeal was detected in a region of falling friction. They also modified the rig to introduce additional longitudinal creepage. For a longitudinal creepage of 2% the level of lateral creep force was reduced and the shape of the lateral friction curve was modified so that the falling regime developed only at higher values of

yaw angle (in this case above  $1^\circ$  or a creepage of 1.7%). Monk-Steel et al. [72] also compared various falling friction characteristics (see also [7]) and showed that, compared with Kraft, the slope of Rudd's model was too severe whereas that of Périard's model was too shallow.

Hsu et al. [41] performed curve squeal and friction coefficient measurements on another 1:3 scale twin disc rig. The forces were measured using strain gauges on the web of the rail roller. The adhesion coefficient did not have a clear trend, with regions that could be interpreted as falling and other regions where it was not. Squeal occurred for yaw angles above  $1.1^\circ$  (creepage of 1.9%); above  $0.4^\circ$  (creepage of 0.7%) when damping was added to the rail disc. Huang [11] utilized the same rig and obtained new data from it. In this case a clear falling friction characteristic was found for dry contact. With water added to the contact zone, the friction coefficient was found to be higher than for dry contact and it had a falling region for positive creepage, while it was constant for negative creepage. Huang [11] modified Kraft's [27] formula:

$$\mu = \mu_0[1 - \lambda \exp(-\kappa/|\gamma_0|)] \quad (4.2)$$

in which the constants  $\lambda$  and  $\kappa$  can be chosen to tune the maximum reduction of friction at large sliding velocity and the rate of decrease respectively. The second exponential term in Eq. (4.1) was found to be unnecessary for the region of small relative velocities relevant for squeal.

Another rig was adopted by Koch et al. [60] to analyze the effect of rolling speed, lateral position of the contact point, angle of attack and vertical load. This used a 1:4 scale model of a wheelset on a very large roller on which the track was mounted. Squeal was detected for angles of attack above  $0.45^\circ$  (creepage of 0.8%), the sound level increased with speed, vertical load had a negligible effect and lateral position was un-important until flanging; with flange contact, no squeal was observed. Importantly, they did not measure any negative slope. They assumed this was due to measuring the average friction instead of the transient one. For dry friction the slope was positive until an angle of attack of around  $1.1^\circ$  (creepage of 1.9%) above which it was constant. Also with water the friction was lower and constant with increasing creepage. Later Collette [46] repeated measurements on the same rig and again measured squeal in the absence of a negative slope. The author pointed out that the vertical dynamics could play an important role to explain squeal even in the absence of negative slope. Although this is addressed in the paper by introducing a fluctuating vertical force on a single-degree-of-freedom mass-on-moving belt system, the phenomenon would be similar to mode-coupling as described Sect. 2.4.

Measurements and theoretical modelling for curve squeal in a controlled environment were presented by Liu and Meehan [33, 34, 73–75]. Measurements were made on a twin disc test rig, with a wheel of radius 0.213 m and a roller of radius 0.085 m; in most cases these showed a clear trend of squeal occurring with falling friction. Angle of attack and rolling speed increase the noise levels and higher humidity makes squeal more likely. Additionally, by adopting friction modifiers,

the negative slope from the friction curve was removed and the friction level decreased. However in some cases this did not result in completely removing squeal. Two possible explanations were given. First, as the friction curve measured is an average over a number of vibration cycles, the authors' hypothesis is that it could be still negative if measured instantaneously. Additionally mode coupling was mentioned as a possible mechanism of squeal with constant friction slope.

Jie et al. [76] performed measurements on roller rig with a whole wheelset; the two rollers can be driven independently. Squeal was associated with negative slope in the friction curve above  $0.7^\circ$  (creepage of 1.2%). Squeal was also observed in the range just before the falling regime. The measured squeal noise spectrum contained several peaks, some of which (but not all) matched resonance frequencies of the wheel observed in the measured driving point mobility. The corresponding wheel modes were not identified.

From this summary it is clear that most of the measurements have found a falling friction coefficient with increasing sliding. It has been pointed out that the friction coefficient measured in these rigs comes from the ratio of average forces over a number of cycles and it is not the instantaneous one, which might take a different shape. What happens at small amplitudes/high frequencies may thus be different from the quasi-static behaviour that can be measured. Koch et al. [60] used this argument to suggest that the instantaneous friction curve may fall even though the curve from the average forces does not. The methods of measuring the normal and tangential forces in the various test rigs also differ, for example using strain gauges on the roller [41] or on the mounting frame [36].

From the papers reviewed, only two authors Koch et al. [60] and Collette [46] have reported squeal in the absence of measured negative slope for dry conditions. However the data were collected from the same test rig, presumably with the same approach. Liu and Meehan [75] also found squeal with friction modifiers where a positive slope was obtained. By contrast, results from seven test rigs produced falling friction. Table 3 summarises this by grouping the papers listed above according to the quantities measured and highlighting whether falling friction was detected or not.

## ***4.2 Field Measurements of Curve Squeal***

There are many measurements of squeal in different situations; some recent ones will be reviewed briefly here. However, it has to be remembered that it is difficult to draw general conclusions as the phenomena may differ from one situation to another. Eadie et al. [77] identified 'top-of-rail' squeal as occurring in the frequency range 1–5 kHz and flanging noise in the range 5–10 kHz. Bullen and Jiang [78] gave algorithms for detecting squeal. They distinguished between curve squeal, which occurs at the inner wheel, has high levels, is persistent and tonal, and flanging noise which occurs at the outer wheel, is less loud, intermittent and more "broad-band" (see also [1]).

### 4.2.1 Suburban Trains

Glocker et al. [48] (see also [79]) reported a series of measurements of suburban trains on a 200 m radius curve and track with timber sleepers. The actual gauge was slightly wider than nominal at 1450 mm. In 62 out of 83 events squeal could be uniquely attributed to the inside of the curve. Of these, 32 events were attributed to the leading inner wheel; the main squeal frequency was 4.1 kHz. Squeal at the outside of the curve was also observed but much less frequently. Additionally some flanging noise was observed from the outside wheel with a much wider range of frequency peaks.

Vincent et al. [80] measured sound with microphones adjacent to the four wheels of a bogie. Tests were conducted on a metro vehicle with monobloc wheels on a curve of radius 75 m at different speeds between 10 and 40 km/h. Squeal occurred at frequencies corresponding to 0-nodal-circle axial modes with 2, 3 and 4 nodal diameters, with natural frequencies 450 Hz, 1.1 and 2.0 kHz; different modes squealed at different stages of the curve. The leading inner wheel always dominated the squeal.

In an unpublished study by the authors at a new line in London, UK, squeal was found on a curve of radius 180 m at 800 Hz (corresponding to a circumferential mode) and at 1.2, 2.3 and 4 kHz (axial modes with 3, 4 and 6 nodal diameters). At another curve, the same trains produced strong peaks at 7.25 and 9.4 kHz; this noise appeared subjectively to be ‘flanging’. The corresponding wheel modes were either radial modes with 8 and 10 nodal diameters or axial modes with 9 and 11 nodal diameters, as in each case both modes types occur close to the peak frequency.

### 4.2.2 Freight Trains

Extensive field trials have been conducted in Australia on both suburban and freight trains, including monitoring the effect of friction modifiers [1, 2, 81–83]; the angle of attack of each passing wheelset has also been monitored. Two main categories of squeal were identified by Anderson et al. [1, 81]. In the first, named ‘friction controlled’, a moderate level of squeal was generated by approximately 10% of passing stock. Squeal could be controlled by top-of-rail friction modifiers and is also affected by environmental conditions, its occurrence therefore appearing random. The second category, ‘steering controlled’, often leads to severe squeal associated with particular vehicles (less than 2%). In such cases squeal was found to be caused by freight vehicles with high angles of attack associated with poor lubrication of the centre bowl (where the bogie pivots relative to the vehicle body) [1]. A third category is called ‘systemic’ in which the majority of vehicles squeal. It is suggested that the underlying effects involve one or both of the friction controlled and steering controlled types but that they are not isolated to a small proportion of rolling stock or friction conditions.

Jiang et al. [84] reported measurements on a 284 m radius curve in Sydney, Australia. The majority of squeal events from freight trains were associated with the outer wheel; nevertheless these were identified as squeal rather than flanging noise. Correlation with angle of attack showed a higher probability of squeal and potentially higher noise levels with increasing angle of attack: below 15 mrad less than 0.1% of wheels squealed and noise levels were below 110 dB; this increased to 10% of wheels for 25–35 mrad with noise levels of up to 130 dB. Conversely the occurrence of flanging noise showed no obvious relationship with angle of attack. Jiang et al. [85] gave further experimental evidence which showed that squeal events from the outer wheel could be dramatically reduced by good lubrication of the outer rail gauge face. Squeal frequencies were identified as being predominantly in the region 1–3 kHz although both lower and higher frequency events were also found.

For heavy haul trains on a large radius curve (1000 m radius) squeal was detected by Fourie et al. [56, 86] at the trailing inner wheel of some unloaded wagons when the outer wheel was in flange contact. At this wheel the angle of attack was estimated to be very small while longitudinal creepage (estimated from the rolling radius difference) was above 1.2% and exceeded saturation. Squeal occurred mainly around 4–5 kHz and was identified with a circumferential mode with 2 nodal diameters and radial modes with 6 and 7 nodal diameters. The dependence of frequency on wheel radius was also shown. It was suggested from the proximity of pairs of modes that mode coupling is responsible, although it appears that falling friction associated with longitudinal creepage cannot be ruled out.

### 4.2.3 Trams

Trams are usually fitted with resilient wheels which have higher damping than monobloc wheels, typically greater by at least a factor of 10. However, trams also negotiate very tight curves, which increases the likelihood of squeal.

Van Ruiten [22] presented squeal noise measurements on three tram systems in the Netherlands for speeds of 15–20 km/h. All were fitted with resilient wheels of various types; measurements were also reported with a variety of track systems. Squeal was found to occur mainly in the 500, 1250–1600 and 2500 Hz one-third octave bands irrespective of the track system and this was associated with the axial modes with 2, 3 and 4 nodal diameters. Mostly the highest levels were measured at the inside of the curve.

Corradi et al. [87] presented a series of measurements on a tram in Milan, Italy with resilient wheels on a very sharp curve with radius 17.5 m and grooved rails. The vehicle speed was 10 km/h. Wheel vibration was also measured during running and it was found that both inner and outer wheels exhibited high vibration levels, although the amplitude on the inner wheels was the highest. The noise levels were similar on both sides of the tram. These measurements are interesting in that the peak frequency of squeal, around 1.5 kHz, did not correspond to a mode of

vibration, the nearest modes being at 1273 and 1423 Hz, both of which have  $n = 3$ , one being predominantly axial and the other radial. In [42] this frequency shift was associated with two-point contact; however, it may also be evidence of mode coupling. Measured damping ratios were also presented in [87] which are between 0.004 and 0.014.

Vincent et al. [80] also measured squeal from a tram fitted with resilient wheels on a 60 m radius curve with grooved rails. It was found that in most cases the highest noise levels were related with the leading inner wheels, but in one case the rear outer wheel was also observed to squeal for a trailer bogie with independent wheels when the speed was higher. All axial modes between  $n = 3$  and 9 nodal diameters were excited (1.2–8.1 kHz). Vincent et al. [80] also measured the modal damping of the resilient wheel, finding damping ratios between 0.002 and 0.008.

In [88], Merideno et al. found that squeal occurred for the trams in Vitoria, Spain which have resilient wheels; the squeal frequencies correspond to the axial wheel modes with  $n = 2$  (780–800 Hz). The curve radius in the tests was 25 m.

#### 4.2.4 Check Rail Contact

The introduction of new trains in the UK in the 1980s led to a severe curve squeal problem with noise levels of 130–145 dB measured close to the wheels [7]. Measurements were carried out with microphones close to each wheel of a bogie on the line between Llandudno and Blaenau Ffestiniog in Wales, on which there are many curves with radius 200 m fitted with check rails. It was identified that squeal occurred at the leading inner wheel and was associated with radial modes with 2–5 nodal diameters (2.2–4.5 kHz). It was determined that these modes were excited by contact between the back of the wheel flange and the check rail.

#### 4.2.5 Summary

The various measurements reviewed here are summarised in Table 4, arranged in order of curve radius. Clearly squeal can occur at a wide range of frequencies; results have been noted between 450 Hz and 8 kHz. Usually the leading inner wheel of a bogie dominates the squeal: the main exception to this was the measurements on freight wagons by Jiang et al. [84] where the majority of squeal events were associated with the outer wheel (it is not stated whether this was the leading or trailing axle). Corradi et al. [87] found squeal on both inner and outer wheels of a tram.

The modes excited are nearly always  $(n,0)$  axial modes, consistent with the models described in Sect. 3. Some special cases have been identified where this is not the case: (i) Fourie et al. [56, 86] where the dominant mode was circumferential, (ii) the case of check rail contact [7] described in Sect. 4.2.4 where the radial modes were excited and (iii) Corradi et al. [87] where the squeal frequency did not correspond closely to a modal frequency. The squeal from the trams in [87] may be affected by contact between the flange and the groove rail due to the very sharp radius.



**Table 4** Summary of curve squeal measurements

Reference	Train type	Curve radius	Dominant frequency (Hz)	Wheel modes	Wheel	Notes
Corradi et al. [87]	Tram	17.5 m	1500	(3,0) + (3,R)	Inner and outer	Resilient wheels
Merideno et al. [88]	Tram	25 m	800	(2,0)	n/a	Resilient wheels
Vincent et al. [80]	Tram	60 m	1200–8100	(3,0) - (9,0)	Leading inner	Resilient wheels
Van Ruiten [22]	Tram	n/a	500, 1250, 1600	(2,0), (3,0), (4,0)	Inner	Resilient wheels
Vincent et al. [80]	Suburban	75 m	450, 1100, 2000	(2,0), (3,0), (4,0)	Leading inner	
Unpublished	Suburban	180 m	800, 1200, 2300, 4000	(0,C), (3,0), (4,0), (6,0)	n/a	
Glocker et al. [48]	Suburban	200 m	4100	(6,0) with (4,R) + (2,2)	Leading inner	
Thompson [7]	Suburban	200 m	2200, 2800, 3600, 4500	(2,R) - (5,R)	Leading inner	Check rail
Jiang et al. [84]	Freight	284 m	1000–3000	n/a	Outer	Large AoA (AoA measured)
Fourie et al. [56, 86]	Freight	1000 m	4000–5000	(2,C), (6,R), (7,R)	Trailing inner	Longitudinal creep

## 5 Mitigation

A range of mitigation measures is available to tackle curve squeal; these are discussed, for example, in [7, 89–92]. These include lubrication and friction modifiers, wheel and rail damping treatments, improved curving behaviour and changes to rail transverse profiles. In discussing noise mitigation measures, it should be emphasised that the desirable outcome is the elimination of squeal or reduction in its occurrence. Although many sources quote noise reductions these have limited value as they cannot be applied to other situations.

### 5.1 Lubrication and Friction Modifiers

There have been many attempts to control squeal using lubrication and friction modifiers. Friction modifiers [93, 94] are intended to replace the falling friction characteristic by a flat or even increasing ('positive') friction characteristic [70] while maintaining the level of friction coefficient in a range suitable for adhesion

and braking requirements. On the other hand oil-based lubricants often lead to lower friction levels and should therefore be avoided on the rail head. Lubricants, such as oil-based grease, are often applied on the wheel flange or rail gauge face. As well as their possible effect on squeal excitation they modify the curving behaviour of the vehicles and reduce wear. If the dominant excitation mechanism is mode coupling, the introduction of ‘positive’ friction via a friction modifier may still not suppress the squeal, although the general lowering of friction level will help.

Eadie et al. [77, 93, 94] reported a number of field tests of friction modifiers applied to the top of the rail, which were successful in reducing squeal noise. These were applied by a trackside applicator system. They were also shown to have a beneficial effect on reducing corrugation growth in curves. Suda et al. [95] described an on-board system used to spray friction modifier onto the rail head which was found to reduce the presence of squeal.

Liu and Meehan [75] investigated the friction and squeal performance of friction modifiers on a twin disc test rig. They found that the negative slope of the friction curve was replaced by a positive friction characteristic with a lower level of friction. Nevertheless squeal was not always suppressed. They hypothesised that the instantaneous friction curve could still have a negative slope but it is also possible that mode coupling was influencing the squeal.

Of the two main categories of squeal identified by Anderson et al. [1, 81], it is stated that ‘friction controlled’ squeal could be controlled by top-of-rail friction modifiers. In the second category, ‘steering controlled’, top-of-rail friction modifier is often only partially effective. It is stated that gauge face lubrication does not influence squeal but can often influence flanging noise, although this is not always the case [1]. However, Curley et al. [82] summarised the results of 16 lubrication scenarios applied in sequence to a single curve with radius 290 m where freight traffic regularly squealed. At this location squeal was successfully mitigated by gauge face lubrication on the outer rail whereas top-of-rail friction modifiers on the inner rail were not successful. This suggests that the outer wheel was squealing, as found by Jiang et al. [84].

Water can also be used to mitigate squeal noise; indeed experience shows that squeal often disappears during rain. In the measurements of Corradi et al. [87] on a tram in Milan, by applying water over both rails, the curve squeal disappeared completely. However, although not reported, it was observed that high squeal levels occurred after rain when the track was starting to dry out. Liu and Meehan [74] found, by monitoring squeal noise in a test rig in a controlled environment, that squeal is more likely at higher humidity levels.

A water mist spray system was used in the early 2000s as a trial on a 300 m radius curve at Barnt Green, near Birmingham, UK [92]. Monitoring of the site showed that the mist spray system reduced the occurrence of squeal from 14 to 2.5% of the time [92]. However, in the winter the system had to be drained. The system was later removed [91] and replaced by a system applying a friction modifier.

## 5.2 Wheel Damping Treatments

Wheel damping treatments have long been seen as a potential solution for curve squeal yet in practice they are not always successful. To understand this, the models are again helpful. According to the falling friction model, if the damping level can be increased so that it exceeds the negative damping of the friction force (Eq. 2.5), the system should be stable. This can lead to dramatic noise reductions from only moderate increases in damping. However, where mode coupling exists the picture is less clear and an increase in damping does not always stabilise the system, see Fig. 8. Resilient wheels have a much higher initial damping than solid wheels but squeal can still occur with them in tight curves.

There are many types of wheel damper that are commercially available, including tuned absorbers, constrained layer treatments and ring dampers [7, 89–91], see Fig. 12a–c. Also shown in Fig. 12d is a resilient wheel. It is unfortunate that most published results on the effect of wheel dampers focus on noise reductions, which are situation-dependent, whereas the modal damping values achieved would be more generally useful.

Bühler and Thallemer [96] reported results of applying tuned absorbers on the wheels. In one case, over a range of curves, squeal was initially found at frequencies 2–8 kHz for curve radii less than 170 m and this was eliminated by the introduction of the wheel absorbers. However, in another case with a squeal frequency of 700 Hz no improvement was observed.

Constrained layer damping applied to the wheel web was successful in suppressing the severe squeal problem in the UK caused by flange-back excitation by contact with a check rail [7] (see Sect. 4.2.4). Recent measurements have shown that the average damping ratio was increased from  $6 \times 10^{-5}$  to  $7 \times 10^{-4}$ . Although this is still quite low, the squeal was completely eliminated (yielding reductions in

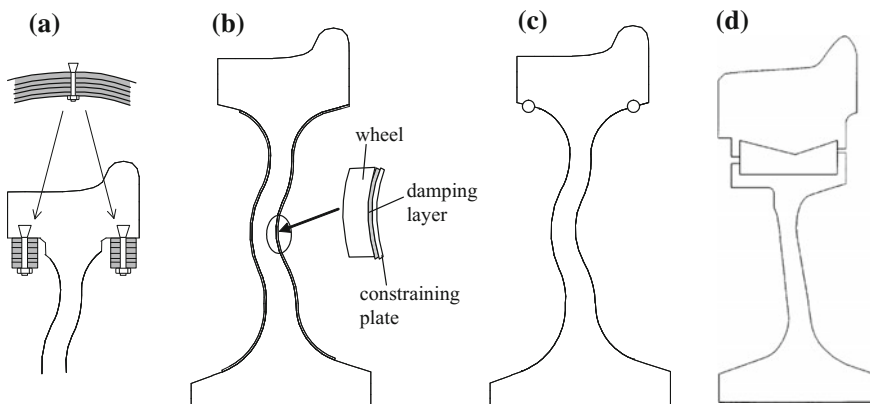


**Fig. 12** Examples of wheel damping treatments: **a** tuned absorbers; **b** constrained layer damping; **c** ring dampers; **d** resilient wheel

overall noise level of more than 30 dB). Jones and Thompson [97] described a calculation method for determining the damping of wheels with constrained layer treatments based on a finite element model.

Merideno et al. [88] described the development of a damper system applied to eliminate squeal in trams occurring at 780–800 Hz. Due to the limited space available on the small resilient wheels, the damper was attached on the inside of the wheel tyre and consisted of a cantilevered plate attached to a damping layer. This is described as a tuned constrained layer treatment and in fact resembles typical tuned absorber systems. The damper successfully eliminated squeal.

Ring dampers are potentially attractive as the added mass is minimal. They are considered for example in [46, 98, 99]. These consist of a metal ring that sits in a groove in the inner side of the tyre. It is believed that friction between the ring and the groove leads to increased damping although the mechanism is not fully understood. Their damping effect is smaller than other systems but is often sufficient to suppress squeal; the mechanism is also nonlinear making the effect amplitude-dependent.

Marjani and Younesian [100] presented a theoretical study of the use of piezoelectric patches on the wheel surface as a means of introducing damping. These are shunted through either a resistance shunt circuit or a resonant shunt circuit. Modest increases in modal damping were reported.

Active control of vibration is another potential technique for controlling wheel vibration. Heckl and Huang [101] proposed a simple active control system as a means of preventing squeal. A simple feedback control system was used based on a filtered signal centred on the squealing mode. It was claimed that the energy requirement is much less than conventional active control. The system was applied to a small scale test rig and was shown to suppress squeal noise. To the authors' knowledge such an active control system has not been applied on a railway vehicle.

### ***5.3 Rail Damping and Track Dynamics***

It is potentially attractive to consider treatments that can be applied to the track at sites where squeal occurs, rather than having to treat whole fleets of vehicles that pass the site. One such treatment is the use of rail dampers, e.g. [102]. However, there is no direct evidence that rail dampers are effective in reducing squeal [7]. Although the rail vibrates during curve squeal, its amplitude is often (although not always) much smaller than that of the wheel. Rail dampers are usually installed to increase the track decay rate to reduce rolling noise; typical reductions of rolling noise are between 2 and 6 dB depending on the rail pad stiffness [7]. A higher track decay rate would also reduce the rail component of squeal noise (which may be significant e.g. in flanging noise) but it would not affect the wheel component. On the other hand, if the mechanism is mode coupling, rail dampers may have an influence by increasing the damping of 'modes' of the rail (see Sect. 3.6.1 [58]).

At the site in London, UK, mentioned in Sect. 4.2.1, rail dampers were fitted to the curve in 2015. Following installation it appears that there was a noticeable reduction in the occurrence of curve squeal. However, as friction modifiers had also been applied at the curve prior to the installation of dampers, it is not certain this improvement was due to the rail damping. Nevertheless, it appears that they played a part. Anecdotally it appears that the rail dampers have been successful in reducing the longer duration squeal events which previously occurred at the site.

As reported by Jiang et al. [103], squeal has been found to occur more severely after replacing timber sleepers by concrete. The reasons for this are unclear, but in the study the track mobilities, decay rates and dynamic gauge were investigated. The point mobility of the track with concrete sleepers showed clearer resonances (which may lead to stronger mode coupling) while the track with timber sleepers had a higher decay rate. The authors claim that this will remove energy from the wheel and therefore mean less squeal propensity but it can be pointed out that undamped wave propagation in an infinite rail also removes energy from the wheel. Finally the track with timber sleepers is more flexible leading to an increase in dynamic gauge spreading during a train passage. This can lead to changes in curving behaviour and also to the location of the contact patch on the wheel (see Sect. 5.5).

Chen et al. [55], by performing FE complex eigenvalue analysis, found that changing the stiffness of the rail support can suppress or eliminate curve squeal. However their model of a short length of rail is unlikely to represent the behaviour of an infinite track adequately.

## 5.4 *Improved Curving Behaviour*

As noted in Sect. 2.1, the yaw stiffness of the primary suspension is required to provide stability of running at high speed, preventing hunting, but this can have an adverse effect on the curving behaviour. If the wheelsets can be arranged to align radially to the curve this will prevent the large angles of attack and hence squeal will not be generated. This also has benefits in reducing wear and rolling contact fatigue. For example, Axiom's LN25 bogie has a radial arm design suspension which allows greater yaw angles than the industry standard Y25 bogie. A recent study [104] has shown that the LN25 bogie will have a reduced likelihood of curve squeal as a result. In [96] it is reported that on the MOB in Switzerland less squealing was observed with bogies which allow radial steering, however no details were given.

Anderson et al. [1, 81] found at some sites that a small number of freight wagons caused large squeal levels. These events were identified with wagons in which the centre-bowl lubrication was ineffective, leading to large angles of attack. Targeted maintenance helped to reduce these severe events. Moreover, it is well known that increasing wheel conicity improves curving behaviour (and reduces critical speed). High conicity profiles reduce the angle of attack although the authors are unaware of any paper that relates conicity with squeal.

Passive steering mechanisms including cross-bracing between the axles of a bogie have been applied on various vehicles to achieve ‘radially steered wheelsets’ [6]. One example of this is the cross-braced bogie, introduced in the early 1980s [105] and applied particularly on freight wagons. However, in a theoretical study [106] it was found that a well-optimised conventional bogie may offer curving performance close to, or even better than, that of radial bogies.

As well as such passive systems, there has been considerable interest recently in active control of vehicle suspensions. Bruni et al. [107] gave a review of monitoring and control systems applied to railway vehicle dynamics. Of interest here are active primary suspensions in which the yaw of the wheelsets is modified by actuation with the aim of improving curving behaviour while maintaining stability at high speed. Systems based on independently rotating wheels were also reviewed, in which case active control is required also to provide steering and guidance, this being provided passively in the case of the solid wheelset. Various prototype systems have been demonstrated [107] and it can be expected that such mechatronic bogies will be introduced in the future.

As an alternative to the control of the primary suspension, active control of yaw in the secondary suspension has also been considered [107]. This applies a yaw torque to the bogie to improve stability; in curved track curving performance can be improved by using the yaw torque to equalise the lateral forces on the two axles. Such systems have been implemented in an operational system [107].

## ***5.5 Rail Profiles, Surface Treatments and Changes to Gauge***

Hiensch et al. [108] described a two-material rail intended to be resistant to rolling contact fatigue and to reduce squeal noise. Surface coatings were applied either during rolling of the rails or by laser cladding. However, field tests did not show any reduction in curve squeal [91]. Similarly, in [96] it was reported that two unspecified systems for rail running surface conditioning were evaluated in Switzerland. They did not eliminate squeal but gave small reductions in noise level (2–5 dB(A)).

De Beer et al. [36] showed that the lateral contact position on the wheel affects the occurrence of squeal; being able to control this could in principle be used as a form of noise control [36]. The wheel they studied on their test rig was symmetrical and only showed squeal for contact positions to one side of the centreline. For a more realistic asymmetric wheel design the dependence on contact position is more complex [7].

One way to move the contact patch location on the wheel is to modify the rail transverse profiles. Asymmetrical profiles from Austria are reported in [109] (see also [90]). However, a pilot study with such profiles in Switzerland only showed positive effects for one type of passenger train [91]. At a site at Wollstonecraft,

NSW, Australia with 200 m radius, application of asymmetric rail profiles proved unsuccessful [1]. In the Netherlands, a special anti-squeal rail profile was tested in Den Haag on a 200 m radius curve [91]. The profile did not reduce the number of squeal events, but the average sound level per squeal event was reduced by 3 dB. On a second test section with the anti-squeal rail profiles, the inner rail was impregnated with tungsten carbide (a material with a very high hardness). This reduced the number of squeal events from 74 to 26%. The average sound level of the squeal events was again reduced by 4 dB.

The contact position can also be modified by varying the track gauge, although this also affects the angle of attack. It will depend on the wheel design whether gauge widening or narrowing is preferable. It can also be postulated that the presence of two-point contact may reduce the likelihood of squeal. The presence of high longitudinal creepage can also be effective in eliminating the falling friction characteristic from lateral creep [72] but may itself excite circumferential modes [86].

## 6 Concluding Remarks

Curve squeal remains a difficult problem, with the phenomenon appearing random rather than deterministic. Nevertheless, some success has been achieved in recent years using deterministic models to represent squeal behaviour. The main outstanding controversy is the relative importance of the falling friction mechanism compared with mode coupling. It is the authors' opinion that falling friction should not be ruled out as there is strong evidence for the existence of falling friction characteristics. However, the measurements of friction that are available from test rigs are quasi-static. What happens at small amplitudes and high frequencies may be quite different from this quasi-static behaviour that can be measured and indeed may not contain a negative slope at all. Mode coupling may contribute to an explanation for why some wheels squeal more than others; angle of attack is also important.

It should be recognised that squeal is not a single phenomenon and different phenomena may require different modelling approaches and different treatments. Although most cases reported involve 0-nodal-circle axial modes excited at the leading inner wheel, some unusual occurrences have been highlighted where different phenomena are involved. Even for the axial modes at the leading inner wheel, the dominant mode may vary over a wide frequency range, with values of  $n$  from 2 to 9. The reasons for this are not clear.

Curve squeal is almost always associated closely with one or more wheel modes. Nevertheless the importance of the rail has also been highlighted. The review has not covered rail vibration measurements or the contribution of the rail radiation to noise; its importance will vary depending on the excitation mechanism. Where the squeal frequency is very close to the natural frequency of the wheel, the rail vibration will exhibit the same frequency components but its response will be small compared with the wheel. However, where the squeal frequency is not exactly at a wheel mode the relevance of the rail response will increase.

Much of the data from field measurements reviewed is extensive, but it has to be commented that no dataset is complete. In particular, the friction characteristic is usually missing; no field test results are available for lateral friction characteristics. Modal identification of the wheels is only possible for test trains, not for service trains. The frequency response of the rails may also be important but is not often measured in the context of squeal investigations. The curving behaviour of the vehicles, particularly the angle of attack, is also very important but has only been reported in very few cases.

Finally, it has been pointed out that the effect of wheel dampers should preferably be expressed in terms of their effects on the modal damping as well their success in eliminating squeal. Tests of rail dampers are rare and more data is needed on their success or otherwise.

There remain many difficulties to be overcome to arrive at a full understanding of curve squeal allowing its control in all situations. It is clear that to achieve this will involve aspects of vehicle dynamics, tribology and vibroacoustics and the various forms of curve squeal will only finally be solved and explained by suitable collaboration between these fields.

## References

1. Anderson, D., Wheatley, N., Fogarty, B., Jiang, J., Howie, A., Potter, W.: Mitigation of curve squeal noise in Queensland, New South Wales and South Australia. In: Conference on Railway Engineering. pp. 625–636, Perth, Australia (2008)
2. Hanson, D., Jiang, J., Dowdell, B., Dwight, R.: Curve squeal: causes, treatments and results. In INTER-NOISE and NOISE-CON Congress and Conference Proceedings, vol. 249, pp. 6316–6323. Melbourne, Australia (2014)
3. Rudd, M.J.: Wheel/rail noise—part II: wheel squeal. *J. Sound Vib.* **46**(3), 381–394 (1976)
4. Remington, P.J.: Wheel/rail squeal and impact noise: what do we know? What don't we know? Where do we go from here? *J. Sound Vib.* **116**(2), 339–353 (1987)
5. Remington, P.J.: Wheel/rail rolling noise: what do we know? What don't we know? Where do we go from here? *J. Sound Vib.* **120**(2), 203–226 (1988)
6. Wickens, A.H.: *Fundamentals of Rail Vehicle Dynamics, Guidance and Stability*. Swets & Zeitlinger, Lisse (2003)
7. Thompson, D.J.: *Railway Noise and Vibration: Mechanisms, Modelling and Mitigation*. Elsevier, Oxford (2009)
8. Kalker, J.J.: *Three Dimensional Elastic Bodies in Rolling Contact*. Kluwer academic publishers, Dordrecht (1990)
9. Vermeulen, P.J., Johnson, K.L.: Contact of nonspherical elastic bodies transmitting tangential forces. *J. Appl. Mech.* **31**(2), 338–340 (1964)
10. Shen, Z.Y., Hedrick, J.K., Elkins, J.A.: A comparison of alternative creep-force models for rail vehicle dynamic analysis. In: Proceedings of 8th IAVSD Symposium, Cambridge MA, Swets and Zeitlinger, Lisse, pp. 591–605 (1983)
11. Huang, Z.Y.: *Theoretical Modelling of Railway Curve Squeal*. Ph.D. thesis, University of Southampton, UK (2007)
12. Hoffmann, N., Fischer, M., Allgaier, R., Gaul, L.: A minimal model for studying properties of the mode-coupling type instability in friction induced oscillations. *Mech. Res. Commun.* **29**(4), 197–205 (2002)



13. Hoffmann, N., Gaul, L.: Effects of damping on mode-coupling instability in friction induced oscillations. *J. Appl. Math. Mech.* **83**(8), 524–534 (2003)
14. Sinou, J.J., Jezequel, L.: Mode coupling instability in friction-induced vibrations and its dependency on system parameters including damping. *Eur. J. Mech.-A/Solids* **26**(1), 106–122 (2007)
15. Johnson, K.L.: *Contact Mechanics*. Cambridge University Press, Cambridge (1985)
16. Kinkaid, N.M., O'Reilly, O.M., Papadopoulos, P.: Automotive disc brake squeal. *J. Sound Vib.* **267**(1), 105–166 (2003)
17. Ghazaly, N.M., El-Sharkawy, M., Ahmed, I.: A review of automotive brake squeal mechanisms. *J. Mech. Des. Vibr.* **1**(1), 5–9 (2013)
18. Ouyang, H., Nack, W., Yuan, Y., Chen, F.: Numerical analysis of automotive disc brake squeal: a review. *Int. J. Veh. Noise Vib.* **1**(3–4), 207–231 (2005)
19. Dorf, R.C., Bishop, R.H.: *Modern Control Systems*, 11th edn. Prentice Hall. (2008)
20. De Beer, F.G., Janssens, M.H.A., Kooijman, P.P., van Vliet, W.J.: Curve squeal of railbound vehicles (part 1): frequency domain calculation model. In: *Proceedings of Internoise*, vol. 3, pp. 1560–1563. Nice, France (2000)
21. Von Stappenbeck, H.: Das Kurvengeräusch der Straßenbahn. Möglichkeiten zu seiner Unterdrückung. *Z. VDI* **96**(6), 171–175 (1954)
22. Van Ruiten, C.J.M.: Mechanism of squeal noise generated by trams. *J. Sound Vib.* **120**(2), 245–253 (1988)
23. Nakai, M., Chiba, Y., Yokoi, M.: Railway wheel squeal: 1st report, on frequency of squeal. *Bull. Jpn. Soc. Mech. Eng.* **25**, 1127–1134 (1982)
24. Nakai, M., Chiba, Y., Yokoi, M.: Railway wheel squeal: 2nd report, mechanism of specific squeal frequency. *Bull. Jpn. Soc. Mech. Eng.* **27**, 301–308 (1984)
25. Nakai, M., Chiba, Y., Yokoi, M.: Railway wheel squeal: 3rd report, squeal of a disk simulating a wheel in internal resonances. *Bull. Jpn. Soc. Mech. Eng.* **28**, 500–507 (1985)
26. Schneider, E., Popp, K., Irretier, H.: Noise generation in railway wheels due to rail-wheel contact forces. *J. Sound Vib.* **120**(2), 227–244 (1988)
27. Kraft, K.: Der Einfluß der Fahrgeschwindigkeit auf den Haftwert zwischen Rad und Schiene. *Arch. für Eisenbahntechnik* **22**, 58–78 (1967)
28. Fingberg, U.: A model of wheel-rail squealing noise. *J. Sound Vib.* **143**(3), 365–377 (1990)
29. Périard, F.: *Wheel-Rail Noise Generation: Curve Squealing by Trams*. Ph.D. thesis, Technische Universiteit Delft (1998)
30. Heckl, M.A., Abrahams, I.D.: Curve squeal of train wheels, part 1: mathematical model for its generation. *J. Sound Vib.* **229**(3), 669–693 (2000)
31. Heckl, M.A.: Curve squeal of train wheels, part 2: which wheel modes are prone to squeal? *J. Sound Vib.* **229**(3), 695–707 (2000)
32. Heckl, M.A.: Curve squeal of train wheels: unstable modes and limit cycles. *Proc. R. Soc. Lond. A: Math. Phys. Eng. Sci.* **458**, 1949–1965 (2002)
33. Liu, X., Meehan, P.A.: Wheel squeal noise: a simplified model to simulate the effect of rolling speed and angle of attack. *J. Sound Vib.* **338**, 184–198 (2015)
34. Meehan, P.A., Liu, X.: Analytical prediction and investigation of wheel squeal amplitude. In: Anderson, D., et al. (eds.) *Noise and Vibration Mitigation for Rail Transportation Systems*. NNFN, vol. 139, pp 69–80. Springer, Heidelberg (2018)
35. Kooijman, P.P., Van Vliet, W.J., Janssens, M.H.A., De Beer, F.G.: Curve squeal of railbound vehicles (part 2): set-up for measurement of creepage dependent friction coefficient. In: *Proceedings of Internoise*, vol. 3, pp. 1564–1567. Nice, France (2000)
36. De Beer, F.G., Janssens, M.H.A., Kooijman, P.P.: Squeal noise of rail-bound vehicles influenced by lateral contact position. *J. Sound Vib.* **267**(3), 497–507 (2003)
37. Thompson, D.J., Hemsworth, B., Vincent, N.: Experimental validation of the TWINS prediction program for rolling noise, part 1: description of the model and method. *J. Sound Vib.* **193**(1), 123–135 (1996)

38. Monk-Steel, A., Thompson, D.J.: Models for railway curve squeal noise. In: VIII International Conference on Recent Advances in Structural Dynamics, Southampton, UK (2003)
39. Barman, J.F., Katzenelson, J.: A generalized Nyquist-type stability criterion for multivariable feedback systems. *Int. J. Control* **20**(4), 593–622 (1974)
40. Huang, Z.Y., Thompson, D.J., Jones, C.J.C.: Squeal prediction for a bogied vehicle in a curve. In Schulte-Werning, B., et al. (eds.) *Noise and Vibration Mitigation for Rail Transportation Systems*. NNFM vol. 99, pp. 313–319. Springer, Heidelberg (2008)
41. Hsu, S.S., Huang, Z., Iwnicki, S.D., Thompson, D.J., Jones, C.J., Xie, G., Allen, P.D.: Experimental and theoretical investigation of railway wheel squeal. *Proc. Inst. Mech. Eng. Part F: J. Rail Rapid Transit* **221**(1), 59–73 (2007)
42. Squicciarini, G., Usberti, S., Thompson, D.J., Corradi, R., Barbera, A.: Curve squeal in the presence of two wheel/rail contact points. In: Nielsen, J.C.O., et al. (eds.) *Noise and Vibration Mitigation for Rail Transportation Systems*. NNFM, vol. 126, pp. 603–610. Springer, Heidelberg (2015)
43. Xie, G., Allen, P.D., Iwnicki, S.D., Alonso, A., Thompson, D.J., Jones, C.J., Huang, Z.Y.: Introduction of falling friction coefficients into curving calculations for studying curve squeal noise. *Veh. Syst. Dyn.* **44**(sup1), 261–271 (2006)
44. Giménez, J.G., Alonso, A., Gómez, E.: Introduction of a friction coefficient dependent on the slip in the FastSim algorithm. *Veh. Syst. Dyn.* **43**(4), 233–244 (2005)
45. Chiello, O., Ayasse, J.B., Vincent, N., Koch, J.R.: Curve squeal of urban rolling stock—part 3: theoretical model. *J. Sound Vib.* **293**(3), 710–727 (2006)
46. Collette, C.: Importance of the wheel vertical dynamics in the squeal noise mechanism on a scaled test bench. *Shock Vib.* **19**(2), 145–153 (2012)
47. Brunel, J.F., Dufrenoy, P., Naït, M., Muñoz, J.L., Demilly, F.: Transient models for curve squeal noise. *J. Sound Vib.* **293**(3), 758–765 (2006)
48. Glocker, C., Cataldi-Spinola, E., Leine, R.I.: Curve squealing of trains: measurement, modelling and simulation. *J. Sound Vib.* **324**(1), 365–386 (2009)
49. Pieringer, A.: A numerical investigation of curve squeal in the case of constant wheel/rail friction. *J. Sound Vib.* **333**(18), 4295–4313 (2014)
50. Pieringer, A., Kropp, W.: A time-domain model for coupled vertical and tangential wheel/rail interaction—a contribution to the modelling of curve squeal. In: Maeda, T., et al. (eds.) *Noise and Vibration Mitigation for Rail Transportation Systems*. NNFM, vol. 118, pp. 221–229. Springer, Heidelberg (2012)
51. Pieringer, A., Baeza, L., Kropp, W.: Modelling of railway curve squeal including effects of wheel rotation. In: Nielsen, J.C.O., et al. (eds.) *Noise and Vibration Mitigation for Rail Transportation Systems*. NNFM, vol. 126, pp. 417–424. Springer, Heidelberg (2015)
52. Zenzerovic, I., Pieringer, A., Kropp, W.: Towards an engineering model for curve squeal. In: Nielsen, J.C.O., et al. (eds.) *Noise and Vibration Mitigation for Rail Transportation Systems*. NNFM, vol. 126, pp. 433–440. Springer, Heidelberg (2015)
53. Zenzerovic, I., Kropp, W., Pieringer, A.: An engineering time-domain model for curve squeal: tangential point-contact model and Green’s functions approach. *J. Sound Vib.* **376**, 149–165 (2016)
54. Pieringer, A., Torstensson, P.T., Giner, J., Baeza, L.: Investigation of railway curve squeal using a combination of frequency- and time-domain models. In: Anderson, D., et al. (eds.) *Noise and Vibration Mitigation for Rail Transportation Systems*. NNFM, vol. 139, pp 81–93. Springer, Heidelberg (2018)
55. Chen, G.X., Xiao, J.B., Liu, Q.Y., Zhou, Z.R.: Complex eigenvalue analysis of railway curve squeal. In: Schulte-Werning, B., et al. (eds.) *Noise and Vibration Mitigation for Rail Transportation Systems*. NNFM, vol. 99, pp. 433–439. Springer, Heidelberg (2008)
56. Fourie, D.J., Gräbe, P.J., Heyns, P.S., Fröhling, R.D.: Analysis of wheel squeal due to unsteady longitudinal creepage using the complex eigenvalue method. In: Anderson, D., et al. (eds.) *Noise and Vibration Mitigation for Rail Transportation Systems*. NNFM, vol. 139, pp 55–67. Springer, Heidelberg (2018)

57. Wang, C., Dwight, R., Li, W., Jiang, J.: Prediction on curve squeal in the case of constant wheel rail friction coefficient. In: Anderson, D., et al. (eds.) *Noise and Vibration Mitigation for Rail Transportation Systems*. NFM, vol. 139, pp XXX–XXX. Springer, Heidelberg (2018)
58. Ding, B., Squicciarini, G., Thompson, D.J.: Effects of rail dynamics and friction characteristics on curve squeal. In: XIII International Conference on Motion and Vibration Control and XII International Conference on Recent Advances in Structural Dynamics (MoViC/RASD), Southampton (2016)
59. Bleedorn, T.G., Johnstone, B.: Steerable steel wheel systems and wheel noise suppression. In: Conference Rec IAS 12th Annual Meeting, Los Angeles, California (1977)
60. Koch, J.R., Vincent, N., Chollet, H., Chiello, O.: Curve squeal of urban rolling stock—part 2: parametric study on a 1/4 scale test rig. *J. Sound Vib.* **293**(3), 701–709 (2006)
61. Logston, C.F., Itami, G.S.: Locomotive friction-creep studies. *ASME J. Eng. Ind.* **102**(3), 275–281 (1980)
62. Ertz, M.: Creep force laws for wheel/rail contact with temperature-dependent coefficient of friction. In: 8th Mini Conference on Vehicle System Dynamics, Identification and Anomalies, Budapest (2002)
63. Lang, W., Roth, R.: Optimale Kraftschlussausnutzung bei Hochleistungs-Schienenfahrzeugen. *Eisenbahntechnische Rundsch.* **42**, 61–66 (1993)
64. Polach, O.: Creep forces in simulations of traction vehicles running on adhesion limit. *Wear* **258**(7), 992–1000 (2005)
65. Zhang, W., Chen, J., Wu, X., Jin, X.: Wheel/rail adhesion and analysis by using full scale roller rig. *Wear* **253**(1), 82–88 (2002)
66. Harrison, H., McCanney, T., Cotter, J.: Recent developments in coefficient of friction measurements at the rail/wheel interface. *Wear* **253**(1), 114–123 (2002)
67. Gallardo-Hernandez, E.A., Lewis, R.: Twin disc assessment of wheel/rail adhesion. *Wear* **265**(9), 1309–1316 (2008)
68. Fletcher, D.I., Lewis, S.: Creep curve measurement to support wear and adhesion modelling, using a continuously variable creep twin disc machine. *Wear* **298–299**, 57–65 (2013)
69. Fletcher, D.I.: A new two-dimensional model of rolling–sliding contact creep curves for a range of lubrication types. *Proc. Inst. Mech. Eng. Part J: J. Eng. Tribol.* **227**(6), 529–537 (2013)
70. Matsumoto, A., Sato, Y., Ono, H., Wang, Y., Yamamoto, M., Tanimoto, M., Oka, Y.: Creep force characteristics between rail and wheel on scaled model. *Wear* **253**(1), 199–203 (2002)
71. Janssens, M.H.A., van Vliet, W.J., Kooijman, P.P., De Beer, F.G.: Curve squeal of railbound vehicles (part 3): measurement method and results. In: *Proceedings of Internoise*, vol. 3, pp. 1568–1571, Nice, France (2000)
72. Monk-Steel, A.D., Thompson, D.J., De Beer, F.G., Janssens, M.H.A.: An investigation into the influence of longitudinal creepage on railway squeal noise due to lateral creepage. *J. Sound Vib.* **293**(3), 766–776 (2006)
73. Liu, X., Meehan, P.A.: Investigation of the effect of lateral adhesion and rolling speed on wheel squeal noise. *Proc. Inst. Mech. Eng. Part F: J. Rail Rapid Transit* **227**(5), 469–480 (2013)
74. Liu, X., Meehan, P.A.: Investigation of the effect of relative humidity on lateral force in rolling contact and curve squeal. *Wear* **310**(1), 12–19 (2014)
75. Liu, X., Meehan, P.A.: Investigation of squeal noise under positive friction characteristics condition provided by friction modifiers. *J. Sound Vib.* **371**, 393–405 (2016)
76. Jie, E., Kim, J.Y., Hwang, D.H., Lee, J.H., Kim, K.J., Kim, J.C.: An experimental study of squeal noise characteristics for railways using a scale model test rig. In: J. Pombo (ed.) *Proceedings of the Third International Conference on Railway Technology: Research, Development and Maintenance*, Cagliari, Sardinia, Italy (2016)
77. Eadie, D.T., Santoro, M., Kalousek, J.: Railway noise and the effect of top of rail liquid friction modifiers: changes in sound and vibration spectral distributions in curves. *Wear* **258**(7), 1148–1155 (2005)

78. Bullen, R., Jiang, J.: Algorithms for detection of rail wheel squeal. In: 20th International Congress on Acoustics 2010, ICA 2010—Incorporating Proceedings of the 2010 Annual Conference of the Australian Acoustical Society. pp. 2212–2216 (2010)
79. Stefanelli, R., Dual, J., Cataldi-Spinola, E.: Acoustic modelling of railway wheels and acoustic measurements to determine involved eigenmodes in the curve squealing phenomenon. *Veh. Syst. Dyn.* **44**(sup1), 286–295 (2006)
80. Vincent, N., Koch, J.R., Chollet, H., Guerder, J.Y.: Curve squeal of urban rolling stock—part 1: state of the art and field measurements. *J. Sound Vib.* **293**(3), 691–700 (2006)
81. Anderson, D., Wheatley, N.: Mitigation of wheel squeal and flanging noise on the Australian network. In: Schulte-Werning, B., et al. (eds.) *Noise and Vibration Mitigation for Rail Transportation Systems*. NNFm, vol. 99, pp. 399–405. Springer, Heidelberg (2008)
82. Curley, D., Anderson, D.C., Jiang, J., Hanson, D.: Field trials of gauge face lubrication and top-of-rail friction modification for curve noise mitigation. In: Nielsen, J.C.O., et al. (eds.) *Noise and Vibration Mitigation for Rail Transportation Systems*. NNFm, vol. 126, pp. 449–456. Springer, Heidelberg (2015)
83. Jiang, J., Hanson, D., Dowdell, B.: Wheel squeal—insights from wayside condition monitoring measurements and field trials. In: Anderson, D., et al. (eds.) *Noise and Vibration Mitigation for Rail Transportation Systems*. NNFm, vol. 139, pp. 41–53. Springer, Heidelberg (2018)
84. Jiang, J., Dwight, R., Anderson, D.: Field verification of curving noise mechanisms. In: Maeda, T., et al. (eds.) *Noise and Vibration Mitigation for Rail Transportation Systems*. NNFm, vol. 118, pp. 349–356. Springer, Heidelberg (2012)
85. Jiang, J., Anderson, D.C., Dwight, R.: The mechanisms of curve squeal. In: Nielsen, J.C.O., et al. (eds.) *Noise and Vibration Mitigation for Rail Transportation Systems*. NNFm, vol. 126, pp. 587–594. Springer, Heidelberg (2015)
86. Fourie, D.J., Gräbe, P.J., Heyns, P.S., Fröhling, R.D.: Experimental characterisation of railway wheel squeal occurring in large-radius curves. *Proc. Inst. Mech. Eng. Part F: J. Rail Rapid Transit* **230**(6), 1561–1574 (2016)
87. Corradi, R., Crosio, P., Manzoni, S., Squicciarini, G.: Experimental investigation on squeal noise in tramway sharp curves. In: *Proceedings of the 8th International Conference on Structural Dynamics, EURO-DYN 2011*, Leuven (2011)
88. Merideno, I., Nieto, J., Gil-Negrete, N., Landaberea, A., Iartza, J.: Constrained layer damper modelling and performance evaluation for eliminating squeal noise in trams. *Shock and Vibration* (2014)
89. Nelson J.T.: *Wheel/rail noise control manual*, TCRP Report 23 (1997)
90. Krüger, F.: *Schall- und Erschütterungsschutz im Schienenverkehr*. Expert Verlag, Renningen (2001)
91. Elbers, F., Verheijen, E.: *Railway noise technical measures catalogue*, UIC report UIC003-01-04fe (2013)
92. Oerth, J.: *Combating curve squeal, phase II, final report*, UIC (2005)
93. Eadie, D.T., Santoro, M., Powell, W.: Local control of noise and vibration with KELTRACK™ friction modifier and protector® trackside application: an integrated solution. *J. Sound Vib.* **267**(3), 761–772 (2003)
94. Eadie, D.T., Santoro, M.: Top-of-rail friction control for curve noise mitigation and corrugation rate reduction. *J. Sound Vib.* **293**(3), 747–757 (2006)
95. Suda, Y., Iwasa, T., Komine, H., Tomeoka, M., Nakazawa, H., Matsumoto, K., Nakai, T., Tanimoto, M., Kishimoto, Y.: Development of onboard friction control. *Wear* **258**(7), 1109–1114 (2005)
96. Bühler, S., Thallemer, B.: How to avoid squeal noise on railways: state of the art and practical experience. In: Schulte-Werning, B., et al. (eds.) *Noise and Vibration Mitigation for Rail Transportation Systems*. NNFm, vol. 99, pp. 406–411. Springer, Heidelberg (2008)
97. Jones, C.J.C., Thompson, D.J.: Rolling noise generated by railway wheels with visco-elastic layers. *J. Sound Vib.* **231**(3), 779–790 (2000)

98. Wetta, P., Demilly, F.: Reduction of wheel squeal noise generated on curves or during braking. In 11th International of Wheelset Congress, Paris (1995)
99. Brunel, J.F., Dufrénoy, P., Demilly, F.: Modelling of squeal noise attenuation of ring damped wheels. *Appl. Acoust.* **65**(5), 457–471 (2004)
100. Marjani, S.R., Younesian, D.: Suppression of train wheel squeal noise by shunted piezoelectric elements. *Int. J. Struct. Stab. Dyn.* (2016)
101. Heckl, M.A., Huang, X.Y.: Curve squeal of train wheels, part 3: active control. *J. Sound Vib.* **229**(3), 709–735 (2000)
102. Thompson, D.J., Jones, C.J.C., Waters, T.P., Farrington, D.: A tuned damping device for reducing noise from railway track. *Appl. Acoust.* **68**(1), 43–57 (2007)
103. Jiang, J., Ying, I., Hanson, D., Anderson, D.C.: An investigation of the influence of track dynamics on curve noise. In: Nielsen, J.C.O., et al. (eds.) *Noise and Vibration Mitigation for Rail Transportation Systems. NNFM*, vol. 126, pp. 441–448. Springer, Heidelberg (2015)
104. Toward, M., Squicciarini, G., Thompson, D.J.: Reducing freight wagon noise at source. *Int. Railway J. March*, 47–49 (2015)
105. Illingworth, R., Pollard, M.G.: The use of steering axle suspensions to reduce wheel and rail wear in curves. *Proc. Inst. Mech. Eng.* **196**(1), 379–385 (1982)
106. Garcia, J.F., Olaizola, X., Martin, L.M., Gimenez, J.G.: Theoretical comparison between different configurations of radial and conventional bogies. *Veh. Syst. Dyn.* **33**(4), 233–259 (2000)
107. Bruni, S., Goodall, R., Mei, T.X., Tsunashima, H.: Control and monitoring for railway vehicle dynamics. *Veh. Syst. Dyn.* **45**(7–8), 743–779 (2007)
108. Hiensch, M., Larsson, P.O., Nilsson, O., Levy, D., Kapoor, A., Franklin, F., Nielsen, J., Ringsberg, J., Josefson, L.: Two-material rail development: field test results regarding rolling contact fatigue and squeal noise behaviour. *Wear* **258**(7), 964–972 (2005)
109. Kopp, E.: Fünf Jahre Erfahrungen mit asymmetrisch geschliffenen Schienenprofilen. *Eisenbahn Techn. Rundsch.* **40**, 665 (1991)

# Wheel Squeal: Insights from Wayside Condition Monitoring



J. Jiang, D. Hanson and B. Dowdell

**Abstract** This paper summarises the insights gained by analysing wayside condition monitoring data from a curve of 300 m radius in Sydney over a three year period. The aim of analysing a large dataset is to derive statistically significant results on how angle of attack, speed, rail lubrication and rail grinding influence wheel squeal. The key finding is that the generation of severe wheel squeal is strongly determined by the angle of attack, which is consistent with the theory: severe squeal was almost entirely absent when the angle of attack was less than 10 mrad, and rose with increasing angle of attack. Squeal was therefore associated only with basic three piece bogies as these were the only bogies to return high angles of attack. Other freight bogie types, such as the one-piece freight bogies, three-piece freight bogies fitted with cross-bracing or steering arms, all steered well around the curve and did not squeal. Other factors, such as speed, rail lubrication and rail grinding, would influence wheel squeal generation when combined with high angles of attack. These factors were found to influence squeal behaviour, but are secondary for controlling wheel squeal compared with solving the poor steering performance of the three-piece freight bogies.

## 1 Introduction

Wheel squeal is a high pitched and very loud noise generated from the wheel/rail interface when a train travels around a tight curve. It often occurs in the frequency range where our ears are the most sensitive, and is therefore very annoying for receivers near the track.

---

J. Jiang (✉) · D. Hanson · B. Dowdell  
Infrastructure and Services Division, Transport for NSW, 18 Lee Street,  
Chippendale, NSW 2008, Australia  
e-mail: [jiandong.jiang@transport.nsw.gov.au](mailto:jiandong.jiang@transport.nsw.gov.au)

© Springer International Publishing AG, part of Springer Nature 2018  
D. Anderson et al. (eds.), *Noise and Vibration Mitigation for Rail Transportation Systems*, Notes on Numerical Fluid Mechanics and Multidisciplinary Design 139,  
[https://doi.org/10.1007/978-3-319-73411-8\\_2](https://doi.org/10.1007/978-3-319-73411-8_2)

Wheel squeal is a major impact from freight rail operations on tight curves in NSW, particularly in the Sydney Metropolitan area. It has defied resolution for decades. Addressing noise from freight trains, particularly wheel squeal, is a key activity under the NSW Freight and Ports Strategy to support greater movements of freight by rail.

The generation mechanism of wheel squeal is complex: it involves not only the wheel/rail interface, the wheel dynamic properties, but also the rolling stock steering performance and track dynamics. This is evident from the continuing efforts in modeling curve squeal from 1970s up to now, which is summarised by Thompson [1]. Therefore, the TfNSW squeal noise abatement strategy includes methods that address all parts of the interacting system; the rolling stock, the wheel/rail interface and the track. For example, work at the wheel/rail interface has demonstrated the profound effect of gauge face lubrication in reducing wheel squeal at sites where the outer wheel, as opposed to the inner wheel, which was found to be the primary source of wheel squeal [2]. Poor steering on certain designs of freight bogie has been found, however, to be the primary causative factor in the generation of wheel squeal. Basic three-piece bogies with poor steering were found to be exclusively responsible for wheel squeal on curves with moderate curve radius (from 300 to 500 m) [3]. Recent results from a very tight curve show that only basic three-piece bogies squeal on that curve too (160 m radius) [4]. Bogie designs that provide good steering (cross braced, one-piece, steering arms) do not generate squeal. Previous work has shown the upgrade from timber to concrete sleepers resulted in significant increase of wheel squeal [5], demonstrating how the track form can also influence squeal.

As part of the overall strategy, wayside noise monitors have been installed at several sites across the network. In particular, noise and angle of attack, i.e. the angle of a wheelset relative to the tangent of the rail in a curve, were measured simultaneously at one site on the main north line. This paper is dedicated to the analysis of the huge amount of data accumulated from this wayside system over the past three years. The aim is to derive statistically robust results on the influence of angle of attack (AoA), speed, rail lubrication, and rail profiles on wheel squeal. The observed result, its consistency with theory, and the implication for mitigation are also discussed.

## 2 Methodology

Figure 1 shows a photograph of the wayside noise and AoA monitoring system. The system is located near the mid-section of a curve of 300 m radius and 110 mm super-elevation on the main north rail line in Sydney. The wayside system only monitors trains travelling on one track towards the city centre and on the downhill (1:52 grade). The rail traffic is mixed passenger and freight trains.

The data from the wayside system includes noise level, AoA, lateral position, and speed for each passing wheel. For instance, Fig. 2 shows the axle-by-axle noise

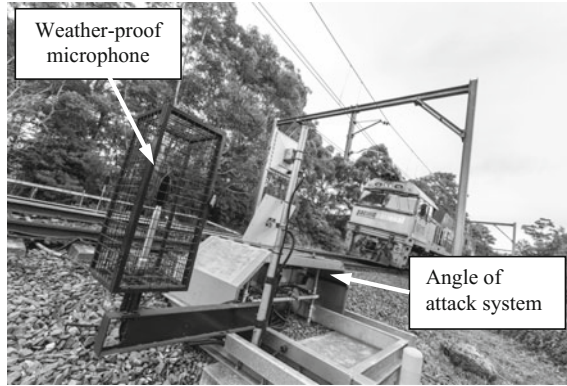


Fig. 1 A photograph of the wayside angle of attack and noise monitoring system

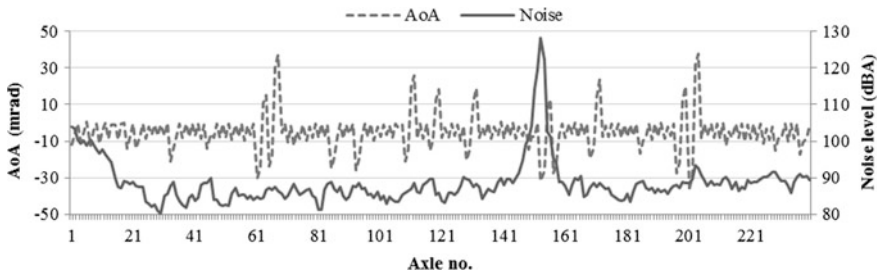


Fig. 2 An example of axle-by-axle noise at 1.2 m from near rail and angle of attack values of a freight train passby: the noise peak was a wheel squeal event which was associated with large angle of attack. Note the negative angle of attack values indicates the wheel tends to attack the high rail

and AoA of a freight train passby with one severe wheel squeal occurrence, which was associated with a large AoA. The negative sign of the AoA values indicates the wheel tends to attack the high rail, and vice versa, the positive value indicates that the wheel tends to attack the low rail. This example shows that the analysis of the noise and wheel steering performance helps to gain insight into wheel squeal generation and the performance of mitigation methods.

Wheel squeal was observed to occur at a wide range of noise levels, from the level equivalent to the background rolling noise, to well over 120 dBA when it is measured near the rail. In this paper, only severe wheel squeal, defined as exceeding 120 dBA measured 1.2 m from the rail, was analysed, considering all other noise sources, such as flanging noise, locomotive noise, or rolling noise, rarely exceeded this level. Furthermore, we are mostly interested in how often and under what conditions the most severe category of squeal occurs. Passenger trains do not generate severe squeal at this site, and therefore are excluded in the analysis.



A dataset including nearly 2,000,000 wheel passes over a three year period, from 04/2013 to 04/2016, was analysed. Of these many wheel passes, 2490 severe squeal events were detected. Both rails of the monitoring site were lubricated by a wayside rail gauge face lubricator during the monitoring period. Squeal occurrence over the three year period was compared to the result before the installation of the rail gauge face lubricator. In addition, rail grinding was conducted twice at the monitoring site during the three-year period. The effect of rail grinding on squeal was also examined.

### 3 Angle of Attack and Wheel Squeal

One of the key findings is that the generation of severe wheel squeal is strongly determined by the steering performance, quantified by the AoA, which is primarily a function of the bogie design. This finding has been previously established [6], but is reinforced here based on the analysis of this larger data set.

Figure 3 shows the AoA distribution of 1.8 million freight wheelset over the three-year monitoring period (from 04/2013 to 04/2016). The majority (more than 85%) of the freight wheels steered well through the 300 m radius curve with AoAs less than 10 mrad. In the small AoA region, there were two distinct peaks: one was around 0 mrad, and the other was around 7 mrad. These two peaks correspond to the normal steering of the trailing and leading axes, respectively. Only a small portion (less than 15%) of AoA values exceeded 10 mrad, and spread widely to over 40 mrad. Note the number of axles in each AoA bin exceeds 3000 in the distribution plot. The wide spread of AoA values is considered unusual for a curve of 300 m radius, but does offer a good opportunity to examine the correlation between AoA and squeal.

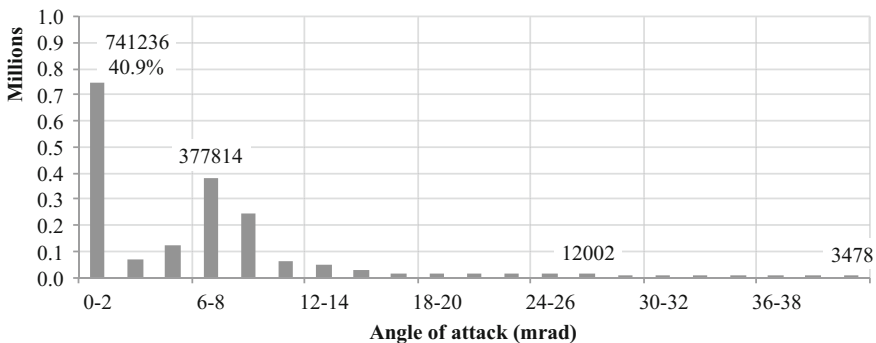


**Fig. 3** Distribution of the angle of attack values measured from the wayside system over a 3 year period. Note, the high incidence at (0–2) and (6–10) denote proper steering performance for trailing and leading wheelsets, respectively

The rate of squeal occurrence with the corresponding AoA values is shown in Fig. 4. Squeal occurrence rate was calculated as the ratio of the number of severe squeal occurrences in each AoA bin divided by the count of axles in that bin. The result shows a remarkably strong determination of AoA on squeal incidence. Essentially there was no or extremely low incidence of severe wheel squeal when the AoA was less than 10 mrad. Squeal incidence increased linearly with increasing AoA in the range from 10 to 35 mrad, and then experienced a more rapid increase when the AoA exceeded around 35 mrad.

To illustrate this nonlinear trend, a 6th order polynomial is added to the chart. The high R-squared value 0.99 indicates a good fit of the nonlinear trend, and strong determination of AoA on squeal.

In order to understand what caused the large AoAs, the AoA data is broken down by freight bogie types. Figure 5 shows the cumulative distribution of AoA separated by freight bogie types. Three-piece bogie was observed as the only bogie type which returned larger than expected AoA values frequently. All the other bogie types, such as the one-piece bogies, two-piece bogies with primary suspension, three-piece freight bogies fitted with cross-bracing or passive steering, or Scheffel bogies, all steered well, and their leading axles' AoA can be well predicted as a ratio of the bogie length (or axle spacing) divided by the curve radius. In addition, the leading axles of locomotives also returned high AoAs around 12–13 mrad as expected due to their longer wheelbase, and were responsible for a very small amount of severe wheel squeal.

The conclusion from this analysis is that for freight wagons only three piece bogies returned large AoA values and were responsible for squeal generation. Despite the strong determination of AoA on squeal, the squeal incidence was generally low, less than 10% even with extremely high AoAs. The low occurrence rate indicates that some other factors must play a role in squeal generation. The following sections examine the other factors which also contribute to wheel squeal generation.

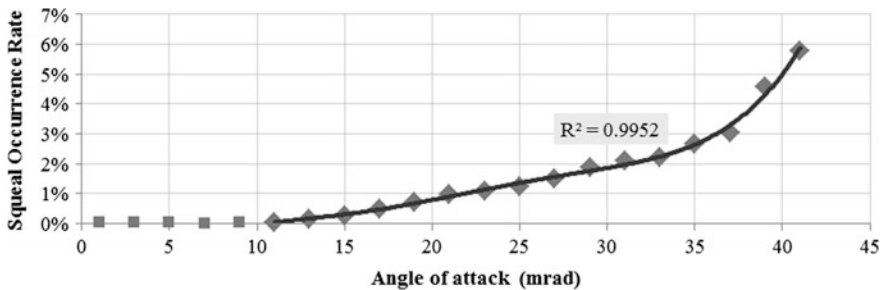


Fig. 4 Severe squeal incidence with angle of attack: a 6th order polynomial is fitted the data points starting at 11 mrad

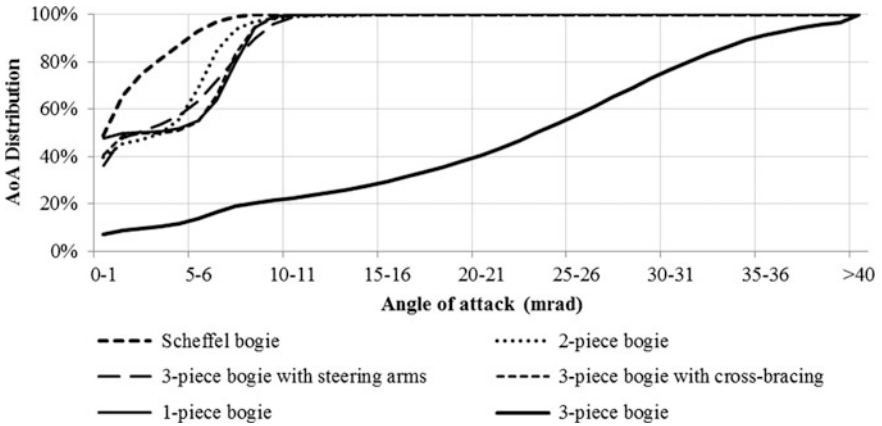


Fig. 5 Cumulative distributions of angle of attack values separated by freight bogie types

### 4 Effect of Speed on Wheel Squeal

The influence of speed on squeal is analysed in two ways: single variable analysis based on speed only, and the combination of speed and AoA analysis.

In the single variable analysis, only those AoA values exceeding 10 mrad were included as the small AoA values have been proved to have no or little influence on squeal. The speed distribution for AoAs exceeding 10 mrad is approximately Gaussian, with the average speed centring around 47 km/h, the maximum speed less than 70 km/h in general, and the standard deviation 8.5 km/h.

Overall, severe squeal occurrence was found to increase linearly with increasing speed. Figure 6 shows the rate of severe squeal occurrence for each speed bin. The high R-squared value 0.83 as shown in the figure indicates a good fit of the linear trend.

Additional analysis taking both speed and AoA into account also revealed similar results. Figure 7 shows the squeal occurrence rate with AoA and speed.

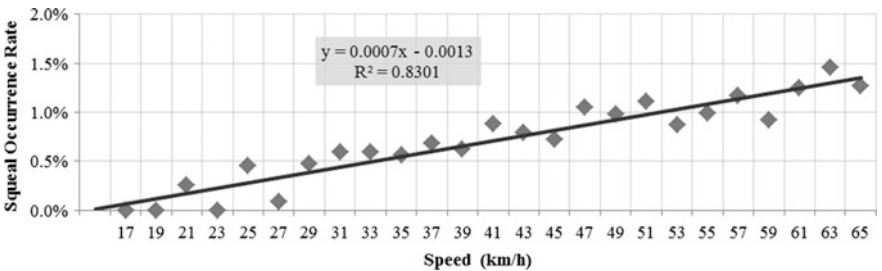


Fig. 6 Severe squeal incidence with speed: a linear trend fits the data points well with high R-squared 0.83

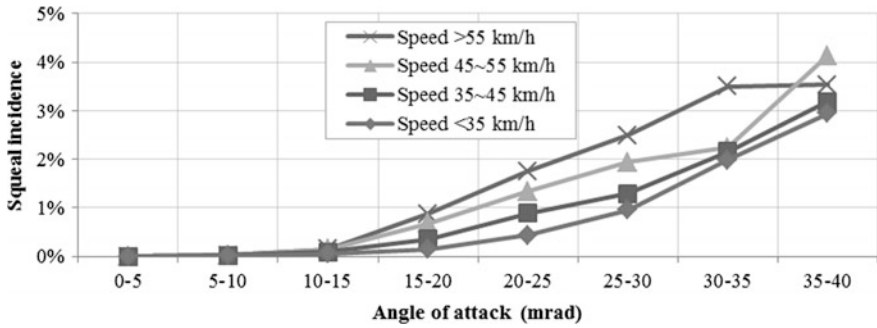


Fig. 7 Severe squeal occurrence rates with angle of attack and speed

Note the number of speed and AoA bins was reduced to maximise the number of samples in each bin. The squeal occurrence rate was observed to increase linearly with increasing AoA and speed in general. However, for speed greater than 55 km/h and AoA exceeding 35 mrad it is considered as an exception due to the reduced number of samples in that speed and AoA range.

## 5 The Influence of Rail Friction on Wheel Squeal

Rail gauge face lubrication was also found to have a profound effect in reducing wheel squeal in 2012 where the predominant squeal ‘mechanism’ was contact between the gauge corner/wheel flange throats [1]. For example, Fig. 8 shows the time history of noise of a freight train passing a curve: severe squeal events were observed at location 1 without lubrication, and the squeal events were eliminated at location 2 where the outer rail gauge face was lubricated [1].

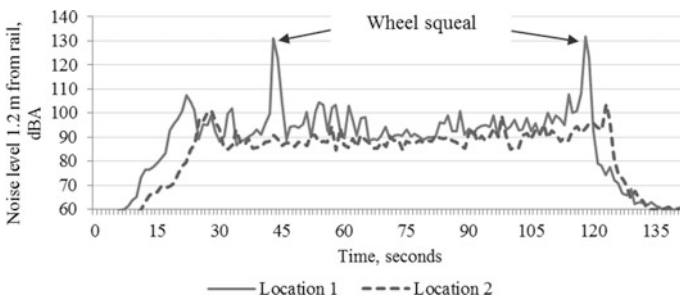
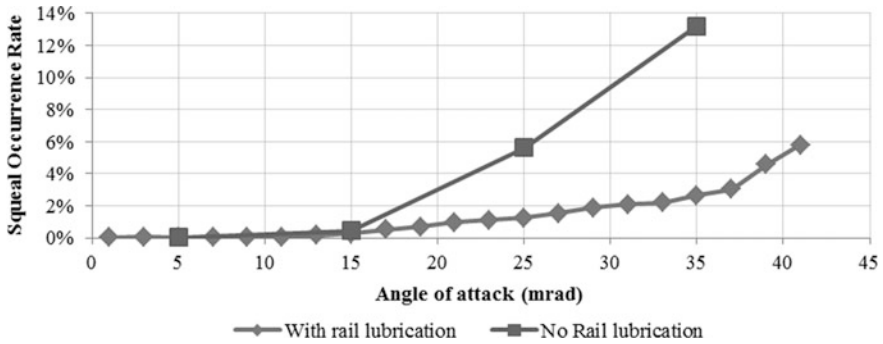


Fig. 8 Noise time history for a freight train passing the test curve, where Location 1 was without lubrication, while Location 2 was with the high-rail gauge face lubricated (Note locations 1 and 2 were on the same curve and similar except for the lubrication) [1]



**Fig. 9** Severe squeal occurrence rates with and without rail gauge face lubrication at the monitoring site

Since the 2012 trial, modern electronic track lubricators were installed at several sites to improve the rail gauge face lubrication. The resultant incidence of squeal at these sites was reduced, as expected. Squeal occurrence at the AoA monitoring site when the rail was not lubricated (from Ref [1]) was compared with that of the 3-year average when the rail was lubricated (see Fig. 9). Significant reduction of squeal incidence was observed across the entire AoA range when the rail was lubricated.

## 6 The Influence of Rail Grinding on Wheel Squeal

Rail grinding is carried out regularly across the Sydney Metropolitan network to restore the rail profile, remove surface cracks, defects and rail corrugation. During the three year monitoring period, rail grinding was conducted twice at the monitoring site. Wheel squeal was observed to rise sharply immediately after rail grinding on both occasions.

For instance, Fig. 10 shows a comparison of the severe squeal occurrence rate before and after rail grinding occurred on 25/08/2013. In the month before rail grinding, squeal occurrence rate (for the AoA values greater than 10 mrad) was generally less than 3%. Rail gauge face lubrication was applied before rail grinding, switched off temporarily during grinding and was switched on immediately after grinding. In the 1st month after rail grinding, squeal incidence was more than doubled, to nearly 20% for AoA values exceeding 40 mrad.

Similarly, rail grinding at the same location on 26/10/2015 led to increased number of wheel squeal events for the week immediately after grinding. However, the increase of noise this time was less significant compared with the 2013 result.

In both instances, a wide facet at the gauge corner of the rail was formed due to rail grinding, preventing conformal rail/wheel contact and restricting the distribution of lubrication from reaching the important gauge corner contact areas. The

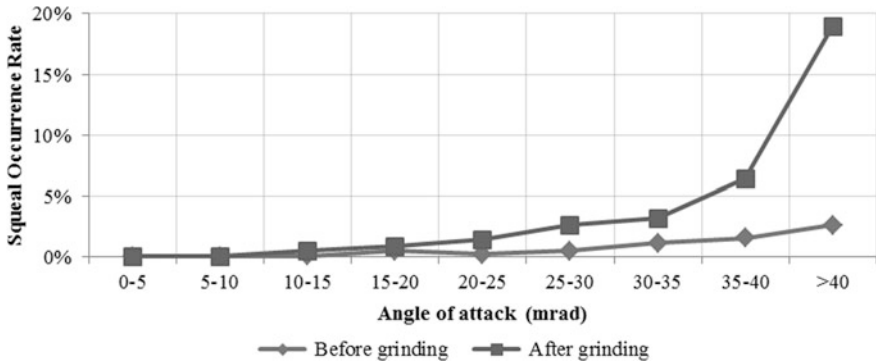


**Fig. 10** The occurrence rate of severe wheel squeal increased significantly at the monitoring site after rail grinding occurred on 25/08/2013

resulting two-point wheel/rail contact also impaired the steering performance of the three-piece bogies by reducing the rolling radius difference across the rails which provides steering.

## 7 Discussion

### 7.1 Bogie Design, Angle of Attack, and Wheel Squeal

It is generally accepted that the lateral creep (or equivalently the AoA) is responsible for the generation of wheel squeal: a prerequisite of AoA value exceeding a certain threshold, around 10 mrad, is required for squeal occurrence [7]. The result from the wayside monitoring data was consistent with the theory: no or extremely low severe squeal occurrence rate when AoA was less than 10 mrad, and squeal occurrence rates rose with increasing AoA values. However, the nonlinear increase of squeal occurrence when AoA exceeded 35 mrad is not predicted by the simple model as shown in [7], and is not fully understood at this stage.

The existing theory for estimating the AoA is proved to be valid for rigid bogies: the leading wheel's AoA can be calculated approximately as the ratio of the bogie length (or axle spacing) divided by the curve radius; while the trailing wheel aligns with the curve radially. However, this theory fails to predict the AoA behaviors of three-piece bogies, which tend to warp fundamentally and frequently return larger than expected AoAs.

So, why do only the 3-piece bogies return larger than predicted AoA values? This can be explained with the railway vehicle curving dynamics. Geometrically, a rigid bogie requires yaw or rotation relative to the wagon body to a position where the trailing axle aligns with the curve centre and with nearly '0' AoA. Physically, the turning moments, a combination of the "steering moment" (due to longitudinal

creep forces) and the “warp moment” (due to the lateral creep forces) have to overcome the rotational resistance from the bogie/wagon interface. If the combined turning moments fall short of the overall rotational resistance, the bogie will rotate less, not rotate at all, or even rotate to the opposite direction to give rise to larger than expected AoA values. The “steering moment” or longitudinal creep forces are often insufficient to overcome the rotational resistance alone, due to factors such as rail lubrication, or two-point contact between the wheel and rail. When this occurs, the “warp moment” becomes critical to rotate the bogie. Rigid bogies, such as the one-piece bogies or bogies with cross-bracing, with very high warp stiffness, are always able to overcome the overall rotational resistance regardless of substantially reduced “steering moment” or excessive rotational resistance. However, 3-piece bogies tend to warp before rotating when the “steering moment” reduces or the rotational resistance increases, leading to increased AoA values.

This analysis shows that not only the geometry of the bogie and track layout design, but also the warp stiffness of the bogie, is critical in the steering and noise performance of a bogie in curving. Furthermore, as pointed out in [8], the poor noise performance of the three piece bogies is also related with high wheel/rail wear and increased fuel consumption.

## ***7.2 The Influence of Speed on Wheel Squeal***

The linear dependence of squeal occurrence on speed as observed from the data was also consistent with the theory. For example, the simplified model [7] predicts that squeal noise level is proportional to speed.

Despite the linear dependence of squeal occurrence on speed, it is considered that speed restriction is not an efficient method for controlling squeal in practice as both the data and the theoretical model predict that wheel squeal will occur at very low train speed, and squeal is not eliminated unless the train stops running.

However, the knowledge of the influence of speed on squeal does help us to understand why the noise may vary between sites if the speed varies significantly. For a given AoA, the squeal at sites with similar rail profile and friction conditions can differ substantially, and the speed profile at these two sites may explain this difference. For example, at two locations on the Main North, which both carry the same freight traffic and have similar rail profiles and lubrication states, the squeal occurrence differed by around 50%. At one site, the average speed was around 66 km/h whereas as the other site it was 46 km/h. The relationship shown in Fig. 6 accurately predicts this 50% increase. Speed is still a secondary factor, however. Only unbraced three piece bogies squeal and speed has no influence on the squeal noise performance of bogie designs that steer properly.

### ***7.3 The Influence of Rail Conditions on Wheel Squeal***

Rail gauge face lubrication was found to have the potential to eliminate wheel squeal if it was generated from the high rail side. This indicates the synergistic benefits of reliable rail lubrication, not only in reducing the severe wheel flange/rail gauge wear and rolling resistance, but also in reducing noise. However, rail gauge face lubrication alone will not address wheel squeal generated from the wheel tread and top of rail interface. A complementary top of rail friction modification is required to better mitigate wheel squeal, particularly at sites where squeal is mostly generated from the wheel/tread/top of rail.

Rail grinding was also found to have impact on wheel squeal. It was considered that excessively wide facet left around the high rail gauge corner had contributed to the increase of squeal noise: (1) the wide facet prevented the grease from being transported to the contact area near the gauge corner, and (2) more severe two-point contact resulted from rail grinding leading to increased contact stress and potential breakdown of the lubricant film.

### ***7.4 Factors Influencing AoA***

It is important to understand how speed, rail lubrication or friction, and wheel/rail profiles, affect AoA since AoA plays a determining role in squeal generation.

Not surprisingly, rail lubrication and rail profiles, which influence the steering capability of unbraced three-piece bogies, have a profound impact on their AoA performance. In other words, AoAs of unbraced three piece bogies were found to be very sensitive to rail lubrication and rail profiles. For example, it was observed that the number of large AoAs increased by several times when the rail was changed from dry to well lubricated condition, but in the meantime the number of severe squeal events was substantially reduced.

Speed, or cant efficiency/deficiency, are found to have very little influence on the AoA of three-piece bogies. However, it is very often being mistakenly thought that speed or cant have an impact on AoA. In particular, in the case a trailing three piece bogie attacking the low-rail due to warp/rotation issue, people may falsely attribute speed or excessive cant as the cause.

Opposite to the three piece bogies, the rigid bogies with consistent and good steering performance are found to be insensitive to all the above mentioned factors.

### ***7.5 Application to Other Railway Systems***

The principles developed in this paper regarding wheel squeal occurrence are believed to be universal. The influence of AoA, speed, rail lubrication and grinding on wheel squeal, although observed only from freight traffic traversing one



particular site, should be applicable to other curved sites and with different rail traffic. In doing so, the user should be aware the context under which the figures were observed and account for the local differences between sites to provide an accurate prediction of squeal occurrence. To this end, our intention is to develop an empirical model that will account for these local factors by taking AoA, speed, rail friction and profile conditions into account to predict wheel squeal occurrence.

## 8 Conclusions

A dataset with over one million wheel passes and two thousand severe wheel squeal events, captured from a wayside monitoring system at a curved site of 300 m radius, were analysed. The analysis provides statistically significant insight into the mechanisms of wheel squeal generation, and the effectiveness of potential mitigation measures. For freight wagons these insights included:

- Wheel squeal is caused by poor bogie steering, and on the curves observed in this study, only unbraced three-piece bogies steer poorly. This is due to the weak bogie warp stiffness of these bogie designs which leads to high AoA. Other bogie types, such as the one-piece bogies, two-piece bogies with primary suspension, three-piece freight bogies fitted with cross-bracing or passive steering, or Scheffel bogies, steer well and do not squeal.
- Once bogie design factors have been accounted for, other factors relating to the track and wheel/rail interface become important:
  - (1) Rail gauge face lubrication was effective in reducing or eliminating wheel squeal if the noise was generated from the wheel flange and rail gauge corner interaction.
  - (2) Rail grinding may have an adverse effect on wheel squeal if it is not done properly resulting in an excessively wide facet at the rail gauge corner.
  - (3) The occurrence rate of severe squeal was found to be proportional to speed, relating to the established relationship between speeds and squeal noise level. However, this relationship is weak, and so speed restriction is not considered as an effective mitigation method as squeal still occurs at very low speed.

## References

1. Thompson, D.J., Squicciarini, G., Ding, B.: A state-of-the-art review of curve squeal noise: phenomena, mechanisms, modelling and mitigation. In: Anderson, D., et al. (eds.) *Noise and Vibration Mitigation for Rail Transportation Systems*. NNFM, vol. XX, pp. XXX–XXX. Springer, Heidelberg (2018)
2. Curley, D., Anderson, D.C., Jiang, J., Hanson, D.: Field trials of gauge face lubrication and top-of-rail friction modification for curve noise mitigation. In: Nielsen, J.C.O., et al. (eds.)

- Noise and Vibration Mitigation for Rail Transportation Systems. NNFM, vol. 126, pp. 449–456. Springer, Heidelberg (2015)
3. Jiang, J., Anderson, D., Dowdell, B., Wang, C.: The impact of angle of attack on curve noise. In: Proceedings of the World Congress on Rail Research, Sydney, Australia (2013)
  4. Hanson, D.: Wheel Squeal on the Flemington Goods Loop. Internal TfNSW Correspondence (2016)
  5. Jiang, J., Ying, I., Hanson, D., Anderson, D.C.: An investigation of the influence of track dynamics on curve noise. In: Nielsen, J.C.O., et al. (eds.) Noise and Vibration Mitigation for Rail Transportation Systems. NNFM, vol. 126, pp. 441–448. Springer, Heidelberg (2015)
  6. Jiang, J., Dwight, R., Anderson, D.: Field verification of curving noise mechanisms. In: Maeda, T., et al. (eds.) Noise and Vibration Mitigation for Rail Transportation Systems. NNFM, vol. 118, pp. 349–356. Springer, Heidelberg (2012)
  7. Rudd, M.: Wheel/rail noise—part 2: wheel squeal. *J. Sound Vib.* **46**, 381–394 (1976)
  8. Hanson, D., Jiang, J., Dowdell, B.: Freight wagon steering—insights from wayside condition monitoring measurements. In: Proceedings of the Conference on Railway Excellence (CORE), Melbourne (2016)

# Analysis of Railway Wheel-Squeal Due to Unsteady Longitudinal Creepage Using the Complex Eigenvalue Method



D. J. Fourie, P. J. Gräbe, P. S. Heyns and R. D. Fröhling

**Abstract** Railway wheel-squeal is a major source of noise nuisance in the proximity of curves where squeal occurs. Wheel-squeal results from frictional instability in the wheel-rail contact patch due to the creep forces generated during vehicle guidance. In the present study, an investigation of railway wheel-squeal due to mode-coupling instability is performed by implementing complex eigenvalue analysis using finite element software. The results of the study show that squeal in 1000 m radius curves can be attributed to the coupling of doublet wheel modes in the presence of saturated longitudinal creepage. More specifically the model validates the experimentally obtained squeal frequencies.

## 1 Introduction

Railway wheel-squeal can be defined as the high amplitude singing of a railway wheel with pure tone components. Squeal is a major source of railway generated noise nuisance in built-up areas.

Railway wheel-squeal belongs to the class of self-excited vibrations. In the case of railway wheel-squeal, the self-excitation results from frictional instability in the wheel-rail contact as a result of the creep forces generated during vehicle guidance. Two possible mechanisms of frictional instability responsible for railway wheel-squeal are identified in literature, namely (i) negative damping introduced to the wheel-rail contact by decreasing friction with increasing relative velocity [1–7]

---

D. J. Fourie (✉) · P. J. Gräbe  
Chair in Railway Engineering, University of Pretoria, Pretoria, South Africa  
e-mail: danie.fourie4@transnet.net

D. J. Fourie · R. D. Fröhling  
Transnet Freight Rail, Room 420, NZASM Building, 6 Minnaar Street,  
Pretoria 0001, South Africa

P. S. Heyns  
Department of Mechanical and Aeronautical Engineering, University of Pretoria,  
Pretoria, South Africa

and (ii) mode-coupling [8, 9]. All of the above references to literature identify unsteady lateral creepage as the main cause of squeal. Longitudinal creepage and wheel flange rubbing that are also generated at the wheel-rail interface during vehicle guidance is not considered relevant to squeal. Instead unsteady longitudinal creepage is believed to be relevant to corrugation formation [7, 10, 11] whilst wheel flange rubbing is considered relevant to broadband flanging noise [11, 12].

Contrary to the widely accepted belief that longitudinal creepage is not considered relevant to squeal, Fourie et al. [13], recently demonstrated the importance of longitudinal creepage as an energy source for squeal. In their in-field study Fourie et al., identified lateral displacement of the wheelset leading to high levels of longitudinal creepage at the wheel-rail contact of the squealing wheel as the key kinematic parameter influencing squeal in the 1000 m radius test curves. Vehicle dynamics simulations have shown that the combination of worn wheel and rail profiles cause affected Scheffel [14] self-steering bogies underneath empty freight wagons to over-steer in the test curves. Over-steering causes both wheelsets of the bogie to displace laterally towards the outside of the curve causing high levels of longitudinal creepage [15]. The simulations also showed that the squealing wheels are subject to predominantly longitudinal creepage with little lateral creepage.

In the present study, an investigation of railway wheel squeal due to mode-coupling instability is performed by complex eigenvalue analysis (CEA) using finite element software. CEA can predict the existence of unstable or undamped roots, which will cause noise in systems with unsymmetric stiffness matrix inputs due to sliding friction.

## 2 Literature Review

### 2.1 Mode-Coupling Instability

Mode-coupling instability results when the oscillation frequencies of two structural modes of an undamped system come, as a function of the control parameter, closer and closer together until they merge and a pair of a stable and an unstable mode is formed [16]. Once the modes are dynamically locked together, energy can be efficiently transferred between the modes, resulting in instability. The friction coupling changes not only the natural frequencies, but also their mode shapes thus bringing them closer and making them identical when the modes merge.

### 2.2 Complex Eigenvalue Analysis (CEA)

Automotive disc brake squeal is another area in which frictional induced instability is a major source of noise nuisance. In the context of automotive disc brake squeal, most production work in industry uses the finite element method to perform CEA

on a discretized model of the disc brake assembly [17]. Commercial finite element software like NASTRAN, ABAQUS and ANSYS has the complex eigenvalue brake squeal analysis capability built into the software.

An important consideration in CEA is how to linearise the non-linear contact and friction phenomena around the steady sliding state. One approach employed in NASTRAN is to simulate the contact/friction interface using linear friction-loaded springs [17]. Linear friction-loaded springs are the most common way of incorporating friction into a finite element model. Another approach employed in ABAQUS is that contact constraints in the normal direction are mathematically imposed, whilst the friction coupling is calculated based on the principle of virtual work for a system involving Coulomb friction [18, 19]. After finite element discretization, this contribution leads to an unsymmetric stiffness matrix which explains any friction induced instability arising in the model from a mathematical point of view.

In contrast to the friction-loaded spring formulation, the virtual work formulation relates frictional stiffness not only to the coefficient of friction  $\mu$  and equivalent contact area and pressure, but also to the tangential mode shape component of the radial modes as a result of the tangential friction force.

### 3 FE Model

The procedure for creating the linear wheel-rail interaction model to study mode-coupling instability includes the following steps: (i) constructing FE models for the wheel and rail, (ii) using a non-linear analysis in MSC Marc to calculate the normal contact stiffness matrices as well as the unsymmetric friction stiffness matrices using the bsqueal command (the friction coupling acts between the normal and longitudinal-tangential directions to correspond with saturated longitudinal creepage in the absence of lateral creepage), (iii) adding the effects of wheel-rail normal and frictional contact stiffness to create the contact-coupled wheel-rail system model, (iv) extracting the real eigenvalues and mode shapes of the contact-coupled wheel-rail system using MSC Nastran, (v) extracting the complex eigenvalues using the subspace projection method in MSC Nastran.

#### 3.1 Model Detail

The mesh for the wheel (916 mm diameter freight wheel) and rail (UIC60E1) were constructed in 2D using predominantly four node quadrilateral elements. These elements were then revolved and extruded respectively to create a single flexible wheel and a 10 m section of rail as seen in Fig. 1 (full length of rail not shown).

The rail model includes discrete supports at 650 mm centers and the wheel is located at a point mid-way between such support points on the rail. These discrete

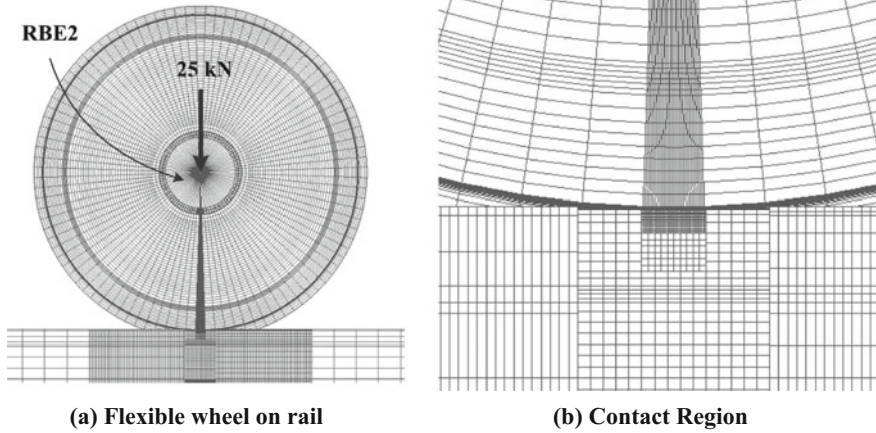


**Fig. 1** Finite element model (full length of rail not shown)

supports are modelled by grounded CBUSH elements (Nastran generalized spring-and-damper structural elements), which have stiffness and damping in three orthogonal directions. The CBUSH elements represent the rail pad stiffness and damping, whilst the connection to ground simulates the sleeper contact. Two CBUSH elements alongside one another were used to represent each rail pad. The connection between the grounded CBUSH point elements and the 3D solid elements of the rail was modelled with RBE3 interpolation elements. The RBE3 elements do not add additional stiffness to the connection and ensure that the CBUSH stiffness and damping is distributed to an area similar to that of the sleeper seat. The assumed rail pad properties corresponding to a soft pad are shown in Table 1.

To complete the model of the wheel, RBE2 rigid body elements were used to represent the omission of the axle. The RBE2 connection was modelled between all the nodes at the inner edge of the hub and a node located at the radial center of the wheel. The omission of the axle results in negligible errors for mode shapes with two or more nodal diameters [11]. The central node was constrained in all three rotations as well as the two tangential displacements. The wheel load was applied in the model vertical direction at the center node.

The mesh density of the wheel was controlled by defining mesh seeds, whilst that of the rail was controlled by defining different regions that were meshed

**Table 1** Rail pad properties

Direction	Rail pad stiffness (N/m)	Viscous damping coefficient (Ns/m)
Vertical	$1 \times 10^8$	5000
Lateral	$5 \times 10^7$	40,000
Longitudinal	$5 \times 10^7$	40,000

independently and then “glued” together. Elements in the contact area were created with a nominal edge length of 1 mm in an attempt to capture the contact characteristics at a sufficient resolution (see Fig. 1b). The material data used for the analysis is a Young’s modulus of 210 GPa, a Poisson’s ratio of 0.3, a density of  $7850 \text{ kg/m}^3$  and a structural damping coefficient of 0.0002 for both the wheel and rail.

### 3.2 Normal/Friction Contact Coupling

The first iteration of the model used the formulation of the friction-loaded spring as employed directly in NASTRAN. Steadily increasing the magnitude of the contact normal spring stiffness from a small value until numerical instability was reached did not render any of the experimentally obtained squeal frequencies unstable (see Sect. 4.2 for the experimentally obtained squeal modes). In this case the coefficient of friction  $\mu$  was set to 0.6.

A second iteration of the model set the contact normal spring stiffness constant whilst varying the frictional stiffness. This can be seen as increasing the frictional work, whilst keeping the normal contact conditions constant. The equivalent contact spring normal stiffness for the known wheel-rail contact conditions was calculated using the contact area and displacement results available from the non-linear MSC Marc contact analysis in step (ii). Results presented in the rest of the paper assume a normal contact Hertzian stiffness of  $20 \times 10^9 \text{ N/m}$  whilst the equivalent frictional stiffness representing the frictional work varied from  $12 \times 10^9 \text{ N/m}$  to  $2400 \times 10^9 \text{ N/m}$ . The frictional stiffness represents tangential displacements due to normal force variations. If the frictional stiffness depends solely on the Hertzian stiffness multiplied by the coefficient of friction, the only component of the normal force that is translated to a tangential force variation is that due to the contact spring. To include friction force variations due to normal force variations induced by dynamics of the wheel and rail in the contact point it is assumed that the frictional stiffness be greater than 0.6 of the Hertzian stiffness.

## 3.3 Model Results

### 3.3.1 Mode Shapes

The following discussion deals with the two nodal diameter circumferential (2,C) doublet mode pair that was found predominantly unstable during the in-field investigation of Fourie et al. [13]. Figure 2a, b show the system mode involving the (2,C) sine mode for contact-coupled representations with and without the frictional coupling present at the wheel-rail contact. Without friction, the (2,C) sine mode has a nodal point in the contact longitudinal-tangential direction and an anti-node in the

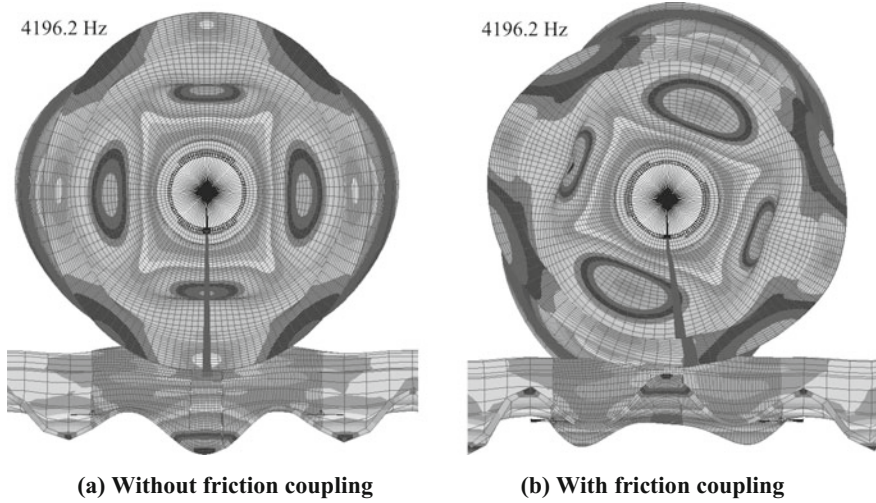
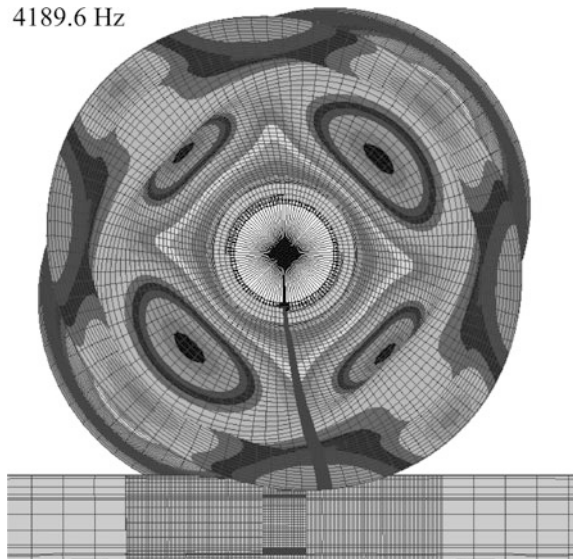


**Fig. 2** System mode involving (2,C) sine doublet mode

contact normal direction. Because the frictional coupling represents tangential displacement due to normal force variations, the (2,C) sine mode rotates itself with respect to the contact to allow simultaneous normal and longitudinal-tangential displacement with respect to the contact as shown in Fig. 2b. Figure 3 shows the system mode involving the (2,C) cosine doublet mode having an anti-node at the contact in the contact longitudinal-tangential direction and a node in the contact normal direction.

**Fig. 3** System mode involving (2,C) cosine doublet mode





Comparing Figs. 2b and 3 it can be seen that the frictional coupling rotates the sine mode to become spatially very similar to the cosine mode, for these otherwise spatially orthogonal modes.

From the work of Huang et al. [20] it is known that modes should satisfy two conditions for them to merge i.e. become identical in frequency and mode shape. These conditions are (i) that the separation between the frequencies of the two modes of a statically coupled system is sufficiently small, and (ii) that their component-wise mode shapes are compatible. Compatibility implies that the system modes display similar component modal displacements at  $\mu = 0$  and can easily become identical when  $\mu$  is increased.

Because the mode shapes of the (2,C) sine and cosine doublets are identical, but spatially orthogonal, the rotation of the (2,C) sine mode due to the imposed longitudinal friction force is crucial for allowing the two modes to become spatially similar. This mode rotation due to the imposed friction in addition to the inherent closely spaced frequencies of doublet modes means that the criteria for mode merging as discussed by Huang et al. are particularly well fulfilled by doublet modes.

### 3.3.2 Merging of Doublet Modes

To demonstrate the phenomenon of mode-coupling instability, which is believed to be the primary cause of friction-induced dynamic instability leading to wheel-squeal in the test curves, CEA was repeated by varying the equivalent frictional stiffness representing the frictional work from  $12 \times 10^9$  N/m to  $2400 \times 10^9$  N/m whilst holding the equivalent Hertzian normal contact stiffness at  $20 \times 10^9$  N/m. The discussion is again limited to the two nodal diameter circumferential (2,C) doublet mode pair that was found predominantly unstable during the in-field investigation of Fourie et al.

#### Model Results Without Material and Rail Pad Damping

Figure 4 shows how, in the absence of material and rail pad damping, the (2,C) doublets move closer and closer as a function of the frictional stiffness until they merge and a new stable-unstable mode pair results. Evident from Fig. 4a is that the doublet modes become coupled at 4193 Hz. At a frictional stiffness of zero these modes occur at 4189.6 and 4196.2 Hz. Figure 4b displays the level of damping of the stable and unstable modes available from the CEA analysis. Initially the damping of both modes is zero as the system is stable and no material and rail pad damping is included in the model. Once the system becomes unstable the damping of the coupled modes grows positively and negatively.

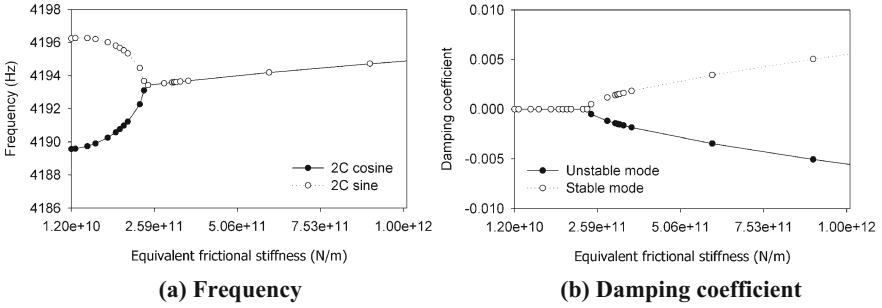


**Fig. 4** Merging modes as a function of equivalent frictional stiffness

### Model Results with Material and Rail Pad Damping

Figure 5 shows the frequency and damping results of the same model, but with material and rail pad damping considered in the model. Comparing Figs. 5a and 4a it becomes evident that when damping is considered in the model, the frequencies of the stable and unstable modes do not remain identical after becoming coupled. Also, comparing Figs. 5b and 4b it becomes evident that the onset of instability occurs at a lower value of frictional stiffness when damping is present in the model.

## 4 Model Calibration and Comparison with Experimental Results

In addition to the (2,C) doublet mode pair, the model also showed other pairs of modes coupling to form stable-unstable mode pairs. The onset of the coupling of the mode pairs and the number of modes with negative damping is dependent on the frictional stiffness value. Assuming that the frictional stiffness is linearly proportional to the top-of-rail friction coefficient and that negative damping is

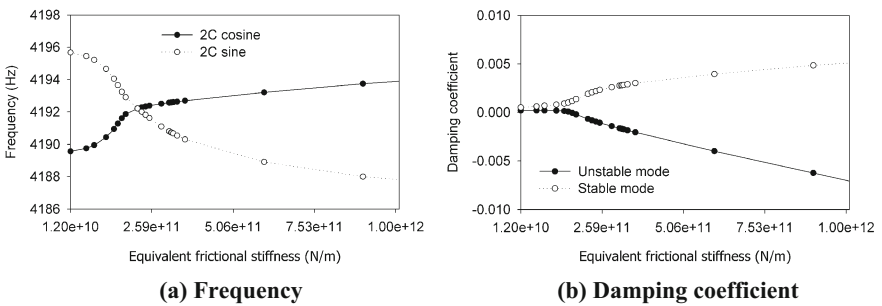


**Fig. 5** Merging modes as a function of equivalent frictional stiffness

equivalent to the occurrence of squeal, allows the frictional stiffness to be calibrated from coefficient of friction measurements combined with the known absence/occurrence of squeal from sound measurements. Once the frictional stiffness in the model has been calibrated using the experimental results, the stability results of the model can be used to compare it to the experimentally measured squeal frequencies for model validation.

#### ***4.1 Experimental Results***

Tonal squeal is emitted by some trailing inner wagon wheels on empty heavy haul trains traversing 1000 m radius curves on the iron ore export line in South Africa. No squeal events are emitted by the wheels of loaded heavy haul trains.

#### ***4.2 Squeal Frequencies***

Figure 6 shows the spread of measured squeal frequencies against wheel diameter for the modelled wheel type. This wheel type corresponds to wheel type A in [13]. Also shown in the figure is the experimentally obtained eigenfrequencies of the wheel eigenmodes most likely to be involved in squeal i.e. (i) the six nodal diameter radial doublet modes (6,R), (ii) the two nodal diameter circumferential doublet modes (2,C) and (iii) the seven nodal diameter radial doublet modes (7,R). For a 916 mm diameter wheel mounted underneath an empty wagon and in contact with the rail, the (6,R) doublet modes occur at 3942 and 3970 Hz, the (2,C) doublets at 4249 and 4261 Hz and the (7,R) doublets at 4743 and 4760 Hz. The squeal frequencies for a 916 mm diameter wheel are 3935, 4220 and 4722 Hz, as estimated from Fig. 6.

#### ***4.3 Top-of-Rail Friction Modification***

Field measurements have shown that top-of-rail friction modification is successful in eliminating squeal from the empty heavy haul trains in the 1000 m curves.

During the field measurements with top-of-rail friction modification, a hand-pushed Tribometer was used to evaluate the effect of the top-of-rail friction coefficient on the emitted squeal noise. The dry top-of-rail coefficient of friction was 0.64. During dry top-of-rail conditions all empty trains had at least one squeal event occurring with very high amplitude. With the adequate spread of friction modifier in the curve, the coefficient of friction reduced to 0.43 and no squeal events emanated from the empty trains. At a coefficient of friction of 0.52 some weak instances of audible squeal was again observed from the empty trains.

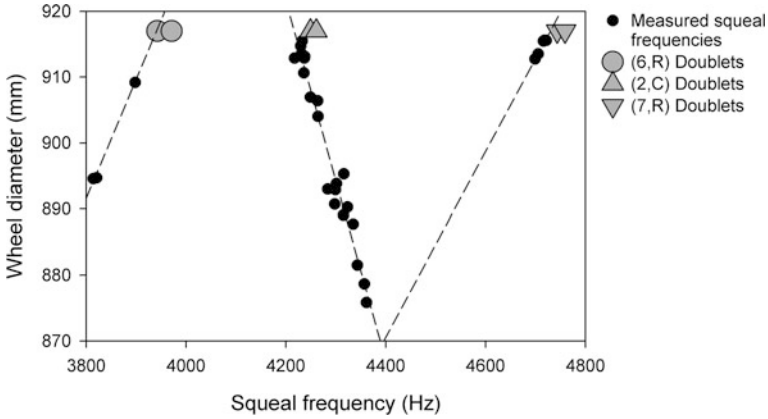


Fig. 6 Comparison between wheel eigenfrequencies and squeal frequencies

#### 4.4 Model Calibration

It is evident from Fig. 6 that squeal for the modelled wheel occurs predominantly due to the (2,C) doublet mode pair, with very few occurrences due to the (6,R) and (7,R) mode pairs. Hence calibration of the frictional stiffness was done using the damping results of the unstable mode that results from coupling of the (2,C) doublet mode pair. Knowing that squeal does not occur at  $\mu = 0.43$  (mode positively damped), that weak instances of squeal starts occurring at  $\mu = 0.52$  (mode slightly negatively damped) and that squeal with a very high amplitude occurs at  $\mu = 0.64$  (mode more negatively damped), allows for the calculation of a range of frictional stiffness for dry rail conditions in the test curves. The calculated range of frictional stiffness for  $\mu = 0.64$  is  $207 \times 10^9$  N/m to  $232 \times 10^9$  N/m.

#### 4.5 Comparison of Model and Experimental Results

Modes with negative damping in the linear CEA analysis indicate potential squeal modes. Not all modes with negative damping in the simulation results will however be found in experimental results. This is because the linear stability analysis only indicates the tendency of divergence and not which mode(s) eventually grow into high amplitude limit cycles [17].

The potential squeal frequencies simulated with a frictional stiffness of  $216 \times 10^9$  N/m are summarised in Table 2. This frictional stiffness falls within the range of expected frictional stiffness calculated for  $\mu = 0.64$ . The table also summarises the associated negative damping coefficient of the unstable mode, the coupled modes leading to the instability as well as the related experimental squeal frequency if any.

**Table 2** Comparison of potential squeal modes with measured squeal frequencies for a 916 mm diameter wheel

Coupled modes	Unstable frequency (Hz)	Damping coefficient ( $\times 10^{-3}$ )	Measured squeal frequency (Hz)
(0,C) mode and a rail mode	731	-0.35	-
(2,C) Doublet mode pair	4192	-0.67	4220
(7,R) Doublet mode pair	4694	-1.44	4722
Two rail modes	5159	-0.32	-
(8,0) <sup>a</sup> Cosine mode and a rail mode	5425	-3.66	-
(8,R) Doublet mode pair	5558	-1.20	-

<sup>a</sup>Wheel's eight nodal diameter axial mode

Evident from Table 2 is that the model accurately predicts two of the three experimental squeal frequencies for a frictional stiffness of  $216 \times 10^9$  N/m. Coupling of the (6,R) doublet modes that also produced squeal in the test curves only occur in the model at a frictional stiffness of  $264 \times 10^9$  N/m. It is however noteworthy that the squeal model can accurately predict all three frequencies found during the experimental campaigns. Provided that the "correct" frictional stiffness is selected, it is still unclear at this point which parameter(s) determine which of the three known squeal frequencies will form the limit cycle and this will be the subject of future research.

## 5 Conclusion

This study modelled railway wheel-squeal due to mode-coupling instability with longitudinal creepage as the energy source. In contrast to current studies that do not consider longitudinal creepage to be relevant to squeal, the results of this research demonstrates the importance of longitudinal creepage as an energy source for squeal. The study further also provides strong evidence that the measured phenomenon is consistent with mode-coupling instability and more specifically the coupling of doublet modes of the wheel. To achieve mode-coupling instability the doublet modes should satisfy the condition that the one doublet has a large mode shape component at the wheel-rail contact in the longitudinal direction whilst the other has a large mode shape component at the wheel-rail contact in the radial direction. In the presence of saturated longitudinal creepage the doublet with the radial anti-node at the wheel-rail contact will rotate itself with respect to the rotational axis of the wheel to allow simultaneous normal and longitudinal-tangential displacement with respect to the contact. Rotation of this mode due the friction coupling makes it spatially very similar to the other doublet mode having the

longitudinal anti-node at the wheel-rail contact for the otherwise spatially orthogonal modes. This mode rotation due to the imposed friction in addition to the inherent closely spaced frequencies of doublet modes means that the criteria for mode merging (modes having small frequency separation and having similar component modal displacements at  $\mu = 0$  that can quite easily become identical when  $\mu$  is increased) are particularly well fulfilled by doublet modes.

Although CEA can predict potential squeal modes as unstable vibration modes, not all modes will eventually grow into limit cycles, i.e. not all unstable modes will be found in experimental results. This is because linear CEA only indicates the tendency of modes to diverge. It is however noteworthy that the squeal model could accurately predict all three squeal frequencies found in the experimental results.

## References

1. Rudd, M.J.: Wheel/rail noise—part II: wheel squeal. *J. Sound Vib.* **46**(3), 381–394 (1976)
2. Periard, F.J.: Wheel-Rail Noise Generation: Curve Squealing by Trams. Ph.D. Thesis, Delft University of Technology, Netherlands (1998)
3. Heckl, M.A., Abrahams, I.D.: Curve squeal of train wheels, part 1: mathematical model for its generation. *J. Sound Vib.* **229**, 695–707 (2000)
4. De Beer, F.G., Janssens, M.H.A., Kooijman, P.P.: Squeal noise of rail-bound vehicles influenced by lateral contact position. *J. Sound Vib.* **267**, 497–507 (2003)
5. Thompson, D.J., Monk-Steel, A.D.: A Theoretical model for curve squeal. Report for UIC project Curve Squeal. Institute of Sound and Vibration Research, University of Southampton, UK, 23 Feb 2003
6. Chiello, O., Ayasse, J.B., Vincent, N., Koch, J.R.: Curve squealing of urban rolling stock—part 3: theoretical model. *J. Sound Vib.* **293**, 710–727 (2006)
7. Huang, Z.Y., Thompson, D.J., Jones, C.J.C.: Squeal prediction for a Bogied vehicle in a curve. In: Schulte-Werning, B., et al. (eds.) *Noise and Vibration Mitigation for Rail Transportation Systems*. NNFM, vol. 99, pp. 13–319. Springer, Heidelberg (2008)
8. Glocker, C., Cataldi-Spinola, E., Leine, R.I.: Curve squealing of trains: measurement, modelling and simulation. *J. Sound Vib.* **324**, 695–702 (2009)
9. Pieringer, A.: A numerical investigation of curve squeal in the case of constant wheel/rail friction. *J. Sound Vib.* **333**, 4295–4313 (2014)
10. Grassie, S.L., Kalousek, J.: Rail corrugations: characteristics, causes and treatments. *J. Rail Rapid Transit* **207**(1), 57–68 (1993)
11. Thompson, D.J.: *Railway Noise and Vibration: Mechanisms, Modelling and Means of Control*, 1st edn. Elsevier, Oxford (2009)
12. Anderson, D., Wheatley, N., Fogarty, B., Jiang, J., Howie, A., Potter, W.: Mitigation of curve squeal in Queensland, New South Wales and South Australia. In: *CORE 2008: Rail; The Core of Integrated Transport*. Perth: Railway Technical Society of Australasia, Engineers Australia, pp. 625–636
13. Fourie, D.J., Gräbe, P.J., Heyns, P.S., Fröhling, R.D.: Experimental characterization of railway wheel squeal occurring in large-radius curves. *J. Rail Rapid Transit* **230**(6), 1561–1574 (2016)
14. Scheffel, H.: A new design approach for railway vehicle suspension. *Rail Int.* **638**, 638–651 (1974)

15. Fourie, D.J., Gräbe, P.J., Heyns, P.S., Fröhling, R.D., Spangenberg, U.: New insights into curve squeal mitigation measures. In: Proceedings of the 11th International Heavy Haul Association Conference, Cape Town, South Africa, pp. 705–712 (2017)
16. Hoffmann, N., Fischer, M., Allgaier, R., Gaul, L.: A minimal model for studying properties of the mode-coupling type instability in friction induced oscillations. *Mech. Res. Commun.* **29**, 197–205 (2002)
17. Ouyang, H., Nack, W., Yongbin, Y., Chen, F.: Numerical analysis of automotive disc brake squeal: a review. *Int. J. Veh. Noise Vib.* **1**(3-4), 207–231 (2005)
18. Kung, S.W., Stelzer, G., Belsky, V., Bajer, A.: Brake squeal analysis incorporating contact conditions and other nonlinear effects. SAE Paper, 2003-01-3343 (2003)
19. Bajer, A., Belsky, V., Zeng, L.J.: Combining a nonlinear static analysis and complex eigenvalue extraction in brake squeal simulation. SAE Paper, 2003-01-3349 (2003)
20. Huang, J., Krousgrill, C.M., Bajaj, A.K.: Modeling of automotive drum brakes for squeal and parameter sensitivity analysis. *J. Sound Vib.* **289**(1), 245–263 (2006)

# Prediction of Wheel Squeal Amplitude



Paul A. Meehan and Xiaogang Liu

**Abstract** The prediction of vibration amplitude of wheel squeal noise is investigated using a concise mathematical model which has been validated with results from a rolling contact two disk test rig. The model is used to perform an energy-based analysis to determine a closed form solution to the steady state limit cycle amplitude of creep and vibration oscillations during squealing. The analytical solution is first shown to compare well with a numerical solution using an experimentally tuned creep curve with full nonlinear shape. The predicted squeal level trend is then shown to compare well with that recorded at various crabbing (lateral sliding) velocities for the test rig at different rolling speeds. The analytical solution provides insight into why the sound pressure level of squeal noise increases with crabbing velocity. The results highlight the primary importance of crabbing velocity (and angle of attack) and provide important theoretical insight into the mechanisms governing wheel squeal amplitude.

## 1 Introduction

Wheel squeal is a high pitched tonal noise that can occur as a train negotiates a curve (corner) of a railway line. This phenomenon has plagued the railway industry for many years and continues to rise in importance as railway usage increases and subjective human noise tolerance decreases. Although much research insight has been obtained into the mechanisms of squeal over the past decade the occurrences and amplitude of wheel squeal still appear unpredictable as it is sensitive to a wide range of parameters that naturally vary in the field and has remained difficult to determine except via complex and lengthy simulation. Much modelling of wheel squeal has been performed particularly following the renowned works of Rudd [1]

---

P. A. Meehan (✉)  
University of Queensland, Brisbane, Australia  
e-mail: meehan@uq.edu.au

X. Liu  
Wuhan University of Technology, Wuhan, China



and reviews by Remington [2] and Thompson et al. [3] in which the fundamental mechanism due to lateral creepage was consolidated. Curve squeal is generally thought to originate from the unstable vibratory response of a railway wheel when subject to large creep forces whilst negotiating corners. The conventional mechanism from the literature is that the unstable excitation of the squealing wheel originates from a lateral ‘stick-slip’ mechanism in the contact region analogous to the bowing of a violin string. In particular, when a bogie negotiates a curve of a track, there is a misalignment between the rolling velocity and the wheel velocity, namely angle of attack, leading to a crabbing velocity, i.e., lateral sliding velocity.

Referring to Fig. 1, the squeal mechanism depends on the behavior of the lateral traction ratio (lateral tangential force  $Q_y$  divided by the normal force  $N$ ) and lateral creepage ( $\approx$  angle of attack) conditions during the excitation of a railway wheel [4, 5]. The friction coefficient and shape and slope of the traction/creepage curve is affected by the so-called third body of the contact; an interfacial layer consisting of any lubricants, contaminants and material generated as a result of the contact interaction [6]. If the crabbing velocity (or angle of attack) is large enough its oscillations will be centered in the full sliding region (c). The negative slope in the creep curve at (c) can be shown to be associated with negative damping of creep oscillations and hence squeal instability. This leads to self-excited “stick-slip” oscillations, which in turn excite wheel vibrations and radiated sound. It is noted that, conversely, some recent research contends that a modal coupling phenomenon between the normal and tangential dynamics may cause the instability eg. [7]. Pure tone components of squeal, are generally related to wheel natural frequencies that correspond to out-of-plane wheel bending (or axial) modes.

Much research on the modelling of squeal has been performed in the past with differences in modelling details of wheel/rail mechanical impedances (analytical [8–12], FEM [4, 13, 14]), vertical dynamics [4, 14], contact forces and wheel sound radiation [4, 13, 14]. Some have also included wheel/rail roughness or wheel rotation effects [9, 10]. Recently, a transient analysis of the lateral creepage of the wheel was performed to account for nonlinearities of friction forces and resultant excited wheel modes appeared to match field observations better [15]. Notably, a time domain model was presented by Heckl and Abrahams [11], which focused on the squeal noise generated by a flat round disc excited at one point along the edge

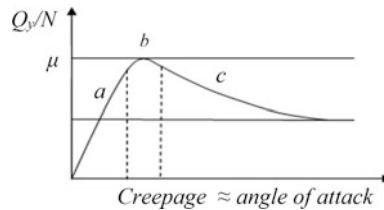


**Fig. 1** Traction/creepage characteristic of railway wheel-rail contact. **a** Region of slip/adhesion, **b** point at which full sliding first occurs and **c** negative slope region of increased sliding causing negative damping of creep oscillations

by a dry-friction force dependent on the disc velocity. This paper concluded that curve squeal is an unstable wheel oscillation that grows to a limit cycle oscillation, whose velocity amplitude is equal or very close to the crabbing speed. Furthermore, the simulation results of Chiello et al. [16] also showed that the vibration velocity stabilises below the lateral sliding velocity. This was investigated further by the present authors in [17] in which a numerical power balance analysis was identified as important, however an analytical prediction was not achieved.

Despite these considerable efforts, there has been uncertainty in fully understanding and theoretically predicting trends of how squeal noise varies with important parameters such as crabbing velocity and angle of attack. In particular models have in general involved too much complexity to be able to efficiently predict squeal amplitudes and perform detailed investigation of the effects of critical parameters on squeal sound levels. The present research investigates the prediction of vibration amplitude and sound pressure level of wheel squeal noise using a concise mathematical model which is compared with results from a rolling contact two disk test rig. This paper will first describe the testrig and mathematical methodology used for squeal investigation. Subsequently, a limit cycle analysis of squeal is provided to obtain a closed form solution to the squeal vibration amplitude that is then compared to numerically and experimentally found trends.

## 2 Methodologies

The experimental results presented in this paper have been obtained previously in [20] and are obtained using a rolling contact two disc test rig developed for the investigation of squeal noise (described in the following for convenience in Sect. 2.1). A theoretical model for squeal in the time domain [20] is reviewed in Sect. 2.2 before analytical methodology for determining the amplitude of squeal oscillation is described in Sect. 2.3.

### 2.1 *Experimental Methods*

A rolling contact two disc test rig [20] is used to investigate the occurrence of squeal as shown in Fig. 2a.

The normal and lateral forces  $F_1$  and  $F_2$  between the upper and lower wheel can be measured with strain gauge bridges  $S_1$ – $S_4$  as marked in Fig. 2b and this method is introduced in details in [18]. Some parameters of this test rig are listed in Table 1.

The angle of attack between the upper and lower wheel can be adjusted and measured using the method introduced in [17]. The test rig was run at various crabbing velocities and the sound was recorded with a microphone placed 5 cm

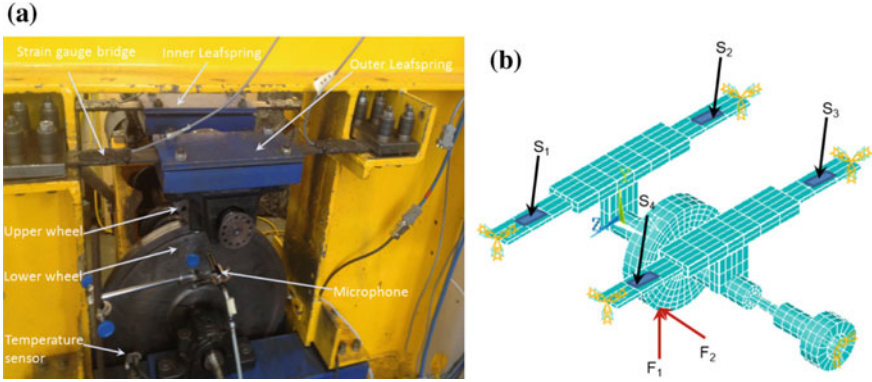


**Fig. 2** Rolling contact two disc test rig used for the investigation of squeal noise **a** front view of the test rig, **b** the FEM model of the test rig structure [18]

**Table 1** Parameters of the test rig

Description	Value
Radii of longitudinal and tangential curvature for the lower wheel ( $R_1, R_{1t}$ )	0.213 m, 0.300 m
Thickness of the lower wheel (rim, web)	0.026 m, 0.015 m
Density ( $\rho$ )	7800 kg/m <sup>3</sup>
Inner radius of lower wheel ( $R_1'$ )	0.0325 m
Young's modulus of upper and lower wheel ( $E$ )	175 GPa
Radii of longitudinal and tangential curvature for the upper wheel ( $R_2, R_{2t}$ )	0.085 m, 0.040 m
Thickness of the upper wheel	0.080 m
Poisson's ratio ( $\nu$ )	0.28
Angle of attack range	0–26 mrad
Creep coefficient ( $C_{22}$ )	3.14
Normal loading ( $W$ )	1000 N
Modal mass ( $m$ )	3.1 kg
Modal damping ( $c$ )	42 Ns/m
Modal stiffness ( $k$ )	$1.6 \times 10^8$ N/m

away from the lower wheel and 80 cm above the ground as displayed in Fig. 2. The vibration characteristics of the test rig are investigated with experimental modal tests conducted with a hard tip impact hammer and analysed using the finite element method. The vibration characteristics of the lower wheel were acquired from finite element analysis and the modal tests correlate well with the results of sound recording [19].

### 2.2 Theoretical Modelling

Wheel squeal may be concisely modelled based on the conceptual diagram of Fig. 3. An important parameter, the crabbing velocity arises due to the misalignment between the wheel velocity and rolling velocity as shown in Fig. 3a. The lateral force  $Q$  arises at the contact point due to the crabbing velocity according to the rolling frictional behaviour. In the lateral direction, the dominant vibration of the wheel is analogous to the frictional self-excited oscillation of mass connected to a spring and damping on a rolling belt as demonstrated in Fig. 3b.

The equations of motion for this system may be derived as shown in [20]. The wheel squeal vibration mode can be described by an effective spring-mass-damper system that can be expressed as,

$$m\ddot{y}(t) + c\dot{y}(t) + ky(t) = Q(\zeta, t) \tag{1}$$

where  $m$  is the modal mass,  $c$  is the modal damping coefficient,  $k$  is the modal stiffness which also account intrinsically for the modal participation from the lateral force  $Q$ . The modal parameters of the dominant mode were curve fitted from a receptance spectrum of a modal test [20] and are listed in Table 1. The lateral force  $Q$  can be calculated with,

$$Q = -\mu(\zeta)W, \tag{2}$$

where the creepage dependent lateral adhesion ratio in rolling contact  $\mu(\zeta)$  can be expressed as [20],

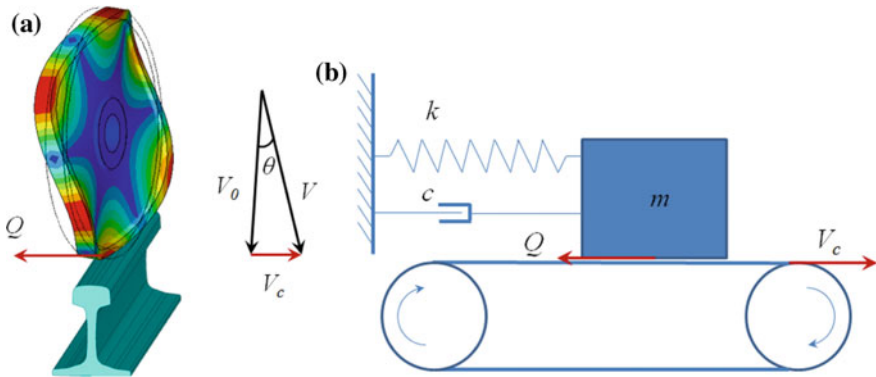


**Fig. 3** a 3D model of a squealing wheel rolling on rail top, b SDOF friction self-excited oscillation in lateral direction

$$\mu(\zeta) = \begin{cases} \mu_s \left\{ \zeta' - \frac{1}{3} \zeta'^2 + \frac{1}{27} \zeta'^3 \right\} \left\{ 1 - 0.5e^{-0.138/|\zeta V_0|} - 0.5e^{-6.9/|\zeta V_0|} \right\} & \text{for } \zeta' \leq 3 \\ \mu_s \left\{ 1 - 0.5e^{-0.138/|\zeta V_0|} - 0.5e^{-6.9/|\zeta V_0|} \right\} & \text{for } \zeta' > 3 \end{cases} \quad (3)$$

where  $\mu_0$  is the stationary friction coefficient. The lateral creepage  $\zeta$  is the ratio of the lateral relative velocity between the wheel and rail divided by rolling speed  $V_0$ ,

$$\zeta = (V_c + \dot{y}(t))/V_0 \quad (4)$$

where  $\dot{y}(t)$  is the vibration velocity of the wheel and  $V_c$  is crabbing velocity. The lateral crabbing velocity between two wheels can be calculated with angle of attack  $\theta$  and rolling speed  $V_0$ , i.e.,  $V_c = V_0 \sin \theta$ . As the angle of attack is normally less than  $3^\circ$ , the crabbing velocity can be approximated accurately as,

$$V_c = \theta V_0 \quad (5)$$

The  $\zeta'$  in Eq. (3) is a normalised creepage that can be described with,

$$\zeta' = \frac{\zeta G a b C_{22}}{\mu_0 W} = \frac{\zeta k_3}{W} \quad (6)$$

where  $G = E/2(1 + \nu)$ . The values used for elastic modulus  $E$ , Poisson's ratio  $\nu$ , the constant  $C_{22}$  and the normal loading  $W$  are listed in Table 1. The dimensions of the elliptical contact patch,  $a$  and  $b$ , are determined by the contact theory of Hertz [21].

When the effect of viscous damping is considered, the power input due to the lateral force and damping dissipation can be expressed as,

$$P_{Qd} = Q\dot{y}(t) - c(\dot{y}(t))^2 \quad (7)$$

where  $c$  is the modal damping of the dominant mode listed in Table 1.

### 2.3 Analysis of Wheel Squeal to Predict the Steady State Amplitude

The equations of motion (1–7) may be solved for limit cycle analysis to analytically determine the amplitude of wheel squeal under simplified assumptions. This provides an almost instantaneous solution that may be used to investigate a wide range of conditions and how the vibration amplitude compares with the crabbing velocity analytically. In order to obtain such an efficient solution, a simplification of the creep behaviour described in (3) is used. In particular, it is assumed that the full

creep behaviour can be characterised by linear slopes,  $k_1$  and  $k_2$ , for the slip and full sliding regions, respectively, as described by:

$$\mu(\zeta) = \begin{cases} k_1 \zeta' & \text{for } \zeta' \leq 1 \\ k_1 + k_2 \{\zeta' - 1\} & \text{for } \zeta' > 1 \end{cases} \quad (8)$$

Wheel squeal is characterised by an initial growth in vibration until a steady state amplitude is reached. This process is governed by an energy balance process based on the effective positive or negative damping characteristic of the slopes of the creep curve. In particular, solving Eqs. (1), (2), (4) and (8) for small oscillations about a nominal crabbing velocity  $V_c$  yields,

$$m\ddot{y}(t) + (c + k_{1,2}k_3/V_0)\dot{y}(t) + ky(t) = 0 \quad (9)$$

where  $k_{1,2}$  represents the local slope of the creep curve under nominal conditions. Equation (9) is in the form of the well known second order vibrating system that has its stability determined by the sign of the effective system damping term  $c + k_{1,2}k_3/V_0$ . A negative system damping term indicates instability and system energy input to vibrations causing them to grow in amplitude. In particular, for small vibrations, in the fully sliding region of the creep curve, the negative slope of  $k_2$  causes a positive power input to the squeal vibration which causes them to grow if it is greater than the power output due to damping  $c$ . The vibration amplitude grows to cause larger creep oscillations that start to impinge on the positive slip side of the creep curve. This positive slope  $k_1$  of the creep cycle causes a negative power input (or power output) to the vibration which acts like additional damping to  $c$  and causes them to decay. The vibration will continue to grow until a balance is achieved between the power input and output over the different slopes of the creep curve so that a steady state (limit cycle) amplitude is reached. Hence the wheel squeal steady state vibration amplitude may be determined by solving equations of motion (1)–(8) to determine when the energy,  $E$ , from the positive and negative sloped sides of the creep curve is zero, or mathematically,

$$\begin{aligned} E &= \int_0^{\frac{2\pi}{\omega}} P_{Qd} dt = 2 \left( \int_0^{t_c} P_{Qd} dt + \int_{t_c}^{\frac{\pi}{\omega}} P_{Qd} dt \right) \\ &= A(4(V_o W - k_3 V_c)(k_2 - k_1) \sin(\omega t_c) \\ &\quad + A\omega((2\omega t_c + \sin(2\omega t_c))(k_2 - k_1)k_3 - 2\pi(k_2 k_3 + cV_o))/2V_o = 0 \end{aligned} \quad (10)$$

where  $t_c$  is the time in the vibration cycle at which critical creep occurs (between the positive and negative sides of the creep curve). It has been assumed that the wheel vibration displacement is small and hence adequately represented by a sinusoid of amplitude  $A$ . This time  $t_c$  may be determined as a function of vibration velocity amplitude by solving Eqs. (4) and (6) for the critical creep  $\zeta' = 1$  to obtain the squeal vibration amplitude as

$$\begin{aligned}
 A\omega &= (V_c - \zeta_c V_0) / \cos(\omega t_c) \quad \text{where } \sin(2\omega t_c) - 2\omega t_c \\
 &= 2\pi(V_0 c_d + k_2 k_3) / (k_3(k_1 - k_2))
 \end{aligned}
 \tag{11}$$

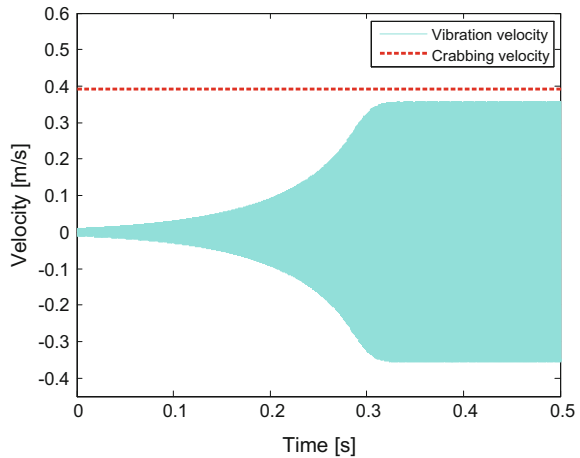
Equation (11) is a transcendental equation which can be easily solved for the critical value of  $\omega t_c$  using any root finding function. Hence solution for the squeal amplitude via Eqs. (11) is almost instantaneous and allows a wide range of parameter investigations to be carried out.

### 3 Results

It was of interest to first compare the analytical results described by solution to Eqs. (11) to the numerical solution to the exact equations of motion in Eqs. (1)–(8). In particular the following parameters were investigated to compare with previous results in [20]. The parameters chosen were: crabbing velocity 0.39 m/s, testrig rolling speed 800 rpm (17.8 m/s) and other parameters described in Table 1. Figure 4 shows the exact time history solution for squeal vibration velocity and these conditions using the exact creep curve described by Eq. (3). The steady state vibration velocity is shown to settle at approximately 0.35 m/s, a value close to but under the crabbing velocity (0.39 m/s). Alternatively, the analytical solution with an approximate creep curve described in Fig. 5 with  $k_1 = 0.27$  and  $k_2 = -0.02$  is found by solving Eq. (14) and (12) to be 0.33 m/s.

The analytical solution is found to be very close to the numerical solution. Figure 5a shows the creep oscillation range and highlights that the steady state squeal amplitude is achieved via creep oscillations spanning both the positive and negative sloped regions of the curve to enable a balance of energy. This is highlighted further by inspecting the power input for both numerical and analytical

**Fig. 4** The simulated vibration velocity at a crabbing velocity of 0.39 m/s (from [20])



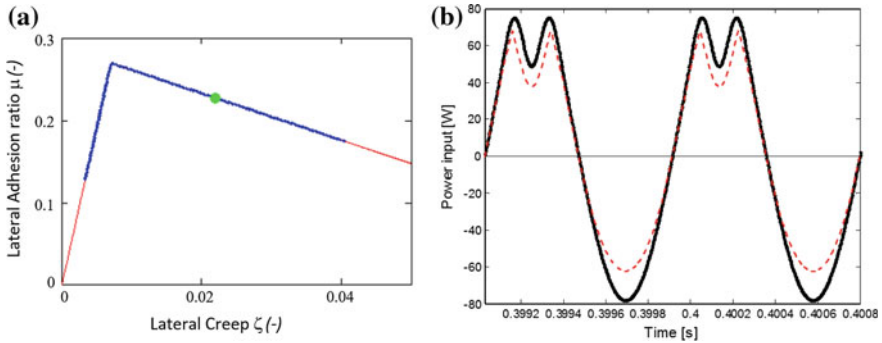


**Fig. 5** **a** The approximated creep curve (-), analytical solution for creep oscillations range (-) and quasistatic lateral creepage ( $\bullet$ ) corresponding to a crabbing velocity of 0.39 m/s. Note change of slope occurs at  $\zeta' = 1$ . **b** The power input near 0.4 s for both simulation (-) and analytical (-) prediction (Adapted [20])

conditions as shown in Fig. 5b. Figure 5b highlights that although the analytical solution underpredicts the simulated power input of the numerical solution, the trend is similar. In particular, there is a reduction and splitting of the positive peaks of the power due to the creep passing below the critical creep and hence passing on the positive side of the creep curve. This reduces the power input to the squeal vibration cycle and hence balances the energy to achieve a steady state amplitude. The difference in amplitude between the analytical and numerical solution is most likely due to the simplified estimate of the creep curve in the analytical model. Note that the squeal velocity shape was found to be very close to that of a sinusoid although the power input shown in Fig. 5b differed substantially.

Figure 5 and Eq. (4) also highlights that the steady state vibration velocity amplitude will always be less than the crabbing velocity if the creep remains positive. It was of interest to investigate whether this holds for a range of crabbing velocities using the efficient model. Figure 6 shows a plot of solutions for the steady state vibration amplitude versus crabbing velocity using the analytical solution.

**Fig. 6** The vibration velocity amplitude (-) versus crabbing velocity (.)

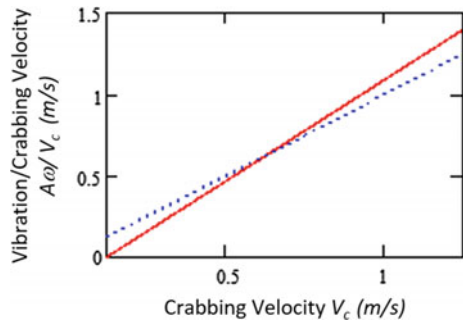
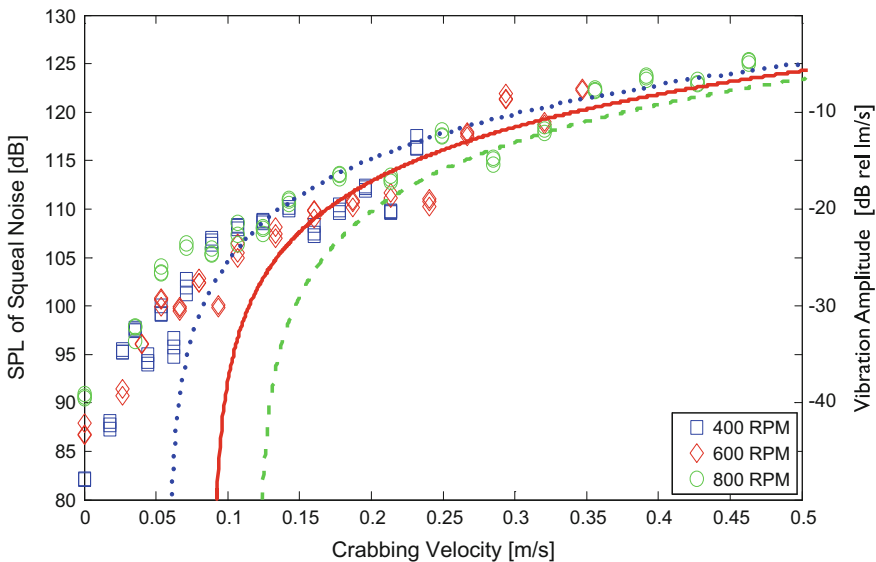




Figure 6 highlights that the vibration velocity amplitude is proportional to the crabbing velocity but is not always less than the crabbing velocity. In particular, for higher values of crabbing velocity of greater than approximately 5 times the critical slip, the vibration velocity amplitude becomes greater than the crabbing velocity. However realistically these correspond to conditions of angle of attack in the order of 35 mrad and hence unlikely under typical railway conditions.

It was of interest to investigate the effect of crabbing velocity on sound pressure level SPL. In this case the sound power is proportional to the vibration velocity squared [3]. The analytical predictions based on solution to Eqs. (12) and (14) were plotted with real experimental recordings on the two disk testrig under the same squeal conditions. The sound generated by the rolling contact two disc test rig was recorded with a microphone placed 5 cm away from the lower wheel and 80 cm above the ground as marked in Fig. 2a. The recorded sound data was analysed and presented in Fig. 7 along with the analytical solutions.

The results in Fig. 7 show that the experimental trend of squeal sound pressure level increasing with crabbing velocity is well predicted by the analytical solution for crabbing velocities greater than 0.15 m/s. This is consistent for squeal conditions. Below 0.15 m/s the trend is not well matched because the experimental noise level is no longer dominated by squeal ie other sources such as rolling noise is largely contributing which is not modelled by the analytical solution. In particular, the analytical solution drops off rapidly when squeal does not occur when the crabbing velocity is less than the critical creep velocity. The dropoff occurs at



**Fig. 7** The sound pressure level of squeal noise versus crabbing velocity; experimental and analytical prediction for 400 (.), 600 (-) and 800 (-) RPM

different values for different rolling speeds because it is assumed in this model that the critical creep is independent of speed. There is evidence that this spread is less in reality because the critical creep reduces with increasing speed.

## 4 Conclusions

A mathematical model integrating the contact mechanics with the modal vibration of the wheel is used to theoretically predict the vibration velocity amplitude of wheel squeal. The limit cycle analysis results show that the vibration velocity amplitude reaches a steady state approaching the crabbing velocity under reasonable conditions in agreement with previous research. Theoretically this is shown to be due to the limit cycle analysis demanding that steady state squeal oscillations be large enough to encompass both positive and negative sloped regions of the creep curve in order to obtain an energy balance for nonlinear steady state squeal amplitudes. However, it is also shown that the vibration velocity may exceed the crabbing velocity under very high angle of attack conditions. The efficient theoretical model is then used to predict the effect of crabbing velocity on wheel squeal noise amplitude and the results compare very favourably with the trend found experimentally.

## References

1. Rudd, M.J.: Wheel/rail noise part II: wheel squeal. *J. Sound Vib.* **46**(3), 381–394 (1976)
2. Remington, P.J.: Wheel/rail squeal and impact noise: what do we know? What don't we know? Where do we go from here? *J. Sound Vib.* **116**(2), 339–353 (1985)
3. Thompson, D.J., Jones, C.J.C.: A review of the modelling of wheel/rail noise generation. *J. Sound Vib.* **231**(3), 519–536 (2000)
4. de Beer, F.G., et al.: Squeal noise of rail-bound vehicles influenced by lateral contact position. *J. Sound Vib.* **267**(3), 497–507 (2003)
5. Kooijman, P.P. et al.: Curve squeal of rail bound vehicles, part 2: set-up for measurement of creepage dependent friction coefficient. In: *Proceedings of the Inter Noise 2000, Nice (France)* (2000)
6. Descartes, S., et al.: Presence and role of the third body in a wheel–rail. *Wear* **258**(7–8), 1081–1090 (2005)
7. Pieringer, A.: A numerical investigation of curve squeal in the case of constant wheel/rail friction. *J. Sound Vib.* **333**(18), 4295–4313 (2014)
8. Nakai, M., et al.: Railway wheel squeal (2nd report, mechanism of specific squeal frequency). *Bull. JSME* **27**(224), 301–308 (1984)
9. Nakai, M., et al.: Railway wheel squeal (squeal of a rotating disk). *JSME Int. J. Ser III Vibr. Control Eng. Eng. Ind.* **32**(3), 406–412 (1989)
10. Nakai, M., Akiyama, S.: Railway wheel squeal (squeal of a disk subjected to periodic excitation). *J. Vib. Acoust.* **120**(2), 614–622 (1998)
11. Heckl, M.A., Abrahams, I.D.: Curve squeal of train wheels, part 1: mathematical model for its generation. *J. Sound Vib.* **229**(3), 669–693 (2000)

12. Heckl, M.A.: Curve squeal of train wheels, part 2: which wheel modes are prone to squeal? *J. Sound Vib.* **229**(3), 695–707 (2000)
13. Schneider, E., et al.: Noise generation in railway wheels due to rail-wheel contact forces. *J. Sound Vib.* **120**(2), 227–244 (1988)
14. Fingberg, U.: A model of wheel-rail squealing noise. *J. Sound Vib.* **143**(3), 365–377 (1990)
15. Brunel, J.F., et al.: Transient models for curve squeal noise. *J. Sound Vib.* **293**(3), 758–765 (2006)
16. Chiello, O., et al.: Curve squeal of urban rolling stock—part 3: theoretical model. *J. Sound Vib.* **293**(3–5), 710–727 (2006)
17. Liu, X., Meehan, P.A.: Investigation of the effect of lateral adhesion and rolling speed on wheel squeal noise. *Proc. Inst. Mech. Eng. Part F: J. Rail Rapid Transit.* **227**(5), 469–480 (2013)
18. Liu, X., Meehan, P.A.: Investigation of the effect of relative humidity on lateral force in rolling contact and curve squeal. *Wear* **310**(1–2), 12–19 (2014)
19. Liu, X., Meehan, P.A.: Wheel squeal noise: a simplified model to simulate the effect of rolling speed and angle of attack. *J. Sound Vib.* **338**, 184–198 (2015)
20. Liu, X., Meehan, P.A.: Investigation of the effect of crabbing velocity on squeal noise based on a rolling contact two disc test rig. In: *12th International Conference of Contact Mechanics CM2015, Colorado (USA)* (2015)
21. Johnson, K.L.: *Contact Mechanics*. Cambridge University Press, Cambridge (1985)

# Investigation of Railway Curve Squeal Using a Combination of Frequency- and Time-Domain Models



A. Pieringer, P. T. Torstensson, J. Giner and L. Baeza

**Abstract** Railway curve squeal arises from self-excited vibrations during curving. In this paper, a frequency- and a time-domain approach for curve squeal are compared. In particular, the capability of the frequency-domain model to predict the onset of squeal and the squeal frequencies is studied. In the frequency-domain model, linear stability is investigated through complex eigenvalue analysis. The time-domain model is based on a Green's function approach and uses a convolution procedure to obtain the system response. To ensure comparability, the same sub-models are implemented in both squeal models. The structural flexibility of a rotating wheel is modelled by adopting Eulerian coordinates. To account for the moving wheel–rail contact load, the so-called moving element method is used to model the track. The local friction characteristics in the contact zone are modelled in accordance with Coulomb's law with a constant friction coefficient. The frictional instability arises due to geometrical coupling. In the time-domain model, Kalker's non-linear, non-steady state rolling contact model including the algorithms NORM and TANG for normal and tangential contact, respectively, is solved in each time step. In the frequency-domain model, the normal wheel/rail contact is modelled by a linearization of the force-displacement relation obtained with NORM around the quasi-static state and full-slip conditions are considered in the tangential direction. Conditions similar to those of a curve on the Stockholm metro exposed to

---

A. Pieringer (✉)  
CHARMEC/Division of Applied Acoustics,  
Chalmers University of Technology, Gothenburg, Sweden  
e-mail: astrid.pieringer@chalmers.se

P. T. Torstensson  
CHARMEC/Department of Applied Mechanics,  
Chalmers University of Technology, Gothenburg, Sweden

J. Giner  
Centro de Investigación en Ingeniería Mecánica,  
Universitat Politècnica de València, Valencia, Spain

L. Baeza  
Institute of Sound and Vibration Research,  
University of Southampton, Southampton, UK

severe curve squeal are studied with both squeal models. The influence of the wheel-rail friction coefficient and the direction of the resulting creep force on the occurrence of squeal is investigated for vanishing train speed. Results from both models are similar in terms of the instability range in the parameter space and the predicted squeal frequencies.

## 1 Introduction

Creep forces at the wheel/rail interface allow for steering of railway vehicles. In unfavorable conditions in small radius curves, this ability may coincide with the generation of a high-frequency tonal noise referred to as curve squeal. Curve squeal originates from self-excited vibrations of the railway wheel and occurs at frequencies corresponding to its axial normal modes [1].

At the squeal frequencies, the wheel mobility exceeds that of the rail making the wheel become the dominating noise source [1]. Hence, in the development of models for squeal prediction, it is of fundamental importance to accurately capture the high-frequency dynamic wheel behaviour. Studies in the literature typically apply a non-rotating wheel modelled using the finite element method [2–4]. Fayos et al. [5] adopted Eulerian coordinates to develop a model of a rotating flexible wheelset that fully accounts for inertia forces such as gyroscopic forces and centrifugal stiffening. In [6], Pieringer et al. investigated the influence of wheel rotation on squeal predictions using the wheel model from [5, 7]. While wheel rotation did not impact on the tendency to squeal and the resulting lateral contact forces in this study, it was recommended to investigate the influence of wheel rotation on the radiated sound.

The track represents a complex structure in terms of modelling. Cross-sectional deformation occurs already at frequencies around 200 Hz [8], which implies that the three-dimensional dynamic behaviour of the rail has to be accounted for at higher frequencies. One modelling alternative is to use waveguide finite elements that combine a discretization of the two-dimensional cross-section geometry of the rail with an analytical wave-type solution along the rail [4, 9]. Koh et al. [10] presented a mathematical formulation of a railway track adopting Eulerian coordinates referred to as the Moving Element Method (MEM). Its functionality was demonstrated for the case of a rail modelled with Euler-Bernoulli beam elements.

Models for curve squeal can be formulated either in the frequency or in the time domain. Frequency-domain models require a linearization of the mechanical system and are in general computationally efficient. These models can only predict the onset of unstable vibrations in the linear regime. Time-domain models have the capability to include non-linearities but involve a higher computational cost. They can model the non-linearities in the contact zone during the build-up of unstable vibrations. Therefore, they cannot only predict which modes are prone to squeal, but also the ultimate squeal amplitudes (i.e. the limit cycle).

Two instability mechanisms for squeal noise identified and explained in the literature are: a negative friction-velocity slope associated with “negative damping” [11] and geometrical coupling enabled by a non-symmetric stiffness matrix [12]. Most available models for curve squeal in the literature are formulated in the frequency domain and adopt the negative friction-velocity slope as instability mechanism, e.g. the models [11, 13–15]. In the related research area of brake squeal, the geometrical-coupling mechanism in combination with linear complex eigenvalue analysis is recognized as one of the most accepted investigation procedures. More recently, the geometrical coupling mechanism has also been adopted in time-domain models for curve squeal [4, 16].

In this paper, curve squeal of rail vehicles is investigated using a combination of models for complex linear stability analysis in the frequency domain and non-linear wheel/rail interaction in the time domain. The model for complex stability analysis of railway tread brake squeal presented in [17] is further developed to simulate curve squeal. The model for non-linear wheel/rail interaction has been presented in [4]. The same submodels are used in both squeal models as far as possible to ensure comparability. Frictional instability due to geometrical coupling is considered. A similar study had been presented in [18], but the implementation of the model for the linear complex stability analysis has been updated since then and the numerical results in this paper replace the results from [18]. Furthermore, the time-domain model now includes the effect of the contact angle.

The application of two different types of model allows the comparison and evaluation of a frequency- and time-domain approach for curve squeal. In particular, the capability of the linear stability analysis to predict the onset of squeal and the squeal frequencies is evaluated. Conditions similar to those of a 120 m radius curve on the Stockholm metro exposed to severe curve squeal are studied [19].

## 2 Curve Squeal Models

In this section, the frequency- and the time-domain models for curve squeal are described.

### 2.1 Submodels

Both the frequency- and the time-domain model for curve squeal include a wheel model, a track model and a contact model. These submodels are presented in the following.

### 2.1.1 Wheel Model

The structural dynamics of a rotating wheel is modelled using a mathematical formulation that adopts Eulerian coordinates [7]. This formulation allows for inertial forces caused by gyroscopic and Coriolis effects to be accounted for by a linear system of differential equations.

A C20 wheel is modelled with 8560 solid quadratic elements (20-node) and 122,880 degrees-of-freedom (dofs). The wheel radius is 0.39 m and the wheel mass is approximately 657 kg. The wheel material is assumed elastic isotropic with elastic modulus 207 GPa, Poisson's ratio 0.29 and density 7820 kg/m<sup>3</sup>. The wheel is modelled as clamped at the hub inner surface. Wheel modal damping is introduced in accordance with the approximate values proposed by Thompson [1]. The number of dofs of the wheel model is reduced through a modal expansion retaining a truncated set of 200 eigenmodes corresponding to a highest eigenfrequency of about 13 kHz. Point receptances of the wheel calculated at the wheel contact node are shown in Fig. 1.

### 2.1.2 Track Model

A rail supported by a uniform viscoelastic Winkler bedding is modelled by an implementation of the so-called Moving Element Method (MEM) introduced in [10]. This method accounts for the wheel motion by using a rail mesh that moves in the longitudinal direction at the vehicle speed.

A BV50 (50 kg/m) rail of length 42 m is modelled with 20,168 solid quadratic elements (20-nodes) corresponding to a total of 406,065 dofs. The longitudinal element length is 5 cm throughout the model. Cyclic boundary conditions are modelled at the rail ends. An elastic isotropic rail material with elastic modulus 207 GPa, Poisson's ratio 0.3 and density 7860 kg/m<sup>3</sup> is assumed. The Winkler bedding is modelled with a uniform distribution of vertical stiffness and damping equivalent to a discrete rail support of approximately  $k_{w,z} = 43.7$  MN/m and  $c_{w,z} = 12.6$  kNs/m, respectively (sleeper span 0.6 m). The stiffness and damping in the

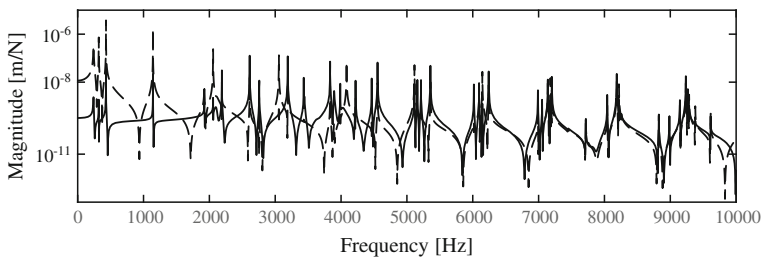


**Fig. 1** Magnitude of wheel receptance calculated for excitation at the wheel contact node. —: Vertical point receptance, - - -: lateral point receptance

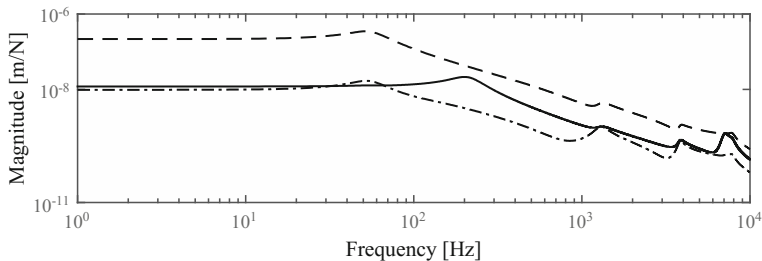


**Fig. 2** Point receptance at the rail contact node in vertical (—) and lateral (---) directions. - · - · -: Vertical-lateral cross receptance

longitudinal and lateral directions are modelled as  $0.1 k_{w,z}$  and  $0.8 c_{w,z}$ , respectively. Modal expansion retaining a truncated set of the 2500 lowest frequency eigenmodes is performed. Point receptances calculated at the rail contact node are shown in Fig. 2.

### 2.1.3 Wheel/Rail Contact Model

The wheel/rail contact is solved using an implementation of Kalker's variational method [20], which includes the algorithms NORM and TANG for normal and tangential contact, respectively. This is a three-dimensional, non-linear and non-steady state rolling contact model that relies on the assumption that wheel and rail can be locally approximated by elastic half-spaces. The local friction model applied in each contact element is Coulomb's law. Details about the implementation are found in [21].

In [22], simulations for conditions corresponding to those in the studied curve on the Stockholm metro resulted in a lateral displacement and a large angle of attack (AoA) of the leading wheelset in a bogie of approximately  $y = 14$  mm and  $\psi = 21$  mrad. This case is modelled here for the low rail contact. The vertical preload is 55 kN. A nominal S1002 wheel profile and BV50 rail profile with inclination 1:40 are used. The contact angle is 5.1 mrad. The definitions of the AoA and the contact angle are given in Fig. 3.

In the non-linear time-domain simulation, NORM and TANG are solved in each time step giving the contact pressure distribution, the tangential tractions and the division of the contact zone into stick and slip zones. The stability analysis requires the coupled equations of motion to be linearized around the quasi-static curving condition. In these simulations, the normal contact problem is modelled by the linear normal contact stiffness  $k_n = 1.057$  GN/m corresponding to the slope of the force-displacement curve obtained with NORM at the vertical preload.

For large AoA as considered here, the complete contact zone is in slip at the onset of unstable vibrations. In the limit cycle obtained in the time-domain



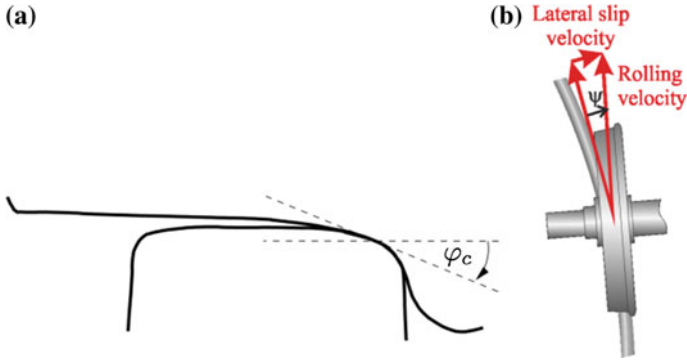


**Fig. 3** Definition of **a** the contact angle  $\varphi_c$  and **b** the angle of attack (AoA)  $\psi$ . The AoA is positive for the shown underradial position of the wheel and negative for an overradial position

simulation, the contact zone changes periodically between full slip and partial slip. As the stability analysis only considers the onset of unstable vibrations, it is sufficient to model full slip in the wheel/rail contact in this numerical approach.

In order to allow for a direct comparison with the frequency-domain approach, time-domain simulations are performed for the linearized wheel/rail system as well.

## 2.2 Solution Procedure

Both squeal models incorporate the wheel, track and contact models described in Sects. 2.1.1–2.1.3. The solution procedure for the linear stability analysis and the time-domain model are briefly described in the following.

### 2.2.1 Linear Stability Analysis

Linear stability is investigated through complex eigenvalue analysis. The homogenous equations of motion of the wheel/rail system are cast into first-order (state-space) form as:

$$\mathbf{A}\dot{\mathbf{z}} + \mathbf{B}\mathbf{z} = \mathbf{0} \quad (2.1a)$$

$$\mathbf{A} = \begin{bmatrix} \mathbf{C} & \mathbf{M} \\ \mathbf{M} & \mathbf{0} \end{bmatrix}, \quad \mathbf{B} = \begin{bmatrix} \mathbf{K} & \mathbf{0} \\ \mathbf{0} & -\mathbf{M} \end{bmatrix}, \quad \mathbf{z} = \begin{bmatrix} \mathbf{q} \\ \dot{\mathbf{q}} \end{bmatrix} \quad (2.1b)$$

where  $\mathbf{q}(t)$  is the modal displacement vector and  $\mathbf{M}$  contains the mass matrices of the wheel and rail.  $\mathbf{C}$  and  $\mathbf{K}$  are the potentially non-symmetric (e.g. caused by the

friction coupling and inertia effects due to rotation) wheel and rail damping and stiffness matrices, respectively. Unstable eigenmodes of the coupled vehicle-track system are indicated by positive real parts of the associated eigenvalues.

### 2.2.2 Time-Domain Model

In the time-domain model, wheel and rail are represented by impulse response functions (Green's functions) that are calculated from the wheel and rail receptances at the contact point by inverse Fourier transform. As the wheel and the rail model incorporate effects of the train speed, the movement of the contact point around the wheel and along the rail is included in the Green's functions. Instead of performing a time integration, the wheel and rail displacements are obtained by convolving the time series of contact forces with the pre-calculated Green's functions. This procedure is relatively computationally efficient. The contact forces are calculated by solving NORM and TANG online in each time step. The detailed solution procedure is described in [21].

## 3 Numerical Results

Dynamic wheel/rail interaction at the inner wheel of the leading wheelset in a C20 bogie during curving on a 120 m radius curve is modelled. The results presented in the following have been calculated for vanishing vehicle speed. The influence of the vehicle speed will be investigated in future work. The frequency range up to 10 kHz is considered.

### 3.1 Linear Stability Analysis

Onset of instability is investigated for varying friction level and direction of the resulting creep force. Eigenvalues that develop positive real parts are outlined in Fig. 4. In the following, the eigenmode associated with the largest magnitude positive real part is referred to as the dominating unstable eigenmode. Instability is predicted from friction coefficient 0.2 and 0.5 upwards for the wheel in a purely underradial ( $\varphi = 90^\circ$ ) and overradial steering position ( $\varphi = 270^\circ$ ), respectively. In addition, Fig. 4 shows the dominating unstable eigenmode to be influenced by the direction of the resulting creep force. For example instability is not predicted for a resulting creep force acting in the longitudinal direction ( $\varphi = 0$  or  $\varphi = 180^\circ$ ) independent of the friction level.

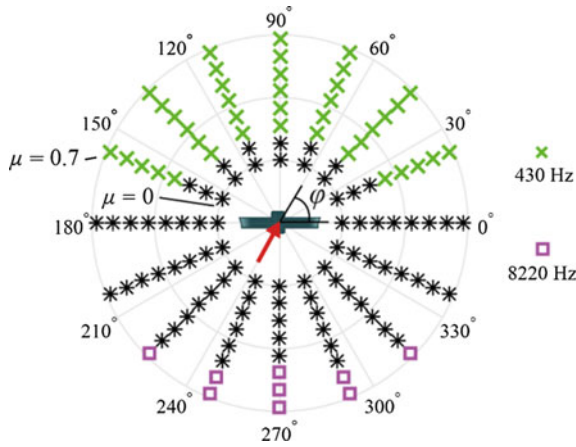


**Fig. 4** Largest magnitude real part of eigenvalues calculated for varying directions of the resulting creep force (acting in angle  $\varphi$  with respect to the vehicle running direction) and a wheel/rail friction coefficient in the range between 0 and 0.7. Unstable modes are outlined with a cross or a square. Black stars correspond to stable conditions

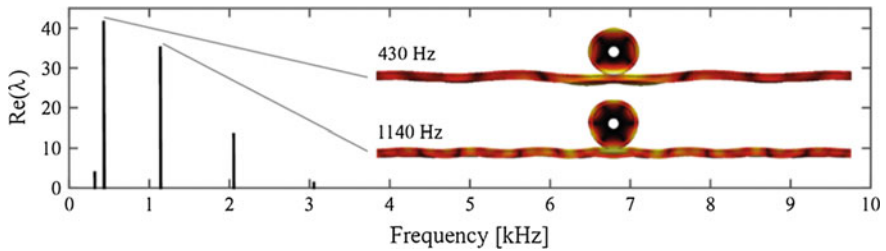


**Fig. 5** Real parts of eigenvalues calculated for  $\varphi = 90^\circ$  and  $\mu = 0.7$ . Eigenmodes associated with the largest magnitude real parts are outlined

The spectrum of the real parts of the eigenvalues calculated for  $\mu = 0.7$  and  $\varphi = 90^\circ$  is shown in Fig. 5. The dominating unstable eigenmode at 430 Hz is found to correspond to a coupled wheel/rail vibration comprising the axial wheel mode with two nodal diameters (and zero nodal circles) and bending of the rail primarily in the lateral direction. The eigenmode corresponding to the peak at eigenfrequency 1140 Hz involves a vibration of the wheel mode with three nodal diameters.

Figure 6 shows the spectrum of the real parts of the eigenvalues calculated for  $\mu = 0.7$  and  $\varphi = 270^\circ$ . Positive real parts result at approximate frequencies 8220 and 9264 Hz, which correspond to axial wheel modes with 10 and 11 nodal diameters, respectively.

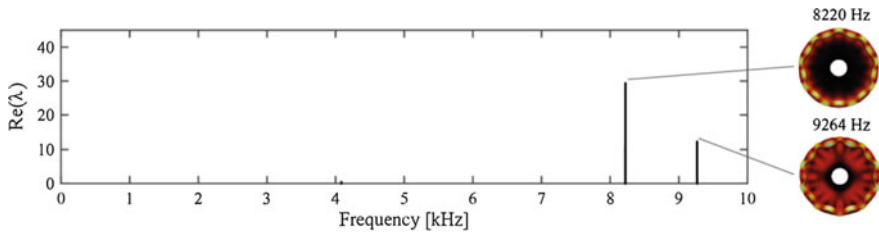


**Fig. 6** Real parts of eigenvalues calculated for  $\varphi = 270^\circ$  and  $\mu = 0.7$ . Eigenmodes associated with positive real parts are outlined. The contribution from the track in the current eigenmodes was found insignificant (not shown here)

### 3.2 Time-Domain Simulations

The calculations for creep force directions  $\varphi = 90^\circ$  and  $\varphi = 270^\circ$  and the friction coefficient  $\mu$  varying from 0.1 to 0.7 have been repeated with the time-domain model both including the linear and the non-linear contact model. A pure lateral creepage with absolute value of 2% has been assumed. The time step is  $1.8 \times 10^{-5}$  s and the spatial resolution in the contact area is 0.25 mm in the longitudinal direction and 1 mm in the lateral direction. The total simulated time is 3.5 s. If squeal occurs in the linear model, the amplitude of the vibration grows to infinity. In the non-linear model, a limit-cycle with finite amplitude is reached, where the contact zone changes periodically between full slip and partial slip.

The results are given in Fig. 7 in terms of the main frequency component in the spectrum of the lateral contact force. For comparison, the corresponding results from the stability analysis are repeated. The power spectra of the lateral contact force obtained for the case  $\mu = 0.7$  and creep force directions  $90^\circ$  and  $270^\circ$  are given in Figs. 8 and 9, respectively.

For the case with the wheel in an underradial steering position shown in Fig. 7a, results obtained from linear time-domain simulations agree with those from the stability analysis in terms of the instability range (i.e. instability from  $\mu = 0.2$  upwards)

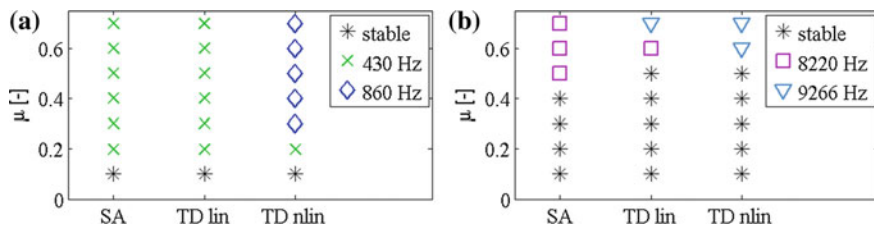


**Fig. 7** Frequency of the largest peak in the lateral contact force spectrum calculated with linear time-domain simulations (TD lin) and non-linear time-domain simulations (TD nlin) in comparison to the frequency belonging to the largest positive real part from the linear stability analysis (SA) for different friction coefficients  $\mu$ : underradial steering position with  $\varphi = 270^\circ$  (a) and overradial steering position with  $\varphi = 90^\circ$  (b)

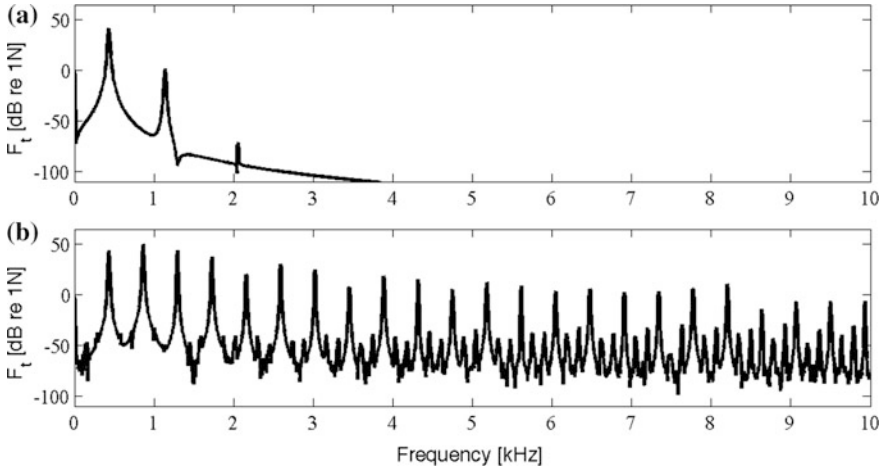


**Fig. 8** Power spectrum of the lateral contact force for  $\varphi = 90^\circ$  and  $\mu = 0.7$  obtained with the linear time-domain model (a) and the non-linear time-domain model (b)

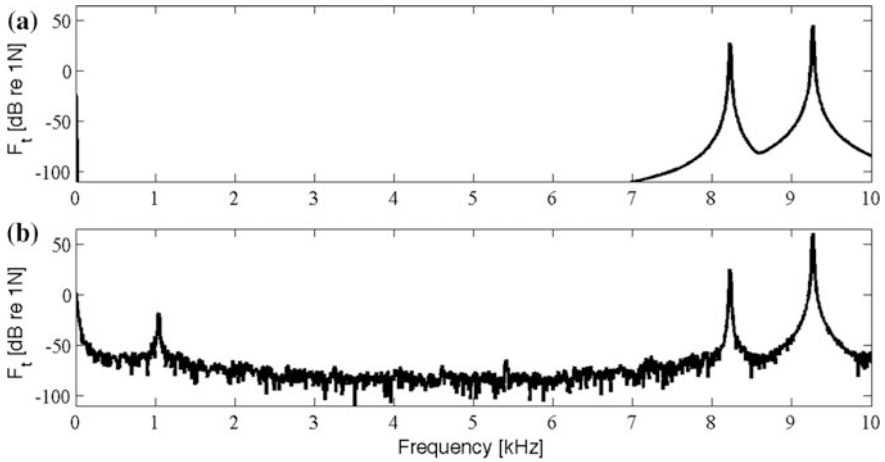


**Fig. 9** Power spectrum of the lateral contact force for  $\varphi = 270^\circ$  and  $\mu = 0.7$  obtained with the linear time-domain model (a) and the non-linear time-domain model (b)

and the main frequency component at 430 Hz. The three peaks in the spectrum of the lateral contact force for  $\mu = 0.7$ , see Fig. 8a, agree with the three largest magnitude real parts of eigenvalues in Fig. 4. The simulations with the non-linear time-domain model still give the same instability range and involve the same mode at 430 Hz, see Fig. 7a, but the spectrum of the lateral contact force now also contains higher harmonics as exemplified in Fig. 8b. The peak magnitude of the second harmonic is observed to exceed that of the fundamental frequency for most cases.

For the case of an overradial steering position shown in Fig. 7b, results from the time-domain simulations are still similar to the stability analysis, but instability initiates at a slightly larger friction coefficient (0.6 instead of 0.5) and the main frequency component shifts from 8220 to 9266 Hz for most squeal cases. A comparison of Figs. 6 and 9 shows that for  $\mu = 0.7$  the same main unstable modes are detected with both models, but the order is reversed.

### 3.3 Discussion

Similar results have been obtained from the linear stability analysis and the linear time-domain simulations. The minor differences in the results are attributed to the remaining modelling differences. Currently, the time-domain model does not, for example, include the longitudinal dynamics of wheel and track, but only the lateral and vertical, while all three directions are included in the stability analysis. Another difference follows from the fact that the first value of the Green's functions in the time-domain model is set to zero. This value describes the instantaneous displacement at excitation by a force at the contact point of the wheel (or rail). By setting the first value of the Green's function to zero in the time-domain approach, the local instantaneous deformation at the contact point is accounted for only in the contact model, while in the linear stability analysis an additional contribution from the structural flexibility of the wheel and rail is included.

Comparing the linear and non-linear time-domain simulations reveals on the one hand the non-linear characteristics of squeal since large magnitude higher-order harmonics may be present, and the dominant frequency may differ between linear and non-linear simulations. On the other hand, for most of the investigated cases, the linear time-domain simulations and the linear stability analysis predict unstable frequencies in agreement with those obtained from non-linear time-domain simulations. In this discussion, it should be kept in mind that the magnitude of the real part of unstable modes in the stability analysis only provides the rate of growth of the instability and is not a selection criterion between different unstable modes.

## 4 Conclusions

In this paper, two different numerical approaches for railway curve squeal have been presented: a model for linear complex stability analysis and a model for non-linear time-domain simulations.

Both squeal models have been applied for conditions similar to those of a 120 m radius curve on the Stockholm metro exposed to severe curve squeal. Results from both models are similar in terms of the instability range in the parameter space and the predicted squeal frequencies. Minor differences can partly be attributed to the different nature of the squeal models and the fact that the magnitude of the real part

of unstable modes in the stability analysis is not a selection criterion between different unstable modes. Another possible reason for the minor differences obtained in squeal predictions are small modelling differences in the squeal models.

## References

1. Thompson, D.: *Railway noise and vibration: Mechanisms, Modelling and Means of Control*. Elsevier, Oxford (2009)
2. Fingberg, U.: A model for wheel-rail squealing noise. *J. Sound Vib.* **143**, 365–377 (1990)
3. Chiello, O., Ayasse, J.-B., Vincent, N., Koch, J.-R.: Curve squeal of urban rolling stock—part 3: theoretical model. *J. Sound Vib.* **293**, 710–727 (2006)
4. Pieringer, A.: A numerical investigation of curve squeal in the case of constant wheel/rail friction. *J. Sound Vib.* **333**(18), 4295–4313 (2014)
5. Fayos, J., Baeza, L., Denia, F.D., Tarancón, J.E.: An Eulerian coordinate-based method for analysing the structural vibrations of a solid of revolution rotating about its main axis. *J. Sound Vib.* **306**(3–5), 618–635 (2007)
6. Pieringer, A., Baeza, L., Kropp, W.: Modelling of railway curve squeal including effects of wheel rotation. In: Nielsen, J.C.O., et al. (eds.) *Noise and Vibration Mitigation for Rail Transportation Systems*, pp. 417–424. Springer, Berlin Heidelberg (2015). (NNFM 126)
7. Martínez-Casas, J., Mazzola, L., Baeza, L., Bruni, S.: Numerical estimation of stresses in railway axles using train-track interaction model. *Int. J. Fatigue* **47**, 18–30 (2013)
8. Andersson, C.: *Modelling and simulation of train-track interaction including wear prediction*. Ph.D. thesis, Department of Applied Mechanics, Chalmers University of Technology, Göteborg, Sweden (2003)
9. Nilsson, C.-M., Jones, C.J.C., Thompson, D.J., Ryue, J.: A waveguide finite element and boundary element approach to calculating the sound radiated by railway and tram rails. *J. Sound Vib.* **321**, 813–836 (2009)
10. Koh, C.G., Ong, J.S.Y., Chua, D.K.H., Feng, J.: Moving element method for train-track dynamics. *Int. J. Numer. Meth. Eng.* **56**(11), 1549–1567 (2003)
11. Rudd, M.J.: Wheel/rail noise - part II: wheel squeal. *J. Sound Vib.* **46**(3), 381–394 (1976)
12. Hoffmann, N., Fischer, M., Allgaier, R., Gaul, L.: A minimal model for studying properties of the mode-coupling type instability in friction induced oscillations. *Mech. Res. Commun.* **29**(4), 197–205 (2002)
13. Heckl, M.A.: Curve squeal of train wheels, part 2: which wheel modes are prone to squeal? *J. Sound Vib.* **229**(3), 695–707 (2000)
14. de Beer, F.G., Janssens, M.H.A., Kooijman, P.P.: Squeal noise of rail-bound vehicles influenced by lateral contact position. *J. Sound Vib.* **267**, 497–507 (2003)
15. Squicciarini, G., Usberti, S., Thompson, D.J., Corradi, R., Barbera, A.: Curve squeal in the presence of two wheel/rail contact points. In: Nielsen, J.C.O., et al. (eds.) *Noise and Vibration Mitigation for Rail Transportation Systems*, pp. 603–610. Springer, Berlin Heidelberg (2015). (NNFM 126)
16. Glocker, Ch., Cataldi-Spinola, E., Leine, R.I.: Curve squealing of trains: measurements, modelling and simulation. *J. Sound Vib.* **324**, 365–386 (2009)
17. Torstensson, P.T., Pieringer, A., Baeza, L.: Towards a model for prediction of railway tread brake noise. In: *The ISMA Conference on Noise and Vibration Engineering (ISMA 2014)*, Leuven, Belgium, 3543–3556 (2014)
18. Pieringer, A., Torstensson, P.T., Giner, J.: Curve squeal of rail vehicles: linear stability analysis and non-linear time-domain simulation. In: Pombo, J. (ed.) *Proceedings of the Third International Conference on Railway Technology: Research, Development and Maintenance*. Civil-Comp Press, Stirlingshire, Scotland (2016)

19. Torstensson, P.T., Nielsen, J.C.O.: Monitoring of rail corrugation growth due to irregular wear on a railway metro curve. *Wear* **267**(1–4), 556–561 (2009)
20. Kalker, J.J.: *Three-Dimensional Elastic Bodies in Rolling Contact*. Kluwer Academic Publishers, Dordrecht (1990)
21. Pieringer, A.: *Time-domain modelling of high-frequency wheel/rail interaction*. Ph.D. thesis, Department of Civil and Environmental Engineering, Chalmers University of Technology, Göteborg, Sweden (2011)
22. Torstensson, P.T.: *Rail corrugation growth on curves*. Ph.D. thesis, Department of Applied Mechanics, Chalmers University of Technology, Göteborg, Sweden, 2012



**Part II**  
**Policy, Regulation and Perception**

# State of the Art Review of Rail Noise Policy



**B. E. Croft and B. Hemsworth**

**Abstract** For many rail noise practitioners, “rail noise policy” is synonymous with “noise limits” or numerical criteria to be applied in various situations. In this context, the task of reviewing rail noise policies around the world might be simplistically reduced to tables and lists of numbers. However, the intention of this state of the art review is to address the broader policy picture. This has as much to do with how (and why) rail noise is managed and regulated, and how rail noise reduction is achieved, as it does with limits and criteria. This paper describes the strategic approach taken by rail networks and regulatory authorities in managing rail noise internationally. It includes review of policies, and the instruments through which regulations are implemented (including noise criteria, limits, access charges etc.). The geographic scope of the review primarily encompasses Europe, North America and Australia, with some limited discussion of other areas. The paper considers how noise policy is applied in a range of contexts, such as new rail projects, upgraded/expanded rail projects, developments near railways, new/upgraded rolling stock, and existing rail operations (including noise abatement). In each geographical region, the key existing and historical rail noise issues are discussed, to understand why particular policies and approaches have been developed, and how effective those policies have been. The outlook for future rail noise policies around the world is also considered.

---

B. E. Croft (✉)

SLR Consulting (Canada), 1620 West 8th Avenue, Vancouver, BC, Canada  
e-mail: bcroft@slrconsulting.com

B. Hemsworth

Brian Hemsworth Noise Consultant LLP,  
16 Whistlestop Close Mickleover, Derby DE3 9DA, UK

## 1 Introduction

A number of rail noise policy reviews have been compiled over recent years. Many have concentrated on the European context [1–3]—this is partly because the European Union focus on research and development has led the rest of the world in this area. In addition, Europe has seen recent significant changes in approaches to rail noise policy, such as the introduction of Technical Specifications for Interoperability (TSI's) [4] and the Environmental Noise Directive (END) [5].

This review aims to take a more international perspective, and to consider the differences between geographical regions in approaches to rail noise policy. The scope of the review primarily encompasses Europe, North America and Australia, with some discussion of other areas where possible within the limitations of the experience of the authors.

Many agencies around the world will review the practices of other jurisdictions when they are developing their own policies. As a consultant, it is common to be tasked with summarizing the approaches applied elsewhere, when a particular local issue is to be addressed in the development of guidelines or criteria for rail noise. A comprehensive review of worldwide noise policies and regulations was prepared by the International Institute of Noise Control Engineering (INCE) in 2009 [6], which includes tables identifying parameters and numeric criteria that are applied in various locations and circumstances to define an acceptable level of rail noise and noise from other sources. Rather than generating a list of numerical railway noise criteria, the objective of this particular paper is to consider a broader policy picture. This has as much to do with how (and why) rail noise is managed and regulated, and how rail noise reduction is achieved, as it does with limits and criteria. In particular, this review considers which regional factors might affect the development of constructive rail noise policies. To develop effective policies, it is important first to define the objectives of the policy, and the reasons guidelines are needed.

The structure of this paper is firstly to examine the reasons for introducing regulation of noise emitted by railways. Different policy instruments and approaches to manage rail noise are then discussed. Recent policy developments are reviewed on a geographic basis to identify approaches used around the world, which policies have been found to be effective, and also which factors act as constraints or barriers to effective policy development. Finally, potential future policy directions are identified.

## 2 Background

### 2.1 *The Introduction of General Noise Regulations*

Environmental noise regulation in most countries started with general noise control acts rather than any railway specific policies. Legislation started to appear in the

1970s, initially to control the noise emitted by road traffic and aircraft [6]. Often, noise from other transportation noise sources was targeted for regulation before noise from railways. In several jurisdictions railway vehicles have been omitted or excluded from general environmental noise regulations applicable to other sources—for example this is typically the case in Australia [7–9]. Conversely, in the US, noise from freight rail vehicles was included with other sources in regulations “to promote an environment for all Americans free from noise that jeopardizes their health or welfare” [10].

## ***2.2 Reasons to Promote Expansion of Railways***

Railways are recognised as being an efficient and environmentally sustainable mode of transport. According to the International Energy Agency (IEA) and the International Union of Railways (UIC) [11], “the transport sector was responsible for 23.1% of global CO<sub>2</sub> emissions in 2012. 3.6% of transport emissions were due to the rail sector, while railways transported over 8% of the world’s passengers and goods.” As of 2012, road transport held 31.3% of combined passenger and freight modal share, shipping held 56.8% and aviation 3.7%. Increasing the proportion of movement of both people and freight by rail is desirable to reduce CO<sub>2</sub> emissions from road traffic and aviation, and to reduce dependence on oil. To this end, the 2011 European Commission Transportation White Paper [12] calls for completion of a European high-speed rail network by 2050, in addition to shifting 50% of long distance road freight (over 300 km) onto rail or waterborne transport by 2050. Transportation planning approaches elsewhere in the world similarly aim to create modal shifts to rail.

With environmental and economic reasons to promote railways in mind, it is understandable that rail operators might argue that restricting noise from railways may be counter-productive. Surely the benefits of railways outweigh the disadvantages, and noise impacts to a relatively small proportion of the population are a small price to pay? A common refrain is “the railway has been here for over a hundred years, it was here first, what right do nearby residents have to complain?” Despite the many reasons to promote increasing use of rail, concerns around harmful effects of noise are increasing all the time. Increasing population density and traffic growth are causing complaints about noise from existing lines—what was once a bearable impact of a few trains passing each day is increasingly severe. It is evident that effective policies are required to balance adverse noise impacts against the benefits of railways to wider society.

## ***2.3 Responsibility for Railway Noise***

Responsibility for regulating or managing noise from railways varies, see [6] for a comprehensive global summary.

In Europe, while some aspects of noise control policy are managed on a national level, the European Union is also able to enact policies that affect railway noise across international borders.

In America, the Noise Control Act of 1972 [10] stated “that while primary responsibility for control of noise rests with State and local governments, Federal action is essential to deal with major noise sources in commerce, control of which require national uniformity of treatment”. Thus, the US Noise Control Act required the development of railroad noise emission standards, which were prepared by the federal Environment Protection Agency and published in 1974 [13]. However, these standards applied specifically to freight, not to transit or electric passenger services. Transit system noise is controlled by district policy and design criteria, but transit projects will generally follow federal guidelines, particularly if some funding is from the federal government. Canada has followed a similar reasoning, with noise from freight railways being federally regulated [14], even though noise from other sources is treated on a provincial level.

The federal or central government is also responsible for railway noise policy in Korea and Japan [6].

In Australia, responsibility for railway noise lies at the state level of government. This leads to differences in approaches between states—some states take an active role in managing railway noise emissions while others effectively do not restrict railway noise emissions. Similarly in South Africa, while national noise control regulations exist [15], legislative responsibility for administering the regulations has devolved to provincial and local authorities.

## ***2.4 Sources of Railway Noise***

Thompson [16] summarises the various sources of railway noise including rolling noise; curve squeal; bridge noise; aerodynamic noise; ground vibration and ground-borne noise; traction noise (including diesel engines); warning signals (on trains and fixed installations); track maintenance equipment; and shunting noise. While almost all of these noise sources exist on railways worldwide, their relative importance varies considerably with geographic location.

### **2.4.1 Factors Contributing to Geographic Variation in Railway Noise Sources**

Two of the key factors contributing to geographic variation in the relative importance of different railway noise sources are the proportion of electrified tracks, and the typical speed of trains. Worldwide, over 30% of track kilometers are electrified, but the national share of electrified tracks varies considerably (Fig. 1, from [11]). Italy and Korea have the highest proportions of electrified track at over 70%. Europe, Russia and Japan also have a high level of electrification, above 60% of all

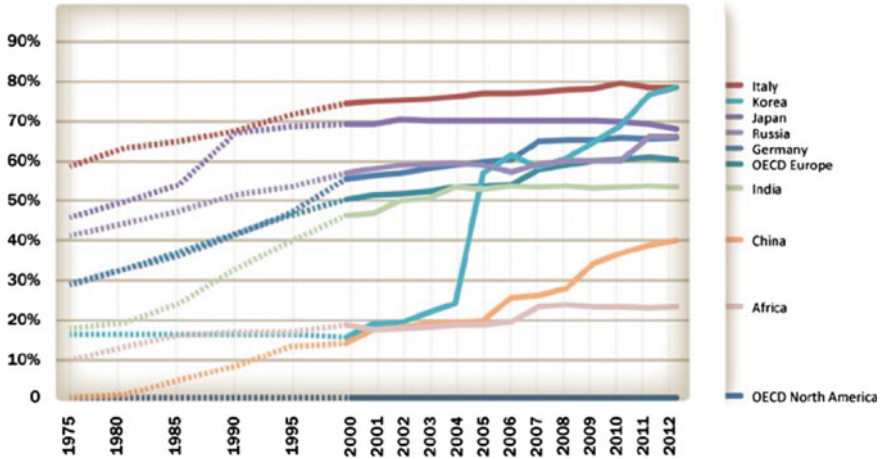


Fig. 1 Share of electrified railway tracks over time for selected countries. Reproduced from [11]

track kilometers. North America has clearly the lowest proportion of electrified tracks. Australian data is not shown in Fig. 1, but there around 10% of all open track kilometers are electrified [17].

In relation to speeds, “low” speeds below 130 km/h are relatively common on freight and intercity lines in North America and Australia, and on suburban, metro or transit rail systems. “Moderate” speeds up to about 200 km/h are common in Europe and parts of Asia. High speed trains >200 km/h are most common in Europe and Asia.

### 2.4.2 Overview of Potential Geographic Variation in Railway Noise Sources

Rolling noise is present on all conventional railways and non-magnetically levitated (maglev) high speed railways. Since it is proportional to speed, it is often the dominant noise source for conventional electrified railways. Rolling noise is a key issue in Europe and parts of Asia where typical speeds are moderate to high and the majority of traffic operates on electrified tracks. Elsewhere, rolling noise is present but other noise sources may be more important in some circumstances.

Aerodynamic noise is only an issue in those areas with high speed trains, and even then only for the upper end of the speed range when it takes over from rolling noise as the dominant contributor to the overall level.

Curve squeal is a localized issue and not directly restricted geographically. However, curve squeal is not commonly a concern on intercity or freight lines with moderate to high speeds, since increased speeds require larger radius curves and the likelihood of curve squeal is increased for smaller radius curves. This means that in addition to metro or transit systems worldwide, curve squeal is likely to be a

particular issue in Australia and North America, where lower typical speeds are sometimes related to winding routes with tighter radius curves.

Traction noise, while present at low levels everywhere, is a particularly important issue for non-electrified networks. In much of Europe and parts of Asia, the noise from diesel locomotives is largely irrelevant, while in North America and Australia it is a key cause of complaints. The lower typical speeds of trains in these areas compound this issue, since the noise source is not speed dependent and so a slower speed means the noise is present for a longer time.

Warning signals include train horns as well as warning bells on active level crossings. While safety rules vary from country to country, in general train horns are required to be sounded on approach to all passive level crossings. Grade separated crossings do not require warning signals. Requirements to sound horns on approach to active level crossings vary, but generally less horn sounding is required for active level crossings than for passive level crossings. This means that the importance of this type of noise is relative to the proportion of grade separated crossings, and also the proportion of active and passive level crossings. Geographic differences may therefore be expected in the prevalence of annoyance related to this type of noise. Horn noise is an important issue in America [18] and Canada [19], and also in Australia despite being alleviated in some areas through noise pollution reduction programs [20]. Figure 2 (from [18]) illustrates the importance of this noise issue, with operation of a freight line through an urban area. North American train operating rules require horns to be sounded for 15 s on approach to each crossing, in a repeated or prolonged pattern of short and long blasts, generating maximum noise levels between 96 and 110 dBA at 100 feet (30 m) in front of the locomotive [21]. Since freight lines operate on a 24 h basis, noise complaints from nearby residents are understandable.

Shunting noise is another localized issue that is not directly restricted geographically. Shunting noise is only a concern where freight rail yards are located in close proximity to residential areas. Geographic differences in importance might be expected depending on historical land-use planning differences, and also the timeframe of rail yard planning and construction. Older railyards may not have been designed with noise control in mind, or residential land uses may have encroached over time. For example, in Canada much of the freight rail infrastructure pre-dates noise policies, and guidelines for new residential developments near rail lines have been introduced relatively recently [22]. Shunting noise remains a cause of complaint near many existing rail yards.

## ***2.5 Treatment of Railways Relative to Other Noise Sources***

As previously mentioned, railways are sometimes excluded from general environmental noise control legislation. Where this is the case, guidelines or policies for rail noise management may still be implemented outside of general noise control policies,

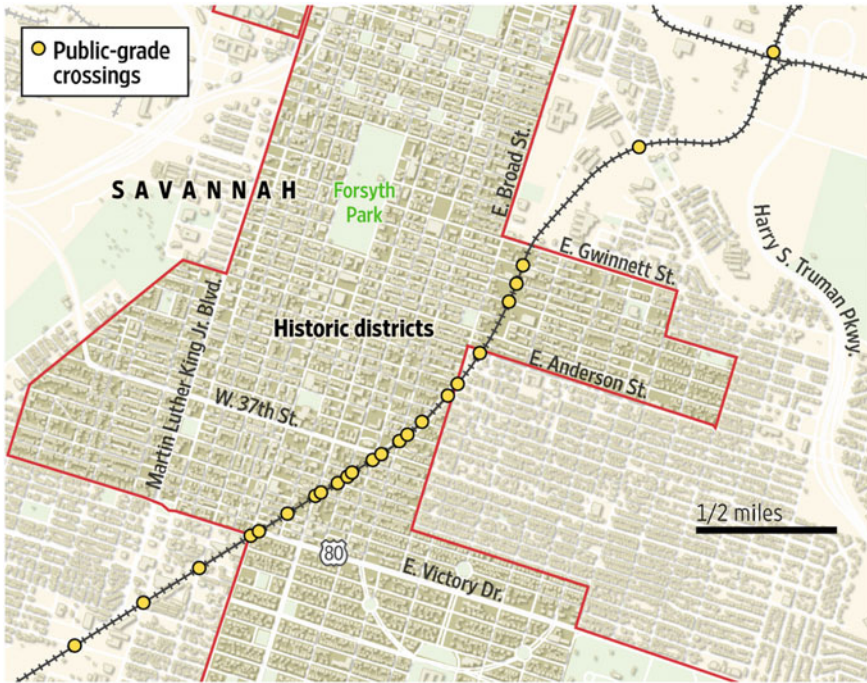


**Fig. 2** Required horn sounding locations on freight line through Savannah, Georgia (USA). Reproduced from [18]

with an option to treat railway noise differently to noise from other sources. A common justification for treating railway noise differently is research into annoyance.

The International Union of Railways (UIC) published a comprehensive review of the so-called “railway noise bonus” or Noise Annoyance Correction Factor (NACF) in 2010 [23]. They conclude that “there is a large amount of evidence that the NACF assumes values of 5 dB or more for the majority of common noise exposure levels. Only for very low levels, the NACF may approach to zero.” Reduced annoyance due to railway noise relative to road traffic noise at the same  $L_{den}$  level is particularly applicable to “general annoyance”, with more uncertainty in relation to sleep disturbance and health effects.

International Standard ISO 1996-1:2016 [24] also includes informative annexes relating to the prevalence of a population to be highly annoyed by noise from various sources, using the community tolerance level (CTL) formulation from Schomer et al. [25] and a regression formulation from Miedema and Oudshoorn [26]. The regression formulation does not attempt to distinguish differences between different train types. The CTL formulation divides trains into “low” and “high” vibration conventional rail, on the basis of perceptible vibration or rattles



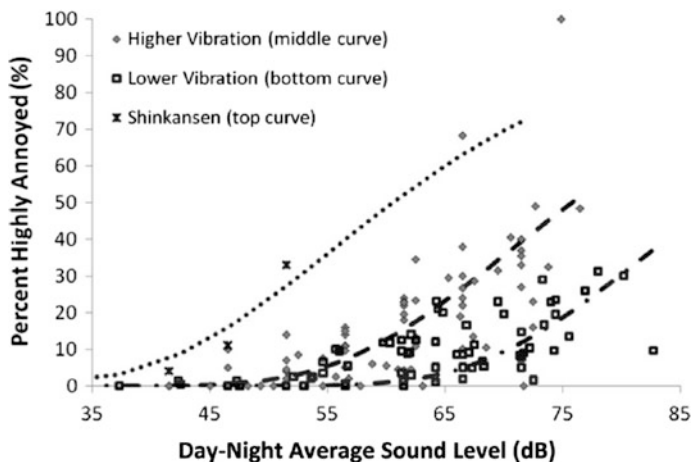


**Fig. 3** Effective loudness functions overlaid on corresponding rail noise survey data. Reproduced from [25]

being identified as important in the original surveys on annoyance due to rail noise. In [24], “low vibration” is defined to include only conventional electric passenger trains operating on vibration-isolated track or on ground that is not conducive to vibration propagation. All other conventional (i.e. not high-speed) rail types are categorized as “high vibration”. Using the CTL approach, high annoyance due to noise from low vibration railways is thought to occur at a level almost 10 dB higher than high annoyance due to road traffic noise. For high vibration railways, high annoyance occurs at lower noise levels than road traffic, by 2.5 dB.

The databases of conventional railway annoyance studies referenced in the ISO 1996-1:2016 annex are based on European and Japanese studies. Data referenced in the studies as originating from North America and Australia relates only to road traffic or aircraft noise, not to railways. Europe and Japan operate the highest proportion of electrified railways in the world [11]. Therefore, annoyance due to noise associated with diesel freight trains or other noise sources such as curve squeal may not be well represented even by the “high vibration” categories in ISO 1996-1. High speed trains are also excluded from the ISO 1996-1 standard, except for a note that the difference in community tolerance level to high speed railway relative to road traffic noise can be severe (i.e., more annoyance may be caused by high speed railways than conventional railways or roads). The variation in annoyance between low and high vibration conventional trains, and high speed trains (Shinkasen) is illustrated in Fig. 3, reproduced from [25].

### 3 Approaches to Rail Noise Management

Noise policies and guidelines are a tool for governments to manage noise impacts, and to balance the benefits of railways against their impacts. For the purpose of this discussion, policies relating to railway noise can be broadly introduced in five main categories: emission limits on individual vehicles, operator incentives, impact assessment limits on received noise levels (for rail infrastructure projects), land use planning controls, noise abatement programs (for existing rail infrastructure) and population-wide targets.

#### 3.1 *Noise Limits on Individual Rail Vehicles*

The introduction of noise limits applicable to individual rail vehicles was initiated first in America, where the prevalence of diesel powered freight trains contributed to a noise issue that has not much affected many other parts of the world where electric freight trains are commonly used. The American Environment Protection Agency (US EPA) published noise emission standards in 1974 [13] that identified limits on noise from freight trains, with A-weighted criteria for stationary and moving scenarios, as well as limits on noise from rail yard operations such as coupling noise and rail retarders. In relation to locomotives, more stringent limits for newly manufactured trains were phased in over several years, with the requirements for locomotives manufactured after 31 December 1979 remaining in place to this day. Electric passenger trains were excluded, and curving noise was not addressed.

In Australia, diesel freight trains are prevalent. Locomotive noise limits have been applicable to new diesel freight locomotives introduced to the NSW rail network since the late 1980s [27], but elsewhere in Australia no limits apply to this noise source.

In Europe, limits on the noise produced by individual rail vehicles were introduced much later in 2002 in the form of Technical Specifications for Interoperability (TSIs). Since noise from a new electric railway depends strongly on the design of the track as well as the design of the vehicle, restricting noise from electric rolling stock requires some effort over and above simply specifying a maximum rolling stock noise level for acceptance. The TSI approach has been an important step in overcoming this issue. The current TSIs were released in 2014 [4].

Outside of Europe, there remain very few restrictions on the noise from individual electric rail vehicles. Noise impacts are assessed when required under planning regulations, and noise limits for individual vehicles can be specified at the procurement stage of new projects.

### **3.2 *Incentives to Reduce Noise***

Noise-differentiated track access charges (NDTACs) are an alternative to implementing noise limits on individual vehicles, since they provide an incentive for rail operators to minimise their noise emissions. The concept of NDTACs was developed in Europe to address the higher noise levels generated by freight wagons with cast-iron brake blocks, to encourage retrofitting of existing wagons with composite brake blocks known to reduce wheel roughness and hence rolling noise levels by around 10 dB.

A framework for harmonizing NDTACs has been agreed, but remains voluntary despite a European Commission (EC) proposal for mandatory introduction of noise-differentiated track access charges [3]. According to [28] uptake of the voluntary measures has been slow, with only Germany and the Netherlands introducing comprehensive NDTAC schemes. For EU countries that choose to implement NDTAC, the agreed framework requires either a bonus or reduced charges for quiet wagons. It also includes an option to penalise or apply a surcharge to non TSI-compliant wagons from 2021.

As a further incentive to quiet freight trains in the EU, public funding is also made available to compensate operators for the cost of retro-fitting noisy freight wagons. It is thought that placing a time limit on the availability of financial compensation (up to 2021) in addition to the potential for surcharges after this date will incentivise earlier retro-fitting of wagons by operators [28].

NDTACs have not been implemented outside of Europe, perhaps because the issue of noisy freight wagons due to cast-iron brake blocks is not important elsewhere. However, the principal could be applied to other noise sources. A reduction in diesel locomotive noise emissions could potentially be incentivised under similar a similar policy approach to that adopted in Europe for rolling noise.

### **3.3 *Impact Assessment Noise Limits at Receiver Locations***

In comparison to the relative lack of noise limits applicable to rail vehicles, noise limits applicable at receiver locations have been introduced in many jurisdictions, as summarised in [6]. These limits have typically been introduced to address the introduction of new rail lines or changes to existing situations. These “impact assessment” criteria enable a structured approach to the provision of noise mitigation, in the event that pre-defined acceptable noise levels are exceeded.

This type of regulation is one of the most common means of rail noise management. Historically, there are many countries where railways have been operating for decades. Any change to the status quo with the potential to impact on previously unaffected populations has the potential to cause concern, and including mitigation measures in the design of new rail projects is an effective means to control impacts within acceptable levels.

### ***3.4 Land Use Planning Controls***

Land use planning controls here is used to refer to conditions that are placed on new developments near existing railway corridors. Examples of this type of guideline are found in Australia, e.g. [29], and in Canada [22].

As stated in [22], “As cities in Canada continue to urbanize, and as they place a greater emphasis on curbing urban sprawl, demand for new forms of infill development is growing, including on sites in proximity to railway corridors. In particular, commercial and industrial properties in proximity to railway operations, and in some cases the buildings situated on those properties, are increasingly being converted to residential uses. At the same time, both the passenger and freight operations of railways are growing steadily, leading to an increasing potential for conflicts between rail operations and adjacent land uses.”

Other examples of this type of regulation can be found worldwide in standards and building codes, which commonly define acceptable internal noise levels for new dwellings.

### ***3.5 Noise Abatement Programs***

Noise abatement programs target existing noise hotspots. Abatement programs are a policy instrument that aims to bridge the gap between infrastructure environmental impact assessment limits and land use planning policies. In a situation where growth in rail traffic (particularly freight traffic) is increasing over time, existing residential areas located near rail lines are increasingly subjected to noise that is well above desirable levels, and that would be considered unacceptable if either the rail line or the residences were newly proposed.

An example of a noise abatement program applied to freight rail is the NSW Freight Noise Attenuation Program [30]. This program offers building treatments to eligible individual noise-affected older properties, and is additional to programs targeting noise at source and noise related to new developments. The program uses an LAeq based eligibility criterion, then prioritises treatment for locations that are subject to curve squeal noise, excessive diesel freight locomotive noise and high numbers of night-time noise events. The treatment is free to long-term owners, or cost-sharing is applied if the owner has held the property for less than seven years.

### ***3.6 Population-Based Targets***

The generally increasing awareness of the health impacts and cost to society of noise exposure is also driving population-based targets and approaches to noise management. These policies are not rail-specific, but railway noise is a component of the wider picture.

The World Health Organisation (WHO) has led the way with population based targets, including the 1999 Guidelines for Community Noise [31] and the 2009 Night Noise Guidelines for Europe [32].

In Europe, the END [4] requires member states to prepare and publish (every 5 years) noise maps and noise management action plans for cities, and for major transportation noise sources including roads, railways and airports. The END itself does not set limit or target values for noise, nor does it prescribe measures to be included in action plans, leaving these up to the discretion of member states. The END noise mapping process enables large-scale reviews of the number of people affected by noise in Europe, and the implications for the health and well-being of populations [33]. Planning and public health departments elsewhere in the world are starting to follow the lead of the EU, particularly on city noise mapping, including in Australia [34] and North America [35].

## 4 Recent Geographic Developments and Future Directions

This section aims to provide a high-level overview of recent and proposed rail noise policy developments around the world. The policy developments and geographic regions discussed are not a comprehensive list—the intention is to provide examples of policy trends, and to highlight changes that have been implemented since the more comprehensive INCE review [6].

### 4.1 Asia

In Korea, the LAeq based management standards for noise were revised in 2010, to reduce the night-time noise goal at residential and other noise-sensitive land uses to 60 dBA. In 2015, additional consideration of the LMax parameter was adopted in circumstances with less than 30 train passbys per day. The new approach requires measured noise levels to be corrected, based on the difference between the maximum noise level of train passbys and the background noise level. It is understood the change was triggered by community complaints related to maximum noise level [36].

In Japan, specific limits for high speed (Shinkasen) and conventional trains have been in place for many years and have not changed recently. A LMax (slow response) criterion for noise from Shinkasen was introduced in 1975. For conventional railways a LAeq approach has been applied since 1995 [6]. It is interesting that the historically different approach to noise limits for high-speed and conventional trains is complementary to the finding of increased annoyance due to Shinkasen trains at the same day-night average sound level (see Fig. 3).

## 4.2 *Australia*

Several Australian states have either introduced new rail noise policies recently, or are in the process of developing new policies.

In Western Australia, the State Planning Policy addressing rail noise [37] is currently under review and a revised policy is expected towards the end of 2016. It is understood that the triggers for the current review include:

- Increasing urban in-fill resulting in more people living within close proximity to existing railways.
- Increasing complaints about noise and vibration from nearby residents.
- Increase in sleep disturbance due to freight train movements at night or early in the morning.
- Greater concern about sleep disturbance and related health impacts.
- Greater expectations of the public that the government will ensure houses are not subject to excessive noise levels from trains.

In Queensland, a statewide noise map is being developed to support planning policies. Under the Queensland Development Code, new residential buildings in transportation corridors are required to be designed and constructed to mitigate transport noise impacts [38]. Large scale noise modelling and mapping for both road and rail networks allows noise categories to be developed based on predicted noise exposure levels to streamline the planning process.

Rail noise policy in NSW is a combination of several complementary approaches, including limits on noise applicable to new freight locomotives, limits at receivers and a freight noise abatement program as previously described. A detailed summary of historical, current and proposed regulatory approaches is provided in [27]. Since freight train noise is a key issue in NSW, regulatory reforms are currently being developed that will recognise the contribution of both rolling stock operators and infrastructure/systems operators to overall noise, and facilitate noise mitigation measures for issues such as curve squeal that require a joint effort to be resolved [39].

## 4.3 *Europe*

The recent UIC State of the Art Report [3] provides a summary of EU policy and legislation relating to rail transport noise in Europe. Here, there is a sense that the fundamental sources of railway noise are now well understood. Rolling noise is by far the most significant issue, and the challenge in managing this issue has become one of implementation—in particular, how to implement a shift to all freight trains using quieter brake blocks. National approaches within the EU show a variety of approaches, the following examples are described in [3]:

- Italy has legislation requiring 7% of the annual track maintenance budget to be spent on noise mitigation.
- Germany spends 150 million Euro each year on noise abatement, and intends to reduce perceived noise levels by half (−10 dB) by 2020.
- Germany, the Netherlands and Switzerland are collaborating on NDTACs.
- Belgium has focused on track acoustic roughness, introducing a monitoring process and corrective grinding program to maintain noise below reasonable limit values.
- The Netherlands has commenced a noise mitigation operation, expected to be implemented by 2023. It will include 540 km of rail dampers, 140 km of barriers (120 km of these will be higher than 7 m), and treatments to 3000 dwellings. They have also introduced a system of noise ceilings around the whole network, based on the actual noise levels from 2005 to 2007. Future actual noise levels are not permitted to exceed the ceiling levels.
- Switzerland completed retro-fitting all freight wagons in its fleet with “quiet” brake blocks in 2015, and has introduced legislation to ban freight vehicles that do not meet the TSI limits by 2020.
- The Austrian network now incorporates 850 km of noise barriers and has had a “noise renovation program” in place since 1993 to treat dwellings, with an estimated total cost of 800 million Euro.

While national initiatives such as these have been effective, they are limited in that the majority will only address noise from the freight wagons registered to a particular country, or operating on a particular network [3].

The European Commission has identified in [28] that there is a risk that excessive levels of railway noise can lead to “uncoordinated unilateral actions by Member States along the most important European rail corridors. These unilateral actions could take the form of national restrictions on rail freight traffic, in particular speed restrictions and restrictions on operating at certain times, especially at night. As freight trains operate mostly at night, such measures would likely result in bottlenecks which, in turn, would have adverse effects on European economies and the railway sector. Furthermore, the restrictions would doubtless lead to a reverse modal shift from rail to road, with a related increase in negative economic, environmental and social impacts.” Both Germany and Switzerland have announced their intention to ban vehicles that do not meet the TSI limits in coming years—Switzerland from 1 January 2020, and Germany after the end of 2020.

In Europe, there is a balancing act between protecting citizens from excessive railway noise while keeping the railway sector competitive and acceptable in terms of public perception. There is also a challenge to develop joint, consistent regulations across the EU members, so that the principles of interoperability and the open market can be achieved.

In 2015, revisions to Annex II of the END were introduced to define common EU methods for calculating exposure to different noise levels [40]. The common methods comprise a set of formulas and coefficients to be used to calculate noise levels at the facade of the buildings, including noise from railways. The

implications for railways are expected to particularly relate to modelling and prediction requirements to consider railhead roughness, rail pad stiffness, track base, rail joints and the radius of curvature of the track. The common approaches may give rise to assessment differences in future noise mapping rounds.

In future, Annex III of the END will describe common methods for calculating the burden of disease caused by exposure to specific noise levels. The methods will include dose-effect relations for a set of health endpoints such as cardiovascular disease, annoyance and sleep disturbance [41]. This revision will follow the current review of the health effects of noise that is being performed by the WHO. The WHO is currently working on revised Community Noise Guidelines for Europe, which are expected to present state-of-the-art evidence on the health effects of noise and updated recommendations on acceptable exposure levels. The guidelines will assess several environmental noise sources, including rail, and will also consider specific settings such as residences and other sensitive land uses. In addition, the guidelines will review the evidence on health benefits from noise mitigation and interventions to decrease noise levels [42].

#### ***4.4 North America***

A recent policy development in America was the development of a guidance document for noise and vibration impacts from high speed rail, released in 2012 [43]. This document addresses noise from high-speed trains using both traditional steel-wheel on steel-rail technologies and from maglev systems, with speeds from 90 to 250 mph (145–400 km/h). This manual is intended to promote consideration of high speed rail options, and complements the existing guideline addressing conventional train speeds [44].

In Canada, collaboration between railway operators and municipalities has led to the development of updated guidelines for planning new residential developments near railway operations [22]. These “proximity” guidelines address safety issues in addition to noise.

### **5 Constraints and Challenges to Effective Policy**

The fundamental objectives of rail noise policies are to benefit society. The environmental noise generated by railways is both a health issue, and a quality of life issue, and there is increasing evidence from European studies that these are related. People who are annoyed by noise over long periods of time may eventually experience more serious effects. On a population level, the burden of these long term noise effects on society is beginning to be quantified, and used as justification for addressing noise issues [45].



There are also political objectives to rail noise policy. Complaints about railway noise are a political issue—it is important that communities that are exposed to noise are treated fairly, and the policies applied are perceived to be reasonable and appropriate. There are many examples of projects or situations where communities perceive that the noise limits and criteria being applied do not adequately reflect their individual experience. For example, the use of the term “railway noise bonus” to describe railway noise annoyance correction factors was not perceived well by residents along noisy railway lines [23]. In Australia and North America, explaining the noise impact of projects involving freight trains operating at night in terms of their “average” noise (LAeq) can be difficult. Even more challenging is explaining to a sleepless resident that for safety reasons the rail operator has no responsibility to mitigate the impacts of noise from locomotive horns. Regulators and policy makers are constantly required to balance opposing factors with a view to the overall benefit to society of a sustainable mode of transport. This section discusses some key constraints and challenges to the development and implementation of effective rail noise policies.

## ***5.1 Technical Factors***

Railway noise is a technical specialty even within the more general discipline of acoustics. As described in Sect. 2.4, understanding the sources of railway noise is an important factor in developing meaningful policies and guidelines. To a railway acoustic specialist, the influence of rail acoustic roughness, track decay rate and rail dampers are key factors in policies to control rolling noise. These factors may not be familiar to other acousticians, let alone to policymakers, local government planners or the general population.

Another example of the challenges associated with technical factors is the challenge of addressing the potential for sleep disturbance due to individual high noise events. Most building codes and planning requirements for new residential buildings specify internal LAeq night-time noise levels, while awakening reactions may be better correlated to the maximum noise level or the typically short rise time for railway noise events [46].

## ***5.2 Geographic Factors***

As discussed in Sect. 2.4, the railway noise issues requiring control through policy instruments are not the same everywhere. Europe is focused on rolling noise and policies to implement retrofitting of composite brake blocks to freight wagons. In Asia, the rapid progress in construction of high speed train lines means the focus is on both aerodynamic noise and rolling noise. In Australia and North America, many complaints relate to diesel locomotive noise, horn noise, shunting noise and

curve squeal, in addition to rolling noise from electrified transit systems. Rolling noise from slow freight trains is relatively low on the priority list. The widely applied databases of conventional railway annoyance studies are derived from European and Japanese studies, so their applicability to projects involving curve squeal or diesel freight locomotives may be questioned.

To be effective, policies need to be tailored to the key issues in the region—while awareness of the approaches used elsewhere is important, sometimes local problems require more local solutions.

### ***5.3 Cost of Implementation***

The direct cost of implementing rail noise mitigation measures is an obvious constraint on effective rail noise policy. This is particularly the case when economic benefits of a reduction in noise are not immediately obvious, or when assessments of the benefits are limited to direct benefits.

In Europe, quantifying the cost of noise in relation to human health impacts has provided an additional economic argument for reducing noise. Elsewhere, consideration of benefits tends to be restricted to more tangible factors such as the reduction in value of noise-affected properties, and the direct cost of implementing noise mitigation. The high population density in Europe combined with high social or cultural expectations of amenity is likely to be a factor in Europe considering the economic benefits of improved health, when this benefit is not commonly included in cost-benefit analyses elsewhere.

### ***5.4 Mechanisms to Evaluate Policy Effectiveness***

Historically, the benefits of some noise mitigation measures and rail noise policies have been difficult to quantify. For example, reducing the number of noisy events may provide a subjective benefit, but not be reflected in the quantitative parameters used to assess projects. In relation to policy development, it is important to understand the end goal, and to consider the means available to assess the effectiveness of the policy in practice. In Europe, there is a mechanism in place to evaluate regulations for fitness, within the Regulatory Fitness and Performance initiative (REFIT) and the Better Regulation program of the European Commission. The effectiveness of the END is currently being evaluated, and several working papers describing the preliminary findings are available [47]. The factors to be reviewed are (as summarized in [48]):

- Relevance—the extent to which an intervention’s objectives are pertinent to needs, problems and issues to be addressed.

- Coherence—the extent to which the intervention logic is non-contradictory/the intervention does not contradict other interventions with similar objectives;
- Effectiveness—the extent to which objectives set are achieved and the main drivers and barriers to achieving the objectives.
- Efficiency—the efficiency of management and implementation arrangements. The extent to which the desired effects are being achieved at a reasonable cost.
- EU added-value—the value added of action at EU level that would be difficult or inappropriate to achieve at national level alone.

Outside of the EU, the mechanisms for evaluating the effectiveness of policies generally less clearly developed. An exception is the regulatory evaluation taking place in NSW at present. Here, the EPA has considered the main environmental regulation issues for the rail sector, and outlined a range of potential options to address these issues [49]. Following identification of a preferred option for regulatory reform based on a qualitative assessment of each of the potential options, a cost-benefit analysis has been undertaken of the most viable options to achieve the regulatory objectives.

## 6 Conclusions

The noise from railways is a global issue to be addressed by regulators and policy makers. Railways are recognised as being an efficient and environmentally sustainable mode of transport. Transportation planning approaches worldwide aim to create modal shifts to rail. At the same time, concerns around harmful effects of noise are increasing. Increasing population densities and traffic growth is causing complaints about noise from existing lines—with growth in rail traffic, what was once a bearable impact is increasingly severe. It is evident that effective policies are required to balance adverse noise impacts against the benefits of railways to wider society.

The term “railway noise” encompasses noise from many different sources including rolling noise, curve squeal, aerodynamic noise, ground-borne noise, traction noise, warning signals and shunting noise. While almost all of these noise sources exist on railways worldwide, their relative importance varies considerably with geographic location. Two of the key factors contributing to geographic variation in the relative importance of different railway noise sources are the proportion of electrified tracks for freight traffic, and the typical speed of trains. Rolling noise is a key issue in Europe and parts of Asia where typical speeds are moderate to high and the majority of traffic operates on electrified tracks. Elsewhere, rolling noise is present but other noise sources may be more important in some circumstances. In particular, geographic factors mean that curve squeal, traction noise, horn noise and shunting noise are likely to be more important than rolling noise outside of Europe and parts of Asia.

Worldwide, railway noise policies commonly reference studies into annoyance caused by various transportation noise sources. It is important to note that the railway responses included in databases of annoyance studies largely originate from Europe and Asia. While recent analysis of the databases has included consideration of differences between low and high vibration train types, the annoyance due to noise associated with diesel freight locomotives or other noise sources such as curve squeal may not be well represented by the existing survey data.

In Europe, rail noise policy is adapting rapidly. Recent developments have included revision of the TSIs, a review of the END, introduction of common noise assessment methods, and harmonised approaches to NDTACs which have been implemented in several countries. Quantifying the cost of noise in relation to human health impacts has provided an additional economic argument for reducing railway noise.

In North America, the pace of policy development is slower, but progress is being made in the development of guidelines to address noise from high speed trains, and in updating policies for new residential developments in proximity to railway operations.

In Australia several states have either introduced new rail noise policies recently, or are in the process of developing new policies. The triggers for these reviews (or objectives to be addressed by revised policies) are typically related to noise from freight trains, curve squeal, night-time noise impacts, sleep disturbance and health impacts, and increasing development of residential land uses near rail operations.

This paper has examined the reasons for introducing regulation of noise emitted by railways. Different policy instruments and approaches to manage rail noise have been discussed and future policy directions have been identified. In developing railway noise policies, it is important that the objectives are clearly defined, and that a review mechanism is included to assess the effectiveness in the long term.

**Acknowledgements** The assistance of the following people in providing advice and comments on the rail noise policy situation in their geographic region is gratefully acknowledged: Mark Kanowski, Adrian Jongens, James Nelson, Jiyoun Hong, Miranda Ludlow, Paul Maddock, Thu Lan Nguyen, Gustaf Reutersward, Nicholas Craven, Hideki Tachibana.

## References

1. Oertli, J.: Railway noise control in Europe: current status. In: Nielsen, J.C.O., et al. (eds.) Noise and Vibration Mitigation for Rail Transportation Systems. NNFN, vol. 126, pp 1–6. Springer, Heidelberg (2015)
2. Verheijen, E., Elbers, F.B.J.: Exploring bearable noise limits and emission ceilings for the railways part I: national and European legislation and analysis of different noise limit systems (UIC Project ‘Bearable limits and emission ceilings’), dBvision, 25 Oct 2011
3. de Vos, P.: Railway Noise in Europe State of the art report. International Union of Railways (UIC), Mar 2016

4. 2014/1304/EU. Commission Regulation (EU) No 1304/2014 of 26 November 2014 on the technical specification for interoperability relating to the subsystem ‘rolling stock—noise’ amending Decision 2008/232/EC and repealing Decision 2011/229/EU
5. 2002/49/EC. Directive of the European Parliament and of the Council of 25 June 2002 relating to the assessment and management of environmental noise—Declaration by the Commission in the Conciliation Committee on the Directive relating to the assessment and management of environmental noise
6. Tachibana, H., Lang, W.W.: Survey of Legislation, Regulations, and Guidelines for Control of Community Noise. I-INCE publication no. 09-1 (2009)
7. NSW State Government: Protection of the Environment Operations (Noise Control) Regulation 2008
8. Victoria State Government: State Environment Protection Policy (Control of Noise from Commerce, Industry and Trade) No. N-1 No. S31, 16/5/1989, Gazette 15/6/1989 (as varied in 1992, 2001)
9. Queensland State Government: Environmental Protection (Noise) Policy 2008
10. US Congress: Noise Control Act of 1972, 86 Stat. 1248, Public Law 92-574
11. IEA and UIC: Railways Handbook 2015: Energy Efficiency and CO<sub>2</sub> Emissions
12. European Commission: White Paper Roadmap to a Single European Transport Area—Towards a competitive and resource efficient transport system. COM/2011/0144 final (2011)
13. US Environmental Protection Authority: Railroad Noise Emission Standards, Part 201 of Title 40 of the Code of Federal Regulations (1974)
14. Canada Transportation Act, S.C. 1996, c.10
15. South African government: Noise Control Regulations GN R154 in Government Gazette No. 13717 date 10 Jan 1992
16. Thompson, D.J.: Railway Noise and Vibration Mechanisms, Modelling and Means of Control. Elsevier (2009)
17. Bureau of Infrastructure, Transport and Regional Economics (BITRE): Yearbook 2014 Australian Infrastructure Statistical Report (2014)
18. Stevens, L.: In Savannah: 24 Hours, 192 Horn Blasts. The Wall Street Journal, 30 Apr 2015. <http://www.wsj.com/articles/towns-force-railroads-to-address-complaints-about-noise-delays-1430420433>
19. Lee, J., Barrett, J.: Railway noise tops complaint to New Westminster city hall. Vancouver Sun, 1 Jun 2013. <http://www.vancouversun.com/news/Railway+noise+tops+complaint+Westminster+city+hall/8468038/story.html>
20. <http://www.epa.nsw.gov.au/noise/keychanges.htm>. Accessed 30 June 2016
21. Electronic Code of Federal Regulations, Title 49 Subtitle B Chapter II Part 229, Railroad locomotive safety standards. <http://www.ecfr.gov/cgi-bin/ECFR?page=browse>. Accessed 30 June 2016
22. Federation of Canadian Municipalities and the Railway Association of Canada: Guidelines for New Development in Proximity to Railway Operations May 2013
23. UIC: The railway noise bonus—discussion paper on the noise annoyance correction factor—Final Report (2010)
24. ISO 1996-1:2016. Acoustics—Description, measurement and assessment of environmental noise—part 1: Basic quantities and assessment procedures
25. Schomer, P., Mestre, V., Fidell S., Berry B., Gjestland T., Vallet M.: Role of a community tolerance value in predictions of the prevalence of annoyance due to road and rail noise. *J. Acoust. Soc. Am.* **131** (4) (2012)
26. Miedema, H.M.E., Oudshoorn, C.G.M.: Annoyance from transportation noise: relationships with exposure metrics DNL and DENL and their confidence intervals. *Environ. Health* **109** (2001)
27. Hanemann, J.M., Maddock, P.: Between the wheel and the track: A regulator’s reflections on rail noise regulation in NSW. In: Anderson, D., et al. (eds.) *Noise and Vibration Mitigation for Rail Transportation Systems*. NNFM, vol. XX, pp XXX–XXX. Springer, Heidelberg (2018)

28. European Commission: Commission Staff Working Document Rail freight noise reduction (2015)
29. NSW Department of Planning: Development near rail corridors and busy roads—interim guideline (2008)
30. Transport for NSW: Freight Noise Attenuation Program: Policy (Jul 2015)
31. WHO: Guidelines for Community Noise (1999)
32. WHO: Night Noise Guidelines for Europe (2009)
33. Houthuijs, D.J.M., et al.: RIVM Report 2014-0130 Health implication of road, railway and aircraft noise in the European Union: Provisional results based on the 2nd round of noise mapping (2014)
34. Hinze, B., Noise mapping in Australia: completed studies, goals and outcomes. Internoise San Francisco (2015)
35. City and County of San Francisco Planning Department: Noise Map. Accessed 3 Jul 2016 at [http://default.sfplanning.org/publications\\_reports/library\\_of\\_cartography/Noise.pdf](http://default.sfplanning.org/publications_reports/library_of_cartography/Noise.pdf)
36. Hong, J: Personal communication by email, 22 June 2016
37. WA State Planning Policy 5.4 Road and Rail Noise and Freight Considerations in Land Use Planning (SPP5.4). <http://www.planning.wa.gov.au/publications/1182.asp>
38. Queensland Development Code MP 4.4—Buildings in a transport noise corridor (2010). <http://www.hpw.qld.gov.au/SiteCollectionDocuments/mp-4-4-buildings-in-transport-noise-corridors.pdf>
39. NSW EPA: Review of regulation of the ‘railway systems activities’ under the Protection of the Environment Operations Act 1997: Position Paper (Aug 2014)
40. Commission Directive (EU) 2015/996 of 19 May 2015 establishing common noise assessment methods according to Directive 2002/49/EC of the European Parliament and of the Council
41. [http://ec.europa.eu/environment/noise/policy\\_dev\\_en.htm](http://ec.europa.eu/environment/noise/policy_dev_en.htm). Accessed 3 Jul 2016
42. World Health Organization website <http://www.euro.who.int/en/health-topics/environment-and-health/noise/activities/development-of-who-environmental-noise-guidelines-for-the-european-region>. Accessed 20 June 2016
43. Hanson, C.E., Ross, J.C., Towers, D.A.: High-Speed Ground Transportation Noise and Vibration Impact Assessment. For U.S. Department of Transportation Federal Railroad Administration (2012)
44. U.S. Department of Transportation (U.S. DOT), FTA. Transit Noise and Vibration Impact Assessment, Report No. FTA-VA-90-1003-06, May 2006
45. WHO: Burden of disease from environmental noise Quantification of healthy life years lost in Europe (2011)
46. Basner M., et al.: ICBEN review of research on the biological effects of noise 2011–2014. *Noise Health* 17:57-82 (2015). Available from: <http://www.noiseandhealth.org/text.asp?2015/17/75/57/153373>
47. [http://ec.europa.eu/environment/noise/evaluation\\_en.htm](http://ec.europa.eu/environment/noise/evaluation_en.htm). Accessed 3 Jul 2016
48. Evaluation of Directive 2002/49/EC relating to the assessment and management of environmental noise Workshop working paper 2 The Evaluation of the END—emerging findings 23rd Sept 2015
49. NSW EPA: Review of regulation of railway systems activities: Cost-benefit analysis (2016)

# Supporting Decision Making and Management of Freight Rail Noise Using GIS



L. Basutu and K. Sharpe

**Abstract** For policy makers, understanding the magnitude and impact of rail noise in the community is critical to the design and implementation of effective noise mitigation programs and projects. Traditionally, policy makers have used noise monitoring and modelling to address specific questions and concerns about the level of noise and impact on the community. Though useful, current monitoring and modelling data is not easily accessible or easily analysed in a comprehensive manner. A key challenge for policy makers is to collate information from a variety of sources and present it in a format that is easy to understand and can be used to inform the delivery and evaluate the effectiveness of rail noise mitigation over time. To address this, Transport for NSW has developed a Geographical Information System (GIS) that gathers, centralises and displays different types of freight rail noise data collected from across the Sydney rail network. This system integrates:

- Complaints data i.e. the number and nature of complaints received per year for each suburb;
- Noise monitoring data collected continuously by our network of permanent noise monitoring stations located at Cardiff, Narara, Koolewong, Leura, Emu Plains, Otford and Jannali;
- Results of short term noise monitoring undertaken across the network to identify rail noise hotspots and in response to complaints; and,
- Data such as treatment areas associated with our Freight Noise Attenuation Program.

This system enables us to communicate the magnitude of the noise impacts and to track the progress we are making on reducing these noise impacts. This paper outlines how we use this system as a tool to facilitate more effective, efficient and evidence based decision-making.

---

L. Basutu · K. Sharpe (✉)  
Transport for NSW, 18 Lee Street, Chippendale, Australia  
e-mail: kyle.sharpe@transport.nsw.gov.au

L. Basutu  
e-mail: laurena.basutu@transport.nsw.gov.au

# 1 Introduction

For policy makers, understanding the magnitude and impact of rail noise in the community is critical to design and implementation of effective noise mitigation schemes. Traditionally policy makers have used noise monitoring and modelling to address specific questions and concerns about the level of noise and impact to the community. The Europeans are still using this method. Under the European Union's (EU) Environmental Noise Directive (END) each member state is required to prepare noise maps every five years. The EU uses these maps, not only to determine the EU community's exposure to environmental noise but also to provide the evidence required to develop environmental noise management action plans that prevent and reduce rail noise to preserve the environmental noise quality [2].

Though useful for the development of rail noise mitigation strategies, there are several challenges in using noise monitoring data for decision-making, including:

- Difficulty in accessing accurate noise monitoring data—in government, rail noise monitoring is conducted by a number of different agencies and stored in various manners. Obtaining this data for analysis is a challenge.
- Difficulty in analysing noise monitoring data—often there is too much data available to be processed in a timely or meaningful manner. A situation can arise where the amount of data precludes its effective and timely use [7].

Using noise prediction programs, such as SoundPlan, can help address these issues but these modelling programs also have their limitations. The main ones being, that:

- The internal parameters of noise models cannot be easily adjusted to suit the local environment or changed to fit empirical results from noise monitoring [6].
- The predicted results are based on a number of assumptions made by the modeller about the geographical and rail traffic conditions of the area for a particular period in time. Even though these models use monitoring data to verify their predictions there is no effective way for them to account for any changes that may occur over time for example an increase in rail traffic.
- The cost of developing and maintaining “dynamic” noise models is very high [6].

A key challenge for rail noise policy makers is to assemble noise monitoring, complaint, noise mitigation and geographical data so they can quantify and qualify noise problems, implement mitigation programs and evaluate the effectiveness of these programs [7]. We have developed a Geographical Information System called the Rail Freight Noise Information System as an alternative to conventional noise prediction packages. Transport for NSW's Geospatial Team developed the system and are responsible for its ongoing maintenance and functionality updates. This system, introduced in early 2016, gathers and centralises different types of freight rail noise data collected from across the Sydney rail network and helps inform our decisions on rail noise mitigation measures.



## 2 The Rail Freight Noise Information System

The Rail Freight Noise Information System (RFNIS is an internal Transport for NSW tool used by a dozen or so staff to manage freight rail noise in NSW.) The system collects, stores, and visualises rail noise data as thematic layers linked by geography. The system presents, as layers:

- Complaints data, that is, the number of complaints received per year, for each suburb since 2013, and the nature of these complaints e.g. wheel squeal, locomotive noise etc.;
- Data collected continuously by our permanent noise monitoring stations located at seven sites across the network;
- Results of short term noise monitoring undertaken periodically at numerous sites across the network to identify rail noise hotspots;
- Results of short term noise monitoring conducted at residences in response to complaints; and,
- Areas where we are rolling out mitigation treatment for the Freight Noise Attenuation Program.

Additional features of RFNIS include functions that allow the user to:

- Select attributes in each layer to find out detailed information i.e. the user can select a short term noise monitoring location and find out the daytime and night time noise level at that location, the monitoring start date and the date when this information was last updated;
- Measure the distance between multiple points; and,
- Show the “street view” for a road by clicking a location on the map.

## 3 Data Management Using RFNIS

As outlined previously, one of the main barriers to effective decision making is the lack of easy access to rail noise monitoring and complaints data related to a particular location. Prior to the introduction of the RFNIS all noise and noise related data we collected was stored in various spreadsheets at disparate locations and analysis was manual, laborious and time consuming. The RFNIS eliminates this problem by collating all the available information in one location. TfNSW uses a simple four-step procedure to process all the rail noise monitoring and complaints data using RFNIS (see Fig. 1).

The RFNIS accommodates an unlimited amount of information and is updated weekly and it is the ‘single source of truth’ upon which decision makers can rely to provide up to date and accurate information regarding freight rail noise in NSW [7].

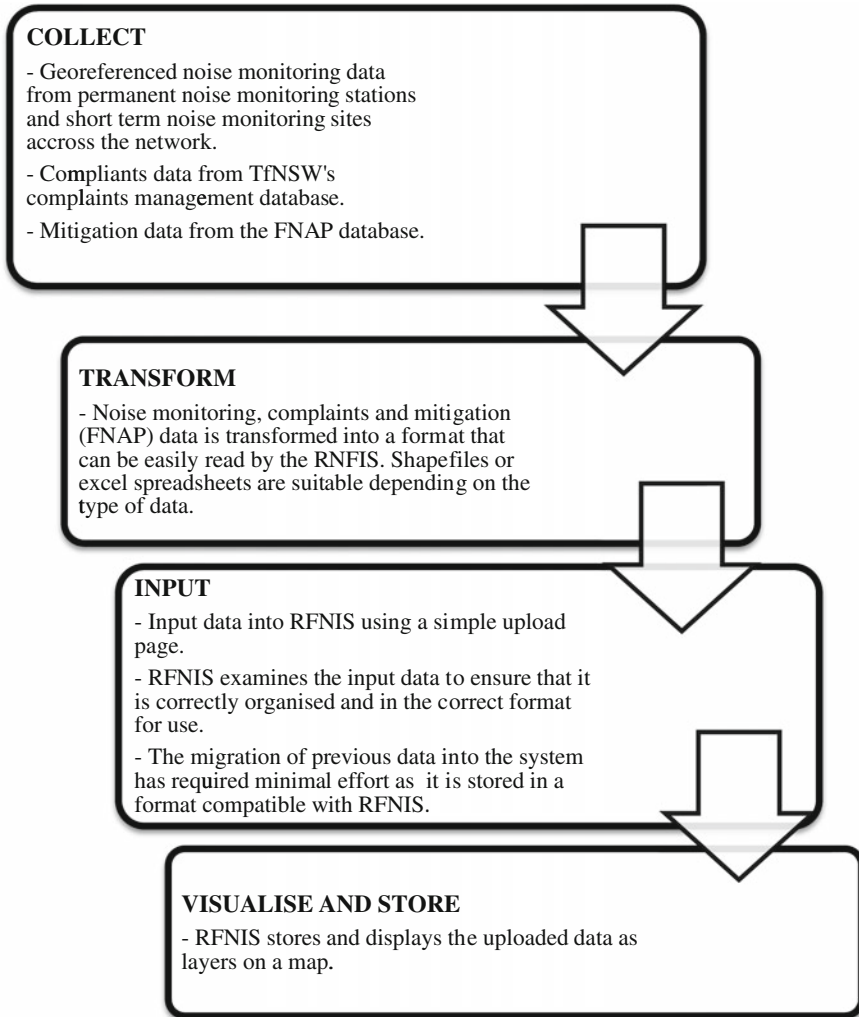


**Fig. 1** RFNIS data processing procedure

## 4 Decision Making Using RFNIS

### 4.1 A Framework for Decision Making Using RFNIS

TfNSW has developed a framework, adapted from traditional spatial analysis, which allows users to apply the RFNIS to freight noise issues [1] (Fig. 2).

Sections 4.1.1–4.1.4 describe each stage in detail.

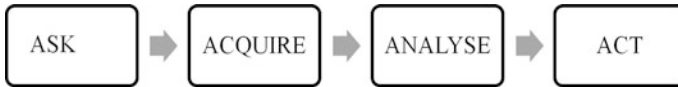


**Fig. 2** Framework for decision-making using RFNIS

#### **4.1.1 Ask**

In this stage, the decision maker asks, “What is the problem I am trying to solve?” or “What am I trying to decide?” Defining the question helps us decide what information and type of analysis is required to solve the issue. It also decides how we should present the results of the analysis.

#### **4.1.2 Acquire**

We collect all the data needed to answer the question posed in stage 1 and display it in the RFNIS. During this stage, the user must ensure that the data gathered is up to date and accurate.

#### **4.1.3 Analyse**

Once we have gathered and displayed the required information in the RFNIS the data can be analysed by mapping two or more types of data relating to the same area one on top of the other. This allows us to examine the relationships between the data and determine where different types of characteristics occur together [7].

#### **4.1.4 Act**

We then use the results of the analysis to come to a decision regarding the question posed in stage 1. The results of the analysis can also be used as evidence to justify the decision made and can be shared with stakeholders using annotated maps, an excel spread sheet or map hyperlinks, depending on the audience.

### **4.2 Decision Making Using RFNIS—A Case Study**

We can best describe how TfNSW uses RFNIS to solve problems by using an example. This section provides a case study of how the framework described in Sect. 3 is to determine whether a property is eligible for treatment under the Freight Noise Attenuation Program (FNAP).

The FNAP offers noise reduction treatments to homes affected by high levels of freight rail noise along NSW Government managed rail corridors between Nowra and Newcastle, and Lithgow. The program prioritises treatment to homes located in areas that experience the highest levels of average night noise. The program aims to treat up to 200 homes per year [8].

#### 4.2.1 Ask

In this case, the user needs to determine whether a property is eligible for treatment under the FNAP.

To be eligible for FNAP properties must comply with a number of eligibility criteria. The property [8]:

- is no more than 100 m from the nearest NSW Government rail corridor carrying freight trains
- is not part of a building that is more than three levels above the ground
- is directly facing the rail corridor
- experiences an average of at least 70 dB during the day or an average of at least 65 dB at night.<sup>1</sup>

#### 4.2.2 Acquire

The user gathers the required data, as defined in the “ask” stage and inputs it into the RFNIS. The RFNIS displays this information as layers (Fig. 3). In this case, the RFNIS displays:

- A Basemap (aerial image with streets) layer
- The Rail dBA (day time and night time) layer
- The FNAP Catchments layer
- The FNAP Applications layer
- The NSW Rail Network layer.

#### 4.2.3 Analyse

The first stage in the analysis is to locate the property in the RFNIS. Once the property has been located, the user:

---

<sup>1</sup>Night time is defined from 10 pm to 7 am.

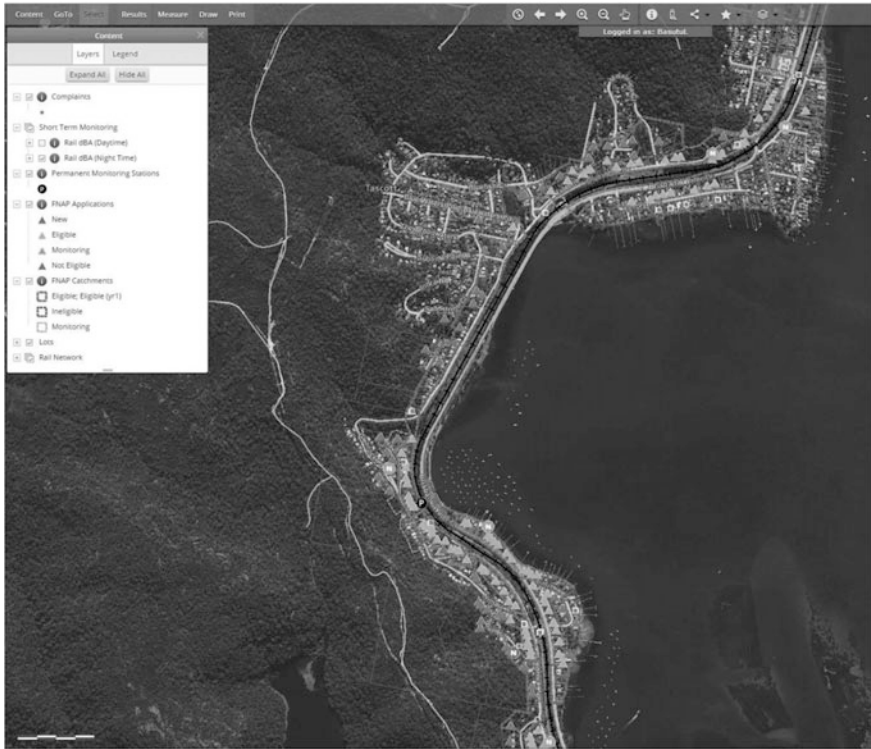


**Fig. 3** Required data displayed in RFNIS

- Visually inspects the property and its surrounds in RFNIS using the street view tool to determine whether it adjacent to a NSW government rail corridor, directly faces the rail corridor and is no more than three levels above ground
- Uses the measurement tool in RFNIS to ensure that the property is no more than 100 m from the corridor.

If the property meets these conditions, the user turns on the “FNAP Catchments layer” and determines whether the property is already in an eligible or ineligible catchment. If the property is in either an eligible or ineligible catchment then the property’s eligibility is the same as that of the catchment.

If the property is not in a defined catchment, the user turns on the “Short Term Monitoring” layer to check if there is monitoring data for the area where the property is located. If there is noise-monitoring data, the user calculates the day and night noise level at the property. If either the calculated day or night level is greater or equal to the eligibility criteria then the property is eligible for the FNAP. If the calculated day or night level is less than the eligibility criteria then the property is ineligible for the FNAP.

If TfNSW has no noise monitoring data in the area then the user will note down the property address and organise for noise monitoring to be undertaken.

#### **4.2.4 Act**

From the results of the analysis, the user is able to determine whether a property is eligible or ineligible for the FNAP or whether further monitoring is required. The outcome of the analysis can be displayed visually using coloured icons for ineligible, eligible and monitoring statuses on a map of the area.

## **5 Benefits of Using RFNIS**

TfNSW has realised a number of benefits using RFNIS to facilitate the management of freight rail noise. The key benefits are summarised in Sects. 5.1–5.4 below.

### ***5.1 Evidence Based Decision Making***

Studies show that 80% of the data collected, stored, managed and used as evidence to support decisions made by local governments has a geographic component [3, 5, 9]. Simply put, it is not only important for decision makers to know *what* is happening, it is also important for them to understand *where* and *when* the problem or issue is happening. RFNIS presents the temporal and spatial data necessary to investigate rail noise issues. This has made it easier to understand the impact of freight rail noise on the community. In the future RFNIS will help TfNSW to communicate the magnitude of freight rail noise issues to diverse audiences contributing to greater collaboration and understanding between stakeholders [4].

### ***5.2 Improved Management of Rail Noise Mitigation Programs***

A key use of the RFNIS is for the management of the FNAP. As this program progresses, we need a clear view of the progress of all the ongoing activities, e.g. how many applications have been received from a particular location, how many residences in that location are eligible for treatment, how many homes in that area have already been treated, and which homes are currently being treated. The RFNIS has been able to take this information from the FNAP database and display it on a map showing where these activities are occurring and, to some extent, whether

these activities are falling behind. The system's ability to produce maps has made it simple to provide stakeholders with a quick snapshot of the program.

### ***5.3 Improved Complaints Management***

As RFNIS stores all the freight rail noise related data—noise levels, complaints and mitigation program details—in one central, easily accessible location using the system has enabled TfNSW to respond more quickly and completely to complaints about freight rail noise. Over time, increased efficiency in complaints management will help to enhance the public's perception of TfNSW's management of rail noise issues.

### ***5.4 Improved Record Keeping***

The use of RFNIS provides TfNSW with a framework for the management of different types of freight rail noise data as all the available data is stored in one location, an infinite amount of information can be put into the system and it can be updated with current data at any time. The system also provides users with a number of reporting tools such as maps, annotated maps and spreadsheets.

## **6 Conclusions and the Future of RFNIS**

Rail noise occurs in both space and time. The RFNIS provides us with a tool that captures not only a diverse range of information on rail noise, but presents this data in terms of both spatial and temporal contexts. We use this system to communicate with various stakeholders in a manner that is easy to understand, and to simplify and improve both record keeping and complaints management. RFNIS is still at an early stage of its development, yet it already provides more useable information than any noise models available to TfNSW.

In time, we aim to improve the system's functionality and ability to analyse data by expanding its capabilities. The system will become integral to FNAP by allowing TfNSW to input information about FNAP applications and catchments directly into the system (possibly via an automated web portal that will also manage the program). Asset management will become a core function by incorporating remote sensing and condition monitoring data, and network access and efficiency will become a key feature by including real time train running data.

In future, the system can be adapted and improved to run automatic multi-criteria queries such as identifying all eligible FNAP participants based on distance, noise level, catchment, etc., thereby eliminating manual work involved in managing the

FNAP program. This will lead to business efficiencies reducing the time and effort required to process applications and allowing us to focus on key activities such as noise monitoring and evaluation. We are also exploring the possibility of integrating data from RFNIS into other NSW Government GIS platforms for example the Planning Portal maintained by the Department of Planning and Environment which is used by Councils and Developers to inform property development.

All of the information we need to achieve these goals exists in various forms—the RFNIS can be the vehicle to bring it together and make collective sense of it.

## References

1. ESRI.: What is GIS. (Online) Available at: <http://www.esri.com/what-is-gis/howgisworks> (2016). Accessed 26 Apr 2016
2. European Commission.: Environmental Noise Directive. (Online) Available at: [http://ec.europa.eu/environment/noise/directive\\_en.htm](http://ec.europa.eu/environment/noise/directive_en.htm) (2015). Accessed 19 Apr 2016
3. Garson, G.D., Biggs, R.S. (eds.): Analytic Mapping and Geographic Databases. SAGE Publications Inc., Newbury Park (1992)
4. Joyce, K.: “To me it’s just another tool to help understand the evidence”: public health decision-makers’ perceptions of the value of geographical information systems (GIS). *Health Place* **15**, 831–840 (2009)
5. OGRIP: White Paper on the Ohio Location Based Response System. Office of Information Technology, Columbus (2004)
6. Pamanikabud, P., Tansatcha, M.: Geographical information system for traffic noise analysis and. *Environ. Model. Softw.* **18**, 959–973 (2003)
7. Tomlinson, R.F.: A geographic information system for regional planning. In: Stewart G.A (ed.) *Land Evaluation*, pp. 200–210. MacMillan, Melbourne (1968)
8. Transport for NSW.: Freight Noise Attenuation Program: Policy. Transport for NSW, Sydney (2015)
9. Williams, R.E.: Selling a geographical information system to government policy makers. s.l., URISA (1987)



# Between the Wheel and the Track: A Regulator's Reflections on Rail Noise Regulation in NSW



J. M. Hanemann and P. Maddock

**Abstract** Noise impacts from the operational rail network in NSW have been regulated since 1970. Regulation has evolved over that time in response to growth and partial privatisation of the rail industry, progressive understanding of the sources and causes of, and mechanisms to address, rail noise and increased community expectations regarding health and amenity impacts. This paper considers the range of regulatory and other approaches that have been applied to rail noise in NSW to date, reflects on the successes and learnings of those approaches and presents the current proposal for progressing towards achieving a level of rail noise that is acceptable by the community.

## 1 Introduction

The New South Wales (NSW) rail network comprises approximately 6400 km of operational rail track.

This network is currently operated by three railway system operators<sup>1</sup> (Fig. 1):

- Sydney Trains (metropolitan areas)
- the Australian Rail Track Corporation (ARTC) (interstate rail network, metropolitan freight network and the Hunter Valley network)
- John Holland Rail Pty Ltd (on behalf of Transport for NSW (TfNSW)) (country regional network).

---

<sup>1</sup>Under the *Border Railways Act 1922*, sections of the Victorian rail network extend into NSW. V/Line holds an environment protection licence (EPL) for 'railway systems activities' in NSW as three of the railway lines it operates in Victoria extend a short distance into NSW to Tocumwal, Moulamein and Deniliquin.

J. M. Hanemann (✉)

NSW Environment Protection Authority, P.O. Box 668, Parramatta, NSW 2124, Australia  
e-mail: jacinta.hanemann@epa.nsw.gov.au

P. Maddock

NSW Environment Protection Authority, Sydney, Australia

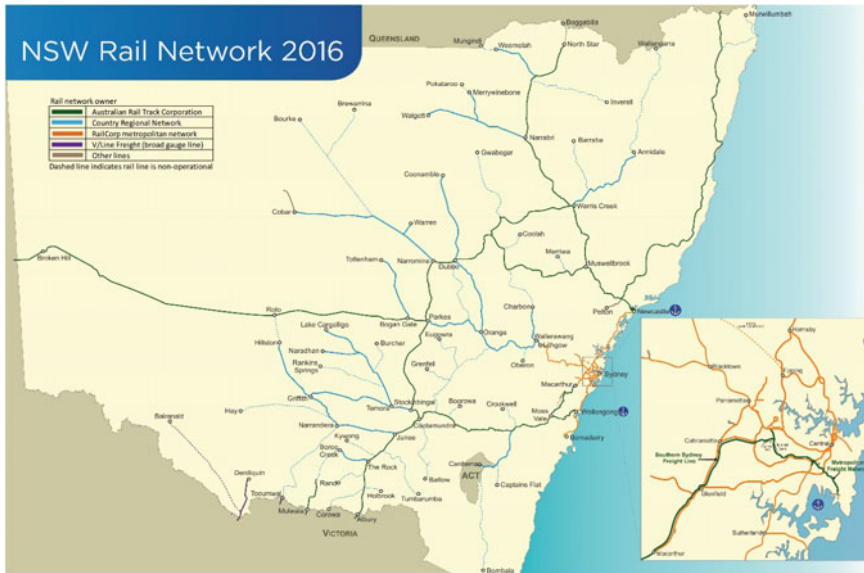


Fig. 1 The NSW rail network February 2016 [1]

The railway system operators grant rolling stock operators access to their networks under contractual network access agreements.

In NSW, rolling stock operators transport passengers and a wide range of freight: such as coal and other minerals, grain, cotton, meat, wine, wool, steel and steel products, and general containerised cargo [2]. Most passenger services in the Sydney metropolitan area are powered by electric locomotives and much of the other rail activity in NSW is powered by diesel locomotives.

Rail freight plays a critical role in transporting bulk commodities and containerised freight in NSW. The NSW Government is committed to enhancing rail freight movement and specifically, to doubling the proportion of container freight movement by rail through the NSW Ports by 2020 [2]. NSW's major ports associated with trade are Port Botany, the Port of Newcastle and Port Kembla. Each of these ports is located in urbanised environments, with the supporting rail network traversing NSW's key and densely populated cities of Sydney, Newcastle and Wollongong respectively.

The NSW Government is currently expanding Sydney's passenger rail network by investing in new services and upgrading existing infrastructure.

The growth of the NSW rail freight and passenger networks brings many benefits to the environment and wider community. However, there is a risk of adverse local impacts associated with this growth and these need to be appropriately managed to minimize the impacts on the environment and health and amenity of the community and ensure that the community's acceptance of rail operations does not

become an issue for the growth of freight transport by rail. The NSW Environment Protection Authority (EPA), as the primary environmental regulator in NSW, is responsible for ensuring these risks are managed.

## **2 Key Environmental Impacts Associated with the Network**

Although air emissions associated with the operation of the rail network have been an emerging issue in recent years, noise is the primary environmental issue associated with the rail network in NSW.

Noise can be annoying, result in speech interference, affect concentration and disturb sleep. Prolonged exposure to excessive noise levels has been associated with a range of health effects. The impacts of noise depend on the noise level, its characteristics and how it is perceived by the person affected. When communities are impacted by noise, local complaints have the potential to escalate to become a broader issue if the noise and relationship with the community is not managed well.

A report commissioned by TfNSW [3] estimates that over 12,000 residences were affected by rail noise exceeding 60 dB LAeq, 24 h in the Sydney metropolitan region of which approximately 80% were exposed to noise from freight operations or a mixture of freight operations and passenger services.

In general terms, the key sources of noise from railways can be split between the wheel-rail interface and engine and exhaust noise sources [4]. Examples include:

- Rolling noise which is influenced by speed, wheel roughness, rail pad stiffness and the roughness of the rail;
- Wheel squeal and flanging;
- Noise from locomotives generated by the engine, exhaust, brake and radiator fans, air intake grills and, where relevant, turbochargers and ancillary equipment. Engine idling and low frequency noise from diesel locomotives can be particularly annoying.

Other specific sources of noise that can affect communities alongside a railway include noise from brake squeal, noise from freight wagons 'booming' when empty, and noise from bunching and stretching of wagons. In some instances, vibration or regenerated noise can also occur.

## **3 Regulation of Rail Noise in NSW**

Regulation of rail noise is challenging. The NSW Government supports the rail industry and recognises the range of benefits that it brings to the environment (lower greenhouse gas emissions) and wider community. Rail transport is a vital

component for achieving sustainable cities. However, these benefits need to be balanced with the impacts on the health and amenity of the community in proximity to the operational rail network. While noise impacts are associated with both the passenger and freight rail networks, the degree of impact from rail freight is more significant and is therefore the focus of this paper.

In Australia, rail noise is regulated at a state, not national, level. Rolling stock operators, however, haul freight across state boundaries and are therefore subject to a range of regulatory regimes for rail noise. The rail industry considers that NSW's regulation of rail noise is the most stringent in Australia.

Regulation of rail noise in NSW has been approached in a strategic manner since 1970. It has developed incrementally in response to changes in the rail industry and community expectations, understanding of rail noise issues, learnings from regulatory approaches implemented and development of environment protection policy. A cornerstone of the regulation is the implementation of reasonable and feasible measures to minimise rail noise.

### **3.1 1975–1999**

Historically, the Pollution Control Act 1970 and Noise Control Act 1975, administered by the former State Pollution Control Commission (SPCC), formed the basis for noise control in NSW.

The Pollution Control Act 1970 was the earliest regulatory instrument available in NSW to manage noise issues. Its principal role was to provide the means to issue licences and approvals. Licensing provisions applied to a range of scheduled premises, including “premises used for the operation of railways systems, whether the Rail Access Corporation or any other persons”. Licensing, however, only applied to proclaimed areas, being all the Sydney Metropolitan area and the Blue Mountains, and did not apply elsewhere in NSW. A single licence was issued to the State Rail Authority (later the Rail Access Corporation) for the metropolitan rail network.

Under the Noise Control Act 1975, the occupier of a premises was required to obtain a Pollution Control Approval if new plant was to be installed or replaced on the premises where changes to the operation of plant was likely to cause or increase noise pollution. This provision applied across the state and was used to control noise emissions from locomotives being introduced to the NSW network.

The Noise Control Act 1975 (as amended by the Noise Control (Amendment) Act 1984) also introduced a number of important concepts for noise control in NSW including the definition of offensive noise and the introduction of instruments to manage noise such as noise abatement orders and noise abatement directions. Although the Pollution Control Act 1970 remained the principal means to manage railway noise through a licence, the Noise Control Act 1975 introduced important

noise management concepts which were later adopted in the Protection of the Environment Operations Act 1997 (POEO Act) to manage railway noise.

Treagus [5] noted that noise was recognised as a significant issue in NSW from the 1970s onwards. This coincided with the proposal for a site for Sydney's second airport and the publication of associated noise contours, which lead to significant community concern.

Growing community and political interest provided an imperative for the SPCC to develop the Environmental Noise Control Manual (ENCM) in 1985 to offer practical guidance on issues as diverse as motor sport, helicopters and garbage collection. The ENCM included advice on noise from rail signaling systems and rail traffic noise, with the latter introducing the following noise criteria: 'planning levels' of LAeq, 24 h 55 dB(A) and LAmax 80 dB(A), and 'maximum levels' of LAeq, 24 h 60 dB(A) and LAmax 85 dB(A).

The 'maximum levels' were reflected in the State Rail Authority licence, which included the following provisions for noise:

...rail services should not exceed LAeq, 24-h 60 dB(A) or LAmax of 85 dB pass by noise 1 m from a residential property

This did not apply to development encroaching onto existing rail lines or where a Pollution Reduction Program (PRP) was in place to manage noise levels. It is worth noting that the planning levels in the ENCM are more stringent than those set out in the licence issued under the Pollution Control Act 1970.

### 3.1.1 Development of the Locomotive Noise Emissions Limits

The introduction of Class 81 locomotives in 1987 prompted numerous noise complaints which led to an investigation by the SPCC and the subsequent development of locomotive noise criteria agreed with the State Rail Authority. The criteria were derived by balancing what could feasibly be achieved for the locomotives against ensuring adequate levels of protection for the community (Table 1).

Subsequently, the following criteria was applied by the EPA for new locomotives operating on the NSW rail network [6].

So by the late 1980s, the SPCC had developed noise criteria applicable at property facades introduced by *Pollution Control Act 1970* and the ENCM and noise limits for individual locomotives, to manage rail noise in NSW.

In addition, in the early 1990s the State Rail Authority was required by the SPCC/EPA to develop a Noise and Vibration Code of Practice. The key objective of the policy was 'minimising problems caused by noise and vibration from railway activities' [7] including through forward planning (explicitly considering the noise and vibration environment at the same time as the operational/development aspects), putting in place measures to reduce the extent of existing noise and vibration problems and using best available technology economically achievable [7]. The outcomes of this Code of Practice are unclear.

**Table 1** EPA locomotive noise emission criteria

Operating condition	Speed and external location	External noise limit
Idle with compressor radiator fans and air conditioning operating at maximum load occurring at idle	Stationary, 15 m contour	70 dB(A) LAmax
All other throttle settings under self load with compressor, radiator fans and air conditioners operating	Stationary, 15 m contour	87 dB(A) LAmax 95 dB linear max
All service conditions	0–50 km/h, 15 m from centre line of track	87 dB(A) LAmax 95 dB linear max

Tonality requirements were included on the basis of third octave band analysis.

No third octave band below 160 Hz to exceed 15 dB(A) above both adjacent bands.

No third octave band 160–400 Hz to exceed 8 dB(A) above both adjacent bands.

No third octave band above 400 Hz to exceed 5 dB(A) above both adjacent bands.

In addition (and unless otherwise stated) the overall linear noise level was not to exceed the overall A-weighted noise level by more than 15 dB.

### 3.2 1999-Current

The POEO Act commenced in 1999. It provided a single licensing arrangement to replace the different licences and approvals required under previous separate Acts relating to air pollution, water pollution, noise pollution and waste management.

A similar approach to regulation of rail noise under the Pollution Control Act 1970 and Noise Control Act 1975 was continued under the POEO Act. Railway systems (including the track, maintenance facilities, workshops and rolling stock) involving the construction, maintenance or operation of railway systems, with more than 30 km of track and excluding systems operated for heritage value, remained a licensable activity. However, all railway networks greater than 30 km in length, regardless of whether they were managed by a private or public entity, were now required to be licensed. Further, a single licence/approval covered the network and the rolling stock operators as rolling stock was deemed to be operated by the railway system operator.

While the licences no longer included façade based noise criteria, the objective of the licences were:

- to minimise noise levels, to the extent practicable, of railway operations and their impact on communities surrounding the railway network; and
- through the use of Pollution Reduction Programs, to progressively reduce noise impacts towards the same façade based noise criteria.

The licences also contained the noise limits for locomotives being introduced to the NSW rail network that were developed when the 81 Class was introduced to the

network. Later, the requirement for approval was extended to locomotives that had been substantially modified since last being operated on the NSW rail network with the intent of having all locomotives operating in NSW assessed against the noise criteria within a decade.

These locomotive noise limits, and PRPs, were the principal means of reducing the noise impacts of the rail network under the licensing regime under the POEO Act.

### 3.2.1 Locomotive Noise Emissions Limits

Although the noise limits were developed in conjunction with SRA on the basis of what could be feasibly achieved by the 81 class in 1987, the rail industry (largely the rolling stock operators) has since contended that the noise limits are too stringent and have curtailed the growth of the rail industry in NSW. The rail industry has raised further concerns regarding the applicability of the limits to more powerful locomotives.

In response to industry concerns, in 2004 the EPA included an alternate locomotive approval pathway. The EPA could approve a locomotive that did not meet all of the noise limits, provided that: the noise emission performance of the locomotive is consistent with best practice, all feasible and reasonable mitigation measures have been implemented and the non-compliances will not result in unacceptable environmental impacts. In 2015, the EPA removed the requirement for 'all service conditions' (dynamic test). This was largely because there was no quantitative standard for the rail condition (which may significantly impact the noise results).

Approximately 70% of the locomotives operating on the network meet the noise requirements. Almost all of these have been approved for operation under the alternate approval pathway. An exception to this is the SDA1 Class and 1100 Class of locomotives, introduced to the NSW network in 2012, which substantially met the noise limits.

The locomotive noise emissions limits have been an effective way of reducing rail noise. A Freight Locomotive Wayside Noise Survey, conducted in 2013, analysed 607 freight passby events across five locations around the network and found that 'all the locomotives identified as having high LCmax levels or subjective noise impacts were introduced to NSW prior to the EPA approval process' [8].

The extension of the requirement to 'substantially modified' locomotives has been less successful. It was presumed that locomotives would require a major overhaul every eight to ten years and therefore every locomotive operating within NSW would have been substantially modified and assessed against the noise criteria within a decade. However, this has not been the case, either because many locomotives have not been substantially modified or because the EPA/railway operator has not been notified when rolling stock operators have done so.

### **3.2.2 Pollution Reduction Programs**

The EPA can require licensees to develop and implement PRPs to improve their environmental performance and reduce pollution. PRPs are legally binding and may require licensees to undertake studies before implementing steps to address environmental problems. There have been a range of PRPs placed on the rail industry in relation to noise.

#### **2001–2006**

Between 2001 and 2006, the EPA required RailCorp to undertake a program of PRPs. These involved identifying areas along the network which exceeded the noise goals and developing an implementation plan of mitigation measures that aim to address noise at these locations. These measures included actions targeting five priority lines as well as whole of network actions. The PRPs also involved RailCorp developing a communication plan for residents adjacent to the five priority lines as well as a noise monitoring program to evaluate the noise mitigation measures. RailCorp was required to report to the NSW EPA every six months throughout the five year PRP period.

The success of these PRPs following the conclusion of the five year period was inconclusive as the results of noise monitoring undertaken following the introduction of the mitigation measures are highly variable and limited (in terms of sample size). Many of the actions undertaken by RailCorp under the PRP appear to relate to asset management (with potential side benefits in terms of noise) rather than targeted noise management/reduction actions.

#### **2007–2012**

The next series of PRPs were focussed on:

1. establishing a baseline for noise performance of the rail network to inform a strategic approach to address long-term rail noise issues. This included monitoring the passby noise performance of freight locomotives on the rail network, monitoring locomotive and wagon axle alignment to identify rolling stock with the capacity to cause wheel squeal from misaligned axles; and
2. implementing works to address more immediate and discrete noise issues. This included the installation of Top of Rail Friction Modifier Applicators at known squeal hot spots and a review of safety related practices that cause a noise nuisance, specifically sounding horns and using detonators.

These programs resulted in some noise improvements across the network with repairs made to defective wagons and some localised noise improvements due to reduced squeal and changes in horn usage.

### **3.2.3 Other NSW State Programs Relevant to Rail Noise**

A number of other NSW State guidelines and programs relevant to rail noise were developed in this period.



### Rail Infrastructure Noise Guidelines

New and redeveloped heavy and light rail projects must be assessed in accordance with the Rail Infrastructure Noise Guideline (RING) [9]. This sets out noise trigger levels, which if likely to be exceeded, feasible and reasonable mitigation must be identified to reduce noise (Table 2).

The RING also includes advice on assessing noise from rail traffic-generating developments where land use development other than rail projects are likely to generate additional rail traffic on an existing rail network.

Where the LAeq noise level increases are predicted to be more than 2 dB(A) and exceeds the noise trigger levels for existing rail lines, feasible and reasonable noise mitigation must be considered.

### Guidelines for Development Near Rail Corridors and Busy Roads

The NSW planning system seeks to ensure that noise sensitive property, encroaching on existing rail corridors, is designed to ensure acceptable internal noise amenity [10]. Developers of residential dwellings must ensure that the following LAeq levels are not exceeded:

- In any bedroom in the building—35 dB(A) at any time 10 pm–7 am
- Anywhere else in the building (other than a garage, kitchen, bathroom or hallway): 40 dB(A) at any time.

### Freight Noise Attenuation Program

The final part of the noise control regime are Noise Abatement Programs to offer mitigation to those already adversely affected by rail noise.

One such scheme administered by Transport for NSW, the Freight Noise Attenuation Program [11], offers architectural treatments to eligible properties

**Table 2** Noise trigger levels for heavy rail affecting residential land uses

Type of development	Noise trigger level dB(A) external	
	7 am–10 pm	10 pm–7 am
New rail line development	60LAeq (15 h) or 80LAFmax	55LAeq (9 h) or 90LAFmax
Redevelopment of existing rail line	Development increases existing LAeq(period) rail noise by 2 dB or more, or existing LAmx rail noise by 3 dB or more and predicted noise level exceed	
	65LAeq (15 h) or 85LAFmax	65LAeq (15 h) or 85LAFmax

affected by freight rail noise on freight corridors between Nowra and Newcastle and west to Lithgow. The eligibility criteria is for an occupied residence within 100 m of a freight corridor experiencing at least 70 dB during the day and 65 dB during the night.

## **4 Regulatory Reform**

### ***4.1 Assessment of the Current Regulatory Regime***

‘In the mid-1990s, structural reforms to the NSW rail industry were introduced to support the implementation of national competition policy, most notably to enable third party operators to use the NSW rail network’ [12]. Access to the network was provided by the NSW Rail Access Regime established by the NSW Government in 1996. In 2004, this was replaced by the NSW Rail Access Undertaking following the transfer of the control of the Hunter Valley Coal Network and the Interstate Lines to the ARTC, wholly owned by the Australian Government, under long term lease arrangements [12].

The current licensing regime holds railway system operators legally responsible for the activities of the third party rolling stock operators and assumes that railway system operators can pass on their licensing obligations to the third party rolling stock operators through these access agreements. The railway systems operators have long contended this is not the case. As these obligations have largely not been passed to the rolling stock operators, the rolling stock operators are not directly accountable to the EPA for their environmental performance. This is a concern because many of the noise impacts associated with the rail network arise from issues that are fully or partly the responsibility of rolling stock operators. Using the licensing regime to enforce environmental responsibilities and achieve acceptable environmental performance by the rail industry has therefore had limited success [13].

As a consequence of this, the EPA has developed rail regulatory reforms.

### ***4.2 Future Regulation***

The EPA, in consultation with TfNSW, Sydney Trains and ARTC, undertook a review of ten regulatory options for the NSW operational rail sector, and determined that the most effective and practical framework would be to license rolling stock operators in addition to railway systems operators [13]. This framework is expected to result in significantly better environmental outcomes than the current framework as it recognises both rolling stock operators and railways systems operators contribute to noise impacts and are therefore responsible for resolving

them. It provides an effective mechanism for addressing issues that require joint management, such as wheel squeal.

The EPA published a position paper on the proposed regulatory framework for stakeholder comment in August 2014. Forty six submissions were received. There was broad support for the proposal from the community, railway systems operators and other agencies. Rolling stock operators were generally opposed to the proposal, citing concerns regarding the potential costs of regulation.

The EPA is intending to proceed with the proposed regulatory change and, in May 2016, released a draft of the amendment regulation for consultation. The EPA is proposing a transitional period for rolling stock operators to hold environment protection licences once an amendment regulation is implemented. Rolling stock operators will need to apply for a licence within six months of the amendment regulation being implemented and the EPA will need to issue the licence within ten months of the amendment regulation being implemented.

The analysis of noise monitoring data from across the Sydney metropolitan network by TfNSW and under the PRPs has led to recent and significant improvements in understanding wheel squeal and passby noise and identifying the appropriate measures to address these issues. Based on the work by TfNSW, the NSW Asset Standards Authority is in the process of developing industry standards around wagon steering, lubrication and track profiling.

The EPA intends that the licences for rolling stock operators will include requirements to address noise impacts from the network. The licences will include limits for noise emissions from locomotives and redress the issue of substantially modified locomotives (outlined in Sect. 3.2.2). The licences may also reference the industry standards around wagon steering, lubrication and track profiling if appropriate, include monitoring and the trialing or implementation of other mechanisms to reduce noise. The EPA will establish a number of working groups across interested stakeholders to inform the development of the licences.

## 5 Conclusion

Effective management of noise impacts from the operational rail network requires:

- the sources and causes of rail noise to be well understood;
- performance standards to be established for the rail industry that are protective of the environment and health and amenity of the community. These could include emission limits for locomotives and standards for other rolling stock and criteria for railway infrastructure and adjacent developments. These may be established by the industry or regulatory or planning authorities, but need to be enshrined in enforceable instruments;
- railway systems operators and rolling stock operators to be accountable for their environmental performance and to work collaboratively to address existing operational rail issues;

- rolling stock operators and rolling stock manufacturers to develop or source best practice technology for the future and existing locomotive and wagon fleets; and
- ongoing collaboration between industry, government and community.

Noise impacts from the operational rail network in NSW has been regulated since 1970. Regulation has evolved over that time in response to growth and partial privatisation of the rail industry, progressive understanding of the sources and causes of, and mechanisms to address, rail noise and increased community expectations regarding health and amenity impacts.

With the current leaps in understanding of the sources and causes of and mechanisms to address rail noise, the proposed amendments to the regulatory framework for rail in NSW, the growing acceptance by the rail industry for the need for a social licence to operate and a greater willingness by the rail industry to work collaboratively with regulators to address rail noise issues, progress towards achieving a level of rail noise that is acceptable by the community and supports the growth of freight transport by rail is on track.

## References

1. Freight Network Improvement, Transport for NSW: NSW Rail Network 2016 (3 Feb 2016)
2. Transport for NSW: NSW Freight and Ports Strategy (February 2013)
3. SLR Consulting on behalf of Transport for NSW: Sydney Rail Network Noise Review (25 Jan 2013)
4. Transport for NSW: NSW Rail Noise Database Stage III Measurements and Analysis (January 2015)
5. Treagus, R.: Government environmental noise policy—a personal account of the last 35 Years. In: Proceedings of Acoustics 2011 (2–4 Nov 2011)
6. NSW EPA: Technical Background Document for the NSW Rail Noise Policy Development (January 2002)
7. State Rail Authority State Rail Noise and Vibration Code of Practice (1995)
8. SLR Consulting Australia Pty Ltd: Epping to Thornleigh Third Track High Noise Locomotive Paper (June 2015)
9. NSW EPA: Rail Infrastructure Noise Guideline (2013)
10. NSW Planning: Development near rail corridors and busy roads—Interim Guidelines (2008)
11. <http://freight.transport.nsw.gov.au/documents/fnap-eligibility-factsheet.pdf>
12. Transport for NSW: Review of NSW Rail Access Regime—Issues Paper (November 2012)
13. NSW EPA: Review of regulation of the ‘railway systems activities’ under the Protection of the Environment Operations Act 1997: Position Paper (August 2014)

# Abatement of Railway Noise in Germany



R. Weinandy, P. Appel and T. Myck

**Abstract** One of the most important environmental issues in densely populated areas is the problem of noise. Road traffic and railway noise and airports located in close proximity to the city is not only annoying for residents; it also leads to serious health issues and has an enormous negative economic impact. Due to this, it is of primary importance for city planners, engineers and politicians to make our cities quieter. An important source for railway noise is freight trains that operate around the clock. However, railway traffic has an important function for a sustainable mobility in Germany and Europe. Therefore, it is planned to transfer more traffic from the roads, waterways, or aircrafts towards the railway. Both the politicians and the majority of the people support this. In contrast to that is the enormous ecological “Achilles’ heel”, the noise emissions. Especially during the nights, the noise exposure is up to 25 dB(A) above the threshold given by the World Health Organization, which is to be aspired in terms of a precautionary health protection of the people. Noise is a frequent reason for complaints and of high relevance with respect to any expansion, upgrade or construction measures of railway infrastructure. Along one of the most used railway corridor Rotterdam-Genoa, the opposition from residents is very high. Numerous people in Germany are protesting against railway noise, especially in the Middle Rhine valley. Under the Directives on rail traffic across Europe, the EU Commission has established pan-European noise thresholds for new types of rolling stock in the Technical Specifications for Interoperability (TSI). These emission values are valid for new rolling stock also in Germany. Since 1974 (western states of Germany) and 1990, respectively (eastern states of Germany), rail traffic on new lines is regulated in the 16th BImSchV (Traffic Noise Protection), which establishes noise immission limits for the protection of local neighborhoods. The most important consequence of the noise thresholds of the TSI is, that particularly noisy rolling stock fitted with cast iron block brakes is no longer permitted to be homologated (wagons of this type entering the market are no longer permitted). The challenge is now to replace these brakes in especially noisy freight wagons in the current rolling stock with quieter

---

R. Weinandy (✉) · P. Appel · T. Myck  
German Environment Agency, Woerlitzer Platz 1, D-06844 Dessau-Rosslau, Germany  
e-mail: rene.weinandy@uba.de

braking systems. As a financial incentive for rail operators to refit such rolling stock with quieter brakes, noise dependent track access charges are implemented in Germany. Additionally, there are a number of technical and legal measures available. In Switzerland and Germany for example, a ban is proposed for noisy freight wagons (non-compliant with TSI) from 2020 on. Access restrictions can yield a high level of protection and are efficient to protect the people from railway noise. The presentation will give an overview on these measures to abate efficiently the emissions of the rail freight traffic.

## 1 Introduction

Environmental noise is an important issue causing one of the most common public complaints in Germany and within the EU. Noise causes health risks, like cardiovascular effects, cognitive impairment, and psychological disorders such as depression and has an enormous negative economic impact. The most important source for railway noise is freight trains that operate around the clock, which is an enormous ecological problem. During nighttime, the noise exposure in hot spot regions is up to 25 dB(A) above the threshold given by the World Health Organization (WHO) [1], which is to be aspired in terms of a precautionary health protection of the people. Therefore, noise is of high relevance with respect to any expansion, upgrade or construction measures of railway infrastructure and it is widely agreed to enlarge noise protection measures. Further details on the general measures are presented in a position paper on the European strategies and priorities for railway noise abatement [2]. There are a number of technical measures available, e.g. retrofitting of the freight wagons to alternative brake systems. Moreover, legal measures like the Technical specification for interoperability relating to the subsystem ‘rolling stock’—noise TSI Noise exists [3]. This TSI Noise constitutes general requirements for the transnational railway traffic in Europe including noise emission thresholds of the rolling stock. The presentation will give an overview on technical measures to abate efficiently the emissions of the rail freight traffic.

## 2 Technical Measures to Abate Railway Noise

Mainly due to their braking technology, rail freight traffic is the predominant noise source in Europe, followed by high speed and inner-urban railway lines. Most freight trains still use cast iron brakes. Wheel roughness together with rail roughness is the main source of rolling noise in conventional rail, the main cause of wheel roughness being the use of cast iron brakes. This problem is even more urgent considering that these trains often operate at night. Therefore, it is necessary to replace the cast iron brakes by new composite or similar brakes, which has already started in Germany and shall be finally achieved by 2020. However, this is not

enough to solve the problem of railway noise. The German Environment Agency recommends various measures to reduce noise. The presentation concentrates on technical measures to abate efficiently railway noise in Germany. Some of them are already in use (e.g. disk brakes), other are currently in discussion (e.g. shielded bogies). However, all measures are taken into account in order to abate railway noise. Further details can be obtained from a recent study [4], which was commissioned by the German Environment Agency.

## 2.1 Disk Brakes

Freight trains still use cast iron brakes and are therefore much noisier. Wheel roughness in combination with rail roughness is the main source of noise in conventional rail, the main cause of wheel roughness being the use of cast iron brakes. This is a problem especially along freight corridors on which most of the rail traffic is operated at night. A prominent example is the Middle Rhine Valley, which is part of the European freight corridor between Rotterdam and Genoa. Disk brakes as shown in Fig. 1 are an alternative option for new freight wagons, which are an effective measure to abate railway noise [4].

New freight wagons with disk brakes have lower operational costs than those with new composite K-Blocks and can be quieter than wagons with other brake systems. The investment costs of disk brakes are about 23.000 € higher than new composite K-Blocks. However, the life cycle costs including investment and maintenance of wagons with disk brakes with a mileage over 65.000 km per year



**Fig. 1** Disk brakes, in this case a wheel disk brake

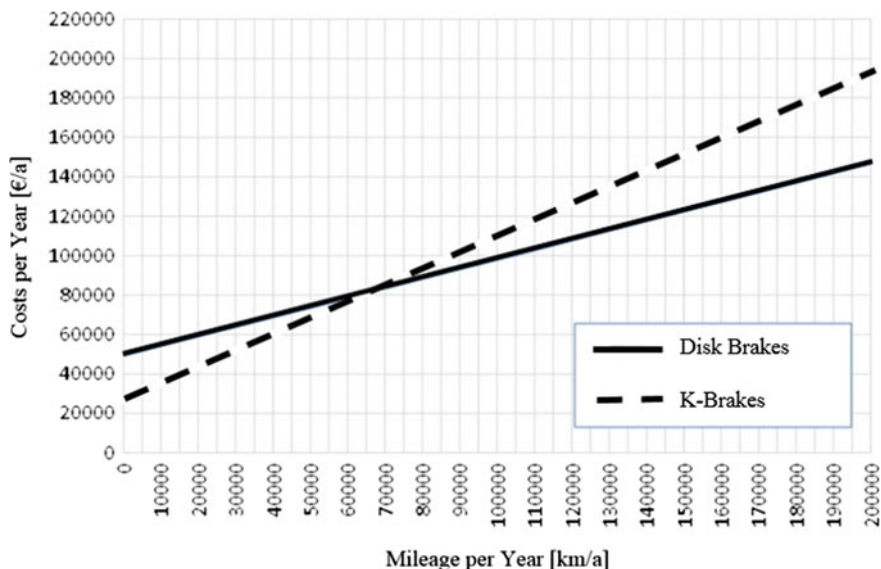


Fig. 2 Mileage in km and costs in € per year for freight wagons with disk brakes and K-brakes

are lower (Fig. 2) and the wagons generate less noise—up to 6 dB(A)—compared to wagons with K-Blocks [4].

The reason is that the disk brakes do not get in contact with the wheel-surface and therefore the wheels do not become rough. For wheel-mounted disk brakes, reduction of vibrations of the wheel is a further effect. The disadvantages are that disk brakes cannot grind the flat spots at the wheels and have a higher weight than conventional brakes. Moreover, they cannot be combined with block brakes in one train, because they require a different mechanism of control (electric instead of pneumatic). Furthermore, disk brakes are expensive to install. Therefore, exchange of an existing wagon is unlikely. Disk brakes are a solution only in shuttle trains (one type of wagons in the entire train) and for new wagons. An additional advantage would be that these trains might run faster than block braked trains. Due to the poor availability of data so far, this two effects are not subject of the assessments of the costs in the study. If the disk brakes are more widely used in future, the more data will be available.

## 2.2 Optimized Wheel Geometry

The noise reduction potential of optimized wheels (for details see Fig. 3) is up to 4 dB(A) [5]. Due to the construction of the wheel, a disk brake is necessary in order to reduce the thermal stress, which is otherwise induced by conventional brakes. The reason is that the optimized wheels are effective for a reduction of noise but not



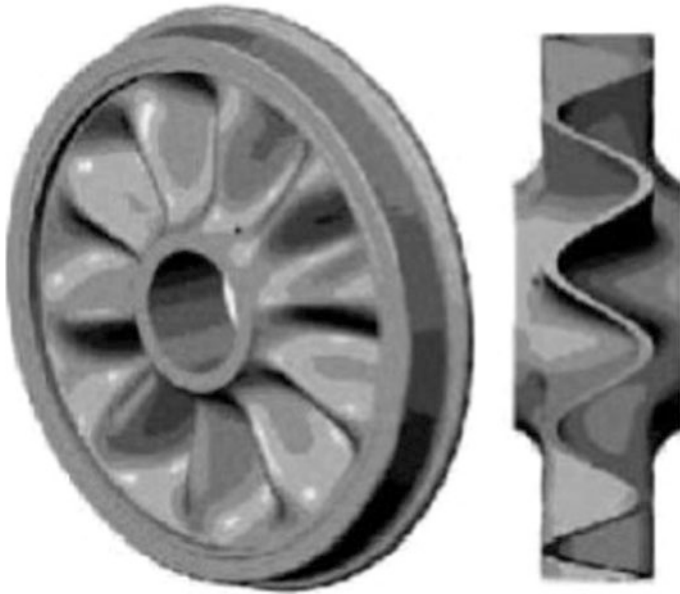


**Fig. 3** Optimized wheel geometry

for an optimum heat dissipation. Another problem is that most of the optimized wheels available are not already used on a larger scale. It is likely that maintenance cost will not increase, because of the same wear and tear like conventional wheels with disk brakes.

### **2.3 Shielded Bogies and Wheels**

Without a low-rise noise barrier, the shielded bogie (Fig. 4) has a reduction potential of 1–2 dB(A) [6]. This is mainly due to noise reflection towards the ground. To enhance this effect further, it is possible to use an integrated soundproofing material to decrease the level of noise before it is reflected to the ground. Moreover, with a low-rise noise barrier, a reduction of up to 10 dB(A) is possible and in combination with an integrated soundproofing material it can be further increased up to 18 dB(A) [4].

Shielded wheels (Fig. 5) reduce the noise by 2 dB(A) [7]. The technical principle is similar to the functionality of the shielded bogie. The noise will be reflected towards the ground. It is also in this case possible to integrate a soundproofing material. The best performance can be achieved by a combination of low-rise noise barriers and soundproofing material.



**Fig. 4** Shielded bogie

It is to be mentioned that both measures makes the inspection and the brake tests difficult. Furthermore, special attention must be given to the international and national loading gauge.

#### ***2.4 Noise Absorber Blinds at the Cooling Air in- and Outlet***

In order to abate the noise of the complete train, it is indispensable to address not only the noise sources of the freight wagons but also those of the locomotives. Therefore, the next measures are directed towards the locomotives. Noise Absorber blinds at the cooling air in- and outlet can be used to minimize the noise of driving, standstill and acceleration. Because of the lamellas, the air particles are diverted and the kinetic energy of the air particles will be converted into heat. The absorber blinds should be designed in a way to ensure that the engine gets enough air for cooling. It is easy to install this measure in stock and not expensive. The noise reduction potential is up to 5 dB(A). However, it should be mentioned that this reduction applies to the cooling air source only, not to the entire train. It will not be reflected in a reduction of the exposure by 5 dB(A). In Fig. 6, a demonstration locomotive, the Blue Tiger with such a device installed is depicted [8].



Fig. 5 Shielded wheels



Fig. 6 Noise absorber blinds at the Blue Tiger

## 2.5 *Optimized Blade Shape for the Cooling Fan*

For the noise reduction, it is necessary to optimize the blade shape for the cooling fan. As the noise absorber blinds, the optimized blade shape helps to minimize the noise of driving, standstill and acceleration by reducing the noise of the cooling fan. The costs for this measure is estimated to be 1.000 € for a new locomotive and 12.000 € for existing stock. The higher costs for stock is due to the need to adapt the electronics. The noise reduction is up to 6 dB(A) [9].

## 3 Conclusions

Unlike road traffic noise, which occurs virtually everywhere, rail traffic noise is more localized to specific transport corridors. However, depending on the type of train and the volume of trains, high levels of noise can be generated, especially along freight corridors on which most of the rail traffic is operated during the night.

The EU Commission has established pan-European noise emission thresholds for new types of rolling stock in the Technical Specifications for Interoperability (TSI). These values are valid for new rolling stock also in Germany. The 16th BImSchV (Traffic Noise Protection) establishes noise immission limits for the protection of local neighborhoods on new lines. The current challenge is to replace the cast iron brake blocks in the existing noisy freight wagons with quieter braking systems. In Switzerland and in Germany, a ban is proposed of noisy freight wagons from 2020 on. However, access restrictions can yield a high level of protection and are efficient to protect the people from rail noise. Moreover, the establishment of ambitious noise thresholds is necessary, but it does not include current freight wagons or locomotives, which typically have an operating life of around 40 years. In terms of noise abatement, however, the existing rolling stock cause the major problem of rail noise. Therefore, it is indispensable to refit freight wagons with quieter braking systems and further measure like the shielded bogies and wheels. Moreover, the locomotives should be applied with noise abatement technology too; some are described in this paper. In a recent study [4], more than 25 of those measures for the freight wagon, the locomotive and the infrastructure were analyzed. It is to be stated here, that all the presented measures to abate rail noise are more costly than the conventional parts. However, such a calculation should always take into account that noise itself is not only harmful for the people but it is expensive too, e.g. due to the health costs, the losses of value of properties and re-modelling costs for buildings like soundproof windows.

An efficient abatement of rail noise including legal, technical and operating measures is necessary in order to reduce health risks as well as to improve the life quality of people. Therefore, the German Environment Agency encourages respective research studies and the German Government is considering national legislation to abate efficiently railway noise.

## References

1. WHO Regional Office for Europe: Night Noise Guidelines for Europe, Copenhagen (2009)
2. WG Railway Noise of the European Commission: Position Paper on the European Strategies and Priorities for Railway Noise Abatement, (2003)
3. Commission Decision of 23 December 2005 concerning the technical specification for interoperability relating to the subsystem 'rolling stock— noise' of the trans-European conventional rail system (2006/66/EC) (2006)
4. IGES Institut GmbH; Technische Universität Berlin, Fachgebiet Schienenfahrzeuge; IVE Ingenieurgesellschaft für Verkehrs- und Eisenbahnwesen mbH; Prof. Dr. Eckhard Pache: Strategien zur effektiven Minderung des Schienengüterverkehrslärms (Strategy for an effective reduction of noise by rail freight transport) (2017)
5. Hecht; Zogg: Lärmdesign moderner Triebfahrzeuge am Beispiel der Lok 2000-Serie. Anwendung von Telemetrie, Intensitäts- und Arraymesstechnik. In: ZEV+DET Glaser Annalen **119**(9/10), 467 (1994)
6. Johannsen: Der Einfluss der Oberflächenimpedanz auf das Abstrahlverhalten eines Schürze-Niedrigschallschirm-Systems. Berlin (2005)
7. Hecht, W.: Low Noise Train (LNT) Präsentation Wien (Austria). Report Nr. **27/02**. (2002)
8. Hecht; Czolbe 2008: BMU-Projekt Lärminderungsmaßnahmen an drei Großdiesellokomotiven BlueTiger. In: ZEVrail Glasers Annalen **132**, 11–12 (2008)
9. Voith Turbo: Wirkt in einem Zug. Antriebstechnik, [http://resource.voith.com/vt/publications/downloads/1970\\_d\\_g\\_1480\\_d\\_atm\\_broschuere\\_gear\\_units\\_2012-09.pdf](http://resource.voith.com/vt/publications/downloads/1970_d_g_1480_d_atm_broschuere_gear_units_2012-09.pdf). (2014)

**Part III**  
**Predictions, Measurements and Modelling**

# Quantifying Uncertainties in Measurements of Railway Vibration



K. A. Kuo, G. Lombaert and G. Degrande

**Abstract** Predictions of railway-induced vibration levels should be accompanied by the caveat that uncertainties exist regardless of the prediction technique used—whether it be empirical methods based on in situ measurements, or numerical models with measured or estimated parameter inputs. This paper investigates sources of uncertainty present in field measurements. Using data from an extensive in situ measurement campaign, variability due to changes in receiver position, the averaging of multiple hammer impacts and time lapse between measurements are quantified. Results are used to conservatively estimate the following uncertainty levels: 1–2 dB for installation of measuring equipment; 5 dB for temporal changes of 14 months; 5 dB at below 10 Hz when using an average of 20 hammer impacts to determine transfer functions; and at least 2–5 dB variation for 10 m longitudinal offset in measurement location.

## 1 Introduction

Reducing uncertainty in vibration predictions in the built environment has both social and economic significance, and for this reason, various prediction models have been developed. Forward-modelling approaches require detailed knowledge of a large range of material and geometrical parameters. The level of confidence in these model predictions is dependent on the uncertainty that exists in both the model and the input parameters, such as the dynamic soil characteristics, wheel/rail unevenness and vehicle properties. Research efforts are focussing on identifying and quantifying these sources of uncertainties [1–7].

In practice, vibration predictions are made using simplified empirical methods, such as those developed by the U.S. Department of Transportation [8, 9]. These methods avoid the need for extensive soil characterisation tests by directly mea-

---

K. A. Kuo (✉) · G. Lombaert · G. Degrande  
Department of Civil Engineering, KU Leuven, Kasteelpark Arenberg 40,  
3001 Leuven, Belgium  
e-mail: kirsty.kuo@kuleuven.be

asuring the vibration transmission through the soil. But sources of uncertainty still exist for measurement-based prediction methods: the choice of equipment, measurement procedure, measurement location and processing of data will all affect the final results obtained. Apart from following ‘best-practice’ procedures, vibration consultants currently have little insight into how to manage these uncertainties. This paper aims to provide some guidance in this area, by examining the results of an extensive field measurement campaign [10] and seeking to draw conclusions regarding the magnitude of some uncertainty sources. Details of the measurement campaign are presented in Sect. 2, Sect. 3 provides the data for various sources of uncertainty, and Sect. 4 discusses what insights can be gained from this study.

## 2 Field Measurement Campaign

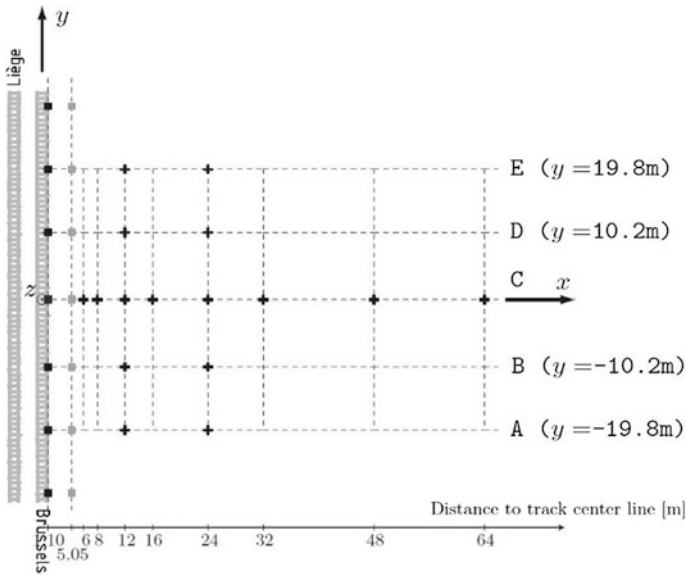
In 2011 and 2012, measurement campaigns [10] were carried out at a site in Lincet, Belgium, located on the high speed line L2 between Brussels and Liège. The high-speed line consists of two classical ballasted tracks with continuously welded UIC 60 rails that are supported every 0.60 m by resilient studded rubber pads on a prestressed monoblock concrete sleeper. Four types of train operate on the line: InterCity (IC) trains of type IC-A and IC-O and the Thalys and ICE high speed trains. The railway line is constructed in an excavation and runs parallel to highway E40, separated by an embankment. A photograph of the site is shown in Fig. 1.

Figure 2 shows the experimental setup used. Sixteen high sensitivity seismic accelerometers (PCB 393 series) measuring free field vertical acceleration were installed along five measurement lines located perpendicular to the track. Five receivers are located at 12 m from the track, and another five at 24 m from the track, with each pair of adjacent receivers offset by a longitudinal distance of

**Fig. 1** Photograph of the site in Lincet







**Fig. 2** Measurement setup in the free field at the site in Lincent, indicating the receiver points (✚) and the source points at the track (■) and at the soil’s surface adjacent to the track (■)

approximately 10 m. Receivers are referred to here by the letter of the corresponding measurement line (A–E), followed by the distance to the track center line, e.g. A12, C24. The data were recorded using a National Instruments PXI-1050 chassis with four 4472B modules. The Nyquist frequency is 500 Hz.

The free field response during the passage of 103 trains was measured in 2011. Transfer functions were obtained in 2011 and 2012 using an impact hammer with a mass of 5.5 kg and a soft tip equipped with a force sensor (PCB 086D50). Two impact locations, the edge of the sleeper and an aluminium foundation installed at the soil’s surface at a distance of 5.05 m from the centre of the track were used. The free field response was obtained by summing the acceleration time signals for 100 hammer impacts at each impact location, then windowing and integrating to obtain the velocity response. An averaged mobility between each source and receiver could then be computed using the forcing history.

### 3 Sources of Measurement Uncertainty

#### 3.1 Longitudinal Variation

Variability of the free-field vibrations in the track’s longitudinal (y) direction is investigated by considering accelerations obtained at adjacent receivers during various train passages. It is expected that variation between two adjacent receivers

will be primarily due to differences in soil characteristics, with wheel-rail unevenness and variation in the track accounting for some (smaller) effect. Figure 3 shows the difference in vibration velocity levels between adjacent receivers located at 12 and 24 m, recorded during 30 passages of IC-A trains (159–211 km/h) travelling in the direction of Brussels. There is no obvious influence of train speed on the difference in the vibration velocity levels. The scatter in the velocity levels for each train passage is believed to be a result of variations in train properties, including wheel/rail unevenness, and measurement noise, whereas the general trend is representative of the longitudinal variation of soil and track characteristics (geometry and materials), and measurement equipment installation.

To obtain a clearer indication of the variation between adjacent receivers during train passages, we calculate the average difference in vibration velocity levels and the interval in which there is 95% confidence that the true average difference can be found (assuming a Gaussian probability distribution). This confidence interval is calculated using the narrow-band velocity spectrum and assuming independent errors for each frequency, before being averaged over the one-third octave bands.

The difference between the vibration velocity levels for each of the four types of train (IC-A, IC-O, Thalys, ICE) at adjacent channels C12 and D12 is shown in Fig. 4. Similar results are observed for all trains, especially the IC-A and IC-O trains. This similarity is also present in the results for channels C24 and D24, shown in Fig. 5. It is difficult to draw conclusions on the influence of the train type due to the small number of recorded passages for Thalys and ICE trains. For this reason, all types of train passages are included in Fig. 6, which shows the average difference in vibration velocity levels between adjacent receivers. The variance is of the order of  $\pm 2$ –5 dB.

To investigate the relative contributions of the soil and track characteristics, we can examine the point source transfer mobility (TMP) measurements, which characterise the direct propagation path between the point of impact and the receiver. Figure 6 shows the difference in TMP obtained using more than 100 impacts on the sleeper of the track. In each case the response has been recorded at the receiver located at the same longitudinal distance along the track as the impact location. As this measurement technique does not involve a train passage, the influence of the vehicle-track interaction has been removed.

### 3.2 *Sampling of Hammer Impacts*

It is recommended that all transfer functions include the average of at least 20 hammer impacts [8, 9]. As over 100 impacts were recorded at each source location, the variability due to sampling of the hammer impacts can be investigated. The 100-plus hammer impacts at  $y = 10$  m were randomly sampled to obtain

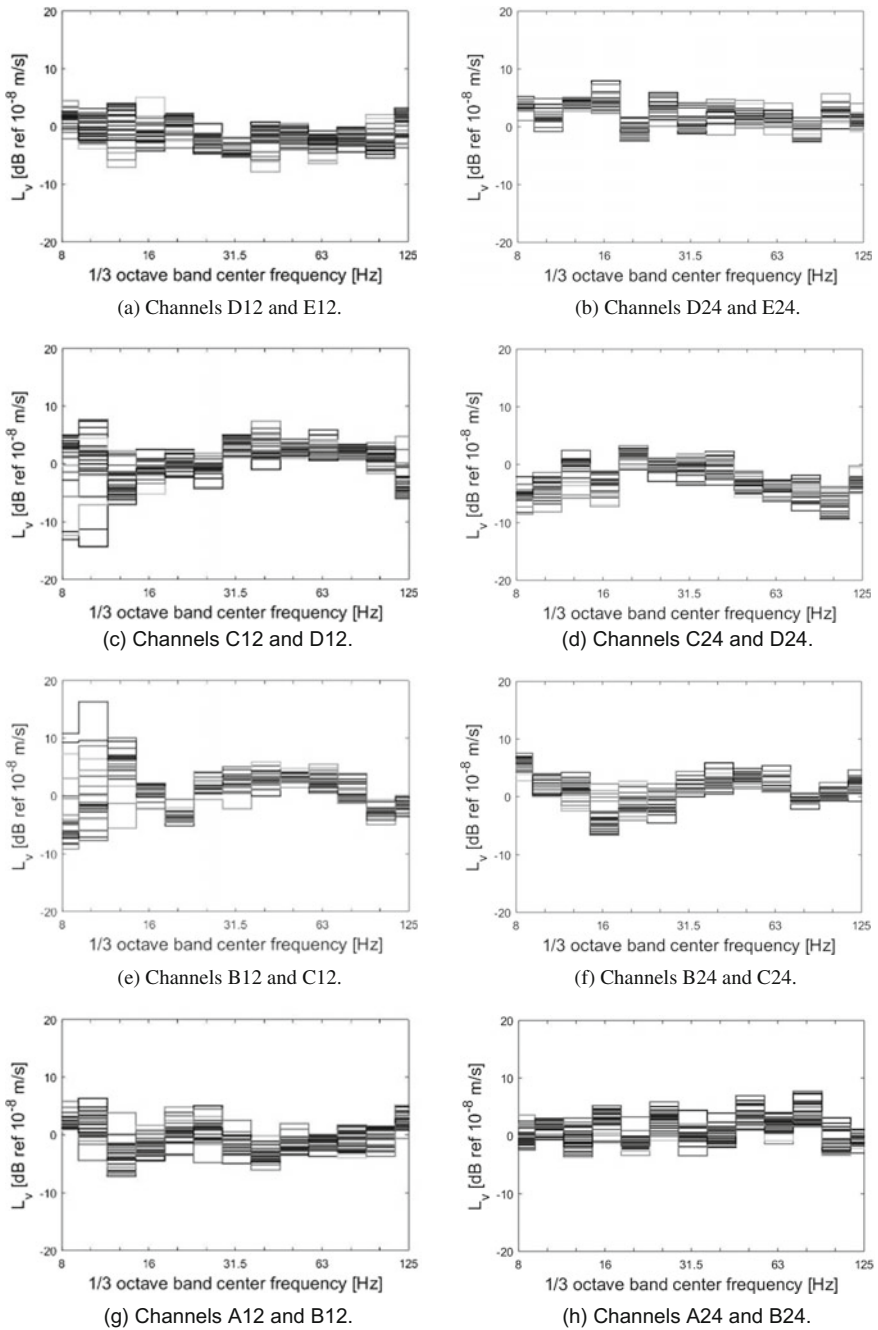


**Fig. 3** The difference in vibration velocity levels between adjacent receivers located at 12 and 24 m, recorded during the passage of 30 IC-A trains (159–211 km/h) to Brussels. The train speed is indicated by the line shade

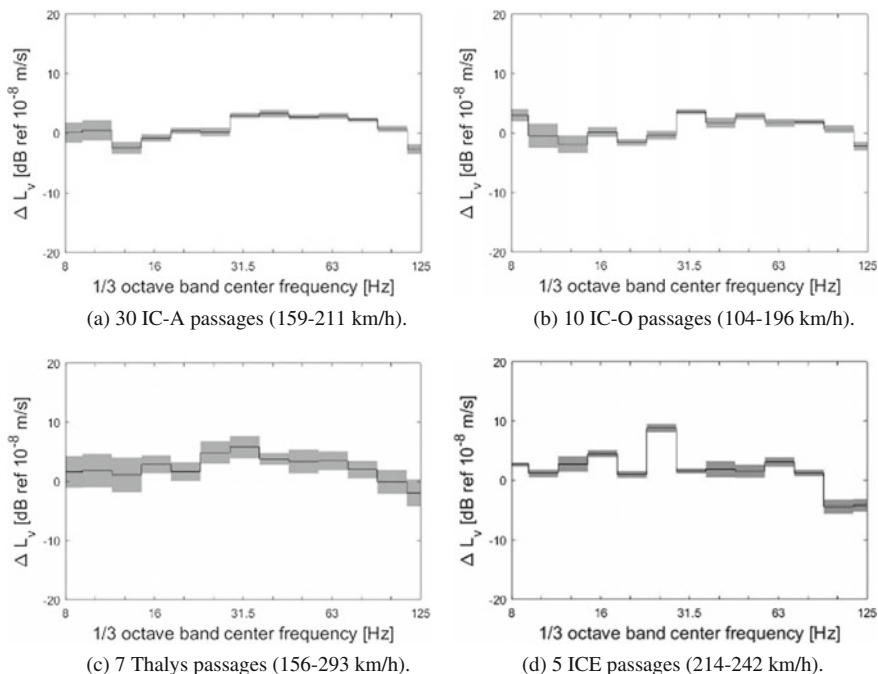


**Fig. 4** The average difference in vibration velocity levels between adjacent receivers C12 and D12 for each train type, recorded during the passage of trains to Brussels, with 95% confidence interval of the average difference in vibration velocity levels shown in grey

25 realisations of a 20-impact set. The point source transfer mobilities obtained from each of these 25 realisations with receiver location C12 are shown on the left of Fig. 7. On the right of this figure, the difference between the average of the 25 realisations and the TMP determined using all 100-plus impacts is shown. It can be seen that the use of a 20-impact set consistently results in an overestimate of the TMP of approximately 5 dB at the frequency band centered on 8 Hz, with the overestimate reducing to and remaining at 0 dB from 16 to 125 Hz. This same trend is observed for other source and receiver locations, and is due to the low signal-to-noise level present at low frequencies.

### 3.3 Time Lapse Between Measurements

Transfer functions between an aluminium foundation located on the soil adjacent to the track and the free field were measured in identical positions (to the extent of our capabilities, with positional error of the order of 1–2 cm) in March 2011 and

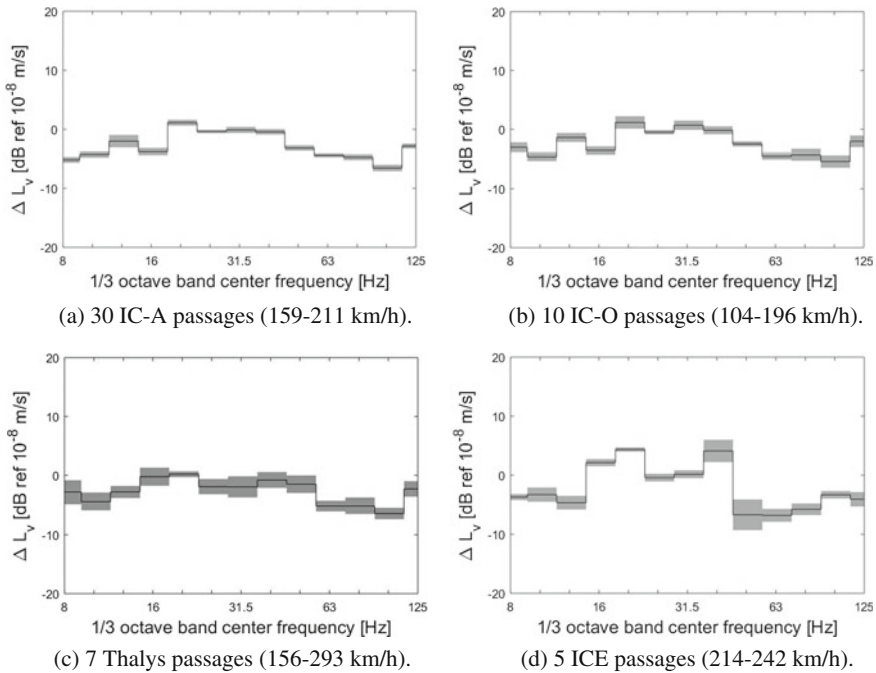
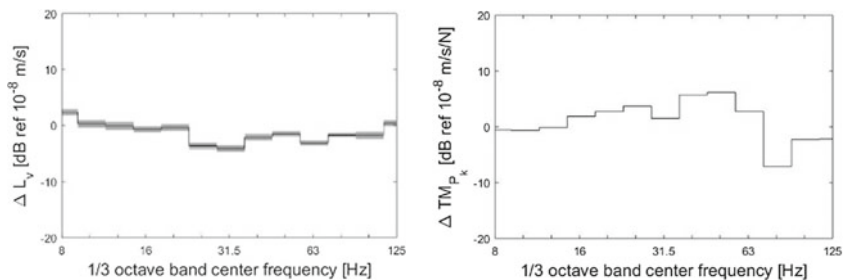
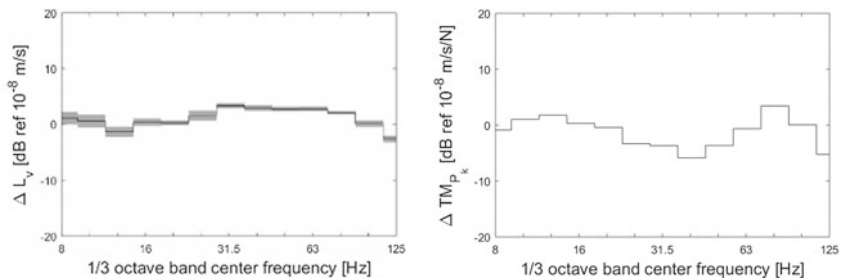


**Fig. 5** The average difference in vibration velocity levels between adjacent receivers C24 and D24 for each train type, recorded during the passage of trains to Brussels, with 95% confidence interval of the average difference in vibration velocity levels shown in grey

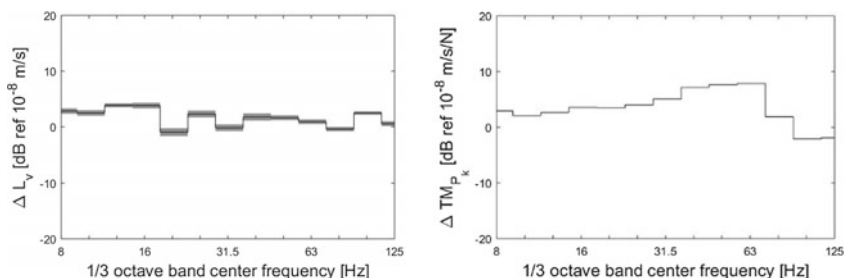
May 2012. Figure 8 shows the difference in point source transfer mobilities obtained 14 months apart, using more than 100 hammer impacts on the soil’s surface, adjacent to the track. The source is located at longitudinal distances of  $\pm 10$ ,  $\pm 30$ ,  $\pm 50$ ,  $\pm 70$  m and the receivers are C12 and C24. The magnitude of the variation is generally 0–5 dB, but can reach up to 10 dB. Similar results are observed for different receivers. This variation could be due to changes in the soil conditions (effects of precipitation, erosion, creep, general disturbance), small variations in the location and installation of the sensors and the aluminium foundation, and noise in the measurements. To assess the influence of the installation of the aluminium foundation, Fig. 8 also shows transfer functions measured using two different installations of the foundation on the same day, with an unchanged sensor installation. The foundation is located at  $y = 0$  m and the receivers are C12 and C24. As the variation observed at C12, C24 and other receivers (not shown here) is generally of the order of 1–2 dB, it can be concluded that the installation of the foundation is not a major contributor to the variation observed in Fig. 7.



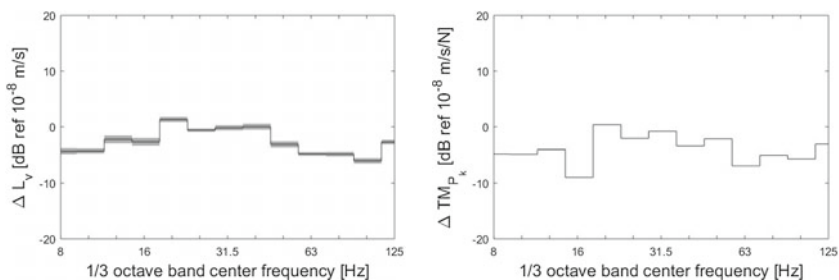
(a) Channels D12 and E12.



(b) Channels C12 and D12.

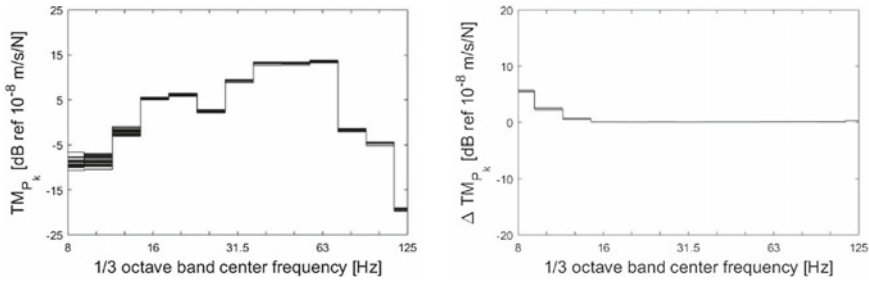


(c) Channels D24 and E24.

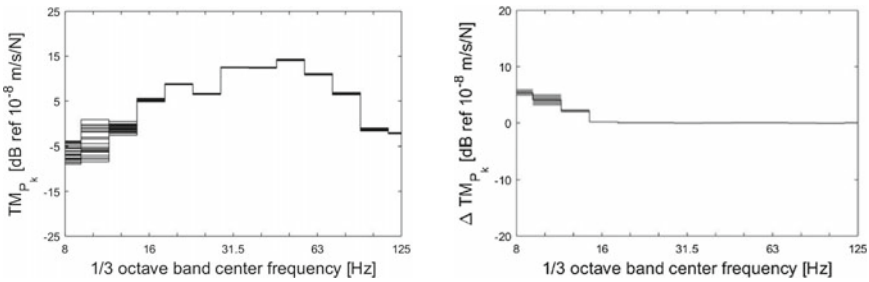


(d) Channels C24 and D24.

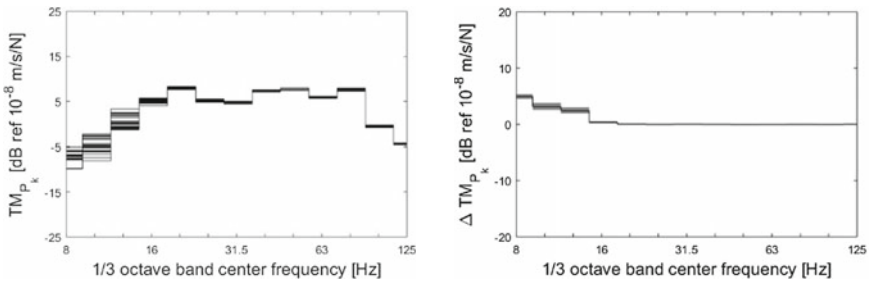
**Fig. 6** The average difference between adjacent receivers calculated using vibration velocity levels recorded during the passage of 52 trains of type IC-A, IC-O, Thalys and ICE to Brussels (left), and point source transfer mobilities obtained using more than 100 impacts on the sleeper of the track (right). 95% confidence interval shown in grey



(a) TMP measured with impacts on track.



(b) TMP measured with impacts on soil (2011).

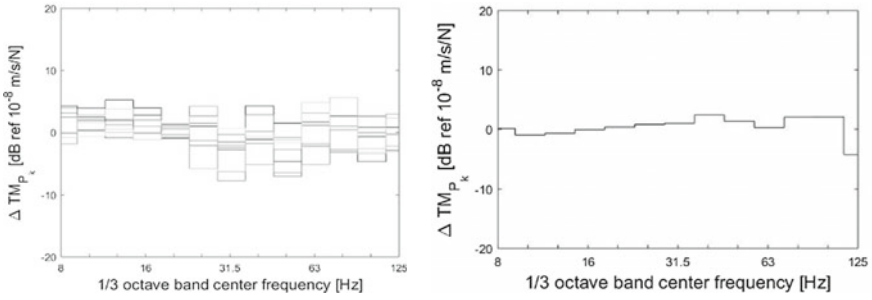


(c) TMP measured with impacts on soil (2012).

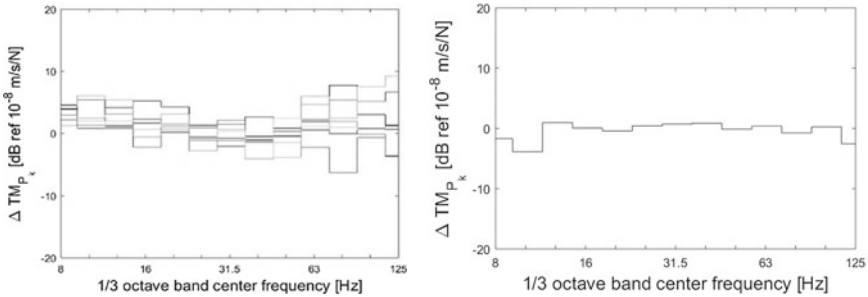
**Fig. 7** The point source transfer mobilities obtained using 25 realisations of a 20-impact data set (left) and the difference between the average of the 25 realisations and the TMP determined using all 100+ impacts (right). The 95% confidence interval shown in grey, the source is located at  $y = 10$  m on the track, and the receiver is C12

## 4 Discussion

The main sources of measurement uncertainty can be considered to be associated with four general categories: choice of equipment; measurement procedure; measurement location; and data processing. Each and every measurement taken in the field contains multiple uncertainties, and it would be a difficult (perhaps even impossible) task to design a study that could be used to isolate and quantify each



(a) Receiver C12.



(b) Receiver C24.

**Fig. 8** The difference in point source transfer mobilities obtained in 2011 and 2012 using more than 100 hammer impacts on the soil's surface, adjacent to the track, where the longitudinal ( $y$ ) position of the source is indicated by the line shade (left); and using two different foundation setups at  $y = 0$  (right)

uncertainty in turn. For this reason, this paper has sought to infer uncertainty levels by applying an understanding of railway-induced vibrations to the available data. The following limitations apply to this paper's findings:

- (1) The measured data is from a single site, which had been specially selected for model validation purposes [10] due to its relatively flat site topography and lack of surrounding buildings. Many railway sites will not have such a simple geography.
- (2) The limited size of the collected data set means that it is not possible to draw accurate conclusions on some aspects of the study, for example, the influence of train type on free-field vibration levels.
- (3) Uncertainties due to choice of equipment have not been considered here, but cannot be assumed to be negligible. A single set of equipment was used during each of the two measurement campaigns in 2011 and 2012. However, some accelerometers used in 2011 were replaced by other sensors in 2012, and the positions of the original accelerometers were interchanged for the second campaign.



- (4) It cannot be assumed that the vibration response is linear in time, nor space, nor in its dependence on operating conditions, even if all measurement uncertainties could be eliminated. Hence measurement variability will always be present.

The data presented in this paper relates to the two categories of measurement procedure (sampling of hammer impacts, installation of the foundation, timing of measurements) and measurement location (longitudinal variation of soil properties, longitudinal variation of train-rail effects). The main findings are as follows:

The variation due to sampling of hammer impacts has been shown to occur primarily at frequencies below 10 Hz. This is generally not a critical region for railway-induced vibration, and therefore the FRA recommendation for use of 20-impact sets is endorsed by this study. If data is needed below 10 Hz, more than 50 impacts should be used.

The installation of the source foundation has been shown to have a very small influence (1–2 dB) on the repeatability of measurements.

The passing of time shows a moderate influence (0–5 dB) on the free-field transfer functions. As there was no observable disturbance at the site, this is primarily attributed to seasonal effects and long-term changes such as erosion. Greater seasonal variation may be expected at a 6-month interval. As measurements for empirical predictions often occur months or even years before construction of new railways/buildings, this effect is relevant for the vibration consultant and further investigation of this is proposed.

Perhaps the most striking aspect of this study is the variation occurring in the vibration velocity levels between adjacent receivers for a single train passage (Fig. 3), with weak observable correlation to train speed and train type. This variation is significantly reduced when the average response of multiple train passages is calculated (Fig. 6). Due to this observation, it is recommended that vibration velocity levels used in empirical prediction methods are the averaged response of at least five, and preferably ten, train passages.

The longitudinal measurement location has been shown to influence both the vibration velocity levels and transfer functions by 2–5 dB as a result of local variations in the soil and track characteristics.

## References

1. Jiang, S., et al.: Railway rolling noise predictions: field validation and sensitivity analysis. *Int. J. Rail Transp.* **1**, 109–127 (2013)
2. Jones, S., et al.: Prediction uncertainties and inaccuracies resulting from common assumptions in modelling vibration from underground railways. *J. Rail Rapid Transit* **226**, 501–512 (2012)
3. Costa, P., et al.: Influence of soil non-linearity on the dynamic response of high-speed railway tracks. *Soil Dyn. Earthq. Eng.* **30**, 221–235 (2010)
4. Degrande, G. et al.: Quantifying and reducing uncertainty in structural dynamics, Project OT/13/59, Research Council KU Leuven, Department of Civil Engineering, KU Leuven, Oct 2013–Sept 2017

5. Triepaischajonsak, N., et al.: Ground vibration from trains: experimental parameter characterization and validation of a numerical model. *J. Rail Rapid Transit* **225**, 140–153 (2011)
6. Kuo, K.A., et al.: The effect of a twin tunnel on the propagation of ground-borne vibration from an underground railway. *J. Sound Vib.* **330**(25), 6203–6222 (2011)
7. Jones, S., Hunt, H.E.M.: Predicting surface vibration from underground railways through inhomogeneous soil. *J. Sound Vib.* **331**(9), 2055–2069 (2012)
8. Hanson, C.E., et al.: Transit noise and vibration impact assessment, Report FTA-VA-90-1003-06. U.S. Department of Transportation, Federal Transit Administration (2006)
9. Hanson, C.E., et al.: High-speed Ground Transportation Noise and Vibration Impact Assessment, HMMH Report 293630-4. U.S. Department of Transportation, Federal Railroad Administration (2005)
10. Verbraken, H.: Prediction of railway induced vibration by means of numerical, empirical and hybrid methods, Ph.D. thesis, Department of Civil Engineering, KU Leuven (2013)

# Reproducibility of Railway Noise Measurements—Influence of Weather and Test Site Conditions



Jens C. O. Nielsen, E. Augis and F. Biebl

**Abstract** Requirements on monitoring stations to guarantee good reproducibility of measured railway noise data from one test site to another are investigated by field measurements and numerical simulations. Based on data from a monitoring system installed at Deutsch-Wagram in Austria, the influence of weather conditions (temperature, rain and snow) on pass-by noise levels and rail vibration is assessed. The influence of temperature on track decay rates (TDR) has been determined from pass-by analysis (PBA). It is concluded that the track superstructure design used at Deutsch-Wagram (60 kg/m rails, rail pads with dynamic stiffness in the order of 700–1000 kN/mm, and monobloc concrete sleepers on ballast) is appropriate for noise monitoring since the variation of measured noise levels for the studied range of weather conditions has a standard deviation of less than 2 dB. For such a track design, it is not essential to apply a correction procedure to account for seasonal variations (except in the case of snow). Further, a numerical parameter study of the influence of TDR and ground conditions (horizontal ground surface level relative to top of rail, and ground impedance based on a single value effective flow resistivity parameter) on predicted noise level is performed using TWINS. It is found that for ground surfaces with low sound reflection, the influence of ground surface level (when varying from 0.2 to 2 m) on predicted pass-by noise level is in the order of 1 dB.

---

J. C. O. Nielsen (✉)

Department of Applied Mechanics/CHARMEC, Chalmers University of Technology,  
41296 Gothenburg, Sweden

e-mail: jens.nielsen@chalmers.se

E. Augis

SYSTRA, 72 rue Henry Farman, 75513 Paris Cedex 15, France

F. Biebl

psiacoustic, Lastenstrasse 38, 1230 Vienna, Austria

## 1 Introduction

Monitoring stations (measurement sites) are track based installations providing data of the running behaviour and conditions of passing trains. Examples of sensors are strain gauges or accelerometers on the rails or sleepers to determine wheel-rail contact forces and detect out-of-round wheels, and microphones to measure noise emission. The use of such measurement sites brings commercial benefits to rolling stock and infrastructure managers. For example, early detection of wheel defects leads to a reduction of infrastructure and vehicle deterioration, allowing for condition-based maintenance of rolling stock. Track access fees can be applied to promote use of track-friendly and low-noise vehicles. The present work was performed in 2012–2014 within the UIC-funded project HRMS (Harmonisation of Running behaviour and noise on Measurement Sites) [1, 2].

For the image of the railway system and the acceptance of new railway lines, low noise emission is a major concern. Existing monitoring systems are based on different track designs and methods to evaluate measured railway noise levels. For cross-border operation of rail vehicles, a harmonisation of these methods is advisable. Limiting values for pass-by noise generated by various types of vehicles are given in [3]. EN ISO3095 [4] sets a standard for the certification of rail vehicles (type testing), where measurements should be measured on a TSI (Technical Specification for Interoperability) compliant test section. This means that (acoustic) rail roughness, vertical and lateral TDR, as well as environmental and meteorological conditions need to fulfil certain requirements. Although EN ISO3095 provides requirements that partly can be adopted for the definition of permanent infrastructure noise monitoring systems, there are currently no dedicated standard or commonly agreed rules for such systems.

## 2 Survey of Noise Monitoring Systems

In the HRMS project, monitoring systems currently in operation in Europe were surveyed. The survey was distributed to infrastructure managers in Austria, Belgium, Finland, France, Germany, the Netherlands, Norway, Poland, Sweden, Switzerland and Spain. In 2014, according to the survey, only the Austrian and German railway networks owned and operated permanently installed (track based) noise monitoring systems.

The Austrian system *acramos*<sup>®</sup>, provided by the company *psiacoustic* and owned by the Austrian federal railways ÖBB-Infrastruktur AG, is mainly used for research purposes. No specification of maximum noise level has been defined. The system is installed at two sites. In Germany, three noise monitoring systems (*AkuMon*) owned by DB Netz AG are currently in operation. Their most complete system is composed of two microphones located at the normative position (7.5 m from track centre and 1.2 m above top of rail), one accelerometer on one rail, a weather station

and wheel sensors. In Belgium, two noise monitoring systems were being evaluated by Infrabel: Gotcha developed by Lloyd's Register and a system developed and provided by Schenck.

Common features of the four systems include installation on tangent ballast track, continuously welded 60 kg/m rails, concrete monobloc sleepers on ballast and rail pads with relatively high dynamic stiffness (700–1000 kN/mm). For similar rail roughness levels, this design is favourable since track with stiff rail pads contribute less to the total noise than track with softer rail pads, meaning that the contribution of wheel noise to the total pass-by noise is more significant. Further, the track is elevated about 1 m above the surrounding soil and free sound propagation conditions are fulfilled. The ground surface on either side of the track is relatively sound absorbing on all test sites (mainly soil, grass or gravel). The weather stations include a rain detector, and wind, temperature and humidity are also measured. Noise and vertical rail vibration are measured by all systems. Based on PBA [5], the rail acceleration signal can be used to derive and investigate the stability of track dynamics indicators, such as TDR and combined wheel/rail roughness. All systems allow for real-time post processing of pass-by noise and the vibration quantities that need to be assessed when applying EN ISO 3095:2013 [4]. Data transfer to a central server is fast, but no post-analysis has been applied to obtain vehicle specific noise signals, or to detect and identify wheel defects and/or vehicle parameters affecting noise (e.g. type of brake block).

### 3 Field Assessment of Influence of Weather Conditions

EN ISO 3095:2013 [4] requires the surroundings around the microphone to be free of sound absorbing elements (free sound propagation is required), including high vegetation or snow. Weather conditions such as rain, temperature, humidity and air pressure should be recorded, but in principle noise type testing of vehicles is allowed also in rainy conditions and at any temperature. The Noise TSI [3] requires the track to be free of ice, frost or snow, but measurements at temperatures below 0 °C are allowed.

The noise monitoring system, see Fig. 1, installed at Deutsch-Wagram (Austria) has been in operation since 2006. Two wheel sensors, installed to trigger the monitoring system, are used to determine the speed and type (based on axle distance pattern) of the train. Each microphone is located at a distance of 7.5 m from track centre and at 1.2 m above the top of the rail. The pass-by noise level, here simplistically denoted  $L_p$ , reported in this study is the A-weighted equivalent continuous sound pressure level evaluated over train passing time  $T_p$  [4].

To evaluate the influence of weather conditions on the reproducibility of the railway noise measurements, data recorded during a period of about one year has been analysed (4000 trains). Datasets from two different train categories, freight trains and passenger trains have been assessed (rejecting braking and accelerating trains). Most of the freight trains have been assumed to have cast iron brake blocks.



**Fig. 1** Noise monitoring station at Deutsch-Wagram in Austria

All passenger traffic included two coupled class 4020 EMU (electric multiple units) train sets used on regional rail routes. Each EMU consisted of a traction unit (4020), a centre unit (7020) and a steering unit (6020) with 12 axles and a total length of 69 m.

### 3.1 Influence of Temperature

The influence of temperature  $T$  on dynamic rail pad stiffness and TDR was investigated in [6]. It was concluded that increasing temperature leads to a reduction of rail pad stiffness, and that decreasing temperature results in increasing cut-on frequency and decay rates of waves propagating along the rail above cut-on. In this study, data has been classified with respect to three temperature intervals:  $T < 0$  °C,  $5$  °C  $< T < 15$  °C and  $T > 20$  °C. For freight traffic, the influence of temperature interval and vehicle speed on pass-by noise level is shown in Fig. 2. For each temperature interval, trends of A-weighted pass-by noise level versus train speed have been determined by linear regression. The slope coefficient  $N$  ('speed exponent', see [7]) is in the order of 30 for all three temperature intervals. A low influence of temperature on noise level is observed. At speeds higher than 80 km/h, the average pass-by noise level at  $T < 0$  °C is only about 1 dB below the noise levels at higher temperatures.

For each studied weather situation (three temperature intervals, rain or no rain, snow or no snow), the average value and standard deviation of pass-by noise level  $L_{p,80 \text{ km/h}}$  have been determined after correcting the measured noise levels with respect to train speed by applying the common relation  $L_{p,80 \text{ km/h}} = L_p - N \log_{10}(v/80)$ ,  $N = 30$ . For both train categories, it was concluded that the average noise level measured in the interval  $5$  °C  $< T < 15$  °C was higher than at  $T < 0$  °C, but surprisingly also slightly higher than the noise level measured at  $T > 20$  °C. The average noise level for temperatures in the mid-interval was 0.4 dB higher than at  $T > 20$  °C, and around 1 dB higher than at  $T < 0$  °C. On the other hand, it was observed that vertical rail vibration level (A-weighted particle velocity level) was monotonically increasing with increasing temperature. TDR were determined based

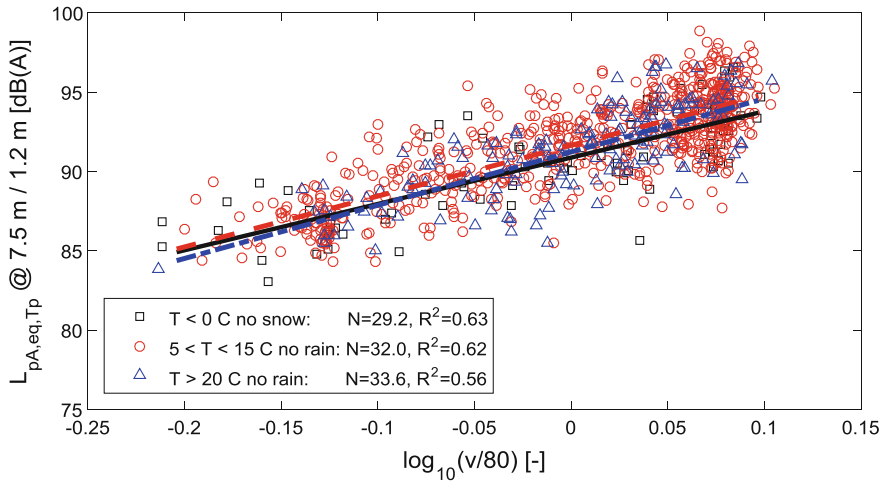


**Fig. 2** Influence of train speed and temperature interval on  $L_p$  at 7.5/1.2 m: freight traffic at Deutsch-Wagram

on measured rail accelerations and PBA analysis [5]. In the frequency interval of main interest 315–2000 Hz (as maximum A-weighted noise levels were recorded in the interval 400–1600 Hz), vertical TDR were decreasing with increasing temperature, see Fig. 3. This is in agreement with the findings in [6]. Generally, the vertical TDR of the measurement section is high (significantly higher than TSI limit values), meaning that the contribution of track noise to total noise is low compared to the wheel noise contribution. This may explain the stability of noise levels when varying the temperature (wheel noise contribution is not related to TDR).

Given the track design at Deutsch-Wagram with stiff rail pads, it can be assumed that the contribution of sleeper noise (unfortunately not analysed in this study) in this frequency interval (see above) may be of the same order as that of the rail, and

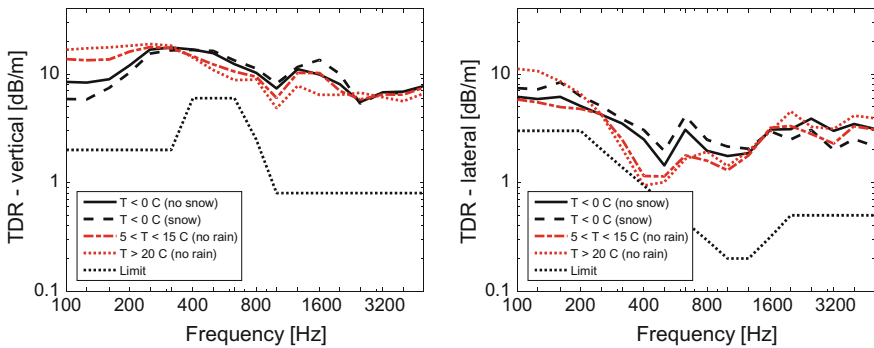


**Fig. 3** (left) Vertical and (right) lateral TDR measured at Deutsch-Wagram in different temperature intervals

is increasing with decreasing temperature (increasing rail pad stiffness). This effect would compensate the decreasing rail noise contribution with decreasing temperature, and could explain that maximum measured noise levels are observed when the temperature is in the mid-interval although rail vibration levels are continuously increasing with increasing temperature. Thus, the observed attractive feature for a monitoring station (stability of noise level versus temperature) may be a consequence of these two compensating effects.

### ***3.2 Influence of Rain***

For passenger trains, an average noise reduction of 0.5 dB was observed when comparing noise levels measured in rainy conditions to those measured in dry conditions, the temperature interval being equal. A reduction appeared in the whole frequency range but was mostly noticeable from 2 to 4 kHz. This effect was noted for both pass-by noise and rail vibration levels. For freight trains, the influence of rain was negligible. It is concluded that noise level measured at Deutsch-Wagram in rainy conditions does not require a systematic rain-related correction procedure.

### ***3.3 Influence of Snow***

The influence of snow depth  $d$  on pass-by noise level was found to be significant, and this category was therefore divided into three different intervals:  $d < 10$  cm,  $10 < d < 20$  cm and  $d > 20$  cm. For  $d < 10$  cm, noise reductions of 1.6 dB for freight trains and 0.9 dB for passenger trains were observed (compared to the situation without snow and  $T < 0$  °C). In the medium snow depth interval, noise reductions increased to 3.1 dB for freight trains and 1.7 dB for passenger trains. Finally, for  $d > 20$  cm, the reduction reached about 8.0 dB for freight trains and 6.4 dB for passenger trains. For such snow depths, a significant screening effect is added to the sound absorption effect. The snow shields part of the rail and the microphone (snow on the windshield).

### ***3.4 Summary***

Based on the discussed statistical analysis, the average levels and standard deviations of pass-by noise  $L_p$  are summarised in Table 1. The analysis shows that the standard deviation of  $L_p$  (after speed correction) is between 1.5 and 2.0 dB for most studied cases. This moderate variation, combined with a high stability of average noise levels versus temperature, indicates a good reproducibility of noise data measured with the system at Deutsch-Wagram. However, in the presence of snow,



**Table 1** Influence of weather conditions on pass-by noise level  $L_{p, 80 \text{ km/h}}$  dB(A): mean value  $E(L_p)$  and standard deviation  $\sigma(L_p)$ . Based on data from 4000 trains measured during one year at the monitoring station at Deutsch-Wagram

Train category	Temperature interval	No snow, no rain		Rain		Snow	
		$E(L_p)$	$\sigma(L_p)$	$E(L_p)$	$\sigma(L_p)$	$E(L_p)$	$\sigma(L_p)$
Passenger trains, rough wheels	$T < 0 \text{ }^\circ\text{C}$	84.3	1.6			81.9	2.8
	$5 \text{ }^\circ\text{C} < T < 15 \text{ }^\circ\text{C}$	85.4	1.6	84.9	1.6		
	$T > 20 \text{ }^\circ\text{C}$	84.9	1.7	84.4	1.9		
	All temperatures	85.1	1.6				
Freight trains	$T < 0 \text{ }^\circ\text{C}$	90.9	1.9			87.3	3.5
	$5 \text{ }^\circ\text{C} < T < 15 \text{ }^\circ\text{C}$	91.7	1.9	91.4	2.0		
	$T > 20 \text{ }^\circ\text{C}$	91.2	1.9	91.4	2.1		
	All temperatures	91.5	1.9				

the standard deviation is increased to 3.5 dB and a further analysis reveals that noise level is strongly affected by snow depth. Thus, to decrease the variance of noise level in the presence of snow, a correction factor depending on snow depth needs to be applied to the results. In rainy conditions, the standard deviations for both train categories and two temperatures intervals ( $5 \text{ }^\circ\text{C} < T < 15 \text{ }^\circ\text{C}$  and  $T > 20 \text{ }^\circ\text{C}$ ) are very similar to those observed in dry conditions.

It is concluded that the track design at Deutsch-Wagram is appropriate for noise monitoring since measured noise levels are relatively insensitive to temperature and precipitation. For such a track design, it is not essential to apply correction factors to account for seasonal variations (except in the case of snow). This situation is expected to be different for monitoring stations with softer rail pads as the track related noise at these stations is significantly affected by the influence of temperature on TDR.

#### 4 Numerical Assessment of Influence of Ground Conditions

The relative contributions of rolling noise from different sources (wheel, rail and sleeper) can be studied by a numerical model, such as TWINS [7]. The contributions from different noise sources are influenced by various factors such as train speed, combined wheel/rail roughness level spectrum and track design. For example, the stiffness of the rail pads influences TDR and the frequency above which the sleepers are dynamically decoupled from the rails, while train speed and shape of the roughness level spectrum influence which frequencies are dominating the excitation of the dynamic wheel-rail interaction. The influence of temperature

(TDR), ground surface level and ground impedance at a noise monitoring station is studied in this section. The calculated sound pressure levels are presented without A-weighting.

For validation, the TWINS model was first compared with measurements performed at Deutsch-Wagram. Information on track superstructure design, rail roughness level, ground surface level and microphone position was provided by ÖBB. The rail pad stiffness used in the model was given by ÖBB but also determined by tuning the calculated vertical and lateral TDR to those measured at Deutsch-Wagram in two different temperature intervals. The tuned vertical rail pad stiffness for  $T > 0$  °C and  $T < 0$  °C were 700 and 900 kN/mm, respectively. Wheel roughness was not measured. Instead, a wheel roughness level spectrum based on measurements on freight wheels with cast iron tread brakes in Sweden was used as input. TDR, measured at Deutsch-Wagram in different temperature intervals, were used as input to the TWINS model.

Sound pressure level (SPL) was calculated using the SPLM module in TWINS. The radiation from the rail is represented by uncorrelated point sources distributed along the rail. The power of each of these point sources is determined by the TDR in the vertical and lateral directions. Monopole radiation is assumed for the vertical waves and dipole radiation for the lateral waves. The sleeper radiation is based on a baffled plate model. As for the rail, the sound power radiated by each sleeper is related to the TDR measured in the vertical direction.

Although there was acceptable agreement in shape of measured and calculated sound pressure level spectra (at 7.5/1.2 m), the predicted spectrum was lower than the measured one. Reasons for the disagreement could be that the wheel model and wheel roughness spectrum applied in the model are not consistent with the conditions at the test site. There was also uncertainty about what ground impedance to use in the model, see Fig. 1, which shows a mix of ground conditions (ballast, concrete and soil). Although there is some disagreement, it is assumed that the model is sufficiently accurate for relative predictions of the influence of weather and ground conditions on SPL.

#### ***4.1 Direct and Reflected Sound Waves***

The calculated sound pressure level at a given receiver position is determined by the direct sound wave and the reflected sound wave. The reflected sound wave includes a so-called “ground wave” term. In this study, the ground is assumed to be flat (horizontal) with properties described by a complex-valued acoustic impedance  $z_n$ . At some frequencies, the reflected sound wave at the receiver is in phase with the direct sound wave and the two contributions can be added, while at other frequencies there is destructive interference. The amplitude reflection coefficient  $R$  (ratio of the reflected to the incident wave amplitudes, with  $\theta$  being the angle of the incident wave relative to the normal of the horizontal plane) is calculated, see [8], as

$$R(\theta) = \frac{z'_n \cos \theta - 1}{z'_n \cos \theta + 1} \tag{4.1}$$

with  $z'_n = z_n/\rho_0c_0$ . The material model by Delany and Bazley [9, 10] expresses  $z'_n$  in terms of a single effective flow resistivity parameter  $\sigma_e$ . According to [9, 11], typical values of  $\sigma_e$  are 50 krayls (kPa·s/m<sup>2</sup>) for snow, 200 krayls for grass and 3200 krayls for dense ground. In the model, the relation between effective flow resistivity and ground impedance is expressed as

$$z'_n = 1 + 9.08 \left( \frac{1000f}{\sigma_e} \right)^{-0.75} + 11.9i \left( \frac{1000f}{\sigma_e} \right)^{-0.73} \tag{4.2}$$

The reflection coefficient  $R$  influences the amplitude and phase of the reflected wave.

## 4.2 Influence of Ground Surface Level and Ground Impedance

Freight traffic with cast iron tread brakes on ISO 3095:2013 rail, track superstructure design according to the test site at Deutsch-Wagram, train speed 80 km/h and axle load 20 tonnes have been used as input. In the TWINS integration of sound pressure, the noise radiated by four wheelsets (nearside and farside wheels) have been considered. At the selected train speed, the wheel roughness spectrum generates a local maximum in the roughness excitation at about 400 Hz.

As discussed above, the test site should allow for free sound propagation. According to ISO 3095:2013 [4], the ground needs to be essentially flat and within a level from 0 to 1 m below the top of the rail. In [3], the level of the ground surface is specified to be within 0 to 2 m relative to the top of rail.

The influence of ground surface level and ground impedance on total SPL at 7.5 m from track centre (1.2 m above top of rail) is illustrated in Fig. 4(left). Within the studied interval of ground surface levels and for a given effective flow resistivity (type of ground surface) corresponding to either snow or grass, it is observed that the variation in SPL is within 1 dB. For more reflective ground conditions (dense ground), the influence of ground surface level on SPL is higher, in the order of 2 dB. The local minimum in SPL at 1.0 m is due to destructive interference of the direct and reflected sound waves emitted by the rail and sleepers in the 400 Hz band. For low ground surface levels, there is constructive interference between the direct and reflected waves leading to higher noise levels. Figure 4(left) also illustrates that different ground surface conditions has a significant influence on the SPL. For example, the high absorption of the reflected sound wave when there is dry snow on the ground ( $\sigma_e < 50$  krayls) leads to 1.5–4 dB lower SPL compared to the case with compacted dense ground ( $\sigma_e$  in the order of 3200 krayls).

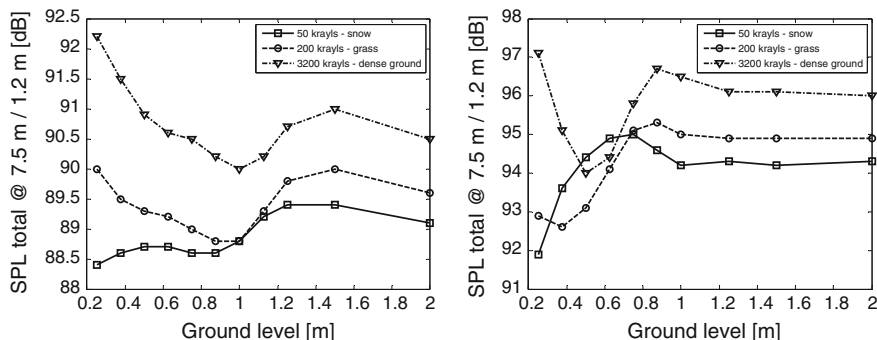


**Fig. 4** Influence of ground impedance and ground surface level on calculated SPL at 7.5/1.2 m (not A-weighted). Input: (left) measured TDR based on pass-by analysis (PBA) from Deutsch-Wagram: 5 °C < T < 15 °C, no rain. (right) calculated TDR based on rail pad with vertical stiffness 120 kN/mm

**Table 2** Relative difference of predicted SPL at 7.5/1.2 m compared to case with effective flow resistivity 400 krayls and ground surface level 1 m. Track decay rate based on PBA from Deutsch Wagram: 5 °C < T < 15 °C, no rain

[m]\[krayls]	50	100	200	400	800	1600	3200	6400	12,800
2.0	0	0.2	0.5	0.8	1.1	1.3	1.4	1.5	1.6
1.50	0.3	0.6	0.9	1.2	1.5	1.8	1.9	2.0	2.1
1.25	0.3	0.4	0.7	0.9	1.2	1.4	1.6	1.7	1.8
1.125	0.1	0.1	0.2	0.4	0.7	0.9	1.1	1.2	1.3
1.0	-0.3	-0.4	-0.3	0	0.3	0.6	0.9	1.0	1.1
0.875	-0.5	-0.5	-0.3	0.1	0.5	0.9	1.1	1.3	1.4
0.75	-0.5	-0.4	-0.1	0.4	0.8	1.1	1.4	1.6	1.7
0.625	-0.4	-0.3	0.1	0.5	0.9	1.3	1.5	1.7	1.8
0.50	-0.4	-0.2	0.2	0.6	1.1	1.5	1.8	2.0	2.2
0.375	-0.5	-0.2	0.4	1.1	1.6	2.1	2.4	2.7	2.8
0.25	-0.7	0	0.9	1.7	2.3	2.8	3.1	3.4	3.5

For comparison, Fig. 4(right) illustrates the influence of ground conditions on SPL for the same rail and sleeper design but with an alternative, more resilient, rail pad (vertical stiffness 120 kN/mm). Calculated TDR are used as input. As expected the more resilient rail pad leads to higher SPL. However, for snow or grass and ground surface levels higher than 0.6 m, the influence of ground surface level is within 1 dB. Again, more reflective ground conditions increase the influence of ground surface level on SPL.

The influence of ground surface level and (a wider range of) effective flow resistivity on SPL is summarised in Table 2. The table shows the relative difference between a given combination of ground surface level and effective flow resistivity and the case where ground surface level = 1.0 m and effective flow resistivity = 400 krayls.

It is concluded that for reflective ground conditions corresponding to  $\sigma_e \geq 400$  krayls, there is a strong influence of ground surface level. For more absorbing ground conditions, the influence of ground level is within about 1 dB.

Thus, to obtain consistent measurement results between different noise monitoring stations having the same superstructure design but possibly different ground surface levels, highly reflective ground conditions should be avoided. Grass/soil is preferred over ballast/concrete/asphalt.

### 4.3 Influence of Temperature

Based on the TWINS model of the noise monitoring station at Deutsch-Wagram, the relative difference in predicted SPL when using TDR measured at  $5\text{ °C} < T < 15\text{ °C}$  (no rain) or at  $T < 0\text{ °C}$  (no snow) as input was studied in HRMS. It was concluded that for all studied ground conditions (ground surface level and ground impedance), the influence of temperature on SPL is less than 0.5 dB. According to the measurements at Deutsch-Wagram, see Table 1 (freight), the average SPL at  $5\text{ °C} < T < 15\text{ °C}$  (no rain) is 0.8 dB higher than at  $T < 0\text{ °C}$  (no snow), which is in good agreement with the results from TWINS.

For comparison, a similar study was also performed based on a more resilient rail pad (natural rubber). Input data on rail pad stiffness at two different temperatures was taken from [6];  $T = 15\text{ °C}$ : vertical stiffness 120 kN/mm, and  $T = -15\text{ °C}$ : vertical stiffness 300 kN/mm. The predicted SPLs were based on calculated TDR. In this case the influence of temperature was significant, in the order of 4 dB, due to the large influence of temperature on TDR.

## 5 Requirements on Monitoring Systems for Reproducibility of Noise Data

The requirements on a noise monitoring system depend on the targeted application, such as noise mapping, rolling stock fleet noise performance, identification of type of brake blocks, detection of wheel defects and hotboxes, etc. Previously, it has been shown that data from long-term monitoring sites is reproducible if corrected with respect to train speed and rail roughness [12, 13].

System requirements to ensure reliable and reproducible pass-by noise measurements were defined in HRMS [2]. This includes recommendations regarding hardware (microphones, sensors, weather station, data acquisition system), track requirements (superstructure design, continuously welded rails, etc.), acoustical environment and meteorological conditions (free sound propagation, background noise level, level and impedance of ground surface) and measurement locations (microphones at 7.5 m from track centre and 1.2 m above top of rail, accelerometer positions).

For a track based system, the most relevant parameters influencing measured noise levels are train speed, rail roughness level and TDR. To ensure the reproducibility of noise measured for several pass-bys of the same train at one or several monitoring stations, the noise and vibration levels need to be determined for a reference speed, e.g. 80 km/h. Rail roughness level and variation of TDR should be assessed at regular intervals to control track related noise contribution. Correction procedures to account for such deviations were described in HRMS [2].

The track design used at Deutsch-Wagram is favourable since track with stiff rail pads generally contribute less to the total noise than track with softer rail pads, meaning that the contribution of wheel noise to the total pass-by noise will be more significant. This statement has been confirmed by the stability of statistically averaged pass-by noise levels recorded at the monitoring site at Deutsch-Wagram (in the absence of snow, all speed corrected average noise levels emitted by passenger trains are within  $\pm 1$  dB; the same statistical stability being observed for freight traffic). Further, the statistical analysis reported here reveals that pass-by noise levels are relatively insensitive to temperature variations. Rain does not significantly affect pass-by noise levels, but as expected, the influence of snow is significant and strongly depends on snow depth. The typical variation (standard deviation) of pass-by noise levels after speed correction is between 1.5 and 2.0 dB for most studied train configurations and weather conditions (excluding the situations with snow). This moderate standard deviation combined with a great stability of average noise levels versus temperature indicate a good reliability of noise data measured with the acramos<sup>®</sup> system at Deutsch-Wagram.

Based on a numerical analysis with TWINS (calibrated for the conditions at Deutsch-Wagram), it was concluded that for ground surfaces with low sound reflection, the influence of ground surface level (when varying from 0.2 to 2 m) on predicted pass-by noise level is in the order of 1 dB. The influence of constructive or destructive interference of direct and reflected sound waves on measured noise levels can be significant for reflective ground surfaces and therefore such ground conditions should be avoided.

In conclusion, it is argued that the track form (design) used at Deutsch-Wagram (60 kg/m rails, stiff rail pads and monobloc concrete sleepers on ballast) is appropriate for noise monitoring since measured noise levels are relatively insensitive to weather conditions. For such track, it is not essential to apply a correction procedure to account for seasonal variations (except in the case of snow). The situation is different for monitoring stations with low stiffness rail pads as these stations are significantly affected by the influence of temperature on TDR and track related noise meaning that a correction procedure of measured noise levels is required. Further, the contribution of wheel noise to total pass-by noise is more significant for monitoring stations with stiff rail pads.

## References

1. Saliger, F., Schmitt, L., Zottl, W.: HRMS—Harmonisation of Running Behaviour and Noise Measurement Sites. Transport Research Arena, Paris, p 9 (2014)
2. HRMS—Harmonisation of Running Behaviour and Noise on Measurement Sites, UIC report, Train track interaction sector, p 154 (non-public report) (2014)
3. TSI Noise, Technical Specification for Interoperability, Subsystem: Conventional Rolling Stock, Scope: Noise, Official Journal of the European Union (April 2011)
4. ISO 3095:2013, Railway applications: acoustics—measurements of noise emitted by railbound vehicles
5. Dittrich, M.G.: Track decay rate measurements using the PBA technique. In: Proceedings of EURONOISE 2006. Tampere, Finland, 2006
6. Broadbent, R.A., Thompson, D.J., Jones, C.J.C.: Evaluation of the effects of temperature on rail pad properties, rail decay rates and noise radiation. In: Proceedings 16th International Congress on Sound and Vibration. Krakow, Poland, July 2009
7. TWINS v3.0c, TNO Science and Industry, Delft, The Netherlands, 2006
8. Thompson, D.: Railway noise and vibration – mechanisms, modelling and means of control. Elsevier, Oxford (2009)
9. Delany, M.E., Bazley, E.N.: Acoustical properties of fibrous absorbent materials. *Appl. Acoust.* **3**, 105–116 (1970)
10. Embleton, T.F.W., Piercy, J.E., Daigle, G.A.: Effective flow resistivity of ground surfaces determined by acoustical measurements. *J. Acoust. Soc. Am.* **74**(4), 1239–1244 (1983)
11. Kragh, J., Plovsing, B., Storeheier, S.A., Jonasson, H.G.: Nordic Environmental Noise Prediction Methods, Nord2000—Summary Report. General Nordic sound propagation model and applications in source-related prediction methods. Report AV 1719/01 (31 May 2002)
12. Verheijen, E.: Statistical analysis of railway noise: how long-term monitoring helps improving short-term measurements. In: Proceedings NAG/DAGA International Conference on Acoustics, Rotterdam, The Netherlands (2009)
13. Verheijen, E., van den Roovers, M.S., Brink, J.W.: Railway noise statistics by monitoring stations—input for Dutch prediction method RMR and track access charging. In: Schulte-Werning, B., et al. (eds.) *Noise and Vibration Mitigation for Rail Transportation Systems*. NNFM, vol. 99, pp. 165–171. Springer, Heidelberg (2008)

# Train Speed Estimations from Ground Vibration Measurements Using a Simple Rail Deflection Model Mask



V. Jurdic, O. Bewes, K. Burgemeister and David J. Thompson

**Abstract** The speed of passing trains is conventionally estimated using Doppler speed guns, or optical sensors. However in many cases, these techniques are not applicable when the measured trains are not visible (for example in tunnels) or close access to the track is not possible. An alternative method to estimate train speed from ground vibration measurements is presented in this paper. The method takes advantage of the relation between vibration levels and the cyclic repetition of the excitation forces created by the wheels. A train mask, expressed in the wavelength domain, is derived from a simple rail deflection model induced by the train wheels. The vibration spectrum at very low frequency and the train mask are qualitatively compared to match the various peaks. Vibration and train speed measurements have been undertaken near St Denys station, Southampton. Very good agreements have been observed between the direct train speed measurements and the proposed estimation method.

## 1 Introduction

The vibration induced by a nearby passing train is highly dependent on its speed. However during many measurement surveys, the train speed cannot be measured or estimated by traditional techniques such as Doppler speed guns, or optical sensors. In most cases, the measured trains are not visible or close access to the track is not possible. The knowledge of train speed allows the operating condition (and its variability) of the measured trains to be assessed. Vibration models can then be used

---

V. Jurdic (✉) · O. Bewes  
Arup, 8 St Thomas Street, Winchester SO23 9HE, UK  
e-mail: vincent.jurdic@arup.com

K. Burgemeister  
Arup, Melbourne, Australia

D. J. Thompson  
Institute of Sound and Vibration Research,  
University of Southampton, Southampton, UK



to predict vibration for changing train speed, track modifications or wheel/rail roughness. The validation of such models requires also accurate estimation of the speed of the reference trains.

Recent studies (Ni et al. [1]; Kouroussis et al. [2]) propose speed estimation methods based on ground vibration measurements. These methods derive the train speed from the various peaks in the vibration spectrum at very low frequency and by considering the train dimensions. However these methods can be relatively complex or lead to significant errors. This paper presents an alternative method to estimate train speed from ground vibration measurements. The method is based on a similar concept but considers a simple model for the rail deflection induced by the train wheels to derive a train ‘mask’ which is matched to the vibration spectrum.

## 2 Concept

Techniques by Ni et al. [1] and Kouroussis et al. [2] use train ground vibration measurements to estimate the train speed. These approaches take advantage of the relation between vibration levels and the excitation forces created by the wheels. At a specific receiver location, the cyclic repetition of the wheel passage induces the principal excitation frequency and harmonics in the vibration spectrum, defined by:

$$f_{c,n} = n \frac{v_0}{L_c} \quad (n = 1, 2, 3, \dots) \quad (2.1)$$

where  $L_c$  is the coach length and  $v_0$  the train speed.

Ni et al.’s method [1] requires an initial estimation of the fundamental frequency. The harmonics are then detected in the vibration measurement via a recursive calculation. The train speed is estimated by:

$$v_0 = \min_n \left( \frac{L_c f_{c,n+1}}{n+1} - \frac{L_c f_{c,n}}{n} \right) \quad (2.2)$$

Significant errors have been observed when the initial estimation of the fundamental frequency is poor or the frequency content of the measurements might be contaminated by resonance phenomena.

Kouroussis et al. [2] define a similar method to estimate the train speed from ground vibration measurements. This method combines three approaches based on cepstrum analysis, running rms, and a theoretical spectral model. The theoretical model includes a soil transmissibility function  $H(f)$ —to consider the amplitude attenuation due to the propagation and the ground damping—and the vehicle excitation forces  $F(f)$ . This excitation function is given as a series of Dirac functions, assumed to represent the excitation of each wheelset. The train speed is estimated using a non-linear regression with the initial speed value calculated using the principal frequency.

This study proposes a simplified method, using a theoretical spectrum or “mask”, defined further in Sect. 3. The mask is defined as a spectrum in the wavelength domain. For an estimated speed  $v_{est}$ , the wavelength spectrum can be expressed as a frequency spectrum through the relation  $f = v_{est}/\lambda$ . The speed  $v_{est}$  can then be altered to shift the mask on the frequency spectrum of the measured vibration. Once the best fit is obtained, the estimating speed corresponds to the train speed  $v_0$ .

Due to the characteristic dimensions of a train (few tens of metres for the carriage length and few metres between two wheels on the same bogie), the frequency analysis is only necessary over a small frequency range (generally from 0.1 to 50 Hz). Rather than using the Fast Fourier Transform (which provides a large frequency range but with poor frequency resolution), it is more appropriate to use a numerical integration according to the Fourier Transform (FT) definition for the ground vibration square signal  $V^2(t)$ :

$$FT_v(f) = \int_{-\infty}^{\infty} V^2(t) e^{-i2\pi ft} dt \quad (2.3)$$

By using a Fourier Transform, the vibration spectrum can be generated with very fine resolution and limited to very low frequency.

### 3 Definition of the Train Mask

#### 3.1 Rail Deflection Model

To illustrate the generation of ground vibration waves, Kouroussis et al. [2] calculate the vertical deflection  $w$  of the track subjected to a load  $P_{wheel}$  by using the Euler-Bernoulli beam theory. In the moving coordinate system linked to the train, the  $i$ th wheel at position  $x_i$  induces the deflection:

$$w(x_i) = \frac{P_{wheel}}{8E_r I_r \beta^2} e^{-\beta x_i} [\cos \beta x_i + \sin \beta x_i] \quad (3.1)$$

where  $E_r$  and  $I_r$  are respectively the Young’s modulus and second moment of area of the rail. The coefficient  $\beta$  is function of the track stiffness (ballast and railpad stiffness,  $k_b$  and  $k_p$  respectively), approximated by:

$$\beta = \sqrt{4} \frac{1}{4E_r I_r} \left( \frac{L}{k_b} + \frac{L}{k_p} \right)^{-1} \quad (3.2)$$

$L$  being the sleeper spacing.

To generate a train mask it is necessary to know the position of each wheel along the train. With this information, the rail deflection  $w(x)$  can be modelled along the

whole train. Without this information it's not possible to generate the train mask. For passenger trains, the rolling stock configuration is well defined and therefore this method is well suited for these type of trains. For freight trains, this method is however more difficult to apply. The wagon composition can vary significantly a large set of masks might need to be tested to obtain the best fit.

In practice, the vibration received at a fixed point during the passage of a train is the combination of the quasi-static and dynamic load components as described by Lombaert et al. [3]. However both components are dependent on the positions of the wheels along the track. Because this method is based on the locations of the wheels and not based on the absolute levels of the induced vibration, a simple model describing only the rail deflection (due to the quasi-static load) is proposed here.

In the moving train coordinate system, the Fourier transform of the rail deflection function can be taken to give its energy spectral component in terms of wavenumber  $k$ :

$$FT_W(k) = \int_{-\infty}^{\infty} w^2(x)e^{-i2\pi kx} dx \tag{3.3}$$

In this study, the mask is only providing an estimation of the location of the spectral component of the rail deflection. Therefore the track stiffness has been given an arbitrary value per metre of rail of 485 and 540 MN/m<sup>2</sup> for the ballast and railpad stiffness, respectively. The mask and measured vibration spectra are also normalised to their highest spectral component.

Expressed in terms of the wavelength  $\lambda = 1/k$ , the Fourier transform  $FT_W$  defines the train mask used in this study. Figure 1 presents the rail deflection function and the train mask for a Class 395 (Javelin) train. Note that on the bottom figure, the wavelength axis is displayed with the value increasing toward the left.

The train mask presents various peaks at discrete wavelengths. The peaks can be classified into two categories:

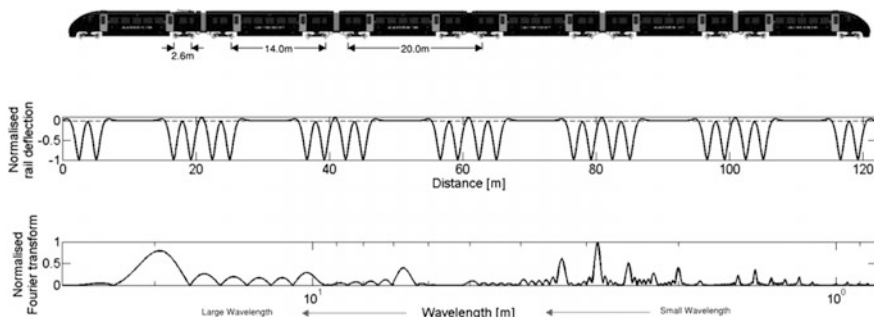


**Fig. 1** Train dimension, rail deflection model and train mask for a Javelin (Class 395)

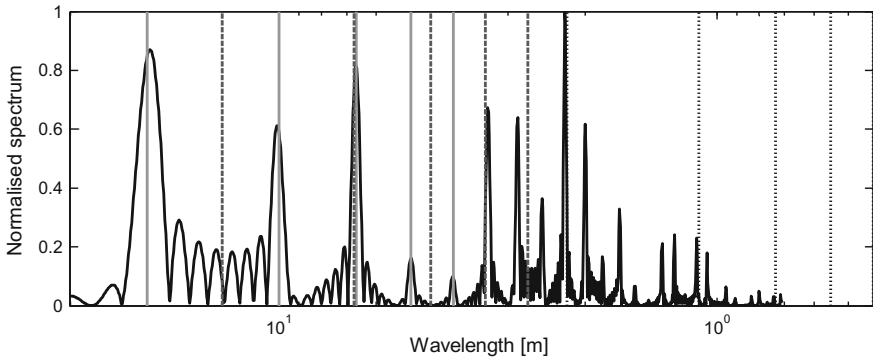


**Fig. 2** Train mask of a Javelin with the corresponding train characteristic wavelengths. (Plain Grey: carriage length, Dashed: inter-bogie length, Dotted: wheelbase length)

- *Principal peaks* occurring around 20, 10, 5 m,... These peaks are close to the carriage length and its harmonics. (Blue dimension in Fig. 2 and blue lines in Fig. 2)
- *Secondary peaks* occurring between the principal peaks. These peaks are an artefact of the finite cyclic distribution of the wheel forces. If the trains were infinitely long the secondary peaks would not be present. Note that the number of secondary peaks between two principal peaks is exactly two less than the number of carriages.

Ni et al. [1] and Kouroussis et al. [2] assumed that the principal peaks occur at wavelength corresponding to the carriage, inter-bogie and wheelbase lengths and their harmonics. Figure 2 shows the Javelin train mask with the corresponding carriage, inter-bogie and wheelbase lengths and their harmonics.

Figure 2 suggests that the cyclic repetition of the wheel forces generates peaks at a wavelength close to but not exactly corresponding to the carriage length. This is due to the non-equally spaced distribution of the wheels along the train. For a theoretical regular distribution of the wheels along the trains, the peaks would occur exactly at the wavelength corresponding to the carriage length. Note also that for a train with a larger number of carriages, the peaks would become closer to the wavelength corresponding to the carriage length.

Moreover, the principal peaks are also located at the carriage wavelength and its harmonics, and not at the inter-bogie and wheelbase wavelengths.

## 4 Validation

### 4.1 Survey Methodology

Measurements were carried out near St Denys station, Southampton, UK, to validate the train mask estimation method.

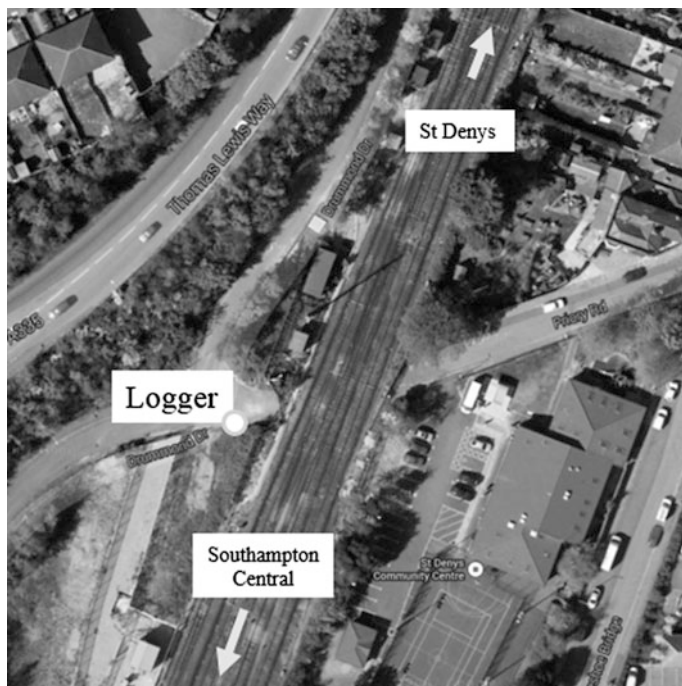


**Fig. 3** Vibration and speed measurements during the validation survey, near St Denys station, Southampton, UK

- Continuous recording of the ground vibration at approximately 10 m from the closest track, shown in Fig. 3.
- Measurements of the train speed using a Doppler radar.
- Video recording to allow train identification and train speed estimation using a reference point.

32 trains were observed with a large combination of services and rolling stock, as summarised in Table 1. Due to the variability of the wagon composition of freight trains, the four freight trains recorded have not been considered in the analysis.

The majority of the recorded trains did not stop at St Denys station but the Class 377 trains are generally slowing to take the junction after St Denys station towards Havant.

## 4.2 Train Speed Estimation Process

For each train passage, the vibration time history and the video section have been extracted from the continuous vibration and video recordings.

**Table 1** Summary of the trains observed during the validation survey near St Denys station

Train class	Number of measured trains	Comments
Class 158	2	Non-stopping trains and trains stopping at St Denys
Class 159	4	Non-stopping trains and trains stopping at St Denys
Class 220	4	4 or 5 coaches—non-stopping trains
Class 377	5	Non-stopping trains
Class 444	4	10 coaches, non-stopping or in transfer trains
Class 450	9	4, 8 and 12 coaches, non-stopping or in transfer trains
Freight	4	Not included in this study

#### 4.2.1 Estimation Using the Train Mask Method

For each observed train type, a train mask has been produced based on its key geometric parameters, summarised in Table 2, allowing the placement of the wheels along the train length. Each individual train has been analysed using the train mask method.

#### 4.2.2 Estimation Using the Video Recording

The train speed can be also estimated using a reference point on the video frame. The head to toe train passage time and the train length gives a second train speed estimation.

**Table 2** Geometric parameters of the measured trains

Train class	Number of carriages	Carriage length (m)	Inter-bogie length (m)	Wheelbase length (m)
Class 158	2	23.2	15.8	2.6
Class 159	3	23.2	15.8	2.6
Class 220	4 or 5	23	15.9	2.25
Class 377	4	20	14.2	2.6
Class 444	5 or 10	23	15.8	2.6
Class 450	4, 8 or 12	20	14.2	2.6

### 4.3 Limitation of Doppler Radar

Doppler radar equipment is very accurate ( $\pm 2$  up to 320 km/h). However it can suffer from angular interference. When measuring with a radar, the optimum angle for measuring is head-on to the train. However, in practice, for safety reasons and to prevent disturbing the drivers, the measurement must be performed to the side of the track.

To obtain accurate measurements, it is recommended to have a distance between 50–300 m to minimise the angular interference. As the train reaches the radar gun, the angle between the train and the radar beam increases and the train gets too close to be measured properly; the speeds can fluctuate when it gets too close.

At the validation site, it was not possible to have the optimal conditions for the measurement of the train speed. The radar measurements are therefore likely to be slightly different to the real train speed.

### 4.4 Results

Figure 4 is an example of the vibration measurement of a Class 450 Desiro train (top) and the matching between the measured vibration spectrum and the train mask. The match has been performed manually to ensure that a maximum of peaks are coinciding between 1 and 15 Hz. Generally, a very good fit is obtained between the vibration spectrum and the train mask. Occasionally (seven cases) the vibration spectrum could not be fitted to the train mask, either because no obvious peaks were present in the spectrum, or the peaks could not be matched with those in the train mask.

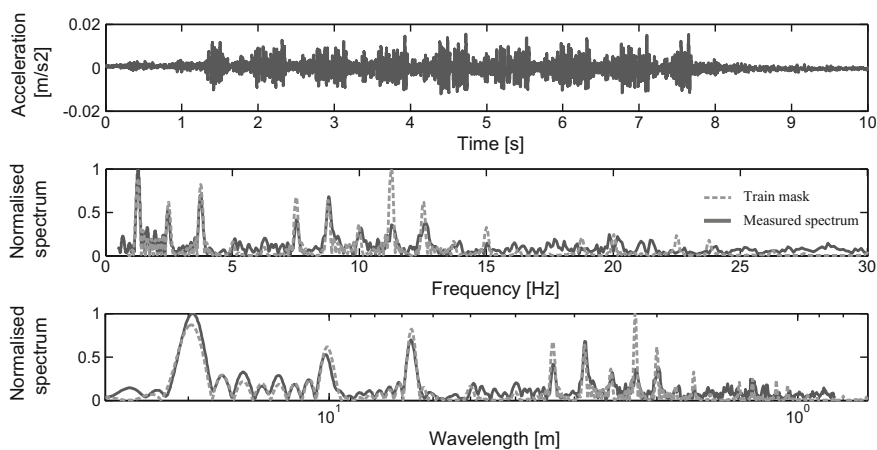
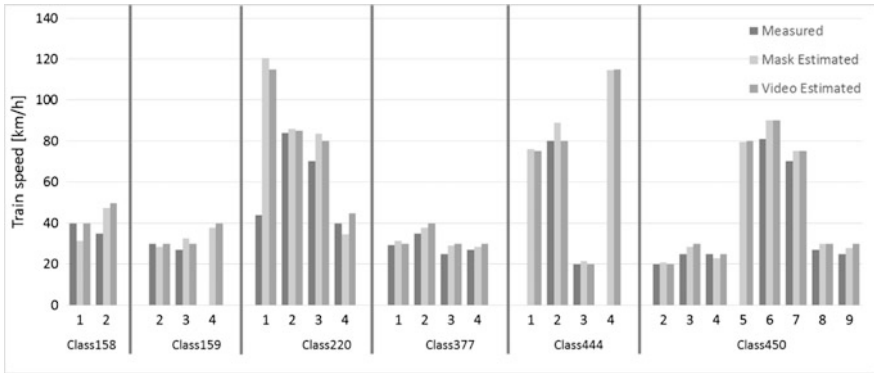


Fig. 4 Example of the measurements and mask matching for a Class 450 Desiro



**Fig. 5** Comparison between the measured train speed and the speeds estimated using the mask, and the video recording

mask. In one case (first measured Class 159 train), significant interference occurred in the measured train vibration spectrum. This spectrum could not be used to estimate the train speed.

Figure 5 summarises the measured and estimated train speed using either the video or the train mask methods. During the survey, the radar gun batteries needed to be replaced and the speed of four trains could not be measured.

Figure 6 presents the estimated train speed using the mask versus the speed measured using the Doppler radar (Fig. 6a) and the speed estimated using the video recording (Fig. 6b).

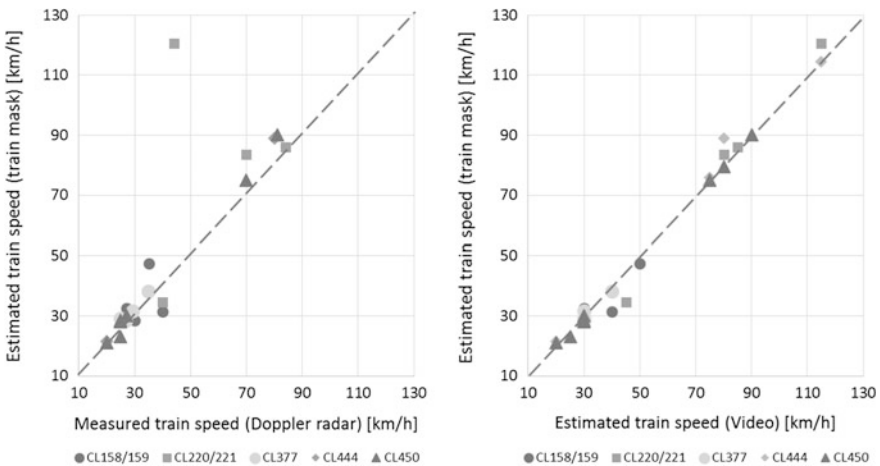


**Fig. 6** Train mask estimated speed versus the measured speed and the video estimated speed



Very good agreement can be observed between the three speed estimation methods. The proposed mask method provides an accuracy of  $\pm 5$  m/s with the Doppler radar and  $\pm 3.6$  m/s with the video estimation method. The train mask method is therefore an accurate alternative method to estimate the train speed from vibration measurements, assuming the wheel distribution of the measured train is well defined.

## 5 Conclusions

A simple method to estimate the train speed has been presented. The train speed is obtained by manually best-fitting a train mask onto the measured vibration spectrum. The train mask is derived from a simple model of rail deflection, due to the forces applied by the train wheels. The train mask and vibration spectrum are normalised to their highest level since the fitting process is performed only on the peak locations and not the peak amplitudes.

The train masks present various principal peaks that are related to the carriage length. Secondary peaks, with significant lower amplitude, are also present between the principal peaks.

The influence of the wheel force distribution and of the train speed variation has been studied. Non-homogeneous wheel force distribution tends to amplify the secondary peaks in the mask. When the train is changing speed during the measurements, the vibration spectrum is likely to be affected at small wavelengths (typically below 4 Hz). However the method will still provide reasonable results when applied for the large wavelength components.

A validation survey has been undertaken near St Denys station at Southampton with vibration and speed measurements, and video recording of the train passage. The speed of the train has been estimated using a reference point on the video and using the developed train mask method. Very good agreements have been observed between the three train speed estimation methods and those for various commuter train types and operating conditions. The proposed mask method for freight trains is more difficult to apply due to the more random wheel distribution along different freight train. Currently the method has only been applied in situations where the wheel distributions are known. Further work is required to understand the errors associated with using approximations of the train mask when the wheel distribution is unknown.

## References

1. Ni, S.-H., Huang, Y.-H., Lo, K.-F.: An automatic procedure for train speed evaluation by the dominant frequency method. *Comp. Geotech.* **38**(4), 416–422 (2011)
2. Kouroussis, G., Connolly, D.P., Forde, M., Verlinden, O.: Train speed calculation using ground vibrations. *Proc. Inst. Mech. Eng. Part F: J. Rail Rapid Transit* **0**, 1–18 (2013)
3. Lombaert, G., Degrande, G., Francois, S., Thompson, D.J.: Ground-borne vibration due to railway traffic: a review of excitation mechanisms, prediction methods and mitigation measures, keynote paper of the IWRN11 conference (2013)

# Groundborne Railway Noise and Vibration in Buildings: Results of a Structural and Acoustic Parametric Study



D. E. J. Lurcock, David J. Thompson and O. G. Bewes

**Abstract** Two parametric studies have been conducted in order to examine the influence of a number of building and room parameters on the groundborne noise and vibration levels in a room. The studies have each utilised a three-dimensional finite element (FE) approach, validated with site measurements. It was found that changing the floor thickness had a limited effect on floor vibration, whereas changing the floor area was found to be more important, due to shifting the floor mode frequencies. Structural damping was shown to be important, and should therefore be specified carefully when modelling building vibration. The FE model of a typical domestic room demonstrated that there is significant variation in groundborne noise at different room positions due to the influence of acoustic modes. It is therefore recommended that the low frequency procedure detailed in ISO 16283-1 be adopted for specifying and measuring groundborne noise in such rooms. The parametric study showed that the room reverberation time, room size and presence of furniture each have a moderate effect on the sound pressure level. Whilst the installation of wall linings was predicted to provide only a marginal improvement in sound pressure level, this effect is dependent on the relative contributions of the wall, ceiling and floor surfaces. Results from the parametric studies are being used to inform semi-empirical prediction formulae for groundborne noise and vibration.

---

Data used for this paper is available from: <http://dx.doi.org/10.5258/SOTON/396986>.

D. E. J. Lurcock (✉) · D. J. Thompson  
Institute of Sound and Vibration Research, University of Southampton,  
Southampton SO17 1BJ, UK  
e-mail: d.lurcock@soton.ac.uk

O. G. Bewes  
Arup Group Ltd, London, UK

© Springer International Publishing AG, part of Springer Nature 2018  
D. Anderson et al. (eds.), *Noise and Vibration Mitigation for Rail Transportation Systems*, Notes on Numerical Fluid Mechanics and Multidisciplinary Design 139,  
[https://doi.org/10.1007/978-3-319-73411-8\\_13](https://doi.org/10.1007/978-3-319-73411-8_13)

## 1 Introduction

When predicting the exposure of a building's occupants to noise and vibration from a railway, there are two primary transmission paths to consider: airborne and groundborne. In many cases, the airborne path is the dominant path of interest. However, when vibration is of concern or where airborne noise is limited for example through the presence of tunnels or noise barriers, the groundborne transmission path becomes important. Whilst for many railway situations airborne noise can be predicted with a reasonable degree of certainty (for example to within a few decibels), this is not generally the case for groundborne noise and vibration, with such predictions often citing uncertainties of 10 dB or so (e.g. [1]). This is due to the number and complexity of components in the transmission path including: vehicle, track and tunnel dynamics; intervening ground factors; foundation type; building structure, layout and geometry; room surface finishes, dimensions and layout.

The most popular prediction approach is the use of empirical formulae derived from measurements (e.g. [2, 3]). Whilst this kind of approach has the advantage of being easy to use, it is not possible to account for even basic building design changes. An alternative is the use of finite element (FE) analysis. Whilst FE modelling can account for design changes, it is often prohibitively expensive in terms of the time required to construct and solve such models. Since mitigation options have significant implications for the cost, complexity and risk of a project, there exists a strong requirement for improvements in the prediction methodologies. The aim of the research presented here is to study the influence of various structural and acoustic parameters on the resulting groundborne noise and vibration levels within rooms in buildings. The work is based on FE modelling and measurements. Results are presented for vibration transmission within the building and sound radiation in rooms.

This research is being undertaken as part of an Engineering Doctorate programme at the University of Southampton, and is funded by the EPSRC and the acoustics division of Arup Group Ltd.

## 2 Building Vibration

### 2.1 Basement Vibration Measurements

Measurement data from twelve different buildings has been collected. These buildings were of various types and sizes, but were all affected by groundborne vibration from underground railways. Most of the buildings were located in London, UK with two located in New York, USA. The measured vibration levels at basement level are given in Fig. 1, along with the calculated (arithmetic) average of all the measurements. These are given as the slow-weighted maximum vertical velocity levels in decibels, relative to  $10^{-9}$  m/s. It is seen that the various sites

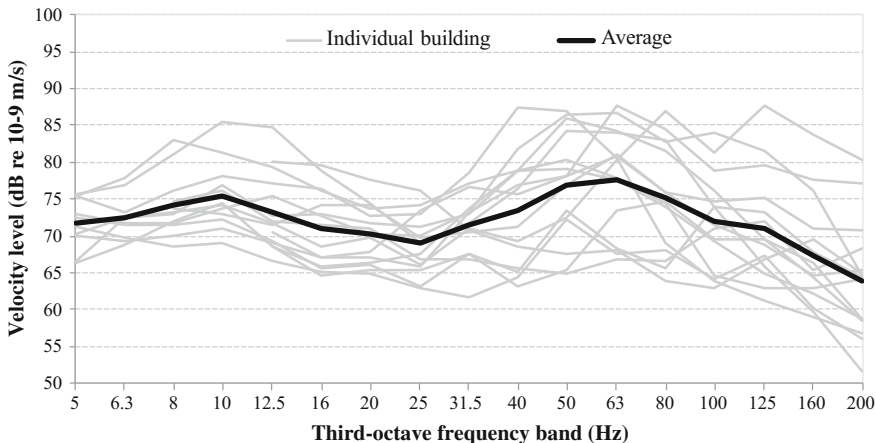


**Fig. 1** Measured basement vibration in twelve buildings, maximum slow-weighted vertical velocity level (dB re  $10^{-9}$  m/s)

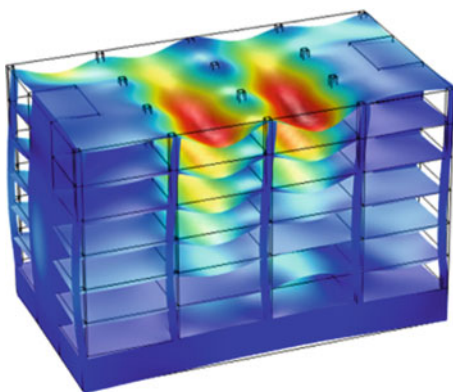
exhibit a similar shape in the frequency spectrum, with broad peaks at around 10 and 63 Hz. The upper peak is believed to be associated with the coupled wheel/track resonance which commonly occurs around this frequency [4, 5]. The 10 Hz peak may be associated with an anti-resonance of the vehicle primary suspension although it is remarkable that a similar peak is found at a range of locations.

## 2.2 *Finite Element Model*

A 3-D FE approach has been developed [6], which has been validated against measurements from existing buildings. A model of a generic six-storey concrete frame building has then been developed and used as the basis for an extensive parametric study, with vibration levels evaluated at each floor mid-span and column position. The building is excited by a uniformly distributed force across the base slab and results are normalised to the vibration of the foundation. As an example a view of the operational deflection shape at 10.2 Hz is given in Fig. 2. At this frequency, vibration increases with height up the building due to the influence of the fundamental building mode, and the vibration levels are greatest at the central portions of the floor slabs due to the influence of floor modes. It is important to note that not all floor slabs exhibit the same mode frequencies. This is due to differences in their boundary conditions.

The FE model was created and solved using COMSOL Multiphysics. Plate elements were used for the floor slabs and walls, with solid elements for the columns. The number of degrees of freedom for the default model was 224,250. Structural damping was modelled with a constant loss factor by making the material

**Fig. 2** FE model of building, operational deflection at 10.2 Hz



Young's modulus of elasticity complex. Solutions were obtained in the frequency domain in the range 4–200 Hz, and the vertical velocity at each floor mid-span and column position was evaluated.

### 2.3 Parametric Study

The default model was used as a basis for an extensive parameter study, which included building geometry, material parameters and the presence of structural items such as shafts and internal walls. Results are shown below of the vertical mid-span floor vibration at the third storey relative to the vibration at the basement. For example, results are shown in Fig. 3 for different thicknesses of the floor slabs. Additionally, the overall A-weighted velocity levels at each storey have been determined, as these are directly related to the radiated noise levels. These have been calculated by assuming that the vibration spectrum at basement level is equal to that of the measurement average, represented by the dark line in Fig. 1. This spectrum is added to the results calculated from the FE model. These results are shown in Fig. 4 relative to the A-weighted level in the basement for the variation in floor slab thickness. Note that in these and subsequent figures, an asterisk in the legend denotes the default model parameter value.

From the results shown in Figs. 3 and 4, the floor slab thickness, within the relatively narrow range of values chosen (0.25–0.30 m), is shown to have only a small influence on vibration levels, with the overall vibration levels reduced slightly by using the thicker slabs.

The effect of variations in the size (length and width) of the floor sections between columns is shown in Figs. 5 and 6. The slab size has a small influence on the vibration level, primarily by shifting the natural frequencies of the floor modes. In addition, the larger floor sections effectively increase the mass of each storey leading to a reduction in the natural frequency of the building modes. This effect

**Fig. 3** Mid-span vibration at 3rd floor, relative to basement: different values of floor slab thickness

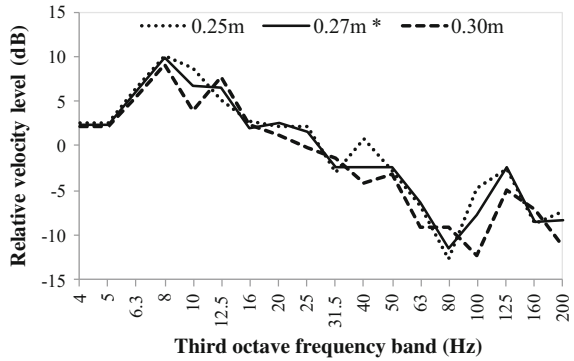


**Fig. 4** Mid-span A-weighted velocity relative to basement: different values of floor slab thickness

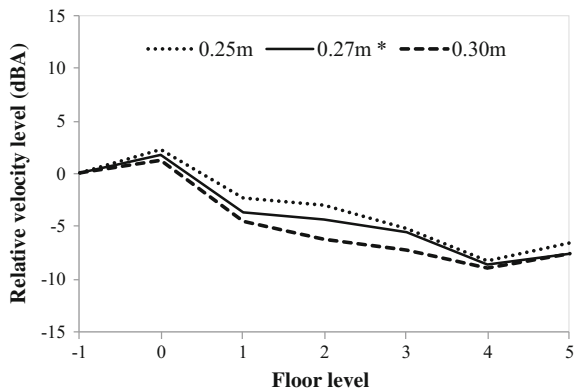
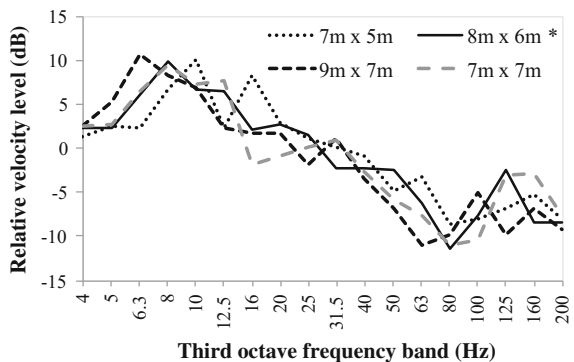


**Fig. 5** Mid-span vibration at 3rd floor, relative to basement: different values of floor slab sizes



might not be observed in practice, since the overall building dimensions would normally be constrained; possible changes in floor section area would most likely be accommodated by altering the layout of supporting columns whilst maintaining the overall building dimensions.

**Fig. 6** Mid-span A-weighted velocity relative to basement: different values of floor slab sizes

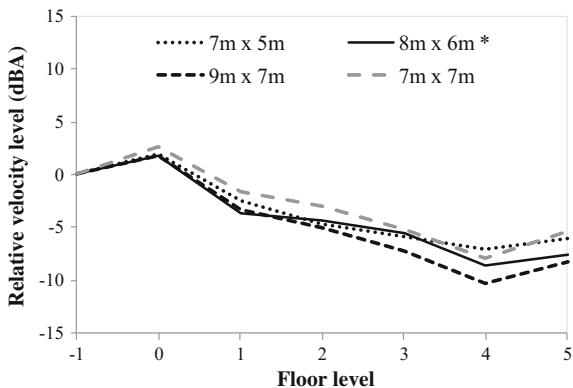


**Fig. 7** Mid-span vibration at 3rd floor, relative to basement: different values of damping (loss factor)

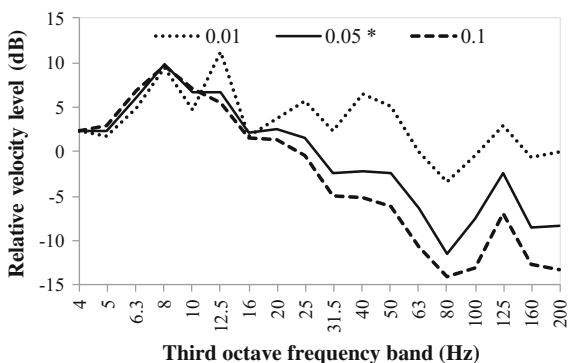
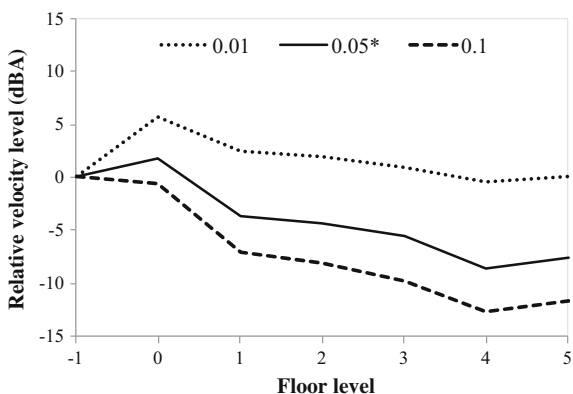


**Fig. 8** Mid-span A-weighted velocity relative to basement: different values of damping (loss factor)



Figures 7 and 8 show the effect of varying the damping loss factor. This can have an important influence on the result, and can account for differences of up to about 10 dB for a six storey building, when considering loss factors in the range 0.01–0.1.



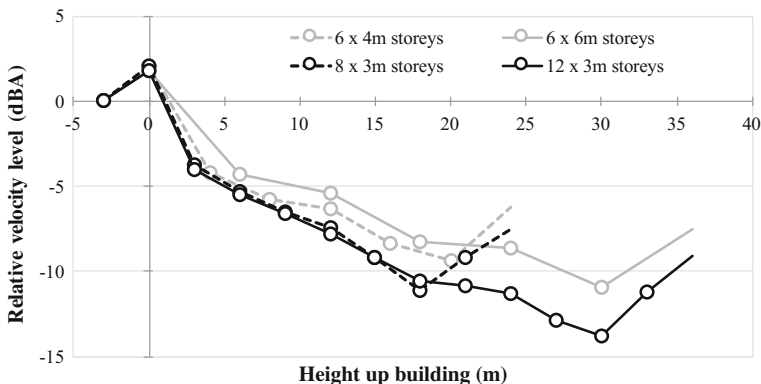


**Fig. 9** Mid-span A-weighted velocity relative to basement: different building/storey height configurations. Each storey is marked with a circle marker. The roof is shown as the far right end of each line, with marker omitted

Figure 9 shows the influence that both the number of storeys and the storey height can have on a building. It suggests that the number of storeys is a more important parameter than the storey height, such that for two buildings of otherwise equal height, the building with the greater number of storeys is likely to exhibit slightly lower floor vibration levels at a given height.

Other building parameters have also been investigated, from which an empirical prediction approach has been developed. The proposed empirical prediction is based upon knowledge of the dominant building and floor natural frequencies and shows good agreement with the model and measurement data, but is not presented here due to space constraints.

### 3 Re-radiated Noise

The re-radiated noise is often estimated from the floor vibration using empirical formulae such as that proposed by Kurzweil [7]. In the present study an FE model has been developed to study the radiation of sound within a room due to structural vibration.

#### 3.1 Finite Element Model

For the FE model of the room, the sound pressure was determined by coupling an air volume to a simplified structural representation of the rest of the building. The building is modelled as a 2 × 2 arrangement of floor slabs that are each 8 m 6 m. The floors are modelled as reinforced concrete with a thickness of 1 m for the

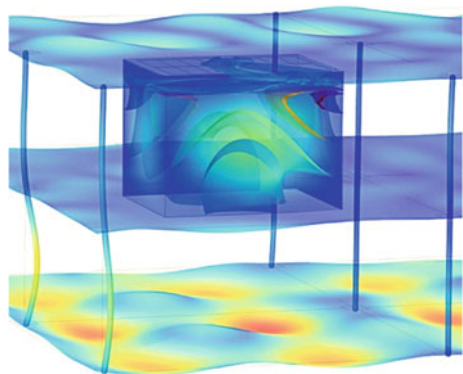
basement, and 270 mm for the upper floors. The columns are 500 mm diameter columns of reinforced concrete, each with a height of 3 m. The basement is excited with a uniformly distributed force that has a vertical component five times that of its lateral components.

The room has dimensions  $4 \times 3 \times 2.6$  m. Its walls are 200 mm thick concrete block construction, and are structural, extending from the floor to the soffit. The room has an internal ceiling of 15 mm thick plasterboard, mounted on a framework that is rigidly connected to the soffit, and with an air-filled cavity of 0.4 m above the ceiling.

A view of the operational deflection and sound pressure iso-surfaces at 91 Hz for the default room model is given in Fig. 10. The model was solved in the frequency domain (1325 frequencies between 16 and 281 Hz) using COMSOL Multiphysics. The number of degrees of freedom was 88,809 for the default room model. Damping was provided to the structural components by including a complex component to the Young's modulus values. Damping was included in the air volume via its coupling with the structural model and through the specification of an additional frequency-dependent air attenuation value. Appropriate values for the air attenuation value were determined through a separate model investigation. For the generic room geometry, it was found that an air attenuation value of 0.35 dB/m provided equivalent damping to a reverberation time of 0.5 s.

Whilst much of the literature for groundborne noise assessment does not specify the location(s) in the room to be used for noise evaluation (e.g. [2, 3, 7]), some of the literature states that the evaluation position should be near the centre of the room, but avoiding the very centre of the room due to its prominent modal features (e.g. [8, 9]). This advice is also given in ISO 14837-1:2005 [10], which adds that measurements may be consistent with the ISO 140 series of standards (concerned with the measurement of sound insulation in buildings). This ISO 140 series has since been superseded by the ISO 16283 series. This contains new guidance recommending that at low frequencies the sound pressure level may be appropriately described by a weighted logarithmic average of the average sound pressure levels at

**Fig. 10** FE model of room, operational deflection and sound pressure iso-surfaces at 91 Hz



corner and distributed room positions (based on the findings of Simmons [11] and Hopkins [12]). The low frequency sound pressure level is then given by:

$$L_{LF} = 10 \log \frac{2 \times 10^{\frac{L_{room}}{10}} + 10^{\frac{L_{corner}}{10}}}{3} \quad (\text{dB re } 2 \times 10^{-5} \text{Pa}), \quad (3.1)$$

where:

$L_{room}$  is the average sound pressure level for the distributed room positions, in dB;

$L_{corner}$  is the average sound pressure level for the corner positions, in dB.

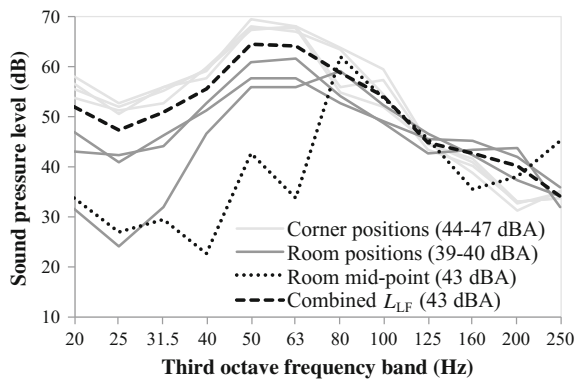
In this paper, the predicted sound pressure levels presented correspond to the combined  $L_{LF}$  values. The corner positions used in the calculations are 0.5 m from the nearest room surfaces.

### 3.2 Parametric Study

Results are presented for the default room and for various parameter changes. The results for the default room model are assigned an indicative sound pressure level that corresponds to a room measurement made by the author, with a spectrum that is typical for groundborne noise from railways. The results for other cases are calculated by applying the difference between the parametric study and default room model results to this representative spectrum.

The sound pressure level at different positions within the model room is shown in Fig. 11. This shows that there are large differences in the sound pressure level at low frequencies, up to about 100 Hz (for this room). Corner positions exhibit sound pressure levels around 6 dBA higher than the room positions. As such, the measurement location is likely to have a significant influence when assessing groundborne noise in rooms. The combined  $L_{LF}$  value represents a reasonable compromise

**Fig. 11** Groundborne sound pressure level at various evaluation locations within the room



between the corner and room positions, having the benefit of including all the room modes, whilst giving overall sound pressure levels that are more representative of the more centrally occupied areas in the room. It is therefore recommended that consideration be given to specifying this parameter when defining groundborne noise criteria and/or making measurements and predictions.

The influence of room absorption has been investigated by altering the air attenuation value in the model to achieve reverberation times that were a factor of two greater than or less than the default condition. The results are shown in Fig. 12. These demonstrate that the room absorption will have an influence on the sound pressure level at the upper frequency range of consideration, such that when considering overall A-weighted sound pressure levels, doubling the reverberation time (across the whole frequency range) could account for an increase in noise level of about 2 dBA. There is no change at low frequency where there are no room modes.

The effect of the size of the room was investigated, with results presented in Fig. 13. The smaller room has the dimensions (l × w × h) 2.7 × 2 × 2.6 m; the default room has dimensions 4 × 3 × 2.6 m; the larger room has dimensions 6 × 4 × 2.6 m. The change in room size shifts the natural frequencies of acoustic room modes as well as those of vibrational modes of the floor and ceiling structures. The significance of this frequency shift on the sound pressure level is dependent on

**Fig. 12** Groundborne sound pressure level: different reverberation time conditions

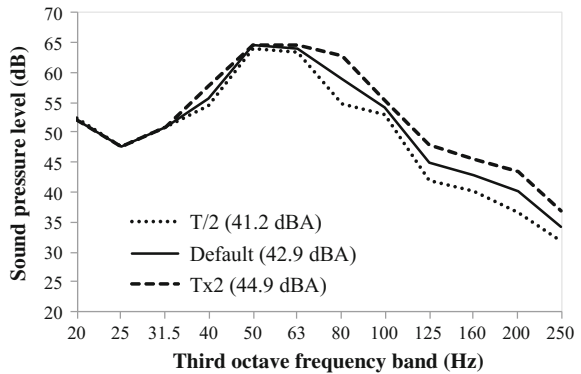


**Fig. 13** Groundborne sound pressure level: different room sizes (floor area)

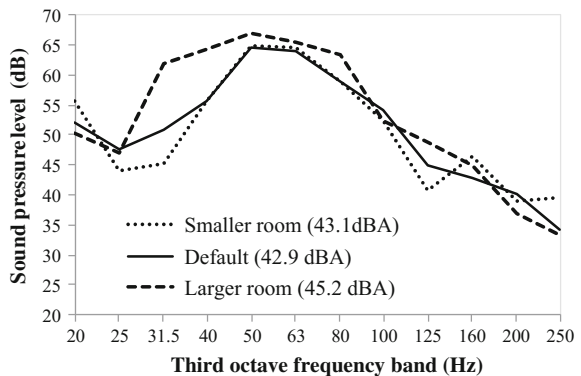
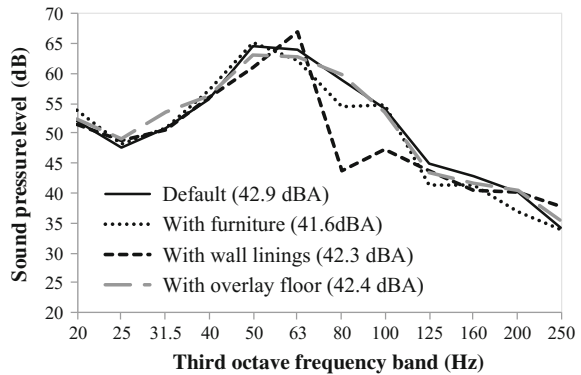


**Fig. 14** Groundborne sound pressure level: other factors



the input spectrum. In addition, changing the geometry of a room affects the reverberation conditions as well as the amount of radiating area, and could potentially change the dominant radiating surfaces from walls to the ceiling/floor or vice versa (determination of relative surface noise contributions is an aspect that requires further investigation). In these examples, the room length and width have been altered by a factor of 1.5. Making the room smaller did not have an appreciable effect for this input spectrum and room size, but increasing the room size led to a slight increase in noise level of about 2 dBA.

Figure 14 shows the influence of various other factors on the predicted sound pressure level. The addition of furniture consisting of a bed, a wardrobe and a chest of drawers, leads to an increase in absorption and scattering and the furniture also provides a small barrier effect for the nearby radiating surfaces. Nevertheless, the inclusion of the furniture itself is predicted to lead to a reduction in sound pressure level by only around 1 dBA. The inclusion of a shallow overlay floor surface consisting of 18 mm chipboard on an 8 mm foam layer, is shown to have a negligible effect on the sound pressure level (<1 dBA). The inclusion of wall linings (13 mm plasterboard on 50 mm studs rigidly attached to the concrete walls, with air in the cavity) is found to affect the sound pressure level between 63 and 100 Hz, although the actual overall A-weighted level is not affected. Performance of the wall linings would be expected to improve at higher frequencies through the inclusion of mineral fibre insulation in the cavity, although such benefits will also be dependent on the relative amount of sound transmission via the floor and ceiling.

Additional room parameters have been investigated, and work is underway on developing a suitable empirical prediction approach for groundborne noise in rooms.

## 4 Conclusions

Parametric studies have been conducted on 3-D FE models of a building and a room in order to investigate the influence of various structural parameters on the levels of railway groundborne noise and vibration. The study of vibration propagation within

the building indicates that changing the floor thickness over a range of reasonable values has a negligible influence on the groundborne vibration, whereas changing the floor area had a more prominent effect due to shifting of the floor natural frequencies. The structural damping was shown to have an important effect on the calculated groundborne noise levels in buildings, and therefore it should be specified through careful measurement.

The room acoustics FE models showed that the groundborne noise level varies considerably within a typical room, and it is therefore recommended that the low frequency procedure detailed in ISO 16283-1 be adopted for specifying and measuring groundborne noise in small rooms. Through a parametric study it was shown that the room reverberation time, room size and presence of furniture each have a moderate effect on the sound pressure level. Whilst the installation of wall linings was predicted to provide only a marginal improvement in sound pressure level, this effect is dependent on the relative contributions of the wall, ceiling and floor surfaces.

## References

1. Jones, S., Kuo, K., Hussein, M.F.M., Hunt, H.E.M.: Prediction uncertainties and inaccuracies resulting from common assumptions in modelling vibration from underground railways. *Proc. Inst. Mech. Eng. Part F J. Rail Rapid Transit.* **226**, 501–512 (2012)
2. Remington, P., Kurzweil, L., Towers, D.A.: Low-frequency noise and vibration from trains. In: Nelson, P.M. (ed.) *Transportation Noise Reference Book*. Butterworth & Co., London (1987)
3. Hanson, C.E., Towers, D.A., Meister, L.D.: *Transit Noise and Vibration Impact Assessment*. Office of Planning and Environment, Federal Transit Administration (2006)
4. Thompson, D.J.: *Railway Noise and Vibration: Mechanisms, Modelling and Means of Control*, Elsevier Ltd (2009)
5. Jin, Q., Thompson, D.J., Lurcock, D.E.J.: Prediction of building vibration induced by underground trains using a coupled waveguide finite/boundary element method: 12th International Workshop on Railway Noise. Terrigal, Australia (2016)
6. Lurcock, D.E.J., Thompson, D.J., Bewes, O.G.: Attenuation of railway noise and vibration in two concrete frame multi-storey buildings: 11th International Workshop on Railway Noise. Uddevalla, Sweden (2013)
7. Kurzweil, L.: Ground-borne noise and vibration from underground rail systems. *J. Sound Vib.* **66**, 363–370 (1979)
8. Ashdown Environmental Limited, *Vibration and Groundborne Noise Calculation Procedures for the Channel Tunnel Rail Link: Volume 1 of 2* (1995)
9. CrossRail, *CrossRail Information Paper D10—Groundborne Noise and Vibration* (2008)
10. British Standards Institution: *Mechanical vibration—Ground-borne noise and vibration arising from rail systems—Part 1: general guidance*, BS ISO 14837-1:2005
11. Simmons, C.: Measurement of sound pressure levels at low frequencies in rooms. Comparison of available methods and standards with respect to microphone positions. *Acta Acustica United with Acustica* **85**, 88–100 (1999)
12. Hopkins, C., Turner, P.: Field measurement of airborne sound insulation between rooms with non-diffuse sound fields at low frequencies. *Appl. Acoust.* **66**, 1339–1382 (2005)

# Identifying Noise Levels of Individual Rail Pass by Events



Matthew Ottley, Alex Stoker, Stephen Dobson and Nicholas Lynar

**Abstract** Technology associated with acoustic data capture has advanced significantly, with commercially available Sound Level Meters allowing engineers and consultants to capture large amounts of multi-channel data relating to train noise. Whilst this extended dataset can provide vital information, manually scrutinizing large amounts of data to isolate individual train pass-bys can be time consuming and problematic. This paper investigates the implementation of automated, remote (un-manned) systems that can be installed on-site, allowing train pass-by noise levels to be recorded with minimal user guidance. The efficacy of acoustic and ground vibration sensors to accurately identify train noise levels and train direction is investigated.

## 1 Introduction

The technology available for noise measurement and analysis has progressed rapidly over the last decade. The quantity of data available has increased dramatically with the advent of large solid state storage and remote connectivity of devices. It is now common to record spectral levels every second and continual high quality audio for weeks on end. Previously, noise data loggers were generally only capable of recording average noise levels over predefined periods (e.g. day and night times). New generation devices are capable of recording individual train pass-bys and there are generally two measurement and analysis options.

One option is to construct customised, dedicated measurement solutions tailored to rail noise measurements, such as the Transport for NSW Wayside Noise and Vibration Monitoring System [1]. These systems are typically installed inside the

---

M. Ottley (✉) · A. Stoker · N. Lynar  
Marshall Day Acoustics, 4/46 Balfour Street, Chippendale, NSW, Australia  
e-mail: sydney@marshallday.com

S. Dobson  
Marshall Day Acoustics, 6 Gipps Street, Melbourne, VIC, Australia  
e-mail: melbourne@marshallday.com

rail corridor and operated by (or on behalf of) the infrastructure owners. The advantage of such systems is that they can be designed to capture very detailed data for specific applications. Their disadvantage is that they lack flexibility and may be unattractive for consultants as their single application nature means they can be difficult to justify (in terms of upfront investment) unless continuous monitoring work is likely. Also the systems generally need to be installed within the rail corridor, requiring co-ordination and co-operation from the network operator, involving a level of bureaucracy as well as the inherent risks of working within an operating rail corridor.

An alternative option to a dedicated measurement system is to use commonly available measurement equipment, such as an advanced noise logger (logging noise parameters every second and recording continuous audio). The advantage of more general purpose equipment is that it can be deployed on other sites when not in use for rail projects. The limitation of advanced noise loggers is that it can be difficult to extract train pass-by information from the large data set collected.

Where the noise logger is located close to the train line and the ambient acoustic environment is relatively free of other extraneous noise simple software triggering (based on level and duration of noise events) can be used to identify rail pass-bys. Unfortunately sites are more often affected by a range of other extraneous ambient noise (such as nearby roads or aircraft overflights) that can interfere with simple noise triggers, leading to either extraneous noise falsely identified as trains or train pass-bys being missed.

This paper examines the potential to use general purpose measurement equipment to be deployed in such a way as to deliver robust noise level results, minimize data analysis time (i.e. reduce man hours required to sort data) and identify key data related to train pass-bys. The focus is on the tools available to quantify the following for individual pass-bys:

- Time of pass-by
- Duration of pass-by
- $L_{AE}/SEL$  of pass-by
- $L_{Amax}$  of pass-by
- Type of train (passenger vs freight)
- Train direction.

On previous projects data acquisition has utilized two advanced noise loggers separated by at least 50 m along the rail corridor. Simple threshold triggers, based on threshold noise levels and duration, are used to identify pass-bys. The time difference between the pass-by at each logger is used to determine train direction. For locations further away from the track the triggers on the logger(s) close to the track can be used to create a time window for pass-bys at loggers located more remotely from the track. This system works well in many instances but has limitations where the site is subject to significant ambient noise that may activate the threshold triggers (particularly if near roads or subject to aircraft overflights).



The other disadvantage to this approach is that multiple advanced noise loggers are required in order to determine train direction or to create trigger windows for sites located some distance from the rail line.

## **2 Methodology**

### ***2.1 System Design***

This paper explores the use of ground vibration sensors to generate trigger windows to capture train pass-by noise. Train passage generates a unique ground vibration event which can be used to identify pass-bys. Two vibration sensors are typically set on ground, close to the rail corridor boundary with a sufficient separation to generate leading and lagging vibration events. The vibration output is used to generate trigger periods to automatically extract noise data from a noise logger typically located at a more remote distance from the tracks. For this study, the equipment comprised a 01 dB Duo Smart Noise Monitor and an 8 Channel Instantel Minimate III Plus with external geophones.

The Duo is an advanced IEC Class 1 noise monitoring platform with 1/3 octave capability, discrete time period acquisition as low as 100 ms, high quality signal recording, advanced trigger coding and utility functions for high capacity memory storage and remote connectivity. The post processing software used for the Duo data is dBTrait.

The Minimate III Plus, now practically a legacy vibration monitoring platform, is primarily used for blast and construction monitoring. It was utilized for this study as it is robust and relatively inexpensive system although the minimum histogram discrete time period of two seconds is less than ideal and for this deployment, requiring a 90 m separation between the geophones to obtain sufficient definition of the leading and lagging vibration events. The post processing software used for the Minimate data is Blastware.

The noise logger was installed just outside the rail corridor, between the vibration sensors.

### ***2.2 Data Processing and Analysis***

The data processing procedure from each monitoring device is set out below.

Step 1: Process vibration data to identify each rail pass-by.

Vibration data was first exported from Blastware as an ASCII file for import to 01 dB dBTrait software. Threshold coding was then applied in dBTrait to establish the time and duration of each vibration event above ambient levels.

Each of the two vibration channels was analyzed individually. The two data sets were then compared to find overlapping events, with non-correlated events excluded. The time difference (leading and lagging) between the first sample of each pass-by on the two sensors was then used to determine the direction of the train (with the leading event indicating direction the train was coming from).

The duration of the coded event can be used to classify the train as either passenger or freight. The exact duration threshold for classification of trains will vary from site to site but in Sydney passenger train sets tend to vary from approximately 80–160 m [2], suggesting a passing period of 5–10 s at 60 km/h. Based on site observations passenger trains tend to be less than 20 s duration on the Sydney network.

Step 2: Transfer event coding sequence to noise histogram.

Within dBTrait the coded event sequence was then applied to the noise data, with the software outputting the  $L_{AE}$  and  $L_{Amax}$  parameters for each event.

### 3 Results

#### 3.1 Test Location 1

A location for initial system testing was found in St Peters, Sydney. The location was on the southern side of the rail corridor, with four rail lines adjacent, ranging from 8 to 30 m from the measurement locations. The site was within a park with relatively low ambient noise levels from street level, but was exposed to regular aircraft overflights. The site location is shown in Fig. 1.



**Fig. 1** Site 1 showing vibration sensor (V) and noise logger (N) locations

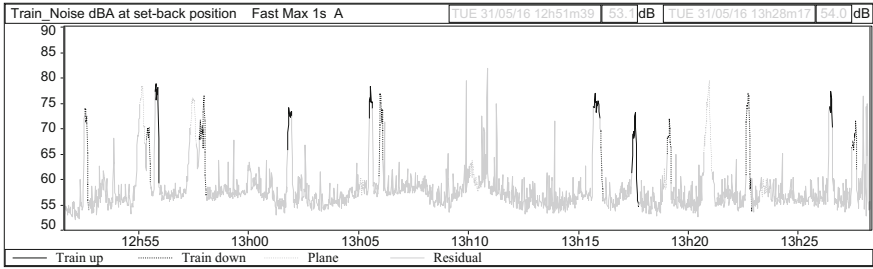


Fig. 2 Time histogram of manually coded results

The measurements were carried out over approximately 40 min whilst an operator was in attendance in order to identify each individual pass-by manually (Fig. 2), for comparison with derived results.

For comparison with the vibration encoding, the noise data was passed through a simple threshold coding for events greater than 70 dB, resulting in 28 events being identified (Fig. 3).

A more refined noise coding was also used to exclude any noise events that exceeded 70 dB for less than 5 s, resulting in 11 events being identified (Fig. 4). For the vibration coding technique, identified vibration events (Fig. 5) are merged with the measured noise histogram (Fig. 6) to identify the noise levels associated with the individual train pass by events.

The results of the different analysis methods are summarised in Table 1. Note that the  $L_{eq} (37min)$  column provides the  $L_{eq}$  contribution over the entire measurement period from only the identified events. The  $L_{AE}$  total column provides the sum of all  $L_{AE}$  levels from individual events.

Note that whilst the vibration auto-coding only identified 13 of the 14 observed events there was one observed event that included the simultaneous passing of two trains in opposite directions. A review of the histogram from the second vibration sensor showed two events, confirming two trains passing simultaneously in opposite directions.

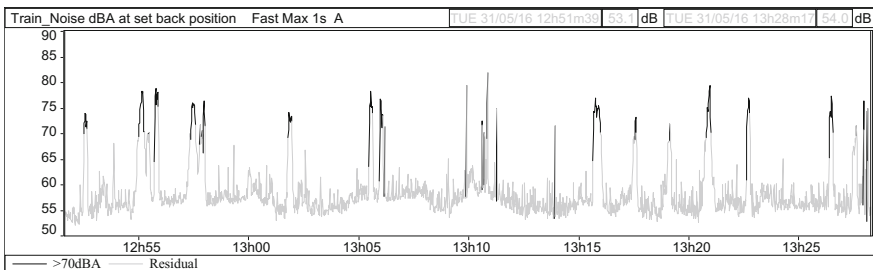


Fig. 3 Time histogram of simple >70 dBA threshold coding results

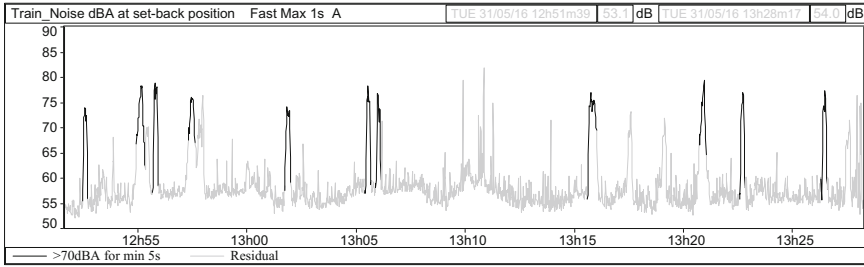


Fig. 4 Time histogram of refined >70 dBA and >5 s duration threshold coding results

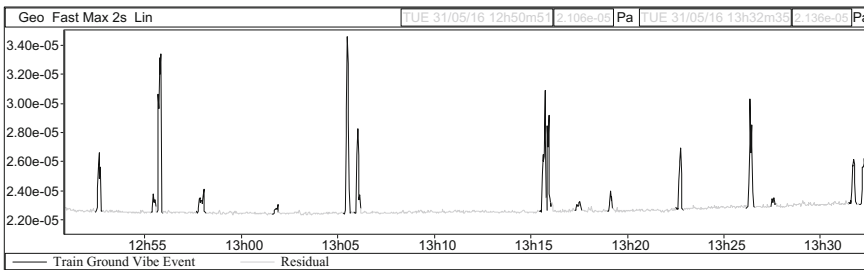


Fig. 5 Time histogram of identified vibration trigger events

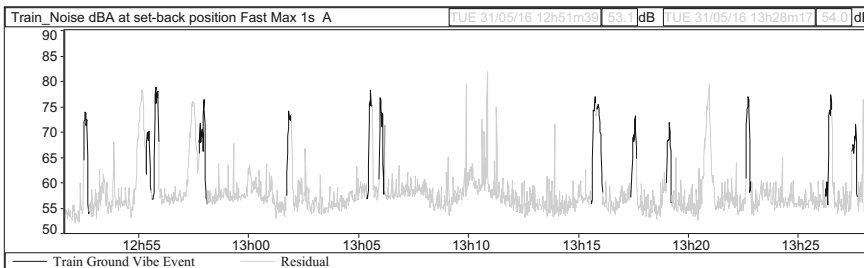


Fig. 6 Time histogram of merged vibration trigger events and noise data

The simple noise threshold coding identified twice as many noise events than there were train pass-bys. The noise threshold coding with minimum duration excluded most of the spurious events but also failed to identify some rail passbys (which were just below 70 dB) whilst not rejecting all aircraft overflights.

From Figs. 4 and 5 and Table 1 the vibration coding method identifies levels from all train passbys and excludes extraneous airborne noise sources (in this case predominantly from aircraft overflights). The method accurately identifies  $L_{AE}$  and

**Table 1** Summary of processed results from Site 1

Event coding	Number of events	L <sub>AE</sub> range (dB)	L <sub>Amax</sub> range (dB)	L <sub>AE</sub> total (dB)	L <sub>Eq</sub> (37min) (dB)	Highest L <sub>Amax</sub> (dB)
Noise threshold coding: >70 dB	28	63–86	70–82	95	62	82
Noise threshold coding: >70 dB and >5 s duration	11	80–86	74–80	95	62	80
Vibration coding	13	77–86	70–79	94	61	79
Attended coding (operator observed)	14	70–86	69–79	93	60	79

L<sub>Amax</sub> levels for individual passbys. Importantly the overall L<sub>AE</sub>/L<sub>Aeq</sub> levels for the period and highest L<sub>Amax</sub> levels for the period are more accurately identified, and are lower than the levels taken from noise threshold coding.

### 3.2 Test Location 2

To expand on the results from Test location 1, as well as to capture freight movements, which were not experienced during the measurement period at Test location 1, a second survey was carried out. The site for the second survey was at Asquith, on the northern edge of Sydney. The equipment was deployed for a 24 h period in order to capture overnight freight operations. The monitor locations were between 12–18 m from the two adjacent rail lines. A sub-arterial road was located approximately 4–6 m from the monitor locations. The site location is shown in Fig. 7.

**Fig. 7** Site 2 showing vibration sensor (V) and noise logger (N) locations



On analysis of the vibration results it was discovered that the vibration levels due to train pass-bys were not sufficiently above the noise floor of the vibration sensors to confidently identify the trains. The noise floor of the vibration sensor was in the order of 0.3 mm/s and at the measurement locations the vibration levels from rail passbys were less than 1 mm/s in most instances, making identification of train events unreliable.

## 4 Discussion

The work at location 2 was important as it showed that the proposed method of using standard vibration loggers designed for construction work would not be sufficient to confidently deploy the system without carrying out initial baseline monitoring of several pass-bys to ensure sufficient signal to noise. One option to improve the system would be to use higher sensitivity geophones with a lower noise floor. A second option, which would allow much clearer identification of trains, and allow rejection of other ambient vibration sources, would be to monitor vibration in 1/3 octaves and identify trains based on their signature vibration levels in the 30–60 Hz range [3].

Identification of train type (passenger verses freight) from vibration levels is another possibility that could be examined with further work, particularly if more sensitive vibration logging equipment was used.

There were some difficulties encountered on site with running 90 m of vibration cable, and this would preclude the use of the system on many sites. Use of suitable wireless ground vibration sensors would be beneficial. Use of vibration equipment with a finer sampling resolution (<2 s) would also reduce the distance required between vibration sensors in order to identify the lead/lag time between sensors, required to determine train direction.

An added benefit of the vibration sensing system examined in this paper is that it can provide a robust trigger for automated photographic snapshots (or video) of train pass-bys. These could be used to confirm train type, locomotive type/number etc. Several software options exist that could be tailored to automatically extract text (such as locomotive numbers) from the photographs. A further extension of this work could include the use of a video device triggered from each vibration sensor, with the sensors separated by a known distance, for calculation of speed between the two points.

One limitation that does exist in the method described is that the system does not discern if an extraneous noisy event occurs simultaneously with a train pass-by. For example if an aircraft passes at the same time as a train the recorded event will include noise from both the train and the aircraft. Such events may give rise to statistically outlying noise levels in the dataset. If required these outlying data points could be identified and the audio recordings manually reviewed to exclude data points if appropriate.

## 5 Conclusion

Investigations were undertaken to examine the possibility of using commonly available measurement equipment in order to measure and identify individual rail pass-bys with a high degree of certainty using a highly automated analysis system. The system included an advanced noise logger and a multi-channel vibration logger with two sensors located some distance apart. Vibration data from each site was processed first and threshold coding applied to establish the time and duration of each vibration event. Each of the two vibration channels was analysed individually and the time difference (leading or lagging) between the first sample of each pass-by on the two sensors was then used to determine the direction of the train. The coded event sequence was then applied to the noise data, with the software outputting the  $L_{AE}$  and  $L_{Amax}$  parameters for each event.

Provided the vibration recordings had sufficient signal to noise the vibration coding method accurately identified all train passbys and excluded extraneous airborne noise sources (except for extraneous noise that occurred simultaneous to a train pass-by). The method identified  $L_{AE}$  and  $L_{Amax}$  levels for individual passbys more accurately than threshold coding directly on the noise histogram. Importantly the overall  $L_{AE}/L_{eq}$  levels for the period and highest  $L_{Amax}$  levels for the period are more accurately identified, and are lower than the levels taken from direct threshold coding of the noise histogram.

## References

1. Jiang, J.: Wayside Noise and Vibration Monitoring System Installation and Technical Manual Version 1.0, Transport for NSW (2015)
2. Sydney Trains. Our Fleet. <http://www.sydneytrains.info/about/fleet/> (2016). Accessed 1 June 2016
3. Nelson, P.M. et al: Transportation Noise Reference Book. Butterworths (1987)

# A Modified Turnout Noise Model and Field Validation



W. Ho, B. Wong and T. Cai

**Abstract** This paper presents a modified empirical model for prediction of noise emanating from turnouts and crossovers. Existing empirical models use a generic correction factor on top of normal rolling noise, assuming turnout is also a dipole line source. Field measurements were conducted at various setbacks to validate the noise model. It is found that turnouts behave as monopole point source rather than dipole line source. The distinct noise source characteristics of turnout necessitate a different set of modelling equations. Calculation of Railway Noise (CRN) tends to underestimate the noise contribution from turnout, particularly at close distance or large angle of view, with a discrepancy of 4–7 dB(A). The modified noise turnout can address such discrepancies by adopting monopole point source assumption. Noise and vibration sensors were also placed at the track to study the relative noise contribution from rail, sleeper and wheel. The empirical relationship between noise level and various dependent parameters are derived. The noise level has higher dependence on train speed which an empirical relation of  $35\log(\text{speed})$  rather than  $20\log(\text{speed})$  in analytical models. However, it shows little dependence on unsprung mass, probably due to the fact that the wheelset is not a rigid body, the gear box and traction motor does not have significant addition to effective mass.

## 1 Introduction

Discontinuity in railway turnouts and crossovers momentarily exerts large contact force on the wheel and track causing wheel and track to vibrate and radiate noise. Turnout noise usually has a dominant contribution to the overall noise level and creates potential annoyance to receivers in the vicinity. A reliable prediction model for turnout noise is vital in railway noise assessment.

---

W. Ho (✉) · B. Wong · T. Cai  
Wilson Acoustics Limited, Unit 601, Block A, Shatin Industrial Centre,  
Shatin, N.T, Hong Kong SAR, China  
e-mail: who@wal.hk

© Springer International Publishing AG, part of Springer Nature 2018  
D. Anderson et al. (eds.), *Noise and Vibration Mitigation for Rail Transportation Systems*, Notes on Numerical Fluid Mechanics and Multidisciplinary Design 139,  
[https://doi.org/10.1007/978-3-319-73411-8\\_15](https://doi.org/10.1007/978-3-319-73411-8_15)



### ***1.1 Existing Empirical Approach***

Existing railway noise models assess impact noise from rail joints by adding a correction factor, e.g. +2.5 dB(A) over 18 m rail segment in UK's Calculation of Railway Noise (CRN) [1]; +5 dB(A) over 18 m rail segment in US's Transit Noise and Vibration Impact Assessment (FTA) [2]; +6 dB(A) over 10 m rail segment in Australia's Rail Infrastructure Noise Guideline [3]. These noise models are too generic and may not truly reflect the nature of turnout noise. For instance, measurement at near field show that the noise level decays at a rate of  $-6$  dB per doubling distance, which explicates that the turnout resembles a very localized point source. Using a line source model tends to underestimate the noise increment at receivers close to the track, but overestimate the noise increment at far field. Moreover, the assumption on dipole radiation pattern significantly underestimated the noise increment when the receiver is at a longitudinal setback from turnout.

### ***1.2 Existing Analytical Approach***

There are model which calculates the contact force using non-linear contact spring, the contact force is then converted to an equivalent wheel rail roughness spectra, and fed into TWINS model [4, 5] to derive the subsequent wheel and track dynamic response via Finite Element Analysis. However, such model requires computational expensive calculation. Moreover, it is incompatible with CRN or other empirical approach due to different model assumptions, input parameters and prediction flow. Therefore the analytical models cannot be readily implemented for general noise assessment purpose.

### ***1.3 Scope of Present Study***

The present study aims to develop a more realistic model for turnout noise. This modified model follows a similar prediction algorithm as in CRN but adopts point monopole source assumption. The reference sound exposure levels (SEL) of point switch and crossing frog are determined from trackside measurements. A different set of train speed correction, distance correction, angle of view correction and screening effect by barrier are derived. Field measurements were conducted to validate the point monopole source assumptions and prediction accuracy.

## 2 Noise Source Characteristics

### 2.1 Noise Radiation from Rail, Sleeper and Wheel

When the train passes a point switch or crossing frog, the discontinuity causes vertical displacement of the wheel and track, resulting in an abrupt change in contact force. The rail, sleeper and wheel will be set to vibration. To quantify the relative noise contribution from different components, vibration sensors are placed under rail and on sleepers to study the noise characteristics. The noise source identification provides insight on potential mitigation treatment at source.

As illustrated in Fig. 1, the rail vibrates predominantly in the frequency range of 200–400 Hz, while the sleeper vibrates predominantly in the frequency range of 250–630 Hz. These correspond to the noise peak at 200–630 Hz. Track components have major noise contribution to turnout noise in the low frequency regime below 630 Hz.

Above 630 Hz, the noise spectra between Old Train and New Train deviate by 4–8 dB. On the other hand, Track vibration level drops significantly above 630 Hz, and there is no significant discrepancy between the old and new train. This implies that noise is probably emanating from the train instead of the track.

The noise radiation from wheel is further manifested through the comparison of noise spectra for individual bogies. For New Train, all bogies are partially covered by undercar skirt. While for Old Train, trailer bogies are partially covered by skirt

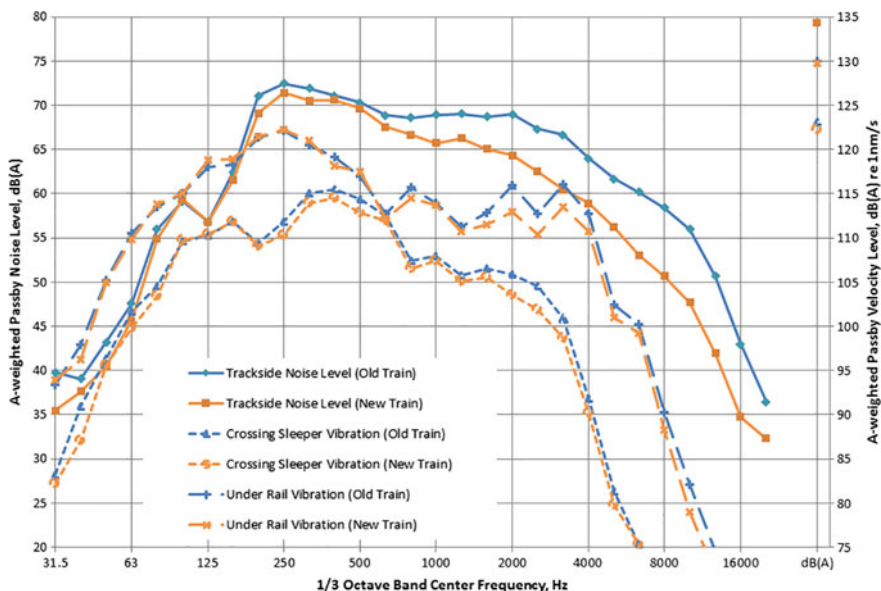


Fig. 1 Correlation between rail and sleeper vibration and passby noise level at 40 km/hr

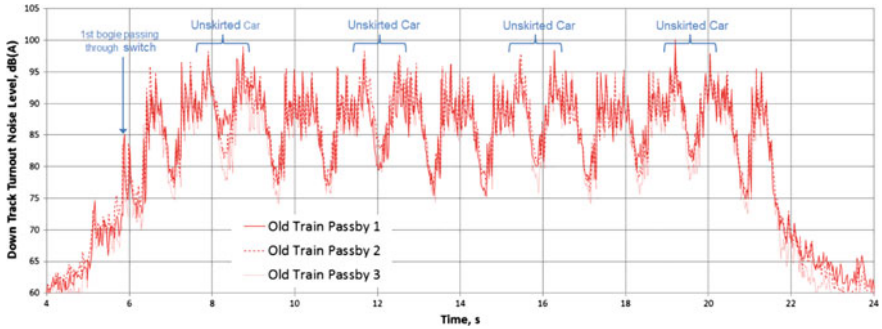


Fig. 2 Typical train passby noise time history

and motor bogies are exposed. If noise is mainly radiated from the wheel, it is anticipated that the undercar skirt will have more salient noise screening effect.

Typical passby noise time history of Old Train is illustrated in Fig. 2. The exposed bogies on the 2nd, 5th, 8th and 11th motor cars showed a higher noise level than other bogies. Their noise spectra are compared in Fig. 3. The major discrepancy lies above 630 Hz at which exposed bogies has about 6 dB higher noise level. Below 630 Hz there is insignificant difference as undercar skirt has little screening effect for noise radiation from track.

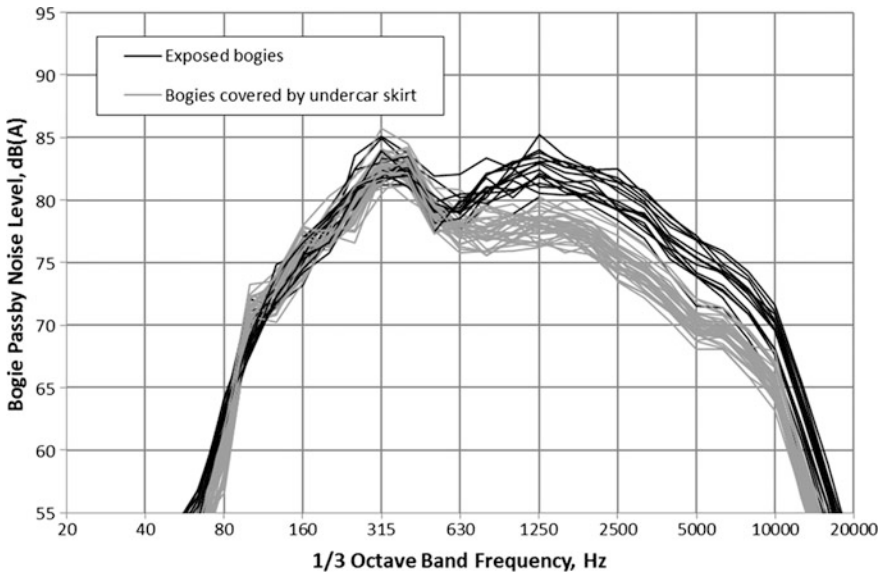


Fig. 3 Noise spectra comparison between covered and exposed bogies

### 2.2 Equivalent Source Length

The distance relation for point source and dipole line source are respectively as follows:

$$\text{Point source : } -20 \log \frac{d}{d_{ref}} \tag{1}$$

$$\begin{aligned} \text{Dipole line source : } & -10 \log \left[ \frac{l^2}{4d^2 + l^2} + \frac{1}{2d} \tan^{-1} \frac{l}{2d} \right] \\ & + 10 \log \left[ \frac{l^2}{4d_{ref}^2 + l^2} + \frac{1}{2d_{ref}} \tan^{-1} \frac{l}{2d_{ref}} \right] \end{aligned} \tag{2}$$

where  $d$  is the setback distance,  $d_{ref}$  is the reference distance of 25 m,  $L$  is the train length. By examining the theoretical distance attenuation against measured value, the assumption for point source or line source can be validated.

Microphones are placed at various setback distance pointing at the crossing frog. Maximum noise level is plotted against distance as shown in Fig. 4. The noise level decreases with distance following the relationship of approximately  $20 \log(d/d_{ref})$ . This relation holds even when the microphone is placed at 3 m from turnout.

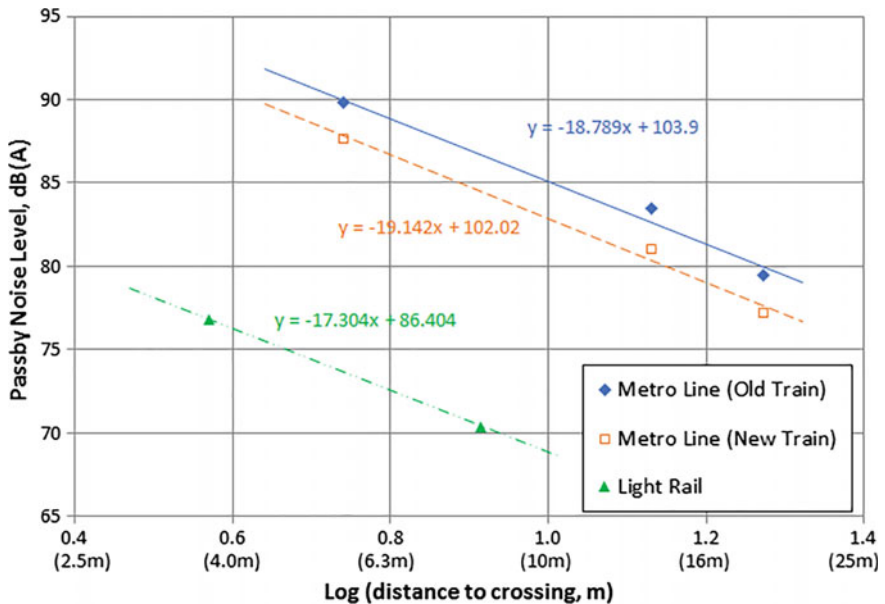


Fig. 4 Passby noise level against distance from turnout

**Table 1** Comparison of SEL between bogies passing through point switch and crossing frog

	Crossing frog	Point switch
Measured SEL for one bogie	86.3 dB(A) at 7.5 m	74.2 dB(A) at 14.1 m
SEL corrected to a reference distance of 25 m	75.8 dB(A)	69.7 dB(A)

This explicates that the turnout resembles a very localized point source. The noise radiation is confined within a very short section of the track, with equivalent source length less than 3 m.

### 2.3 Relative Source Strength Between Switch and Crossing

As the wheel rolls over a wider gap at the crossing frog, the crossing frog radiates significantly more sound energy than point switch. When a train runs to the diverging track it would pass through two crossing frogs, compared to one when running on straight through track of the crossing. Consequently, higher noise level would be produced. In order to establish a reliable turnout noise model, each individual switch and crossing shall be modelled as a separate noise radiation point. Thus it is necessary to quantify the relative source strength between switch and crossing.

In normal circumstances the noise from switch would be masked by that from crossing, except the first or last bogie when the train is just running through the switch but not yet arrive at the crossing. For easy visualization this switch noise level is indicated in the passby time history in Fig. 2. The sound exposure level (SEL) for the 1st bogie is extracted and compared with that from crossing frog. Both SEL are corrected to a reference distance of 25 m based on point source assumption. The result is presented in Table 1. The SEL of crossing frog is 6 dB(A) higher than that of point switch.

## 3 Parametric Study

Impact noise from turnout depends on various parameter including train speed, unsprung mass, axle load and condition of turnout. A parametric study is conducted to examine the relationship between noise level and these dependent parameters.

### 3.1 Train Speed Dependence

The relationship between passby noise level and train speed is illustrated in Fig. 5. The passby noise level increases with speed following the relation of  $35\log(\text{speed})$ .

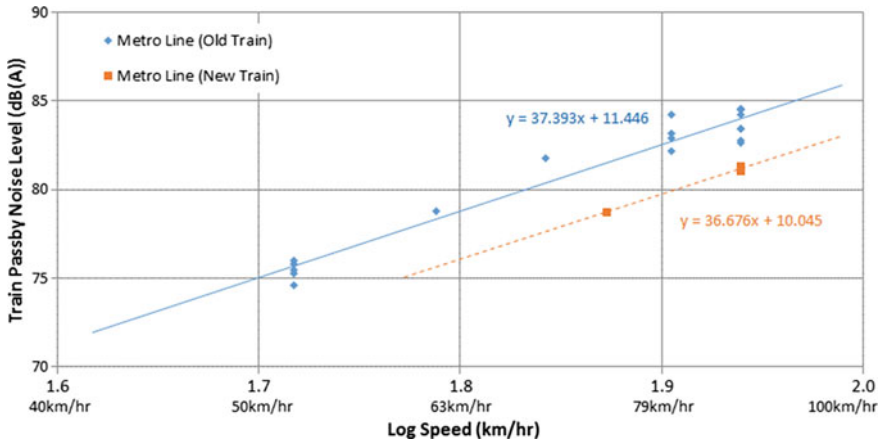


Fig. 5 Passby noise level against train speed

A similar speed dependence has also been identified for maximum noise level. Since the time for the train to pass through the turnout decreases as train speed increases, consequently SEL increases with train speed according to  $25\log(\text{speed})$ .

Theoretical analysis has shown that sound power level from rail joints increases according to approximately  $20\log(\text{speed})$  for step up joints and dipped joints, and less than  $10\log(\text{speed})$  for step down joints [4, 5]. The measured speed relationship of  $37\log(\text{speed})$  is significantly higher than theoretical value. It is even higher than the speed relation of  $30\log(\text{speed})$  for normal rolling noise. Such discrepancies deserve further investigation. Nevertheless, the measured speed relationship is adopted in the present noise model.

### 3.2 Effect of Unsprung Mass

The relationship between turnout noise level and unsprung mass is illustrated in Fig. 6. For Old Train, 2 dB(A) adjustment has been applied to motor bogies, to correct for the screening effect if undercar skirts is installed. The maximum noise level marginally increases from 95 to 96 dB(A) as unsprung mass increases from 1400 to 1800 kg. For New Train, the maximum noise level marginally increases from 94 to 95 dB(A) as unsprung mass increases from 1350 to 1840 kg. The unsprung mass is found to have insignificant effect on turnout impact noise.

British Rail Joint Model [6] suggested that the dynamic contact force for a dipped rail joint increases with unsprung mass according to  $10\log(\text{unsprung mass})$ . The measured empirical relationship is  $7\log(\text{unsprung mass})$ . Turnout noise has little dependence on unsprung mass due to non-rigidity of wheel set. The first

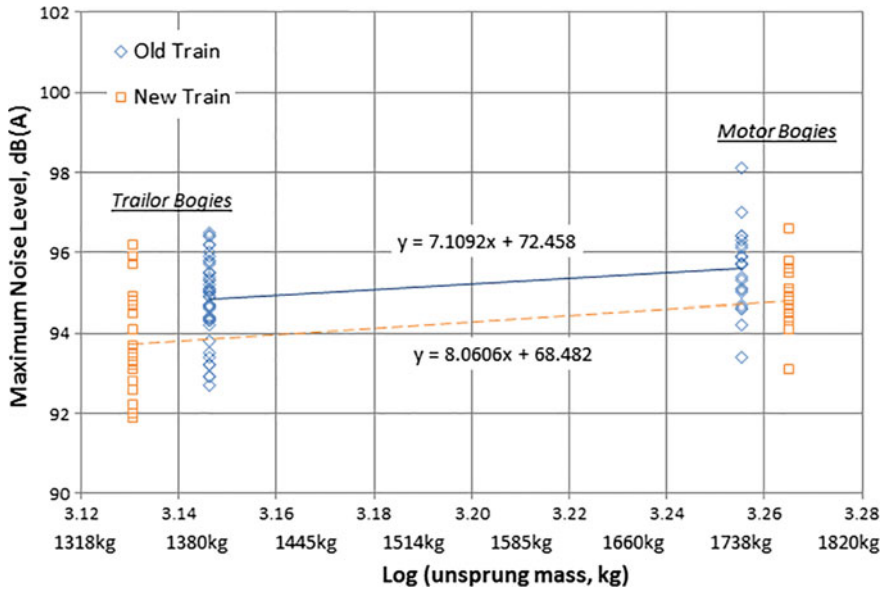


Fig. 6 Maximum noise level against unsprung mass

flexural mode of wheelset occurs at around 100 Hz, above 100 Hz the wheelset is no longer a rigid body. In other words, only the wheel mass at the turnout side contribute to the overall effective mass of the wheelset, the motor and gearbox on the motor bogie has little contribution to the modal mass at the noise radiation frequencies.

### 3.3 Future Studies

Impact noise from turnout also depends on the axle load. Since all the noise and vibration measurements are being conducted on operating metro lines in Hong Kong, there is insufficient variation on axle load to establish an empirical relationship.

Also, owing to limited track access site inspection has not been conducted to quantitatively describe the turnout condition such as gap width and step size. Our routine noise monitoring showed around -2 to 3 dB(A) difference between a newly replaced turnout and a well-maintained turnout.

Thus, these parameters remain the work for future research.

### 4 Modified Turnout Noise Model

Base on the measurement findings, a modified turnout noise model is established as summarized in Table 2. The SEL for turnout is derived by trackside measurement close to turnout, while the SEL for plain track is derived by measurement at adjacent control section. A distance correction of  $20\log(d/d_{ref})$  is applied based on point source.

One particular point of interest is the angle of view correction. Calculation of Railway Noise (CRN) assumes a dipole radiation pattern as the same for rolling noise. The noise evanesces abruptly as view angle increases. However, since the noise is mainly radiating from vertical motion of the rail and baffled sleeper, field measurement indicates that the turnouts can be better represented by a monopole. This is further elucidated in the subsequent field validation section. Consequently, a modified angle of view correction is adopted, whereas the  $\sin\alpha$  term accounts for the increase in slant distance to the turnout.

Another point to note is the screening effect. The CRN correction for line source and derived by integrating the barrier effect for infinitesimal point sources. While in the modified model, the screening effect is directly referenced to Maekawa equation for a point source, the screening effect is a function of the angle of view. Moreover, the turnout emanates noise predominantly in the low frequency regime between 200 and 500 Hz, in contrary to rolling noise which is predominantly at  $\sim 800\text{--}1000$  Hz, making it more difficult to be screened by noise barrier. A noise frequency peak at around 315 Hz is assumed in the modified model.

**Table 2** Comparison between the CRN and the modified turnout noise model

	CRN	Modified turnout noise model
Reference SEL (25 m and 80 kph)	+6 dB(A) relative to plain track [i.e. 87.3 dB(A)] distributed over 20 m track	86.6 dB(A) for crossing, 80.6 dB (A) for switch, localized point source
Correction for train speed	$+ 20\log \frac{V}{V_{ref}}$	$+ 25\log \frac{V}{V_{ref}}$
Distance correction	$- 10\log \frac{d}{d_{ref}}$	$- 20\log \frac{d}{d_{ref}}$
Angle of view correction	$- 10\log \left[ \frac{\pi\theta}{180} - \cos 2\alpha \cdot \sin\theta \right] - 5$	$20 \log(\sin \alpha)$
Screening effect by noise barrier	<p>for <math>0.4 &lt; \delta &lt; 0</math> (<i>illuminated</i>)  <math>\Delta L = 0.88 + 2.14 \log(10^{-3} + \delta)</math></p> <p>for <math>0 &lt; \delta &lt; 2.5</math> (<i>shadow</i>)  <math>\Delta L = -7.75 \log(5.2 + 203\delta)</math></p> <p>for <math>\delta &gt; 2.5</math> (<i>shadow</i>)  <math>\Delta L = -21</math></p> <p>where <math>\delta</math> is the path difference</p>	$\Delta L = -7 - 20 \log \left( \frac{(2\pi N)^{1/2}}{\tan h(2\pi N)^{1/2}} \right)$ where Fresnel Number $N = \frac{2}{\lambda} \delta \cdot \sin\alpha$ $\delta$ is the path difference $\alpha$ is the angle of view



## 5 Field Validation

To validate the model assumptions and prediction accuracy, microphones are placed at various setbacks from the crossing frog at up track turnout, to capture the noise from both up track (UT) and down track (DT). In CRN model, the turnouts are modelled as 20 m line source as indicated by the two rectangular boxes in Fig. 7. In the modified model, the turnouts are modelled as 4 monopole point sources (2 point switches and 2 crossing frogs) as indicated by the four dots. A  $-2.5$  dB(A) correction has been applied for the further microphone to account for wall reflection. In Fig. 8, the predicted noise level is compared against measured values. It can be observed that the CRN significantly underestimated turnout noise.

The discrepancy between point source and line source assumption can be observed from UT noise level. Within 20 m, the noise level decreases at a rate of 3 dB per doubling distance in CRN model, and 6 dB per doubling distance in modified model. The discrepancy is more salient when the microphone is placed very close to the track, as the sound energy is concentrated at a point close to the microphone rather than evenly distributed over a line. At longer distance the noise contribution from turnout diminish, the noise level converges to that from plain track and the discrepancy become smaller. The discrepancy on monopole and dipole assumption can be observed from DT noise level, where the microphone has a longitudinal setback of 18 m from the crossing. Under dipole assumption a large angle of view correction is applied. The noise contribution from turnout) is much less than that from plain track. In that sense, turnout noise from DT would be masked by plain track rolling noise and become inaudible, even despite a +10 dB (A) correction for turnout instead of +6 dB(A). This is not in line with site observation whereas impact noise from turnout is still dominant.

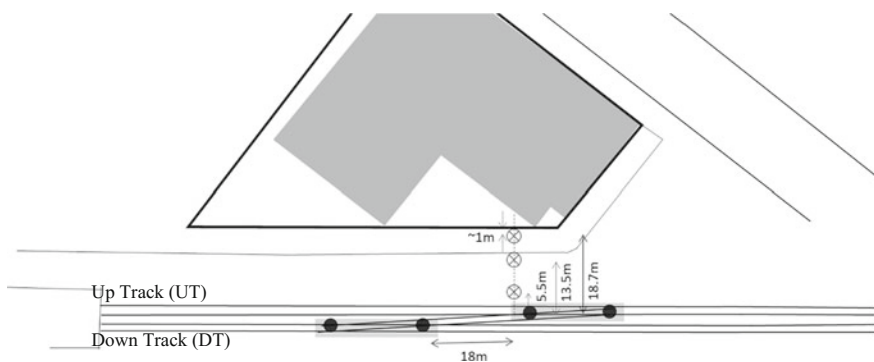


**Fig. 7** Site map for field validation

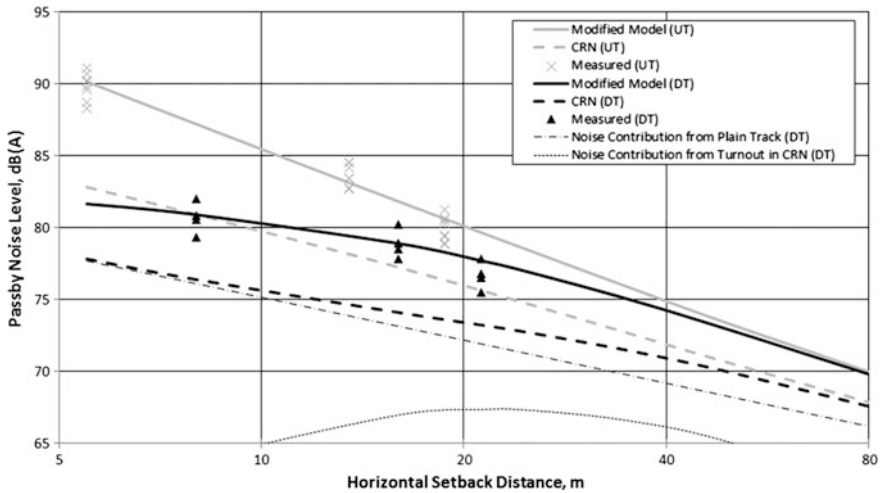


Fig. 8 Comparison between measured and predicted noise levels

## 6 Conclusions

A modified turnout noise model was established. This modified model follows a similar prediction algorithm as in CRN but adopts point monopole source assumption. The reference sound exposure levels of point switch and crossing frog are determined from trackside measurements. A different set of train speed correction, distance correction, angle of view correction and screening effect by barrier are derived. Field measurements were conducted to validate the model assumption and prediction accuracy. It is found that CRN tends to underestimate the noise contribution from turnout, particularly at close distance or large angle of view, with a discrepancy of 4–7 dB(A). The modified noise turnout can address such discrepancies.

Noise and vibration sensors were also placed at the track to study the relative noise contribution from different components. Noise and vibration spectra suggest rail and sleeper have major contribution to turnout noise in the low frequency regime below 630 Hz. The empirical relationship between noise level and various dependent parameters are investigated. The noise level has higher dependence on train speed which an empirical relation of  $37\log(\text{speed})$  rather than  $20\log(\text{speed})$  in analytical models. However, it shows little dependence on unsprung mass, probably due to the fact that the wheelset is not a rigid body.

## References

1. The Department of Transport: Calculation of Railway Noise. UK (1995)
2. Federal Transport Administration 2006: Transit Noise and Vibration Impact Assessment. Washington
3. Environment Protection Authority State of NSW: Rail Infrastructure Noise Guideline. NSW EPA (2000)
4. Thompson, D.J., Gautier, P.E.: TWINS: A Prediction Model for Wheel-Rail Noise Generation. In: Proceedings of InterNoise (1993)
5. Thompson, D.J.: Railway Noise and Vibration 1st Edition Chapter 10. Elsevier Science, pp. 344–358 (2009)
6. Wu, T.X., Thompson, D.J.: On the Impact Noise Generation due to a Wheel Passing over Rail Joints. Institute of Sound & Vibration Research (2001)

# Railway Noise: A New Paradigm for SNCF Acousticians



F. Poisson, D. Laousse, F. Dubois, B. Faure and E. Bongini

**Abstract** The environmental noise of the railway system is an important weakness for the acceptability of this means of transportation, but it could also be considered as an opportunity for radical innovation. Saying so, we postulate that “noise and sound” could be both, a physical and a societal item. Railway industries, operators and infrastructure managers work to understand the physical mechanisms responsible for noise in order to reduce it. To be compliant with the regulations and preserve the traffic, infrastructure managers and operators spent their money into mitigation measures, mainly at source or on propagation path (noise barriers). Considering the increase of passenger and/or freight traffic, an automatic approach for mitigation measures implementation could no longer be adopted. SNCF has developed since 2010 an expertise in innovative design methodology using the DKCP method (Define-Knowledge-Concept-Project), based on C–K theory of innovative design (Concept–Knowledge) developed at Mines ParisTech, to revisit research topics and roadmaps in a radical way. That method has been applied to deal with challenge to design acoustics futures. Theoretical foundations of this innovative method are briefly presented in the paper. Then, the application of the method to define a new roadmap of research projects in railway noise is described in detail as well as the first implementations of the subsequent projects. The paper focuses on some examples of innovative projects. Now, for SNCF noise and sound experts, the paradigm has changed and the main objective of this paper is to share this new experience with railway colleagues.

---

F. Poisson (✉) · B. Faure · E. Bongini  
SNCF Innovation and Research Department, Physics of the Railway System,  
40 av. des terroirs de France, 75611 Paris cedex 12, France  
e-mail: [franck.poisson@sncf.fr](mailto:franck.poisson@sncf.fr)

D. Laousse  
SNCF Innovation and Research Department, Innovation and Prospective  
Group/Mines ParisTech, Center for Management Science, Paris, France

F. Dubois  
SNCF Innovation and Research Department, User Experience Group, Paris, France

## 1 Introduction

The acceptability of the railway transport is a key issue to develop this mode. Train pass-by, railway stations, depots, marshaling yards are in most of the cases noisy locations. At these places, the soundscape is representative of the railway system and is in mind of everybody. Then, “noise and sound” could be, both, a physical and a societal item where we could work on to design research objects that participate to enlarge, and even regenerate, acoustics projects.

Since a long time ago, railway industries, operators and infrastructure managers work to understand the physical mechanisms responsible for noise in order to reduce it. The rolling noise which is the main noise source at classical speed has been deeply investigated [1]. Nowadays, modeling tools are available and input data like rail roughness and track decay rates can be measured. For the aerodynamic noise [2], analytic approach was the first one. For 10 years, computational fluid dynamics can be used to deal with a complete train set and predict aerodynamic noise. Due to the increase of train performances and passenger and driver comfort, more and more equipment are installed on the train which potentially induces a noise increase. Then, the modeling of the global pass-by noise according to the train operation has been developed, based on the prediction of each noise source. These tools are used by train manufacturers for the design of the next train generation and also by operators to investigate deeply some acoustic hotspots. Using prediction tools, parametric studies have been conducted to develop the appropriated mitigation measures to tackle the noise at source and along the propagation path to the residents.

This approach is the main response to the legal constraints in Europe for many years. On one side, train manufacturers use pass-by noise prediction tools to design new train generations. Noise limits at standstill, during pass-by and in acceleration phase are imposed through Technical Specification for Interoperability [3]. A new rolling stock must be compliant with all the rules of the Technical Specification for Interoperability to be certified to run on European network. On the other side, operators manage the traffic noise limited by national laws with noise barriers along the track and insulated windows for residents.

In this context, innovation focuses onto the development of new mitigation measures to improve acoustic performances of the railway system. These performances are assessed through noise indicators defined to reflect the annoyance of residents. The relevance of these indicators, mainly based onto A weighted sound pressure levels, is often discussed by residents.

Considering the increase of passenger and/or freight traffic, an automatic approach for mitigation measures implementation could no longer be adopted. For some classical lines in France, the main cost of the increase of capacity is the installation of noise mitigation measures, compared to signaling and track upgrades, to be compliant with national rules. This compliance is not a guarantee of acceptance of residents.

In this context, the paradigm of the environmental railway noise needs to be revisited. Particularly, one of our main objects of study which has to constitute the basic guideline of our innovation is the perception of “receptors” i.e. nearby residents and clients, when exposed to the soundscapes whose we—SNCF—are partially or totally responsible. The main objective is to develop a research program which leads to a huge increase of acceptance and a compliance with regulation laws.

SNCF has developed since several years an expertise in innovative design methodology using the DKCP method (Define-Knowledge-Concept-Project), based on C–K theory of innovative design (Concept–Knowledge), to revisit research topics and roadmaps in a radical way. That method has been applied to deal with challenge to design acoustics futures. The new concepts are translated into a roadmap gathering research projects.

Theoretical foundations of this innovative method will be briefly presented in Sect. 1. Then, the application of the method to define a new roadmap of research projects in railway noise will be described in detail as well as the first implementations of the subsequent projects. The paper will focus also on some examples of innovative projects.

Now, for SNCF noise and sound experts, the paradigm has changed to open on more applied and conceptual research and the main objective of this paper is to share this new experience with railway colleagues.

## 2 Prospective and Innovative Design Methodology

SNCF has developed since 2010 an expertise in innovative design methodology using the DKCP method, to revisit research topics and roadmaps in a radical way. In a word, C–K theory of innovative design was tailored by Theory and Method of Innovative Design Chair at Mines ParisTech [4, 5], first to understand scientifically design reasoning, then to create radical innovation workshop guidelines. Main idea was that radical innovation roots are not in K- production (academic work) but more on C-exploration (Concept). In another word, new concept elaboration delivers research questions to be deepened by R&D.

After 6 years of practice (2010–2016), 57 workshops have been managed by Innovation and Prospective team all-around SNCF on engineering and services topics. For example, on rolling stock maintenance, electrical feeding by direct current or unmanned vehicles (Drones), Mass Transit railway operations, ...

All these DKCP workshops have been named LABs and MiniLAB, depending on the size and topic to investigate. A LAB concerns a complete firm function like railway operations (Mass Transit), energy or infrastructure/rolling stock global maintenance so about 80 experts are mobilized for a year workshop sponsored by executive committee member. For MiniLABs, topic is more specific—signaling, unmanned vehicles...—with 30 experts on design duty and sponsored by technical domain top manager.

LAB and MiniLAB are managed as structured and collaborative process in the unknown. Here, LAB members have to accept that it's important to keep the unknown alive for the longest time possible, to go out of dominant design or acoustics mainstream. For acoustician experts, the MiniLAB was focused on inventing new, and unknown for the moment, futures for acoustics. MiniLAB was entitled "Ambient soundscape" and not "new questions for acousticians" to engage contributors in something different than acoustics mainstream.

Being more prospective to explore new question defined on-the-way could be scary for some but, in our view, it's the only way to be innovative. After 57 LAB and MiniLAB, we have learned that innovative design workshops are twofold linking closely social dimension (LAB is a community of actors) and cognitive dimension (LAB is a deep conceptual exploration) [4].

Once the challenge accepted, MiniLAB was organized to manage contributors as co-designers of acoustics futures objects and competencies. Saying so, we postulate that radical innovation is a matter of changing objects and their identity (Ambient soundscape is quite different from classic railway acoustics field) and consequently expertise needed (questions could be different, mixing different previous topics).

### **3 Minilab in Acoustics**

#### ***3.1 Participants***

As presented in paragraph 2, a group of people must be defined to participate to the MiniLab. All SNCF acousticians, from infrastructure and rolling stock departments, dealing with environmental noise or acoustic comfort, have been invited. Acousticians from SNCF group (SYSTRA and AREP) have been including too. Some others people have been invited for their global expertise in sustainable development and comfort. Experts in other domains have be also included to enlarge the "K"nowledge. Even if the target is a roadmap of research projects, the group is not restricted to researchers. Engineers, measurement engineers but also marketing profiles can be included.

#### ***3.2 "D"efine Phase: Defining Framework***

The objective of the MiniLab must be clearly defined and shared with all the participants to let them accepting to "design in the unknown", out of their formal expertise. In a more classical application of the DKCP methodology, an initial concept called "C0" is defined. It is a sentence which defined the target and which is neither true nor false. For example, "a flying boat" can be considered as the "C0" of the hydropter project. In our case, the objective is not to define a new object. The

output of the MiniLab will be a roadmap of research projects in acoustics. Some disruptive innovations will be included in the roadmap but it is not the only one perspective. The work carried out will be the opportunity to share a common research program in acoustics between all the stakeholders. Then, the objective was defined as the following: define the roadmap of research projects in acoustics (environmental noise and acoustic comfort) for the next 10 years.

### 3.3 “K”knowledge Phase: Opening on State of the Non-art

The input of knowledge was organized during 4 full days. It was specific knowledge called “state of the non-art” to open on new visions and not only on “state of the art” which is closely linked to dominant design we wanted to escape.

Thirteen presentations from academics or private companies have been organized. Speakers make a presentation during 45 min. Then, participants are split into 2 groups. They point out “key points” and “weak signals” and prepare 3 questions. All participants met again and each group representative asks the two questions to the speaker. The third question is used if one of the two first has been already asked by the previous group. This organization leads to a common understanding of the presentation and deeper questions. The 4 days are spread over 4 months, then a member of the organizing committee make a short summary of the previous “K” days.

In acoustics, topics introduced during the “K” phase are presented in Table 1.

**Table 1** List of topics presented during the “K3” phase

Topics	Type	University/company
Soundscape management	Academic	CRESSON
Sound perception and sound design	Academic	IRCAM
Acoustic drivers and innovation in HS2	Private company	ARUP
Mediation about environmental noise	Association	CIDB
Environmental psychology	Academic	Psy ECCA
To learn from acoustics of the biosphere	Academic	Fondation Cousteau
Managing transportation noise in the urban soundscape	Academic	University Lisboa
Health impact of transportation noise	Academic	IFSTTAR
New-sub systems for sound absorption	Academic	LAUM
Nonlinear damping system	Academic	LMA
Acoustic comfort in railway stations	Private company	Active audio
Mobility and life quality in urban area	Academic	IRCAM
Ethnology and noise	Academic	Museum d’Histoire Naturelle



Speakers are invited to participate to the full “K” day. All of them have appreciated the discussion with participants and also with others speakers. For each presentation, a summary sheet is realized to capitalize the knowledge and share it with missing participants.

### 3.4 “C”oncept Phase

The “C”oncept phase is organized during one or two days with all the K-phasis participants. The main objective is to elaborate disruptive concepts based on initial (K-phasis inputs) knowledge and additional one from each participant mediated by conceptual work. Concept-phasis could be considered as design method core heart as it opens on new topics on a guided and structured way. DKCP innovative design method takes into account main weakness of more classical creativity method (brainstorming, design thinking) which postulate that innovation is only a matter of having “good” ideas and to implement them. On the contrary, for innovative design scholars, innovation is more about formal design reasoning than choosing between predefined trends (design thinking) or associating words and images (brainstorming).

Animation method was based on “conceptual projectors”, some kind of provocative vision to force participants to go outside their expertise comfort zone and to propose new and fresh ideas. These provocative visions are decided by project-team integrating K-phasis results (ideas with a conceptual potential) and new inputs to guide participants design reasoning on specific topics. Research on design methods has shown that better results could be reached by guiding and structuring way of thinking [5]. In that, conceptualization workshop is a major input to elaborate a first conceptual tree on stage, during C-phasis, by making primary “conceptual partitions” [5].

Concepts are organized in a tree to give a global picture of dominant design (left branch) and potential disruptions (all branches starting from dominant design).

A tree is not right or false as it gives a conceptual potential vision knowing that there are several possibilities to organize disruptive branches and concepts associated. Two examples are given on Figs. 1 and 2.

Figure 1, the tree was elaborated by project team based on ideas proposed during conceptual workshop, but extended by over-conceptualization afterwards. The C-tree has to be considered as an editing work dedicated to make logical conceptual partitions by differentiation between two ways of acting on a specific topic: existing way and alternative way which is supposed to be innovative [5]. Again, project-team conceptual editing work goes far from classic synthesis dedicated to format rough data from C-seminar. But, even if it’s an assumed conceptual editing posture, project-team goes back to participants in a special session to obtain consensus on conceptual proposals. In other words, guiding and structuring design

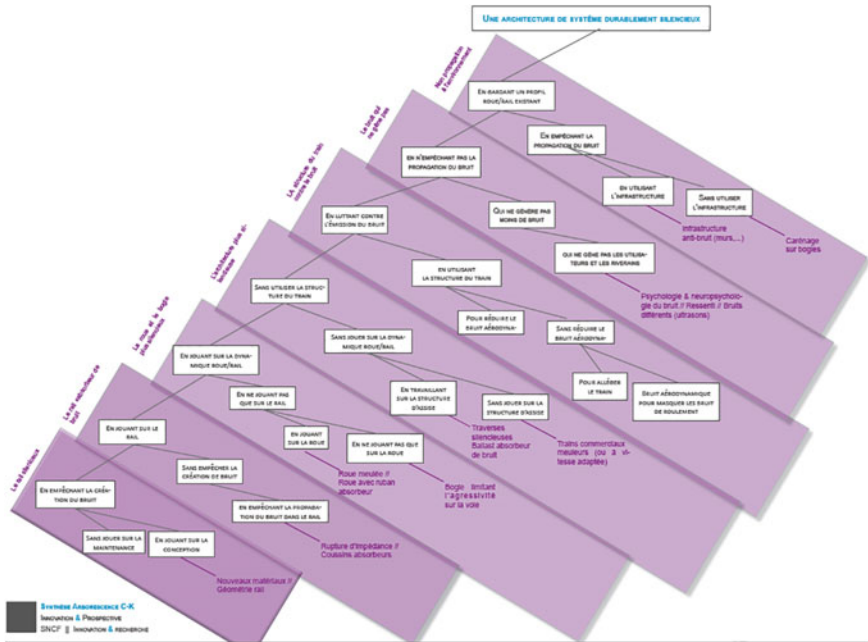


Fig. 1 Examples of concepts tree

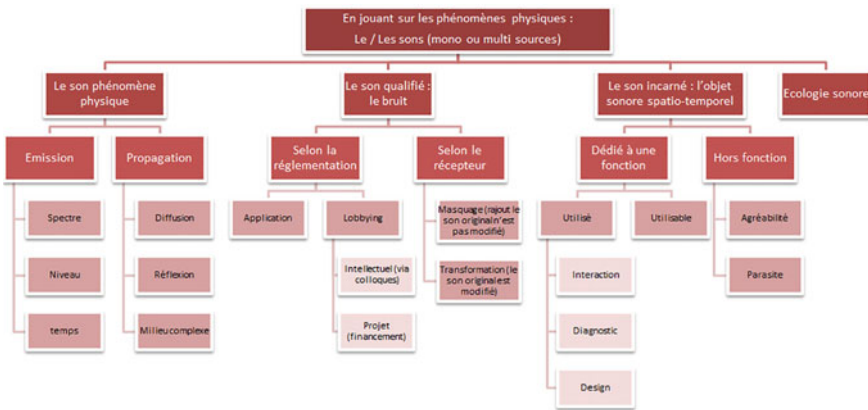


Fig. 2 Examples of concepts tree

group reasoning and giving editing value to conceptual tree means that project team endorse a creativity authority role [5] but under design group control, so C-tree is a collective expression despite tree building is an expert work to switch from heuristic mind-mapping to real conceptual tree.

Back to Fig. 2, we'll see now how to read a C-tree organized in a three dimension scale:

- Left branch is dominant design or acoustics as usual;
- From the left to the right, each branch grasp a specific concept from less to most disruptive concept,
- From top to bottom of each branch, each concept is more and more detailed until it's possible to transform it in a project.

This type of presentation is traditional for all innovative design workshops based on CK Theory to formalize results, so was Soundscape MiniLab (acoustics) management.

### 3.5 *“P”roposals/“P”rojects Phase: Exploration Strategy Elaboration*

The Proposals/Projects phase aims at defining projects based on established concepts of the previous phase. Distinction has to be made between Proposals (early concept) and Projects (implementable concepts). In a CK tree, all outputs are kept alive even if implementation isn't possible according to CK spirit to give a global view of topic under investigation. Otherwise, proposals would have disappeared as firms see them as “moonshots” or too fundamental research.

Proposals projects take place at the bottom of the concept tree of Fig. 2. The most disruptive projects are located on the right. Here, project team has to complete CK tree by defining an exploration strategy which is cornerstone of future research roadmap. Exploration strategy elaboration means identifying relevant knowledge to make a project to formalize “Knowledge part” of CK Tree. Among relevant knowledge for projects, missing knowledge (things we don't know for the moment) has to be highlighted as it's the main driver for research projects.

Even with a large incertitude on each project, their characteristics must be defined:

- Start: short/mid/long term
- Duration
- Cost estimation: person/month, investment...
- Partnership: academics, private companies...
- ...

A SWOT analysis can be added on each project datasheet. Each branch of the tree is not converted in project. Some projects cover a larger part of the tree and put together several concepts.

Examples of project are presented in the next paragraphs. The projects are completely different and show the diversity of the results provided by the method.

## 4 Examples of Projects

One of the outputs of the method, is a Ph.D. thesis launched with the French laboratory CSTB (Centre Scientifique et Technique du Bâtiment). In times of progressive urbanization, a growing section of the human population is exposed to noise pollution. Noise measurement and classical indicators are not able to describe the soundscape. The possibility to listen to an acoustic simulation is a powerful tool of prevention. It becomes a different way to communicate with residents, without noise maps or acoustic indicators. The main objective of the Ph.D. is to include the railway noise source in existing noise simulation tools of CSTB.

Another example concerns the acoustic comfort of train passengers. Noise could be seen as a tool for quality and reliability. Identifying squeak and rattle noises could be a maintenance tool. Based on acoustic measurement in running conditions and signal processing, the noisy locations could be identified to guide the maintenance inside coaches.

DKCP method has been also applied to a major modernization program for display and public announcement systems in stations.

The complete list of research projects cannot be discussed for confidentiality reasons. Only two other projects are detailed in the following paragraphs. The first one is related to a new concept of noise barrier that can be easily defined, build and tested. The second one is a concept that can influence the development of railway stations and must be promoted to the architects.

### 4.1 Discrete Noise Barrier

During the presentation of the “Laboratoire d’Acoustique de l’Université du Maine” (LAUM), Vincent Tournat has presented some examples of meta-material with specific acoustics characteristics. Based on the principle of locally resonant sonic materials [6], an appropriate arrangement of periodic elements is able to provide an attenuation in a given frequency band. Some examples presented Fig. 3 show noise barriers made with bamboo or rigid square-rod scatters.

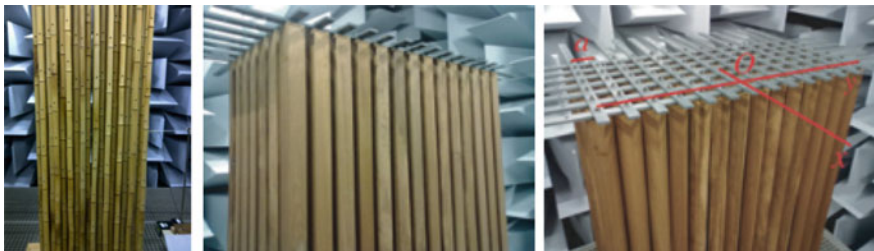


Fig. 3 Examples of meta materials (left: [7], center and right: [8])

Performances of damping materials used in the noise barriers can also be improved by adding some rigid inclusions in porous materials. The combination of rigid inclusions with a periodic structure leads to another increase of performances [8]. Small Helmholtz resonators can be also directly included in the porous material [9]. These new materials made of periodic structures can facilitate the integration of noise barriers in urban area. They must be deeply investigated with academics to fit their performances to the railway noise characteristics. As the band gap is not as large as classical noise barrier, listening tests can be used to define the appropriate band gap.

## 4.2 *Smart Railway Station*

«Smart railway station» is a concept which has been defined during the «C» phase, based on several presentations of the “K” phase. Railway stations are often noisy locations. Noise sources are numerous: train pass-by, standstill trains, public address system.... Railway stations become multimodal places including buses, cars, bicycles and commercial gallery with more and more services proposed to the citizens. This high concentration of activities leads also to an increase of the environmental noise.

An alternative concept consists in spreading the railway station over a large area. The main building disappears for smaller ones located at the extremity of each platform. The “smart railway station” is perfectly integrated into the environment (green roofs, rainwater harvesting, absence of noise) and with the territory (shared services, attractiveness of the region). Services are installed in shops along the street. Parked trains are located outside the station. The main objective is to avoid the concentration of noise sources, especially in urban area. Inside the station, the idea is to clearly differentiate spaces from interior ambiances, with asymmetric and adapted acoustic treatment, to help visually impaired people, to prevent information overload and improve flow management.

To promote this concept, a classical research project is not suitable. Another approach has been imagined. A competition of young researchers in urban design and environmental noise can be organized to illustrate this concept. Based on uses of people and environmental noise reduction, concepts defined by the teams of students can be illustrated with scale models. The concepts can be also evaluated by a jury of people in charge of railway station design to guarantee the appropriation by our colleagues.

## 5 Conclusion

In a context where the main role for acousticians was to respond to the constraints of the law, SNCF has decided to renew its roadmap of research projects in acoustics. A prospective design method called DKCP has been used to define a new

roadmap of research projects. The group of SNCF acousticians has met periodically during 6 months to run the method step by step. A large field of knowledge has been discovered and shared in the group of experts during the “K”knowledge phase. Then, new concepts have been elaborate together. A tree of the new concepts has been used as an intermediate phase to define the new roadmap of research projects.

This method is the opportunity to build a community of experts with a common basis of knowledge. The group defines a common roadmap and supports it for the following years.

For an acoustical point of view, the topics of interest have enlarged. Technical definition and validation of mitigation measures are not the only ones targets. The resident is becoming the main interest, the main target. Then, new competences are needed to carry out the corresponding projects. It can be provided by the integration of new collaborators inside SNCF combined with the appropriated partnerships.

Then, a new paradigm has been defined and shared by SNCF acousticians to deal with environmental noise. The use of a scientific approach was the guaranty to reach innovative concepts including disruptions.

## References

1. Thompson, D.J.: *Railway Noise and Vibration: Mechanisms, Modelling and means of control*. Elsevier Ltd, Amsterdam (2009)
2. Poisson F.: *Railway Noise Generated by High-Speed Trains*. International Workshop of Railway Noise (2013)
3. *High-speed Rolling stock Technical Specification for Interoperability*, 21th of February 2008
4. Hatchuel, A., Le Masson, P., Weil, B.: *Design Theory and Collective Creativity: A Theoretical Framework to Evaluate KCP Process*. International Conference on Engineering Design, Stanford, USA (2009)
5. Hatchuel, A., Le Masson, P., Weil, B., Agogu , M., Kazak i, A., Hooge, S.: *Multiple Forms of Applications and Impacts of a Design Theory—Ten Years of Industrial Applications of C–K Theory* (2013)
6. Liu, Zhengyou, Zhang, Xixiang, Mao, Yiwei, Zhu, Y.Y., Yang, Zhiyu, Chan, C.T., Sheng, Ping: *Locally resonant sonic materials*. *Science* **8**, 1734–1736 (2000)
7. Lagarrigue, C., Groby, J.P., Tournat, V.: *Sustainable sonic crystal made of resonating bamboo rods*. *J. Acoust. Soc. Am.* **133**(1), 247–254
8. Romero-Garcia, V., Lagarrigue, C., Groby, J.P., Richoux, O., Tournat, V.: *Tunable acoustic waveguides in periodic arrays made of rigid square-rod scatterers: theory and experimental realization*. *J. Phys. D Appl. Phys.* **46**, 305108 (2013)
9. Lagarrigue, C., Umnova, O., Groby, J.-P., Tournat, V., Dazel, O.: *Absorption of sound by porous layers with embedded periodic arrays of resonant inclusions*. *J. Acoust. Soc. Am.* **134** (6), 4670–4680 (2013)

# Ageing Cuts Down the Track Homogeneity Causing Differences Between Calculations and Measurements of Railway Noise



H. Venghaus

**Abstract** At tracks with high accumulated axle loads per year the ageing effects of the rail pads will change track parameters causing different noise radiation than calculated by general data sets. This observation initiated the R&D-project Factor X, funded by Schweizerischen Bundesbahnen (SBB). The changes due to ageing effects act in different ways on the overall system. First effect of the axle loads acting on the rail pads will lead to a loss in pad thickness over time with the consequence of a decreased clamp forces at the rail foot. This reduced clamping force allows a higher grade of rail movement presented as increased local mobility of the rail head, leading to increased noise radiation. The second observed ageing effect was the loss of stiffness of the rail pads under the impact of accumulated axle loads. This effect leads to a decoupling of the rail from the sleeper, again leading to increased noise radiation. With an increased accumulated axle load the spread of the ageing effect of the rail pads becomes more stochastic. A consistent prediction method about the changes of parameters is impossible to be given. A well-proven method of enhancing the basic data set for calculation is achieved by measuring and calculating the TDR of the track under investigation. As the calculation method of the TDR data mainly depends on the local mobility of the rail at the starting position of a measurement grid, the uncertainty of the calculated TDR also depends on variations from sleeper bay to sleeper bay due to the wear state of the rail pads. This uncertainty of calculated TDR data can be reduced efficiently by increasing the number of measurement grids along a track section, allowing an analysis of the deviation over several measurements. Due to the duration of one measurement grid containing 29 positions, a new measurement method with a reduced number of positions in a grid is presented. By a choice of appropriate positions the loss in precision of calculating TDR is almost negligible.

---

H. Venghaus (✉)  
ACCON GmbH, 86926 Greifenberg, Germany  
e-mail: [helmut.venghaus@accon.de](mailto:helmut.venghaus@accon.de)

## 1 Introduction

A R&D-project “Factor X” funded by Schweizerischen Bundesbahnen (SBB) finalised in 2015 [1], was set up to investigate the deviation of calculated noise radiation at railway tracks from measured data at local track sections. For this purpose, measurements at several different railway lines across Switzerland were carried out. At every location, some of the rail pads were taken as samples for an additional laboratory analysis. The subject area of the R&D-project had its topics in:

- analysis of vibration of rail and sleeper with/without rail damper
- analysis of vertical local mobility of rail
- analysis of vertical and horizontal TDR

including ageing aspects of worn track parameters.

For a qualified determination of TDR in EN15461 [2], a homogeneous track section is required. Therefore the local mobility of the rail head should be tested at a minimum of 3 positions across the test section. At least 2 of these positions the frequency-response curves should be similar to obtain a qualified series of measurements for the generation of TDR values.

In EN 15461, specifications are missing about the distances between these test locations and the amount of deviation between the frequency response curves that is allowable for the track to be accepted as “homogeneous”.

The following chapters may give an overview on the influence of aged rail pads on radiated noise, including the variation of vertical mobility of rails, causing an uncertainty in the determination of track decay rates (TDR).

To overcome the peculiarities mentioned above, a new method for determining the TDR by a reduced number of measurement positions is presented, allowing a higher number of measurements along a track section to calculate a more precise TDR and allowing a calculation of uncertainty for the track section under investigation.

## 2 Deviation of the Vertical Local Mobility of a Rail

In Fig. 1 a 3-dimensional diagram is presented, showing the vertical local mobilities of a rail head being in duty for more than 20 years. The annual axles load passing this track section is about  $44.2 \times 10^6$  tons/a. The travelling speed of the trains is from 80 km/h (mainly freight trains) up to 120 km/h (mainly passenger trains).

The measurement positions at rail head were all taken above sleepers, 19 sleepers in a row, with center position at  $MP00 = 0$  m.

The main differences of the vertical mobilities are observed in the frequency range below 1 kHz correlating to the pinned-pinned frequency of a UIC 60 rail and 0.6 m spacing. Those deviations in the upper frequency range are assumed to be caused by errors during measurements.



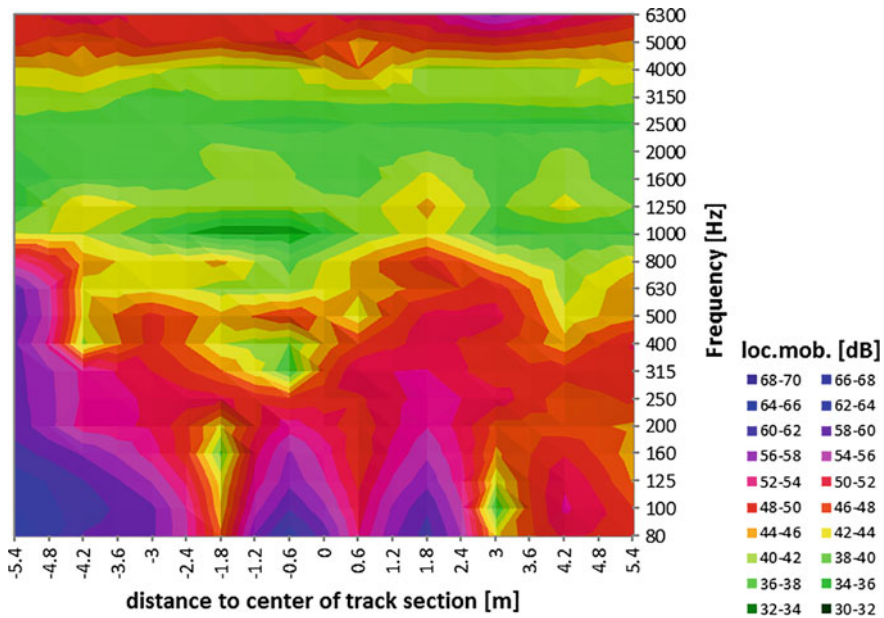


**Fig. 1** Vertical local mobilities of a rail head measured at 19 positions—all above sleepers

After the first measurement campaign the clamps at the rail foot were untightened and afterwards fixed again by a fixed torque of 180 Nm, still leaving the worn rail pads at their positions. In Fig. 2 the diagram of the local mobilities after maintenance work is presented.

Comparing both diagrams there are 2 important results to be mentioned

- A re-fixation of the clamps at rail foot by a constant torque of 180 Nm reduces the vertical local mobilities at the rail head up to 10 dB (frequency dependent)
- The deviation of the local mobilities is reduced from  $\pm 8$  dB (before) down to  $\pm 3$  dB after re-fixation of the clamps at the rail foot.

These results will lead to the assumption that clamps at the rail foot and rail pads changes their properties over years, if no basic maintenance work is carried out but with the opportunity of being restored to initial conditions.

## 2.1 Loss of Pad Thickness

The axle loads are acting on rail, rail pad and sleeper like heavy roller mill. The weakest part in this assembly is the rail pad, absorbing most of the energy impact induced by the rolling wheels. Due to these acting forces the rail pad will loose of its thickness over the years. In Fig. 3 the remaining thickness of 27 worn rail pads taken from different tracks in Switzerland versus the estimated summed axle load is

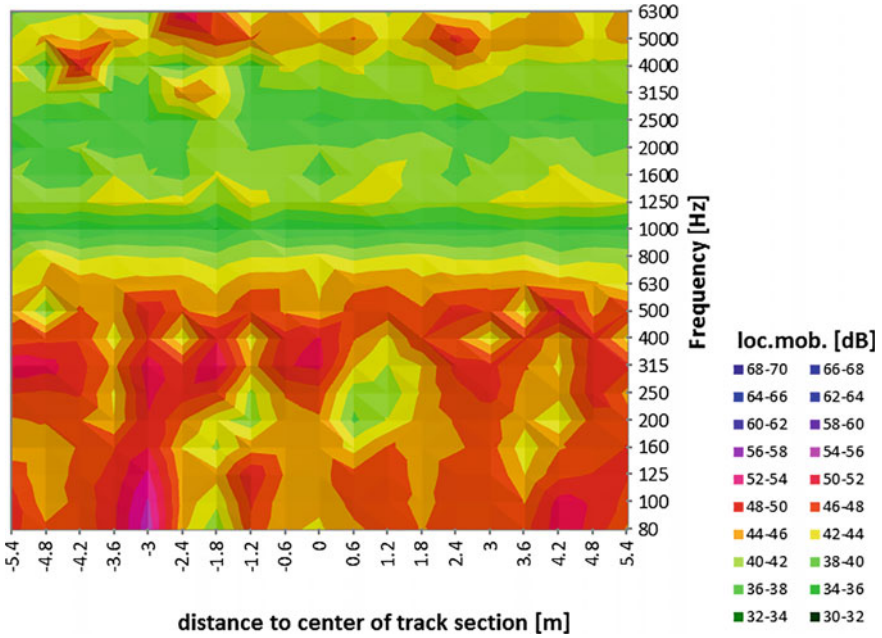
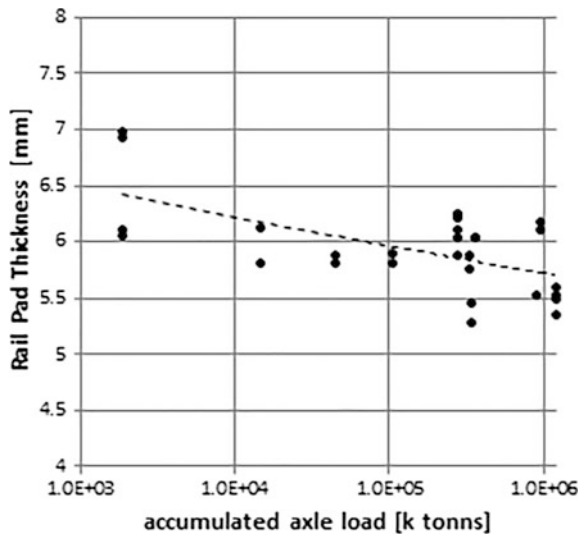


**Fig. 2** Vertical local mobilities of a rail head measured at 19 positions—after re-fixation at 180 Nm

**Fig. 3** Remaining thickness of 27 rail pads versus summed axle load



presented. All rail pads are of the same type Zw 661a and the original thickness is  $d = 6.5 \text{ mm} \pm 0.2 \text{ mm}$ .

As another result from Fig. 3 can be drawn that with increasing summed axle load the deviation of remaining pad thickness is increasing. This result will give an answer to the great deviation in local mobilities present in Fig. 1, considering the changes of the acting forces of the clamps on the rail foot.

In Fig. 4 the set up of clamp, screw, sleeper and rail is presented. By tightening the screw the force of the central bending spring is transferred to the toes, keeping the rail foot at its place.

The strength of the clamping force is defined by the distance between the toe (limited downwards by the rail foot) and the central spring (limited by the screw; highlighted by the orange colored arrow in Fig. 4). Assuming that the screw is absolutely fixed and will not move over time, but on the other side the rail pad is getting thinner under the accumulated load of the passing axles, the distance between spring and toes will increase over time, which means a reduced force of the spring. In Fig. 5 the change of the “toe load” (as an alias of “spring force”) is drawn versus thickness of the rail pad, causing a different deflection of the central spring of the clamp at the rail foot.

The results presented in Fig. 5 are only valid for this tested set up, W30-Vossloh clamp, worn Zw 661a rail pad, UIV 60 rail on a B70 concrete monobloc sleeper.

**Fig. 4** Set up of clamp, rail, rail pad and sleeper (*source* Vossloh)



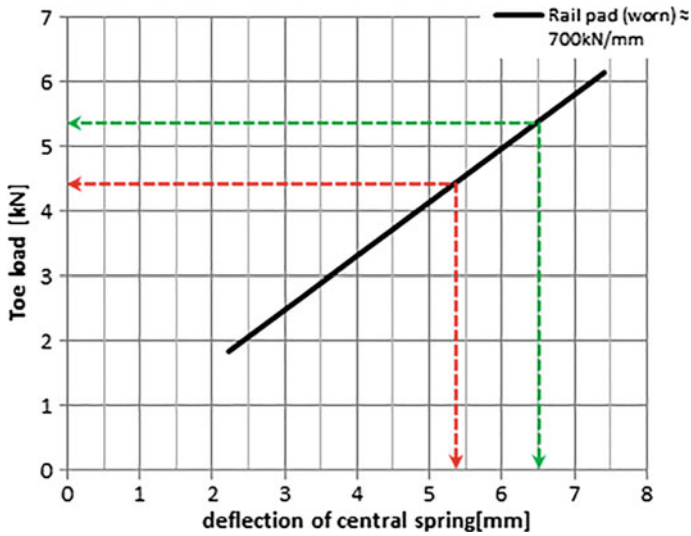


Fig. 5 Change of the toe load versus varying deflection of the central spring

As the contact from rail to sleeper via rail pad is defined by the clamping force in the absence of axle loads, the local mobility and in consequence the determination of TDR is depending on the thickness of the rail pads and the residual clamping force.

## 2.2 Loss of Pad Stiffness

Many factors that affect the fatigue crack nucleation and growth process in rubber were identified in recent years, but many of them remain unknown up to now. Factors that influence the fatigue life of rubber are broadly classified as being related to the mechanical loading history, to environmental conditions, to formulation of the rubber compound, and to certain aspects of the stress-strain constitutive behavior, with the specialty of nearly oppositional reactions of different rubber compounds to the same impact.

During the research of the Faktor X study several rail pads were exchanged by new ones, for testing worn rail pads at a servo hydraulic actuator at the laboratories of Studiengesellschaft fuer unterirdische Verkehrsanlagen (STUVA) in Cologne—Germany. The tests at the STUVA laboratories used a nearly rectangular time signal at a frequency of about 2 Hz to load the pads. This signal was chosen as it was felt to better represent the loading of a train than the conventional sinusoidal signal defined in EN 13146-9 [3]. The frequency approximates to the axle passing frequency of a train travelling at 80 km/h, the loading is representative of axle loads up to 23 t.

The majority of rail pads used in the Swiss railway network are of the type Zw 661a. These ethylene-vinyl-acetate (EVA) pads have a manufacturer's reported static stiffness of around 700 kN/mm.

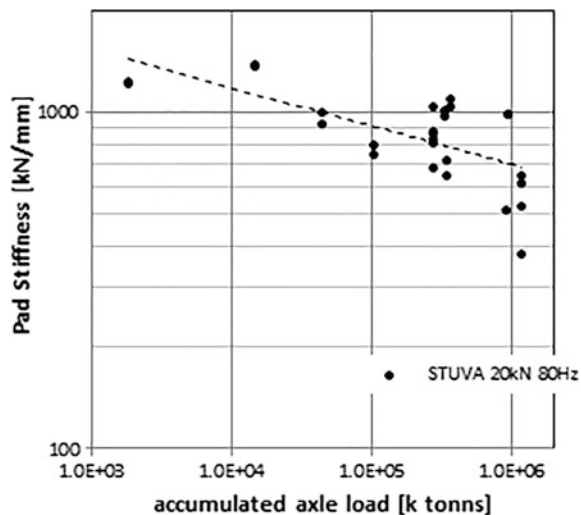
Figure 6 suggests that pad stiffness may decrease with accumulated axle load. This effect could account for the differences in TDR between the nominally similar new and old rail pads at the same location. A similar finding was observed by Kaewunruen and Remennikov [4], who suggested a linear deterioration of the stiffness of about  $-2.18$  kN/mm at an accumulated axle load of 1 MGT whereas the results from the work here suggest at a linear regression analysis a deterioration of about  $-3.06$  kN/mm.

It has to be mentioned that the reduction of pad stiffness in relation to accumulated axle load presented in Fig. 6 is only valid for the tested rail pad of the type Zw 661a made of the rubber compound EVA. It is assumed that due to the effect of heavy roller mills the long molecules are cracked resulting in a reduced stiffness of the pad and in parallel reducing its thickness.

The logical outcome of this observation would stand for a very rapid destabilization of the molecular structure of pads made by EVA, as a reduced thickness of rubber pads—not exposed to heavy loads—will gain in an increased stiffness. Hence rail pads made of different rubber compounds may cause different ageing characteristics.

At a special track section the old worn rail pads Zw 661a—original static stiffness of about 700 kN/mm—were replaced by new rail pads with an original static stiffness of about 200 kN/mm. In vertical direction nearly no differences of the TDR taken from both systems was observed. In lateral direction there was a slight difference to be observed which assumed to be generated by the change of the torque of the screws from an unsystematic to a systematic clamping force.

**Fig. 6** Decay of the rail pad stiffness versus summed axle load measured at STUVA test rig



### 3 Deviation of the TDR

The deterioration of the thickness of worn rail pads and the deterioration of the stiffness of worn EVA rail pads are the main reason for an increased decoupling effect of the rail observable by TDR data tending towards lower values [5]. Both changes of rail pad parameters—thickness and stiffness—are getting more stochastic at high accumulated axle loads. It is assumed that this stochastic effect is leading to dissimilar local mobilities of the rail head. At an UIC60 rail at 0.6 m spacing these deviations is observed mainly in the frequency range below 1 kHz in vertical direction.

As the local mobility at the starting position of the grid will mainly affect the TDR, changes of the local mobility will lead to remarkable deviations of calculated TDR when the starting position is moved by a short distance. In Fig. 7 the data of vertical and horizontal TDR is presented developed at a very old track. The different TDR are values are taken at different sections of the track at a distance of about 20 m.

Although at both sections there is nearly the same trend over frequency the deviation of the TDR is significant. It is assumed that these deviations are caused by worn rail pads, as this track was mainly used by heavy freight trains.

Developing TDR by carrying out measurements at a higher number of grids at a certain track section would open the possibility to calculate the variance of TDR, representing a higher reliability of the calculated data.

The disadvantage of this measure is the strongly increasing time consumption, as each duration of measuring a grid at 29 positions (recommendation by ISO 15461) will take more than 30 min (without disturbances by passing trains). During the

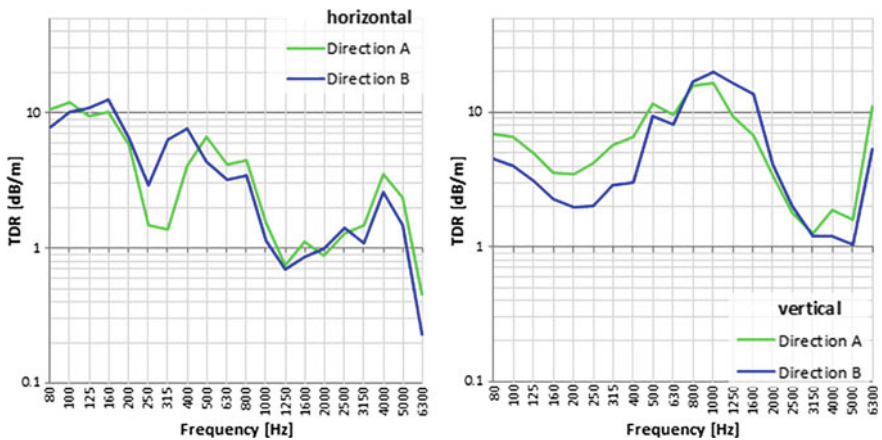


Fig. 7 Vertical and horizontal TDR at different sections of a very old track

DEUFRAKO R&D-project STARDAMP M. G. T. Toward [5, 6] suggested a reduction of the grid down to 13 positions. The evaluation of this suggestion was done by a strategic analysis procedure of 10 different measurement grids at different track sites, pointing out that an appropriate reduction of position within a grid, new TDR data can be generated with low deviation relative to the original TDR. In Fig. 8 some examples of reduced number of grid positions are shown on the left side of the graphic (logarithmic scale of distances), on the right side of the graphic the responding deviation (full frequency range) is presented.

Suggesting that the main part of the radiated noise of track, sleepers and rails is radiated in the frequency below 2 kHz the frequency dependent deviation of TDR data gained by the reduced number of measurement positions compared to the original grid will occur in the frequency range from 200 Hz up to 1.6 kHz. In Fig. 9 the deviation  $\Delta TDR(f)$  normalized to the original  $TDR_{orig}(f)$  calculated by the data gathered at 10 different track sections at different sites. It can be taken from Fig. 9 that a reduction of appropriate measurement positions down to 11 will keep the deviation at a very low stage. The increased deviations at 2.5 and 4 kHz with opposite sign are not explainable yet.

The choice of the reduction of appropriate positions is not finalized yet, the presentation in this paper reflects the studies done up to now.

The aim of this idea is to demonstrate a new way of carrying out the measurements for TDR calculations at reduced duration without losing precision in a considerable manner. On the other hand the reduction of measurement position accelerates the progress in one layout of a measurement grid, allowing the execution of additional measurements. Comparing the estimated deviation by a reduced number of measurement positions in a grid to the real existing deviations at track at nearby sections, it is quite obvious that it is of a big advantage to have a higher number of measurement grids.

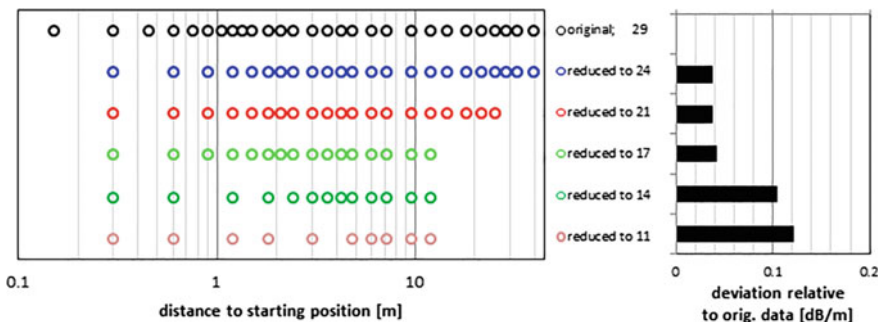


Fig. 8 Reduction of positions in grid and resulting deviation from original TDR

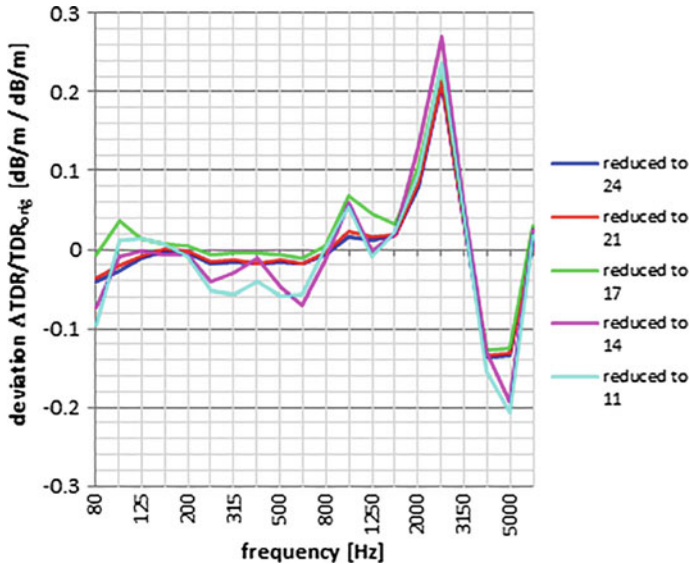


Fig. 9 Decay of the rail pad stiffness versus summed axle load measured at STUVA test rig

## 4 Conclusions

Results from the R&D-project Factor X, funded by the SBB, pointed out that the thickness of worn rail pads is decreasing under the impact of an increasing accumulated axle load. This effect will reduce the toe load of the clamps at the rail foot in direct relation.

The second result is the observed decrease of stiffness of worn EVA rail pads Zw 661a under the impact of an increasing accumulated axle load.

Hence both observed changes of the rail pad parameters will reduce the coupling forces of the rail to sleeper and track, generating lower TDR data values, hand in hand with an increased noise radiation. The measured noise levels are higher than calculated noise based on general data.

These results are assumed to be the main part of reasons of differences between measured noise data at tracks versus calculated data.

To come closer to reality very often TDR data measured at track are taken to improve the calculation basis. At old track sections with worn rail pads the local mobility of the rail head will change importantly within short distances along track. As the calculation method of the TDR given by ISO 15461 is relying on the initial measurement position of the grid, the calculated TDR may vary significantly by a minor shift of the measurement grid along track.

Hence a method is recommended which is based on a reduced number of measurement positions completed by additional measurement grids shifted along track. The duration of measuring each grid is reduced, but by the higher number of



TDR data allows an analysis of the deviation. As the measurement grid of a reduced number of positions may lead to some loss in precision, the win in precision by an increased number of TDR data is much more important.

Due to the experiences won during Factor X study it is recommended to switch to the new method presented in this report, especially in the case of old tracks.

## References

1. Venghaus, H.: Erprobung Schienendämpfer—Bestimmung Faktor X—Stardamp Tool Welche Faktoren aus dem Trassenaufbau beeinflussen die Wirkung von Schienendämpfern. Eine Studie durchgeführt an den Monitoringstationen der SBB, Bern (2015)
2. EN 15461 Railway Applications—Noise Emission—Characterisation of the Dynamic Properties of Track Sections for Pass by Noise Measurements
3. EN 13146-9 Railway Applications—Track—Test Methods for Fastening Systems—Part 9: Determination of Stiffness; EN 13146-9:2009 + A1:2011
4. Kaewunruen, S., Remennikov, A.M.: Response and Prediction of Dynamic Characteristics of Worn Rail Pads Under Static Preloads. In: 14th congress of sound and vibration ICSV14, 9–12 July. Cairns Australia
5. Thompson, D.J.: Railway Noise and Vibration. Elsevier, Oxford (2009)
6. Toward, M.G.T., Thompson, D.J.: Stardamp Project—Laboratory Test Method for Acoustic Rail Dampers, 2010–2012 funded by the Deufrako

# Track Condition Assessment Using Primary Suspension Data



Y. K. Siow, D. Y. Foo, T. N. Nguyen and W. L. Chia

**Abstract** Primary suspension of trains can be a useful tool, given its generic commonality across metro systems. This paper presents the findings from its use for track condition assessment. It is premised on the understanding that suspension movement represents a filtered reflection of track undulations and geometry changes. The findings tap on measurements from in-service passenger trains, which cover the system on an almost daily basis over a 2-year period. The movement profiles are plotted against track length and presented with trackform and train speed information. A general reference is provided for tangent and curve tracks before detail analyses based on known track maintenance activities were made. An interesting note is that part of track system had undergone re-sleepering during this period. This provides an opportunity for condition assessment on pre- and post re-sleepering activity. Results on a specific track section chart the change and improvement from track tamping activities. These and other observations provide a sense of the utility that can be accorded using suspension data. The motivation is to progressively develop a data-driven measure to reflect track condition, for a build-up of time-slice references from periodic back-end analyses. This could be used to prioritize maintenance activities.

## 1 Introduction

Track undulations exert an influence on the suspension movement of trains under dynamic conditions. Together with suspension stiffness and the bogie set-up, they determine the range of motion of the primary suspension. In this paper, a track condition measure is developed with the use of suspension data from two in-service passenger trains of the same type, that are equipped with the train-borne condition monitoring system for the power rail. The 6-car train configuration of 4 motorised-cars in the middle and a trailer-car on each end, gives a total of

---

Y. K. Siow (✉) · D. Y. Foo · T. N. Nguyen · W. L. Chia  
SMRT Trains Ltd, SMRT Bishan Depot, 300 Bishan Road, Singapore 579828, Singapore  
e-mail: siowyukwee@smrt.com.sg

12 bogies. Sensors are installed on one trailer-car bogie (the second last) per train. An outline of the measurement set-up is provided, followed by a description of the data processing approach. In principle, track influences over a 20 m moving window are aggregated to give a measure for each track chainage increment. The typical influences to the suspension movement like passenger load and vehicle dynamics at transitions between tangent and curve tracks are discussed.

In the results sections, reference track length plots from the four track-forms found on SMRT operated metro lines are first presented. The four track-forms on SMRT network included ballasted timber (BLT\_Timber) and ballasted concrete (BLT\_Concrete) sleepers for viaduct sections, concrete slab track (CST) and floating slab track (FST) for tunnel sections. The layout is oriented towards utility on an operating metro and to ease comparison across track-forms and time. In the results and discussions, a more detailed treatment is provided for a 2 km ballast track section that has undergone major maintenance. The paper is concluded with key observations surfaced by the presented measure before a closing brief on future work.

## 2 Background

Track Condition Index (TCI) or Track Quality Index (TQI) is conventional measure, which is used by railway to assess the quality of track [1–3]. There are mainly 8 types of evaluation methods being adopted throughout the world to assess the track quality of a whole track segment. The 8 types of methods included SD Index, Q Index, P Index, Track Roughness Index, Track Geometry Index, CN's Track Quality Index, SNCF's Mean Deviation Indices and Chinese Track Quality Index [1]. There are also other types of measure that based on accelerometer measurement, which are related to train ride comfort research [4, 5].

Currently in SMRT, the monitoring of track condition relies heavily on Multi-Function Vehicle (MFV) and manual inspection during engineering hours. However, the trend of condition monitoring has been continuously going towards trolley based and train borne system [4]. This inspection method has advantages such as more frequent inspection; increase productivity and more data availability for analysis. These become the motivation of equipping passenger train with sensor in an effort to have better assessment of track condition.

The primary suspension data from in-service trains can be used to assess the condition of the whole track system, under actual loading condition and on a regular basis. Time slice analyses can be performed to determine consistency and highlight relative changes for maintenance intervention. In addition, the individual track-form such as tangent and curve on both viaduct and tunnel sections can be extracted to have a clearer view on the characteristic. As a result, the track maintenance can be prioritized.

### **3 Measurement Set-up**

A condition monitoring system was developed to be equipped onto in-service passenger trains. The primary suspension measurement is actually part of this system, which monitors the vertical position of the power rail. Figure 1 depicts the layout and the mounting location of the displacement sensors used to capture primary suspension movement. The main hardware components are:

#### ***3.1 Displacement Sensors***

Two displacement sensors were mounted on both left and right side of the primary suspensions with customized brackets for collecting the suspension readings. The measurement range of the displacement sensor used is  $\pm 25$  mm with output of 0–5 VDC.

#### ***3.2 Train Tachogenerator***

The train tachogenerator produced 132 pulses per revolution with nominal 0-10 VDC conditioned square pulse output to the on-board field computer to determine the train speed and travel distance.

#### ***3.3 On-board Compact Field Computer***

A programmable compact field computer was installed in the train and used to record and process all the data from the displacement sensors and tachogenerator together with timestamp information. The sampling frequency of the measured data is 200 Hz. The train speed (km/h) and travel distance (m) were computed by the field computer based on the square pulse output from the tachogenerator and the wheel diameter information for location indication. The field computer also captures the location information from the markers at stipulated track locations. This is used with the tacho signal to derive the location information of the train.

The on-board monitoring system was powered by 110 VDC from train's Auxiliary Power Supply (APS). Therefore, the system is capable of continuous measurement, eliminating the need for attended data capture. The monitoring system automatically stores the measured data to a memory card, which can be accessed remotely.

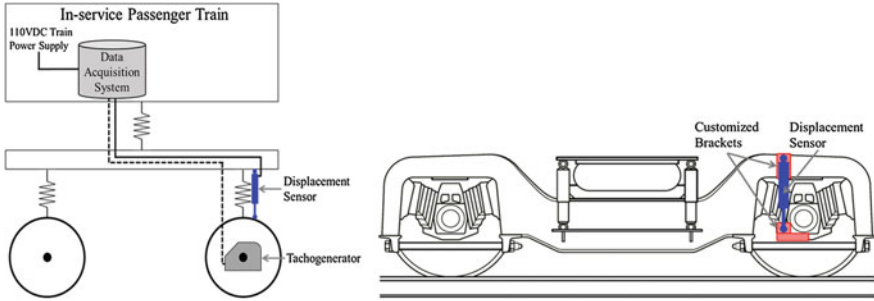


**Fig. 1** On-board monitoring system and mounting location of the displacement sensor

Measurement data from the displacement sensor and tachogenerator shown in Fig. 1 are central to the capture of track undulations and its relationships with key analysis parameters (train speed and track chainage) respectively. To provide a sense of the bogie layout dimensions, in relation to track length window and resolution used for data processing, the above axle-to-axle spacing is about 3 m. The nearest adjacent bogie is in the adjacent train car and both these bogies are within a 10 m zone.

## 4 Data Processing

In the preceding section, the instrumentation for the measurement of suspension movement is outlined. Observations from the collected data confirm the expected coherence between the LHS and RHS measurements. It was also observed that this pair of measurements change and differ when a train negotiates the banking of the track at curve sections, which is part of normal vehicle dynamics. This change is normalized in the computation of the *Track Condition Index under Dynamic condition based on suspension data*. Specifically, the step change in suspension, experienced at stations where passenger load varies, is mitigated by a moving average over a long distance. This is used to offset the localized (20 m window) suspension reading in the calculation, to minimize and work around the step change influence of passenger load. All computation uses only one suspension measurement. The acronym *Dyn\_TCI\_susp (mm<sup>2</sup>)* is coined and referred to in the remaining sections of this paper.

The data capture based on a sampling frequency of 200 Hz was designed to accord the data points with a track resolution of about 0.1 m, at the top operating train speed. The first processing step is to rebase the data from a time dimension to a length dimension and to associate it to the common chainage reference used to describe track locations. The identification of non-steady train speed sections follows to preclude them from further analysis. Note that beyond the computation of *Dyn\_TCI\_susp*, for each short track-length section of 100 m or 200 m, the mean, variance and peak value are calculated to accord an overall measure, for the purpose of comparison. A sample of these values is presented in Table 1.

In the computation of the *Dyn\_TCI\_susp*, the objectives for the track condition (undulation) measure are to characterize the track influences in the immediate vicinity of the sensor-mounted bogie; and to provide a realistic representation of the rate of change of these influences along the track chainage. The impact of a fixed change in suspension movement due to changes in passenger loading is minimized together with that arising from changes due to banking of track at curve sections. This is essentially achieved by high pass filtration of the suspension data, where the “low frequency” content of these impacts is omitted. The “power density” is subsequently calculated for the suspension data, with respect to track length, based on a 20 m moving window. The outcome is a “power density” based on a central moving average, where a data point at a certain track chainage encompasses all the suspension information, 10 m before and after that particular chainage.

## 5 Result

The plots in Figs. 2, 3 and 4 are the *Dyn\_TCI\_susp* for a variety of track sections. Figures 2 and 3 are reference measures for tangent and curve tracks respectively, based on short track-length sections for six different track-forms. The information on the 12 sets of plots are paralleled in Table 1 where the corresponding mean, variance and peak value are presented. It should be noted that the three figures has common track sections that could be identified by the arbitrary track chainage. Subplots (d) and (f) in Figs. 2 and 3 are the same tangent and curve track sections, measured 1.5 years apart. They reflect the track condition at two steady operating states—before and after re-sleepering work, and are snap-shots of the improvement achieved. The same two track sections are part of Fig. 4, which shows 4 time slices across the same 1.5 years. This 2 km track section consists of both tangent and curve tracks, as demarcated by the boundaries for the three zones. It charts the changes in track condition brought about by the re-sleepering work from timber sleepers to concrete sleepers.

<u>Viaduct</u>		<u>Tunnel</u>	
<b>BLT_Timber</b>	: Ballasted Timber Sleeper	<b>CST</b>	: Concrete Slab Track
<b>BLT_Concrete</b>	: Ballasted Concrete Sleeper	<b>FST</b>	: Floating Slab Track

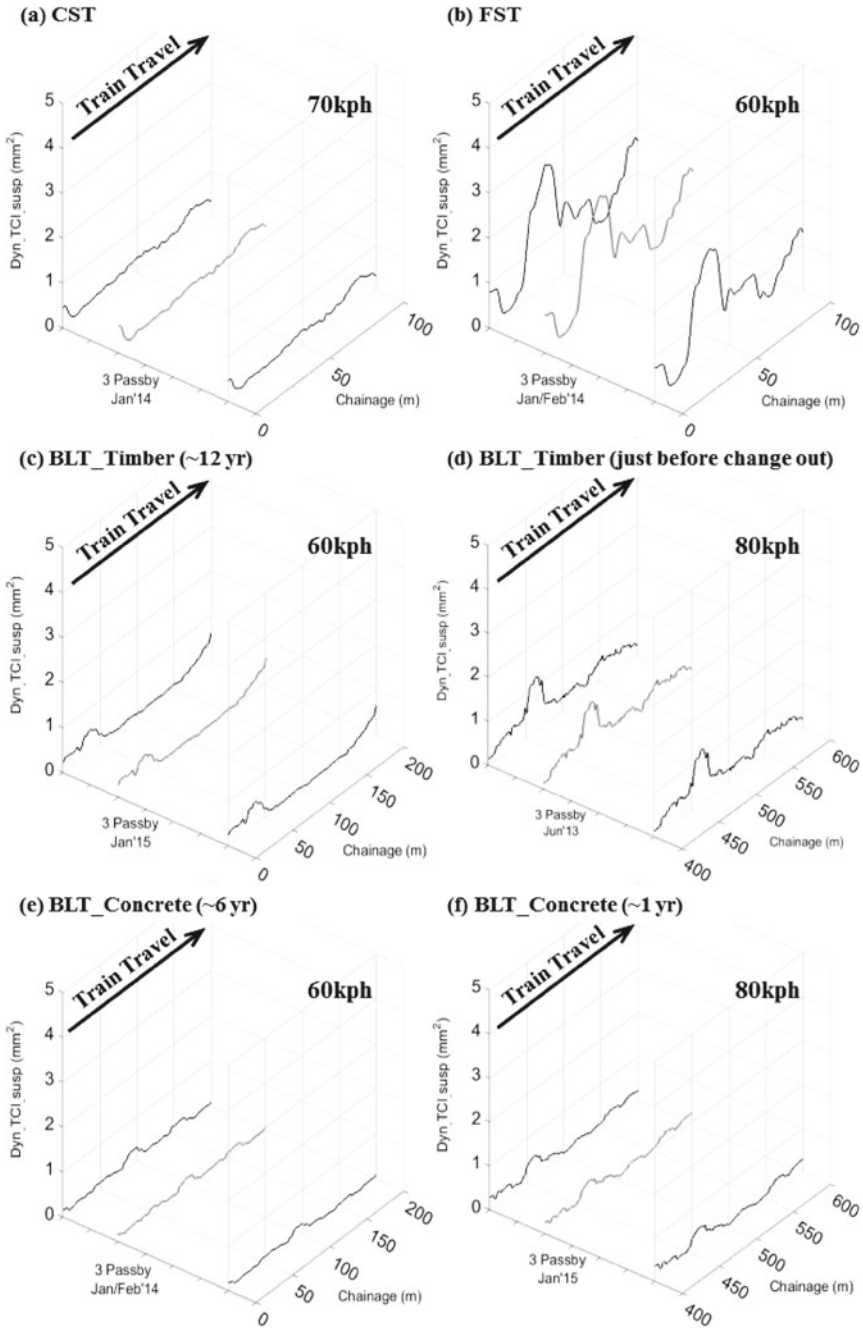


Fig. 2 Dyn\_TCI\_susp—Reference measurement for tangent track

<u>Viaduct</u>		<u>Tunnel</u>	
<b>BLT_Timber</b>	: Ballasted Timber Sleeper	<b>CST</b>	: Concrete Slab Track
<b>BLT_Concrete</b>	: Ballasted Concrete Sleeper	<b>FST</b>	: Floating Slab Track

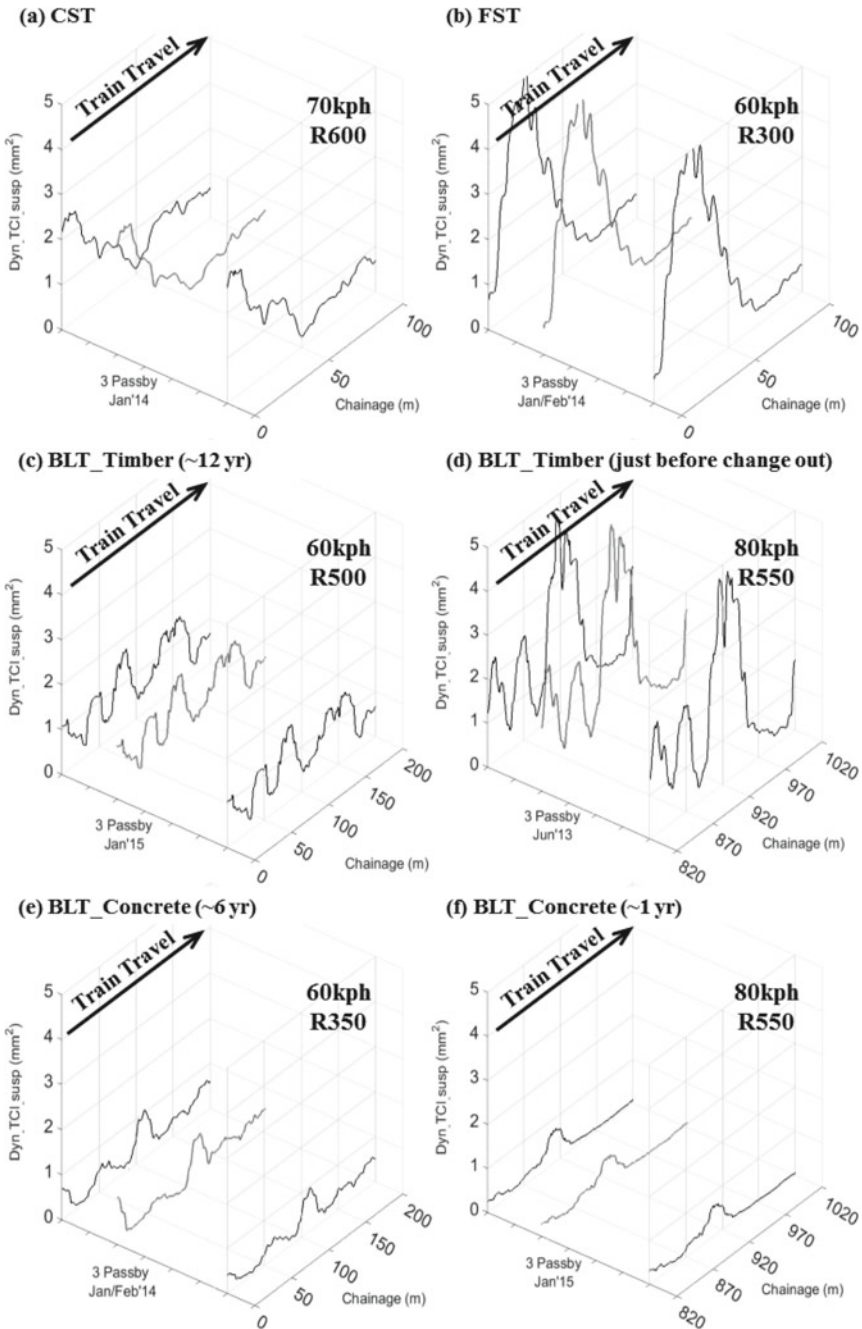
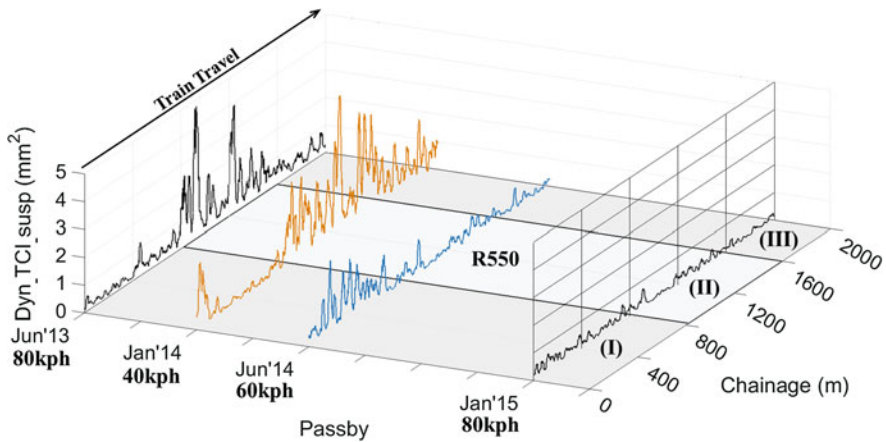


Fig. 3 Dyn\_TCI\_susp—Reference measurement for curve track





**Fig. 4** Ballast track sleepers change out—improvement over 1.5 years

The interest is on steady speeds of >60 km/h, as it represents the normal range of in-service train operating speed. The speeds for the 12 sets of plots in Figs. 2 and 3 are all in this range. In the comparison between tangent and curve tracks, it is clear that the latter registers higher *Dyn\_TCI\_susp* across the board. In Fig. 4, the 2 km track section has a normal operating speed of 80 km/h as reflected by the two steady operating states in the 1st and 4th time-slice. In between these time periods, the implemented speed restrictions (in tandem with track maintenance activities like re-sleeping and tamping) are reflected by the lowered speeds of 40 and 60 km/h. In the 2nd time-slice (Jan 2014), which has a steady train speed of 40 km/h, track tamping activities is known to be in progress in **zones 2** (curve) and **3** (tangent). Note the comparison between the 1st (Jun 2013) and 2nd (Jan 2014) time-slices, at the curve section (**zone 2**); the index in the latter registers prominently higher values despite a lower train passby speed by half. The chronology of observations into the 3rd and 4th time-slices, indicates that improvement for the curve section (**zone 2**) is the greatest, after re-sleeping.

In Table 1, the highest respective values are noted by the bold and larger font size. It is clear the FST has the highest *Dyn\_TCI\_susp* across all track-forms. The less obvious observation is that the index registers a greater level of gradation on curve tracks than tangent tracks, between track-forms.

**Table 1** Statistic of *Dyn\_TCI\_susp* for tangent and curve track

	(a) CST	(b) FST	(c) Ballast timber (~ 12 year)	(d) Ballast timber (just before change out)	(e) Ballast concrete (~ 6 year)	(f) Ballast concrete (~ 1 year)
<i>Tangent track</i>						
Mean, $\mu$ (mm <sup>2</sup> )	0.3	<b>1.1</b>	0.2	0.4	0.1	0.2
Variance, $\sigma^2$ (mm <sup>4</sup> )	<0.1	<b>0.4</b>	<0.1	0.1	$\ll$ 0.1	<0.1
Peak (mm <sup>2</sup> )	0.6	<b>2.5</b>	0.6	1.2	0.3	0.5
<i>Curve track</i>						
Mean, $\mu$ (mm <sup>2</sup> )	1.1	<b>2</b>	0.9	1.7	0.3	0.2
Variance, $\sigma^2$ (mm <sup>4</sup> )	0.5	<b>2.9</b>	0.1	1.8	<0.1	<0.1
Peak (mm <sup>2</sup> )	2.9	<b>5.7</b>	1.7	4.8	1.0	0.7

## 6 Discussion

The presented data acquisition set-up is neither as detailed as a conventional track geometry measurement nor as complex as an accelerometer based data acquisition system. The suspension data used is in fact incidental and collected as part of the train borne system used to monitor the condition of the vertical position of the power rail. The inherent benefit of such a set-up is continuous data acquisition, as long as the relevant trains are deployed. Over time, a large data set is accumulated on an almost daily basis, to provide a good time resolution and the option to choose quality data that meets the requirement for processing (steady train speed in this case). The track condition index, *Dyn\_TCI\_susp*, which is based on suspension data collected under dynamic conditions is intended to provide a severity or condition indication of track health. The assumed relationship is that higher track undulations reflect a less healthy track condition. A higher *Dyn\_TCI\_susp* should be interpreted as having lower track stability.

In the presented plots in Figs. 2 and 3, it should be noted that the 100 and 200 m short track lengths are only intended to provide a reference. Note that the 12 sets of data are from five different station-to-station track sectors; and the 36 plots were all derived from 15 individual train passby measurements. The first impression is that the 12 graphs show repeatability within each 3-plot set, demonstrating consistency in results and hence the inferred utility of the *Dyn\_TCI\_susp*. Also note the chainage in subplots (d) and (f). These track sections are exactly that presented in Fig. 3. (I.e. these 200 m sections are extract from the 2 km section.)

Figure 2 shows the reference *Dyn\_TCI\_susp* for the different combination of track forms for **tangent tracks**. Amongst the 6 graphs presented for the different tangent track-forms and years in operations, the FST shows the highest variation and peak values at index of around 2.5. The second highest registered index levels came from the ballast track-form with timber sleepers just before change out. Its peak values are at index of around 1.5. The remaining four generally registers at index of  $<0.5$  with peak values that are at index of  $<1$ .

Figure 3 shows the equivalent reference *Dyn\_TCI\_susp* for **curve tracks**. Similar to the tangent track results, the FST and the ballast track-form with timber sleepers just before change out register the highest peak values and variance. Both their peak values are at index of around 5. The remaining 4 track-forms in decreasing order of peak values are CST, BLT\_Timber ( $\sim 12$  year), BLT\_Concrete ( $\sim 6$  year) and BLT\_Concrete ( $\sim 1$  year). The youngest ballast track-form generally has index levels of  $<0.5$  and a peak value that is at index of  $<1$ .

Based on the results in Figs. 2 and 3, and Table 1, the reflected order of track undulations under dynamic condition by the *Dyn\_TCI\_susp* is in alignment with intuitively known baseline expectations—Curve track has more undulation than tangent track; FST has more undulations than CST; a younger ballast track-form has lower undulation than that, just before a sleeper change out. The results have also brought out some surprises in relation to track-form comparison—On curve track, CST is not necessarily more than or as stable as ballast track; FST is registering higher or equivalent peaks than the worst ballast track-form. A reasonable counter to these two points is that the presented curve tracks have different curvatures; hence direct comparisons between track-forms do not hold. On the observed higher undulations in FST, it may also be explained by the design of the FST, which is to absorb energy by moving, in order to limit the vibration energy being propagated. A general comparison between tangent and curve tracks indicated that the *Dyn\_TCI\_susp* is better at providing gradation of measure for the latter. This observation, to some extent, is also in alignment with the intuitive expectation that more issues tend to manifest at curve tracks than tangent tracks.

Figure 4 shows a 2 km section of ballast track condition over a span of 1.5 years, in four time slices, 6 months apart. It should be noted that result consistency was checked with three passby, but not presented here. Note the two steady state operating speed where train passes at 80 km/h, represented by the 1st and 4th time slice. The two intermediate time slices represent different stages of sleeper change out and tamping activities. Zone (I) Tangent Track: The 1st and 4th time slice did not show much change. However variation could be seen in the two intermediate time slices, reflecting the sleepers change out or tamping activities. Zone (II) Mainly Curve Track: The improvement between the 1st and 4th time slice is evident. Zone (III) Tangent Track: The observations are similar to that in Zone (I). The only difference is the timing of track maintenance activities. One interpretation is that track maintenance started from Zone (III) and progressed towards Zone (I).

## 7 Conclusion

The presented measure of track condition index, *Dyn\_TCI\_susp*, is based on suspension data collected under dynamic conditions. It is analogous to a Power Density Function with length (track length) in place of the time parameter, using a 20 m moving window. The measure was applied on three track-forms—Concrete Slab Track (CST), Floating Slab Track (FST), Ballast Track (BLT), where the first two are typically found in tunnels while ballast track is typically found on viaducts. For ballast track, the results are further categorized into timber and concrete sleepers. The outcome shows that the *Dyn\_TCI\_susp* is able to clearly differentiate between tracks with low and high undulations. By extension, this differentiation allows a range of quantifiable threshold of acceptance to be set by user, based on experiences from conventional measure of track quality from maintenance record.

A reference *Dyn\_TCI\_susp* across the varied track-forms found on SMRT operated metro lines, was provided. The repeatability of the results for a given track section is demonstrated by the observed consistency over three data sets derived from three different train passby of suspension measurements. In general, tangent tracks register lower index levels compared to curve tracks. For tunnel track-forms, the peak values for tangent tracks are at index of around 0.5 and 2–2.5 for CST and FST respectively; for curve tracks, they are at index of around 2.5 and 3–5 respectively. In general, FST registers higher mean, variation and peak values compared to CST. For ballast track (BLT), the peak values fluctuate over a much larger range, up to index of around 4. The fluctuation could be accounted for by the variety of the presented BLT track-forms. They include concrete and timber sleepers at different stages of their operating life. It is noted that for BLT tangent and curve tracks that underwent re-sleepering, the improved *Dyn\_TCI\_susp* register index values below 0.5 in general.

In the more detailed treatment on a 2 km section of ballast track, the *Dyn\_TCI\_susp* was charted over a 1.5 years over four time slices, to capture a major track maintenance activity (re-sleepering). Improvement is observed for tangent and curve tracks, between the two steady state track conditions in Jun 2013 and Jan 2015. The Jun 2013 plot shows high variation of the index with the curve section registering peaks at index of around 2–4; and the tangent section registering peaks at index of around 1. The significantly improved track condition in Jan 2015, as reflected by the plots, showed index levels that are generally below 0.5 with the curve and straight sections registering peaks at index of around 0.7 and 0.5 respectively.

The discussed application scope of the presented *Dyn\_TCI\_susp* can only utilize suspension data that is measured under steady train speed, to avoid inclusion of influences that are not track related. Extending this point to track feature, anecdotal evidence indicates that gaps at crossings and curve transitions give rise to an increased index level. More development work is needed to determine such increases in index can be managed. Future work will includes simplifying the index into a simple 3-tier rating for each fixed track-length section. This will likely progressed with the use of peak values and statistical measures like mean and variance.

Given the presented results, the *Dyn\_TCI\_susp* has shown to provide a consistent baseline. At the minimum, it can be deployed for comparative assessment going forth, as more development work is needed to explore its use as a form of absolute measure for track condition, to guide maintenance work.

**Acknowledgements** This research paper is made possible through the help and support from various parties, including: co-authors, colleagues, supervisors, family and friends. Especially, I would like to dedicate my acknowledgement of gratitude toward the following significant advisors and contributors. First and foremost, I would like to thank Permanent Way department for their support for the on-site measurement and track maintenance work information. Second, I would like to thank Rolling Stock department for their support in the provision of trains for the installation of the train-borne condition monitoring system. Finally, I sincerely thank my colleagues in Technology Management Office for their data repository, which allows the management of track measurement data in a systematic manner.

## References

1. Liu, R., Xu, P., Sun, Z., Zou, C., Sun, Q.: Establishment of track quality index standard recommendations for Beijing metro. *Discrete Dyn. Nat. Soc.* **2015**, 1–9 (2015). <https://doi.org/10.1155/2015/473830>
2. CEN: Railway Applications-Track-Track Geometry Quality, in Part 1: Characterization of Track Geometry. CEN, Brussels, Belgium (2008)
3. FRA: Federal Railroad Administration Track Safety Standards Compliance Manual. Federal Railroad Administration, Washington, DC, USA (2008)
4. Mori, H., Sato, Y., Ohno, H., Tsunashima, H., Saito, Y.: Development of compact size onboard device for condition monitoring of railway tracks. *J. Mech. Syst. Transp. Logistics JMTL* **6**(2), 142–149 (2013). <https://doi.org/10.1299/jmtl.6.142>
5. Hodge, V.J., O’keefe, S., Weeks, M., Moulds, A.: Wireless sensor networks for condition monitoring in the railway industry: a survey. *IEEE Trans. Intell. Transp. Syst.* **16**(3), 1088–1106 (2015). <https://doi.org/10.1109/tits.2014.2366512>

# Modelling Framework for Electromagnetic Noise Generation from Traction Motors



F. Botling, I. Lopez Arteaga and S. Leth

**Abstract** Electromagnetic noise from traction motors is often the single most dominating noise source from trains at low train speeds. This electromagnetic noise is tonal and annoying for both passengers on the train and people near the track and on the platform. A thorough understanding of the cause and the prediction of the electromagnetic noise is needed to be able to design low noise components. This paper describes a real time multi-physics modelling framework for prediction of the audible electromagnetic noise generated by traction motors fed by power converters. The cause of the electromagnetic noise is influenced by several different domains. To be able to fully simulate the final acoustic sound, all these domains needs to be modelled and simulated together. Simulations of some relevant operational conditions for acoustic noise generation has been performed and discussed. Some of these results have been compared to real measurements from a converter fed traction motor.

## 1 Introduction

Various simulation models for electromagnetic noise generation from traction motors have been developed by researchers dealing with low noise motor design [1–3]. However, most of these models focus on modelling only in one or a few of the domains contributing to the final generated sound. To accurately and effectively

---

F. Botling (✉) · I. Lopez Arteaga · S. Leth  
The Marcus Wallenberg Laboratory for Sound and Vibration Research (MWL),  
KTH Railway Group, KTH Royal Institute of Technology,  
SE-100 44 Stockholm, Sweden  
e-mail: botling@kth.se

F. Botling  
Bombardier Transportation Sweden AB, Gothenburg, Sweden

I. Lopez Arteaga  
Department of Mechanical Engineering, Eindhoven University of Technology,  
5600MB Eindhoven, The Netherlands

simulate the total generated noise, the contribution of all the different physical domains related to the noise generation needs to be connected and modelled in the same simulation environment. This paper presents a complete and structured multi-physics modelling framework for the simulation of electromagnetic noise generated by traction motors. The different domain models are separated by well-defined physical interfaces making it possible to simulate and investigate the effects from each of the domains, and their relation to the final generated sound.

## 2 Background

The characteristics of electromagnetic generated noise are very complex and contain narrow banded harmonic components spread in a wide frequency range. The spectral content is also varying with the operational conditions as e.g. train speed and load conditions. Figure 1 shows the spectral content of the electro-magnetic noise generated during acceleration of a train from stand still.

Electromagnetic noise from traction motors is caused by effects in many different domains depicted in Fig. 2.

1. Converter Control: Control of the power electronics to generate a pulse with modulated (PWM) converter voltage i.e. voltage pulses of different widths to create a quasi-sinusoidal voltage.
2. Electrical domain: The converter voltage determines the input currents to the motor and is affected by both converter and motor electronics.
3. Electro-magnetic domain: The motor currents generate magnetic flux dependent motor forces in both tangential and radial direction.
4. Structural domain: Radial motor forces distributed both in space and frequency induce structural vibrations in the stator shell.
5. Acoustic domain: Radial stator vibrations cause radiated acoustic pressure waves.

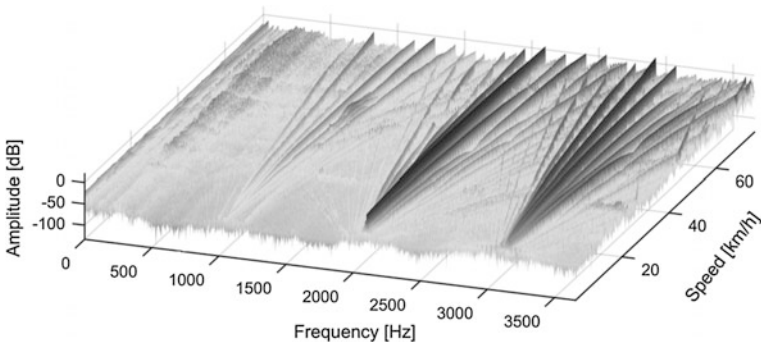


**Fig. 1** Electromagnetic acoustic spectra of a traction motor during acceleration from stand still. Frequency range between 0 and 3500 Hz on the horizontal axis, and train speed from 0 to 70 km/h on the vertical axle

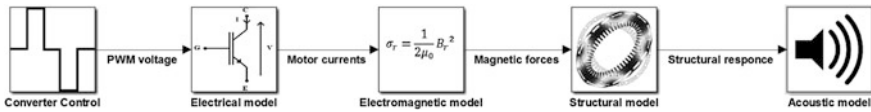


Fig. 2 Modelling framework

### 3 Simulation Framework

A simulation framework has been developed to predict the effects in each domain related to the final acoustic noise. The spectral content of the electromagnetic noise is mainly determined by the converter control strategy and the operational conditions of the motor [4], but the structural response of the motor is important for the vibration amplitudes of the narrow banded components.

#### 3.1 Real Time Based Simulations

The converter control domain is one of the most complex domains to simulate accurately. A complete control system for converter control of a traction motor for train applications typically consists of several millions lines of code. One way to simulate the behaviour of a full converter control system is by using the real converter control-unit hardware and software, and simulate the mechanical and electrical interaction with the rest of the train in real time. This type of simulator is often called a Hardware-In-the-Loop (HIL) simulator, or a Real-Time-Simulator (RTS). The software models for the simulated train-environment are based on Matlab/Simulink models converted to code running on high performance real-time simulator hardware (dSPACE). The simulations are running with fixed time steps normally within 20–50  $\mu$ s, corresponding to a maximum acoustic bandwidth of 10–25 kHz.

#### 3.2 Converter Control

The most common type of traction motors for rail applications is the 3-phase asynchronous motor. To be able to control both the torque and the rotational speed of the motor the power fed to the motor must be converted to a 3-phase voltage with variable amplitude and frequency. The amplitude and frequency of the 3-phase converter voltage are created by a pulse with modulated (PWM) DC voltage. The PWM control signals for controlling the power converter electronics are calculated by the real converter control unit based on input signals calculated from the RTS simulator. In the RTS simulator these PWM control signals are inputs to a



power converter electronics model that calculates the 3-phase output converter voltage that is connected to the traction motor.

### 3.3 Electrical Induction Motor Model

The induction motor consists of three distributed stator windings surrounding a rotor built up from metal bars short-circuited by conducting end rings. 3-phase induction machines are usually mathematically represented by complex equations, using so called space vectors [5]. These equations are often described as equivalent circuit diagrams making it possible to use a simple and compact representation of the motor. The induction machine can be represented by the following complex equations:

$$u_s = R_s i_s + \dot{\psi}_s \tag{1}$$

$$\dot{\psi}_r = -R_r i_r + j\omega \psi_r \tag{2}$$

$$\psi_s = L_{s\sigma} i_s + L_m i_m \tag{3}$$

$$\psi_r = L_{r\sigma} i_r + L_m i_m, \tag{4}$$

where  $u, i$  and  $\psi$  represents the converter voltage, motor current and flux linkage. The resistance and inductance of the motor is denoted  $R$  and  $L$ , and the suffix  $s, r$  and  $m$  stands for the rotor, stator and mutual relations. These equations are described by the equivalent circuit diagram in Fig. 3.

The electrical interaction in the air-gap between the rotor and the stator is modelled as the mutual inductance  $L_m$  with the corresponding air gap flux linkage  $\psi_m$ . The flux density  $B$  through a winding is given by the flux linkage divided by the area  $S$  and the number of winding turns  $N$ .

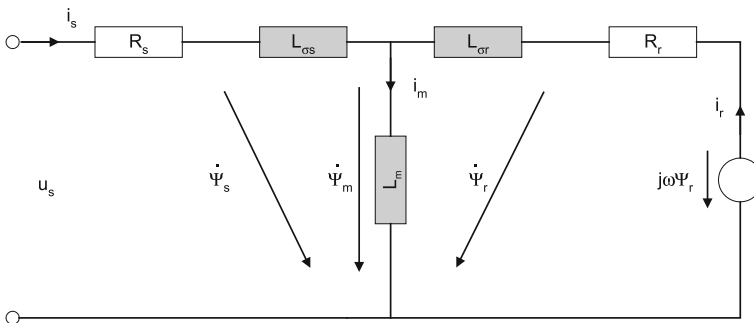


Fig. 3 Equivalent circuit diagram of the traction motor

### 3.4 Electromagnetic Forces

The complex valued air gap flux density  $B$  described in Sect. 3.3 can be used to calculate both the tangential and the radial forces created in the air gap between the stator and the rotor. The tangential force component corresponds to the wanted torque of the motor, but there are also a radial force component causing unwanted radial forces. The Maxwell stress tensor can be used to calculate the radial force in the air gap [6] as:

$$\sigma_{radial} = \frac{1}{2\mu_0} B_{radial}^2, \quad (5)$$

where  $\mu_0$  is a magnetic constant and  $B_{radial}$  is the radial magnetic field in the air gap. The radial force acting on the structure is causing structural vibrations that will result in radiated sound. The spatial distribution of the force on the stator is important for the excitation of certain vibration patterns (structural modes) of the stator [7]. Only the structural modes that co-insides with the force distribution will give structural vibration response.

### 3.5 Structural Model

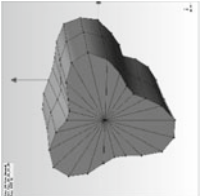
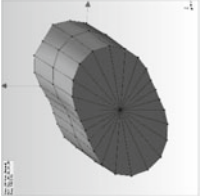
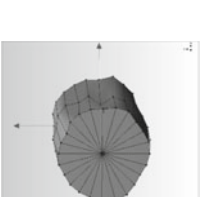

The structural model used in the RTS simulations is based on a reduced order modal model. The modal parameters (eigen frequency  $\omega_n$ , mode shape  $\varnothing_{pn}$  and damping  $\zeta$ ) were derived from an experimental modal analysis performed on a real traction motor [8]. Table 1 shows some of the structural modes with their corresponding eigen frequency derived from the experimental modal analysis. If preferred, other methods as analytical and numerical methods can be used for determining the modal parameters for the modal model.

The vibration level in one or several points on the stator can be calculated by a summation of the contributing vibration levels from all of the force positions. This can be expressed as the transfer matrix  $\mathbf{H}$

$$\mathbf{H} = \begin{bmatrix} h_{11} & \cdots & h_{1Q} \\ \vdots & \ddots & \vdots \\ h_{P1} & \cdots & h_{PQ} \end{bmatrix}, \quad (6)$$

where  $Q$  is the number of force positions and  $P$  is the number of vibration responses. The elements in the matrix  $\mathbf{H}$  can be expressed as the sum of contributions from a number of vibrational modes of the structure. The interaction of the different force contributions will result in only a few possible vibrational modes. The important vibrational modes are determined by the spatial distribution of the exited force. For a motor with two magnetic pole pairs, the PWM generated forces

**Table 1** Mode shapes from experimental modal analysis

	$m = 0$	$m = 2$	$m = 3$	$m = 4$
$n = 0$	 <p style="text-align: right;"><b>2915 Hz</b></p>	 <p style="text-align: right;"><b>749 Hz</b></p>	 <p style="text-align: right;"><b>1476 Hz</b></p>	 <p style="text-align: right;"><b>2357 Hz</b></p>

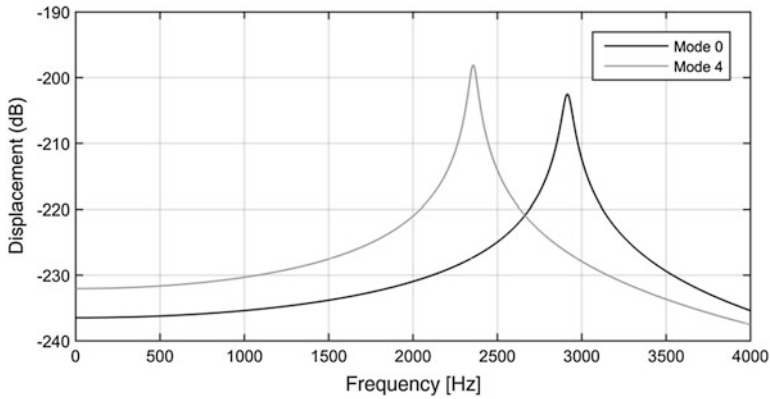


**Fig. 4** Displacement as function of frequency for the two structural modes 0 and 4

will only be of order 0 and 4 [9]. The frequency characteristics for a mode can be expressed as a second order transfer function in Laplace transform as:

$$G(s) = K_n \cdot \frac{\omega_n^2}{s^2 + 2\zeta\omega_n s + \omega_n^2} \tag{7}$$

where  $K_n$  is equivalent to the inverted stiffness,  $\omega_n$  is the natural frequency and  $\zeta$  the damping of the system. The vibration response for the two modes 0 and 4 can be plotted by using Eq. 7 with the modal parameters derived from the experimental modal analysis. Figure 4 shows the displacement response for mode 0 in black and mode 4 in grey. It can be seen that the resonance peaks are at the eigen-frequencies corresponding to the values in Table 1.

### 3.6 Acoustic Domain

The radiated acoustic sound power can be calculated based on the vibration velocities  $v_n$  on the stator using Eq. 8, where  $\sigma$  is the radiation efficiency,  $\rho_0$  is the density of air,  $c$  is the speed of sound,  $S$  is the area of the vibrating body and  $v_n^2$  is the squared spatial average of the vibration velocity.

$$W = \sigma\rho_0cS\langle v_n^2 \rangle \tag{8}$$

The radiation efficiency is assumed to be one ( $\sigma = 1$ ) for this type of application. The equivalent sound pressure levels (SPL) at some distance from the motor can then be estimated from the calculated acoustic power. The squared surface velocities are hence directly proportional to the sound pressure levels from the motor.

The simulated sound pressure levels are calculated in real time based on the simulated stator vibration velocities.

## 4 Simulation and Experimental Results

The simulations were performed in the real time simulator and validated against measurements of a real traction motor fed by a PWM controlled converter. The measurements were performed in the Bombardier Power Lab in Västerås, Sweden.

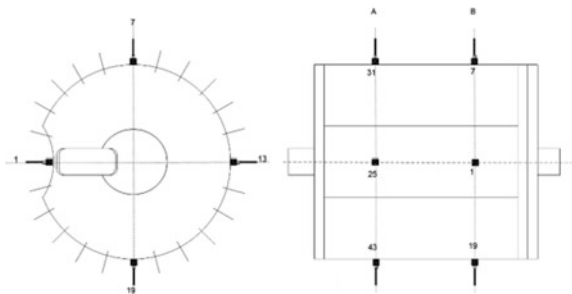
### 4.1 Experimental Study

During the experimental studies the traction motor was driven by converter fed operation in a Power Lab, and measurements of vibration levels and the acoustic response were performed. There were 48 accelerometers mounted in two circumferential rings with 24 accelerometers evenly distributed on each circumferential ring seen in Fig. 5. The acoustic response were measured with one to four microphones depending on the test case. Motor currents and motor rotational speed were also measured.

### 4.2 Electromagnetic Force

The electromagnetic radial force acting on the stator surface can be calculated from the squared magnetic flux according to Eq. 5. The structural modes of interest are the two modes 0 and 4, seen in Table 1, corresponding to the two dominant spatial orders of the electromagnetic force. Several other structural modes still exists, but they are not important to include in the model as long they are not excited by the electromagnetic force. To be able to simulate the structural response in the time

**Fig. 5** Measurement setup of 48 accelerometers mounted on the stator



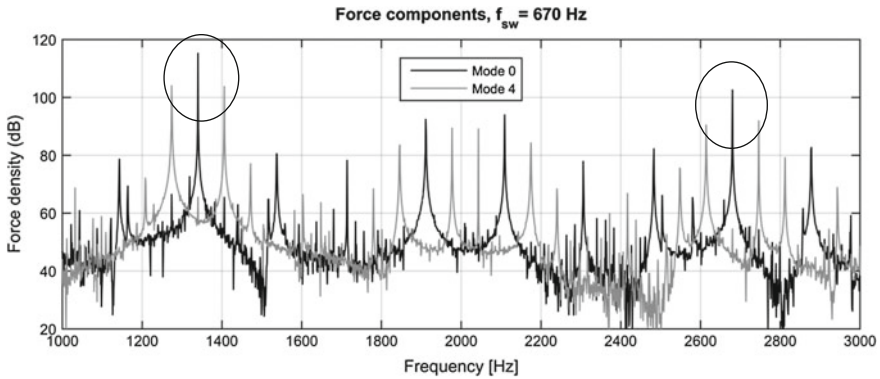


**Fig. 6** Simulated electromagnetic force components

domain for the two structural modes, the electromagnetic force corresponding to these two modes must be calculated separately for each mode. The structural response is governed by the characteristic equations illustrated in Fig. 4 for the two modes respectively. Figure 6 shows the simulated force density components corresponding to the spatial orders of mode 0 in black and mode 4 in grey. Dominating force components are found in the region of two and four times the switching frequency marked by circles.

The components corresponding to these six most dominating force components in Fig. 6 is used for validation of the simulation results. The frequencies and modes for these components can be calculated analytically [6], and is depending on both the used PWM switching frequency  $f_{sw}$  and the frequency corresponding to the rotational speed of the motor  $f_m$ . Table 1 shows the frequencies and modes for these six dominating components with their analytical expressions. Both the analytically calculated frequencies and modes corresponds well to the simulation results in Fig. 6.

### 4.3 Structural Response

#### 4.3.1 Simulated Structural Response

The structural vibrations are calculated as the input electromagnetic force acting on the structural modal model. The vibration levels are calculated separately for the two modes. The resulting absolute vibration amplitude is depending on a number of different physical constants for each of the calculation steps. In this study a global constant is used and tuned against the amplitude of one frequency component in one measurement point. All the simulations are then using the same global constant. The resulting vibration levels for the two modes, mode 0 in black and mode 4 in grey, are shown in Fig. 7. It can be seen that the force components closer to the

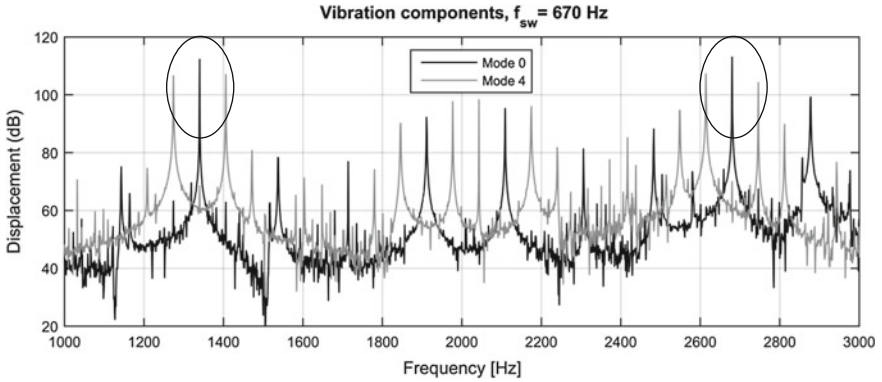


Fig. 7 Simulated vibration components

structural resonances (2300–2900 Hz) are causing higher vibration amplification compared to components far from the resonances. However, even at lower frequencies (1200–1500 Hz) the structural vibration response is high due to the high levels of magnetic force excitation.

### 4.3.2 Measured Structural Response

As a comparison, the average vibration levels measured from the 48 accelerometers are shown in Fig. 8. The simulations in Fig. 7 are showing the pure electromagnetically induced vibrations. The measured vibrations in Fig. 8 are also including contributions from mechanical induced vibrations from e.g. other machines in the Power Lab at levels around 60 dB. It is however possible to see the characteristics

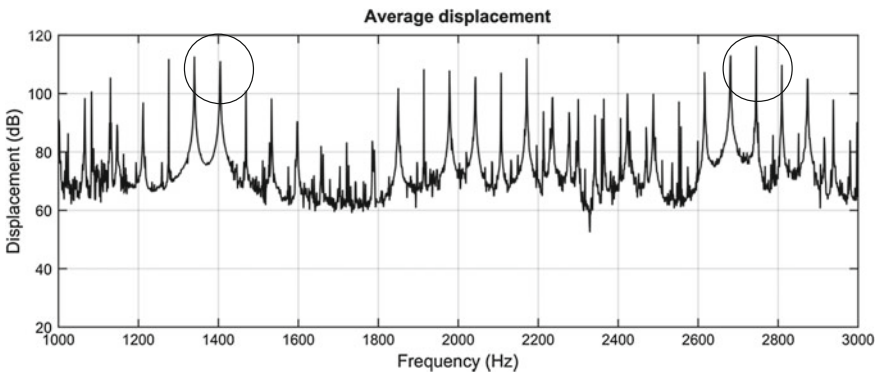


Fig. 8 Measured vibration components

of the narrow banded vibration components similar to the simulated ones in Fig. 7. The measured frequencies for the six components in Table 2 corresponds well to both the simulated and the analytically calculated values. The measured modes (deflection shapes) for these frequency components has earlier been validated against analytical expressions [10]. The measured vibration levels from components around three times the switching frequency are significantly larger than the simulated values, however acoustic measurements does not show any significant levels in this frequency region. This discrepancy for three times the switching frequency must be further studied.

### 4.3.3 Model Validation

In Fig. 9 the simulated vibration responses for mode 0 and 4 for the six frequency components according to Table 2 is compared with the measured average displacements and 2 times the standard deviation (STD) of the measured values. The simulated vibration response for mode 0 and 4 are shown by the black and grey curves. The measured average vibration levels for each of the six frequency components are plotted as circles, and 2 times the standard deviation for each component are marked with diamonds. The first five frequency components matches the measured average responses quite well, but the last point at 2745 Hz seems to be different. This component is still within 2\*STD but due to the large spread in the vibration measurements it is hard to draw any conclusion if it is the simulated or measured response that is not correct or neither of them. However, by studying the components 4 and 6, these components shall from the theory be of the same magnitude just as the components 1 and 3 are, in both simulations and measurements in the left part of Fig. 9. The simulated amplitudes for component 4 and 6 corresponds well with this theory, but not the measured amplitudes for component 6. This indicate that the measured value for component 6 may be the erroneous one.

**Table 2** Frequencies for the six dominating components

Component	Frequency (Hz)	Mode (sign = rotation)	Analytical expression
1	1275	-4	$2f_{sw} - 2f_m$
2	1340	0	$2f_{sw}$
3	1415	4	$2f_{sw} + 2f_m$
4	1615	-4	$4f_{sw} - 2f_m$
5	2680	0	$4f_{sw}$
6	2745	4	$4f_{sw} + 2f_m$



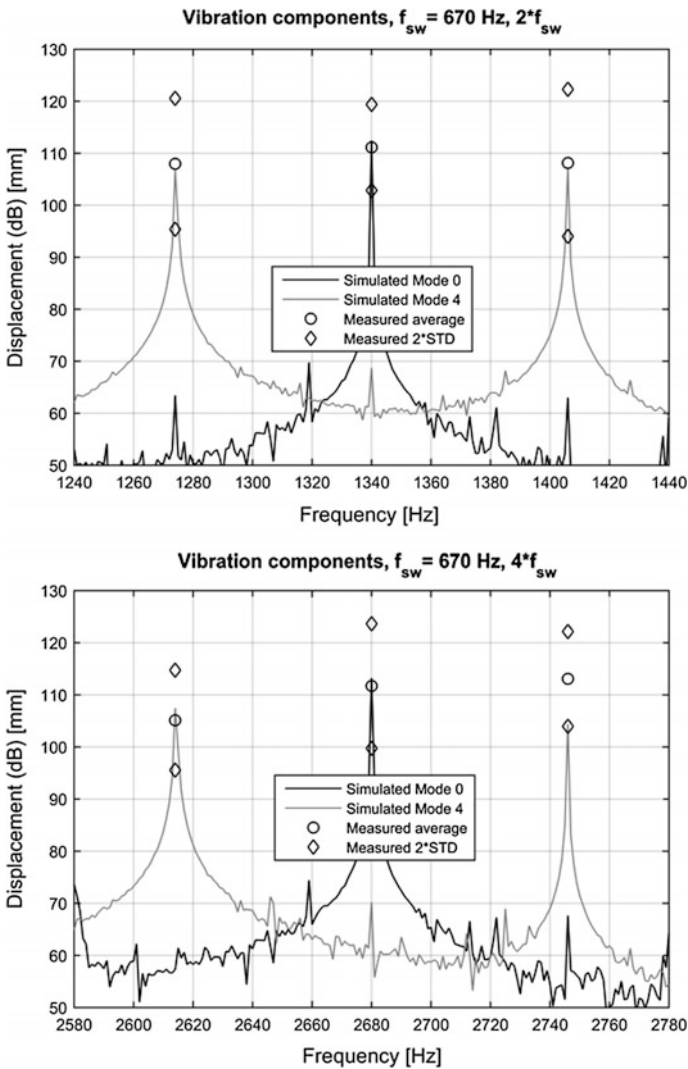


**Fig. 9** Simulations compared with average measured vibration levels and 2\*STD standard deviation of the measurements

#### 4.4 Sound Pressure Level

The sound pressure level from the motor can be simulated in real time as described in Sect. 3.6. The sound pressure level caused by the electromagnetic forces depends on many different factors. In the following sections simulation and measurements are studied and briefly discussed for some of the most important operational conditions. Full results of these studies will be presented in a future publication.

#### 4.4.1 Sound Pressure Level as Function of Torque

Intuitively one may think that the electromagnetic noise from a motor is highly influenced by the applied torque, and is sometimes also claimed in the literature [11]. However, Eq. 5 shows that the sound depends only on the magnetization flux and not on the torque. To be able to produce a certain torque from a motor, a minimum value of flux is always needed. Anyhow, when possible, flux reduction can be applied to minimize the electromagnetic noise from a motor. To investigate the influence of the torque, simulations were performed with constant flux and different levels of applied torque. The simulation results did not give any change of the sound pressure level during the different load conditions. Hence, the sound level can be constant while e.g. the torque is increased as long as the flux is constant. This result has also been verified by measurements in the Power Lab.

#### 4.4.2 Sound Pressure Level as Function of Flux

To investigate the influence of the magnetic noise with changing flux levels, tests with constant low torque and increased flux levels were conducted both as simulations and by measurements in the Power lab. If the torque was kept constant at a level of 5% and the magnetic flux was changed, the simulations gave a steady increase of the simulated sound pressure level. Hence, the sound level will increase in proportion to the increase of the flux. Similar results were obtained from measurements in the Power Lab, but with slightly different absolute SPL levels.

#### 4.4.3 Sound Pressure as Function of Motor Speed

During a run-up the train is accelerating with full tractive effort. In this case both the amplitude and the frequency of many of the acoustic components will vary as the speed is increasing, as shown in Fig. 1. It is not possible to characterize the perceived sound and annoyance based on total sound pressure level measurements alone. Graphs with third octave band responses are also not enough to give a good representation of the perceived noise when the acoustic components are narrow banded. A better representation of the perceived noise can be made by plotting a high frequency resolution spectrogram or preferably by listening to the acoustic simulation results, see Fig. 1. Figure 10 shows the simulation result of a spectrogram of a run-up. The highest acoustic energy can be seen in the regions of 2 and 4 times the switching frequency marked with ovals.

The maximum A-weighted sound pressure level is still one important parameter often specified in legal and customer requirements. The possibility to simulate the total sound pressure levels during a run up gives valuable information of critical speed regions and of the overall SPL level. The simulated and measured A-weighting total sound pressure level during a run-up is plotted in Fig. 11, at a

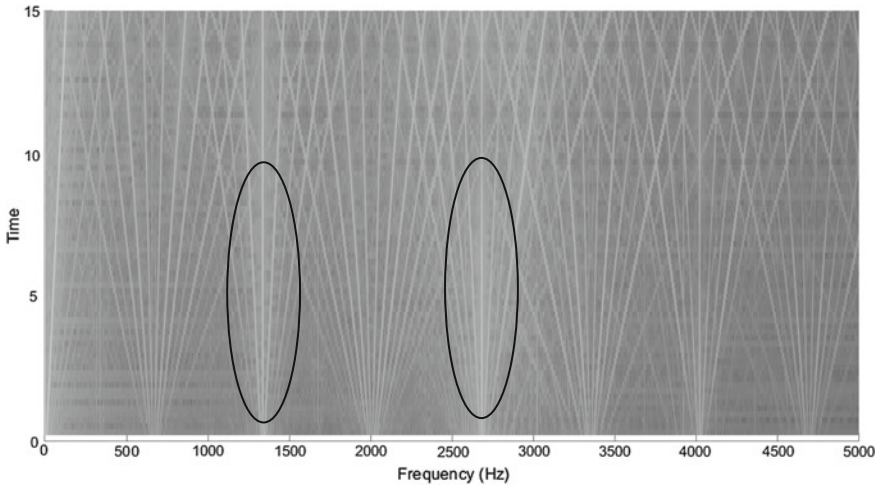


**Fig. 10** Spectrogram of simulated run-up

microphone distance of 1.0 m. The constant acceleration of the train starts at around 20 s, and the train reaches 45 km/h at around 130 s. The simulated and the measured levels are close and shows a similar behaviour.

## 5 Conclusion

A real time multi-physics modelling framework for simulation of the audible electromagnetic noise generated by traction motors has been presented. The five main physical domains important for the generated sound have been simulated, explained and discussed. The simulation model is capable of calculating the electromagnetic forces, structural vibrations and the total sound pressure level in real time. Simulation results of the electromagnetic force harmonics show good correlation to analytical expressions. Compared to measured data, the simulated vibration components have correct frequencies and the mode shapes are correctly predicted compared to both analytical expressions and measured operational deflection shapes. The simulated vibration amplitudes are shown to be within 2 times of the standard deviation of the measured values and is predicting the correct trends for relation between the levels of the 6 most important frequency components. However, due to large spread in the measurements and that one of the measurement points may not be correct, the conclusions so far on agreement for the predicted amplitudes are tentative and both the measured and calculated results needs further investigations for more final conclusions. Simulations of the total sound pressure level over all frequencies during a constant acceleration of the train shows good agreement with measurements.

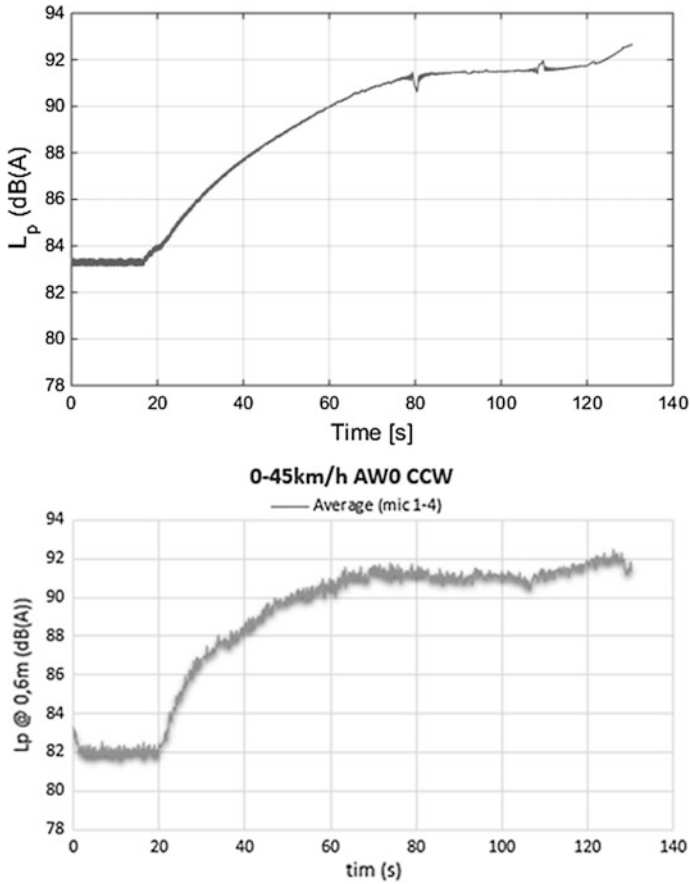


**Fig. 11** Simulated (left) and measured (right) SPL during constant acceleration from stand still to 45 km/h

**Acknowledgements** The authors would like to thank the KTH Railway group at the Royal Institute of Technology in Stockholm, Sweden, and to Propulsion and Controls, at Bombardier Transportation AB in Västerås, Sweden.

## References

1. Braunisch, D., Ponick, B., Bramerdorfer, G.: Combined analytical–numerical noise calculation of electrical machines considering nonsinusoidal mode shapes. *IEEE Trans. Magn.* **49** (4), 1407(9) (2013)
2. Saito, A., Suzuki, H., Kuroishi, M., Nakai, H.: Efficient forced vibration reanalysis method for rotating electric machines. *J. Sound Vib.* **334**, 388(16) (2015)

3. van der Giet, M.: Asymptotic Fourier decomposition of tooth forces in terms of convolved air gap field harmonics for noise diagnosis of electrical machines. *Int. J. Comput. Math.* **28**, 804–818 (2009)
4. Tsoumas, I.P., Tischmacher, H.: Influence of the inverter's modulation technique on the audible noise of electric motors. *IEEE Trans. Ind. Appl.* **50**(1), 269–278 (2014)
5. Munoz, A.R., Lipo, A.: Complex vector model of the squirrel-cage induction machine including instantaneous rotor bar currents. *IEEE Trans. Ind. Appl.* **35**(6) (1999)
6. Besnerais, J.L., Lanfranchi, V., Hecquet, M., Brochet, P.: Characterization and reduction of audible magnetic noise due to PWM supply in induction machines. *IEEE Trans. Ind. Electron.* **57**(4), 1288–1295 (2010)
7. Verdyck, D., Belmans, R.J.M.: An acoustic model for a permanent magnet machine: modal shapes and magnetic forces. *IEEE Trans. Ind. Appl.* **30**(6), 1625 (1994)
8. Botling, F., Amlinger, H., Lopez Arteaga, I., Leth, S.: Vibro-acoustic modal model of a traction motor for railway applications. In: *Proceeding of the 34th International Modal Analysis Conference 2016*, Orlando
9. Franck, D., van der Giet, M., Hameyer, K.: Active reduction of audible noise exciting radial force-density waves in induction motors. In: *IEEE International Electric Machines & Drives Conference*, pp. 1213–1218, May 2011
10. Amlinger, H., Botling, F., Arteaga, I.L., Leth, S.: Operational deflection shapes of a PWM-fed traction motor. In: *IMAC XXXIV*, Orlando, 2016
11. Ruiz-González, A., Meco-Gutiérrez, M.J., Vargas-Merino, F., Heredia-Larrubia, J.R.: Reducing acoustic noise radiated by inverter-fed induction motors controlled by a new PWM strategy. *IEEE Trans. Ind. Electron.* **57**(1) (2010)

# Design and Performance of a Permanent Vibration Monitoring System with Exceedance Alarms in Train Tunnels



S. Rajaram, James T. Nelson and H. J. Saurenman

**Abstract** Sound Transit has installed nine permanent vibration monitors (VMS) to continuously monitor the revenue service train 1/3 octave vibration velocity in the University of Washington (UW) campus area. The monitors allow verification that the vibration levels generated from the newly opened University Link (U-Link) extension light rail operations are within the thresholds established in the Master Implementation Agreement (MIA) signed by UW and Sound Transit. There are also three wheel flat detectors located along the light rail alignment outside of the campus area to serve as an early warning system that allows Sound Transit operations to implement mitigation measures in real time before trains with wheel flats reach the vibration-sensitive zone in the University of Washington. This paper discusses the design of the vibration monitoring program and the functioning of the system during the first three months of U-Link revenue service. Some of the key results are that the system is functioning as designed and consistently records and notifies vibration events that exceed alarm thresholds. The vibration levels from train passbys have been well below the MIA thresholds and preliminary investigation indicates that the alarms are not caused by the trains. A surprising result, however, is that several non-train vibration sources that coincide with train recording sessions are generating alarms. Vehicular traffic on adjacent roadways and mechanical equipment such as sump pumps located in the vicinity of the VMS units are suspected as the potential sources of vibration alarms.

---

S. Rajaram (✉)  
Sound Transit, 401 S Jackson St., Seattle, WA 98104, USA  
e-mail: Shankar.rajjaram@soundtransit.org

J. T. Nelson  
Wilson Ihrig & Associates, Emeryville, CA, USA

H. J. Saurenman  
ATS Consulting, Pasadena, CA, USA

# 1 Introduction

Sound Transit’s University Link (U-Link) light rail extension opened for revenue service in March 2016. The new alignment extends the Central Link Light Rail Train operations to the University of Washington (UW) football stadium. The UW campus has vibration-sensitive research equipment housed in approximately 25 buildings. As part of the agreement with UW, Sound Transit is required to install and maintain a permanent vibration monitoring system that demonstrates that the stringent 1/3 octave band vibration velocity limits for each of the UW building are not exceeded during train operations [1, 2].

The vibration monitoring program consists of three wheel flat detectors (WFDs) located before the trains enter the campus area for early warning as shown in Fig. 1, and nine 1/3 octave vibration monitoring system (VMS) units in the train tunnels within the UW campus as shown in Fig. 2 [3]. The WFDs are programmed to trigger alarms when the wheel condition might cause vibration levels that approach or exceed the MIA thresholds. The locations of the WFD allow sufficient time for Sound Transit train operators to reduce speeds before the trains reach the UW campus area. Each of the VMS units has two data loggers and two geophones to provide redundancy. The primary data logger is the default recorder for train passbys, but in case of malfunction of the primary data logger, the VMS monitor will automatically switch to the alternate data logger and geophone system. The VMS units are located every 300 ft in each of the tunnels in the UW campus area, with monitors at interleaved positions to maximize coverage. The MIA

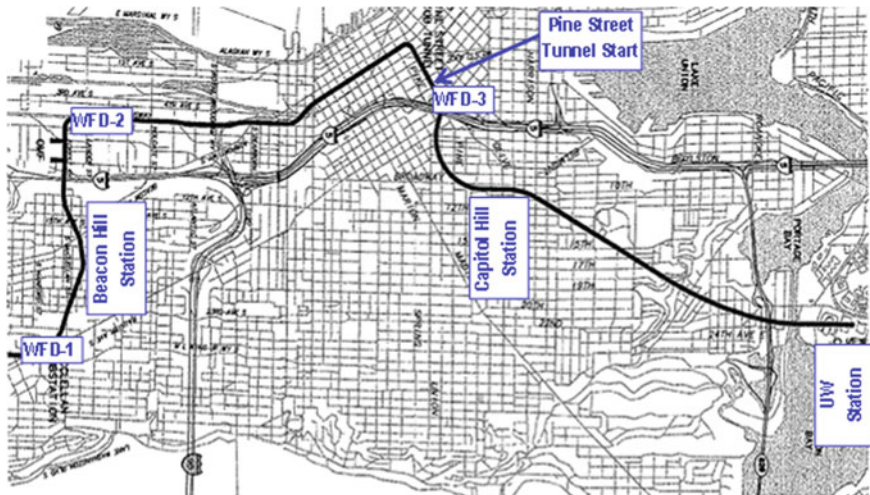


Fig. 1 WFD units on the northbound track before the newly-opened extension to UW

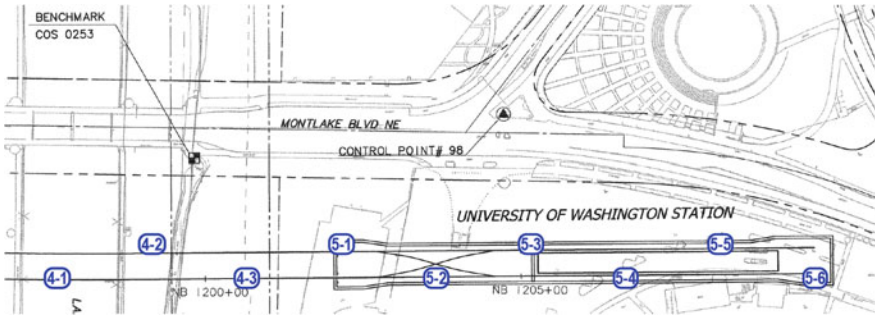


Fig. 2 VMS units in the U-link tunnel near UW station

between Sound Transit and UW requires that the vibration monitoring system be reliable.

The WFDs and the VMS units are programmed with two levels of alarms. The first level is a warning alarm and the second (and higher) level is the exceedance alarm. In case of the WFDs, the VMS alarm trigger levels were calibrated with light rail vehicles (LRVs) with wheel flats and with no wheel flats. The data from the WFD would be shown for multiple passes of the same vehicle to demonstrate repeatability of the wheel flat detection. An interesting observation was that the wheel flat amplitude tended to go down with more runs during the same day, indicating that the flat spot maybe smoothing, although that was never verified.

The traffic on adjacent streets on the ground and mechanical equipment in the vicinity of the VMS units appear to produce low frequency vibration that is detectable by the VMS, and high enough to trigger the VMS alarms. This paper discusses the design of the vibration monitoring program, the calibration tests and the functioning of the system during revenue service operations.

## 2 Description of Vibration Monitors and Early Warning System

This section describes the key features of the design and functioning of the VMS and WFD systems.

### 2.1 Vibration Monitors

Nine VMS units that generate alarms are in the UW campus area. The VMS units have two trigger settings, (1) warning, and (2) alarm. The alarm was set at the vibration limit for each building. The goal for the warning was set at 10 decibels



below the exceedance. However, at many VMS units, the warning alarm levels at individual frequencies are set higher to avoid false alarms from ambient vibration sources. Each VMS unit has a backup system with an independent data logger and geophone. The backup system also records train vibration along with the default system. However, the backup system does not send triggers to the train control center unless the default system fails. Thus, the VMS system is a redundant monitoring system designed for very high reliability.

## ***2.2 Wheel Flat Detectors***

The three WFDs comprise the early warning system that allows Sound Transit's operators to implement mitigation measures before trains with wheel flats reach the University area. The WFDs also have two trigger settings, (1) warning, and (2) alarm. The WFDs use an array of accelerometers that trigger appropriate alarms if the measured acceleration levels are above a reference baseline that is built into the WFD system. The WFD alarm settings are calibrated to the VMS vibration alarm settings as discussed later in this document. Similar to the VMS units, the WFDs also have a backup system.

## ***2.3 VMS Monitors Averaging and Windowing Function***

The average train speed in the vicinity of UW campus is 30–35 mph. For a 4-car train, this would result in durations of approximately 8 s for each train passby event at each VMS location. Because the vibration limit for UW extends to as low as the 2 Hz 1/3 octave band, the type of windowing function required to populate each 1/3 octave band bin during an 8-second passby window is critical. The monitors digitize the geophone signals and Fourier transform the time domain data with an 8-second conversion time after windowing the data with a Hamming window, yielding an 0.125 Hz bandwidth resolution. The signals are deconvolved in the frequency domain to compensate for the low frequency roll-off of the geophone. Several overlapping analyses with an 87.5% overlap were energy averaged to provide an effective averaging time of eight seconds, the results of which are then convolved with 1/3 octave frequency responses to obtain 1/3 octave band vibration velocity levels. These data are exported each second and compared with thresholds. The eight-second averaging time is intended to reduce the uncertainty of the measurement of the root-mean-square vibration velocity during train passage. This approach was compared with infinite impulse response 1/3 octave 3-pole Butterworth filters and shown to be in good agreement, within a fraction of a decibel. The choice of the analysis procedure was made by the VMS supplier.

## ***2.4 Relationship Between Train Vibration in the Tunnels and UW Building Vibration***

The VMS systems rely on vibration attenuation estimates (VAE) between the VMS monitoring points and various laboratories. These VAEs were defined by extensive testing on the UW campus. The challenge for the monitoring system is that the low frequency VAEs are poorly known. In fact, so far, only the ground vibration at the 31.5–63 Hz 1/3 octave bands appears to be sufficient to define the VAEs between the tunnel wall monitors and sensitive laboratories. This is to be expected, since the design of the transit system is intended to render ground vibration levels to be below the MIA thresholds, which represent the background vibration at the sensitive laboratories. The VAEs are thus approximate at best, and likely over-predict the ground vibration at sensitive receivers. The VAEs will likely be revised downward with time as data are collected, especially if rail corrugation or excessive roughness develops in the wheels and rails. Presently, ground vibration from operating trains is virtually undetectable in the presence of background vibration at the sensitive laboratories.

## ***2.5 Train-in-Zone***

Both data loggers in each VMS unit continuously record vibration data and send it to the main server. The train-in-zone (TIZ) is a feature implemented in the VMS system that assigns track circuits to each VMS unit and ‘informs’ the main server whether to store the recorded data or to discard them. If the TIZ confirms train occupancy in the track sections assigned to a particular VMS unit, then the main server stores and notifies the train control center of any warnings or exceedances. If there is no train occupancy in the relevant track sections, the data gets discarded. One of the challenges in having many monitors at a terminal station is that there is almost always a train, which can make for long recording sessions even when the trains are not moving. It increases the probability for false alarms from non-train events. Sound Transit developed a more advanced TIZ program after few months of revenue service that would count a moving train as track occupancy and discount any stationary train to reduce false alarms.

## **3 Performance of the WFD System**

The WFD alarm settings are based on a composite of correlation tests using a test vehicle and monitoring of pre-revenue and revenue train recordings for several months. Table 1 shows a summary of WFD alarm settings, including measured WFD data during calibration tests and the number of warnings and alarms during

**Table 1** Summary of alarm settings for the wheel flat detectors

	MLK (WFD-1) embedded track	S lander (WFD-2) ballast & tie track	Pine street (WFD-3) direct fixation track
<i>Measured WFD values during calibration tests (4-car test train with flat wheel, 7 train passbys)</i>			
Test train speed (KPH)	48	32	48
Maximum (Sensor A)	0.036	0.032	0.028
Minimum (Sensor A)	0.021	0.020	0.021
Average (Sensor A)	0.027	0.026	0.025
<i>WFD threshold settings June 2016</i>			
Warnings	0.045	0.045	0.045
Alarms	0.055	0.055	0.055
<i>Typical weekly average number of warnings and alarms during revenue service between March–June 2016</i>			
Warnings	20–25	0	20–25
Alarms	2	0	4
<i>WFD threshold settings between June–September 2016</i>			
Warnings	1	0.5	1
Alarms	0.5	0.5	0.5

*Note* The WFD readings are unitless quantities generated from Cepstrum analysis of the vibration acceleration signal when the train passes over the WFD and is compared to wheel motion signals

revenue service trains. The WFD alarms were set very conservatively (lower levels) during testing and the pre-revenue phase and were carefully revised up before the commencement of revenue service. The goal was to make sure that trains with the risk of causing potential vibration exceedances in the UW campus area are not overlooked; however, overly conservative settings would mean that too many trains are slowed and the train schedule is disrupted. The alarm settings between March and June 2016 resulted in approximately 25 warnings and 4 alarms from revenue service trains. The wheel flat detectors were successful in identifying vehicles with wheel flats. A key observation was that the trains generating WFD alarms did not result in VMS alarms during this time indicating that the WFD alarm settings were still conservative and could be revised upwards. The settings were increased in June 2016 and the number of warnings and alarms reduced as shown in Table 1.

## 4 Performance of the VMS System

There have been 57 alarms and numerous warnings generated by the VMS units during the first year of U-Link Extension revenue service, including 40 alarms in the first three months, and summarized in Table 2. All alarms were generated at low

**Table 2** Summary of alarms from vibration monitoring system since U-link opening

Frequency	6.3 Hz		12.5 Hz						16 Hz			20 Hz		
Monitor#	5-1	5-2	4-1	4-2	4-3	5-1	5-2	5-4	4-1	4-2	4-3	5-1	4-1	4-3
# of Alarms	15	17	5	4	9	1	2	1	9	4	8	1	3	4

frequencies; 6.3, 12.5, 16 and 20 Hz 1/3 octave bands. About 30% of the alarms were generated at multiple VMS units.

### 4.1 Suspected Exceedance Alarm at 6.3 Hz

Fifteen alarms were due to suspected exceedances at 6.3 Hz generated simultaneously by VMS 5-1 and 5-2. The following are the key points about the 6.3 Hz alarms:

- A sample of the time history that generated an alarm at 6.3 Hz is shown in Fig. 3. This time history plot indicates that the vibration levels at 6.3 Hz fluctuate by approximately 20 dB, including some sharp peaks of approximately 40 VdB (without the alarm event).
- The 6.3 Hz vibration levels resulting in alarms were consistently between 50 and 52 VdB at monitor 5-1. For all 6.3 Hz alarm events, the vibration level at monitor 5-1 was approximately 1 dB higher than at monitor 5-2. These observations indicate that the 6.3 Hz alarms are potentially from the same source.
- In the example illustrated in Fig. 3, the alarm event took place at 12:10:10 PM and was more than 1 min away from the closest train event identified by the peaks in the 40 Hz vibration level signature, clearly establishing that the trains did not cause the alarm in vibration at 6.3 Hz.

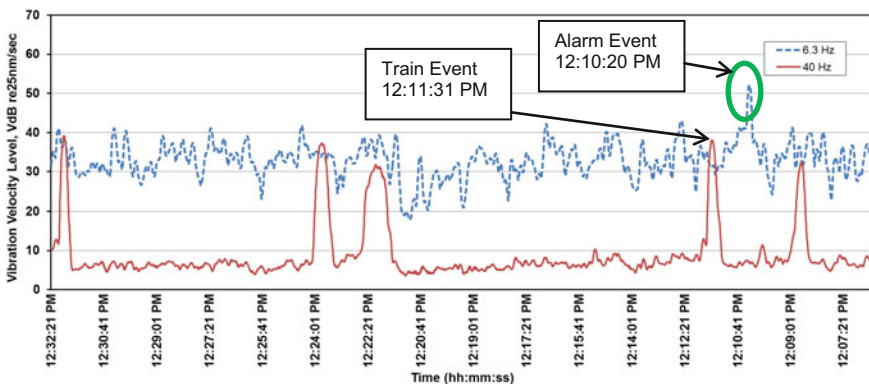


**Fig. 3** Alarm#16, time history of a 6.3 Hz alarm at VMS 5-1

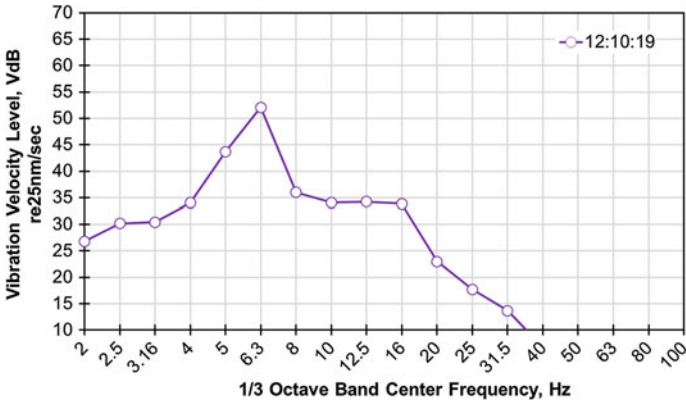


Fig. 4 Vibration spectra of 6.3 Hz alarm

- Figure 4 shows the spectral curve of the alarm event. The 6.3 Hz peak is sharp without any other distinct peak. Also, the vibration level at 40 Hz is less than 10 VdB, confirming that the alarm was not due to a train event. The spectral shape also indicates that the sharp 6.3 Hz peaks are potentially caused by an occasional heavy truck or bus above certain axle loads and speeds. The 6.3 Hz alarms did not occur during typical quiet periods for heavy vehicle traffic such as nighttime or early evenings.

## 4.2 Suspected Exceedance Alarm at 12.5 Hz

Many alarms were due to suspected exceedance at 12.5 Hz that were primarily generated by VMS units 4-1, 4-2 and 4-3. VMS units 5-1 and 5-4 generated one alarm and VMS 5-2 generated two alarms. The following are the key points about the 12.5 Hz alarms:

- A sample of the time history from an alarm generating event at 12.5 Hz is shown in Fig. 5. This time history plot shows that the alarm event lasted more than 20 min and is clearly not due to train movement.
- Figure 6a shows the spectral curve of the alarm event when there was no train and Fig. 6b shows the spectral curve with the train. In both cases the 12.5 Hz shape and level remained unchanged; however, as expected the vibration levels at 40 Hz increased to 40 VdB re 25 nm/s with the trains. This establishes that the alarm event was not caused by the train. In this example of 12.5 Hz alarm spectra, it is noteworthy that the 16 Hz level is about 50 VdB as shown in Fig. 6a, b.

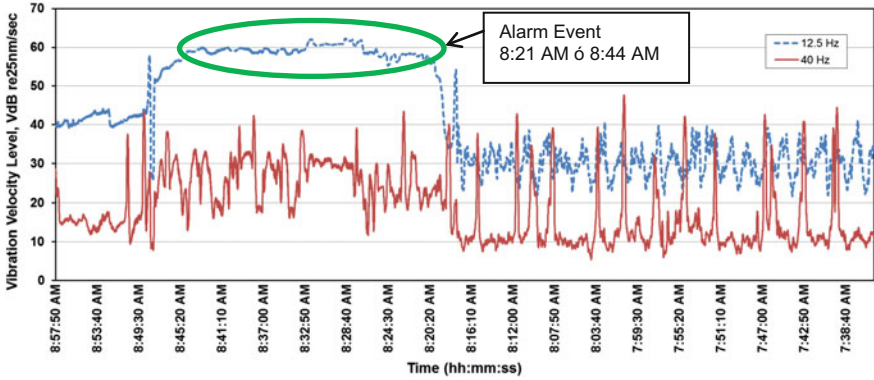


Fig. 5 Alarm#20, time history of a 12.5 Hz alarm at VMS 4-3

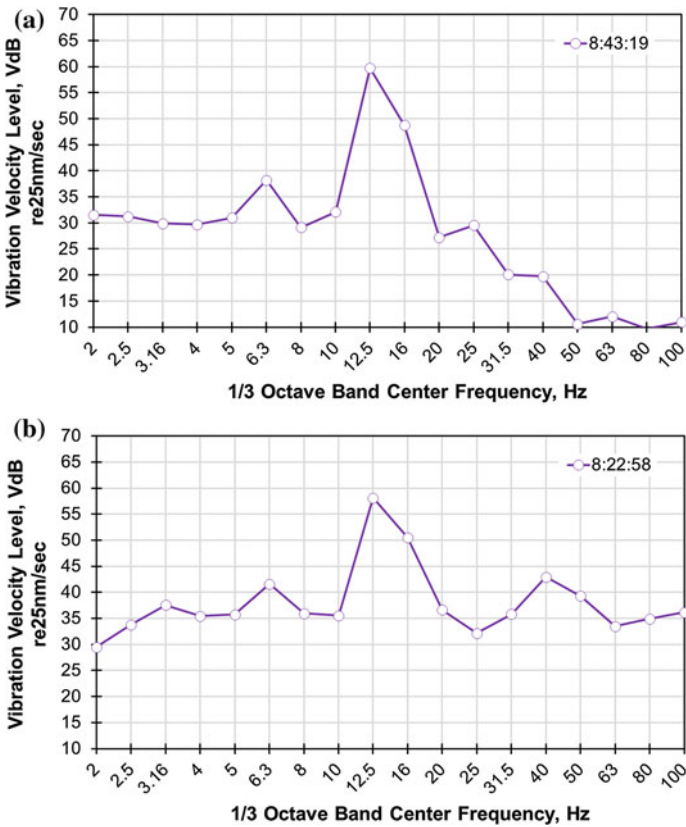


Fig. 6 Vibration spectra of 12.5 Hz alarm a without train b with train

### 4.3 Suspected Exceedance at 16 Hz

Many alarms were due to suspected exceedances at 16 Hz that were primarily generated by VMS units 4-1, 4-2 and 4-3. VMS unit 5-1 generated one alarm.

The following are the key points about the 16 Hz alarms:

- A sample of the time history from a 16 Hz alarm generating event is shown in Fig. 7. This time history plot shows that the alarm event lasted more than 20 min, suggesting that the vibration source was some kind of mechanical equipment such as a pump. This event generated alarms simultaneously at monitors 4-1, 4-2 and 4-3.
- Figure 8 shows the spectral curve of the alarm event. The 12.5 Hz level is also above the remaining spectrum, indicating that the sources exciting monitors 4-1, 4-2 and 4-3 at 16 Hz could also have another complementary source at 12.5 Hz. For example, sump stations comprise a small jockey pump and two large pumps or a combination of a large and a small pump. Another plausible source of vibration is the Montlake Boulevard draw bridge motors that use two different speeds.

### 4.4 Suspected Exceedance at 20 Hz

There were several alarms due to suspected exceedance at 20 Hz that were all generated by VMS units 4-1 and 4-3. A sample of the time history from an alarm generating event at 20 Hz is shown in Fig. 9. This time history plot shows that the alarm event lasted about two minutes. Figure 10 shows the vibration spectra of the 20 Hz alarm. A sharp peak occurs at 20 Hz and a subtle peak occurs at 40 Hz, possibly a second harmonic. The vibration source is suspected to be mechanical equipment, the location of which is unknown.

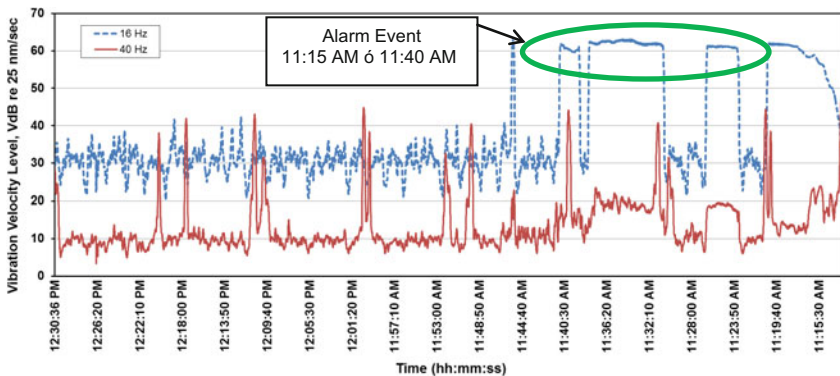


Fig. 7 Alarm#7, time history of a 16 Hz alarm at monitor VMS 4-3

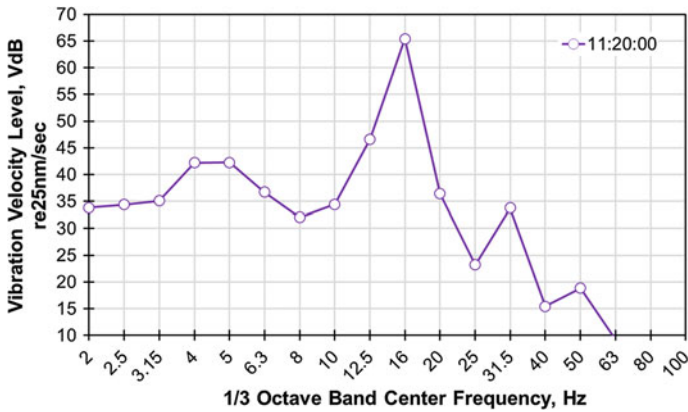


Fig. 8 Vibration spectra of 16 Hz alarm at VMS 4-3

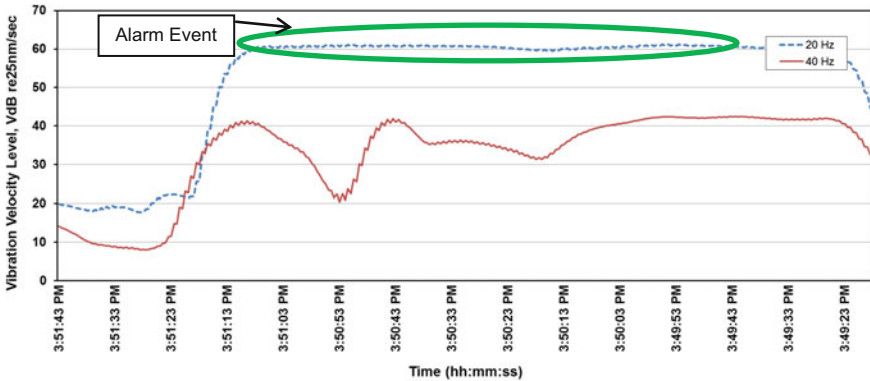


Fig. 9 Alarm#5, time history of a 20 Hz alarm at VMS 4-1

### 4.5 Train Vibration

This section presents the vibration spectra due to train movements at the different monitors when there were no unusual background events with high vibration amplitudes. Figure 11a shows the vibration spectra of the straight through train movement in the northbound (NB) and southbound (SB) directions recorded at VMS 4-2. If rail roughness increases over time, vibration levels would likely increase, probably at 40–60 Hz due to rail corrugation.

Figure 11b shows the vibration spectra for diverging train movements across the double crossover diamond located south of UW Station. The double crossover consists of moveable-point frogs and a flange bearing diamond. Below 25 Hz, the vibration energy from trains did not exceed 35 VdB re 25 nm/s. If the crossover



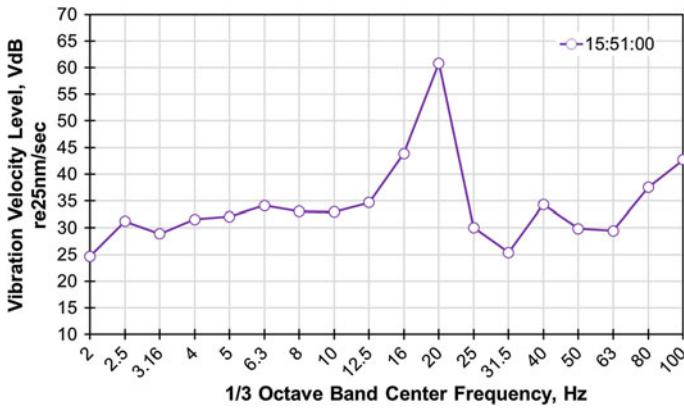


Fig. 10 Vibration spectra of the 20 Hz alarm at VMS 4-1

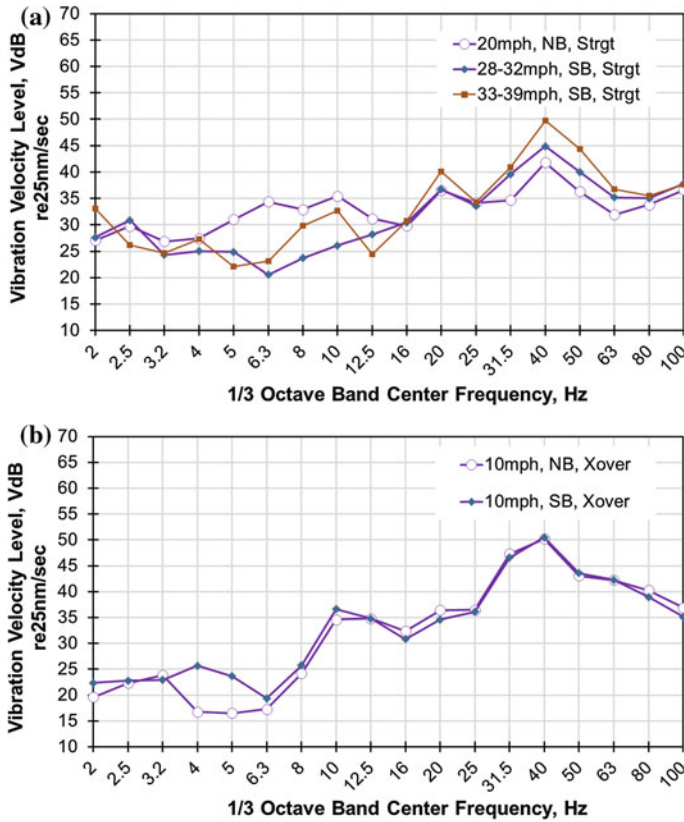


Fig. 11 Vibration spectra of train vibration at a VMS 4-2, and b VMS 5-2

ramp or flange-way wears excessively or is damaged, vibration may increase over a broad range of frequencies. Based on the data presented here, the likelihood of trains causing low frequency vibration exceedances seems negligible, especially for ground rail and well maintained special trackwork. The monitoring system is designed to detect wear or damage of track components and allow maintenance prior to generating vibration in excess of thresholds.

## 5 Conclusions

The following are the key conclusions from the functioning of the VMS and WFD systems during the first year of revenue service on the U-Link system:

- The VMS and WFD systems have met the primary design goal of capturing and notifying all events with vibration levels that are at or in excess of the warning and/or exceedance thresholds.
- Calibrating each WFD's warning and alarm settings to match the most sensitive VMS unit is an iterative process that requires robust data during normal revenue operations. We anticipate that it will require up several years of revenue service before the WFDs are fully optimized.
- All warnings and alarms generated during the first year since commencement of U-Link revenue service were caused by non-train sources at or below 20 Hz.
- The VMS data collected so far establishes that the vibration levels from train events are substantially lower than the thresholds. The levels can be expected to increase if there is substantial long-term degradation in the tracks or the crossover rails. The monitoring system is designed to detect such degradation in time for scheduling maintenance to avoid exceedances. Considering that the monitors are located at 300 foot intervals near the UW campus, the VMS units serve as track health monitors. Long-term trend analysis from the VMS data can be used to demonstrate good maintenance of the rails and fleet wheels, a major concern for the University of Washington.

## References

1. Master Implementation Agreement for Sound Transit Entry to the University of Washington Seattle Campus, June 29 (2007)
2. Amendment to Master Implementation Agreement for Sound Transit Entry to the University of Washington Seattle Campus, June 5 (2014)
3. Gamache, R.: U835 EMI, Vibration and Wheel Flat Detection and Monitoring System, Final Design Document, Prepared for Sound Transit, April 2 (2015)

# The Uncertainty Associated with Short-Term Noise Measurements of Passenger and Freight Trains



C. Weber and L. Zoontjens

**Abstract** When assessing the potential impacts from passenger or freight train operations, it is necessary to undertake noise measurements at representative locations. It is important to recognise that the level of uncertainty associated with these measurements is significant and should be included in the assessment. Rail noise emissions vary each day due to many parameters such as speed, rolling stock type, wagon type, track and wheel condition, minor timetable changes and weather conditions. Measurement data also varies as a result of the type of sound level meter used, measurement locations used and other operator factors. Limited guidance is available which identifies the number of train passby events of each type that are required to obtain a reliable estimate of long-term overall noise levels. Guidance in relation to the uncertainty associated with the measurement of  $L_{Aeq(periode)}$  and  $L_{Amax}$  noise levels from rail traffic is provided in Draft International Standard ISO/DIS 1996-2. However, in the literature this guidance has not been reviewed in the context of Australian conditions and assessment criteria. This paper expands on the information provided in the draft standard via the analysis of noise measurements at a variety of independent sites across the rail network in Sydney Australia. Nine sites are based on unattended measurements undertaken over a continuous period of one week. Two sites are based on unattended measurements undertaken over a continuous period of up to six months. At each site, the standard uncertainty associated with the short-term measurement of five, ten, twenty and sixty train passbys of each type are compared with the longer-term measurement results. The uncertainty results are compared with the default values in the draft standard. Guidance is provided in relation to the reliability of undertaking short-term measurements and the associated uncertainty in utilising this information to calculate long-term noise levels. The paper provides guidance on how the uncertainty associated with varying

---

C. Weber (✉)

Renzo Tonin & Associates, Level 1, 418A Elizabeth Street,  
Surry Hills, NSW, Australia  
e-mail: conrad.weber@renzotonin.com.au

L. Zoontjens

SLR Consulting, 589 Hay Street, Jolimont, WA, Australia  
e-mail: lzoontjens@slrconsulting.com

operating conditions and measurement locations can be accounted for as part of the noise compliance stage (where attended noise measurements are utilised to assess compliance with noise criteria or predictions).

## 1 Introduction

When measuring or assessing the potential impacts from passenger or freight train operations, it is necessary to undertake noise measurements at representative locations. When summarising the overall noise levels measured, it is important to recognise that source noise emissions from rail operations will vary, and that all scientific measurements have some degree of error. These factors lead to uncertainty in the true result. This is particularly important where assessments are to be made against a fixed noise limit.

### *1.1 Uncertainty, Confidence Intervals and Coverage Factors*

Uncertainty is the measure of dispersion or variance that may be expected with a claimed performance value, often represented by the term  $U_{95}$ . The subscript '95' means a 95% confidence interval. It represents the estimated range in which the true value lies for 95 out of 100 repeated events, e.g. a  $U_{95}$  of 5 dB indicates that the true value is expected to be within  $\pm 5$  dB of the estimates provided for 95% of all observations. 95% represents the most common level of preferred confidence for acoustic measurements [1] and is normally defined as the measured level  $\pm 2$  standard deviations (i.e. coverage factor of 2). Reference [2] notes that "Cognizant authorities may set other coverage probabilities. A coverage factor of 1.3 will, e.g., provide a coverage probability of 80%".

### *1.2 Uncertainty of Short-Term Measurements to Quantify Long-Term Measurements*

This paper examines the uncertainty associated with undertaking short-term noise measurements for the purpose of quantifying longer-term overall noise levels. It expands on guidance in relation to the uncertainty associated with the determination of  $L_{Aeq(\text{period})}$  and  $L_{Amax}$  noise levels provided in Ref. [2], based on measurement data obtained at several sites in Sydney, Australia.

Guidance is provided on the number of passenger and freight train passby measurements that are required in order to provide a 95% confidence  $U_{95}$  that long-term noise levels will be within a given tolerance level.

## 2 Measurement Sites and Methodology

### 2.1 Train Types

Unattended noise measurements have been undertaken at eleven independent sites across the rail network in Sydney Australia. Each measurement location includes a mix of passenger and freight train operations.

The passenger trains comprised a mix of electric multiple unit double deck rolling stock classes, including older and newer generation trains. According to the NSW Rail Noise Database [3], source noise levels from older generation trains (S, K and C Sets) are up to 5 dB higher than newer generation trains (A and M Set).

The freight trains comprised up to four diesel-electric locomotives hauling freight, coal or grain wagons with a typical overall length of 250–1500 m. According to Ref. [4], more than 100 locomotive classes are permitted to operate on the NSW rail network, some of which have been operating since the 1950s. More than a 10 dB variation in source noise levels exists between different classes of diesel locomotives and wagons [3].

### 2.2 Measurement Locations and Methodology

For the noise measurements presented in this report, no distinction has been made in relation to the class of passenger rolling stock, freight locomotive or wagon type. The distinction of passenger and freight trains for Sites A to I has been made on the basis of the passby time of the measurement. A measurement duration of less than 40 s is assumed to represent passenger trains, and a measurement duration of 40 s or greater is assumed to represent freight trains. These assumptions form part of the variability in the noise levels measured and this classification methodology is accounted for in the overall uncertainty analysis in Sect. 4.

At eight sites (A to I), measurements were undertaken over a continuous period of nominally one week. At two measurement sites (J and K), noise measurements have been obtained from two permanent noise monitoring stations for a period of 16 and 26 weeks, respectively. A general description of each measurement location, site characteristics and the number of train passbys measured is provided in Table 1. For the purpose of this study, the precise measurement locations are not important. All measurements are free field without significant influence from sound reflections off nearby buildings or structures.

**Table 1** Measurement sites

Site	Number of passenger trains	Number of freight trains	Measurement distance to near track (m)	Approximate track grade	Track curvature (m)
A	539	76	19.0	1 in 75	Straight
B	252	66	9.0	1 in 40	220
C	235	61	10.0	1 in 40	Straight
D	902	110	14.0	1 in 75	250
E	1370	95	7.5	1 in 75	Straight
F	545	123	20.0	1 in 180	550
G	696	150	12.0	1 in 300	550
H	850	128	12.0	1 in 200	300
I	894	113	33.0	Level	Straight
J	4680	936	11.8	1 in 60	280
K	20,800	624	10.8	1 in 40	640

### 3 Summary of Measurement Results

#### 3.1 $L_{Aeq(Period)}$ Noise Levels

##### 3.1.1 Guidance Based on ISO/DIS 1996-2

According to Clause 7.3.1 of Draft International Standard ISO/DIS 1996-2 [2] and Cook [5], the Experimental Standard Deviation of the Mean (ESDM)<sup>1</sup> associated with the calculation of overall  $L_{Aeq(Period)}$  noise levels from the  $L_{AE}$  of individual passbys can be estimated on the basis of the following formula:

$$ESDM = C/\sqrt{n} \quad (3.1)$$

where  $n$  is the number of measurements and  $C$  represents the standard deviation ( $\sigma$ ) of the  $L_{AE}$  (single event sound exposure level) measurements.

As can be seen from Sect. 3.1.5, Formula 3.1 underestimates the true uncertainty for noise measurements expressed in decibels.

Reference [2], notes that  $C$  is estimated to be 10 dB if the sampling is made regardless of the operating conditions and can be lowered to 5 dB if the sampling takes into account the relative occurrence of the different train classes (freight, passenger, etc.). The standard further notes that a more accurate ESDM can be determined from the statistics of direct  $L_{AE}$  measurements of individual passbys (this paper presents this approach).

<sup>1</sup>Note that in Draft International Standard ISO/DIS 1996-2, The ESDM is referred to as the standard uncertainty of the source ( $u_{sou}$ ).

### 3.1.2 Measurement Uncertainties

A summary of the measurement results is provided in Table 2 (for passenger trains) and Table 3 (freight trains). The standard deviation ( $\sigma$ ) of the  $L_{AE}$  measurements (column 2) is calculated for the full data set of the passenger and freight train passbys at each measurement location. Note that  $\sigma$  represents the standard uncertainty of a single passby event and can be compared directly with the 5 dB estimate for C in Ref. [2].

In columns 3–7, a calculation of the Experimental Standard Deviation of the Log Mean (ESDLM) is made based on 5, 10, 15, 20 and 60 passenger or freight passbys. This was determined by log averaging consecutive passby events ( $\overline{L_{AE}}$ ) and repeating this analysis for the entire data set. The ESDLM was evaluated on the basis of 26 weeks of 1-week long measurement results for Site K and 16 weeks of 1-week long measurements results for Site L. The number of train passbys at Sites K and L was held constant for each week.

### 3.1.3 Calculation of $L_{Aeq(Period)}$ Noise Levels

The  $\overline{L_{AE}}$  noise measurements can be utilised in conjunction with the number of trains ( $n$ ) and the duration of the assessment period ( $T_{period}$ ) to calculate the  $L_{Aeq(period)}$  noise level for each train type according to Eq. 3.2.

$$L_{Aeq(period)} = \overline{L_{AE}} + 10 \log_{10}(n) - 10 \log_{10}(T_{period}) \quad (3.2)$$

### 3.1.4 Discussion of Measurement Uncertainties

Noise emissions from individual train passbys can be highly variable due to many parameters including speed, rolling stock type, wagon type, wheel condition and other intermittent effects (i.e. wheel flanging or squeal). On this basis, calculating the  $L_{Aeq(period)}$  noise level on the basis of a small number of passby events presents a risk that the small data set may not be representative of the long term noise levels. To highlight this point, the Maximum Range values in Tables 2 and 3 represent the maximum observed range in  $L_{Aeq(period)}$  noise levels (i.e. highest minus lowest) that were calculated from the smaller sample sets.

For example, with reference to Table 2 and Site D, it can be seen for the full data set (902 passenger train passbys), that  $\sigma$  is 4.4 dB. This means that that probability of any single passenger train passby having an  $L_{AE}$  noise level within  $\pm 4.4$  dB of the full data set average is 68% (representing 1 standard deviation). For 95% confidence, this range would be  $\pm 8.8$  dB.

If the  $L_{AE}$  values from 5 consecutive passenger train passbys ( $n = 5$ ) are measured and log averaged, then on the basis of the measurement results, the ESDLM

**Table 2**  $L_{Aeq}$  measurement results—passenger trains

Site	$\sigma$ of full data set (dB)	ESDLM ( $\sigma$ of $\overline{L_{AE}}$ ) for reduced data set (dB)					Maximum range in $\overline{L_{AE}}$ noise levels for reduced data set (dB)				
		n = 5	n = 10	n = 15	n = 20	n = 60	n = 5	n = 10	n = 15	n = 20	n = 60
A	6.3	2.5	1.6	1.3	1.2	0.7	16	10	6	5	3
B	5.0	3.6	3.1	2.7	2.5	1.2	21	16	14	12	6
C	5.9	3.0	2.3	2.0	1.6	0.7	14	10	8	7	3
D	4.4	2.7	2.2	2.0	1.9	1.4	16	13	11	10	6
E	3.4	2.4	2.0	1.7	1.6	1.0	15	11	9	7	4
F	3.8	2.3	1.9	1.7	1.5	0.9	14	10	8	8	4
G	4.9	2.4	1.8	1.6	1.4	0.9	20	16	13	11	5
H	4.1	2.4	2.0	1.7	1.6	1.1	20	17	13	10	5
I	4.4	2.3	1.6	1.4	1.2	0.9	12	8	7	5	3
J	4.2	n = 182, ESDLM = 1.0 dB					n = 182, Range = 4 dB				
K	3.0	n = 800, ESDLM = 0.4 dB					n = 800, Range = 1.3 dB				

**Table 3**  $L_{Aeq}$  measurement results—freight trains

Site	$\sigma$ of full data set (dB)	ESDLM ( $\sigma$ of $\overline{L_{AE}}$ ) for reduced data set (dB)					Maximum range in $\overline{L_{AE}}$ noise levels for reduced data set (dB)				
		n = 5	n = 10	n = 15	n = 20	n = 60	n = 5	n = 10	n = 15	n = 20	n = 60
A	2.9	1.5	1.1	0.8	0.6	–	8	5	3	2	–
B	8.7	6.2	4.2	2.7	2.2	–	26	20	11	6	–
C	4.4	3.3	2.6	2.3	1.8	–	12	9	9	6	–
D	6.6	4.1	3.1	2.4	2.3	1.0	15	13	11	7	3
E	4.0	2.0	1.3	0.9	0.7	–	11	6	4	4	–
F	5.6	3.2	2.2	1.7	1.4	0.5	13	10	8	6	2
G	4.8	2.6	1.8	1.5	1.3	0.4	13	7	6	5	2
H	7.0	3.5	2.4	1.8	1.3	0.5	18	10	7	6	2
I	4.5	2.3	1.9	1.5	1.1	0.2	10	8	7	5	1
J	4.5	n = 35, ESDLM = 0.9 dB					n = 35, Range = 4 dB				
K	3.6	n = 20, ESDLM = 1.5 dB					n = 20, Range = 6 dB				

Note Where the total number of freight train passbys is less than 100, statistical results for n = 60 passbys are not presented

( $\sigma$  of  $\overline{L_{AE}}$ ) is reduced to 2.7 dB. As the number of consecutive measurements increases (n = 5, 10, 15, etc.), ESDLM decreases as expected.

For Site D, it can also be seen that for 5 consecutive passbys the maximum range in  $\overline{L_{AE}}$  noise levels observed was 16 dB. This range of 16 dB (the difference between the highest and lowest  $\overline{L_{AE}}$  noise levels) approximately represents  $\pm 3$  standard deviations ( $6 \times 2.7 \text{ dB} = 16.2 \text{ dB}$ ). As the number of consecutive measurements increases, the maximum range in  $\overline{L_{AE}}$  noise levels decreases.



### 3.1.5 Comparison of Measurement Results with ISO/DIS 1996-2

Rearranging Formula 3.1, it can be seen that the C can be defined in terms of the ESDM and the number of measurements (n). On the basis of the measurement data in Table 2, the ESDLM of the passenger train noise levels is presented in Fig. 1 and compared with the default  $C = 5$  and  $C = 10$  values from Ref. [2].

It can be seen from Fig. 1 that the measured C values from all but two sites (Site B and Site D) lie within the 5–10 dB range. Measurement data which follow Formula 3.1 (based on ESDM) would be represented in the figure as a horizontal line (with C constant). For the measurement results (based on ESDLM), there appears to be a general trend for C to increase marginally as the number of measurements (n) increases. This observation is consistent with Ref. [6] which investigates the uncertainty of normally distributed dB power sums. For a  $\sigma$  of 5 dB, the variation in C with the number of measurements (Fig. 1) has been derived from the results in Ref. [6].

As Formula 3.1 is based on the arithmetic average of decibel noise levels, rather than the log average, Formula 3.1 underestimates the uncertainty of  $\overline{L_{AE}}$  noise levels as the number of measurements increases. On this basis, it is recommended that the uncertainty of the source noise levels is based on measurements of ESDLM (or the uncertainty of normally distributed dB energy addition if the  $\sigma$  of the full data set is to be used).

## 3.2 $L_{Amax, 95\%}$ Noise Levels

In several states of Australia, the noise assessment criteria for rail operations includes a requirement for maximum noise levels to be evaluated based on the  $L_{Amax, 95\%}$  noise parameter. This is generally described as the maximum noise levels not exceeded by 95% of train passbys in the relevant assessment period [7].

One common method of evaluating the  $L_{Amax, 95\%}$  is based on a statistical approach which assumes that  $L_{Amax}$  noise levels are normally distributed. Annex H of Ref. [2] includes a polynomial function which relates the percentage exceedance to the number of standard deviations above or below the arithmetic mean. For this approach, the  $L_{Amax, 95\%}$  is estimated based on the arithmetic mean of the  $L_{Amax}$  passby events plus 1.61 standard deviations. This figure is close to the 1.64 value commonly found in standard Normal Distribution tables [8].

Another approach often implemented within a spreadsheet program such as Microsoft® Excel is the percentile function method. Using this method, the 95th percentile will always be less than the maximum value measured.

The view of the authors' is that the percentile function method is the preferred approach for evaluating  $L_{Amax, 95\%}$  noise levels as this method more closely represents the definition of this noise parameter in Australian guidelines.

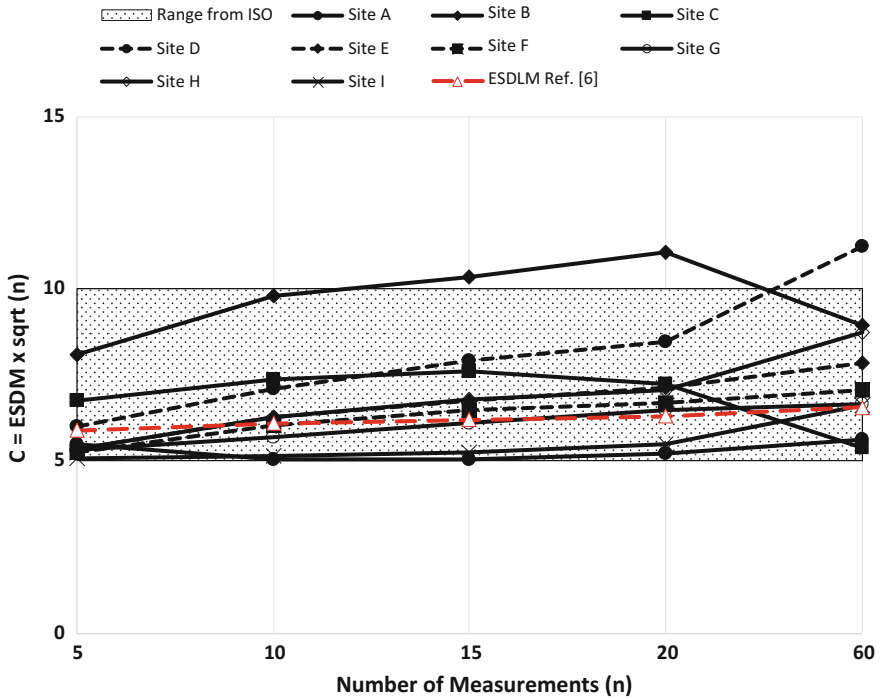


Fig. 1 Comparison of measured standard uncertainties with ISO/DIS 1996-2

Consistent with guidance provided in Ref. [2], measurement results at all sites indicated higher uncertainties for  $L_{Amax}$  levels compared with  $\overline{L_{AE}}$  levels. The  $L_{Amax, 95\%}$  noise assessment parameter is thus more volatile than the  $\overline{L_{AE}}$  and  $L_{Aeq(periode)}$  noise assessment parameters and has a higher level of measurement uncertainty.

## 4 Implications for Measurement Surveys and Compliance Monitoring

### 4.1 Overall Measurement Uncertainty and Budgeting

When evaluating overall noise levels associated with measurement surveys and comparing these results with predictions and/or design criteria, the uncertainty associated with the measurement equipment, weather conditions, assessment locations, measurement methods and residual noise needs to be considered.

Evaluation of the overall uncertainty is based on the Guideline for the Uncertainty of Measurement (GUM) [9]. The preferred uncertainty budget method [2] has been utilised to identify all major sources of uncertainty.

## 4.2 Uncertainty Budget Approach

The GUM [9] provides detailed guidance on how to calculate the  $U_{95}$ , the differences between Type A (practical) and Type B (theoretical) evaluations, distribution types (e.g. normal, triangular, rectangular, etc.), ranges, etc., and how to evaluate the combined uncertainty. Table 4 provides a summary of the uncertainty budget calculations relating to noise compliance measurements. In the example given, the uncertainty of the source noise levels  $u_{\text{sou}}$  ( $\sigma$  of  $\overline{L_{AE}}$  or  $\sigma$  of  $L_{A\text{max}, 95\%}$ ) is the largest contributor to the combined uncertainty.

The example illustrates that for a  $U_{95}$  with the calculated  $L_{A\text{eq}(\text{period})}$  noise levels within  $\pm 3.0$  dB of the true value,  $u_{\text{sou}}$  must be 1.2 dB. Tables 2 and 3 indicate that the number of measurements required to reduce the  $\sigma$  of  $\overline{L_{AE}}$  noise levels to 1.2 dB or less is typically 20 passbys or more. The number of passbys required to achieve this result is not constant, but varies between measurement sites and the operating conditions of the rolling stock.

For the  $L_{A\text{max}, 95\%}$  noise parameter, measurement results indicated that the  $U_{95}$  is unlikely to be better than  $\pm 5.0$  dB. This was based on a  $\sigma$  of  $L_{A\text{max}, 95\%}$  of 2.3 dB. Typically, this equates to approximately 20 passbys or more.

## 4.3 Recommendations for Reducing the Level of Measurement Uncertainty

All scientific measurements have some degree of error. Even when measurements are made of a steady noise source in a free field, the standard uncertainty of a Class 1 sound level meter is 0.5 dB, which corresponds to a  $U_{95}$  of  $\pm 1$  dB.

With reference to the example uncertainty budget in Table 4, the overall uncertainty can be reduced most effectively by focusing on the parameters with the largest uncertainty. In this example, the uncertainty of the source (train passby results) and the train passby detection method.

In cases where short-term measurements are required in order to calculate  $L_{A\text{eq}(\text{period})}$  noise levels, attended measurements provide the most effective means of reducing the level of uncertainty. Omitting operator blunders, attended measurements ensure that extraneous noise from non-rail sources and adverse meteorological conditions are excluded from the measurement results. Attended measurements can also effectively identify train types, speeds, direction and noise characteristics that may not form part of the assessment (e.g. horn noise). In the

**Table 4** Example uncertainty budget, dB

Parameter/ quantity	Standard uncertainty $u_j$ (dB)	Distr. type	Sensitivity coefficient $c_j$ (dB)	Uncertainty contribution $c_j u_j$ (dB)	Comments
Sound level meter	$u_{slm}$ 0.5	Normal	1	0.5	Class 1, Ref. [2, 11]
Weather conditions	$u_{met}$ 1.0	Triangular	$1/\sqrt{6}$	0.4	Estimated uncertainty based on engineering judgment and small measurement distance ( $<50$ m)
Meas. location	$u_{mea}$ 0.0	Normal	1	0.0	No correction for free field based on Ref. [2]
Train passby detection method	$u_{detection}$ 1.0	Rect.	$1/\sqrt{3}$	0.6	Maximum error of $\pm 1$ dB assumed with rectangular distribution
Source	$u_{sou}$	Normal	1	1.2	$\sigma$ associated with number of measurements ( $n$ ) (from ESDLM). Example value of 1.2 used here
Residual noise	$u_{resid}$ 0.0	Normal	1	0.0	Residual noise assumed to have nil influence at small measurement distances
Rounding to nearest dB	$u_{rounding}$ 0.5	Rect.	$1/\sqrt{3}$	0.3	Final noise level rounded to nearest dB
Combined standard uncertainty				1.5	From ISO GUM [9]
$u(L_m) = \sqrt{\sum_1^n (c_j u_j)^2}$					
Expanded uncertainty for $U_{95}$ (95% confidence)				3.0	For 95% confidence that calculated $L_{Aeq(periode)}$ noise level is within $\pm 3.0$ dB of the true value

context of compliance measurements, short-term attended measurements can also be efficiently undertaken at many locations across project areas.

Automated train detection systems can be utilised effectively if they are able to accurately identify the type of rolling stock and exclude extraneous noise from non-rail sources and adverse weather. Large sample sizes associated with automated systems assist in reducing the level of measurement uncertainty. Measurement uncertainty can also be reduced by categorising rolling stock classes with a similar noise profile.

The assessment location can have a significant influence on the measurement uncertainty. Free field measurements undertaken close to the railway corridor reduce the level of measurement uncertainty. When measurements are undertaken near building facades, in shielded locations or at large distances, additional uncertainties must be accounted for (refer Ref. [2]).

#### ***4.4 Uncertainties Associated with Compliance Monitoring***

On most projects, noise monitoring is required to verify if operational noise levels comply with the project criteria. If compliance measurements are to be undertaken in accordance with, for example Ref. [2] or ISO 3095:2013 [10], this requires the uncertainty to be quantified. At any particular location, the measured noise levels will have a  $\pm$  tolerance based on the measurement uncertainty with an associated confidence level. For the examples provided in this paper, this could be for example,  $\pm 3$  dB for  $L_{Aeq(\text{period})}$  noise levels or  $\pm 5$  dB for  $L_{Amax, 95\%}$  noise levels, both with a confidence level of 95%.

When comparing the results of noise measurements with environmental noise limits, it is often not clear whether the noise limits include or exclude a compliance tolerance. The required confidence levels are also not often stated. Consider an example where the project noise criterion is 60 dBA and no other guidance is provided. If the measured noise level is determined to be 59 dBA  $\pm 3$  dB with a confidence level of 95%, it is inconclusive whether the measurements comply with or exceed the criterion (Ref. [5]). For this example, uncontested compliance would only be achieved if the measured noise level was 57 dBA or less.

An example approach used on a project in Sydney involved noise measurements at several independent locations. By examining the measurement results from multiple locations, it was possible to examine whether there was a clear trend for the measured noise levels to be higher or lower than the noise criterion and predicted noise levels. This approach allowed for locations with inconclusive results to be accepted if the average noise levels across all sites complied with the criterion level or were below the predicted levels.

#### ***4.5 Worked Example for Mixed Passenger/Freight Train Operations***

This example considers a subset of the  $L_{AE}$  measurement results from one track at Site J. Measurements were undertaken of 20 passenger and 20 freight train passbys. The  $\sigma$  of  $\overline{L_{AE}}$  for each data set is shown in Table 5. The ESDLM ( $\sigma$  of  $\overline{L_{AE}}$ ) has been interpolated from Ref. [6] with  $n = 20$ .

**Table 5** Noise levels and uncertainties for passenger and freight train example

Train Type	$\overline{L_{AE}}$ Noise level (dBA)	$\sigma$ of full data set (dB)	ESDLM ( $\sigma$ of $\overline{L_{AE}}$ ) for n = 20 (dB)	Number of trains in 24 h	Calculated $L_{Aeq(24hour)}$ noise level (dBA)
Passenger trains	93.3	4.2	1.13	26	58.1
Freight trains	107.5	4.5	1.23	5	65.1
Overall	–	–	–	–	65.9

In a typical day, there are 26 passenger train passbys and 5 freight train passbys. The  $L_{Aeq(24hour)}$  contribution from passenger and freight trains is determined from Formula 3.2 to be  $L_{Aeq(24hour)}$  66 dBA (rounded to nearest dB). The standard uncertainty of the  $L_{Aeq(24hour)}$  noise level (1.1 dB) is estimated from Formula 4.1 (from Ref. [2]).

$$u_{Leq,ref} = \sqrt{\sum_{i=1}^n \left| \frac{N_{ref,i} 10^{0.1\overline{L_{E,i}}}}{\sum_{i=1}^n N_{ref,i} 10^{0.1\overline{L_{E,i}}} \right| u_{L_{E,i}}^2} \tag{4.1}$$

Substituting the calculated standard measurement uncertainty of 1.1 dB into the source uncertainty ( $u_{sou}$ ) row of Table 4, the combined standard uncertainty of the measurement is 1.4 dB. For a coverage factor of 2 for  $U_{95}$ , the calculated  $L_{Aeq(24hour)}$  noise level results is expressed as 66 dBA  $\pm$  2.8 dB with a confidence level of 95%.

## 5 Conclusions and Recommendations

The measurement results presented in this study identify that the variability of the source noise levels from passenger and freight train operations represent the greatest source of uncertainty in the noise measurement chain. The uncertainty associated with train noise is not constant, but varies on the basis of operating conditions at each site. Uncertainty in the source levels can be minimised by increasing the number of averages in the data set, attended monitoring, improved train detection methods, excluding extraneous events and accurately categorising train types with similar noise characteristics.

The measured  $\sigma$  of passenger and freight train  $L_{AE}$  noise levels was approximately 5 dB and generally consistent with guidance provided in Draft International Standard ISO/DIS 1996-2. When evaluating the  $\sigma$  of log average  $L_{AE}$  noise levels ( $\overline{L_{AE}}$ ) for 5, 10, 15, 20 and 60 passbys, the ESDM formula in Draft International Standard ISO/DIS 1996-2 (Eq. 3.1) was found to under-estimate the source

uncertainty. Evaluation of source uncertainty based on normally distributed dB power sums (Ref. [6]) is preferred.

The source uncertainty associated with the measurement of  $L_{Amax, 95\%}$  noise levels is higher than for  $\overline{L_{AE}}$  noise levels. This observation is consistent with guidance provided in Draft International Standard ISO/DIS 1996-2.

For the measurements in this study, there is a 95% confidence that the calculated noise levels are within  $\pm 3$  dB of the true  $L_{Aeq(Period)}$  noise levels when at least 20 train passbys of each type under the same operating conditions are measured. For the  $L_{Amax}$  assessment parameter, the uncertainty increases to approximately  $\pm 5$  dB for the same number of train passbys.

As measurement uncertainties are more frequently quantified by practitioners, additional guidance is required in relation to setting of noise criteria, compliance tolerances and confidence levels. This is to minimise situations where it is inconclusive whether measurement results are above or below the criterion. One approach used on a project in Sydney involved noise measurements at several independent locations and investigating whether there was a clear trend for the measured noise levels to be higher or lower than the noise criterion and predicted noise levels.

## References

1. Brinkmann, K. et al.: Treatment of Measurement Uncertainties in International and European Standards on Acoustics, Acoustique & Techniques No. 40, "Uncertainty-Noise" Le Mans (2005)
2. ISO/DIS 1996-2: Acoustics—Description, measurement and assessment of environmental noise—Part 2: Determination of environmental noise levels
3. Transport for NSW, 2015.: The Rail Noise Database. [Online] Available at: <http://www.asa.transport.nsw.gov.au/ts/asa-standards>. Accessed 1 June 2016
4. Schulten, C., Weber, C., Croft, B., Hanson, D.: Considerations in modelling freight rail noise. *Acoust. Aust.* **43**, 251–263 (2015)
5. Cook, R.: Assessment of Uncertainties of Measurement for Calibration & Testing Laboratories—Appendix IX Assessment of Compliance with Specifications. National Association of Testing Authorities, Australia (2002)
6. Nasell, I.: Some properties of power sums of truncated normal random. *Bell Syst. Tech. J.* **46** (9) (1967)
7. NSW Environment Protection Authority: Rail Infrastructure Noise Guideline (2013)
8. Walpole, R., Myers, H.: Probability and Statistics for Engineers and Scientists (5th ed.)—Appendix A.3, Macmillan Publishing Company (1993)
9. ISO/IEC Guide 98-3, Uncertainty of measurement—Part 3: guide to the expression of uncertainty in measurement (1995)
10. ISO3095:2013: Acoustics—railway applications—measurement of noise emitted by rail-bound vehicles
11. Payne, R.: Uncertainties associated with the use of a sound level meter. National Physics Laboratory (UK) Report DQL-AC 002 (2004)

# Rail Ground-Borne Noise and Vibration Prediction Uncertainties



C. Weber and P. Karantonis

**Abstract** On projects where there is limited or only high-level information relating to source, path and receiver components, the uncertainty associated with ground-borne noise and vibration predictions can be large and prediction uncertainties of up to 10 dB(A) have been reported and sometimes applied as a safety factor (engineering margin) on underground railway projects. However, this simplistic and somewhat ad hoc approach is not well founded quantitatively. Furthermore, during the detailed design stage of projects, such large safety factors can be very costly in terms of the required mitigation measures. The uncertainty associated with some modelling input parameters can be quantified and minimised via repeated measurements, however many other parameters and the uncertainty associated with predictions can only be established via published data or engineering judgement. On a recent underground railway tunnel project, a quantitative approach was used with the aim of improving estimates of prediction uncertainties and to better advise the design team of the level of design risk associated with the predictions. Field measurements were also utilised to reduce the uncertainty associated with the ground-borne noise and vibration predictions. Prediction uncertainties were determined on the basis of the methodologies described in the ‘Guide to the expression of uncertainty in measurement’ (GUM) and by establishing an uncertainty budget for each part of the ground-borne noise and prediction process (source, path and receiver). For each modelling input parameter (or source of uncertainty), an estimate of the likely range (minimum and maximum) of values was made on the basis of measurement results, published data and engineering judgement. This paper presents the uncertainty budget calculations where for each parameter, an estimate of the standard uncertainty (uncertainty contribution)

---

C. Weber (✉) · P. Karantonis  
Renzo Tonin & Associates, Level 1, 418A Elizabeth Street,  
Surry Hills, NSW, Australia  
e-mail: conrad.weber@renzotonin.com.au

P. Karantonis  
e-mail: peter.karantonis@renzotonin.com.au



has been made on the basis of the half range, the probability distribution and associated distribution divisor. This paper focuses on the results and outcomes at a representative receiver above the railway tunnel which was selected to establish and illustrate the uncertainties in the modelling predictions. The combined standard uncertainty at this location was calculated at 2.5 dB(A) for the source parameters, 2.0 dB(A) for the path parameters and 2.2 dB(A) for the receiver parameters. The combined standard uncertainty for the whole prediction path was calculated to be 3.9 dB(A). A Monte Carlo simulation with 100,000 iterations was also undertaken to provide an independent calculation of the combined standard uncertainty.

In summary, the prediction uncertainty analysis found:

- the predicted ground-borne noise levels are expected to lie within  $\pm 3.9$  dB(A) [ $\pm 1\sigma$ ] of the mean with 68% confidence;
- by adding an engineering margin of  $1\sigma$  or 3.9 dB(A) to the predicted noise level, the probability of the actual (or true) noise level being less than the predicted noise level is 84%, or conversely, the risk that the actual noise level will be higher than the predicted noise level is 16%; and
- for a 90 and 95% confidence that the actual (or true) noise level will be less than the predicted noise level, the following engineering margins should respectively be added to the modelling results: 5.0 and 6.4 dB(A).

## 1 Introduction

### 1.1 *Railway Ground-Borne Noise and Vibration*

Ground-borne noise and vibration (GBNV) modelling has been undertaken for a recent railway tunnel project, based on the guidance contained in International Standard ISO14837-1:2005 [1]. The standard provides guidance in relation to the key factors to be considered when predicting GBNV for rail operations and guidance on modelling methods. Three key factors are identified in the propagation of GBNV, and comprise:

1. source vibration levels occurring at the wheel-rail interface and supporting track form,
2. vibration transferred between the tunnel and the ground surface via the surrounding ground, and
3. vibration levels occurring within the building and associated ground-borne noise levels.

For underground railways, vibration is transmitted through the track structure, through the ground mass and into building structures. This vibration has the potential to be perceptible to building occupants as tactile vibration but is usually manifested as ground-borne noise.

The extent of vibration is influenced by several physical aspects such as: mass of train (axle load and unsprung mass); train speed and length; condition of rail surface (e.g. alignment, roughness and defects such as corrugations etc.); condition of wheels (e.g. roughness, flats or other wheel defects etc.); type of track structure and form (e.g. stiffness or softness of rail track bed and fasteners, tunnel type, etc.); ground type between tunnel and receiver buildings; distance between tunnel and receivers, tunnel depth and construction type of receiver buildings.

## ***1.2 Modelling Parameters and Uncertainties***

The standard [1] identifies three primary methods for predicting ground-borne noise and vibration. These include parametric models (algebraic and numerical solutions), empirical models of various types, and semi-empirical models, which involve a combination of parametric and empirical components.

The modelling for this project was based on a combination of measurement data obtained from an underground railway line with similar ground conditions, with interpolation and extrapolation of these results for situations where different source, ground or receiver conditions occurred. Where corrections were required, these were calculated using a variety of parametric and empirical methods. The GBNV prediction algorithms had been previously validated via field measurements on another underground rail scheme.

The calculated GBNV along an underground rail corridor are based on numerous parameters and assumptions considered during the design phase. Some parameters can be easily quantified with a good degree of certainty, while other parameters can only be estimated based on very little available data and information, causing these to have lower certainty.

For the subject rail tunnel, the parameters quantified and used in the predictions are presented in Table 1. An estimate of the prediction uncertainties was undertaken in order to quantify and advise the design team of the level and range of design risks that are associated with the rail GBNV predictions.

It is important to recognise that all scientific predictions (and measurements) have some degree of error. Therefore, when predicting the potential impacts from GBNV from underground rail operations, there are errors or uncertainties that will occur with predictions. Prediction uncertainties were determined on the basis of the methodologies described in the GUM [2].

For each modelling input parameter (or source of uncertainty), an estimate of the likely range (minimum and maximum) of values was made on the basis of field measurement results, published data and engineering judgement. An uncertainty budget was established for each part of the ground-borne noise and prediction process (refer Table 1), based on guidance in Ref. [3].

**Table 1** Modelling parameters and description of uncertainties

No.	Modelling parameters	Description of uncertainty
<i>Source parameters</i>		
1	Source level measurement resolution	Error associated with rounding up or down measurement results to the nearest decimal place
2	Variation in source vibration levels between sites	Range based on measurement results at several locations in similar rail tunnels
3	Measurement equipment uncertainties	Error associated with measurement instruments used in the source vibration measurements
4	Measured speed variation	Accuracy of train speed measurements undertaken for the source vibration measurements
5	Predicted rail roughness variation	Assumed $\pm 2.5$ dB variation in rail roughness compared with levels compliant with ISO 3381 [4]
6	95th percentile correction	Assumed standard deviation of source variance for 95% of train passbys—assumed between 2 to 4 dB. For this project, noise compliance was assessed on the basis of the 95th percentile (highest 1 in 20) passby noise level
7	Logarithmic summation errors when calculating overall dB(A) levels	Previous measurements indicate logarithmic sum of 1/3 octave band spectra measured in the field are on average 0.5 dB(A) higher than low-frequency band limited L <sub>Amax</sub> , slow levels, but found to vary from 0 to 1 dB(A)
<i>Path parameters</i>		
8	Train speed variation	Assumed speed variation of actual train speeds +0%, -5%
9	Train speed relationship	Assumed variation from 15 log to 25 log [5–7]
10	Fastener corrections	Assumed $\pm 2$ dB variation in calculation of insertion loss of proposed fasteners for the project
11	Stiffness variations	Assumed variation in overall track stiffness due to production tolerances
12	Rail vehicle unsprung mass variation	Attenuation varies depending on unsprung mass of rail vehicles proposed to be used on the line
13	Frequency band corrections	Potential error if path correction spectra is shifted $\pm 1/3$ octave band
14	Ground conditions from source to receiver	Variation in excess attenuation values per 10 m distance between tunnel and receiver on ground surface
15	Attenuation calculation method—source to receiver	Error associated with calculation method of attenuation between source and receiver—two different methods utilised to estimate range
<i>Receiver parameters</i>		
16	Distance calculation error	From ground contour maps, assumed accuracy of $\pm 1$ m vertically at receiver locations
17	Coupling losses and building amplifications	Standard deviation of coupling loss and amplification values determined from field measurements at several locations
18	Conversion from vibration to noise levels	Based on [6, 7]

## 2 Uncertainty, Confidence Intervals and Coverage Factors

This paper examines the uncertainty associated with undertaking GBNV predictions. To illustrate the methodology and procedure followed, a representative receiver above the railway tunnel was selected to establish uncertainties in the modelling predictions.

The GUM [2, 3] provides detailed guidance on how to calculate the  $U_{xx}$ , the differences between Type A (statistical) and Type B (any other non-statistical means) evaluations, distribution types (e.g. normal, triangular, rectangular, etc.), ranges, etc., and how to evaluate the combined uncertainty.

A Type A uncertainty analysis is typically based on determining the standard deviation (standard uncertainty) of measurement results. A Type B uncertainty analysis involves estimating the uncertainty of the input parameter on the basis of published data, calculations, engineering judgement or common sense. Type A and Type B analyses are considered in this example.

For some Type B evaluations, it is only possible to estimate the upper and lower limits of uncertainty. It may then be assumed that either the value is equally likely to fall anywhere in between, (i.e. a rectangular or uniform distribution) or that there is a greater chance that the value will fall close to the mean of the possible data range (i.e. a normal or triangular distribution). Other distribution types are also possible.

### 2.1 Uncertainty Budgets

A summary of the uncertainty budget calculations is provided in Table 2. For each GBNV modelling input parameter, an estimate of the standard uncertainty (uncertainty contribution) has been made.

For some input parameters (e.g. speed variations and unsprung mass), the minimum and maximum assumptions which are utilised to establish the range in possible values must be converted into decibels before the uncertainties can be combined. Thus a 5% change in the accuracy of train speed measurement was determined to be equivalent to a 0.4 dB change in GBNV levels.

Individual standard uncertainties can be combined validly by ‘summation in quadrature’ (also known as ‘root sum of the squares’), which is called the combined standard uncertainty and denoted by  $u_c$ :

$$\text{Combined uncertainty} = \sqrt{a^2 + b^2 + c^2 + \dots \text{etc.}} \quad (2.1)$$

The approach of summing the uncertainties works well where calculations of prediction results involve the summation of a series of values. For example, when calculating GBNV levels, calculations begin with source vibration 1/3 octave band spectra to which corrections are added or subtracted to in order to derive predicted

**Table 2** Uncertainty calculations

Parameter	Assumptions		Half range or standard deviation dB(A) - $c_i$	Probability distribution type	Distribution divisor ( $1/u_i$ ) normal $1\sigma$ rectangular $\sqrt{3}$ triangular $\sqrt{6}$	Uncertainty contribution $c_i u_i$ dB(A)	Uncertainty squared, $(c_i u_i)^2$
	Min	Max					
<i>Source parameters</i>							
Measurement equipment uncertainties	-0.4 dB	0.4 dB	0.4	Normal	1.0	0.4	0.2
Vibration source level variations	min Vib	max Vib	3.1	Rectangular	1.7	1.8	3.2
Measured speed variation	-5%	5%	0.4	Rectangular	1.7	0.3	0.1
Predicted rail roughness variation	-2.5 dB	2.5 dB	2.5	Rectangular	1.7	1.4	2.1
95th percentile correction	3.3 dB	6.6 dB	1.6	Rectangular	1.7	0.9	0.9
Log sum errors when calculating overall dB(A)	-1.0 dB	0.0 dB	0.5	Triangular	2.4	0.2	0.0
<i>Combined standard uncertainty—source</i>							
<i>Path parameters</i>							
Train speed variation	-5%	0%	0.3	Normal	1.0	0.3	0.1
Train speed relationship	15 log	25 log	0.3	Rectangular	1.7	0.2	0.0
Fastener corrections	-2 dB	2 dB	2.0	Triangular	2.4	0.8	0.7
Stiffness variations	-15%	15%	1.4	Triangular	2.4	0.6	0.3
Rail vehicle unsprung mass variation	950 kg	750 kg	0.8	Rectangular	1.7	0.4	0.2

(continued)

Table 2 (continued)

Parameter	Assumptions		Half range or standard deviation dB(A) - $c_i$	Probability distribution type	Distribution divisor ( $1/u_i$ ) normal $1\sigma$ rectangular $\sqrt{3}$ triangular $\sqrt{6}$	Uncertainty contribution $c_i u_i$ dB(A)	Uncertainty squared, $(c_i u_i)^2$
	Min	Max					
Frequency band corrections	Move spectra 1/3 octave		2.3	Rectangular	1.7	1.3	1.8
Ground conditions from source to receiver	2 dB per 10 m	1 dB per 10 m	1.3	Rectangular	1.7	0.8	0.6
	Method 1	Method 2	0.9	Rectangular	1.7	0.5	0.3
Attenuation calculation method				<i>Combined standard uncertainty—path</i>			
<i>Receiver parameters</i>							
Distance calculations	-1 m	1 m	0.2	Rectangular	1.7	0.1	0.0
Building coupling losses/amplifications	-1.8 dB	1.8 dB	1.8	Normal	1.0	1.8	3.2
Conversion from vibration to noise	-31 dB	-27 dB	2.0	Rectangular	1.7	1.2	1.3
Resolution (nearest decibel)	-0.5 dB	0.5 dB	0.5	Rectangular	1.7	0.3	0.1
				<i>Combined standard uncertainty—receiver</i>			
Combined standard uncertainty from GUM [2]				$u(L_m) = \sqrt{\sum_1^n (c_i u_i)^2}$			
Expanded uncertainty for $U_{68}$ (68% confidence)				k = 1			
Expanded uncertainty for $U_{95}$ (95% confidence)				k = 2			

levels at receiver locations. In this and similar cases, parameter uncertainties are treated equally and are unweighted. For cases where calculations involve the multiplication, division, power or logarithm of values (e.g. when adding vibration or noise components to arrive at total levels), relative or fractional uncertainties must be used in order to weight the effect of parameter uncertainties on the combined standard uncertainty (refer Ref. [2]).

## 2.2 Confidence Intervals and Coverage Factors

Uncertainty is the measure of dispersion or variance that may be expected with a claimed performance value, often represented by the term  $U_{xx}$ . The subscript 'xx' means a xx% confidence interval. It represents the estimated range in which the true value lies for xx out of 100 repeated events, e.g. a  $U_{95}$  of 5 dB indicates that the true value is expected to be within  $\pm 5$  dB of the estimates provided for 95% of all observations.

Once the combined standard uncertainty is determined, it may be required to re-scale the result. The combined standard uncertainty may be thought of as equivalent to 'one standard deviation' ( $1\sigma$ ), but it may be preferred to have an overall uncertainty stated at another level of confidence. This re-scaling can be done using a coverage factor,  $k$ . Multiplying the combined standard uncertainty,  $u_c$  by a coverage factor gives a result which is called the expanded uncertainty, usually shown by the symbol  $U$ , i.e.  $U = ku_c$ . A coverage factor  $k = 2$  results in a confidence level of 95%. The most common level of preferred confidence for acoustic predictions often lies between 68% ( $\pm 1\sigma$ ) and 95% ( $\pm 2\sigma$ ), which can be referred to as having a coverage factor of 1 and 2, respectively.

## 3 Uncertainty Calculations

### 3.1 Uncertainty Predictions Based on GUM

For each parameter used in predicting project GBNV levels, an estimate of the standard uncertainty (uncertainty contribution) has been made on the basis of the methodologies described in the GUM [2]. Table 2 presents a summary of the uncertainty calculations.

The combined standard uncertainty is calculated to be 2.5 dB(A) for the source parameters, 2.0 dB(A) for the path parameters and 2.2 dB(A) for the receiver parameters. The combined standard uncertainty for the entire prediction path is calculated to be 3.9 dB(A). This indicates that the predicted ground-borne noise levels are expected to lie within  $\pm 3.9$  dB(A) [ $\pm 1\sigma$ ] of the predicted levels with

68% confidence and within  $\pm 7.8$  dB(A) [ $\pm 2\sigma$ ] of the predicted levels with 95% confidence.

For compliance with specifications or design noise targets, predictions with confidence intervals of 84% ( $+1\sigma$ ) or 95% ( $+1.64\sigma$ ), are commonly found in standard Normal Distribution tables, for example Ref. [8]. That is, there is:

- 84% confidence that the true level will be below the predicted level plus  $1\sigma$  [i.e. plus  $1 \times 3.9 = 3.8$  dB(A)]
- 90% confidence that the true level will be below the predicted level plus  $1.28\sigma$  [i.e. plus  $1.28 \times 3.9 = 5.0$  dB(A)]
- 95% confidence that the true level will be below the predicted level plus  $1.64\sigma$  [i.e. plus  $1.64 \times 3.9 = 6.4$  dB(A)].

### 3.2 *Uncertainty Predictions Based on Monte-Carlo Simulation*

In order to validate the combined standard uncertainty of the predictions presented in Table 2, a Monte Carlo simulation was performed.

For each modelling input parameter, a pseudo-random number was generated within a spreadsheet and the corresponding prediction error was determined on the basis of the half range or standard deviation, and associated probability distribution function (normal, rectangular or triangular). For each iteration, the total prediction error was calculated by arithmetically summing the prediction errors associated with each modelling input parameter. This process was repeated for 100,000 iterations.

The results of this analysis yielded a standard deviation (combined standard uncertainty) of 3.9 dB(A) in the prediction errors, consistent with the GUM analysis method in Table 2.

## 4 **Methods Used to Reduce Modelling Uncertainty**

With reference to the example uncertainty budget calculations in Table 2, the overall uncertainty can be reduced most effectively by focusing on the modelling input parameters with the largest uncertainty. For this project, the GBNV input parameters found to have the largest uncertainty were: vibration source levels; rail roughness levels; ground conditions/attenuation between source and receivers; building coupling losses/amplifications; the vibration spectrum shape; and the algorithm conversion of vibration to noise. Field vibration and noise measurements from the subject project and other similar projects were reviewed to assist with reducing the uncertainty of some of these key parameters:



- **Vibration Source Levels:** The variation in source vibration levels at otherwise identical measurement sites with similar track forms were established on the basis of measurement data from an existing railway tunnel. One-third octave band vibration measurements of multiple train passbys were undertaken at multiple locations with known track forms, rolling stock and train speeds. Corrections to the measured vibration levels were made to account for minor differences in the proposed track forms, rolling stock and speeds. The uncertainty associated with these corrections form part of the uncertainty predictions.
- **Rail Roughness Levels:** The typical variation in rail roughness was investigated via a review of rail roughness measurements undertaken on a comparable railway scheme. Within the wavelength range critical to ground-borne noise (greater than 100 mm for train operations less than 100 km/h), the measured rail roughness levels were typically lower than the rail roughness limit spectrum in ISO 3381-2005 [4] and ISO 3095-2005 [9] at all locations. For modelling, it was assumed that the rail roughness levels will be maintained to these standards or better throughout the life of the rail system and that this would be achieved via the periodic measurement of rail roughness and acoustic rail grinding.
- **Ground conditions/attenuation:** Between the tunnel and ground surface, vibration attenuation occurs due to two primary factors: geometric spreading (via body waves) and excess attenuation (due to material damping). For train vibration (where the length of the train is large compared with the propagation distance), vibration levels attenuate in a cylindrical pattern at a rate of 3 dB per doubling in distance [5, 6, 7]. Additional losses due to material damping are frequency dependent, with greater losses occurring at higher frequencies (smaller wavelengths). Excess attenuation values were determined from transfer mobility measurements and vibration measurements above the project tunnel during tunneling construction works.  
Excess attenuation values at a number of locations across all data sets were found to be generally comparable and were adopted for modelling purposes.
- **Building Coupling Loss/Amplification and Conversion Factors from Vibration to Noise:** Attended noise and vibration measurements were conducted at multiple sensitive receiver locations in close proximity to the project tunnel. The purpose of the measurements was to quantify: vibration propagation between tunnels and ground surface; coupling loss and amplification (difference in ground-borne vibration levels outside building and floor vibration levels inside building), and conversion of floor vibration levels to audible noise. A statistical approach, based on the measurement results at multiple locations was utilised to calculate the standard deviation of the results.

The uncertainty budget calculations in Table 2 include the benefits of the above field test inputs.

## 5 Conclusions and Recommendations

On projects where there is limited or only high-level information relating to the source, path and receiver components, the uncertainty associated with GBNV predictions can be large. On the basis of some references [10, 11], prediction uncertainties of up to 10 dB(A) have been reported and sometimes applied as a safety factor (engineering margin) on underground railway projects. During the detailed design stage of projects, large safety factors can be very costly in terms of the required mitigation measures.

Field measurement data was utilised on this project to reduce the uncertainty associated with key modelling input parameters (source, propagation path and receiver). For other input parameters, the uncertainty was established via published data and engineering judgement. The overall prediction uncertainty was calculated on the basis of guidance in the GUM and independently validated via Monte Carlo simulation.

Assessment of the modelling uncertainty on the basis of a quantitative approach based on GUM provides the additional benefit of quantifying the probability (confidence level) of the prediction uncertainty. Rather than simply stating that the prediction uncertainty is accurate to  $\pm 5$  dB or  $\pm 10$  dB, the prediction uncertainty based on GUM for this project can be stated as follows:

- the predicted ground-borne noise levels are expected to lie within  $\pm 3.9$  dB(A) [ $\pm 1\sigma$ ] of the predicted levels with 68% confidence, or within  $\pm 7.8$  dB(A) [ $\pm 2\sigma$ ] of the predicted levels with 95% confidence;
- by adding an engineering margin of one standard deviation [3.9 dB(A)] to the predicted noise level, the probability of the actual (or true) noise level being less than the predicted noise level is 84%, or conversely, the risk that the actual noise level will be higher than the predicted noise level is 16%; and
- for a 90 and 95% confidence that the actual (or true) noise level will be less than the predicted noise level, the following engineering margins should respectively be added to the modelling results 5.0 and 6.4 dB(A).

In summary, by undertaking field measurements and establishing uncertainties for all input modelling parameters, the overall confidence in the GBNV predictions was quantified using GUM, and found to be significantly better than originally estimated. This in turn assisted in reducing engineering design margins with subsequent project mitigation cost reduction benefits.

## References

1. International Standards, ISO 14837-1:2005—Mechanical vibration—Ground-borne noise and vibration arising from rail systems (2005)
2. ISO/IEC Guide 98-3, Uncertainty of measurement—Part 3: Guide to the expression of uncertainty in measurement, ISBN 92-67-10188-9, 1st Edition 1993, corrected and reprinted 1995 (GUM:1995)

3. Craven, N.J., Kerry, G.: School of Computing, Science & Engineering, The University of Salford. A Good Practice Guide on the Sources and Magnitude of Uncertainty Arising in the Practical Measurement of Environmental Noise Edition 1a—May 2007
4. International Standards, ISO 3381-2005 Railway applications—Acoustics—Measurement of noise inside railbound vehicles, ISO (2005)
5. Hassan, O.A.B.: Train-Induced Ground-borne Vibration and Noise in Buildings. Multi-Science Publishing Co., Ltd., Essex (2006)
6. Nelson, P.: Chapter 16 Low Frequency Noise and Vibration from Trains (Remington, Kurzweil and Towers), in Transportation Noise Reference Book, Butterworths (1987)
7. Transit Noise and Vibration Impact Assessment, United States Federal Transit Association (2006)
8. Walpole, R., Myers, H.: Probability and Statistics for Engineers and Scientists (5th ed.)—Appendix A.3, Macmillan Publishing Company (1993)
9. International Standards, ISO 3095:2005 Railway applications—Measurement of noise emitted by railbound vehicles (2005)
10. Hunt, H., Hussain, M.: Accuracy, and the prediction of ground vibration from underground railways, 5th Australasian Congress on Applied Mechanics, Australia (2007)
11. KTE Rail Tunnel Project—Hong Kong—[http://www.epd.gov.hk/eia/register/report/eiareport/eia\\_1842010/EIA/html/8%20-%20GB%20Noise.htm](http://www.epd.gov.hk/eia/register/report/eiareport/eia_1842010/EIA/html/8%20-%20GB%20Noise.htm). Available online—accessed 4 July 2016

# Genset Locomotives: Implications for Type Testing in NSW



D. R. McGregor

**Abstract** All new locomotives need a “type” approval from the Environment Protection Authority to operate on the New South Wales rail network. To be approved, the locomotive type must meet noise criteria or:

- have noise emission performance consistent with current best practise
- have all reasonable and feasible measures for minimising non-compliance with the criteria and
- not result in unacceptable environmental impacts.

The noise criteria include overall A-weighted limits in all throttle settings, an overall Z-weighted limit for every throttle setting except for low idle, and limits on tonality for noise less than 1000 Hz. A multiple engine “genset” locomotive uses a system of at least two smaller engines to provide the same tractive effort provided by a large engine, and allows engines to be switched off when they are not needed. Two genset models can be used in NSW as they were approved by the EPA after testing against Environment Protection Licence noise criteria and best practise. In this paper I:

- briefly explain the testing and approval process for locomotives in NSW
- use a simple model to explore potential differences in exhaust noise tonality between gensets and conventional diesel-electric locomotives
- consider some implications of those differences.

---

D. R. McGregor (✉)

Technical Assessments and Advice, NSW Environment Protection Authority,  
PO Box A290, Sydney, NSW 1232, Australia  
e-mail: [info@epa.nsw.gov.au](mailto:info@epa.nsw.gov.au)

## 1 Introduction

### 1.1 *How Are Locomotives Tested for Noise Emissions in NSW?*

In New South Wales, the *Protection of the Environment Operations Act 1997* requires “railway systems activities”<sup>1</sup> to be licensed by the Environment Protection Authority. Almost all rail track in NSW is covered by one of three environment protection licences: 3142 (Australian Rail Track Corporation), 12208 (Sydney Trains) and 13421 (John Holland Rail, who maintain the NSW Country Regional Network).

Environment protection licences 3142, 12208 and 13421 require all new locomotives operated on the rail network to have a “type” approval from the EPA to operate [1]. To be approved, the locomotive type must meet noise criteria or:

- have noise emission performance consistent with current best practise
- have all reasonable and feasible measures for minimising non-compliance with the criteria and
- not result in unacceptable environmental impacts [2–4].

The noise criteria include overall A-weighted limits in all throttle settings, an overall Z-weighted limit for every throttle setting except for low idle, and limits on tonality for noise less than 1000 Hz [2–4]. To limit tonality, the licences require that  $L_{ZEq(30s)}$  in each third-octave band does not exceed the level of the adjacent bands on both sides by:

- (a) 5 dB if the centre frequency of the band containing the tone is above 400 Hz
- (b) 8 dB if the centre frequency of the band containing the tone is between 160 and 400 Hz, inclusive
- (c) 15 dB if the centre frequency of the band containing the tone is below 160 Hz [2–4].

The approach to tonality in railway systems licences mirrors the simplified method for assessing the audibility of tones in ISO 1996-2 [5].

Noise testing against the criteria must be consistent with the requirements of a stationary vehicle type test according to AS 2377-2002: *Acoustics—Methods for the measurement of railbound vehicle noise*, except:

- all parameters must be obtained over 30 s and 15 m from the track centre
- measurements are not required at 30 m, directly in front or behind the locomotive, or 3.5 m above the rail head
- two additional parameters are required:  $L_{Zmax(F,30s)}$  and  $L_{1/3oct,eq(30s)}$  [2–4, 6].

---

<sup>1</sup>As defined in clause 33, Schedule 1 of the *Protection of the Environment Operations Act 1997* (NSW)

## 1.2 *What Is a Genset Locomotive?*

Multiple engine locomotives have been used in the USA since 1963, when EMD produced the first DD35 slave locomotive [7]. The most powerful diesel-electric locomotive ever built was a multiple engine locomotive, the 4.92 MW EMD DDA40X, which entered service in 1969 [8].

A genset locomotive uses at least two smaller engines to provide the same tractive effort as one large engine. This allows one or more engines to be switched off when they are not needed. The name “genset” refers to the use of generator sets, each containing an engine and generator, and is used similarly in electricity generation.

In its simplest form, a multiple engine locomotive could operate all engines at all times. To improve efficiency, complex control systems have developed which allow each engine to operate independently. This includes:

- starting another engine after one is already operating
- controlling engine speeds to improve efficiency while meeting power demands
- stopping an engine when another is still operating
- limiting engine idle time [9].

Patent US7431005B2 [9], which is held by a manufacturer of genset locomotives, describes a number of scenarios for controlling engines in genset locomotives. Engine control is based on variables including notch position, engine output, vehicle speed, brake pressure, battery voltage and ambient temperature. For example:

- Between idle and notch 2, only one engine may operate.
- From notch 3, a second engine may be started after 3 s, as long as the first engine is producing more than 90% of its rated power and the locomotive’s speed is more than about 1.8 m/s.
- In notches 4–8, the speed of the engines may be controlled by the throttle position [9].

## 2 **Modelling Approach**

To explore potential differences between exhaust noise from conventional and genset locomotives, I developed a simple model of cylinder behaviour based on thermodynamic theory. I used that model to derive exhaust noise waveforms, at the outlet, for a 6 cylinder diesel engine at 51,200 samples per second and:

- 800 RPM
- 1500 RPM
- 2000 RPM.

I then combined engine exhaust noise waveforms to simulate sound pressure levels at 15 m from two engines in a genset where:

- One engine is running at 1500 RPM and the other at 800 RPM.
- One engine is running at 2000 RPM and the other at 800 RPM.
- One engine is running at 2000 RPM and the other at 1500 RPM.

I also explored the influence of the phase difference between the engines in a genset, by modelling two engines both operating at 2000 RPM.

By combining the waveforms in this way I assumed that each engine and exhaust system in the locomotive was identical and each exhaust outlet was in the same location relative to the observer.

To simplify analysis I also assumed that directivity effects were negligible, and that distance attenuation occurred only by hemispherical dispersion.

The engine I modelled was a 6 cylinder diesel with the following general specifications:

- compression ratio 15 and ratio of rod length to cylinder stroke 1.8
- cylinder bore of 0.159 m and stroke 0.159 m
- exhaust valve diameter 0.0604 m
- total displacement 19 L.

## 2.1 *Single Cylinder Model*

I developed a simple cylinder model by calculating the properties of air in the cylinder at discrete time steps and using the following simplifying assumptions:

- Engine rotational speed is constant in each operating condition.
- Air in the cylinder is an ideal gas, has constant specific heats and the ratio of specific heats is  $k = 1.4$ .
- The engine does not have a turbocharger or intercooler.
- The intake valve is large enough that, while it is open, cylinder air temperature and pressure are equal to atmospheric.
- Compression, prior to fuel addition, is isentropic: heat is not exchanged with the cylinder walls. The cylinder pressure  $P_2$  and temperature  $T_2$  at time step 2 can be calculated from the pressure  $P_1$  and temperature  $T_1$  at time step 1 and the volume ratio  $V_1/V_2$  [10]:

$$T_2 = T_1 \left( \frac{V_1}{V_2} \right)^{k-1} \quad (2.1)$$

$$P_2 = P_1 \left( \frac{V_1}{V_2} \right)^k \quad (2.2)$$

- Fuel injection occurs as heat addition at constant pressure. The cylinder temperature  $T_2$  at time step 2 can be calculated from the temperature  $T_1$  at time step 1 and the volume ratio  $V_2/V_1$  [10]:

$$T_2 = T_1 \left( \frac{V_2}{V_1} \right) \tag{2.3}$$

- Expansion following fuel addition is isentropic.
- I chose exhaust valve opening and closing times typical of medium duty diesel engines and assumed sinusoidal valve movement between those boundaries.
- The exhaust valve is a converging nozzle, and flow is isentropic. Mass flow through the exhaust valve depends on the pressure in the cylinder, the exit Mach number and the effective area of the valve:
  - I determined the exit Mach number ( $M$ ) from the ratio of specific heats  $k$ , cylinder pressure  $p_0$  and ambient pressure  $p$  [11]:

$$\frac{p_0}{p} = \left( 1 + \frac{k-1}{2} M^2 \right)^{\frac{k}{k-1}} \tag{2.4}$$

$$\text{Then } M = \sqrt{\frac{2}{k-1} \left[ \left( \frac{p_0}{p} \right)^{\frac{k-1}{k}} - 1 \right]} \tag{2.5}$$

- When  $M$  was less than 1, I calculated the mass flow  $\dot{m}$  through the valve from the cylinder pressure  $p_0$ , ratio of specific heats  $k$ , gas constant  $R$ , cylinder temperature  $T_0$ , Mach number  $M$  and valve effective area  $A$  [11]:

$$\dot{m} = p_0 \sqrt{\frac{k}{RT_0}} MA \left( 1 + \frac{k-1}{2} M^2 \right)^{\frac{k+1}{2(1-k)}} \tag{2.6}$$

- When  $M$  was equal to or greater than 1, I calculated mass flow  $\dot{m}$  through the valve from the cylinder pressure  $p_0$ , valve effective area  $A$ , ratio of specific heats  $k$ , gas constant  $R$  and cylinder temperature  $T_0$  [11]:

$$\dot{m} = p_0 A \sqrt{\frac{k}{RT_0}} \left( \frac{k+1}{2} \right)^{\frac{k+1}{2(1-k)}} \tag{2.7}$$

- I calculated the density  $\rho$  of air exiting the exhaust valve from the density  $\rho_0$  of air in the cylinder, ratio of specific heats  $k$  and Mach number [11]:



$$\rho = \rho_0 \left( 1 + \frac{k-1}{2} M^2 \right)^{\frac{-1}{k-1}} \quad (2.8)$$

- I calculated the exhaust gas velocity  $v$  from the mass flow  $\dot{m}$  and density  $\rho$  of air exiting the valve and area  $A_e$  of the exhaust outlet [11]:

$$v = \frac{\dot{m}}{\rho A_e} \quad (2.9)$$

- Assuming hemispherical dispersion, I calculated the instantaneous sound pressure  $p_{\text{sound}}$ , at distance  $r = 15$  m from the exhaust outlet, from the exhaust area, gas density and velocity [12]:

$$\langle p_{\text{sound}}^2 \rangle = \frac{W_M \rho c}{2\pi r^2} \quad (2.10)$$

$$\text{Where } W_M = \frac{A_e \rho v^3 M}{2} \text{ and } M = \frac{v}{c} \quad (2.11)$$

$$\text{So } p_{\text{sound}} = \sqrt{\frac{A_e \rho^2 v^4}{4\pi r^2}} \quad (2.12)$$

My model provided the cylinder pressure-volume diagrams in Fig. 1, and the sound pressure waveforms at 15 m from the exhaust outlet in Fig. 2.

## 2.2 Engine Model

To derive engine exhaust waveforms I combined six, single cylinder exhaust waveforms, each offset from the last by  $120^\circ$  crankshaft angle. The engine exhaust waveforms, at 15 m from the exhaust outlet, are shown as a time series in Fig. 3.

## 3 Engine Tonality

This section describes the results of my modelling, showing variations in tonality which could occur in genset locomotives. Tonality in the genset model depended on the speed and phase differences between the engines used. I used Sinus Samurai software to analyse the model waveforms described in Sect. 2 as WAVE files.

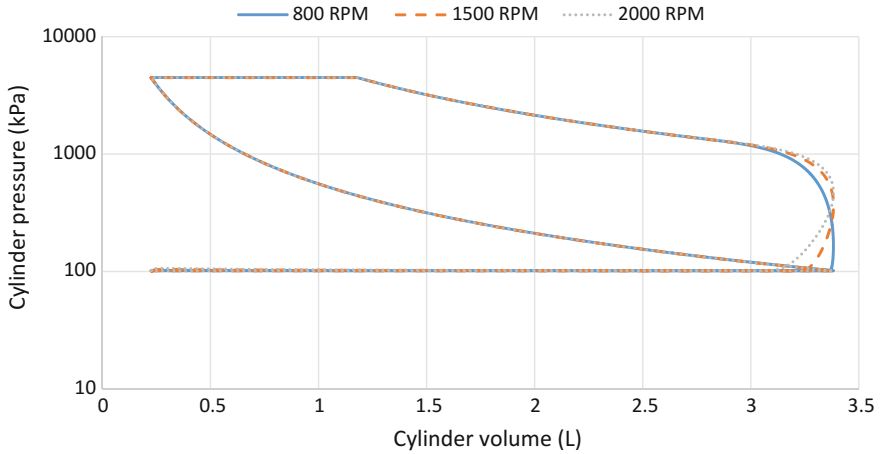


**Fig. 1** P-V diagrams for the simple cylinder model at 800, 1500 and 2000 RPM

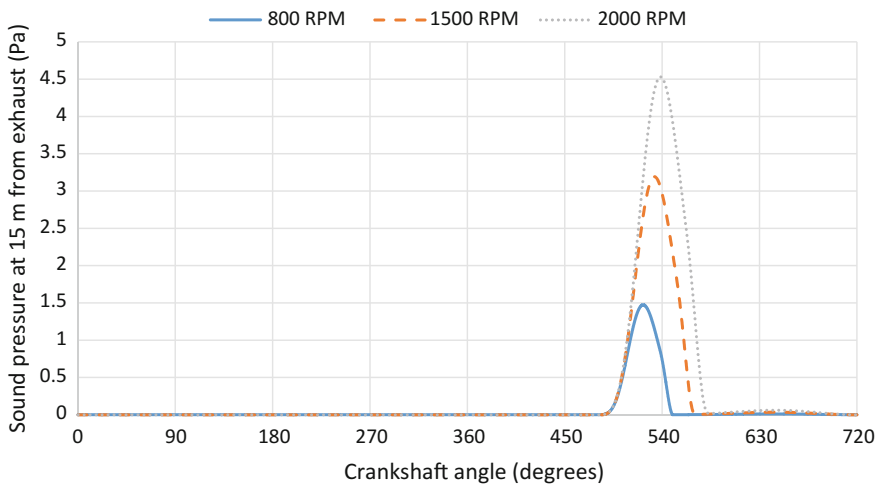


**Fig. 2** Modelled exhaust sound pressure waveform for a single cylinder at 800, 1500 and 2000 RPM

### 3.1 Tonality for a Single Engine

Figure 4 shows  $L_{eq(30s)}$  third octave spectra at various engine speeds for the engine modelled. A number of tones occurred depending on engine speed:

- At 800 RPM the engine was tonal in the 40 and 80 Hz bands
- At 1500 RPM the engine was tonal in the 80 and 160 Hz bands
- At 2000RPM the engine was tonal in the 100 and 200 Hz bands.

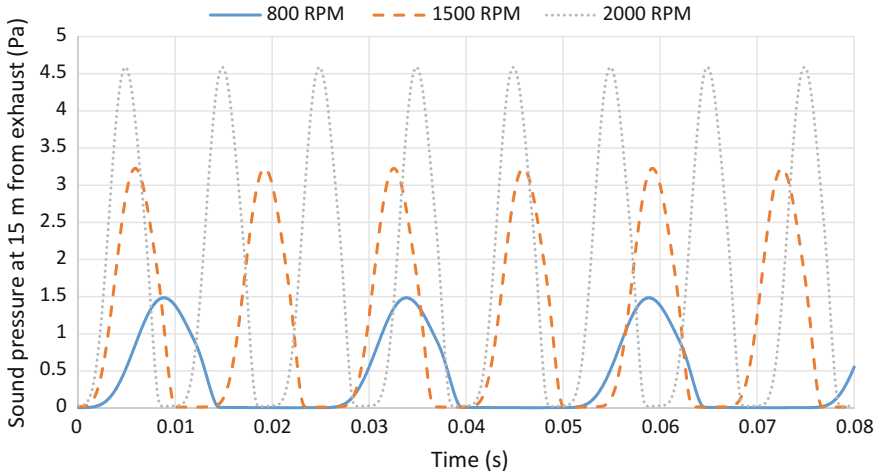


**Fig. 3** Modelled exhaust waveforms for the engine running at 800, 1500 and 2000 RPM

The single engine  $L_{eq(30s)}$  third octave spectra indicate that the modelled engine would require treatment before being used in a locomotive on the NSW rail network.

### 3.2 Tonality for Two Engines Running at Different Speeds

Figure 5 shows  $L_{eq(30s)}$  third octave spectra for a genset running three different combinations of engine speeds:

- One engine at 1500 RPM and the other at 800 RPM (1500/800 RPM)
- One engine at 2000 RPM and the other at 800 RPM (2000/800 RPM)
- One engine at 2000 RPM and the other at 1500 RPM (2000/1500 RPM).

The 1500/800 RPM and 2000/800 RPM spectra were still tonal in the bands where the single engines were tonal:

- When one engine was running at 1500 RPM and the other at 800 RPM, the genset was tonal in the 40, 80 and 160 Hz bands.
- When one engine was running at 2000 RPM and the other at 800 RPM the engine was tonal in the 40, 100 and 200 Hz bands.
- When one engine was running at 2000 RPM and the other at 1500 RPM the engine was not tonal in any band.

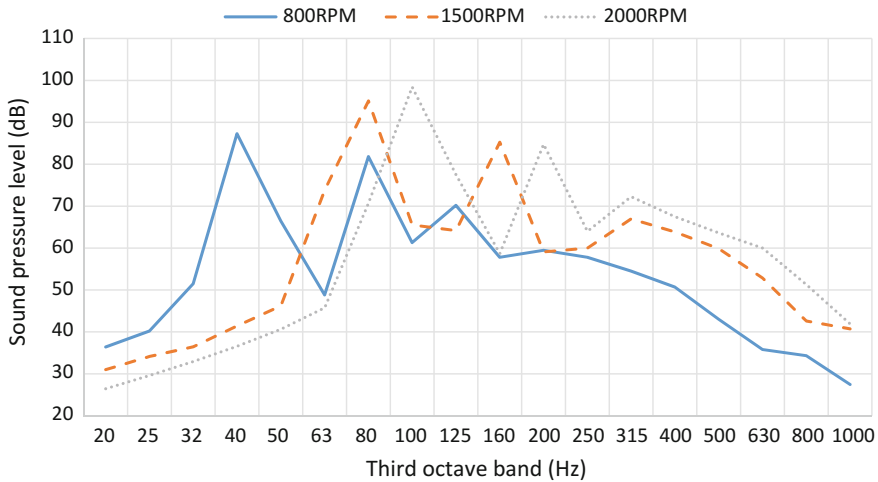


Fig. 4 Third octave spectra for modelled engines

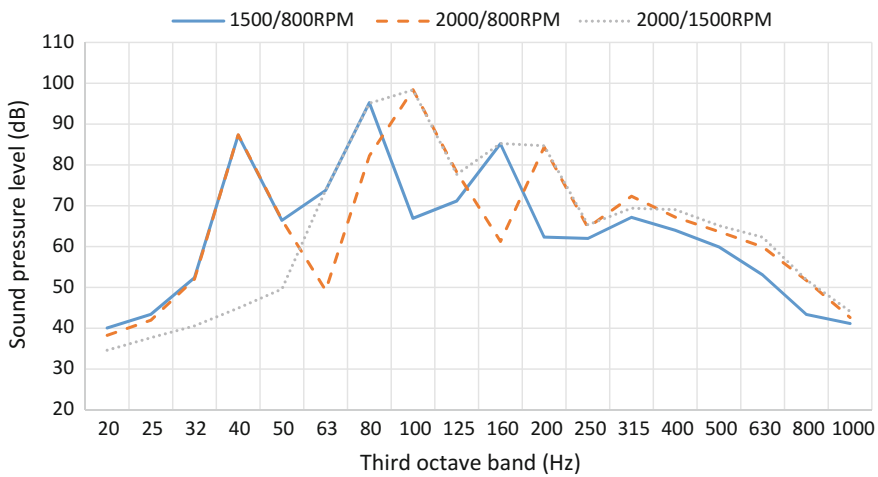


Fig. 5 Comparison of genset third octave spectra for different engine speeds

These results indicate that noise from a genset locomotive may be tonal in some notch settings but not tonal in other notch settings, because of the interaction between exhaust pressure waves from each engine.

It is also possible that in some notch settings tones in adjoining bands<sup>2</sup> would obscure one another but still be perceived as tonal by an observer. The way such a

<sup>2</sup>See for example 80 and 100 Hz bands in the 2000/1500 RPM case.

combination of tones might be perceived will not be explored in this paper, but may be explored in future work.

### ***3.3 Tonality for Two Engines at the Same Speed***

Figure 6 compares the third octave spectra for a genset where both engines were operating at 2000 RPM:

- While both engines were in phase, the tones that existed for an individual engine were maintained in the 100 and 200 Hz bands.
- When the 100 Hz tones from the engines were close to 90° out of phase, the first harmonic at 200 Hz was reduced so that the genset was not tonal in the 200 Hz band.
- When the 100 Hz tones from the engines were close to 180° out of phase, the primary 100 Hz tone reduced so that band was not tonal, but tones occurred in the 200, 400 and 630 Hz bands.

This means that noise from a genset locomotive may be tonal or not tonal depending on the phase difference between the two engines at the time of measurement. Depending on the control system used this may occur in any notch setting where both engines operate at similar speeds.

## **4 Recommendations**

### ***4.1 The EPA Should Consult with the Rail Industry on Whether to Change Locomotive Test Methods***

Theoretical model results indicate that exhaust noise tonality could vary more for a genset locomotive than a conventional diesel-electric locomotive. This means that current locomotive type test requirements may not adequately assess operational noise emissions from gensets, depending on the design of each locomotive.

The EPA is changing the way railway activities are licensed in NSW. This will involve consulting with locomotive owners and operators, discussing: the issues identified in this paper, how genset locomotives are used in service, and whether current type tests are adequate for genset locomotives or should be changed.

Methods which may improve genset locomotive testing include manually operating each engine independently. This would enable possible tonality to be assessed at each engine speed and phase difference combination which is allowed by the engine control system.

Real world testing of genset locomotives, and consideration of possible interactions in multiple engine locomotives, may help manufacturers reduce noise

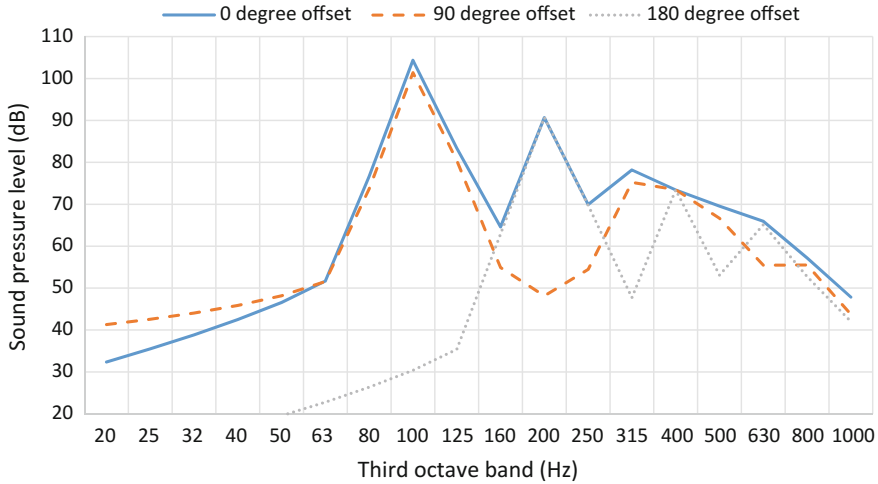


**Fig. 6** Comparison of genset third octave spectra for engines at 2000 RPM, depending on the 100 Hz phase difference Sound pressure levels for the 180° offset case, in the third octave bands 20–40 Hz, were below 20 dB

impacts without reducing efficiency. For example, engines may be able to be made to run out of phase with each other at all times, to minimise phase-generated tones.

### 4.2 The Engine Model Should Be Refined

The engine model used should be expanded to account for turbocharger, intercooler and exhaust effects. It should also be verified by measurement of a variety of engine types.

### References

1. State of NSW, Environment Protection Authority: Review of regulation of ‘railway systems activities’ under the *Protection of the Environment Operations Act 1997*, position paper, online: <http://www.epa.nsw.gov.au/resources/epa/14657railpospap.pdf>. Accessed 27 Apr 2016
2. State of NSW, Environment Protection Authority: Environment Protection Licence 3142, online: <http://www.epa.nsw.gov.au/prpoeoapp/ViewPOEOLicence.aspx?DOCID=72984&SYSUID=1&LICID=3142>. Accessed 27 Apr 2016
3. State of NSW, Environment Protection Authority: Environment Protection Licence 12208, online: <http://www.epa.nsw.gov.au/prpoeoapp/ViewPOEOLicence.aspx?DOCID=62682&SYSUID=1&LICID=12208>. Accessed 27 Apr 2016
4. State of NSW, Environment Protection Authority: Environment Protection Licence 13421, online: <http://www.epa.nsw.gov.au/prpoeoapp/ViewPOEOLicence.aspx?DOCID=33621&SYSUID=1&LICID=13421>. Accessed 27 Apr 2016

5. International Organization for Standardization: Acoustics—Description, measurement and assessment of environmental noise—Part 2: Determination of environmental noise levels, ISO 1996-2:2007. International Organization for Standardization, Geneva (2007)
6. Australia, Standards: Acoustics—Methods for the measurement of railbound vehicle noise, AS 2377-2002. Standards Australia, Sydney (2002)
7. Strack, D.: Union Pacific’s DD35 Double Diesels, online: <http://utahrails.net/articles/up-dd35.php> (2007). Accessed 3 May 2016
8. Oxlade, J.: Union Pacific “Double Diesel” Locomotives, online: <http://www.worldrailfans.info/Articles/US/DoubleDiesels.shtml> (2003). Accessed 3 May 2016
9. Hawkins, W.C., McManus, S.J.: Engine start/stop control for multiple engine OHV based on operating conditions. US7431005B2 (2008)
10. Çengel, Y.A., Boles, M.A.: Thermodynamics an Engineering Approach, 7th edn. McGraw-Hill, New York (2011)
11. Potter, M.C., Wiggert, D.C., Hondzo, M. Shih, T.I-P.: Mechanics of Fluids (3rd edn.). Thomson Learning, Pacific Grove CA (2002)
12. Bies, D.A., Hansen, C.H.: Engineering Noise Control: Theory and Practice, 4th edn. Taylor & Francis, New York (2009)

**Part IV**  
**Rail Roughness, Corrugation**  
**and Grinding**



# Routine Measurement of Long Wavelength Irregularities from Vehicle-Based Equipment



Stuart L. Grassie

**Abstract** RCA equipment supplied by RailMeasurement Ltd is used routinely on reprofiling trains to show when irregularities have been brought within limits stated in reprofiling specifications and on other vehicles to help schedule reprofiling. It has been shown previously that these measurements correlate well with those made using the CAT instrument, which is widely used to take measurements of rail irregularities for acoustic purposes. The measurements presented here from routine use of RCA equipment illustrate several interesting features. For example, the distribution of irregularities along the track varies little in time despite the maintenance that would have been undertaken during the almost two year period over which measurements are shown for one line. There is strong evidence that long wave (1–10 m) irregularities are relatively low on non-ballasted trackforms that have been well laid and well maintained, whereas such irregularities are both more variable and generally more severe on ballasted track. Conventional grinding brings about a substantial reduction in irregularities in the 40–1000 mm wavelength range, with a modest reduction at best at longer wavelengths and a substantial increase at shorter wavelengths. The increase arises from the well-known “grinding signature” i.e. the pattern that is imprinted at the wavelength that a grinder moves forward during one rotation of a grindstone. As a result, there is very little ground rail on which irregularities are lower than the EN ISO 3095:2013 limit line for smooth rail for wavelengths of less than 35 mm. A specific reprofiling technique, such as offset or shuffle-block grinding, would be required to reduce irregularities in this wavelength range. Irregularities on metro systems are extremely variable, with little if any consistency between nominally similar trackforms (such as sleepers laid in concrete) on different metros. There is some evidence that the newest metro systems for which data are presented here do have lower long wave irregularities.

---

S. L. Grassie (✉)

RailMeasurement Ltd, The Mount, High Street, Toft, Cambridge CB23 2RL, UK  
e-mail: [stuart.grassie@railmeasurement.com](mailto:stuart.grassie@railmeasurement.com)

## 1 Introduction

There are many references to measurement of irregularities on both wheels and rails. Measurements of sufficient accuracy for use in railway noise prediction date from about the 1970s, in particular with work from both the USA [1] and UK [2]. A survey, of irregularities on both wheels and rails on the Dutch railway system, was undertaken in the 1990s by Dings and Dittrich [3]. They commented on the type of material for block-braked wheels, suggesting that a reduction of 7–10 dBA in pass-by noise could be obtained only if cast-iron blocks were no longer used. If severe rail corrugation were removed, this offered the possibility of reducing noise by 10 dB with block-braked wheels and 17 dBA with disc-braked wheels. Fodiman and Staiger, following the NOEMIE project in the early 2000s, proposed an initial TSI (Technical Specification for Interoperability) limit for acoustic roughness on rails [4]. Measurements taken at sites on 6 European railway systems indicated that rails were often smoother than the proposed limit in the mid-wavelength range, but with some quite large exceedences at shorter wavelengths (<25 mm) and at the higher end of the wavelength range considered (100–315 mm). Further input from the NOEMIE project came from Verheijen [5], who commented that one of the objectives of the project was to consider how to extend the wavelength range of measurements from the 100 mm to which they were then limited by the 1.2 m straight-edge based systems that were then commonly used. Results were mentioned from an early comparison test undertaken in Utrecht that included both the RM1200E straight-edge based device [6] and the CAT (Corrugation Analysis Trolley) [7]. A difference of as little as 1 dB was found between the two instruments for measurements in the wavelength range 2–25 cm. For rails in service, the range of roughness was found to be as great as 40 dB in some one-third octave bands. Verheijen attempted to consider the requirements of various parties who have an interest in rail roughness: in particular those whose concern is reprofiling and those whose concern is wheel/rail noise.

A common problem with these earlier surveys, as mentioned explicitly by Verheijen [5], is that the wavelength range that could be measured reliably with a straight-edge based instrument was inherently limited. For example, the wavelength range for measurements on rails was limited to 100 mm in Ref. [3] and 315 mm in Refs. [4, 5]. This limitation was entrenched in the European Standard for measurement of rail roughness related to rolling noise generation, which considers the wavelength range 3–250 mm [8]. In a so-called “road test” that was undertaken in developing this Standard, it was demonstrated that substantially identical measurements were obtained for this wavelength range by a variety of straight-edge based equipment and the CAT [9, 10].

At a substantially similar time, research teams in the UK [11] and Sweden [12] undertook work to combine CAT measurements with those from a Track Recording Car. By pushing the CAT at a rather higher speed than normal (about 1.5 m/s), apparently reliable measurements of railhead irregularities were obtained up to a wavelength of about 1.5 m. Measurements covering the wavelength range

6.3–2000 mm have been presented by Grassie from several users of the CAT worldwide [13]. These show particular characteristics of irregularities on different types of railway system (heavy haul, light rail, mixed traffic and metro). Effects are also shown of different reprofiling techniques and of the growth of corrugation after reprofiling.

In a study undertaken to limit ground-borne noise and vibration from a new metro line to sensitive research laboratories, the frequency range of interest is considered to be 3.16–100 Hz [14]. If ground-borne noise and vibration were a significant problem, and if the 3.16 Hz limit were assumed, it would be necessary to measure and control irregularities of 6 m wavelength for metro trains at 70 km/h, and proportionately longer wavelengths for higher speed traffic. Routine measurement of such long wavelength irregularities is considered here.

## 2 Equipment and Measurements

The RCA (Rail Corrugation Analyser) made by RailMeasurement Ltd [15] was designed for routine use in reprofiling trains to show if irregularities were being brought within specified limits e.g. those in Ref. [16]. It was demonstrated in Ref. [17] that measurements made with the RCA (Fig. 1) correlate well with those made using the CAT up to a wavelength of about 5 m, and that the repeatability of the RCA is superior at wavelengths of more than about 1 m. This finding provides some confidence in use of the RCA equipment.

Measurements are presented here from routine use of the RCA equipment. On two railway systems the measurements come from surveys that were undertaken to help plan reprofiling. In one of these cases (Sect. 3), examples are presented from a remarkable history of measurements undertaken of the same metro line over a



**Fig. 1** RCA (Rail Corrugation Analyser)

period of several years. Most measurements come from reprofiling trains on metro systems. These metro systems are extremely varied: from some of the oldest in the world to some of the newest.

Long wave measurements are very much better on long runs or where the measuring speed is relatively high. The longer runs here e.g. those for which data are shown in Figs. 2 and 3 are at least 500 m long and in one case the data are from a run of almost 10 km. On metro systems, relatively short sections are often ground: data are shown in Fig. 4 for sections of 95–400 m length. Grinding is commonly undertaken at speeds of only a few km/h to reduce short wavelength irregularities, particularly on the later passes when measurements are made. This tends not to be a problem on main lines and high speed railways, where sections of at least 1 km in length may be ground at speeds of 15 km/h or more.

Particular attention is paid here to the trackform, as this appears significantly to influence long wavelength irregularities and what is essentially the quality of track geometry at wavelengths of 3–10 m. This is consistent with measurements shown in Ref. [18], where installation of the Pandrol Vanguard fastening system in a metro line reduced both irregularities in the 1 m wavelength range and ground-borne vibration measured above the line. These results are of great significance to those systems where ground-borne vibration is critically important: Crossrail in London is a particularly interesting example.

### 3 Long Term Measurements on a Metro System

Few if any long-term measurements exist of irregularities at the same location on the same railway system. An early example is monitoring that was undertaken with an ancestor of the CAT on British Rail in the 1970s [19].

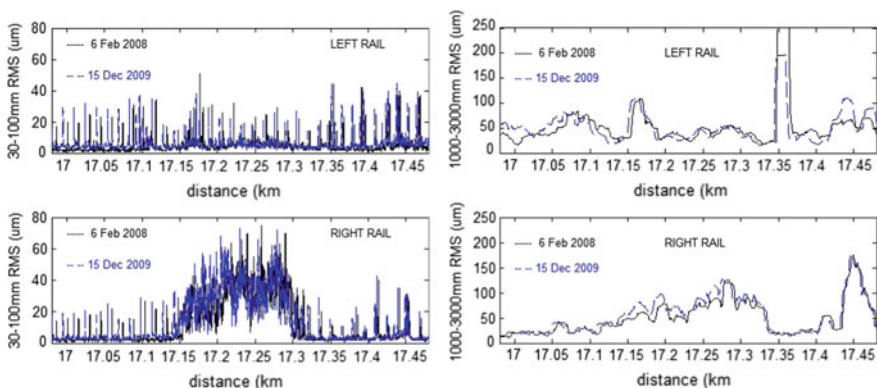


**Fig. 2** Irregularities measured on the same 0.5 km inter-station section of a metro line 22 months apart

A comprehensive set of RCA data has been provided for several lines on a metro system that were taken every few months over a period of several years. Measurements of one inter-station section taken almost two years apart are shown in Fig. 2.<sup>1</sup> The detailed history of reprofiling on this line is no longer known, but it is highly likely that grinding was undertaken as conscientiously as measurement during this period, thereby removing corrugation in the curve at 17.1–17.35 km. Yet both short and long wavelength irregularities follow almost exactly the same pattern. In another example from the same line, a section of track was rerailed, thereby giving a very much lower level of discrete irregularities at welds. Nevertheless, the pattern of irregularities in the 30–100 and 1000–3000 mm wavelength ranges was almost identical over an interval of 3 years.

## 4 Irregularities on Different Railway Systems

As noted in Sect. 2, RCAs are used on some railway systems to provide routine surveys of rail corrugation whereas on others, and indeed more commonly, they are used on reprofiling trains to show whether residual corrugation is within specification. Roughness spectra for both rails are shown in Fig. 3 for the wavelength range 0.005–10 m from three very different railway systems. The spectra are superposed on the upper limit line from Ref. [20] extended from 40 cm to 10 m. There are two sets of data for a metro (the location shown in Fig. 2); data from three separate sections of line on a system that carries primarily freight and a small amount of passenger traffic; and pre-grind data from two different locations on the same high-speed railway system.

There are interesting characteristics of these sets of measurements. At long wavelengths (1–10 m), there is a similar level of irregularities for both the metro and the high-speed line, whereas irregularities on the freight line are very much higher. The most likely reason for this, and one that is consistent with comments later in this paper, is that both the metro and the high-speed line have relatively recent non-ballasted trackforms, albeit of different designs. These lines appear to have been constructed with very good geometry which has been maintained. On the other hand, long wave irregularities on the ballasted railway system are both more variable and, in general, more severe than on the non-ballasted trackforms.

Irregularities on the high-speed line in the mid-wavelength range (30–1000 mm) are extremely low, particularly given that these are pre-grind measurements. Only the metro line shows much sign of corrugation, at about 80 mm wavelength on one

---

<sup>1</sup>The measurements shown are moving averages of RMS amplitudes of irregularity calculated every 2 mm for a particular “moving window”. The window is of 500 mm length for the 30–100 mm wavelength range and 15 m for the 1000–3000 mm wavelength range. See e.g. Annex D of Ref. [16]. The scale for the 1000–3000 mm data has been selected to show detail for most of the runs on both dates at the cost of missing the very local maximum at 17.35 km on the left rail for 6 February 2008.

**Fig. 3** Roughness spectra from relatively high speed measurements of three railway systems

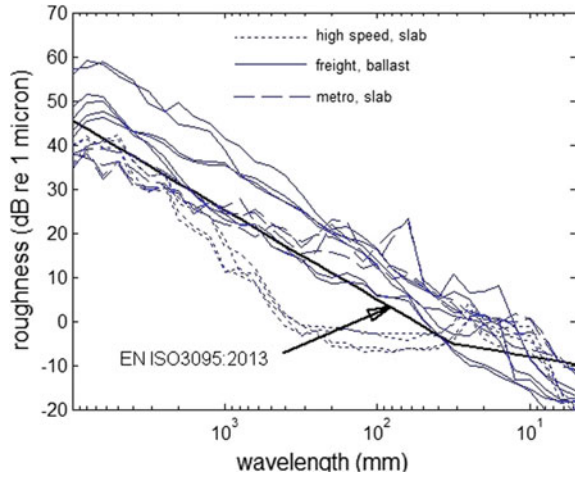
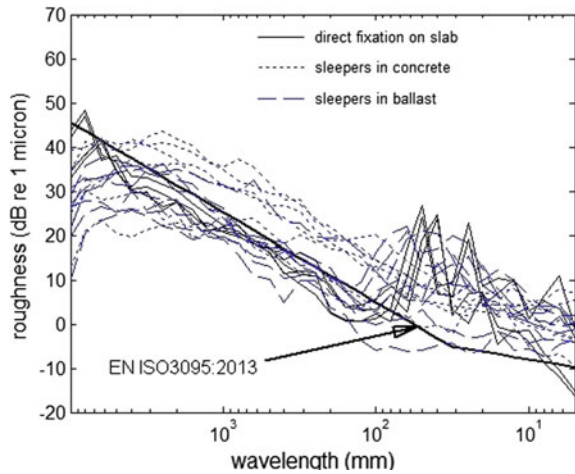


**Fig. 4** Roughness spectra from several metro lines, before grinding



rail (see also Fig. 2). In all but one case (one of the sets of measurements from the freight line), the periodic “grinding signature” gives rise to pronounced peaks in the spectrum at the fundamental wavelength (at about 30 mm or less) and usually also at the first harmonic. These effects are also discussed in Sect. 5. Consequently on the high-speed line the spectra of roughness significantly exceed the EN ISO3095 limit for the wavelength range 8–40 mm but at no other wavelengths. Some other form of rail treatment, such as “acoustic grinding” [21] or the slightly less effective “offset grinding” [13], would be required to reduce irregularities in this wavelength range and the consequential noise.

Roughness data are shown from 5 metro systems in Fig. 4 for the wavelength range 5 mm–10 m. Some of these lines were built almost a century ago whereas others are less than a decade old. The reliability of measurements for wavelengths

of substantially longer than 1 m may be somewhat questionable given the relatively low speed at which all measurements were taken. A basic “sanity check” was made on the many sets of data from these metro systems by comparing pre- and post-grind measurements. Where grinding appeared to bring about a consistent and substantial change (5 dB or more) in roughness at wavelengths of >1 m, the measurements have been omitted.

Consistently high levels of long wavelength irregularity are found on one relatively old system in which the trackform comprises sleepers set into concrete, whereas a substantially lower level of irregularities is found on an even older metro with a similar trackform. There is also a consistent variation in long wavelength irregularities on the two metros for which the trackform comprises sleepers laid in ballast within tunnels of a generously large, rectangular cross section. Long wave irregularities are consistently low for different sections of track on a modern metro system with a direct fixation trackform laid on concrete slab. Pronounced corrugation exists on all trackforms at wavelengths of 30–80 mm. The periodic grinding “signature” at typically 30 and 15 mm wavelengths has persisted in several cases. This is a remarkably common phenomenon on ground rail.

## 5 Effects of Reprofilng

Several references exist showing effects of reprofiling on railhead irregularities, not least Ref. [13] in which the effects are shown over the wavelength range 5–2000 mm. The findings in Ref. [13] come from several users of the CAT instrument measuring track that has been reprofiled (ground or milled) by different contractors. A rather narrower range of measurements is shown here. All of the data shown here are from conventional grinding using stones that rotate about an axis normal to the rail surface.

The change in roughness brought about by grinding is shown in Fig. 5. The measurements have been separated into those from a high speed and metro system in which there are different slab trackforms, and measurements from several other metro systems with different trackforms. On the non-ballasted track systems (Fig. 5a) it is shown quite consistently that irregularities with wavelengths of more than about a metre are changed relatively little by reprofiling. The pronounced increase in irregularities at a wavelength of about 2 m on the metro in Fig. 5a is the manifestation of a poor “set-down” that was inadvertently made in the middle of this grinding site. This system was ground to treat a section of particularly severe corrugation at about 50 mm wavelength: this has been very successful. The reduction of 25 dB is equivalent to reducing the RMS amplitude to about 5% of its level before grinding. On the high-speed system, grinding brings about a relatively modest reduction in roughness of about 2–8 dB at wavelengths of 30–100 mm. On both systems, the grinding signature brings about an increase of about 5 dB in roughness in the 31.5 and 16 mm one-third octave bands on the metro and high speed systems respectively. The corresponding grinding speed is simply  $v = f\lambda$

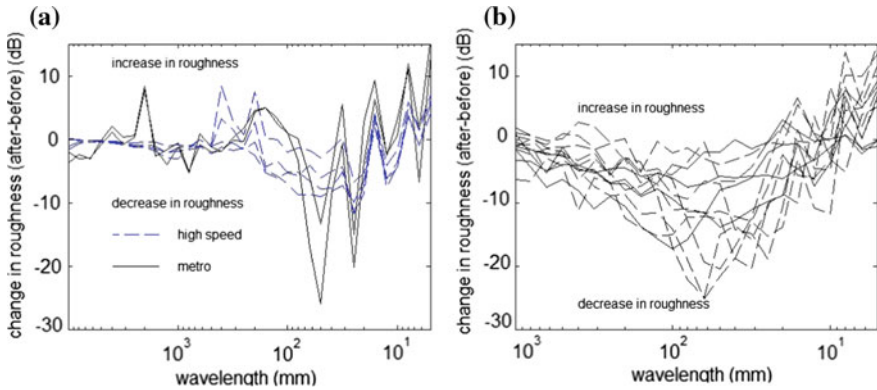


**Fig. 5** Change in roughness as a result of reprofiling **a** slab track **b** other metro systems

where  $f$  is rotational frequency of the grinding motors (typically 50–60 Hz) and  $\lambda$  is the wavelength of the grinding signature i.e. the distance that the train moves forward in one rotation of the grinding stone. For  $\lambda = 31.5$  mm,  $v = 1.6$  m/s (5.7 km/h). It is critically important when grinding to remove corrugation to ensure that the wavelength of the grinding signature or one of its harmonics does not coincide with the corrugation wavelength: this is a significant constraint on the grinding speed.

The change in roughness associated with reprofiling the several other metros (Fig. 5b) has similar characteristics to those shown in Ref. [13]. There is typically a significant reduction in corrugation (15–25 dB) at the corresponding wavelength, and an increase in short wavelength irregularities, particularly at those wavelengths associated with the grinding signature and its harmonics. It is shown in Ref. [13] that these periodic irregularities usually decrease in severity quite quickly after grinding, although it is clear from Figs. 3 and 4 that there is some residual periodicity even just before the track is next ground.

## 6 Conclusions

There is no shortage of measurements of rail roughness in the reference material on wheel/rail noise. The majority of these references are restricted to relatively short wavelengths of 0.315 m or less, primarily as a consequence of the limitations of measuring equipment based on straight edges of at most 1.2 m length. The current EN ISO3095 for acoustic testing of vehicles specifies limits on rail roughness to wavelengths of 0.4 m. There are several references in which measurements made using the CAT instrument are not limited by the length of a straight edge datum, but whose reliability is nevertheless limited to wavelengths of about 2 m. Measurements are presented here from so-called RCA (Rail Corrugation Analysis)



equipment whose common use is on reprofiling trains to show whether irregularities have been brought within specified limits. The RCA equipment is also used to help schedule reprofiling. The measurements presented here have been obtained from routine use of the RCA equipment: they were not obtained as part of an experiment or a controlled test but primarily from maintenance shifts in which the equipment was used on grinding trains. Most of these sets of measurements are from sites of at least 100 m, while some are from sites of more than 10 km length.

Results are presented from an unusual series of measurements in which a metro line was monitored every few months for a period of several years. Despite the maintenance that would have taken place during this time (whose details are no longer known), the distribution and severity of irregularities along the track, in both short and long wavelength ranges, changes very little.

One third octave spectra of irregularities are presented for the wavelength range 5–10 m for several railway systems. There is convincing evidence that a relatively modest level of long wavelength (1–10 m) irregularities exists on at least some non-ballasted trackforms. On ballasted track, long wave irregularities are both more variable and, in general, more severe. Data are presented for sites on five different metro systems with significantly different trackforms. There is considerable variation in long wavelength irregularities on these systems. Long wave irregularities are consistently low for different sections of track on a modern metro system with a direct fixation trackform laid on concrete slab, but there is otherwise little consistency from one type of trackform to another or even between sites on the same metro system.

A few sets of data are presented showing the change in roughness as a result of grinding. Grinding does not significantly reduce irregularities at wavelengths of longer than a metre for any of the cases examined here. It is, however, extremely effective at reducing irregularities at shorter wavelengths, particularly for wavelengths of 30–100 mm that are typical of short-pitch corrugation on metros and main lines. On the other hand, conventional grinding using stones that rotate about an axis normal to the rail give rise to severe periodicity at the wavelength associated with the grinding signature, or the distance that the grinder moves forward in one rotation of the grinding stone. It is critically important that this wavelength does not coincide with the characteristic wavelength of corrugation. The periodicity associated with the grinding signature is still apparent in many cases when the track is next ground.

These measurements were obtained using equipment that was in routine use for rail maintenance or planning of maintenance. The RCA would appear from the results presented here and in a previous reference [17] to offer a means of obtaining reliable and accurate measurements of railhead irregularities over an extremely wide wavelength range, from the shortest wavelengths of interest for rolling noise to the longest of interest for ground-borne noise and vibration. These measurements can moreover be obtained for an almost unlimited distance.

**Acknowledgements** RailMeasurement Ltd is indebted to the many clients and users of RCA equipment for providing the results on which this paper are based.

## References

1. Remington, P.J., Rudd, M.J., Ver, I.L., et al.: Wheel/rail noise, parts I-V. *J. Sound Vib.* **46**, 359–451 (1976)
2. Thompson, D.J.: Wheel-rail noise generation, parts I-V. *J. Sound Vib.* **161**, 387–482 (1993)
3. Dings, P.C., Dittrich, M.G.: Roughness on Dutch railway wheels and rails. *J. Sound Vib.* **193**, 103–112 (1996)
4. Fodiman, P., Staiger, M.: Improvement of the noise technical specifications for interoperability: the input of the NOEMIE project. *J. Sound Vib.* **293**, 475–484 (2006)
5. Verheijen, E.: A survey on roughness measurements. *J. Sound Vib.* **293**, 784–794 (2006)
6. Diehl, R.J., Holm, P.: Roughness measurements—have the necessities changed? *J. Sound Vib.* **293**, 777–783 (2006)
7. Grassie, S.L., Saxon, M.J., Smith, J.D.: Measurement of longitudinal rail irregularities and criteria for acceptable grinding. *J. Sound Vib.* **227**, 949–964 (1999)
8. Railway applications—noise emission—rail roughness measurement related to rolling noise generation, European Standard EN 15610:2009, May 2009, CEN, rue de Stassart 36, B-1050 Brussels, Belgium
9. Railway applications—noise emission—road test of draft standard for rail roughness measurement prEN15610:2006, March 2008, CEN, rue de Stassart 36, B-1050 Brussels, Belgium
10. Jones, C.J.C., Létourneaux, F., Fodiman, P.: Testing a new rail roughness measurement standard. In: *Proceedings of Euronoise/ Acoustics '08*, Paris, 29 June–4 July 2008
11. Triepaischajonsak, N., Thompson, D.J., Jones, C.J.C., Ryue, J., Priest, J.A.: Ground vibration from trains: experimental parameters and validation of a numerical model. *J. Rail Rapid Transit, Procs of I mech E* **225F**, 140–153 (2011)
12. Spännar, J.: Measured rail corrugation growth. In: *Proceedings of 8th International Conference on Contact Mechanics and Wear of Rail/Wheel Systems (CM2009)*, Firenze, Italy, September 15–18, 2009
13. Grassie, S.L.: Rail irregularities, corrugation and acoustic roughness: characteristics, significance and effects of reprofiling on different types of railway system. *J. Rail Rapid Transit, Procs of I mech E* **226F**, 542–557 (2012)
14. Nelson, J.T., Watry, D.L.: Vibration control on Sound Transit. In: Nielsen, J.C.O., et al. (eds.) *Noise and Vibration Mitigation for Rail Transportation Systems*. NNFM, vol. 126, pp. 313–320. Springer, Heidelberg (2015)
15. <http://railmeasurement.com/rail-corrugation-analyser-rca/>. Accessed 15 June 2016
16. Railway applications—track—acceptance of works—Part 3: Acceptance of rail grinding, milling and planing work in track, European Standard EN 13231-3:2006, May 2006, CEN, rue de Stassart 36, B-1050 Brussels, Belgium
17. Grassie, S.L.: Measurement of long wave irregularities on rails. In: Nielsen, J.C.O., et al. (eds.) *Noise and Vibration Mitigation for Rail Transportation Systems*. NNFM, vol. 126, pp. 643–649. Springer, Heidelberg (2015)
18. Bewes, O.G., Jakielaszek, L.J., Richardson, M.L.: An assessment of the effectiveness of replacing slab track to control groundborne noise and vibration in buildings above an existing railway tunnel. In: Nielsen, J.C.O. et al. (eds), *Noise and Vibration Mitigation for Rail Transportation Systems*. NNFM, vol. 126, pp. 393–400. Springer, Heidelberg (2015)
19. Grassie, S.L.: Short wavelength rail corrugation: field trials and measuring equipment. *Wear* **191**, 149–160 (1996)
20. Acoustics—Railway applications—Measurement of noise emitted by railbound vehicles, European Standard EN ISO 3095:2013, August 2013, CEN, rue de Stassart 36, B-1050 Brussels, Belgium
21. Asmussen, B., et al.: Status and perspectives of the ‘Specially Monitored Track’. *J. Sound Vib.* **293**, 1070–1077 (2006)

# Noise Reduction Measure for Trussed Non-slab Bridges



Shinji Mori, Minoru Kobayashi and Junichiro Osawa

**Abstract** In this paper, we introduce that noise reduction can be realized by corrective grinding at rail joints of the bridge section. The noise level was reduced by about 4 to 5 dB before and after rail corrective grinding. Also in the frequency characteristic analysis, the noise reduction effect was recognized in a wide frequency band of 50 to 8 k Hz. Furthermore, In light of the results delivered by this corrective grinding, we implemented corrective grinding at rail joints in a continuous, roughly 250-m section, and measured noise levels. Approximately 10 dB noise level was reduced before and after rail corrective grinding, and the noise level was reduced in all frequency bands.

## 1 Introduction

In 1927, Tokyo Metro Co., Ltd. began operating the first subway in Asia in Tokyo, Japan. Presently the company operates nine subway lines over 195.1 km of track. Most of the lines in the urban center of Tokyo run through tunnels, while many of the lines outside the urban center run above ground. Nearly all the bridges in the above-ground sections are trussed non-slab bridges, designed in the 1960s with emphasis on controlling construction costs. Residential development progressed near the bridges and population grew along the lines into the 1980s, and these developments have resulted in increasing demand to reduce the noise created by passing trains. The low weight limits that accompany the low-cost design of the trussed non-slab bridges make it difficult to add soundproof panels and the like across the lengths of the bridges. Similarly, the option of welding rail joints to create continuous welded rails (CWR) is often impossible to implement on bridges due to restrictions such as limitations on longitudinal force due to CWR. We exhausted our imaginations to find radical ways to overcome these difficulties and reduce noise on above-ground bridges, and settled on corrective grinding at rail

---

S. Mori (✉) · M. Kobayashi · J. Osawa  
Tokyo Metro Co., Ltd., 3-19-6, Higashiueno, Taito-ku, Tokyo, Japan  
e-mail: s.mori.k4y@tokyometro.jp

joints on trussed non-slab bridges where it was relatively easy to implement. In this paper, we introduce this method of reducing noise.

## **2 Selecting a Target Bridge and Measuring Noise**

### ***2.1 Target Bridge***

About the target bridge:

Name: Arakawa-Nakagawa Bridge

Section: Electrified double-track section

Length: 1270 m

Rail mass: 50 kg/m

Sleepers: compound sleeper

Line: Tozai Line, Tokyo Metro (use only by trains)

Construction: October 1966 to September 1968

Superstructure: Warren through-truss

Track construction: Ballastless.

### ***2.2 Measurement Locations***

We conducted measurements along the Tozai Line between Minami-sunamachi and Nishi-kasai Stations, near the 19,436 m point (from the line origin) at the continuous truss at the 15th span (“T15”), and near the 19,511 m point (from the line origin) at the continuous truss at the 16th span (“T16”). We measured only the A Line at each location. Measured section at T15 is at rail joints, and is at welded joints at T16. Table 1 and Figs. 1, 2, 3, 4, 5 and 6 show information about the measurement locations. These are based on Ref. [1].

## **3 Noise Source Analysis**

The first step of this research was to analyze the noise sources on the bridge. After identifying the sources, we calculated the respective proportions of noise attributable to the rolling stock and the bridge structure.

**Table 1** Measurement locations (T15, at rail joints, T16, at welded joints)

No.	Data	Measurement locations		T15	T16
1	Vibration	A line	Rails	✓	✓
2			Sleepers	✓	✓
3			Vertical girders	✓	✓
4			Lateral girders	✓	✓
5			Diagonal chords	✓	
6	Noise	A line	Near rails	✓	✓
7			Near vertical girders	✓	✓
8			Near lateral girders	✓	✓
9			Truss height	✓	
10		Structure center	Floor system center	✓	✓
11		Ground level	12.5 m below girders	✓	✓
12			Below girders	✓	✓

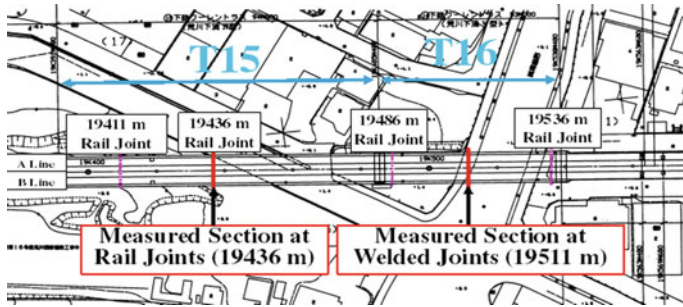


**Fig. 1** Overview of target bridge

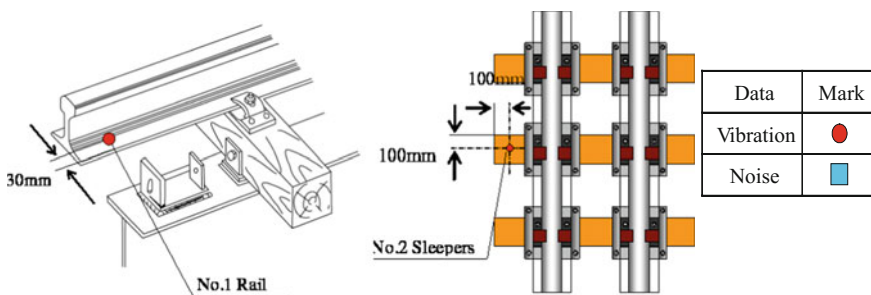


**Fig. 2** Measurement locations—rails, sleepers

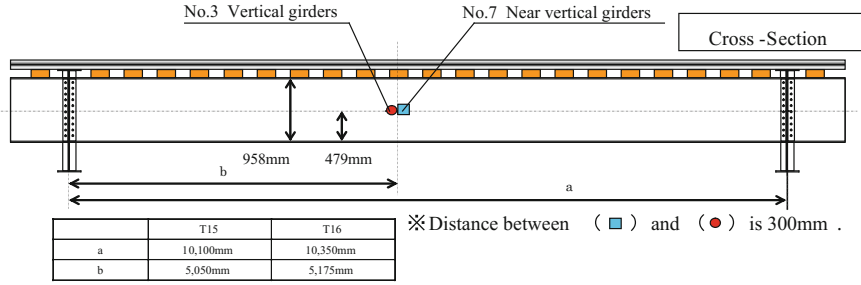


Fig. 3 Measurement locations—vertical girders

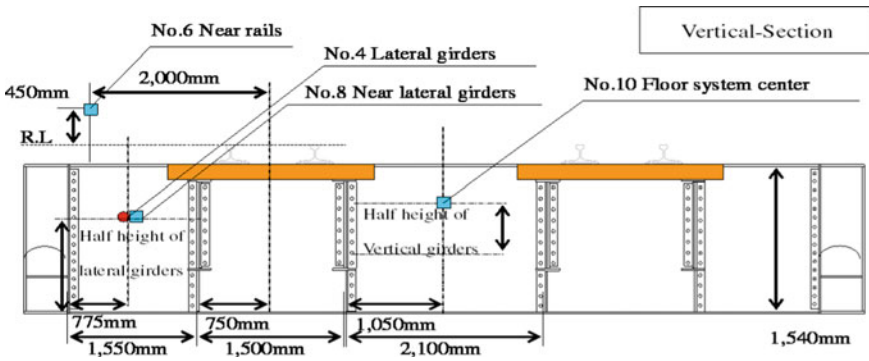


Fig. 4 Measurement locations—near rails, lateral girders, floor system center

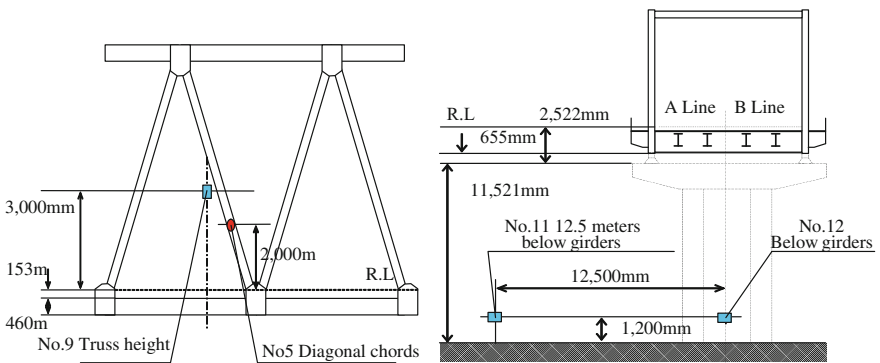
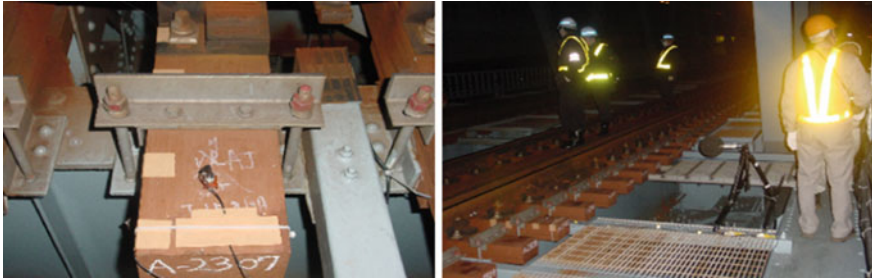


Fig. 5 Measurement locations—diagonal chords, truss height, below girders, 12.5 m below girders



**Fig. 6** Examples—sleepers (vibration), near rails (noise)

### 3.1 Hypotheses and Analytical Procedure

We hypothesized that the two main noise sources on the target bridge are the bridge structure and the rolling stock. All noise sources were assumed to be non-directional, finite line sound sources. In our analysis, we supposed that each sound source had the total radiated sound power in the center of each member. We set the location of the source of rolling stock noise at the center of the near-side rails, at the level of the rails, in addition we set the location of the source of structure-borne noise horizontally at the center of the near-side rails, and vertically at half the height of the vertical girders.

We defined structure-borne noise as the combination of radiated sound from the members we measured at the measurement locations at T15 and T16: sleepers, vertical girders, lateral girders and diagonal chords.

The rolling stock is a combination of noise generated between the rails and wheels and noise generated by equipment on trains (Fig. 7).

The main analytical procedure is as follows.

Step 1: Categorize sound sources (rolling stock and bridge structure)

We used actual measured values of noise to calculate the sound power levels of the rolling stock and the bridge structure. The respective sound power levels of these two noise sources were unknown; thus, actual measured values of noise at two measurement locations were required to derive them. After consideration, we determined that using data from near the rails and from the center of the floor system was appropriate for this experiment.

Step 2: Analyze degree of noise attributable to structure-borne noise

We estimated the sound power levels of each noise source by dividing the sound power of the entire structure-borne as derived in Step 1. It was calculated by A-weighted vibration velocity levels actual measurements of vibration acceleration and by the radiated sound area of the members. We conducted this analysis on the A Line at T15 and T16.

Step 3: Analyze degree of noise at 12.5 m below girders.

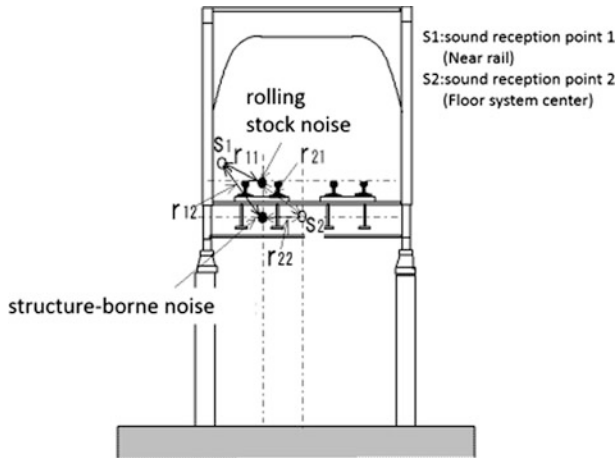


Fig. 7 Image of analysis

We used the sound power of noise sources to calculate the noise level for each source at 12.5 m from below girders. We incorporated decay due to distance and diffraction into our calculations. Note that we used A-weighted values for sound power levels and noise levels in this analysis.

### 3.2 Input Data

Table 2 shows A-weighted vibration velocity levels of each noise source calculated by actual measurements of vibration velocity. Table 3 shows the radiated sound area of the members.

These two values are input to calculate the sound power levels of each noise source.

### 3.3 Results

Table 4 shows our calculations of sound power levels for each noise source on the A Line at T15 and T16. The results revealed the following:

Table 2 A-weighted vibration velocity level (dB)

	T15	T16
Sleeper	104.2	89.1
Vertical girders	96.4	91.8
Lateral girders	95.2	83.6
Diagonal chords	88.1	88.1



**Table 3** Radiated sound area (m<sup>2</sup>/m)

	T15	T16
Sleeper	3.6	3.5
Vertical girders	11.5	11.2
Lateral girders	3.6	3.1
Diagonal chords	11.9	16.0

**Table 4** Calculation result of sound power level (dB)

Noise source		T15	T16
Rolling stock noise		111.3	104.4
Structure-borne noise	Sleeper	108.0	92.4
	Vertical girders	105.3	100.1
	Lateral girders	98.6	86.9
	Diagonal chords	98.5	96.6
	Total	110.5	102.4

**Table 5** Calculation result of noise level at 12.5 m from below girders (dB)

Noise source		T15	T16
Rolling stock noise		91.5	84.5
Structure-borne noise	Sleeper	88.3	72.7
	Vertical girders	85.6	80.4
	Lateral girders	78.9	67.2
	Diagonal chords	78.8	76.9
	Total	90.8	82.7

- (1) The sound power level of rolling stock noise was the highest of all sound at both T15 and T16. This is a distinct attribute of the target bridge; the reference [2] we cited shows that structure-borne noise was around 4 dB higher than rolling stock noise at a different bridge.
- (2) The second-highest sound power level was sleepers at T15 and it was vertical girders at T16.

Table 5 shows our calculations of noise levels on the ground level, 12.5 m from below girders. These measurements show that rolling stock noise contributed most to noise at T15 and T16, followed by sleepers at T15 and vertical girders at T16. These match the sound power level results.

The results from Tables 4 and 5 demonstrate that it is most important and effective to address rolling stock noise at both T15 and T16.

## 4 Noise Attribute Analysis

Next, we measured noise levels and analyzed frequency attributes on the bridges at rail joints (T15) and at welded joints (T16). We expected noise to be louder at rail joints than welded joints. Nonetheless, we analyzed both in order to confirm the facts and fully understand the extent of noise. Note that we used A-weighted values for noise levels and frequency characteristics in this analysis.

### 4.1 Comparing Noise Levels

Figure 8 shows a comparison of noise levels near the rails at T15 and T16. The results revealed the following:

- (1) The overall noise level at welded joints (T16) was lower than that at rail joints (T15). This allowed us to confirm that noise at rail joints is higher than noise at welded joints.
- (2) Our measurements showed noise levels of 95 to 100 dB(A) near the rails on A Lines at T16.

### 4.2 Comparing Noise Frequency Characteristic

Figure 9 shows a comparison of 1/3 octave band spectra near the rails at T15 and T16. The results revealed the following:

- (1) The basic features of the frequency characteristic, such as noise peaking around a frequency of 1 kHz, are similar for T15 and T16 near both rails.
- (2) The data show higher frequencies of noise at rail joints at T15 on the A Line than that at welded joints at T16.

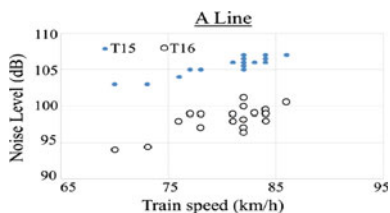


Fig. 8 Comparison of noise levels near rails

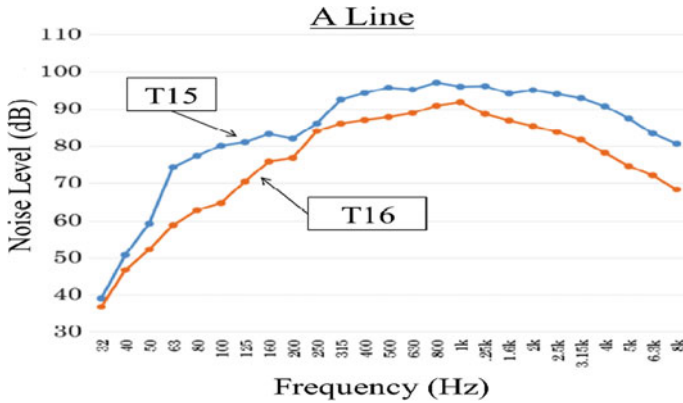


Fig. 9 Comparison of frequency characteristic

The above data show that noise levels are considerably higher at rail joints than at welded joints. This means that controlling noise at joints is the more effective way to reduce noise.

## 5 Noise Reduction Through Corrective Grinding

The analysis of noise sources and attributes from Sects. 2.1 and 3 showed that reducing rolling stock noise at rail joints would be the most effective way to reduce noise. Thus, we implemented corrective grinding on the rails of the A Line at rail joints at T15. Next we analyzed the effects of the corrections by comparing the results of noise measurements and frequency characteristic before and after the corrections. Note that we used A-weighted values for noise levels and frequency characteristics in this analysis.

### 5.1 Overview of Corrective Grinding Method

During this research, we used a rail grinder to implement corrective grinding. A rail grinder is a corrective grinding device developed by the East Japan Railway Company for the purpose of improving precision after rails are welded.

Rails are ground by pushing an abrasive belt rotating in the longitudinal direction with respect to the rails along a roller, which moves back and forth along the rails longitudinally when pushed. The top and sides of the head of the rail can be corrected, and each corrective stroke can adjust 150 to 1000 mm of rail.

We used the following procedure to implement corrective rail grinding during this research.

- (1) Measure unevenness in the heads of rails with a 1-m gauge, mainly at rail joints.
- (2) Correct the higher side of the unevenness. Generally, the higher side is on the preceding rail with respect to the motion of the trains. Thus, the preceding rail is often corrected to the height of the succeeding rail.

When the difference is greater than 1 mm, spread out the correction around 1 m from the joint.

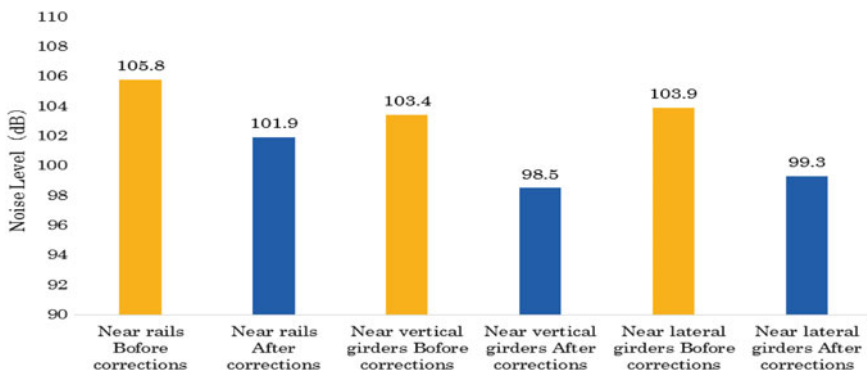
## 5.2 Noise Levels Before and After Corrective Grinding

Figure 10 shows changes in noise levels at T15 on the A Line as a result of corrective grinding, expressed as energy average values of noise levels at train speeds from 77 to 83 km/h as measured before and after corrective grinding. Before corrective grinding, the unevenness was about 1 mm, but after corrective grinding, it became close to 0.

According to these results, noise levels at each measurement location at T15 obviously reduced. The mean change was a decrease of around 4 or 5 dB near the rails and vertical girders, lateral girders. This means that corrective grinding at rail joints is highly effective in reducing noise.

## 5.3 Frequency Characteristic Before and After Corrective Grinding

Figure 11 shows analysis of the frequency of noise before and after corrective grinding at T15 on the A Line. For this paper, we analyzed frequencies near the rails and at the center of the floor system.



**Fig. 10** Noise levels before and after corrective grinding (dB)

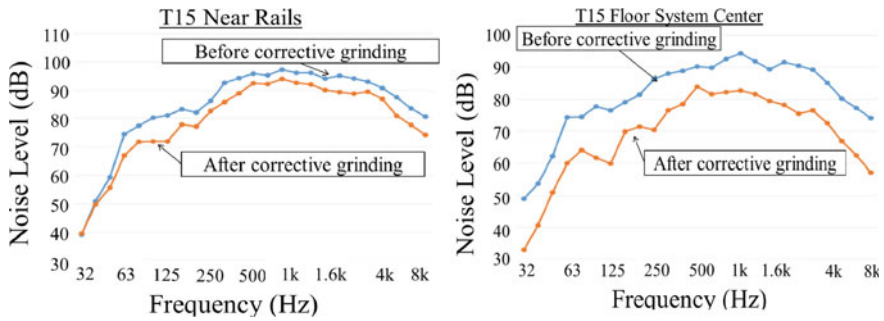


Fig. 11 Frequency characteristic before and after corrective grinding (dB)

The frequency analysis shows that corrective grinding effectively reduced noise across a wide range of frequencies (from 50 to 8 k Hz) at each measurement location at T15. In particular, the corrections reduced noise significantly at the Floor System Center. We also analyzed frequencies at T16, but the corrections at T15 caused hardly any change. These results also show that corrective grinding at rail joints was highly effective in reducing noise.

## 6 Corrective Grinding in Long Sections

In light of the results delivered by this corrective grinding, we implemented corrective grinding at rail joints in a continuous, roughly 250-m section around T15, and measured noise levels. The target section included the A and B Lines between the points 19,226 and 19,476 m from the line origin, and the noise was measured from the ground level, below girders at 19,351 m. We measured noise on the day of the corrections, and on the day after; in other words, we implemented the corrections during the night after the first day’s measurements. We took measurements on the second day at the same time of day as on the first day. We measured noise for 10 passing trains on each day. Note that we used A-weighted values for noise levels.

### 6.1 Noise Levels Before and After Corrective Grinding

Figure 12 shows analysis of the noise levels before and after corrective grinding. The corrections resulted in noise reductions of 8.4 dB on the A Line and 10.0 dB on the B Line. Since each full train is roughly 200 m long, we expect that correcting a 250-m section would give an increased benefit of reduced noise over a correction in a single location.

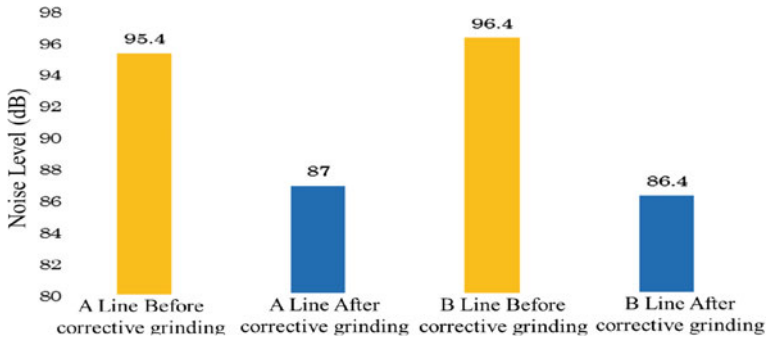


**Fig. 12** Noise levels before and after corrective grinding (dB)

## 7 Conclusion

Our investigation of the noise sources on a trussed non-slab bridge clearly showed the degree of noise attributable to rolling stock at rail joints. Our data also clearly show that we were able to use corrective grinding at rail joints to achieve high noise reduction effects as changing to continuous welded rails. The corrective grinding method can reduce noise that reaches people living near these bridges, and the reduced vibrations can improve the durability of bridge members. We intend to periodically measure noise to investigate the durability of corrective grinding at rail joints and to standardize corrective grinding at bridge joints.

## References

1. Yukio, S., Akira, N., Kenzo, T., Shigeru, M.: Track, Revised edn. Japan Railway Civil Engineering Association, Daito-ku (1997)
2. Hansaka, M., Sugimoto, I., Nagakura, K., Mamada, S.: Analysis of contribution of structure-borne noise radiated from each member and examination of materials to reduce noise. Railway Tech. Res. Inst. Rep. **21**(2), 21 (2006)

# Effects of Rail Lateral Dynamic Deflection and Vibration Level on Rail Corrugation Development



A. Wang, Z. Wang, Z. Zhang, N. Xu, X. Qiao and M. Du

**Abstract** To seek the generation and development mechanism of rail corrugation, the relationship between track support stiffness change of the rail system and wheel-rail system dynamic receptance is investigated. The mechanism of “variation of difference between wheel and rail receptance” has been studied recently as one of the main reasons to cause the short wavelength rail corrugation. It can clearly describe the basis of rail corrugation generation. Based on this new understanding, reduction in the variation difference of wheel-rail receptance and rail vibration in the lateral direction can effectively prevent the formation and development of rail corrugation. The effects of rail deflection and lateral vibration on the rail corrugation development have been demonstrated with two types of rail fasteners with different lateral stiffnesses on a curved track. Rail roughness levels have been monitored using the CAT system every month for a period of the rail grinding circle under normal traffic condition. A new resilient baseplate system, with a similar vertical stiffness but high lateral stiffness relative to the Egg baseplate, was installed and compared with the existing Egg system on an curved track with radius of 350 m on Nanjing Metro Line 1 in order to compare rail corrugation development of two systems. It is concluded that one of the key means to slow down the corrugation growth is to reduce the difference of wheel-rail receptance and control the rail dynamic deflection and vibration level in the lateral direction. Rail roughness growth on the track with Egg baseplate is about 15 dB(A) higher than that on the track with the high lateral stiffness resilient baseplate in about 6 months period after the rail was ground.

---

A. Wang (✉)

Shanghai University of Engineering Science, 333 Longteng Road,  
Shanghai 201620, People’s Republic of China  
e-mail: anbin.wang@sues.edu.cn

A. Wang · Z. Wang · Z. Zhang · N. Xu  
Luoyang Ship Material Research Institute, Luoyang 471003  
People’s Republic of China

X. Qiao · M. Du  
Nanjing Metro Operation Co., Ltd., Nanjing 210012, People’s Republic of China

## 1 Introduction

Rail corrugation, developed at different levels during rail transit operation, not only increases the wheel-rail noise and vibration, but also accelerates the fatigue failure of track and vehicle components, seriously threatening operational safety. Since the late 70s, a large number of scholars and researchers engaged in research in this area [1–3]. For seeking the generation and development mechanism of rail corrugation, a great deal of theoretical and experimental studies were carried out. However, because many factors affect the interaction between vehicle and track [4, 5], such as the dynamic characteristics of the bogie system and rail system, material properties and wheel-rail rolling contact conditions, the running condition of the vehicle and the wheel-rail surface irregularity roughness, the researchers still have not come to an agreement on the rail corrugation generation and development mechanism and means of control [6, 7]. In this paper, by studying the support stiffness changes of the rail system [8] and the wheel-rail system dynamic receptance relationship, the mechanism “variation of difference between wheel and rail receptance” is first proposed, that can effectively describe the reasons of rail corrugation generation for the short wavelength in frequency range between about 200 and 1200 Hz. Experimental verifications were made in different metro lines with the same conclusion, that the vibration difference of wheel-rail receptance, discrete support and the support stiffness variation are the main reasons of rail corrugation generation. Based on this new mechanism, decreasing the variation difference of wheel-rail receptance and rail vibration will effectively inhibit the formation and development of rail corrugation.

Two rail fastening systems with different lateral stiffness have been investigated to study the effect of the difference of wheel-rail lateral receptance on the development of rail corrugation. Investigation was carried out on a curved track under normal operation traffic excitation. Rail roughness levels have been monitored every month for rail grinding cycle to compare those two different track forms.

## 2 Rail Lateral Dynamics and Rail Roughness Growth

### 2.1 *Characteristic Frequency of Discontinuous Support System*

Rail corrugation is a typical rail roughness phenomenon. During train operations, periodic wear marks appeared on the rail surface along the longitudinal direction. These marks have fixed wave length. It is easy to notice the wear marks on the rail head with evident wave crest and trough. Due to the complicated nature of wheel-rail interactions, which involve dynamics, contact and friction mechanics and their cross-disciplines, rail corrugation is considered as the consequence of a quasi-periodic normal load in combination with a considerably constant tangential



traction, which may arise from applied traction and braking, steering forces or a combination of all. The so-called “wavelength-fixing mechanism” is the resonance of vehicle’s unsuspended mass (“P2 resonance”) or the “pinned-pinned resonance” of the rail [1].

The “pinned-pinned resonance” was shown to be the dominant mechanism of wavelength-fixing. This pinned-pinned frequency  $f$  can be calculated with the equation below [5]:

$$f = \frac{\pi}{2l^2} \sqrt{\frac{EI}{m_r}} \left\{ 1 - \frac{1}{2} \left( \frac{\pi r_g}{l} \right)^2 \left( 1 + \frac{2(1+\nu)}{K} \right) \right\} \quad (1)$$

$E$  is the modulus of elasticity of rail steel,  $I$  is the moment of inertia of the rail,  $m_r$  is the rail mass per unit length,  $l$  is the fastener spacing,  $r_g$  is the radius of gyration,  $\nu$  is Poisson’s ratio, and  $K(\approx 0.34)$  is the shear constant of the cross section.

The wavelength and wave amplitude are both important parameters to define the rail corrugation level. Therefore the corrugation excitation frequency of the running train can be calculated if the train speed is known, i.e.

$$f_c = s/\lambda \quad (2)$$

where  $f_c$  is frequency,  $s$  is train speed and  $\lambda$  is wavelength of corrugation. This is useful to identify the vibration source on the corrugated track. Changing the train speed may affect the wavelength of corrugation but may not effectively inhibit the rail corrugation formation.

## 2.2 Comparison of Theoretical Analysis and Test Result

In order to eliminate the effect of the different factors, such as the axle load, vehicle speed, curve radius and the wheel rail surface conditions on measurement results, frequency response functions of the track system can be used. The frequency response function can identify system’s natural characteristics such as track stiffness, resonance frequencies etc. This can be conducted to measure the track response when tracks are excited by an impact force using instrumented hammer. Track vibration propagation decay rate can be also obtained through multi-point transmission response function.

Figure 1 shows a simple model of a typical rail system, including the representation of continuous rail, discrete support spring and damping. The vertically and horizontally dynamic flexibility and constraints due to foundation are considered in the model.

The dynamic characteristics of track system can be described by the formula of discretely supported Timoshenko beam model:

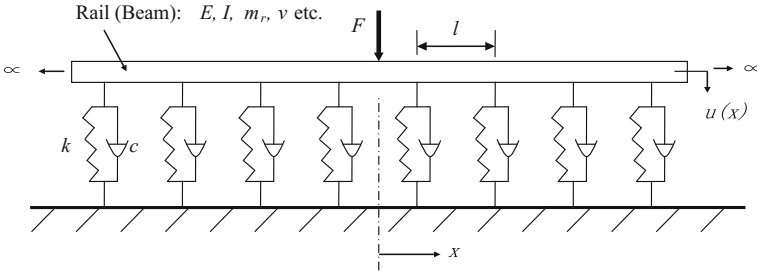


Fig. 1 Track model

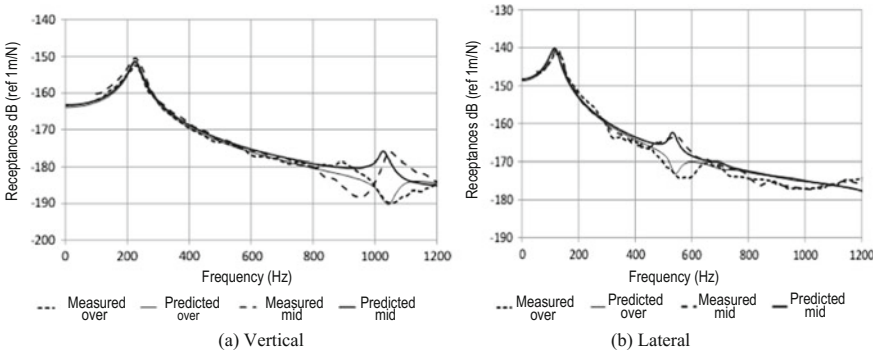


Fig. 2 Rail receptances

$$-m_r \omega^2 u + GA\kappa(\phi' - u'') + \sum_{n=1}^N ku\delta\{x - x_n\} = Fe^{i\omega t} \delta(x) \tag{3}$$

$$-\rho I \omega^2 \phi + GA\kappa(\phi - u') - EI\phi'' = 0 \tag{4}$$

where,  $u$  is the vertical displacement of the rail vibration at the position  $x$ ,  $\phi$  is the angular displacement of rail vibration at position  $x$ ,  $p$  is the density of the rail per unit length,  $A$  is the cross-sectional area of the rail,  $G$  is the shear modulus of the material of the rail,  $k$  is the stiffness of the rail support fastener  $k = k_0(1 + i\eta)$ ,  $\eta$ ,  $\eta$  is the damping loss factor,  $x_n$  is the position of the rail support,  $F$  is the excitation force acting on the rail.

Figure 2 shows the rail receptance spectrum just above the support and at the 1/2 span of adjacent fasteners in the vertical and transverse directions. Theoretical calculations and field test results are drawn on the same graph, and good match were found. The theoretical and test parameters are shown in Table 1. The equivalent lateral parameters correspond to the position at the rail head [9].

From the theoretical calculations and the site tests, that in the no-load track system with 60 kg rails, ordinary track bed, 75 MN/m vertical support stiffness

**Table 1** Track parameters in the vertical and lateral directions

Vertical bending rigidity	$EI/m^2$	$6.42 \times 10^6$	Lateral bending rigidity	$EI/m^2$	$1.05 \times 10^6$
Vertical shearing rigidity	$GA/N$	$5.92 \times 10^5$	Lateral shearing rigidity	$GA/N$	$3.85 \times 10^5$
Vertical equivalent density	$\rho A/ \text{kg m}^{-1}$	60.4	Lateral equivalent density	$\rho A/ \text{kg m}^{-1}$	39.3
Vertical supporting stiffness	$k/ \text{MN m}^{-1}$	75	Lateral supporting stiffness	$k/ \text{MN m}^{-1}$	13.0
Supporting spacing	$l/m$	0.625	Damping loss factor	$\eta$	0.2
Shear constant	$\kappa$	0.34	Poisson ratio	$\nu$	0.3

fastener and 0.625 m support span, the P2 resonance frequency is 220 Hz in the vertical direction, and 110 Hz in the lateral direction; the p-p frequency in the vertical direction is about 1050 Hz, and in the lateral is about 550 Hz.

### 2.3 Variation of Discontinuous Support Rail Receptance

As shown in Fig. 2, due to the discontinuous support of the rail, there is a large dynamic receptance difference at the p-p frequency in the bearing positions and between. At the support position, the rail receptance at the p-p frequency is shaped like a valley, and in the middle span is peak shaped. Most rail corrugation occurs primarily below 800 Hz, close to the lateral p-p frequency. Figure 3 shows the lateral rail receptance along the rail at the p-p frequency 550 Hz. It can be seen from the figure, the rail receptance change at p-p frequency exceeds 10 dB. This wide variation of rail dynamic response will greatly increase the track dynamic

**Fig. 3** Rail lateral receptance along the track direction

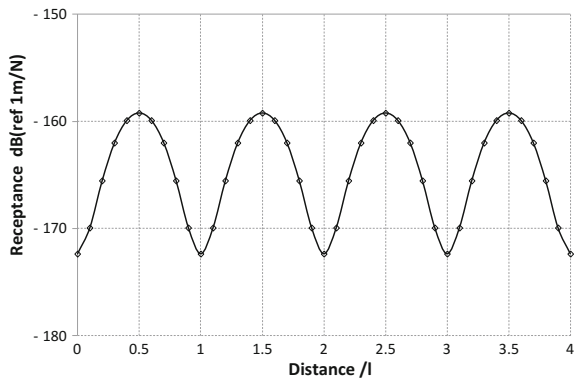
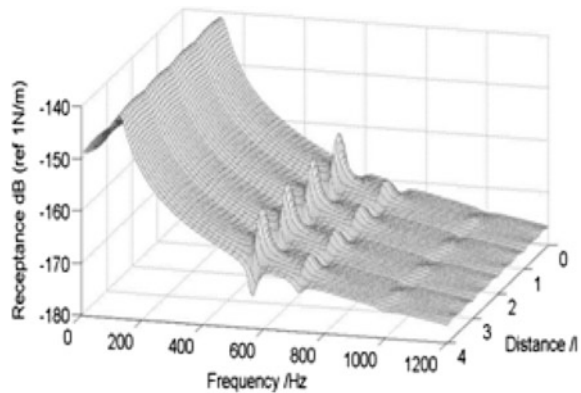


**Fig. 4** Rail lateral receptance spectrum along the track



instabilities; Fig. 4 shows the lateral rail receptance spectrum in different locations, from which the receptance along the rail at different frequencies are shown [9].

## 2.4 The Wheel-Rail Receptance Difference Variation and the Rail Corrugation Generation

### 2.4.1 Wheel-Rail Receptance Level Difference

The receptance spectrum in dB of a 60 kg rail and a typical wheel at each contact point are shown in Fig. 5. The level difference of receptances between the wheel and rail are plotted in Fig. 6 for both track vertical and lateral directions. The rail receptance in the vertical direction below the p-p frequency is much higher than that of the wheel except at the wheel modal frequency around 500 Hz. If the same wheel-rail interaction force applied, the vibration displacement of the rail should be greater than that of the wheel [9].

### 2.4.2 Generation and Development of Rail Corrugation

#### (1) Vertical impact effect:

Due to the difference variation between wheel-rail receptance caused by contact forces between rail and wheel along the track direction, the contact force of wheel-rail interaction is a kind of non-steady-state dynamic force  $F$  as shown in Fig. 7a. Under the vertical excitation of this unsteady wheel-rail dynamic force as well as the wheel-rail roughness irregularity, there is a difference in vibration displacement between the rail and the wheel, which results in the unsteady rolling mode of “contact—separation—impact—contact” in range below certain frequency such as p-p frequency. At the same train speed and track structure condition, if there

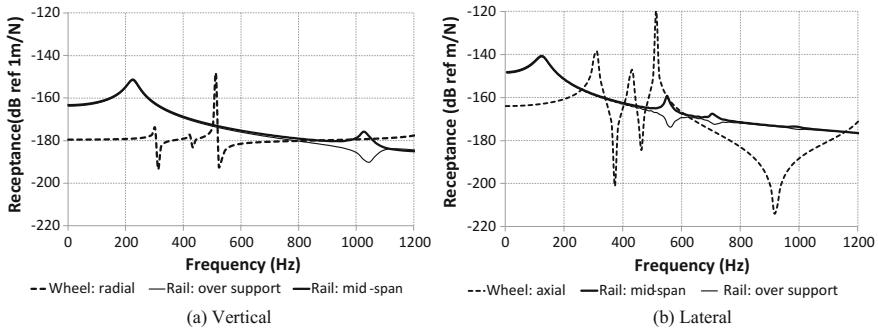


Fig. 5 “Wheel-rail” receptance in the vertical direction

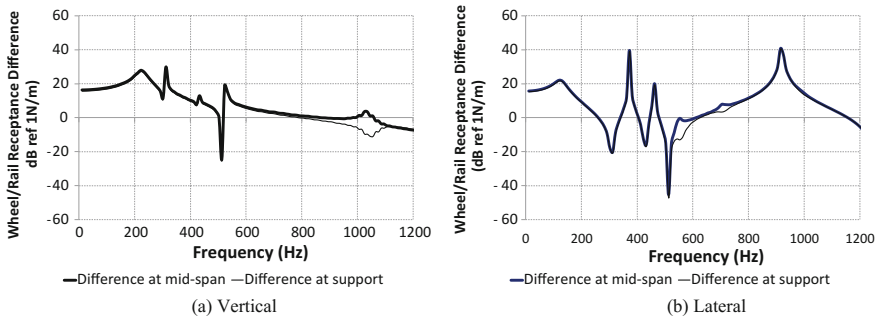


Fig. 6 The difference of receptances between wheel and rail

is a large vibration displacement difference between rail and wheel at certain frequency, this “contact—separation—impact—contact” model will cause the periodic variation of wheel-rail interaction forces and the consequence is the generation of regular rail wearing marks along the rail length.

**(2) Horizontal sliding wearing effects:**

When the wheels roll along the rails, except the longitudinal sliding and rolling, there is also the lateral sliding occurring in the wheel-rail contact surface because of the gradient tread design at the wheel-rail contact tread. Also due to the existence of the lateral wheel-rail dynamic receptance difference, especially at p-p frequency band, and the variation of receptance in the longitudinal direction, the lateral periodic vibration displacement occurs and causes wheel-rail contact surface wear. When the train is moving at a constant speed, the rail lateral vibration and the vertical component on the contact surface will cause force fluctuations and horizontal alternating sliding. The wheel-rail vertical-horizontal interaction model is shown in Fig. 7b. Since the receptances of wheel and rail are different and their difference together with wheel-rail contact forces changes along the rail, the standing wave shape wearing will occur in the longitudinal direction. Figure 8

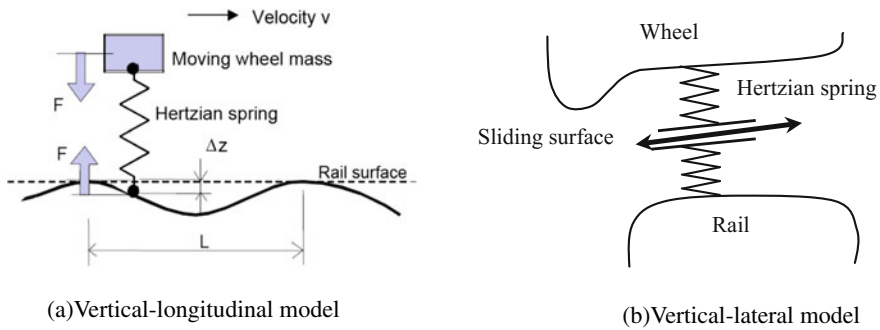
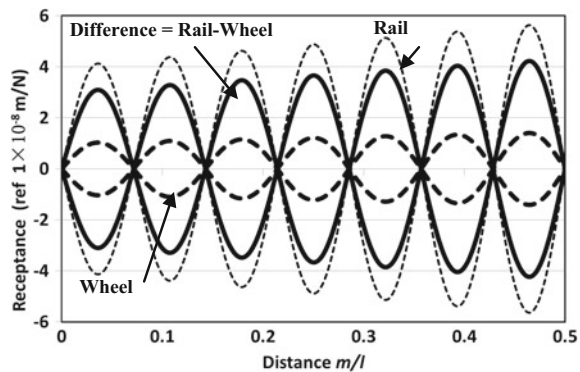


Fig. 7 Wheel-rail rolling contact interaction

Fig. 8 Wheel-rail receptance amplitude simulation



shows the simulation results of receptances of rail and wheel, and their difference at the mid span between two supports. In practice, because of the ellipse shape of the wheel-rail Hertz contact zone and the running tread band width, the lateral vibrating and sliding wear trace is wide.

As the above analysis shows, the short wavelength rail corrugation is generated mainly by the wheel-rail periodic interaction variation because of the variable difference of wheel-rail receptance under the fixed train speed, especially at the lateral p-p frequency caused by the discontinuous support track structure.

### 3 On Site Test

#### 3.1 Test Site

In order to find out the effects of track lateral receptance on the rail corrugation growth on the tracks under normal traffic conditions, a trial was carried out on a curve track on Nanjing Metro Line 1 with two different fastening systems, Egg

baseplate with lateral stiffness of 5 MN/m and a new type of baseplate with high lateral stiffness of 15 MN/m. The site is located between Shuanglong Road station and Nanjing South Station.

The Egg baseplates were original installation between kilometer posts K7+429 and K7+917 for 488 m long, where the last rail grinding was made on 19 December 2014. The Egg baseplates in the section between K7+600 and K7+675 had been replaced with new baseplates on 16 January 2015, about four weeks after rail grinding. Adjacent two similar sections, K7+600 to K7+675 for new baseplate track, and K7 + 675 to K7 + 750 for Egg baseplate track, with curvature of 350 m were selected to compare the roughness level with the Egg baseplate track and the new baseplate track every month between February and July 2015 within the rail grinding cycle.

### ***3.2 Rail Roughness Measurements***

The rail roughness level was measured using CAT “Corrugation Analysis Trolley” system [10]. Five measurements had been made at monthly intervals.

Measurement wavelength validated for the range of interest from 8 to 800 mm. This is satisfied with the frequency range between 20 and 2500 Hz for noise and vibration when the train speed is around 70 km/h for the metro system. In order to evaluate the effects of rail roughness growth to rail vibration and its noise radiation, rail roughness has been converted with A-weighting into dB(A) levels with known train speed on each site and neglecting any effect of filtering in the wheel-rail contact. This data conversion can represent the effect of rail roughness on the noise level.

### ***3.3 Rail Corrugation Test Analysis***

Figures 9 and 10 show measured roughness spectrum over time for track fitted with Egg fasteners. The 1st measurement was in Feb. 2015, which is about 6 weeks after the rail was ground. For both low and high rails, corrugation already clearly shown with peaks at one third octave wavelength of 80 and 40 mm at the low rail, and 63 and 31.5 mm on the high rail. Following five measurements were at monthly intervals, as seeing in Figs. 9 and 10, roughness increased as time progressed, which indicates the development and on-set of rail corrugation. Multi wavelength corrugation patterns are shown with dominant peaks at wavelength of 80 and 40 mm on low rail and 63 and 31.5 mm on high rail.

On the track sections fitted with new baseplates of higher lateral stiffness, roughness measurements were taken at the same time and results are shown in Figs. 11 and 12. The 1st measurement shows the roughness peaks at the same wavelength as shown in Figs. 9 and 10, this is because these new baseplates were fitted to replace original Egg baseplates two weeks after track grinding was carried

**Fig. 9** Eggs fastener roughness spectrum-low rail

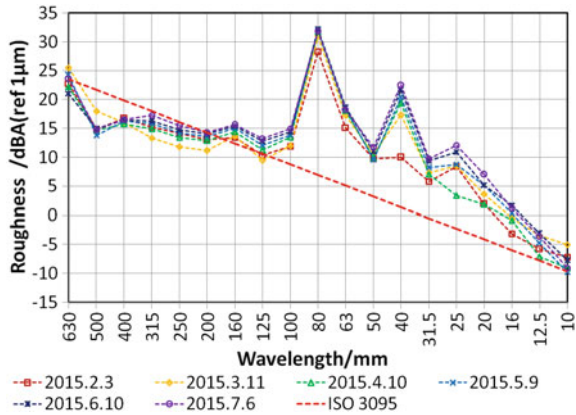
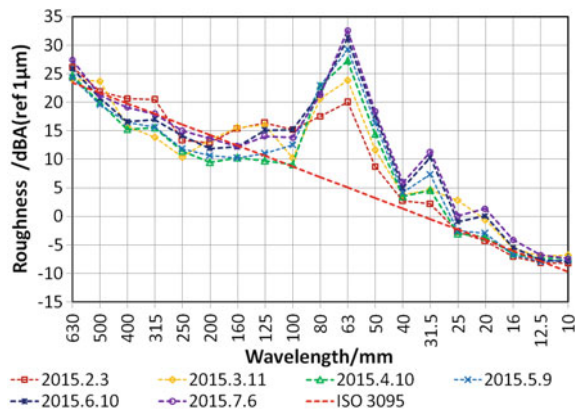


**Fig. 10** Eggs fastener roughness spectrum-high rail



out, and by then corrugation already developed. The further five measurements demonstrated that track roughness reduced over the time at the dominant peak of 80 mm wavelength on low rail, overall reduction on the high rail. The results are very encouraging and suggesting track with new baseplates can effectively control the rail corrugation development on rail tracks with direct-fixation fasteners.

On the low rail, for Egg baseplate track section, in five month time with six monthly roughness measurements, the average rail roughness growth rate is over 0.7 dB per month at 80 mm wavelength and 2.5 dB per month at wavelength 40 mm. At the same time period, for new baseplate track section, rail roughness reduction rate is 2.5 dB per month at 80 mm wavelength, rail roughness increase rate is 1.0 dB per month at 40 mm wavelength.

On the high rail, for Egg baseplate tracks, the average rail roughness growth rate is 3.0 dB per month at 63 mm wavelength and 1.9 dB per month at wavelength 31.5 mm; for new baseplate track, rail roughness reduction rate is 0.24 dB/per month at 63 mm wavelength and 1.5 dB per month at 31.5 mm wavelength.

In summary, according to the six monthly continuous track roughness measurements within two sections fitted with Egg baseplates and new higher transverse



**Fig. 11** New baseplate roughness spectrum-low rail

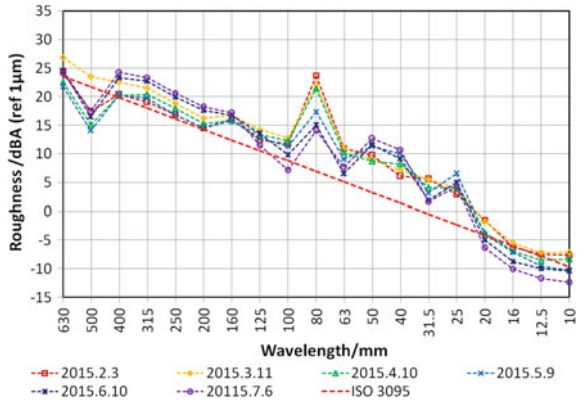


**Fig. 12** New baseplate roughness spectrum-high rail

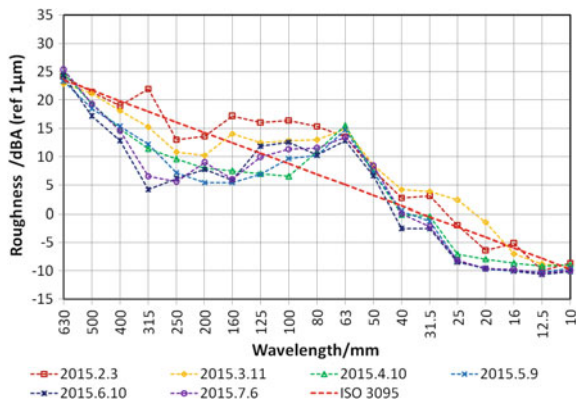
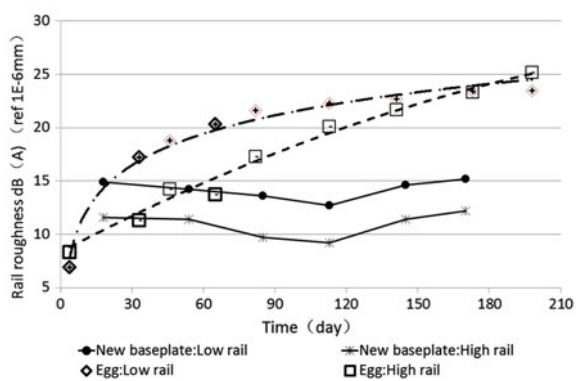


**Fig. 13** Two types rail fastener with the change of roughness level



stiffness baseplates respectively, the overall roughness growth rate is 1.8 dB per month for Egg baseplates tracks, and  $-0.8$  dB (i.e., reduction) per month for new baseplate track. Figure 13 gives the total roughness levels over the time of track sections with two types of rail fastening systems. Rail roughness growth on the

track with Egg baseplate is about 15 dB(A) higher than that on the track with the high lateral stiffness resilient baseplate in about 6 months period after rail grinding.

## 4 Conclusions

The difference of wheel and rail receptance and its variation is one of main factors of rail corrugation generation and development on a discrete support track. Theoretical prediction and site measurement of the receptance and their pinned-pinned frequencies have demonstrated a good agreement.

Rail roughness growth on the track with Egg baseplate is about 15 dB(A) higher than that on the track with the high lateral stiffness resilient baseplate in about 6 months rail grinding cycle. Comparison of effect of two types of baseplates on rail corrugation has found that increase of transverse stiffness of baseplates can effectively control the generation and development of corrugation.

## References

1. Grassie, S.L., Kalousek, J.: Rail corrugation: characteristics, causes and treatments. *Proceedings of the Institution of Mechanical Engineers, J. Rail Rapid Transit.* **207F**, 57–68 (1993)
2. Wang, A., Cox S.J.: Effect of rail pad stiffness on rail roughness growth and wayside noise levels on high speed track. In: *The 6th World Congress on Railway Research*, Edinburgh, UK (2003)
3. Ilias, H.: The influence of rail pad stiffness on wheelset/track interaction and corrugation growth. *J. Sound Vib.* **227**, 935–948 (1999)
4. Collette, C., Horodincu, M., Preumont, A.: Rotational vibration absorber for the mitigation of rail rutting corrugation. *Veh. Syst. Dyn.* **47**(6), 641–659(19) (2009)
5. Grassie, S.L., Cox, S.J.: The dynamic response of railway track with flexible sleepers to high frequency vertical excitation. *Proc. Inst. Mech. Eng.* **198D**(7), 117–124 (1984)
6. Gomez, I., Vardillo, E.G.: An analytical approach to study a special case of booted sleeper track rail corrugation. *Wear* **251**, 916 (2001)
7. Kalousek, J., Johnson, K.L.: An investigation of short pitch wheel and rail corrugations on the Vancouver mass transit system. *Proceedings of the Institute of Mechanical Engineering, J. Rail Rapid Transit.* **206**, 127–135 (1992)
8. Wang, A., Wang, Z., Zhang, P., Xu N., Zhang, Z., He, K.: Study on the mechanism of discontinuous support stiffness on the development of rail corrugation. In: *21st International Congress on Sound and Vibration*, Beijing, China, July 2014
9. Wang, A., Wang, Z., Zhang, P., Xu, N.: The mechanism of rail corrugation generation and development—variation of difference between wheel and rail receptance. In: *22nd International Congress on Sound and Vibration*, Florence, Italy, July 2015
10. Grassie, S.L., Edwards, J.W., Jones, C.J.C., Verheijen, E.: Benchmark testing of equipment to measure rail roughness. In: *Proceeding of the 8th International Workshop of Railway Noise*, Buxton, UK (2004)

# Impact of Rail Dampers on the Mainline Rail Roughness Development



Christoph Gramowski and Patrick Suppin

**Abstract** To investigate the rail damper influence on the long-term development of rail roughness, a frequent measurement schedule was executed at an Austrian mainline. To get representative results also for further networks a common used track type was chosen, consisting of concrete sleepers with sleeper pads, 60E1 rail profile and soft rail pads. The latter allows a relative high noise emission of the rail. One track section was measured where the rail dampers of Schrey & Veit GmbH are installed, an adjacent track section serves as reference section (without rail dampers). The ‘natural’ roughness of this track section is low but differs at one of the four sections. Due to conventional rail grinding and the subsequent train operation, all roughness levels become similar after about three months. The following and two-monthly repeated measurements show the slight increase and a ‘tonal’ peak which disappears after 2–6 months. After a 13 month interval no further changes are visible. The overall results are showing low and widely similar rail roughness values for both sections at both rails. For this track/vehicle/rail damper constellation, the rail dampers are no obstacle to reach again the very low rail roughness levels. Although differing in many parameters, further measurement results (mainline and metro network) are leading to related results. Additional investigation of the mechanical interactions of the system vehicle—rail—rail damper is needed, to tune the dampers for an increased effect on roughness development, especially in curves.

---

C. Gramowski (✉)

Schrey & Veit, Graf-von-Sponheim-Straße 2, 55576 Sprendlingen, Germany  
e-mail: christoph.gramowski@sundv.de

P. Suppin

Psiacoustic, Vienna, Austria

## 1 Introduction

Rail dampers are used to mitigate the rail rolling noise radiation by increasing the track decay rate in the related frequency range. Beside the direct impact on the track damping (reducing the vibration transmission) the change in track dynamics can also change the running rail surface roughness. Therefore it is possible that the rail-wheel excitation is influenced. The worst case scenario would be that the rail roughness increases and reduces the dampers' acoustic benefit.

Speaking in a long-term view, different possibilities exist for the rail roughness development. The pass-by noise measurements, which are usually executed shortly after the rail damper installation, are not detecting long-term effects and can therefore not be used for validated conclusions. When keeping the vehicle operation impact constant, a time period of at least about six month is required.

From the currently existing knowledge no clear conclusion can be expected. This applies also to the inverse interaction from an increased rail roughness to the altered rail damper reaction which can in turn influence the surface roughness.

Therefore, additional information is needed to assess the rail damper benefit in a long-term correct way by manufacturing companies, network managers and related authorities.

Different rail damper types are currently in operation throughout the world. Furthermore, the different track types and also several vehicle types are leading to numerous possible configurations. Therefore, track-vehicle configurations, that are often present at mainline noisy track sections, were chosen. An international team from measurement institute psiacoustic GmbH, damper manufacturer Schrey & Veit GmbH and network manager ÖBB-Infrastruktur AG arranged a project to investigate this issue.

The project outcome is important for applying rail dampers in planning processes where a legally secured noise calculation is required. These calculation results have to be accurate for the entire rail damper's lifetime.

## 2 Frequent Rail Roughness Measurements

The analysis is based on rail roughness measurements at a track section before and, in a frequent two-month interval, after rail damper installation. The overall measurement period was 13 month due to converging roughness level values in the last measurement runs, see Fig. 1.

Furthermore an adjacent track section with similar track construction but without rail dampers ('reference section') was measured to quantify 'global' changes in track dynamics caused by temperature differences, etc. This procedure is similar to the assessment specification for innovative noise reduction measures [1] that was set-up for the German Konjunkturpaket II [2]. To start with as much as possible equal rail roughness, both sections had been ground (conventional maintenance

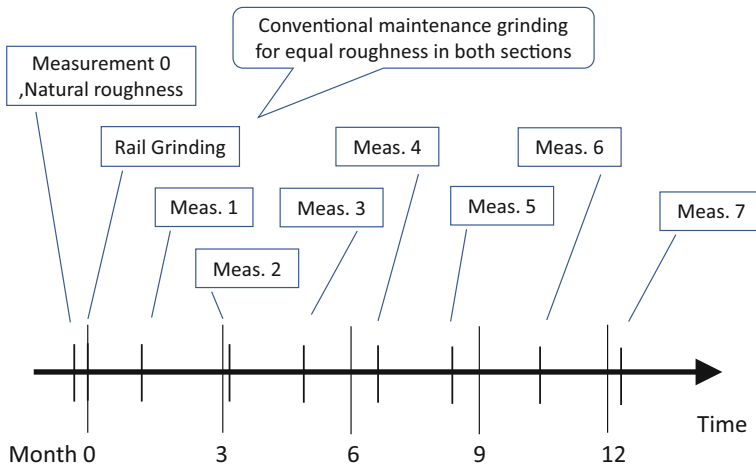


Fig. 1 Time scale of the roughness measurements

grinding), followed by a five week period with common train operation to reduce the grinding pattern and maintain the typical track roughness.

The ‘natural’ (without any measures) roughness at this track section is the final result of numerous parameters from track, vehicles and operation. Therefore no absolute equal spectra had been expected at all four rail sections and an initial rail roughness measurement (‘before grinding’) was agreed to quantify this.

Supported by railway network manager ÖBB-Infrastruktur AG a straight track section at a west Austrian mainline was appointed. Here, the track specifications from ISO 3095 [3] are met, but no further track works had been scheduled for the project timeframe. The track type is made of a typical European configuration with concrete sleepers (fitted with sleeper pads), rail profile 60E1 (prev. UIC60) and a Vossloh fastening system with soft rail pads Zw700. The latter allows the rail to vibrate ‘unconstrained’ starting from a low ‘cut-on’ frequency (frequency  $f_{c2}$  according Thompson [4] is about 240 Hz) and therefore emit a high rolling noise level. Furthermore, this effect was expected to increase the rail dampers’ influence on roughness development.

The train operation is from different vehicle classes (freight and passenger) with about 45 trains per direction per day.

The rail dampers are manufactured by Schrey & Veit GmbH and from type VICON AMSA 60 VS, a tuned mass-spring sandwich system with rail fixation by a clip spring. Rail dampers are applied at a length of 100 m. Figure 2 shows a view of the track section with installed rail dampers in the foreground. All rail roughness measurements had been executed according EN 15610:2009 [5] by psiacoustic GmbH (see Fig. 3).

**Fig. 2** View of the track section



**Fig. 3** Roughness measurement



### 3 Roughness Development

The analysis is differentiated for each track section and also for each rail. Roughness spectra are presented in Figs. 4, 5, 6 and 7. Note the ISO 3095 limit at the diagrams backgrounds.

An important finding from the results ‘before grinding’ is that not all sections are in the same ‘natural’ roughness condition although operated with the same trains at similar train speeds and consisting of the same track type. Especially Rail 1 in the reference section exceeds slightly the ISO 3095 limit. However, the absolute levels are low without ‘tonal’ peaks.

The differences of Rail 1 are not completely neutralized by the grinding action and the following train operations, but, resulting from the measurements in June 2014, an equal level is reached at both rails. This is an objective start of the monitoring time frame.

Test section with dampers (15m), Rail 1

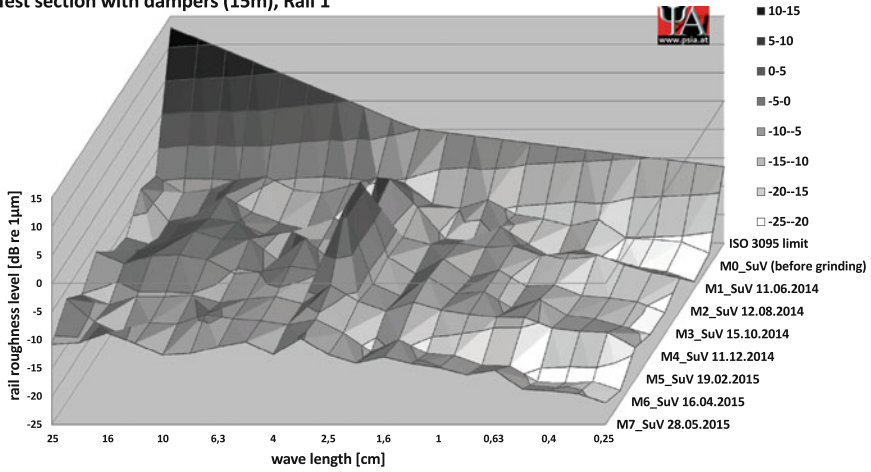


Fig. 4 Rail roughness, rail 1, damper section

Test section with dampers (15m), Rail 2

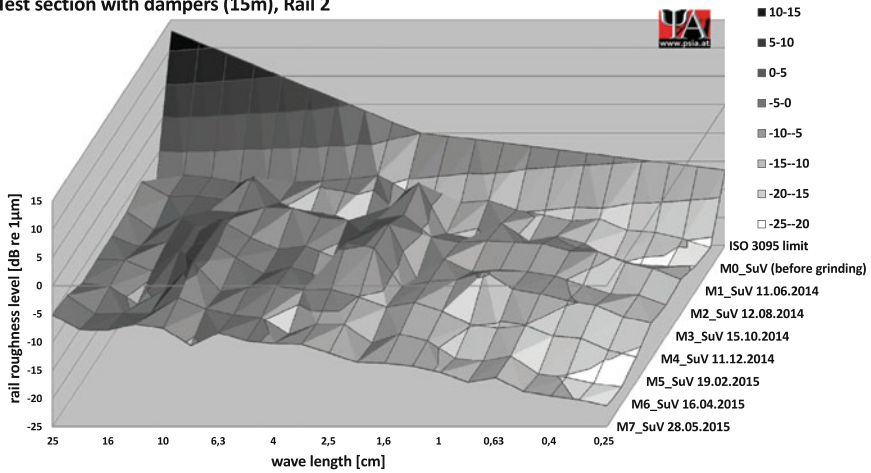


Fig. 5 Rail roughness, rail 2, damper section

In the following period all roughness levels are slightly increasing. An interesting phenomenon takes place at Rail 1 when a remarkable ‘tonal’ peak develops at the 3.15 cm wavelength. After about 2–6 month it disappears at the rail damper section earlier compared to the reference section. The reason for this peak is unknown, especially the appearance at only one rail.

Roughness levels in the other wavelength bands are more or less equal; differences are within the general measurement accuracy. After about October 2014 the

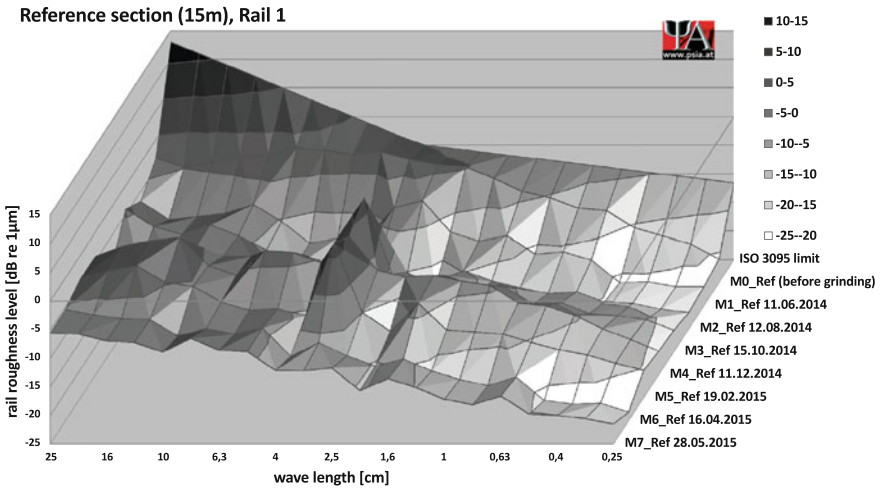


Fig. 6 Rail roughness, rail 1, reference section

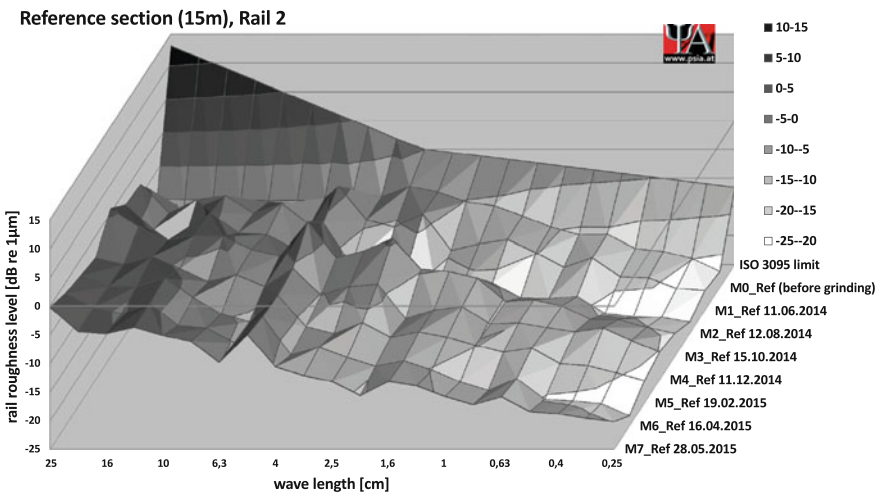


Fig. 7 Rail roughness, rail 2, reference section

3.15 cm bands of Rail 1 roughness are reaching the adjacent levels and remain constant at the final measurement in May 2014.

In general, from the Rail 1 reference section result ‘before grinding’ it can be expected (when compared to following results) that also the Rail 1 damper section will show a similar decrease. But, due to the overall low roughness levels, a further reduction is not realistic.

The overall assessment shows that rail dampers at this track type are not increasing the rail roughness, although it is on a notable low level. Therefore no



disadvantageous effect on the noise performance can be expected for this track/vehicle/rail damper configuration.

## 4 Discussion

From the initial roughness measurement ‘before grinding’, the ‘natural’ roughness is clearly not equal at all four rail sections. Therefore, an analysis approach according to the above mentioned analysis specification (from German innovative noise reduction measures) is not optimal due to the assumption of equal starting conditions. Also, the reason for this analysis specification was to suppress ‘global’ influences on the track itself which can determine the before/after result comparison of applied measures. However, the results presented here are from changes at the track itself (roughness).

After finishing the above presented results, additional measurement results have been published. In an eight-year analysis the French network manager SNCF Infra investigated the influence of rail roughness on a straight mainline track [6]. A similar conclusion was found due to widely equal roughness spectra at both rail damper and reference sections, therefore no rail damper effect can be assessed at this site.

At metro networks the rail roughness change due to rail dampers was assessed two times. One section was on straight and open track with damper type VICON AMSA GV [7], the other one in a curved tunnel with damper type VICON AMSA VS. Although caused by different dynamic interactions, a roughness resp. corrugation reduction process was found on both sections. ‘Corrugation’ describes with a periodic irregularity a special case of ‘roughness’ [8].

Even if the theoretical background of these results is investigated in first steps (e.g. Croft [8] or Wu and Wang [9]), a deeper approach together with validations at a statistically sufficient number of test sites requires a huge effort. This seems to hinder further activities in this interesting field—especially when keeping in mind that none of these rail dampers are individually tuned to reduce rail roughness. Main difference to the mentioned investigations is that both authors are modelling the rail damper by discrete single mass spring systems. However, the Schrey & Veit rail damper at the Austrian field tests introduce a multi mass spring system to the rail; this reduces the comparability of results. Nonetheless most of the authors concluded an improving effect of rail dampers on rail corrugation resp. roughness.

## 5 Outlook

Further measurements on the Austrian section are ordered to investigate an extended timeframe. Preliminary results, obtained six months after executing the last above presented result, seem to confirm the current project outcome. An additional measurement is scheduled in summer 2016.

Upcoming investigations will focus on the rail dampers' influence at curved track roughness and corrugation. Additional generation parameters have to be considered for objective results. The generation mechanism of 'corrugation' differs from that of 'roughness'. Existing experience from a mainline curve of ÖBB-Infrastruktur AG show the accelerated corrugation development after damper installation, but also opposite results are achieved at different light rail tracks (see Chapter "[Prediction of Wheel Squeal Amplitude](#)"). New tests with defined boundary conditions and a similar monitoring approach are foreseen.

Nevertheless, corrugation in curve sections is an important maintenance cost factor and any constructive mitigation measure is very welcome.

## References

1. DB Systemtechnik: Innovative Maßnahmen zum Lärm- und Erschütterungsschutz am Fahrweg — Grundlegende Anforderungen an Nachweismessungen zur quantitativen Bewertung von infrastrukturbasierten Innovationen zur Minderung des Schienenlärms, Munich 2010
2. Möhler, U., Liepert, M., Martens, A.: Innovative noise mitigation measures in the framework of "Konjunkturpaket II" in Germany. In: Nielsen, J.C.O., et al. (eds.) *Noise and Vibration Mitigation for Rail Transportation Systems*. NNF, vol. 126, pp. 181–187. Springer, Heidelberg (2015)
3. ISO 3095:2013: Acoustics—Railway applications—Measurement of noise emitted by railbound vehicles
4. Thompson, D.: *Railway Noise And Vibration: Mechanism, Modelling and Means*. Elsevier, Oxford (2009)
5. EN 15610:2009: Railway applications—Noise emission—Rail roughness measurement related to rolling noise generation
6. Margiocchi, F., Poisson, F., Gramowski, C., Tartary, J.P.: A 8-years' complete assessment of rail damper performances on an operated track in France. In: *Proceeding of the WCRR, Milan (Italy)* (2016)
7. Kampfraath, P.: Effectiveness of rail dampers at retarding the formation and growth of rail corrugation. In: *Proceeding of APTA Rail Conference, Montréal (Canada)* (2014)
8. Croft, B.E.: Modelling the effect of rail dampers on wheel-rail interaction forces and rail roughness growth rates. *J. Sound Vib.* **323**, 17–32 (2009)
9. Wu, T.X., Wang, Y.R.: Modeling wheel-track interaction with rail vibration damper and its application for suppressing short pitch rail corrugation. In: Nielsen, J.C.O., et al. (eds.) *Noise and Vibration Mitigation for Rail Transportation Systems*. NNF, vol. 126, pp. 361–368. Springer, Heidelberg (2015)

**Part V**  
**High Speed Rail Noise**

# Estimation of Aerodynamic Bogie Noise Through Field and Wind Tunnel Tests



T. Uda, N. Yamazaki, T. Kitagawa, K. Nagakura  
and Y. Wakabayashi

**Abstract** A method has been developed to determine the aerodynamic noise from the bogie of a high-speed train using a two-dimensional microphone array in a wind tunnel. First, the flow velocity under the train car in the rail direction was measured in a field test. Second, the flow distribution was simulated in the wind tunnel. Third, aerodynamic noise generated by a bogie was estimated from the source distribution measured using a two-dimensional microphone array. Finally, the noise generated from the lower part of the car, which was obtained by adding the aerodynamic noise and the rolling noise estimated by the TWINS model, was compared with the result obtained from the field test. It was found that the estimated noise shows good agreement with the measurement obtained in the field test. The estimated lower part noise levels were consistent with the actual experimental measurements. This conclusion suggests that this method is appropriate to estimate aerodynamic bogie noise quantitatively. It is also shown that below 500 Hz the contribution of the aerodynamic bogie noise is more than those of the rolling and machinery noise.

## 1 Introduction

In Japan, the wayside noise of Shinkansen railway lines raised a strong social demand for environmental controls in the 1990s, and since then many attempts have been made to reduce the noise [1, 2]. To reduce railway noise, it is essentially important to clarify the sound source and contribution to the total noise [3–5]. The noise generated by Shinkansen trains mainly consists of (1) pantograph aerodynamic noise, (2) aerodynamic noise generated from the upper part of the cars, (3) bridge noise and (4) noise generated from the lower parts of the cars (lower part

---

T. Uda (✉) · N. Yamazaki · T. Kitagawa · K. Nagakura  
Railway Technical Research Institute, 2-8-38, Hikari-cho,  
Kokubunji-shi, Tokyo, Japan  
e-mail: uda.toki.92@rtri.or.jp

Y. Wakabayashi  
East Japan Railway Company, Tokyo, Japan

noise) [6]. It is generally known that the lower part noise has the greatest contribution to the total noise and consists of aerodynamic, rolling, and machinery noise. Among these noise sources, the aerodynamic noise is dominant above about 300 km/h. However, the contribution of aerodynamic noise (aerodynamic bogie noise) has not been explicitly estimated. In this study, an attempt will be made to quantitatively estimate aerodynamic bogie noise using both field and wind tunnel tests. In the first step, the flow velocity component in the rail direction under Shinkansen cars will be shown through field tests. Next, a method to simulate the flow velocity distribution in a wind tunnel test will be developed. Then, the contribution of the aerodynamic bogie noise is estimated using the results of the noise source distribution measured with a two-dimensional microphone array. Finally, the method will be validated by comparing the estimated lower part noise with the results obtained in the field measurements.

## 2 Field Test: Flow Velocity Measurement Under the Train Car

### 2.1 Measurement Methods

In this section, methods are described to measure flow velocity distributions under the vehicle floor during the passage of a train. On a slab-track in the Shinkansen line, eight one-dimensional hot-wire anemometers (KANOMAX ANEMOMASTER MODEL6141) are installed in line along the sleeper direction (Fig. 1). An illustration of installed hot-wire anemometers on the slab track is shown in Fig. 2. The coordinate origin is set at the surface of the rail head (R.L.) on the center of the track. The traveling direction of the vehicle is defined as the positive direction of the  $x$ -axis, the direction to the right of an observer facing the rear of the train is the positive direction of the  $y$ -axis, and the vertical direction is the positive direction of the  $z$ -axis. Seven sensors (S2–S9 except S8) are installed at a height of  $-15$  mm ( $z = -15$  mm).

Time histories of the velocity under vehicles are measured as Shinkansen trains passed over them. The measured quantity is the magnitude of the velocity component perpendicular to a hot-wire anemometer:



**Fig. 1** Example of rolling stock passing over hot-wire anemometers installed on slab track

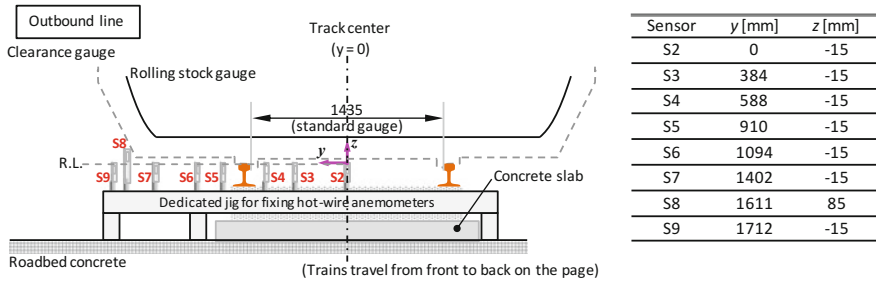


**Fig. 2** Illustration of hot-wire anemometers installed on slab track

$$V_{\text{measured}} = \sqrt{V_x^2 + V_z^2}. \tag{2.1}$$

It is noted that  $V_y$  is not measured and  $V_z$  is small compared to  $V_x$ .

An axle detector is used to measure train speed. The outputs from the hot-wire anemometers and axle detector are recorded with a data recorder. The sampling frequency of the A/D conversion was 2 kHz, and the anti-aliasing filter had a cut-off frequency of 1 kHz.

## 2.2 Data Analysis

The details of the flow distribution under the floor differ from one train to another even when they have the same type of rolling stock. Therefore, it is better to average the data of flow velocity to investigate the characteristics of the flow under the floor. For each type of rolling stock, measured time-series data is analyzed according to the following procedure:

- (1) Measured flow velocity magnitude is treated as normalized by the train speed.
- (2) Time-series data is normalized using train length and speed.
- (3) Time-series data is ensemble-averaged.

## 2.3 Measurement Result

### 2.3.1 Flow Velocity Distribution in the Rail Direction

In this measurement, the results are expressed in the ground-fixed coordinate system. This is because the under-floor flow velocities are measured on the ground side. Figure 3 shows the averaged normalized velocity for E5 series Shinkansen. The velocities shown in Fig. 3 are averaged over 13 trains at speeds in the range of

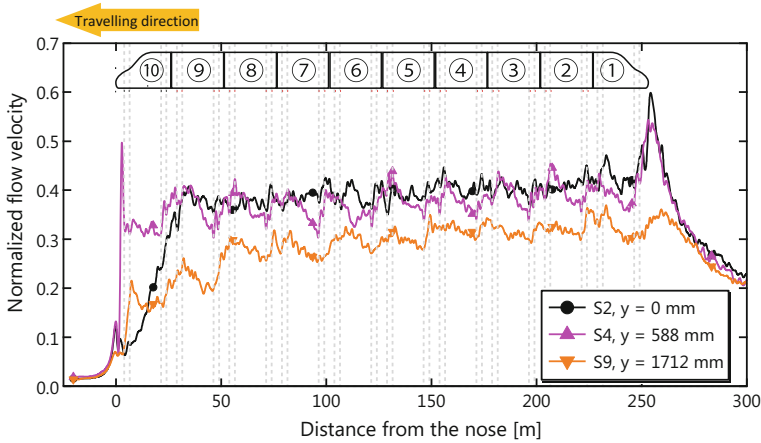


**Fig. 3** Averaged velocity for E5 series Shinkansen in the ground-fixed coordinate system; the horizontal axis shows the distance from the leading edge of the leading vehicle, and the vertical axis shows the averaged magnitude of the normalized flow velocity under the floor

254–317 km/h. The horizontal axis shows the distance from the leading edge of the leading vehicle, while the vertical broken lines denote the edge position of the bogie section for each vehicle. It can be seen that the overall trend of the under-floor velocity is that it gradually increases toward the rear of the train. This is due to the growth of the boundary layer thickness under the train. It is found that clear peaks appear during the passage of the nose and tail of the train.

For the velocity on the individual cars obtained by S2 and S4 sensors, it can be stated that flow velocity increases at the backward and forward bogie sections and decreases at the position between two bogies in a car. This result indicates that under-floor flow at the bogie section is affected due to pressure loss and regains strength again through the path under side covers in the intermediate section without bogies.

### 2.3.2 Flow Velocity Distribution in the Sleeper Direction

Figure 4 shows the normalized flow velocity distribution in the sleeper direction. The position indicator, P0, indicates the leading position of the front bogie in the leading vehicle whereas P1 and P2 indicate the leading and trailing positions of bogie section in intermediate cars (No. 8 to No. 2 cars are averaged). The measured velocity is normalized by pass-by train speed. It is found that the under-floor velocity at rail level in the ground-fixed coordinate system does not exceed 0.5. This suggests that the under-floor velocity is kept more than 0.5 in the train-fixed coordinate system. For the difference between the leading and intermediate vehicles, the flow velocity distribution in the sleeper direction is in the range of 30–40% of the train speed in the intermediate vehicles. In the leading car, however, the flow

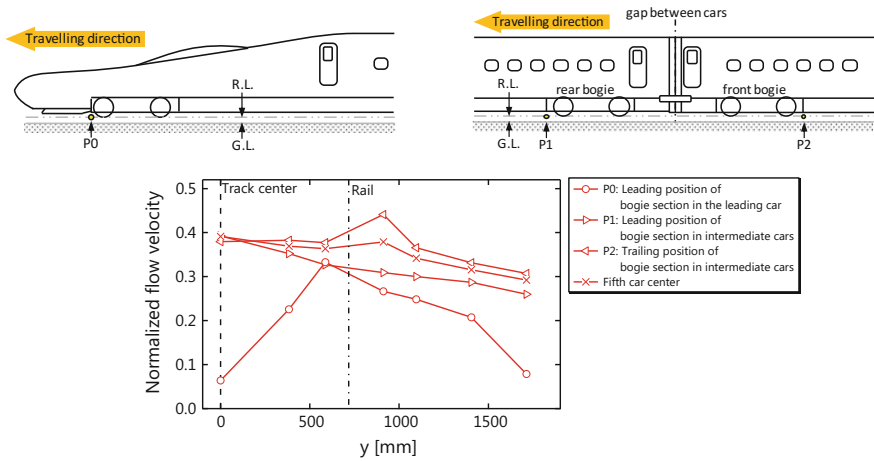


**Fig. 4** Velocity profiles along the sleeper direction for E5 series Shinkansen in the ground-fixed coordinate system; the horizontal axis shows the distance from the track center, and the vertical axis shows the averaged magnitude of the normalized flow velocity under the floor

velocities at the entrance of bogie section are lower than 25%. This suggests that, in the train-fixed coordinate system, the leading vehicle is exposed to high-speed airflow, which may lead to greater aerodynamic noise. In the intermediate vehicles, the flow velocities decrease as  $y$  position (distance from the track center) increases. This is due to the turbulent boundary layer in the intermediate vehicle. It is also found that, at  $y = 910$  mm, the under-floor flow is influenced by the wheels.

Through this field test, it is indicated that the under-floor flow distribution for the leading and intermediate vehicles in wind tunnel tests should be simulated separately to evaluate the aerodynamic bogie noise at two vehicles quantitatively.

### 3 Wind Tunnel Tests

Figure 5 shows the setup of the wind tunnel test. The  $x$ ,  $y$ , and  $z$  directions are defined as the main flow, horizontal, and vertical directions, respectively. A 1/7-scale train model is installed on the ground plate with two supporting struts at the front and rear model cars. An acoustic barrier shown in Fig. 5b is set at the side of the train model to screen the noise propagating from the strut located at the train head. This is because the strut is exposed to high-speed airflow.

#### 3.1 Bogie Section

Figure 6 shows the test conditions for the bogie section. As shown in Fig. 6a, the bogie model is installed inside the cavity. During the measurement of the



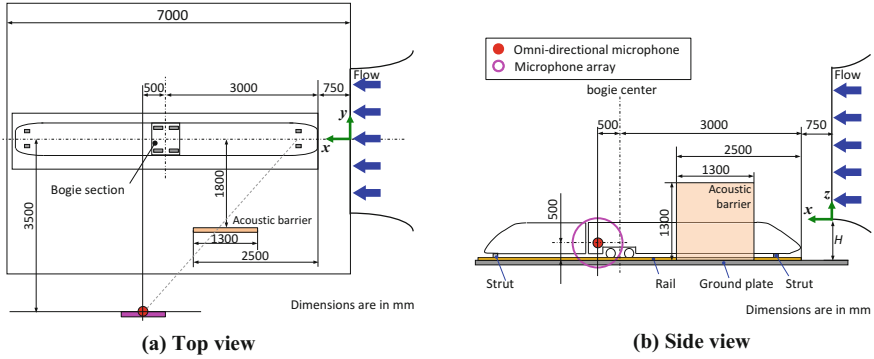


Fig. 5 Schematic of the experimental setup of a wind tunnel test

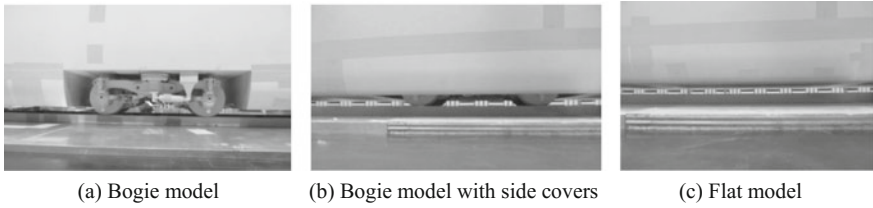


Fig. 6 Schematic of the experimental setup of a wind tunnel test

aerodynamic bogie noise, both sides of the bogie are fully covered (Fig. 6b) as E5 series Shinkansen in Japan. Background noise is defined as the data measured under a flat condition without bogie section and cavity (Fig. 6c).

### 3.2 Flow Velocity Profile Adjustment

Based on the results reported in Sect. 2, the flow velocity distribution at the front and intermediate bogies measured in the field test is simulated to investigate the aerodynamic bogie noise of the leading vehicle and the intermediate vehicle in the wind tunnel test. The flow velocity distribution is simulated with a focus on two points. First, the flow velocity in the sleeper direction at the intermediate vehicle is approximately 40% of the train speed at the track center ( $y = 0$  mm) and decreases gradually to 30% toward the side of the body in the ground-fixed coordinates. Second, at the leading vehicle, the flow velocity is lower than that at the intermediate vehicle in the ground-fixed coordinates.

We develop two experimental methods to adjust the velocity profile (noting that the velocity is plotted in the ground-fixed coordinate system), as follows:

- (1) Using a free shear layer around the nozzle exit.
 

This method is intended to decrease the flow velocity around the bogie section. Figure 7a shows the schematic of the free shear layer around the nozzle exit with a velocity gradient. The velocity at the inlet of the bogie section was adjusted by changing the relative height position of the model,  $H$ , between the lower edge of the nozzle exit and the ground level.
- (2) By installing flow adjustment parts under the car.
 

As shown in Fig. 7b, a pair of elliptically shaped parts is installed on the rail located upstream of the bogie section. The reduced-velocity region downstream of these flow adjustment parts changes depending on the widths of  $L_1$  and  $L_2$  (Fig. 7b). This hydrodynamic phenomenon helps us simulate an appropriate velocity distribution of the field test.

After applying these two methods together, the flow distributions in the sleeper direction for the leading and intermediate vehicles are properly adjusted as shown in Fig. 8. It is confirmed that the results from the field test and wind tunnel test are consistent.

### 3.3 Methods for Estimating Aerodynamic Bogie Noise

This section describes the procedures used to estimate the aerodynamic bogie noise in the wind tunnel test. The aerodynamic bogie noise is measured using a two-dimensional microphone array. The array has a radius of 1 m and consists of 66 microphones, and the distance between the train center and the array is 3.5 m. The distribution of aerodynamic bogie noise sources up to a 2 kHz band in a

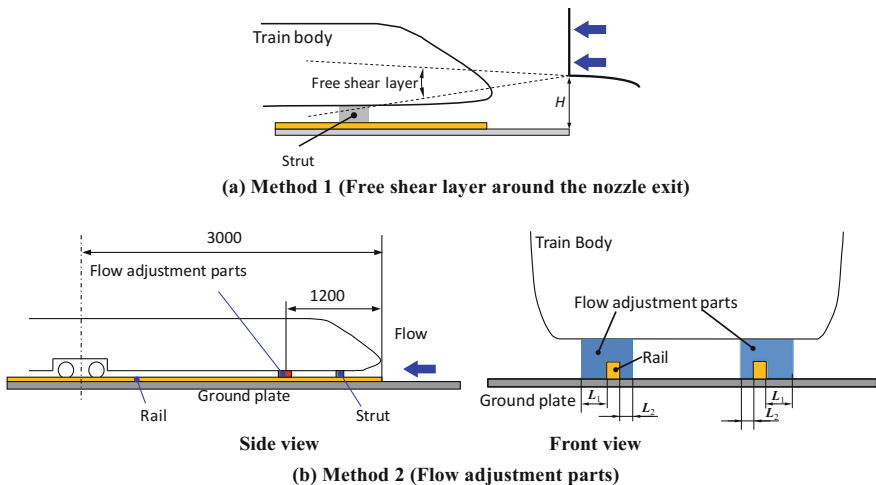
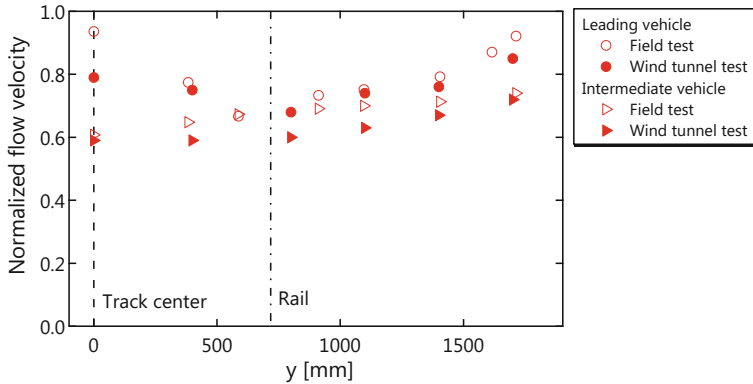


Fig. 7 Methods used to adjust the flow distribution under the train car model



**Fig. 8** Flow velocity distribution in the sleeper direction at the leading position of bogie section in the train-fixed coordinate system

full-scale model is then obtained by applying a conventional delay-and-sum beamforming algorithm. Finally, the sound source distribution around the bogie section is integrated to obtain the integrated sound pressure level (SPL). This integrated SPL, however, generally disagrees with the SPL with the omni-directional microphone installed at the array center. Then an omni-directional microphone is installed at the array center to modify the integrated SPL using the following equation.

$$C(f) = L_{\text{integral}}^{\text{bogie}}(f) - L_{\text{omni}}^{\text{bogie}}(f), \tag{3.1}$$

where “bogie” indicates the measured value of the bogie condition without side covers (Fig. 6a). Using this conversion coefficient, the SPL in the wind tunnel,  $L^w$ , is calculated as follows:

$$\begin{aligned}
 PW_{\text{bogie\_cover}} &= 10^{\frac{L_{\text{integral}}^{\text{bogie\_cover}}(f) - C(f) + A_w(f)}{10}} \\
 PW_{\text{flat}} &= 10^{\frac{L_{\text{integral}}^{\text{flat}}(f) - C(f) + A_w(f)}{10}} \\
 L^w &= 10\log_{10}(PW_{\text{bogie}}) - 10\log_{10}(PW_{\text{flat}})
 \end{aligned}
 \tag{3.2}$$

where,  $PW$  indicates squared pressures and  $L_{\text{integral}}^{\text{bogie\_cover}}(f)$  and  $L_{\text{integral}}^{\text{flat}}(f)$  are the SPL integrated over an area around the bogie section in the two-dimensional SPL distribution measured by the microphone array. The superscripts “bogie\_cover” and “flat” indicate the measured value of the bogie condition with side covers (Fig. 6b) and flat condition (Fig. 6c) respectively.  $A_w(f)$  indicates the A-weighting frequency characteristics. The signal-to-noise ratio (SNR) in this condition is more than 5 dB below the 1 kHz band and sufficient to estimate the coefficient  $C$ .

Finally, the noise level measured at 2 m from the center of the track and 0.4 m above the railhead (*noise measurement point N*) is estimated. Using the  $L^w$  measured in the wind tunnel test, the noise level at point N is calculated by Eq. (3.3):

$$\begin{aligned} L^F &= L^w + 20 \log_{10}(r\alpha/r_d) + 10 \log_{10}(n) \\ &= L^w + 22 \text{ [dB]} \end{aligned} \quad (3.3)$$

where  $1/\alpha$  ( $=1/7$ ) is the model scale and  $n$  ( $=2$ ) is the number of bogies.  $r$  ( $=3.5$  m) is the distance from the model center to the microphone array in the wind tunnel test as shown in Fig. 5 and  $r_d = 2.717$  m is the distance between the train center and the noise measurement point N in the field test.

### 3.4 Validation of the Estimated Aerodynamic Bogie Noise

In order to validate the proposed methods, the estimated aerodynamic bogie noise is compared with the lower part noise in the field test. Because the lower part noise consists of the rolling and machinery noise in addition to the aerodynamic bogie noise, estimated rolling and machinery noise obtained from a previous study [7] is added to the noise level calculated by Eq. (3.3). Figure 9a shows a comparison of the lower part noise from the intermediate vehicle estimated in the wind tunnel test with the results obtained from the field tests at 320 km/h. To estimate the lower part noise, the rolling and machinery noises are combined according to previous study [7]. The estimation error is defined as the averaged SPL difference between the field test and the estimation in each 1/3 octave frequency band. The total estimated lower part noise levels are consistent with those from the field test within an estimation error of approximately 2 dB. This demonstrates that the proposed method is valid for quantitatively estimating aerodynamic bogie noise. The results also show that the aerodynamic bogie noise estimated from the wind tunnel tests, which has a peak at approximately 400 Hz, is close to those from the field test in a frequency range from 125 to 500 Hz. This suggests that, in this frequency range, aerodynamic noise plays a greater role in the lower part noise than the rolling and machine noises.

Figure 9b shows the lower part noise for the leading and intermediate vehicles at 320 km/h. The difference in noise between the cars was approximately 4 dB in both the field studies and wind tunnel tests. Table 1 shows the mean flow velocities,  $V_L$  and  $V_M$ , for the leading and intermediate vehicle, respectively. In Case 1, the velocity is obtained by averaging the flow velocity over the all sleeper positions, whereas in Case 2, the velocity is obtained at the centerline ( $y = 0$  mm). It is assumed that the power of the aerodynamic noise increases in proportion to the 6th power of the flow velocity, and the difference in SPL between the two cars is estimated as follows:

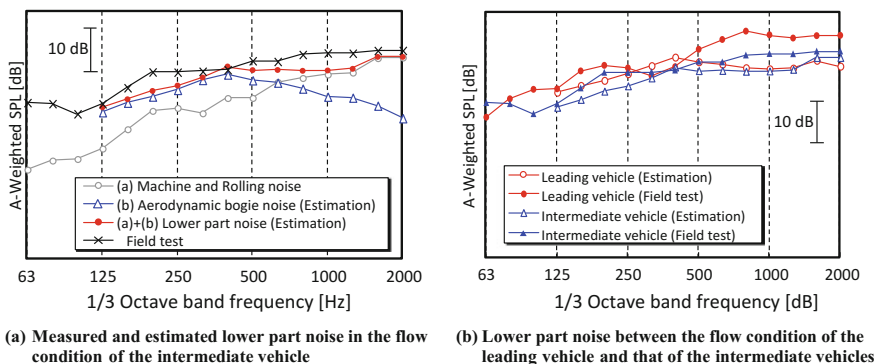


Fig. 9 Measured and estimated lower part noise at 320 km/h

Table 1 Effect of the flow velocity on the difference in noise level

		$V_L$	$V_M$	$\Delta L$ (dB)
Case 1	Averaged velocity over whole region	0.76	0.64	4.8
Case 2	Velocity at $y = 0$	0.79	0.59	1.5

$$\Delta L = 60 \log_{10}(V_L/V_M) \tag{3.4}$$

In Case 1, the difference in the noise level is estimated at approximately  $60\log_{10}(0.76/0.64) = 5$  dB, which agrees well with the results shown in Fig. 9b. However, the noise level difference in Case 2 is  $60\log_{10}(0.79/0.59) = 8$  dB, which is much greater than the results in Fig. 9b. This difference suggests that flow distribution along the sleeper direction has a significant influence on the aerodynamic bogie noise and should be simulated correctly to evaluate the aerodynamic bogie noise through wind tunnel tests.

## 4 Conclusions

Using wind tunnel tests, we developed a method for quantitatively estimating aerodynamic bogie noise. The flow distribution in the sleeper direction under a train car was obtained through field testing, while the velocity distributions of the leading and intermediate vehicle were precisely simulated in a wind tunnel test. Aerodynamic bogie noise was then estimated from the noise source distribution obtained by a two-dimensional microphone array. The estimated lower part noise including the aerodynamic bogie noise obtained through the proposed method was consistent with the results obtained in the field test. It was shown that the contribution of the aerodynamic bogie noise is greater than that of both the rolling and

machinery noise, especially below 500 Hz. From examining the aerodynamic bogie noise of the middle and the leading vehicles, it was concluded that flow distribution along the sleeper direction should be correct to evaluate the aerodynamic bogie noise through wind tunnel tests.

## References

1. Iglesias, E.L., Thompson, D.J., Smith, M.G.: Component-based model for aerodynamic noise of high-speed trains. In: Nielsen, J.C.O., et al. (eds.) *Noise and Vibration Mitigation for Rail Transportation Systems*. NNFM, vol. 126, pp. 481–488. Springer, Heidelberg (2015)
2. Thompson, D.J., Iglesias, E.L., Liu, X., Zhu, J., Hu, Z.: Recent developments in the prediction and control of aerodynamic noise from high-speed trains. *Int. J. Rail Transp.* **3**(3), 119–150 (2015)
3. Mellet, C., Létourneaux, F., Poisson, F., Talotte, C.: High speed train noise emission: latest investigation of the aerodynamic/rolling noise contribution. *J. Sound Vib.* **293**(3–5), 535–546 (2006)
4. Poisson, F., Gautier, P.E., Létourneaux, F.: Noise sources for high speed trains: a review of results in the TGV case. In: Schulte-Werning, B., et al. (eds.) *Noise and Vibration Mitigation for Rail Transportation Systems*. NNFM, vol. 99, pp. 71–77. Springer, Heidelberg (2008)
5. Masson, E., Paradot, N., Allain, E.: The numerical prediction of the aerodynamic noise of the TGV POS high-speed train power car. In: Maeda, T., et al. (eds.) *Noise and Vibration Mitigation for Rail Transportation Systems*. NNFM, vol. 118, pp. 437–444. Springer, Heidelberg (2012)
6. Kurita, T., Wakabayashi, Y., Yamada, H., Horiuchi, M.: Reduction of wayside noise from shinkansen high-speed trains. *J. Mech. Syst. Transp. Logist.* **6**(2), 1–12 (2011)
7. Kitagawa, T. et al.: The noise generated from the lower part of Shinkansen cars running at high-speed. *J. Environ. Eng.* **7**(1), 66–75 (2012) (in Japanese)

# Aerodynamic Noise Reduction of Brake Disc for High-Speed Trains



N. Shiraishi, Y. Wakabayashi, T. Kurita, T. Fujimoto  
and Y. Ichikawa

**Abstract** Wayside noise reduction arises as a major issue when increasing the Shinkansen's operating speed. We have been working on reduction of noise from the lower part of train cars, a major source of Shinkansen noise. First, using the experimental train "FASTECH360", we identified the noise source from around wheels. We confirmed that noise from around the wheels was aerodynamic noise generated from air through the ventilation route of brake discs. Thus, we developed a low-noise brake disc for new Shinkansen Trains "Series E5." Next, we used test equipment to investigate the mechanism of noise generation of the rotating wheel with a low-noise disc attached to further improve the low-noise disc. As a result, we found that: (1) Air through the ventilation route generated noise over 700 Hz and this noise consists mostly of noise generated by rotating wheels with low-noise brake discs; (2) Circumference gap generated noise around 500 Hz; (3) Bolt holes generated noise around 2500 Hz.

## 1 Introduction

Increasing maximum operating speed is one of the most effective ways to cut Shinkansen travel time. To achieve operation at higher speeds, it is necessary to reduce wayside noise, since it is necessary to keep wayside noise levels within those of existing Shinkansen trains, even at higher speeds. It has been acknowledged that the reduction of noise emitted from not only pantographs but also the lower part of cars can effectively reduce wayside noise even in Shinkansen surrounded with noise barriers [1, 2]. Thus, we have been studying ways to reduce

---

N. Shiraishi (✉) · Y. Wakabayashi · T. Kurita  
East Japan Railway Company, 2-479, Nisshin-Cho, Saitama-Shi,  
Saitama 331-8513, Japan  
e-mail: nobuo-shiraishi@jreast.co.jp

T. Fujimoto · Y. Ichikawa  
Nippon Steel & Sumitomo Metal Corporation, 5-1-109, Shimaya,  
Konohana-Ku, Osaka-Shi, Osaka 554-0024, Japan

aerodynamic noise from brake discs attached to both sides of each wheel to reduce noise from the lower-part of cars. First, we identified noise from wheels as a main source of the lower-part noise which, through running tests using our experimental train FASTECH360 [3], was found to be aerodynamic noise emitted from brake discs. Based on the running test results, we developed a low-noise brake disc for new Shinkansen “Series E5” trains. We investigated aerodynamic noise sources of the rotating low-noise brake disc using test equipment to further improve the low-noise brake disc. In this paper, we describe development of the low-noise brake disc and clarification of aerodynamic noise sources of the rotating low-noise brake disc.

## 2 Development of Low-Noise Brake Disc

### 2.1 Study of Reducing Noise from Lower Part of Cars on Running Tests

We carried out a study to reduce noise on experimental train FASTECH360S running tests. Figure 1 shows a schematic diagram of noise source distribution measured using a spiral microphone array. Figure 2a shows noise source distribution of FASTECH360S, and strong noise sources were observed around bogies, especially the wheels. Thus, we focused on this noise and carried out running tests to reduce brake disc aerodynamic noise by blocking the cooling ventilation route on the back side of the brake disc at the side of the wheel. We blocked ventilation route by closing inner circumferential gap using aluminum tape, as shown in Fig. 3. Figure 2b shows the result. From the comparison of Fig. 2a and b, we confirmed that noise from around wheels was aerodynamic noise generated from air through the ventilation route of brake discs, thus the noise can be reduced by blocking the ventilation route.

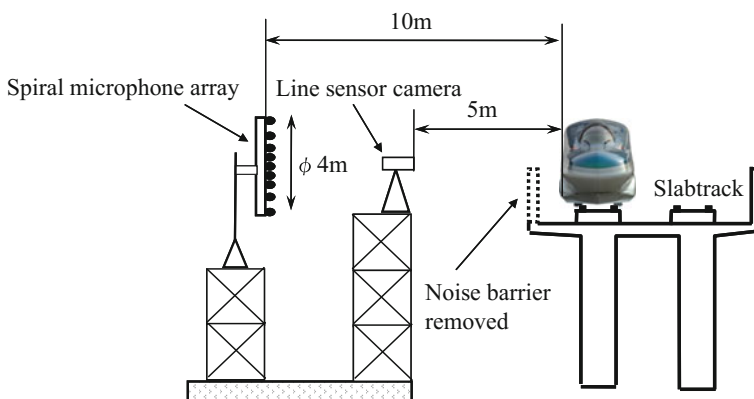


**Fig. 1** Schematic diagram of measurement using spiral microphone array



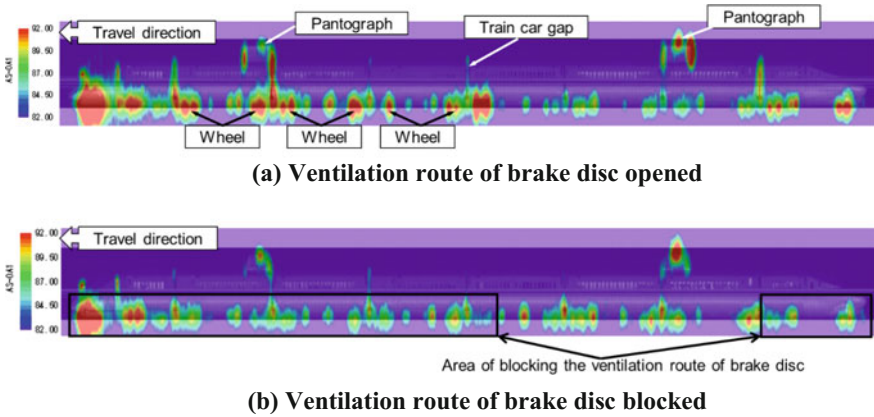


Fig. 2 Noise source distribution of FASTECH360S using spiral microphone array (340 km/h)

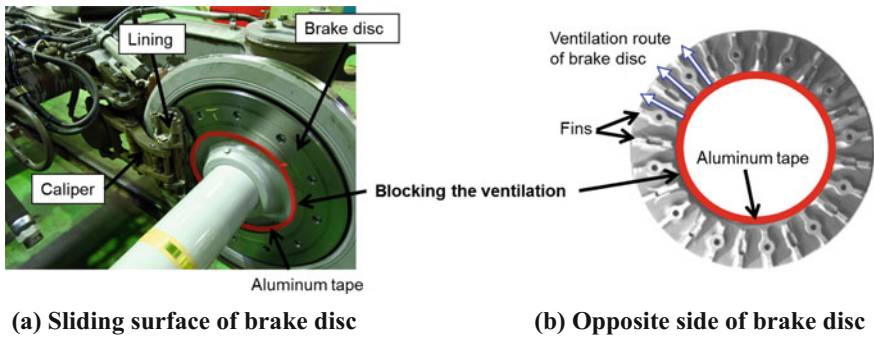


Fig. 3 Blocking ventilation route of brake disc

## 2.2 Noise Analysis of Running Test Results

We investigated noise near a train using a microphone, as shown in Fig. 4. Figure 5 shows that noise around bogies was reduced approximately by 3 dB by blocking ventilation routes of the brake disc. From comparison of noise spectra at peak values, blocking ventilation routes of brake disc can reduce noise within a frequency range of 500 to 3000 Hz. Thus, we confirmed that aerodynamic noise within this frequency range is generated from the ventilation route at the back of brake disc and by blocking the ventilation route of brake disc, we can reduce the noise levels around bogies by approximately 3 dB.

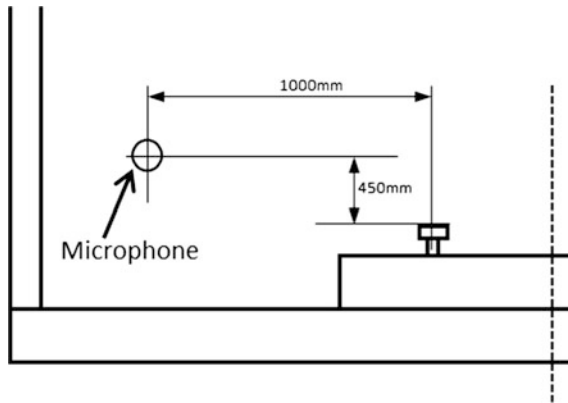


Fig. 4 Position of microphone

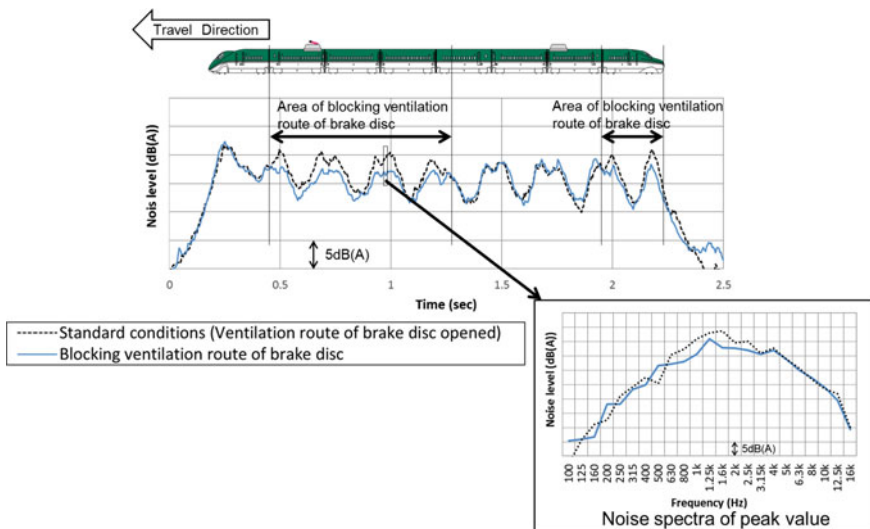
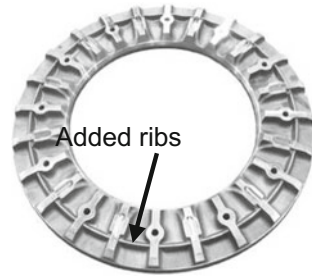


Fig. 5 Comparison of time histories of noise (Time constant of 10 ms) and noise spectra of peak value

### 2.3 Development of Low-Noise Brake Disc

We developed low-noise brake disc to reduce aerodynamic noise of the brake discs by reducing air flow rate through the ventilation route, as shown in Fig. 6. Since brake disc must maintain a flow rate required for cooling, we added ribs in the middle of the ventilation route on the brake disc to reduce air flow rate through the ventilation route to ascertain extent. This low-noise brake disc is applied to JR-East new commercial Series E5 trains.

Fig. 6 Low-noise brake disc



### 3 For Further Reducing Noise Around Wheels

#### 3.1 Investigation of Noise Around Wheels with Low-Noise Brake Discs

Figure 7 shows noise source distribution of FASTECH360Z equipped with the low-noise brake discs. Some noise is still observed around wheels. We investigated relation between the train speeds and the peak values of sound pressure levels at 1000 Hz band (1/1 octave) around wheels in the noise source distribution map to reveal the cause of the noise generation. Figure 7 shows that sound pressure power increases approximately in proportion to the sixth or fifth power of the train speed, and we found that aerodynamic noise is dominant in noise from around wheels. We therefore focused further reducing aerodynamic noise of the low-noise brake disc.

#### 3.2 Experiment of Measuring Aerodynamic Noise Generated from Rotating Brake Disc

##### 3.2.1 Test Method

We rotated wheels with a brake disc alone using rolling test equipment to investigate aerodynamic noise of the rotating low-noise brake disc in detail, as shown in

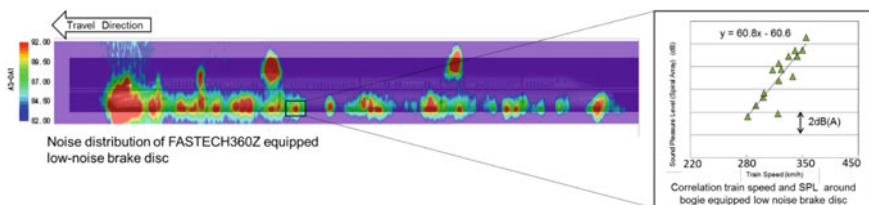


Fig. 7 Noise distributions of FASTECH360Z and relation between train speeds and SPLs around bogie

Fig. 8 [4] and measured the aerodynamic noise generated from the rotating brake disc. Figure 9 shows the position of the microphone. Rotating speeds are adjusted to wheel speeds of 270, 320 and 360 km/h.

### 3.2.2 Aerodynamic Noise Generated from Rotating Brake Disc

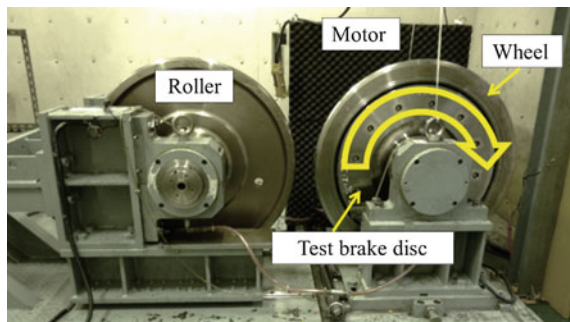
We conducted experiments under two differing conditions to investigate the aerodynamic noise level generated by rotating brake disc, as shown in Fig. 10. In case A, brake discs are investigated under standard conditions (all openings free). In case B, all openings of brake disc (inner circumference gap, outer circumference gap, bolt holes) are blocked with aluminum tape. Brake caliper with linings was placed at the regular position in both cases. Figure 11 shows the result at 360 km/h. From comparison between case A and case B, the noise of brake discs was reduced within a wide frequency range by closing all openings (case A  $\rightarrow$  B), and reduced by 23 dB. From this result, we confirmed that a large amount of aerodynamic noise is generated from openings of low-noise brake disc, and we can measure aerodynamic noise from rotating brake discs by using this experimental method.

### 3.2.3 Test Conditions of Investigating the Noise Sources of Low-Noise Brake Disc

Next, we conducted experiments under different conditions by changing each opening (closed or opened) (Fig. 12) and with and without the brake caliper to identify noise sources of the low-noise brake disc in detail, as shown in Table 1.

We compared noise spectra of case A (all openings free with the brake linings) and case G (all openings free without the brake linings) at a wheel speed of 360 km/h to evaluate the effect of the lining, as shown in Fig. 13. The presence or absence of brake linings has no effect on the noise level generated from a rotating wheel with a low-noise brake disc.

**Fig. 8** Rolling noise test equipment (Rotated by motor, not by roller wheel)



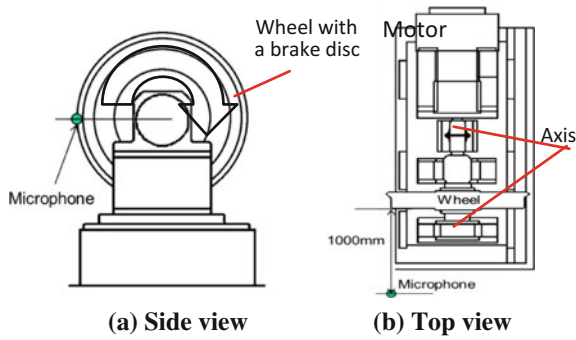


Fig. 9 Position of microphone. a Side view, b top view

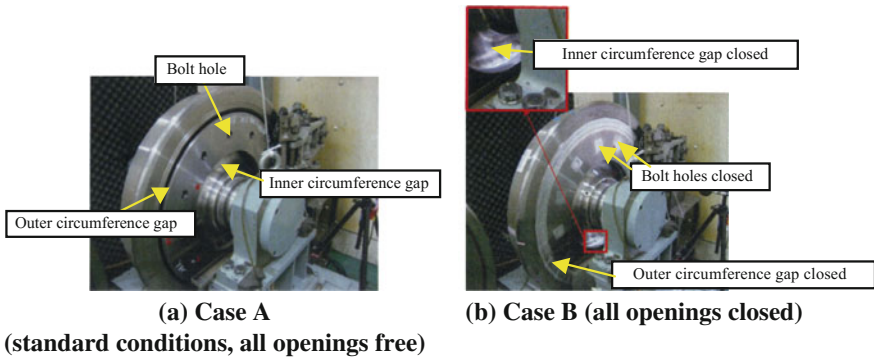
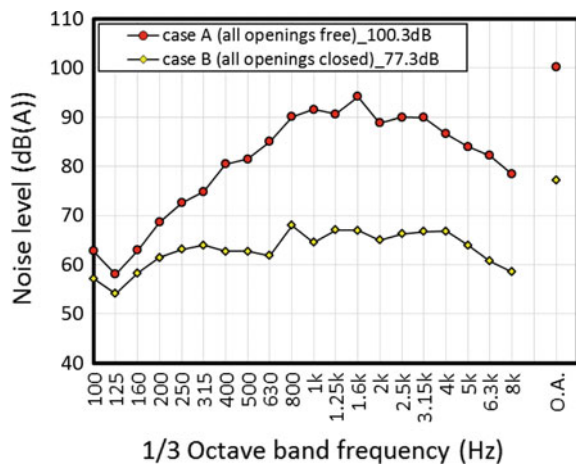
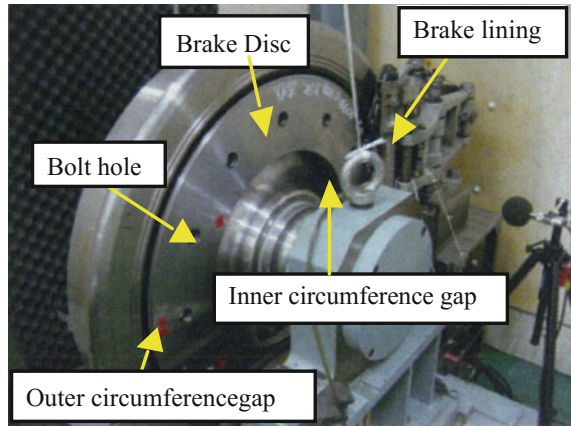


Fig. 10 Experiment cases

Fig. 11 Comparison of noise spectra between case A (all openings free) and case B (all openings closed) at a wheel speed of 360 km/h



**Fig. 12** Names of parts opening of brake disc



**Table 1** Test conditions

Case	Condition of brake disc			Brake lining
	Bolt holes	Inner circumference gap	Outer circumference gap	
Case A (standard conditions, all openings free)	–	–	–	With
Case B (all openings closed)	Closed	Closed	Closed	
Case C (only outer circumference gap open)	Closed	Closed	–	
Case D (only inner circumference gap open)	Closed	–	Closed	
Case E (only bolt holes open)	–	Closed	Closed	
Case F (only bolt holes closed)	Closed	–	–	
Case G (all openings free without brake lining)	–	–	–	Without

### 3.2.4 Noise Source in Ventilation Route and Circumferential Gap of Low-Noise Brake Disc

Figure 14 shows noise spectra of case A (all openings free), case C (only outer circumference gap opened), and case D (only inner circumference gap opened) at a wheel speed of 360 km/h. We confirmed that by blocking the ventilation route we can efficiently reduce noise in the low-noise brake disc within a frequency range over 700 Hz. From this result, we confirmed that a high volume of aerodynamic noise is generated from air flow through the ventilation route of the low-noise brake disc.

From comparison between case C and D, we confirmed as follows:

**Fig. 13** Comparison of noise spectra among case A (all openings free with brake lining) and case G (all openings free without brake lining) at 360 km/h

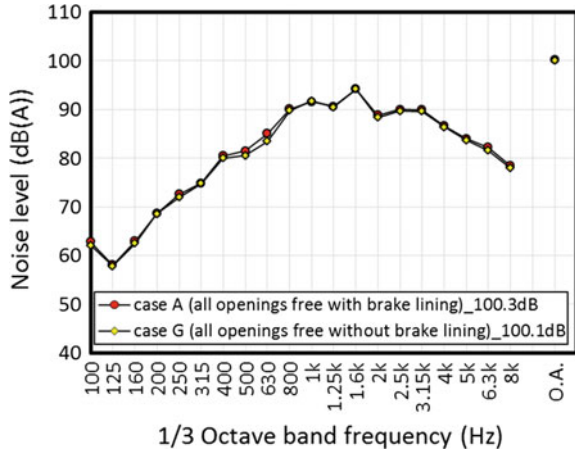
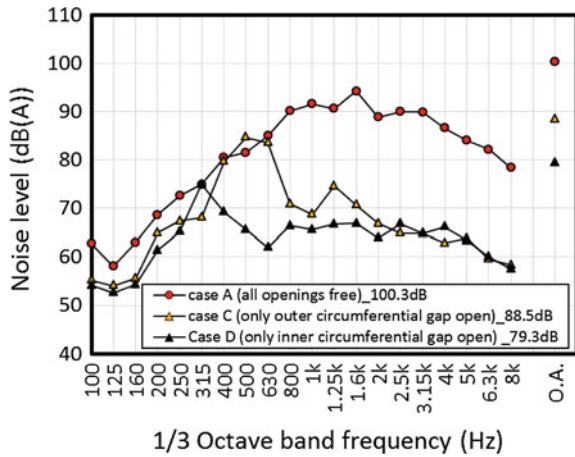


**Fig. 14** Comparison of noise spectra among case A (all openings free), case C (only outer circumferential gap open), and Case D (only inner circumferential gap open) at wheel speed of 360 km/h

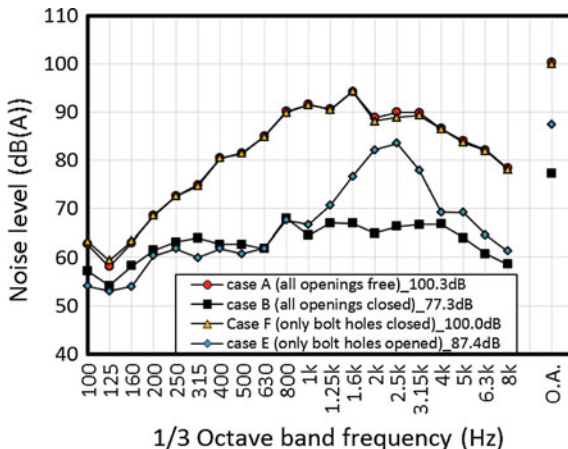


- Noise around 300 Hz is generated when inner circumferential gap alone is opened.
- Noise in a frequency range of 400–600 Hz is generated when outer circumferential gap alone is opened.

**3.2.5 Noise from Bolt Holes**

We compared noise spectra among case A (all openings free), B (all openings closed), E (only bolt holes opened), and F (only bolt holes closed) at a wheel speed of 360 km/h to confirm noise level from bolt holes, as shown in Fig. 15. When comparing case A (bolt holes open, other openings opened) with F (bolt holes

**Fig. 15** Comparison of noise spectra among case A (all openings free), case B (all openings closed), case E (only bolt holes opened), and case F (only bolt holes closed) at wheel speed of 360 km/h



blocked, other openings opened), we observed that brake disc noise level did not change. However, when comparing case B (all openings closed) with E (bolt holes open, other openings blocked) a level of noise of around 2500 Hz was generated. From these results, we confirmed that the 2500 Hz was generated from the bolt holes, though this 2500 Hz sound hardly affects the overall noise level when all openings are free.

### 3.2.6 Contribution of Each Noise Source

Figure 16 shows overall level of each case at a wheel speed of 360 km/h. In case A, all openings of brake disc (inner circumference gap, outer circumference gap, bolt holes) are free. In cases B, C, D, and E, ventilation route is blocked. From comparison of cases A and C (or B, D, and E), noise was reduced by more than 12 dB (100 dB → 88 dB) by blocking ventilation route. Thus, we confirmed that noise generated from the ventilation route is dominant in aerodynamic noise of low-noise brake disc.

Moreover, we evaluated the contribution of other noise sources using case B (all openings closed) as a benchmark. From comparison of cases B and C (only outer circumference gap opened), noise level increases by 11 dB (77 dB → 88 dB) by opening outer circumference gap alone. From comparison of cases B and D (only inner circumference gap opened), noise increases by 2 dB (77 dB → 79 dB) by opening inner circumference gap alone. From comparison of cases B and E (only bolt holes opened), noise increases by 10 dB (77 dB → 87 dB) by bolt holes alone.

From the above, we surmised the noise level of each noise source by comparing cases.

Outer circumference gap: 87 dB subtracting 77 dB (case B) from 88 dB (case C)  
 Inner circumference gap: 74 dB subtracting 77 dB (case B) from 79 dB (case D)



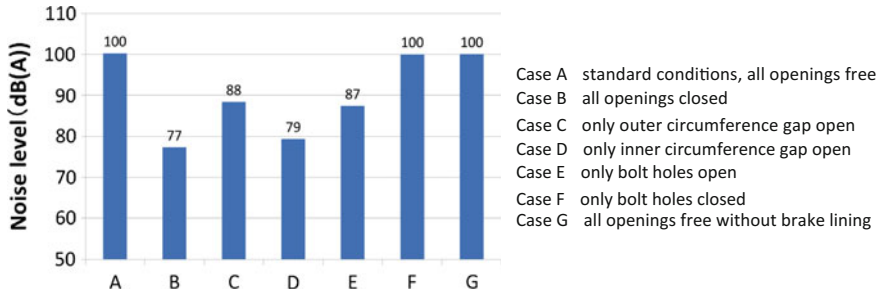


Fig. 16 Overall level of each case at 360 km/h

Bolt holes: 86 dB subtracting 77 dB (case B) from 87 dB (case E)

Ventilation route: 99 dB subtracting other noise sources (87, 74, 86 dB) from 100 dB (case A).

Therefore, each noise sources of low-noise brake disc can be ranked in following order.

Ventilation route  $\gg$  Outer circumference gap > Bolt holes > Inner circumference gap.

## 4 Conclusion

In this paper, we conducted a study to reduce noise from lower parts of train cars, especially noise around wheels. First, we focused on aerodynamic noise of brake discs and developed a low-noise brake disc through running tests using FASTECH360. Next, to further reduce noise around wheels, we investigated aerodynamic noise sources of the low-noise brake disc using test equipment. We obtained the following results.

- (1) From running test results using FASTECH360, we confirmed that noise from around bogie and wheels was mainly aerodynamic noise generated from air through the ventilation route on the back of the brake discs, and we developed a low-noise brake disc with ribs.
- (2) From experiment results of the low-noise brake disc using our test equipment, we confirmed that (A) noise over 700 Hz is generated by air through the ventilation route at the back of the disc, (B) noise around 500 Hz is generated from circumference gap, and (C) noise around 2500 Hz is generated from bolt holes.
- (3) Contribution of each noise source of the low-noise brake disc was found to be in the following order:  
 Ventilation route  $\gg$  Outer circumference gap > Bolt holes > Inner circumference gap.

## References

1. Kitagawa, T., Nagakura, K.: Aerodynamic noise generated by Shinkansen cars. *J. Sound Vib.* **231**(3), 913–924 (2000)
2. Kurita, T., et al.: Reduction of wayside noise from Shinkansen high-speed trains. *J. Mech. Syst. Transp. Logist.* **4**(1), 1–12 (2011)
3. Wakabayashi, Y. et al.: Noise measurement results of Shinkansen high-speed test train (FASTECH 360S, Z). In: *Proceedings of the 9th International Workshop on Railway Noise, Munich (Germany)*, pp. 63–70 (2008)
4. Fujimoto, T. et al.: Evaluation of rolling noise property and establishment of vibro-acoustic model (in Japanese). In: *Proceeding of the 16th Transportation and Logistics Conference 2007*, pp. 63–66 (2007)

# Development of New Noise Reduction Equipment for the Slits on Tunnel Hoods



Masaaki Matsunuma and Nobuyuki Kimura

**Abstract** High speed-trains entering long tunnels sometimes cause an explosive sound at the exit, caused by a micro-pressure wave. Tunnel hoods have been installed to mitigate this phenomenon. In general, Shinkansen tunnel hoods have slit windows in their side wall. On one hand these side slit windows are effective for micro-pressure waves; but on the other hand, they cause traveling noise from trains to escape from tunnel hoods. To make matters worse, the faster trains travel, the louder traveling noise becomes. In this study, new noise reduction facilities for slit windows of tunnel hoods have been developed. The scale model experiments in this study proved the effectiveness in noise reduction.

## 1 Introduction

High speed-trains entering long tunnels sometimes cause an explosive sound at the exit, caused by micro-pressure wave [1]. Tunnel hoods have been installed to mitigate this phenomenon. In general, Shinkansen tunnel hoods have slit windows in their side wall. This is because these side slit windows can make length of tunnel hoods shorter. It is true that these side slit windows are effective for micro-pressure waves, but traveling noise from trains escape to outside from side slit windows. To make matters worse, the faster trains travel, the louder traveling noise becomes; proportionately with traveling speed to the sixth power. So far, countermeasures against explosive sounds have been considered important around the tunnel portal; but, to operate Shinkansen at faster speed in the future, traveling noise from side slit windows must be even further mitigated. In this study, new noise reduction facilities for side slit windows of tunnel hoods have been developed. The scale-model experiments in this study proved their effectiveness in noise reduction.

---

M. Matsunuma (✉) · N. Kimura  
Frontier Service Development Laboratory, Research and Development Center  
of JR East Group, East Japan Railway Company, A2-479, Nisshin-cho,  
Kita-ku, Saitama-city, Saitama-Pref 331-8513, Japan  
e-mail: masaaki-matsunuma@jreast.co.jp

## 2 Target of Development

The main function of installing tunnel hoods is to reduce micro-pressure waves. For that purpose, one of the most basic solutions against micro-pressure waves is to lengthen tunnel hoods. But, in most cases, railroad companies lack space to lengthen tunnel hoods. Moreover, the foundational structures of tunnel hoods tend to be large. On the other hand, slit windows on side walls of tunnel hoods have an effect similar to the lengthening of tunnel hoods (Fig. 1). Thus, slit windows on side walls have usually been applied to reduce micro-pressure waves. However, the faster high-speed trains travel, the louder the noise they generate. For trains to travel faster the traveling noise from side wall slit windows should be controlled. Therefore, the main target in this project is to reduce the traveling noise leaking from slit on side walls. Thus, our target is to develop new ducts especially for slit windows of tunnel hoods.

## 3 Newly Developed Slit-Vented Side Walls for Tunnel Hoods

As a measure for noise-reduction, we devised duct frames to install in existing slit windows on tunnel hoods (Fig. 2: 'A-type'), including a 'vane type' (Fig. 3: B-type) and a 'louver type' (Fig. 4: C-type). The scale model size is 1/25. The difference from the conventional duct is that the 'vane type' has a vane in the duct and the 'louver type' has a louver.

It should be noted that noise-reductive materials (polyurethane foam, etc.) can be applied to the internal surface of each type (Fig. 5).

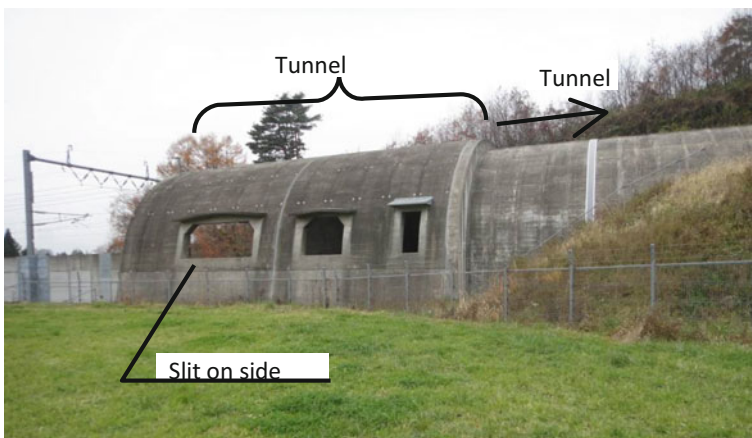


**Fig. 1** Example of tunnel hoods with slit windows on its side wall

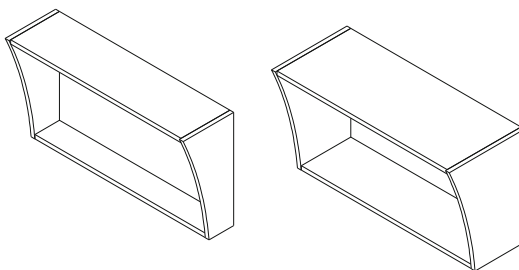


Fig. 2 A-type

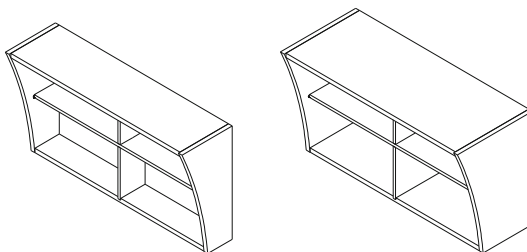


Fig. 3 B-type

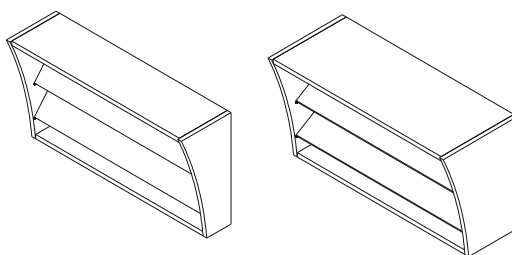


Fig. 4 'C-type'



Fig. 5 Each type with polyurethane foam

## 4 Method of the Scale Model Experiments

### 4.1 Outline of Scale Model Experiments

We used 1/25 scale model of tunnel hood, made of stainless steel, set in the fully anechoic chamber (Fig. 6). Slit windows are made in the center of the model. Figure 7 shows the ‘louver type’ set in the slit windows.

### 4.2 Noise Source for Experiments

In general, Shinkansen noise sources are classified into four major categories: structure noise, noise from lower parts of cars, aerodynamic noise, and pantograph noise. In the scale model, the noise line source was set at the three locations shown in Fig. 8. The total noise is calculated by applying the three line sources to the spectrum curves of noise characteristically emitted by Shinkansen trains.

- (1) Noise from lower parts of cars (and rail)
- (2) Aerodynamic noise from upper part of car body
- (3) Pantograph noise.

### 4.3 Measurement Point

We define the centerline of the scale model of the tunnel hoods as a reference surface. The measurement point is set on a perpendicular plane 25 m away from center line on the near side of track (Fig. 9).

Fig. 6 Model of tunnel hood



**Fig. 7** 'Louver type' set on the slit windows

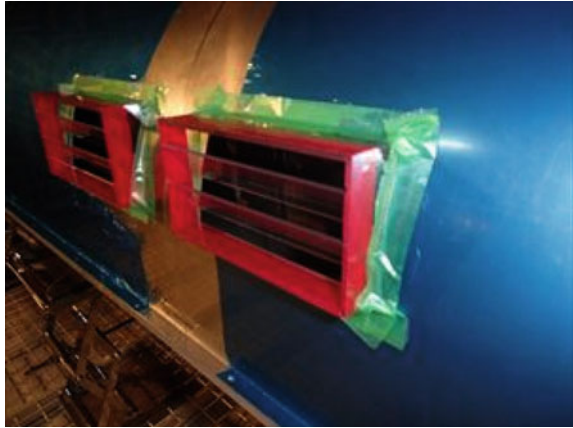


**Fig. 8** Noise source of experiment

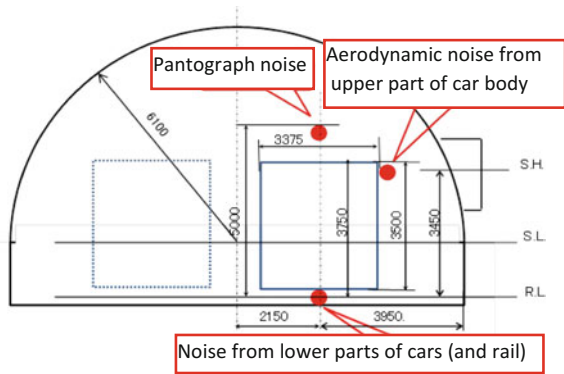


**Fig. 9** Measurement point

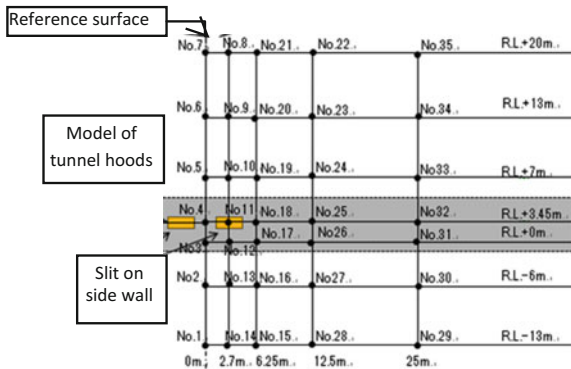


**Table 1** Parameters of the scale model experiments

Type	Length <sup>a</sup>	Noise-absorbing Polyurethane foam (thickness = 5 mm)	Train position on double track	Definition of case name (example)
Slit only	–	–	Near side (N)	“CLA-N” means long louver type, with polyurethane foam when the trains are on near side
Duct type (A)	L = 500 mm	Present (A)	Far side (F)	
Vane type (B)	(S)	Absent (N)		
Louver type (C)	L = 1000 mm (L)			

<sup>a</sup>...“Length” is described by actual scale

#### 4.4 Parameters of the Scale Model Experiments

The model for experiments had two different sizes (500 and 1000 mm in length) for different types of new facilities. Experiments with/without polyurethane foam were conducted. The experiments were also performed on both sides of a double track. The parameters for the experiments and the naming convention used are shown in Table 1.

#### 4.5 Model Scaling

The models were produced at a scale of one twenty-fifth of the normal size. Therefore, the center frequency should be divided by 25. For example, the value of 25 kHz in the experiments is converted to the value of 1 kHz at normal scale.

### 5 Results of the Scale Model Experiments

The results from each experimental scale model were analysed to provide the distribution of noise as contour maps.

#### 5.1 Slit Only

In the ‘slit only’ model the distribution of noise values obtained is shown in Fig. 10. The horizontal axis shows horizontal distance from the reference surface, which is defined as the same distance from the two slit windows. The vertical axis shows the elevation height above the rail.



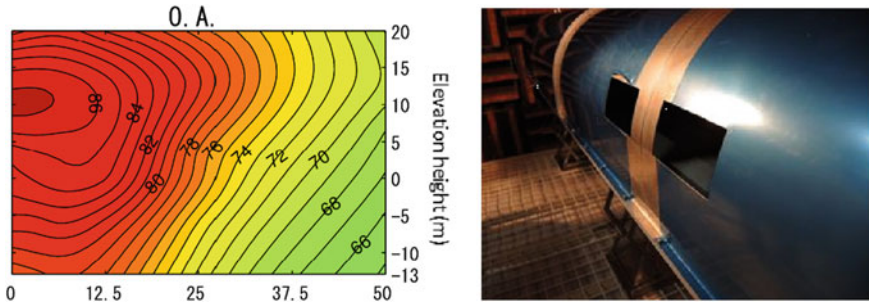


Fig. 10 Noise contour of ‘slit only’ model

### 5.2 A-Type

In case of ‘ALA,’ the noise level was reduced by 3 dB on the average, compared to the ‘slit only’ model (Fig. 11). Elevation height of peak of noise is about ten meters from track height, which is similar to the ‘slit only’ model.

### 5.3 B-Type

In case of ‘BLA,’ the noise level was reduced by 5 dB on the average, compared to the ‘slit only’ model (Fig. 12). Elevation height of peak of noise is about ten meters from track height, which is similar to ‘slit only’ model.

### 5.4 C-Type

In the case of ‘CLA,’ the noise level was reduced by 10 dB on the average, compared to the ‘slit only’ model (Fig. 13). The interval of contour line is wider, compared with others.

### 5.5 Comparison About Noise Value of Each Types

Figure 14 shows the total noise when the train noise source was simulated to travel on the near side of a double track. We defined the elevation height of track rail as base line (R.L.). In Fig. 14, we compare the noise level measured in the scale model experiments (Figs. 11, 12, 13 and 14) at elevation levels of -6, 3.5, and 7 m. The horizontal axis shows the test scenarios and vertical axis shows the total noise level at three points. Compared with the case of ‘slit only’(S-N), the longer louver type with noise absorbers enabled reduction of noise by 16.6 dB.

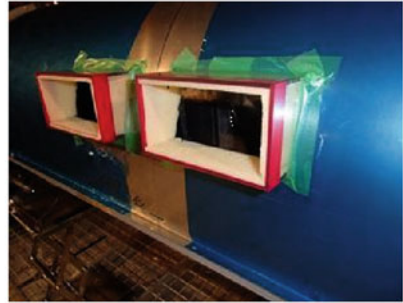
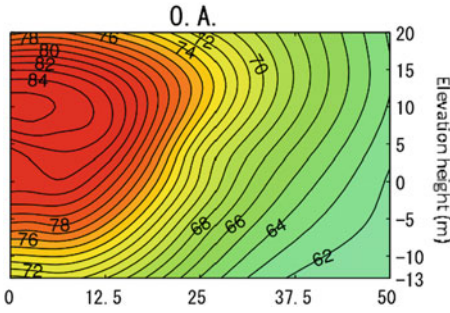


Fig. 11 Noise contour of 'A-type' model

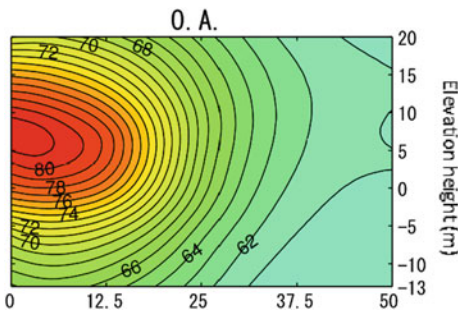


Fig. 12 Noise contour of 'B-type' model

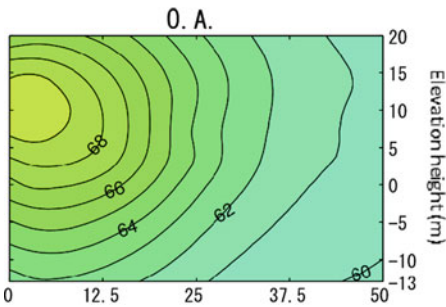


Fig. 13 Noise contour of 'C-type'

### 5.6 Effectiveness in Noise Reduction [2, 3]

Regarding duct containing noise-absorbing material noise reduction is proportional to side length and inversely proportional to the square measure of duct.

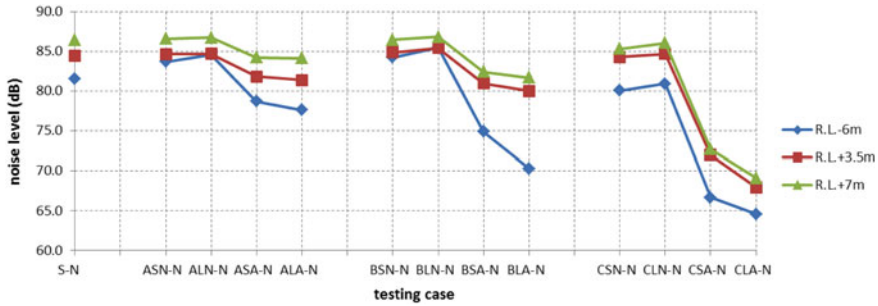


Fig. 14 Total noise results from the scale experiments

$$R = K \cdot P/S \tag{5.1}$$

R: Attenuation

K: Factor of proportionality depending on sound absorption coefficient

P: Side length of duct

S: Square measure of duct.

The tendency for “vane type” to be more effective than “duct type” seems to follow to Eq. (5.1).

### 5.7 Comparison with Actual Tunnel Hoods

At a certain site of high-speed train tunnel, difference of noise around tunnel hoods between slit side and non-slit side reached about 8 dB. In the case of “louver type,” noise reduction effects overtake this value. Therefore, “louver type” can be expected to have sufficient effect.

## 6 Conclusion

New noise-reduction facilities have been developed through this project. We obtained the following results.

- (1) New noise control designs for the slit-vented tunnel hoods were investigated. The reduction in noise emissions for each design were confirmed by a 1/25 scale experiments.
- (2) The new noise control tunnel hoods included vane-type and louver-type design. Both types were investigated using scale models.

- (3) As a result of the scale experiments, the louver-type design with absorptive lining was found to reduce noise level by up to 16.6 dB more than the existing slit-only design.

## References

1. Kato, I., Shinohara, Y.: Wayside environmental measures for Shinkansen speed increases. *JR East Tech. Rev.* 26, 73–76 (2013) (in Japanese)
2. Institute of Noise Control Engineering in Japan: *Hand Book of Noise Control Engineering* (2001) (in Japanese)
3. Bruel, P.V.: *Sound Insulation and Room Acoustics*, pp. 159–165. Chapman & Hall, London (1951)

# Reduction of Aerodynamic Noise Emitted from Pantograph by Appropriate Aerodynamic Interference Around Pantograph Head Support



T. Mitsumoji, Y. Sato, N. Yamazaki, T. Uda, T. Usuda  
and Y. Wakabayashi

**Abstract** Reduction of aerodynamic noise emitted from a pantograph head and its support is one of the important subjects for the speed-up of high-speed trains from an environmental point of view. In this study, to reduce aerodynamic noise emitted from the pantograph head and its support, suitable arrangement of a pantograph head which has a smooth cross section profile, was investigated. The flow field measurement in the wake domain of the pantograph shows that turbulent intensity can be reduced by setting the pantograph head at a suitable position. The reduction of turbulence in the wake domain is caused by appropriate aerodynamic interference between the pantograph head and its support. Furthermore, the results of the aerodynamic noise measurement show that the suitable pantograph head arrangement efficiently reduces aerodynamic noise.

## 1 Introduction

In Japan, Shinkansen trains run through densely populated areas. Therefore, reduction of wayside noise caused by Shinkansen trains is necessary to preserve surrounding environments along the railway lines. Since the sound power of aerodynamic noise grows at a rate between the 6th and 8th power of the train speed, aerodynamic noise is the dominant source for the high-speed train operations [1–3]. Among aerodynamic noise emitted from various parts of the Shinkansen train, the

---

T. Mitsumoji (✉) · Y. Sato · N. Yamazaki · T. Uda · T. Usuda  
Railway Technical Research Institute, 2-8-38, Hikari-cho, Kokubunji-shi, Tokyo, Japan  
e-mail: mitsumoji.takeshi.84@rtri.or.jp

Y. Wakabayashi  
Advanced Railway System Development Center, R&D Center of JR East Group, 2-479,  
Nisshin-cho, Kita-ku, Saitama-shi, Saitama, Japan

pantograph, especially pantograph head and its support (see Fig. 1a), is one of the dominant aerodynamic noise sources [2–5].

A previous study has proposed a smooth profile pantograph head (see Fig. 1c) which achieves both aerodynamic noise reduction and stabilization of lift force characteristics by applying optimization technique with the help of CFD analysis [6]. However, the smooth profile pantograph head mounted on the currently used pantograph head support can not reduce aerodynamic noise sufficiently. The reason turned out to be that the aerodynamic interference between the pantograph head and its support causes intensive turbulence resulting in significant broad band aerodynamic noise [7]. The former study also clarified that an improved pantograph head support which set the pantograph head to be apart from the pantograph head support can reduce aerodynamic noise efficiently [7, 8]. However, the detailed mechanism of the aerodynamic noise reduction by improving arrangement of the pantograph head and its support has not yet been completely understood.

In this study, a suitable position of the smooth profile pantograph head relative to the pantograph head support was investigated by evaluating turbulent intensity in the wake domain using PIV (Particle Image Velocimetry) and flow visualization techniques in wind tunnel tests. Based on these results, several types of improved pantograph head support arm which supports the smooth profile pantograph head at a required position were mounted on a pantograph of a Shinkansen train, and aerodynamic noise measurement in the wind tunnel was carried out. As a result, it is clarified that setting the pantograph head at a suitable position can generate appropriate aerodynamic interference and reduce broad band aerodynamic noise sufficiently.

## 2 Flow Field Evaluation with 1/1.6 Scaled Pantograph Model

### 2.1 Details of the Wind Tunnel Test

To investigate the relation between the position of the smooth profile pantograph head relative to its support and the wake turbulence, PIV measurement and flow

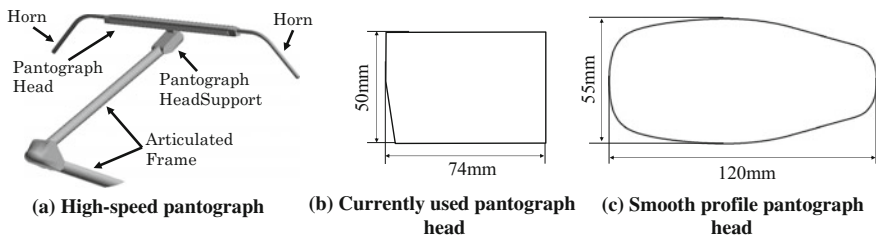
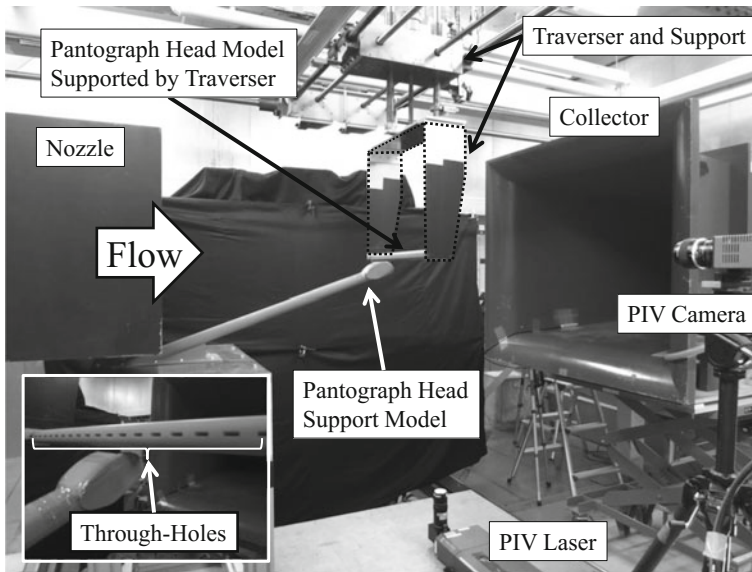


**Fig. 1** Shape of high-speed pantograph and pantograph head

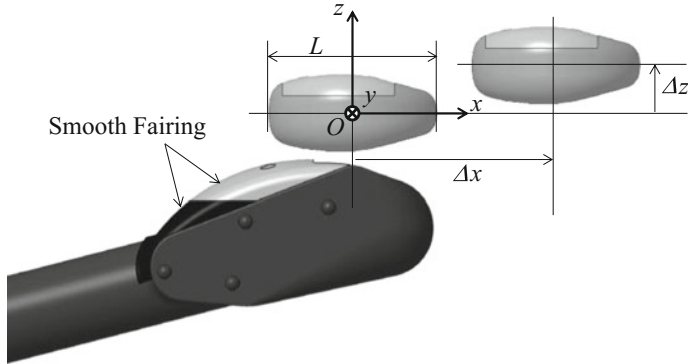
visualization were carried out in RTRI's small scale low-noise wind tunnel (the nozzle size is  $720 \text{ mm} \times 600 \text{ mm}$ , the maximum flow speed is  $150 \text{ km/h}$ ). Figure 2 shows the configuration of the wind tunnel test. The 1/1.6 scaled pantograph model which consists of only upper articulated frame, pantograph head support, and the smooth profile pantograph head was installed in the test section with knuckle forward orientation. The smooth profile pantograph head model with through-holes was mounted on a traversing mechanism which enables to set the pantograph head at arbitrary position relative to the pantograph head support. The length of the pantograph head model in the sleeper direction was  $515 \text{ mm}$ . Each through-hole had  $12.6 \text{ mm} \times 3.8 \text{ mm}$  rectangular cross section and 16 through-holes were installed on the pantograph head model at  $12.6 \text{ mm}$  intervals [6, 9]. A smooth fairing was attached on the pantograph head support as shown in Fig. 3. In this wind tunnel test, the pantograph horn was not installed.

Figure 3 shows the definition of the coordinate system and pantograph head position in this wind tunnel test. The center of the smooth profile pantograph head when the pantograph head model is equipped with the currently used pantograph head support is defined as the origin. In this paper, pantograph head position is indicated with the dimensionless position  $(\Delta x/L, \Delta z/L)$ , where  $\Delta x$  and  $\Delta z$  indicate displacement of the pantograph head relative to the position of the pantograph head which is mounted on the currently used pantograph head support, and  $L$  indicates the pantograph head length in the rail direction.

The measurement plane of the PIV was set at the  $y = 0$  i.e. the center plane of the pantograph head in the sleeper direction. Three hundred pairs of PIV images



**Fig. 2** Configuration of the PIV measurement



**Fig. 3** Definition of coordinate system and pantograph head position

were taken under each test condition. Mean and RMS velocity field in the  $y = 0$  plane were obtained by statistical calculation of 300 instantaneous velocity fields derived by the PIV image. The wind speed  $U_0$  was set at 10 m/s with due consideration of traversing mechanism strength. The Reynolds number based on the width of the pantograph head support is  $3.8 \times 10^4$ .

The measurement plane of the flow visualization was set at  $z = -0.26L$ , which includes the center point of the gap between the bottom of the pantograph head and the top of the pantograph head support. The wind speed  $U_0$  was set at 5 m/s so that visualization smoke particles would not diffuse. Reynolds number for the flow visualization is  $1.9 \times 10^4$ .

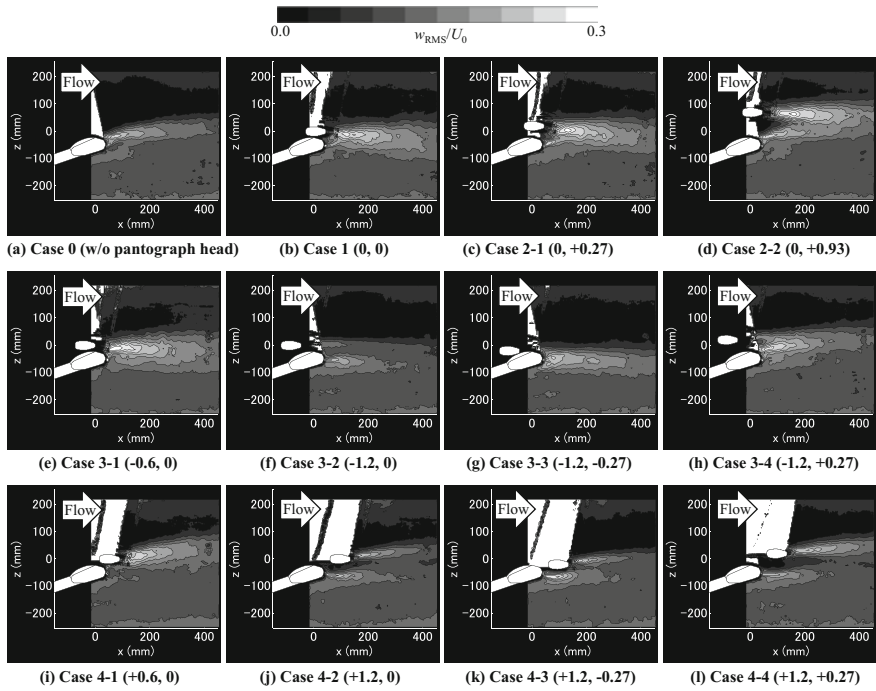
## 2.2 Results of the PIV Measurement

Figure 4 shows  $z$ -directional turbulent intensity obtained by the PIV measurement. The white domain on the upper left area of each figure is a shadow domain where the laser sheet was blocked out by the pantograph head or the pantograph head support. The caption of each figure indicates the appellation of the test conditions together with dimensionless pantograph head positions.

Comparing Case 1 (Fig. 4b, pantograph head is set at  $(0, 0)$ ) with Case 0 (Fig. 4a, without pantograph head), it can be found out that turbulent intensity of Case 1 is larger than that of Case 0. Flow interference between the pantograph head and its support generates wake turbulence.

In Case 2-1 (Fig. 4c) and Case 2-2 (Fig. 4d), where the pantograph heads are set apart from the pantograph head support in the vertical direction so that the flow interference is weakened, turbulent intensity is not reduced efficiently. Especially in Case 2-2, where the pantograph head is set widely apart from the pantograph head support, turbulent intensity behind the pantograph head is still large. Therefore, to





**Fig. 4**  $z$ -directional turbulence intensity distribution measured by PIV ( $y = 0$  plane,  $U_0 = 10$  m/s)

reduce the wake turbulence, it is not sufficient to simply set apart the pantograph head from its support so that the flow interference is weakened. In the cases where the pantograph head is shifted to the upstream domain (Case 3-1 (Fig. 4e)—Case 3-4 (Fig. 4h)), turbulent intensity distribution sensitively depends on the pantograph head position. Among these cases, the most drastic turbulent intensity reduction is observed for Case 3-2 (Fig. 4f).

In the cases where the pantograph head is shifted to the downstream domain (Case 4-1 (Fig. 4i)—Case 4-4 (Fig. 4l)), turbulent intensity distribution depends on the pantograph head position. The turbulent domain splits into two regions and turbulent intensity is smaller especially in Case 4-2, Case 4-3, and Case 4-4 than that of Case 4-1 or Case 1. Among these cases, the most effective turbulent intensity reduction is observed in Case 4-2 (Fig. 4j). From these results, it is concluded that setting the pantograph head at a suitable position leads to generation of appropriate aerodynamic interference, resulting in a reduction of turbulent intensity in the wake domain.

### 2.3 Results of the Flow Visualization

The PIV measurement described in the previous section were carried out only in the  $y = 0$  plane. However, to understand the flow field around the pantograph head and its support, additional flow field information is necessary since the wake turbulence has three-dimensional distribution. Therefore, the flow visualization in the  $x$ - $y$  plane which is orthogonal to the above-mentioned PIV measurement plane was carried out.

Figure 5 shows the flow visualization results for typical pantograph head positions. In Case 1 (Fig. 5b), where the pantograph head is set at  $(0, 0)$ , remarkable flow separation can be observed around the pantograph head support and the flow in the wake region is turbulent. In contrast, in Case 3-2 (Fig. 5a) and Case 4-2 (Fig. 5c), where drastic reduction of turbulent intensity is observed in the PIV measurement, remarkable flow separation around the pantograph head support is no longer observed and the flow in the wake domain is less turbulent.

From these results, it is concluded that the suitable pantograph head arrangement prevents remarkable flow separation around the pantograph head support and reduces wake turbulence.

### 2.4 Conclusion of the Flow Field Measurement

For the reduction of the wake turbulence, it is not sufficient only to reduce aerodynamic interference by simply setting the pantograph head apart from its support. As shown in Case 3-2 and Case 4-2, the remarkable flow separation around the pantograph head support can be prevented and the wake turbulence can be reduced by setting the pantograph head at suitable position. This is due to appropriate aerodynamic interference between the pantograph head and its support.

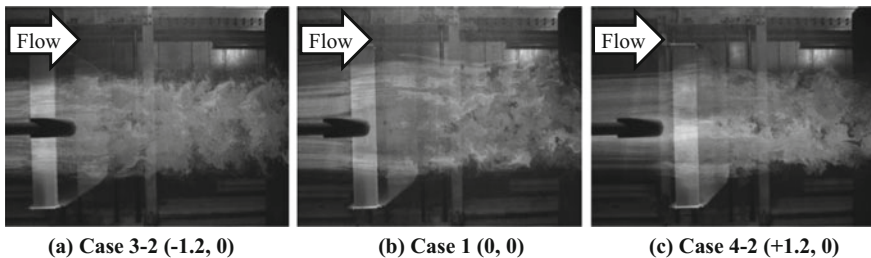


Fig. 5 Flow visualization results in the  $x$ - $y$  plane ( $z = -0.26L$  plane,  $U_0 = 5$  m/s)

### 3 Aerodynamic Noise Measurement with Actual Shinkansen Pantograph

#### 3.1 Details of the Wind Tunnel Test

To investigate the aerodynamic noise reduction effect of setting the pantograph head at suitable position, aerodynamic noise measurement was carried out in RTRI's large scale low-noise wind tunnel (nozzle size is  $3 \text{ m} \times 2.5 \text{ m}$ , maximum flow speed is  $400 \text{ km/h}$ ). Figure 6 shows the wind tunnel test setup. A Shinkansen pantograph was installed in the open type test section. An omnidirectional microphone for aerodynamic noise measurement was set obliquely downward of the pantograph as shown in Fig. 6 and 1/3 octave band analysis with A-weighting was carried out. In the flow direction the microphone position was set at the center of two insulators supporting the pantograph. The microphone was set at  $5 \text{ m}$  laterally from the center of the pantograph head, which corresponds to the center line of the nozzle, and at  $2.616 \text{ m}$  downwards from the top of the pantograph head respectively. The wind speed  $U_0$  was set at  $111 \text{ m/s}$  ( $400 \text{ km/h}$ ). The Reynolds number is  $6.7 \times 10^5$ .

In this wind tunnel test, the aerodynamic noise reduction effect of applying several types of the improved pantograph head support arm as shown in Fig. 7 was assessed. The smooth profile pantograph head model with through-holes was applied in all the cases except for Case 0 and Case 6. In this section, the definition and the description of the pantograph head position are the same as the ones explained in the Section “[Details of the Wind Tunnel Test](#)”. The pantograph head

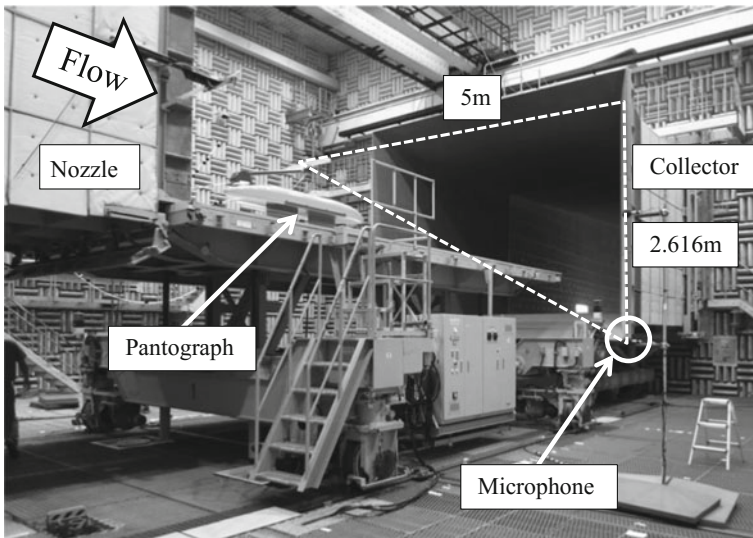


**Fig. 6** Configuration of the aerodynamic noise measurement

positions in the cases of Case 0 (Fig. 7a) to Case 4-3 (Fig. 7h) are indicated in Fig. 4. Case 5 is a supplementary test case, where the pantograph head support is covered with the full-coverage fairing so that the flow interference can be reduced by its smooth shape. Case 6 is the case in which the currently used pantograph head and its support are applied. In Case 6 the smooth fairing as shown in Fig. 3 was not installed. In all of these test conditions, pantograph horns were not installed.

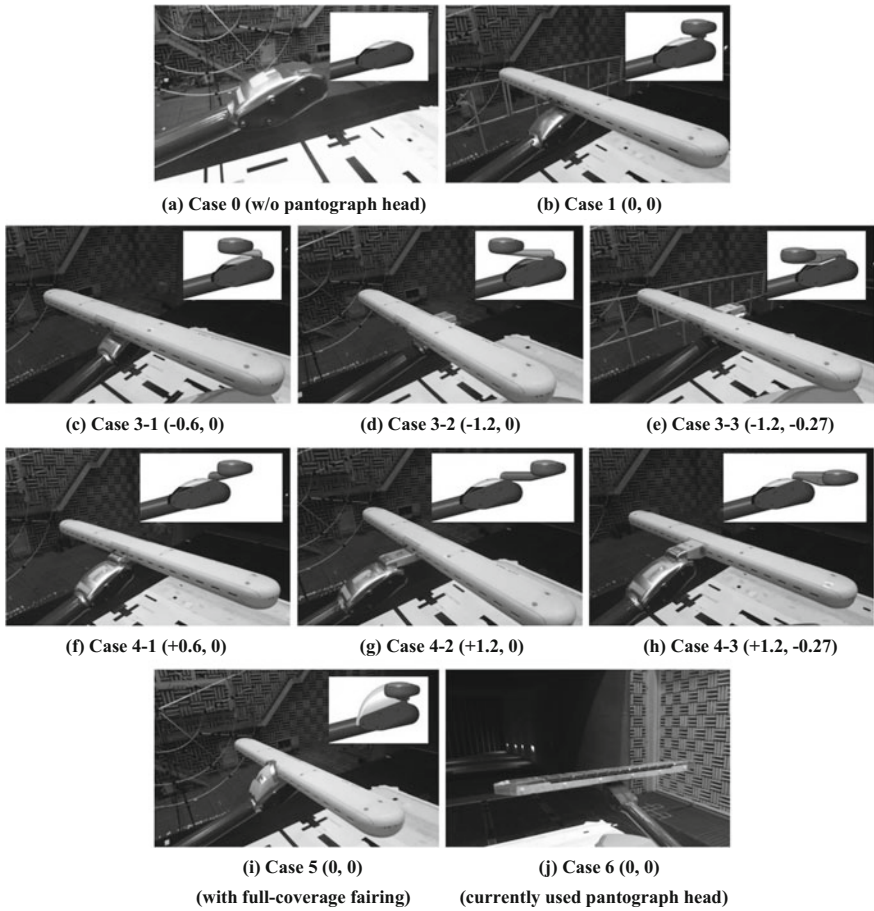


**Fig. 7** Test cases for aerodynamic noise measurement

### 3.2 Results and Conclusion of the Aerodynamic Noise Measurement

Figure 8 shows the aerodynamic noise measurement results. Figure 8a, which is a comparison among the upstream offset cases, indicates that the smooth profile pantograph head (Case 1) can considerably reduce aerodynamic noise in the frequency range above 400 Hz compared to the currently used pantograph head (Case 6). The overall noise level of Case 1 is 3.1 dB(A) lower than that of Case 6. In comparison with Case 1, the noise level of Case 3-1, where the pantograph head is displaced at  $(-0.6, 0)$ , can be reduced in the frequency domain between 500 to 1.25 kHz, and the overall noise level of Case 3-1 is 0.8 dB(A) lower than that of Case 1. Furthermore, the noise level of Case 3-2, where the pantograph head is displaced at  $(-1.2, 0)$ , can be reduced in the frequency domain above 500 Hz, and the overall noise level of Case 3-2 is 1.4 dB(A) lower than that of Case 1. However, the noise level of Case 3-3, in which the pantograph head is displaced at  $(-1.2, -0.27)$ , increases in the frequency domain above 2 kHz in comparison to Case 1. As a consequence, the overall noise level reduction compared with that of Case 1 is no more than 0.3 dB(A). In these upstream offset cases, the lowest noise level case is Case 3-2. This result is consistent with the flow field measurement results

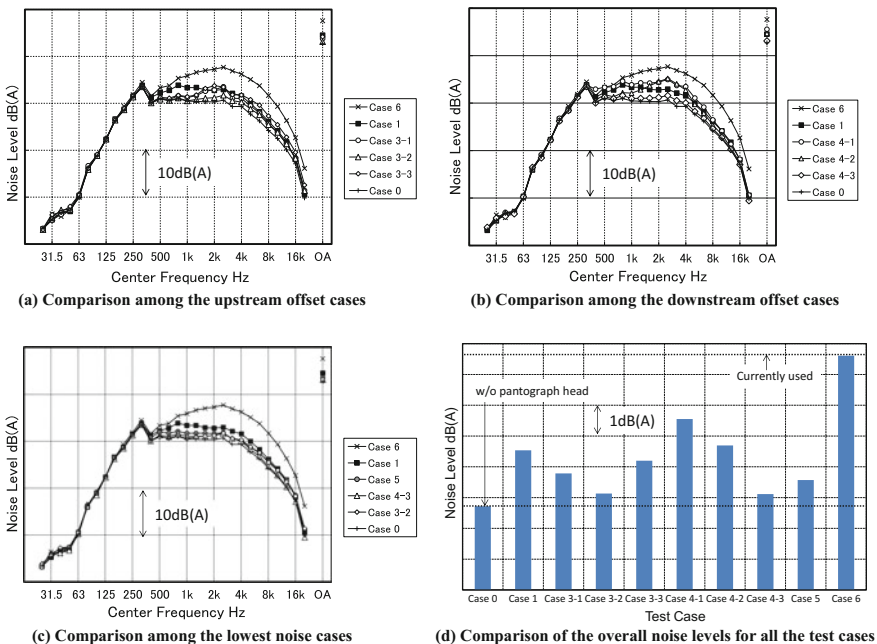


**Fig. 8** Aerodynamic noise measurement results ( $U_0 = 111$  m/s, 1/3 octave band analysis with A-weighting)

described in Chapter “[Wheel Squeal: Insights from Wayside Condition Monitoring](#)”.

Figure 8b shows a comparison of the noise level among the downstream offset cases. In comparison with Case 1, the noise level of Case 4-1, where the pantograph head is displaced at  $(+0.6, 0)$ , increases in the frequency domain above 315 Hz, and the overall noise level of Case 4-1 is 1.0 dB(A) higher than that of Case 1. The noise level of Case 4-2, where the pantograph head is displaced at  $(+1.2, 0)$ , in the frequency domain between 400 and 1.25 kHz is reduced compared with that of Case 1. However, the noise level of Case 4-2 increases in the frequency domain between 1.6 and 4 kHz compared with that of Case 1. As a consequence, the overall noise level of Case 4-2 is 0.2 dB(A) higher than that of Case 1. On the contrary, the noise level of Case 4-3, where the pantograph head is displaced at  $(+1.2, -0.27)$ , remarkably decreases in the frequency domain above 400 Hz in comparison with that of Case 1. The overall noise level of Case 4-3 is 1.4 dB(A) lower than that of Case 1. Of these downstream offset cases, results in Case 4-3 show the lowest noise level. This result is not consistent with the flow field measurements described in Chapter “[Wheel Squeal: Insights from Wayside Condition Monitoring](#)”. The reasons for this are considered to be the difference of the test conditions, such as the existence of the pantograph head support stay arm which aligns in front of the pantograph head and the difference of Reynolds number.

Figure 8c shows comparison of the noise level among Case 3-2 and Case 4-3, including Case 5, where the full-coverage fairing was applied to Case 1. According to Fig. 8c, the noise levels of Case 3-2 and Case 4-3 are lower in the frequency domain between 400 to 1.6 kHz than that of Case 5. As a consequence, Case 3-2 and Case 4-3 produce 0.5 dB(A) lower overall noise level than that of Case 5. From these results, it is concluded that setting the pantograph head at the appropriate position can reduce the aerodynamic noise more effectively than applying the full-coverage fairing to the pantograph head support.

## 4 Conclusion

To reduce the aerodynamic noise emitted from the pantograph head and its support, suitable arrangement of the pantograph head which has a smooth cross section profile, was investigated. First, the flow field measurements in the downstream domain of the pantograph were carried out. As a result, it is shown that it is not sufficient for the reduction of wake turbulence only to reduce aerodynamic interference by simply setting the pantograph head apart from its support. On the other hand, it is clarified that the remarkable flow separation around the pantograph head support can be prevented and the wake turbulence can be reduced by setting the pantograph head at a suitable position. This is due to appropriate aerodynamic interference between the pantograph head and its support. Next, the aerodynamic noise measurement with the Shinkansen pantograph was carried out. As a consequence, setting the pantograph head at an appropriate position can reduce

aerodynamic noise more effectively than applying the full-coverage fairing to the pantograph head support. Finally, it is concluded that the aerodynamic noise emitted from the smooth profile pantograph head and its support can be reduced by setting the pantograph head at a suitable position.

## References

1. Moritoh, Y., Zenda, Y., Shimizu, Y., Nagakura, K.: Aerodynamic noise of highspeed railway cars. In: STECH'93 (1993)
2. Moritoh, Y., Zenda, Y., Nagakura, K.: Noise control of high-speed Shinkansen. *J. Sound Vib.* **193**(1), 319–334 (1996)
3. Nagakura, K.: The method of analyzing Shinkansen noise. *Q. Rep. RTRI* **37**(4), 210–215 (1996)
4. Yamazaki, N., Nagakura, K., Ikeda, M.: Acoustic source localization of pantograph using a 2-D microphone array. *RTRI Rep.* (in Japanese) **17**(11), 1–6 (2003)
5. Kurita, T.: Development of external-noise reduction technologies for Shinkansen high-speed trains. *J. Environ. Eng.* **6**(4), 805–819 (2011)
6. Ikeda, M., Suzuki, M., Yoshida, K.: Study on optimization of panhead shape possessing low noise and stable aerodynamic characteristics. *Q. Rep. RTRI* **47**(2), 72–77 (2006)
7. Ikeda, M., Mitsumoji, T.: Numerical estimation of aerodynamic interference between panhead and articulated frame. *Q. Rep. RTRI* **50**(4), 227–232 (2009)
8. Ikeda, M., Mitsumoji, T., Sueki, T., Takaishi, T.: Aerodynamic noise reduction in pantographs by shape-smoothing of the panhead and its support and by use of porous material in surface coverings. *Q. Rep. RTRI* **51**(4), 220–226 (2010)
9. Ikeda, M., Takaishi, T.: Perforated pantograph horn aeolian tone suppression mechanism. *Q. Rep. RTRI* **45**(3), 169–174 (2004)

# Application Effect of Chinese High-Speed Railway Noise Barriers



Yanliang Li and Zhiqiang Li

**Abstract** As the construction of high-speed railway in China is increasingly completed, noise pollution along the railway has gained serious attention. Noise barriers play an important role in reducing high-speed railway noise and are widely used around the world. Researchers from Germany, France, Japan, England and America have enriched the structures, theories and prediction models of high-speed railway noise barriers for the past several decades (Yin et al., *J Railway Energy Saving Environ Prot Occup Safety Health* 5(4):148–151, [1]). The development of noise reduction theories for barriers has three main stages: geometric and wave acoustics theory, empirical and semi-empirical theories, and finite element and boundary element theories (Wu, *J Sound Vib* 6(3):85–88, [2]). The Chinese criteria “Technical guidelines for environment impact appraisal, Acoustic environment” (Technical guidelines for environment impact appraisal, Acoustic environment, [3]) and “The specifications for noise barriers’ acoustical design and measurement” (The specifications for noise barriers’ acoustical design and measurement, [4]) provide the formulae for predicting the an infinitely long noise barrier’s insertion loss. According to the noise source distribution of the high-speed train, East China Jiaotong University established a formula for predicting the insertion loss of the high-speed railway noise barriers (Lei, *China Railway Sci* 26(4):1–4, [5]). Southwest Jiaotong University established a finite element model to estimate the insertion loss based on finite element theory and results of a high-speed train’s noise source identification (NSI) (Zhou et al., *J Mech Eng* 49(10):14–10, [6]). To lay a solid technical foundation for further research, comprehensive investigations and measurements of the application effect of high-speed railway noise barriers are necessary. According to the data obtained from integration tests and commissioning in recent years, noise reduction effects of noise barriers with different materials and heights, and noise measurement points at different positions are summarized

---

Y. Li (✉) · Z. Li  
China Academy of Railway Sciences,  
No. 2 Daliushu Road, Haidian District, Beijing, China  
e-mail: liyl@rails.cn



(Gu et al., J Energy Sav 5(4):143–147, [7]) . Regarding the high-speed railway noise as an equivalent line noise source, the insertion loss formulas from “Technical guidelines for environment impact appraisal, Acoustic environment” and “The specifications for noise barriers’ acoustical design and measurement” are verified by test data, and the height of the equivalent line noise source of the train moving at 300 km/h is suggested at 2 m from the bottom of the barrier. Furthermore, the prediction of the barrier’s insertion loss is more accurate by separating the noise sources into different lines based on the primary results of NSI.

## 1 The Application Status of Chinese Railway Noise Barrier

The study and application of railway noise barriers in China began approximately 30 years ago. Relative development history can be divided into three stages: the fundamental research stage from 1985 to 1995; the demonstrating project application stage from 1995 to 2005, and the large-scale application stage from 2005 to now. Based on the series criteria reference maps, many kinds of noise barriers have been constructed along the Chinese high-speed railway, with a combined length exceeding 4000 km [1, 2].

According to the operating speed, the Chinese high-speed railway barriers are classified into the 250 km/h dedicated passenger line barriers and 350 km/h dedicated passenger line barriers. According to the style of tracks, there are subgrade barriers and bridge barriers. Based on the main materials used in the barrier, the noise barriers can be classified as metallic noise barriers or non-metallic noise barriers. Most of the barriers are metallic plate-inserted barriers, which account for 90% of the total. The most common heights of the high-speed railway noise barrier are 2.15 and 2.95 m, which are used on the bridge and subgrade respectively. In some special sections, 0.5 or 1.0 m acrylic transparent plates are added on the top of the barrier to achieve better effect.

## 2 Field Measurement Results

The evaluation parameter of noise a barrier’s acoustical performance is insertion loss ( $IL$  in short hereinafter). “The specifications for noise barriers’ acoustical design and measurement” (HJ/T 90-2004) and “Dynamic test guidance for passenger dedicated railway project completion acceptance” (TB/T 90-2004) specify the measurement methods and requirements of a noise barrier’s  $IL$ . The measurement method is called “the indirect method” and the relative equation is illustrated as (2.1)

**Table 1** Rail lines used in this paper

Rail line	Barrier style	Height (m)	Length (m)	Railway
L1	Metallic plate-inserted	2.15 m on bridge 2.95 m on subgrade	>300	Ballastless track
L2	Metallic plate-inserted	2.95 m on subgrade	300	Ballastless track
L3	Nonmetallic plate-inserted	2.95 m on subgrade	400	Ballasted track
L4	Metallic plate-inserted	2.15 m on bridge	690	Ballastless track
L5	Metallic plate-inserted	2.95 m on subgrade	500	Ballastless track
L6	NSI test			Ballastless track

$$IL = (L_{\text{ref},a} - L_{\text{ref},b}) - (L_{\text{r},a} - L_{\text{r},b}) \quad (2.1)$$

$L_{\text{ref},b}$  A-weighted sound level at reference point without noise barrier;

$L_{\text{ref},a}$  A-weighted sound level at reference point with noise barrier;

$L_{\text{r},b}$  A-weighted sound level at standard test point without noise barrier;

$L_{\text{r},a}$  A-weighted sound level at standard test point with noise barrier.

The data used below in this paper were acquired from several high-speed railway Integration Tests. A short introduction of these lines is given in Table 1.

## 2.1 Relationship Between Barrier IL and Speed of Electric Multiple Unit

The main noise source of high speed railways was widely agreed to be divided into 4 main parts: wheel and rail noise, aerodynamic noise, current collecting system's noise and structure-borne noise. The heights of these noise sources were different and the percentage of each part changed with the speed of Electric Multiple Units (EMU), which led to changes in the noise barrier  $IL$  at the same time.

Figure 1 shows the relationship between the barrier  $IL$  and EMU's speed. The tested barriers were metallic plate-inserted barriers along L1 in Table 1. The heights of the barriers were 2.15 m on bridge and 2.95 m on subgrade respectively, and both were 2.05 m from the top surface of the rails. Figure 1 illustrates that as the speed of EMU increased, the  $IL$  of the noise barrier decreased, which indicated that aerodynamic noise and current collecting system noise increased with speed and raised the height of the equivalent line noise source. As a consequence, the noise reducing effect of the barriers decreased.

To study the noise barrier  $IL$  effect at different heights, four testing points were set at 25 m away from the middle of the nearest track along L2. These points were at 0, 1.5, 3.5 and 5.0 m above the top surface of the rails (indicated as 25 m-0 m, 25 m-1.5 m, 25 m-3.5m and 25 m-5 m respectively). These points were all in the barrier's acoustic shadow for wheel and rail noise, partially in the barrier's acoustic

**Fig. 1** Relationship between barrier *IL* and EMU speed (25 m-0 m)

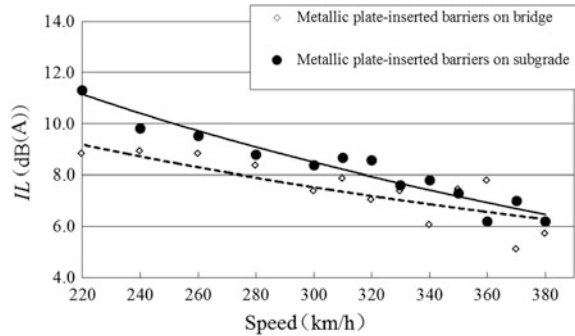
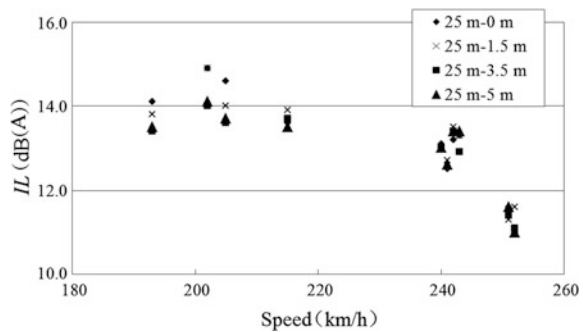


**Fig. 2** *ILs* of noise barriers at different testing heights



shadow for aerodynamic noise, and not in the barrier’s acoustic shadow for current collecting system noise. The result from Fig. 2 revealed that *ILs* at different heights were almost the same. This indicated that current collecting system noise contributed less energy, with wheel and rail noise and aerodynamic noise being the main sources.

## 2.2 Relationship Between Barrier *IL* and Measurement Positions

The effectiveness of noise barriers must consider the height and length. The extra barrier which is longer than the protected zone is called the additional length [8]. As shown in Fig. 3, differences between the *ILs* at the middle and at the end of the barriers were tested during the Integration Test of L3. The measuring points were set at 30 and 60 m away from the middle of the nearest track and 1.2 m above the ground. These are indicated as 30 m-1.2 m and 60 m-1.2 m in Fig. 4. It is noted that the measuring points at the end of the barriers were set at 10 m horizontally away from the end and still in the acoustical shadow of the barriers. The tested noise barriers were non-metallic plate-inserted barriers. From 30 to 60 m, *ILs*

**Fig. 3** Measuring point distribution (unit: meter)

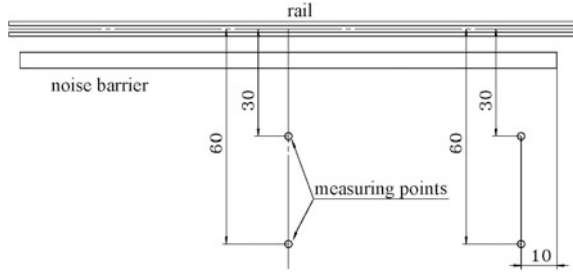
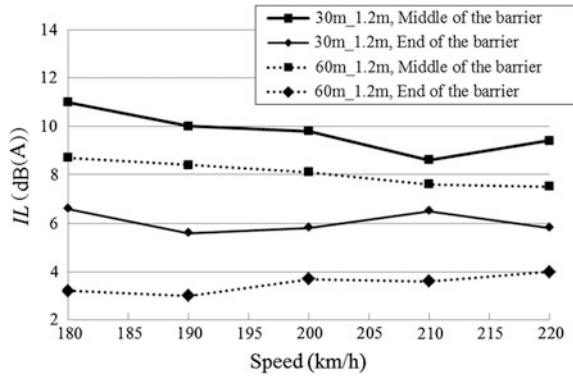


**Fig. 4** *ILs* with different distances and at the middle or end of the noise barriers



reduced 1–3 dB(A) at the middle and 2–5 dB(A) at the end of the barriers. For the same distances, *IL* at the end of the barriers was much smaller than those at the middle, which meant a longer additional length was necessary.

### 3 Comparison of the Calculated and Measured *ILs*

Representing fast moving EMU’s noise source with a line source and assuming the length of noise barrier was long enough, according to “Technical guidelines for environment impact appraisal, Acoustic environment”, the barrier *IL* was estimated using Eq. 3.1 below:

$$IL = \begin{cases} -10 \lg \frac{3\pi\sqrt{(1-t^2)}}{4 \arctan \sqrt{\frac{1-t}{1+t}}} & t = \frac{40f\delta}{3c} \leq 1 \\ -10 \lg \frac{3\pi\sqrt{t^2-1}}{2 \ln(t + \sqrt{t^2-1})} & t = \frac{40f\delta}{3c} > 1 \end{cases} \quad (3.1)$$

- f* frequency
- c* sound speed
- δ* acoustic path difference.

To calculate the acoustic path difference, the height of the equivalent line noise source is required, which has a significant influence on the calculation result. Based on the noise data of L4 (bridge with 2.15 m barriers) and L5 (subgrade with 2.95 m barriers), this paper estimated the equivalent height of the line noise source for a speed of 300 km/h. Assuming the height of line noise source was 0.5, 1 or 2 m and calculating the *ILs* using Eq. (3.1) separately, a comparison of the calculated and measured results is shown in Figs. 5 and 6. The results show that an equivalent line noise source at 2 m coincided well with the measured results.

Despite the consistency, there were differences between the calculated and measured *ILs*. The reasons can be concluded as follows: first, the EMU noise source contains several components which are complexly distributed, whereas the approximate equivalent was more simple; and second, the barrier’s acoustic insulation was not perfect at all frequencies, and sound leakage was inevitable.

In general, even though the calculation of Eq. 3.1 was does not fit the measurement data perfectly, it is still advisable. The equivalent heights of EMU line noise sources at different speeds could be determined in the same way.

**Fig. 5** Comparison of calculated and measured *ILs* of barriers on bridge

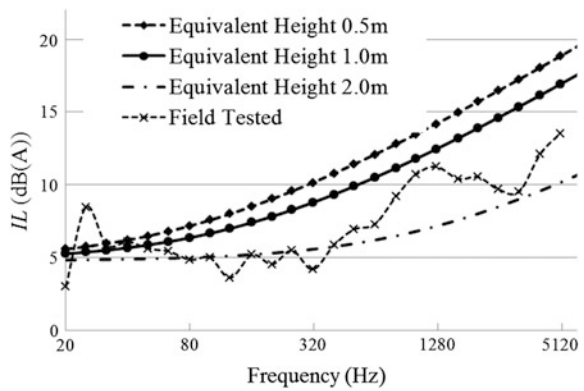
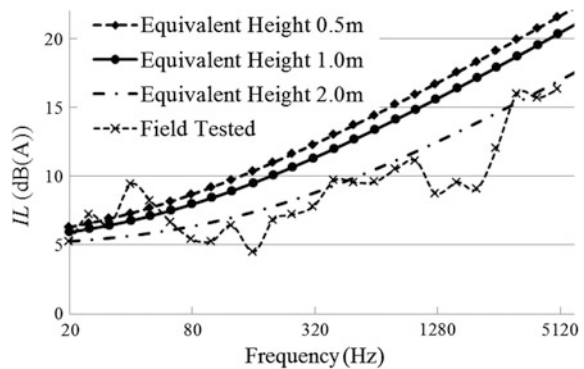


**Fig. 6** Comparison of calculated and measured *ILs* of barriers on subgrade



The study of NSI could be used to improve the prediction accuracy of a noise barrier's *IL* [9]. Up to now, China Academy of Railway Sciences, the Third Railway Survey and Design Institute Group Corporation, Central South University, Southwest Jiaotong University and Beijing Jiaotong University have carried out related research. The testing results showed that wheel and rail noise was the most significant source, which accounted for 50% of the whole energy when the speed was 300–350 km/h. Assuming the wheel and rail noise accounted for 50%, aerodynamic noise 30%, current collecting system noise 20%, and the equivalent heights were 0.5, 2 and 4.5 m respectively. The whole energy was measured during Integration Test of L6 and given as a 1/3 octave spectrum. The *IL* of each noise source was calculated and the overall A-weighted *IL* was obtained. In this way, the overall calculated *IL* was 5.2 dB(A), while the measured *IL* was 5.0–6.0 dB(A) for a speed of 350 km/h.

Dividing the noise source into several sources to predict the barrier's effect was complicated but more accurate. To obtain improved predictions, deeper research in NSI is suggested.

## 4 Conclusion

As the EMU's speed increases, the noise contribution from upper sources increased, the height of the equivalent line noise source was raised, and as a result, the noise barrier effectiveness was reduced.

As the distance from the middle of the nearest track to the measurement position was increased, the *IL* of the noise barrier was reduced. The barrier *IL* was reduced at locations near the end of the barrier, compared with the middle of the barrier. A long enough additional length is therefore strongly suggested.

Assuming the high-speed railway noise source can be modelled as an equivalent line noise source to calculate the barrier effect was partially useful and effective. Dividing the noise source into several sources according to their own characteristics and heights provided a more accurate prediction. Deeper research in noise source identification and more measurements are needed to make clear each component's height and proportion.

## References

1. Yin, H., Liu, L.H., Li, Y.L., et al.: The research status and development trend of China's high-speed railway noise barrier. *J. Railway Energy Saving Environ Prot Occup Safety Health* 5(4), 148–151 (2015). (in Chinese)
2. Wu, H.Y.: Advances on insertion loss theory of road barrier. *J. Sound Vib.* 6(3), 85–88 (2006). (in Chinese)
3. Technical guidelines for environment impact appraisal, Acoustic environment. HJ2.4-2009 (in Chinese)

4. The specifications for noise barriers' acoustical design and measurement. HJ/T 90-2004 (in Chinese)
5. Lei, X.Y.: Calculation method for high-speed railway noise. *China Railway Sci.* **26**(4), 1–4 (2005). (in Chinese)
6. Zhou, X., Xiao, X.B., He, B., et al.: Numerical model for predicting the noise reduction of noise barrier of high speed railway and its test validation. *J. Mech. Eng.* **49**(10), 14–19 (in Chinese)
7. Gu, X.A., Guo, H.Y., Zhou, T.J., et al.: The research and development survey of railway sound barrier in China. *J. Railway Energy Saving Environ Prot Occup Safety Health* **5**(4), 143–147 (2015). (in Chinese)
8. Zhang, L.J., Zhang, B., Hu, W.C., et al.: The comparative analysis of theory and measurement about the protective effect of additional length of the high-speed rail sound barrier. *Sound Vib. Control* **34**(s1), 75–77 (2014). (in Chinese)
9. Su, W.Q., Pan, X.Y., Ye, P.: The study of acoustic computing model for the noise barrier of high-speed railway. *China Railway Sci.* **34**(1), 126–130 (2013). (in Chinese)

# Experimental Research on the Characteristics of the Noise Source of the Chinese High-Speed Railway



Lanhua Liu and Zhiqiang Li

**Abstract** Being familiar with the level and characteristics of a high-speed railway's noise sources is the theoretical foundation for better noise control. Based on a large number of field experiments relating to Chinese high-speed railway noise sources, the work described in this paper assessed the characteristics of the noise sources at bridge sections and embankment sections in the speed range of 200–300 km/h and 300–350 km/h separately. The paper discusses the relationship between the noise production and the train speed. In the end, the comparison of high-speed railway noise source levels in China and those in foreign countries like France and Germany showed that the noise source levels in these countries were almost the same.

## 1 Introduction

High-speed railways have been constructed and operated in nearly 20 countries and regions all over the world. By the end of 2015, the total length of the Chinese high-speed railway had exceeded 19,000 km, accounting for over 60% of the entire high-speed railway network on earth. According to Chinese urban planning and the “13th Five Year Plan”, at least 11,000 km more high-speed railways would be constructed and 80% of the cities in China would be connected by 2020. The construction and development of the Chinese high-speed railway has made a great contribution to the development of the Chinese economy. High-speed railway has become the backbone of modern cities' transport system. However, the noise of high-speed railways has limited its development and should be effectively controlled according to the request of state and citizens. Mastering the characteristics of the high-speed railway noise source was the significant theoretical foundation for noise control and reduction.

---

L. Liu · Z. Li (✉)

China Academy of Railway Sciences, No. 2 Daliushu Road,  
Haidian District, Beijing, China  
e-mail: qiangzhili123456@126.com



## 2 Research Content and Method

Researchers from China and other countries have done much work to study the characteristics of high-speed railway noise sources and the laws that rule their interrelations. Japanese scientists since 1960s and French and German scientists since 1980s have carried out research relating to high-speed railway noise. Related research in China did not start until the end of the 20th century. Many tests have been carried out during integration and large-scale combined tests. Research includes noise source identification, noise source characteristics, sound field distribution, laws of sound radiation and effects of noise reducing measures [1–4]. The noise source characteristics of different kinds of EMUs at different tracks were also tested and compared. The testing method was based on “Railway applications-Acoustics Measurement of noise emitted by rail bound vehicles (ISO-3095)” and “Acoustic measurement of railway locomotive vehicle’s radiation noise (GB-T5111)”. The tested trains were typical EMUs which were still in active service or newly produced.

## 3 Testing Result and Analysis

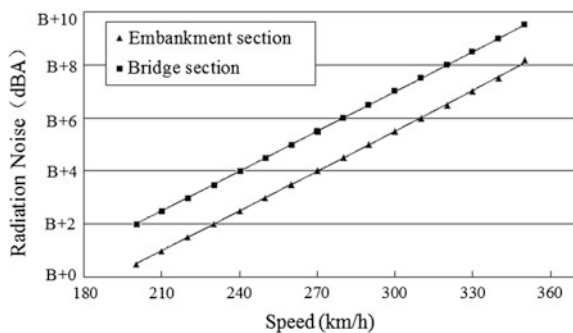
### 3.1 Testing Result and Analysis of High-Speed Railway Noise Source

The measured results of noise source levels from more than 30 railways and 40 testing sections were statistically analyzed. The noise source levels of Chinese high-speed railway from 200 to 350 km/h are shown in Fig. 1. Note that for the data security, “B” on vertical axis in Fig. 1 and other Figures below means the same base value.

According to the regression analysis of data in Fig. 1, the relationship between speed and noise source level could be expressed as equations below.

From 200 to 300 km/h on bridge section:

**Fig. 1** The noise source levels at different speeds and on different railway situations



$$TEL = (27 \sim 30) \times \lg\left(\frac{v}{v_0}\right) + B_1 \tag{3.1}$$

From 200 to 300 km/h on embankment section:

$$TEL = (26 \sim 29) \times \lg\left(\frac{v}{v_0}\right) + B_2 \tag{3.2}$$

here  $v_0 = 200$  km/h,  $200 \text{ km/h} \leq v \leq 300 \text{ km/h}$ .

From 300 to 350 km/h on bridge section:

$$TEL = (39 \sim 43) \times \lg\left(\frac{v}{v_0}\right) + B_3 \tag{3.3}$$

From 300 to 350 km/h on embankment section:

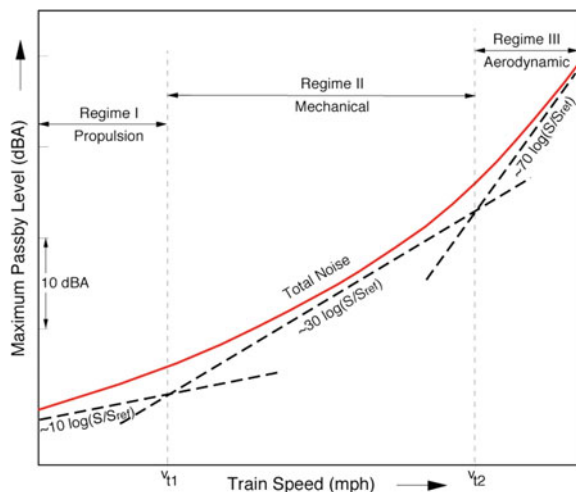
$$TEL = (36 \sim 40) \times \lg\left(\frac{v}{v_0}\right) + B_4 \tag{3.4}$$

here  $v_0 = 300$  km/h,  $300 \text{ km/h} < v < 350 \text{ km/h}$ .

From Eqs. 3.1–3.4, it could be concluded that the noise source level increases along with the EMU’s speed in general. The increment factors are different depending on whether the speed ranges are below or above 300 km/h. In the range of 200–300 km/h, the increment factors are 26–30 and in the range of 300–350 km/h, the increment factors are 36–43.

The difference in increment factors for different speed ranges is due to the change of the dominant noise source components. Based on the theoretical result in Fig. 2, the increment factor is 30 in the speed range where wheel and rail noise is

**Fig. 2** The theoretical relationship between noise source levels and train speeds



the main noise source, and 70 in the speed range where the aerodynamic noise is the main noise source. According to the field tests and theoretical results, when the speed is 200–300 km/h, the main noise source is wheel and rail noise; when the speed exceeds 300 km/h, the proportion of aerodynamic noise and pantograph system's noise increases and plays an important role. At present, for environmental noise prediction purposes, it was recommended that the increment factor is assumed to be 30 according to the 44th suggestion draft of Ministry of Chinese Railway's Planning and Development Department. The predicted levels were in accordance with the test results when the speed range was below 300 km/h. There were discrepancies when the speed exceeded 300 km/h and parameter modifications were needed.

### 3.2 Time Domain and Frequency Spectrum Characteristics of High-Speed Railway Noise

The time domain of EMU's noise at a speed of 350 km/h is shown in Fig. 3 and the 1/3 octave frequency spectrum is shown in Fig. 4. The measurement distances were 25 m from the axis of the outer track and 3.5 m above the rail head. As illustrated in Fig. 3, when the EMU passed by the measuring point at high speed, the sound level changes significantly and could be 40 dBA higher than the background noise. The maximum steepness of the rise of the sound level is more than 8 dBA/s. The sudden and powerful noise could easily cause people along the railway to be annoyed and anxious. According to Fig. 4, the spectrum of EMU's noise is wide band and sharply reduced over 4000 Hz. The relatively higher sound levels are found mainly

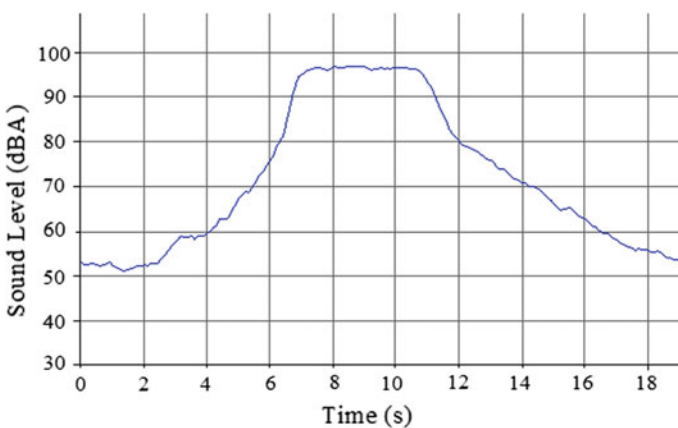


**Fig. 3** Time domain of the high-speed railway noise at the speed of 350 km/h

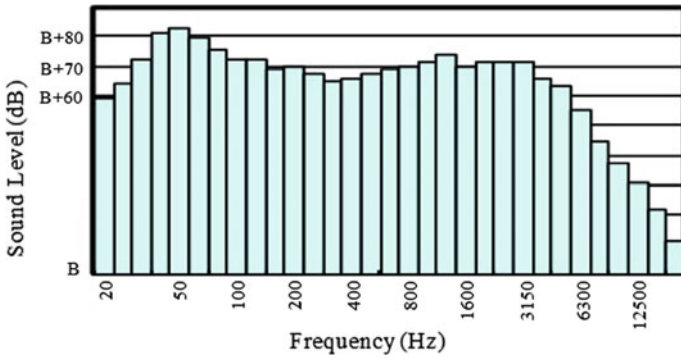


Fig. 4 Frequency spectrum of the high-speed railway noise at the speed of 350 km/h (Leq)

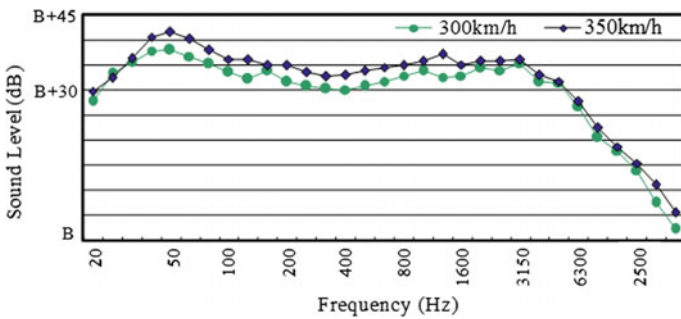


Fig. 5 Comparison of 1/3 octave frequency spectrum at the speed of 300 and 350 km/h (Leq)

in low frequencies from 31.5 to 125 Hz. Based on this linear frequency spectrum, the main power of the A-weighted noise would distribute from 500 to 5000 Hz.

Figure 5 provides a comparison of 1/3 octave frequency spectra of high-speed railway noise at the speed of 300 and 350 km/h. When the speed increases, sound levels at all frequencies increase, and the low-frequency (below 2000 Hz) components increase faster than the high-frequency components. This might be explained by the fact that the low-frequency components are caused mainly by aerodynamic noise, which is more sensitive to speed.

### 3.3 Comparison of the Noise Source Level of 3 Kinds of EMU in China

Based on the latest measurements, the noise source levels of three different kinds of EMUs with speeds from 300 to 350 km/h were compared. These were designated as EMU1, EMU2 and EMU3, where the lower number indicates a later production.

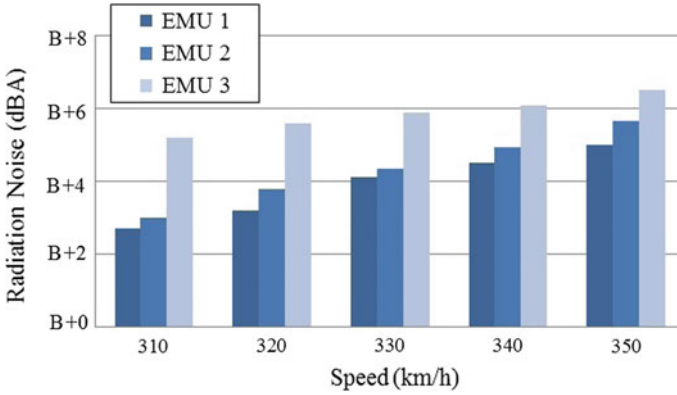


Fig. 6 The comparison of 3 Chinese EMUs’ noise source level (TEL)

As shown in Fig. 6, the noise source levels of EMU3 were the highest and those of EMU1 were the lowest at all speeds. Based on the production time, as more advanced noise reducing measures were implemented in the latest EMUs, the noise source level has been reduced continuously. The measures taken include increasing the slenderness ratio (the ratio of length and radius of gyration), optimizing the EMU’s head unit and smoothening the surface of the EMU. These measures have reduced the air resistance by 10–15% and the aerodynamic noise by nearly 1 dBA. In addition, a new pantograph which had baffles at the sides assisted in reducing the aerodynamic noise caused by the electric power system [5, 6].

## 4 Comparison with Other Countries

### 4.1 Relationships Between Noise Source Levels and Speeds in Other Countries

Researchers from Japan, France and Germany have investigated the high-speed railway noise source characteristics over the years, and have acquired their own trains’ relationships between the noise source levels and the speeds before 2000. The results of these studies are summarized in Table 1 [6, 7].

Table 1 Relationships between the noise source levels and speeds (200–300 km/h)

Nation	Regression equations	Measurement point
Germany	$TEL = 33.6 * \lg(v/v_0)$	25 m-3.5 m
France	$TEL = 40.7 * \lg(v/v_0)$	25 m-3.5 m
Japan	$TEL = 58.2 * \lg(v/v_0)$	25 m-1.3 m

Note for measurement point: the first number is the axis of the outer track, and the second number is the height above the rail head.

According to Table 1 and Eqs. 3.1–3.4, the increment factor of Chinese high-speed railway noise was relatively smaller than that of other countries, which indicated that the present optimization of Chinese EMUs is already better than foreign high-speed trains from before 2000.

### 4.2 Comparison of Noise Source Levels in Different Countries

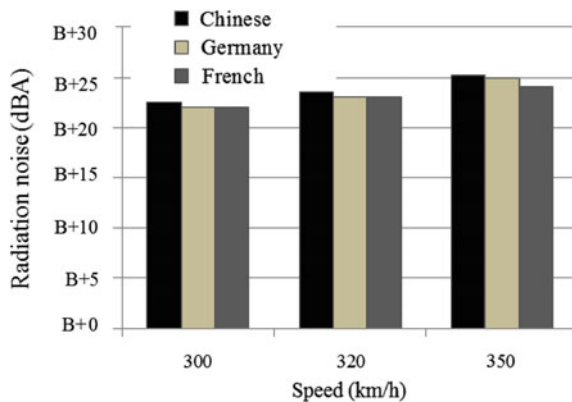
The level of high-speed railway noise had shown a clear reduction in every country, as was illustrated in Table 2, which indicated that the high-speed railway technologies were constantly being improved.

**Table 2** High-speed railway noise source levels of different countries (TEL)

Nation	Speed (km/h)	Noise source level (dBA)		
		1980s	1990s	Present
France	200	–	87	86
	270	97	92	90
	300	97	94	92
	350	–	–	94
Germany	200	86	84	84
	250	90	88	88
	300	93	92	92
	350	–	–	95
Japan	200	87	67*	–
	250	–	73*	74*
	300	–	77*	75*

\*The results were obtained at noise barrier sections

**Fig. 7** The comparison of Chinese, German and French high-speed railway noise



Note that the measurement points are the same points as in Table 1, in addition, the Japanese data with \* behind were tested at noise barrier sections and the height of barriers was 2 m.

Figure 7 presents a comparison of Chinese, French and German high-speed railway noise source levels, which indicates that the Chinese railway noise source levels are almost the same as other countries' and the differences are no more than 1 dBA.

## 5 Conclusions

1. The increment of the radiated noise level with the logarithm of the speed is about 36–43 in the speed range from 300–350 km/h; When the EMU passes by the measuring point at high speed, the sound level increases rapidly with a steep rise.
2. High-speed railway noise has a broadband character and the lower-frequency components increase faster than the higher-frequency components when the speed increases.
3. The Chinese and foreign countries' high-speed railway noise is almost the same for similar speeds; The current difference is no more than 1 dBA at present.

## References

1. Zhang, S.G.: Noise mechanism, sound source localization and noise control of 350 km/h high-speed train. *China Railway Sci.* **30**(1), 86–88 (2009)
2. Deng, J.: The Beijing-Tianjin inter-city railway noise characteristics research. Master's thesis of Southwest Jiaotong University, pp. 4–6 (2010)
3. Xing, S.M., Liu, Y., Zhang, X.P.: Noise test and analysis of express train-set. *Sound Vib. Control* **3**, 79–88 (2009)
4. Yu, W.Z., Wang, C., Mao, D.X., et al.: Noise characteristics of chinese high-speed railway. *Environ. Pollut. Prev. Control* **31**(1), 74–77 (2009)
5. Gu, X.A.: The application of the control technology of the noise source and the effect of its noise reduction of Beijing-Shanghai High-speed railway. *J. Railway Energy Saving Environ. Prot. Occup. Safety Health* **3**(1), 1–3 (2013)
6. Yin, H., Li, Y.Z., Gu, X.A.: Study of the noise characteristics of running trains of high-speed railway. *J. Railway Energy Saving Environ. Prot. Occup. Safety Health* **36**(5), 221–223 (2009)
7. Wang, G.L., Liu, D.D.: Characteristics of Chinese high-speed railway noise. *Railway Rolling Stock* **2**, 6–8 (2001)

# Psychoacoustic Evaluation of Noises Generated by Passenger Seats for High Speed Trains



J. Sapena and R. Caminal

**Abstract** Passenger acoustic perception is one of the main factors in order to evaluate the comfort in a High Speed Train (HST). While current measurement standards for interior noise (ISO 3381) only take into account objective measurements, some aspects of the soundscape inside a high speed train are not considered. Noise produced by the vibration of different interior assemblies, like squeak and rattle, are evaluated subjectively during commissioning tests. The first topic treated by this study is the development of a methodology for the specification of squeak and rattle (SR) noise produced by passenger seats. A correlation between a subjective assessment of rattle noise and psychoacoustic parameters is done. The novelty of this study is to take into account these anomalies as a part of the correlation and to find a method to allocate targets to seat suppliers during project development to reduce costs by avoiding expensive retrofit works. Another aspect related to the acoustic perception of a product is the sound quality associated to its functioning. Interior components are normally static components where a specific noise signature is not expected, but a passenger seat can have a dynamic operation by the passengers which could influence the perceived quality of the final product. Perceived quality is often used to target designs for different type of users and applications. It is applied widely in the automotive industry but no references exist for a rolling stock application. A methodology has been applied to assess the sound quality of passenger seats for typical operating noises of a seat like reclining, armrest, footrest, seat tray, etc. This part of the study allows the establishment of psychoacoustic targets for those operations in order to achieve a desired level of perceived quality. The methodology that has been used for both topics is based on jury tests of different acoustic recordings, using a statistically significant sample of participants of different ages and social positions. During this survey, people were asked to evaluate the acoustic comfort of the interior soundscape of high speed trains, and to evaluate also the robustness, quality and annoyance of some devices

---

J. Sapena (✉)  
ALSTOM, 48 Rue Albert Dhalenne, 93482 Saint-Ouen Cedex, France  
e-mail: [juan.sapena@alstomgroup.com](mailto:juan.sapena@alstomgroup.com)

R. Caminal  
Ingeniería para el Control del Ruido (ICR), Barcelona, Spain



linked to the train seats. The subjects rated the response on a scale with several categories according to certain criteria. In summary, two methodologies are proposed: one for the specification of squeak and rattle noises related to high speed train operation and another one for the perceived sound quality of passenger seat operation.

## 1 Introduction

Interior noise in a passenger train is one of the main aspects to take into account to assess the global comfort of passengers. ALSTOM integrates in the design cycle of rolling-stock global comfort aspects by choosing the right ratio between the different aspects of global comfort. Thermal, visual, ergonomic, vibrational and acoustic comfort performances shape the passenger experience and a global balance of all these aspects will give an overall indicator of the global comfort perceived. Acoustic comfort (or discomfort) perceived by passengers is an important part of this, especially for high speed rolling stock. From the acoustic point of view, a train operating at a certain speed is a set of noise sources and train assemblies. The mechanical interaction between them will generate a specific interior noise signature. Some components of this noise signature are related to parts generating SR noises. SR due to its type of transient signature could be perceived as non-comfortable for passengers. In other industries, like automotive [1], SR has been deeply studied and some authors propose also methods to predict it [2]. For rolling-stock, the state-of-the-art of simulations is still far away from predicting SR but it is very important to allocate targets of SR to interior components in order to avoid costly modifications once a component has been already sourced and installed in a train.

Several studies have been done in the past to understand and to find the correlation between psychoacoustic parameters and acoustic discomfort in a train but always focusing on stationary noises (constant speed) and tonal noises without taking into account specific SR phenomena [3–5]. Previous work from the authors of this study [6] was focused in the development of a testing methodology to reproduce SR noises in a train passenger seat with the objective of quantifying and allocating targets to seat suppliers. The methodology was based on the recording of real vibration patterns in a seat installed in a high-speed train. Those vibration patterns were applied to the seat through the use of a quiet multi-axial vibration shaker in a semi-anechoic room to reproduce possible SR noises as seen in Fig. 1. One of the conclusions of the study was that it was needed to obtain a wider psychoacoustic analysis in order to have a robust indicator that related the SR noises of the seat to acoustic discomfort. The work in this paper uses data from the previous work as input for psychoacoustic studies to refine the acoustic targets for seats SR.

In this study the process to establish the targets consisted of a subjective assessment by a wide population of the annoyance perceived by a passenger due to



**Fig. 1** Left, Multi-axial low noise vibration table in a semi-anechoic room. Right, Seats installed in the vibration table together with a binaural recording system

seat noises. This was followed by a correlation of the different psychoacoustic parameters to subjective responses. A final adjustment of the target levels was done with a reduced number of listeners where background noise of the train was added to the measured seat noise signals in the test bench.

Another aspect related to the noise signature inside a train is the sound quality of a product, in this case of a seat. Seats operations are one of the main interactions between passengers and the train. We recline the seat, we use the tray in front, we change the position of the foot-rest, we move the arm-rest up and down. All these operations could generate different types of noise signatures that could affect, positively or negatively, our passenger experience. This study proposes a methodology to take into account these noise signatures in order to allocate targets of sound quality to different seat operations. Sound quality is a wide concept but to simplify it has been centered into three aspects: quality, robustness and annoyance.

## 2 Seat Noises Assessment Through Jury Tests

### 2.1 Jury Test for Squeak and Rattle Noise Annoyance

During the development of the test bench methodology of SR noise for seats [6], it was shown that the measurement position that presented a clear detection of SR events was the position behind the seat. In this case, noise perceived was a rattle due to the seat tray vibration in its “closed” position. This measurement position was chosen for the assessment of annoyance through jury tests. One of the difficulties of the previous work was to establish the right vibration levels to be applied to the seat in order to reproduce the life cycle of a seat and the different types of track qualities where a train can be operated. Running test to obtain vibration patterns were performed in a well maintained high speed track with brand new seats installed. The vibration levels measured in these operating conditions at 320 km/h seldom produced rattling noise. Nevertheless, vibration inputs applied to a seat in

real service operation of rolling stock during its life cycle can be more severe due to bad running conditions (track quality) and wear of seats due to continuous use by passengers and induced vibration. In order to represent those degraded conditions, the vibration inputs applied to the seat were amplified by a factor of two. With this factor applied, rattling noise appeared clearly in all events.

In this work, an initial jury test with a small number of participants (6) was done with the objective to define the questionnaires and the procedure to be followed during the jury tests. The outputs of this initial jury were the questions to be answered, duration of the listening juries, number of participants and the procedure to be followed. In order to have a statistically representative sample of train passengers a wide survey was done with 83 participants of different ages, status, nationality (most of them European) and gender.

All the recordings were done using a binaural recording system. The jury tests procedure included:

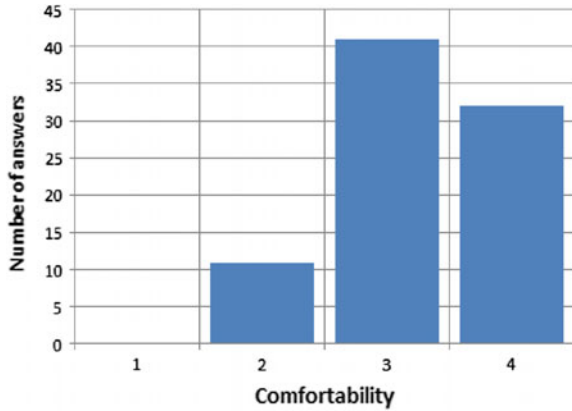
- Binaural listening of 30 s of test bench measurements with rattle explaining that they are in high speed train running at constant speed at 320 km/h at different levels of excitations, positions and seat configurations.
- Binaural listening of 30 s of test bench measurements (with an amplification factor of 2) of a seat with rattle tray noise explaining to the listeners that they should imagine that they will listen to that noise during a 2 h trip. The listeners are not informed of what type of noise and what is the origin of that noise.
- The listeners were allowed to re-listen the recordings to obtain a more accurate opinion.
- Following the above, the listener answers the question: “do you feel that this environment is comfortable?”
- The subjects evaluated the presented sounds based on a bipolar scale, whose ends were labelled with an adjective and its antonym (comfortable/uncomfortable). The chosen scale had four degrees in order to avoid a neutral rating.

The listeners rated the response on a scale going from 1 to 4 (1 being comfortable and 4 uncomfortable). The results of this jury tests can be seen in Fig. 2 where it can be concluded that for most of the listeners the noise was perceived as uncomfortable.

## ***2.2 Jury Test for Seats Operation Sound Quality***

The operations of seat parts were recorded using a binaural recording system. Seat operation noise recordings were done in two different trains with different seats. The type of operations recorded were armrest movement up and down, footrest movement up and down, reclining from normal to reclined position and tray opening and closing. The measurement dummy was placed in different positions adjacent to the seat to be evaluated.

**Fig. 2** Results of listening jury test of a seat rattle vibration with a comfort scale of 1 being comfortable and 4 being uncomfortable



A pre-jury test was done to select the most representative recording positions and to choose the right questions to ask during the definitive jury tests. The final jury was done with the same number of participants as the SR jury tests (83). The procedure for the evaluation of seat operation noises included:

- An initial set of listeners (50) were informed that they are in a train and they listen some noise events. No information about the type of event was shown (“blind” test)
- Binaural listening to the seats operation in random order
- The listeners were allowed to re-listen the recordings to obtain a more accurate opinion
- After listening, the subjects answered the following questions: “do you feel that this noise is produced by a robust device?”, “do you feel that this noise is produced by a quality device?” and “Is that noise event disturbing for you?”
- The subject evaluates the presented sounds based on a scale from 1 to 4 whose ends are labelled as low robustness (scale 4) to high robustness (scale 1), low quality (scale 4) to high quality (scale 1) and high annoyance (scale 4) to low or inexistent annoyance (scale 1)
- A second set of listeners (33) were informed of what type of noise they were listening to and performed the assessment following the same procedure as the “blind” tests (“known noise origin” test).

The objective of asking three questions was to determine if the listeners are able to distinguish different perceptions related to robustness (feeling of a device of being robust and therefore not easily broken with a long expected durable life), quality (wide definition that includes a perception of cost and good design) and disturbance (how disturbing could be that noise when we listen to it). The results of the jury for seat operation noises can be seen in Fig. 3.

By comparing the blind tests results with the results from the known noise origin test in Fig. 3, it was seen that listeners tend to assign a worse score when the origin of noise is known in most of the cases for the three parameters asked. The differences are

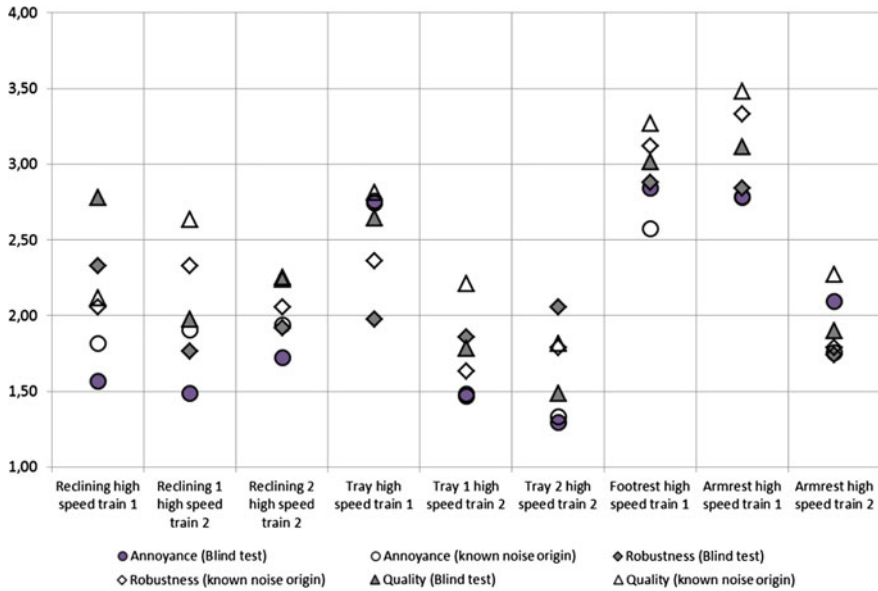


**Fig. 3** Assessment of Annoyance, Robustness and quality for different seats operations for blind tests and known noise origin tests. Confidence interval between 0.2 and 0.3

relevant since the average scores differences between “blind” and “known” tests are higher than the confidence interval observed (confidence interval between 0.2 and 0.3) of both tests in almost all the noise events. This means that depending on the seat operation, the listeners set a *malus* of perception to the noise events in function of the preconceived notion of the device they are evaluating.

A Pearson’s correlation coefficient was calculated to evaluate if the three different questions were significantly different. The result can be seen in Table 1. On one hand, quality and robustness presented a higher correlation between them than annoyance versus quality/robustness. This means that listeners would not be able to distinguish between the two questions, especially in the jury test with known origin of noise. A higher number of noise samples in different seats would be needed to confirm if robustness and quality are considered as equivalent terms to represent the sound quality of the seat.

**Table 1** Correlation coefficients of jury tests results for 9 type of seat operating noises

Type of jury test	Robustness		Annoyance	
	Blind	Known origin	Blind	Known origin
Quality	0.47	0.72	0.41	0.48
Annoyance	0.24	0.42	1	1

### 3 Targets Setting for SR Seat Noises

#### 3.1 Psychoacoustic Parameters Study

One of the conclusions of the previous work [6] was that SPL  $L_{pAeq}$ , Loudness  $N_{ave}$ , Sharpness  $S_{ave}$  or Roughness  $R_{ave}$  could be good psychoacoustic indicators to represent the annoyance perceived by the SR noises of seats. In this study, in order to refine noise allocation, different amplification of vibration patterns, seat configuration and measurement positions has been analyzed in order to have a broader range of the psychoacoustic indicators. A correlation between all the different psychoacoustic indicators has been calculated. The results can be seen in Table 2.

With the analysis done it was seen that  $L_{pAeq}$  and  $N_{av}$  presented a very high correlation together with  $R_{av}$ . A combination of  $L_{pAeq}$  and  $S_{av}$  sharpness were found to be possible candidates to represent the annoyance of SR of seats because of its lower correlation. Nevertheless, with the data used for this study (only one type of train with one type of perceived SR from one seat) there wasn't enough variability of data to obtain a statistically relevant model combining the different parameters to predict the annoyance perceived by passengers. A wider sampling of different type of seats with different rattle noises would have allowed applying a multiple regression technique [3] to obtain a predictive model of annoyance.

#### 3.2 Allocation Methodology

Test bench assessment with vibrations amplified with a factor of 2 indicated a clear perception of annoyance for most of the listeners (see Sect. 2.1). This amplification factor corresponded to a specific dB(A) level. In order to allocate a target of annoyance to a seat supplier a new jury test was performed with a reduced number of participants (14). In this final jury test, different recordings were used with different amplification factors from  $\times 1$  up to  $\times 2$  in steps of 0.2. The binaural recordings were mixed with real background noise of the train running at 320 km/h and a dedicated filtering was applied to obtain different sharpness of the rattle noises. A total number of 8 synthesized recordings were obtained.

A criterion to find the lower threshold of annoyance was set corresponding to a detection of rattle annoyance of more of the 50% of the assessments. This criteria was accomplished with an amplification factor of 1.4. This amplification factor resulted in a specific dB(A) and sharpness limit targets. As a conclusion, a seat

**Table 2** Correlation coefficients of different Psychoacoustic parameters (SPL  $L_{pAeq}$ , Loudness  $N_{ave}$ , Sharpness  $S_{ave}$  or Roughness  $R_{ave}$ )

	$L_{pAeq}$	$N_{av}$	$S_{ave}$	$R_{ave}$
$L_{pAeq}$	1	0.99	0.83	0.96
$N_{av}$	-	1	0.83	0.83
$S_{av}$	-	-	1	0.83

tested with whatever amplification factor exceeding that psychoacoustic criterion will be considered as annoying and therefore not considered appropriated for a high speed train application.

## 4 Targets Setting for Sound Quality of Seat Operations

### 4.1 Psychoacoustic Parameters Study

Seat operation noise events present transient behavior and cannot be analyzed as stationary signals. Therefore, specific transient analysis to obtain psychoacoustic parameters [7] was done.

The objective psychoacoustic metrics obtained were:

- Loudness 5th percentile,  $N_5$  and loudness maximum,  $N_{max}$ , time-varying loudness (DIN 45631).
- Sharpness median ( $S_{50}$ ) and 5th percentile ( $S_5$ )—time varying sharpness (DIN 45631).
- Roughness average,  $R_{ave}$ .
- SPL levels with  $LA_{Smax}$ ,  $LA_{Fmax}$ ,  $LA_{Imax}$ ,  $LA_{5S}$ ,  $LA_{5F}$ ,  $LA_{5I}$ .
- Loudness based impulsiveness [7],  $N_I$  refers to the degree of impulsive content perceived in a sound.

Correlation between all these parameters from all the different seat operation events can be seen in Table 3. In order to reach a significance (p-value) < 0.05 with the number of samples used (9), a correlation coefficient higher than 0.67 is needed. SPL parameters are highly correlated between them. Sharpness and Roughness are more independent than the other variables. Loudness ( $N_5$ ) and impulsiveness present a high correlation between them and a lower correlation to SPL levels. Sharpness and roughness presented lower correlations between the different parameters and also between them. Several parameters are giving different information regarding perception without a clear trend to choose some of them as indicators to obtain a model of sound quality (robustness, quality and disturbance). As a conclusion, the following psychoacoustic parameters were selected to compare subjective versus objective assessments:  $N_5$ ,  $S_5$ ,  $LA_{Fmax}$ ,  $R_{ave}$ .

### 4.2 Psychoacoustic Parameters Correlation Versus Sound Quality

With the results analyzed in Sect. 4.1 a correlation between a set of psychoacoustic parameters of seat operation versus the subjective assessment of the listeners was done. Correlation coefficients between sound quality perceptions (robustness,





quality and disturbance) and selected psychoacoustic parameters from Sect. 4.1 (Loudness  $N_5$ , Sharpness  $S_5$ ,  $LA_{Fmax}$  and  $R_{ave}$ .) for two different seat operations (reclining operation and seat tray opening/closing) were obtained.

Considering that only 3 samples for each one of the type of seat operation noises were available for the jury tests, correlation coefficients higher than 0,98 represent a significance (*p-value*) of 0.127. This significance is still not good enough to confirm the predictability of the psychoacoustics parameters but indicates a trend in the selection of the most significant ones.

From the analysis of the correlation coefficients in Tables 4 and 5, it was observed that Loudness has a very high correlation with annoyance perception responses from the jury test answers for both cases (reclining and tray). Roughness presented a lower correlation and therefore it shouldn't be considered as a good indicator of annoyance.

For the reclining operation none of the parameters observed presented a good enough correlation with robustness and quality. The different type of noise signatures for reclining seat operations was one of the reasons for the bad correlation. Depending on the type of seat operation the diversity of noise signatures generated is wide. A way to improve that correlation could be either increasing the number of samples by testing in different seats or a previous classification in function of type of noises.

For the seat tray operation (open/close), loudness correlates in the same way for robustness and quality while the other parameters gave a non-significant correlation to perceptions evaluated.

From these analyses it is proposed to evaluate annoyance of seat operation noises by the loudness parameter ( $N_5$ ) because, even with a small number of samples, it provides a high correlation. Another conclusion from the study is that listeners could hardly differentiate between robustness and quality. Only by using a higher number of samples could a clearer significance of one of the parameters proposed with robustness/quality (considered as only one perception) be obtained.

**Table 4** Correlation coefficients of different psychoacoustic parameters for reclining operation

Reclining	$N_5$	$S_5$	$LA_{Fmax}$	$R_{ave}$
Robustness	0.13	0.68	0.01	-0.40
Quality	0.35	0.82	0.24	-0.18
Annoyance	0.99	0.90	0.96	0.77

**Table 5** Correlation coefficients of different psychoacoustic parameters for seat tray open/close

Tray	$N_5$	$S_5$	$LA_{Fmax}$	$R_{ave}$
Robustness	0.96	-0.85	0.68	0.56
Quality	0.95	-1.00	0.97	0.93
Annoyance	1.00	-0.96	0.86	0.78

## 5 Conclusions, Further Work and Challenges

Two preferred metrics, dB(A) ( $L_{pAeq}$ ) and Sharpness ( $S_{ave}$ ) are proposed to predict the annoyance of SR noises of rolling stock passenger seats. Using these two metrics, a methodology has been proposed to establish acceptance targets during the development of a new seat. The application of this methodology will allow important cost reductions to stakeholders by avoiding seat retrofitting when SR noises appear in commercial service. Moreover, the methodology proposed can objectivize the contractual agreements between rolling stock manufacturers, seat suppliers and train operators regarding SR noises by predicting the annoyance of SR noise before installing seats.

It will be possible to increase the predictability of the metrics proposed by an optimal combination of them. This will be possible including in the model several seats with different types of SR generated. Another important aspect to improve is the predictability of SR generated noises before testing in it a test bench. Return of experience in the use of combination of materials coming from other industries should be used during new design developments.

Another important challenge for the future is how to extrapolate SR target allocations to other interior parts of rolling stock (e.g. interior trimmings, windows stores, luggage racks, internal doors, gangways) and how to perform tests to verify those targets.

Regarding seat operation noises, a methodology has been proposed to evaluate the sound quality of seats with a preferred metric, the 5th percentile of Loudness ( $N_5$ ). Participants in the jury tests were not able to identify clear differences between requested perception based on robustness and quality.

As for SR noises, a wider sampling of different type of seats with the different type of operation signatures is needed to improve the predictability of different metrics by combining them. Target allocation for sound quality aspects of seat operations will require a wider comparison of the same type of seat operation noises in different type of seats.

## References

1. Trapp, M., Chen, F.: Automotive Buzz, Squeak and Rattle: Mechanisms, Analysis, Evaluation and Prevention, Book. Butterworth-Heinemann, Oxford (2011)
2. Shorter, P., Cotoni, V., Chaigne, S., Langley, R., Predicting the Acoustics of Squeak and Rattle. SAE Technical Paper 2011-01-1585, 2011. <https://doi.org/10.4271/2011-01-1585>
3. Gibert, O., Sapena, J.: Development of a prediction model of acoustic discomfort in high-speed train passenger cars. In: Euronoise 2009, Edinburgh, Scotland, 26–28 Oct 2009
4. Mzali, M.: Perception de l'ambiance sonore et evaluation du confort acoustique dans les trains, Ph.D., Université Paris VI, France (2002)

5. Boulet, I., Rabau, G., Meunier, S., Poisson, F.: Psychoacoustical Indicators of Acoustical Comfort Inside Trains for Background Noise and Emergent Signals. International Congress on Acoustics, Madrid (2007)
6. Sanei, N., Sapena, J.: Squeak and Rattle Specification Methodology for Passengers Seat in High Speed Trains. International Congress in Sound and Vibration, Beijing (2014)
7. Willensem, A., Rao, M.: Characterization of Sound Quality of Impulsive Sounds using Loudness Based Metric. International Congress on Acoustics, Sydney (2010)

# Active Noise Control of Interior Noise of a High-Speed Train Carriage



Yanju Zhao, Renzhong Shuai, Leiwei Zhu, Peng Lin and Zongcai Liu

**Abstract** The traditional method of controlling high-speed train noise involves passive noise reduction methods, such as sound insulation, vibration reduction and so on. These approaches are only effective in controlling high-frequency noise however, whereas high-speed train noise at 300 km/h includes lower frequency components. In order to eliminate low and mid-frequency noise, this paper proposes a project based on an adaptive noise control system. The running state of the system was simulated by means of the FXLMS algorithm. The active noise control system performance was tuned through testing within a high-speed train. The result shows that the active noise control system is able to reduce lower frequency noise inside the vehicle.

## 1 Introduction

Vibration and noise reduction measures are a key consideration in the design of high speed trains. Field test results show that the interior noise of high-speeds train is mainly concentrated in the low and mid-frequency range. It is known that sound absorption and insulation measures have less effect on low and mid-frequency noise.

Active Noise Control (ANC) is achieved by introducing a canceling “anti-noise” wave through an appropriate array of secondary sources [1, 2]. These secondary sources are interconnected through an electronic system using a specific signal processing algorithm for the particular cancellation scheme. The advantage of active control is that the additional mass is small, and the low frequency noise cancellation performance is good. Therefore ANC has been widely used in manufacturing, industrial and automotive industries. So far there have been few applications in rail.

---

Y. Zhao (✉) · R. Shuai · L. Zhu · P. Lin · Z. Liu  
CRRC Qingdao Sifang Co. Ltd, No. 88 Jinhongdong Road, Chengyang District,  
Qingdao, China  
e-mail: zhaoyanju215@163.com

This paper describes the development of an active noise control system for a cabin on a high speed train. According to the ANC principle, a multi reference feed forward algorithm controlling a number of loudspeakers was used. Based on the ANC development process, line tests and static transfer function tests were conducted. Algorithm simulation using the test data was then used to predict the noise control effect. Finally, according to the simulation, the ANC system performance was verified in an operational vehicle line test.

## 2 Active Noise Control Principles

The basic idea behind ANC has been known for more than 70 years. Producing an opposing signal (anti-noise) with the same amplitude as the noise to be reduced (unwanted noise), but with the opposite phase, yields a significant reduction in the noise level [3]. According to the superposition of waves, two waves with equal amplitude and identical phase have an additive effect, resulting in a doubling of the overall amplitude. On the other hand, two waves with equal amplitude but opposite phase have a subtractive effect, resulting in a decrease in the overall amplitude. The phase describes the relative position of the wave in its rising and falling cycle. If two waves are in phase, they rise and fall together. However, if they are exactly out of phase, one rises as the other falls, and so they cancel out one another. ANC tries to eliminate sound components by adding the exact opposite sound. The level of attenuation is highly dependent on the accuracy of the system for producing the amplitude and the phase of the reductive signal (anti-noise).

Due to the sound field changing with time, and the frequency, amplitude, phase, sound source volume velocity and other information being non-steady-state, the control system must be adaptive. Considering the application in railway passenger vehicle interior noise control, an active noise control mechanism based on FXLMS algorithm (Fig. 1) was proposed.

According to ANC theory, an ANC system should have four major components:

- Reference accelerometer: the accelerometer that receives the noise source which generates the internal noise (unwanted noise).
- Error microphone: the microphone that senses the noise at the point at which noise reduction is required, and monitors how well the ANC system performs.

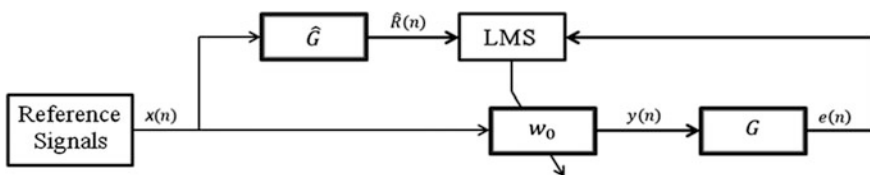


**Fig. 1** Active noise control mechanism

- Speaker: the device that physically produces the anti-noise.
- Controller: a signal processor (usually digital) that drives the speaker. In the simplest case, the DSP controller multiplies the reference microphone signal by minus one and sends it to the speaker to produce the anti-noise.

### 3 Line and Static Transfer Function Test

The initial task was to identify the number and location of both the speakers and the reference sensors which are used to control the algorithm. The location of the microphones used for the system feedback will also need to be identified. This can be achieved using a modelling exercise based on measurements taken in a carriage under operating line test and static conditions [4, 5].

#### 3.1 Line Test

To support the modelling phase, the interior noise and surface vibration at selected points was measured under operating conditions at a number of vehicle speeds, Fig. 2 shows the test points, which included:

- seven noise measuring points:

One noise measuring point at a height of 1.6 m above floor level, and six noise measuring points at a height of ears of the passenger (a height of 1.2 m above floor level).

- twenty four vibration measuring points:

Eight vibration measuring points at the floor of the car-body, eight vibration measuring points at the sidewall, eight vibration measuring points at the roof and side of the roof.

These measurements were used to define the reference signals.

The acoustic and structural operational data were acquired simultaneously on a moving train. The requirement for simultaneous acquisition dictated the number of transducers which could be used and the final arrangement included eight microphones and twenty four accelerometers. The acoustic data and the structural response were acquired at 4096 Hz.

The data were measured under a total of eight operating conditions: at vehicle speeds of 200, 250, 300 and 350 km/h with the train travelling both forwards and backwards.

The tonal characteristics seen in the acoustic response are also seen in the mean structural response (Fig. 3) suggesting that these features are, at least partially, structurally transmitted.

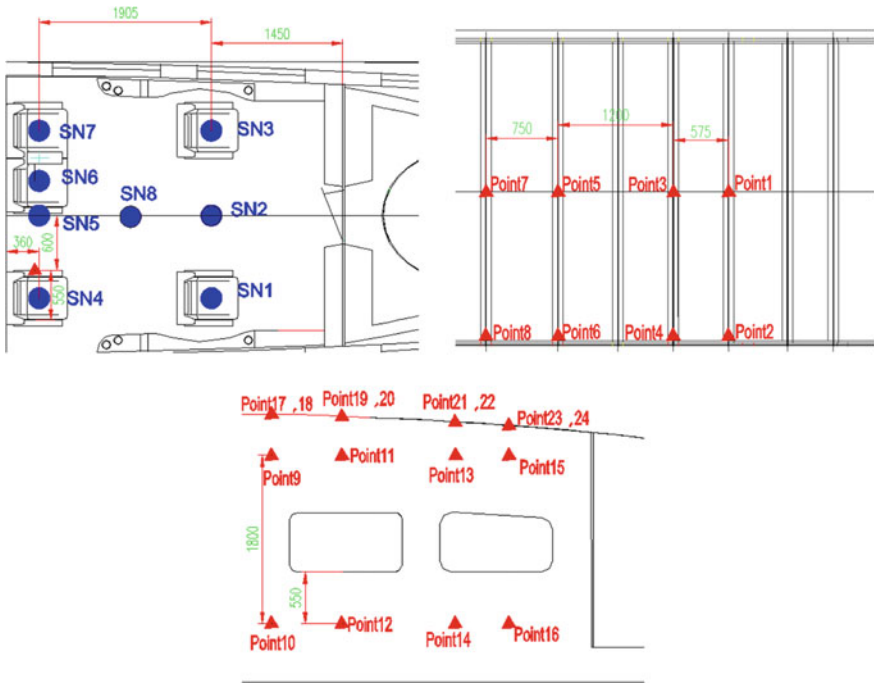


Fig. 2 Line test of ANC reference signal

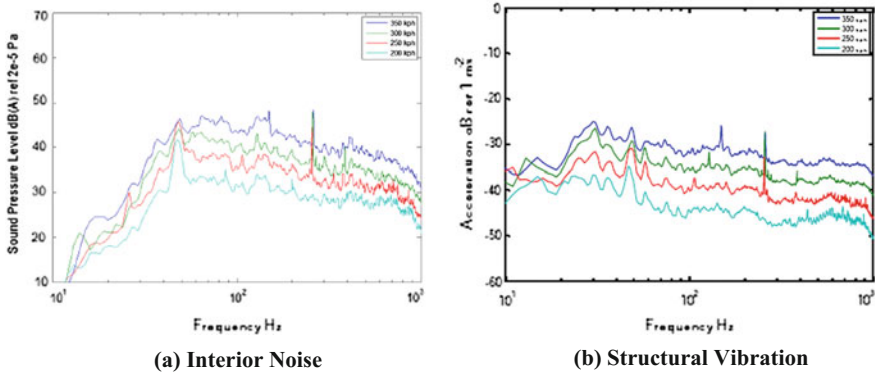


Fig. 3 Comparison of the Spectra at four test speeds train travelling forwards

### 3.2 Static Transfer Function Test

Transfer functions were also measured between potential actuator locations and the control points at which the noise was measured, as shown in Fig. 4. The noise point was same as shown in Fig. 2. This paper presents an overview of the data recorded following initial analysis prior to the modelling of the system.

The transfer functions between the potential loudspeaker sites and the seven microphone locations were measured with the vehicle static. A speaker was used to excite the cavity and the transfer function between the speaker drive voltage and the sound pressure level at each microphone was measured. A band width of 2048 Hz was used and the excitation was band limited pink noise. The frequency response functions measured were subsequently converted to impulse response functions suitable for the model (Fig. 5).

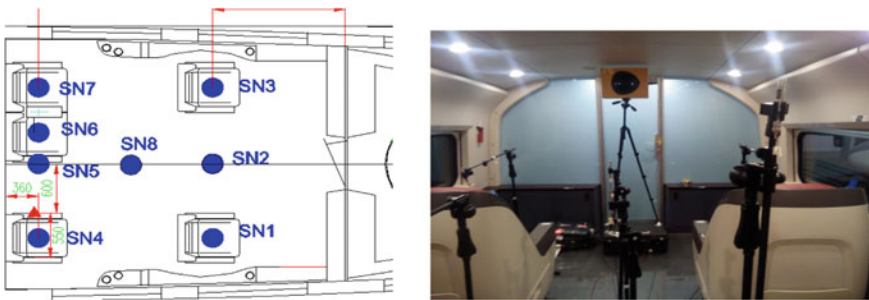
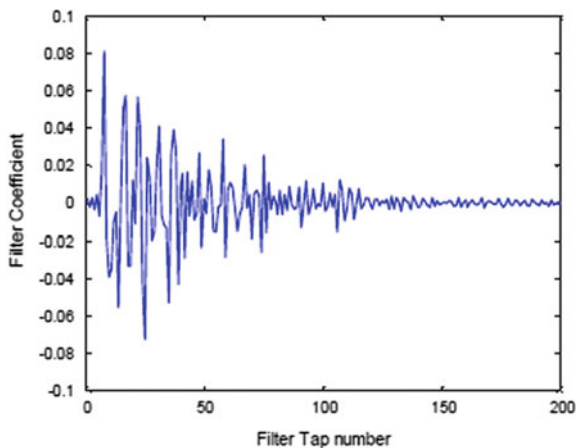


Fig. 4 The ANC static test of transfer functions

Fig. 5 Impulse response function, Actuator 1 to Microphone 1





### 4 The Algorithm Simulation and Analysis

According to the ANC principle, a multi reference feed forward algorithm controlling a number of loudspeakers was used. The simulation model was the established using this algorithm. This modelling procedure allowed the system architecture to be defined and an estimate of the achievable noise reduction to be made.

In the algorithm modelling the most important parameters are the convergence coefficient and output gain [6]. Convergence coefficient can be calculated from the test data. The value of output gain may vary according to experience and simulation results. Figure 6 shows the waveform of the residual noise signal represented by different output gain values. In this project, after much iteration, the gain value was selected as 0.1.

As an example, Fig. 7 shows the simulated system performance for the case of the train travelling forward at 350 km/h. As can be seen, the control effect was obvious, especially in the low-frequency region, resulting in an overall noise reduction of 6 dB (A).

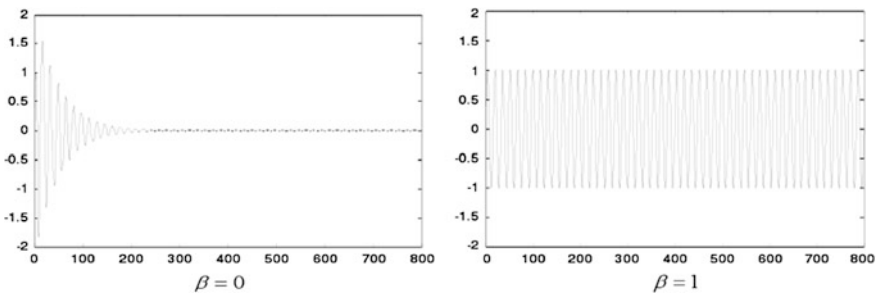
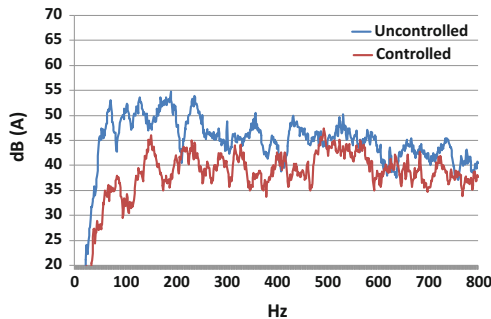


Fig. 6 The waveform of the residual noise signal represented by different output gain values

Fig. 7 The result of simulation predict







**Fig. 10** Test picture

The results of the in-service performance tests are shown in Fig. 11. As these results show, the active control system can effectively reduce low frequency noise 3–6 dB especially below 300 Hz in the human head region. An overall noise reduction of 5 dB (A) was achieved.

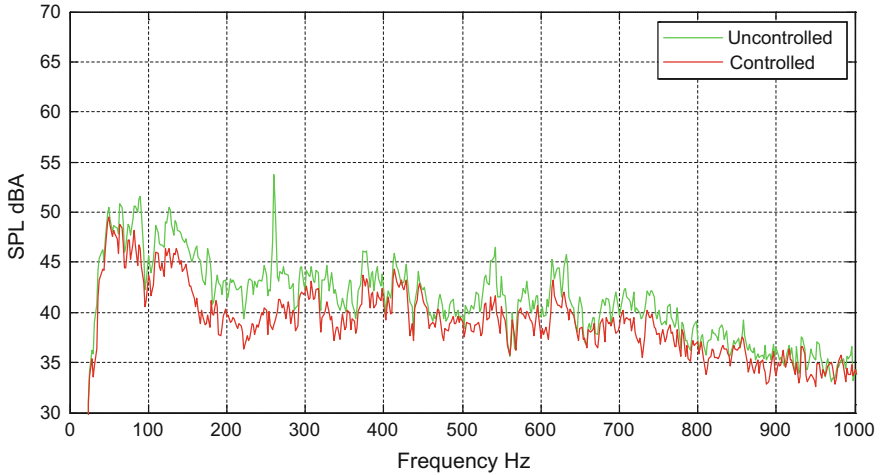


**Fig. 11** Test result

## 6 Conclusion

The performance of an active noise control system, targeted at low and mid frequency noise inside a high speed train passenger cabin, was demonstrated through in-service testing. The system delivered enhanced passenger comfort and reduced the interior noise level by between 3 and 6 dB(A) in the controlled frequency range.

## References

1. Elliott, S.J.: *Signal Processing for Active Control*. Academic Press, New York (2001)
2. Kuo, S.M., Morgan, D.R.: Active noise control: a tutorial review. *Proc. IEEE* **87**(6), 943–973 (1999)
3. Leug, P.: Process of silencing sound oscillation; Germany, 655508[P]. 1933-01-27
4. Sutton, T.J., Elliott, S.J., McDonald, A.M., et al.: Active control of road noise inside vehicles. *Noise Control Eng. J.* **42**(4), 137–147 (1994)
5. Otte, D., Sas, P., Van de Ponsele, P.: Noise source identification by use of principal component analysis. In: *Proceedings of Inter-noise*, p. 88 (1988)
6. Johansson, S., Claesson, I., Nordebo, S.: Evaluation of multiple reference active noise control algorithms on Dornier 328 aircraft data. *IEEE Trans. Speech Audio Process.* **7**(4), 473–477 (1999)

# Development of a Suspended Floor Structure for a Railway Vehicle



K. Yamamoto, T. Goto, M. Asahina, Y. Akiyama and N. Imaoka

**Abstract** The interior noise of a passenger cabin mainly comprises the transmitted noise and structure-borne noise. To reduce the level of the interior noise, new countermeasures against the structure-borne noise from the floor panel are required. In this study, we verified the vibration characteristics of a car body and clarified that the vertical vibration of the side structure is less than that of the floor structure, which supports the floor panel. On the basis of this result, we devised a new floor structure, wherein the floor panels are suspended from the side panel. Moreover, we evaluated the effectiveness of the design by numerical analysis and excitation tests using a test vehicle. Here we outline the suspended floor structure, predict the noise reduction effect by numerical analysis, test the vibration reduction effect, and compare the results with those for a conventional fixed floor structure in a Shinkansen-type test vehicle.

---

K. Yamamoto (✉) · T. Goto · M. Asahina · Y. Akiyama  
Railway Technical Research Institute, 2-8-38, Hikari-Cho, Kokubunji-Shi, Tokyo, Japan  
e-mail: katsu@rtri.or.jp

T. Goto  
e-mail: goto.tomonori.98@rtri.or.jp

M. Asahina  
e-mail: asahina@rtri.or.jp

Y. Akiyama  
e-mail: akiyama@rtri.or.jp

N. Imaoka  
Japan Transport Engineering Company, 3-1, Okawa, Kanazawa-Ku, Yokohama, Japan  
e-mail: imaoka@j-trec.co.jp

## 1 Introduction

To improve the comfort levels of passengers in a railway vehicle cabin, the interior noise should be reduced. The interior noise of a railway vehicle is broadly classified into “rolling noise,” “mechanical noise,” and “aerodynamic noise” [1]. A portion of rolling or mechanical noise power, which is generated in a bogie, propagates to the car body structure through the air springs, dampers, and traction links between the car body and the bogie as vibrations; the power radiates from the floor or the interior panels into the cabin as structure-borne noise [2, 3]. Moreover, the exterior noise around the car body caused by the rolling noise, aerodynamic noise, or mechanical noise transmits through the car body structure and interior panels as transmitted noise.

The previous approaches to the interior noise have focused on the method for reducing the noise level. Therefore, on the basis of the characteristics of the interior noise or vibrations of a car body and bogie, numerous countermeasures have already been incorporated in the vehicles. In general, countermeasures against transmitted noise are based on the mass law, whereas those against structure-borne noise are based on vibration isolation. As a result of these countermeasures, the interior noises in high-speed trains are kept low. However, new countermeasures for reducing noise level or maintaining noise quality are continuously being developed in preparation for higher speeds or reductions in vehicle weight [1].

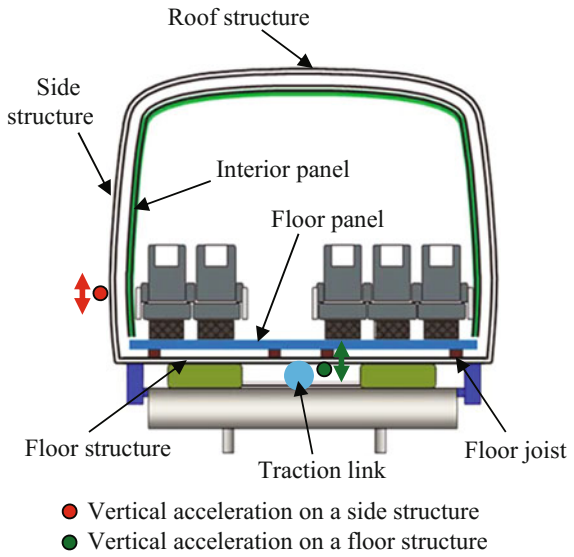
Although common countermeasures such as the floating floor structure have been widely applied to high-speed vehicles [4], we attempted to devise a new countermeasure without reference to the conventional methods. Therefore, we re-evaluated the vibration characteristics of a car body structure and the transmission mechanism of structure-borne noise from a bogie via the floor panel and subsequently devised a new floor structure: the suspended floor structure.

In this paper, we describe the vibration characteristics of the car body structure and the mechanism of structure-borne noise of a railway vehicle and then outline the suspended floor structure as a new countermeasure against structure-borne noise. Moreover, we use numerical analysis to evaluate the reduction effect of noise emitted from the floor panel and conduct excitation tests using a test vehicle to study the vibration reduction effect on a floor panel.

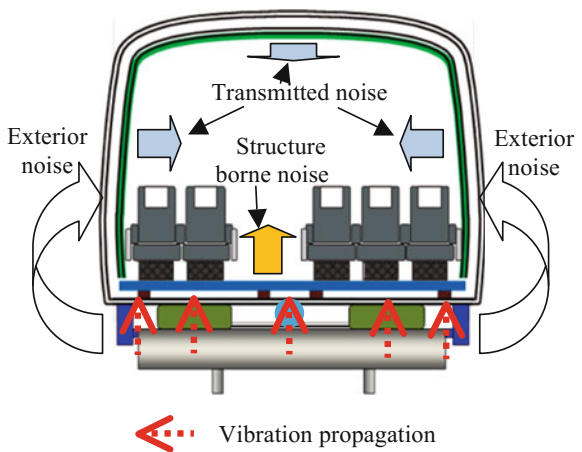
## 2 Interior Noise of a Railway Vehicle

Figure 1 shows a cross-sectional view of a Shinkansen vehicle. The car body structure comprises a roof, side, floor, and gable, as shown in Fig. 2. Floor panels in the cabin are fixed to the floor joist, by which the floor panels are connected to the floor structure panel. The interior noise in a cabin is generally evaluated on the basis of an overall value of an A-weighted sound pressure level. The frequency characteristics of the A-weighted sound pressure level at the center of a Shinkansen

**Fig. 1** Cross-sectional view of a Shinkansen vehicle



**Fig. 2** Interior noise in the cabin



vehicle cabin are shown in Fig. 3 [5]. For both an open section and a tunnel section of track, the sound pressure level is highest in the frequency range from 100 to 400 Hz. Attempts to reduce the overall value of the A-weighted sound pressure level should preferably focus on the frequency range where the sound pressure level is greatest. The previous studies have mentioned that the interior noise in the frequency range from 100 to 400 Hz penetrated from the floor as structure-borne noise.

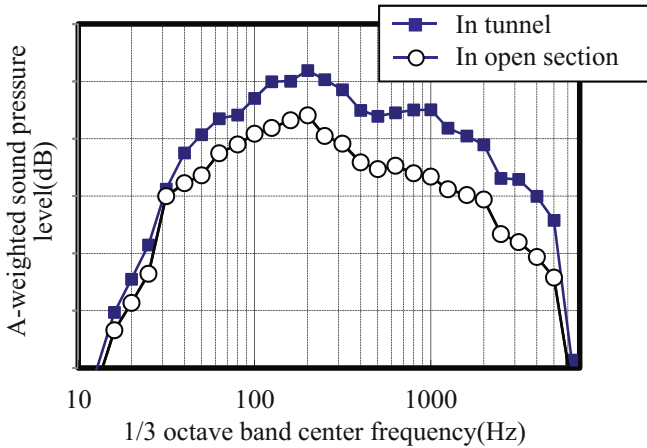


**Fig. 3** Frequency characteristics of the interior noise in a Shinkansen vehicle

### 3 Vibration Characteristics of a Car Body Structure

In previous testing, we evaluated the vibration characteristics of a car body structure with acceleration sensors placed on the structure panels in the normal vibration direction; i.e., vertical vibrations were measured for the floor structure or roof structure, and lateral vibrations were measured for the side structure. Thus, the vertical vibrations of the side structure have not been well characterized.

To re-evaluate the vibration characteristics of a car body structure and the mechanism of the structure-borne noise from a bogie into a cabin via the floor panel, we measured the vibrations in the vertical direction of the floor and side-structure panels of a Shinkansen-type test vehicle owned by the Railway Technical Research Institute. The appearance of the test vehicle is shown in Fig. 4. The test vehicle was constructed on the basis of an actual commercial Shinkansen vehicle with a double-skin structure and includes interior panels and seats.

**Fig. 4** The Shinkansen-type test vehicle at the Railway Technical Research Institute





**Fig. 5** Exciter mounted to a yaw damper frame

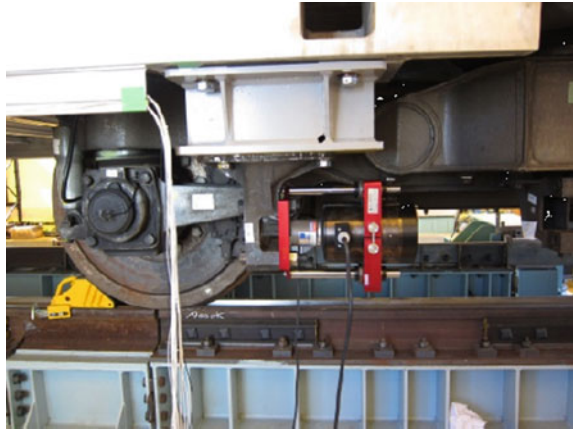
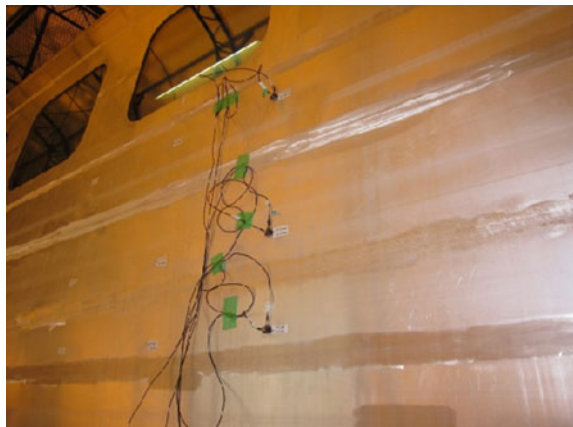


**Fig. 6** Accelerometers on the side structure panel



An exciter was mounted to the frame of a yaw damper in the side of the car body, as shown in Fig. 5, and accelerometers were attached to the side and floor structure panels in the vertical and lateral directions, as shown in Fig. 6.

A comparison of the vertical vibration characteristics at the center of the floor and side structure panels is shown in Fig. 7. The vibration frequency characteristics indicate that the vibration of the floor structure panel was greater than that of the side structure panels in the frequency range from 200 to 400 Hz; this frequency range falls within the dominant range of the interior noise in railway vehicles. This result suggests that the floor structure panel is likely to vibrate in response to anti-plane vibrations, whereas the side-structure panels are less likely to vibrate in response to in-plane vibrations. Therefore, a larger vibration of the floor structure is transmitted to the floor panel through the floor joist and the structure-borne noise emits to the cabin in the dominant frequency range of interior noise.

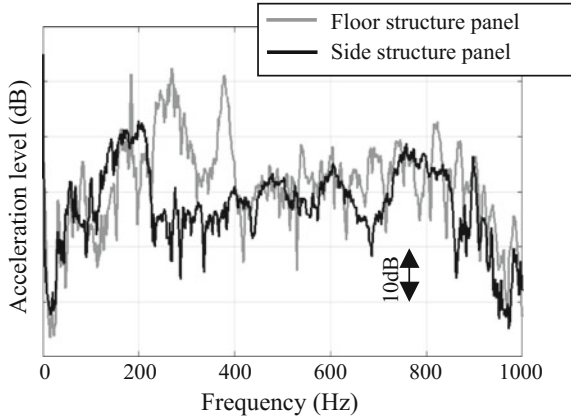


Fig. 7 Comparison between the vibrations of floor and side structure panels

### 4 The Suspended Floor Structure

On the basis of the vibration characteristics shown in Fig. 7, we devised a suspended floor structure for the railway vehicle as a method for reducing the structure-borne noise from the floor panel. Figure 8 shows a schematic of the proposed structure. Whereas the floor panel is fixed to the floor joist, which is supported by the floor structure in a conventional vehicle, in the new structure, the floor panel is suspended from the side structure by suspension members. Because the floor panel is connected to the side structure rather than being supported by the floor structure, vibration propagation from the floor structure to the floor panel will be completely isolated. The vibrations are transferred to the floor panel only from the side structure; therefore, the vibration and radiated noise of the floor panel should be reduced.

The suspension member is selectable from among, for example, rod-like bars, plates, or wires. Preferably, however, the suspension member should fit in the space

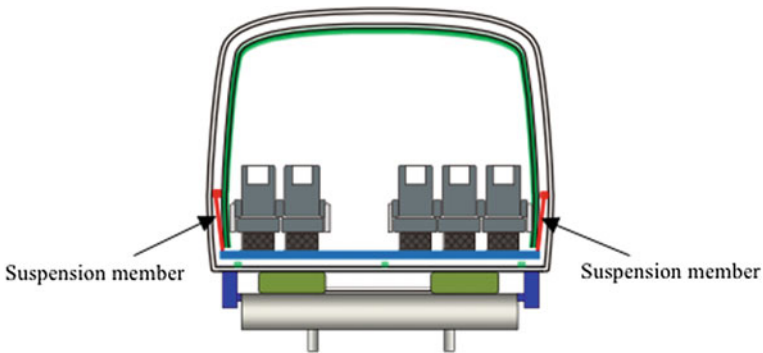


Fig. 8 The suspended floor structure

between the structure panel and interior panel. Additionally, the insertion of a vibration insulator into the joint between the floor panel and suspension member or inside the suspension member is expected to result in further vibration reduction.

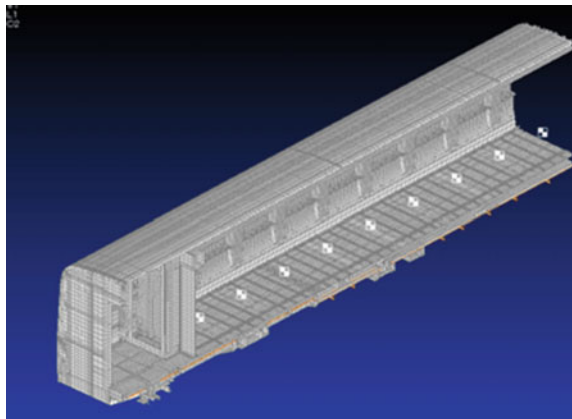
We well recognize that several problems with the suspended floor structure need to be solved before such railway vehicles can be used commercially; these problems are discussed in Sect. 7.

## 5 Numerical Analysis of the Suspended Floor Structure

### 5.1 Overview of the Numerical Analysis

To compare the noise that radiates from the floor panel between the fixed and suspended floor structures, we performed a numerical analysis using a detailed car body model of a Shinkansen-type test vehicle equipped with interior panels and seats. Figure 9 shows the analysis model based on this vehicle. The vibration characteristics of the car body structure or interior panels were calculated using the NASTRAN program. The vibration data of the interior panel or floor panel were converted into air partial velocity and input to a cabin space model as the boundary condition. The noise characteristics in the cabin were calculated using a boundary element method by the SYSNOISE program. In this analysis model, the suspension members were rigid bars with links that could swing in the lateral direction. Here, full-scale model analysis would exceed the model's capacity of calculating the vibration or interior noise of the vehicle. Therefore, the model was reduced to one-fourth scale and was treated as a space with a symmetry plane in the longitudinal and lateral directions. Although the vibration calculations using the NASTRAN program included a deck in the model, the analysis of the interior noise by the SYSNOISE program included only a cabin. All seats were modeled in their actual shape, but their weight was modeled as a mass point on the floor.

**Fig. 9** The analysis model of a Shinkansen-type test vehicle



## 5.2 Comparison Between Fixed and Suspended Floor Structures

Figure 10 shows a comparison of the air particle velocity near the floor panel at 316 Hz between the fixed and suspended structures, as calculated using the SYSNOISE program. The color change of the entire area of the figure from red or yellow to green or blue indicates a reduced air particle velocity; in particular, the air particle velocity was reduced by more than 10 dB in the left area, which is located above a bogie. The characteristics of the air particle velocity can be regarded as noise characteristics; near any structure, the noise emitted from the floor panel is expected to be reduced. On the basis of this numerical analysis result, the suspended floor structure is expected to effectively suppress the noise power in the cabin.

## 6 Verification Test of the Suspended Floor Structure in a Test Car

### 6.1 Outline of the Verification Test

We performed excitation tests using a test car to verify the effectiveness of the suspended floor structure. Under ordinary circumstances, the effectiveness would be evaluated on the basis of the change in noise characteristics in the cabin. However, such measurements are difficult because the floor panels covering a large area would have to be replaced with suspended floor panels. Therefore, in these tests, we compared the vibration characteristics between fixed and suspended floor panels. Additionally, several different materials and lengths of suspension members were tested and their effectiveness was evaluated. The conditions used in the verification tests are summarized in Table 1.

Here, when the floor panel was suspended using wire, the panel could freely move in the horizontal plane. Such floor panel movement is undesirable; therefore, band plates were tested to inhibit the swing in the longitudinal direction.

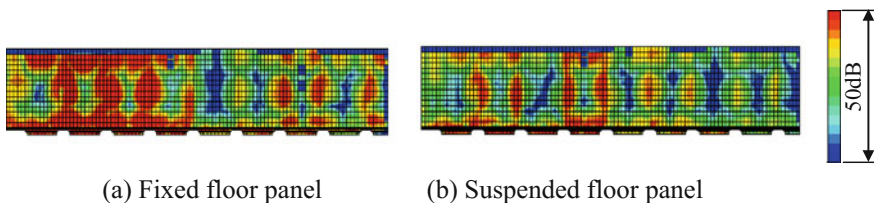


**Fig. 10** Comparison of the air particle velocity emitted from fixed and suspended floor panels

**Table 1** Verification test conditions

No.	Fixture condition	Material of the suspension member (on one side)	Length of the suspension member	Excitation point
1	Fixed on the floor joist			Yaw damper frame/traction link
2	Suspended	3 short wires	550 mm ( $\phi$ 1 mm)	Yaw damper frame
3		2 long wires	1475 mm ( $\phi$ 6 mm)	Traction link
4		2 vertical long band plates	1475 mm (SUS w: 115, t: 1)	Traction link
5		2 horizontal long band plates	200 mm (SUS w: 835, t: 1)	Traction link

### 6.2 Vibration Reduction Effect of the Suspended Floor Panel

The vibration characteristics of the conventional fixed floor structure and the suspended floor structure were compared by excitation tests of a test car. Figure 11 shows a comparison of the vibrations when the floor panel was suspended with three wires on each side from the under hem of a window. Compared to the vibration level of the fixed floor panel, the vibration level of the suspended floor panel was reduced by approximately 10 dB in the frequency range between 200 and 400 Hz.

Figure 12 shows the results when the floor panel was suspended with two long wires on each side from around the upper hem of a window. The vibration of the floor panel was reduced more than in the case of the short wires (Fig. 11); it suppressed approximately 5–10 dB in the entire frequency range compared to the fixed floor panel. These two results suggest that wire is a suitable suspension member and that long wire is beneficial to vibration reduction of the floor panel regardless of the excitation point.

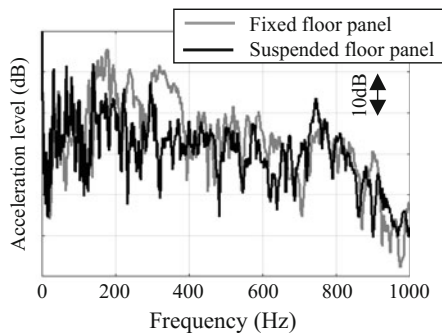
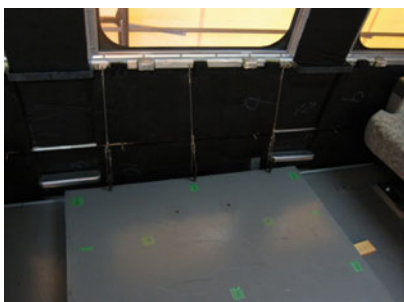


**Fig. 11** Floor panel suspended by short wires (! 1 \$ \$)

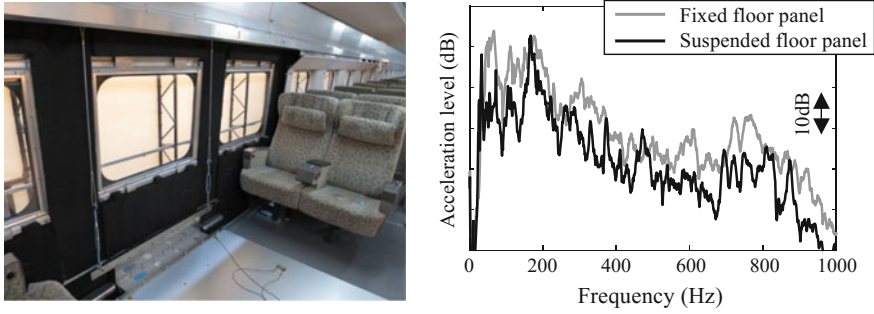


Fig. 12 Floor panel suspended by long wires (! 6 \$ \$)

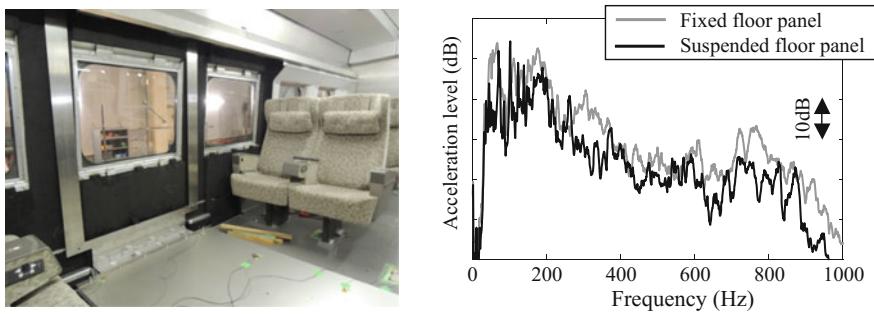


Fig. 13 Floor panel suspended by vertically long band plates

The vibration changes when a vertically long band plate was used as the suspension member are shown in Fig. 13. A comparison with Fig. 12 reveals a smaller vibration reduction effect in the case of the band plate, especially in the frequency range from 380 to 600 Hz near the fixed floor panel. These differences between different suspension-member materials are attributed to differences in their attenuation characteristics against vibration propagation; i.e., the wire dissipates vibration during propagation.

Finally, the vibration characteristics in the case of a horizontally long band plate are shown in Fig. 14. This suspension member was shorter and exhibited weaker attenuation characteristics than the other investigated suspension members; therefore, the vibration level increased and decreased with the frequency range. Moreover, the peak vibration occurred in locations where vibration was caused by the suspension member itself.

On the basis of these four results, we verified that the suspended floor structure can potentially reduce the vibration input to the floor panel; we speculate that the emission noise from the floor would also be reduced.

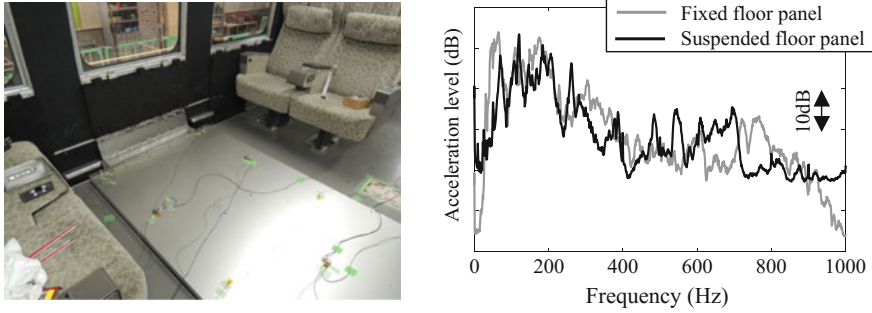


Fig. 14 Floor panel suspended by a horizontally long band plate

## 7 Approach for Applying to Commercial Railway Vehicles

We proposed an outline of a suspended floor structure and evaluated its ability to reduce noise as a fundamental verification through numerical analysis and actual tests using a Shinkansen-type test vehicle. Although the results show that the new floor structure can reduce the interior noise when the floor panels are suspended from the side structure panel, this design has not yet reached a stage where it can be applied to a commercial railway vehicle. Several problems need to be solved to enable commercial use of this design.

One of the remaining problems is the stiffness of the floor panel. Because the conventional fixed floor panel is supported by the floor joist near its center, substantial stiffness is not needed. However, in the suspended floor structure, the floor panel is suspended from its lateral edges; therefore, the weight of the seats and passengers must be supported by the floor panel, which, in the case of a Shinkansen-type vehicle, is approximately 3-m long. Thus, the stiffness of the floor panels should be increased. However, increasing the stiffness of the panels introduces the problem of increasing the weight of the lightweight, high-speed train. The floor panel must be redesigned with effective additional reinforcement without substantially increasing its weight.

Another problem is the frequency characteristics of the suspended member and the floor panel. Because the floor panel is suspended like a swing with no buffer on either side, we expect that low-frequency vibrations that affect ride comfort will be reduced by the inertial forces in the lateral direction of the floor panel and in the link mechanism of the suspension member. However, a fundamental eigen frequency of the floor panel and suspension member appears to occur in the low-frequency range. To avoid affecting ride comfort, the frequency characteristics of these will need to be designed to be in a higher range, for example 50–100 Hz; in this frequency range the influence on both ride comfort and interior noise is smaller.

## 8 Conclusion

We proposed a new suspended floor structure as a countermeasure against structure-borne noise from the bogie of a railway vehicle.

1. The vibration level of the side structure is lower than that of the floor structure in the railway vehicle.
2. As a countermeasure against structure-borne noise, we proposed a new floor structure in which the floor panel, which is supported by a floor joist to the floor structure in a conventional vehicle, is suspended from the side structure.
3. On the basis of numerical analysis, the noise emitted from the floor panel is expected to decrease when the suspended floor panel is applied to a railway vehicle.
4. Excitation tests were performed to evaluate the vibration reduction effect of the suspended floor structure in an actual Shinkansen-type test vehicle; the suspended floor structure was verified to be effective.
5. A longer suspension member composed of wire was found to substantially reduce vibration.

## References

1. Thompson, D.: Railway Noise and Vibration, pp. 465–467 (2009)
2. Asahina, M., et al.: Application of transfer path analysis to the vibration and noise of a railway vehicle. In: Proceeding of 7th International Symposium on Speed-up and Sustainable Technology for Railway and Maglev Systems (STECH2015), Chiba, Japan
3. Asahina, M., et al.: Study on the Application of Transfer Path Analysis to the Structure Borne Sound from the Bogies of Railway Vehicles, Proceeding of Inter Noise 2016, Hamburg, Germany
4. Fan, R., et al.: Experimental study of the effect of viscoelastic damping materials on noise and vibration reduction within railway vehicles. *J. Sound Vib.* **319**(1–2), 58–76 (2009)
5. Yamamoto, K., et al.: Investigate the interior noise of railway vehicle, *RRR* **73**(8) (2016) (In Japanese)



# Study on Sound Absorption Seats in High Speed Trains



Xiaojun Deng, Yanju Zhao, Haijin Zhang and Peng Lin

**Abstract** Learning from the successful application of the sound absorption seats in the music halls and theaters and also based on the features of the noise spectrum in high speed trains a sound absorption seat design which applies specifically to the high-speed trains is put forward in this paper. High performance absorbing materials and perforated plates are selected and designed. Finally, seats of full train carriage were made and tested in the high-speed train on the railway. The test results showed that the installation of the sound absorption seats results in the noise level at the standard point in the passenger compartment decreases by 1.5 dB compared with that of the normal seats.

## 1 Introduction

Currently sound absorption seats are widely applied in the concert halls, opera houses, meeting rooms and places having strict limits on noise. By comparing the reverberation time before and after the installation of seats it is shown that seats account for 30–50% of the gross amount of that absorbed in the whole hall. This significantly reduces the noise and improves the sound quality [1–4]. However, studies on sound absorption seats in the high-speed train are rare. This paper aims to study sound absorption seats designed to absorb the reverberant sound in the high-speed train with the purpose of reducing noise.

---

X. Deng  
School of Mechanical, Electronic and Control Engineering, Beijing Jiaotong University,  
Beijing 100044, China

X. Deng · Y. Zhao (✉) · H. Zhang · P. Lin  
CRRC Qingdao Sifang Locomotive and Rolling Stock Co. Ltd, Qingdao, China  
e-mail: zhaoyanju215@163.com

## 2 Design of Sound Absorption Seats

A seat in the high-speed train is made up of cushion, backrest, support structure, fire-proof plate and some other parts. The cushion and backrest are filled with elastic materials. Details are shown in Fig. 1.

In order to improve the absorption effect of the seat, specialized acoustic design is made for the limited area where the seat contacts the air. As for the backrest and the cushion in contact with people, elastic sound-absorbing materials are used to improve the absorption performance of the backrest while ensuring the materials are elastic and fire-proof. Sound absorption material is also used outside of the backrest to enlarge the absorbing area of the whole seat to improve the absorption effect. With regard to the backrest plate, cushion support plate and fire-proof plate, they are all perforated sound absorption boards which further improves the performance by setting their parameters according to the absorption bands. Specific materials, perforated boards selection and designs are as follows.

### 2.1 Studies on Properties of Sound-Absorbing Materials and Layer Structure

In order to meet the requirement of being fire-proof in the high speed train, it is necessary to add a layer of flame retardant adhesive outside of the sound-absorbing material which was then wrapped by the seat cover. Therefore studies on properties of the layer structure of the sound-absorbing material, seat cover and the flame retardant adhesive seem to be essential.

Here different sound-absorbing materials will be selected, and then absorption coefficient tests will be made on them as well as on their layer structure. Polyurethane foam is a sound-absorbing material with elasticity, low price and good performance that can meet the requirements of backrest and cushion being elastic.

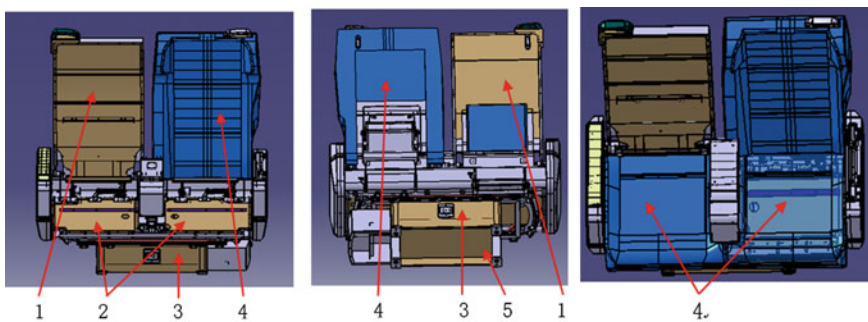


**Fig. 1** Basic structures of seats (1. Backrest rivet support plate; 2. Cushion support plate; 3. Chassis plate; 4. Components of backrest; 5. Fire-proof plate)

As a result, it is widely used in the seats now. In order to find a material which works better in sound absorption, a comparison is made between polyurethanes with 50 mm thickness from different manufacturers and of different foaming capacities. Silicone foam is a new type of sound-absorbing material with elasticity. Due to its higher density, 30 mm thick is going to be used in this test.

Figure 2 is the comparison of the absorption coefficients of different materials tested in the standing wave tube. As is shown above, the absorption performances of polyurethane foam 1, foam 2 and foam 3 are barely different in the low frequency stage. When it comes to the frequency stage of 400–1100 Hz, polyurethane foam 1 performs better. The melamine material performs poorly in the stage of 200–400 Hz but performs the best of all the materials in the range of 700–1100 Hz. This is a comparison only between materials themselves. In order to verify the properties of the layer structure made up of the absorbing materials, the flame retardant adhesive and the seat cover, sound absorption tests are made again when the materials, the adhesive and the cover are composed. The results are presented in Fig. 3.

Compared with Fig. 2, it is shown in the Fig. 3 that in the layer structure, the polyurethane foam 1, which itself performs well in sound absorption, performs also very well among all the elastic sound-absorbing materials. The melamine material tests above show that flame retardant adhesive and the seat cover increase the absorption coefficient and thus lead to better performance in absorbing sound across the whole frequency range.

**Fig. 2** Comparison of absorption coefficient of different material

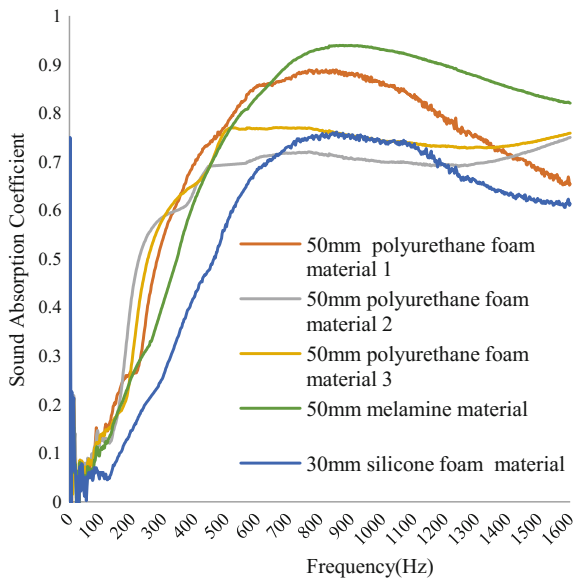
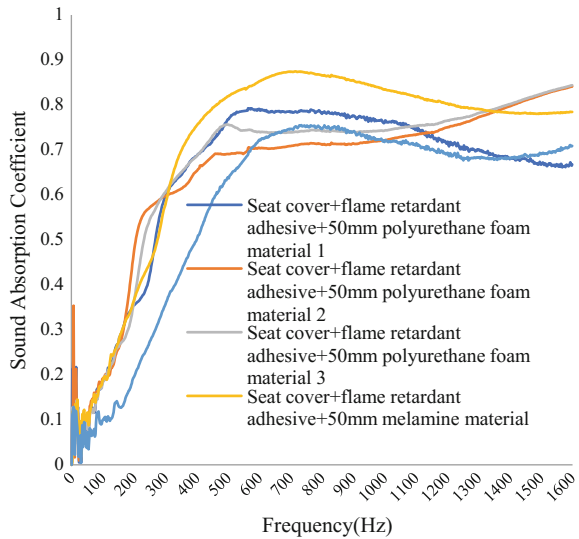


**Fig. 3** Test result of sound-absorbing materials, flame retardant adhesive and seat cover



## 2.2 Study on the Design of Perforated Plates

The sound absorption mechanism of the perforated plate is that each perforation in the plate and its corresponding air layer or the sponge material with small holes work together into a system which is similar to Helmholtz resonator. The resonant sound-absorbing structure of the perforated plate can be viewed as a parallel connection of many Helmholtz resonance absorbers.

In order to determine the optimal parameters of the perforated plate, several optional perforated plate designs are made, calculated with a formula according to the mechanism [5, 6]. Then sound-absorbing performances of perforated aluminum with various thickness, apertures and perforation rates will be tested in the standing wave tube. The results are presented in Fig. 4. As can be seen, different apertures and perforation rates result in different absorption bands. The thicker the plate, the absorption band is more likely to go toward low frequency. The smaller the aperture, the higher the absorption coefficient across a wider the band. The noise spectrum of the high speed train is mainly concentrated in the mid and low frequency range 200–800 Hz. As shown in Fig. 4, a perforated plate with 1 mm thick, 1 mm aperture and 3.14% perforated rate and one with 1.4 mm thick, 5 mm aperture and 1% perforated rate have a higher absorption coefficient in the frequency range 200–800 Hz. Therefore, these two types of plates are selected to be applied into the sound absorption seat design.

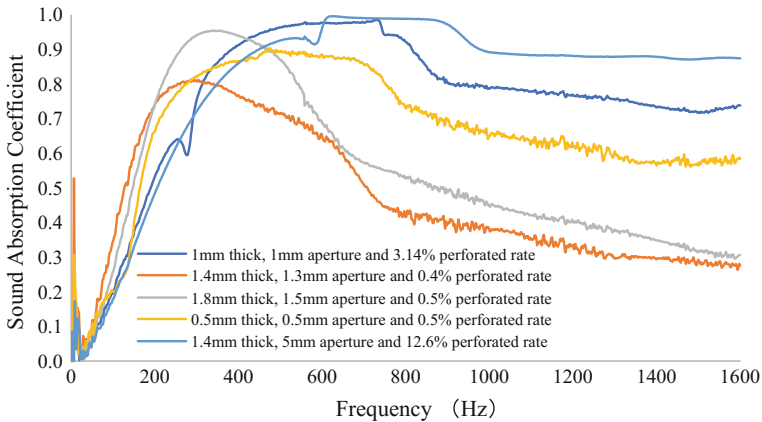


**Fig. 4** Absorption coefficient tests of different perforated plates with different parameters

### 2.3 Design of the Sound Absorption Seat

A seat in the high speed train is made up of cushion, backrest, support structure, chassis plate, fire-proof plate and some other parts. Cushion and backrest are filled with elastic materials. According to the features of seat structure and test results above, designing scenarios of sound absorption seats are as follows:

- (1) Backrest plate area is relatively large and thus contributes more to absorbing noise in the passenger room. According to tests and simulation experiments, designing the aluminum backrest into perforated absorbing plate with 1.4 mm thick, 5 mm aperture and 1% perforated rate would be helpful to absorb high-frequency noise.
- (2) Stick melamine sound-absorbing material of 50 mm thick to the backrest perforated plate in order to enlarge the absorption area of the seat. In this way, it can not only absorb the noise in the train, but also form a Helmholtz resonator structure with the perforated plate, which enhances the absorption effect.
- (3) Design the cushion into perforated plate with 1.4 mm thick, 5 mm aperture and 1% perforated rate, and mount melamine sound-absorbing materials beneath the cushion.
- (4) Design the protective panel and baseplate into perforated plate with 1.4 mm thick, 1.5 mm aperture and 3.14% perforated rate in order to absorb the low frequency noise coming from the train floor (Fig. 5).

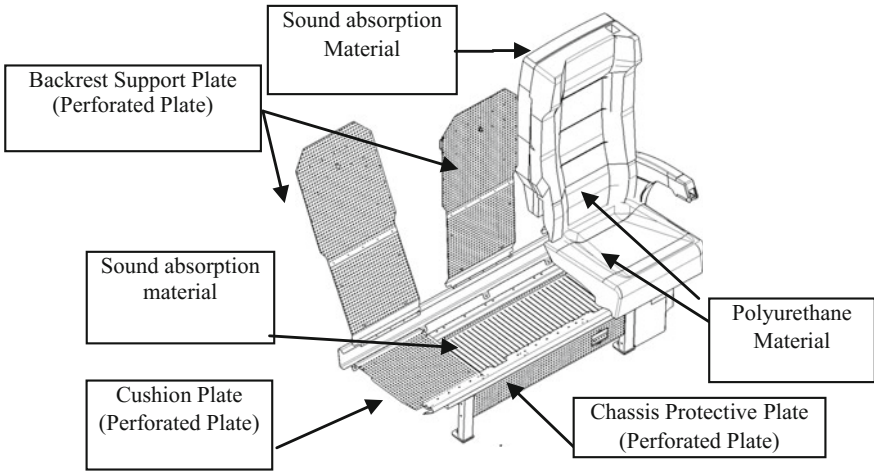


Fig. 5 Design scheme of sound absorption seat

### 3 Analysis of Sound Absorption Test in the Laboratory

According to the sound absorption design, seat models were made and tested inside a reverberation chamber [7, 8]. The volume of the chamber was 227 m<sup>3</sup> and the frequency range of the of the sound was 50–5000 Hz, 122 dB re 1pW. In order to make a comparison, 15 sound absorption seats and 15 normal seats were arranged into 3 rows in the reverberation room, in accordance with way seats are currently arranged inside trains. Testing set-up of the seats inside the test chamber is shown in Fig. 6.

Before the seats are put into the reverberation chamber, the gross volume of absorbed sound  $A_1$ , according to Sabine formula, can be represented as:

$$A_1 = \frac{55.3V}{c_1T_1} + 4m_1V \tag{3.1}$$

Fig. 6 Absorption coefficient test of the sound absorption seats



After installing the seats, the gross volume of absorbed sound  $A_2$  can be represented as:

$$A_2 = \frac{55.3V}{c_2T_2} + 4m_2V \tag{3.2}$$

In the formula:  $T_1, T_2$ -respectively stands for the reverberation time of the empty room and that of the room equipped with seats

$V$ —volume of the reverberation chamber,  $m^3$ ;  
 $c_1, c_2$ —respectively stands for sound velocity of the empty room and that of the room equipped with absorption materials, m/s;  
 $m_1, m_2$ —respectively stands for air absorption attenuation coefficient of the empty room and that of the room equipped with absorption materials.

If the interval between the two measured times is relatively short or the difference of the inner temperature and the humidity between them is small it can be approximated that  $c_2 = c_1 = c, m_2 = m_1 = m$ . Then the change of the sound volume absorbed before and after the installation of the seats can be expressed as:

$$\Delta A = \frac{55.3V}{c} \left( \frac{1}{T_2} - \frac{1}{T_1} \right) \tag{3.3}$$

Considering that the area of the absorption material and the surface area of the reverberation room are both small, the sound absorption coefficient of the floor that is covered by the seats is very small, which represented as:

$$\alpha_s = \frac{\Delta A}{S} = \frac{55.3V}{cS} \left( \frac{1}{T_2} - \frac{1}{T_1} \right) \tag{3.4}$$

In the formula:  $S$ —area of the seats to be tested,  $m^2$ ;  
 $\alpha_s$ —random incidence sound absorption coefficient of the seats to be tested.

Therefore, as long as the reverberation time before and after the installation of the seats, the volume of the reverberation chamber and the area of the seats to be tested are tested out, the random incidence sound absorption coefficient can be obtained via the formula (3.4). The test results are shown in Fig. 7.

As can be seen from the test results, compared with that of the normal seats, the sound absorption coefficient of the absorption seats is improved in the range 160–4000 Hz, especially in the range of 250–600 Hz, in which the coefficient increases from 0.45 to 0.8. This results proves that the sound absorption seats design is effective.

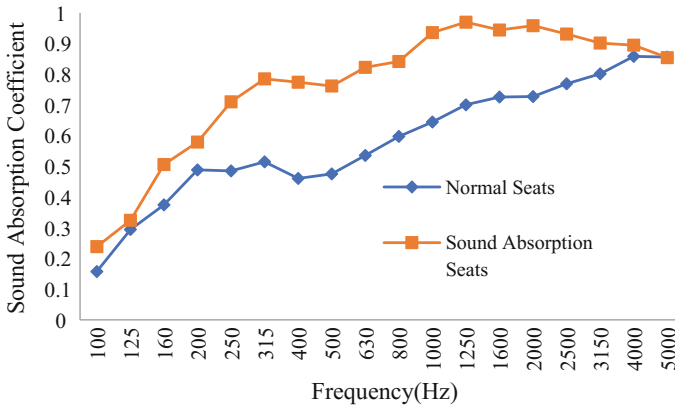


Fig. 7 Comparison between test results of sound absorption seats and normal seats

### 4 Analysis of Results from in Situ Railway Experiments

To further verify the sound absorption effect of the absorption seats, a full train of seats are made and arranged in a real high-speed train to test the sound pressure level at the standard points in the middle and at both ends of the carriage (1.2 m from the floor). The test condition is open air with a train velocity of 300 km/h (Fig. 8).

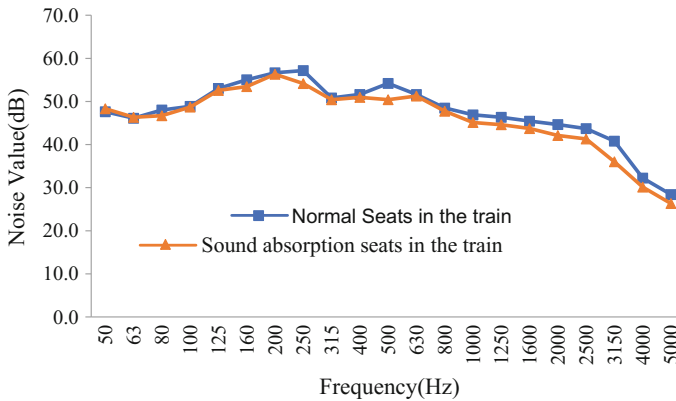
After installing the sound absorption seats, the noise decreases because the seats enlarge the sound absorption area and thus absorb more of the reverberation noise. Figure 9 is the comparison of the frequency spectrum in the middle of the train before and after the installation of the sound absorption seats. As is shown in the figure, the noise in the whole frequency band, especially in the middle and the high frequency bands, decreases due to the sound absorption seats.

Table 1 is the noise comparison before and after the installation of the sound absorption seats. It can be seen that the sound absorption seats play a positive effect

Fig. 8 Railway test in the train







**Fig. 9** Comparison of noise spectrum of the standard point in the middle of the train

**Table 1** Contrast of noise between sound absorption seats and normal seats in the train

Open wire 200 km/h	End 1 (dB)	Middle (dB)	End 2 (dB)
Normal seats in the train	66.7	66.5	67.5
Sound absorption seats	65.7	65	66.6
Noise reduction	1.0	1.6	0.9

on reducing the noise in the middle of the train which decreases by approximately 1.5 dB. However, the effect is relatively poor at both ends where the noise decreases by around 1 dB. This is mainly because both ends are close to the inner door and the number of the seats is relatively small. Consequently the absorption area is accordingly smaller which in turn reduces the absorption effect of the seats. In general, the sound absorption seats are advantageous since they neither add any extra weight nor take up extra interior space.

## 5 Conclusion

In this thesis, a sound absorption seat design to be fitted in a high-speed train is put forward. On the premise of ensuring that the materials are elastic and fire-proof, high-performance sound absorption materials and a perforated plate is applied to the backrest and cushion. Through tests in the lab and in a real train, it can be seen that after the installation of the sound absorption seats the noise in the middle of the train decreases by 1.5 dB and the noise at both ends 1 dB. This proves that the sound absorption seats play a positive effect in sound absorption while at the same time take up no extra interior space nor add no extra weight. Therefore it is predicted that the sound absorption seats can be widely used in the future.

## References

1. He, H.: Innovation and development of Chinese high-speed railway. *China Railway* **12**, 5–8 (2010)
2. Zhou, C.: Situation and prospects of high-speed railway's development. *Sci. Technol. Exch.* **2**, 38–42 (2005)
3. Zhong, X.: Study on sound absorption of theater seats and audience. *J. Tongji Univ. (Nat. Sci.)* **3**, 333–337 (1997)
4. Yu, B., Zhang, K.: Analysis and research on sound absorption of theater seats. *Environ. Eng.* **33**, 18–20 (2015)
5. Ma, D.: Accurate theory and design of micro-perforated absorber plate. *J. Acoust.* **22**(5), 385–393 (1997)
6. Zuo, Y., Zhou, J.: Sound absorption performance and application of perforated panel absorber. *China Mech. Eng.* **18**, 778–780 (2007)
7. GBJ47-1983, Specification for Sound Absorption Coefficient Measurement by Reverberation Chamber Method
8. Lu, J., Jin, Y., Geng, C.: Measurement of sound absorption of seats in the auditorium by Reverberation Chamber Method. *Entertainment Technol.* **7**, 29–32 (2011)

**Part VI**  
**Structure-Borne Noise**  
**and Ground-Borne Noise**

# On the Propagation and Prediction of Rail-Induced Ground-Borne Vibration Within Sandy Soils



Binghui Li and Luke Zoontjens

**Abstract** The propagation and attenuation characteristics of railway generated ground-borne vibration within Perth, Western Australia is unique to other Australian states and territories given that predominant superficial ground conditions for the central metropolitan region are layered sandy soils. For reliable prediction of ground-borne vibration from proposed rail operations at grade or within underground tunnel structures in the Perth metropolitan area, it is therefore essential that these sandy soil characteristics are well understood. In this context, this study investigates the prediction methodologies for rail-induced ground-borne vibration within sandy soils, for both at grade and underground cases. The paper firstly presents the surface geology of the Perth metropolitan region, followed by a brief theoretical review on the propagation and attenuation of ground-borne vibration under various ground conditions. The paper then investigates the empirical methodologies for predicting the ground-borne vibration from surface rail operations based on vibration measurements for the at-grade passenger rail operations carried out at multiple sites within both the Perth and Sydney metropolitan region. A borehole vibration testing at two specific borehole locations east of Perth was carried out and the subsequent data analysis and results are presented. The implications of the testing results on implementing the empirical predictions for the ground-borne vibration propagation from underground rail system operations, particularly with the presence of distinctive ground layers, are also discussed.

## 1 Introduction

The Perth metropolitan region, on a geologic setting, is within the large-scale Perth Basin which is an onshore and offshore sedimentary basin of a north to north-northwest trending, extending about 1300 km along the southwestern margin of the Australian continent [1, 2]. The underlying cretaceous-Tertiary formations of

---

B. Li (✉) · L. Zoontjens  
SLR Consulting Australia Pty Ltd, 503 Murray Street, Perth, WA 6000, Australia  
e-mail: bli@slrconsulting.com

© Springer International Publishing AG, part of Springer Nature 2018  
D. Anderson et al. (eds.), *Noise and Vibration Mitigation for Rail Transportation Systems*, Notes on Numerical Fluid Mechanics and Multidisciplinary Design 139,  
[https://doi.org/10.1007/978-3-319-73411-8\\_38](https://doi.org/10.1007/978-3-319-73411-8_38)

the Perth Basin within the Perth metropolitan area, including Osborne Formation, Molecap Greensand, Poison Hill Greensand and Kings Park Formation, are predominantly sandstones or siltstones which form the basement of the geological structure of the region.

In terms of a smaller scale geomorphic setting, the Perth metropolitan region is part of the Swan Coastal Plain which is a strip of around 34 km wide on the Indian Ocean coast, bonded to the east by the Gingin and Darling Fault Scarps [3]. In general, the superficial formations for the Swan Coastal Plain consist of:

- Ascot Formation of fine to coarse sand with a maximum thickness of 25 m in the southern and northern Perth areas, and is widespread as a basal unit of the superficial formations; Where present, the Ascot Formation lies unconformably on other cretaceous-Tertiary formations;
- Guildford Formation along the eastern margin of the Plain, over much of the eastern Perth region, and materials are dominated by silts and clays (mud) of up to 35 m thick;
- Bassendean Sand is present in the central area of the Plain, over much of the central Perth region, and materials are predominantly medium-grained sand, with a maximum thickness of about 80 m;
- Tamala Limestone extends along the coastal strip of the Perth region, consisting of a creamy-white to yellow, or light-grey, calcareous aeolianite. The upper surface of the limestone is generally exposed and leached to unconsolidated layer of sand.

Figure 1 shows a recent study result classifying the layers of unconsolidated solid material covering the bedrock basement into four main categories based on the dominant layer of material type and thickness, from the analysis of numerous geological borehole survey data within the central Perth region [4]. In general, the site classification results are in line with the superficial formations within the region recorded in the literature as described above.

Overlaying the existing Perth passenger rail network with the site classification map Fig. 1, it can be concluded that the majority of the rail routes are laying over ground with sandy ground conditions, particularly for the rail routes within the central area, and rail lines to the north and south.

## 2 Propagation of Ground Vibration

Vibration waves that propagate through an elastic solid ground can be classified into two general categories: body waves and surface waves.

Body waves, including compressional [i.e. dilatational/longitudinal or primary (P)] waves and shear [i.e. transverse or secondary (S)] waves, propagate through ground media. The two wave speeds,  $C_P$  and  $C_S$ , correspond to compressional and shear wave motions, are directly related to the elastic solid material properties:



Fig. 1 Site classes defined within the central Perth metropolitan region [4]

$$C_P = \sqrt{\frac{\lambda + 2\mu}{\rho}}; \quad C_S = \sqrt{\frac{\mu}{\rho}} \quad (2.1)$$

where  $\lambda$  and  $\mu$  are the Lamé constants:

$$\lambda = \frac{\nu E}{(1 + \nu)(1 - 2\nu)}; \quad \mu = \frac{E}{2(1 + \nu)} \quad (2.2)$$

$E$  is Yong's modulus,  $\nu$  is Possion's ratio and  $\rho$  is the density of the material. The compressional wave travels faster than the shear wave, as indicated in the comparison between the two speeds in (2.1).

For horizontally layered solid media, the shear wave contribution can be decomposed into the component in a horizontal plane (i.e. horizontal polarization, SH wave) and the component in a vertical plane (i.e. vertical polarization, SV wave), and their motions are completely uncoupled [5]. In such cases, only the SV wave is considered as it is most relevant to the vertical forces induced by rail system operations on the rail tracks.

Surface waves, including Rayleigh (R) waves and Love (L) waves, propagate only in the presence of a free boundary and parallel with the ground surface, with the wave amplitude decaying exponentially with depth [6]. Rayleigh waves are typically related to the P-SV wave component interactions, and are always generated when a free surface presents in a continuous body. However, Love waves are related to the SH wave component, and can exist only under certain restrictive layering conditions, where the shear wave velocity in the upper layer is less than that in the underlying half-space.

The Rayleigh wave velocity  $C_R$  can be approximately related to the shear wave velocity  $C_S$  as [7]:

$$\frac{C_R}{C_S} \approx \frac{(0.87 + 1.12\nu)}{(1 + \nu)} \quad (2.3)$$

Most materials have Poisson's ratio values ranging between 0.0 and 0.5. Therefore, from Eq. 2.3 the Rayleigh wave has a speed of 87–95% of the corresponding shear wave speed, depending on the Poisson's ratio of the material.

For the basic theoretical vibration propagation model for an idealized half-space homogeneous solid ground, the attenuation of vibration with distance comprises two components: radiation damping loss due to geometric spreading of each wavefront, and material damping losses as a result of energy dissipation in the ground medium [8, 9]. In general, the amplitude at a distance  $r$  from the vibration source  $A$  can be represented as [10]:

$$A(r : r_0) = \left(\frac{r_0}{r}\right)^n A_0(r_0) \exp(-\alpha(r - r_0)) \tag{2.4}$$

where  $A_0$  is the amplitude at a reference distance  $r_0$  from the vibration source,  $n$  is the spreading factor and  $\alpha$  is the material absorption coefficient. For material damping loss, it is assumed that the material absorption coefficient is linearly dependent on frequency:

$$\alpha = \pi \eta f r / C \tag{2.5}$$

where  $\eta$  the loss factor and  $C$  is the speed of the appropriate wave type under consideration. The attenuation of the vibration level  $L_A$  then can be presented as [9]:

$$\Delta L_A = 27.29 \eta f r / C \tag{2.6}$$

For the case of surface vibration propagation, Fig. 2 demonstrates different waves generated by the vertical oscillation of a flat plate on the ground surface as the surface point vibration source [11]. The resulting ground vibrations generate both Rayleigh waves and body waves. The body waves propagate radially outwards from the impact point along a hemispherical wave front, while the Rayleigh waves propagate radially outwards along a cylindrical wave front, with the normalized displacement amplitudes (mode shapes) as a function of depth shown in Fig. 2. Studies [12, 13] showed that Rayleigh waves are the dominant wave type for such surface vibration sources, typically 67% of the total input energy transmitted into Rayleigh waves, 26% of the input energy into shear waves, and the remaining 7% into compressional waves (Table 1).

The vibration propagation in layered ground is more complex as the layered structure of the ground has a significant effect on the propagation of both surface and body waves [14]. Numerical modelling based on specific software tools (e.g. [15]), with relevant model parameters inputs such as the layer depths, wave speeds

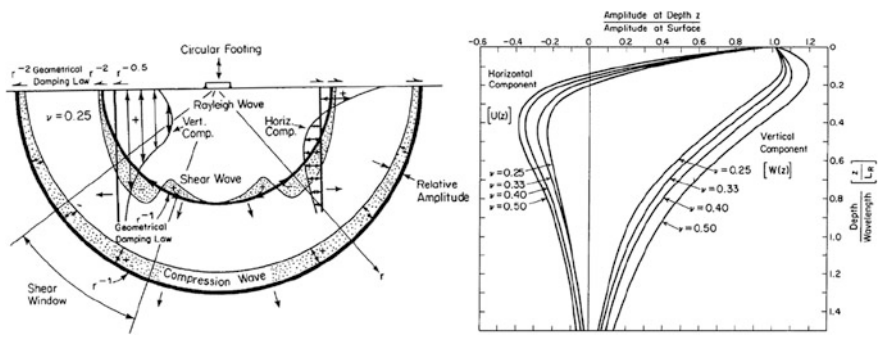


**Fig. 2** Left: distribution of displacement waves from a circular footing on a homogeneous elastic halfspace [11]; Right: Rayleigh wave normalized mode shapes of various Poisson's ratios in a homogeneous elastic halfspace [12]



**Table 1** Radiation damping/geometrical spreading laws for various basic vibration source models [9]

Geometrical spreading	Source model	Physical source examples	Wave type	Monitor location	Spreading factor, $n$
$\frac{1}{r^n}$	Line—surface	Highway/Rail line	Rayleigh	Surface	0
			Body	Surface	1
	Point—surface	Footing Impact	Rayleigh	Surface	0.5
			Body	Surface	2
	Line—buried	Rail Tunnel	Body	Interior	0.5
	Point—buried	Buried Explosion	Body	Interior	1

and ground material damping, is normally undertaken to illustrate the vibration propagation mechanisms within layered ground. Site vibration transmission tests are generally performed in order to determine ground soil properties as well as to validate the modeling predictions [9].

### 3 Empirical Propagation Model for Passenger Rail Systems at Grade

SLR has undertaken numerous measurements on the surface ground vibration from passenger rail operations at grade within the central Perth metropolitan area, predominantly within the areas of East Perth and Burswood where the sandy soils are the dominant ground type, as described in Sect. 1. The measurements were undertaken at various distances from the track centerline with trains travelling at various speeds. For each train pass-by, the maximum root-mean-square (RMS) vibration velocity level of one-second duration ( $L_{v,RMS,1s}$ , dB re 1 nm/s) was recorded and then corrected to reference train speed of 80 km/h, based on the following speed adjustment factor [16]:

$$adjustment(dB) = 20\log_{10}(speed/speed_{ref}) \tag{3.1}$$

For each measurement location, the 95th percentile of the vibration levels was then derived based on measurements of multiple train pass-by events.

Figure 3 presents the maximum one-second RMS vibration velocity levels  $L_{v,RMS,1s}$  from the passenger rail pass-bys at multiple measurement distances from the track centerline for metro Perth. The 3rd order polynomial regression of the 95th percentile vibration velocity levels, with extrapolated values extending to the distance range of five to 50 m from the track centerline, is also plotted in the figure.

For comparison, results of similar vibration measurements undertaken from passenger rail operations at grade within the central Sydney metropolitan area are also presented in Fig. 3. As recorded in the literature, the Sydney sandstone,

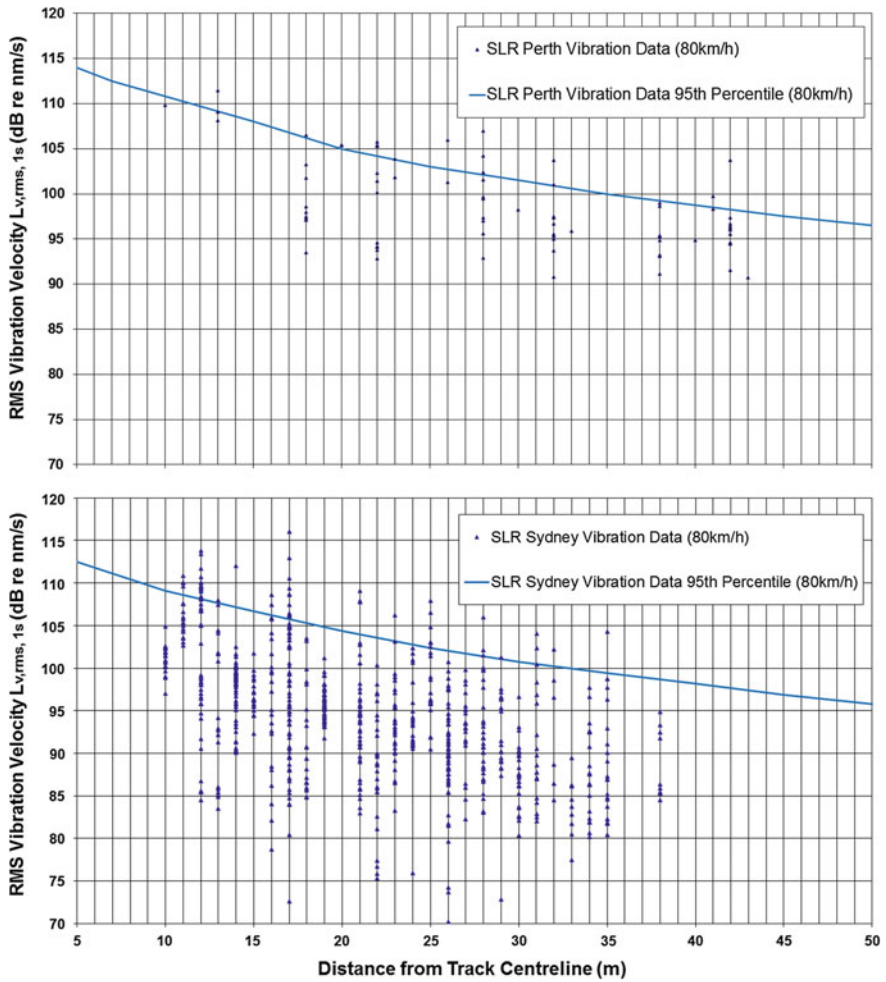


**Fig. 3** Vibration levels from surface passenger rail operations within Perth (top) and Sydney (bottom) metropolitan area, and the polynomial regression (3rd order) of 95th percentile vibration levels versus distance from the track centerline

namely the Sydney Basin Hawkesbury Sandstone, forms the ground foundation for much of the region of Sydney [17, 18]. As for any typical ground conditions, a top layer of unconsolidated ‘weathered’ material [10] is still expected for the Sydney region.

As evidenced in Fig. 2, Rayleigh waves are the dominant wave type for the rail systems at grade when the measurement locations are also on the ground surface.

In fitting the regression curves of the 95th percentile vibration levels into the basic propagation model as described in the Formula (2.4) for the two regions, cylindrical spreading is assessed as the best fit spreading law for both cases, so that

**Table 2** Ground conditions and ground vibration model parameters for passenger rail system at grade within the central metropolitan regions of Perth and Sydney

Region	Ground conditions	Spreading factor, $n$	Dominant 1/3-octave frequency band, Hz	Rayleigh wave speed, m/s	Loss factor, $\eta$
Perth	Sandy soils with Sandstone basement	1 (Cylindrical Spreading)	32	150–350	0.027–0.062
Sydney	Sandstone foundation with top ‘weathered’ unconsolidated layer		50	200–300	0.018–0.027

the remaining damping loss in general varies linearly with distance from the track centerline.

Comparisons between ground condition and the resulted basic vibration model parameters for passenger rail system at grade for the region of Perth and Sydney are summarized in Table 2.

The vibration spectral data from the measurements show that, for Perth region, the 1/3-octave band with center frequency of 32 Hz generally dominates the vibration spectra, while for Sydney region the highest energy predominantly lays within the 1/3-octave band with center frequency of 50 Hz. Based on historical surface shear wave velocity measurements [19] and Rayleigh-shear wave speed relationship Formula (2.3), the Rayleigh wave speeds within the region of Perth are estimated as the range 150–350 m/s and for region of Sydney as the range 200–300 m/s.

In accordance with Formula (2.6), the loss factor for the ground material within the Perth region is estimated to be the order of 0.027–0.062, which roughly reflects published attenuation characteristics of sandy soil [9]. The loss factor of 0.018–0.027 is estimated for the ground material within the Sydney region and is closer to the loss factor for rock materials [9], distinctively lower than that of the sandy soil in Perth.

## 4 Borehole Vibration Attenuation Measurements

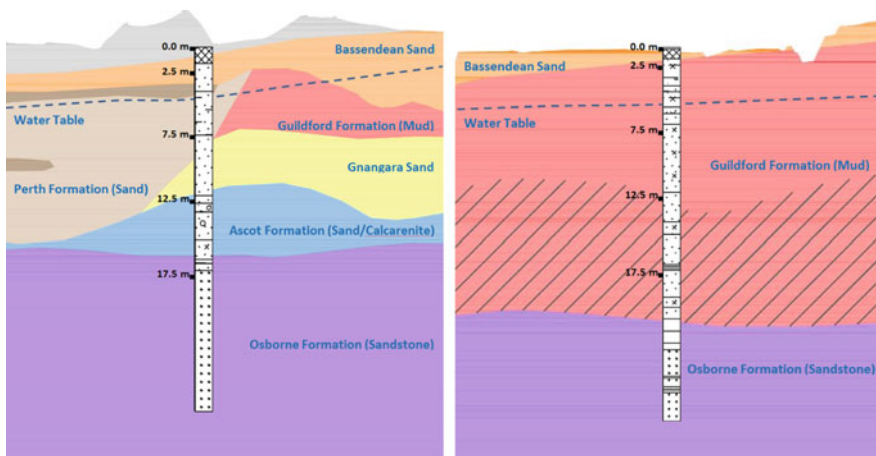
To investigate vibration propagation and attenuation specifically for local sandy soil conditions, borehole vibration attenuation testing was undertaken at several sites east of Perth. The measurement setup comprised a 40 kg weight dropped from a height of 1.5 m to strike the ground, with a Down Hole Accelerometer Clamping (DHAC) system equipped with an accelerometer to measure the vibration response and a hydraulic expansion plate used to rigidly clamp the system in place within the borehole at the depth of interest. A surface reference accelerometer was also mounted at a location near the ground vibration source position.

Figure 4 presents the two boreholes tested at four depths (2.5, 7.5, 12.5 and 17.5 m), with their corresponding local geotechnical layer and water table information. As can be seen, for both locations the ground conditions vary in sand type, particularly along the vertical borehole columns. In general, the borehole columns comprised various sandy materials above the sandstone basement.

The measured acceleration waveforms from the testing vibration source at five geophone locations (top to bottom—surface location, locations at depths of 2.5, 7.5, 12.5 and 17.5 m) and their corresponding spectrograms are illustrated in Fig. 5. Based on the vibration signal arrival time differences measured at the four vertical measurement depths of the first borehole, as marked up in the Fig. 5, the average compressional wave speed  $C_P$  is approximately 1.68 km/s, and the average shear wave speed  $C_S$  is approximately 0.63 km/s. The high compressional wave speed for the sandy layers is expected to be due to their saturated conditions with the presence of low-depth ( $\sim 4.5$  m) water table below the local ground [20], as shown in Fig. 4.

The received average one-third octave vibration velocity spectral levels for the two boreholes as in Fig. 5 are presented in Fig. 6. Combined with the local ground conditions of the two boreholes, the corresponding vibration level variations over the testing depths clearly illustrate the significant effects on the vibration attenuation due to the distinctive ground layer presence.

At the two borehole locations, due to the dominant Rayleigh wave propagation, significantly higher vibration levels were recorded at the surface location throughout the frequency range. Relatively higher vibration levels were received at the location of 2.5 m for the frequency range above 50 Hz, as a result of the combination of Rayleigh wave propagation and body wave reflection from the water table.



**Fig. 4** The two boreholes to be tested with four testing depths (2.5, 7.5, 12.5 and 17.5 m) and the local geotechnical layers and groundwater table information

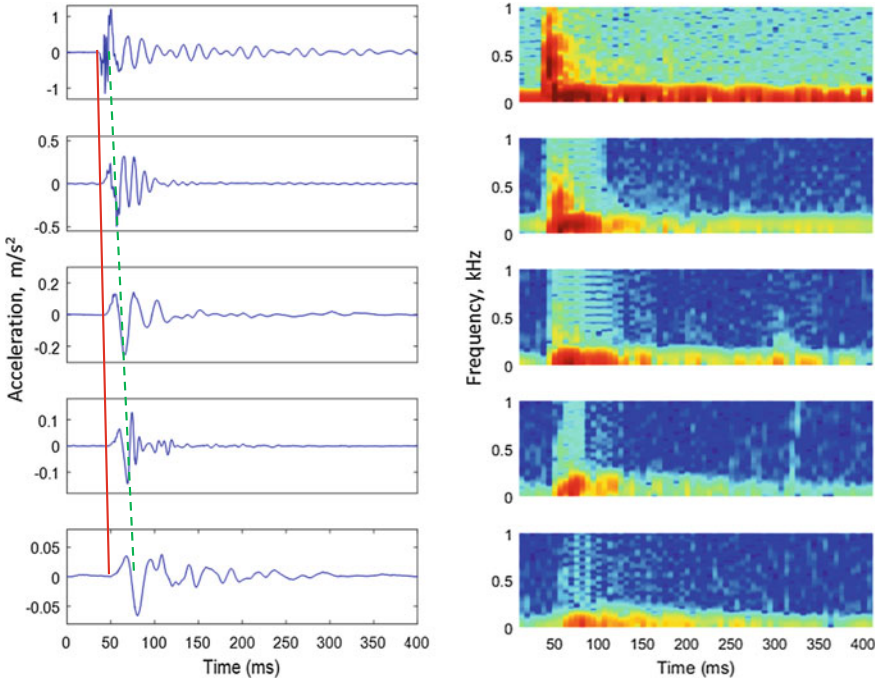


**Fig. 5** Left—measured acceleration waveforms at five geophone locations (from top to bottom—surface location, borehole locations at depths of 2.5, 7.5, 12.5 and 17.5 m), and vibration signal arrival time differences for compressional waves (red) and shear waves (blue); Right—spectrograms of the corresponding waveforms

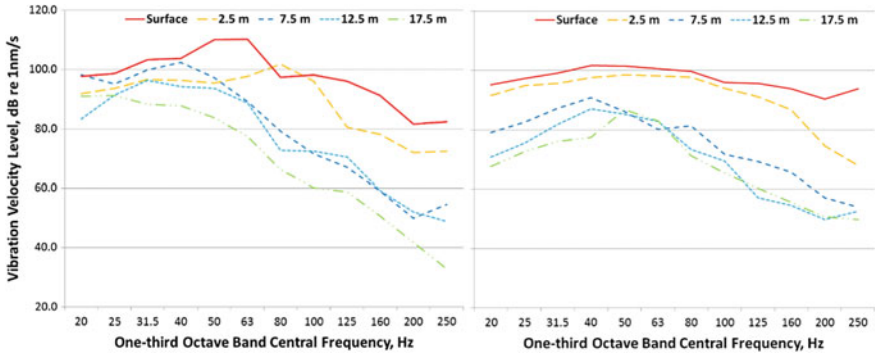


**Fig. 6** Received average vibration velocity one-third octave spectral levels (dB re 1 nm/s) at five geophone locations (surface location and borehole locations at depths of 2.5, 7.5, 12.5 and 17.5 m) for the two testing boreholes

The presence of sandstone basement at the first borehole location at a depth of approximately 16 m causes the received vibration levels at the depth of 17.5 m noticeably lower than the levels at depth of 7.5 and 12.5 m over the entire frequency range. This vibration level contrast, however, doesn't occur at the second borehole location, as the testing depth of 17.5 m is within the same sandy layer as the depth of 12.5 m at this location.

Further analysis also shows that the vibration attenuation versus distance from the vibration source demonstrates no clear correlation with the spreading loss over the frequency range, which indicates that, the presence of distinctive ground layers and influence of Rayleigh wave propagations distort significantly the vibration level variations over the ground depth. Detailed ground vibration propagation in such layered ground can be further investigated based on numerical modelling [15, 21] and is considered for future work.

## 5 Conclusions and Discussions

A review of relevant literature shows that layered sandy soils are the dominant superficial ground conditions for the majority of the central metropolitan region of Perth, Western Australia.

Rayleigh waves are the dominant wave type for the rail system operations at grade when the measurement locations are also on the ground surface. On this basis, the principal vibration propagation for passenger rail operations at grade in the Perth region can be estimated with the basic theoretical model as described in the Formula (2.4), with the model parameters being derived empirically based on numerous measurements on the flat surface ground vibration from passenger rail operations within the central Perth metropolitan area.

To investigate ground vibration attenuation characteristics from the underground rail systems during construction and operation phases, borehole vibration measurements with vibration testing source on the surface can be undertaken based on the principle of reciprocity. Results from borehole vibration testing at two specific borehole locations east of Perth demonstrate that the presence of distinctive ground layers including water table and sandstone basements (which are the common features for the ground conditions over the majority of the Perth region) combined with the Rayleigh wave mode shape penetrations over the ground layers, cause complex vibration wave fields which could not be possible to be depicted based on basic theoretical model. Advanced numerical modelling (e.g. [21]) is suggested to be undertaken for the prediction and validation process and is considered for future work.

## References

1. Playford, P.E., Cockbain, A.E., Low, G.H.: Geology of the Perth Basin Western Australia. *Geol. Soc. W. Aust. Bull.* **124** (1976)
2. Cadman, S.J., Vuclovic, V.: Perth Basin, WA. Australian Petroleum Accumulations Report 10, Bureau of Resources Sciences, Canberra (1994)
3. Davidson, W.A.: Hydrogeology and groundwater resources of the Perth region, Western Australia. *W. Aust. Geol. Surv. Bull.* **142** (1995)
4. McPherson, A., Jones, A.: Appendix D: Perth Basin geology review and site class assessment. In: Jones, T., Middelman, M., Corby, N. (compilers) *Natural Hazard Risk in Perth, Western Australia*. pp. 313–344. Geoscience Australia, Canberra (2005)
5. Brekhovskikh, L.M., Godin, O.A.: *Acoustics of Layered Media I—Plane and Quasi-Plane Waves*, Springer Series on Wave Phenomena, Series Volume 5. Springer, Berlin (1990)
6. Foti S.: Multistation methods for geotechnical characterization using surface Waves. Ph.D. thesis, Chapter 3 Rayleigh Waves (2000)
7. Achenbach, J.D.: *Wave Propagation in Elastic Solids*. North-Holland, Amsterdam (1973)
8. Richart, F.E., Hall, J.R., Woods, R.D.: *Vibrations of Soils and Foundations*. Prentice-Hall, Englewood Cliffs, New Jersey (1970)
9. Gutowski, T.G., Dym, C.L.: Propagation of ground vibration: a review. *J. Sound Vib.* **49**(2), 179–193 (1976)
10. Thompson, D.: *Railway Noise and Vibration: Mechanisms, Modelling and Means of Control*, 1st edn. Elsevier, Oxford (2009)
11. Lamb, H.: On the propagation of tremors over the surface of an elastic solid. *Philos. Trans. R. Soc. A* **203**, 1–42 (1904)
12. Miller, G.F., Pursey, H.: On the partition of energy between elastic waves in a semi-infinite solid. *Proc. R. Soc. Lond. Ser. A Math. Phys. Sci.* **233**(1192), 55–69 (1955)
13. Woods, R.D.: Screening of elastic surface waves by trenches. *J. Soil Mech. Found. Div. ASCE* **94**(4), 951–979 (1968) (July)
14. Ewing, W.M., Jardetzky, W.S., Press, F.: *Elastic Waves in Layered Media*. Graw-Hill Book Company INC, New York (1957)
15. Schevenels, M., François, S., Degrande, G.: An ElastoDynamics toolbox for MATLAB. *Comput. Geosci.* **35**(8), 1752–1754 (2009)
16. FTA: Transit noise and vibration impact assessment, U.S. Department of Transportation Federal Transit Administration (2006)
17. Rust, B.R., Jones, B.G.: The Hawkesbury Sandstone south of Sydney, Australia; Triassic analogue for the deposit of a large, braided river. *J. Sediment. Res.* **57**(2), 222–233 (1987)
18. Flannery, T. (ed.): *The Birth of Sydney*, Melbourne. The Text Publishing Company (1999)
19. Collins, C., Kayen, R., Carkin, B., Allen, T., Cummins, P., McPherson, A.: Shear wave velocity measurement at Australian ground motion seismometer sites by the spectral analysis of surface waves (SASW) method. In: *Earthquake Engineering in Australia*, Canberra, 24–26 Nov 2006
20. Keceli, A.: Soil parameters which can be determine with seismic velocities. *Jeofizik* **16**, 17–29 (2012)
21. Degrande, G., Lombaert, G.: Wave propagation in layered ground, RIVAS Training Workshop—“Reducing railway induced ground vibration by interventions on the transmission path”, Berlin, 23 May 2013

# Modelling of Ground-Borne Vibration When the Train Speed Approaches the Critical Speed



J. Y. Shih, David J. Thompson and A. Zervos

**Abstract** When trains run on soft ground, large deflections of the track and vibration of the ground can occur when the train speed approaches the speed of Rayleigh waves in the ground. Modelling is helpful to understand and mitigate such critical velocity effects. Here, a three-dimensional time-domain model of a load moving on a track and ground has been developed with the finite element software ABAQUS. This allows nonlinear soil properties to be considered. In order to validate the approach, the vibration of the track and ground induced by a high speed train is compared with those from the site measurements carried out in the late 1990s at Ledsgård, Sweden. Due to the particularly soft soil at this site, it is necessary to adopt a nonlinear soil model due to the large deflections induced by the high-speed train. It is shown that using a linear model based on the small strain soil parameters leads to results which underestimate the displacements. Laboratory test data allow the nonlinear characteristics to be obtained. These have previously been used by various authors in an equivalent linear model. Here this approach is compared with a fully nonlinear model.

## 1 Introduction

Due to the demands of increasing population as well as environmental concerns, there is an urgent need for higher train speeds and increased capacity of the railways in many countries. As the train speed increases, however, track deflections can become larger. Particularly large displacements can occur when the speed of the train approaches the speed of waves in the ground and embankment, known as the

---

J. Y. Shih (✉) · D. J. Thompson

Faculty of Engineering and the Environment, Institute of Sound and Vibration Research,  
University of Southampton, Southampton SO17 1BJ, UK  
e-mail: j.shih@bham.ac.uk

A. Zervos

Infrastructure Research Group, Faculty of Engineering and the Environment,  
University of Southampton, Southampton, UK



critical velocity. These large displacements may lead to damage of the track components and may cause environmental impact for the neighbourhood. As a result, good design of high-speed railways depends on an accurate assessment of such critical velocity effects so that they can be avoided. In addition, better understanding of the stresses in the subgrade and the amplitudes of vibration of the whole system can lead to reductions in the cost of maintenance and an improvement in the quality of the railway system.

A number of theoretical models have been developed by various authors in an attempt to understand and predict such phenomena. Approaches adopted include semi-analytical models [1–4] and numerical models [5–11] based on finite element and boundary element approaches. Both frequency domain [1–4, 6, 8, 9] and time domain [5, 7, 10, 11] approaches have been considered. In predicting environmental ground vibration from trains, linear elastic models of the soil are normally used, which is generally justified by the fact that the strains are small. However, when the track deflections increase, as the train speed approaches the critical velocity, nonlinear effects may become important [2, 3, 6], especially in the region near the track. Of particular interest in this regard is the soft soil site at Ledsgård, south of Gothenburg in Sweden, where field tests were carried out in the late 1990s with trains running at or near the critical velocity [2, 3] as well as extensive soil investigations [5, 6].

According to laboratory tests, soil stiffness depends on cyclic strain amplitude, as well as a number of other factors such as mean principal effective stress, plasticity index, void ratio, over-consolidation ratio, and the number of loading cycles [12]. It is particularly important, in modelling nonlinear soil behaviour, especially at shear strains larger than  $\sim 10^{-5}$ – $10^{-4}$ , to determine the dependence of the shear modulus on the strain [13]. With increased strain level, reductions in soil stiffness (stiffness degradation) and increases in damping ratio are obtained using cyclic triaxial tests [12, 14–16] and can be described by a shear modulus reduction curve and corresponding curve of damping ratio as a function of shear strain.

To include these effects in a model of the track and ground, several authors have used equivalent linear models [2, 3, 5, 6, 17]. An equivalent linear model involves an iterative procedure that can approximate nonlinear behaviour efficiently and can be more numerically stable than a fully nonlinear calculation. From an initial calculation, an ‘effective’ shear strain is determined from the time-varying strains. This is then used with the measured curves of shear modulus and damping at different shear strains to calculate updated values of the shear modulus and damping ratio applying to the motion. The model is run again until the strains obtained correspond to the assumed modulus. The effective shear strain used in this process is chosen as a proportion of the maximum strain in order to characterise the motion. From seismic tests a value of 0.65 times the maximum shear strain is used for this purpose [12]. In [2, 3, 5] such an equivalent linear model was used for the soft soil site of Ledsgård and good agreement was found with site measurements of track deflections. In these models, however, the stiffness reduction, based on an approximate effective strain level, was applied to all elements within a given soil layer. A more advanced approach was implemented by Costa et al. [6] in which the shear modulus

was adjusted according to the maximum effective shear strain in each element of the 2D cross-section, resulting in a transverse inhomogeneity in the ground. It was found that a number of iterations were required to reach a value of shear modulus that was consistent with the corresponding strain level. This approach gave good agreement with the measurements.

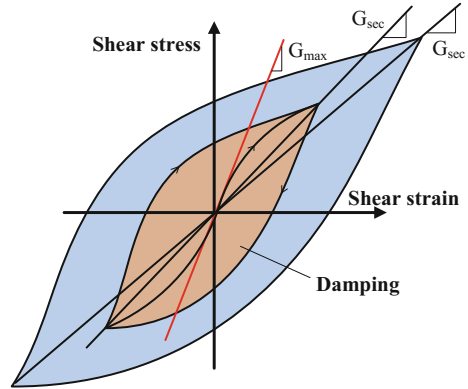
The nonlinear stress-strain behaviour of soils can be represented more accurately by cyclic nonlinear constitutive models that follow the actual stress-strain path during cyclic loading. This behaviour can be characterized by a backbone curve and a series of rules that govern unloading-reloading behaviour, stiffness degradation, and other effects such as irregular loading, densification, pore pressure generation, etc. A popular cyclic model was given by Iwan [18] based on a series of parallel Jenkin elements, which consist of a linear spring in series with a frictional slider, to describe the backbone curve and the yield level. This model was adopted by Gomes Correia and Cunha [19] to study the effect of subgrade nonlinearity on the track response induced by a high-speed train. Such cyclic models can represent the development of permanent strains, hardening under drained conditions or stiffness degradation under undrained conditions due to pore pressure development. A more complex nonlinear model was used by Fernandes [20] to represent the ballast and soil nonlinearity beneath a railway track. The dynamic response after five cycles of loading due to moving axles was obtained and permanent displacements were modelled for understanding the behaviour of the soil and ballast degradation. However, the model is very complex and requires many parameters to construct the soil constitutive model.

A simpler nonlinear model is introduced here that is based on the shear modulus reduction curve. At each time step the soil stiffness in each element is determined based on the instantaneous octahedral shear strain. This is implemented in a user-defined subroutine within the software ABAQUS. Plastic behaviour is not considered here as it can be considered to be small compared with the transient dynamic deflections and the objective of the present work is not to study track settlement. Finally, the results are compared with site measurements from Ledsgård [6]. The influence of the soil nonlinearity on the critical speed and stress-strain behaviour for the embankment and ground is investigated when the train speed approaches the critical speed.

## 2 Nonlinear Soil Model

During cyclic loading, the soil stress-strain behaviour typically follows a nonlinear hysteresis loop, as shown in Fig. 1. The slope of the stress-strain curve can be identified as the soil stiffness; when it is loaded in shear this is the shear modulus. The dissipation energy, which is related to the damping ratio, can be determined from the area of the loop. The secant shear modulus is defined in terms of the maximum values of stress and strain as indicated in Fig. 1. As the amplitude of the loading increases, this modulus reduces in the example shown, with the maximum

**Fig. 1** Shear stress-strain path during cyclic loading



shear modulus occurring for very small amplitudes. The ratio of the secant shear modulus at a given strain level to the maximum shear modulus can be identified as the shear modulus reduction associated with this amplitude. Figure 2a shows shear modulus reduction curves obtained from cyclic triaxial tests at different amplitudes, for material samples obtained at Ledsgård [6]. In contrast to the stiffness, the damping ratio tends to increase when the strain level increases, as shown in Fig. 2b.

A new material constitutive model has been developed in a user subroutine UMAT in the commercial finite element program, ABAQUS, based on shear modulus reduction curves such as these. This subroutine operates on each integration point by receiving variables such as the incremental strain vector and the previous stress vector, and returns the current stress vector and updated Jacobian matrix (current tangent modulus matrix). The new Young’s modulus is obtained from the modulus reduction curve which is given in terms of the shear strain value. However, due to the fact that a moving train induces a complex three-dimensional deflection which involves multiple strain components, the octahedral shear strain is used as the strain index to evaluate the value of modulus reduction for each time step. This is given by

$$\gamma_{oct} = \frac{1}{3} \sqrt{(\epsilon_{xx} - \epsilon_{yy})^2 + (\epsilon_{yy} - \epsilon_{zz})^2 + (\epsilon_{xx} - \epsilon_{zz})^2 + 6(\gamma_{xy}^2 + \gamma_{yz}^2 + \gamma_{xz}^2)} \quad (2.1)$$

From the new Young’s modulus, determined from the modulus reduction curve, the new constitutive matrix

$$[D] = \begin{bmatrix} \lambda + 2\mu & \lambda & \lambda & 0 & 0 & 0 \\ \lambda & \lambda + 2\mu & 0 & 0 & 0 & 0 \\ \lambda & \lambda & \lambda + 2\mu & 0 & 0 & 0 \\ 0 & 0 & 0 & \mu & 0 & 0 \\ 0 & 0 & 0 & 0 & \mu & 0 \\ 0 & 0 & 0 & 0 & 0 & \mu \end{bmatrix} \quad (2.2)$$

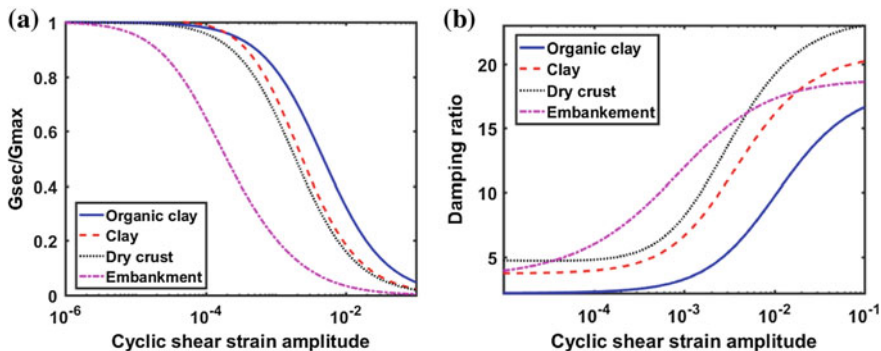


**Fig. 2** Nonlinear soil characteristic from Ledsgård **a** shear modulus reduction curve; **b** damping ratio [6]

is obtained, in which

$$\lambda = \frac{\nu E}{(1 + \nu)(1 - 2\nu)}; \quad \mu = \frac{E}{2(1 + \nu)} \tag{2.3}$$

with  $E$  the Young’s modulus and  $\nu$  the Poisson’s ratio. The stress matrix is then updated for the next time step  $i + 1$  based on this new tangent constitutive matrix

$$\{\sigma\}_{i+1} = [D]_i \{\varepsilon\}_i \tag{2.4}$$

and the strain which is updated by the strain increment  $d\varepsilon$

$$\{\varepsilon\}_i = \{\varepsilon\}_{i-1} + \{d\varepsilon\}_i \tag{2.5}$$

The stress and strain vectors are given by

$$\{\sigma\} = \{ \sigma_{xx} \quad \sigma_{yy} \quad \sigma_{zz} \quad \tau_{xy} \quad \tau_{yz} \quad \tau_{xz} \}^T \tag{2.6}$$

$$\{\varepsilon\} = \{ \varepsilon_{xx} \quad \varepsilon_{yy} \quad \varepsilon_{zz} \quad \gamma_{xy} \quad \gamma_{yz} \quad \gamma_{xz} \}^T \tag{2.7}$$

Changes to the damping ratio are not considered here. A constant damping ratio is used based on Rayleigh damping. In this approach the damping matrix is proportional to the mass and stiffness matrices with the factors  $\alpha$  and  $\beta$  as follows

$$[C] = \alpha[M] + \beta[K] \tag{2.8}$$

To determine  $\alpha$  and  $\beta$ , two frequencies,  $\omega_1$  and  $\omega_2$ , are chosen at which the target damping ratio  $\zeta$  is to be matched. Then

$$\alpha = \frac{2\xi\omega_1\omega_2}{\omega_1 + \omega_2}, \quad \beta = \frac{2\xi}{\omega_1 + \omega_2} \quad (2.9)$$

The mass-proportional component of damping can be incorporated directly in the ABAQUS FE code for built-in constitutive models and is assumed not to vary with strain level. However, for a user-defined material, the stiffness-proportional damping must be incorporated in the user-defined material subroutine, UMAT. This can be achieved by adding the corresponding stress term, where  $\beta$  is assumed constant:

$$\{\sigma_d\}_{i+1} = \beta[D]_i\{\dot{\epsilon}\}_i \quad (2.10)$$

where  $\dot{\epsilon}$  is the strain rate, to the stress resulting from the elastic responses at each integration point. As a result, the total stress can be calculated by

$$\{\sigma_T\}_{i+1} = \{\sigma\}_{i+1} + \{\sigma_d\}_{i+1} \quad (2.11)$$

### 3 Numerical Model

#### 3.1 FE Model

A three-dimensional FE model has been constructed of the track and ground at the site at Ledsgård. Soil properties are available from various in situ tests, including cross-hole, SASW and SCPT tests [5, 6]. In addition to the embankment, three main soil layers were identified, referred to as dry crust, organic clay, and clay. Measured shear wave speeds as a function of depth are shown in Fig. 3a along with the values assumed here. The lower clay layer is assigned a shear wave speed that varies with depth. The material properties used for the various layers are listed in Table 1.

The FE mesh is shown in Fig. 3b. Use is made of symmetry about the track centreline. It has been found that, provided that the model is large enough, there is

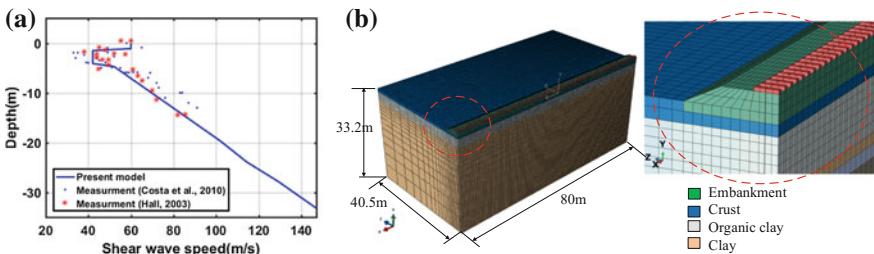


**Fig. 3** Soil and railway embankment geometry and shear wave speed at Ledsgård based on soil investigations; **a** shear wave speed profile; **b** three-dimensional track/ground FE model

**Table 1** Embankment/ground properties

	Thickness (m)	P-wave speed (m/s)	S-wave speed (m/s)	Density (kg/m <sup>3</sup> )	Damping ratio (%)
Embankment	1.4	470	250	1800	12
Crust	1.1	500	60	1500	7
Organic clay	3.0	500	42	1250	4
Clay	29.1	1500	50–122.9	1470	7

no benefit in using absorbing elements at the boundaries [21]. A cuboid model with fixed boundaries with a width of 40.5 m and a depth of 33.2 m is used. A damping model with a sufficiently large mass-proportional term should be used, allowing the energy to be dissipated sufficiently to avoid the reflections interrupting the results [21]. The target damping ratios for the four different materials are listed in Table 1. Rayleigh damping coefficients are obtained from Eq. (2.10) for target frequencies of 3 and 20 Hz. This frequency range is chosen to correspond to region where the measured vibration spectra close to the track has its maximum [5, 6]. The length of the model required to achieve steady state depends on the load speed [21], with longer models required if the load speed approaches or exceeds the critical speed. Here, an 80 m long model is used which is found to be sufficient for convergence.

Fully-integrated quadratic cuboid elements are used for the whole ground model. Linear Timoshenko beam elements are used for the rail. To represent the railpads linear springs with stiffness  $4.7 \times 10^8$  N/m are used to connect the rail to each sleeper. Discrete sleepers with a spacing of 0.67 m are considered. The half-sleeper length, height, mass density, Young's modulus and Poisson's ratio are 1.3 m, 0.2 m, 2500 kg/m<sup>3</sup>,  $3 \times 10^{10}$  N/m<sup>2</sup> and 0.15, respectively. The ballast is included in the embankment layer and this in turn is embedded to a depth of 0.4 m into the upper ground layer. The smallest element size is set to be 0.5 m in the vicinity of the track, which is sufficient for accurate modelling of local deflections up to around 50 Hz. However, the element size is increased gradually with a stretch factor of 1.2 in both the vertical and horizontal directions, as shown in Fig. 3b. This prevents the mesh size becoming too large and has been shown to be acceptable provided that far field wave propagation does not occur. The total number of degrees of freedom is 1.76 million.

### 3.2 Results for Moving Loads

Results are presented for moving axle loads, i.e. neglecting surface roughness excitation. Details of the train, X2000, are available from the literature [6]. Multiple loads are applied on the rail at the locations of the various axles and these are moved along the track according to the train speed. For the northbound train, with the locomotive leading, only two vehicles (eight axles) are considered, because the

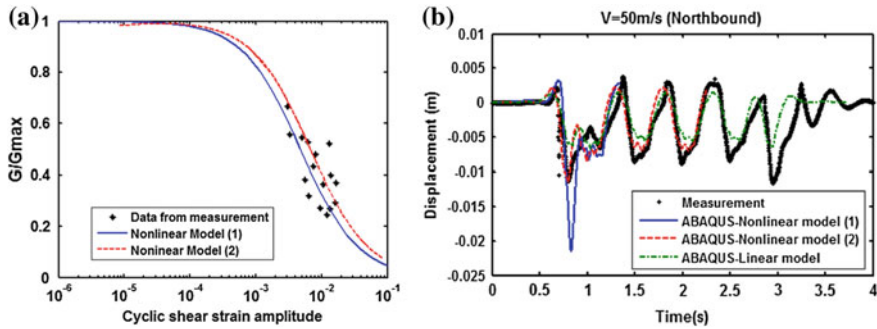


**Fig. 4** Nonlinear model; **a** shear modulus reduction curve for organic clay layer; **b** displacement comparison between linear, nonlinear models and measurement for load speed 50 m/s (northbound)

maximum deflections occurred for the front vehicle. However, the full train set is considered for analysis of the southbound direction. For linear analysis a single moving load is used with superposition to determine the response to the whole train.

The parameters for the organic clay are the most important for the behaviour of the whole system as this is the softest layer, see Table 1. Measurement data for this material, obtained from triaxial tests [6], is shown in Fig. 4a in the form of the shear modulus reduction. Two fitted lines are given which are used in the material constitutive model described in Sect. 2 to represent the soil nonlinearity. These two nonlinear models as well as a linear model based on the unreduced parameters in Table 1, are compared with the measurements. Results for a train speed of 50 m/s are shown in Fig. 4b. Good agreement with the measurements is found by using the second nonlinear model, which is slightly stiffer than the first one. The peak deflection from the first nonlinear model is almost double that from the second one. When the first load is suddenly applied, large strains occur in the surface layers immediately beneath the load, leading to stiffness degradation and particularly high track deflections for the softer nonlinear model 1. This deflection spreads into adjacent areas of the soil so that the region of influence increases and the local strains are lower for the later axle loads, leading to smaller stiffness degradation. On the other hand, the results from the linear model tend to be too small compared with the measurement.

The maximum upward and downward displacements for different train speeds are shown in Fig. 5a. Results are shown from the site measurements, the linear model and the second nonlinear model. The critical speed, at which the maximum deflection occurs, is found at around 55–60 m/s. A similar value is also found in the literature [2, 3, 6]. Good agreement is found with the nonlinear model. The maximum displacement at the critical speed, at around 15 mm, is roughly double the result due to the static load. On the other hand, the linear model predicts a critical speed of around 70 m/s, which is  $\sim 15\%$  higher than the results from the nonlinear model. Furthermore, the maximum deflections close to the critical speed are much

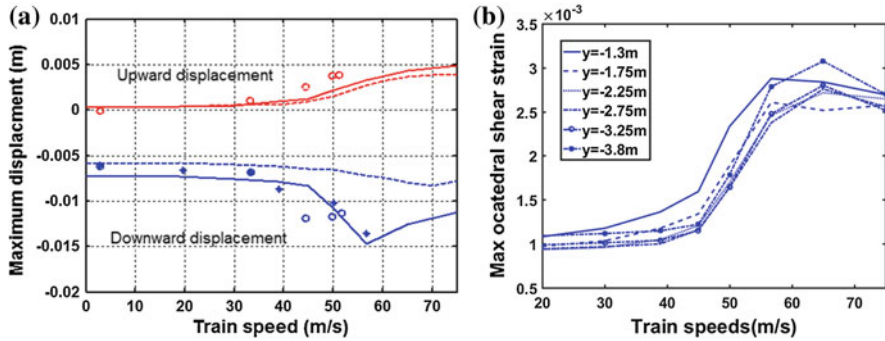


**Fig. 5** Assessment of critical speed; **a** displacement -: nonlinear model; - - -: linear model; o: northbound measurement data; \*: southbound measurement data; **b** maximum octahedral strain level for organic clay layer at different load speed

smaller than for the nonlinear model. It is clear that soil nonlinearity should be considered for this site at the higher train speeds, although the results from the linear model agree reasonably well with the measurement for speeds lower than 40 m/s.

Figure 5b shows the maximum octahedral shear strains at different depths within the organic clay layer obtained from the nonlinear model for different train speeds. The strain level increases significantly when the load speeds are higher than around 45 m/s. Furthermore, the strain level at higher speeds is around three times larger than the results at low speed. Comparing these values with the modulus reductions curves in Fig. 4a it can be seen that the modulus will be reduced to between 90 and 70% of the small strain stiffness (according to model 2).

The maximum octahedral shear strains are shown in Fig. 6 as a function of the depth for two different train speeds. Results are shown for linear and nonlinear models. As can be seen, the strain levels are typically  $10^{-3}$  which is too large to allow use of the small strain approximation (see Fig. 4a). Nevertheless, for the load speed of 19 m/s, the results of the linear and nonlinear models are very similar, except at the embankment. Figure 7a compares the track deflections under the train with measurements, showing good agreement even for the linear model. In contrast, as shown in Fig. 7b, for a train speed of 56.7 m/s the results from the linear model are around 40% smaller than the measurements whereas the nonlinear model gives good agreement. Figure 6b shows that the strain level in the organic clay layer is around 30% higher for the nonlinear model than the linear model.

Finally, the octahedral shear strain at the top surface of the organic clay layer for a load speed at 56.67 m/s is shown in Fig. 8. The strain level from nonlinear model is not only larger than the result from the linear model but the shape of the propagation is different. A clear wave shaped pattern occurs for the nonlinear model. This is because the load speed is higher than the wave speed in the ground, whereas for the linear model it is still below the critical speed. Furthermore, even though the



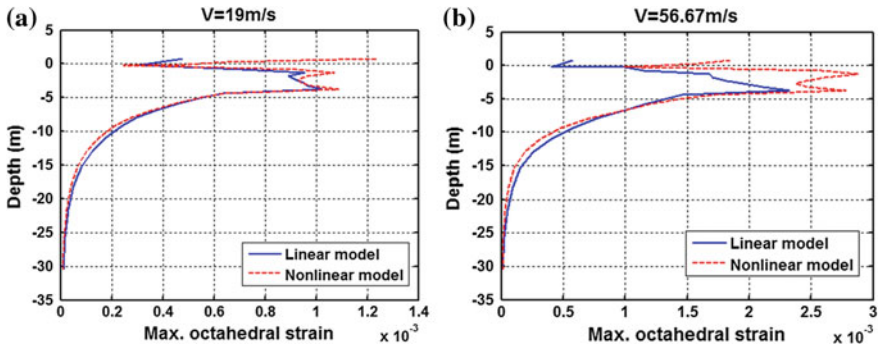


Fig. 6 Maximum octahedral shear strain against depth from northbound analysis for two different load speeds; a 19 m/s; b 56.7 m/s

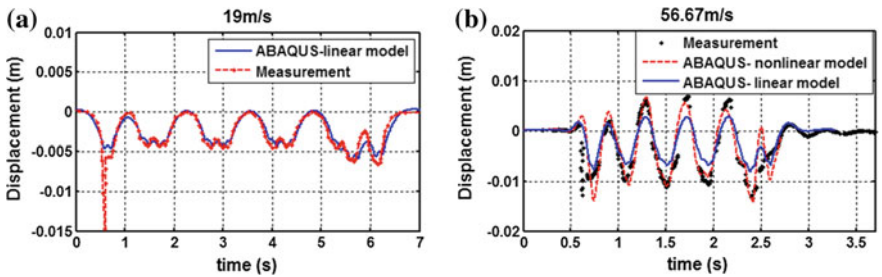


Fig. 7 Displacements for southbound train for two different speeds; a 19 m/s; b 56.7 m/s

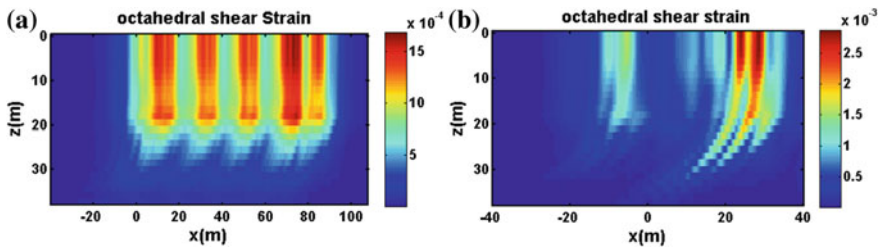


Fig. 8 Octahedral shear strain from linear and nonlinear model at load speed 56.67 m/s (Northbound); a linear model; b nonlinear model

strain level decreases significantly away from the track, octahedral shear strains of around  $10^{-3}$  still can be found at 30 m away from the track for the nonlinear model, as shown in Fig. 8b.

## 4 Conclusions

A three-dimensional vehicle/track/ground model that includes soil nonlinearity has been developed that operates in the time domain. Soil nonlinearity has been implemented within the FE model in terms of shear modulus degradation. Good agreement has been found compared to site measurements at the soft soil site in Ledsgård, Sweden. The effect of soil nonlinearity becomes significant at this site when the load speeds approach or exceed the critical speed. The maximum track displacements for load speeds close to the critical speed are around twice those found at lower speeds. The maximum strain levels in the subgrade increase by around a factor of three.

The critical speed obtained from the linear model is higher than that obtained from the nonlinear model. The displacements from the linear model are underestimated, especially for speeds approaching the critical speed. Nevertheless, good agreement is found for lower speeds. Two different shear modulus reduction curves have been considered here in the nonlinear model, both of which are consistent with soil data obtained in triaxial tests. The results are found to be very sensitive to the choice of this curve.

**Acknowledgements** The work described has been supported by the EPSRC under the Programme Grant EP/H044949/1, 'Railway Track for the 21st Century'.

## References

1. Sheng, X., Jones, C.J.C., Petyt, M.: Ground vibration generated by harmonic load acting on a railway track. *J. Sound Vib.* **225**, 3–28 (1999)
2. Kaynia, A.M., Madshus, C., Zackrisson, P.: Ground vibration from high-speed trains: prediction and countermeasure. *J. Geotech. Geoenviron. Eng.* **126**, 531–537 (2000)
3. Madshus, C., Kaynia, A.M.: High-speed railway lines on soft ground: dynamic behaviour at critical train speed. *J. Sound Vib.* **231**, 689–701 (2000)
4. Krylov, V.V.: Generation of ground vibrations by superfast trains. *Appl. Acoust.* **44**, 149–164 (1995)
5. Hall, L.: Simulations and analyses of train-induced ground vibrations in finite element models. *Soil Dyn. Earthq. Eng.* **23**, 403–413 (2003)
6. Costa, P.A., Caçada, R., Cardoso, A.S., Bodare, A.: Influence of soil non-linearity on the dynamic response of high-speed railway tracks. *Soil Dyn. Earthq. Eng.* **30**, 221–235 (2010)
7. El Kacimi, A., Woodward, P.K., Laghrouche, O., Medero, G.: Time domain 3D finite element modelling of train-induced vibration at high speed. *Comput. Struct.* **118**, 66–73 (2013)
8. Sheng, X., Jones, C.J.C., Thompson, D.J.: Modelling ground vibration from railways using wavenumber finite- and boundary-element methods. *Proc. R. Soc. A Math. Phys. Eng. Sci.* **461**, 2043–2070 (2005)
9. Yang, Y.B., Hung, H.H., Chang, D.W.: Train-induced wave propagation in layered soils using finite/infinite element simulation. *Soil Dyn. Earthq. Eng.* **23**, 263–278 (2003)
10. Kouroussis, G., Verlinden, O., Conti, C.: Ground propagation of vibrations from railway vehicles using a finite/infinite-element model of the soil. *Proc. Inst. Mech. Eng. Part F J. Rail Rapid Transit.* **223**, 405–413 (2009)

11. Shih, J.Y., Thompson, D., Zervos, A.: Assessment of track-ground coupled vibration induced by high-speed trains. In: 21st International Congress on Sound and Vibration, pp. 13–17 (2014)
12. Kramer, S.L.: *Geotechnical Earthquake Engineering*. Prentice-Hall Inc, Upper Saddle River (1996)
13. Beresnev, I.A., Wen, K.: Nonlinear soil response a reality? *Bull. Seismol. Soc. Am.* **86**, 1964–1978 (1996)
14. Ishibashi, I., Zhang, X.: Unified dynamic shear moduli and damping ratio of sand and clay. *Soils Found.* **33**, 182–191 (1993)
15. Iwasaki, T., Tatsuoka, F., Takagi, Y.: Shear moduli of sand under cyclic torsional shear loading. *Soils Found.* **18**, 39–56 (1978)
16. Kokusho, T.: Cyclic triaxial test of dynamic soil properties for wide strain range. *Soils Found.* **20**, 45–60 (1980)
17. Thach, P.-N., Liu, H.-L., Kong, G.-Q.: Vibration analysis of pile-supported embankments under high-speed train passage. *Soil Dyn. Earthq. Eng.* **55**, 92–99 (2013)
18. Iwan, W.D.: On a class of models for the yielding behavior of continuous and composite systems. *J. Appl. Mech.* **34**, 612–617 (1967)
19. Gomes Correia, A., Cunha, J.: Analysis of nonlinear soil modelling in the subgrade and rail track responses under HST. *Transp. Geotech.* **1**, 147–156 (2014)
20. Fernandes, V. A. Subject: Numerical analysis of nonlinear soil behavior and heterogeneity effects on railway track response (2014)
21. Shih, J.Y., Thompson, D.J., Zervos, A.: Modelling scheme for railway vehicle/track/ground dynamic interaction in the time domain. In: *Proceedings of 24th UK Conference on Association for Computational Mechanics in Engineering* (2016)

# Influence of Soil Properties and Model Parameters on Vibrations Induced by Underground Railways for Deep Stratified Alluvial Deposits



Hailing Xing, Tong Jiang, Jiahua Liu and Tianxing Wu

**Abstract** Thin-layer method (TLM) is presented and applied to model the ground vibrations induced by underground railways located in deep stratified soft-soil deposits. The numerical model is calibrated by vibration levels recorded from arrays of accelerometers placed both in the railway tunnel and on the ground surface in Shanghai metro. Then a parametric study is performed to investigate the effect of dynamic soil properties on the vibration levels calculated using TLM. These properties include the soil material damping and Poisson ratio. Lastly, the study is focused on the influence of model parameters, such as model dimensions. Vibration levels and transfer functions on ground surface is calculated using different parameters for comparison. Calculation results illustrate that both the dynamic soil properties and model parameters have noticeable influence on modeling free-field vibrations from underground railways.

## 1 Introduction

Researches of ground-borne vibration from underground railways have gained great interest in recent years all over the world. In urban areas, this kind of ground-borne vibrations may not only disturb occupants in surrounding buildings, but also cause malfunctioning of vibration-sensitive equipment [1]. Environmental impact assessments related to vibrations and re-radiated noise are usually required for sensitive subjects such as building structures or services. For these purposes,

---

H. Xing (✉) · J. Liu

Technical Research Center of Shanghai Shentong Metro Group Co. Ltd, Bld. 1, 909 Guilin Road, Shanghai 201103, China  
e-mail: hailin2353@163.com

T. Jiang

Research Institute of Structural Engineering and Disaster Reduction, Tongji University, Shanghai, China

T. Wu

Institute of Vibration, Shock and Noise, Shanghai Jiao Tong University, Shanghai, China

empirical prediction methods are usually adopted to quantify these vibrations. However, parameters for those methods are obtained from experimental data for some special cases and the empirical prediction methods can give only qualitative results in most cases. Consequently, analytical, semi-analytical and various numerical methods are extensively used to predict ground-borne vibrations as well as to complement empirical prediction results.

Even though the problem of vibration induced by underground railways is by nature three-dimensional (3D), two-dimensional (2D) models have been widely used. It has been noted that a main disadvantage of 3D model is their high computational cost at present. According to Anderson and Jones [2], the computing time of numerical analysis with 3D model is 1000–2000 times longer than a similar 2D one. A lot of research has been done in recent years to develop a so-called 2.5D predictive model, as reviewed by Galvin et al. [3] and Rieckh et al. [4]. However, the 2.5D methodology must apply both Floquet and Fourier transform, which is relatively complicated and time-consuming. On the other hand, it was previously observed that the results obtained with 2D models could satisfy engineering requirements. Furthermore, Anderson and Jones [2] have shown that 2D models could be acceptable for relative changes of soil and tunnel. Aiello and his coworkers [5] carried out 2D finite element analysis and found that results of 2D model were acceptable for engineering predictions. Therefore, a 2D model is selected to determine relative differences between different soil parameters on vibration level.

Here, the TLM is proposed to analyze vibrations induced by underground railways. TLM is a semi-analytical and semi-numerical approach to solving elastic wave propagation problems in a stratified half-space [6, 7]. According to TLM, the semi-infinite soil is discretized in the vertical direction into a number of thin-layer elements while analytical wave propagation equation is used in the horizontal direction. All these allow a semi-infinite half space to be meshed with far fewer elements than with finite element method, without any artificial boundary element in horizontal direction. This method has been successfully applied to analyze the free-field vibration of stratified soil deposits [8, 9].

In this paper, researches on ground-borne vibrations induced by underground railways are firstly reviewed. Section 2 briefly describes the basic theory of TLM and its application on modeling ground vibration generated by a harmonic load. Section 3 presents a typical deep stratified alluvial deposit in Shanghai and also gives the dynamic soil properties. Section 4 presents a numerical study with the TLM for deep stratified alluvial deposits in Shanghai area. Those numerical results are compared with measured results to calibrate the TLM model. Section 5 demonstrates the influence of dynamic soil properties (material damping and Poisson ratio) and dimensions of the numerical model on the free field response of underground railways. Section 6 summaries some important conclusions of this study.

## 2 Numerical Model with Thin-Layer Method

The basic theory of TLM, which includes the full derivations of governing equations for semi-infinite soil profile and their fundamental solutions, has been proposed by Kausel and Roesset [6], and Jiang and Tajimi [7]. For the problem of a tunnel buried in stratified soil, the governing equations of dynamic soil-tunnel interaction were derived by flexible volume method as follows.

The equilibrium equation of the soil-tunnel system is given by

$$\{F\} = [S(i\omega)]\{u\} \tag{1}$$

where  $\{u\}$  and  $\{F\}$  are displacement response and the exciting force matrix;  $S(i\omega)$  is the impedance matrix and  $\omega$  denotes circular frequency. Using the flexible volume method, as illustrated in Fig. 1, the impedance matrix  $[S(i\omega)]$  in Eq. (1) is

$$[S(i\omega)] = [K_T] - [K_T^G] + [A(i\omega)]^{-1} - \omega^2 ([M_T] - [M_T^G]) \tag{2}$$

where  $[K_T]$  and  $[K_T^G]$  are stiffness matrix of tunnel elements and the corresponding artificial soil elements which are excavated, respectively;  $[M_T]$  and  $[M_T^G]$  are mass matrix of tunnel elements and the corresponding artificial soil elements which are excavated, respectively;  $[A(i\omega)]$  denotes the complex dynamic flexible matrix obtained by TLM for soil layers without tunnel [7].

In 2D model, dynamic excitation is assumed as time-dependent loads or displacements acting on the ballast on which track is fixed. In this situation, Eq. (1) can be expressed as

$$\begin{Bmatrix} \{F_1\} \\ \{0\} \end{Bmatrix} = \begin{bmatrix} [\bar{S}_{11}] & [\bar{S}_{12}] \\ [\bar{S}_{21}] & [\bar{S}_{22}] \end{bmatrix} \begin{Bmatrix} \{u_1\} \\ \{\bar{u}_2\} \end{Bmatrix} \tag{3}$$

where  $\{F_1\}$  and  $\{u_1\}$  are force and displacement vectors for nodes on which dynamic excitations are applied, respectively;  $\{\bar{u}_2\}$  is the displacement vector of the remaining nodes. The free field response of the model is now decoupled and then the interaction forces of all nodes can be obtained by substituting Eq. (2) into Eq. (3)

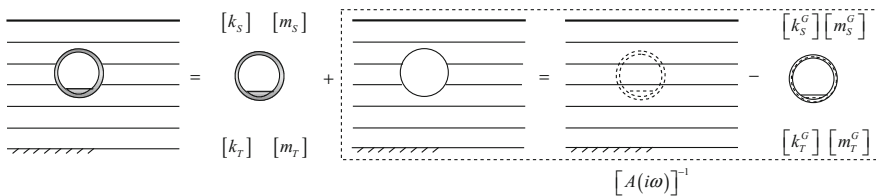


Fig. 1 Sketch of the flexible volume method for TLM model

$$\{F_G\} = [A(i\omega)]^{-1} \left\{ \begin{array}{l} \{u_1\} \\ -[\bar{S}_{22}]^{-1}[\bar{S}_{21}]\{u_1\} \end{array} \right\} \quad (4)$$

The displacement of ballast bed  $\{u_1\}$  can be measured in situ and then employed as input excitation in Eq. (4) to calculate all the unknown interaction forces  $\{F_G\}$  by using the fundamental solutions of the TLM.

The tunnel and ballast bed are discretized and analyzed with the finite element method. The sizes of tunnel elements are carefully handled because they will otherwise influence the results of the numerical modeling. The TLM derivation illustrated above used a fixed boundary condition at the bottom to simulate rigid bedrock. When the TLM is used to analyze a horizontally layered soil with a tunnel, an absorbing boundary on the base of the vertical finite TLM domain is applied to model the surrounding soil.

### 3 Characteristics of the Site and Tunnel

The alluvial plain area where Shanghai city is located on is a plain filled with soft Quaternary deposits whose thickness varies from 200 to 300 m. A typical soil profile is given in detail by Jiang and Tajimi [7]. The soil profile from ground surface to a depth around 100 m is shown in Table 1 for simplicity. The dynamic soil properties, thickness and soil type for each layer are also summarized in Table 1.

The tunnel investigated here in this paper is of the conventional bored-tunnel type with a segmented concrete lining with an external radius of 3.1 m and a wall thickness of 0.3 m. The tunnel lining is composed of six circumferential segments for each ring, which are connected by bolts in both circumferential and longitudinal direction. The Young's modulus, Poisson's ratio and density of the concrete tunnel wall and slab track are 35000 MPa, 0.25 and 2500 kg/m<sup>3</sup>, respectively (Fig. 2).

### 4 Numerical Example

Vibration measurements were performed on a site near line 8 of Shanghai metro. The vibrations in the tunnel were also been measured in situ. The depth of soil layer on the top of the tunnel is 8.3 m. The other dimensions of the tunnel are the same as specified in Sect. 3. More than 20 acceleration time series recorded during passage of the underground trains were used as input excitations for vibration level calculation on the ground surface. Figure 3 illustrates the vibration levels measured in situ and calculated using the TLM. The numerical and test results show good

**Table 1** Soil properties of deep stratified alluvial deposits in Shanghai

No.	Layer thickness (m)	Soil type	Density (kg/m <sup>3</sup> )	$v$ (m/s)	Poisson's ratio	Notes
1	1.0	Back-fill	1890	74	0.35	
2	3.2	Silty clay	1850	89	0.30	
3	2.1	Muddy silt clay	1850	85	0.30	
4	11.3	Muddy silt clay*	1790	108	0.30	
5	26.4	Silty clay	1820	220	0.25	
6	4.0	Fine silty clay	1930	190	0.25	
7	3.4	clay	2040	195	0.25	
8	8.1	Fine silty sand	1920	230	0.25	
9	16.9	Silty clay with sand	1950	220	0.25	for 70 m-model
10	2.2	Fine silty sand	1920	263	0.25	
11	3.8	Fine sand with gravel	1960	267	0.25	
12	3.0	Fine sand	1920	272	0.25	
13	6.7	Gravelly sand	1940	279	0.25	
14	4.4	Fine sand	1930	287	0.25	
15	6.7	Fine silty sand	1920	296	0.25	for 100 m-model

\*Muddy silt clay, high plasticity

agreement with each other, particularly when the distance from the tunnel-center is less than 20 m.

## 5 Parameter Studies

The soil is usually modeled as an elasto-dynamic medium, characterized by the shear modulus or shear wave velocity, the density, Poisson's ratio and the material damping ratio. Those dynamic characteristics can be determined by in situ tests. Although the accurate determination of soil properties is important for reliable vibration predictions, the uncertainty associated with them is high and the predictions in the free surface field are expected to be less reliable [1]. The soil material damping ratio, for example, varies mainly between 0.03 and 0.05 when it is used in numerical simulations [1, 10]. As for the TLM and its applications on the deep stratified alluvial deposits, a parametric study is necessary.



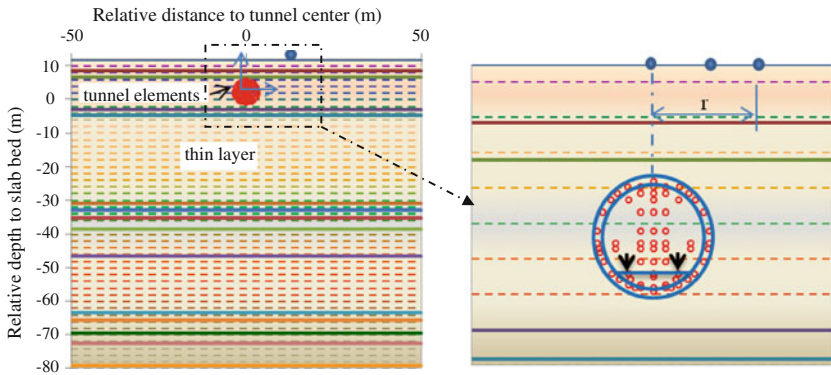
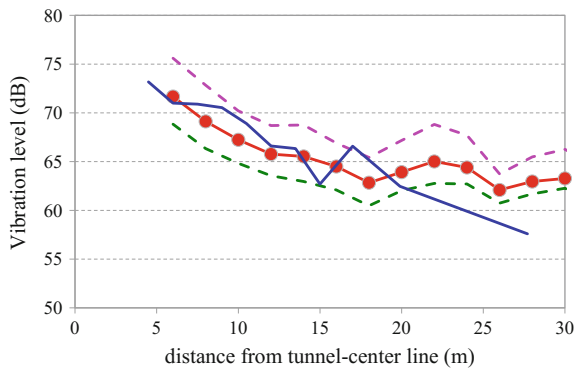


**Fig. 2** Sketch of the soil profile and the numerical model

**Fig. 3** Comparison of vibration levels on ground surface. The maximum, average and minimum value of vibration levels are plotted with the dashed (pink), solid with dots (red) and dashed (green) curves, respectively. Vibration levels measured in situ are plotted with solid (blue) curve



The transfer functions are computed for comparisons using the TLM for each frequency. The transfer function is defined as the response of the model for a unit load applied on the driving point, i.e., the element node on which the rail is located. After the computation of the transfer functions, the response during the passage of a train is calculated by adding the contribution of dynamic forces or displacements in the frequency domain.

Vibration acceleration level is also adopted for comparisons of results obtained with various model and soil parameters. Vibration acceleration level (VL) is defined as 20 times the logarithm to base 10 of the weighted root mean square (RMS) value of the vibration acceleration with respect to a reference value  $10^{-6} \text{ m}^2/\text{s}$ . Principal frequency weightings curves specified by ISO 2631 [11] for vertical vibrations are adopted. The response of tunnel-soil system is considered in a frequency range between 1 and 80 Hz for a unit harmonic displacement or load applied on the track slab. Acceleration time histories measured in line 2 and line 8 of Shanghai metro are chosen as input for vibration analysis of the ground. Therefore, unless otherwise specified, the tunnel is assumed to be embedded in the soil deposit with 8.5 m-depth soil layer on top of it.

## 5.1 Parametric Study of Soil Properties

### 5.1.1 Effect of Damping Ratio

First, the damping ratio of each soil layer in the numerical model is assumed to be given. Here in this paper, four values, i.e. 0.01, 0.02, 0.03 and 0.05 are specified for soil damping ratios. Transfer functions of observation points on the free-field surface are computed using those damping ratio, as shown in Fig. 4. Damping ratios, which change slightly, can have significant effects on the vibration at the surface. In Fig. 4a the transfer functions of ground surface on top of the tunnel (at a horizontal distance of 0 m from the tunnel center) are depicted. The increase of the damping ratio decreases the transfer function, especially at frequencies higher than 40 Hz. The higher the frequency is, the greater the influence of damping ratio is. Moreover, a bigger distance between target position and the tunnel-center line may lead to a lower frequency range in which the damping ratio will have obvious influence. For example, when the point on free-field surface is 5 m from the tunnel center, the variation of damping ratio has a very slight influence on the transfer functions in a frequency range between 0 and 20 Hz, as shown in Fig. 4b. However, when the point is 20 m from the tunnel center, the corresponding frequency will be 0–6 Hz. All these results are in accord with the influence of material damping on wave propagation.

The effects of changing damping ratios on the free-field surface vibration are shown in Fig. 5, which shows the acceleration vibration level as a function of the lateral distance from the tunnel. Increasing the damping ratio of the soil decreases the response at free-field surface. At distances larger than 20 m from the tunnel, a difference of more than 10 dB is observed for the damping ratio 0.01 and 0.05. Moreover, the influence of damping ratio on vibration level increases as the lateral distance becoming larger.

### 5.1.2 Effect of the Poisson's Ratio

To study the effect of Poisson's ratio on vibration levels, the analysis is performed with a given Poisson's ratio for all soil layers in the numerical model. The vibration levels and their attenuations on the free-field surface for the site with different Poisson's ratio of soil are shown in Fig. 6. As a general trend, the increase of Poisson's ratio results in a decrease of vibration level at the free-field surface. That the vibration level curves are nearly parallel to each other, which implies that the influence of Poisson's ratio is nearly independent of the lateral distances or locations.

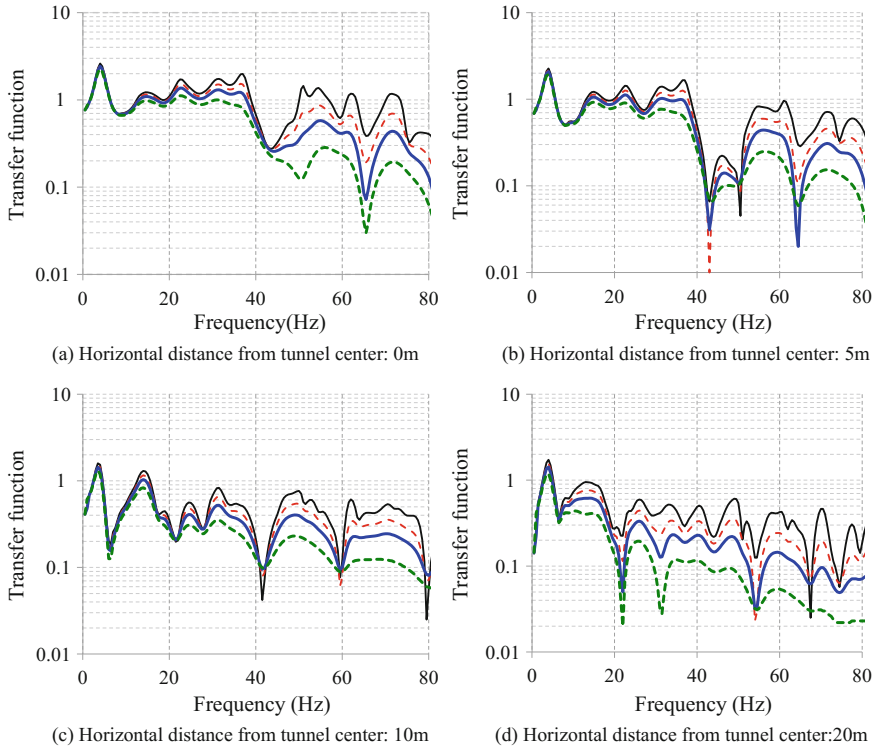


**Fig. 4** Transfer functions obtained with different damping ratio for 4 points on free-field surface of the soil deposit. The transfer functions corresponding to damping ratio 0.01, 0.02, 0.03 and 0.05 are plotted with the solid (black), dashed (red), bold solid (blue) and bold dash (green) curves, respectively

**Fig. 5** Vibration levels calculated with different damping ratio. Vibration levels corresponding to damping ratio 0.01, 0.02, 0.03 and 0.05 are plotted with the solid (black), dashed (red), bold solid (blue) and bold dash (green) curves, respectively

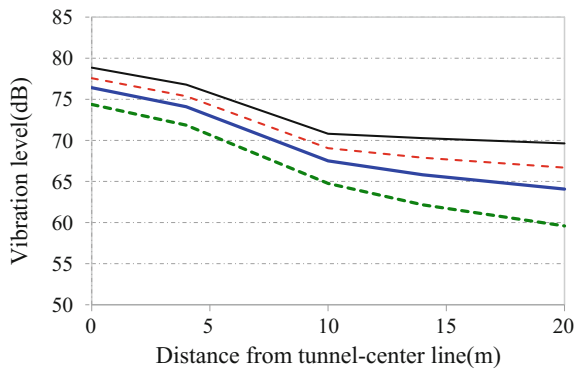
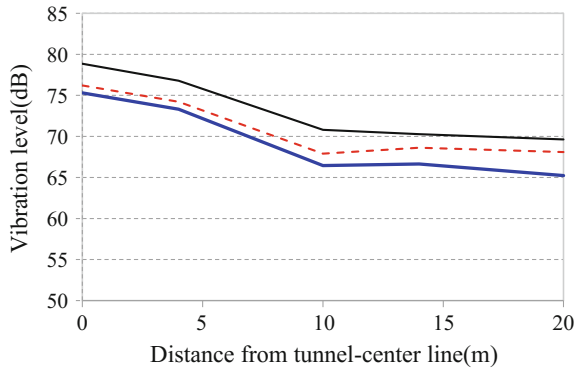


**Fig. 6** Vibration levels calculated with different damping ratio. Vibration levels corresponding to Poisson’s ratio 0.1, 0.2 and 0.3 are plotted with the solid (black), dashed (red) and bold solid (blue) curves, respectively



### 5.2 Model Parameter

In this section, the analysis is performed assuming that depths of the numerical model are 70, 100 and 270 m, respectively. The soil profile and properties from surface to a depth of about 100 m are the same as given in Table 1, and the rest are also taken from the same typical soil profile, which is elaborated by Jiang and Tajimi [7]. As for the 70 m-depth model, only the first 9 layers in Table 1 are selected. The transfer functions of the free-field surface are calculated using the same soil properties for a specific layer. Results are compared in Fig. 7. The results of the 270 m-model are nearly the same with the 100 m one. Only little influence is observed when the depth of overlying soil layer is 70 m. A numerical model at a depth of 100 m is recommended for the TLM when it is applied to analyze those deep stratified alluvial deposits in Shanghai.

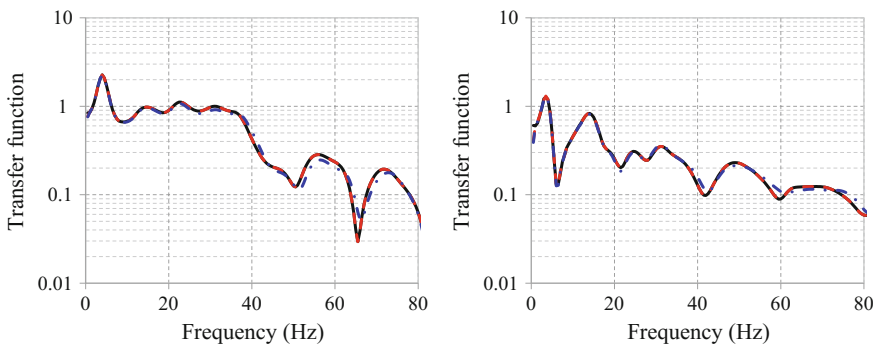


**Fig. 7** Transfer functions calculated with different model or element sizes. Transfer functions corresponding to a depth of 270, 100 and 70 m are plotted with the solid (black), dashed (red) and dash-dot (blue) curves, respectively

## 6 Conclusion

This study provides a better understanding in the context of the TLM and its application to modeling ground-borne vibration induced by underground railway. The TLM is introduced as an efficient semi-analytical and semi-numerical means of simulating deep stratified alluvial deposits for ground vibration problems induced by underground railway. Comparisons between numerical predictions and measurements on a specific site in Shanghai were carried out and the TLM seem to provide fairly satisfactory results. Parametric studies are performed in order to figure out the influence of dynamic soil properties on numerical results. The material damping ratio is an important parameter for vibration levels in the free field, particularly at large lateral distances from the tunnel-center and high frequency band. The influence of Poisson's ratio on vibration levels in the same model is also considered. Furthermore, the vertical size of numerical model is demonstrated and a proper depth is suggested for accurate predictions in the free field using the TLM.

## References

1. Gupa, S., Stanus, Y., Lombaert, G.: Influence of tunnel and soil parameters on vibrations from underground railways. *J. Sound Vib.* **327**, 70–91 (2009)
2. Anderson, A., Jones, C.J.C.: Coupled boundary and finite element analysis of vibration from railway tunnels—a comparison of two- and three-dimensional models. *J. Sound Vib.* **293**, 611–625 (2006)
3. Galvin, P., Francois, S., Schevenels, M., Bongini, M., Degrande, G.: A 2.5D coupled FE-BE model for the prediction of railway induced vibrations. *Soil Dyn. Earthq. Eng.* **30**, 1500–1512 (2010)
4. Rieckh, G., Kreuzer, W., Waubke, H., Balazs, P.: A 2.5D Fourier-BEM model for vibrations in a tunnel running through layered anisotropic soil. *Eng. Anal. Boundary Elem.* **36**, 960–967 (2012)
5. Aiello, V., Boiero, D., D'Apuzzo, M., Socco, L.V.: Experimental and numerical analysis of vibrations induced by underground trains in an urban environment. *Struct. Control Health Monit.* **15**, 315–348 (2008)
6. Kausel, E., Roesset, J.: Stiffness matrices for layered soils. *Bull. Seismol. Soc. Am.* **71**(6), 1743–1761 (1981)
7. Jiang, T., Tajimi, H.: *The soil-structure interaction analysis method*. Tongji University Press, Shanghai (2009). (in Chinese)
8. Jiang, T., Cheng, C.S.: Environmental vibration induced by elevated railway traffic using thin-layer method. *J. Vib. Eng.* **20**, 623–627 (2007). (in Chinese)
9. Jiang, T., Yue, J.Y.: Analysis of environmental vibration induced by subway in Shanghai and Chengdu by using thin layer method. In: *Proceedings of the 5th International Symposium on Environmental Vibration 2011*, Nanjing, China

10. Jones, S., Hunt, H.: Predicting surface vibration from underground railways through inhomogeneous soil. *J. Sound Vib.* **331**, 2055–2069 (2012)
11. ISO 2631-1, Mechanical vibration and shock—Evaluation of human exposure to whole-body vibration—Part 1: General requirements (1997)

# Attenuation Properties of Ground Vibration Propagated from Subway Tunnels in Soft Ground



K. Tsuno and M. Furuta

**Abstract** Ground-borne noise and vibration caused by passing trains in subway tunnels are sometimes perceived in near-by buildings and may pose a problem for residential buildings and facilities requiring silence and freedom from vibration. Field measurements were carried out in this research both in subway tunnels located in the soft ground and on the ground surface at 21 locations in and around the Tokyo area to measure the attenuation property of the ground. The attenuation properties are analyzed for each 1/3 octave band by applying an empirical equation to the measurement results. The material damping coefficient  $\alpha$  is obtained for each 1/3 octave band and the relational equation between frequency and material damping coefficient  $\alpha$  is proposed. The relational equation enables calculation of the vibration attenuation in the ground with empirical equation considering geometrical and material damping.

## 1 Introduction

Ground-borne noise and vibration caused by passing trains in subway tunnels are sometimes perceived in near-by buildings. Although the level of noise and vibration is normally small as compared with those caused by train passage on the ground or viaducts, they may pose a problem in residential buildings and facilities requiring silence and freedom from vibration. To evaluate the ground-borne noise and vibration on the ground surface or in buildings, it is required to properly predict vibration attenuation in the ground.

Numerical calculation is an effective tool to predict the vibration attenuation in the ground. However, a simpler prediction method is desired at the schematic design stage, in which soil properties required for numerical calculation are not

---

K. Tsuno (✉)

Railway Technical Research Institute, 2-8-38 Hikari-Cho, Kokubunji-Shi, Tokyo, Japan  
e-mail: tsuno.kiwamu.00@rtri.or.jp

M. Furuta

NIPPON KOEI CO., LTD, Kudan kita, Chiyoda-ku, Tokyo, Japan

available yet and ground-borne noise and vibration needs to be roughly estimated at many locations. Although the vibration attenuation in the ground is affected by frequency, many existent empirical equations for subway-induced vibration do not take into account its frequency characteristics. This research therefore investigates the attenuation properties based on the field measurement [1, 2] and proposes the simple prediction method of vibration attenuation which takes into account the frequency characteristics.

## **2 Field Measurement**

### ***2.1 Outline of Field Measurement***

#### **2.1.1 Measurement Location**

As measurement data both in subway tunnels and on the ground surface have not been sufficiently accumulated, especially in soft ground condition, this research carries out field measurement at 21 locations in and around Tokyo area. The condition of measurement location is described in Tables 1 and 2. The tunnels are located in soft ground, namely alluvial or diluvial ground. There are 14 and 7 locations for field measurement of shield tunnels and cut and cover tunnels, respectively. The diameter of shield tunnels is 5.3–12.7 m and the depth of cover is 11.5–28.3 m. The structure of cut and cover tunnels are double-track ones with one-layer and two-spans and the cover depth ranges from 2.7 to 9.0 m. The length of one vehicle is 20 m at ordinary subway system. At site SE, SJ, SM, SN, SO, SP and SQ, the small linear-motor metro transport system is used and the vehicle length is 16 m.

#### **2.1.2 Measurement and Analysis Method**

Vibration acceleration is simultaneously measured both in the tunnels and on the ground surface with piezoelectric accelerometers, charge amplifiers and data recorders. In the tunnels, steel cubes or plates with piezoelectric accelerometers are fixed on tunnel lining and occasionally on track bed. Vibration acceleration is measured in the tangential or vertical direction (Z-direction) and radial or horizontal direction (Y-direction) in the tunnels. On the ground surface, steel cubes or plates are also fixed with plaster of Paris or stake and vibration acceleration in the vertical direction (Z-direction) is mainly measured.

The measured acceleration data during train passage are analyzed with a 1/3 octave band analyzer at time constant of 0.63 s. Average levels are calculated based on the levels of six or more passing trains after eliminating the data strongly influenced by wheel damage, background and other obstacles.



**Table 1** Outline of measurement location at shield tunnel

Site	SD	SE	SF	SG	SH	SI	SJ	SK	SL	SM	SN	SO	SP	SQ
Cover depth (m)	15.8	11.5	12.1	12.3	12.9	12.9	13.9	14.1	15.5	15.6	20.1	24.5	28.3	28.3
Track structure*	B	R	B	C	B	R	R	R	C	C	R	R	R	R
Tunnel outer diameter (m)	10.4	5.3	7.3	7.3	7.3	7.3	8.5	7.3	12.7	8.5	5.3	5.3	5.3	5.3
Number of measurement location	Tunnel	3	4	4	5	5	4	5	3	4	4	3	3	4
	Ground	11	3	3	3	3	3	3	3	3	4	3	4	5
Number of train set	8car	8car	8car	8car	8car	8car	8car	8car	8car	8car	8car	8car	8car	8car
Average train speed (km/h)	45	63	68	63	69	68	48	68	60	63	38	45	40	40

\*B Ballast track, C Concrete direct fastened track, R Vibration isolation sleeper track

**Table 2** Outline of measurement location at cut and cover tunnel

Site	CB	CC	CD	CE	CF	CG	CH
Cover depth (m)	2.7	4.1	6.8	7.0	8.0	8.0	9.0
Track structure*	BR	B	R	R	C	BR	C
Number of measurement location	Tunnel	1	2	3	2	1	1
	Ground	4	3	5	4	6	4
Number of train set	3car	8car	8car	10car	6car	10car	10car
Average train speed (km/h)	44	48	40	68	63	61	70

\**B* Ballast track, *BR* Ballast track with ballast mat, *C* Concrete direct fastened track, *R* Vibration isolation sleeper track

## 2.2 Measurement Results

### 2.2.1 1/3 Octave Band Spectrum

1/3 octave-band spectra obtained at shield and cut and cover tunnels are shown in Fig. 1, in which the reference value of vibration acceleration level is  $10^{-5} \text{ m/s}^2$  according to the rule and regulation of vibration level meter in Japan.

The vibration acceleration spectra in the tunnels tend to gradually increase from 10 to 40 Hz and have wide-range frequency components including high frequency

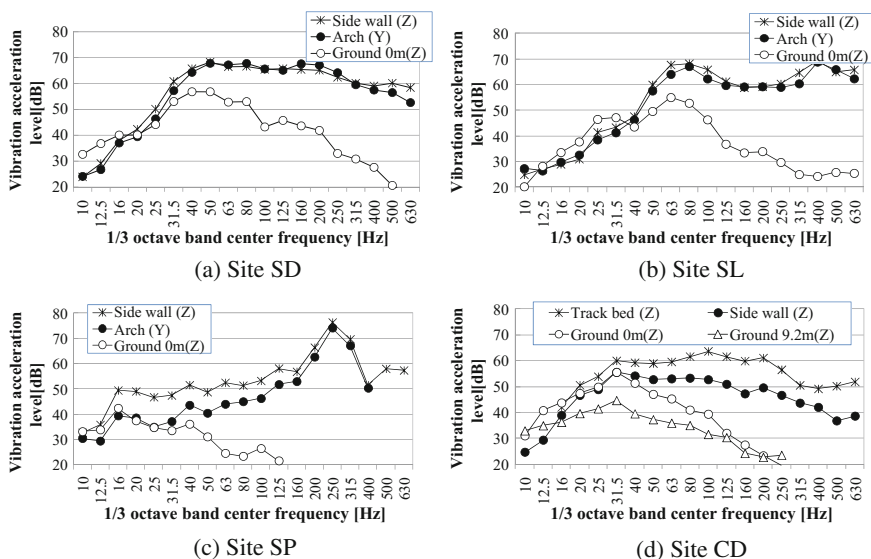


**Fig. 1** Vibration acceleration level in 1/3 octave band (ref  $10^{-5} \text{ m/s}^2$ )

ones more than 100 Hz. On the other hand, the spectra on the ground surface have absolute peaks from 40 to 80 Hz at the shield tunnels and 31.5–63 Hz at the cut and cover tunnels. At site SN and SP, linear-motor metro transport system is applied with vibration isolation sleeper tracks and peaks are observed at 16–20 Hz on the ground surface. In these figures, it is observed that the high frequency components more than 100 Hz, which are observed in the tunnels, attenuate in the ground.

### 2.2.2 Attenuation in the Ground

The attenuation in the ground is investigated for every 1/3 octave band based on the measurement data. Relative acceleration level  $\Delta L_{VA}$  (dB) is defined as;

$$\Delta L_{VA}(f) = L_{VA}(f) - L_{VA0}(f) \tag{2.1}$$

where  $L_{VA}(f)$  (dB) is vibration acceleration level in the vertical direction of ground surface at  $f$  (Hz),  $L_{VA0}(f)$  (dB) is the level at reference point in tunnels at  $f$  (Hz) and  $f$  (Hz) is 1/3 octave band center frequency. Reference points are set up on the arch in the radius direction in the shield tunnels and on the lower part of side wall in the vertical direction in the cut and cover tunnels. Figure 2 shows the relationship between frequency and relative acceleration level at representative locations. The attenuation in the ground becomes larger with increasing frequency.

Figure 3 shows the relationship between the propagation distance and relative acceleration level at the bands of 16, 31.5, 63 and 125 Hz. Propagation distance is defined as shown in Fig. 4 in this research. At 16 and 31.5 Hz, some plots show positive values, which indicates amplification, and distance attenuation is not clear. On the other hand, the distance attenuation is observed at 63 and 125 Hz. The figures show that distance attenuation becomes clearer as frequency increases.

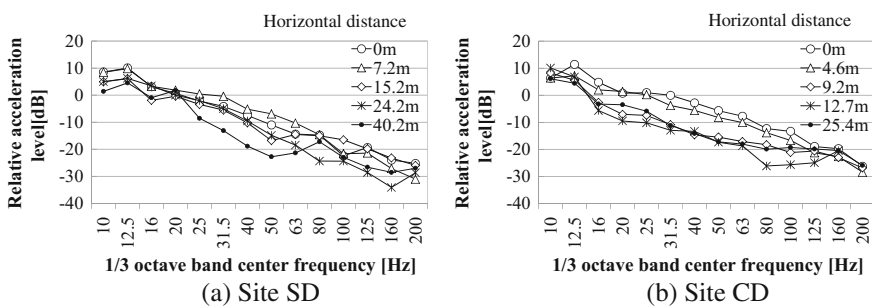


Fig. 2 Relative acceleration level in 1/3 octave band

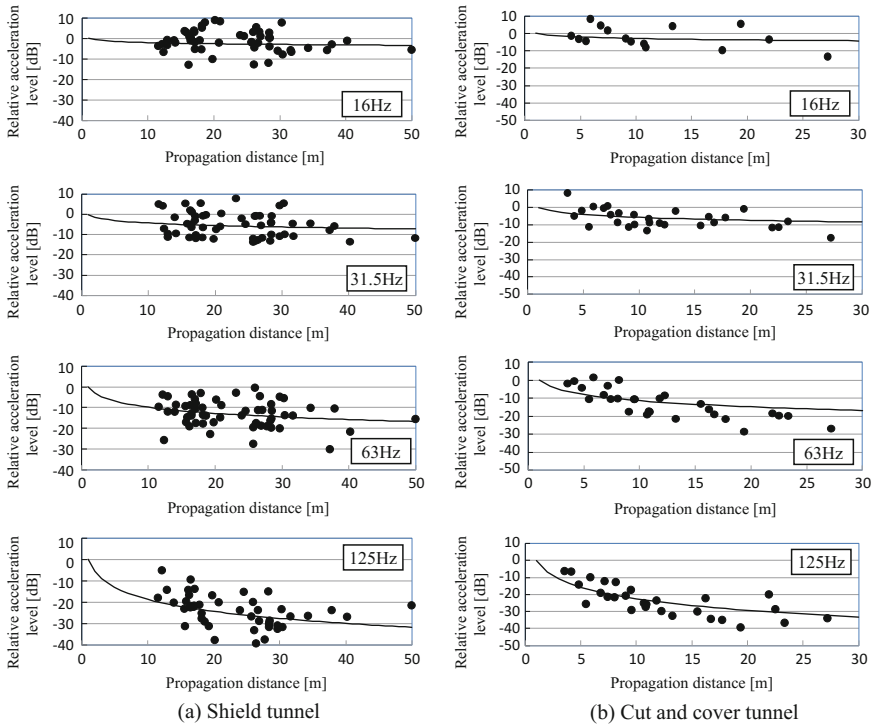


Fig. 3 Relative acceleration level in representative 1/3 octave bands

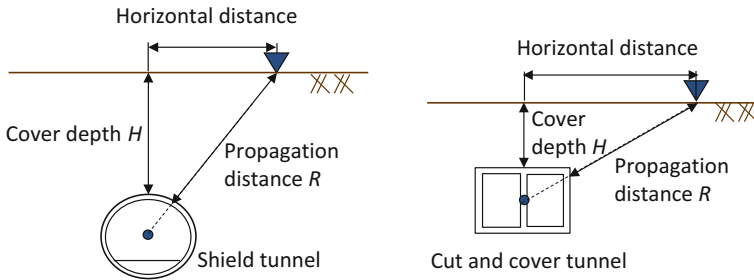


Fig. 4 Definition of propagation distance

### 3 Prediction Method of Attenuation in the Ground

#### 3.1 Logarithmic Regression Formula

The attenuation properties in the ground are analyzed based on the following logarithmic regression equation;

$$L_{VA}(f) - L_{VA0}(f) = -A \log_{10}(R/R_0) \tag{3.1}$$

where  $L_{VA}(f)$  (dB) is vibration acceleration level in the vertical direction of ground surface at  $f$  (Hz),  $L_{VA0}(f)$  (dB) is the level at reference point in tunnels at  $f$  (Hz),  $f$  (Hz) is 1/3 octave band center frequency,  $A$  is a coefficient regarding vibration attenuation in the ground,  $R$  (m) is the propagation distance and  $R_0$  (m) is the distance from the source to the reference point. The value of  $R_0$  is assumed to be 1.0 m in this research.

The coefficient  $A$  is calculated with respect to each 1/3 octave band and each measurement site by means of the least square method based on the relationship between the propagation distance and relative acceleration level. Figure 5 shows the relationship between frequency and average coefficient  $A$  and suggests that the coefficient  $A$  becomes larger with increasing frequency.

The following equation is obtained with a regression analysis for the vibration attenuation from shield tunnels.

$$A = 0.15f \tag{3.2}$$

The equation for cut and cover tunnels is also obtained as follows.

$$A = 0.18f \tag{3.3}$$

Figure 6 makes a comparison of coefficient  $A$  between the shield tunnels and cut-and-cover tunnels. The results of shield tunnels denote the same tendency of those of cut and cover tunnels in the sense that the coefficient  $A$  becomes larger with increasing frequency. On the other hand, the coefficient  $A$  of cut and cover tunnels is larger than that of shield tunnels more than 80 Hz. It is considered to be one of the reasons for the larger value  $A$  of cut and cover tunnels that the cover depth of cut and cover tunnels is smaller than that of shield tunnels and that vibration is propagated through the comparatively soft ground with larger damping factors.

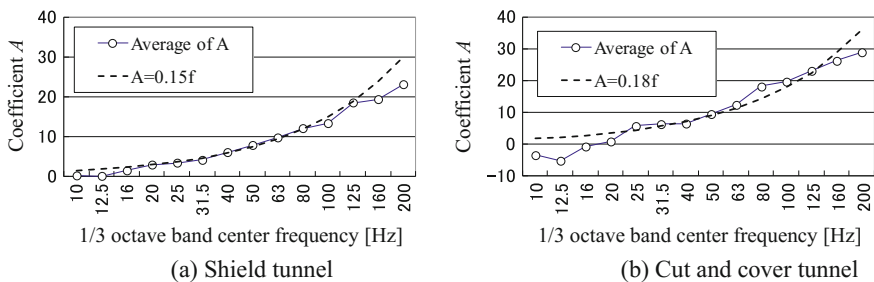
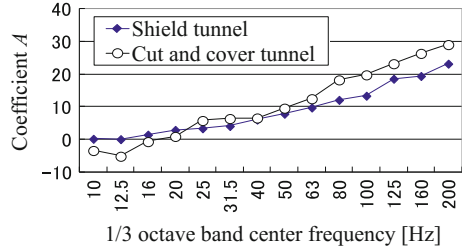


Fig. 5 Relationship between frequency and coefficient  $A$

**Fig. 6** Comparison of coefficient  $A$  between shield tunnel and cut and cover tunnel



### 3.2 Empirical Equation

#### 3.2.1 Fundamental Equation

To investigate the attenuation properties in the ground, the following equation is applied as a fundamental equation [3];

$$U_R = U_0 e^{-\alpha(R-R_0)} (R/R_0)^{-n} \tag{3.4}$$

where  $U_R$  is vibration amplitude at the point of distance  $R$ ,  $U_0$  vibration amplitude at the reference point,  $n$  the geometrical damping coefficient,  $\alpha$  the material damping coefficient,  $R$  propagation distance from the reference point and  $R_0$  distance from the source to the reference point. The equation takes into account both geometrical and material damping.

The geometrical damping coefficient  $n$  is assumed to be 0.5 in this research, considering that tunnels are infinitely long structures existing in the ground and vibration propagated from tunnels is body wave from buried line source. The Eq. (3.4) is changed to the following one by representing it in vibration acceleration levels in the 1/3 octave bands (dB);

$$L_{VA}(f) - L_{VA0}(f) = -10 \log_{10}(R/R_0) - 8.68\alpha(f)(R - R_0) \tag{3.5}$$

where  $L_{VA}(f)$  (dB) is vibration acceleration level in the vertical direction of ground surface at  $f$  (Hz),  $L_{VA0}(f)$  (dB) is the level at reference point in tunnels at  $f$  (Hz),  $f$  (Hz) is 1/3 octave band center frequency,  $R$  (m) is the propagation distance,  $R_0$  (m) is the distance from the source to the reference point and  $\alpha(f)$  is material damping coefficient at  $f$  (Hz).

#### 3.2.2 Investigation of Material Damping Coefficient $\alpha$

The material damping coefficient  $\alpha$  is calculated with respect to each 1/3 octave band and each measurement site. As there are multiple measurement points on the ground surface, the values of  $\alpha$  are calculated by means of a regression analysis. Figure 7 shows the relationship between frequency and material damping

coefficient  $\alpha$  with respect to each measurement location. This figure indicates that the values of  $\alpha$  tend to increase with increasing frequency. Most of material damping coefficient  $\alpha$  is negative in the frequency band of 10–40 Hz with comparatively short wave length.

### 3.2.3 Relational Equation Between Material Damping Coefficient $\alpha$ and Frequency

As it is observed that the material damping coefficient  $\alpha$  is correlated with frequency as described in Fig. 7, the  $\alpha$  is expressed as a function of frequency as;

$$\alpha = af - b \tag{3.6}$$

where  $\alpha$  is material damping coefficient,  $f$  (Hz) frequency and  $a$  and  $b$  positive constant.

Regarding the shield tunnels, the average values of  $\alpha$  at 14 locations are calculated with respect to each 1/3 octave band as shown in Fig. 8a. The coefficients of

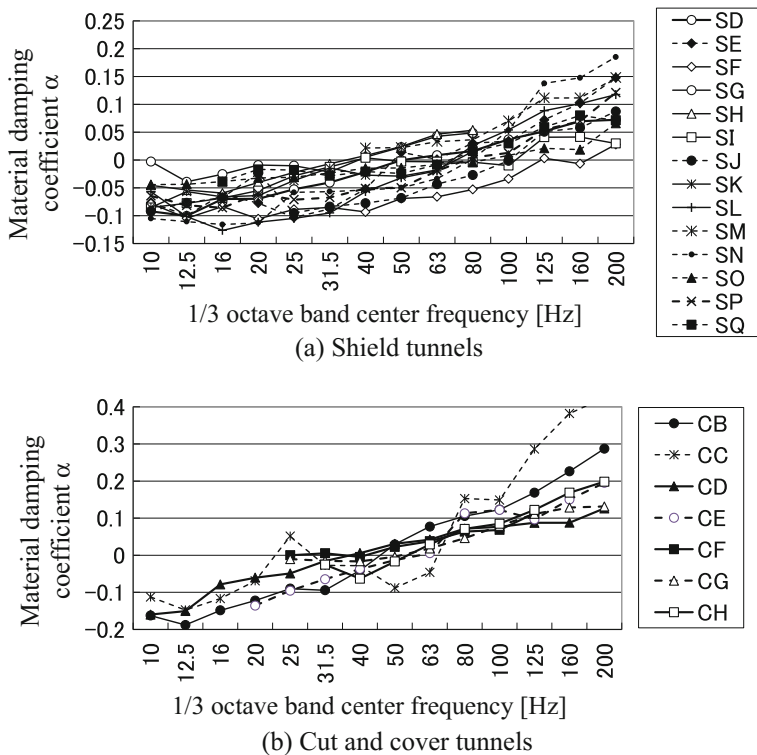


Fig. 7 Relationship between frequency and material damping coefficient  $\alpha$

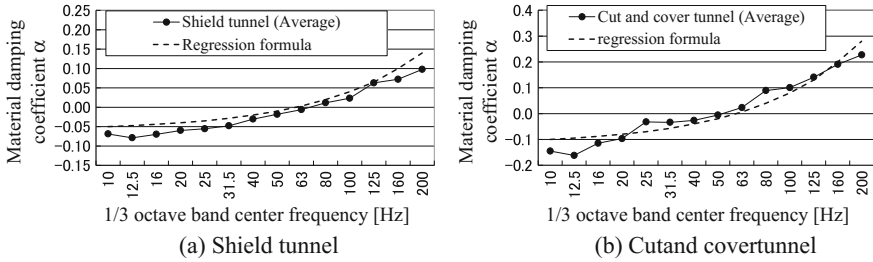


Fig. 8 Average material damping coefficient  $\alpha$

$a$  and  $b$  are decided to be 0.001 and 0.06 respectively by a regression analysis, and the following equation regarding the material damping coefficient  $\alpha$  and frequency  $f$  (Hz) is obtained.

$$\alpha = 0.001f - 0.06 \tag{3.7}$$

Figure 8b shows the average values of  $\alpha$  at 7 locations regarding the cut and cover tunnels. The following relational equation is obtained for the cut and cover tunnels.

$$\alpha = 0.002f - 0.12 \tag{3.8}$$

The attenuation in the ground can be predicted by using the Eqs. (3.5) and (3.7) for shield tunnels and the Eqs. (3.5) and (3.8) for cut and cover tunnels.

### 3.3 Investigation of Damping Factor

Numerical calculation simulating the subway-induced vibration, such as a finite element analysis, necessitates the damping factors. This research calculates the values of damping factors on the basis of attenuation property obtained in (3.2).

The relationship between damping factor and material damping coefficient  $\alpha$  is expressed as the following equation;

$$\alpha = \frac{2\pi fh}{V_s} \tag{3.9}$$

where  $f$  (Hz) is frequency,  $h$  the damping factor and  $V_s$  ( $m/s^2$ ) shear wave velocity. If the 2nd term on the right side of the Eqs. (3.7) and (3.8) is influenced by the amplification near the ground surface and is ignored, it is possible to calculate  $h/V_s$  by means of the relationship between frequency  $f$  and the material damping coefficient  $\alpha$ .



**Table 3** Calculated  $h/V_s$  and damping factor  $h$  (shield tunnel)

Site	SD	SE	SG	SH	SI	SK	SM	SO	SP	SQ
$h/V_s$	0.00015	0.00021	0.00018	0.00027	0.00013	0.00018	0.00014	0.00008	0.00017	0.00011
$h$ (%)	3.0	4.3	2.7	3.4	1.6	2.3	2.4	1.6	4.1	2.7

**Table 4** Calculated  $h/V_s$  and damping factor  $h$  (cut and cover tunnel)

Site	CB	CC	CD	CE	CG	CH
$h/V_s$	0.00040	0.00049	0.00021	0.00027	0.00016	0.00024
$h$ (%)	6.2	7.7	2.8	7.3	3.0	5.5

The average shear wave velocity is determined based on the data of PS logging or by converting the N-values into shear velocity based on the method described in the railway design standard in Japan. The calculated  $h/V_s$  and damping factors  $h$  are shown in Tables 3 and 4. The calculated damping factors  $h$  range from 1.6 to 4.3% in the shield tunnel and from 2.8 to 7.7% in the cut and cover tunnel.

## 4 Conclusion

The attenuation properties of ground vibration propagated from subway tunnels are investigated based on the field measurement data at 21 locations in and around the Tokyo area. The following conclusions are derived.

- (1) Vibration acceleration spectra in the tunnels have wide-range frequency components including high frequency ones above 100 Hz, while those on the ground surface have peaks at 40–80 Hz at the shield tunnels and 31.5–63 Hz at the cut and cover tunnels. In the case of linear-motor metro transport system with vibration isolation sleeper, the spectra have peaks at 16–20 Hz on the ground surface.
- (2) Attenuation in the ground becomes larger with increasing frequency. Distance attenuation also becomes clearer as frequency is higher.
- (3) Coefficient  $A$  in logarithmic regression equation is calculated with respect to each 1/3 octave band based on the measurement data and becomes larger with increasing frequency. Relational equation between frequency and coefficient  $A$  is obtained.
- (4) The material damping coefficient  $\alpha$  with respect to each 1/3 octave band is calculated and became larger with increasing frequency. The relational equation between frequency and material damping coefficient  $\alpha$  is proposed for shield tunnels and cut and cover tunnels. This equation enables calculation of the vibration attenuation in 1/3 octave bands with the empirical equation considering geometrical and material damping.

- (5) Damping factors are calculated based on the measurement data. The calculated damping factors range from 1.6 to 4.3% at shield tunnels and 2.8–7.7% at cut and cover tunnels.

## References

1. Tsuno, K., Furuta, M., Fujii, K., Kusakabe, F., Nagashima, O.: Wide-range attenuation properties of ground vibration propagated from subway shield tunnel. *J. Jpn. Soc. Civ. Eng.* **792**(III-71), 185–198 (2005)
2. Tsuno, K., Furuta, M., Orihara, K., Akagi, H.: Wide range attenuation properties of ground vibration propagated from cut-and-cover tunnel. *J. Jpn. Soc. Civ. Eng.* **70**(3), 83–91 (2014). (in Japanese)
3. Bornitz, G.: *Über die Ausbreitung der von Grozklolbenmaschinen erzeugten Bodenschwingungen in die Tiefe*, J. Springer (1931)

# Effects of Tuned Slab Damper on Low Frequency Ground Vibration Levels on Metro Systems



G. Xu, A. Wang, Y. Li, Y. Fan, Z. Zhang, Z. Wang, G. Dong and J. Liu

**Abstract** This paper describes a method to reduce slab low frequency vibration using tuned slab dampers on a metro track. Track frequency response functions have been compared between a standard slab track and the track with optimized tuned slab damper. Slab and track bed vibration measurements were also carried out on the same track with and without tuned damper respectively under the same traffic conditions. The results demonstrate that for slab with tuned damper, low frequency slab vibration level is reduced by more than 10 dB under normal metro traffic conditions.

## 1 Introduction

Trains passing along railway tracks excite vibrations because of the roughness on the wheels and rail. As this roughness consists of components with a wide range of wavelengths, therefore exciting a wide range of frequencies. In addition, there are parametric excitations at particular frequencies that are related to the geometry of the system, for instance the frequency associated with axles, bogies, and vehicles passing above a given position; or frequency linked to wheels passing over the

---

G. Xu (✉)

School of Civil Engineering and Transportation, South China University of Technology, 381 Wushan Road, Guangzhou 510641, People's Republic of China  
e-mail: xghscut@163.com; x.gh@mail.scut.edu.cn

A. Wang

Shanghai University of Engineering Science, 333 Longteng Road, Shanghai 201620, People's Republic of China

A. Wang · Y. Li · Y. Fan · Z. Zhang · Z. Wang

Luoyang Ship Material Research Institute, 40 North Binhe Road, Luoyang 471003, People's Republic of China

G. Dong · J. Liu

Shanghai Shentong Metro Co, 909 Guilin Road, Shanghai 201102, People's Republic of China

© Springer International Publishing AG, part of Springer Nature 2018

D. Anderson et al. (eds.), *Noise and Vibration Mitigation for Rail Transportation Systems*, Notes on Numerical Fluid Mechanics and Multidisciplinary Design 139, [https://doi.org/10.1007/978-3-319-73411-8\\_42](https://doi.org/10.1007/978-3-319-73411-8_42)

fasteners; or frequency related to the pinned-pinned resonance of tracks; and so on. The frequencies excited are determined by dimensions of the track and vehicles, and by the train speed.

There are particular frequencies associated with resonances in the train track system. These characteristic frequencies are not affected by train speed. They include body and bounce modes of the vehicle. But of particular interest here is the so-called loaded track resonance frequency in which the unsprung mass of the vehicle bounces on the stiffness of the track.

The problem addressed is with specific reference to metro transit systems. The range of parametrically excited frequencies is limited, because there are a number of constraints that apply to all metro systems that tend to enforce a degree of conformity. For example, stations on different systems tend to be similar distances apart, and with practical limitations on acceleration, braking, and passenger safety and comfort, metro train speeds lie within a relatively narrow range. Vehicle lengths, bogie and axle spacings, and fastener spacings also tend to lie within restricted bands.

For the ground borne vibration problem at metro systems, the most dominant range of frequencies is below 100 Hz which mainly concerns the excitations from both fastener passing frequency and the loaded track resonance frequency. To control the ground borne vibration, understanding the influence of track dynamic behavior and effective mitigation measures on metro track systems is important.

This paper describes a method to reduce slab low frequency vibration by applying tuned slab dampers on a metro track. Track frequency response functions have been compared between a standard slab track and the track with optimized tuned slab damper. Slab and track bed vibration measurements were also carried out on the same track with and without tuned damper respectively under the same traffic conditions. The results demonstrate that a tuned slab damper effectively reduces low frequency slab vibration level, and more than 10 dB reduction can be achieved under normal metro traffic conditions.

## 2 Theory of Tuned Slab Dampers on Metro Track

### 2.1 Theory of Dynamic Vibration Absorber

J. Ormondroyd proposed the theory of dynamic vibration absorber in 1928 [1–3]. According to this theory, a tuned mass-spring-damper system is added as the dynamic vibration absorber to the main vibration system. When the added tuned system resonates, the reacting force of the added tuned system can reduce the vibration of the main system.

The dynamic vibration absorber can be effective when the excited forces distribute in particular frequency ranges.

To introduce the theory of designing a dynamic vibration absorber for a single degree of freedom for a main vibration system ( $k_1$ - $m_1$ - $c_1$ ), a combined system can be simplified as a two degree of freedom vibration system when adding a vibration

absorber ( $k_2$ - $m_2$ - $c_2$ ) to the main vibration system as shown in Fig. 1, a harmonic force  $F e^{i\omega t}$ , is assumed to apply on the main vibration system.

The equation of motion based on Newton’s laws can be established as below [4–7]:

$$m_1 \ddot{x}_1 + c_2(\dot{x}_1 - \dot{x}_2) + k_2(x_1 - x_2) + c_1 \dot{x}_1 + k_1 x_1 = F e^{i\omega t} \tag{1}$$

$$m_2 \ddot{x}_2 + c_2(\dot{x}_2 - \dot{x}_1) + k_2(x_2 - x_1) = 0 \tag{2}$$

where  $m_1$   $k_1$  and  $c_1$  are mass, stiffness, and damping respectively for the main vibration system;  $m_2$ ,  $k_2$  and  $c_2$  are mass, stiffness, and damping respectively for the tuned system;  $x_1$  is displacement of  $m_1$  and  $x_2$  is displacement of  $m_2$ .

Supposing the solution of the steady forced vibration displacement is

$$\{x\} = \{X\} e^{i\omega t} \tag{3}$$

Substituting this form of solution into Eqs. (1) and (2) gives the complex displacement response amplitude of the main system.

$$\bar{x}_1 = \frac{(k_1 k_2 - m_2 k_1 \omega^2 + i k_1 c_2 \omega)}{\left[ m_1 m_2 \left( \frac{k_1}{m_1} - \omega^2 \right) \left( \frac{k_2}{m_2} - \omega^2 \right) - c_1 c_2 \omega^2 \right] + i \omega [c_2 k_1 + c_1 k_2 - \omega^2 (m_1 c_2 + m_2 c_1 + m_2 c_2)]} \cdot \frac{F}{k_1} \tag{4}$$

Defining:

$$\delta_s = F/k_1, \omega_{1n} = \sqrt{k_1/m_1}, \omega_{2n} = \sqrt{k_2/m_2}, \alpha = \omega_{2n}/\omega_{1n}, \gamma = \omega/\omega_{1n}$$

$$\mu = m_2/m_1, \zeta_1 = c_1/2m_1\omega_{1n}, \zeta_2 = c_2/2m_2\omega_{2n}.$$

The dimensionless form response amplitude for  $\bar{x}_1$  is:

$$\frac{X_1}{\delta_s} = \sqrt{\frac{(\alpha^2 - \gamma^2)^2 + (2\alpha\gamma\zeta_2)^2}{(\alpha^2 - [1 + 4\alpha\zeta_1\zeta_2 + (1 + \mu)\alpha^2]\gamma^2 + \gamma^4)^2 + (2\gamma\{(\alpha^2 - \gamma^2)\zeta_1 + \alpha[1 - (1 + \mu)\gamma^2]\zeta_2\})^2}} \tag{5}$$

**Fig. 1** Model of dynamic vibration absorber

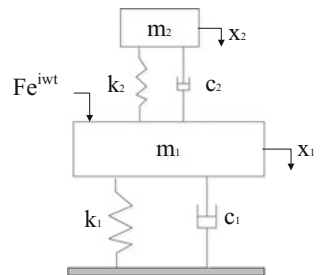
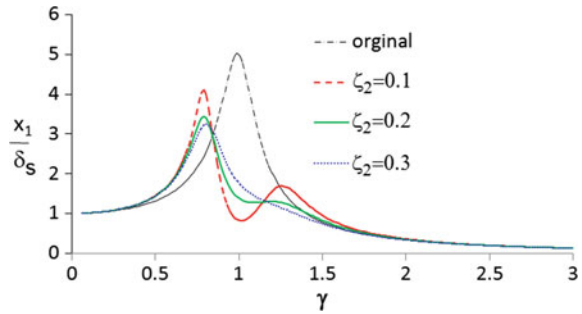


**Fig. 2** Displacement amplitude of main system



Here  $X_1$  is the amplitude of complex displacement  $\bar{x}_1$ .

To illustrate this result, Fig. 2 shows the dimensionless form of the amplitude plotted against frequency ratio  $\gamma$  ( $\alpha = 1$ ,  $\mu = 0.3$ ).

As shown in Fig. 2, the displacement response amplitude of the system with a dynamic vibration absorber is lower than that of the original system in a frequency range near the frequency  $\omega_{1n}$ . In this way, the dynamic vibration absorber system can reduce the vibration of the main system in a particular frequency range.

If the natural frequency is equal to the excitation frequency of the main vibration system, the vibration amplitude can be reduced near the excitation frequency.

## 2.2 Application of Dynamic Vibration Absorber on Metro Track

To reduce the vibration of the metro system at particular frequency range, a dynamic vibration absorber can be introduced with a special design.

By adding optimized tuned slab dampers (the so called dynamic vibration absorber) for metro track system [8], vibration energy of the metro slab can be absorbed, and hence the vibration of the slab can be reduced.

Figure 3 shows a slab track system with tuned slab damper. This system is composed by slab mat, slab, block pad, mass block, and resilient baseplates in which the mass block and block pad forms a tuned slab damper. By matching the stiffness of the block pad, mass of the block and also the stiffness of the baseplate and the slab mat with slab mass, the combination track system can achieve high-level vibration damping of the track.

As shown in Fig. 3, tuned slab damper which is composed of rubber pad and mass block is added on the combination track system. Natural frequency of the tuned slab damper is specially designed to reduce the vibration of track slab.

Mass, stiffness and damping of the added system are the main factors for designing a dynamic vibration absorber for main system.

For example, when the train passes the fasteners, the excitation frequency of the rail for the slab is  $f_1 = v/L$ , where  $v$  is the speed of train,  $L$  is the fastener spacing.

**Fig. 3** Track with tuned slab damper

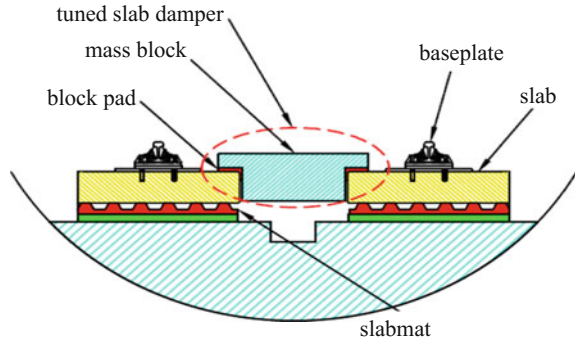
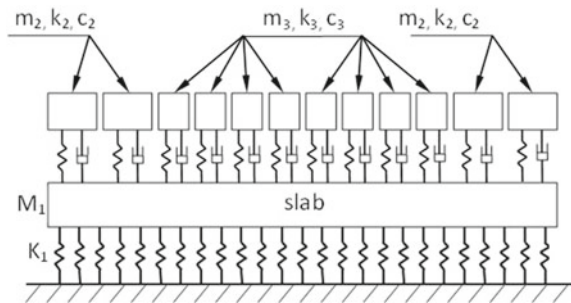


**Fig. 4** Track model with tuned slab dampers



Take the speed of train as 80 km/h, the fastener spacing as 625 mm, then the fastener passing excitation frequency is 35.6 Hz. Suppose the mass of a track slab is 5000 kg. A tuned slab damper system can be designed as below: choose the mass ratio as  $\mu = 0.3$ , frequency ratio  $\alpha = 0.77$ , the tuned slab damper's natural frequency  $f_2 = 27.4$  Hz, the damping ratio of the tuned slab damper is  $\zeta_2 = 0.23$ , the tuned slab damper's stiffness is  $k_2 = 44.4$  kN/mm.

In order to make it easy to assemble, divide the above tuned slab damper into 12 parts (2 types), every part constitutes a small tuned slab damper, as seen in Fig. 4.

### 3 Simulation of Vibration Reduction Effect of Tuned Slab Damper

#### 3.1 Simulation Model

For the simulation, the standard 60 kg rail is selected. Slab panel is 5 m long and 2.4 m wide with thickness of 0.2 m; Slab mats are under the slab panel, which has a thickness of 0.03 m and area stiffness of 0.018 N/mm<sup>3</sup>. Stiffness of fasteners is 60 MN/m for standard tracks, and 8 MN/m for tracks with tuned dampers.

In the simulation model, rails are modelled using beam elements, track system is modelled using hexahedral elements, and fasteners are simplified by springs with the space of 0.625 m. Material parameters are shown in Table 1.

The simulation model based on the simplified methods mentioned is shown in Fig. 5. Simulation model is shown in Fig. 6. To consider the effect of vehicle on track system, the unsprung mass of 850 kg is adopted. The response position of the slab is on the center of the slab, and the one on foundation is 300 mm to the edge of slab, the same as on site measurement.

**Table 1** Material parameters of simulation model

Item	Density/kg m <sup>-3</sup>	Modulus of elasticity/MPa	Poisson ratio
Rail	7850	210,000	0.3
Slab	2500	32,500	0.2
Slab mat	1200	3	0.49
Foundation	1500	2000	0.25

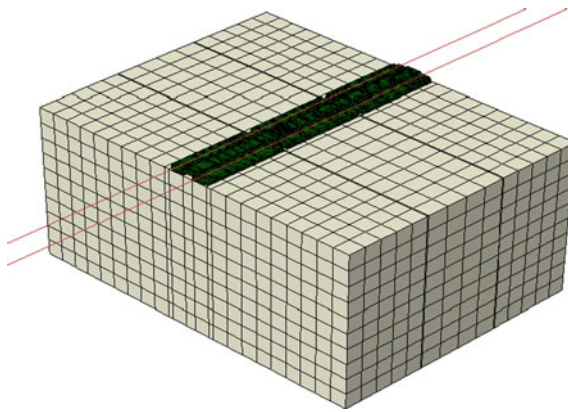


**Fig. 5** Simulation model

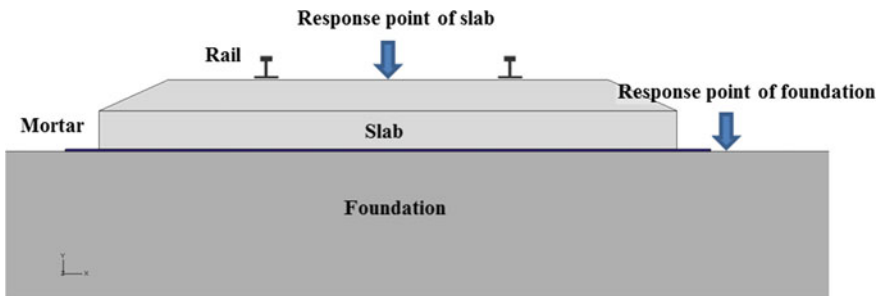


**Fig. 6** Response points of track system



## 3.2 Simulation Results

### 3.2.1 Analysis of Resonance Frequency of Tuned Dampers on Slabs

The vibration reduction performance of tuned slab damper is analyzed based on the mathematical model. Figure 7 shows the comparison of vibration acceleration between slabs without and with tuned slab damper (tuned damper to slab mass ratio  $\mu = 0.3$ ). Several response peaks between 22 and 35 Hz on the line representing acceleration of slab without dampers are no longer shown on the acceleration response of track with tuned damper slab. The resonance of slab vibration is cancelled out. From the result, the resonance frequency of tuned damper is around 27 Hz, agreed well with design value discussed in Sect. 2.2 above.

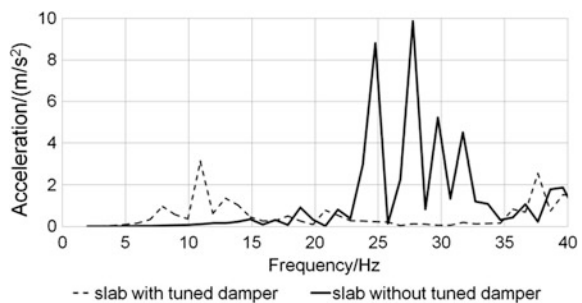
### 3.2.2 Effect of Mass Ratio on Vibration Reduction Performance

The vibration amplitude is inversely proportional to the mass ratio, the higher the mass ratio is, and the lower the slab vibration amplitude is. To analyze the effect of mass ratio on vibration reduction performance, vibration acceleration of slabs with tuned slab dampers for 4 different mass ratios, are calculated. The results are shown in Fig. 8, where  $\mu = 0$  representing slabs without tuned dampers. From Fig. 8a, in frequency range of 20–40 Hz, the vibration is considerably reduced, more reduction with higher mass ratio. From Fig. 8b, insertion loss and mass ratio are in the direct ratio, and the insertion loss is up to 15 dB when mass ratio is 0.3.

### 3.2.3 Vibration Reduction Effect of Tuned Slab Dampers on Slabs and Track Bed

To analyze the effect of tuned slab dampers on slabs and track bed, frequency response functions of conventional standard slab track, combined slab track system and combined slab track with tuned slab damper (mass ratio  $\mu = 0.3$ ) are simulated. The results are shown in Fig. 9. For the slab response as shown in Fig. 9a, although

**Fig. 7** Comparison of vibration between two kinds of slabs



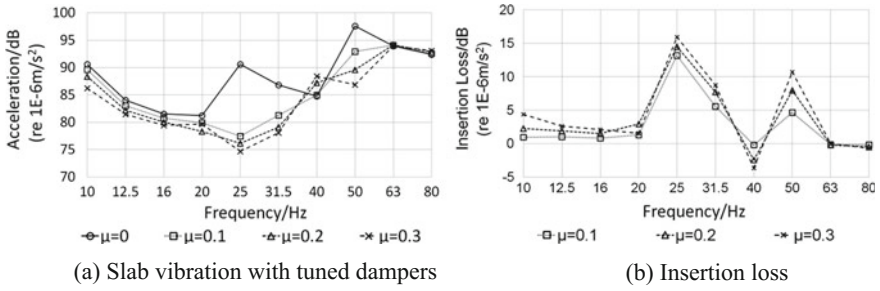


Fig. 8 Comparisons of slabs vibration level with different tuned mass

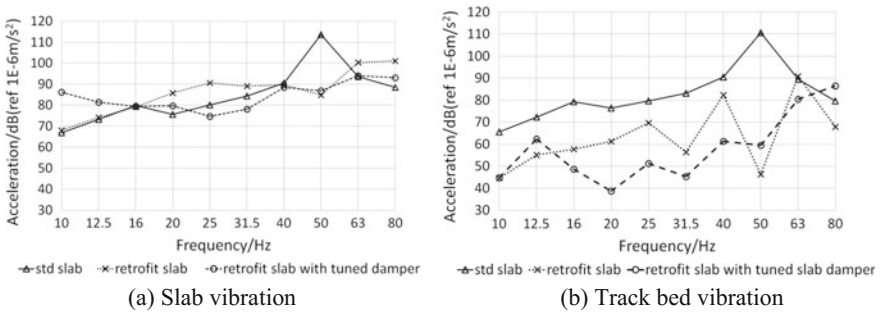


Fig. 9 Vibration comparison of slabs and foundations

combined slab track showed reduced vibration levels in 40–63 Hz range, The response increased in frequency range of 20–31.5 Hz. For the track bed response as shown in Fig. 9b, both combined slab tracks with and without tuned slab damper show vibration reductions, but the reduction with tuned slab damper system is much higher.

Considering the overall combined vibration reduction ability on both slab and track bed, the tuned slab damper system demonstrated promising and superior performance.

## 4 Frequency Response Function Test

### 4.1 Lab Test Method

To exclude the influence of axle load, vehicle speed, line curvature and wheel/rail surface conditions and other factors, and to gain a more accurate understanding of the vibration characteristics and vibration transfer law on different track structures, tests are carried out under controlled conditions. This way, the dynamic

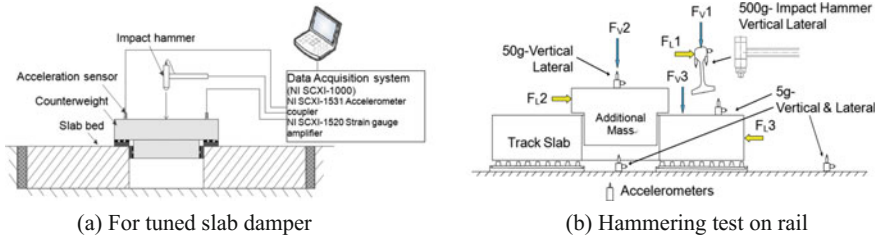


**Fig. 10** Schematic diagram of track transfer response function test

characteristics of the system parameters under ideal conditions, such as track vibration isolation and vibration characteristics of track slab can be obtained. The track is excited with an instrumented hammer, and the measurement of various vibration responses is at the same positions as under traffic condition.

To verify the performance of slab low frequency vibration attenuation by tuned slab dampers on a metro track, laboratory tests are carried out in two conditions on a 1:1 size combined slab trials section. Test 1 is on a standard slab track setting, and 2 on the track with optimized tuned slab dampers. Tests of track transfer response function include:

- (1) resonance frequency of tuned slab damper;
- (2) transfer response function from rail to track slab;
- (3) transfer response function from rail to track bed.

Figure 10 shows the direction and position of exciting force and response transducer. The excitation and two vibration response positions are above the cross-section of the fastener and 1/2 span of two fasteners respectively. Responses are measured at several different positions to eliminate the deviation of the system itself and experiments.

## 4.2 The Frequency Response Function Analysis

Track transfer response functions, vibration response functions of slab and track bed are discussed to illustrate the vibration attenuation influence of tuned slab dampers on a metro track. The resonance frequency of tuned slab damper is also shown in Fig. 11 to determine whether the design requirements are achieved.

### 4.2.1 The Resonance Frequency of Tuned Slab Damper Analysis

The result of resonance frequency of tuned slab damper is obtained by hammering test on the laboratory's 1:1 scaled combined slab trials section. Figure 11 shows that the vertical natural frequency is around 27 Hz and lateral natural frequency is around 15 Hz.

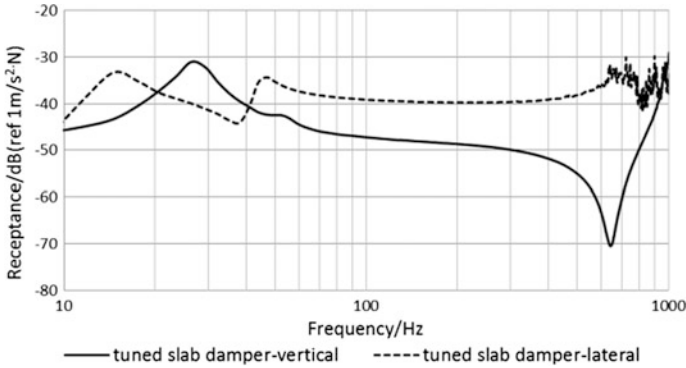


Fig. 11 The resonance frequency of tuned slab damper

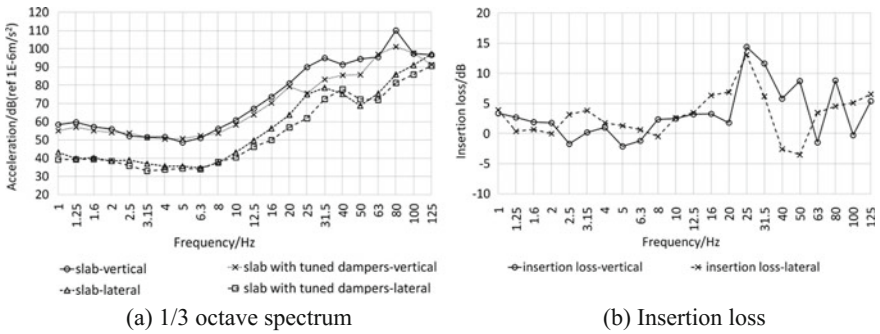


Fig. 12 Track slab acceleration level and insertion loss

### 4.2.2 The Track Slab Transfer Function Analysis

Figure 12 shows the track slab vibration acceleration level and insertion loss of a standard slab track and the track with optimized tuned slab dampers. In the frequency range between 20 and 40 Hz, the vibration levels in both vertical and lateral directions are significantly reduced on the track with optimized tuned slab dampers, especially at central frequency of 25 Hz band, the vertical vibration amplitude has been reduced up to about 15 dB, and the lateral vibration amplitude reduced about 13 dB.

### 4.2.3 The Slab Bed Transfer Function Analysis

Figure 13 shows the vibration acceleration level of slab bed with the standard slab track and the track with optimized tuned slab dampers and their insertion loss. In the low frequency range below 125 Hz, the track bed vibration peak on the track

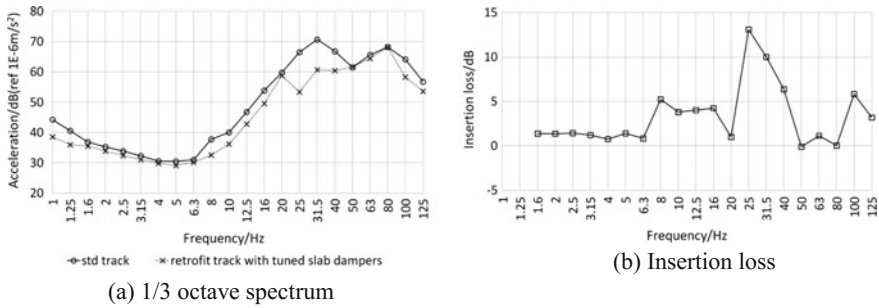


Fig. 13 Slab bed vertical acceleration level and insertion loss

with optimized tuned slab dampers is less than ordinary slab track, especially at 25 Hz frequency band for more than 13 dB reduction. The results demonstrate that tuned slab dampers are very effective in reducing the transmission of vibration energy from track to foundation.

## 5 On Site Test Under Traffic Conditions

### 5.1 Track Vibration Measurements

The test site is a viaduct with span of 30 m. The track has a curvature of 600 m located between Longyang road station and Zhangjiang station in Shanghai Metro Line 2. The original track is a standard slab track fitted with 60 kg rail and type DT-VII baseplate in spacing of 625 mm. The track was retrofitted with pre-cast slab supported on the slab mat and fitted with new resilient baseplates. The pre-cast slab panel is a framed shape where there is room to attach the tuned slab damper in the center area. The same rails were kept before and after the track retrofitted. The same test train was used to present a traffic condition at different speeds. Figures 14 and 15 show the vibration sensors arrangement schematic diagrams for both original normal track and retrofit track.

Fig. 14 Sensors arrangement (std track)

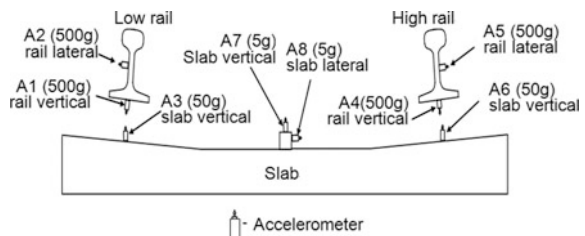
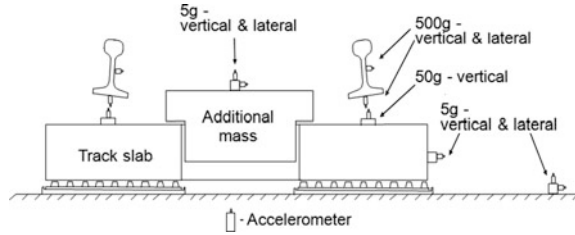


**Fig. 15** Sensors arrangement (retrofitted track)



### 5.2 The Test Results Under Traffic Condition

The test train was used to simulate the traffic condition at different nominal speeds of 20, 40 and 60 km/h respectively to present some different excitations. Track and viaduct vibration measurements have been conducted for both original standard track and refitted track with the same rolling stock system. Wayside noise and in-car noise have also been measured to check the effect on track noise radiation.

Track bed vibration acceleration levels for the low frequency range are shown in Fig. 16 in the vertical direction and Fig. 17 in the lateral direction. The total vertical acceleration levels at train speed of 60 km/h on the track bed are 100.2 and 86.9 dB

**Fig. 16** Track slab bed vertical vibration

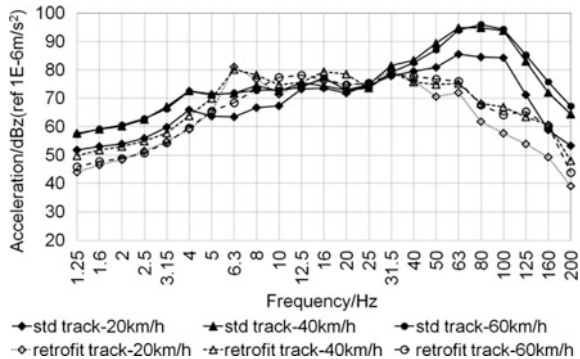
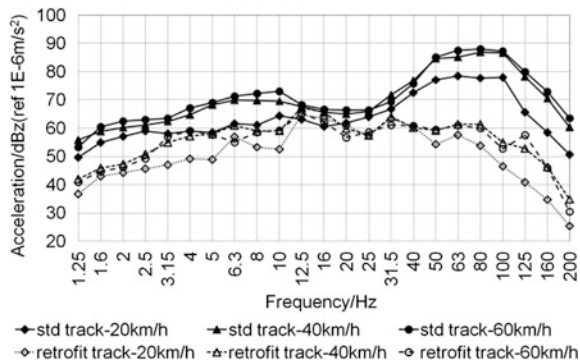


**Fig. 17** Track slab bed lateral vibration



with standard slab and retrofit slab respectively. This indicates an insertion loss of 13.3 dB in the vertical direction. The total lateral acceleration levels at train speed of 60 km/h on the track bed are 93.7 and 72.2 dB with standard slab and retrofit slab respectively. This indicates an insertion loss of 21.5 dB in the lateral direction.

## 6 Conclusions

For low frequency ground vibration control on metro system, the effects of the combined slab track system with tuned slab dampers are analyzed, simulated, and measured in laboratory on full scale test rig, and under traffic conditions. By introducing the tuned slab damper into a combined slab track system, the vibration of the slabs in the low frequency range is significantly reduced by about 15 dB based on the simulation and laboratory test. On-site tests also show the vibration reduction of track bed is more than 13 dB in the vertical direction and 22 dB in the lateral direction on the combined slab track with tuned slab damper compared with those on ordinary standard track system at train speed of 60 km/h. This indicates that the tuned slab damper is effective for controlling the low frequency track vibration on a metro system.

## References

1. Liu, Y.Z., Yu, D.L., Zhao, H.G., et al.: Review of passive dynamic vibration absorber. *Chin. J. Mech. Eng.* **43**(3), 14–21 (2007)
2. Brock, J.E.: A note on the damped vibration absorber. *J. Appl. Mech.* **13**(4), A-284 (1946)
3. Den Hartog, J.P.: *Mechanical Vibration*, pp. 112–132. McGraw-Hill Book Company, New York (1947)
4. Wei, C.F.: Time-Domain Conversion and the Application Research of Track Irregularity Power Spectrum, pp. 26–28. Southwest Jiaotong University, Chengdu (2011)
5. Zhai, W.M.: *Vehicle-Track Coupling Dynamics*, pp. 175–178. China Railway Publishing House, Beijing (1997)
6. Chen, G.: *The Analysis on Random Vibration of Vehicle-Track Coupling System*, p. 153. Southwest Jiaotong University, Chengdu (2000)
7. Liu, J.B., Wang, Z.Y., Du, X.L., et al.: Three-dimensional visco-elastic artificial boundaries in time domain for wave motion problems. *Eng. Mech.* **22**(6), 46–51 (2005)
8. Liu, W.F., Liu, W.N., Yuan, Y.: Study on isolation efficiency of floating slab track using a numerical prediction model of metro traffic induced vibrations. *Journal of the China Railway Society* **34**(9), 81–86 (2009)

# Optimal Design of Wave Barriers for the Reduction of Vibration Levels



C. Van hoorickx, M. Schevenels and G. Lombaert

**Abstract** In order to reduce ground vibration levels in a building, wave barriers can be introduced in the soil between the source and the building. In this contribution, the wave barriers are optimized using topology optimization to discover novel, effective design geometries. The objective is to minimize the amount of stiffer material introduced in the soil while satisfying the required vibration criteria in the building. In this way, an optimal geometry is determined that considerably reduces the required amount of stiffer material, outperforming rectangular wall barriers using the same amount of material. To make the design less sensitive to geometric imperfections, a worst case robust approach is applied. The resulting smaller sensitivity with respect to geometric imperfections also ensures that a posteriori design simplifications have a minimal impact on the barrier's performance.

## 1 Introduction

Railway induced vibrations may lead to the malfunctioning of sensitive equipment. Extensive research has been performed to search for effective vibration measures [1]. Three categories of reduction measures are distinguished, namely at the source, the transmission path, and the receiver [2]. The present work considers wave barriers to hinder ground transmission.

Currently, only a limited number of simple design geometries for mitigation measures have been investigated. However, current flexibility in construction methods, such as jet grouting, provides opportunities for further improvement.

---

C. Van hoorickx (✉) · G. Lombaert  
Department of Civil Engineering, Structural Mechanics Section, KU Leuven,  
Kasteelpark Arenberg 40, 3001 Leuven, Belgium  
e-mail: cedric.vanhoorickx@kuleuven.be

M. Schevenels  
Department of Architecture, Architectural Engineering, KU Leuven,  
Kasteelpark Arenberg 1, 3001 Leuven, Belgium



To discover novel design geometries, topology optimization [3] is applied. Wave barrier effectiveness can be quantified by comparing the calculated one-third octave band velocity spectra in specific receiver points in the building to generic vibration criteria for sensitive equipment [4].

As full control of the built geometry is difficult in constructing underground structures, the optimized design should be robust with respect to geometrical imperfections [5]. A worst case approach is applied to improve the robustness of the design [6]. The robust designs can be simplified with almost no deterioration of performance.

## 2 Problem Description and Methodology

### 2.1 Problem Description

Figure 1 shows the problem considered in this paper. A building is located at the surface of a homogeneous elastic halfspace, representing the soil. The soil is a typically sandy soil having a mass density of  $2000 \text{ kg/m}^3$ , a longitudinal wave velocity of  $400 \text{ m/s}$ , and a shear wave velocity of  $200 \text{ m/s}$ . The building has a total width of  $12 \text{ m}$ , a total height of  $12 \text{ m}$ , and is a four-story frame consisting of four floors and two spans. The thickness of the walls is  $0.25 \text{ m}$ , while the thickness of the slabs is  $0.20 \text{ m}$ . The walls and slabs are made of reinforced concrete with a mass density of  $2500 \text{ kg/m}^3$ , a Young's modulus of  $30 \text{ GPa}$ , and a Poisson's ratio of  $0.25$ .

The halfspace is excited at the surface by a vertical load at a distance of  $25 \text{ m}$  from the building. A line load with a uniform peak amplitude of  $45 \text{ N/m}$  in the frequency range between  $4$  and  $80 \text{ Hz}$  is applied, as a first approximation of an actual train loading. The aim is to reduce the vibration levels at specific points and

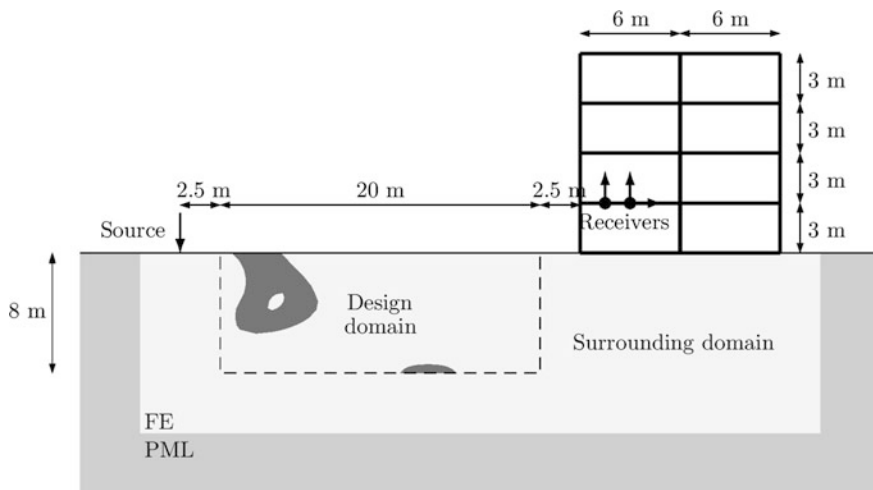


Fig. 1 The two-dimensional optimization problem

directions inside the building, in this case on the first floor in the span closest to the source. A horizontal receiver is considered in the middle of the floor, while two vertical receivers are considered at one fourth and in the middle of the floor span.

To reduce the vibration levels at these receiver points, a design domain with dimensions  $8 \times 20 \text{ m}^2$  is considered in the elastic halfspace, located between the source and the building. In this design domain a stiffer material is introduced. This material is given the characteristics of grout: a mass density of  $2000 \text{ kg/m}^3$ , a longitudinal wave velocity of  $950 \text{ m/s}$ , and a shear wave velocity of  $550 \text{ m/s}$ .

The elastodynamic problem is solved using a two-dimensional finite element model with four-node elements in plane strain. An element size of  $0.25 \text{ m}$  is used, corresponding to ten elements per shear wavelength of the soil at a frequency of  $80 \text{ Hz}$ , the upper limit considered here. In the design domain, however, the mesh size is reduced to  $0.125 \text{ m}$  to achieve a design with sufficient detail. The building is modeled using beam elements adapted to plane strain with an element size of  $0.25 \text{ m}$ . The finite element equilibrium equations are written as:

$$\hat{\mathbf{K}}\hat{\mathbf{u}} = \hat{\mathbf{p}} \quad (2.1)$$

where  $\hat{\mathbf{p}}$  is the load vector,  $\hat{\mathbf{u}}$  is the displacement vector, and  $\hat{\mathbf{K}}$  is the dynamic stiffness matrix. At the boundaries of the finite element mesh, appropriate radiation boundary conditions prevent spurious wave reflections. In this paper, Perfectly Matched Layers (PML) are used [7].

## 2.2 Topology Optimization

For finding the optimal distribution of the stiffer material in the design domain, topology optimization is used. The material distribution is parameterized with element densities  $\bar{\rho}_e$  for each element  $e$  in the design domain. If the element density is equal to 0, element  $e$  has the properties of the homogeneous halfspace, while if it is equal to 1, element  $e$  has the properties of the stiffer material. In order to solve the optimization problem with a gradient based method, a continuous interpolation of the element densities between 0 and 1 is used to interpolate the material properties. The Solid Isotropic Material with Penalization (SIMP) interpolation is applied, that avoids so-called gray designs with intermediate densities [8].

The (physical) element densities  $\bar{\rho}_e$  are obtained from the design variables  $\rho_e$  of the optimization problem by applying a projection filter [9]:

$$\bar{\rho}_e = \frac{\tanh(\beta\eta) + \tanh(\beta(\tilde{\rho}_e - \eta))}{\tanh(\beta\eta) + \tanh(\beta(1 - \eta))} \quad (2.2)$$

where  $\beta$  is a sharpness parameter, controlling the smoothness of the projection, and  $\eta$  is the projection threshold. This equation projects filtered densities  $\tilde{\rho}_e$  higher than the projection threshold  $\eta$  towards 1, while filtered densities  $\tilde{\rho}_e$  lower than the

projection threshold  $\eta$  are projected towards 0. The filtered densities  $\tilde{\rho}_e$  are obtained from:

$$\tilde{\rho}_e = \frac{\sum_{i=1}^{N_e} w_{ei} v_i \rho_i}{\sum_{i=1}^{N_e} w_{ei} v_i} \tag{2.3}$$

with  $N_e$  the number of elements in the design domain,  $v_i$  the volume of element  $i$ ,  $w_{ei} = \max(R - r_{ei}, 0)$  a weighting function which depends on the filter radius  $R$  and the center-to-center distance  $r_{ei}$  between elements  $e$  and  $i$ . In this paper, the filter radius  $R$  is equal to 6 elements or 0.75 m, the projection threshold  $\eta$  is set to 0.5 and the sharpness parameter  $\beta$  has an initial value of 1 and is continuously increased such that the value of 32 is reached after 300 iterations.

### 2.3 Optimization Problem

To quantify the effectiveness of the wave barriers, the calculated one-third octave band velocity spectra are compared with generic vibration criteria (VC) for sensitive equipment (Fig. 2c) [4]. These criteria are specified in terms of the maximum allowable RMS velocity in the one-third octave bands between 4 and 80 Hz. The VC criteria impose less stringent vibration limits in the frequency range between 4 and 8 Hz, where the limit is that of constant acceleration instead of constant velocity. For the VC-C criterion, for example, the maximum allowable RMS velocity is equal to 12.5  $\mu\text{m/s}$  between 8 and 80 Hz, while for lower frequencies, it increases to a value of 25  $\mu\text{m/s}$  at 4 Hz.

The aim is to distribute the material in the design domain in order to meet the intended vibration criteria. However, since there is a cost in the amount of material that is stiffened, the volume of the wave barrier is minimized. The problem is

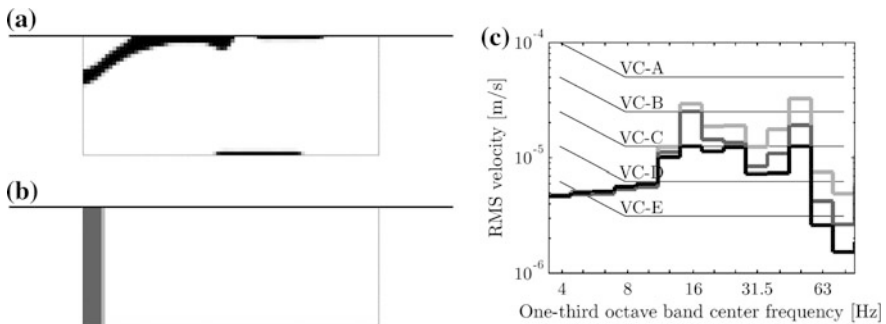


**Fig. 2** **a** Topology optimized design, **b** rectangular design with a depth of 8 m and the same volume as the optimized design, and **c** the maximum one-third octave band RMS spectra of the velocity at the receivers for the original homogeneous halfspace (light gray), for the rectangular design (dark gray), and for the optimal design (black)

formulated as a minimization problem, where the volume is minimized and the vibration levels are constrained to the vibration criteria:

$$\begin{aligned}
 \min_{\rho_e} \quad & \sum_{e=1}^{N_e} v_e \bar{\rho}_e \\
 \text{s.t.} \quad & \hat{v}_{m,i}^{\text{RMS}}(\bar{\rho}_e) \leq \hat{v}_m^{\text{VC}} \quad m = 1 \dots N_{\text{band}} \\
 & \quad \quad \quad \quad \quad \quad \quad \quad i = 1 \dots N_L \\
 & 0 \leq \rho_e \leq 1 \quad e = 1 \dots N_e
 \end{aligned} \tag{2.4}$$

where  $N_{\text{band}}$  is the number of one-third octave bands (14 between 4 and 80 Hz),  $N_L$  is the number of receiver points (3 in this paper),  $\hat{v}_{m,i}^{\text{RMS}}$  is the RMS velocity in the one-third octave band  $m$  at receiver location  $i$ , and  $\hat{v}_m^{\text{VC}}$  is the value of the maximum allowable RMS velocity in the one-third octave band  $m$ .

The optimization problem is solved using the method of moving asymptotes (MMA) [10]. Before applying this gradient-based method, the derivatives of the objective function with respect to the physical densities have to be calculated. To efficiently calculate the gradient, the adjoint method is used [3].

### 3 Topology Optimized Design

Figure 2a shows the topology optimized design, obtained from solving the optimization problem in Eq. (2.4), where the amount of material is minimized while the vibration levels have to meet the VC-C criterion. The maximum one-third octave band RMS spectra of the velocity at the receivers is shown in Fig. 2c for the original homogeneous halfspace and for the wave barrier. While the vibration levels in the original halfspace exceed even the VC-B criterion, they remain below the VC-C criterion after the introduction of the topology optimized design in the soil.

The design has a total cross sectional area equal to 6.8% of the design domain, or 10.9 m<sup>2</sup>. As the objective is to minimize the volume of the wave barrier, this optimized design is compared with a rectangular wave barrier with the same depth as the design domain (8 m) and the same volume as the optimized design, shown in Fig. 2b. The rectangular wall barrier is placed at the left hand side of the design domain, as this results in the best performance. Also for this design, the maximum one-third octave band RMS spectra of the velocity at the receivers is shown in Fig. 2c. Although the performance is better than for the original halfspace, the VC-B criterion is (slightly) exceeded in the one-third octave band with a center frequency of 16 Hz. Therefore, the optimized design is much more effective in reducing the vibration levels than the rectangular design.

Figure 3 shows for excitation at different frequencies (16, 25, and 50 Hz) the real part of the displacement field for the homogeneous halfspace, for the rectangular wall barrier with a volume of 10.9 m<sup>2</sup>, and for the topology optimized barrier. The rectangular wall barrier mainly reflects the incoming waves, and is therefore

more effective at higher frequencies, where the dimensions of the wall barrier are large enough compared to the wavelengths of the incoming Rayleigh waves. The topology optimized design also partly reflects the incoming waves at higher frequencies, but also redirects a part of the transmitted waves into the soil, away from the surface, lowering the vibration levels in the building.

In the optimized design, stiffer material is introduced in three main areas: (1) the top left structure containing an inclined and horizontal part, (2) a horizontal structure at the surface, and (3) a horizontal structure at the bottom. In Fig. 4, first the top left structure is isolated, and then only the inclined part of this structure is considered. The maximum one-third octave band RMS spectra of the velocity at the receivers is shown in Fig. 4c.

Removing the horizontal structure at the surface and at the bottom leaves the performance largely unaffected. However, at the one-third octave bands with a center frequency of 16 and 50 Hz, the VC-C limit is now exceeded. The corresponding real part of the displacement field is shown in Fig. 5a–c for excitation at 16, 25, and 50 Hz. At low frequencies, the Rayleigh waves, having a larger penetration depth, are disturbed by the bottom structure, while at frequencies around 50 Hz, the structures at the top and the bottom of the design domain can cause destructive interference.

The horizontal part of the top left structure mainly improves the lower one-third octave bands (with a center frequency between 16 and 31.5 Hz). The real part of the displacement field after removing the horizontal part of the top left structure is

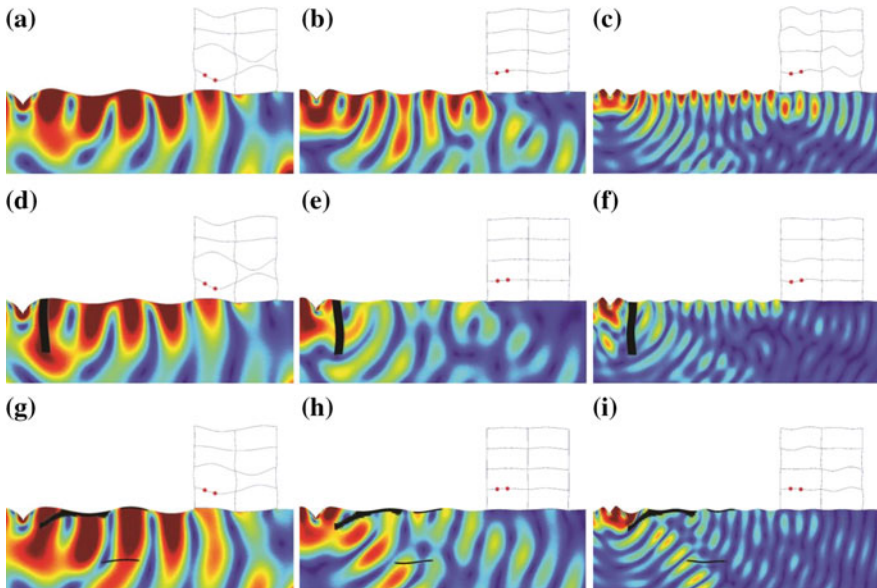


**Fig. 3** Real part of the displacement field in the homogeneous halfspace for excitation at **a** 16 Hz, **b** 25 Hz, and **c** 50 Hz, with the rectangular wall barrier in Fig. 2b for excitation at **d** 16 Hz, **e** 25 Hz, and **f** 50 Hz, and with the topology optimized design in Fig. 2a at **g** 16 Hz, **h** 25 Hz, and **i** 50 Hz

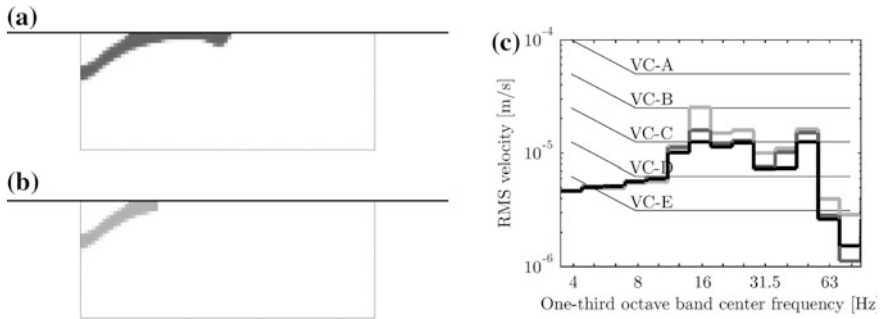


**Fig. 4** **a** Top left structure of the topology optimized design, **b** the inclined part of this structure, and **c** the maximum one-third octave band RMS spectra of the velocity at the receivers for the optimized design (black), the top left structure of this design (dark gray), and the inclined part of this structure (light gray)

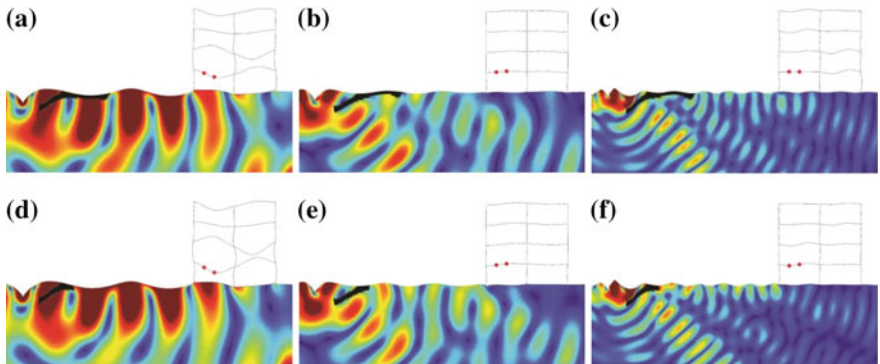


**Fig. 5** Real part of the displacement field in the homogeneous halfspace with the top left structure of the design for excitation at **a** 16 Hz, **b** 25 Hz, and **c** 50 Hz, with only the inclined part of this structure for excitation at **d** 16 Hz, **e** 25 Hz, and **f** 50 Hz

shown in Fig. 5d–f for excitation at 16, 25, and 50 Hz. At low frequencies, the structure becomes too small compared to the wavelength of the incoming wave and, as a result, there is almost no vibration reduction. At higher frequencies, however, the inclined part still causes the incoming waves to be redirected into the soil, so that the performance of the inclined part is still better than for the wall barrier.

### 4 Robust Design

The optimized design in Fig. 2a may be very sensitive to deviations in the geometry. The influence of geometric deviations can be modeled by varying the projection threshold  $\eta$  in Eq. (2.2) [6]. For low values of the projection threshold,

for example 0.25, the projection of the filtered densities to the physical densities also includes lower values, increasing the dimensions of the stiffer material; these designs are called dilated. For high values of the projection threshold, for example 0.75, the projection of the filtered densities to the physical densities only includes the higher values, decreasing the dimensions of the stiffer material; these designs are called eroded. For the dilated design, the maximum RMS velocity in the one-third octave bands for the different receiver locations is equal to  $9.38 \mu\text{m/s}$ , which is well below the VC-C criterion with a maximum allowable RMS velocity of  $12.5 \mu\text{m/s}$ . For the eroded design, however, the maximum RMS velocity is equal to  $32.13 \mu\text{m/s}$ , thereby exceeding even the VC-B criterion with a maximum allowable RMS velocity of  $25 \mu\text{m/s}$ .

The resulting intermediate design is shown in Fig. 6. The cross-sectional area is equal to 13.4% of the design domain, or  $21.4 \text{ m}^2$  and is therefore much larger than the one of the topology optimized design in Fig. 2a. This design is, however, robust with respect to geometric imperfections. For the dilated, intermediate, and eroded design, having a cross-sectional area of 26.7, 21.4, and  $16.2 \text{ m}^2$ , respectively, the maximum RMS velocities are 12.1, 11.4, and  $12.5 \mu\text{m/s}$ , all meeting the VC-C criterion.

The real part of the displacement field for excitation at 16, 25, and 50 Hz is shown in Fig. 7. The deep part at the left side of the design partly reflects the incoming waves and partly guides them into the soil, away from the surface. The horizontal part ensures that also the low frequency wave transmission is reduced.

For practical construction, it may be desirable to simplify the design. Since the design in Fig. 6 is robust to thickness variation, simplifying the geometry is not expected to significantly affect the design performance. Two simplified designs are shown in Figs. 8 and 9, where a simplified shape with straight edges is intuitively positioned at the location where the stiffer material is concentrated in the optimized

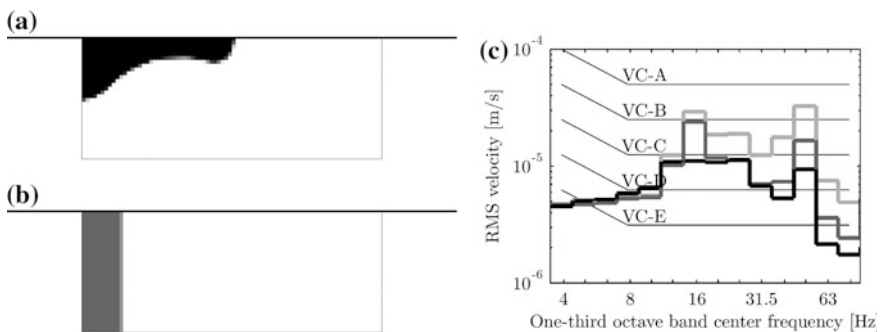


**Fig. 6** **a** Robust topology optimized design, **b** rectangular design with a depth of 8 m and the same volume as the optimized design, and **c** the maximum one-third octave band RMS spectra of the velocity at the receivers for the original homogeneous halfspace (light gray), for the rectangular design (dark gray), and for the robust design (black)

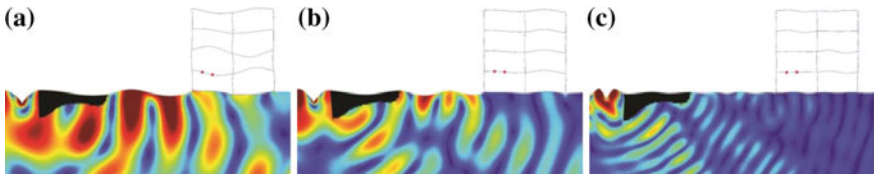


**Fig. 7** Real part of the displacement field in the homogeneous halfspace with the robust design for excitation at **a** 16 Hz, **b** 25 Hz, and **c** 50 Hz

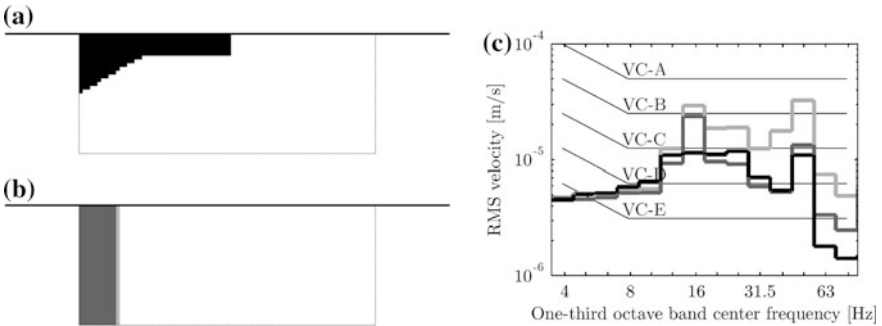


**Fig. 8** **a** First simplified design, **b** rectangular design with a depth of 8 m and the same volume as the optimized design, and **c** the maximum one-third octave band RMS spectra of the velocity at the receivers for the original homogeneous halfspace (light gray), for the rectangular design (dark gray), and for the simplified design (black)

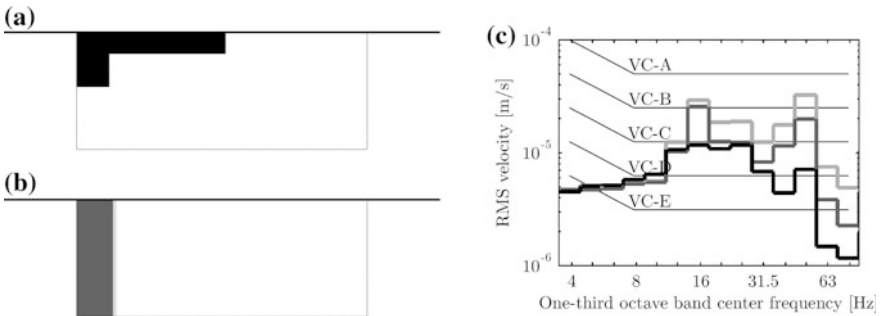


**Fig. 9** **a** Second simplified design, **b** rectangular design with a depth of 8 m and the same volume as the optimized design, and **c** the maximum one-third octave band RMS spectra of the velocity at the receivers for the original homogeneous halfspace (light gray), for the rectangular design (dark gray), and for the simplified design (black)

design. Both designs have more or less the same amount of material as the robust design (13.1% of the design domain) and the VC-C criterion is still met for all one-third octave bands.



## 5 Conclusion

In this paper, topology optimization is used to design wave barriers for the reduction of elastodynamic wave transmission. The volume of the wave barriers is minimized while the vibration levels have to meet stringent vibration criteria. Topology optimization leads to designs which meet the vibration criteria and outperform a rectangular wave barrier using the same amount of material. To make the design less sensitive to geometric imperfections, a worst case approach is adopted. A larger amount of material is needed, but the resulting design is robust with respect to geometric imperfections, making it possible to simplify the topology with almost no deterioration of performance.

**Acknowledgements** The first author is a doctoral fellow of the Research Foundation Flanders (FWO). The financial support is gratefully acknowledged. The authors are members of KU Leuven-BOF PFV/10/002 OPTEC-Optimization in Engineering Center.

## References

1. Coulier, P., François, S., Degrande, G., Lombaert, G.: Subgrade stiffening next to the track as a wave impeding barrier for railway induced vibrations. *Soil Dyn. Earthq. Eng.* **48**, 119–131 (2013)
2. Lombaert, G., Degrande, G., François, S., Thompson, D.J.: Ground-borne vibration due to railway traffic: a review of excitation mechanisms, prediction methods and mitigation measures. In: Nielsen, J.C.O., et al. (eds.) *Noise and Vibration Mitigation for Rail Transportation Systems, Notes on Numerical Fluid Mechanics and Multidisciplinary Design*, vol. 126, pp. 253–287. Springer, Heidelberg (2015)
3. Bendsøe, M.P., Sigmund, O.: *Topology Optimization: Theory, Methods and Applications*. Springer, Berlin (2003)
4. Gordon, C.G.: Generic vibration criteria for vibration-sensitive equipment. In *Proceedings of the SPIE Conference on Vibration Control and Metrology*, vol. 1619, pp. 71–85, San Jose, California, USA (November 1991)
5. Jansen, M., Lombaert, G., Schevenels, M.: Robust topology optimization of structures with imperfect geometry based on geometric nonlinear analysis. *Comput. Methods Appl. Mech. Eng.* **285**, 452–467 (2015)
6. Wang, F., Lazarov, B.S., Sigmund, O.: On projection methods, convergence and robust formulations in topology optimization. *Struct. Multi. Optim.* **43**, 767–784 (2011)
7. Harari, I., Albocher, U.: Studies of FE/PML for exterior problems of time-harmonic elastic waves. *Comput. Methods Appl. Mech. Eng.* **195**, 3854–3879 (2006)
8. Bendsøe, M.P.: Optimal shape design as a material distribution problem. *Struct. Optim.* **1**, 193–202 (1989)
9. Guest, J.K., Prévost, J.H., Belytschko, T.: Achieving minimum length scale in topology optimization using nodal design variables and projection functions. *Int. J. Numer. Meth. Eng.* **61**, 238–254 (2004)
10. Svanberg, K.: The method of moving asymptotes—a new method for structural optimization. *Int. J. Numer. Meth. Eng.* **24**, 359–373 (1987)

# Vibration Reduction with Installation of Rail Dampers—A Case Study



B. E. Croft and C. M. Weber

**Abstract** Measurements of ground vibration were taken in a rail tunnel and cross passage, before and after the installation of rail dampers. In addition to lower in-car noise, measurements indicated an immediate reduction in ground vibration, attributed to the rail dampers. While the most significant observed reduction in vibration was at frequencies above those of interest for ground-borne noise control (16–250 Hz), a reduction in average vibration of up to 9 dB was recorded at 150–200 Hz. This paper summarises the measurement results from two parallel rail tunnels. One of the tunnels includes results with and without rail dampers. Results from the opposite tunnel are used as a control data set. As a shuttle service was in operation at the time of the measurements, the same rolling stock was utilised for both tracks. The Pipe-in-Pipe (PiP) model has been used in an attempt to reproduce the measured change in vibration due to the addition of rail dampers. The initially selected model parameters reproduced the vibration reduction, but predicted it would occur at lower frequencies than indicated by the measurements, i.e. at 100–150 Hz. This simple model with the rail dampers represented as pure masses also suggested that vibration may increase above 160 Hz with the addition of rail dampers, but no increase was seen in the measurements at any frequency. Adjusting the model parameters improved the correlation of the modelled and measured insertion gains. Predictions were then made for the insertion gain on the surface immediately above the rail tunnel, to identify the potential for a change in ground-borne noise. A potential modest reduction in surface vibration in a small frequency range around 160 Hz has been predicted as a result of rail damper installation in a tunnel.

---

B. E. Croft (✉)

SLR Consulting, 1620 West 8th Avenue, Vancouver, BC, Canada  
e-mail: bcroft@slrconsulting.com

C. M. Weber

Renzo Tonin & Associates, Level 1, 418A Elizabeth Street, Surry Hills, NSW, Australia  
e-mail: conrad.weber@renzotonin.com.au

## 1 Introduction

The Epping to Chatswood Rail Line (ECRL) is a 13 km long twin tunnel commuter link in Sydney, Australia. One of the project approval conditions required the installation of a vibration monitoring system within the tunnel to identify potential “high noise train” events—essentially, to identify any trains with wheel defects that might increase ground-borne noise levels beyond the approved levels.

The ECRL opened in February 2009 as a limited shuttle service until October 2009. Initially, only a limited number and type of rolling stock operated on the line (four H-Set trainsets each day, four cars per train). A purpose built automated wheel condition monitoring system (AWCMS) was set up to collect and monitor vibration levels during shuttle operations. During this period of vibration monitoring, a separate suite of investigations took place targeting the reduction of in-car noise levels. One outcome of those investigations (summarised in [1, 2]) was a recommendation to retro-fit rail dampers. At the AWCMS location, rail dampers were initially installed on the Up track and on a later date on the Down track.

Following the initial rail damper installation, an immediate overnight step-change reduction in overall vibration levels was observed (this effect was observed after installation of rail dampers on the Down track at a later date). Figure 1 indicates the average vibration spectra measured in the cross-passage for Up and Down track train passbys immediately before and after rail damper installation on the Up track. Both tracks show a decrease in vibration at frequencies below 100 Hz—since no change was made to the Down track, this effect below 100 Hz is not attributable to the rail dampers. Above 125 Hz, a reduction in vibration levels was observed on the Up track following rail damper installation. No significant change in vibration was observed above 125 Hz on the Down track where no rail dampers were installed. The same vehicles operated the shuttle service on both tracks, so the change in vibration observed was clearly attributable to the rail damper installation.

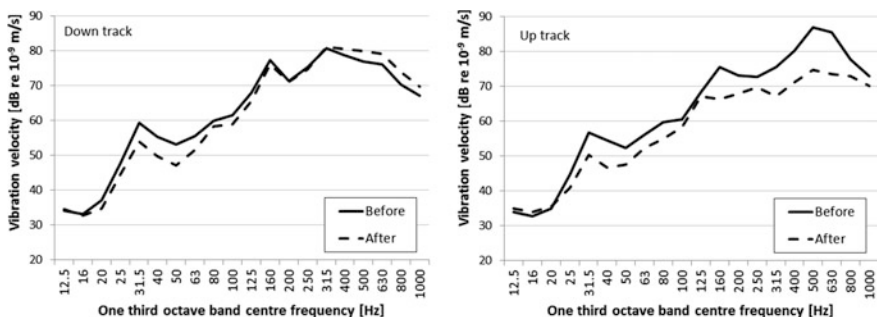


**Fig. 1** Vibration velocity (Lmax slow response) recorded in the cross-passage before and after rail damper installation on the Up track. Each line represents the arithmetic average of 20 events, collected on the two days immediately before and three days immediately after rail damper installation (during an overnight possession)

The objective of the rail damper installation was to reduce airborne noise levels within the tunnel, and in-car noise measurements indicated the installation was successful, with noise reductions observed in the frequency range between 315 and 800 Hz. Examination of the vibration spectrum before and after rail damper installation indicates that the overall vibration level difference was greatest in the one-third octave frequency bands between 400 and 630 Hz, up to 12 dB at 500 Hz. A reduction in average vibration levels of 9 dB was also observed in the 160 Hz one-third octave frequency band.

Ground-borne noise from trains in tunnels is a low-frequency phenomenon. The frequency range of interest for ground-borne noise is approximately 16–250 Hz according to ISO 14837 [3]. This paper investigates the causes of the reduction in measured ground vibration following the installation of rail dampers, and whether the observed vibration reduction at the tunnel depth is likely to lead to measurable or discernible effects at noise sensitive receivers on the surface.

In the ground-borne noise frequency range, rail dampers are expected to behave predominantly as additional masses (since their resonances target higher-frequency rolling noise). The addition of mass above a resilient track component is recognised as a measure to mitigate ground-borne noise and vibration, by reducing the coupled wheel/track resonance frequency. However, although rail dampers increase the mass of the rail by approximately 50% (from 60 kg/m up to 90 kg/m) this increase is small relative to the unsprung mass of the vehicle, which averages 940 kg per wheel for the H-Set (average of motor cars and trailer cars). The shift in the wheel/track resonance frequency is expected to be negligible with the introduction of rail dampers [4].

## 2 Methodology

### 2.1 Overview of Methodology

This paper revisits the historical vibration data to investigate the potential causes of the observed change in vibration following the installation of rail dampers. The Pipe-in-Pipe (PiP) model version 4 [5] is used in this study firstly to investigate the theoretical effects on vibration of adding mass to the rail, without modifying the bending stiffness. The model outputs in the form of insertion gains are compared to the ECRL measurement data. Then, the potential effects of the rail dampers on other model parameters are considered. The insertion gains predicted by the PiP model are then used to test the potential for differences in ground vibration and ground-borne noise due to rail dampers at various tunnel depths, and for a range of potential ground conditions.

## ***2.2 Vibration Measurements***

The AWCMS system incorporated two accelerometers. The first was located equidistant from both rail tunnels on the floor of a cross-passage, and the second was fixed to the Up tunnel wall adjacent to the cross passage, 1 m above top of rail. Before installation, the measurement system was calibrated from front to end in order to verify that the system was performing in accordance with typical acoustic specifications. Calibration of the system was also verified on commissioning. Train passby vibration was recorded in WAV file format for post-processing, with each event triggered by a laser sensor. This sensor was also used to determine the average train speed, which was 65 km/h on both tracks.

## ***2.3 Post-processing Measurement Data***

PiP predicts Power Spectral Density (PSD) of vertical displacement, for an infinite train. Results are presented either at a single frequency on a cross section plot or for all frequencies at a single measurement point. The measured vibration was post-processed to identify the PSD of vertical displacement at the measurement point in the cross passage, for comparison with the PiP predictions. The measured insertion gain with addition of the rail dampers was also calculated. While the absolute PSD level depends on the combined roughness of the wheels and rails, the insertion gain between model cases may be compared directly with the measured insertion gain.

## ***2.4 PiP Model Initial Parameters***

The parameters used initially in the PiP model for the baseline damped and undamped case are summarised in Table 1. The track form at the measurement location is direct fixation track with Delkor “Sydney Egg” baseplates at 0.7 m spacing. This fastener has been represented in the PiP model as a single resilient layer with a dynamic stiffness of 17 MN/m per fastener, neglecting the stiffer rail seat bearing pad. Since floating slab track is not used at this location, a stiff “slab bearing” layer has been used to simulate a rigid connection while incorporating the slab and tunnel invert mass. “Soil” parameters chosen for this initial case are representative of concrete, since the measurement position is in the cross passage with concrete connection to the tunnel.

**Table 1** PiP model parameters

Model component	Parameter	Initial value
Soil	Compression wave velocity	4000 m/s
	Shear wave velocity	2400 m/s
	Density	2450 kg/m <sup>3</sup>
	Shear loss factor	0.01
Tunnel	Elastic modulus	50,000 MN/m <sup>2</sup>
	Poisson's ratio	0.3
	Density	2500 kg/m <sup>3</sup>
	Shear loss factor	0.01
	Outer radius	3.45 m
	Tunnel thickness	0.20 m
Slab	Bending stiffness of slab	4500 MN/m <sup>2</sup>
	Slab bending loss factor	0.05
	Slab mass	4500 kg/m
Rail and baseplate pads	Bending stiffness of one rail	6.1 MNm <sup>2</sup>
	Rail bending loss factor	0.001
	Mass of one rail	60 kg/m (rail only), 90 kg/m (with dampers)
	Railpad/baseplate stiffness	24 MN/m per m of rail
	Railpad/baseplate loss factor	0.2
Train	Average unsprung mass per axle	1880 kg
	Axle spacing (average)	5 m
Tunnel	Depth (surface to tunnel centre)	28.5 m
Cross passage measurement point	Offset from track centre	7 m
	Depth below surface	30 m
Input roughness	Track irregularity	"Track in Average Condition"

### 3 Results

#### 3.1 Measured and Predicted Vertical PSD

Figures 2 and 3 show the measured and predicted vibration at the accelerometer located in the cross-passage before and after rail damper installation. Note that direct comparison of model predictions and measurements may not be meaningful, for several reasons: the actual roughness spectrum during the measurements is unknown; the "measured" displacement PSD is an approximation derived from

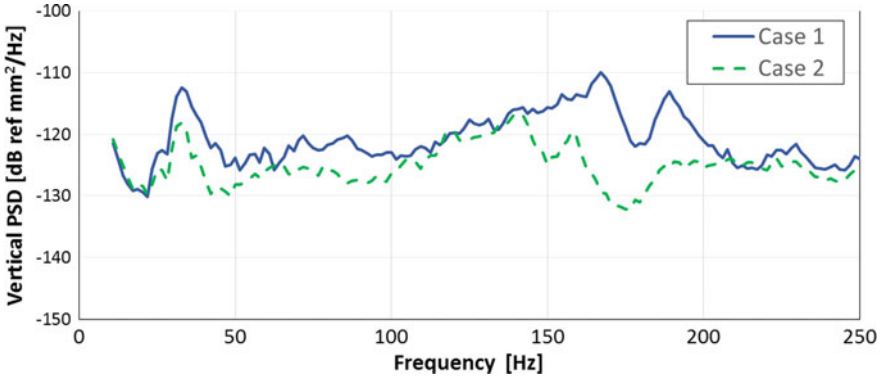


**Fig. 2** Average measured cross-passage vibration before (Case 1) and after (Case 2) rail damper installation

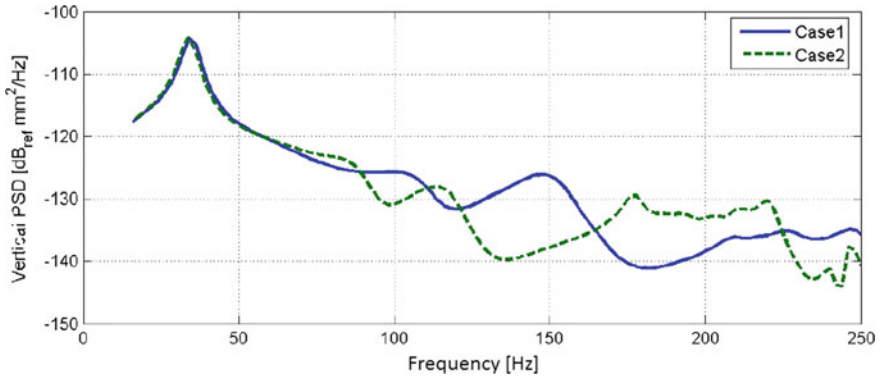


**Fig. 3** PiP predicted cross-passage vibration before (Case 1) and after (Case 2) rail damper installation. Model parameters as shown in Table 1

peak hold slow response vibration velocity for the duration of a passby; uncertainty and variability in model parameters; and the measurement position is relatively close to the track. Since PiP is a pseudo stationary model (there is no change in vibration as the train passes), PiP predictions may not be directly comparable to near-field measurements.

The above factors notwithstanding, the resonance of the unsprung mass on the track stiffness is evident at around 35 Hz in both the measurements and the predictions. The resonance of the rail mass on the track stiffness is evident in the predictions at 100 Hz in the base case, and shifts to around 80 Hz with the addition of the damper mass, as expected for a parallel impedance model of the track. The measured reduction in vibration below 100 Hz is not evident in the predictions, but

since a corresponding reduction was also observed on the control (Down) track this measured change is not attributed to the rail dampers. The measurements indicate a reduction in vibration between 150 and 200 Hz due to the addition of the rail damper mass, whereas the predictions indicate that at this location a reduction in vibration might be expected at lower frequencies, between 100 and 160 Hz. The predicted increase in vibration due to added mass above 160 Hz was not observed in the measurements.

### ***3.2 Measurement Uncertainty***

AWCMS reports on the wheel condition of rolling stock operating on the ECRL network from the time of the original measurements noted that wheel condition was relatively stable, with an approximate overall variation of  $\pm 3$  dB. A “high noise train event” due to poor wheel condition was unlikely in the time period examined for this case study. The standard deviations of the measurements in the cross passage before and after damper installation are summarised in Table 2, and supports the conclusion that vibration velocity in the frequency range of interest for ground-borne noise typically varies by about  $\pm 3$  dB.

### ***3.3 Model Uncertainty and Parameter Investigation***

Due to multiple sources of uncertainty in railway ground vibration modelling, it is unreasonable to expect an overall prediction accuracy greater than 10 dB, but models are useful to determine the insertion gain or change in vibration due to a change in model parameters [6]. For this work, representing the rail dampers as simply increasing the mass of the rail with all other parameters unchanged indicates that adding mass to the rail can reduce vibration by several decibels at some frequencies, but may also increase vibration at other frequencies—in the measurements, no increase was observed at any frequency.

Therefore, the effect of adjustments to the model parameters was tested to determine whether the insertion gains measured with installation of the rail dampers could be predicted more closely.

The Sydney Egg specifications list a static stiffness of 10–14 MN/m, and a dynamic stiffness at 15 Hz no greater than 1.4 times the static stiffness under a 20 kN preload. For the initial model parameter set, dynamic stiffness was assumed to be constant at higher frequencies, and also under a realistic train load of around 50 kN per wheel. The resulting baseplate dynamic stiffness applied for the initial parameter set in Table 1 is 24 MN/m/m along each rail. The effect of increasing the baseplate dynamic stiffness to 50 MN/m/m is shown in Fig. 4—this change



**Table 2** Standard deviation of cross passage measured vibration, 20 trains before and after damper installation (dB)

Frequency (Hz)	12.5	16	20	25	31.5	40	50	63	80	100	125	160	200	250	Av.
Before	2.0	1.6	3.2	1.7	3.9	3.4	2.2	2.3	2.0	2.2	3.0	1.7	1.8	2.4	2.4
After	3.0	3.7	6.2	3.2	6.7	5.5	3.5	3.7	2.5	4.2	2.8	3.5	2.5	2.3	3.8

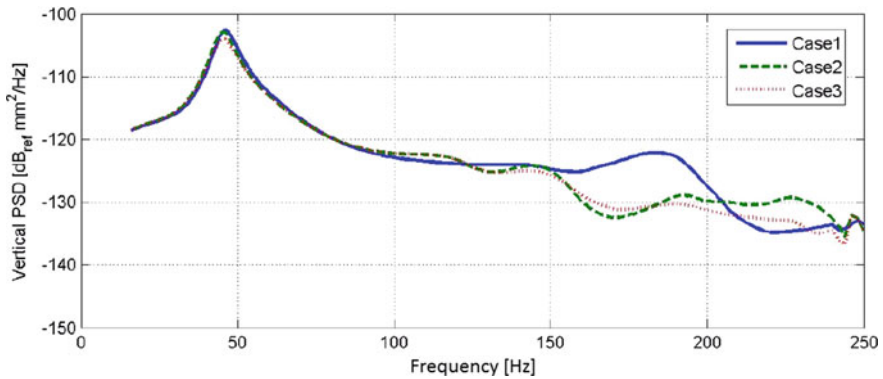


**Fig. 4** PiP cross-passage vibration before (Case 1) and after (Case 2, Case 3) rail damper installation. Model parameters shown in Table 1, except for baseplate dynamic stiffness (50 MN/m/m). In Case 3 the rail bending loss factor is increased to 0.1, in addition to the increased rail mass due to the dampers modelled in Case 2

effectively shifts system resonances to higher frequencies. The fundamental resonance of the unsprung mass on the track stiffness is also unrealistically shifted to a higher frequency—an improved model representation would include frequency dependent stiffness effects to simulate increasing dynamic stiffness with increasing frequency.

With this adjustment to baseplate dynamic stiffness, the model cases with rail dampers then show a reduction in rail vibration in a similar frequency range to that observed in the measurements. The predicted increase in vibration due to added damper mass above 200 Hz is lessened by the addition of damping to the rail bending modes.

Figure 5 shows the comparison between the measured and predicted insertion gain in the cross passage due to the installation of the rail dampers, with the model parameters adjusted to include increased dynamic stiffness values, and with the dampers represented as added mass and increased rail bending loss factor. The measured insertion gain has been adjusted at low frequencies to remove the reduction in vibration that was observed on the control track and that is not attributable to the rail dampers. The agreement between measured and predicted insertion gain is reasonable, when the standard deviation of the measurements is considered. The insertion gain indicates that very little variation in vibration is expected due to the installation of rail dampers at frequencies below 125 Hz, with a reduction in vibration predicted below around 200 Hz in the cross passage.

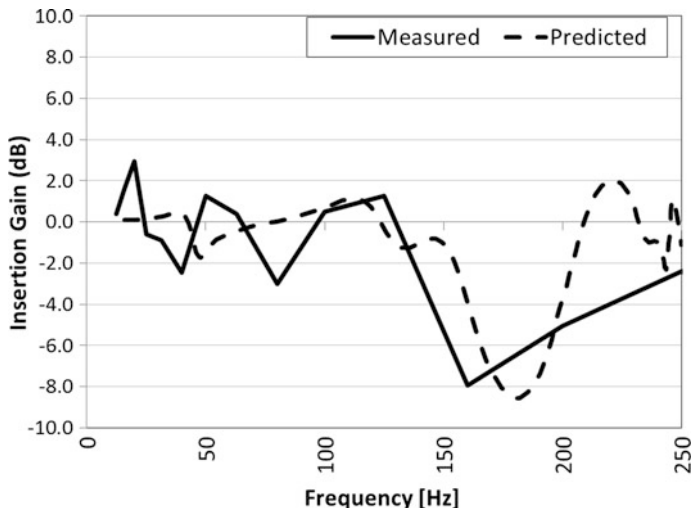


**Fig. 5** Measured and predicted insertion gain in the cross-passage due to rail damper installation on the Up track. Predicted results assume increased dynamic stiffness values, with dampers represented as added mass and increased rail bending loss factor

### 3.4 Predicted Surface Vibration Insertion Gain with Rail Dampers

The PiP model has been used to predict the insertion gain at 160 Hz on the surface immediately above the rail tunnel, to identify the potential for perceptible change in ground-borne noise due to the installation of rail dampers.

In addition to the base case model parameters, three additional cases have been modelled to test the sensitivity of the results to variations in ground parameters. The range of soil parameters considered is shown in Table 3. Of these, the base case parameters were chosen to represent hard rock, representative of vibration propagation through concrete in the vicinity of the cross passage. This base case is the same as used to generate model results elsewhere in this paper. Soil A parameters are taken from [7], for slightly weathered Hawkesbury sandstone with a compression to shear wave velocity ratio of 1.87. The shear loss factor for this soil type is estimated to be 0.2, since it is commonly thought to have a higher loss factor than other hard stone substrates. Soil B shear velocity parameters represent dense soil or soft rock, and Soil C parameters are typical of sandy soil. For these soils, the ratio of compression to shear wave velocity is estimated at 1.75 [8].

The predicted insertion gain contours at 160 Hz for this range of soil types is shown in Fig. 6. Although there are clear differences in the predicted insertion gain due to rail dampers across the various soil types, the predicted vibration on the surface at this frequency gain is predicted to be less with the rail dampers in all cases. The range of potential benefit is greatest for harder soils, with a benefit up to

**Table 3** PiP model “soil” parameters

Soil parameter	Base case	Soil A	Soil B	Soil C
	Concrete/hard rock	Sydney sandstone	Dense soil/soft rock	Sandy soil
Compression wave velocity (m/s)	4000	2600	875	525
Shear wave velocity (m/s)	2400	1400	500	300
Density (kg/m <sup>3</sup> )	2450	2450	2000	1600
Shear loss factor	0.01	0.2	0.1	0.1

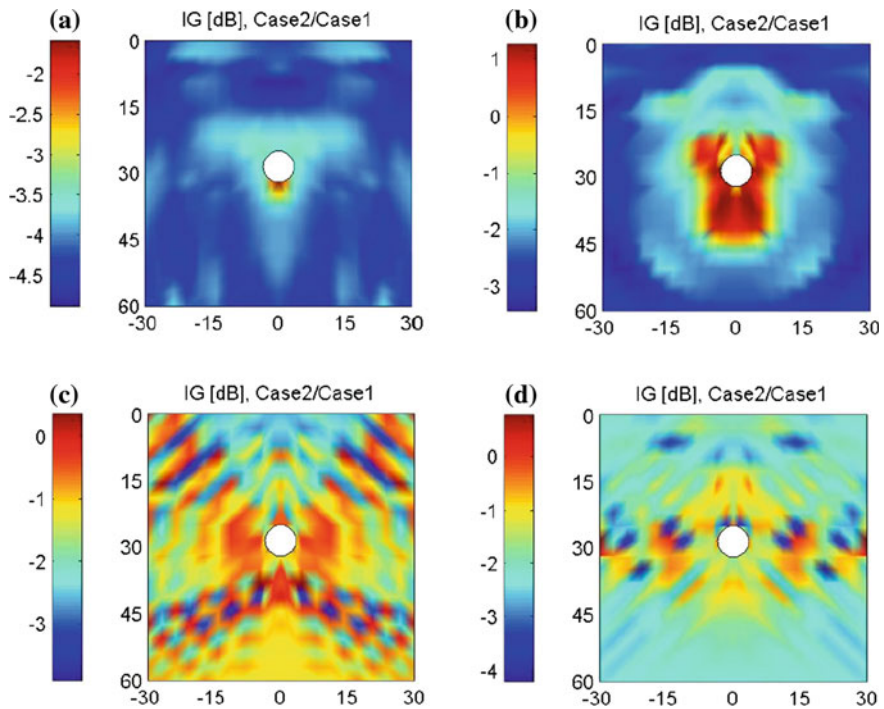


**Fig. 6** Predicted rail damper insertion gain contour at 160 Hz over a 60 m by 60 m cross section: **a** base case concrete/ hard rock, **b** soil A Sydney sandstone, **c** soil B dense soil/ soft rock, **d** soil C sandy soil

around 3 to 5 dB predicted at 160 Hz on the surface. For softer soils, the benefit predicted is in the range 0–3 dB. Note that the model does predict the possibility of vibration increases at other frequencies.

## 4 Conclusion

Measurements of ground vibration in the near field before and after the installation of rail dampers have indicated that rail dampers reduced ground vibration at frequencies above 125 Hz. In the frequency range of interest for ground-borne noise, a reduction in average vibration of up to 9 dB was recorded at around 160 Hz.

A theoretical model has been used in an attempt to simulate the measured change in vibration due to the addition of rail dampers. The initially selected model parameters reproduced the near field reduction in vibration, but predicted it would occur at lower frequencies than indicated by the measurements. Adjusting the model parameters improved the correlation of the modelled and measured insertion gains. Predictions were then made for the insertion gain on the surface immediately above the rail tunnel, to identify the potential for a change in ground-borne noise in the far field.

The model results indicate there is potential for a reduction in surface vibration in a small frequency range around 160 Hz as a result of rail damper installation in a tunnel. The model was also used to investigate whether this reduction might occur for a range of different soil types. The largest predicted benefits were for tunnels in hard rock substrates, with a maximum reduction of around 5 dB predicted on the surface. For softer soil types, the predicted benefit was less.

In relation to the potential reduction in ground-borne noise, this would depend on the magnitude of vibration at different frequencies. If surface vibration and ground-borne noise at a sensitive receiver location is dominated by lower frequencies than around 125 Hz, it is unlikely that the rail dampers would have a noticeable effect on ground-borne noise. However, since A-weighting reduces the influence of these lower frequencies, it is possible in some circumstances that a measurable or noticeable reduction in ground-borne noise at higher frequencies might result from an installation of rail dampers on track in tunnels.

## References

1. Anderson, D., Coker, D.: Reducing in-train noise on the Epping to Chatswood Rail Link. In Proceedings of Conference on Railway Engineering 2010, Railway Technical Society of Australasia
2. Weber, C.M., Haling, J., Brown, G.P., Hanson, D.: In-car noise control for Epping to Chatswood rail link. In: Maeda, T., et al. (eds.) *Noise and Vibration Mitigation for Rail Transportation Systems*. NNFEM, vol. 118, pp. 463–470. Springer, Heidelberg (2012)
3. ISO 14837-1:2005 Mechanical vibration—Ground-borne noise and vibration arising from rail systems—Part 1: General guidance
4. Thompson, D.J.: *Railway Noise and Vibration Mechanisms. Modelling and Means of Control*. Elsevier Science, Oxford (2009)
5. Hussein, M.F.M., Hunt, H.E.M.: A computationally efficient software application for calculating vibration from underground railways. *J. Phys: Conf. Ser.* **181**, 012057 (2009)

6. <http://www2.eng.cam.ac.uk/~hemh/PIP.htm> PiP website accessed 7 May 2016
7. McPherson, A.A., Hall, L.S.: Development of the Australian National Regolith Site Classification Map. *Geoscience Australia Record* 2007/07 (2007)
8. Castagna, J.P., Batzle, M.L., Eastwood, R.L.: Relationships between compressional-wave and shear-wave velocities in clastic silicate rocks. *Geophysics* **50**(4) (April 1985)

# Computation of Ground Vibration Around Pier by Using Axisymmetric Finite Element Method



Jun Kaneda, Hirofumi Ikemoto, Takeshi Ishii and Kunio Saitoh

**Abstract** We conducted on a study on a method of calculating ground vibration around a girder-type viaduct. This work focuses on the motion of the pier caused by the passing trains. Vibration acceleration in the pier at time of train passage was measured. Measurements revealed that vibration consisted chiefly of vertical translational behavior and rotational behavior around the horizontal axis. Analysis of ground vibration by axisymmetric finite element method considering these motions as excitation force characteristics was carried out. It was confirmed that the calculation results reproduce the ground vibration in the frequency range below 40 Hz.

## 1 Introduction

Ground vibration from train traffic can be an issue when trains run at faster speeds. JR East aims to improve the service in the expanded Shinkansen network, become more competitive with airlines and reach the top level of high-speed technology in the world. To achieve that, it is necessary to predict the change in ground vibrations, and apply measures to mitigate vibration if it increases.

Some prediction methods of ground vibration have been proposed in previous studies [1]. The first method is to use empirical models. This method is based on a prediction expression which is determined from statistical accumulated measure-

---

J. Kaneda (✉) · H. Ikemoto

Frontier Service Development Laboratory, Research and Development Center of JR East Group, 2-479, Nisshin-cho, Kita-ku, Saitama-shi, Saitama 331-8513, Japan  
e-mail: j-kaneda@jreast.co.jp

T. Ishii

The Research and Development Initiative, Chuo University, Tokyo, Japan

K. Saitoh

Department of Civil and Environmental Engineering, Chuo University, Tokyo, Japan

ments of ground vibration. This method is applicable if conditions such as ground, structure and vehicle at the prediction point are similar to condition of points where accumulated data were measured. But it is difficult to apply this method if there are major differences in conditions.

The second method is to use numerical models. Ground vibrations are propagated from a vehicle to the ground through tracks and structure. Vibrations at the prediction point are calculated by finite element models or thin layered elements upon which the propagation path is modeled. This method has an advantage in that it is possible to calculate the vibrations without measurements. But, there is a problem in that the more precisely the propagation path is modeled, the more calculation time and computer power is necessary. In order to solve this problem, a method of using divided numerical models (for example vehicle and track model and track, structure and ground model) and a method of using both empirical models and numerical models have been proposed [2, 3].

In sections where speed-up has been proposed, a large number of calculations are required to reflect the difference between various structures and soil characteristics in the section to identify the point where ground vibration has increased. For this reason, it is not practical to apply this to too elaborate a model. Therefore, it is useful to devise a simpler calculation method for ground vibration.

It has been proposed that a method using axisymmetric finite elements as a simple way to predict ground vibration from a viaduct [4, 5]. However, it was not sufficient in grasping the motion of piers at the moment of train passage. Therefore, we measured the motion of the pier. Settings for excitation force characteristics used for calculation were reviewed based on measurement results.

In this paper, first we describe the actual measurement results of the vibration behavior of the piers of the girder-type viaduct. Then, we describe the calculation method based on the vibration behavior. Finally, we show the results of comparison of measured and calculated values. Calculation target is ground vibration in the vertical direction.

## 2 Vibration Measurement of Girder-Type Viaduct

This chapter describes the vibration movement of the pier when a train is passing over the girder-type viaduct. In the previous study [4, 5], vibration behavior at the time of train passage has been treated as vibrating only vertically direction. However, it is envisioned that the actual pier is vibrating both horizontally as well as vertically. Thus we carried out vibration measurements for passing trains attaching three-axis acceleration sensors to piers in order to determine the behavior of the pier.



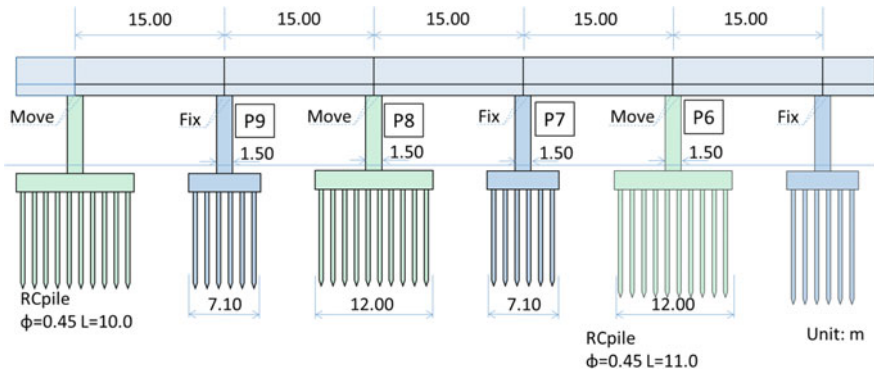


Fig. 1 A schematic of piers of the measurement object

### 2.1 Measuring Method

A schematic of piers of the measurement object is shown in Fig. 1. The span of the viaduct is 15 m. Acceleration sensors were installed in the two neighboring piers: P7 and P8. Four acceleration sensors were attached to each pier at the position shown in Fig. 2. The acceleration time history was recorded at the time of the train passage.

### 2.2 Measuring Result

Lissajous curves of acceleration at the time of a down train passage are shown in Fig. 3. It can be seen that the largest acceleration amplitudes were recorded at the top of the pier in the x-direction. Comparing piers P7 and P8, acceleration amplitude of the pier P8 is large. The ratio of maximum acceleration amplitude is shown in Table 1.

Attention is paid to the difference between acceleration at the top and bottom of the pier. The difference is largest in the bridge axis direction. The difference is

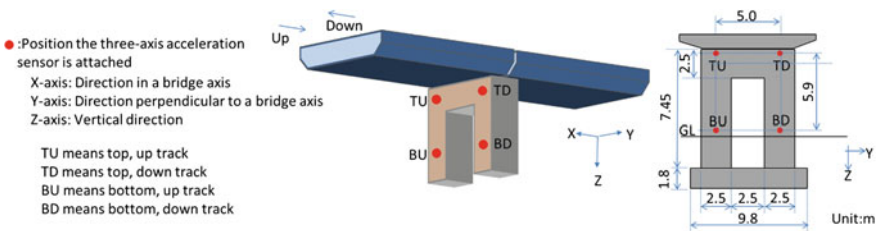


Fig. 2 Attachment position of acceleration sensors

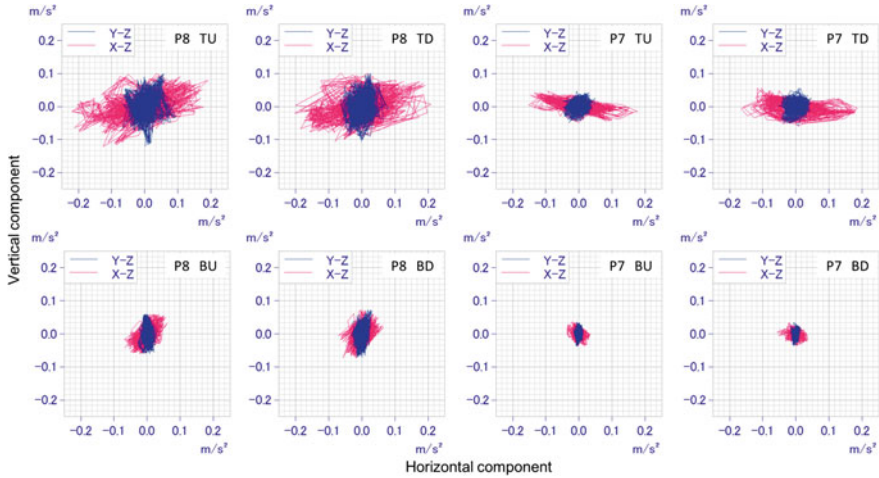


Fig. 3 Lissajous curve of measured acceleration

Table 1 Maximum amplitude ratio

	Amplitude ratio of bottom to top				Amplitude ratio of up side to down side			
	P7		P8		P7		P8	
	Up	Down	Up	Down	Top	Bottom	Top	Bottom
Direction in X-axis	0.21	0.26	0.32	0.32	0.93	0.73	1.00	0.95
Direction in Y-axis	0.29	0.32	0.35	0.42	0.99	0.90	1.10	0.92
Direction in Z-axis	0.78	0.61	0.54	0.70	0.84	1.06	1.07	0.82

second largest in the direction perpendicular to the bridge axis. The difference is smallest in the vertical direction.

Attention is paid to the difference between acceleration at the left and right of the pier. The difference is large in the vertical direction. The difference is small in the bridge axis direction and the direction perpendicular to the bridge axis.

Measurements revealed the movement of pier consisted chiefly of vertical translational behavior and two rotational motions around the horizontal axis as shown in Fig. 4.

Fig. 4 Major motion of the pier

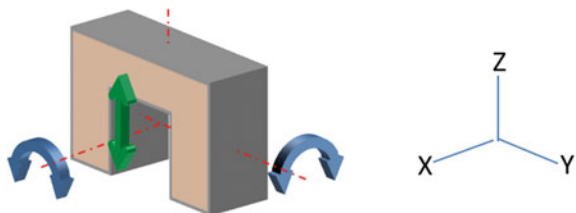
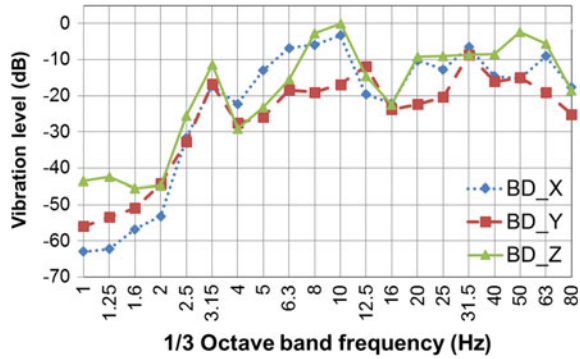
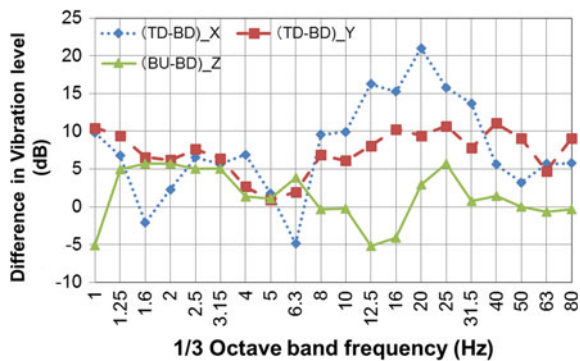


**Fig. 5** Spectrum of vibration level



Now, we describe the frequency characteristics, focusing on the point BD as one of the measuring points close to the ground. Figure 5 shows the 1/3 octave spectrum of the vibration level at the point BD. The spectrum is normalized so that the maximum value is 0 dB. Difference in vibration level is shown in Fig. 6. Differences are shown between top and bottom for X and Y components. The difference between up side and down side is shown for Z component. In relation to X and Y components, the frequency range that shows large vibration level in Fig. 5 matches with the frequency range that indicates a large difference in vibration level in Fig. 6. On the other hand, there is almost no difference in vibration level at the peak frequency for the Z component. This provides further evidence that the pier moved as shown in Fig. 4.

**Fig. 6** Spectrum of difference in vibration level



### 3 Computing Method of Ground Vibration

In this chapter, we describe the method of calculating the ground vibration using the FEM analysis by axi-symmetry model.

#### 3.1 Overview of Computing Method

Vibration propagated from piers to point (A) where vibration was computed is shown in Fig. 7. Vibration of point (A) was influenced by multiple piers. Vibrations at point (A) propagated from each pier were computed according to the following steps.

Step 1: Model a pier and its surrounding ground by the axisymmetric FEM as shown in Fig. 8.

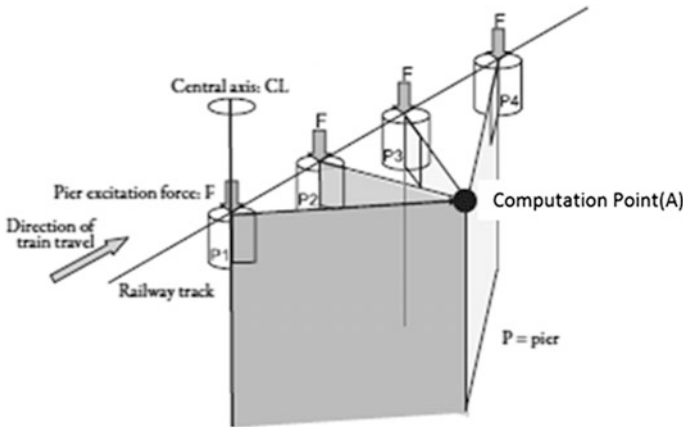
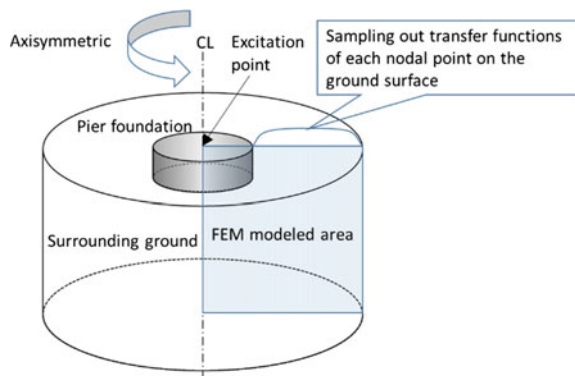


Fig. 7 Image of ground vibration propagation [4]

Fig. 8 Concept of axisymmetric FEM [4]



Step 2: Use model to compute transfer functions between the nodal point at the pier center (the point of excitation) and each nodal point on surface.

Step 3: Determine excitation characteristic for computing vibration at the nodal point (A), so that the acceleration response value at the excitation point matches the acceleration measured at the pier.

Step 4: Use the transfer functions and excitation characteristic to compute the acceleration response at the nodal point that corresponds to point (A).

The steps 1 to 4 are repeated until the computation of vibration propagated from every pier that significantly influences the vibration at point (A) is complete.

Incidentally, piers and the surrounding ground in the computation target area are often regarded as the same. In that case, they can be computed using the same model to save time. The vibration at the Point (A) is calculated by adding the vibration from each of the piers.

### 3.2 FEM Model for Calculating the Transfer Function

In this section, we describe a method of calculating the transfer function. The transfer function is determined by the complex response analysis. The transfer function was determined indicating the relationship between acceleration response to inputted excitation force with “Soil Plus” which is a finite element analysis program produced by ITOCHU Techno-Solutions Corporation. The transfer function is calculated in all surface nodes and the node of the excitation point.

#### 3.2.1 Modeling of the Structure

The shape of the raft is originally rectangular. However, the shape of the raft must be approximated by a circle due to the constraints of the axisymmetric model. Figure 9 illustrates the modeling of rafts and piles. The FEM model is shown in Fig. 10.

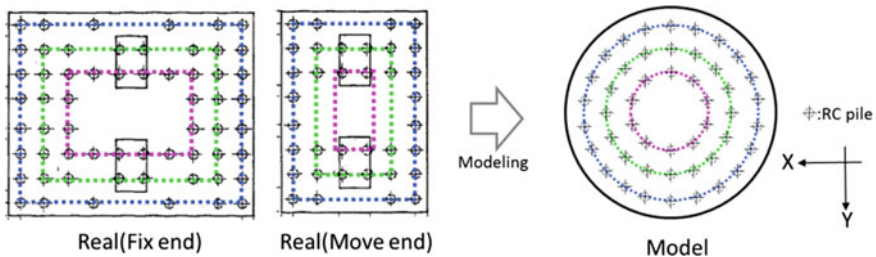


Fig. 9. Modeling of raft and pile

The radius of the raft model was the length from the center of the actual rafts to the end face in the direction perpendicular to the bridge axis.

Only part of a pier was modeled. The Pier was modeled to the height of the acceleration sensor that measures the vibrations used as a reference for determining the excitation force characteristics. The prototype of volume and mass were different from the analyzed model because a rectangular structure was modeled as a circle, or the structure was modeled only in part. The effect is taken into account in the modeling of the excitation force, which will be described later.

### 3.2.2 Modeling of the Ground

The ground was modeled as a linear viscoelastic material using linear elements of 0.2 m in width of 0.167–0.42 m in height. Soil physical properties were determined on the basis of ground survey results. Shear wave velocity  $v_s$ , density  $\rho$ , Poisson’s ratio  $\nu$ , and shear modulus  $G$  shown in Fig. 10. At the lower edge a viscous boundary was set up in order to eliminate the effect of reflection. Similarly, the lateral side was provided with an energy transfer boundary, to be able to represent the escape of vibration waves.

### 3.2.3 Excitation Position

As described above, there are three main behaviors of a pier during the train passage. They are linear motion in the vertical direction, rotational motion around the bridge axis and rotational motion around the horizontal axis perpendicular to the bridge axis. Accordingly, the three transfer functions corresponding to these three kinds of excitation force are calculated. The excitation point for the vertical linear motion was determined as the center point as the pier is regarded not to move in a horizontal direction. The excitation point for rotational motion was determined from the installation position of the vibration sensor for determining the excitation force characteristics.

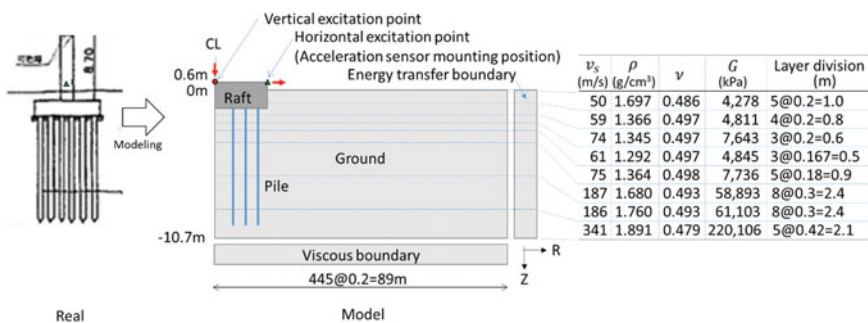


Fig. 10 FEM model

### 3.3 Calculation of Ground Vibration Using the Transfer Function

In this section the procedure for calculating the ground vibration around a pier using transfer function and the acceleration of vibration measured at a pier is described.

#### 3.3.1 Modeling of the Excitation Force Characteristics

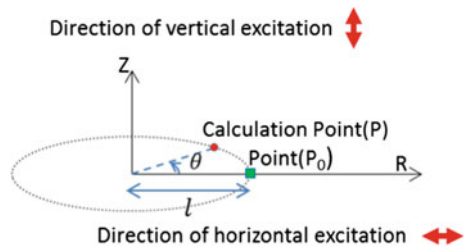
The transfer function obtained in the previous section gives the relation between acceleration response and inputted excitation force. Therefore, it is necessary to determine the excitation force characteristics to be used in the calculation. Excitation force can be determined by multiplying mass and acceleration at the excitation point. However, the model of the structure is made without considering the accuracy of mass. Thus, the effective mass is determined so that the acceleration response value at the excitation point matches the acceleration measured values. Where a vertical response to excitation in horizontal direction is generated at an excitation point, the effective mass of the Z-direction excitation is adjusted so that the sum of the vertical response due to vertical and horizontal excitation agrees with the measured vertical acceleration.

In this way, it is possible to adjust the difference of mass between the model and reality by determining the virtual mass. Excitation force characteristic is determined as a frequency spectrum of the excitation force (i.e. the product of the effective mass and acceleration).

#### 3.3.2 Calculation of Ground Vibration

The relationship between excitation direction and point P (the calculation point) is shown in Fig. 11. Calculation of vibration at point P will be described.

**Fig. 11** Relationship between excitation direction and calculation point



Ground Vibration Caused by Vertical Excitation

Vertical response distribution in the circumferential direction in the axisymmetric model is as shown in Fig. 12a.

Vertical response to the vertical excitation is constant in the circumferential direction. Vibration of the point P is calculated by multiplying the excitation force characteristics to a transfer function at point P<sub>0</sub> (a node corresponding to a distance between point P and model center).

Ground Vibration Caused by Rotational Motion Around a Horizontal Axis

Vertical response distribution in the circumferential direction in the axisymmetric model is as shown in Fig. 12b. Vertical response to the horizontal excitation is variable in the circumferential direction. Ground vibration of the point P can be expressed by the following equation.

$$A_{phz} = A_{phz0} \cdot \cos \theta \tag{3.1}$$

With:

- $A_{phz}$  Vertical response to the horizontal excitation at point P
- $A_{phz0}$  Vertical response to the horizontal excitation in case of  $\theta = 0$ .

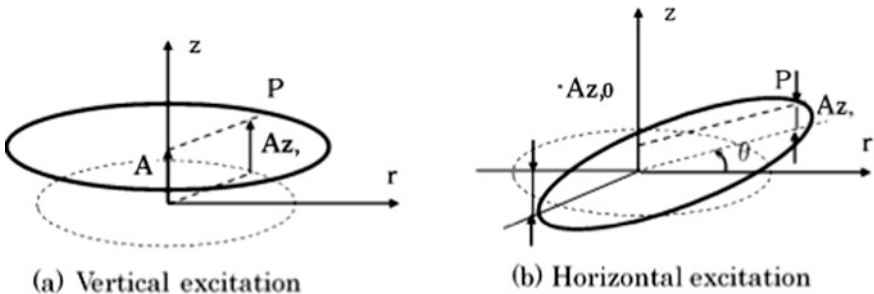


Fig. 12 Vertical response distribution of vertical in the circumferential direction



## Synthesis of Vibration

Ground vibration at point P propagating from a pier is expressed by the following equation.

$$A_{pz} = A_{pxz} + A_{pyz} + A_{pzz} \quad (3.2)$$

With:

$A_{pxz}$  Vertical response to excitation in X-axis direction

$A_{pyz}$  Vertical response to excitation in Y-axis direction

$A_{pzz}$  Vertical response to excitation in Z-axis direction.

Sum of squared accelerations are used for calculation of vibration level due to all the piers considered.

## 4 Comparison Between Calculated Values and Measured Values

In this chapter, a comparison is given between measured values and calculated values. Comparison was carried out at the points shown in Fig. 13f. The 1/3 octave band spectrum of acceleration is shown in Fig. 13a–e.

These figures show the calculated values and the measured values in the case of 10-car train traveling at a speed of 270 km/h. The length of the vehicle is 25 m. The spectrum is normalized so that the maximum measured value at point 75 °C is 0 dB. Four piers which is shown in Fig. 1: P6, P7, P8 and P9 are included in the calculation. It took about 6 h to calculate. When the frequency is below 40 Hz, the calculated values show the same tendency as the measurement values at each point.

Calculation considering only vertical excitation is compared with the calculation using the proposed method, and measurement at point 75 °C in Fig. 14. Focusing on the peak frequency of measurement: 8–10 Hz, calculation that takes into account only the vertical excitation is not able to reproduce the measured values as well as the proposed method. This suggests that the proposed method is effective in improving the accuracy.

On the other hand, the difference between the calculated value and measured values is increased for frequency higher than 40 Hz. This could be because of the damping in the soil. In this calculation, the damping characteristic of the ground is constant regardless of the frequency. It could be that accuracy is improved by considering the damping characteristics according to frequency. Another reasons for the discrepancy at high frequencies could be the modelling of the pier which is no longer rigid. These are the subjects of further study.

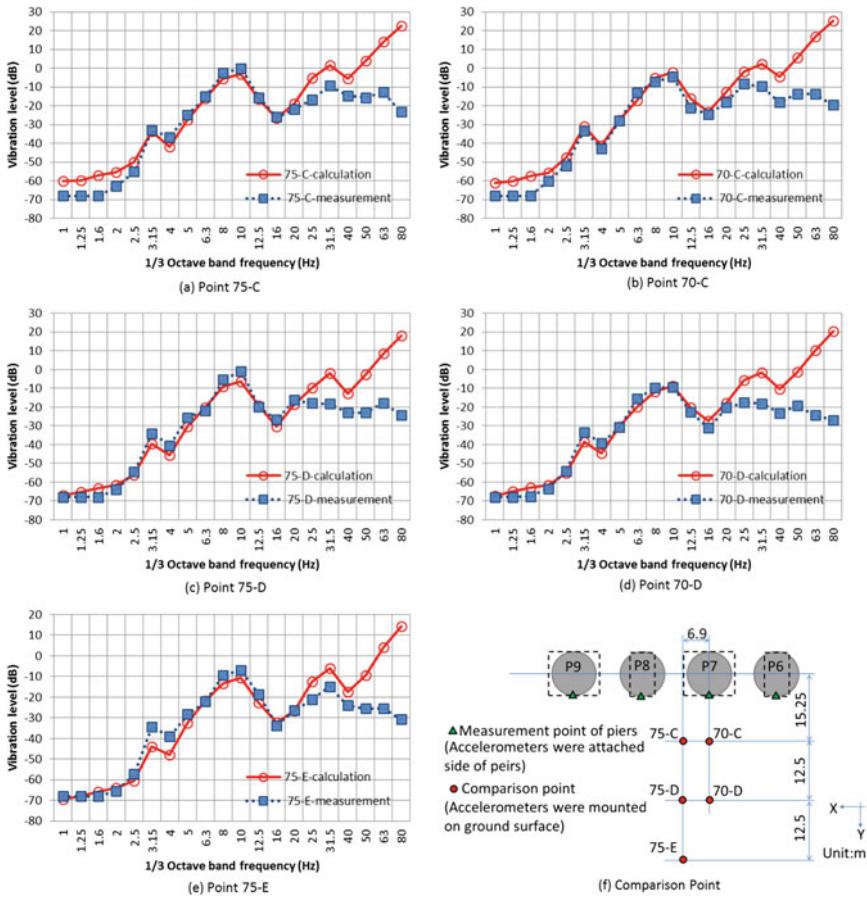
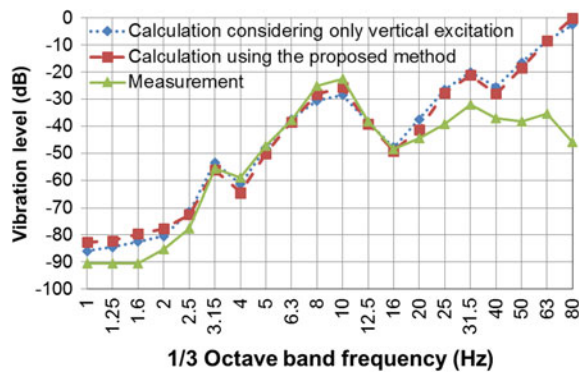


Fig. 13 Comparison between calculated values and measured value

Fig. 14 Calculation considering only vertical excitation



## 5 Conclusion

To conclude, we have conducted a study of a method of calculating ground vibration caused by trains running on girder-type viaducts using the axisymmetric model. The following points became clear as a result of the study.

- (1) The movement of piers caused by passing trains consists chiefly of linear motion in the vertical direction and rotational motion around the two horizontal axes.
- (2) It is possible to reproduce the ground vibration by calculation in considering the three types of excitation force characteristics, namely, linear motion in the vertical direction and rotational motion around the two horizontal axis for frequencies up to 40 Hz.

## References

1. Lombaert, G., et al.: Ground-borne vibration due to railway traffic: a review of excitation mechanisms, prediction methods and mitigation measures. In: Nielsen, J.C.O., et al. (eds.) *Noise and Vibration Mitigation for Rail Transportation Systems*. NNFM, vol. 126, pp. 253–287. Springer, Heidelberg (2015)
2. Yosioka, O., et al.: Prediction analysis of train induced ground vibrations using the equivalent excitation force. *RTRI Rep.* **10**(2), 41–46 (1996)
3. Watanabe, T., et al.: Ground vibration on high-speed railway tunnel. In: Maeda, T., et al. (eds.) *Noise and Vibration Mitigation for Rail Transportation Systems*. NNFM, vol. 118, pp. 299–306. Springer, Heidelberg (2012)
4. Nakade, K. et al.: Development of Design and Construction Method for Highly Effective Ground Vibration Control Work, *JR EAST Technical Review*, No. 14 (2009)
5. Taniguchi, M. et al.: Development of a Method of Analytically Considering Ground Vibration, *JR EAST Technical Review*, No. 21 (2011)

# Development of Orthogonal Resilient Materials for Tuned Mass Dampers



Po-lai Tam, Chi-wah Leung, Chee-leung Mak, Wilson Ho and Ting Cai

**Abstract** For UIC60 and UIC54 rail track, our on-site measurements, together with finite elements analysis (Thompson in *Railway noise and vibration: mechanisms, modelling and means of control*. Elsevier, Amsterdam, 2008 [1]), showed that the pin-pin resonance modes of the rail track in lateral and vertical direction (i.e. the two principal directions perpendicular to the length of rail tracks) are in the frequency ratio of around 1:2. Following our recent development of Tuned Mass Damper (TMD, Fig. 1) (Ho et al. in *Tuned Mass Damper for Rail Noise Control*. Springer, Berlin 2012 [2]), multiple masses were employed so that they oscillate along the shear direction of the resilient layers to form a multiple spring-mass system in both vertical and lateral directions. As the damping mechanism strongly relies on the stiffness of the resilient layer, thus a resilient composite material with anisotropic shear moduli in orthogonal directions can be used to tackle the issue of different pin-pin resonance modes in both lateral and vertical directions. Since the resonance frequency is proportional to the square root of the modulus, with a frequency ratio of  $\sim 2$  between the vertical and lateral pin-pin resonance modes, a ratio of 4 between the shear moduli of the two respective directions is required. In this study, aligned glass fibres were embedded into silicone matrix to form uniform composite resilient layers with orthogonal shear moduli. Their shear stiffnesses were measured by a tensile tester, with the setup for shear modulus measurement based on the International Organization for Standardization ISO-1827. Our results showed that these composites can achieve an orthogonal shear moduli ratio of about 1:1.44. Vibration tests were performed to verify that two natural frequencies were observed in these TMDs using the orthogonal resilient layers, which is not possible for TMDs using isotropic resilient layer materials. Hence, resilient layer material of

---

P. Tam · W. Ho (✉) · T. Cai  
Wilson Acoustics Limited, Unit 601, Block A, Shatin Industrial Centre,  
Shatin, N.T., Hong Kong SAR, China  
e-mail: who@wal.hk

P. Tam · C. Leung · C. Mak  
Department of Applied Physics, The Hong Kong Polytechnic University,  
Hung Hom, Kowloon, Hong Kong SAR, China

orthogonal shear moduli as applied in the TMD is promising for suppressing the two direction pin-pin resonance modes in rail tracks.

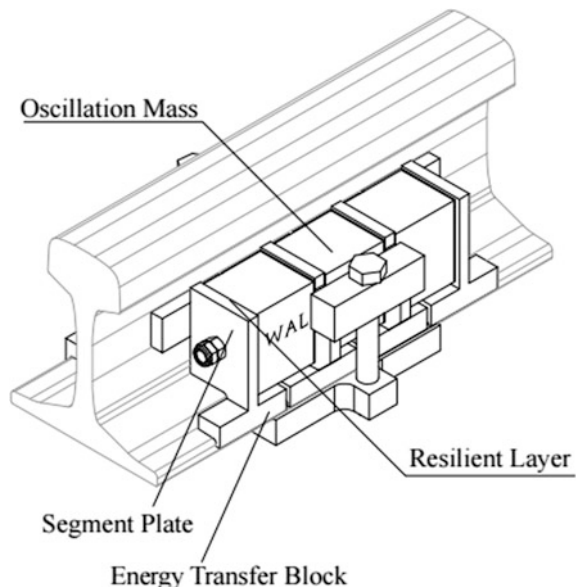
## 1 Introduction

Railway networks have been widely adopted for express transportations alongside with the expansion of cities. Together with vibrations, the noise generated by railway trains is a growing environmental concern. In recent years, the railways are planned even closer to the residential areas and the noise impact on the residents draws more attractions than ever. Substantial regulations have been setup in cities in order to suppress the noise down to acceptable level.

A vast amount of countermeasures have been investigated and employed for mitigating ground-borne and air-borne noises. Wilson Acoustics Limited (WAL) developed a shear type of Multi-Directional Tuned Mass Damper (MDTMD) and was successful applied to reduce rail vibration, noise radiation and rail corrugation at five operational sections in Hong Kong. Owing to the prominent performance of WAL's MDTMD, WAL has obtained a new contract to install the dampers at a 6th operational section.

Previous studies showed the pin-pin resonance modes of rail track in lateral and vertical directions are very different [1]. For multi-directional tuned mass damper (MDTMD), there is a market demand that one oscillation mass could ideally handle vibrations of two different frequencies. To fully utilize the limited space along the rail track and spare oscillation masses for other desired frequencies, we develop an

**Fig. 1** Multi-directional tuned mass damper (MDTMD)



orthogonal resilient material to be used in the current MDTMD design. With the help of these orthogonal resilient layers, the current MDTMD can maintain the single oscillating mass design while possessing different resonance frequencies in the perpendicular directions.

This paper presents the development of the orthogonal resilient materials based on glass fibre/silicone composite, and explores the effects of it on suppressing vibration at multi-frequencies.

## 2 Principle of Orthogonal Resilient Materials

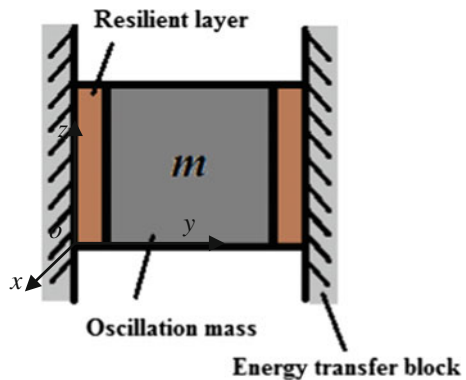
MDTMD is essentially a shear-type tuned mass damper. Based on the design shown in Fig. 1, the resilient layer and oscillation mass are combined to complete a spring-mass system. For a single modulus TMD element, mass and resilient layer are installed in series with screws and bolts, and the mass has a certain dynamic range that allows vibration at different directions to absorb the energy from tracks. The arrangement is shown in Fig. 2.

The thickness of the resilient layer is 1 mm, which enforces the oscillating mass to vibrate along *x*- and *z*- directions, while minimizing the wobbling movement along *y*- direction has been minimized. Here, the resilient layer with the specific shear property provides a restoring force to the mass corresponding to the mass oscillation. By introducing different stiffness of resilient layers, the mass-spring system can be tuned for damping propose at different target frequencies [3]. The resonance frequency *f* depends on the shear modulus of the resilient layer, contact area between oscillation mass and resilient layer, oscillation mass and thickness of resilient layer based on the following equation.

Resonance frequency:

$$f = \frac{1}{2\pi} \sqrt{\frac{2GA}{mb}} \tag{1}$$

Fig. 2 Schematic diagram of single mass module



where in,

$G$  is the shear modulus of the resilient layer

$A$  is the contact area

$M$  is the oscillation mass

$B$  is the thickness of resilient layer.

In the equation, the lateral and vertical motions ( $x$ - and  $z$ - directions) are assumed to be independent. Thus, different resonance frequencies can be achieved by using a resilient layer with anisotropic shear moduli, i.e. a single oscillation mass would be able to suppress two pin-pin resonance modes in two orthogonal directions. The resonance is proportional to the square root of the modulus, with a frequency ratio of  $\sim 2$  between the vertical and lateral pin-pin resonance modes, for example, a ratio of 4 between the shear moduli of the two respective directions is required.

### 3 Preparation of Resilient Damping Layer

To produce an orthogonal resilient material, a fibre-reinforced composite based on silicone and glass-fibre was employed. This orthogonal composite was expected to have a higher shear stiffness in a specific direction, which is the same direction as the aligned fibre i.e. vertical direction in our application [4].

In the resilient material that has been developed, E-glass fibre with diameter of 20  $\mu\text{m}$  was selected as the embedded fibre because of its high acid resistance and ease to acquire. The base matrix was made of a kind of adjusted RTV-2 silicone rubber. During the manufacturing process, silicone mixed with curing agent was poured into a Teflon mould, put into vacuum to remove gas bubbles and put into an oven at 75  $^{\circ}\text{C}$  for three hours for curing. The composite was fabricated layer by layer with alternating silicone and glass fibre, with each silicone layer of 0.5 mm thickness covered by an aligned and well-dispersed glass fibre layer. The composite consisting of five layers of silicone and four layers of glass fibre was produced as described below for MDTMD (Table 1).

## 4 Measurement

### 4.1 Mechanical Properties

The shear moduli measurement of the samples was based on ISO-1827:2011 [5]. A sample holder consisting of four aluminum plates was adopted in order to allow the shear moduli to be measured with a tensile tester (Fig. 3).

Rather than use glue for fixture of samples as suggested by ISO-1827:2011 [5], we conducted the measurements using C-clamps for sample fixture. For the

**Table 1** Parameters for matrix and fibre of composite

	Matrix	Fibre
Materials	RTV-2 Silicone Rubber	E-glass fibre
Young modulus	311 kPa <sup>a</sup>	70 GPa <sup>b</sup>
Shear modulus	107 kPa <sup>a</sup>	–
Diameter	–	20 μm
Mass (g)	12.0	2.8
Mass ratio (%)	81.1	18.9
Cross-section ratio (%)	88.4	11.6

<sup>a</sup>Measured value

<sup>b</sup>Reference [4]

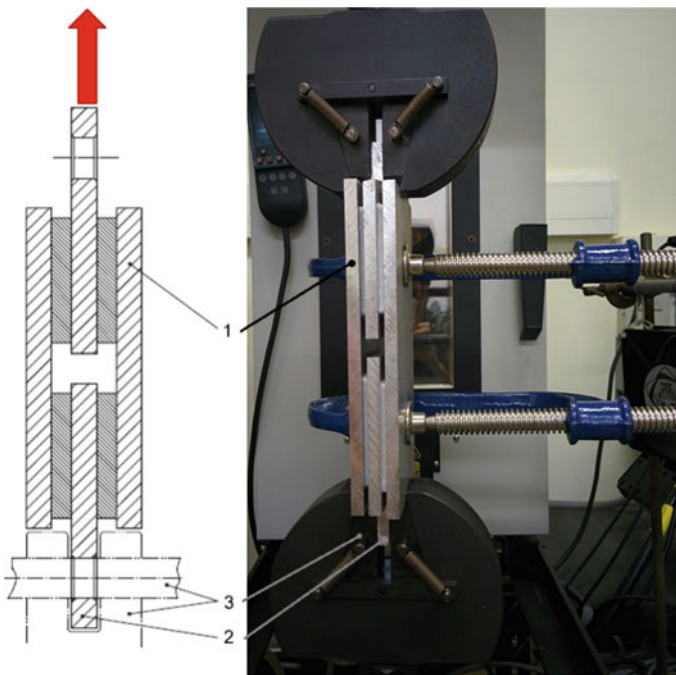


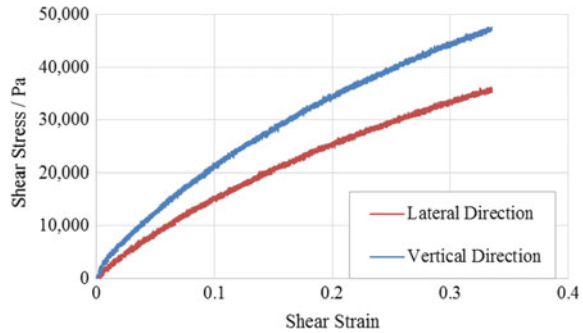
**Fig. 3** Schematic diagram of sample holder [5] and measurement setup, (1)—two external plates, (2)—two internal plates and (3) fixture for tensile loading

specified sample dimension as suggested by ISO-1827:2011, the sample dimension used in the measurement was selected to cater for MDTMD use. The shear moduli of orthogonal composite were measured separately on the lateral and vertical directions to investigate the orthogonal feature of the composite.

Instron 8872 testing system with actuator and load cell capable for 25 kN loading was employed for the tests. A mechanical conditioning was required before



**Fig. 4** Typical shear stress-strain curve of shear tests



measurements, by applying five successive shear-loading cycles from 0 to 0.3 shear strain as recommended the ISO 1827:2011. During the test, the hydraulic actuator was regulated at a travelling rate of 2 mm/min and the test ended when the tensile extension reaches 1 mm, which corresponds to a shear strain of 0.33 for the samples. According to the earlier site measurement of the traffic pass-by, the amplitude of oscillation mass is around 30  $\mu\text{m}$  which the modulus measurement is at considerably higher strain than application. The results were averaged by three successive measurements to eliminate the uncertainties.

Based on the results shown in Fig. 4, the shear moduli of lateral and vertical directions were determined as 159 and 212 kPa, respectively, indicating a shear moduli ratio of 1:1.34.

## 4.2 Vibration Test

By measuring the frequency response along lateral and vertical directions, the natural frequencies of the mass damper along the lateral and vertical directions were determined. The composite samples were installed into a single damper module between the oscillation mass and the segment plates and fixed with screw and bolts following the damper design. Two TMD modules were mounted on a 320 mm long UIC-60 Rail track on both sides, and the rail track with dampers was hanged to avoid resonance from other sources. Three accelerometers in total were employed for measurement, two of them were placed on the oscillation masses of the two TMDs to monitor the vibration along either the lateral or the vertical directions of the corresponding TMD, and one accelerometer was set as a reference on rail track. We studied the spectra of vertical response for vertical impact, vice versa.

Accelerometer sensors V1 and V2 (see Fig. 5) monitored vertical vibration while L1 and L2 monitored lateral vibration, the reference sensor was positioned accordingly at L Ref. for lateral test and V Ref. for vertical test. All spectra in the test were averaged of five impact responses (Figs. 7 and 8).

Figures 7 and 8 show the frequency response curves in vertical and lateral directions, respectively. The oscillation masses have resonance frequencies at 139

**Fig. 5** Schematic side view of the impact point and position of accelerometer on track

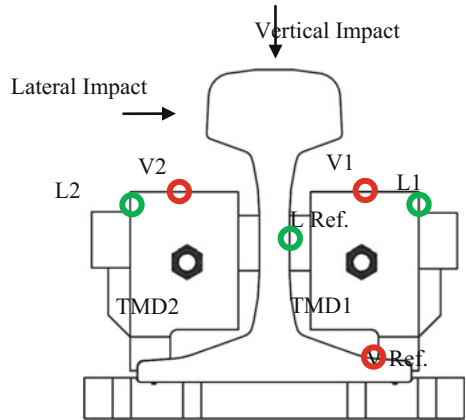


**Fig. 6** Measurement setup for vibration test

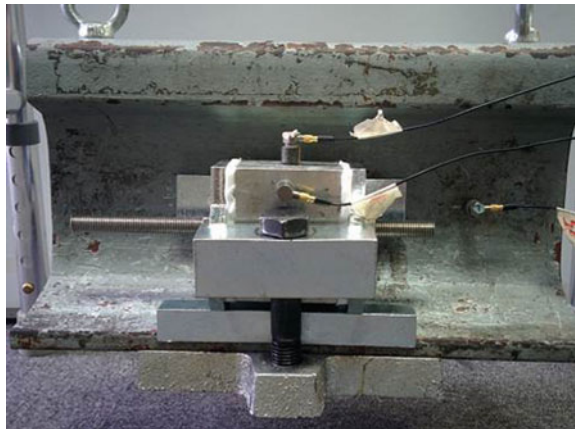


**Fig. 7** Frequency response in vertical test

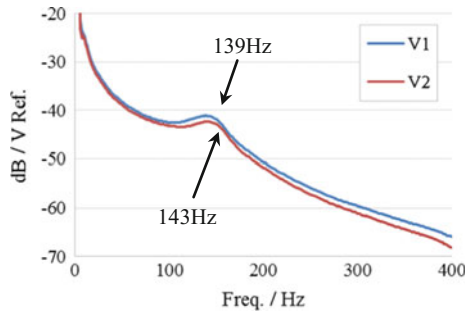
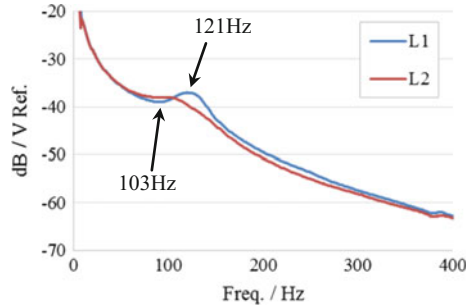


**Fig. 8** Frequency response in lateral test



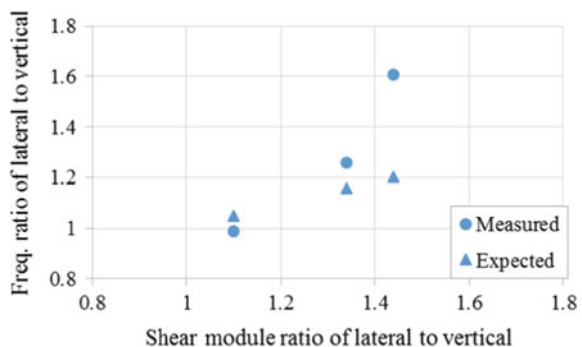
and 143 Hz in the vertical direction, while resonance frequencies at 121 and 103 Hz in the lateral direction. As a result, the average resonance frequencies for the vertical and lateral directions are 141 and 112 Hz respectively.

These results indicate that a clear frequency difference exists in the two resonance modes for the same mass with orthogonal resilient material, which is not possible for resilient layers made by homogeneous materials. Since the shear moduli ratio of the composite is 1:1.34, the resonance frequency ratio is expected to be 1:1.16 according to Eq. (1). The frequency response test showed a ratio of 1:1.26, which is slightly higher than prediction.

Silicone is a viscoelastic materials which has frequency-dependent properties while undergoing a deformation [6]. A higher frequency deformation on viscoelastic materials leads to a higher stiffness [7]. This may explain the effect of resonant frequency difference higher than expected. A viscoelasticity model should be considered, especially in high frequency damping.

The frequency ratio of the three composite samples with different shear moduli ratios were measured by the vibration test. And the results were plotted in Fig. 9. For the sample with the shear module ratio closed to one, the frequency ratio seems to be closed to the expected value from the equation. However, as the shear moduli ratio gets increased, the measured frequency ratios become larger than those values obtained from the equation. More detailed investigations are under progress in order to explore the detailed correlation between frequency ratio and shear moduli ratio.

**Fig. 9** Frequency ratio along lateral to vertical directions against the corresponding shear modulus ratio



However, considering the frequency difference in the two respective directions, it suggests the feasibility of suppressing the two directions pin-pin resonance modes in the rail track using a single resilient layer with orthogonal shear moduli. By increasing the shear moduli ratio through replacing the glass fibres as well as the manufacturing technique, it is expected the resonance ratio of 1:2 could be achieved.

## 5 Conclusions

Damping orthogonal pin-pin resonance modes on rail track by a single tuned mass damper module is presented. Three glass fibre/silicone composites with different shear moduli ratio were fabricated to demonstrate the effect and viability of the concept. By further improving the manufacturing process to increase the shear moduli ratio of the composite, we will be able to achieve the resonance ratio of 1:2 in orthogonal directions.

**Acknowledgements** This work is supported by the Innovation and Technology Fund, HKSAR through the Teaching Company Scheme (UIT/128). Any opinions, findings, conclusions or recommendations expressed in this material do not reflect the views of the Government of HKSAR or the Innovation and Technology Commission.

## References

1. Thompson, D.: *Railway Noise and Vibration: Mechanisms, Modelling and Means of Control*. Elsevier, Amsterdam (2008)
2. Ho, W., Wong, B., England, D.: Tuned mass damper for rail noise control. In: *Noise and Vibration Mitigation for Rail Transportation Systems*, pp. 89–96. Springer, Berlin (2012)
3. Connor, J., Laflamme, S.: *Structural Motion Engineering*. Springer, Berlin (2014)
4. Chawla, K.K.: *Composite Materials: Science and Engineering*. Springer Science & Business Media, Berlin (2012)
5. ISO: Rubber, vulcanized or thermoplastic—Determination of shear modulus and adhesion to rigid plates—Quadruple-shear methods (2011)
6. Goldberg, A.J.: Viscoelastic properties of silicone, polysulfide, and polyether impression materials. *J. Dent. Res.* **53**, 1033–1039 (1974)
7. Shaw, M.T., MacKnight, W.J.: *Introduction to Polymer Viscoelasticity*. Wiley, Hoboken (2005)

# Reduction of Vibration Emissions and Secondary Airborne Noise with Under-Sleeper Pads—Effectiveness and Experiences



Harald Loy, Andreas Augustin and Lukas Tschann

**Abstract** In the railway superstructure under-sleeper pads are primarily used for ballast protection and to improve the track quality. They increase the contact area between concrete sleepers and the top ballast layer, reduce the formation of hollowness beneath sleepers and lower superstructure settlements. But elastic under-sleeper pads can also represent a cost-effective way to reduce the transmission of vibration and structure-borne noise. To this effect the formation of a vibratory system is required. Both effects, improvement of the track quality and formation of a vibratory system, have an impact on the measured insertion loss which is discussed in this article. Derived from this result, the challenges of a computational prognosis of the vibration mitigation effect are described. In the light of experience gained in projects carried out with under-sleeper pads for vibration reduction, the achieved results are presented by means of examples.

## 1 Introduction

Moving trains cause mechanical vibrations from the wheel/rail contact. These vibrations (emission) are carried through the subsoil (transmission) in the form of waves and are often perceived as disruptive at the receiving location (immission). When these effects can be felt by humans, they are considered to be vibrations. As a result the quality of life for residents may be negatively affected to a considerable degree, particularly when the vibrations increase in the occupied rooms because of the effect of resonance or when secondary airborne noise arises as a result of higher frequency parts of the vibrations. The secondary airborne noise is mostly perceived

---

H. Loy (✉) · A. Augustin · L. Tschann  
Getzner Werkstoffe GmbH, Herrenau 5, 6706 Buers, Austria  
e-mail: harald.loy@getzner.com

A. Augustin  
e-mail: andreas.augustin@getzner.com

L. Tschann  
e-mail: lukas.tschann@getzner.com

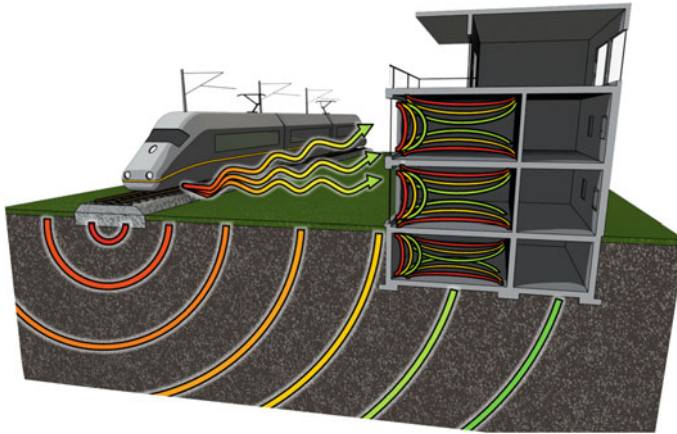


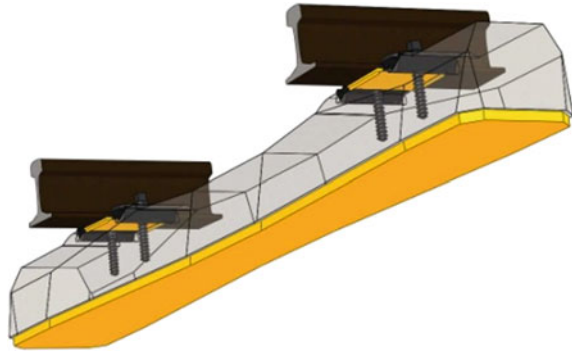
**Fig. 1** Transmission of vibrations in the area around railway lines

as a muffled rumbling sound. This sound may be masked by the primary airborne noise arising from outside. Noise and vibrations are an omnipresent, undesired side effect of our mobility. Suitable measures must therefore be taken to preserve and enhance quality of life, particularly in fast-growing urban areas. It is well known that it is most effective to concentrate on reducing disruptive vibrations directly at the source of the emission (Fig. 1).

## 2 High-Quality Superstructure Systems Based on Evenness and Resilience

The more even the railway superstructure, the lower the force excitation when a train passes. The track panel itself is “floating” in the track superstructure. Repeated dynamic loads lead to changes in the track geometry over time, which leads to additional acceleration of the wheelsets. The forces generated alter the track bed quality. Hollow areas below the sleepers and signs of wear on the wheel and rail surface, both of which arise over time, increase these processes as well as being the result of them. The system vibrates more and more, thereby also increasing the emissions. By tamping and adjusting, the superstructure must be returned to its original position. The length of time this deterioration takes is largely dependent on the initial quality of the track superstructure [1]. The creation of the conditions necessary for a good, durable line that is as inherently stable as possible should therefore be the primary goal when installing new track. In this context, evenness and resilience are important starting points for a high-quality superstructure system. Through the defined arrangement of elastic elements, such as under-sleeper pads, the railway track edges nearer to achieving this goal (Fig. 2).

**Fig. 2** Under-sleeper pad beneath a concrete sleeper



### 3 Increased Contact Area Using Under-Sleeper Pads

Arranging the under-sleeper pads under the concrete sleepers prevents a hard impression directly on the ballast. The upper-most layer of ballast can bed into the padding material, increasing the contact area (from 2–8% without padding, to 30–35% with padding) and thereby also avoiding excessive contact pressures. The larger ballast contact area and more even bedding lead to increased stability of the ballast bed, less track settlement and reduced wear to significant track components (Fig. 3).

As laboratory tests and track measurements show, the lateral resistance of padded sleepers is consistently higher than that of conventional concrete sleepers. With under-sleeper pads, which permit comparably deeper bedding-in of the ballast stones due to their specific material properties, resulting in a larger area of contact ratio, a further increase in lateral resistance was measured [2]. In a padded line with ballast, the formation of voids is almost entirely avoided. This fact in particular shows that the padded concrete sleepers have a significantly better position behaviour. For example, while fairly strongly pronounced voids arose over time between

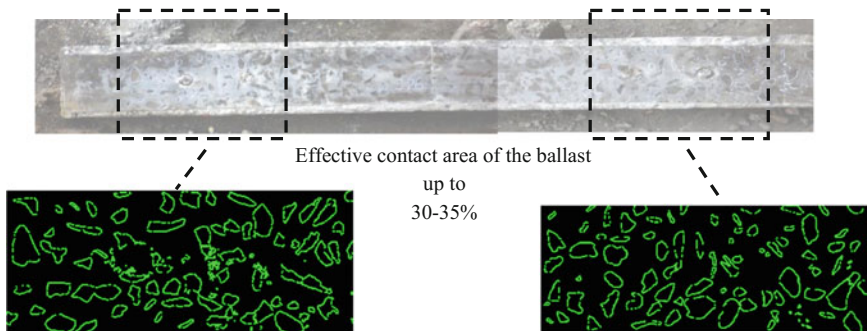


**Fig. 3** Digital contact area analysis on a concrete sleeper with PU under-sleeper pad removed from a track in service (pore scan method)

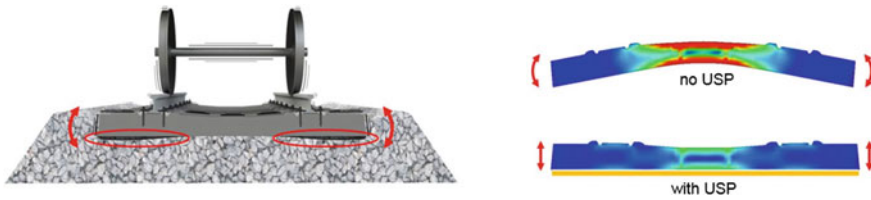


**Fig. 4** Void formation only under unpadded concrete sleepers. Such voids are avoided by using under-sleeper pads, which makes load transfer more even

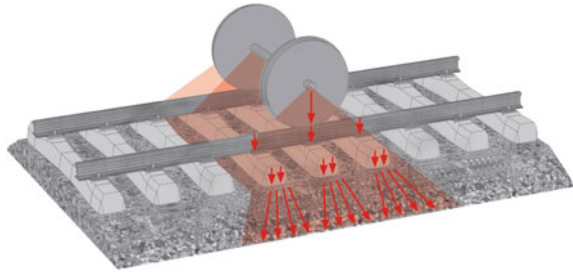
the undersides of the sleepers and the ballast bed in 7 out of 10 unpadded concrete sleepers in the Austrian Federal Railways' network, no void formation could be detected in the measured sections with padding [3]. Deviation in the track quality is significantly lower in padded sections than in unpadded sections. These properties have led to the under-sleeper pads bringing about a significant improvement in the traditional ballasted track. Not least because of this, padded sleepers have become established as the standard form of construction in the Austrian Federal Railways' network. In the mainline network today, concrete sleepers with under-sleeper pads are used as standard in new track and turnout installations (Fig. 4).

#### 4 Vibration Isolation Using Sylomer<sup>®</sup> and Sylodyn<sup>®</sup>

The quality of the railway superstructure has a considerable influence on the occurrence of vibrations. A railway line with improved, long-term track bed behaviour due to under-sleeper pads emits less noise and fewer vibrations thanks to the trains running more smoothly. The use of highly elastic materials can significantly reduce emissions to the surrounding environment by making use of the physical principle of mass force compensation for vibration isolation. The effectiveness of elastic components in the railway superstructure is dependent on variables such as mass, stiffness and damping. A vibratory system is formed, the natural frequency of which is ideally much lower than the excitation frequency, based on the operating principle of a single/multi degree of freedom system. The materials Sylomer<sup>®</sup> and Sylodyn<sup>®</sup> have proven themselves as essential elastic components for the reduction of emissions. Depending on the requirements, these materials can be provided with a more or less pronounced damping property, especially for avoiding excessively high resonance peaks in the natural frequency. With a dynamic stiffness that can be accurately adjusted for any application, under-sleeper pads can be used to their desired potential for track vibration insulation. As a rule, the higher the dynamic efficacy of the chosen polyurethane material (PU), the greater the vibration protection performance (Fig. 5).



**Fig. 5** The load transfer in the railway superstructure can be improved significantly with high-quality elastic elements



## 5 Insertion Loss Measurements Prove the Efficiency

The frequency-dependent vibration-reducing effect of elastic elements is quantified by the insertion loss in accordance with standard DIN V 45673-4 [4]. The insertion loss describes the relative effect of a mitigation measure compared with a reference situation. It shows, for example, how the structure-borne noise changes if under-sleeper pads are installed. Ideally, all other emission influences remain constant here, i.e. the same vehicle, the same speed and identical track roughness, etc. are considered. As the elastic element influences the railway system as a whole, the frequency-dependent insertion loss may vary with other track superstructure properties, other subsoils and/or other vehicle fittings. Figure 6 shows a series of measured insertion losses on different railway lines with various types of under-sleeper pads made from polyurethane material.

As can be seen from the measured insertion losses and frequency determinations, the natural frequencies of the superstructures with sleeper pads generally lie between 30 and 40 Hz. In the range relevant for emitted structure-borne noise,

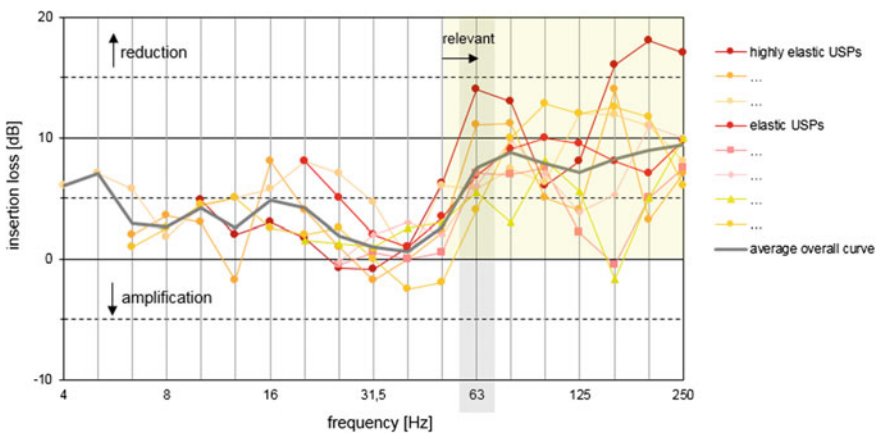


**Fig. 6** Measured insertion losses with various elastic or highly elastic under-sleeper pads made of Sylomer® and Sylodyn®

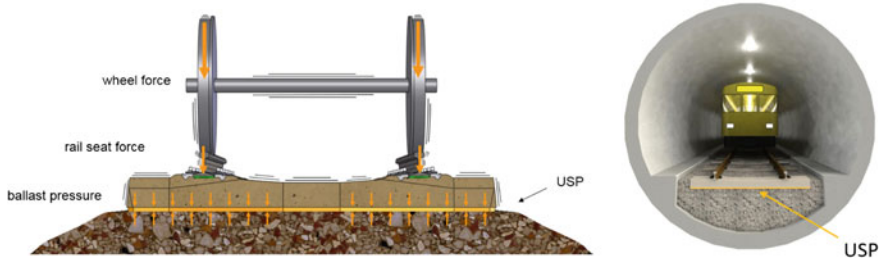


**Fig. 7** Integrating under-sleeper pads in the load transfer path of the superstructure

above 50 Hz (secondary airborne noise constitutes the decisive criterion here), the damping efficiency ranges between approx 4 and 14 dB (63 Hz) across all types of sleeper pads. With regular elastic padding, 4–7 dB are attainable values. Compared with this, there are the highly elastic under-sleeper pads, which should be considered particularly in conjunction with structure-borne noise insulation. They demonstrate the potential of the technology in an exemplary manner: with a ballasted track optimised acoustically in this way, maximum damping efficiencies of 11–14 dB (63 Hz) can be achieved. The measurements prove these types of under-sleeper pads significantly exceeded expectations. For ease of understanding: 10 dB already corresponds to an insulation rate (reduction) of 69%. With frequencies below 50 Hz there is hardly any amplification (–1 to –3 dB), whilst below 25 Hz a further damping efficiency of up to 8 dB is apparent. This is probably largely due to the improved bedding of the sleepers in the ballast bed (fully embedded, no sleepers lying on top of voids) and the enhanced superstructure/vehicle interactions. A reduced damping efficiency occurs in some cases at 100–160 Hz (“two degrees of freedom system” with soft rail pads). Nevertheless, there is almost always a positive effect (reduction). The above findings should be sufficient to prove the fundamental suitability of under-sleeper pads for vibration isolation. However, selecting the correct product is vital. This applies both to under-sleeper pads on open tracks and those in tunnels (Fig. 7).

## 6 Predicting the Vibration-Damping Effect

The findings from track measurements (Fig. 6) show the frequency-dependent effect of under-sleeper pads. One relatively simple option for mathematically forecasting such a vibration-mitigating effect is the impedance model [4–6]. Originally designed for under-ballast mats, this model can, in principle, also be used for calculations involving under-sleeper pads. Here the insertion loss also indicates the ratio of the vibration velocity amplitudes in the ground, without elastic components, to the amplitudes in the ground with elastic components installed. In addition to the spring impedance of the elastic material, the terminating impedance

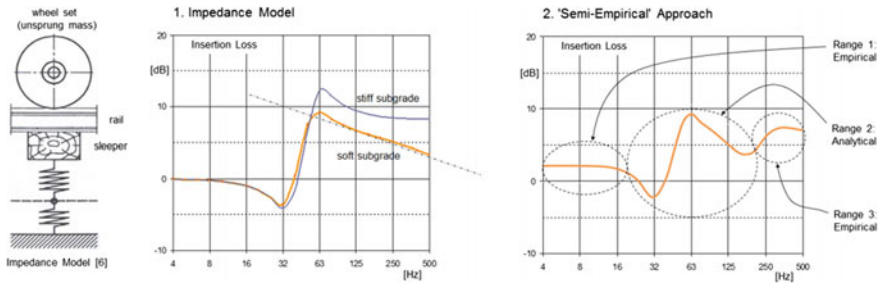


**Fig. 8** Model approaches for forecasting the insertion loss of under-sleeper pads

of the subsoil is taken into account—with a softer subgrade in the frequency range >125 Hz this can typically lead to a falling curve with a decreased effect in the one-third octave band spectrum (cf. Fig. 8: Impedance model—left-hand diagram). A possible reduction in the damping efficiency at 100–160 Hz with the existing soft rail pads could not be shown using this model. Similarly, the positive insertion loss frequently determined in the measurements for the frequency range <25 Hz, due to the improved track bed with padded sleepers, could not be shown.

One possibility for better reflecting the behaviour measured in the track with a prediction model would be to use a “semi-empirical” approach. A model partly based on empirical values using three ranges could more closely describe the reality (cf. Fig. 8: ‘Semi-empirical’ approach—right-hand diagram, Range 1: Offset for improved track bed quality. Range 2: Analytical model considering the alleviative influence of soft rail pads. Range 3: Optional declining curve taking into account the alleviative influence of the subgrade). Use of such an empirical calculation method may, under certain circumstances, require more in situ measurements, to enable more accurate statements concerning the mode of operation of under-sleeper pads with regard to vibration isolation. This is intended merely to provide food for thought here, however it is highly probable that the accuracy of a prediction concerning under-sleeper pads could be improved with empirical data.

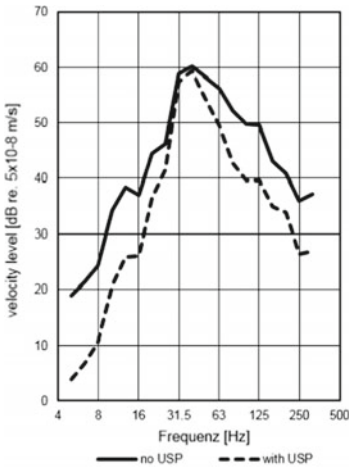
## 7 Project Example: Tunnel

The following example reveals the results of a vibration insulation renovation project for a railway tunnel in Germany [7]. The reason for retrofitting elastic padded sleepers was the high level of secondary airborne noise in the buildings above the tunnel. Numerous complaints from residents led to a law suit, which requires measures to improve the situation. Due to the comparatively high demands and resulting high costs of retrofitting under-ballast mats, the decision was made to opt for a much simpler solution: replacing the unpadded sleepers with padded sleepers. This alternative was also significantly cheaper. Highly effective under-sleeper pads made of Sylodyn® of type SLN1010G from Getzner Werkstoffe

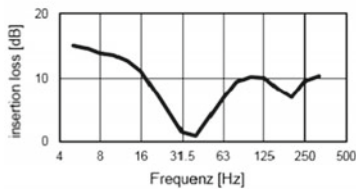
were used. To test the effectiveness, measurements were taken in the tunnel and in a building above the structure (first floor). Figure 9 shows the measured one-third octave band spectra with and without under-sleeper pads, and the associated insertion loss factor.

The analysis of all the results shows a vibration-mitigating effect of between 5 and 10 dB above a frequency of >40 Hz [7] both in the tunnel and in the building after padded sleepers were installed. There is a reduction in the damping efficiency in the natural frequency range in accordance with vibration theory, however amplification does not occur. The suitability of the under-sleeper pad in reducing secondary airborne noise and vibrations has been demonstrated in this renovation project in both the tunnel and inside the building.

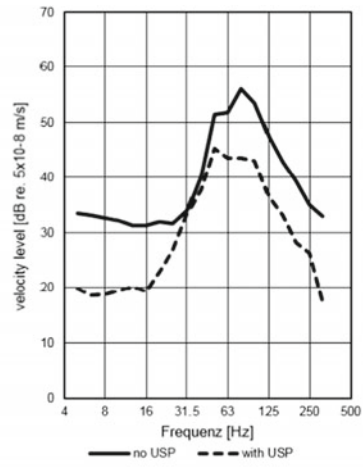
One-third octave band velocity level at the tunnel wall with and without under-sleeper pads:



Insertion loss factor at the tunnel wall:



One-third octave band velocity level in the building with and without under-sleeper pads:



Insertion loss factor in the building:

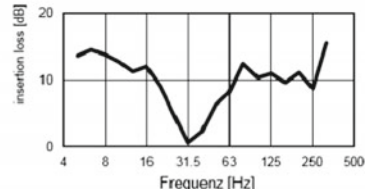


Fig. 9 Measured one-third octave band velocity level with and without under-sleeper pad, type SLN1010G, as well as the associated insertion loss factors as difference spectra

## 8 Project Example: Open Track

The following example shows an extract of the results of investigations into the vibration-damping effect of under-sleeper pads on an open track in Denmark [8]. In this project, highly effective under-sleeper pads made of Sylodyn® of type SLN1010G from Getzner Werkstoffe were used. To quantify the mode of operation of the under-sleeper pad, measurements were performed 7.5 m away from the track. The values shown below were originally calculated as acceleration levels. However, they have been converted to velocity levels to standardise the diagrams. Figure 10 shows the measured one-third octave band spectra with and without under-sleeper pads, and the associated insertion loss factor.

Based on the measured data for this project, the measures implemented produced a vibration-reduction of approx 13.5 dB in the dominant frequency bands. The reduction in damping efficiency in the natural frequency range is clearly visible as expected, however there remains a positive effect (reduction) without the feared break with a reinforcing effect.

One-third octave band velocity level 7.5 m from the track with and without under-sleeper pads:

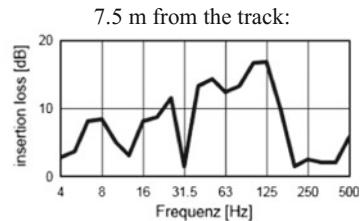
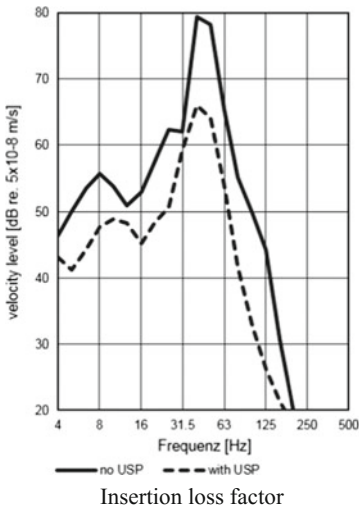


**Fig. 10** Measured one-third octave band velocity level with and without under-sleeper pad, type SLN1010G, as well as the associated insertion loss factor as a difference spectrum

## 9 Latest Developments in Under-Sleeper Pads

Nowadays, under-sleeper pads that are predominantly used to improve the track bed and protect the track ballast consist of a resistant material with a viscoplastic property that has a positive effect on the way the ballast is embedded. On the other hand, sleeper pads that are primarily used for vibration insulation require a softer, dynamically highly elastic material with low damping properties.

As the explanations show, both approaches are necessary for effective vibration protection. Therefore, a combination of different materials may be used to reduce the occurrence of the disruptive vibrations by means of a stable and secure track bed geometry, whilst also reducing the transmission of annoying vibrations using the physical principle of vibration isolation. Figure 11 shows an under-sleeper pad in a sandwich arrangement with multiple functional layers. The soft and acoustically highly effective resilient layer made from Sylo<sup>®</sup> is protectively embedded between a polyamide connecting medium (“mechanical adhesion” mesh) for the sleeper concrete side and a viscoplastic layer for the ballast side. This separation of functions covers multiple aspects and can therefore also cater to combined requirements.

Current development approaches show that it is possible to combine elastic and plastic properties in one material. They form the basis for the latest generation of PU under-sleeper pads. Positive results from various tests performed as part of ongoing research and development already confirm the advanced performance of this material. The demand for optimised innovations that meet market requirements can thus be satisfied with this solution (Fig. 12).

**Fig. 11** USP multiple functional layers

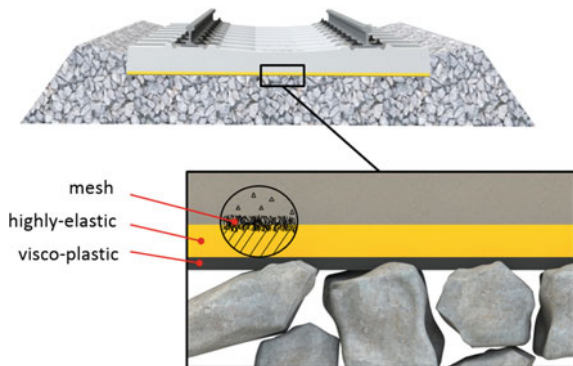




**Fig. 12** The elastic and plastic material properties of under-sleeper pads combined forecasted and desired ballast impressions immediately after removal (left) and three weeks later—complete restoration (right)

## 10 Summary and Conclusion

Railway traffic generates mechanical vibrations, due to the interaction between the rail vehicle and the track, which are transmitted either as structure-borne noise through the ground or as airborne noise. Based on the current understanding of the topic, suitable under-sleeper pads made from Sylomer® or Sylodyn® have been used to reduce the vibrations within the frequency range relevant to structure-borne noise by more than 10 dB. To date, a negative impact on primary airborne noise has not been established. Technically sophisticated under-sleeper pads can represent a cost-effective improvement to the traditional ballasted track, however the choice of material used is of vital importance here.

## References

1. Veit, P., Marschnig, S.: Towards a more sustainable track. *Railway Gaz. Int.* pp. 42–44 (January 2011)
2. Iliev, D.: Versuche mit elastisch besohnten Schwellen – Elastizität, Kontakt-spannungen, Querverschiebewiderstand [Trials using elastically padded sleepers – elasticity, contact stress, lateral resistance]. *Getzner Bahnfachtagung Schwarzenberg/Vorarlberg* (October 2011)
3. Auer, F.: Einfluss von elastischen Komponenten auf das Gleisverhalten [The influence of elastic components on the track behaviour]. *ÖVG Tagung Salzburg 104*, 53–55 (2011)
4. DIN V 45673-4 (2008): Mechanical vibration—Resilient elements used in railway tracks—Part 4: Analytical evaluation of insertion loss of mounted track systems
5. Wettschreck, R.G., Kurze, U.J.: Einfügungsdämm-Maß von Unterschottermatten [Insertion loss factor of under ballast mats]. *ACUSTICA* 58, 177–182 (1985)
6. Müller, G.; Möser, M.: *Taschenbuch der Technischen Akustik* [Pocketbook of technical acoustics]. 3rd edn., p. 545 (2003)
7. Garburg, R.: Aktuelle Erfahrungen und Erkenntnisse aus Sicht der Akustik beim Einsatz von Schwellenbesohlungen - DB Systemtechnik [Current experiences and insights from the perspective of acoustics when using under-sleeper pads—DB system technology]. *Getzner Bahnfachtagung Schwarzenberg/Vorarlberg* (November 2007)
8. COWI to Banedanmark: Experiments with vibration damping effect of Under Sleeper Pads (USP) —Vibration measurements in Dyrehaven at Springforbivej, Document No. A026780-0015 (9 January 2014)

# Sound Transit Prototype High Performance Low Frequency Floating Slab Testing and Evaluation



James T. Nelson, Derek L. Watry, Michael A. Amato,  
Patrick G. Faner, Sarah E. Kaddatz and Thomas F. Bergen

**Abstract** Sound Transit is constructing twin-bored tunnels under the University of Washington campus in Seattle, Washington, USA. The tunnels will include high-performance floating slab track isolation to control ground vibration in research laboratories and satisfy the terms of an agreement between Sound Transit and the university. The agreement includes provisions for liquidated damages in the event that vibration exceeds specified limits for third octave band vibration between 2 and 100 Hz in the laboratories. The floating slab design consists of discontinuous concrete double-ties with high compliance direct fixation fasteners supporting RE115 rail. Four natural rubber main support pads and two bonded natural rubber side pads isolate each slab from the tunnel invert. The nominal design resonance of the floating slab track is 5.5 Hz. The unique floating slab track design incorporates a magnetic field cancellation cable suspended beneath the slab track in an inverted trough. The magnetic field cancellation cable presents unique design challenges for operation, maintenance, and construction. A prototype of the floating slab of length 131 m has been installed in a tunnel that is not on the campus to verify performance. This paper presents and discusses the results of measurements of the dynamic response and vibration isolation effectiveness of the track isolation, and comparisons with theoretical calculations.

## 1 Introduction

The Sound Transit is constructing twin-bored tunnels from downtown Seattle to Lynwood in Washington State (USA), as part of a major expansion of the light rail system. A portion of the tunnels passes through the University of Washington's Seattle campus. Agreements were made between the Sound Transit and the University of Washington to maintain ground vibration within guaranteed limits for

---

J. T. Nelson (✉) · D. L. Watry · M. A. Amato ·  
P. G. Faner · S. E. Kaddatz · T. F. Bergen  
Wilson Ihrig, 6001 Shellmound, Suite 400, Emeryville, CA 94608, USA  
e-mail: jnelson@wiai.com

© Springer International Publishing AG, part of Springer Nature 2018  
D. Anderson et al. (eds.), *Noise and Vibration Mitigation for Rail Transportation Systems*, Notes on Numerical Fluid Mechanics and Multidisciplinary Design 139,  
[https://doi.org/10.1007/978-3-319-73411-8\\_48](https://doi.org/10.1007/978-3-319-73411-8_48)



third octave vibration velocity in up to 24 research laboratories at horizontal distances ranging from 0 to 700 m from the tunnels. Most of these limits represent the existing ambient background vibration environment. The agreement also includes limits for magnetic fields induced by the traction power currents in the catenary and rails. The project and measurements and predictions made at similar tunnels on the Sound Transit system are discussed by Nelson, et al. [1].

The Sound Transit light-rail vehicles are three-piece articulated 70% low floor vehicles with independently rotating wheels on the centre bogie. The motor bogies each have two traction motors with floating gear unit and flexible coupling between the gear unit and axle. Resilient wheels are employed on all bogies. Traction power is supplied by overhead catenary. This type of vehicle is used at a number of light rail systems in the United States, including, for example, the Los Angeles Metropolitan Transit Authority, Portland Tri-Met, New Jersey Transit, and Valley Transportation Authority in San Jose, California.

A high performance low resonance frequency track isolation system is planned to satisfy the agreement between the Sound Transit and the University of Washington. This is the first low frequency double-tie floating slab to be installed at a light rail system in the United States.

Floating slab track are used at a number of heavy rail transit systems, such as the Bay Area Rapid Transit system in San Francisco, the Los Angeles Metro, the Washington Metropolitan Area Transit Authority in Washington D.C., and the Metropolitan Atlanta Rapid Transit Authority in Atlanta Georgia. These isolation systems consist of either continuous poured-in-place slabs such as in Washington, D.C., or discontinuous double ties such as used in Toronto and Atlanta. Floating slab track is not common at US light rail systems. The earliest example of a floating slab track is the double-tie system at the Niagara Frontier Transportation Authority in Buffalo, New York. Thus, the floating slab track isolation system at Sound Transit is to some extent unique for U.S. light rail.

A prototype track isolation system was installed on the University Link south of the Capitol Hill station to demonstrate performance of the floating slab design and further define operating limits for ground vibration. The dynamic responses of the unloaded slabs were measured with a shaker and impact hammer, and results are compared with theoretical responses obtained with a Timoshenko beam model of a discretely supported rail and lumped masses. The floating slab vibration isolation performance was obtained by measuring the third octave force density levels of the Sound Transit vehicles at various speeds with methods outlined by the U.S. Federal Transit Administration [2]. These analyses and testing are discussed below.

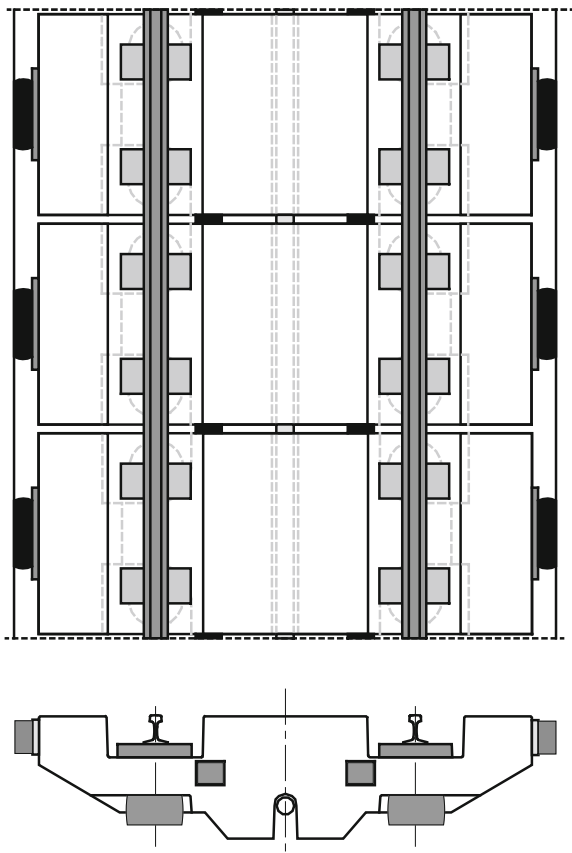
## 2 Design

The prototype design consists of discontinuous 1168 mm “double ties” at 1219 mm pitch supported with natural rubber main support pads and bonded side pads providing an unloaded natural frequency of about 5.5 Hz. The track consists of 115RE

rail supported on high compliance natural rubber bonded fasteners at 610 mm pitch. The nominal dynamic stiffness of the direct fixation fasteners is 14 MN/m. The slabs are precast with heavy-weight concrete. The combined mass of the slabs and track is 5200 kg per slab, giving a mass per unit length of 4275 kg/m. The design of the slab accommodates a traction power cable designed to cancel magnetic fields produced by the traction power currents in the catenary. The cable is suspended beneath the slab in an inverted trough cast into the slabs. The cable runs continuously under the slabs and is spliced to electrical cable risers that connect the cable to the catenary at nominally 18.3 m intervals. Two long splicing slabs are installed at these splices. The length parallel to the rail of each splicing slab is 2388 mm. Eleven double-tie slabs are positioned between the splicing slab sections, giving a total segmental length of 18.3 m. The design resonance of the splicing slab is similar to that of the 1168 mm slabs. The cross-section and plan of the floating slab are illustrated in Fig. 1.

The slab pitch was chosen to be approximately 1.5 times the axle separation (wheel base) of the bogies. Thus, when one axle passes over a slab, the trailing axle

**Fig. 1** Plan and cross-section of floating slab double tie track



passes over the gap between slabs, thus minimizing parametric excitation of the combined vehicle and track system.

The main support pad nominal height and diameter are 190.5 mm and 317.5 mm, respectively. The side pad dimensions are 102 mm thick by 381 mm long by 203 mm high, giving a loaded area of 0.0774 m<sup>2</sup>. Elastomer separation pads are placed between the slabs, though these do not enter directly into the performance.

### 3 Slab Response

The floating slab response was calculated with an idealized lumped parameter model [3] as illustrated in Fig. 2. Concentrated masses and moments of inertia represent each slab, supported by concentrated linear springs and torsional springs to represent the direct fixation fasteners and floating slab natural rubber isolators. The torsional springs represent the torsional reaction of the direct fixation fasteners and isolators to slab rotation. The separation pads were ignored. The calculated transfer compliance response of one of the slabs to rail force (simultaneously applied to both rails) is compared with the measured response in Fig. 3. The measured data were obtained by shaker excitation of the slab and measuring the vertical response with accelerometers.

#### 3.1 Single-Degree-of-Freedom Response

The resonance peak at about 5.5 Hz corresponds to rigid-body motion of the slabs and rail in the vertical direction, controlled by the combined mass of the slabs and

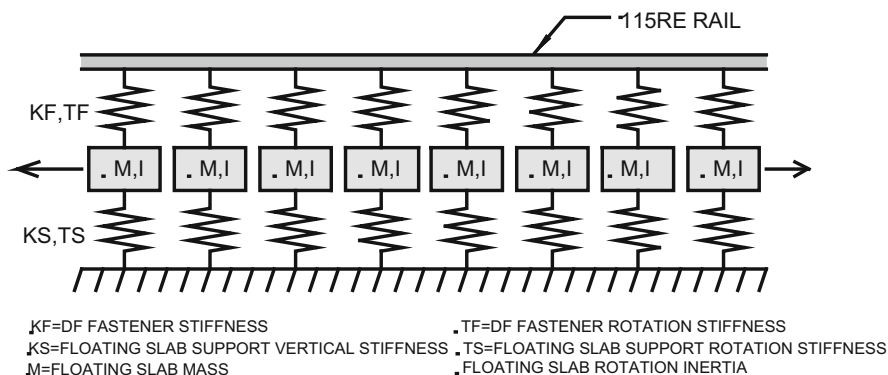
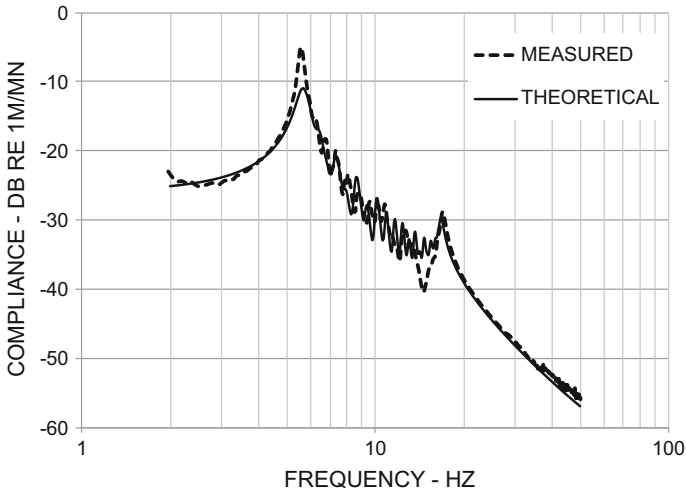


Fig. 2 Lumped parameter model



**Fig. 3** Comparison of theoretical response of slab to rail force

rail resonating on the elastomeric main support and side pad isolators. The phase velocity for waves propagated by the rails along the track at this frequency is essentially infinite in the case of zero material damping of the elastomer. Below 5.5 Hz the vibration does not propagate along the track away from the source, at least in the limiting case of zero material damping of the elastomer. Above 5.5 Hz the vibration energy propagates away from the source, though it is affected by the discrete nature of the slabs, with stop bands and pass bands.

### 3.2 17-Hz Mode

Figure 4 illustrates the mode shape associated with the 17 Hz vibration mode. The rail constrains the slabs and supports the mode in which adjacent slabs are 180 degrees out of phase. The resonance frequency is controlled by the mass of each slab and the combined stiffness of the four direct fixation fasteners, four natural rubber main support pads, and two natural rubber side pads. The mode shown is the simplest mode involving out-of-phase motion of adjacent slabs. The predicted and measured responses agree very closely.

More complicated modes exist, such as groups of two slabs moving out of phase with the next group of two, and so on, modified by the bending stiffness of the rail.

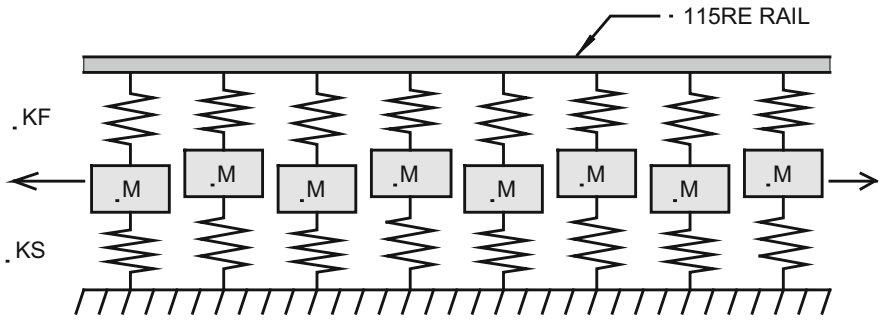


Fig. 4 Mode shape of slabs between rail and invert

### 3.3 Force Cancellation

The appearance of the mode at 17 Hz suggests that there might be increased forced transmissibility at this frequency and perhaps additional modes. However, the phases between slab motions are such that cancellation of forces transmitted by the entirety of the slabs occurs. Figure 5 illustrates the calculated effect of adding the transmitted forces of individual contiguous slabs for symmetric excitation of the rails at a single slab. The transmitted forces at slabs 0, 1, 2 and 3 are shown, together with the sum of these forces. The forces are applied at Slab 0, and Slabs 1, 2, and 3 are contiguous slabs extending in either direction. Finally, the curve labeled “Net Force Transmissibility” is the sum of 20 slabs that were modeled. The converged force transmissibility

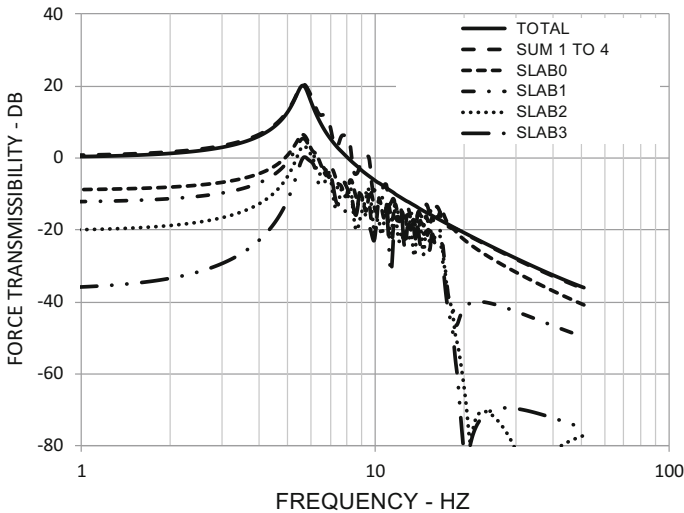


Fig. 5 Partial summation of transmitted forces

asymptotically approaches 0 dB at 0 Hz, with no evidence of a peak at 17 Hz, and the shape approximates the transmissibility curve of a single degree-of-freedom oscillator near the slab design resonance frequency of 5.5 Hz. The net response conforms to the force transmissibility curve of a two-degree-of-freedom oscillator, due to the rail on fastener resonance, as discussed below. This is a general result of discretely supported beams up to the pin-pin mode frequency of the system [4].

### 3.4 Rail-on-Fastener Resonance

Figure 6 compares the theoretical and measured vertical transfer compliance of the slab due to vertical symmetric forces applied to the rail. The measurement was done by impacting the center of the slab and measuring the rail response, which is equal to the forward transfer compliance by reciprocity. The rail-on-fastener resonance frequency is about 90 Hz. Again, the measured and predicted results agree well up through the track resonance frequency, but considerable ripple exists in the response above the track resonance that is not well replicated by the prediction.

### 3.5 Predicted Insertion Gain

Theoretical insertion losses of the combined vehicle and floating slab were calculated with a parallel impedance model of the wheel and rail, using the above described model of the track and a multi-degree-of-freedom model of the vehicle.

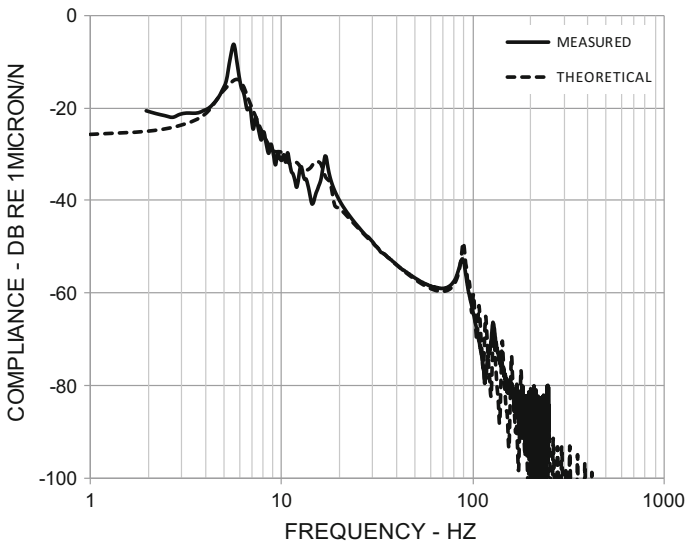
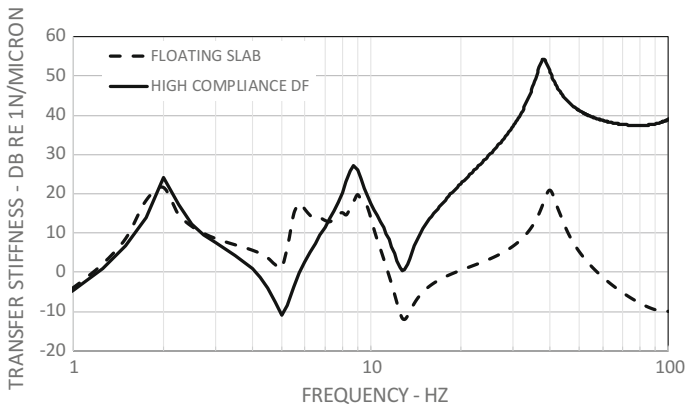


Fig. 6 High frequency transfer compliance of slab to symmetric rail force

The vehicle model includes the wheel sets with resilient wheels, axles, primary suspension, secondary suspension, bogie frame, and one half of the car body mass. The compliance matrix for the four wheels was combined with the compliance matrix for the track at the wheel/rail contact points. Net invert forces were computed for an assumed unit amplitude sinusoidal roughness at each wheel/rail contact. The results for each wheel were incoherently summed. This procedure is based on the assumption that the roughness at each wheel is not coherent with the roughness at any of the other wheels.

The predicted invert force of the floating slab track and vehicle is compared with that of the high compliance fasteners and vehicle in Fig. 7. The force is the sum of all transmitted forces by the track. The peak at about 2 Hz is due to the modelled secondary suspension resonance of the vehicle. A pronounced dip occurs in the transmitted force spectrum at about 5 Hz for the high compliance direct fixation track. The transmitted forces for the floating slab track are higher than those for the direct fixation track near 5 Hz. The predicted transmitted forces are less than those for the direct fixation track at frequencies above 7 Hz. The predicted force at the primary resonance frequency is less for the floating slab than for the direct fixation track, and improves with increasing frequency. The track and wheelset resonance appears in both force spectra at 40 Hz.

Figure 8 illustrates the predicted insertion gain of the floating slab track, calculated as the difference between the curves shown in Fig. 7. The insertion gain is almost 20 dB at the design resonance frequency of 5.5 Hz, is slightly negative at 9 Hz, and approximates that of a single-degree-of-freedom oscillator at frequencies above 10 Hz. The predicted insertion gain at the design resonance is for a loss factor of 10% for the elastomer pads. In practice, the effective insertion gain tends to be much less, as was observed during testing with vehicles.



**Fig. 7** Invert force relative to relative displacement between tire and rail

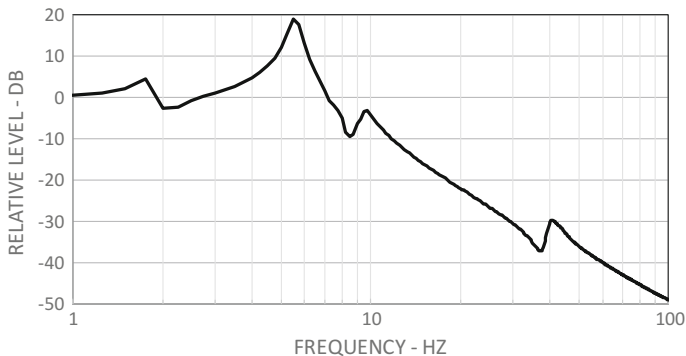


Fig. 8 Floating slab insertion gain

### 4 Performance

The vibration reduction performance of the prototype floating slab under vehicle operation was measured with a two-car test train at various speeds. The procedure involved measuring the force density levels for the floating slab track and rigid invert track. This was done by measuring the vibration levels transmitted to the adjacent tunnel and normalizing the data with the measured line source response between the track and the measurement points. The procedure is described in [1, 2]. The data were further adjusted for measured rail undulation.

The prototype floating slab was installed in one of two bored tunnels with track centers at about 14 m apart. The length of the floating slab test section was 134 m. Vibration velocity levels were measured during passes of a two-car test train of total length 60 m traveling at various speeds on both the prototype floating slab track and a contiguous section of rigid invert track with high compliance fasteners of the same type as used on the floating slabs. The fastener pitch for the rigid invert track was 762 mm. Data were obtained for multiple passes in both directions and background vibration samples were obtained for each pass. The background vibration was similar with or dominated by vibration produced by trains at frequencies below 10 Hz. For these frequencies, the differences between each sample with a train and sample without a train were subjected to a Student’s T test to estimate levels of significance. For those third octaves judged to be significantly above the background vibration during train passage, the background vibration was subtracted from the train vibration plus background vibration. Otherwise, ten decibels were subtracted from the energy mean of the combined train vibration and background vibration. The final results are plotted in Fig. 9.

The line source response levels were measured at each test section and subtracted from the passby vibration levels to obtain the third octave force density levels for each test section. These were further adjusted by the rail vertical undulation and roughness measured at each test location. The rails at the floating slab



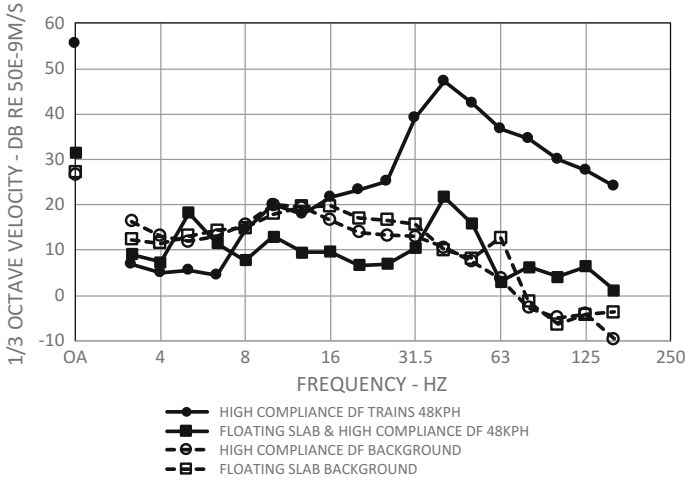


Fig. 9 Measured vibration at safety walks of adjacent tunnels –3-car trains at 48KPH

test section were supplied by a different manufacturer from those installed at the rigid invert test section, and the vertical roughness of the rail at the floating slab test section was significantly greater than that at the rigid invert test section at wavelengths of several meters. The estimated force density levels as adjusted by these combined effects are plotted in Fig. 10.

The force density levels for the floating slab test section relative to the force density levels for the rigid invert test section are plotted in Fig. 11 as insertion gains. Also plotted in Fig. 11 is the theoretical estimate of the insertion gain for the floating slab system, calculated on the basis of the parallel impedance model of the vehicle and discretely supported rail as described above. The measured insertion

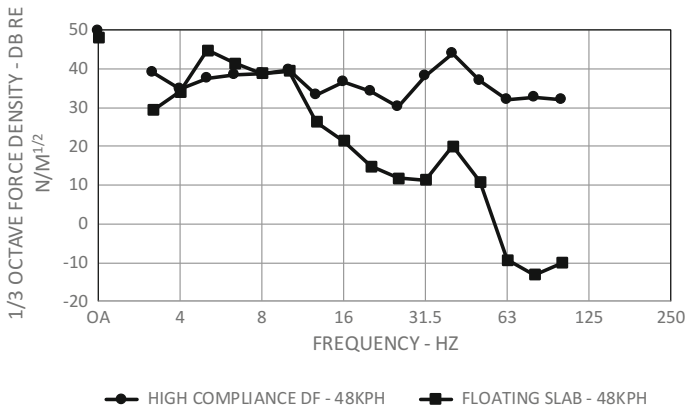
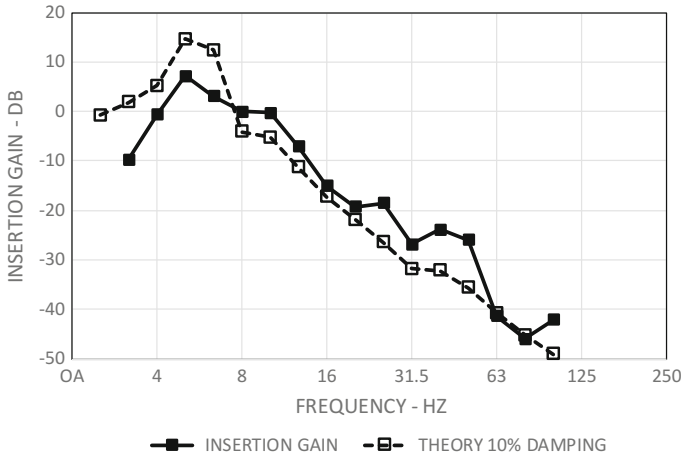


Fig. 10 Estimated force density levels for rigid invert and floating slab



**Fig. 11** Insertion gain—floating slab relative to high compliance direct fixation

gain is higher than the theoretical estimate by approximately 10 dB at about 40 Hz, and less so at other frequencies. The predicted amplification at frequencies up to 6.3 Hz is not realized in the data. Higher speed tests have indicated less amplification than shown for 48 km/hr operation.

## 5 Conclusion

The foregoing illustrates the vibration isolation achievable with a high performance floating slab system, and, moreover, indicates that the vibration isolation performance can be reasonably predicted. Deviations between measured and predicted performance are due to measurement uncertainties, limitations of the theoretical models, and restriction of the input roughness to the vertical direction. In the last case, other mechanisms besides relative roughness between the wheel and rail may cause vibration, such as stick slip oscillations, and parametric excitation. The prototype slab design is planned for the North Link tunnels under the University of Washington campus.

**Acknowledgements** We acknowledge the staff of Sound Transit, McMillen Jacobs Associates, and Parsons Brinckerhoff/PBWorld. This project is the culmination of the concerted effort of many over a period of many years.

## References

1. Nelson, J.T., Watry, D.L.: Vibration control at sound transit. In: Nielson, J.C.O., et al. (eds.) *Noise and Vibration Mitigation for Rail Transportation Systems*. NNFM, Vol. 126, pp. 313–320. Springer, Heidelberg (2012)
2. Hanson, C.F., Towers, D.A., Meister, D.F.: *Transit Noise and Vibration Impact Assessment*, U.S. Federal Transit Administration (2006)
3. Nelson, J.T., Watry, D.L., Amato, M.A.: Dynamic response of high-performance floating slab track. In: *Proceedings of Inter Noise 2015 San Francisco (USA)*
4. This is the result of an unpublished analysis of bi-bloc resilient tie systems conducted by the author as part of a project for the US DOT/TSC (1984)

# Development of a Test Procedure for Stiffness Measurements Appropriate to Ground-Borne Noise Modelling



D. Herron, E. Bongini, B. Faure, R. Potvin and S. Cox

**Abstract** A simple test procedure is proposed to measure the stiffness of rail fastening systems specifically for the purpose of providing suitable input data to predictive models for ground-borne noise. It is therefore intended to provide stiffness data that is appropriate to the frequencies, amplitudes and types of fastening systems that are relevant to studies of ground-borne noise. The stiffness of the fastening system is found to be dependent on vibration amplitude within the range expected in track. The proposed test procedure allows stiffness measurements to be made over a suitable range of amplitudes and would represent only a small addition to existing standard tests for fastening systems in terms of the resources required.

## 1 Introduction

### 1.1 *The Stiffness of Rail Fastening Systems*

The stiffness of rail fastening systems is one of the main parameters used to select an appropriate fastening system for a given situation. While the lateral stiffness and roll stiffness of the fastening system are of interest, it is usually the vertical stiffness that is the main consideration. The vertical stiffness, hereafter referred to as the ‘stiffness’, is relevant to various important considerations, such as the rate of deterioration of the track and the related maintenance requirement, rolling noise, bridge noise and ground-borne noise.

---

D. Herron (✉) · S. Cox  
Pandrol Limited, Addlestone, UK  
e-mail: d.herron@pandrol.com

E. Bongini · B. Faure  
SNCF Research, Paris, France

R. Potvin  
SNCF Infrastructure, Paris, France

While static stiffness measurements are still made, it is accepted that dynamic stiffness measurements are a more suitable indicator of how the fastening system will behave in the track. The resilient elements used in fastening systems normally have a stiffness that is dependent on amplitude, frequency and temperature. These parameters therefore need to be controlled appropriately in a stiffness test.

## ***1.2 The Stiffness Tests Described by the European Standards for Fastening Systems***

The current European standards for the testing of rail fastening systems currently describe three different types of vertical stiffness measurement [1]: (i) Static stiffness, (ii) Dynamic low frequency stiffness, (iii) Dynamic high frequency stiffness. The dynamic low frequency test (type ii above) is normally performed at a frequency of 5 Hz [2, 3]. The results of this type (ii) stiffness measurement are of limited application to noise and vibration issues. This is because the load conditions are representative of the quasi-static excitation in-track, rather than the excitation mechanism of primary interest in railway noise and vibration, that due to wheel-rail roughness.

The dynamic high frequency stiffness test (type iii) is performed using one of three different methods: the direct method, the indirect method and the corrected driving point method [1]. The frequency range for these measurements is stated as 20–450 Hz, except for the corrected driving point method, for which it is given as up to 120 Hz. The amplitude of the dynamic load is chosen so that the rail velocity in the test is equal to an estimate made for the rail velocity in track and a second test is performed at a rail velocity 20 dB lower than this estimated level in track. If no data are available for rail velocity in the track, a rail velocity of 90 dB ref.  $5 \times 10^{-8}$  m/s can be assumed. This test involves much smaller amplitudes of dynamic load and displacement than the type (ii) stiffness measurement, such that they are appropriate to the excitation mechanism (that due to wheel-rail roughness) which is relevant to the type (iii) stiffness measurement. A static preload is applied to the fastening system, in addition to the dynamic load, which represents the pre-loading effect of the quasi-static wheel load.

Type (i) and type (ii) stiffness measurements are made routinely during the development of fastening systems and they are mandatory parts of the approval process for fastening systems that is defined by the European standards [2, 3]. Measurements of type (iii) are not a mandatory part of the approval process and they are made much less frequently than types (i) and (ii), such that there is a lack of type (iii) measurement data for many types of fastening system. The main reasons for this is that the procedure described by [1] for the type (iii) measurement is regarded as difficult to perform and requires skills/equipment that are quite different to those used in the other tests required by the European Standards [2, 3].

### ***1.3 The Requirements of Stiffness Measurement Data for Use in Predictive Models for Ground-Borne Noise***

Predictive models for ground-borne noise are now widely used in urban railway projects and a suitable dynamic stiffness of the fastening system is an important input parameter to these models. This now appears to be the main reason for additional (to the type (i) and type (ii) values that are normally published) stiffness data to be requested of the manufacturer, rather than in relation to studies of rolling noise or bridge/viaduct noise.

The requirements of stiffness data for use in ground-borne noise models are different to those for measurement data to be used in rolling noise or bridge/viaduct noise studies. The frequency range of interest for ground-borne noise is usually from about 30 to 250 Hz, while that for both rolling noise and bridge noise extends to more than 1 kHz. Previous measurement work indicates that the dependence of the fastening system stiffness on frequency is very limited in the relatively low frequency range of interest for ground-borne noise [4–6]. It may therefore be unnecessary to measure the stiffness of the fastening system over this frequency range, such that the measurements could be made at a single frequency that is chosen to allow a simple approach to be taken to the measurement. Ideally, this simple approach would be based on the same rig and measurement equipment as is used for the type (i) and type (ii) stiffness measurements, such that it would be a very small addition to the standard set of tests. This means using the driving point method and a hydraulic actuator to provide the dynamic loading.

The stiffness of the fastening system is normally assumed to be independent of the amplitude of displacement and strain when predictive models are used to study railway noise and vibration. This assumption appears to be valid in cases where rolling noise or bridge/viaduct noise are of interest [7]. However, the lower frequency range of interest for ground-borne noise means that the amplitudes of displacement and strain will be larger. The assumption that the stiffness of the fastening system is independent of amplitude may therefore not apply to ground-borne noise modelling studies.

The dependence of fastening system stiffness on displacement and strain amplitude has been proposed as a possible explanation for difficulties found in forecasting the performance of low stiffness fastening systems with regard to ground-borne noise [8]. While a hydraulic actuator is not normally able to provide the very small amplitude excitation that can be obtained from an electromagnetic shaker, it can provide excitation over a wide range of amplitudes, including those expected in track at the lower end of the frequency range of interest for ground-borne noise. At these frequencies, the quasi-static loading and parametric loading at the sleeper passing frequency in particular may be significant contributors to the dynamic load conditions.

## ***1.4 Aims of This Work***

The primary aim of this work is to establish a procedure for measuring the stiffness of fastening systems in a manner that will provide suitable input data to models for ground-borne noise. This procedure should be a practical addition to the set of tests required by [2, 3], without the need for specialist equipment or a prohibitive increase in the time required to perform the prescribed set of tests. This would be of benefit in helping to generate suitable measurement data for use in ground-borne noise modelling work.

A secondary aim of this work is to investigate the dependence of fastening system stiffness on the displacement/strain amplitude in the resilient element(s) of the fastening system over the range relevant to ground borne noise. It is the relatively low stiffness fastening systems that are of primary interest in this regard, since it is these systems that are expected to show the greatest amplitude dependence and it also these systems that are normally used in cases where ground-borne noise is a major consideration.

## **2 Stiffness Measurements for Fastening Systems with a Single Resilient Element**

### ***2.1 Measurements Made on a Pandrol 5877D Studded Rubber Rail Pad***

Studded rubber rail pads are widely used on both ballasted tracks and slab tracks. A fastening system that contains a single rubber pad would not normally be used in cases where ground-borne noise was a concern, due to its relatively high stiffness. However, such fastening systems are often used as the reference track system in ground-borne noise modelling studies. This allows an insertion loss curve to be produced for each proposed mitigation measure, relative to a well-known track type.

The Pandrol 5877D studded rubber rail pad is used on a number of European railways. It has a nominal installed thickness of 10 mm and a type ii stiffness of approximately 70 kN/mm when measured to the specification for mainline track fastening systems [1, 2]. Type (iii) stiffness measurement data is available for the 5877D pad, from several different sources. An overview of this existing measurement data, which has been obtained by various different methods, is given by [5]. This represents a good basis for an evaluation of the proposed simple test method. Figure 1 presents results for the 5877D rail pad (no other pads are included) obtained in previous work for a static preload of 40 kN [5].

Figure 1 shows large variations between the results obtained in the different tests performed on this rail pad. The results labelled ‘Goose Hill’ were obtained from measurements made in-track. Those labelled ‘Pandrol direct’, ‘TNO revised’ and

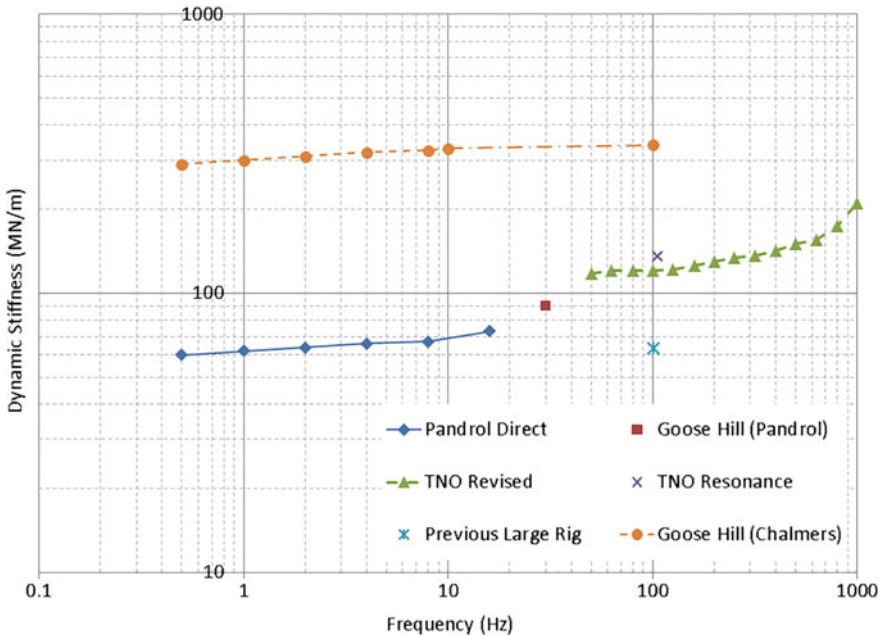


**Fig. 1** Dynamic stiffness of the 5877D rail pad shown against frequency for a static preload of 40 kN

‘TNO resonance’ are from laboratory measurements made using the driving point (Pandrol) and indirect (TNO) methods. While these measurements are available for quite different frequency ranges, this does not explain the differences in the results of the various studies. The difference in the amplitude of the dynamic load and resulting displacement/strain amplitude in the pad in these studies is large and it is expected that this is responsible for the misalignment in the datasets presented in Fig. 1. For example, the ‘Pandrol direct’ results were obtained for a dynamic load amplitude of 10 kN, which results in a pad strain (peak) amplitude of the order of 1%. In contrast, the TNO results were obtained for a pad strain (peak) amplitude of the order of 0.005%. It is expected that the stiffness will be independent of amplitude for peak-peak strain amplitudes below approximately 0.3% for rubber elements, but significant dependence on strain amplitude can be expected above this level [9]. This is a property of the material. Note that the tests performed for large load amplitudes are run for only a short duration, such that no significant build-up of heat in the pad occurs.

The datasets shown in Fig. 1 indicate that the stiffness of the pad is not strongly dependent on frequency in the range below 250 Hz, taken to be the upper limit of the range of interest for ground borne noise here. The results labelled ‘TNO revised’, originally reported in [10], demonstrate this particularly clearly. Together with the expectation that a significant part of the differences found in the results of



the various different measurements made for this pad previously is due to the different strain amplitude levels in these tests, this supports the proposal made in Sect. 1.3 to make a set of measurements using the driving point method and a hydraulic actuator to provide excitation over a large range of load amplitudes. This can be done using the same apparatus as is described for Type (ii) stiffness measurements in Sects. 6.2 and 7.2 of [1]. The load from the actuator is monitored by the actuator control system and the displacement is measured at the input side of the rig using four displacement transducers, from which a mean displacement is found. The actuator provides a dynamic load that oscillates about a mean load value that represents a static preload.

The use of a hydraulic actuator to provide the excitation limits the tests to very low frequencies, because the actuator becomes unstable at higher frequencies. For the actuator used in these tests, which has a modern control system, it can be unstable for frequencies as low as 20 Hz, depending on the conditions of the test. For this reason, all of the measurement data presented in this work has been obtained at a frequency of 15 Hz. While this lies outside the frequency range of interest for ground-borne noise, it is assumed here that the frequency dependence of the pad stiffness in the range from 15 Hz to the frequencies of interest for ground-borne noise is sufficiently small for representative measurements to be made in this way. The results shown in Fig. 1, together with the variability in the material properties of rubber pads (typically  $\pm 10\%$  for a single pad manufacturer, greater than this when several manufacturers are considered), supports this assumption. A set of results obtained using the proposed simple test method for a static preload (or mean load) of 40 kN are presented in Table 1.

Table 1 shows that the stiffness result increases in value by almost a factor of 2 as the dynamic load amplitude is reduced from 7 to 1 kN. In terms of strain amplitude, this is a range from about 1% to just under 0.1%.

If a comparison is made between the results shown in Table 1 and those from previous measurement work that are presented in Fig. 1, good agreement is shown when the comparison is made on the basis of comparable amplitudes. The ‘Pandrol direct’ result, 73 kN/mm at a frequency 16 Hz, for this pad was obtained for a load amplitude of 10 kN. These conditions are comparable to those for the largest amplitude case shown in Table 1 and the results are similar. The ‘TNO revised’ result of 118 kN/mm at a frequency of 50 Hz was obtained for a strain amplitude

**Table 1** Results obtained for the 5877D rail pad using the proposed simple test method and a static preload of 40 kN

Frequency (Hz)	Static preload (kN)	Dynamic load amplitude (kN)	Stiffness (kN/mm)	Displacement amplitude ( $\mu\text{m}$ )	Rail velocity (dB ref. $5 \times 10^{-8}$ m/s)	Peak pad strain amplitude (%)
15	40	7.5	67	111	103	1.11
15	40	2	89	22	89	0.22
15	40	1	118	8	81	0.08

much smaller than the lowest amplitude case shown in Table 1, but the results of these two tests compare well. This is consistent with the expectation that the stiffness is independent of amplitude for small strains [9] and that the effect of the frequency difference between these two tests would be small.

## ***2.2 Note on Amplitudes of Displacement and Strain***

The results presented in Table 1 indicate that the stiffness of the 5877D studded rubber rail pad is dependent on the dynamic displacement/strain amplitude over the range considered in these tests, which was from 111 to 8  $\mu\text{m}$ . In order to comment on the significance of this, the amplitudes of displacement across the fastening system that occur in track need to be understood. It is difficult to quantify the displacement across the fastening system at frequencies above those at which displacement transducers (which would be mounted on the sleeper/slab, close to the fastening system) can be used. However, existing measurement data for the vibration of the rails, obtained using accelerometers, was reviewed for frequencies close to the lower limit of interest for ground borne noise, about 30 Hz, and also at about 100 Hz. From this review it is expected that for conventional fastening systems a representative displacement amplitude would be around 30  $\mu\text{m}$  at a frequency of 30 Hz and 10  $\mu\text{m}$  at 100 Hz. This, together with the results of Table 1, indicates that the amplitudes expected in-track are sufficiently large for the stiffness of the pad to show significant amplitude dependence. For the low stiffness fastening systems that are used as a mitigation measure for ground-borne noise (see Sects. 3 and 4), larger displacement amplitudes occur: up to 80  $\mu\text{m}$  at a frequency of 30 Hz and 20  $\mu\text{m}$  at 100 Hz.

## ***2.3 Measurements on a Complete Fastening System Fitted with the 5877D Rail Pad***

The 5877D rail pad was fitted to a complete fastening system, in which the two clips provided a combined clamping load of approximately 18 kN to a short section of rail. The inertia forces associated with the moving section of rail are very much smaller than the elastic forces in these tests, which were run at a frequency of 15 Hz. The actuator was used to apply the same dynamic load amplitudes as were applied to only the pad in Sect. 2.3. The static preload (or mean load) applied by the actuator in each test was set to 18 kN less than it was for the corresponding test on only the pad, to compensate for the clamping load applied by the clips to the rail in the complete fastening system. The results obtained for a static preload of 22 kN from the actuator, which corresponds to a total static preload on the pad of approximately 40 kN, are shown in Table 2.

**Table 2** Results obtained for the 5877D rail pad in a complete fastening system (with clips), using the proposed simple test method

Frequency (Hz)	Static preload from actuator (kN)	Dynamic load amplitude (kN)	Stiffness (kN/mm)	Displacement amplitude ( $\mu\text{m}$ )	Rail velocity (dB ref. $5 \times 10^{-8}$ m/s)	Pad strain amplitude (%)
15	22	7.5	81	93	102	0.93
15	22	2	118	17	87	0.17
15	22	1	154	6	78	0.06

The stiffness results from the measurements made on the complete fastening system are generally higher than those made for only the pad, by about 25% for the two larger dynamic load amplitude cases and by 35% for the 1 kN load amplitude case. These are significant differences between the results of the test on only a pad and those on a complete fastening system. However, the results of the dynamic low frequency (type ii) stiffness performed on this pad alone and then on a complete fastening system fitted with this pad also differed by almost 25%. Such differences in type (ii) stiffness results between tests on a pad and tests on a complete fastening system are not uncommon. The comparison between results of tests on a pad only and tests on a complete system appears to be very sensitive to the correction used to account for the clamping load from the clips.

### 3 Stiffness Measurements for a Two-Stage Resilient Baseplate

A two-stage resilient baseplate is a type of fastening system that includes two resilient elements, typically separated by a cast iron plate. A lower stiffness can be achieved with this type of fastening system than the conventional type that includes only one resilient element. The type ii. stiffness of these systems is typically in the range from 15 to 30 kN/mm. An example of this type of fastening system is the Pandrol VIPA-SP, which normally includes a studded rubber rail pad between the rail and the cast iron plate, and a studded rubber ‘baseplate’ pad beneath the cast iron plate. The cast iron plate is therefore mounted in the fastening system via resilient elements, such that it is free to vibrate rather than being clamped down rigidly to the track slab or sleeper. Modes of vibration in which the resiliently supported plate moves as a mass or plate in bending may be expected for this type of fastening system, which is not the case for a single-pad fastening system.

A finite element model of the VIPA-SP fastening system was created in previous work [6] and verified by comparing results from the model with measurements for point response at the rail head and with decay rate measurements. Measurements for the type (iii) stiffness of the two pads were made by the indirect method (down to a

frequency of 140 Hz) and used as input data to the model. Under the load conditions appropriate to a static preload of 15 kN on the system, the model predicts the stiffness spectra shown in Fig. 2.

The model predicts a stiffness of 53 kN/mm at low frequencies, for a static preload of 15 kN. The modal response of the fastening system becomes important for frequencies greater than about 200 Hz. The assumption that the frequency dependence of the fastening system stiffness can be neglected for ground-borne noise studies is a reasonable one for this fastening system, and probably also for others of a similar design. This means that simple approach to stiffness measurement described in Sect. 2 can also be applied to the VIPA-SP system.

The proposed simple test method was applied to the VIPA-SP fastening system, for a range of static preloads and dynamic load amplitudes. Results obtained for a static preload are presented in Table 3.

Each of the two studded rubber pads in the VIPA-SP fastening system had a thickness of approximately 12 mm when installed. Mean strain amplitudes are shown in Table 3 based on the displacement measured at the rail and the combined thickness of the two pads. The stiffness of the VIPA-SP fastening system is shown to be dependent on dynamic load amplitude over the range from 5 to 0.5 kN. With the exception of the 5 kN case, the displacement amplitudes in these tests are within the range expected in track for the frequencies of interest for ground-borne noise. In terms of the mean strain amplitude, this is between about 0.3 and 0.05%. The lower end of this strain range is sufficiently small for an amplitude independent stiffness to have been expected. The use of mean strain amplitude here may be responsible for

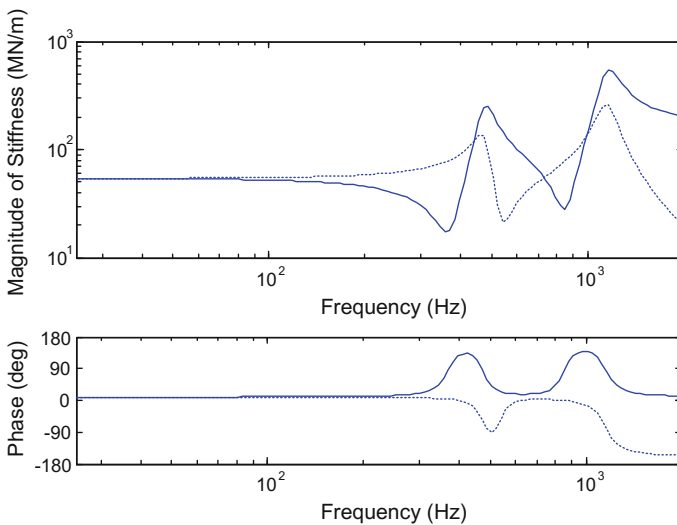


**Fig. 2** Magnitude and phase of the VIPA-SP baseplate stiffness obtained from the finite element model, for excitation but no mass at the rail, shown versus frequency: solid line, direct stiffness; dashed line, transfer stiffness

**Table 3** Results obtained for the VIPA-SP fastening system using the proposed simple test method

Frequency (Hz)	Static preload from actuator (kN)	Dynamic load amplitude (kN)	Stiffness (kN/mm)	Displacement amplitude ( $\mu\text{m}$ )	Rail velocity (dB ref. $5 \times 10^{-8}$ m/s)	Mean strain amplitude (%)
15	15	5	23	221	109	0.89
15	15	2	27	74	100	0.3
15	15	1	30	33	93	0.13
15	15	0.5	38	13	85	0.05

this not being the case, which are a mean for the two pads in the fastening system and also a mean throughout the rather complex geometry of each studded pad. For the lower pad in particular, which is not subject to the clamping load from the clips, the ‘domed’ ends of the studs may be expected to experience dynamic strains locally that are much larger than the mean strain values.

The type (iii) stiffness of 53 kN/mm for the VIPA-SP fastening system found from measurements made for the two studded rubber pads used in this fastening system separately and combined in series [6], by hand calculation or using the finite element model, is significantly higher than the result of the lowest-amplitude test shown in Table 3, 38 kN/mm. Since the stiffness results shown in Table 3 indicate significant dependence on amplitude between the two lowest dynamic load amplitude cases (1 and 0.5 kN), it may be expected that this amplitude dependence would continue to lower amplitudes than can be provided by the actuator. This, together with the much lower dynamic load amplitudes in the previous measurement work [6], may explain the difference between the lowest-amplitude result shown in Table 3 and that from the previous work.

#### 4 Stiffness Measurements for a Very Low Stiffness Baseplate

The Pandrol Vanguard baseplate has a type (ii) vertical stiffness of approximately 5 kN/mm when measured to the loads required by the European standard for Metro track fastening systems. The Vanguard system holds the rail by the web, using rubber wedges that deform in shear, rather than in compression. This allows a very low vertical stiffness to be achieved, whilst retaining good control of rail roll and track gauge. Measurements have been made that show the effect of installing this fastening system as a replacement for more conventional systems at several sites [11]. Measurements have also been made for the dynamic stiffness of the Vanguard system in previous work [12]. Results obtained using the driving point method, without correction for the moving rail mass (18.7 kg), are shown in Fig. 3.

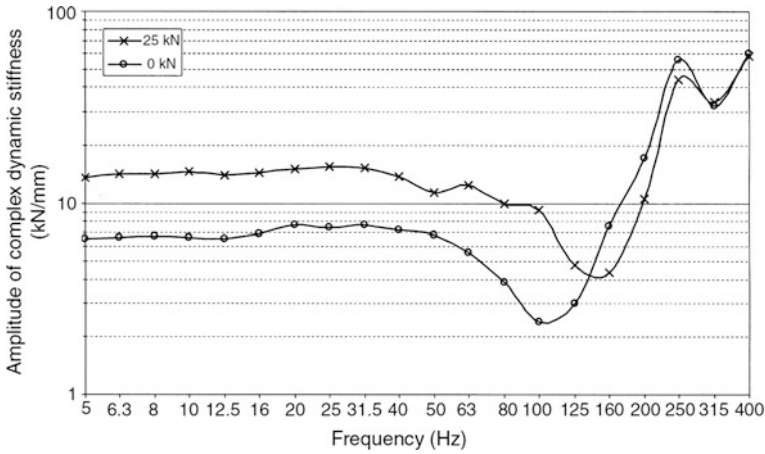


**Fig. 3** Dynamic stiffness of the Pandrol Vanguard fastening system shown against frequency for preloads of 25 and 0 kN, with a rail velocity of 95 dB ref.  $5 \times 10^{-8}$  m/s

**Table 4** Results obtained for the Vanguard fastening system using the proposed simple test method

Frequency (Hz)	Static preload from actuator (kN)	Dynamic load amplitude (kN)	Stiffness (kN/mm)	Displacement amplitude ( $\mu$ m)	Rail velocity (dB ref. $5 \times 10^{-8}$ m/s)
15	25	3.5	8.8	400	114
15	25	1	11.4	88	101
15	25	0.5	13.3	38	94
15	15	3.5	7.8	446	115
15	15	1	9.9	101	103
15	15	0.5	11	46	96

The inertia of the moving rail mass affects the results of the test for frequencies greater than approximately 50 Hz. The excitation was provided by an electromagnetic shaker in these tests, exciting the rail at a velocity of 95 dB ref.  $5 \times 10^{-8}$  m/s. For the 25 kN preload case, the stiffness of approximately 14.5 kN/mm from this previous study provides a reference value for comparison to the results obtained using the proposed simple test method with the Vanguard system, which are shown for two different preloads in Table 4.

The results given in Table 4 show that the stiffness is again amplitude dependent over all of the range tested and also over the range expected in track, up to about 80  $\mu$ m for track built with Vanguard fastening systems in the frequency range of interest for ground-borne noise. The result of 13.3 kN/mm shown in Table 3 for a preload of 25 kN and the smallest dynamic load amplitude used in these tests has been obtained under conditions that are comparable to those under which the

reference result from previous work [12] was obtained, 14.5 kN/mm. In the context of sample-to-sample variability for rubber parts, this represents satisfactory agreement. For the Vanguard system, the hydraulic actuator can provide dynamic excitation to the system that is sufficiently small to compare with measurements made using an electromagnetic shaker and it can also provide excite the system to the larger displacement amplitudes expected in track at the lower end of the frequency range of interest.

## 5 Conclusions

The proposed simple test method has been shown to give results that compare reasonably well with those obtained using more complex methods, when there is a basis for this comparison in terms of the applied preload and the amplitude of strain/displacement of the resilient element(s) of the fastening system. For the single studded rubber pad case and also for the very low stiffness baseplate case, it was possible to obtain results for small enough amplitudes for the results to be very similar to proper type (iii) stiffness measurements and also to obtain results for the larger amplitudes expected in the frequency range of interest for ground-borne noise. The stiffness of the two-stage resilient baseplate appears to be frequency dependent down to smaller amplitudes and this may be due to localised high strains in the lower of the two studded rubber pads in this system. Nonetheless, it is possible to obtain stiffness results for this fastening system for amplitudes that are expected in track at the lower part of the frequency range of interest for ground-borne noise.

The proposed simple test method allows the amplitude dependent stiffness of fastening systems to be evaluated and this method represents only a small addition to the resources required to perform the standard set of tests for fastening systems. It may therefore offer a means to address the problem of there being a lack of stiffness data for many fastening systems. Further work may be required to determine a suitable approach to determining how stiffness data that are available for different amplitudes should be used in models for ground-borne noise, since the amplitudes given by the models are themselves a function of the fastening system stiffness input by the user.

## References

1. EN 13146-9:2009+A1:2011, Railway applications—Track—Test methods for fastening systems. Part 9: Determination of stiffness
2. EN 13481-2:2012, Railway applications—Track—Performance requirements for fastening systems. Part 5: Fastening systems for concrete sleepers

3. EN 13481-5:2012, Railway applications—Track—Performance requirements for fastening systems. Part 5: Fastening systems for slab track with rail on the surface or rail embedded in a channel
4. Thompson, D.J., Van Vliet, W.J., Verheij, J.W.: developments of the indirect method for measuring the high frequency dynamic stiffness of resilient elements. *J. Sound Vib.* **213**(1), 169–188 (1998)
5. Wang, A.: Tests on Studded Rubber Rail Pads to Establish a Technique for High Frequency Stiffness Measurements of Rail Pads, Pandrol Report no. 41369-1 (1997)
6. Herron, D.: Vibration of Railway Bridges in the Audible Frequency Range, Engineering Doctorate Thesis, the University of Southampton, Chapter 5 (2009)
7. Thompson, D.J., Verheij, J.W.: The dynamic behaviour of rail fasteners at high frequencies. *Appl. Acoust.* **51**(1), 1–17 (1997)
8. Desmyter, D. Cox, S.J. Cailliau, J.: Laboratory Measurement of the Vibration Attenuation of the Fastening System. IN: 10th European Congress and Exposition on Noise Control Engineering, Maastricht (2015)
9. Freakley, P.K. Payne, A.R.: Theory and Practice of Engineering with Rubber. Applied Science Publishers Ltd, London, pp. 74–82 (1978)
10. TNO Report TPD-HAG-RPT-960066: Measurements of the high frequency dynamic properties of Swedish rail pads (June 1996)
11. Cox, S.J., Herron, D.: A Review of Measurement Data on the Performance of a Resilient Track Form as a Mitigation Measure for Ground-Borne Noise. In: Proceedings of the 11th International Workshop on Railway Noise, Uddevalla, pp. 679–688 (2013)
12. Morison, C., Wang, A., Bewes, O.: Methods for measuring the dynamic stiffness of resilient rail fastenings for low frequency vibration isolation of railways, their problems and possible solutions. *J. low Freq. noise, Vib. Active Control* **24**(2), 107–116 (2005)



# A Comprehensive Review of Force Density Levels from Sound Transit's Light Rail Transit Fleet



S. Rajaram, James T. Nelson and H. J. Saurenman

**Abstract** Sound Transit has conducted many wayside train vibration measurement campaigns since 2007 to characterize vibration emissions from the trains and track. The vibration emissions are defined by force density levels (FDL) that are usually based on empirical vibration data. Because there are many competing factors that influence the FDLs, correlation of the empirical data with controlling mechanisms is not straightforward. A more robust dataset developed from multiple test campaigns under different conditions is required to develop an overall understanding of the underlying vibration mechanisms. This paper looks at results from seven major vibration test programs between 2007 and 2015 and attempts to tease out the key features of FDLs from the existing Sound Transit LRV fleet. The existing Sound Transit LRV fleet vibration spectra show three distinct frequency regimes. The low frequency peaks in the FDL spectra are predominantly influenced by the primary resonance frequency of the motored truck and the mid frequency peaks are influenced by the center truck characteristics. The track stiffness, damping characteristics and resilient wheel determine the amplitude and shape of the high frequency peaks. Factors such as speed also influence the FDLs. For a given track and vehicle type combination, the key factors that influence FDLs are wheel-rail profile match, maintenance of the wheel-rail surfaces and frictional forces in the wheel-rail interface.

---

S. Rajaram (✉)  
Sound Transit, 401 S Jackson St., Seattle, WA 98104, USA  
e-mail: Shankar.rajaram@soundtransit.org

J. T. Nelson  
Wilson Ihrig & Associates, Emeryville, CA, USA

H. J. Saurenman  
ATS Consulting, Pasadena, CA, USA

## 1 Introduction

The vibration levels generated by light rail vehicles (LRV) are characterized by 1/3 octave band force density levels (FDL) in North America [1]. The FDL uses a well-established testing methodology that has been in use for over 30 years by practitioners in North America, originally developed by Nelson and Saurenman in the 1980s [2]. The FDL is the level in decibels of the force per root track length produced by the train and transmitted to the tunnel invert or ground surface and necessarily includes both the vehicle and track form. The FDLs are derived by measuring the wayside vibration velocity levels from the trains and subtracting the line source transfer mobility magnitude levels in decibels between line source and point receiver points. The line source transfer mobility represents the effects of train length, geometric and excess attenuation, tunnel/soil structure interaction, and soil stratification. The accuracy of the FDL is critical for designing appropriate mitigation measures for new transit alignments and to ensure that the vibration limits are not exceeded at the sensitive receivers.

The FDLs are influenced by the vehicle design, track design, condition of the wheels and rails, and the operating conditions. Studies in Europe predicted that wheel roughness, rail unevenness, and rail roughness contribute to vibration forces at high frequencies [3, 4]. A comparative study of slab and ballasted tracks showed that low frequency vibration of slab tracks will be lower due to superior track quality and high frequency vibration of ballasted track will be lower due to high damping of the ballast [4]. Empirical FDL studies in the US have shown that factors such as rail and wheel roughness, rail-wheel profile match, vehicle dynamics and track stiffness profoundly influence the vibration characteristics [5, 6]. However, it is difficult to isolate the factors that contribute to specific vibration peaks or amplitudes [7, 8].

Since procuring the first set of LRVs in 2007, Sound Transit has performed detailed FDL tests at its Link Light Rail System in Seattle on more than five occasions at different tracks under different conditions [6, 9–11]. These data are used to accurately model vibration due to future light rail extensions to the north and east sides of Seattle. The Sound Transit LRV fleet currently has 62 LRVs with 70% low floor vehicles. The FDLs used for modelling Sound Transit's initial segment were measured for similar vehicles at three ballasted track sites in 2006 at Santa Clara Valley Transit Authority (VTA) in the San Jose area. These vehicles have three sections, with the center section supported on a non-motored center bogie with independently rotating wheels. The end bogies each have two traction motors and flexible couplings between gear units and axles. The vibration characteristics of Sound Transit vehicles are similar to most modern light rail vehicles introduced to service by agencies across North America in the last two decades [5, 7]. The FDL measurement programs on the Link Light Rail System over the last nine years tested a variety of track types and train speeds, mostly under known conditions of the wheel-rail surfaces. The data presented in this paper cover the following track types: ballast and tie (B&T), direct fixation (DF) with standard

resilient fasteners (STDF), DF with high compliance (soft) direct fixation fasteners (HCDF), DF tracks in tunnels and DF tracks in a trench.

The primary goal of this paper is to take a comprehensive look at all of the detailed FDL studies performed at Sound Transit and compare the results. The various parameters that affect the FDLs are discussed in the context of the test results and the most plausible explanations for variations in the FDL spectra are reviewed. The paper also identifies areas that need better understanding so that future FDL test programs at Sound Transit and other transit systems can take advantage of this information and design the tests to improve in those areas. The areas that Sound Transit plans to correlate data in the future are information on track geometry, vehicle dynamics and wheel surface condition measurements.

## 2 Background

This section provides a background on FDLs and Sound Transit's existing fleet.

### 2.1 Force Density Level

The FDL represents the incoherent distribution of forces transmitted to the ground or tunnel invert by the combined vehicle and track. The FDL prediction procedure is based on the premise that the FDL is independent of the wayside measurement position. This empirical method is described in detail in the FTA Guidance Manual and used for the detailed prediction procedure for groundborne noise and vibration that is defined by the following relationship [1]:

$$\text{FDL} = L_v - \text{LSTM} \quad (2.1)$$

All values are in decibels assuming a consistent set of units and decibel references. All levels are based on 1/3 octave band levels. In the US, the force density level in decibels uses a reference magnitude of 1 lb/ft<sup>1/2</sup>.

FDL is a derived quantity that uses measured line source transfer mobilities<sup>1</sup> (LSTM) (also referred to as Line Source Response) and train vibration velocity levels ( $L_v$ ) at an existing train system as shown in Eq. 2.1. LSTM is obtained by combining multiple Point Source Transfer Mobilities or PSTM (also known as the Point Source Response). The PSTM is the level in decibels of the transfer mobility magnitude between a point at the center of the track and the measurement position.

---

<sup>1</sup>The term "transfer mobility" is a complex quantity consisting of a frequency dependent real and imaginary, or magnitude and phase, velocity response to excitation force. The term PSTM is used loosely here to represent the level in decibels of the magnitude of the transfer mobility function.

PSTM characterizes the efficiency of vibration transmission through the soil. To derive the FDL, the train vibration velocity levels ( $L_v$ ) are also measured at the same measurement positions.

## 2.2 Sound Transit Fleet

Sound Transit has 62 LRV 70% low floor vehicles, which are referred to by Sound Transit as ST1 LRV vehicles. Each LRV has a center idling truck and two motored trucks. The AW0 empty vehicle operational weight is 49,450 kg; and the AW2 weight of each LRV based on 74 seated passengers and 120 standing passengers is 63,000 kg. The length of each LRV is 29 m and the wheels are 660 mm in diameter.

## 3 Description of Testing Sites and Conditions

Many studies have been conducted to characterize the wayside vibration from the ST1 fleet since the Startup Phase of the Central Link alignment. Key studies and their results have been selected for discussion in this paper. This section describes the test sites and conditions for the measurements selected from the studies.

Following are the test sites and conditions:

- 2007 Site (South of Downtown (SODO) area, B&T tracks, 1-car test trains) [6]: This test was performed with two 1-car test trains on a ballast and concrete tie (B&T) track section. One of the test cars had a pronounced wheel flat and the other vehicle had only smooth wheels with no flats.
- 2009 Site (Beacon Hill Tunnel, direct fixation tracks with standard fasteners, 4-car test trains) [12]: This test was performed in the Beacon Hill tunnel area using two 4-car test trains with smooth wheels. The rail fasteners used in this section have a nominal vertical static stiffness of 25.4 MN/m at 762 mm pitch. The 2009 tests were performed before profile-grinding of the rails in 2010 and the installation of any rail lubrication system.
- 2012 Site (Beacon Hill Tunnel, direct fixation tracks with standard fasteners, 4-car test trains): This test was performed at the similar location as in 2009 after rail profile-grinding and installation of a top-of-rail lubrication system. The test was performed using two 4-car test trains with smooth wheels. Since the installation of the lubrication systems, this section of the alignment has a very good coat of lubricant on the contact band. The standard fasteners are the same as those tested in 2009 and have a vertical static stiffness of 25.4 MN/m at 762 mm pitch.
- 2013 Site (148th Street Tukwila, direct fixation tracks with standard fasteners, 3-car test trains) [9]: This test was performed in an open cut section adjacent to

Interstate Highway I-5 using 3-car test trains with smooth wheels at speeds ranging from 40 kph (25 mph) to 89 kph (55 mph). This section is approximately 3 km from the closest lubrication system and, based on Sound Transit's field observations, the contact band is typically covered with a thin film of lubricant. The static stiffness of the direct fixation fasteners is 25.4 MN/m at 762 mm pitch.

- 2013 Site (Martin Luther King (MLK) Blvd., B&T tracks, 3-car test trains) [9]: This test was on a ballast and concrete tie track section on MLK Blvd. with the same 3-car test train that was used at the Tukwila test site. Vibration testing was performed at train speeds ranging from 32 kph (20 mph) to 56 kph (35 mph). This site also was within 3 km of the nearest lubrication system and typically has a thin film of lubricant on the contact band.
- 2015 Site (U-Link Tunnel, DF tracks with High Compliance Direct Fixation (HCDF) fasteners, 4-car test trains) [11]: This test was performed in the recently completed U-Link tunnel during the testing phase of the new alignment. This section used HCDF fasteners (Egg fasteners) with a vertical static stiffness of 10.5 MN/m at 762 mm pitch. There was no lubricant on the rails.

All test vehicles used in the different years of testing had wheels with known conditions. The wheels were inspected visually in all cases for surface defects to separate smooth wheels from wheels with defects of differing degrees. All baseline FDL tests were conducted using test vehicles with smooth wheels, except for the one case in 2007 where a pronounced wheel flat condition was part of the test variables. The term "smooth" means wheels that have been in service, but without visible or audible wheel flats. All test sites were on tangent tracks, except for one measurement at Beacon Hill that was on a curve with a radius of approximately 250 m at the test location.

## 4 Force Density Data

This section presents the FDL data for ST1 LRVs collected from vibration tests conducted between 2007 and 2015 on different track types. Figure 1 shows the FDL test results for tangent tracks with (a) STDF fasteners measured in 2012, (b) STDF fasteners measured in 2013, (c) HCDF fasteners in 2015, and (d) B&T measured in 2013. In all cases three distinct regimes exist; (i) A low-frequency regime with a peak between 8 and 10 Hz, (ii) a mid-frequency regime with a peak between 16 and 25 Hz, and (iii) a high-frequency regime with peak energy between 40 and 80 Hz.

Below 12.5 Hz, the FDL data from 2012 and 2013 show similar trends for tracks with STDF fasteners. Both data sets, although collected at different test sites, contain a 10-Hz peak at speeds ranging from 40 to 64 kph. The 2015 FDL data on DF tracks with HCDF fasteners also contain a 10-Hz peak that is comparable to 2012 and 2013 data. The 2013 B&T data also contain a 10-Hz peak FDLs that are

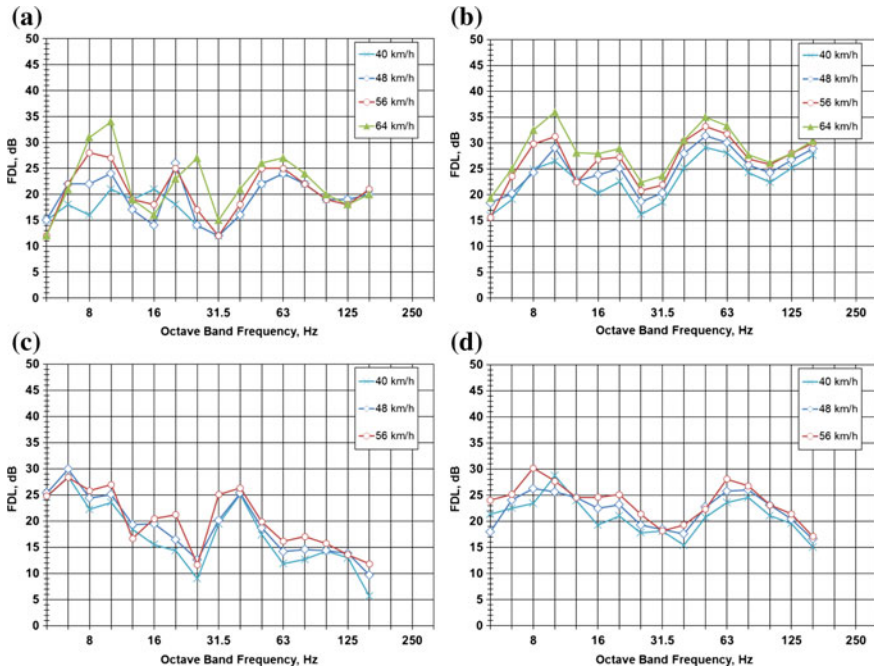


**Fig. 1** FDL on tangent tracks with **a** STDF Fasteners in 2012, **b** STDF Fasteners in 2013, **c** HCDF Fasteners in 2015 **d** B&T Tracks in 2013

in the 25–30 dB range and comparable to the DF track 10-Hz peak FDL. There is also noticeable 8 Hz energy at 56 and 64 kph in all the data presented in Fig. 1. There is an additional 6.3 Hz peak for the 2015 data, which may be related to wheel radial run-out or the measured LSTM uncertainty. Background vibration tended to obscure both train vibration and the LSTM at frequencies below 8 Hz.

There is a strong 20 Hz peak at 48 and 56 kph in the DF tracks data set collected in 2012 and 2013 as shown in Fig. 1a, b. At 64 kph, this peak shifted to 25 Hz in 2012 but remained at 20 Hz in 2013. The HCDF data from 2015 Fig. 1c shows a 20 Hz peak at 56 kph although it was 5 dB lower compared to the standard DF fastener data. At lower speeds there was no 20 Hz peak on the HCDF track. The cause of this peak has not been clearly identified.

The tracks with STDF fasteners (Beacon Hill and Tukwila) showed similarly shaped FDL curves between 40 and 80 Hz with peak vibration energy at 50 and 63 Hz. However, the data from the 2013 site was 5 to 8 dB higher than the 2012 data in this frequency range. The B&T FDL peaks at different speeds are between 63 and 80 Hz. For the HCDF track this peak moved to the lower 1/3 octave band frequency and resulted in a strong peak at 40 Hz. Also, the vibration level above 50 Hz is substantially lower for the HCDF fasteners compared to STDF fasteners, which is beneficial for groundborne noise control.

### 4.1 Vibration Peak Between 8 and 10 Hz

In theory, the low-frequency peak in the FDL could be attributed to a variety of reasons including the primary resonance frequency, wheel rotation frequency, and motor-bogie frame vibration. The vehicle’s specifications indicate that the primary suspension resonance frequency ranges from 4.56 to 5.53 Hz for loading conditions ranging from AW0 to AW4 [13]. A bogie resonance study conducted at the Transportation Test Center (TTCI) in Colorado for Sound Transit suggested that the primary suspension resonance frequency is 8.5 Hz for the unloaded bogie [14]. The vehicle tests conducted in 2012 indicate that the primary suspension resonance is closer to 10 Hz [15]. Nevertheless, the fact that the peak appears at all speeds and all track types suggests that it is a function of the motorized bogie, and the 8–10 Hz FDL peak is predominantly influenced by the primary resonance. The primary resonance is the resonance of the bogie frame and hardware resonating on the parallel combination of the primary suspension and the secondary suspension. The resonance frequency of the car body on the secondary suspension typically is between 1 to 2 Hz.

### 4.2 Vibration Peak Between 20 and 25 Hz

This section discusses the LRV vibration spectral peak in the 20–25 Hz range. Figure 2a is a comparison of FDLs at 48 kph measured on DF tracks between 2009 and 2015. Assuming that the dynamic differences between 3-car and 4-car test trains are insignificant [7], there was a strong 20 Hz peak in 2009, 2012 and 2013. The FDL data from 2015 did not have a strong peak; however, this peak is shifted to 16 Hz. It is not clear if the shift in peak was caused by the softer HCDF fasteners that could have potentially influenced the lateral oscillation of the center truck. Figure 2b shows the comparison of the FDL at 56 kph, indicating that the 20 Hz

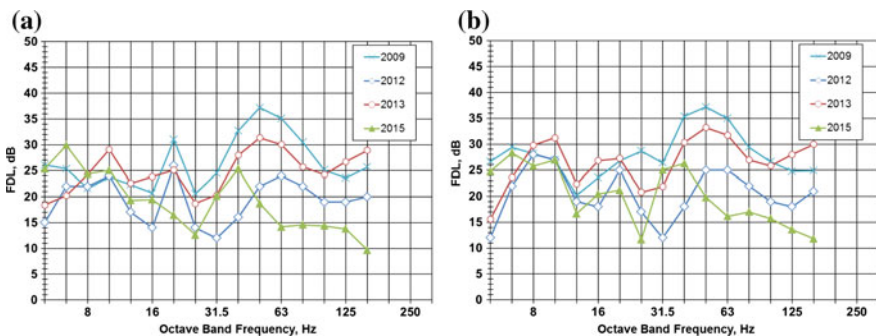


Fig. 2 Comparison of FDL on Tangent DF Track at: a 48 km/h and b 56 km/h

peak appeared in 2015. The 20 Hz peak did not shift in 2012 and 2013 at 56 kph, although the peak was less sharp. In 2009, the 20 Hz peak seems to remain but there is additional higher energy at 25 Hz.

LRV truck vibration tests were performed on two Sound Transit’s test cars, Car 132 and Car 137, in 2012 [15]. Before the tests, all twelve wheels in each car were inspected for deviation from the wheel profile template, peak-to-peak radial runout and wheel diameter. All of the wheels were consistently free of visible defects. The radial runout of the wheels on Car 132 was higher than the radial runout of the wheels on Car 137. Also the wheels on the center bogie of Car 132 were relatively new and had never been trued. The testing involved instrumenting the motor bogie and center bogie frames and bearing box and measuring the vibration acceleration in the vertical and horizontal directions.

For the current discussion, the key results from the center trucks at 48 kph train speeds are presented in Fig. 3a, b. The vertical vibration of the center truck frame showed a peak at 20 and 25 Hz for Car 132 and showed a sharper peak at 25 Hz for Car 137. The bearing box vibration showed a 20 Hz peak for Car 132. There was no 20 Hz peak for Car 137. Wayside vibration was also measured during these tests and the results at 48 kph are shown in Fig. 4. A strong 20 Hz peak was seen for Car 132 but not for Car 137. At higher train speed, the 20 Hz peak seen in Car 132 shifted to 25 Hz. This result combined with other data for the motor bogie seems to indicate that the 20 Hz peak phenomena could be related to the center truck characteristic and not the motor truck. Potential influences at 20 Hz could be higher harmonic wheel rotation frequency caused by wheel run out and wheel tread profile and lateral resonance of resilient wheel tire on its spring. In summary, this test showed that the center bogie is a dominant influence at 20 Hz under certain conditions of wheels and operating speeds but the exact mechanism has not been established. The excitation does not appear to be related to wheel and rail vertical roughness amplitude.

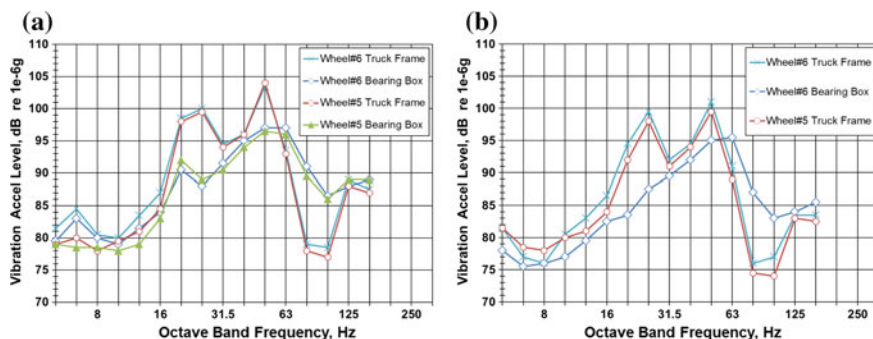
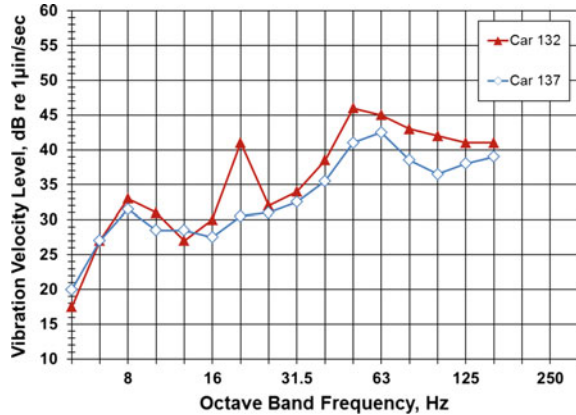


Fig. 3 Vibration of center truck components at 48 km/h: a in Car 132 and b in Car 137



**Fig. 4** Wayside vibration level at 48 km/h in 2012



### 4.3 Vibration Peak Between 40 and 80 Hz

The FDL results shown in Fig. 1 indicate that the frequency at which vibration levels peak between 40 and 80 Hz may be controlled predominantly by the stiffness of the track fastening system. In theory, the track resonance is controlled by the track, resilient wheel, axle set, and higher track stiffness should increase the track resonance frequency assuming the wheel surface condition is the same. The results shown in Fig. 1 tend to confirm this theory. The data for the B&T tracks, consisting of 115RE rail with concrete sleepers and shoulders at 762 mm spacing, with the highest stiffness, shows peak frequency between 63 and 80 Hz. The DF tracks with HCDF fasteners have the least vertical stiffness and the data show the track resonance peak at about 40 Hz. The HCDF track FDL shows a sharp peak at 40 Hz, whereas the data for the other two tracks show a more diffused peak.

Figure 5 shows the FDL collected on tangent B&T track section in 2007 with and without wheel flats. The peak frequency was 63 and 80 Hz for both wheel conditions. The main difference between the two wheel conditions was that the amplitude above 31.5 Hz was higher by 5–10 dB for the wheel flat vehicles. Also, the flat wheel vehicle resulted in FDLs that were virtually independent of train speeds above 31.5 Hz. Similar results were obtained from an extensive wheel-flat study using Sound Transit’s LRV on DF tracks in 2014 [16]. The 2014 study also noted that since the gauge-face lubricator system was installed, the flange wear reduced substantially on the ST1 vehicles. The wheel truing intervals to re-establish the flange approached 130,000 km after the installation of the lubricator system compared to 65,000 km intervals prior to the lubricator system.

Figure 6 shows the difference in vibration level between measurements taken in 2009 and 2012 at the same location in Beacon Hill. The test results show that rail roughness and the wheel-rail profile match can have a major influence on the FDL amplitudes at these frequencies. The difference is remarkable, and the test results showed a 10 dB reduction in vibration levels at higher frequencies in 2012

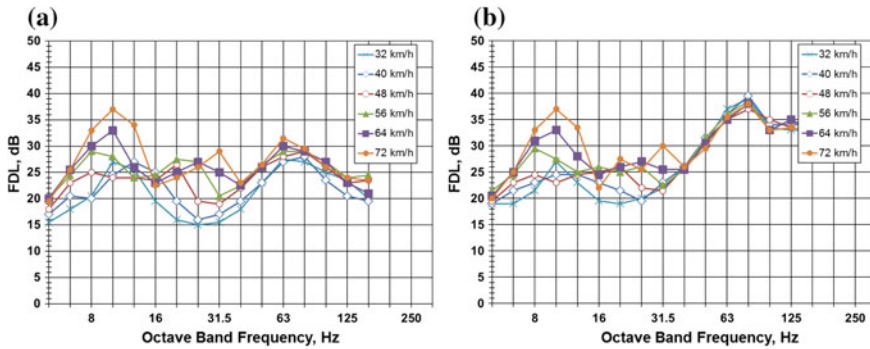
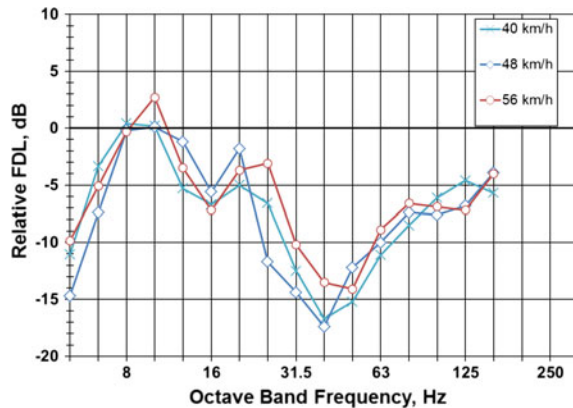


Fig. 5 FDL on tangent B&T track in 2007 with a) No Flat Wheel b) Flat Wheel

Fig. 6 Relative vibration level on same tangent DF track before and after profile grinding (2012 minus 2009)



compared to 2009. The vibration reduction was in the 31.5–100 Hz frequency range. The only known changes in the 2-year period are profile grinding of the track and installation of a rail lubrication system. A similar result was observed after profile grinding on a metro line in Sydney, Australia [17].

Based on the above discussion, it appears that the peak vibration frequency above 31.5 Hz is determined by the track stiffness and wheelset, but other factors such as wheel surface condition, wheel-rail match, and lubrication can influence the FDLs. Other related studies conducted at Sound Transit have also identified rail roughness as a potential variable that can be used to reduce vibration [8].

## 5 Conclusions

Following are key conclusions based on wayside and onboard vibration data collected on the Sound Transit Light Rail system between 2007 and 2015:

- The motor truck most likely influences the vibration levels at very low frequencies particularly at 8–10 Hz. The 10 Hz FDL peaks at all vehicle speeds ranging from 20 to 55 mph are attributable to the primary resonance, which is controlled by the LRV's bogie mass and primary and secondary suspension stiffnesses.
- The FDL peak at 20–25 Hz is perhaps the most difficult to explain. This peak may be influenced by the center truck and how it traverses the rails, both in tangent and curved sections. Modifications to the wheel-rail interface friction by top-of-rail friction modifiers or gauge-face lubricators show a propensity to reduce FDLs in the 20–25 Hz region. There is a host of secondary factors that may or may not alter the FDLs in this frequency range. The 20–25 Hz component does not appear to be directly related to rail or wheel roughness.
- At frequencies above 30 Hz, the FDLs are a function of several factors, including track stiffness, resilient wheel stiffness, axle mass, primary stiffness, track damping, wheel-rail profile match at the interface, surface defects on the wheels, wheel and rail roughness, and, to some extent, the frictional forces at the wheel-rail interface. The Sound Transit B&T tracks consistently show higher vibration levels compared to DF tracks at frequencies above 30 Hz, though rail roughness may be a factor. However, the peak frequency is consistently higher for the B&T tracks along the Sound Transit alignment compared to the DF tracks.
- The FDL peak for the DF tracks shifts to 40 Hz for the HCDF compared to the 50 Hz peaks for the STDF fasteners used in the US. The vibration levels at frequencies above this peak are approximately 5 decibels lower for the HCDF track section compared to the STDF fastener track section.
- Sound Transit's wheel maintenance program initiated after the first few years of revenue service on the Central Link alignment has helped to keep vibration levels lower and extended the life of the wheel treads between truing cycles.

## References

1. Transit Noise and Vibration Impact Assessment, report FTA-VA-90-1003-06, Federal Transit Administration, Washington, D.C. (2006)
2. Nelson, J.T., Saurenman, H.J.: A Prediction Procedure for Rail Transportation Ground-Borne Noise and Vibration, Transportation Research Record 1143, Transportation Research Board, Washington D.C., (Aug 1988)
3. Auersch, L., Rucker, W.: A user-friendly prediction tool for railway induced ground vibration: emission—transmission—immission. In: Schulte-Werning, B., et al. (eds.) Noise and Vibration Mitigation for Rail Transportation Systems. NNFm, vol. 99, pp. 129–135. Springer, Heidelberg (2008)
4. Auersch, L.: The influence of the soil on track dynamics and ground-borne vibration. In: Schulte-Werning, B., et al. (eds.) Noise and Vibration Mitigation for Rail Transportation Systems. NNFm, vol. 99, pp. 122–128. Springer, Heidelberg (2008)

5. Nelson, J.T.: Tri-Met track vibration isolation tests, Technical Report, Prepared for Portland Tri-Met (30 Oct 1998)
6. Nelson, J.T., Watry, D. L.: Sound Transit Kinkisharyo LRV Force Density Level, Technical Memorandum, Prepared for Sound Transit (12 Dec 2007)
7. Rajaram, S., Saurenman, H. J.: Variation in Measured Force Density Levels of Rail Transit Vehicles. In: Proceedings of NoiseCon 2010, Baltimore, MD (USA)
8. Rajaram, S., Saurenman, H.J.: Evaluation of force density levels of light rail vehicles. *Transp. Res. Rec.: J. Transp. Res. Board* **2302**, 21–29 (2015)
9. Rajaram, S., Wolf, S.: Vibration Measurements of Existing Sound Transit Trains, Final Report, Prepared for Sound Transit (22 May 2014)
10. Nelson, J.T., Watry, D. L.: North Link Extension Final Design task 830.2 90% Ground Borne Vibration Predictions, Technical Memorandum, Prepared for Sound Transit (14 Sep 2012)
11. Nelson, J.T., Watry, D. L.: Prototype Floating Slab Performance, Technical Memorandum, Prepared for Sound Transit (17 Oct 2015)
12. Bergen, T. et al.: Northgate Link—Civil Engineering and Architectural Final Design Services Contract No. RTA/LR 0177-09, PCR 143 2013 Beacon Hill Rail Evaluation—Ground Surface Vibration Monitoring, Technical Memorandum, Prepared for Sound Transit (16 Dec 2013)
13. Arrangement of primary suspension, ER2145, CDRL 19-21-6, Revision 1, Kinkisharyo International, L.L.C. (30 Aug 2006)
14. Ketchum, C. D. et al.: Characterization Testing of the Sound Transit Light Rail Vehicle, Report P-011-Draft, Prepared for Parsons Brinkerhoff, Inc. (Feb 2012)
15. Philips, J.E., Nelson, J.T.: North Link final design task 830.017.3 LRT truck vibration test, Technical Memorandum, Prepared for Sound Transit (17 May 2012)
16. Watry, D. L. et al.: U-Link U835 Flat-Hollow Wheel & Passing Vibration Measurements at Beacon Hill, Technical Memorandum, Prepared for Sound Transit, (31 Oct 2014)
17. Lawrence, B.: Effect of Rail Grinding on Rail Vibration & Groundborne Noise: Results from Controlled Measurements, Proceedings of ACOUSTICS 2004, Gold Coast (Australia)

# Estimating Adjustment Factors to Predict Vibration at Research Facilities Based on Measurements in a Subway Tunnel



A. L. Evans, C. G. Ono and H. J. Saurenman

**Abstract** The Sound Transit System in Seattle, Washington recently opened the University Link (U-Link) extension. U-Link extended the existing light rail transit (LRT) system to the southern tip of the University of Washington (UW) campus. The potential for the LRT system to generate vibration that interferes with vibration sensitive research at UW has been a topic of concern and debate for over 10 years. Sound Transit and UW negotiated a Master Implementation Agreement (MIA) that includes specific limits on the maximum vibration levels inside a number of University buildings that can be generated by LRT operations. The limits are in terms of 1/3 octave band vibration velocity levels (RMS) from 2 to 100 Hz. A unique feature of the MIA is that substantial financial penalties may be assessed if the MIA vibration limits are exceeded at any of the 24 buildings identified in the MIA. Part of the MIA agreement is that Sound Transit would install a vibration monitoring system in the subway that will identify all trains that generate vibration levels within 10 decibels of the limit (a warning) and will identify all trains that cause vibration levels that exceed the MIA limit (an alarm). The vibration monitoring system (VMS) consists of monitors at nine locations, three in the University of Washington Station, three in the crossover box immediately south of the UW Station, and three in the bored tunnel portion of the U-Link extension. This paper presents the approach taken to estimate the relationships between the vibration at the VMS sites and the vibration at the buildings identified by UW as vibration sensitive along with some of the unexpected results of the detailed vibration testing that was performed. The relationship between the vibration measured at a monitor and the vibration generated at a sensitive building site is referred to in this paper as a *Vibration Adjustment Estimate* (VAE). Some of the challenges to developing credible estimates of the VAEs were: (1) There were no 1/3 octave bands where train vibration at the measurement sites inside UW buildings had a clearly discernable effect on the ambient vibration; (2) For the 1/3 octave bands of 16 Hz and lower, the vibration at the VMS sites in the subway from train operations is often **lower** than the vibration from trucks and buses on nearby roadways; even though

---

A. L. Evans (✉) · C. G. Ono · H. J. Saurenman  
ATS Consulting, 215 North Marengo Avenue, Pasadena, CA 91101, USA  
e-mail: tevans@atsconsulting.com

the roadway is 60 m from the subway and the VMS sites are at the subway wall about 3 m from the tracks; (3) In some cases, the agreed upon limits are lower than the existing ambient vibration; (4) Because of the long history of discussions about the potential for LRT vibration to interfere with vibration-sensitive research at UW, it was critical that our work be deemed satisfactory and credible by Sound Transit, the Sound Transit vibration consultants, UW, and the UW vibration consultants. The findings of this study are relevant to the next extension of the Sound Transit light rail system to the north (Northgate Link) because the subway for that extension passes substantially closer to many UW research facilities. Northgate Link is currently under construction and is scheduled to be completed in 2021. The findings also are relevant for other rail transit projects that would pass close to vibration sensitive research facilities.

## 1 Introduction

### 1.1 Background

The University of Washington in Seattle, Washington is a world-class university and research center with a wide variety of vibration sensitive research facilities. Concerns about vibration from the proposed Sound Transit light rail transit system have been negotiated by UW and Sound Transit for over a decade. These negotiations resulted in the Master Implementation Agreement (MIA) [1] that was finalized in 2014. Key features of the MIA are limits on the maximum vibration levels that would be generated by LRT operations at 24 UW buildings and the potential for substantial financial penalties if the MIA vibration limits were exceeded at any of the 24 buildings.

The University Link (U-Link) extension that opened in March of 2016 extended the LRT system to the southern tip of the UW campus. The U-Link extension is two bored tunnels up to the UW Station and the crossover structure just south of the UW Station. The UW Station is the current northern terminus of the U-Link extension. The station and crossover structures are cut-and-cover construction. In accordance with the MIA, Sound Transit installed a vibration monitoring system (VMS) in the subway to identify any trains that cause vibration levels that approach or exceed the MIA limits. This paper discussed the process of estimating the relationships between the vibration levels at the VMS monitors and the vibration levels inside the spaces identified as sensitive. These relationships are referred to in this paper as *vibration adjustment estimates* (VAEs). If all values are in dB, the assumed relationship between vibration measured in the tunnel and vibration at the sensitive research facilities is:

$$L_V(\text{Facility}) \cong L_V(\text{VMS}_n) + \text{VAE} \quad (1.1)$$

$L_V(VMS_n)$  is the measured RMS vibration at monitor  $n$  (maximum of 8 s moving average),  $VAE$  is the vibration adjustment estimate from monitor  $n$  to the building, and  $L_V(Facility)$  is the estimate of the resulting vibration level at the research facility. Implicit assumptions in this approach are that: (1) train operations will generate vibration at the sensitive research facilities that can be measured and that (2) the vibration measured at the VMS locations, which are near-field locations, is directly related to the far-field vibration at the buildings. As discussed later, we found that the vibration generated by train operations was generally not discernable at the buildings of concern and that the vibration in the tunnel was not necessarily related to the vibration at the buildings.

Figure 1 shows the buildings that were selected for vibration testing: Wilcox Hall, Winkenwerder Hall, the Center for Human Development and Disability (CHDD), and the UW Medical Center Cyclotron (UWMC). The VAEs for the other 20 buildings are based on the measurements at these four buildings. Some of the other building are substantially farther from the subway than the four that were selected for testing. Significant features of the area are the double crossover just south of the station, Montlake Boulevard approximately 60 m west of the subway, the Montlake Cut water channel approximately 185 m south of the station, and the Montlake Bridge, a drawbridge that crosses the channel. Figure 1 also shows the locations of the nine VMS monitors.

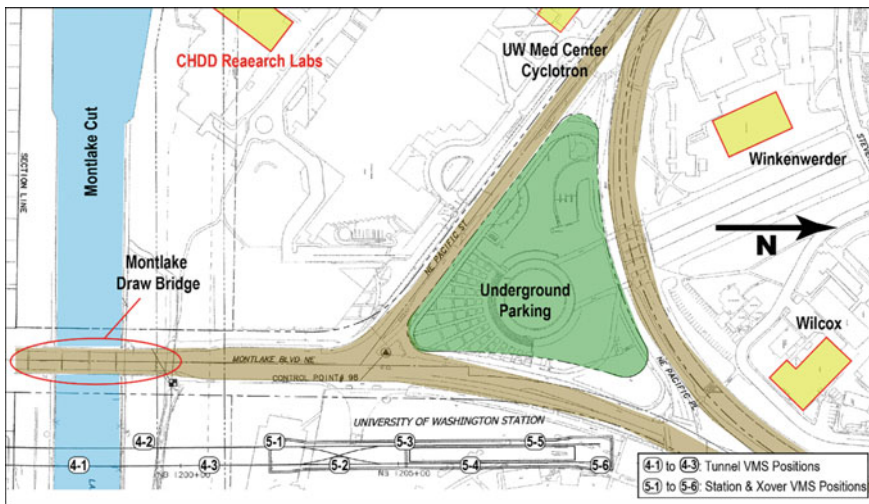


Fig. 1 Locations of four UW buildings selected for testing

## 1.2 Approach for Estimating VAEs

We recognized at the initiation of this project that direct measurements of the VAEs were not feasible because of the distance from the subway to the buildings of concern. Also, the various interceding roadways and structures and the complex interaction between the ground vibration and the resulting building vibration made it unlikely that computer modeling would provide realistic results. Thus we decided that measurements must be performed to estimate the VAEs. Our measurements were performed during the pre-revenue service testing phase of the project and included measurements of test trains and transfer mobility tests using a drop hammer as the vibration source. After careful consideration of feasible approaches for estimating the VAEs, the selected approach was to “leap frog” by combining more than one measurement to achieve the full distance between the VMS sites and the sensitive buildings. The basic steps in our approach were:

1. Use train vibration measurements supplemented with transfer mobility measurements to estimate the relationship between vibration at the VMS sites and vibration at the ground surface. Basically, the transfer mobility measurements were used to verify the relationships derived from the train vibration measurements.
2. The relationship between vibration in the subway and vibration at the ground surface was relatively weak, particularly at low frequencies. As a result, it was necessary at lower frequencies (below 25 Hz) to use the available data to make reasonable estimates of train vibration as a function of distance from the tunnel. The result was a group of curves of train vibration levels as a function of distance from the tunnel. The curves for each 1/3 octave band were estimated as straight lines that were functions of  $\log_{10}$  (distance).
3. The curves from Step 2 were used to estimate the train vibration levels at the distances that the buildings are from the VMS monitor sites, which required extrapolation of the best-fit curves for all 1/3 octave bands.
4. Outdoor-to-indoor transfer function measurements were performed at the four test buildings. The transfer functions were measured following the procedures outlined in the FTA Guidance Manual [2]. This test was performed at increasing distances from the buildings until the vibration from the drop hammer could no longer be detected inside the buildings. The vibration changes from outside to inside were estimated by calculating transfer functions between outdoor and indoor accelerometers. This adjustment was added to the results from Step 3 to estimate the train vibration levels inside the buildings.
5. Our initial VAE estimates were the difference between the vibration levels predicted in Step 4 and the measured vibration levels at the VMS positions.

Two adjustments were made to the initial VAEs. First, for any frequency band where train vibration appeared to have caused ambient vibration to increase, the entire VAE curve was adjusted up so that the predicted vibration in the specific band was equal to the estimated level. Second, for all frequencies where there was no evidence that train vibration caused any change in the ambient vibration, the



VAE at each frequency was adjusted down so that the predicted vibration level was at least 10 decibels lower than the minimum measured ambient vibration.

When these initial VAEs were plugged into the VMS computer system, we discovered that low-frequency ambient vibration often created warnings and occasionally created alarms. This led to performing supplementary measurements to investigate the sources and levels of ambient vibration and to develop final VAEs that would minimize the potential for ambient vibration to generate false warnings and alarms. Exceedances in the 6.3 Hz band were particularly frequent.

## 2 Measurement Programs

The measurements were performed in three phases. The Phase 1 measurements performed in August 2015 consisted of train vibration measurements in the subway, at the ground surface, and at the four test buildings plus transfer mobility measurements from the subway invert to the ground surface and from the ground surface into the four test buildings. One surprising result from analyzing the Phase 1 data is how important the ambient vibration was at the VMS stations. The Phase 2 measurements performed in February 2016 were designed to provide a better understanding of the sources and importance of ambient vibration. Phase 3 also was performed in February 2016. The Phase 3 measurements were designed to increase the reliability of the VAE estimates.

The recording equipment consisted of seismic accelerometers, geophones, a 16-channel analog-to-digital data collection system and four multi-channel data recorders. Synchronization of the recording systems was achieved by connecting all the recorders to the digital data acquisition system and sending a signal to the devices so they all started simultaneously. The recorders were then disconnected and carried to the different recording stations. The equipment was run continuously until the end of each measurement. There was some drift between the recording devices, but, over several hours of recording, the drift was on the order of several milliseconds, which was insufficient to affect the results.

The transfer function measurements were performed using a drop hammer that drops an 18 kg weight from a height of 1.2 m onto a load cell. The impact data were processed to obtain the transfer mobility between the impact force and the vibration velocity response at the measurement positions. Typically, 50 impacts were recorded for each test to maximize the improvement in the signal-to-noise ratio provided by signal averaging.

### 2.1 *Vibration Tests Performed in August 2015*

As discussed above, at the initiation of this project, it was clear that there were a number of hurdles that had to be overcome before credible VAEs could be

developed. A comprehensive initial test program was designed to overcome as many of the hurdles as possible within the time constraints. The time constraint was largely due to Sound Transit staff working overtime to make sure that the system would be ready to open in March 2016. The testing consisted of measurements of vibration from a four-car test train and transfer mobility measurements. The first night of testing included two lines of accelerometers perpendicular to the subway, measurements at each of the nine VMS positions in the subway, and measurements at CHDD and UWMC west of the subway. The primary reason for the accelerometer lines perpendicular to the subway was to provide data on the attenuation of train vibration with increasing distance from the subway. The process and results of these measurements are discussed in further detail in the memo delivered to Sound Transit in December 2015 [3].

The second night of testing focused on the two buildings northwest of the subway. Because of interference from the roadways and an underground parking structure, it was not feasible to install accelerometer lines between the UW Station and these two buildings. A compromise was to measure at the surface parallel to Montlake Boulevard and the northern end of the UW Station and to measure at two locations in a UW utility tunnel that were generally between the UW Station and the two buildings. After completing testing in the subway, transfer function measurements were performed from outside the four test buildings into the sensitive laboratories on the third and fourth night.

A preliminary set of VAEs were developed based on these measurements. Our analysis of the measurements raised some questions about the ambient vibration at the VMS positions and whether vibration from the test train could or could not be identified at CHDD and UWMC. To resolve these questions, two sets of supplementary measurements were performed in February 2016 approximately 4 weeks prior to the line's opening day.

## ***2.2 Supplementary Measurements February 2016 (Phases 2 and 3)***

The main purpose of the Phase 2 and 3 measurements in February 2016 was to clear up questions about the source of the ambient vibration that was causing false alarms in several 1/3 octave bands between 2 and 25 Hz and whether the small increase in ambient vibration as test trains passed two of the test buildings was real. Suspected sources of the ambient vibration causing false alarms were trucks and buses on Montlake Boulevard and, possibly, trucks and buses crossing the Montlake Bridge. The Phase 2 testing of ambient consisted of simultaneous vibration measurements at three of the VMS positions, at the ground surface above the VMS positions, on the sidewalk adjacent to the roadway, and on the foundation of the Montlake Bridge. The Phase 3 measurements consisted of measurements at locations similar to Phase 1 using a test train as the vibration source. The test train was specifically selected to have at least one vehicle with audible wheel flats. The train vibration measurements

included measurements at three of the VMS locations, on the sidewalk near the northwest corner of the Montlake Bridge, in CHDD, in UWMC, and on the sidewalk of Pacific Street outside UWMC. All the February 2016 measurements were performed using geophones instead of seismic accelerometers. The geophones were supplied by another consulting firm that was a key participant in the measurements in February 2016. The process and results of these measurements are discussed in further detail in the memo delivered to Sound Transit in June 2016 [4].

### 3 Testing Results

The recorded vibration and transfer function data were analyzed using MATLAB scripts to obtain 1/3-octave band vibration levels at 1/2-second intervals for the train vibration and the relationships between the exciting force and the acceleration response for the transfer function measurements. The transfer function analysis had a resolution of 0.5 Hz. The transfer function results were integrated in the frequency domain to obtain the relationship between the exciting force and the resulting vibration velocity, which is referred to as the *transfer mobility*. The narrow band transfer mobility and coherence data were energy averaged over the 1/3 octave band limits to obtain an approximation of the 1/3 octave band transfer mobility. When measuring vibration propagation for rail projects, we refer to the relationship between a point vibration source and the response as a *Point Source Transfer Mobility (PSTM)*. When steps are taken to estimate an equivalent relationship between a line vibration source (e.g., a train) and the response at the measurement position, we refer to the result as the *Line Source Transfer Mobility (LSTM)*. In this project we used the PSTM data directly and did not estimate LSTM. Additional information on obtaining PSTM and LSTM data is provided in the U.S. FTA noise and vibration guidance manual [2].

The decibel reference values used for the analysis were based on the non-SI system used in the United States. For this paper the quantities have been changed to more common SI equivalents. Table 1 provides the decibel reference values used in the original analysis and the conversions to the metric standards used in this paper.

**Table 1** Decibel reference quantities

Measure	Standard US	SI Equivalent	Adjust. (US to SI)
Vibration velocity (VdB)	1 $\mu$ in/sec ( $10^{-6}$ in/sec)	1 nm/sec ( $10^{-9}$ m/sec)	+28.1
Point source transfer mobility	1 ( $\mu$ in/sec)/lbf	1 (nm/sec)/N	+15.1

### 3.1 Transfer Mobility Test Results

Two types of transfer mobility tests performed, (1) Measuring the relationship between a vibration source in the subway and the resulting vibration at the ground surface, and (2) Determining how vibration amplitudes change as vibration is transmitted from the soil into a building foundation and to sensitive spaces inside each building.

#### 3.1.1 Subway to Surface Transfer Mobility Results

For the tests with the drop hammer in the subway, the surface accelerometers were located at distances up to 250 m from the subway. While we did not expect the drop hammer to provide a measurable signal at that distance, the hope was that through averaging 50 impacts, the valid data would extend to at least 100 m. Figure 2 shows the PSTM data from the two accelerometer lines extending west of the subway. The distances given in the legends for Fig. 2 are the diagonal distances assuming the subway is 33 m deep at the measurement position. Figure 2a is the PSTM amplitude and 2b is the coherence. In Fig. 2b the coherence is often less than 0.1, which indicates a very weak relationship between the source and the vibration response. When coherence is less than 0.1, the PSTM lines in Fig. 2 are shown in gray to indicate that the data are of questionable validity. The results for the other subway-to-surface transfer mobility tests were similar. Observations from the results shown in Fig. 2 are:

- The relatively low coherence (less than 0.5) for all surface measurement positions, even those directly above the tunnel, indicate that there is significant attenuation of vibration as it travels from the subway structure to the ground surface.
- The low coherence below 16 Hz indicates that the impact vibration source had insufficient low-frequency content to generate signals that exceeded the ambient vibration and that low-frequency vibration propagates poorly from the tunnel.

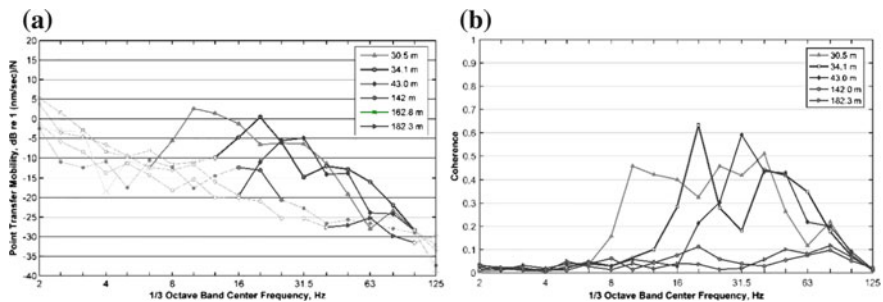


**Fig. 2** Subway-to-Surface PSTM and coherence from impact testing on night 1, phase 1 (August 2015). **a** PSTM amplitude, **b** Coherence. Distances are diagonal distances from subway track centerline

- Due to the poor quality of the PSTM data, the train vibration measurements in the subway and at the surface were used in the transfer function model for predicting train vibration in the sensitive spaces.

### 3.1.2 Outdoor-to-Indoor Transfer Function Results

To determine the transfer function from the ground into the sensitive spaces, vibration impact testing was performed at each of the four test buildings. The tests consisted of exciting the ground using the drop hammer at increasing distances from the test building and comparing the results at fixed locations outside and inside the building. The signal-to-noise ratio decreased as the distance to the drop hammer increased. However, the transfer functions between the two accelerometer positions were similar except at lower frequencies where coherence was poor. In these tests the linear average of 50 impacts was used to improve the effective signal-to-noise for the final transfer function estimate. The transfer functions in “decibel” arithmetic are defined as:

$$TF = CPD_{xy} - PSD_{xx} \tag{3.1}$$

- $CPD_{xy}$  Absolute value of Cross Power Spectral Density between responses at the outdoor sensor and the indoor sensor in decibels.
- $PSD_{xx}$  Absolute value of Power Spectral Density of responses at the outdoor sensor in decibels.

It is assumed that a consistent set of decibel reference values are used.

The final outdoor-to-indoor transfer functions are shown in Fig. 3. These results are for measurement locations at which there was sufficient signal-to-noise ratio in the sensitive space to achieve a reasonably accurate estimate. A note is that the transfer functions were calculated using test results in which the drop hammer was at least 2 m beyond the accelerometer in question. The results indicate that indoor

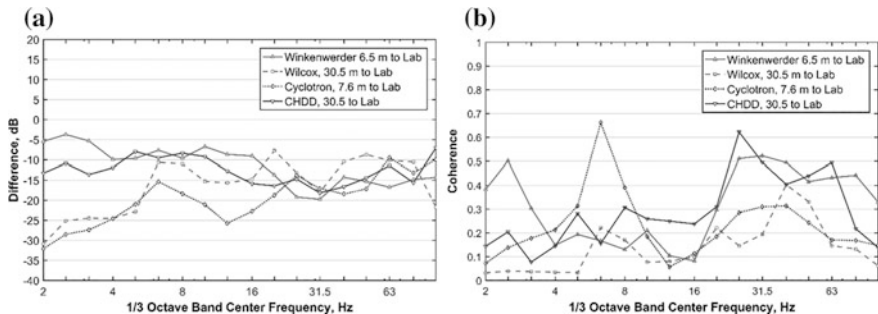


Fig. 3 Measured Outdoor-to-Indoor Transfer Functions. **a** Is the transfer function amplitude, **b** is the coherence

vibration can be expected to be at least 10–15 decibels lower than the outdoor vibration. The results should be used with some discretion because of the relatively low coherences at some frequency bands. However, because the results were reasonable and our process of generating the VAEs included reasonableness checks, these curves were used without modifications.

### 3.2 Train Vibration Test Results

Key issues with the initial VAEs generated from the Phase 1 data were false warnings caused by ambient vibration at the VMS sites and questions about whether there were any 1/3 octave bands where the train vibration could be detected in the test buildings. The Phase 2 and 3 measurements were designed to address these issues.

#### 3.2.1 Measurements in Buildings

An important question is whether there were any frequencies where the train vibration could be detected at the sensitive research facilities. There were indications from the Phase 1 measurements that train vibration in the 40 and 50 Hz bands may have been detectable at CHDD and UWMC. This observation was not supported by the Phase 3 measurements. Figure 4 illustrates the analysis used to draw this conclusion. The curves are the difference in the vibration spectrum as the test train passed CHDD and the ambient vibration immediately before and after the train passage. Each gray line is one train event and the heavy black line indicates the average of all the gray lines. This approach attempts to account for the fluctuating ambient vibration. A positive value indicates that train vibration may have caused ambient vibration to increase. When the average is zero or less than zero, we assumed that the train vibration was at least 10 decibels lower than the average ambient vibration. As seen in Fig. 4, ambient vibration caused a wide fluctuation in

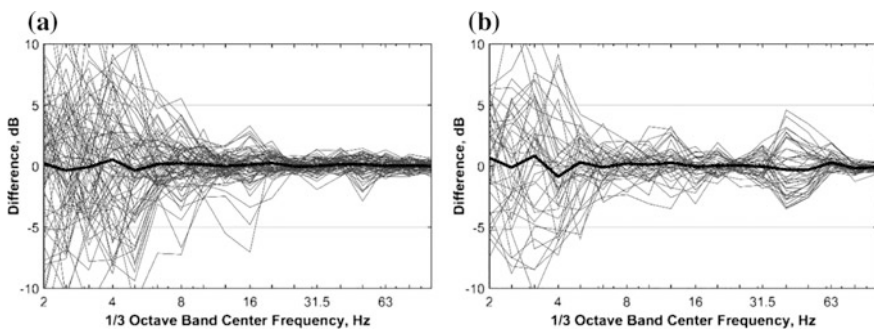


Fig. 4 Train vibration minus ambient vibration. **a** UWMC, **b** CHDD

the results at low frequencies. However, over the entire frequency range at the CHDD and UWMC measurement sites, the average is within 1 decibel of zero. This indicates that the train vibration at all frequencies was at least 10 decibels below the ambient vibration.

### 3.2.2 Comparison of Ambient Vibration and Train Vibration at VMS Sites

One of the key questions about the measurements inside the subway tunnel was why ambient vibration was triggering warnings at low frequencies. This issue was largely resolved by careful inspection of the time histories of the 1/3 octave band levels. Figure 5 is a plot of the 0.5 s rms vibration levels at VMS Monitor 4-2 and the foot of the Montlake Bridge during one of the Phase 3 train vibration tests. The vertical lines indicate when the test train passed monitor 4-2. The train event numbers are at the top of the lines. Figure 5 includes three test train movements in the southbound direction and two in the northbound direction. The average speed in the southbound direction was 64 km/h and the average speed in the northbound direction was 32 km/h. The stacked graphs show the rms vibration levels in the 6.3, 20, and 40 Hz bands. The train vibration at monitor 4-2 and at the Montlake Bridge is clear at 40 Hz, less prominent at 20 Hz, and only slightly evident at 6.3 Hz. As expected, the train vibration in the southbound direction at 64 km/h is greater than the train vibration in the northbound direction at 32 km/h. Except at 40 Hz, there are times when vibration from traffic on the bridge generated higher vibration in the subway than the test train did when traveling in either directions.

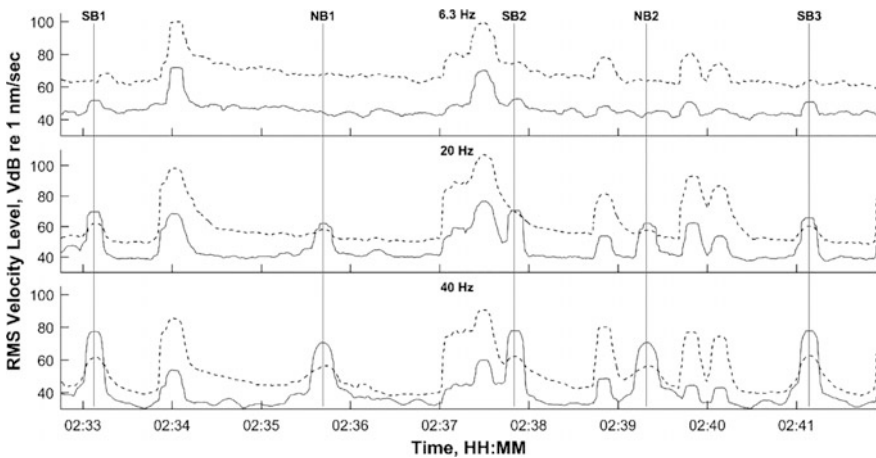
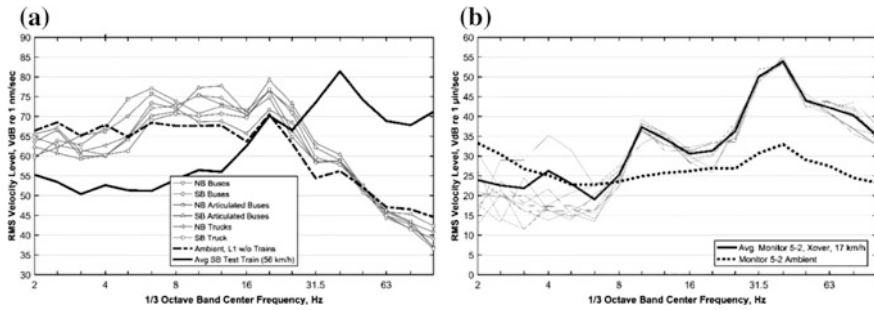


Fig. 5 Stacked RMS time histories. Solid lines are at Monitor 4-2, dashed lines are at foot of bridge



**Fig. 6** Average train Lmax at monitors 4-2 and 5-2 compared to ambient vibration. **a** Train vibration at monitor 4-2 operating in the SB direction compared to average bus and truck vibration. **b** Vibration at monitor 5-2 for diverting moves through the crossover compared to average ambient vibration. Definitions: SB = southbound, NB = northbound, L1 = vibration level exceeded 1% of measurement period

The relative levels of traffic and train vibration is further illustrated in Fig. 6 that compares train vibration and ambient vibration at Monitors 4-2 and 5-2 from two of the Phase 3. In Fig. 6a the light gray lines are the average vibration spectra at Monitor 4-2 as buses and trucks crossed the Montlake Bridge and the solid black line is the average Lmax spectrum of the test train operating in the southbound direction. Figure 6a illustrates that vibration at Monitor 4-2 from trucks and buses crossing the bridge is greater than train vibration at frequencies below 30 Hz.

Figure 6b compares the average ambient vibration at Monitor 5-2 with the Lmax spectra of diverting train moves through the crossover. From Fig. 6b it is evident that, even close to the crossover, ambient vibration from traffic and other sources frequently exceeds the train vibration at frequencies below 8 Hz. Many of the false alarms and warnings occurred at 6.3 Hz.

### 3.3 Derivation of VAEs

Several observations from analysis of the second and third sets of measurements in February 2016 suggested that derivation of the VAEs should be modified. These observations were:

- The estimated levels of train vibration at the anchor frequencies appear to be excessive.
- Low frequency ambient vibration ( $\leq 8$  to 12.5 Hz) measured at the VMS positions often exceeds the levels of train vibration.
- Ambient vibration at the VMS positions has the potential of causing false alarms.



The modified procedure for estimating the VAEs is:

- Step 1: Develop an initial VAE based on the measurements. The initial VAEs were the estimated building vibration minus vibration measured at the VMS positions.
- Step 2: Adjustment for “Anchor Points”. Anchor points are defined as train vibration levels at specific frequencies estimated from the train vibration measurements for the few times that it appeared that train vibration could be extracted from the data. This was a key step in our initial estimates of the VAEs, but was excluded in the generation of the final VAEs because the Phase 3 measurements did not support the anchor point approach.
- Step 3: Cap the predicted vibration at the buildings to 10 dB below the ambient whenever the train vibration was undetectable at the building.
- Step 4: Calculate a final VAE using the capped predicted vibration at the building and the vibration measured by the VMS monitors.
- Step 5: The VAEs at low frequencies ( $\leq 20$  Hz) were capped to avoid false alarms due to ambient vibration from traffic and unidentified vibration sources. This step was not part of the initial VAE estimating process.

$$VAE_{Final/CAP} = \min(VAE_{Final}, MIA - 10 - L_{VMax}(Ambient)) \tag{3.2}$$

In this equation,

- $VAE_{Final}$  the VAE derived in Step 4
- $L_{VMax}(Ambient)$  the maximum vibration in each 1/3 octave band at the tunnel monitors
- $MIA$  the MIA limit in each 1/3 octave band.

## 4 Conclusions and Observations

There were a number of important conclusions and observations from the testing and analysis described in this paper. These include that it is inconclusive whether train vibration can ever be reliably detected at 40 or 50 Hz in CHDD and UWMC. No train vibration was detected at those buildings in the most recent set of measurements (February 2016).

A surprising result is that traffic on the Montlake Bridge is the primary source of 6.3 Hz vibration at the VMS monitor positions in the tunnel. The vibration from traffic on the bridge shows up at the VMS monitors in the tunnel, at CHDD, and at UWMC. Also, flowing vehicle traffic on Montlake Boulevard is probably the primary source of 10–20 Hz ambient vibration in the subway.

Also surprising is that the low-frequency vibration at the VMS locations due to train operations is often lower than the ambient vibration from traffic on the

Montlake Bridge and on Montlake Boulevard. In this case, “low frequency” means 8 Hz and lower. At the lowest frequencies, train vibration was sometimes masked by ambient vibration at the VMS locations even during periods with no traffic on Montlake Boulevard. The key conclusion is that in the UW Station area, it is questionable whether low frequency vibration from LRT operations would ever be higher than vibration from trucks and buses on nearby roadways.

Another conclusion is that using only the train vibration measured at the monitors without considering traffic vibration in the creating the VAEs would provide better estimates of the VAEs, but would lead to numerous false alarms. At low frequencies, an upper limit for the VAEs is needed to ensure that background vibration from traffic or other sources, does not cause false alarms. In the UW Station area, it is questionable whether low frequency vibration from LRT operations would ever be higher than vibration from trucks and buses on nearby roadways.

## References

1. Amendment to Master Implementation Agreement for Sound Transit Entry to the University of Washington Campus (June 2014)
2. US Federal Transit Administration, Transit Noise and Vibration Impact Assessment, Report FTA-VA-90-1003-06 (May 2006)
3. Saurenman, H., Evans, T., Ono, C.: Derivation of Transfer Functions for IEM Vibration Monitoring System. Memorandum from ATS Consulting to Shankar Rajaram, Sound Transit and Ron Gamache, IEM (Dec 2015)
4. Saurenman, H., Evans, T., Ono, C.: Updated Vibration Attenuation Estimates for IEM Vibration Monitoring System. Memorandum from ATS Consulting to Shankar Rajaram, Sound Transit and Ron Gamache, IEM (15 June 2016)

# Mechanism and Reduction Countermeasure of Structure Borne Sound of Reinforced Concrete Viaducts



T. Watanabe, K. Matsuoka and S. Fuchigami

**Abstract** We have developed a new analysis method to analyze effectively the vibration response of the structural members of railway reinforced concrete viaducts. In this paper, numerical experiments to investigate the structure borne sound countermeasures were conducted for high-speed train operation over 320 km/h, considering structure vibration of reinforced concrete rigid frame viaducts. Numerical experiments with the vehicle/track system model were carried out using the program DIASTARSIII developed by Railway Technical Research Institute, which can analyze dynamic interaction between vehicle and railway structures. Furthermore, numerical analysis with the track/structure system model was carried out using the program DIARIST. As a result, we proposed various countermeasures for structure borne sound and quantified their vibration reduction. First, reinforcements of center slab and cantilever slab are effective. Second, vibration reducing track is more effective than softening of the rail pad spring constant. But, the frequency range where reduction effect can be obtained depends a great deal on natural frequency of vibration reducing track. Third, vibration reduction effects by adjusting vehicle parameters are smaller than those by adjusting structure and track parameters in consideration of the feasibility of reduction a vehicle mass.

## 1 Introduction

Structure born sound is generated by a vibration force (hereafter called an “excitation force”) acting on the track due to a train running on track with irregularity of the order of several micrometers, existing on the surfaces of the wheel treads and the rail heads. Track irregularity with a wavelength of the order of several meters in the direction of the railway track also causes the excitation force. Vibration induced by the excitation force propagates to the track consisting of sleepers and track slabs,

---

T. Watanabe (✉) · K. Matsuoka · S. Fuchigami  
Railway Technical Research Institute-1, 2-8-38, Hikari-Cho, Kokubunji-Shi,  
Tokyo 185-8540, Japan  
e-mail: watanabe.tsutomu.30@rtri.or.jp

and also to the structure (girder bridges, viaducts, truss bridges and so on) that supports the track, causing sound to be radiated from the vibrating surfaces of the various members. Structure born sound generated from concrete rigid frame viaducts or other types of concrete bridges has frequency components from several tens of Hz to 1000 Hz. In the case of a high-speed railway the dominant frequency range lies between 30 and 100 Hz.

In order to reduce the structure borne sound, it is effective to conduct the rail and wheel grinding, to reduce train weight and to use low stiffness elastic rail fastening systems and vibration-reducing track.

Although, the vibration-reducing track with a small constant of track-supporting spring is predicted to have a large deformation and there is a concern that it may generate resonance, which consequently degrades running safety and ride comfort of a train, by numerical experiments, we confirmed that it is possible to improve the running safety and ride comfort by applying jointless slab track and uniform elasticity of track-supporting spring [1].

The authors have developed a numerical analysis model to estimate vibration of reinforced concrete (RC) rigid frame viaduct up to about 200 Hz which causes the structure born sound, and have first carried out studies focusing on the parameters of the structure composed of vehicle/track/structure [2]. In this research, we focus on various parameters rather than those of the structure, and numerical experiments to investigate the structure borne sound countermeasures for high-speed train operation over 320 km/h, considering the structure vibration of reinforced concrete (RC) rigid frame viaducts.

## 2 Research Methods

### 2.1 Analysis Methods

Figure 1 shows the structure to be analyzed, and Table 1 shows material properties of each element. We conducted analyses of vibration characteristics RC rigid frame viaduct.

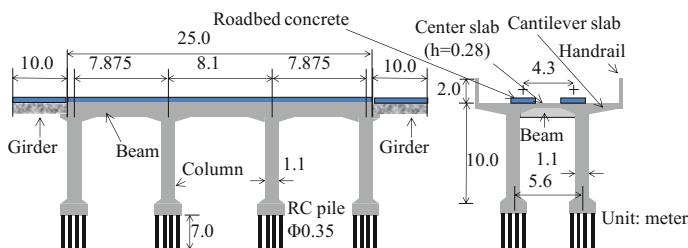


**Fig. 1** A standard 3-span RC rigid frame viaduct and adjustable girders

**Table 1** Material properties

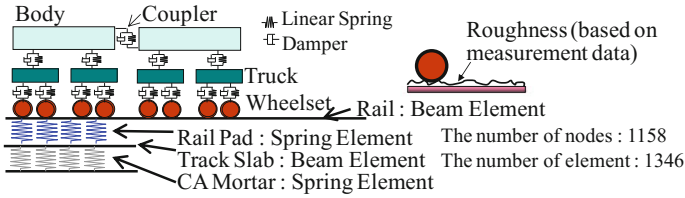
60 kg-Rail (JIS E 1101)	Young modulus $E_R$	200 kN/mm <sup>2</sup> ( $I_R = 3.09 \times 10^{-5} \text{ m}^4$ $A_R = 0.00755 \text{ m}^2$ )
Spring constant of rail pad $K_P$		60 MN/m
Track slab	Dimension	4930 mm × 2340 mm × 190 mm
	Young modulus $E_T$	31 kN/mm <sup>2</sup>
CA mortar	Young modulus $E_{CA}$	3.5 kN/mm <sup>2</sup>
	Thickness $t$	25 mm
Concrete	Young modulus $E_C$	26.5 kN/mm <sup>2</sup>
Damping constant $h$ (ALL modes)		2%

Figure 2 describes an outline of the numerical analysis model. We focused on the difference in dominant frequencies of vibration modes of the track (normally higher than 100 Hz) and structure (normally lower than several hundreds Hz). Therefore we developed a new method in which the analysis model is divided into two parts, namely vehicle/track and track/structure [2]. The vehicle/track model is used for analysis of the excitation force, and it is input into the track/structure model to analyze the vibration of the structure members. Conversion of the excitation from vehicle/track model to track/structure model is done using a constructed program which automates the pre-processing to the lines of excitation forces. The analysis model is separated into two parts along “Lines of Excitation Forces”. This enables the numbers of degrees of freedom of analysis to be greatly reduced compared to the case where the entire system is analyzed at one time.

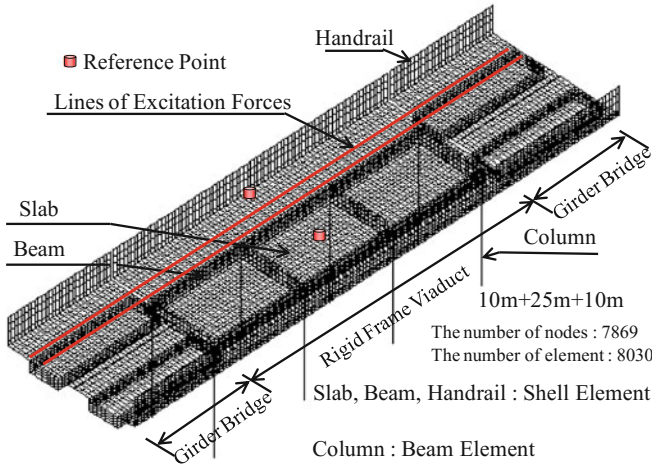
Numerical analysis using the vehicle/track system model was carried out using the program DIASTARSIII, developed by Railway Technical Research Institute [3, 4], which analyzes dynamic interaction between vehicle and railway structure. Furthermore, numerical analysis using the track/structure system model was carried out using the general purpose structure program DIARIST for the track/structure model [5].

## 2.2 Dynamic Model of Vehicle

Figure 3 shows a dynamic model of vehicle. The body, bogies and wheelset are assumed to be rigid bodies. The model shown in Fig. 3 is a 3-dimensional model in which rigid bodies are linked by springs  $K_N$  and dampers  $C_N$  ( $N$  is a suffix in Fig. 3) according to their corresponding characteristics. Each vehicle has 31 degrees of freedom (5 degrees of freedom for the body, 5 degrees of freedom for the bogies, and 4 degrees of freedom for the wheelset). A train is represented by multiple



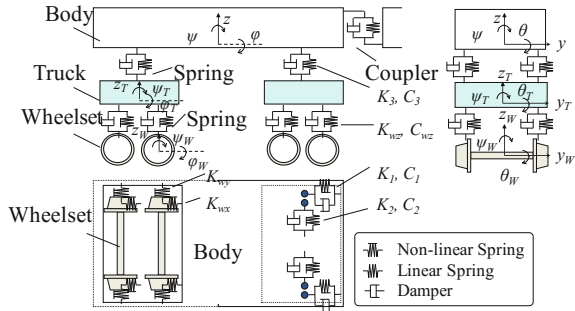
(a) Vehicle/track model



(b) Track/structure model

Fig. 2 The numerical analysis models

Fig. 3 Dynamic model of vehicle



vehicle models linked together by springs  $K_C$  and dampers  $C_C$  attached to the ends of the vehicle models. In this research, the train consists of six Shinkansen vehicles, each with length of 25 m and axle load of roughly 120 kN. Wheelbase is 2.5 m, and distance between two bogies of each vehicle is 17.5 m.

### 2.3 *Dynamic Model of Track and Structure*

The track and structure were modeled with the finite element method. In the case of the vehicle/track system model, as shown in Fig. 2a the rail and track slabs were modeled as beam elements, and the track pads, resilient material (vibration-reduction track) and the cement asphalt (CA) mortar (normal slab track) beneath the track slabs were modeled as spring elements. CA mortar is a material for filling the gap between the track slab and the structure. By using this model, the spring force equivalent to the reaction of resilient materials and the CA mortar can be obtained, and the excitation force was converted into the “Lines of Excitation Forces”, taking into consideration the rail position of the track/structure system model and the load dispersion due to the roadbed concrete, and so on. The spring constant of the track pad used in these analyses was set to three times the nominal value, while making reference to the measurement value of the track spring constant calculated from the results of measuring the displacement of rail and the axle load. In the case of the track/structure system model, shown in Fig. 2b, handrails, cantilever slabs, center slabs and beams were modeled as shell elements, and columns were modeled as beam elements. With regard to the track, only its mass was added to that of slab model, because elasticity of the track is negligible in the case of the track/structure system model. From the prior study, it was found that the effect of footing or the ground on the response of a member in the frequency region (roughly above 20 Hz) that contributes to structure born sound was small, even when the footing or the ground was modeled. For this reason, it was decided to omit them from the model, and assume that the bottom ends of the piers are fixed.

In the case of both models, the basic mesh size was set to 0.15625 m, which is 1/4 of the rail fastening interval (0.625 m). In the case of the vehicle/track system model, the total number of nodal point was 1158 and the total number of elements was 1346, while in the case of the track/structure system model, the total number of nodal points was 7869 and the total number of elements was 8030.

### 2.4 *Dynamic Model of Interaction Force Between Wheel and Rail*

Figure 4a shows a wheel/rail model. We focused on relative displacement between the wheel and the rail. The vertical interaction force of these components was modeled by Hertzian contact springs so that it can be possible to judge the contact condition between the wheel and rails. The vertical relative displacement between the rail and the wheel  $\delta_z$  is expressed by Eq. (1).

$$\delta_z = z_R - z_W + e_Z + e_{z0}(y) \quad (1)$$

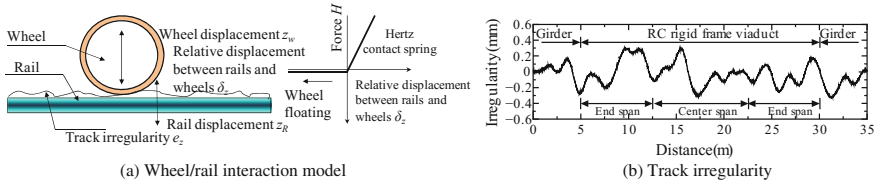


**Fig. 4** Wheel/rail interaction model for vertical direction and track irregularity

where  $z_R$  is a vertical displacement of the rail,  $z_W$  is a vertical displacement of the wheel,  $e_z$  is a vertical track irregularity.  $e_{z0}(y)$  is the amount of change of the wheel radius at the current contact point from initial wheel radius.  $y$  is the longitudinal horizontal displacement of the wheel. When  $\delta_z \geq 0$ , the wheel is in contact with the rail, and when  $\delta_z \leq 0$ , the wheel loses of contact with the rail. The z-direction interaction force  $H$  due to contact of wheel and rail is expressed by Eq. (2).

$$H = H(\delta_z) \tag{2}$$

The interaction force in the horizontal direction is expressed as a creep force unless the wheel flange touches the rail. When the wheel flange contacts with the rail, the wheel load and the interaction force in the horizontal direction act on the rail, causing the rail crown to move in the horizontal direction. As a result, torsion of the rail occurs. The torsion resistance which is generated by the rail and the rail fastener is expressed by a torsional spring element.

Figure 4b shows the track irregularity which was used for analysis. Track irregularity measured by a 1 m-chord was applied to the slab track on the structure to be analyzed. However, it is considered that the excitation force generated by a track irregularity of the order of a wavelength of several meters is not reproduced sufficiently. Consequently, track irregularity measured by a 5 m-chord was added to the track irregularity measured on the slab track of a meter-gauge railway line by a 1 m-chord, although it was not measured on the concerned structure. Thus a 5 m-chord long wavelength component was added to 1 m-chord one. The pseudo peaks due to the measurement wavelength was removed using a filter.

### 2.5 Numerical Analysis Method

In order to carry out efficient numerical analyses, the equation of motion concerning the vehicle, the track and the structure was modal-converted. The equation of motion on the modal coordinate system of the vehicle and structure was solved step-by-step in time increment  $\Delta t$  units by using the Newmark mean acceleration method. However, because the equation of motion is non-linear, iterative calculation has to be iterated within  $\Delta t$  until the residual error becomes sufficiently small. The mode order in the analysis was set to a value that enabled vibration to about



400 Hz to be reproduced, and the analysis time step was set to 0.0005 s. The frequency analysis was conducted for 2 s time history data ( $\Delta f = 0.49$  Hz).

## 2.6 Analysis Cases

Table 2 shows analysis cases. We conducted numerical experiments for RC rigid frame viaduct. CASE 1 is the basic case.

In the CASE 2, we examined parameters related to viaduct (structure). In CASE 2-1, the stiffness of the center slab was set to a value of five times the normal value to study the effect of the stiffness of the center slab. This value was obtained by the currently proposed center slab reinforcing method based on the results of an actual bending stiffness test [6]. In CASE 2-2, beam elements were added at the top of columns to reinforce the cantilevered slabs.

In the CASE 3, we examined parameters related to the track. In CASE 3-1, the spring constant was reduced to half of the basic case to study the effect of applying low stiffness spring constant springs to the rail pad. CASE 3-2, CASE 3-3 and CASE 3-4 are vibration reducing slab track. CASE 3-2 corresponds to the Type G vibration reducing track, which are used in commercial lines in Japan. Spring constant in CASE 3-3 is 10 times smaller than that in CASE 3-2. CASE 3-4 increased the damping constant to 8%, because of the estimation of the effect of damping.

In the CASE 4, we examined parameters related to vehicle. In CASE 4-1, the mass of the carbody was uniformly reduced by 30%, while the spring constant was left unchanged to study the effect of the mass of the vehicle. In CASE 4-2, the unsprung mass was also uniformly reduced by 30%, while the spring constant was left unchanged.

**Table 2** Analysis cases

CASE	Parameter	Notes (Train speed $V = 320$ km/h)
1	–	Basic case
2-1	Viaduct (Structure)	Reinforcement of center slab by Ultra High Strength Fiber Reinforced Concrete [6]
2-2	Viaduct (structure)	Reinforcement of cantilever slab by adding beam element at the top of column.
3-1	Track	Reduction of Spring constant of rail pad ( $K_p = 60$ MN/m $\Rightarrow 30$ MN/m)
3-2	Track	Vibration reducing slab track (Spring constant $K_v = 50$ MN/m) First natural frequency of vertical direction $f_v = 40$ Hz
3-3	Track	Vibration reducing slab track (Spring constant $K_v = 5$ MN/m) $f_v = 5$ Hz, Slab dimension = $20,000 \times 3200 \times 800$
4-1	Vehicle	30% reduction unsprung mass from basic case
4-2	Vehicle	30% reduction carbody mass from basic case

### 3 Analysis Results

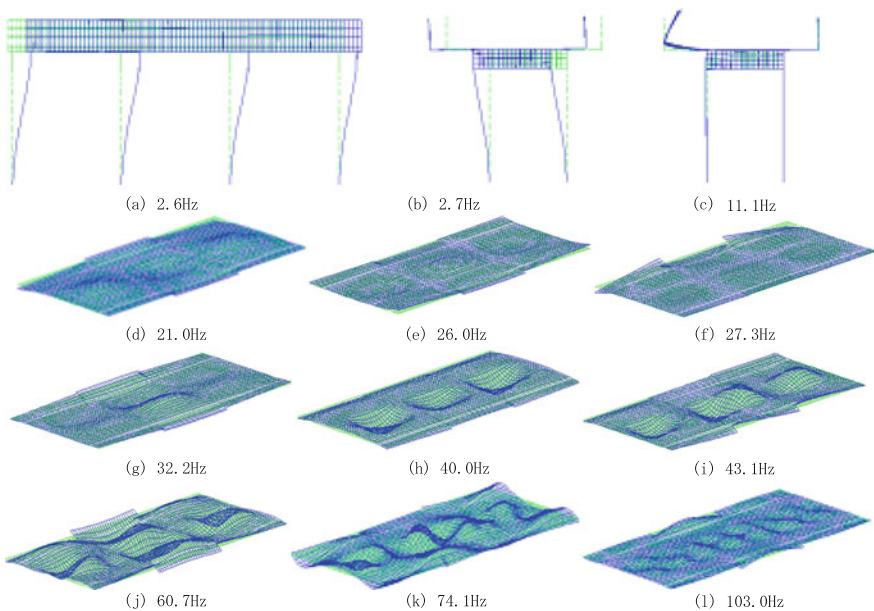
#### 3.1 Vibration Modes

Figure 5 shows the vibration modes and natural frequencies of the RC rigid frame viaduct. The natural vibration modes in the longitudinal direction and in the transverse direction of the viaduct appear at 2.6 and 2.7 Hz, respectively. However, in this model, the bottom end of the column is fixed. If the ground, footing beam and foundation structure are appropriately modeled, the natural frequency may change. The vibration mode of the cantilever slab appears at 11.1 Hz. There are many modes in which cantilever slabs are coupled to center slabs or handrails. Concerning the vibration modes of the center slab, the primary mode appears at 21.0 Hz, and as the order of the mode increases, the number of the nodes and the antinodes increases.

Reference [7] provides a detailed report concerning validation of these vibration modes by measurement. We considered that analysis results were agreement with measurement result.

#### 3.2 Characteristics of Excitation Force

Figure 6 shows the results of time history wave and frequency analysis for the spring reaction force of a specific spring element equivalent to CA mortar in a



**Fig. 5** Vibration modes of RC rigid frame viaduct (Green line: original, blue line: mode shape)

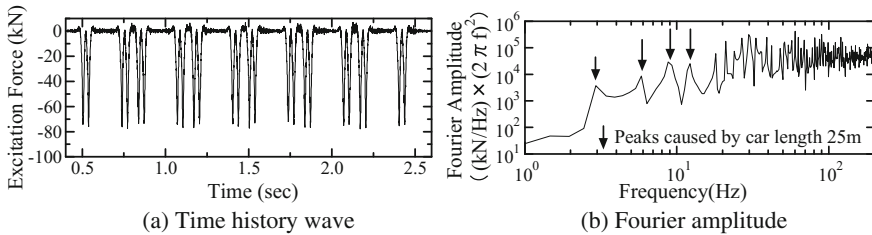


**Fig. 6** Time history wave and Fourier amplitude of excitation force ( $V = 270$  km/h)

vehicle/track system model. The train speed is 270 km/h. From the time waveform, a response peak appears when each axle passes the spring element. Some peaks can be observed at an integral multiple of the primary frequency ( $3 \text{ Hz} = (270/3.6)/25$ ) which is determined by a train speed of 270 km/h and a vehicle length of 25 m.

### 3.3 Frequency Characteristics of Each Structure Member

Figure 7 shows a comparison between measurement and analysis results with respect to the frequency analysis of the response acceleration at the center slab and the cantilever slab of the RC rigid frame viaduct. The train speed is 270 km/h, and the reference points are shown in Fig. 2b. We compared the results of measuring about 10 trains (the number of trains differs for each member) with the analysis results, in consideration of random variations from one measurement to another.

From the above figure, it can be seen that a peak appears at an integral multiple of the basic excitation frequency ( $3 \text{ Hz} = 270/25/3.6$ ) determined by the train speed and the vehicle length.

When comparing measurement and analysis results, both analysis results are roughly within the range of random variation of the measurement results.

Measurement for comparison is performed only in the case of a train speed of 270 km/h, therefore it is necessary to validate this analysis method in the case of other speeds by accumulating data in the future. However, from the above-mentioned comparison, it is confirmed that this analysis method is appropriate. The effect of the various parameters is to be discussed in the following paragraphs.

### 3.4 Effectiveness of Countermeasures of Structure Borne Sound

Figure 8 shows the Comparison between CASE1 and the other CASEs with respect to frequency analysis results of the response acceleration of the RC rigid frame viaduct at the center slab. Train speed is 320 km/h.

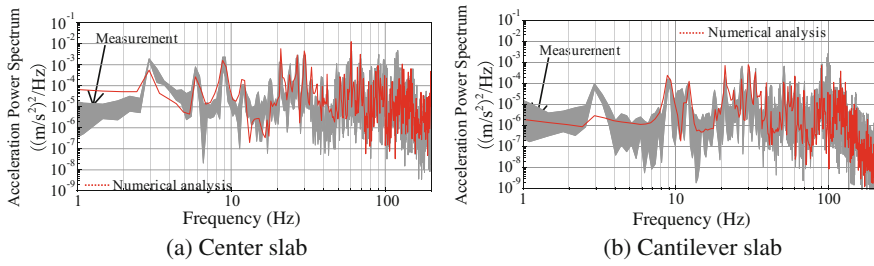


**Fig. 7** Comparison between measurement and numerical analysis with respect to frequency analysis results of the response acceleration of RC rigid frame viaduct ( $V = 270$  km/h)

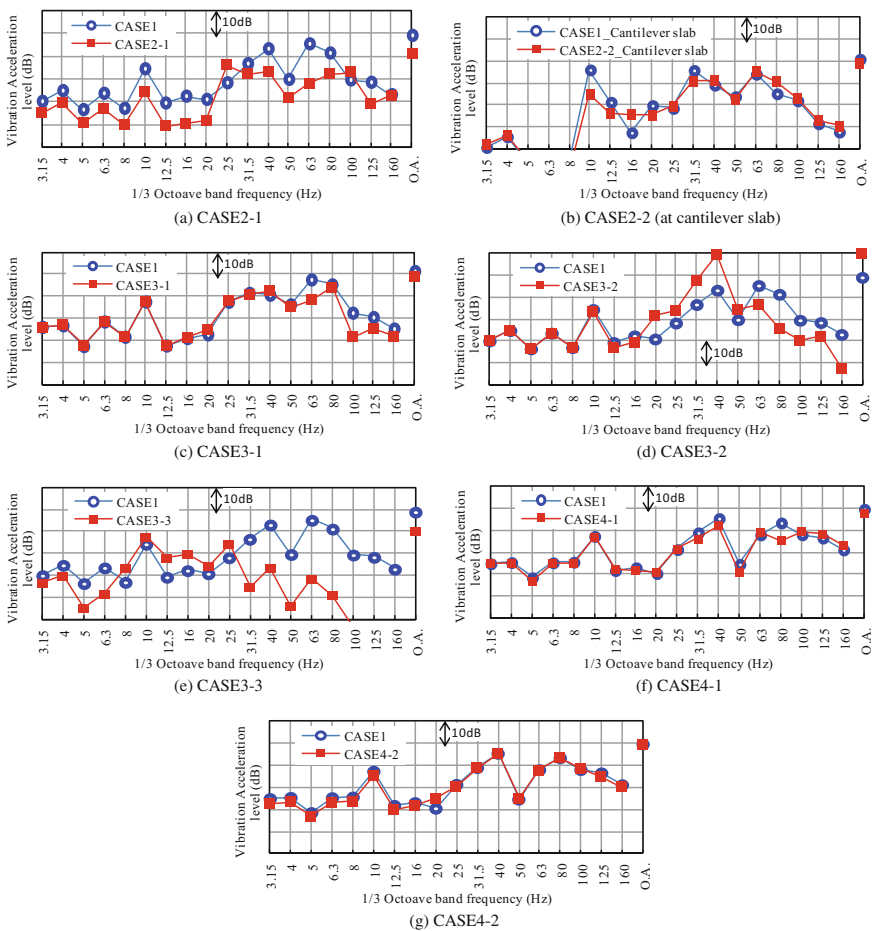


**Fig. 8** Comparison between CASE 1 (basic case) and each case with respect to frequency analysis results of the response acceleration of RC rigid frame viaduct at center slab ( $V = 320$  km/h)

In CASE 2-1 and CASE 2-2, vibration acceleration level is reduced by reinforcement of the center slab and the cantilever slab. Therefore, reinforcement of each member of the structure is effective as the countermeasure of structure borne sound. But it is separately necessary to investigate and develop the construction method by which reinforcement of these members can be achieved.

In CASE 3-1, CASE 3-2 and CASE3-3, we focus on the track parameters. Vibration reducing track (CASE3-3) is more effective than softening of the rail pad spring constant (CASE3-1). Similar to CASE 3-3, the vibration acceleration level of CASE 3-2 is increased compared with CASE 1, at the vicinity of each natural frequency. Above this frequency, vibration acceleration level is decreased compared with CASE 1. In this way, the frequency band at which reduction effect can be obtained depends on a great deal on natural frequency of the vibration-reducing track. But it is also separately necessary to investigate and develop the construction method by which the vibration reducing track with natural frequency 5 Hz can be achieved, with respect to not only new construction but also improvement of existing tracks.

In CASE 4-1 and CASE 4-2, we focus on the vehicle parameters. The vibration reduction effect by managing vehicle parameters is smaller than parameters of the structure and the track. Furthermore, in practice, it is difficult to reduce an unsprung mass and a carbody mass by 30% from basic case.

## 4 Conclusion

The knowledge obtained in this research is summarized below.

- (1) The proposed analysis method is useful to simulate the dynamic response of the RC rigid frame viaduct quickly and effectively.
- (2) Vibration acceleration can be reduced by reinforcement of the center slab and the cantilever slab. Therefore, reinforcement of members of the structure are effective as countermeasures of structure borne sound.
- (3) Vibration reducing track is more effective than softening of the rail pad spring constant, but the vibration acceleration level is increased compared with basic case at the vicinity of natural frequencies.
- (4) Frequency band in which vibration reductions can be obtained depend greatly on natural frequencies of vibration-reducing track.
- (5) Vibration reduction effect of managing vehicle parameters is smaller than managing structure and track parameters in consideration of the feasibility of reduction in vehicle mass.

In addition to the above knowledge, it is necessary to investigate and develop a construction method by which proposed parameter management can be achieved with respect to not only new construction but also improvement of existing tracks.

## References

1. Watanabe, T., Sogabe, M., Yamazaki, T.: A study of running safety and ride comfort of floating tracks for high-speed train. *J. Mech. Syst. Transp. Logistics* **1**(1), 22–30 (2008)
2. Watanabe, T., Sogabe, M., Tokunaga, M.: Analytical study on structural member vibration characteristics of reinforced concrete rigid frame viaducts. *J. Adv. Simul. Sci. Eng.* **2**(1), 16–33 (2015)
3. Wakui, H., Matsumoto, N., Tanabe, M.: A study on dynamic interaction analysis for railway vehicle and structures. *Quart. Rep. RTRI* **35**(2), 96–104 (1994)
4. Tanabe, M., Matsumoto, N., Wakui, H., Sogabe, Wakui: Simulation of a Shinkansen train on the railway structure during an earthquake. *Jpn. J. Ind. Appl. Math.* **28**(1), 223–236 (2011)
5. Sogabe, M., Matsumoto, N., Fujino, Y., Wakui, H., Kanamori, M., Miyamoto, M.: Dynamic response and design of continuous concrete railway bridges in resonance area. *J. Jpn. Soc. Civ. Eng.* **724**, 83–102 (2003)
6. Shirai, T., Kasakura, R., Watanabe, T., Nihei, T.: Development of reinforcement method of RC slab by ultra high strength fiber reinforced concrete. *Proc. Jpn. Concr. Inst.* **36**(2), 1243–1248 (2014)
7. Matsuoka, K., Kaito, K., Watanabe, T., Sogabe, M.: Identification of high-order local vibration properties of RC viaduct under the passing train loads. *J. Jpn. Soc. Civ. Eng.* **67**(3), 545–564 (2011)

# The Factors Associated with the Management of Combined Rail/Wheel Roughness to Control Groundborne Noise and Vibration from the UK's Crossrail Project



R. H. Methold, C. J. C. Jones, C. Cobbing and J. Cronje

**Abstract** Crossrail is currently Europe's largest infrastructure project. The route runs over 100 km from Reading and Heathrow in the west, through new tunnels under central London to Shenfield and Abbey Wood in the east. In addition to the re-configuration and upgrade of surface railway in existing corridors, the scheme consists of the construction of 21 km of twin bored tunnels beneath the heart of London. The Project is the first in the UK to accommodate a combined rail/wheel roughness limit for the purposes of controlling groundborne noise and vibration in overlying buildings from trains operating in the tunnels. The roughness limit is intended to be complied with during the entire operational life of the railway. This paper presents: background on the issues associated with roughness in the wavelength range of interest; the findings of the early work undertaken to identify the risks associated with the limit imposed; roughness data associated with the track designs proposed; and the methods for measuring roughness in the relevant range of wavelengths. This paper has been prepared by the Alstom TSO Costain Joint Venture, the contractor responsible for the system-wide track and fit-out of the central London section of the project, in collaboration with Crossrail Ltd.

---

R. H. Methold (✉) · C. J. C. Jones  
Southdowns Environmental Consultants Ltd., 16 Station Street,  
Lewes, E.Sussex BN7 2DB, UK  
e-mail: rhm@southdowns.eu.com

C. J. C. Jones  
e-mail: cj@southdowns.eu.com

C. Cobbing  
Crossrail Ltd., 25 Canada Square, Canary Wharf, London E14 5LQ, UK  
e-mail: colincobbing@crossrail.co.uk

J. Cronje  
Alstom TSO Costain Joint Venture, 6th Floor, 1 Westferry Circus,  
Canary Wharf, London E14 4HA, UK  
e-mail: james.cronje@ATCsystemwide.co.uk

## 1 Introduction

Crossrail is currently Europe's largest infrastructure project. The railway includes the construction of 21 km of twin bored tunnels beneath the heart of London.

A Joint Venture organisation comprising Alstom Transportation, Travaux du Sud Ouest and Costain Limited (referred to as the ATCjv) has been contracted by the Crossrail project to install the track systems in the central London section of the route which includes the twin bored tunnels. As well as providing input into the final track designs, and the eventual installation of the track systems, ATCjv is also responsible for ensuring that the final track systems installed comply with an acoustical rail roughness limit applicable across the footprint of the tunnelled section of railway; and that the railway can be maintained to meet this limit throughout its life.

The purpose of the roughness limit is to control groundborne noise and vibration within buildings overlying the tunnels.

Whilst a number of rail schemes implement rail-head maintenance measures as part of normal asset management activities, Crossrail is considered to be the first project in the UK to incorporate a published combined wheel/rail roughness limit as part of the construction and operation of the railway to control groundborne noise and vibration.

This paper has been prepared by the ATCjv team currently reviewing the compliance requirements for the roughness limit which includes track designers and UK railway noise and vibration experts from Southdowns Environmental Consultants Ltd., working in collaboration with Crossrail Ltd. (CRL).

## 2 Crossrail Combined Rail/Wheel Roughness Commitments

The Crossrail project gained the necessary powers to build the railway in 2008 through an Act of the UK Parliament (the Crossrail Act 2008). During the passage of the Crossrail Bill through Parliament a number of undertakings and assurances were given to third parties affected by the scheme.

The assurance relevant to this paper is drawn from Crossrail Information Paper D10 (IP D10) [1], and re-produced below:

2.10 The nominated undertaker will put in place measures that will ensure that at no point during the operational life of the Crossrail passenger service will the combined power spectral density of the wheel and rail roughness amplitudes be worse than 30 dB re 1 micron on the 1/3 octave centred on a wavelength of 2 m, decreasing by 15 dB per tenfold reduction in wavelength.

The commitment essentially requires that the wavelength spectrum of roughness must be complied with during the operational life of the railway and the reference to '*measures*' refers to both the means of construction as well as maintenance regimes.



The setting out of the track is relevant to achieving the best possible outcome in terms of overall roughness.

### 3 Technical Considerations

#### 3.1 Description of Roughness

For its effect in producing noise and vibration, the small scale irregularity of the wheel and rail running surfaces can be referred to as ‘*acoustic roughness*’. This forms the origin of vibration that leads both to airborne noise and groundborne noise. A component of roughness at wavelength  $\lambda$  causes vibration excitation and therefore sound radiation at a frequency  $f = v/\lambda$  where  $v$  is the train speed. Since the frequency ranges of the airborne rolling noise and groundborne noise are different, the relevant wavelength range of roughness is also different. At the wavelengths of concern, the rms amplitudes of roughness are of the order of microns and since the resulting noise is directly proportional to the roughness amplitude, it is natural to express the amplitude of the roughness, like noise, in decibel terms. i.e. as roughness level,  $L_r = 20 \log_{10}(r_{\text{rms}}/r_{\text{ref}})$ , where the dB reference value,  $r_{\text{ref}}$ , is  $1 \mu\text{m}$ , i.e.  $10^{-6}$  m. Thus when the rms roughness is  $1 \mu\text{m}$  of amplitude,  $L_r = 0$  dB.

The Crossrail commitments refer to a spectral limit of the roughness by wavelength. This follows the practice of railway noise and vibration specialists and the associated standards in using the one-third octave spectrum presentation (including BS EN 15610 [7]).

#### 3.2 Relevant Wavelengths for Groundborne Noise and Vibration

The roughness wavelengths of interest for Crossrail can be determined by considering the operational speeds of the railway and the vibration frequency range that is important for groundborne noise and vibration. Crossrail trains will operate at a maximum speed of 100 km/h in the tunnels under London, and as such it can be shown that the wavelength range of interest lies between 1.4 and 0.1 m. Most of the available guidance on acoustic roughness relates to the generation and control of airborne noise emissions. There is limited information available on roughness in the wavelengths of interest for groundborne noise and vibration.

### 3.3 Combined Roughness

The roughness commitment is for the *combined* roughness of the wheel and rail. However, the roughness of the wheel and rail is the responsibility of separate rolling stock providers and track fit out contractors. ATCjv is only responsible for the track related matters.

Figure 1 presents the summary results of roughness measurements undertaken on Class 378 wheelsets for the Crossrail project [2]. These data show that even with a 95% confidence interval of the roughness, the measured data at the longest wavelength of 0.5 m are more than 10 dB below the Crossrail IP D10 limit. This evidence suggests that wheel roughness for modern well maintained rolling stock is unlikely in practice to significantly influence the long wavelength combined roughness.

As such it is considered that in the frequency region important for groundborne noise and vibration, the *combined* roughness limit will be met if the track alone achieves the limit.

In the UK, applicable rail grinding specifications and acceptance criteria are found in BS EN 13231 Part 3 [3]. These are presented in terms of wavelength but not in one-third octave bands, and with a single value of acceptance applicable over a range of wavelengths. This leads to a stepped representation when shown graphically. To enable direct comparison of these acceptance criteria with other guideline roughness levels (including from ISO 3095 [4] which is used to identify

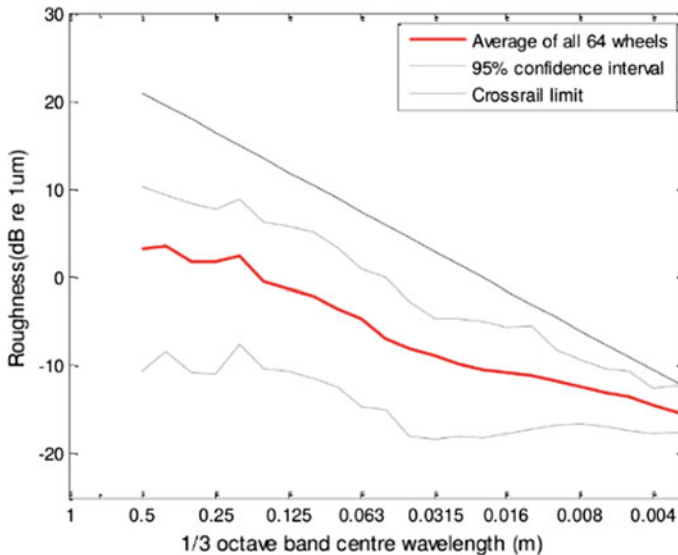


Fig. 1 Class 378 wheel roughness data measured for the Crossrail project

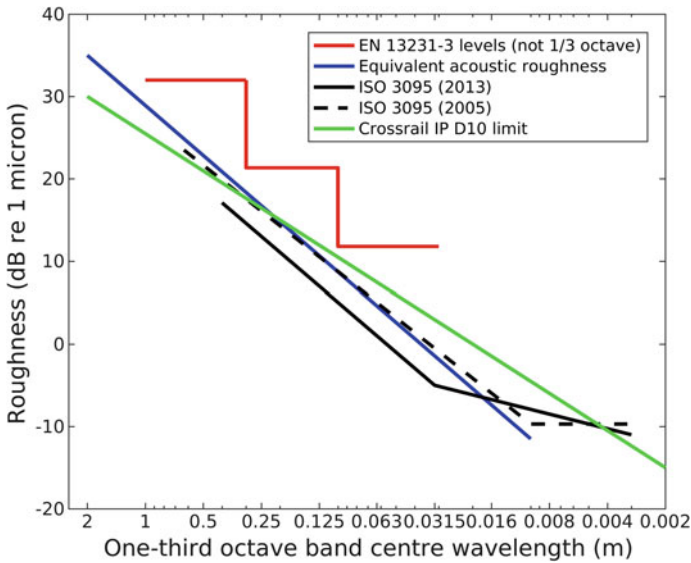


Fig. 2 Comparison of available roughness thresholds with Crossrail requirements

suitable test sites for type testing of rolling stock under the TSI requirements), it has been necessary to derive an equivalent roughness profile.

Figure 2 presents a comparison of the Crossrail IP D10 combined roughness limit, and other reference limits published in standards including ISO 3095 (old and new) [4, 5], and the equivalent roughness that can be calculated from EN 13231 Part 3 [3].

The figure shows that the Crossrail roughness requirement is more onerous than the equivalent acoustic roughness derived from the BS EN 13231 acceptance criteria in the longer wavelengths of interest. It also shows that the Crossrail requirement follows a similar slope in the longer wavelengths when compared to the roughness limit in the 2013 version of ISO 3095.

The IPD10 roughness limit up to a wavelength of 2 m was demonstrated to be reasonable in measurements made by BRR in 1996 [6]. This historic data showed that the combined roughness limit was capable of being achieved by a cast in situ booted sleeper type system within the wavelength range of interest.

## 4 Measurement of Rail Roughness

### 4.1 BS EN 15610

The measurement of roughness is addressed in BS EN 15610: 2009 [7]. The aim of the standard is to assess roughness representative of short track lengths for the

purpose of assessing air-borne rolling noise whereas Crossrail is concerned with monitoring the roughness at a longer wavelength range. This standard is currently under review, but the main expected change will be its extension to include the measurement of wheel roughness.

In BS EN 15610, the minimum record length allowed for analysis up to 0.25 m wavelength is 15 m. This is based on the principle of statistical sample size. In frequency or wavelength analysis, the precision in the estimation of the mean level depends on the product of the total record length and the bandwidth resolution. To limit the uncertainty to a similar amount at 2 m wavelength, a record length of about 120 m is therefore required. In other words, to allow a comparison of the criterion with an evaluation of the level of the 2 m one-third octave band with a certainty of the order of  $\pm 3$  dB, the data should only be compared on the basis of sections of measurement (or running mean windows) about 120 m long.

## 4.2 *Measurement Equipment*

For the current studies, the Project is reviewing the performance of measurement equipment based upon proven technology. The Corrugation Analysis Trolley (CAT) is a device based on running an accelerometer along the rail head.

In recent years the requirements of corrugation surveying and grinding quality monitoring have led to the development of a device called a Rail Corrugation Analyser (RCA) based upon the principles of the CAT but which is vehicle mounted and runs at up to 50 km/h on both rails. The RCA has been used to measure long wavelength acoustic roughness using the processing of BS EN 15610.

Given the longer term requirement to monitor and manage roughness inside the tunnels, the project is keen to accommodate high speed measurement techniques where practicable to maximise the efficiencies of its large-scale roughness management campaigns.

However, the project is also embarking upon research into the effects of various track and rail-head maintenance measures using different techniques, and this will be undertaken on relatively short sections of track under construction. The CAT was selected for this purpose and as such, the project needed to understand that (a) CAT was capable of providing reliable roughness results at wavelengths up to 2 m; and (b) the results gained using a CAT are comparable with those obtained using a RCA.

Prior to ATCjv's involvement, Crossrail's designers tested the CAT's ability to measure the longer wavelengths of roughness up to and beyond 2 m [8]. One test was to measure the roughness of the railhead whilst pushing the CAT at different speeds ranging from 0.5 to 2.0  $\text{ms}^{-1}$ , and applying different integrating time constants. The results of this exercise are reproduced in Fig. 3.

These spectra show that the longer wavelengths of roughness are only measured correctly when the CAT is pushed at the higher speed. At 2 m wavelength the measurement frequency is 1 Hz at 2 m/s trolley speed. The RCA and CAT devices

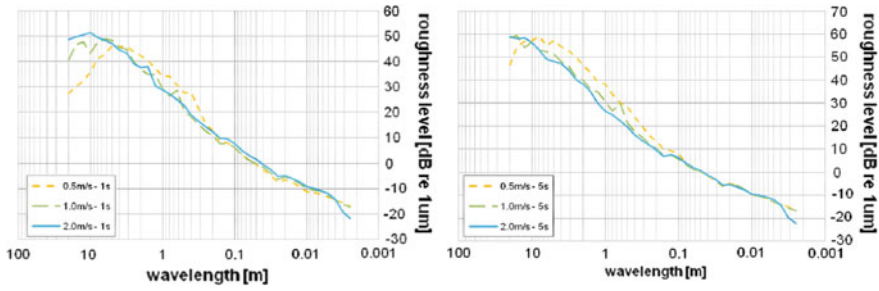


Fig. 3 CAT pushed at different speeds with integration time constant of 1 and 5 s, reproduced from [8]

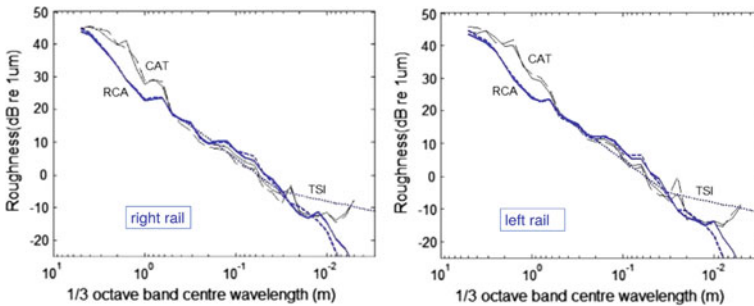


Fig. 4 Comparison of the performance of the RCA and CAT across the wavelength range, reproduced from [9]

were compared in a paper published in 2013 [9]. Figure 4 presents data from that paper which shows that the RCA and CAT measure very consistently in the wavelength range from the 0.63 m one-third octave wavelength band down to the 0.0125 m band. It is surmised that the difference at long wavelength is due to the measurement speed issue identified above, as the CAT was pushed only at walking speed ( $<2 \text{ ms}^{-1}$ ) during these tests. The discrepancy between the CAT and the RCA in Fig. 4 is very similar in character to the differences shown as a result of trolley speed in Fig. 3.

## 5 Control of Rail Roughness

Careful attention to the setting out of the rail must be given to obtain the best possible roughness spectrum, especially for long wavelengths. The overall track construction technique and the applied vertical rail level tolerances are thought to have a major bearing on long wavelength roughness. It should also be noted that

rail straightness (including droops at the rail ends) influences the longer wavelength roughness.

## 5.1 Crossrail Track Systems

The following ballastless track systems are to be installed within the running tunnels:

Standard Track Systems:

- Resilient baseplate system *Delkor Alt1* (Connaught tunnel only)
- Bi-bloc booted sleeper system *Sateba Booted Sleeper (SAT S 312 V S3)*

Enhanced Track Systems:

- Concrete track slab supported on discrete resilient rubber bearings,
- Concrete track slab supported on discrete steel helical spring bearings, and
- *High Attenuation System (HAS)*. Based with a resilient soffit pad beneath mono-bloc slab

The construction techniques proposed for the above Crossrail track systems will utilise a ‘top down’ process whereby the final vertical rail position is achieved by the use of adjustable props or jigs. The rail seats and, where appropriate, sleepers are already fixed to the underside of the rails so that there is no further possible movement in the systems when the final concreting is undertaken to surround and secure the rail support components. This is the preferred technique to control undesirable long wavelength amplitudes.

A study conducted by Crossrail’s trackform designers examined the required tolerances in the track setting out and predicted whether this source of geometrical imperfection alone could be shown to achieve the long wavelength requirements by constructing a simulated worse case roughness vertical profile. The study considered the following in deriving a worse-case scenario for potential long wavelength generation:

- Track installation tolerances in vertical alignment;
- Rail straightness specifications; and
- Construction temporary rail support spacings.

Crossrail’s trackform designers assumed that temporary rail supports or jigs would be placed every 3 sleepers (assuming 0.65 m sleeper spacing) and a maximum deflection between the 1.95 m supports of  $\pm 0.03$  mm during construction of the top down track systems in its study. The results of the study showed that when considered in isolation from any other factors the track geometry tolerances alone would achieve the IPD10 roughness limit.

### 5.2 Grinding/Profiling

After the setting out aspect has been controlled, roughness can be controlled further by rail surface treatment or grinding. This raises the question of the most effective method of grinding to reduce roughness across the wavelength range. In a paper published in 2012, Grassie [10] collected together roughness spectra measured before and after grinding and included the wavelength range up to 2 m. As well as providing more evidence of roughness spectra in the wavelength range this paper also shows evidence of the improvement of roughness that can be expected from grinding/re-profiling operations.

Figure 5 reproduces a figure from [10], showing the change in roughness achieved by grinding. This shows that wavelengths shorter than about 30 mm (and in some cases up to the 63 mm band) are made worse by grinding. They eventually wear smooth again under traffic. These data must be interpreted in conjunction with other figures in that paper, in that a lack of improvement in roughness is not of great importance if the before-grinding spectrum already shows a very smooth rail.

Figure 5 shows a lack of evidence of the efficacy of grinding for the longer wavelengths of 2 m down to about 0.25 m. Other data in that paper did, however, at least show one test in which a reduction was obtained in up to the 2 m wavelength. What these data did not show however, was the effectiveness of the first grind of the newly laid track and whether this introduces any improvement in long wavelength

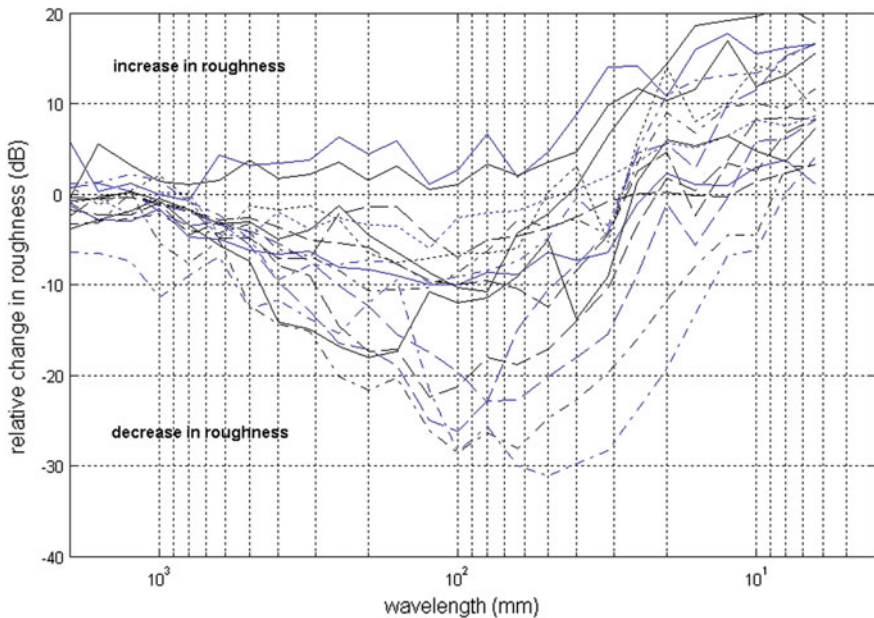


Fig. 5 Change in roughness before to after grinding, reproduced from [10]

roughness, nor whether the particular grinding technique used would have been expected to have altered long wavelength roughness in any case. ATCjv is investigating the benefits introduced by the first grind and to consider further the different types of available rail-head maintenance measures which are summarised below.

### ***5.3 Standard UK Reprofilng***

Notwithstanding the lack of available information on the benefits of an initial grind on newly laid rail, experience of roughness measurement immediately after standard UK railhead profile grinding processes shows the rail head can be left ‘jagged’ after the reprofiling process. Normally, wear by service traffic operating on the line following the reprofiling process, smooths the rail head so that it is close to the ISO 3095: 2013 limit curve and hence the IPD10 limit in the shorter wavelengths.

Experience suggests that about 3 months of normal density operational traffic should be sufficient to provide a smooth railhead.

### ***5.4 High Speed Passive Grinding***

A surface condition similar to that of wear from normal density traffic can be achieved by the use of passive grinding. This is called ‘high speed grinding’ or ‘offset grinding’ (because of the offset angle at which the grinding stones are set). This type of grinding can be carried out using a trailer rack of passive grinding stones. The passive grinding process takes only a small amount of metal off the rail. It leaves the rail smoother than the reprofiler but does not become optimally smooth at short wavelengths until it is subjected to some operational traffic. Even so, experience in the UK where this process has been used in the past has shown that good measurements of roughness can be made straight after rail treatment as the surface is left in a much smoother condition than standard re-profiling.

It is not known whether passive grinding alone (without prior reprofiling grinding), would deliver a compliant rail-head condition at long wavelengths. It is hypothesised that any benefits of standard or high speed grinding is likely to be limited by the length of wheel base of the grinding vehicle.

Research by Grassie [10] shows one test on the effects of the two types of grinding and presents data up to 2 m wavelengths. The data suggests some improvement due to either type of grinding at the longer wavelengths, but no distinguishing improvement as a result of the different techniques applied between 2 m and about 0.25 m.



## 5.5 *Acoustic Grinding (Shuffle Grinding)*

‘Shuffle grinding’ (or special ‘acoustic grinding’) polishes the rail head with longitudinal motion to deliver a smooth rail that is known to be immediately compliant with the ISO 3095: 2013 limit spectrum. This method has been used in the UK previously to prepare tracks for rolling stock passby noise measurement test sites, and is the most likely technique to produce a successful measurement of low roughness over a wide wavelength range.

## 6 Next Steps

Installation of tracks in the Crossrail tunnels is now underway. The rail surface when delivered to site and installed cannot be used for roughness surveys, not least because a useable running band is not evident, and the rail surface is contaminated with factory introduced mill scale and rust. As a consequence the rail surface does not allow the probe of a roughness measuring device to ride smoothly and so reliable measurements cannot be made.

Once the rails are fitted and commissioned, engineering trains will be able to operate on the tracks. However, there are only a few movements per day and the construction rail traffic operate at very low speeds (up to 20 km/h) compared to the eventual service operations. This will not provide a rail surface condition that is comparable to a track worn by normal density operational services.

Therefore, long wavelength roughness surveys have been scheduled to take place after a section of the completed track has been subject to an initial railhead grind or milling process. This is in order to investigate the effectiveness of rail treatment techniques (through grinding or re-profiling) to reduce roughness at the longer wavelengths which is important for controlling groundborne noise and vibration generation.

The project will then use this information to review the maintenance strategy and ensure that in combination with a high speed roughness measuring system, any of the grinding treatments identified as being effective and necessary can be programmed into the asset management plans for the railway.

**Acknowledgements** The authors would like to acknowledge the earlier work undertaken by Crossrail and their designer’s ARUP/Atkins JV on the subject matter discussed in this paper, and Crossrail for their permission to publish the data in this paper. In addition we would like to thank Stuart Grassie of Railmeasurement Ltd. for his kind permission to reproduce and annotate figures from his previous research publications.

This paper was originally presented at the 23rd International Conference on Sound and Vibration (ICSV) in July 2016 and is published in the corresponding proceedings.

## References

1. Crossrail Limited: Crossrail Information Paper D10—Groundborne Noise and Vibration, (2008)
2. Toward, M.: ISVR (for Mott MacDonald—Rolling Stock Division). Consultancy Report Ref: 8831-R02 Measurements of wheel roughness on Class 378 trains, (2012)
3. British Standards Institution: BS EN 13231-3 Railway applications—Track—Acceptance of works—Acceptance of reprofiling rails in track, (2012)
4. British Standards Institution: BS EN ISO 3095 Acoustics—Railway Applications—Measurement of noise emitted by railbound vehicles, (2013)
5. British Standards Institution: BS EN ISO 3095 Acoustics—Railway Applications—Measurement of noise emitted by railbound vehicles, (2005)
6. Jones, C.J.C., Block, J.R.: British Rail Research Report No. RR\SS\96\007 Measurements of rail roughness on booted sleeper track, (1996)
7. British Standards Institution: BS EN 15610 Railway Applications—Noise Emission—Rail Roughness Measurement Related to Rolling Noise Generation, (2009)
8. Jakielaszek, L. for Crossrail Limited: Report Ref: C122-OVE-R-RGN-CRG01-50001. Design package C122—Bored Tunnels. Measurement of acoustic roughness at long wavelengths, (2012)
9. Grassie, S.L.: Measurement of long wavelength irregularities on rails. 11th International Workshop on Railway Noise. Uddevalla, Sweden (2013)
10. Grassie, S.L.: Rail irregularities, corrugation and acoustic roughness: characteristics, significance and effects of reprofiling. Proc. IMechE Part F: J. Rail Rapid Transit **226**(5), 542–557 (2012)

# Verification of the Effectiveness of a Floating Track Slab System After 20 Years of Service



Hanno Töll, Günther Achs, Christoph Kuttelwascher,  
Michael Mach and Mirko Dold

**Abstract** In 2015, verification tests on the effectiveness of a floating track slab system after 20 years of service were carried out in the Römerbertunnel, Austria. The verification-test campaign included a visual inspection of the discrete bearings, of the shear key stabilization for longitudinal displacement, and of the lateral bearings. Furthermore, a test set up according to DIN SPEC 45673-3 in order to verify the natural frequency and the insertion loss of the floating track slab system was carried out. The visual inspection of the system indicated very good condition. The bearings were in correct position and no abnormal distortions or deformation of the bearings were identified. The insertion loss of the floating track slab system measured in situ was referred to a ballasted track located next to the 192 m long floating track slab system section, demonstrating that the effectiveness of the system is even better than the predicted insertion loss during the design phase of the system track. According to the verification tests, the in situ measured natural frequency of the floating track slab system shows good compliance with the theoretical tuning frequency of the system. Based on the measured and inspected results, the effectiveness of the floating track slab system can be verified. The vibration mitigation behavior is still as good as predicted during the design of the system and thus complies with all requirements of Austrian Federal Railways.

---

H. Töll (✉) · G. Achs  
FCP Fritsch, Chiari & Partner ZT GmbH, Marxergasse 1 B, 1030 Vienna, Austria  
e-mail: toell@fcp.at

C. Kuttelwascher · M. Mach  
Austrian Federal Railways (ÖBB), Vienna, Austria

M. Dold  
Getzner Werkstoffe GmbH, Bürs, Austria

## 1 Introduction

In 1996 a heavy mass-spring-system was designed and installed in the Römerbergtunnel at the main East-West track route next to the city of Schwanenstadt in Upper Austria to mitigate vibrations and ground borne noise in the adjacent residential buildings. The Austrian Federal Railways (ÖBB), the infrastructure owner, is permanently inspecting the existing mitigation measures to ensure the effectiveness and functionality of these special track systems. Therefore, an in situ verification campaign was initiated to confirm the correct condition of the track system with vibration measurements and visual inspections [1]. This paper aims at presenting the in situ test set measurements and the results as well as the procedure and outcomes of the visual inspection.

## 2 Verification of the Effectiveness of a Floating Track Slab System

### 2.1 Historic Review

In order to maximize the protection to the adjacent residences from noise and vibration impact, the Austrian Federal Railways have started searching for effective track mitigation measures at a very early stage. The scope was to reduce the generation of vibrations and its propagation at the source. Having this scope, the ÖBB are adopting floating track slab systems (MSS) in order to mitigate vibrations and ground-borne noise impacts since 30 years.

The discrete bearings installed in the Römerbergtunnel at the main East-West track route next to the city of Schwanenstadt in Upper Austria (1996) represent one of the first MSS where Sylodyn [2], a special type of closed-cell elastomer has been installed, a material back then newly developed.

The section with discrete bearings has a length of 192 m, and, additionally, transition zones with full surface bearings have been installed on both ends. The prevailing track system in the tunnel is a ballastless track with track slabs, merging to ballasted standard track (depth of ballast 55 cm) at both ends of the tunnel.

To confirm the effectiveness of this floating track slab system after 20 years of service, ÖBB assigned frequency measurements and visual inspections to FCP.

### 2.2 Design of the Floating Track Slab System

The investigated mass-spring-system in the Römerbergtunnel was planned back in the year 1996 and designed to meet the vibration impact criteria. The investigated floating track slab system consists of a ballastless track system designed as a

continuous reinforced concrete beam supported on discrete elastomeric point bearings (floating slab track).

During the overall design process a consultant [3] implemented investigations while an engineering office [4] dimensioned the elastic bearings. The outcome of the study by the consultant in 1996 [3] determined a required natural frequency of the floating track slab system of 13 Hz for the concerned track section, considering a mass of 6 t per meter and a dynamic bedding modulus of  $1.4 \times 10^7 \text{ N/m}^2$ . In addition, the consultant’s study determined the following requirements in regard to the insertion loss:

- Natural frequency (dynamic): 13 Hz
- Max. amplification at natural frequency: 9 dB
- Lower frequency of effectiveness of MSS: 18 Hz
- Upper frequency of effectiveness of MSS: 71 Hz
- Max. effectiveness: 35 dB
- Effectiveness at 31.5 Hz: 15 dB
- Effectiveness at 40 Hz: 21 dB
- Effectiveness at 50 Hz: 27 dB.

Within the scope of design and final stage phases, the engineering office designed the bearing positions in more detail. Within this study, the natural frequency of the investigated MSS was fixed at 13 Hz. Figure 1 illustrates the cross-section of the MSS in the tunnel area. The dynamic stiffness of the discrete bearings was determined on the basis of material tests by EMPA (Swiss Federal Laboratories for Material Science and Technology) [5].

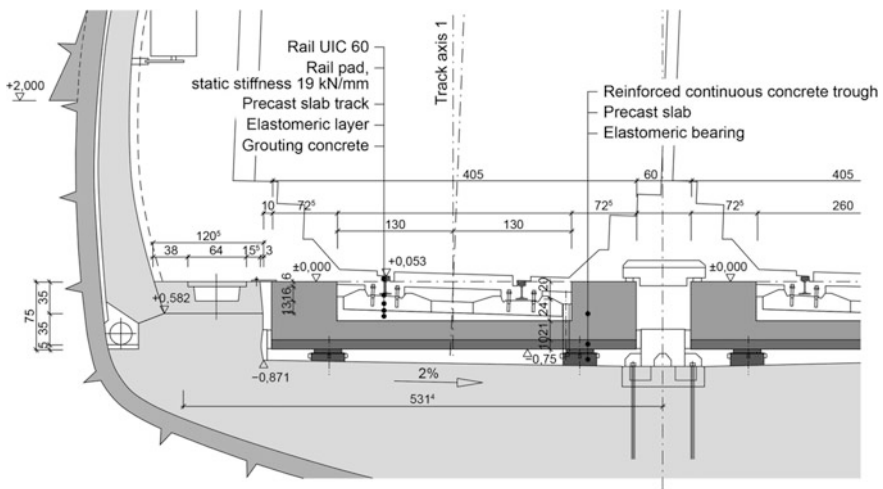


**Fig. 1.** Extract from design documents: cross section of floating track slab system Römerbergtunnel

### 2.3 Visual Inspections of the Bearings

In the course of the measurement campaign, an additional visual inspection of a 60 meters long section of the floating track slab system was carried out. The condition of the discrete bearings (closed-cell elastomer) was very good. The bearings were in the correct position and no abnormal distortions or deformation of the bearings could be identified (Fig. 2).

### 2.4 Inspections of the Track System During Non-operating Rail Traffic

#### 2.4.1 Determination of the Natural Frequency by Measurements

The floating track slab system was examined by using different stimulation methods in order to determine the translational natural frequency. First, at each measurement location, accelerometers were fixed to the floating track slab system. Next, the MSS was impacted in order to make it oscillate. The oscillation was recorded by the accelerometer until the MSS stopped vibrating. By applying a Fast-Fourier-Transformation, the recorded time history signal was transformed into the frequency domain and the natural frequency was determined.

The MSS was stimulated with three different methods, namely a sand bag, a falling weight and a single jump. As these excitation sources do not correspond to a



**Fig. 2.** Visual inspection of discrete bearings

perfect impact able to excite all frequencies of the MSS with the exact same force, the measured natural frequency was around an average of 11 Hz, depending on the stimulation method. The associated modal damping was determined by means of the logarithmic decrement and was around an average of 8.9%, independently from the method used.

#### **2.4.2 Comparison of Measured to Calculated Frequency**

The measured natural frequency is compared to the frequency determined during the design phase back in 1996. The originally requested natural frequency is determined based on a substitute model and is around to  $f_0 = 11.5$  Hz. The measured natural frequency was determined with unloaded track system, so that the measured frequency needs to be adjusted considering the missing dynamic loads (undamped mass of the train) using the following adjustments:

- Measured natural frequency:  $f_0 = 11$  Hz
- Undamped wheelset mass: 750 kg (assumption)
- Length of influence = 10 m, corresponding to the bending line of the system in loaded condition
- Static dead load (track system), without train: approx. 6 t/running meter
- Adjustment of the measured natural frequency =  $11 \text{ Hz}/1.0125 = 10.9$  Hz.

The comparison of measured and calculated natural frequency has a very good correlation.

## ***2.5 Measurements Under Rail Traffic in Service***

### **2.5.1 Basics of the Measurements**

Under regular train operation, a measurement was carried out in order to determine the insertion loss of the floating track slab system compared to a reference test section with ballasted standard track inside the tunnel (reference section). The determination of the insertion loss was made according to the method included in DIN SPEC 45673-3 [6]. The insertion loss of mitigating track systems can be determined based on the comparison of different track systems before and after a change or based on the comparison of so called ‘left and right’ systems.

The comparison before and after is applied to situations, where measurements are carried out before track upgrading and after the installation of vibration mitigating systems. The measurements are carried out at the same test section and same sensor positions.

If test sections with different mitigating systems but same track forms are available on a certain section as it is the case for the Römerbergtunnel, the ‘left and right’ method can be applied.

In order to determine the insertion loss, the vibration caused by different trains running under regular operation was recorded and analyzed at both test sections. The sensor set-up is presented in Fig. 3.

As specified in Fig. 4, the reference test section at chainage km 235,622 was equipped with three accelerometers (denoted as Wil\_1, Wil\_2, Wil\_3) at position 1 and two velocity sensors (denoted as W9 and W10) at position 2. The sensors were placed at respective distances of 10 meters along the track axis.

In the same way, the measurement section with floating track slab system was equipped with three accelerometers (Wil\_4, Wil\_5, Wil\_6) mounted on the tunnel wall and with two velocity sensors (W8 and W11) installed at position 2. The sensors were placed at respective distances of 10 m along the track axis.

The analysis of the vibration velocity level is done in the one-third octave bands on the basis of integration of the time history signals (reference amplitudes of the vibration velocity level  $v_{\text{ref}} = 5 \times 10^{-8}$  m/s).

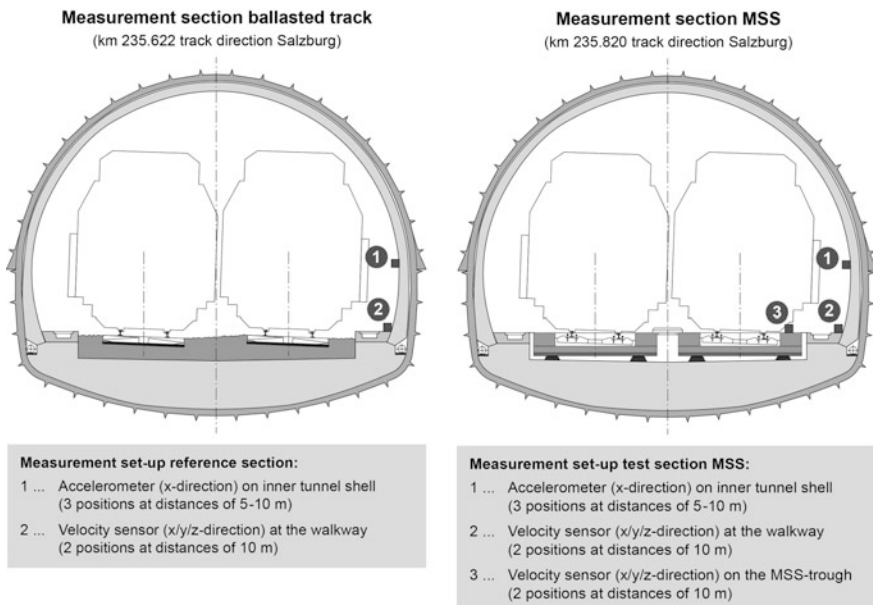


**Fig. 3.** Measurement set-up of reference section and test section of track system for the determination of the insertion loss



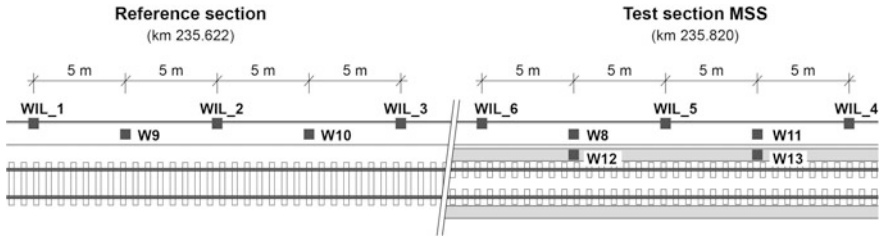


Fig. 4. Measurement positions (Reference section ch. 235.622 and test section with floating track slab system ch. 235.820)

### 2.5.2 Implementation of the Measurement Campaign

The measurement at the Römerbergtunnel was carried out on 14th July 2015. The test sections were equipped in the night from 13th to 14th July when trains were not operating. In the investigated section, the floating track slab system is characterized by discrete point bearings installed over a total length of 192 m. (Sylodyn NF, thickness 45 mm, dimensions 430 mm × 375 mm, Fig. 5).

Out of all recorded train passings, three clusters of uniform train types were listed and one-third octave band spectra within each cluster were analyzed:

- passenger train/long distance train type RailJet: 14 passings,
- passenger train/long distance train type Intercity: 14 passings,
- passenger train/commuter train type Westbahn: ten passings.

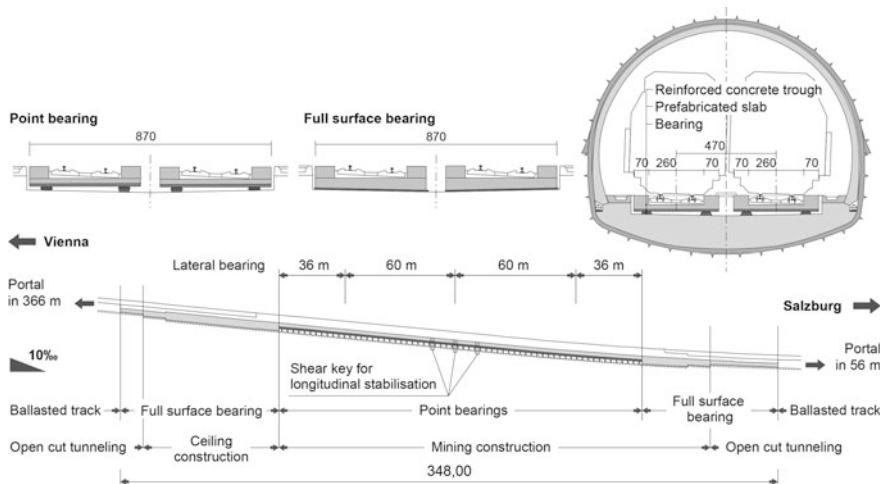


Fig. 5. Overview of the floating track slab system Römerbergtunnel [7]

### 2.5.3 Data Processing and Results

The insertion loss  $D_e$  was determined according to DIN SPEC 45673-3 and it specifies the reduction of one-third octave band levels of ground-borne noise of one test section. (Defined as one-third octave band levels of vibration velocity  $L_{v2}(f_{Tn})$  or acceleration  $La2(f_{Tn})$  in dB)

$$D_e(f_{Tn}) = L_{v1}(f_{Tn}) - L_{v2}(f_{Tn})$$

where:

- $L_{v1}(f_{Tn})$ ...vibration velocity level in one-third octave bands at the reference section, dB re  $5 \times 10^{-8}$  m/s
- $L_{v2}(f_{Tn})$ ... vibration velocity level in one-third octave bands at the section with floating track slab system, dB re  $5 \times 10^{-8}$  m/s.

In order to determine the insertion loss, a force impact is needed. This impact can be an artificial force or the running train. According to DIN SPEC 45673-3, different artificial forces can be used as an exciter, namely a shock impact, a harmonic or a stochastic impact. In all cases, it is always suggested to measure the force input. If this is not feasible, it has to be assured that test and reference measurement sections are excited with the same force input.

In the case of excitation with a running train as it is the case in the Römerbergtunnel, the speed of the passing trains was constant, so that the insertion loss could be determined as follows:

1. Simultaneous determination of  $L_{v1}(f_{Tn})$  and  $L_{v2}(f_{Tn})$  of trains running over both test sections one after each other (train speed  $v$  is constant at both reference and test section).
2. Calculation of  $D_{e,z}(f_{Tn})$  for each train passing (Train type is identical at both reference and test section). In accordance with Fig. 3, the following insertion losses  $D_e$  have been calculated from the difference of one third octave band spectra:

- $D_{e\_WIL1-WIL6} = L_{v\_WIL\_1} - L_{v\_WIL\_6}$
- $D_{e\_WIL2-WIL5} = L_{v\_WIL\_2} - L_{v\_WIL\_5}$
- $D_{e\_W9-W8} = L_{v\_W9} - L_{v\_W8}$
- $D_{e\_W10-W11} = L_{v\_W10} - L_{v\_W11}$

For the measurement of vibrations and determination of insertion losses, velocity sensors type Walesch MST-1005-V and accelerometers types Wilcoxon have been used. Figure 6 is showing the insertion losses calculated from vibration velocity levels measured at the walkway for different train types.

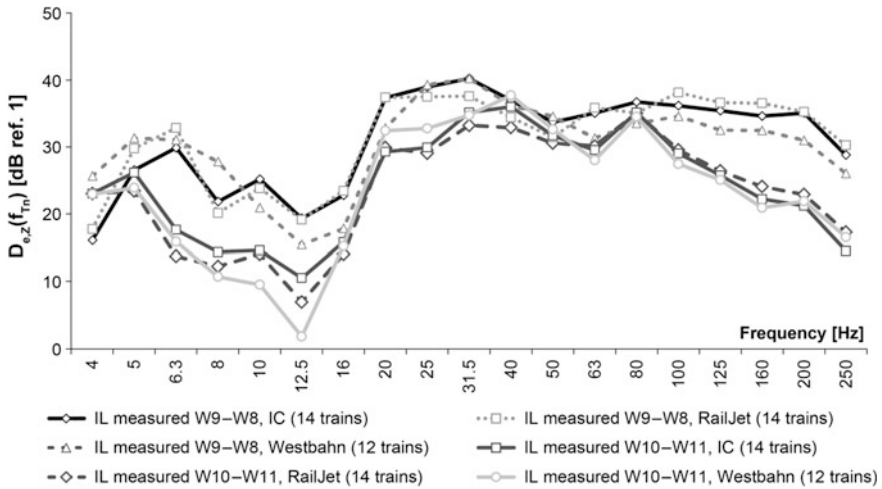


Fig. 6. Average insertion loss calculated out of vibration spectra measured at the walkway for different train type and passing

### 2.5.4 Comparison of Numerically Calculated and in Situ Measured Insertion Loss

The numerical calculation of the insertion loss is based on the model of a multi-mass oscillator, implemented according to DIN 45673-4, Sect. 5.2 [8].

The comparison of the in situ measured insertion loss (min and max peak values) of the numerically determined insertion loss with the initial input data determined by the consultant is shown in Fig. 7.

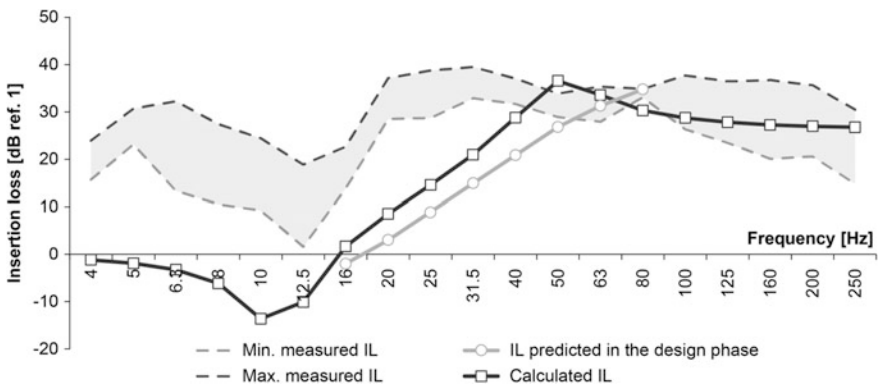


Fig. 7. Comparison of insertion losses of the heavy floating track slab system Römerbergtunnel (calculation, measurement, prediction)

It can be concluded that the measured results are characterized by high scattering in the low frequency domain, but are always higher than prediction and numerical calculation. In the frequency range from 31.5 to 80 Hz, the range of the measured insertion loss is very small and fits to the predicted and calculated levels.

There is a notable discrepancy between the measured and the calculated insertion loss in the lower frequency domain. While the calculated insertion loss behaves as expected showing a typical amplification at 10 Hz, the measured insertion loss contradicts the expectation and is not showing any amplification. This can be justified by different track conditions based on the ‘left and right’ method, requiring a test and a reference track section. In this case, the ballasted reference track section was showing slightly differing soil characteristics and a certain degree of degradation of the ballast, as it is common after 20 years of service, in comparison to the floating slab track system.

### 3 Conclusions

Out of the verification measurements carried out at the floating track slab system Römerbergtunnel, a series of findings in regard to the long term behavior of floating slab track systems could be assessed. The measured results are showing good agreement with the first required natural frequency and the insertion loss expected in the design phase back in the year 1996. A notable discrepancy between the measured and the calculated insertion loss in the lower frequency domain was identified due to slightly differing soil characteristics and a certain degree of degradation of the ballasted reference section. Furthermore, the measured and inspected results are demonstrating that material aging and a loss of the effectiveness of the bearings of closed-cell elastomer did not occur.

The scattering among the insertion loss curves results from the direct comparison of the train passings on the ballasted track with those on the floating slab track system. The vibration mitigation behavior for protection of the adjacent residential buildings is still as good as it was in 1996, despite a daily track loading of 60,000 gross tons.

### References

1. Fritsch, Chiari & Partner Ziviltechniker GmbH, Technischer Bericht „Wirksamkeit Masse-Feder-System – Verifikationsuntersuchungen, km 235,452 bis km 235,800 Römerbergtunnel“. GZ 15/1159, Rev. 00, Wien, 14.12.2015
2. Getzner Werkstoffe GmbH, Brochure Mass-Spring System/7. Sylodyn, 2014
3. Univ. Prof. Dr. Peter Steinhauser, Ergebnisse der Vibrosan-Untersuchung, EB-Operat Masse-Feder-System Römerbergtunnel, Bericht Nr. 487/9601 bzw. Plannummer 2129-03, 07. August 1996

4. Ingenieurbüro für Bau, Verkehr und Umwelt Rutishauser, Untersuchungen zur Ermittlung der geeigneten elastischen Lagerung des Masse-Feder-Systems Römerbergtunnel, 2. April 1996
5. EMPA (EMPA Eidgenössische Materialprüfungs- und Forschungsanstalt, Bericht Nr. 166'363: Bestimmung der Federkennlinie – Dynamische Steifigkeit bei verschiedenen Mittellasten und Frequenzen. Prüfobjekt: Elastomerlager Sylodyn N40840 Troglager Römerberg, Muster Nr. 6, 29. November 1996)
6. DIN SPEC 45673-3 Mechanische Schwingungen – Elastische Elemente des Oberbaus von Schienenfahrwegen – Teil 3: Messtechnische Ermittlung der Einfügungsdämmung im eingebauten Zustand (Versuchsaufbau und Betriebsgleis): August 2014
7. Fritsch, Chiari & Partner Ziviltechniker GmbH, Planunterlagen, EB-Operat Masse-Feder-System Römerbergtunnel, Plannummern 2129-51, 2129-52, 2129-53, 2129-54, 2129-55, 2129-56, 2129-57, 2129-58, 27. June 1996
8. DIN V 45673-4: Mechanische Schwingungen – Elastische Elemente des Oberbaus von Schienenfahrwegen – Teil 4: Rechnerische Ermittlung der Einfügungsdämmung im eingebauten Zustand: July 2008

**Part VII**  
**Wheel and Rail Noise**

# Low Cost Noise Barriers for Mitigation of Rail Noise



L. Basutu, W. Chan, D. Hanson, B. Dowdell and C. Weber

**Abstract** Noise barriers are a widely used mitigation measure for rail noise, particularly for new rail line developments. Precast concrete barriers are typically used for rail noise mitigation as their high mass allows them to effectively mitigate low frequency noise from sources such as freight locomotives. However, there are considerable capital costs associated with the design and the construction of concrete barriers due to the large scale earthworks required for barrier footings and vegetation clearing. As such, there exists an opportunity to reduce the cost of noise barriers by optimising their design to suit the particular noise characteristics at each site. This paper presents an approach for the design of low cost noise barriers for the mitigation of rail noise. This approach involves: Categorising the type of rail noise at the target location. Categories include locomotive noise, squeal noise, rolling noise, bunching and stretching etc. which reflect the frequency content of the noise at the site. Designing the barrier to treat the specific noise type at the site (i.e. specifying barrier material, height and length). Examining the cost components of each barrier design using a life cycle methodology that considers all costs associated with design, construction and maintenance of the barrier. As an illustration of how this design approach can be applied, this paper presents two case studies showing the low cost noise barrier design at two locations on the Sydney Trains Network which experience squeal noise and locomotive noise, respectively. Each design considers the predicted performance and costs of the designed barriers and compares them with industry benchmarks.

---

L. Basutu (✉) · W. Chan · D. Hanson · B. Dowdell  
Transport for NSW, 18 Lee Street Chippendale, Sydney, NSW, Australia  
e-mail: [Laurena.Basutu@transport.nsw.gov.au](mailto:Laurena.Basutu@transport.nsw.gov.au)

C. Weber  
Renzo Tonin and Associates, Sydney, NSW, Australia

## 1 Introduction

Precast concrete noise barriers are a widely used mitigation measure for noise [1, 2]; particularly for new rail line developments as their high mass allows them to effectively mitigate low frequency noise from sources such as freight locomotives. However, there are considerable capital costs associated with the design and construction of concrete barriers due to the large scale earthworks required for barrier footings and vegetation clearing. As such, there exists an opportunity to reduce the cost of noise barriers by optimising their design to suit the particular noise characteristics at each site. For example, light weight, cheaper materials such as steel or PVC could be used to construct noise barriers that mitigate high frequency rail noise from sources such as squeal (frequency band 1000–10,000 Hz) and flanging (frequency band 2000–10,000 Hz).

## 2 Noise Barrier Design Tool

Transport for NSW has developed a simple desktop analytical tool—the Noise Barrier Calculation Spreadsheet—that enables us to design both single and double panel noise barriers and optimise the design of those barriers to suit the particular rail noise type (locomotive noise, squeal noise, rolling noise, bunching and stretching) at the target location. The Noise Barrier Calculation spreadsheet uses the theoretical engineering prediction schemes and experimental results postulated by Maekawa [3], Rathe [4], Kurze and Anderson [5], to determine the noise barrier performance in terms of the diffracted noise component (how much noise is able to pass over and around the barrier determined by the height and length of the barrier) and the calculations by Sharpe [6] and Bies and Hansen [7] to determine the transmitted noise component (how much noise is able to pass through the barrier, determined by material properties) in one-third octave frequency bands. This allows us to specify the appropriate barrier height and material to be used, which will achieve the desired noise mitigation at a receiver experiencing a particular type of rail noise.

## 3 Noise Barrier Field Trial

To test the accuracy of the Noise Barrier Calculation Spreadsheet and calibrate it to real world conditions, a noise barrier field trial was undertaken in Brooklyn NSW.

The objectives of the field trial were to:

- Confirm that the overall insertion loss predicted by the Noise Barrier Calculation spreadsheet for different materials is similar to the measured insertion loss.
- Determine which noise barrier material types have a comparable performance to concrete for different types of rail noise.



### 3.1 Trial Methodology

#### 3.1.1 Site Description

The trial was located in Brooklyn NSW, adjacent to the Main North Line at Kilometrage 55.025 km. The location was selected due to its unique characteristics, including proximity to a tight curve (237 m), differing rail traffic (both passenger and freight), a steep grade (1 in 40), and a large flat area adjacent to the track that was suitable for barrier construction. Noise types identified at the site included locomotive engine noise, squeal, flanging and rolling noise.

#### 3.1.2 Noise Barrier Types and Installation

Four noise barriers were constructed at the trial location. A description of each barrier is listed Table 1.

The barriers were constructed in a U-Shaped configuration (refer to Fig. 1). The front end (facing the rail) of each barrier was installed 14 m from the nearest rail, and oriented parallel to the tangent of the curve. This approximates the distance of the corridor boundary from the nearest track across the network, i.e. a typical barrier location. Each barrier was spaced 3.5 m apart (measured side by side). The panels were installed on 200 mm by 400 mm flange plates and fixed in place by steel posts at each corner. Braces were installed on top of the side panels to prevent movement. No excavation was used during the installation. All air gaps were eliminated.

#### 3.1.3 Noise Measurements

Noise measurements at each barrier were recorded over a two-week period from 10 May 2016 to 24 May 2016 using Ngara noise loggers. The noise loggers were set

**Table 1** Noise barrier types

Barrier type	Front and side dimensions (m)	Surface density of material (kg/m <sup>2</sup> )
Steel Fencing	2.4 (width) × 1.8 (height)	2.75
Modular barrier made from Hollow PVC panels <sup>a</sup>	2.4 (width) × 1.8 (height)	84
Modular barrier made from PVC panels filled with dried sand	2.4 (width) × 1.8 (height)	640
Modular barrier made from PVC panels filled with concrete	2.4 (width) × 1.8 (height)	920

<sup>a</sup>Modular hollow PVC panels were chosen due to their ease of installation and ability to have different infill materials placed inside. Each PVC panel was 2.4 m × 0.6 m × 0.048 m

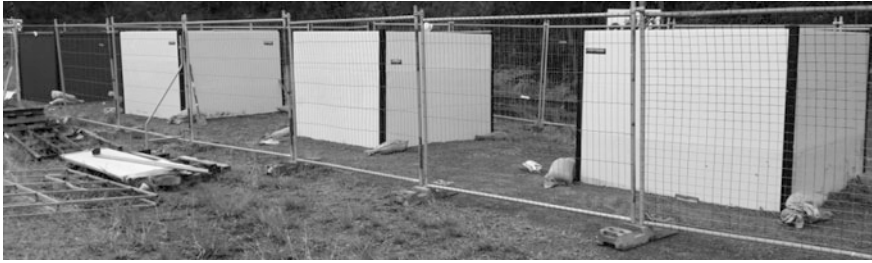


**Fig. 1** Noise barrier configurations (left to right: steel, sand-filled, concrete-filled, hollow)

up to measure the  $L_{Aeq}$  and  $L_{Amax}$  noise levels in consecutive 0.1 s intervals [8]. Audio was recorded continuously in 16 bit 48 kHz Wav format [8].

### Attended Field Insertion Loss Measurements

Attended measurements of insertion loss performance were conducted on 10 May 2016 and 17 May 2016. This was achieved by using a pink noise source raised 2 m above ground level to generate a steady noise at a distance of 7.5 m from the noise barriers, and measuring the sound pressure level inside each barrier and in the free field. The amplitude of the noise source was adjusted such that the free-field noise level at 9 m was 87 dB(A). Noise loggers used to record the noise levels were located within the enclosures (1.2 m behind the barrier) and at the free-field location.

### Unattended Field Insertion Loss Measurements

Unattended noise measurements were recorded over a two-week period. A logger was installed at the center (1.2 m behind the barrier) of each barrier, 1 m above the ground. An additional control logger was installed in a free-field location at the same distance from the nearest rail to identify the baseline noise level, 3 m from the steel fence. The noise measuring set-up is shown in Fig. 2.



**Fig. 2** Unattended noise monitoring set-up

## **3.2 Data Analysis**

Raw data was analysed using Transport for NSW's Trackside Noise software [9]. In the analysis, values for  $L_{Aeq}$ ,  $L_{Amax}$ , and the one-third octave noise spectra ( $L_{Aeq}$ ) for each train passby were determined. The insertion loss of each barrier was calculated by subtracting the measured noise level behind each barrier from the equivalent noise level at the free-field control location. This analysis was undertaken on a one-third octave basis at each centre frequency between 63 and 10,000 Hz.

### **3.2.1 Attended Insertion Loss Measurements**

The measured insertion loss from the pink noise test was compared to the insertion loss calculated by the Noise Barrier Calculation Spreadsheet. This was used to confirm that the overall noise reduction predicted by the Noise Barrier Calculation spreadsheet for different materials was similar to measured noise levels.

### **3.2.2 Unattended Insertion Loss Measurements**

The overall insertion loss performance of each barrier for different rail noise types was determined by identifying both passenger and freight train passbys which exhibited primarily rolling, squealing, flanging or locomotive noise. The noise levels behind each barrier for these train passbys were compared to the noise levels at the free-field control location. This comparison was used to determine which barrier type provided the most attenuation for the different rail noise type investigated.

## **3.3 Results**

### **3.3.1 Attended Field Insertion Loss Measurements Results**

The measured insertion loss for each barrier was compared to the insertion loss predicted by the Noise Barrier Calculation Spreadsheet as shown in Table 2. In all cases the predicted insertion loss is within 2 dB(A) of the measured insertion loss. This means that the Noise Barrier Calculation Spreadsheet can be used to design an appropriate barrier to achieve the desired noise mitigation at a receiver experiencing a particular type of rail noise.

**Table 2** Total measured versus predicted insertion loss for each barrier type using pink noise source

	Noise barrier type			
	Concrete	Steel	Sand	Hollow PVC
Measured insertion loss	12	10	12	11
Predicted insertion loss	13	11	13	13

### 3.3.2 Unattended Insertion Loss Measurements

The results of the unattended insertion loss measurements are presented in Fig. 4. The results show that the concrete and sand-filled PVC barriers exhibit superior performance for frequencies between 63 and 160 Hz. From 160 to 6300 Hz, all PVC barriers exhibit similar performance. Above 6300 Hz, the sand-filled PVC barrier exceeds both the hollow and concrete-filled barrier. The results also show that while the Steel fence performs poorly at lower frequencies, above 2000 Hz it outperforms all of the PVC barriers types (hollow, concrete-filled and sand-filled).

In Fig. 5, the overall insertion loss for different noise types is shown. Steel performs the best for flanging and squeal noise (high frequency), but performs the worst for rolling and locomotive noise (low frequency). The PVC barriers perform similarly across all noise types.

## 4 An Approach for the Design of Low Cost Noise Barriers

The results from the investigation at Brooklyn support the premise that the type of noise barrier can be tailored to the specific rail noise character at a particular site. Building on this understanding, we propose an approach to the design of low cost noise barriers, as outlined in Fig. 6.

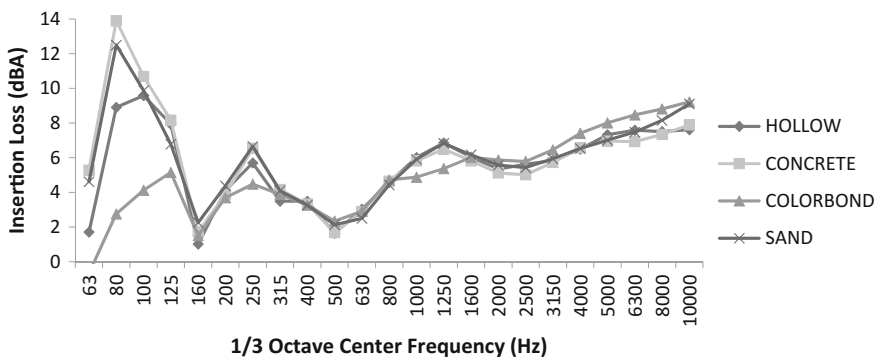


**Fig. 4** Noise barrier insertion loss spectra from over 350 train passbys (passenger and freight)

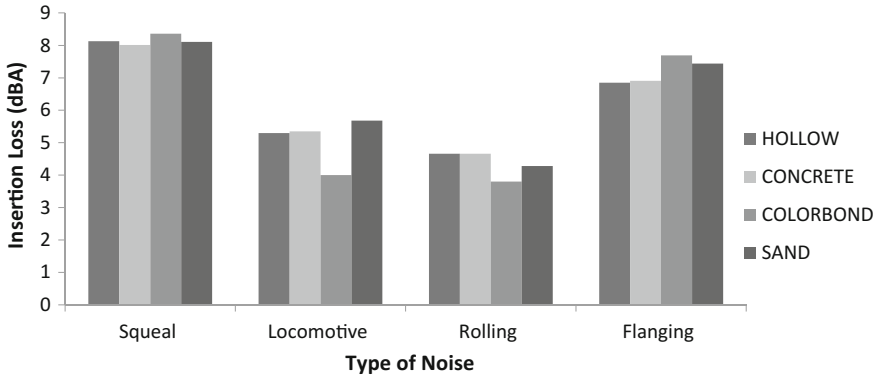


Fig. 5 Noise barrier overall in-field insertion loss

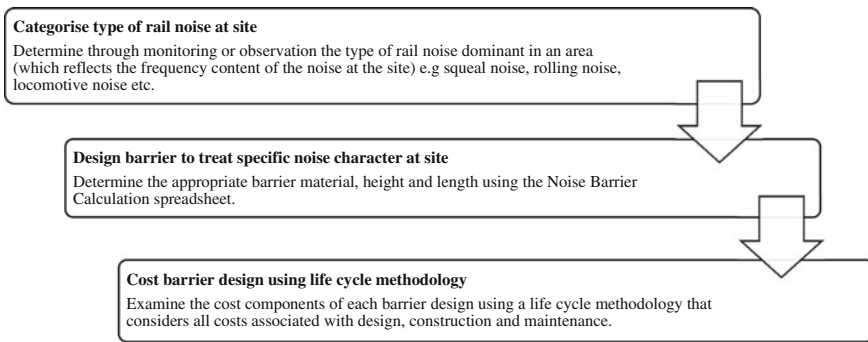


Fig. 6 Approach for the design for low cost noise barriers

### 4.1 Noise Barrier Design Case Study

As an illustration of how this design approach can be applied, two case studies presenting the low cost noise barrier design at locations on the Sydney rail network which experience locomotive noise and curve squeal, respectively, are presented below. Each design considers the predicted performance and costs of the designed barriers and compares them with industry benchmarks.

#### 4.1.1 Case Study 1—Wheel Squeal

There are a number of locations on the network that experience high levels of squeal noise. In this example, we consider a typical application where the receivers are 1.5 m above ground (e.g. a ground floor window) and located 38 m from the rail corridor. This case study considers a 4.2 m high, 400 m long steel noise wall to

be built at the corridor boundary 17 m from the near track. We used the Noise Barrier Calculation Spreadsheet to see how well the proposed noise barrier design performs against a traditional precast concrete noise barrier design. The input parameters used for this analysis are listed below:

- steel: panel thickness—0.00035 m, panel density—7850 kg/m<sup>3</sup>
- Precast Concrete: panel thickness—0.125 m, panel density—2300 kg/m<sup>3</sup>
- Noise source—the third octave spectrum of a squealing train measured by TfNSW with a free-field noise level of 113 dB(A) at 1.2 m.
- Source height—0.5 m.

The results shown in Fig. 7 indicate that a steel barrier is as effective at mitigating squeal noise as a concrete barrier of the same height, particularly at frequencies greater than 2000 Hz. This is because the light weight steel barrier has sufficient mass to mitigate the transmitted noise and the diffracted noise component is dominant.

### 4.2 Case Study 2—Locomotive Noise

Locomotives occasionally stop for long periods adjacent to residents at some locations on the network. In this case study, we considered one such location at which the receiver is 1.5 m above ground and located 39 m from the rail line. That the case study considers a 4.2 m high, 55 m long hollow PVC noise wall built 13 m from the nearest façade of the residence facing the rail in order to mitigate the idling noise. We used the Noise Barrier Calculation Spreadsheet to see how well the proposed noise barrier design performs against a traditional precast concrete noise barrier design. The input parameters used for this analysis are listed below:

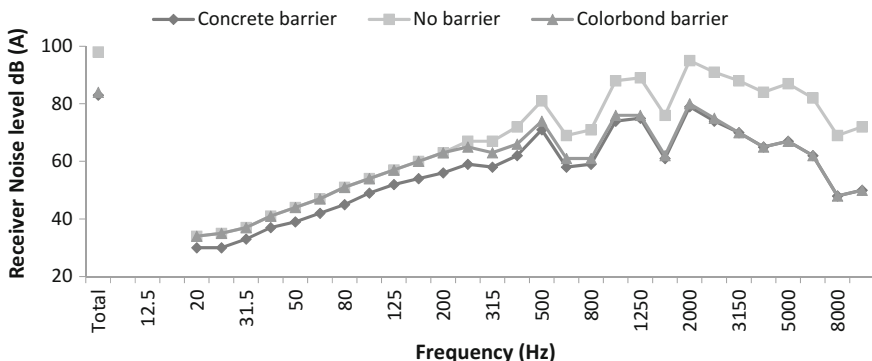


Fig. 7 Performance of steel barrier versus precast concrete barrier—squeal noise

- Hollow PVC: total panel thickness—0.0048 m (Each wall has a thickness of 0.0024 m), panel density—1400 kg/m<sup>3</sup>
- Precast Concrete: panel thickness—0.125 m, panel density—2300 kg/m<sup>3</sup>
- Noise source—the third octave spectrum of an idling train source from the Rail Noise Database [10] with a free-field noise level of 88 dB(A) at 7.5 m.
- Source height—4.0 m.

The results shown in Fig. 8 indicate that a hollow PVC barrier is as effective at mitigating idling noise as a concrete barrier of the same height.

### 4.3 Cost Comparison

The lifecycle costs of competing noise barrier designs, in conjunction with the type of noise targeted for attenuation, should be considered when deciding the most appropriate barrier type to use. To assist in this calculation, the net present cost of a precast concrete barrier and each barrier type used in the field trial over a 40-year lifecycle is presented in Table 2.

In the calculation, a design life of 20 years was assumed for the steel fence, and 40 years for the modular PVC and precast concrete barriers [2]. Generally, it is recommended that 10% of the capital cost be set aside for maintenance [2]. This does not include the cost of graffiti removal, and for the purposes of the net present cost calculation, it was assumed that this amount was consumed evenly over a 40-year lifecycle. An annual inflation rate of 3% and discount rate of 7% was also used in the calculation [11] (Table 3).

Using the figures in Table 2, a net present cost comparison over a 40-year lifecycle between the chosen barrier type in each case study and a precast concrete barrier has been calculated.

In case study 1, the net present cost of the steel fence was A\$288,000 whilst the precast concrete barrier was A\$735,000. This represents a cost saving of \$447,531.

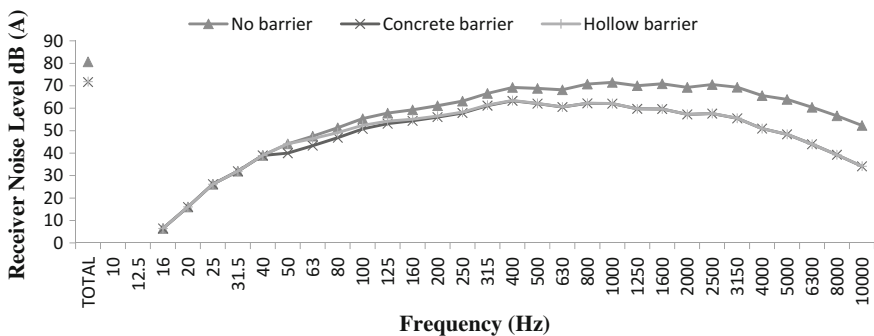


Fig. 8 Performance of hollow PVC barrier versus precast concrete barrier—idling noise

**Table 3** Cost per lineal metre of the barriers considered in this study

Barrier type (4.2 m high)	Capital cost	Maintenance cost (p.a)	Net present cost
Steel <sup>a</sup>	A\$480	A\$1.20	A\$719
Hollow PVC	A\$490	A\$1.23	A\$515
Sand-filled PVC	A\$850	A\$2.13	A\$893
Concrete-filled PVC	A\$900	A\$2.27	A\$952
Precast concrete	A\$1750	A\$4.38	A\$1838

<sup>a</sup>Includes the cost of replacing the steel fence after 20 years

In case study 2, the net present cost of the hollow PVC barrier was A\$28,000 whilst the precast concrete barrier was A\$101,000. This represents a cost saving of A \$73,000.

## 5 Conclusions and Recommendations

Transport for NSW has undertaken an investigation into low cost noise barriers which are tailored to the particular noise characteristics at a target site. The results of this investigation indicate that low cost barriers can achieve the desired noise mitigation at a receiver when compared with traditional concrete barriers.

The approach to designing a low cost noise barrier presented in this paper includes the following steps: categorizing the type of rail noise at the site; designing the barrier to treat the site specific noise character by selecting the appropriate barrier material and barrier height; and costing the barrier using a lifecycle methodology. The effectiveness of this approach has been illustrated using two case studies. Each case study considered the predicted performance and costs of low cost barriers compared to the industry benchmark concrete barrier. In case study 1, a 4.2 m high 400 m long steel noise barrier was found to be as effective at mitigating wheel squeal as a traditional concrete barrier of the same length and height, but cost 61% less over a 40 year life-cycle. In case study 2, a 4.2 m high 55 m long Hollow PVC barrier was found to be as effective at mitigating locomotive noise as a traditional concrete barrier of the same length and height, but cost 72% less over a 40 year life-cycle.

These results support the consideration of low-cost noise barriers for the mitigation of rail noise.



## References

1. Roads and Maritime Service: Noise Wall Design Guideline. Transport for NSW, Sydney (2016)
2. Sevo, B., Jurevicius, D.: Playford Projects Acoustic Barrier Options Analysis, s.l.: s.n. (2011)
3. Maekawa, Z.: Noise reduction by screens. *Appl. Acoust.* **1**(3), 157–173 (1968)
4. Rathe, E.J.: Note on two common problems of sound attenuation. *J. Sound Vib.* **10**(3), 472–479 (1969)
5. Kurze, U.J., Anderson, G.S.: Sound attenuation by barriers. *Appl. Acoust.* **4**(1), 35–53 (1971)
6. Sharpe, B.H.: Prediction methods for the sound transmission of building elements. *Noise Control Eng.* **11**(2), 53–63 (1978)
7. Bies, D.A., Hansen, C.H.: *Engineering Noise Control*, 4th edn. Taylor Francis, New York (2009)
8. Tonin, Renzo: Brooklyn Noise Wall TJ112-01F03(r1). Renzo Tonin, Sydney (2016)
9. CRC for Rail Innovation: *Transport for NSW Trackage Noise v3.0*, Sydney: CRC for Rail Innovation (2014)
10. Transport for NSW: The Rail Noise Database. [Online] Available at: <http://www.asa.transport.nsw.gov.au/ts/asa-standards> [Accessed 7 June 2016] (2015)
11. New South Wales Treasury, Office of Financial Management, 2007. *NSW Government Guidelines for Economic Appraisal*, s.l.: s.n.

# A New Model for the Prediction of Track Sound Radiation



Xianying Zhang, David J. Thompson and Giacomo Squicciarini

**Abstract** The TWINS model is a widely used and well-established model for rolling noise which has been validated against field measurements in terms of overall noise spectra and levels. However, there are still some areas that can be improved. In particular, the radiation from the rail is based on a model of a rail in free space and there are also limitations in the model for the sound radiation from the sleepers. This paper draws on recent research into the effects of the proximity of the rail and sleeper to an absorbing ground on their sound radiation. Moreover, the ballast is acoustically absorbing to some extent because of the gaps between the ballast particles and this can affect the noise radiation by the rail and sleeper. The ballast absorption is represented here using the Johnson-Allard model with measured values of flow resistivity and porosity. Additionally, the Delany and Bazley model is introduced with a higher value of flow resistivity for comparison. These are used to produce the normal impedance of the ballast layer which is introduced in boundary element calculations of the radiation from the rail and sleepers. Comparisons are made first with the sound radiation from a 1:5 scale track model which has been measured reciprocally in the reverberation chamber. It is shown that the impedance using the measured flow resistivity is inadequate for use in the numerical models; probably an extended reaction model would be more appropriate. However, the Delany and Bazley model with the higher flow resistivity gives better agreement with the measurements and is a practical solution. The new models have also been used together with TWINS to predict the sound radiation from an operational track and the results have been compared with an example field measurement. The new models are found to give an improvement at low frequencies, where the sleeper is the dominant noise source.

---

X. Zhang (✉) · D. J. Thompson · G. Squicciarini  
Institute of Sound and Vibration Research, University of Southampton,  
Southampton SO17 1BJ, UK  
e-mail: xianyingzhang96@gmail.com

© Springer International Publishing AG, part of Springer Nature 2018  
D. Anderson et al. (eds.), *Noise and Vibration Mitigation for Rail Transportation Systems*, Notes on Numerical Fluid Mechanics and Multidisciplinary Design 139,  
[https://doi.org/10.1007/978-3-319-73411-8\\_56](https://doi.org/10.1007/978-3-319-73411-8_56)

709

## 1 Introduction

The most important source of railway noise in most situations is rolling noise, which is caused by wheel and rail vibration induced at the wheel/rail contact area. The TWINS model [1, 2] is well-established as a method of predicting the generation of vibration and noise from the railway wheels and track and this has been used successfully to design noise mitigation measures. However, there exist some limitations in this model. In particular, the sound radiation from the rails is calculated under the simplifying assumption that they radiate into free space, whereas in the reality they are located close to the ground. There are also limitations in the way that the sleepers are treated in TWINS. They are assumed to be embedded in a rigid ground and the effect of multiple sleepers is taken into account in a heuristic way [3]. Recently, the authors have developed improved models for the sound radiation from rails in proximity to an absorptive ground using the boundary element method (BEM) and validated them against laboratory experiments [4]. In [5], improved boundary element models for the sound radiation from sleepers have been presented and validated through laboratory measurements for an absorptive ground consisting of melamine foam.

The ballast is also an important component of the track. Railway ballast is a porous medium with absorptive properties which may modify the sound radiation of the rail and the sleeper. Therefore, it is necessary to take these boundary conditions into account in the models for the sound radiation from the track. In this paper, measurements of ballast absorption are presented and two different models are used to represent this. The effects on the sound radiation from the rail and the sleepers are predicted by the boundary element method. Then, the various models are combined to give predictions of the sound radiation from the complete track. Results are shown first for a 1:5 scale track and are compared with corresponding experimental results obtained in the laboratory. Finally, the sound radiation from a full size track is predicted by using the new models together with the TWINS software and comparisons are made with existing field measurements.

## 2 Ballast Absorption and Its Effects on the Track Sound Radiation

### 2.1 Ballast Absorption

Measurements of the absorption of railway ballast obtained in a reverberant chamber have been presented by Broadbent et al. [6]. In that work the results were fitted to a multiple layer model with flow resistivities between 25 and 51 kPa.s/m<sup>2</sup>. However, in [7] the flow resistivity of railway ballast was measured as 200 Pa.s/m<sup>2</sup>.

Due to the difficulties of working with full scale ballast (typical stone sizes are 50 mm) measurements have been made here of the flow resistivity and porosity of

samples of 1:5 scale ballast with the correct gradation [8] at reduced scale. The flow resistivity was measured by passing air through a tube of internal diameter 146 mm filled with ballast samples of 300 and 600 mm thickness. The mean value was found to be  $280 \pm 20 \text{ Pa.s/m}^2$ . In addition the porosity was determined by adding a measured amount of water to a bucket filled with scale ballast and a value of 0.463 was found. These properties of the 1:5 scale ballast are similar to the values for full scale ballast given in [7] but are believed to be more reliable as a correspondingly larger sample of ballast could be included in the test rigs. The absorption coefficient of this reduced scale ballast was also measured in a reverberation chamber [9], as shown in Fig. 1. This is comparable to the result for the equivalent full scale sample from [6], shown in Fig. 2.

**Fig. 1** Absorption coefficient of the 1:5 scale ballast. Comparisons between reverberation chamber measurements and prediction. **a** Thickness 0.03 m; **b** Thickness 0.06 m

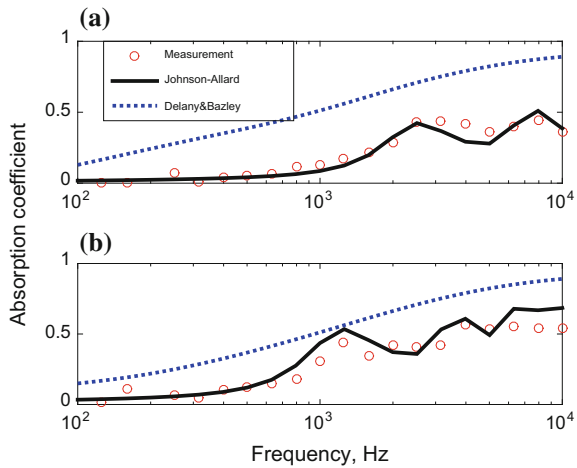
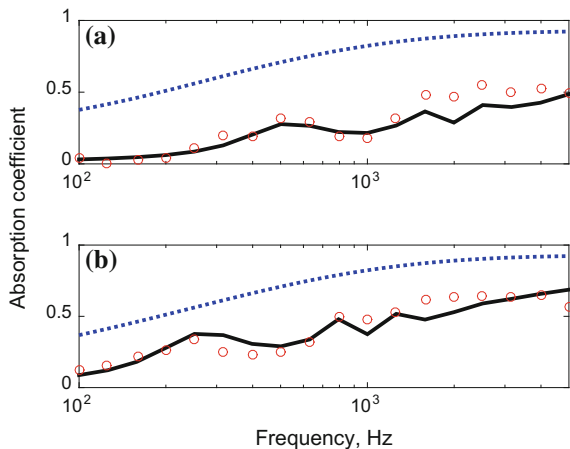


**Fig. 2** Absorption coefficient of the full scale ballast. Comparisons between the measured results from [8] and predictions. **a** Thickness 0.17 m; **b** Thickness 0.33 m



The Johnson-Allard model [10, 11] has then been used with the above parameter values to obtain the normal acoustic impedance. The values of tortuosity and characteristic lengths were chosen to give a good fit to the measured absorption coefficient. This gave a tortuosity of 1.3 and viscous characteristic length of 0.482 mm for the 1:5 scale ballast and values of 1.0 and 1.63 mm for full scale ballast. The results are compared with the corresponding measured diffuse field absorption coefficients in Figs. 1 and 2. Good agreement can be seen between them for both the 1:5 scale and full size ballast.

However, for propagation at grazing incidence above a layer of ballast, the Delany and Bazley model [12] for an infinite layer with a flow resistivity of 50 kPa.s/m<sup>2</sup> has been found to give reasonable predictions [13]. This model will be also used as an alternative to study the influence of the ballast absorption in this paper, even though the flow resistivity used in the model (50 kPa.s/m<sup>2</sup>) is quite different from the measured value (280 Pa.s/m<sup>2</sup>). By using this model, the corresponding absorption coefficients in a diffuse field for the two types of the ballast are also presented in Figs. 1 and 2. The agreement between the predictions and the measured results for both cases is much worse than for the Johnson-Allard model.

## 2.2 Rail and Sleeper Radiation

Two-dimensional boundary element calculations have been carried out for a full scale rail located 50 mm above a layer of ballast using both impedance models described above. In the Johnson-Allard model the thickness of the ballast layer is set to 500 mm, whereas in the Delany and Bazley model it is neglected. The radiation ratio of the rail is presented in Fig. 3, for purely vertical and lateral vibration of the rail. Compared with the result for a rail in free space, as used in TWINS, dips occur below 1 kHz in the results predicted by the Johnson-Allard model with the measured flow resistivity, which are due to the effects of the layer thickness in the impedance. When the Delany and Bazley model with the higher flow resistivity is used, at low frequency the radiation ratio increases for lateral motion, but the radiation ratio for vertical motion reduces, similar to results found for a rigid ground [3]. For both the vertical and lateral motion of the rail, at high frequency the radiation ratio is reduced by around 2 dB because of the absorption of the ballast in either model.

For the sleepers, a three-dimensional boundary element model is used to assess the effect of the ballast absorption on the sound radiation. Three sleepers are included in the model, which are assumed to be vibrating with amplitudes of 0.5, 1 and 0.5 to represent the relative vibration transmitted by the rail excited at a point above the central sleeper [5]. The sleepers are assumed to be fully embedded in the ballast so only their upper surface is visible. Figure 4 shows the radiation ratio obtained using the different models of ballast impedance. These are compared with the result obtained from the model currently implemented in TWINS. The latter is an approximation based on the radiation from a rectangular piston set in an infinite

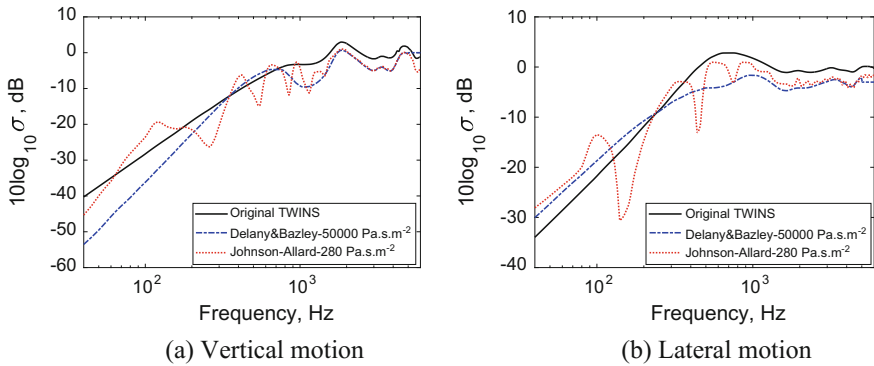
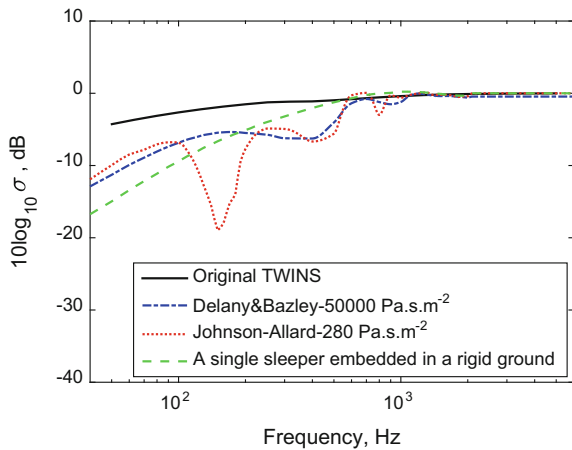


**Fig. 3** Comparison of the results of different models for the radiation ratio of a full size rail, **a** Vertical motion, **b** Lateral motion

baffle with a heuristic correction for the presence of multiple sleepers [4]. The predicted radiation ratio from the sleeper in the current work has allowed for this effect in a more rigorous way. Dips again occur below 1 kHz for the case based on the Johnson-Allard model with the measured flow resistivity.

Although not shown here, measurements on individual 1:5 scale rails and sleepers together with the scale ballast indicate that the results obtained with the Delany & Bazley model with flow resistivity of 50 kPa.s/m<sup>2</sup> are more consistent with the measured data.

**Fig. 4** Comparison of the results of different models for the radiation ratio of the full size sleepers



### 3 Validation Using 1:5 Scale Track

Validation measurements have been carried out using a 1:5 scale model track. This consisted of two 2 m-long rails attached via spring clips to 17 concrete sleepers. These were arranged with a spacing of 0.12 m (corresponding to a full scale distance of 0.6 m). The track was embedded in 1:5 scale ballast, with overall dimensions  $2\text{ m} \times 0.8\text{ m} \times 100\text{ mm}$ , located on the floor of a large reverberation chamber; the depth of ballast beneath the sleepers was 60 mm. The corresponding set up is shown in Fig. 5. Rubber rail pads are also located between the rail foot and the sleepers. These consisted of pieces of neoprene with a thickness of 2.5 mm and dimensions  $45\text{ mm} \times 35\text{ mm}$ . The average stiffness of the railpads has been determined to be 15 MN/m.

#### 3.1 Point Mobility and Decay Rate

The driving point mobility of this scale model track is presented in Fig. 6. Comparison is also made with the corresponding predictions obtained by using an analytical track model, based on a continuously supported infinite Timoshenko beam [14, 15]. Quite good agreement can be seen between the predictions and the measured point mobility, indicating that the track behaves in a similar way to a full size track. The fluctuations in the measurements at high frequencies are due to reflections from the finite length of the rail.

**Fig. 5** Experimental set up for the 1:5 scale whole track embedded in ballast



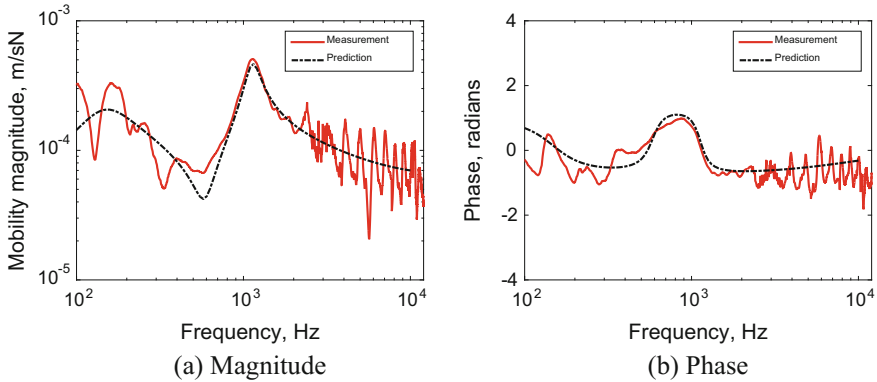
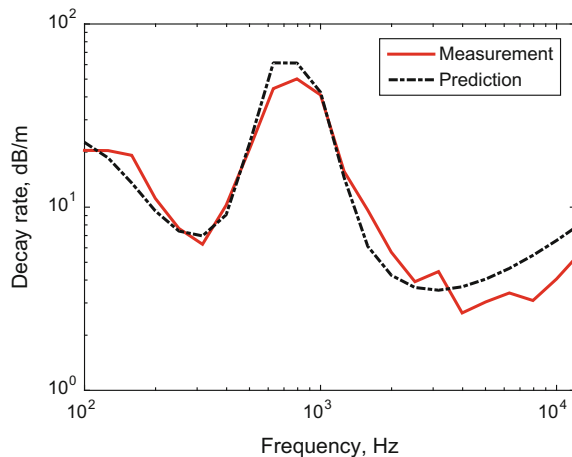


**Fig. 6** Point mobility of the 1:5 scale track. Rail pad stiffness 15 MN/m, loss factor 0.2. Ballast stiffness 1.0 MN/m per half-sleeper, loss factor 1.0, **a** Magnitude, **b** Phase

Measurements based on the method from EN 15461 [16] have also been made to verify that the decay rate for the 1:5 scale track is representative of a real track. In applying this method, the initial point was set at one end of the track and the mobility was measured at 30 positions by moving the impact hammer. Corrections were made for the finite length of the track in processing these measured results [17]. The results are shown in Fig. 7 and compared with the results of the infinite track model [14, 15]. Good agreement can be seen between the predicted decay rate and the measured one. The decay rate has a typical form, with a high value at low frequency, a peak in the region where the sleeper acts as a dynamic absorber, a sudden drop above the resonance of the rail on the pad before rising again at high frequency. Thus, it can be concluded that the 1:5 scale track is a good representation of a real track.

**Fig. 7** Decay rate for an equivalent infinite track for the 1:5 scale track





### 3.2 Sound Power from the Whole Track

The sound power  $W$  radiated by a vibrating object can be written as [18]

$$W = \rho_0 c_0 S \langle \overline{v^2} \rangle \sigma \quad (3.1)$$

where  $\rho_0$  is the density of air,  $c_0$  is the speed of sound,  $S$  is the surface area of the vibrating structure and  $\langle \overline{v^2} \rangle$  is the surface-averaged mean-square velocity normal to the surface in the frequency band of interest. The parameter  $\sigma$  is the radiation ratio or radiation efficiency.

The mean-square velocity of the rails and sleepers for a unit force on the railhead has been measured by applying a reciprocal method. The transfer mobility was measured for vertical excitation at 69 points along each rail (4 points spaced equally along the rail section in each sleeper span), 11 points spaced equally along the central three sleepers, and 3 points spaced equally along all the other sleepers. Two accelerometers were located vertically at the centre of the railhead above the central sleeper, one on each rail. By reciprocity these measurements represent the transfer mobility from a force at the railhead at the centre of the rail to the velocity of the rail or the sleeper.

The sound power from the whole track for a unit force applied at the rail has been measured reciprocally in a reverberation chamber. Comparison is made with the sound power from both the rails and the sleepers determined by using the corresponding measured vibration and the predicted radiation ratios, including the effect of the ballast absorption. The radiation ratio of the rails is estimated by using a weighted average of the results for a rail attached to a rigid ground [3] and a rail 20 mm above the ballast. To estimate the sound power from the sleepers, the radiation ratio is based on three sleepers with vibration amplitudes in the ratio of 0.5:1:0.5, as shown in Fig. 4 for the full size sleepers.

Figure 8 presents the measured sound power from the assembly normalised by the mean square force. The results are shown in 1/12 octave bands. These are compared with the estimated sound power from the two rails and 17 sleepers based on their measured vibration. As can be seen, the sound power from the sleepers dominates the noise up to 2000 Hz (400 Hz at full size) as the rail pads reduce the vibration transmission from the rails to the sleepers at higher frequencies, where the rail dominates.

The radiation ratio of the sleepers embedded in ballast obtained with the Delany and Bazley model gives a better prediction of their sound power than that predicted using the Johnson-Allard model, especially in the frequency range 500–1000 Hz. This discrepancy is related to the dips in the predicted radiation ratio of the sleepers embedded in ballast for the Johnson-Allard model, as shown in Fig. 4. This suggests that the impedance obtained with the measured flow resistivity is not suitable for use in the BEM model, even though good agreement was found with the ballast absorption measured in a diffuse field, as presented in Fig. 1. This is likely to be due

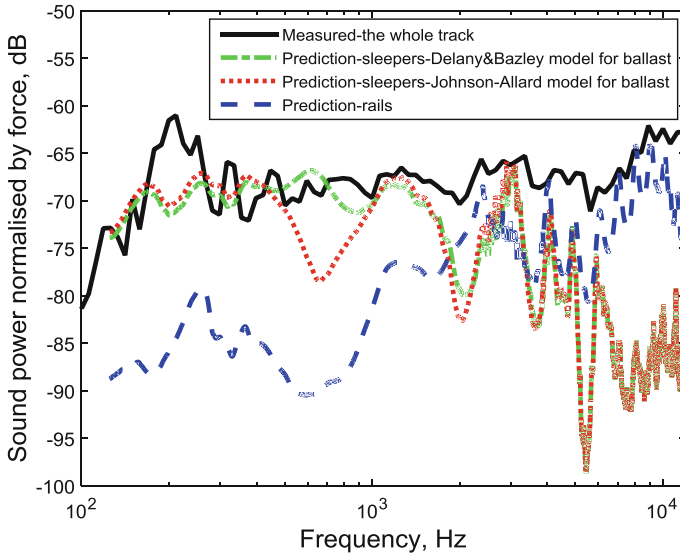


**Fig. 8** Comparison of measurements and predictions for the sound power of the scale model track shown in Fig. 5

to limitations in the assumption of local reaction, implied in the use of an impedance boundary condition in BEM, whereas an extended reaction model is more appropriate [13].

## 4 Application to Operational Track

Finally the current models for the sound radiation from the rail and sleeper are applied to an operational track. The noise from the track is predicted using the TWINS software which is modified to include the results of the new radiation models. These predictions are compared with existing measurements obtained at Fishbourne, UK [19]. The sound pressure spectrum was measured at a point 7.5 m away from the track and 1.5 m above the ground during the passage of Class 377 Electrostar EMUs at a speed of 118 km/h. The rail roughness and track decay rates were measured at the site and wheel roughness measurements were available from similar trains [19]. The pad stiffness was estimated as 120 MN/m for the vertical direction and 13 MN/m for the lateral direction. Results will be shown from the existing TWINS software and additionally two modified predictions including the effects of the ground on the sound radiation from the rail and sleeper, as shown in Figs. 3 and 4.

### 4.1 Prediction of the Sound Radiation from Different Components in the Track

The component of the sound pressure level from the sleepers at the microphone position is presented in Fig. 9. Results are shown for the original model and the updated models. As expected from the radiation ratios shown in Fig. 4, the contribution from the sleepers obtained by using the current models is lower than that obtained based on the original TWINS model. A strong dip can be seen at 160 Hz for the case based on the Johnson-Allard model due to the thickness effect.

The predicted sound pressure component from the rails at the microphone position is shown in Fig. 10. Results are again shown for the original model and the updated models. As can be seen, there are considerable differences between the results of these models at low frequency. However, in this frequency region the sleeper is actually the dominant source. Hence, although the contribution from the rails is obviously modified by the current models at low frequency, this difference will not affect the predicted total noise for a ballasted track such as this.

The sound pressure component from the wheels is shown in Fig. 11. This is unaffected by the changes introduced here. As can be seen by comparison with the other components, the wheel will become the dominant source at high frequencies, above about 2 kHz.

**Fig. 9** Predicted A-weighted sound pressure level of the component from the sleepers

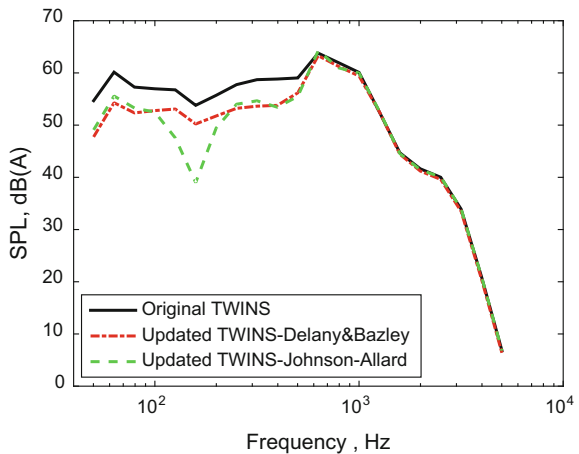


**Fig. 10** Predicted A-weighted sound pressure level of the component from the rails

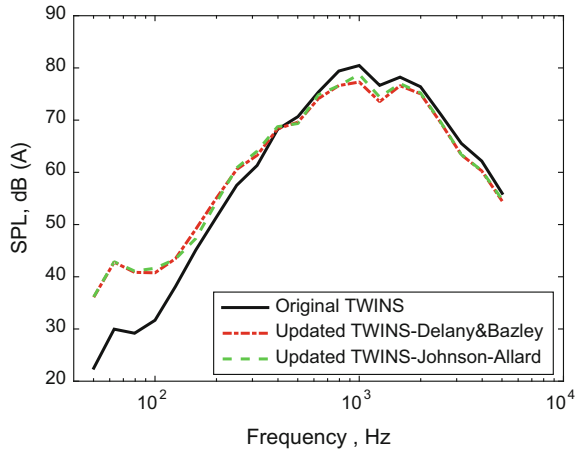
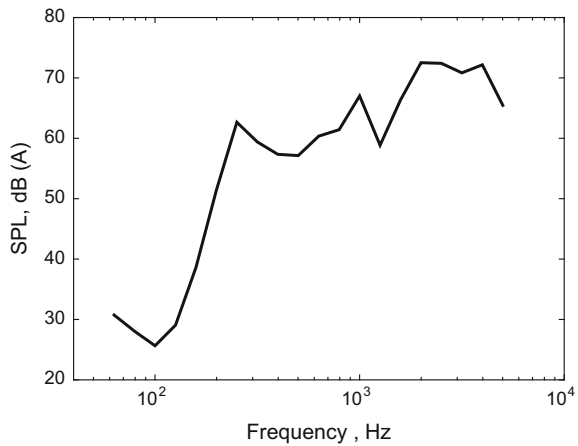


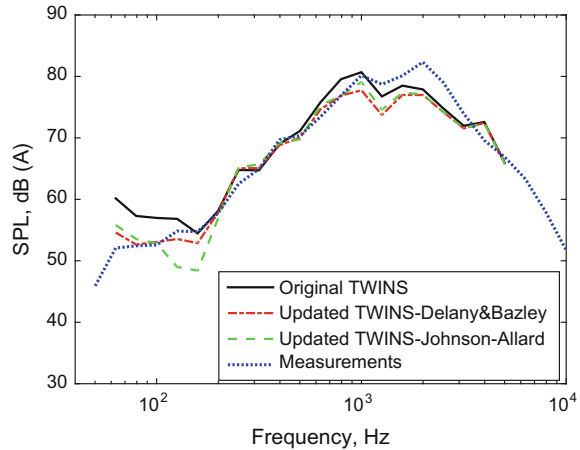
**Fig. 11** Predicted A-weighted sound pressure level of the component from the wheels



**4.2 Prediction of the Sound Radiation from the Whole Track**

The measured and predicted total A-weighted sound pressure levels are shown in one-third octave bands in Fig. 12. Good agreement can be seen between the measurements and the predictions from both the original and updated versions of TWINS, especially bearing in mind that the measured results are subject to a variation of  $\pm 3$  dB(A) in each 1/3 octave band due to variations in train speed, wheel roughness and temperature [19]. The new radiation ratios have a significant effect below 200 Hz, and in the current example show improved agreement with the measurements. The large dip at 125 Hz in the results based on the measured flow resistivity of the ballast is not consistent with the measurements whereas the results for the higher value of flow resistivity show better agreement. The differences

**Fig. 12** Comparison of A-weighted sound pressure spectra between different predictions and the measurements



between the models are smaller at higher frequencies, with a small reduction seen in the rail component between 800 and 1600 Hz. The wheel component dominates the noise above 2 kHz, which remains invariant in the different predictions.

## 5 Conclusions

A new model has been proposed to predict the sound radiation from the track using the boundary element method, taking account of the effects of the ground, including the ballast. Measurements have been performed of the flow resistivity, porosity and diffuse field absorption of 1:5 scale ballast. These are used with the Johnson-Allard model to represent the acoustic impedance. Good agreement can be found between the predicted absorption and the corresponding measurement results. The Delany and Bazley model is also used with a higher value of flow resistivity to obtain an alternative impedance for use in the numerical models. By taking the ballast absorption into account, it is found that the sound radiation from the rails and the sleepers are significantly affected, especially at low frequency. The models have been validated by measuring the sound radiation from a 1:5 scale track and comparing the results with the predictions. It is found that using the impedance derived from the Johnson-Allard model in the BEM models does not give satisfactory results, which is probably due to the need to account for extended reaction in the ballast layer. On the other hand using the Delany and Bazley model with a higher value of flow resistivity gives more satisfactory results. The models have finally been used with the TWINS software to predict the sound radiation from an operational track and comparisons have been made with field measurements. Differences are introduced in the sound radiation components predicted for the rails and the sleepers, particularly at low frequency. Good agreement is seen with field

measurements. The new models are found to give an improvement at low frequencies, where the sleeper is the dominant noise source.

**Acknowledgements** The work described here has been supported by the EPSRC under the programme grants EP/H044949/1, ‘Railway Track for the 21st Century (Track 21)’ and EP/M025276/1, ‘The science and analytical tools to design long life, low noise railway track systems (Track to the Future)’.

All data published in this paper are openly available from University of Southampton repository at <https://doi.org/10.5258/soton/d0013>.

## References

1. Thompson, D.J., Hemsworth, B., Vincent, N.: Experimental validation of the TWINS prediction program for rolling noise, Part 1: description of the model and method. *J. Sound Vib.* **193**, 123–135 (1996)
2. Thompson, D.J., Fodiman, P., Mahé, H.: Experimental validation of the TWINS prediction program for rolling noise, part 2: results. *J. Sound Vib.* **193**, 137–147 (1996)
3. Thompson, D.J., Janssens, M.H.A.: Track Wheel Interaction Noise Software, Version 3.0, Theoretical manual, TPD-HAG-MEMO-960343 (1996)
4. Zhang, X., Squicciarini, G., Thompson, D.J.: Sound radiation of a railway rail in close proximity to the ground. *J. Sound Vib.* **362**, 111–124 (2016)
5. Zhang, X., Thompson, D.J., Squicciarini, G.: Sound radiation of railway sleepers. *J. Sound Vib.* **369**, 178–194 (2016)
6. Broadbent, R.A., Thompson, D.J., Jones, C.J.C.: The acoustic properties of railway ballast. *Euronoise 2009*, Edinburgh
7. Attenborough, K., Boulanger, P., Qin, Q., Jones, R.: Predicted influence of ballast and porous concrete on rail noise, *Internoise 2005*. Brazil
8. BS EN 13450: 2013.: Aggregates for railway ballast
9. Zhang, X., Thompson, D.J., Squicciarini, G.: Effects of railway ballast on the sound radiation from the sleepers, *Euronoise 2015*. Maastricht (Netherlands)
10. Johnson, D.L., Koplik, J., Dashen, R.: Theory of dynamic permeability and tortuosity in fluid-saturated porous media. *J. Fluid Mech.* **176**, 379–402 (1987)
11. Allard, J.F., Atalla, N.: Propagation of sound in porous media: modelling sound absorbing materials. Wiley, Chichester (2009)
12. Delany, M.E., Bazley, E.N.: Acoustical properties of fibrous absorbent materials. *Appl. Acoust.* **3**, 105–116 (1970)
13. Heutschi, K.: Sound propagation over ballast surfaces. *Acta Acustica United Acustica.* **95**, 1006–1012 (2009)
14. Thompson, D.J.: *Railway noise and vibration mechanisms, modelling and means of control*. Elsevier, Amsterdam (2008)
15. Grassie, S.L., Gregory, R.W., Harrison, D., Johnson, K.L.: The dynamic response of railway track to high frequency vertical excitation. *J. Mech. Eng. Sci.* **24**, 77–90 (1982)
16. EN 15461:2008+A1:2010.: Railway applications. Noise emission. Characterization of the dynamic properties of track selections for pass by noise measurements
17. Squicciarini, G., Toward, M.G.R., Thompson, D.J.: Experimental procedures for testing the performance of rail dampers. *J. Sound Vib.* **359**, 21–39 (2015)
18. Fahy, F., Gardonio, P.: *Sound and structural vibration: radiation, transmission and response*, 2nd edn. Elsevier, Oxford (2007)
19. Squicciarini, G., Thompson, D.J., Toward, M.G.R., Cottrell, R.A.: The effect of temperature on railway rolling noise. *J. Rail Rapid Transit.* (2015). <https://doi.org/10.1177/0954409715614337>

# Friction Management as a Sustainable Solution for Controlling Noise at the Wheel-Rail Interface



R. Stock, M. Santoro, T. Makowsky, D. Elvidge and P. Xia

**Abstract** Noise phenomena generated by the rail/wheel interface can pose a major problem for urban railway operations. Friction Management can provide a sustainable strategy to mitigate multiple rail/wheel contact related noise effects including rolling noise, rumbling noise (caused by corrugation), wheel squeal, flanging noise and impact noise. As the term friction management refers to a combined application of gauge face lubrication and top of rail (TOR) friction control, special emphasis needs to be placed on the differences between the two aspects with respect to consumable products and their resultant noise mitigation capabilities. By analysing recent trial results and successful implementations as well as by referring to already published data, the opportunity for managing and controlling noise with optimised Friction Management strategies will be highlighted. This paper will primarily focus on the functional characteristics of a water based, drying friction modifier (FM) that was used in most of the referred studies and implementations. The positive implications of friction management are not only limited to noise mitigation. Consequently a wider, system based implementation approach needs to be considered in order to derive sustainable benefits for quiet and cost efficient railway operations.

## 1 Introduction

Noise phenomena related to wheel-rail contact issues can present a significant challenge for railway operators, especially in densely populated areas. Residential and ridership complaints, regional bylaws regulating allowable noise levels, and possible damaging impacts to vehicles and supporting track infrastructure can significantly impact the economics of railway operations. This paper will discuss the positive effects of Friction Management on mitigation of noise phenomena associated with different specific sources and generation mechanisms.

---

R. Stock (✉) · M. Santoro · T. Makowsky · D. Elvidge · P. Xia  
L.B. Foster Rail Technologies, Corp., 4041 Remi Place, Burnaby  
B,C V5A 4J8, Canada  
e-mail: rstock@lbfoster.com; r.stock@linmag.com

© Springer International Publishing AG, part of Springer Nature 2018  
D. Anderson et al. (eds.), *Noise and Vibration Mitigation for Rail Transportation Systems*, Notes on Numerical Fluid Mechanics and Multidisciplinary Design 139,  
[https://doi.org/10.1007/978-3-319-73411-8\\_57](https://doi.org/10.1007/978-3-319-73411-8_57)

## 2 Friction Management

Depending on the position of the wheel relative to the rail, different functional targets have to be achieved when managing friction between the two contacting bodies. For rail gauge face (GF)/wheel flange contact, the main objective is to reduce wear of both components. Consequently, a GF lubricant or grease is applied to lower the coefficient of friction ( $COF = \mu$ ) at the wheel-rail interface to a minimum threshold value typically  $< 0.25 \mu$ . On the top of rail (TOR), effects like squealing noise, damage development (wear, RCF—Rolling Contact Fatigue, corrugation, shelling, spalling, etc.) and energy consumption can also be positively influenced by proper friction management. The product of choice for TOR friction control is a Friction Modifier (FM), a material that reduces friction to an optimised level ( $0.35\text{--}0.40 \mu$ ) to produce positive benefits without adversely impacting safety of train operations.

Whereas GF lubrication has been in use since the early days of railroading, the concept of using a friction modifier for top of rail friction control was first introduced in late 1980s to mitigate problem wheel squeal and corrugation concerns at the newly commissioned Vancouver, B.C. Canada SkyTrain system [1]. A typical FM consists of a water-based suspension of dry solid materials with no liquid oil or lubricant content. The water acts as a carrier and quickly evaporates, leaving the dry FM particles to modify the rheological properties of the third body layer at the wheel-rail interface. A FM exhibits two main performance characteristics:

- Produces an intermediate coefficient of friction located between dry friction levels and well lubricated low GF friction levels (Fig. 1a). This will positively influence vehicle steering and associated dynamic lateral force generation, wheel-rail damage, and fuel consumption.
- Introduces positive traction characteristics between wheel and rail over relevant creepage ranges/application rates to prevent unwanted stick-slip effects that are associated with noise and damage effects (Fig. 1b).

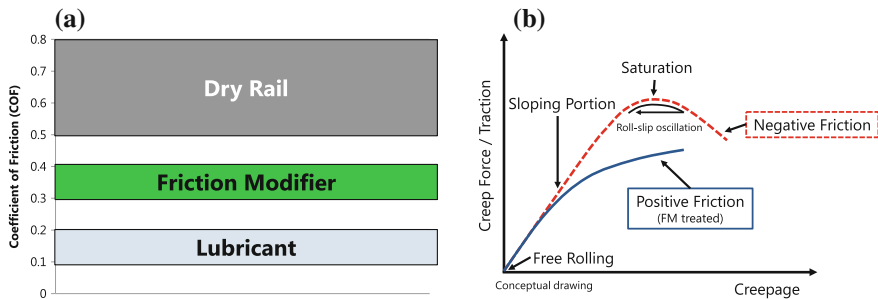


**Fig. 1** a Typical COF ranges for different rail/wheel contact conditions. b Traction creepage relationships for negative and positive friction characteristics



It is worth mentioning that a FM does not act as a traction enhancer. Only high friction levels can be altered by a FM. In the case of low adhesion (e.g. wheel slip) conditions, a FM will not have any impact on the already low friction levels.

Alternative materials have recently been promoted for TOR application. These materials are typically lubricant based (e.g. TOR oil, TOR grease, TOR hybrid products) but may also have solid particle and/or water content. These materials have limited or no field test data confirming noise abatement effectiveness [2]. This paper will focus on test results derived from a specific water-based FM product and refer to the other alternative material types as TOR lubricants.

### 3 Noise Phenomena in a Railway Environment

There can be several different noise phenomena present in a railway operating environment (list not complete) that are associated with the following different formation mechanisms and predominant frequency ranges [3, 4]:

1. **Rolling Noise (30–2500 Hz)**—Dependent on the combined surface roughness of wheel and rail. Undulations with wavelengths between 5 and 250 mm typically contribute to this category. High rail surface roughness (e.g. directly after grinding [5]) can generate increased noise in specific frequency ranges that are perceived as very unpleasant noise by nearby residents.
2. **Excessive Rumble Noise (200–1000 Hz)**—Predominantly caused by rail corrugation. Besides problematic noise, corrugation will also impart significant damage to track and vehicle components, thereby reducing the service life of railway infrastructure. This paper refers to roughness in typical corrugation wavelengths as macro roughness of wheel and rail (or roughness in a **cm** scale).
3. **Wheel Squeal (1000–5000 Hz)**—Produced by frictional instabilities at the top of rail surface caused by negative friction characteristics at the wheel-rail interface. Lateral creepage in curves can initiate wheel roll-slip oscillations that will excite wheel resonance leading to extreme noise emissions. Wheel squeal is typically the most prevalent problematic noise condition for Transit Railways (e.g. Light rail/Metro). Recent investigations also suggest mode coupling as an alternative mechanism for wheel squeal [6].
4. **Flanging Noise (5000–10,000 Hz)**—Hissing or grinding noise associated with high rail wheel flange contact in sharper curves. It can be differentiated from wheel squeal noise by the underlying mechanism as well as the resultant noise frequency range.
5. **Impact Noise from flat spots (50–250 Hz)**—Dependent on vehicle speed. Caused by singular (or quasi-singular) irregularities on the wheel surface producing a partial unloading or even separation of wheel from rail, followed by impact when the two surfaces re-engage.

## 4 Noise Mitigation with Friction Management

### 4.1 *Micro Roughness as Indicator for Rolling Noise Mitigation*

Although roughness on a  $\mu\text{m}$  scale is not directly impacting rolling noise it is used here as an example/indication how effective FM could be used to impact aspects of rolling noise through positively changing the surface roughness conditions of wheel and rail. A test was done at a North American light rail transit system using acrylic dental moulds to produce rail surface roughness replicas before and after a wayside FM application site in service for  $\sim 2$  years. The moulds were then sent to the National Research Council Canada (NRC) for analysis. The NRC performed 11 line scans on a representative  $2 \times 1$  cm area extracted from the TOR test site moulds, with a resolution of  $1 \mu\text{m}$  in scan direction (x direction = 2 cm) and a y distance between each line of 1 mm. The results of these scans (average values over 11 scans) are shown as a distribution plot in Fig. 2. A notable and immediate downward shift in surface roughness and a narrowing of the roughness distribution width was observed after the trackside TOR unit distribution bars (e.g. FM treated rail surface).

Another trial was done on a full scale, linear rail/wheel test rig at voestalpine Schienen GmbH in Austria. Although the trial focused on the impact of FM on RCF and wear, some surface roughness measurements were also recorded. A typical test lasted 100,000 wheel passes with heavy haul-like vertical and lateral loads applied. Tests were done under both dry and FM treated contact conditions. Details regarding general test set-up can be reviewed in [7].

Rail surface roughness measurements were performed after 100,000 loaded wheel passes and on new condition test rails provided by a rail mill, using a Mitutoyo Model SurfTest-212 surface profilometer. This instrument was calibrated before each measurement using a precision reference specimen ( $R_a 2.95 \mu\text{m}$ ). The instrument was also set to an overall 4.0 mm evaluation length and provided a  $R_a$  roughness parameter over this interval (arithmetic means of absolute values =  $\mu\text{m}$ ).

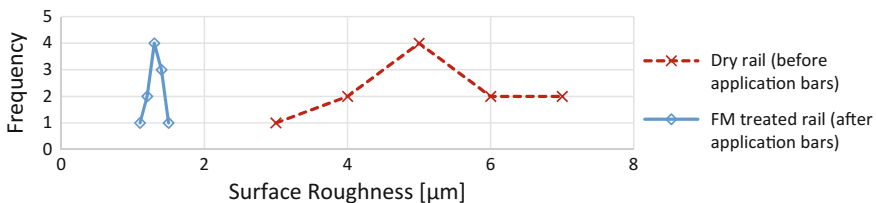


**Fig. 2** Roughness distribution measured on TOR surface replicas extracted before and after FM distribution bars. (Note Notable reduction in rail surface roughness after distribution bars due to FM application)

As the instrument used a stylus detector (parallel to measured surface), surface roughness measurements were performed in the longitudinal rail direction only. Twenty-six rail measurement locations were used, starting at the bottom edge of the gauge side and spaced approximately every 5 mm up around the rail profile until reaching the bottom field side corner. Figure 3a. b shows the Ra measurement plots overlaid on the measured rail profile for a dry test rail and a FM test rail (Note: rail profile recorded using a MINIPROF Rail instrument at the end of each test). A clear reduction in surface roughness for FM treated rail vs. dry rail after 100,000 wheel passes can be noticed for the marked conformal contact areas.

The Ra values listed in Table 1 compare the roughness conditions at two representative locations for each of the noted test rail conditions, as defined by the angle between their tangent to the rail surface and the horizontal line (TOR = 9.9° and Gauge Corner—GC = 35°) [7].

Table 1 results further validates FM ability to reduce rail surface roughness. Although real world track conditions will demonstrate different micro roughness values, FM application is still be expected to positively impact rail surface roughness development (µm).

### 4.2 Rumble Noise (E.G. Corrugation Growth Reduction)

Corrugations (periodic wave structure on the rail surface) can be found on all types of railway systems and track infrastructure. Corrugation can be classified according to the formation mechanism and appearance [8]. Especially for passenger and transit type operations, a specific corrugation type called short pitch corrugation can be predominantly found on the low rail of small to medium radius (50–500 m) curves. The most common sub-type of short pitch corrugation is called rutting corrugation which is attributed to a wavelength-fixing mechanism (excitation of all vehicles at the same location), a damage mechanism (wear), and stick-slip

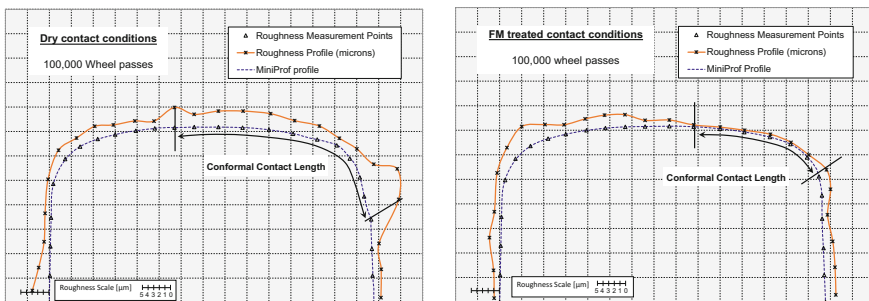


**Fig. 3** Comparison of surface roughness distribution along the transversal rail profile for dry (left graph) and FM treated (right graph) contact conditions after 100,000 wheel passes on a full scale test rig

**Table 1** Comparison of surface roughness results at two selected positions (TOR = 9.9°, GC = 35°) on the transverse rail profile for both test conditions and a new rail

Sample	Rail roughness, $R_a$ ( $\mu\text{m}$ )	
	TOR position	GC position
New	1.75	1.71
“Dry”	2.05	1.27
“FM”	0.49	0.50

oscillations of the wheel set [8]. A friction modifier can address both wear (reducing wear by providing an intermediate coefficient of friction) and stick-slip oscillations (by producing positive friction characteristics at the wheel-rail interface). FM application will additionally improve vehicle steering performance to mitigate or eliminate problematic wavelength-fixing mechanism effects.

Figure 4 contains results from a track test for a European commuter rail system [9]. Corrugations were measured using an Esveld RAILPROF instrument. The original conditions showed severe corrugation growth within 30 days after grinding at the test curve (R = 227 m, rail grade R260, 3% gradient, concrete sleepers on ballast) with a typical corrugation wavelength of 69–82 mm. After the installation of FM application systems in this curve, and grinding to remove existing corrugations, the corrugation growth rate was significantly reduced (Fig. 4). An improvement factor of 27 was recorded for Track 1 (Improvement factor definition: corrugation growth baseline divided by corrugation growth with FM application normalized to average corrugation growth per 30 days). A second adjacent track with the same curvature (Track 2—Data not shown in Fig. 4) demonstrated an improvement factor of 10.

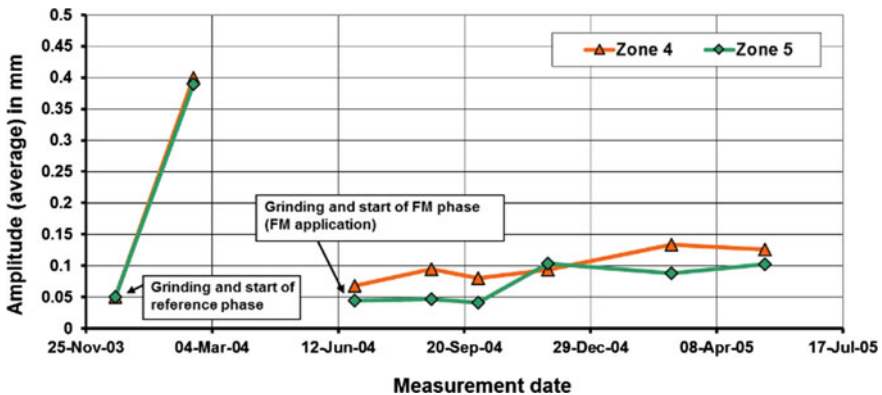


**Fig. 4** Corrugation measurements before and after FM implementation. Several measurements per data point were averaged (peak to peak amplitude)

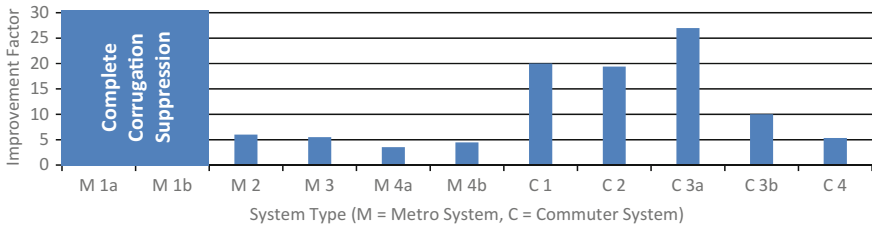


**Fig. 5** Overview of corrugation growth improvement factors for different metro and commuter systems. Curve radius varied between 40 m and 350 m, typical train speed between 30 and 65 km/h

An overview [10] of several additional successful implementations of FM as a means to mitigating corrugation growth is shown in Fig. 5. Corrugation reduction results range from complete growth suppression to a minimum improvement factor of 4, with a corresponding average improvement factor of 11 for this data. The noted variation in data strongly suggests an achievable improvement factor is highly dependent on the local conditions for each site (e.g. track construction, rail metallurgy, curvature radius, train speed, etc.).

Premium rail grades with higher wear resistance, along with an appropriate maintenance strategy (e.g. grinding/milling) removing corrugation and adjusting rail profiles to optimize vehicle steering, are also beneficial in reducing corrugation. Consequently, the best solution for mitigating corrugation growth and associated noise effects is a blended system approach incorporating all three of these key components (e.g. FM application, rail metallurgy, grinding/milling).

### 4.3 Flanging Noise and TOR Squeal Reduction Mitigation

Although flanging noise and TOR squeal are two separate phenomena with distinct frequency spectra, they are reviewed together in this sub-chapter given associated mitigation strategies are similar in nature. Flanging noise is directly related to contact between the wheel flange and rail GF, as derived from high dynamic lateral track loading in sharp curves ( $R < 500$  m). High friction and creepage conditions between the two contacting bodies will generate typical flanging noise significantly increasing noise levels in a broadband spectrum typically above 5000 Hz. GF lubrication is traditionally used to reduce friction levels at the GF/wheel flange interface to thereby mitigate flange noise generation. In some instances, infrastructure owners incorrectly conclude GF lubrication as also successfully mitigating TOR squeal. A closer review of these cases typically reveals unwanted GF grease migration to the TOR surface, reducing both squeal and flanging noise at the same time but consequently introducing negative impacts to train braking and tractive performance.

On TOR, the mechanism for curve squeal generation is associated with a frictional instability under lateral creep conditions in a curve. Due to the negative slope of the traction-creepage curve beyond creep saturation in dry contact conditions (see Fig. 1b), a further increase in creep levels will result in lower COF. This can lead to an unstable wheel response in the form of stick slip oscillations (or more accurately, roll-slip oscillations) causing (squeal) noise radiation [11]. A friction modifier can mitigate the formation of roll-slip oscillations due to its positive traction characteristics over relevant creepage ranges as shown in Fig. 1b. The impact of FM with respect to the mode coupling theory [6] is not examined in this paper. This will be part of possible future work.

An extensive track test was completed at a European Metro system to demonstrate the effectiveness of a water-based FM for squeal noise mitigation. Sound level measurements were performed using a Bruel & Kjaer 2260 Sound level meter equipped with a foam wind screen. The sound level meter was mounted on a tripod 6 meters from the center of the track (on the low rail side of the test curve), with the microphone 1.2 m above the top of rail surface. The sound level range was pre-set to between 50 and 130 dB for train passes (40–120 dB for ambient). The tests were conducted with manual application of the Friction Modifier in accordance to a defined procedure simulating application rates/volumetric output typically used during standard wayside unit operation.

Figure 6 compares baseline results with FM treated results for low rail (LR) only application, and for both high rail (HR) and LR application for a specific train type in a 195 m radius curve. The average sound pressure levels over time (averaged over three train passes per phase) for the two rail application strategy were clearly reduced compared to baseline results over the full length of the train. In the case of LR only application, a peak event was noticed that could be consistently associated with a specific car in the train consist (see Fig. 6: 20–25 Secs data interval on x-axis). For this particular test, the two rail application strategy only was successful in preventing wheel squeal.

The average frequency distribution results shown in Fig. 7 (averaged over three train passes per phase) mirrored the findings of the earlier average sound pressure

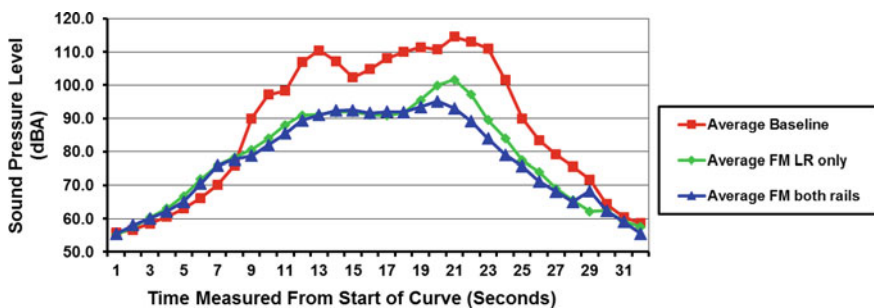


**Fig. 6** Average sound level over time measurements for different FM strategies—1 Rail (LR) versus 2 Rail application

levels analysis. A reduction in sound pressure level was recorded during the two rail FM application test phase (average 9.5 dB), especially in the frequency range associated with TOR squeal (1000–5000 Hz). For the LR only test phase the same data peak anomaly appeared, as caused by a specific car in the train consist (see Fig. 7: ~5000 Hz on x-axis). Figure 7 data further suggests positive FM impacts during the two rail application phase in the frequency range associated with wheel flanging noise (5000–10,000 Hz). It should be mentioned that system GF lubrication was not considered optimized during this trial. Further results with respect to squeal noise mitigation can be found in [11].

Figure 8 shows partial results from a trial in a heavy haul environment (mixed freight trains with 2 lead locomotives) where the baseline condition included optimized GF lubrication for the test curve. Comparing average values two baseline trains with two FM treated trains (averaged), FM application combined with GF lubrication consistently achieved effective noise reduction results in the frequency range above 1000 Hz. This can be attributed to improved steering and reduced flanging of the vehicles due to the FM application [12]. This trial incorporated noise monitoring protocols similar to those previously described for the other test initiatives.

Based on presented data (Figs. 7 and 8) and referenced literature [3, 11] as well as on observations in track the predominant sources of noise differ between heavy haul systems and transit/passenger systems. In a heavy haul environment wheel flange contact typically represents the main source of noise, whereas in transit systems TOR squeal is causing major problems. This needs to be considered when choosing the appropriate implementation strategy (GF lubrication and/or TOR friction control).

#### 4.4 Implications on Impact Noise Generation

Impact noise is caused by irregularities on the wheel and rail surface such as RCF damage (e.g. shelling), flat spots, wheel burns, welds, etc. Friction Management

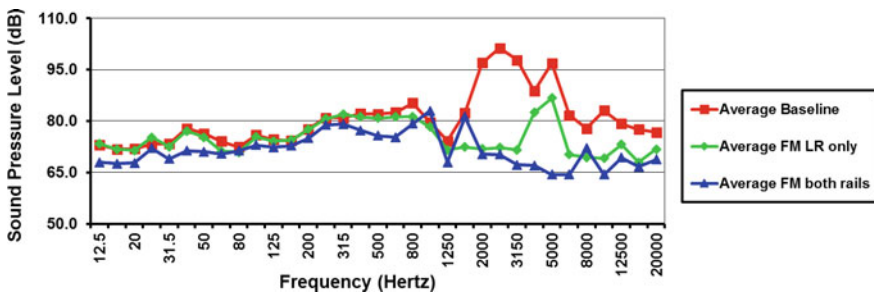
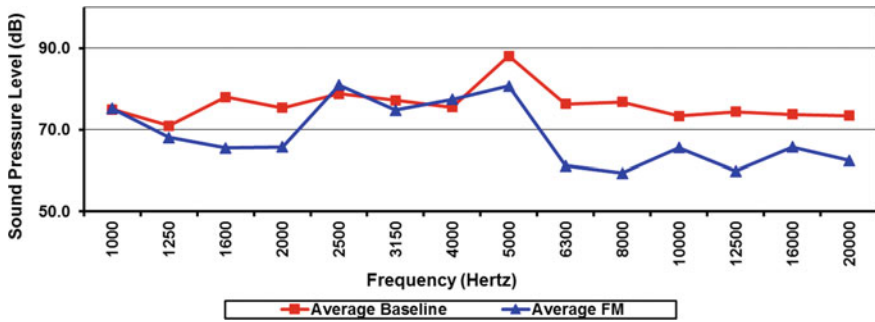


Fig. 7 Frequency distribution for different FM strategies—1 Rail (LR) versus 2 Rail application



**Fig. 8** Noise measurements in a heavy haul environment (1000–20,000 Hz). Average values of two trains per phase (baseline, FM)

(GF and TOR) has been proven to reduce RCF and wear development on rails and is therefore expected to also reduce the occurrence of RCF or wear-related impact noises. A recent study dealing with FM onboard technology operating under North American heavy haul conditions indicates the number of high impact wheel change-outs (impact loads > 400 kN) could be reduced by up to 75% for coal trains equipped with this onboard FM technology [13]. Although noise measurements were not part of this project, a reduction in the development of high impact wheel defects will conversely contribute to a reduction in noise generated by these same defects.

#### 4.5 Other Benefits of Friction Modifiers

Besides the positive impact on noise effects, the use of Friction Modifiers has also been proven to provide additional benefit with respect to track [14], rail/wheel damage [15] and fuel reduction related topics [16].

### 5 Implementation Considerations

The examples given in this paper are primarily based on well planned and rigorously executed trials. When it comes to incorporating an effective GF-TOR Friction Management program, a number of factors must be taken into consideration in order to achieve benefits comparable to those demonstrated in trials:

- **Application Strategy**—Choosing the appropriate application strategy (wayside vs. onboard) is dependent on size of the targeted problem area to be treated (e.g. A few individual sites vs. full network rollout), ownership rights of vehicle and track (e.g. Joint vs. Private ownership), and maintenance access/upkeep requirements.



- **Consumable Selection**—A wide range of consumables offering different cost and effectiveness levels are available, particularly with respect to conventional rail curve greases used for GF friction control. A review of the different product types used for TOR friction control was provided in Chap. 2 of this paper (Page 2). Consumable selection can involve both liquid and/or solid stick product groups depending on application strategy preference (e.g. wayside vs. onboard).
- **Maintenance Considerations**—Maintainability and uptime of GF-TOR friction management systems are among the most important factors for effectively mitigating noise effects. A system that does not consistently or effectively will not produce expected benefits. Even relatively short operating down times can produce irreversible damage requiring unplanned and expensive corrective maintenance actions.
- **Knowledge Management**—With changing employees and management restructuring, the original scope and intent for implementing GF-TOR friction control can get lost. Additionally, lack of an obvious problem (e.g. no curve squeal) can suggest an effective friction management program is not required or economically viable, consequently overriding “bigger picture” consideration of the broader technical and financial benefits of GF-TOR friction control.

## 6 Conclusions

The results presented in this paper highlight how friction management and especially TOR friction control can help to mitigate specific noise problems. Whereas GF lubrication effectiveness is limited to mitigating flanging noise, TOR friction control is able to reduce both TOR wheel squeal and flanging noise (1000–10,000 Hz). Furthermore, TOR friction control has been proven to reduce corrugation growth and positively influence surface roughness on a  $\mu\text{m}$  scale. Recent results also confirm that freight trains with onboard TOR friction control systems can significantly extend wheel life and reduce high impact incidents (e.g. delayed RCF formation on wheel tread).

It is very important to highlight that friction management is not a standalone solution. Similar to vehicle and track representing a system, friction management must be treated as a key component of a broader wheel-rail interface management system. It is important to understand its interaction with other key elements such as rail and wheel metallurgy, track geometry, rail and wheel profiles, and associated wheel and rail maintenance activities that collectively will assist to mitigate problem noise and other key track maintenance concerns.

## References

1. Kalousek, J., Johnson, K.L.: An investigation of short pitch wheel and rail corrugations on the Vancouver mass transit system. *Proc. Inst. Mech. Eng.* **206**(2), 127–135 (1992)
2. Stock, R. et al.: Material concepts for top of rail friction management—classification, characterization and application. *Proc. 10th Int. Conf. Contact Mech. CM2015* **9** (2015)
3. Eadie, D.T., et al.: Railway noise and the effect of top of rail liquid friction modifiers: changes in sound and vibration spectral distributions in curves. *Wear* **258**, 1148–1155 (2005)
4. Lewis, R. and Olofsson, U.: *Wheel-Rail Interface Handbook*. Woodhead Publishing (2009)
5. Schoech, W.: Considerations regarding noise reductions by means of rail grinding. *Rail Eng. Int.* **2015**(1), 4–6 (2015)
6. Thompson, D.J. et al.: A state-of-the-art review of curve squeal noise: phenomena, mechanisms, modelling and mitigation. In Anderson, D., et al. (eds.) *Noise and Vibration Mitigation for Rail Transportation Systems*. NNFM, vol. XX, pp XX–XX. Springer, Heidelberg (2018)
7. Eadie, D.T., et al.: The effects of top of rail friction modifier on wear and rolling contact fatigue: Full-scale rail–wheel test rig evaluation, analysis and modelling. *Wear* **265**, 1222–1230 (2008)
8. Grassie, S.L.: Rail corrugation: characteristics, causes and treatments. *Proc. IMechE, Part F: J. Rail Rapid Transit.* **223**, 581–596 (2009)
9. Eadie, D.T., et al.: Field studies of the effect of friction modifiers on short pitch corrugation generation in curves. *Wear* **265**, 1212–1221 (2008)
10. Beck, M. et al.: Rail corrugation growth in curves—friction management as a sustainable solution. *Proc. 24th Int. Symp. Dyn. Veh. Roads Tracks* **12** (2015)
11. Eadie, D.T., Santoro, M.: Top-of-Rail friction control for curve noise mitigation and corrugation rate reduction. *J. Sound Vib.* **293**(3–5), 747–757 (2006)
12. Roney, M. et al.: Implementation of distributed power and friction control to minimize the stress state and maximize velocity in Canadian Pacific’s heavy haul/heavy grade train operations. *Proc. Inst. Mech. Eng., Part F: J. Rail Rapid Transit* September 1, **224**(5), 465–471 (2010)
13. Elvidge, D. et al.: The effect of freight train mounted TOR-FM on wheel life and defects. *Proc. Third Int. Conf. Railway Technol.: Res. Dev. Maintenance* **17** (2016)
14. Chestney, M. et al.: The effect of top of rail friction control on a European passenger system: The Heathrow Express experience. *Proc. 8th Int. Conf. Contact Mech. Wear Rail/Wheel Syst. (CM2009)* **3**, 591–598 (2009)
15. Sroba, P. et al.: Canadian Pacific railway 100% effective friction management strategy. *Proc. Int. Heavy Haul Assoc. Conf. Rio de Janeiro* 93–102 (2005)
16. Cotter, J. et al.: Top of rail friction control: reductions in fuel and greenhouse gas emissions. *Proc. Int. Heavy Haul Assoc. Conf. Rio de Janeiro*, 327–333 (2005)

# Development of Supported Rail Vibration Models



W. Li and R. A. Dwight

**Abstract** A rail model that allows practical track conditions to be taken into account is presented. This model is based on the semi-analytical finite element method which discretises the cross-section of the rail using conventional finite element method while including the vibration along the rail as travelling waves. Three rail support models are considered: one is based on an *ad hoc* approach which represents the track support as an equivalent layer of springs and the others model the rail support by masses and massless spring-dampers. All of the models are developed to be able to account for multiple layers of rail support, namely, rail pads, sleepers and ballast. The track support parameters, i.e. rail pad stiffness and damping, ballast stiffness and damping are measured in the field via an impact hammer test on a tangent track. The numerical results obtained indicate that the *ad hoc* approach and the lumped mass based models have equally good performance. The 2-node mass element based model is not able to reflect the correct rail vibration behaviour. The usage of mass elements introduces extra degrees-of-freedom and results in additional computation time compared to the equivalent spring based model. It is therefore recommended to use a combination of the *ad hoc* approach to model the track support and the semi-analytical finite element method to model the rail to investigate rail vibration response on a site-by-site basis.

## 1 Introduction

Rail radiated noise is an important component of overall railway noise, resulting from wheel and rail interaction. Rail vibration behaviour has to be characterized in order to predict the acoustic radiation behaviour of a rail. Many rail vibration models have been developed: earlier models were analytical and beam-based, e.g., Euler-Bernoulli beams [1] and the Timoshenko beams [2–4] with and without the track support structures like rail pads and sleepers. Thompson and Vincent [5]

---

W. Li (✉) · R. A. Dwight  
University of Wollongong, Wollongong, Australia  
e-mail: wl948@uowmail.edu.au

presented a model with the rail pads, sleepers and ballast included, represented by an equivalent layer of springs. Both the periodic and the continuous models have been developed, to allow for the periodicity or continuity of the rail support. The effect of random spacing between sleepers on rail vibration has also been considered [6]. All of the beam-based models can take into account the vertical and lateral waves travelling along the rail, i.e. the bending waves. A more sophisticated model based on the Timoshenko beam but including the effect of the torsional wave has been developed by Heckl [7] where the coupling effect of various waves was included. However, a drawback in common for all of these beam-based models is that they are based on the beam assumption, i.e. the cross-section of the rail remains plane across the frequency range which does not hold at high frequencies.

To allow for the deformation of the rail cross-section, numerical models have been developed, usually based on the finite element principle. To model the almost infinite rail is numerically impossible if the conventional finite element software package is to be used. To address this limitation, two approaches that can take the waveguide nature of the rail into account are developed and reported in the literature. One is the 'wave and finite element method' (WFEM) and the other the 'semi-analytical finite element method' (SAFEM). Both of them allow the investigation of rail vibration into high frequencies; however, one excels the other at different conditions. In general, WFEM allows the use of available FE software to build the FE model and the inclusion of the periodic nature of a structure, whereas numerical difficulties may be encountered when solving the governing system of equations [8]. In contrast, SAFEM is better-conditioned in terms of the associated governing equations, but the model has to be developed on a case-by-case basis and periodicity of the waveguide is hard to include. Since it is reported that the impact of discrete support on rail vibration response is insignificant [9], SAFEM is sufficient to model the rail. The current work is based on SAFEM.

Models developed by the usage of SAFEM include [10, 11]. In [11], Bartoli et al. built a free rail model to look at wave propagation along the rail above 10 kHz; Nilsson et al. [12] developed a model to study rail vibration at the frequency range of interest to rolling noise, i.e. under 5 kHz with the rail support represented by a layer of continuous support representing rail pads. The layer of rail pads was modelled by FEs; Li et al. [13] presented a model where rail support is an equivalent layer of spring-mass-spring representing rail pads, sleepers and ballast, respectively. Track properties measured in the field are used therein and their results match those predicted by a Timoshenko beam at low frequencies.

It is arguable that conventional lumped mass and massless springs may also be used to model the track support and may possess similar performance to the *ad hoc* equivalent spring model developed in [13]. In this work the mass and massless spring based track support models are developed and compared against the model presented in [13].

## 2 Method

The governing equation of the SAFE rail model is given by

$$\left( \mathbf{K}_2(-i\kappa)^2 + \mathbf{K}_1(-i\kappa) + \mathbf{K}_0 - \omega^2 \mathbf{M} \right) \hat{\mathbf{U}}(\kappa) = \hat{\mathbf{F}}(\kappa) \quad (2.1)$$

where  $\kappa$  is the wavenumber of the waves travelling along the rail.  $\mathbf{K}_j$  ( $j = 0, 1, 2$ ) and  $\mathbf{M}$  are the system stiffness and mass matrices, respectively.  $\hat{\mathbf{F}}$  is the external force, applied at each node of the model.  $\hat{\mathbf{U}}$  accounts for the displacements at all degrees of freedom of the system. The hat over a variable denotes the Fourier transform of the variable in the spatial domain and  $i$  the imaginary unit. A bold font indicates a variable is a vector/matrix. For more information on the derivation of these matrices, the readers can refer to Li et al. [13].

### 2.1 Equivalent Spring-Mass-Spring Support Model

In this model, the track support is represented by a layer of continuous springs. The spring stiffness  $S$  is given by

$$S = \frac{s_p(-m_s\omega^2 + s_b)}{-m_s\omega^2 + s_b + s_p} \quad (2.2)$$

where  $s_p$  and  $s_b$  are the stiffnesses of the rail pads and ballast per unit length, respectively. The variable  $m_s$  is the sleeper mass per unit length. These parameters can be obtained from field tests. To combine this equivalent spring model with a FE-based rail model, i.e. to obtain a proper stiffness value at each of the nodes on the rail foot bottom,  $S$  is averaged over the width of the rail foot bottom. The stiffness at a node is calculated according to the width of the corresponding element bottom edge. Finally, the effect of the track support can be incorporated into the FE model as an external force, i.e.  $\mathbf{S}\hat{\mathbf{U}}$ , where  $\mathbf{S}$  is the matrix collecting the stiffness at all of the degrees of freedom of the system. For those nodes not on the rail foot bottom, a value of zero is used for the stiffness. It is noted that this model does not add any additional degree of freedom to the rail model and therefore reduces computational burdens significantly compared to models representing rail support components like rail pads with finite elements as in [12]. The modified governing equation then reads

$$\left( \mathbf{K}_2(-i\kappa)^2 + \mathbf{K}_1(-i\kappa) + \mathbf{K}_0 + \mathbf{S} - \omega^2 \mathbf{M} \right) \hat{\mathbf{U}}(\kappa) = \hat{\mathbf{F}}(\kappa) \quad (2.3)$$

## 2.2 Mass and Spring Based Support Models

The models to be presented are based on masses and massless springs. Different from the equivalent model described in Sect. 2.1, both the mass and spring elements depicted herein introduce new degrees of freedom. However, as will be shown, during assembly, only those associated with the mass elements will remain after the application of constraints.

Two different types of mass elements are proposed in this work. One is inspired by the beam model developed by Nilsson and Jones [14] and the other the lumped mass element.

### 2.2.1 Mass Element Model 1

The element is shown in Fig. 1. It is based on the assumption that a lumped mass sits between two nodes, N1 and N2. The non-dimensional distance between two nodes is assumed to be 2. The locations of N1, N2 and the lumped mass are assumed to be  $-1$ ,  $1$  and  $\zeta$ , respectively.

The displacement of the lumped mass in  $x$ ,  $y$  and  $z$  directions is denoted as  $\mathbf{u}_m = (u_m \ v_m \ w_m)^T$ . Similarly the displacements of two neighboring nodes are assumed to be  $\mathbf{u}_{n1} = (u_{n1} \ v_{n1} \ w_{n1})^T$  and  $\mathbf{u}_{n2} = (u_{n2} \ v_{n2} \ w_{n2})^T$ . The superscript  $T$  denotes transpose.

By further assuming the displacement varies linearly across  $(-1, 1)$ , the displacement of the lumped mass is given by

$$\mathbf{u}_m = \frac{1}{2}(1 - \zeta)\mathbf{u}_{n1} + \frac{1}{2}(1 + \zeta)\mathbf{u}_{n2} \quad (2.4)$$

Expanding this into 3D mass displacements yields

$$\mathbf{U}_m = \mathbf{T}\mathbf{q}_m \quad (2.5)$$

where

$$\mathbf{T} = \begin{bmatrix} \frac{1}{2}(1 - \zeta) & 0 & 0 & \frac{1}{2}(1 + \zeta) & 0 & 0 \\ 0 & \frac{1}{2}(1 - \zeta) & 0 & 0 & \frac{1}{2}(1 + \zeta) & 0 \\ 0 & 0 & \frac{1}{2}(1 - \zeta) & 0 & 0 & \frac{1}{2}(1 + \zeta) \end{bmatrix} \quad (2.6)$$

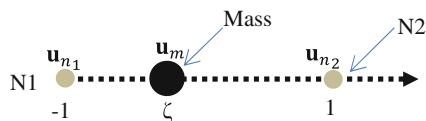


**Fig. 1** Mass element model 1: a lumped mass connected to two nodes.  $\mathbf{u}_{n1}$ ,  $\mathbf{u}_{n2}$  and  $\mathbf{u}_m$  are the displacements of node N1, node N2 and the lumped mass, respectively

and  $\mathbf{q}_m^{(e)} = (u_{n1} \ v_{n1} \ w_{n1} \ u_{n2} \ v_{n2} \ w_{n2})^T$ .

The governing motion equation of the mass in each of the three directions is given by

$$-\omega^2 m_a u_m = f_x \tag{2.7}$$

where  $u_m$  and  $f_x$  can be replaced by  $v_m$  and  $f_y$ ,  $w_m$  and  $f_z$ . Here  $f_x, f_y$  and  $f_z$  are the force components of the external force applied on the mass element in the  $x, y$  and  $z$  direction, respectively. The variable  $m_a$  is the element mass.

For one element, the virtual work of the external force,  $\delta W_m^{(e)}$ , is given by

$$\delta W_m^{(e)} = \int_z \delta \mathbf{q}_m^{(e)H} \mathbf{F}_m^{(e)} dz \tag{2.8}$$

where

$$\mathbf{F}_m^{(e)} = \mathbf{T}^T \mathbf{f}_m^{(e)} \tag{2.9}$$

the superscript  $H$  represents conjugate transpose and  $\mathbf{f}_m^{(e)} = (f_x, f_y, f_z)$ . Superscript  $e$  denotes the variable of interest is element-based and subscript  $m$  denotes the element is a mass element.

The first variation of the kinetic energy,  $\delta T_m^{(e)}$ , is given by

$$\delta T_m^{(e)} = \omega^2 \int_z \delta \mathbf{q}_m^{(e)H} \mathbf{M}_m^{(e)} \mathbf{q}_m^{(e)} dz \tag{2.10}$$

where

$$\mathbf{M}_m^{(e)} = m_a \mathbf{T}^T \mathbf{T} \tag{2.11}$$

Using the above assumptions, it is straightforward to include the mass element into the governing equation of the SAFE rail model which can then be written as:

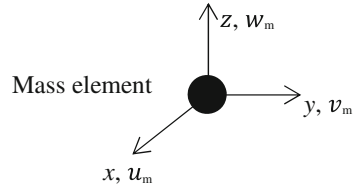
$$\left( \mathbf{K}_2 (-i\kappa)^2 + \mathbf{K}_1 (-i\kappa) + \mathbf{K}_0 - \omega^2 (\mathbf{M} + \mathbf{M}_m) \right) \hat{\mathbf{U}}(\kappa) = \hat{\mathbf{F}}(\kappa) \tag{2.12}$$

where  $\mathbf{M}_m = \bigcup_{e=1}^{n_{mel}} \mathbf{M}_m^{(e)}$ ,  $\hat{\mathbf{F}}(\kappa) = \bigcup_{e=1}^{n_{mel}} \mathbf{F}_m^{(e)}$ ,  $n_{mel}$  is the number of mass elements. It is noted that  $\hat{\mathbf{F}}(\kappa)$  includes all the external forces applied on the rail model including the mass elements.

### 2.2.2 Mass Element Model 2

The second mass element model is based on a lumped mass which has three degrees of freedom per element as shown in Fig. 2.

**Fig. 2** Mass element model 2: a lumped mass.  $u_m, v_m$  and  $w_m$  are the displacements of the mass element in  $x, y$  and  $z$  directions



The kinetic energy of a lumped mass element is given by

$$\delta T_m^{(e)} = \int \delta \mathbf{q}_m^{(e)H} \mathbf{M}_m^{(e)} \delta \mathbf{q}_m^{(e)} dz \tag{2.13}$$

where  $\mathbf{q}_m^{(e)} = (u_m, v_m, w_m)^T$ .  $z$  is the direction along the rail.  $\mathbf{M}_m^{(e)} = m_a \mathbf{I}_{3 \times 3}$  is the equivalent mass matrix.

The work due to external forces on the mass element is given by

$$\delta W_m^{(e)} = \int \delta \mathbf{q}_m^{(e)H} \mathbf{F}_m^{(e)} dz \tag{2.14}$$

where  $\mathbf{F}_m^{(e)} = (f_x, f_y, f_z)^T$  denotes the force applied on the mass element in the  $x, y$  and  $z$  directions. Substituting Eqs. (2.13) and (2.14) into Eq. (2.1) leads to a governing equation same to Eq. (2.12).

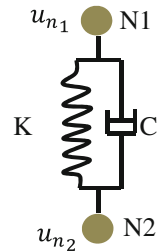
### 2.2.3 Massless Spring-Damper Element

A spring-damper element is shown in Fig. 3. Assumptions made on the spring-damper element include: (1) the spring element is 3D; (2) there is no coupling between different degrees-of-freedom; (3) the spring is massless; and (4) only translational degrees of freedom are considered.

Based on these assumptions, the spring stiffness and damping matrices are given by

$$\mathbf{K}_s^{(e)} = \mathbf{K}_s \mathbf{T}_s \tag{2.15}$$

**Fig. 3** Structure of a spring-damper element: N1 and N2 are the ending nodes of the element;  $K$  and  $C$  are the stiffness and the viscous damping of the spring element, respectively;  $u_{n1}$  and  $u_{n2}$  are the displacements of nodes N1 and N2





$$\mathbf{C}_s^{(e)} = \mathbf{C}_s \mathbf{T}_s \tag{2.16}$$

respectively, where

$$\mathbf{T}_s = \begin{bmatrix} 1 & 0 & 0 & -1 & 0 & 0 \\ 0 & 1 & 0 & 0 & -1 & 0 \\ 0 & 0 & 1 & 0 & 0 & -1 \\ -1 & 0 & 0 & 1 & 0 & 0 \\ 0 & -1 & 0 & 0 & 1 & 0 \\ 0 & 0 & -1 & 0 & 0 & 1 \end{bmatrix} \tag{2.17}$$

$\mathbf{K}_s = \text{diag}(k_1, k_2, k_3, k_1, k_2, k_3)$ ,  $\mathbf{C} = \text{diag}(c_1, c_2, c_3, c_1, c_2, c_3)$ . Here  $k_i$  and  $c_i$  ( $i = 1, 2, 3$ ) represent the stiffness and viscous damping in the  $x$ ,  $y$  and  $z$  direction, respectively.

The governing motion equation is given by

$$\mathbf{S}_s^{(e)} \mathbf{q}_s^{(e)} = \mathbf{F}^{(e)} \tag{2.18}$$

where  $\mathbf{F}^{(e)} = [f_{n1x} \ f_{n1y} \ f_{n1z} \ f_{n2x} \ f_{n2y} \ f_{n2z}]^T$  is the external force applied on the spring element at both of the ending nodes.  $\mathbf{q}_s^{(e)} = [u_{n1x} \ u_{n1y} \ u_{n1z} \ u_{n2x} \ u_{n2y} \ u_{n2z}]^T$  is the displacement of the spring element.  $\mathbf{S}_s^{(e)}$  is the equivalent element stiffness matrix which is given by

$$\mathbf{S}_s^{(e)} = \mathbf{K}_s^{(e)} + i\omega \mathbf{C}_s^{(e)} \tag{2.19}$$

It is noted that  $f_{n1x} = -f_{n2x}, f_{n1y} = -f_{n2y}, f_{n1z} = -f_{n2z}$ , due to the property of a spring. It is noted that node displacements are used directly in Eq. (2.18). A structural damping model may also be used, where the equivalent stiffness matrix is given by

$$\mathbf{S}_s^{(e)} = \mathbf{K}_s^{(e)} (I_{6 \times 6} + i \times \text{diag}(\eta_1, \eta_2, \eta_3, \eta_1, \eta_2, \eta_3)) \tag{2.20}$$

where  $\eta_i$  ( $i = 1, 2, 3$ ) is the structural damping ratio in  $x$  direction ( $\eta_1$ ),  $y$  direction ( $\eta_2$ ) and  $z$  direction ( $\eta_3$ ).

The first variation of the potential energy,  $\delta P_s^{(e)}$ , is given by

$$\delta P_s^{(e)} = \int_z \delta \mathbf{q}_s^{(e)H} \mathbf{S}_s^{(e)} \mathbf{q}_s^{(e)} dz \tag{2.21}$$

The virtual work,  $\delta W_s^{(e)}$ , done by external force is given by

$$\delta W_s^{(e)} = \int_z \delta \mathbf{q}_s^{(e)H} \mathbf{F}_s^{(e)} dz \tag{2.22}$$

where

$$\mathbf{F}_s^{(e)} = \mathbf{T}_s \mathbf{F}^{(e)} \tag{2.23}$$

By further including the spring elements into governing Eq. (2.12), we can get

$$\left( \mathbf{K}_2(-i\kappa)^2 + \mathbf{K}_1(-i\kappa) + (\mathbf{K}_0 + \mathbf{K}_s) - \omega^2(\mathbf{M} + \mathbf{M}_m) \right) \hat{\mathbf{U}}(\kappa) = \hat{\mathbf{F}}(\kappa) \tag{2.24}$$

where  $\mathbf{K}_s = \bigcup_{e=1}^{n_{sel}} \mathbf{S}_s^{(e)}$ ,  $n_{sel}$  is the number of spring elements; the external force  $\hat{\mathbf{F}}(\kappa)$  includes the both those applied on the mass elements and the spring elements as well as those applied on the rail.

The rail model with the proposed support models can then be summarized into a diagram which is shown in Fig. 4.

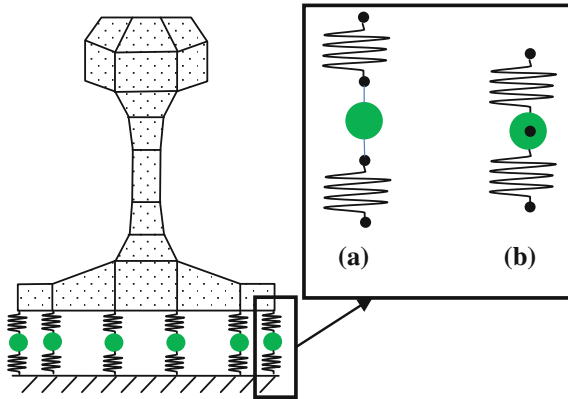


**Fig. 4** SAFE rail model with support represented by mass and spring elements. Mass, spring and mass, from top to the bottom, represent rail pads, sleepers and ballast; **a** and **b** shown on the right hand side of the rail model are mass-spring elements based on the mass element models presented in Sect. 2.2.1 and Sect. 2.2.2, respectively. It is noted that each small dot is a node and each big solid circle is a mass element. It is further noted that the mass element coincides with spring nodes shown in model (b)

**Table 1** Track parameters determined from field tests [13]

Rail (UIC60)	Vertical	Lateral	Longitudinal
Bending stiffness (M N m <sup>2</sup> )	6.42	1.07	–
Timoshenko shear coefficient	0.4	0.4	–
Loss factor	0.03	0.03	–
Mass per unit length (kg)	60	60	–
Young's modulus (GPa)	210	210	–
Poisson's ratio	0.3	0.3	–
Density(kg m <sup>-3</sup> )	7850	7850	–
<i>Rail pad</i>			
Stiffness (M N m <sup>-1</sup> )	600	50	50
Loss factor	0.5	0.5	0.5
<i>Ballast</i>			
Stiffness (M N m <sup>-1</sup> )	10	40	40
Loss factor	0.15	0.03	0.03
Sleeper (Mono-bloc)			
Spacing (m)	0.6	0.6	0.6
Mass (kg)	300	300	300

### 3 Track Parameters

The parameters for the track support components, like stiffness and damping, are shown in Table 1. These parameters were determined by tuning a Timoshenko beam model to the measured rail response [13].

### 4 Results and Discussion

Based on the spring and mass elements proposed in this work, together with the determined track parameters, the forced rail responses are calculated using the three track support models. Their results are compared against each other and the predictions of the *ad hoc* model presented in Li et al. [13]. It is noted that the mass and spring stiffness for each of the mass and spring elements shown in Fig. 4 are the same as those used by Li et al. [13]. The coarse mesh presented in Li et al. [13] is used. A refined mesh is only necessary when acoustic radiation of the rail is of interest. Therein the *ad hoc* model was found to agree with the Timoshenko beam model on the predicted rail responses. The latter has been regularly used in engineering practice. The results are replicated from Li et al. [13] without further explanation.

It is assumed that the lumped mass is located at the middle of the nodes of the proposed mass element in Sect. 2.2.1 in the following calculation, i.e.  $\zeta = 0$ .

The calculated rail mobilities excited by a point force at the top center of the rail head are shown in Fig. 5. Here it shows that (1) a good agreement between the *ad hoc* model and model (b) of Fig. 4 is achieved throughout the frequency of investigation but (2) a big discrepancy is observed between model (a) of Fig. 4 and the other two models at frequencies below 1 kHz.

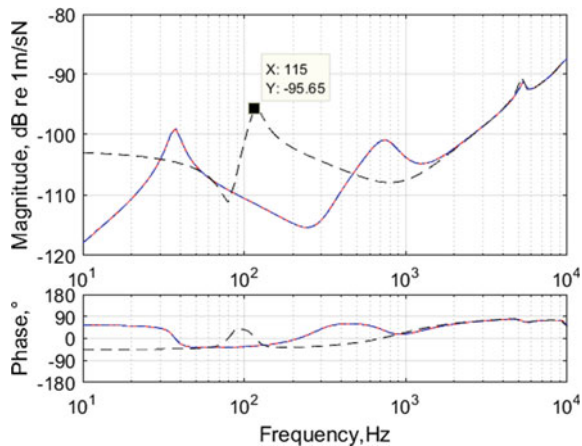
It can be verified using the values given in Table 1 that the first peak of mobility corresponding to the *ad hoc* model as well as model (b) of Fig. 4 is the resonant frequency of rail and sleeper masses on the ballast stiffness and the second peak is the resonant frequency of the rail mass on the rail pad stiffness.

To further understand the discrepancy observed in Fig. 5, a simplified model is built and shown in Fig. 6a. Here  $m_r, m_s, s_p, s_b$  denote rail mass, sleeper mass, pad stiffness and ballast stiffness, respectively. The mass element representing sleepers has two ends, both of which can move freely. The displacements of rail and sleepers are represented by  $u_1, u_2$  and  $u_3$ , respectively. The corresponding governing equation is

$$\left( \begin{bmatrix} s_p & -s_p & 0 \\ -s_p & s_p & 0 \\ 0 & 0 & s_b \end{bmatrix} - \omega^2 \begin{bmatrix} m_r & 0 & 0 \\ 0 & \frac{1}{4}m_s & \frac{1}{4}m_s \\ 0 & \frac{1}{4}m_s & \frac{1}{4}m_s \end{bmatrix} \right) \begin{pmatrix} u_1 \\ u_2 \\ u_3 \end{pmatrix} = 0 \quad (4.1)$$

By solving Eq. (4.1) one can get the only effective natural frequency of the system to be  $\sqrt{\frac{(m_s + 4m_r)s_p s_b}{m_r m_s (s_p + s_b)}}$ , or, 117 Hz by substituting the parameter values, which matches the frequency at the marked position in Fig. 5. Rail mobilities obtained by using the two models of different details are shown in Fig. 6b. Here it shows a good agreement up to the peak. The rail mobility is mass dominant at low frequencies

**Fig. 5** Rail driving point mobilities under a vertical point excitation at the top centre of the rail head calculated by using: — rail with an *ad hoc* support model; - - model a of Fig. 4 and - • - model b of Fig. 4



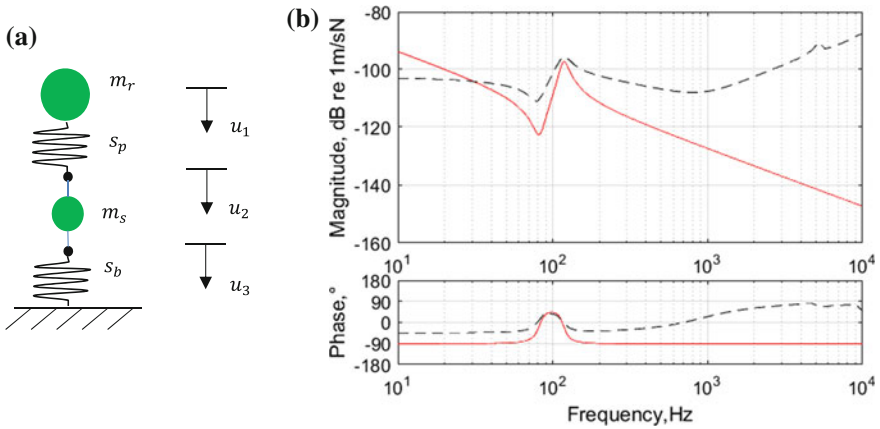


**Fig. 6** Simplified mass-spring-mass model to represent model a of Fig. 4: **a** schema; **b** rail driving point mobilities obtained from: — the simplified model and – – model a of Fig. 4

because the mass element representing the sleepers is capable of free movements at both ends which results in a free and suspended rail. This indicates that model (a) of Fig. 4 is inadequate to represent real track support.

## 5 Conclusions

Rail models based on SAFEM are presented. Three models are proposed to include the track support structures. By comparing the driving point responses at the top center of the rail head under a vertical point excitation, the *ad hoc* model assuming the support to be an equivalent layer of springs is found to agree well with the rail model with the support represented by 1-node lumped mass and massless spring-damper elements. The 2-node mass and massless spring-damper element based model, however, differs from the other two significantly and could not generate rail vibration close to reality. Both of the support models making use of independent mass elements introduce extra degrees-of-freedom, compared to the *ad hoc* model. The *ad hoc* rail model is therefore more computationally efficient and more implementations of the model to cater for real track conditions are recommended.

**Acknowledgements** This work was financially supported by the CRC Rail Innovation Project R128. It was under the assistance of RailCorp that the field measurements were conducted.

## References

1. Knothe, K., Grassie, S.L.: Modelling of railway track and vehicle/track interaction at high frequencies. *Veh. Syst. Dyn.: Int. J. Veh. Mech. Mobility* **22**(3&4), 52 (1993)
2. Grassie, S.L., Gregory, R.W., Johnson, K.L.: The dynamic response of railway track to high frequency lateral excitation. *J. Mech. Eng. Sci.* **24**(2), 91–95 (1982)
3. Grassie, S.L., Gregory, R.W., Johnson, K.L.: The dynamic response of railway track to high frequency longitudinal excitation. *J. Mech. Eng. Sci.* **24**(2), 97–102 (1982)
4. Grassie, S.L., et al.: The dynamic response of railway track to high frequency vertical excitation. *J. Mech. Eng. Sci.* **24**(2), 77–90 (1982)
5. Thompson, D.J., Vincent, N.: Track dynamic behaviour at high frequencies. Part 1: theoretical models and laboratory measurements. *Veh. Syst. Dyn.* **24**(sup1), 86–99 (1995)
6. Wu, T.X., Thompson, D.J.: The influence of random sleeper spacing and ballast stiffness on the vibration behaviour of railway track. *Acta Acustica united Acustica* **86**(2), 313–321 (2000)
7. Heckl, M.A.: Coupled waves on a periodically supported Timoshenko beam. *J. Sound Vib.* **252**(5), 849–882 (2002)
8. Waki, Y., Mace, B.R., Brennan, M.J.: Numerical issues concerning the wave and finite element method for free and forced vibrations of waveguides. *J. Sound Vib.* **327**(1–2), 92–108 (2009)
9. Thompson, D.J.: Wheel-rail noise generation, Part III: rail vibration. *J. Sound Vib.* **161**(3), 421–446 (1993)
10. Hayashi, T., Tamayama, C., Murase, M.: Wave structure analysis of guided waves in a bar with an arbitrary cross-section. *Ultrasonics* **44**(1), 17–24 (2006)
11. Bartoli, I., et al.: Modeling wave propagation in damped waveguides of arbitrary cross-section. *J. Sound Vib.* **295**(3–5), 685–707 (2006)
12. Nilsson, C.M., et al.: A waveguide finite element and boundary element approach to calculating the sound radiated by railway and tram rails. *J. Sound Vib.* **321**(3–5), 813–836 (2009)
13. Li, W., Dwight, R.A., Zhang, T.: On the study of vibration of a supported railway rail using the semi-analytical finite element method. *J. Sound Vib.* **345**, 121–145 (2015)
14. Nilsson, C.M., C.J.C. Jones, Theory Manual for WANDS 2.1 Wave-number-domain FE-BE Software for Structures and Fluids. 2007, University of Southampton, Institute of Sound and Vibration Research

# Characterization of Train Fleet Wheel Condition in a Metro



K. G. Albindo, C. J. Ng, T. P. Ng and W. L. Chia

**Abstract** The wheel condition of a metro fleet (>100 trains) is characterized based on train passby noise and wheel maintenance records over a four-year period. The initial objective was to identify wheel flats from noise measurements. The base unit of measurement is the maximum value of  $L_{Aeq,1s}$  from individual train passbys. These quarterly operation data are processed and ranked on a normalized scale, to provide an indication of the fleet performance. The change in the distribution of the train fleet wheel condition, on the normalized scale, is charted over time with the use of histograms. Further analyses are conducted, with the dataset sub-divided into two parts: the outliers (noisy trains) and the remaining data points. The outlier information is reviewed with wheel maintenance records, in an attempt to generalize descriptors like wheel defect severity, gestation period and location. The remaining data points are used to characterize the performance of each train type within the fleet. A relative performance comparison between the four train types in the fleet is attempted. The noise-based analyses indicate that there is a differentiation in terms of likelihood of wheel defect formation for a given time period and train passby noise emission. Using actual noise measurements and the derived characteristics of each train type, train traffic scenarios are simulated and compared to published National Environment Agency (NEA) guideline. The same baseline information is also used to simulate wheel maintenance optimization, with the objective of not exceeding the NEA noise emission guideline. It incorporates the increased train traffic expected with the new train signaling system. The paper is concluded with discussions on potential maintenance optimization and expected conditions with the increased train traffic.

---

K. G. Albindo (✉) · C. J. Ng · T. P. Ng · W. L. Chia  
SMRT Trains Ltd., 251 North Bridge Road, Singapore 179102, Singapore  
e-mail: kevingunawan@smrt.com.sg

© Springer International Publishing AG, part of Springer Nature 2018  
D. Anderson et al. (eds.), *Noise and Vibration Mitigation for Rail Transportation Systems*, Notes on Numerical Fluid Mechanics and Multidisciplinary Design 139, [https://doi.org/10.1007/978-3-319-73411-8\\_59](https://doi.org/10.1007/978-3-319-73411-8_59)

# 1 Introduction

The main contribution of noise emission from a metro train passby can be attributed to its wheel-rail interaction. Changes to the rolling contact condition arising from either component will affect this dynamic interaction, which influences the noise emission profile. A series of field measurements and laboratory studies had been performed by Thakkar et al. in order to understand the effect of wheel defects on the acoustic emission of wheel-rail interaction [1]. From railway operator perspective, noise emission from railway is regulated by law specific to the country. Assessment of noise pollution from Italian railways was attempted in order to understand the origin of noise emission and reduce its level to the allowable value [2].

In this paper, quarterly noise measurements over a four-year period are presented as an inference to the wheel condition of a metro train fleet. The charted records reflect the condition improvement based on a better (more even) distribution across noise emission levels while keeping a consistently low number of trains with high passby noise emission (outliers). The results provide an account of the train fleet performance with the use of a derived normalized scale (Noise Index) for each of the four train types that make up the fleet; and their respective average rate of Noise Index Escalation to reach a stipulated criterion. This criterion is also used to classify outliers, which are analysed separately by tabulating a sample of results and comparing them with maintenance records, to associate the observed wheel condition for a given Noise Index.

The assignment of a Noise Index to each train passby naturally lends itself to a ranking process to form a prioritization framework for maintenance. It represents an attempt to emulate condition-based maintenance where the outliers are highlighted for maintenance intervention; and the average time between wheel maintenance is calculated for each train type, to keep the passby noise below the stipulated criterion. The process of these characterizations also collated the typical background noise, noise emission profile and proportion of each train type and outliers. These are used to create the basis for noise measurement simulations where comparisons to actual measurements are made at two locations to establish coherence. The simulation is subsequently used to estimate the expected increased noise level with the to-be-completed new signaling system that will see an increase in train traffic throughput. The outcome is discussed in relation to the published NEA guidance of  $L_{Aeq,1 \text{ hr}} 67 \text{ dBA}$ .

## 2 Methodology

### 2.1 Measurement Concept

A time-based wheel maintenance schedule is typically adopted with regular checks in between scheduled wheel maintenance to assess train wheel condition in SMRT. During these regular checks, wheels found to have a certain wheel flat severity



undergo re-profiling as needed. However, flats of varying severity develop between checks from events such as a loss of rolling traction (un-intended wheel slide) from wet rail condition; and variability in condition assessment exists owing to checks being performed by different staff at different times for different trains. The situation is further complicated with a potential judgement call by staff on the expected rate of aggravation of a discovered small wheel flat. From these considerations, the idea of using noise as an unambiguous descriptor and to provide a frame for prioritization over a given timeframe is embarked on. It aims to form a condition monitoring system. The motivations included the creation of periodic snapshots of the train fleet wheel condition and providing a link to published noise emission guidelines.

In most cases of environmental noise, the differentiation of various noise contributors is important. Railway noise can be categorized into three sources: rolling, traction and aerodynamic noise. For train speeds below 200 km/h, the rolling noise is the main source of railway noise compared to the other two sources [3]. In this study, the train operating speed is below 100 km/h, which consequently allows the analysis of train passby noise to establish a correlation between train noise and wheel condition.

Based on the collected data, the noise characteristic from the railway source (train passby) can be differentiated from other noise emitting sources. A departure from background noise level can be observed at the location of measurement during the train approach. An upward progression from the background noise level will culminate and hover at a certain plateau value, before a drop back to the background noise level as the train moves further from the measurement location. This noise profile is distinct from other sources due to the same time period taken for the upward progression and the drop, for a given train passby at constant speed. Based on this distinctive feature, the sound energy value  $(L_{AE})_i$  related to the  $i$ -th single event of train passby can be identified. The equivalent sound level calculated on the two reference periods  $(L_{Aeq,T})$  is a commonly used measurement unit in environmental noise study which is governed by the Eq. (2.1) used in [2].

$$L_{Aeq,T} = 10 \log \left[ \frac{1}{T} \sum_{i=1}^n 10^{0.1(L_{AE})_i} \right] \text{dB(A)} \quad (2.1)$$

where  $T$  is the time period of measurement and  $n$  is the number of train passbys during the period  $T$ .

## 2.2 Measurement Setup

Bies & Hansen describes the three regions of sound field radiated by a source in a free field: the hydrodynamic near field, the geometric near field, and the far field [4]. It is further explained that measurements of the acoustic pressure amplitude in the

near field give no indication of the sound power radiated by the source. For the geometric near field, although radiated sound power can be calculated from a sufficient number of sound pressure measurements, the determination of a sufficient number of measurements becomes a challenge which consequently requires a great number of measurements to determine when further measurements would appear to provide no improvement. It is therefore favorable to perform sound pressure measurement in the far field where the source directivity is well defined.

The presence of other noise contributors during the measurement is inevitable. For example, major roads adjacent to a railway track will affect the measured noise level emission. A measurement method was studied by Italian Railways to discriminate railway noise events from other noise contributors. It uses two measurement points with one of them close to the railway tracks to serve as a reference point [2]. For the measurements used in this paper, an observer is stationed at the measurement location to log information such as time and identification number of each train passby. Any uncertainty or spurious events in the measurements are flagged and excluded from analysis to minimize ambiguity and unwanted influence. The outcome is a set of distilled good quality data from each session of two-hour noise measurement.

Another factor affecting the noise level measurement is the condition of the rail at the measurement site. Cases of rail corrugation were observed at different time periods during the four years at one of the sites. The wheel-rail interaction on corrugated rail is more complex and produce higher noise level than normal rolling noise [5]. The observed influences include significantly higher noise levels that mask the normally observed noise level gradation across the different train passbys. Due to the complexity and insufficient distinction of noise levels within the train fleets, any measurement data affected by corrugation is omitted from analysis. To ensure the quality of measured data, the following criteria are used to determine the suitability of measurement sites:

- Distance between the sound level meter to the track is in the range of 30–60 m
- Line of sight to the track from sound level meter location
- The speed of train passby should be constant
- Absence of any visible rail corrugation.

The noise measurements are conducted using a sound level meter at two locations every quarter. At each location, four sets of two-hour measurement are performed within two-week period. A calibration check is performed before and after each two-hour measurement to ensure the integrity of the captured data. Train number of each passby is recorded in order to assign the measured noise level to the correct train. The noise descriptor value extracted to provide data points for post-measurement processing and analysis is  $L_{Aeq,1s}$ .

### 2.3 *Relationship Between Wheel Flat and Noise Level*

The identification of trains with bad wheel condition was performed on the assumed correlation between the passby noise level and the presence and/or severity of wheel flat. In other words, a higher train passby noise level could indicate the presence of a wheel flat and/or one with a certain level of severity [6]. This assumption is supported by the hybrid model for wheel/track dynamic interaction and noise generation due to wheel flats presented in [7]. The simulation model demonstrates a higher noise emission for a wheel flat of 2 mm depth compared to a 1 mm wheel flat. In Sect. 3.2, a qualitative correlation between wheel flat size and noise level is attempted based on a sample of outlier train passby noise.

### 2.4 *Benchmarking of Train Fleets*

The noise measurements are carried out at two sites to cover the two main lines operated by SMRT. They are namely the North-South Line and the East-West Line. At each site, a series of four two-hour noise measurements are performed within a two-week period to capture a substantial number of train passby. There will be a difference in the absolute noise level, if the same train was to pass the two different measurement sites. This is due to the different environmental characteristics and measurement distance from the track. However, the shape of the noise profile (Fig. 5) of each train passby is generally similar. This shape has a characteristic “plateau” lasting about 6 s. It represents the central portion of a six-car train passing the point that is closest to the sound level meter at a speed of 70–80 km/h. The analogy is that of a moving constant noise emitting line-source where a single point receiver (sound level meter) receives the influence from various portions of the moving line. At the central portion of the moving line-source, the sound level meter registers a “plateau” of maximum noise level. An interesting observation is that if there is a sizeable wheel flat in one of the 12 double-axle bogies of the train, a “peak” manifests itself above this “plateau” of noise level. From the perspective of the microphone, the overall noise level is the contributive sum of different sections of a moving train. At the point where a flat is closest to the microphone, for one that is located in the middle of the train, the noise contributions includes that from the flat and the sections preceding and after it. Should a flat be located on the first or last bogie of the train, contributions from train sections preceding or coming after, will be absent. Hence leading to a relatively muted “peak”.

The data processing collates all eight measurement sets, from the two sites, onto a derived normalized scale (Noise Index). The Noise Index is a relative scale based on the lowest train passby noise recorded in each measurement session. This lowest measured passby noise is assigned a zero index and is dependent on the data set. The gradation, however, from 0 to 10 is always the same and is proportional to the dB scale. The data point for each passby is the maximum  $L_{Aeq,1s}$  of the “plateau” or

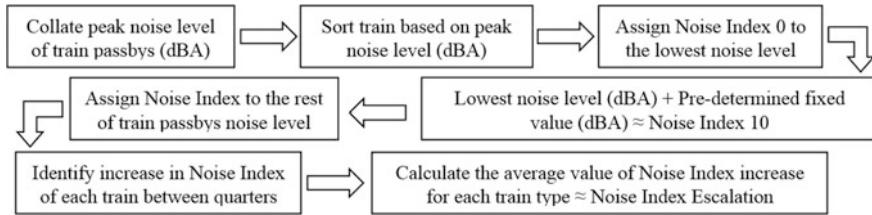


**Fig. 1** Process flow in deriving noise index and noise index escalation

the “peak” if any. Statistical analysis is used to calculate the mean and the percentage deviation from it. Note that the basis behind combining data sets from different time of measurement and different locations is the use of relative scales and the leverage on the large train passby data. In comparing different measurement times, the few quietest trains (likely just after wheel maintenance) passby noise levels are used as the datum and in comparing different locations, a group of trains will invariably appear across all data sets and hence could be used as reference for collation, on the assumption that wheel condition remained the same in the two-week period. The outcome is a relative measure of noise index that has an arbitrarily set scale of 0 to 10 where the noisiest train passby will register higher noise indices. This Noise Index is used to track the wheel condition degradation rate (Noise Index Escalation), which will be discussed in the next section. Figure 1 summarizes the process in deriving Noise Index and Noise Index Escalation.

### 3 Measurement Result and Analysis

#### 3.1 Overall Train Fleet Performance and Characterization Based on Train Type

The train fleet on the two metro mainlines operated by SMRT is made up of four train types. On average, the total number of unique train passby is 60% of the train fleet size, after excluding passby data that are affected by unintended noise influences (like those from road traffic car horn). The performance comparison across the four train types based on Noise Index (NI) is shown in Fig. 2. Train Type 1 is found to be the best performing, registering low NI values over 15 quarters. The wheel condition deterioration rate (Noise Index Escalation) for each train type is also calculated based on data points below the stipulated criterion of NI 6. The same criterion is used to categorize outlier data, which is analyzed in the next sub-section.

The subplots in Fig. 2 each show two envelopes, highlighting the NI of the top two noisiest train passbys. Significant departures between the two are observed on occasions. This is highlighted with the knowledge that wheel maintenance is typically conducted in sequence of train type at regular time/mileage intervals. Hence if

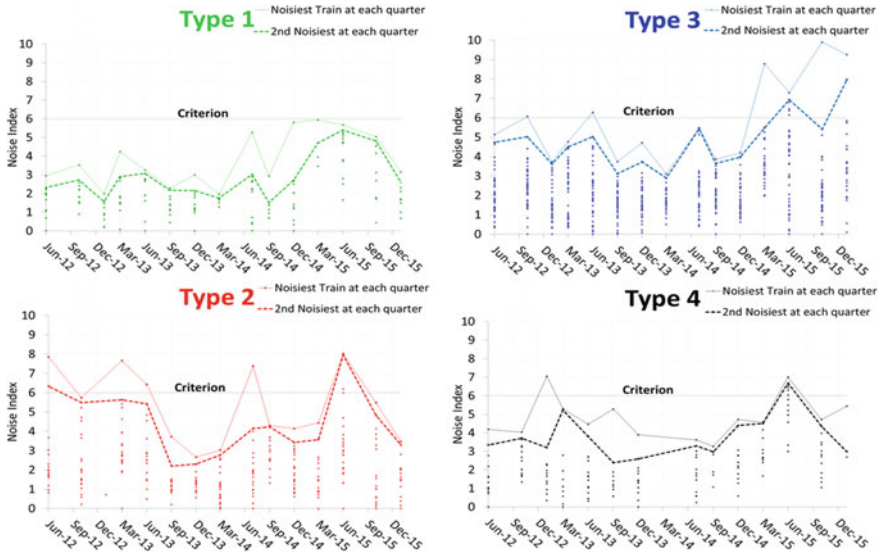
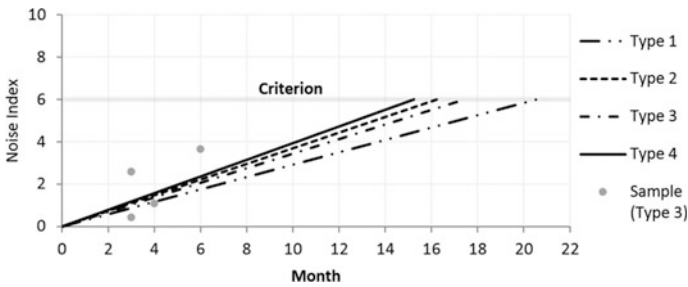


Fig. 2 Comparison of train fleet performance

wheel deterioration rate (by means of noise escalation) is progressive and linear, the data points within each quarter and train type should display the characteristic of a grouped and even spread (i.e. no departures). The envelopes show instances of “outlier” behaviour, where a data point escalates well above rest. Note that the categorization of “outlier” has been defined as data points above the criterion. The subplots also showed that any train type is capable of registering zero NI. By deduction, they represent trains that had undergone wheel maintenance just before the noise measurement. Across the 15 quarters, 2015Q2 (June) registers the greatest number data points (>10) above NI 6. The norm is one or two cases, seen occasionally in some quarterly data.

Figure 3 shows an indication of wheel deterioration rate by train type, through NI Escalation. Each train type is assumed to have a single rate of escalation for data points with NI values <6 i.e. it assumes a simple linear relation between NI escalation and time. An example of this NI escalation for a particular train (type 3) is represented by the data points in Fig. 3. Train Type 1 is shown to be the best performing, taking the longest time (20 months) to deteriorate from 0 to 6. This outcome on best performing train type is consistent with the outcome from Fig. 2. It should be noted that the data used to calculate the average rate of NI Escalation ranged from three months to well over a hundred months. The data spread is not only wide ranging, the degree of overlap between the train types is also significant. Using an example of wheel condition degradation: from newly turned, to wheel circumferential pitting at the contact patch due to surface fatigue [7], to formation of flat from un-intended wheel slide, the process of defect formation will likely not progress in a linear fashion. Further, these discontinuities (pits and flats) would also



**Fig. 3** Noise index escalation for different train types

have a non-linear relationship with the manifested noise level. Despite the flaw on the assumed linear basis for the rates calculated for Fig. 3, the outcome does provide a qualitative comparison between train types.

### 3.2 Outlier Analysis

The choice of NI 6 as the cut-off criterion, for the categorization of outliers, was built on observations of the correlation to wheel maintenance records. This stipulated level seems to correspond well to recorded wheel flat size that approaches 20 mm, which is the limiting threshold for maintenance intervention. This intervention takes account of the number of flats and other defects like pitting. Maintenance guidance points to a basis of audible effect in service. In practice, aside from visual inspection that provides a measure of the flat, intervention threshold based on wheel impact force from a trackside system (Wheel Impact Load Detection - WILD), is used. Table 1 shows a ranking of NI and the corresponding remarks in the maintenance record. The nine train passbys are selected to cover the full range of data points, found to be above the criterion in Fig. 2. They start from NI 6.3 (with flat sizes up to 20 mm), to NI 8.0 and 9.9 (with flat sizes of 35 and 40 mm respectively).

It is observed that two train types (Type 2 and Type 3) have a higher number of outliers than the other two. On the assumption of similar utilisation and preventive maintenance, it means that certain train types or a few trains tend to exhibit outlier behaviour. On this note, there is one train of each type, from Type 2 and Type 3, that repeatedly appears in the outlier list. At the time of this study, the root cause of the repeating high NI was not investigated. However, the potential benefit of an outlier analysis is clear. The empirical information could be used to identify specific trains, with respect to the tendency of wheel flat formation, for added attention.

**Table 1** Correlation between noise index and presence of wheel flat

Train	Noise index	Remarks
Type 3	6.3	Multiple wheel flats were detected
Type 4	6.5	Multiple wheel flats were detected
Type 3	6.9	Wheel flat and pitting were detected
Type 3	7.3	Wheel flat was detected
Type 2	7.4	Wheel flat, pitting, and spalling were detected
Type 2	7.7	Wheel flat, pitting, and spalling were detected
Type 2	8.0	Wheel flat was detected
Type 3	8.8	Wheel flat, metal build up, and spalling were detected
Type 3	9.9	Wheel flat was detected

### 3.3 Maintenance Optimization

As previously described in the methodology section, wheel condition is monitored through fixed schedule maintenance and regular checkup every three weeks. This maintenance approach could potentially be optimized if a frame could be set to provide a feedback on effects of changes to maintenance practice.

Progression of noise level between quarters over four years shows improvement as illustrated in Fig. 4. The time slice analysis of train performance is a reflection of the maintenance system over the four years. The best train fleet’s wheel condition is observed in 2014 where the majority of train fleets has noise index less than the threshold value of 6 as indicated by the dotted line in Fig. 4. In fact, the majority of trains had noise index below 4 in 2014.

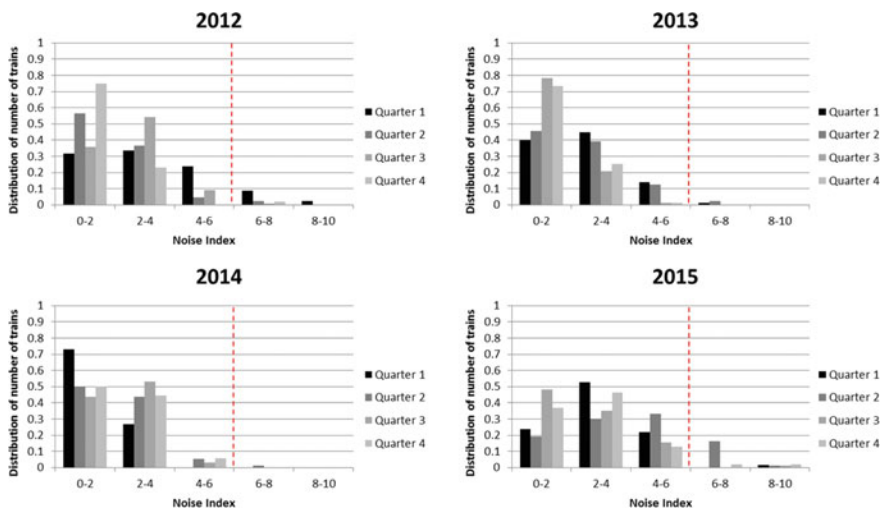


**Fig. 4** Noise index distribution across four years

Although the noise index threshold can be used for an optimization of wheel maintenance, it is indicative that optimization of wheel maintenance was achieved in 2015 based on the noise index distribution which is more spread out compared to 2014. However, it is imperative to understand that this observation is purely based on the time slice analysis of train performance across the years. The distance travelled by each train was not taken into account during the analysis in order to offer a more simplified approach.

An interesting point to note is the reducing number of outliers across the four years of noise measurement. The number of outliers has decreased from 14 to only 1 between 2012 and 2014. In fact, the train fleet number was increased by 10% in 2013 due to the introduction of new trains. Despite the increased train fleet number, outliers have decreased within this time period which shows that the maintenance system is working well. Although the number of outliers in 2015 increased up to 20, almost all of them are identified in the 2nd quarter which was then greatly reduced in the next quarter.

The optimization of the maintenance regime could be attributed to the Wheel Impact Load Detection (WILD) system which was implemented in 2013. In addition, a more distributed noise index level below the threshold in 2015 could be the result of condition based maintenance through the WILD system which complements the regular maintenance regime. The real-time monitoring achieved by the implementation of the WILD system also reduces the response time between the detection of potential wheel defects and wheel maintenance which is an improvement from the quarterly noise measurement.

### 3.4 Increasing Train Traffic Due to New Signaling System

A simulation was done to predict the increase in noise level with increasing train traffic as a result of the implementation of a new signaling system which will reduce train service headway. The profile of noise level from each train type, outlier trains, and environmental noise were averaged to get a single noise profile for each of them. Figure 5 illustrates the identification of train type 3 profile from the collected noise data.

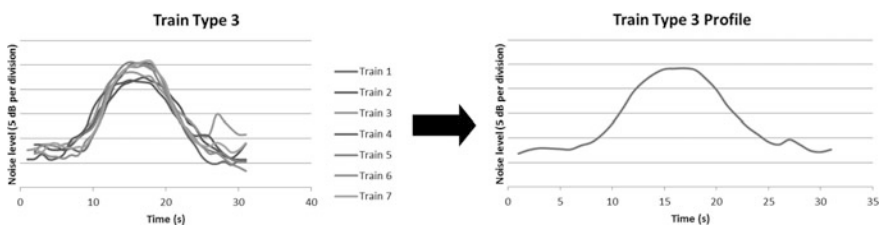


**Fig. 5** Average noise profile for train type 3



**Table 2** Simulation result for increasing train traffic

	Measured $L_{Aeq,1\text{ hr}}$	Simulated $L_{Aeq,1\text{ hr}}$	Simulated $L_{Aeq,1\text{ hr}}$ for increased train traffic
Location 1	63.1 dB (57 trains)	63.1 dB (57 trains)	63.9 dB (72 trains)
Location 2	65.4 dB (57 trains)	65.3 dB (57 trains)	66.2 dB (72 trains)

The number of trains from each type was determined for a one-hour measurement from the observation of train passbys during the noise measurement. Equation (2.1) was used to calculate the  $L_{Aeq,1\text{ h}}$  which includes the profile of four train types, outlier trains, and environmental noise. Simulation of the measured  $L_{Aeq,1\text{ h}}$  value was done with a good result. Using the same train type composition, the number of trains from each type can be calculated for the scenario of increased train traffic from a reduction of train headway. This translated to an increase from 30 to 36 trains passing in an hour, for each direction. Actual measurements of  $L_{Aeq,1\text{ h}}$  and simulated scenarios are provided for a comparison to the stipulated guidance of 67 dBA by NEA.

The noise levels in Table 2, shows that all scenarios are within the NEA stipulated guidance of 67 dBA. The total number of train passbys denoted in the table is for train traffic passing in both directions. It is noted that a 20% increase in train traffic (from 30 to 36 trains per hour for each direction) will lead to a less than 1 dBA increase in  $L_{Aeq,1\text{ h}}$ .

## 4 Conclusion

Characterization of train fleet wheel condition in a metro was done based on train passby noise and wheel maintenance records over a four-year period. Identification of wheel flats through analysis of the maximum  $L_{Aeq,1s}$  value from individual train passbys was performed. Noise measurement data was normalized into a noise index ranking to give the fleet performance over time. Histogram analysis was also done to show the change in the distribution of train fleet wheel condition.

Overall train fleet data was analyzed with further observation on the outlier trains. Performance comparison between the four train types was attempted. The established degradation rate for the overall train fleet and each train type shows differences in the likelihood of wheel defect formation. Together with the wheel maintenance records, correlation between high noise level and the presence of wheel flats is confirmed.

A qualitative comparison between train types was done from the identified degradation rate. Progression of noise level distribution with time shows improvement with a more evenly distributed noise index level in 2015.

Standardized noise profile for each train type was also established for the simulation of train traffic scenario where an increasing number of train passbys is expected with the new train signaling system. The simulation result shows that the noise level is still below the limit stipulated by National Environment Agency (NEA).

To conclude, this paper discusses the noise measurement exercise from time-based and train-centric behavior. A closer look into distance travelled by train fleets might allow another perspective towards wheel maintenance optimization. The performed study and observation reflect the maintenance system in SMRT with progressive transition from rigid maintenance system towards condition-based maintenance system which allows more flexibility in maintenance resource allocation.

**Acknowledgements** This research paper is made possible through the help and support from various parties, including: colleagues, supervisors, family and friends. Especially, we would like to dedicate our acknowledgement of gratitude toward the following significant advisors and contributors. First and foremost, we would like to thank Permanent Way Emergency Response Unit (ERU) team members for their support for the on-site noise measurement and collection of train passby information. Second, we would like to thank Rolling Stock department for their support in the provision of wheel maintenance record and WILD system data. Finally, we sincerely thank our colleagues in Technology Management Office for their data repository which allows the management of noise measurement data in a systematic manner.

## References

1. Thakkar, N., Steel, J.A., Reuben, R., Knabe, G., Dixon, D., Shanks, R.: Monitoring of rail-wheel interaction using acoustic emission (AE). *Adv. Mater. Res.* **13–14**, 161–168 (2006). <https://doi.org/10.4028/www.scientific.net/amr.13-14.161>
2. Scarano, P.: Noise measurement activity by Italian railway, *Proceeding of International Commission for Acoustics 2001 (Rome)*
3. Szwarc, M., Kostek, B., Kotus, J., Szczodrak, M., Czyżewski, A.: Problems of railway noise—a case study. *Int. J. Occup. Saf. Ergon.* **17**(3), 309–325 (2011). <https://doi.org/10.1080/10803548.2011.11076897>
4. Bies, D.A., Hansen, C.H.: *Engineering noise control: theory and practice*. Spon Press/Taylor & Francis, London (2009)
5. Nelson, J.T.: *Wheel/rail noise control manual*. Transportation Research Board, Washington, DC (1997)
6. Lewis, R., Olofsson, U.: *Wheel-Rail Interface Handbook*. Woodland Publishing Limited, Cambridge, UK (2009)
7. Wu, T.X., Thompson, D.J.: *A hybrid model for wheel/track dynamic interaction and noise generation due to wheel flats* (2001)

# Hybrid Model for Prediction of Impact Noise Generated at Railway Crossings



P. T. Torstensson, G. Squicciarini, M. Krüger, Jens C. O. Nielsen  
and David J. Thompson

**Abstract** A hybrid model for the prediction of impact noise at railway crossings is presented. The hybrid model combines the simulation of vertical wheel–rail contact force in the time domain and the prediction of sound pressure level using a linear frequency-domain model. The time-domain model uses moving Green’s functions for the vehicle and track models (accounting for wheel flexibility and a discretely supported rail with space-variant beam properties) and a non-Hertzian wheel–rail contact model. The time-domain and frequency-domain models are coupled based on the concept of an equivalent roughness spectrum. The model is demonstrated by investigating the influence of axle load, vehicle speed and wheel profile on generated impact noise levels. A negligible influence on impact noise is observed for axle loads in the interval 15–25 tonnes. On the other hand, increasing vehicle speed from 80 to 150 km/h, or comparing a nominal S1002 wheel profile with a severely hollow worn profile, result in substantially higher levels of impact noise; for the given wheel and track conditions the differences are in the order of 10 dB(A).

## 1 Introduction

Turnouts (switches and crossings, S&C) provide flexibility of traffic operation in railway networks. A wheel passing over the crossing in a facing move (from the switch towards the crossing) typically results in a high-frequency impact load on the crossing nose; for the trailing move a corresponding impact occurs on the wing

---

P. T. Torstensson (✉) · J. C. O. Nielsen  
Department of Applied Mechanics/CHARMEC,  
Chalmers University of Technology, 41296 Gothenburg, Sweden  
e-mail: peter.torstensson@chalmers.se

G. Squicciarini · D. J. Thompson  
Institute of Sound and Vibration Research, University of Southampton,  
University Road, Southampton SO17 1BJ, UK

M. Krüger  
DB Netz AG, Völckerstrasse 5, 80939 Munich, Germany

rail. Apart from severe material degradation and rail profile damage, a critical consequence of the impact load is noise at levels that may exceed the general rolling noise by several decibels. As a result of the trend of decreasing levels of rolling noise (e.g. achieved by the retrofitting of cast iron to composite brake blocks on freight rolling stock), Deutsche Bahn (DB) expects the awareness of discrete railway noise sources to increase in the future.

Impact noise is generated due to excitation by discrete vertical discontinuities in the running surfaces of wheel and rail. Studies in the literature on wheel–rail impact noise are few and focus mainly on rail joints and wheel flats [1]. In [2], efficient mitigation of impact vibration at a crossing by retrofitting with resilient rail pads was demonstrated by numerical simulations and field measurements. Longitudinal and transverse re-profiling of the crossing rails (optimisation of wheel trajectory) is another potential strategy to mitigate noise. However, the modified rail design must account for the substantial variation in (worn) wheel profiles occurring in traffic [3].

To simulate the dynamic vehicle–track interaction in the crossing panel, a computationally efficient and versatile time-domain method introduced by Nordborg [4] is applied. Vertical wheel–rail contact is solved based on the variational method by Kalker [5]. To account for the longitudinal motion of the wheel, the dynamics of the track is represented by a set of moving Green’s functions. The simulation method accounts for both the parametric excitation due to the discretely supported rail as well as the excitation by periodic and discrete irregularities. This approach has previously been applied for the simulation of high-frequency vehicle–track dynamics [4], prediction of squeal noise [6] and rolling contact fatigue damage [7].

A numerical method for the prediction of impact noise due to excitation by wheel flats was presented in [8]. A hybrid approach was proposed in which the simulations are performed in two steps: (1) calculation of impact load by a time-domain simulation of non-linear high-frequency vertical dynamic vehicle–track interaction, and (2) prediction of noise using the software TWINS [9] in the frequency domain based on excitation by an equivalent roughness spectrum.

The current paper presents a further development of the hybrid approach to investigate impact noise generated at crossings. Conditions similar to those of a crossing located at Loreley (in the Rhine valley) on the track network of Deutsche Bahn (DB) are studied, see Fig. 1.



**Fig. 1** Photograph of studied crossing at Loreley in Germany

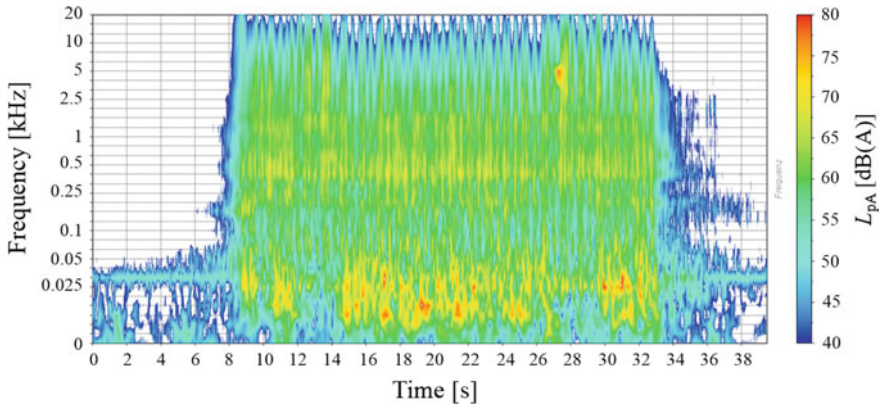


**Fig. 2** Sound pressure level spectrum in 1/3 octave bands measured during passage of a freight train through a crossing at Loreley in Germany, vehicle speed 88 km/h

## 2 Impact Noise Measured on the Rhine-Alpine Rail Corridor

As part of DB's efforts to mitigate the generation of railway noise along the Rhine-Alpine freight corridor, track-side monitoring stations have been erected at several locations along the track. Measurement data is automatically analysed and published on the internet [10]. The sound pressure level is measured at a distance of 7.5 m from the track centre and 1.2 m above the top of the rail. The pass-by time of first and last axle is used to calculate the equivalent sound pressure level of a train.

Figure 2 shows the A-weighted sound pressure level spectrum in 1/3 octave bands measured during the passage of a freight train at speed 90 km/h through the crossing at Loreley (trailing move). The train consists of 22 container wagons each with three 2 axle bogies and composite brake blocks. High sound pressure levels are observed for frequencies below approximately 50 Hz and in the frequency interval between 250–2000 Hz. The corresponding equivalent sound pressure level during the pass-by was 88 dB(A) (normalized to a vehicle speed of 80 km/h).

## 3 Time-Domain Wheel–Turnout Interaction Model

Simulation of impact noise requires accurate prediction of the magnitude and frequency content of the wheel–rail impact load. In the current work, dynamic vehicle–crossing interaction in the frequency interval up to 4 kHz is considered using the software RAVEN [7].

Vertical non-Hertzian wheel–rail contact is modelled using an implementation of Kalker's algorithm NORM [5] by Pieringer [6]. The flexibility of the wheel and rail

in the vicinity of the contact is approximated by elastic half-spaces. The three-dimensional running surfaces of the wheel and crossing are described by linear iso-parametric surface elements of side length 1 mm.

The dynamic response of the rail and wheel are described by the use of impulse response functions, also called Green's functions. These are computed by the inverse Fourier transform of transfer receptances (i.e. frequency response functions of displacement over applied force). To account for the motion of the wheel, so-called moving Green's functions for the crossing panel need to be assembled. For a vertical unit excitation on the rail at position  $x_0$  and time  $t = 0$ , the moving Green's function  $G_{R,v}(x_0, t)$  contains the vertical rail displacement at a point moving away from the excitation at train speed  $v$ . The vertical displacement,  $\eta_R(t)$ , of the rail due to excitation at the wheel–rail contact is calculated by convolution of the vertical contact force,  $F_N$ , and the (moving) Green's function as

$$\eta_R(t) = \int_0^t F_N(\tau) G_{R,v}(v\tau, t - \tau) d\tau \quad (3.1)$$

The crossing and wheel models are briefly described in the following sections.

### 3.1 Wheel Model

A BA319 freight wheel with nominal rolling radius 0.46 m and mass 350 kg is modelled with axi-symmetric elements using the finite element (FE) method. To account for half the wheel axle mass, a lumped mass of 350 kg is added at the wheel centre. Longitudinal and lateral displacements of the nodes on the inner surface of the wheel hub are constrained. The wheel is suspended in its primary suspension, which is modelled as a linear spring,  $k_{PS} = 10.9$  MN/m, and a viscous damper,  $c_{PS} = 50$  kNs/m, coupled in parallel. Based on an eigenvalue analysis for the wheel model, the receptance at the wheel–rail contact is calculated by a modal superposition. Wheelset structural damping is accounted for by introducing a modal damping ratio of 0.001 for all modes. Figure 3a outlines the prescribed node where the vertical wheel–rail contact force is applied in the subsequent time-domain simulation. Wheel structural flexibility in the frequency interval below 4 kHz is considered. The Green's function calculated for excitation at the wheel–rail contact node is shown in Fig. 3b. The corresponding result calculated for an alternative rigid wheel model (neglecting the structural flexibility) is shown for comparison. Both models are considered in the analysis for comparison.

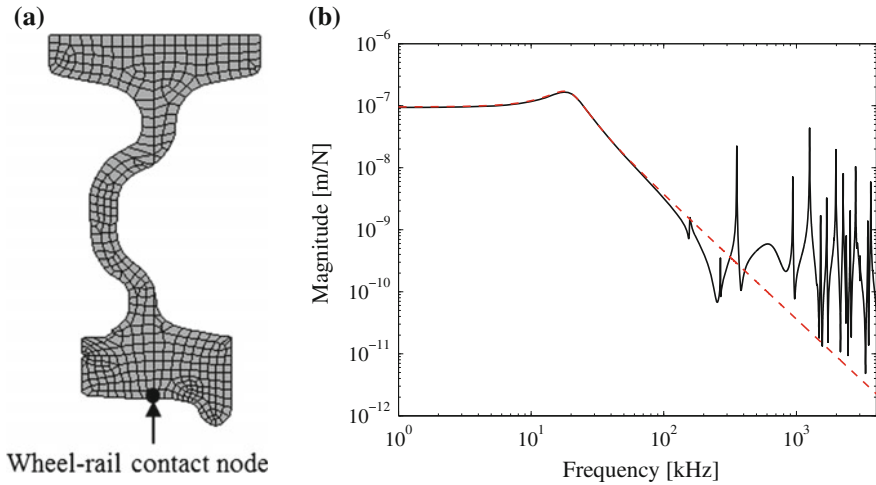


**Fig. 3** **a** Cross-section of wheel FE-mesh with the prescribed excitation node. **b** Magnitudes of vertical wheel point receptance at the wheel-rail contact node. —: Flexible wheel model, - - -: rigid wheel model

### 3.2 Simplified Model of a Railway Crossing

A linear model of part of a crossing panel in a railway turnout has been developed, see Fig. 4. The model contains only the straight rail in the through route that includes the crossing. The discretely supported rail is modelled by undamped Rayleigh–Timoshenko beam finite elements with spatially-varying bending stiffness  $EI(x)$ , shear stiffness  $kGA(x)$ , mass per unit beam length  $m(x)$  and rotational inertia per unit beam length  $mr^2(x)$ . The beam properties were extracted from a more comprehensive FE-model of a 60E1-760-1:15 turnout [11], which includes all the rails in the switch, closure and crossing panels (stock rails, switch rails, closure rails, crossing nose, wing rails and check rails). The variations of cross-sectional area and moment of inertia extracted from [11] and implemented in the present model are illustrated in Fig. 4. In future work, the more comprehensive FE-model could be used for a more accurate description of dynamic properties.

The track model is 70 sleeper bays long with constant sleeper spacing  $L = 0.6$  m and clamped boundaries at the two rail ends. The impact on the crossing nose is prescribed to occur at  $x = 21$  m, which is directly above sleeper 35. Each rail pad and the support under each (half) sleeper are modelled as a discrete linear elastic spring and a viscous damper in parallel. For the rail pads, the stiffness and damping constants are taken as constant:  $k_p = 120$  kN/mm and  $c_p = 25$  kNs/m. The length and inertia  $M_s(x)$  of the sleepers associated with the vibration of the modelled rail

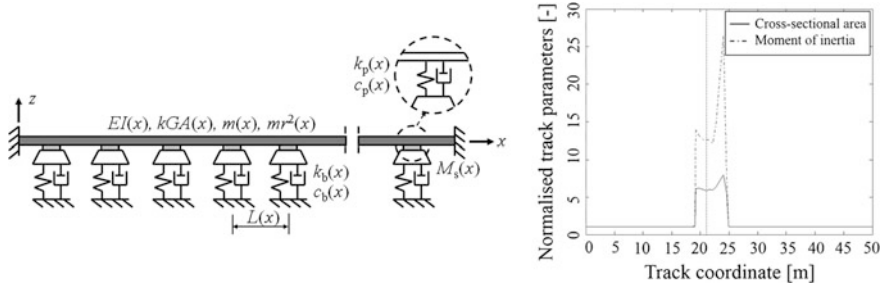


**Fig. 4** Track model with one rail on discrete supports. Variation of cross-sectional rea  $A(x)$  and moment of inertia  $I(x)$  for straight rail including the crossing;  $A(x)$  and  $I(x)$  are normalised with respect to  $A_{ref} = 7.69e-3 \text{ m}^2$  and  $I_{ref} = 3.05e-5 \text{ m}^4$ . Prescribed impact position at crossing is indicated by the vertical dashed line

are assumed to be constant (150 kg) for sleepers 1–25 and 56–69. In between, it is assumed that the sleeper length and mass varies linearly from sleeper 26 (150 kg) to sleeper 55 (300 kg). Uniform sleeper support conditions (constant bed modulus) are assumed and thus the linear variation of ballast/subgrade stiffness  $k_b(x)$  and damping  $c_b(x)$  is proportional to sleeper length.

The level of the vertical point receptance calculated around the crossing panel is shown in Fig. 5a. Examples of moving Green’s functions calculated at three positions along the track model are shown in Fig. 5b.

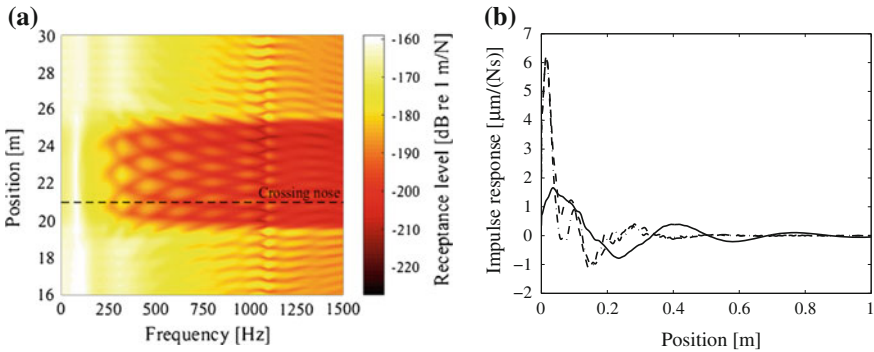


**Fig. 5** **a** Level of vertical point receptance calculated in the vicinity of the crossing panel at steps of 3.75 cm. **b** Moving Green’s functions of the track calculated for vehicle speed 100 km/h. Excitation at the crossing nose (—), and at 10 sleepers before (—) and after (---) the crossing nose



## 4 Hybrid Method for Prediction of Impact Noise at the Crossing

To estimate impact noise levels from the contact forces calculated in the time domain, a hybrid approach has been developed based on the definition of an equivalent roughness [8]. The idea is to find an equivalent roughness spectrum that, in a linear model, gives the same contact force spectrum as would be obtained with a non-linear model that includes the discontinuity. In this linear model, the dynamic properties of the wheel and track must be the same as in the non-linear time-domain model but the non-linear properties of the contact are replaced by a linearised Hertzian contact spring. This roughness spectrum can then be used in a detailed linear model of noise generation, such as TWINS [9], to predict the noise due to the impact.

The first step is to calculate the transfer function between roughness and contact force for a given combination of wheel type, track and contact. By using a “moving roughness” approach, the contact force per unit roughness,  $H_{RF}(\omega)$ , can be obtained as

$$H_{RF}(\omega) = \frac{1}{X_R(\omega) + X_W(\omega) + X_C(\omega)} \quad (4.1)$$

where the denominator includes the summation of rail ( $i = R$ ), wheel ( $i = W$ ) and contact ( $i = C$ ) receptances,  $X_i(\omega)$ . The rail (crossing) and wheel receptances are calculated based on the models presented in Sects. 3.1 and 3.2. The contact receptance is represented by means of a linearised Hertzian contact spring with stiffness calculated for each axleload (1.31 GN/m for 15 t, 1.44 GN/m for 20 t and 1.55 GN/m for 25 t).

Time histories of vertical wheel–rail contact force are calculated using the non-linear model RAVEN described in Sect. 3. These are transformed to the frequency domain,  $F_N(\omega)$ , by a fast Fourier transform (FFT); a time window of 0.7 s centred at the discontinuity is selected to calculate the spectrum. The equivalent roughness,  $r(\omega)$ , is obtained as

$$r(\omega) = \frac{F_N(\omega)}{H_{RF}(\omega)} \quad (4.2)$$

The equivalent roughness calculated based on the rail receptance at the crossing is shown in Fig. 6a together with the TSI limit [12]. The equivalent roughness levels are quite low due to the smooth profile in this case. Results obtained for the flexible and rigid wheel models are almost identical up to 200 Hz and follow the same trends at higher frequency with a maximum difference of 5 dB. Results are also shown for a nominal track in which the track properties do not vary along the length in Fig. 6b. In this case the two wheel models show very similar results. This suggests the differences are related with the crossing model and that the wheel structural flexibility should be accounted for in the time-domain simulations whereas for a regular track this is not necessary [8].

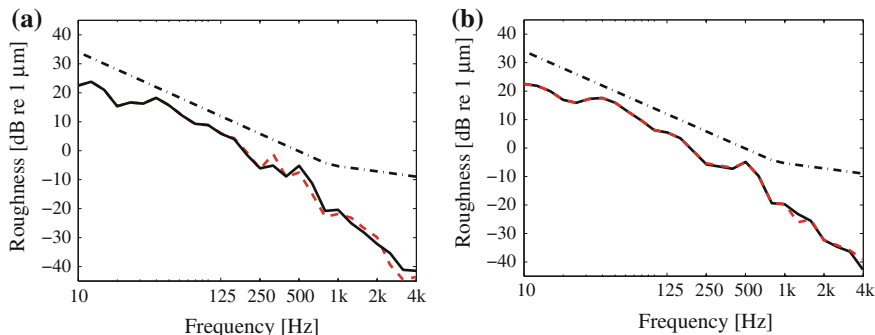


**Fig. 6** Equivalent roughness calculated for the crossing model (a) and for a nominal track (b). —: Flexible wheel model, - - -: rigid wheel model, - · - ·: TSI

## 5 Results

The passage of a freight wheel in the facing move, from the switch panel towards the crossing panel of the through route is considered. The nominal rail geometry is interpolated from rail profiles given at a discretisation distance of 50 mm. Any further track irregularity (such as rail acoustic roughness) is not considered here even if allowed for by the simulation procedure. The lateral position of the wheel centre relative to the track centreline is prescribed and kept constant during the simulation of vertical wheel–rail contact force time history in RAVEN. The TWINS model is then applied to predict the equivalent sound pressure level (SPL) at 7.5 m from the track during the passage of one vehicle with an assumed length of 20 m and comprising four wheelsets. To calculate the noise radiation from the track, a standard track model consisting of a Timoshenko beam mounted on a two-layer support is used in TWINS [9]. The effect of ground reflections is also included and this results in a dip in the spectrum at around 800 Hz. Because no acoustic roughness is accounted for, the results represent the noise generated due to the impact force alone.

The influence of axle load on the predicted magnitudes of vertical wheel–rail contact force and noise radiation has been investigated. Figure 7a shows the time history of the dynamic component of the vertical contact force in the crossing panel. The parametric excitation due to the discrete sleeper supports is observed at positions before 19 m and after 25 m. It is observed that the results calculated for three different axle loads are almost overlapping. A small increase in sound pressure level is predicted for increasing axle load, see Fig. 7b.

Figure 8 indicates a significant influence of the vehicle speed on the vertical wheel–rail contact force and the associated radiated noise. An increase in vehicle speed from 80 to 150 km/h corresponds to an increase in predicted equivalent sound pressure level of 7 dB(A), see Fig. 9a.

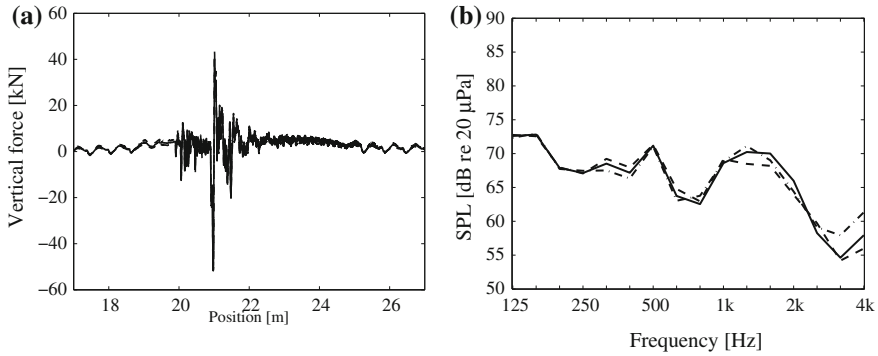


**Fig. 7** **a** Vertical wheel–rail contact force (dynamic component) in the vicinity of the crossing and **b** associated prediction of sound pressure level. Vehicle speed 100 km/h, flexible wheel. —: 15 tonnes, — —: 20 tonnes and - · - ·: 25 tonnes axle load

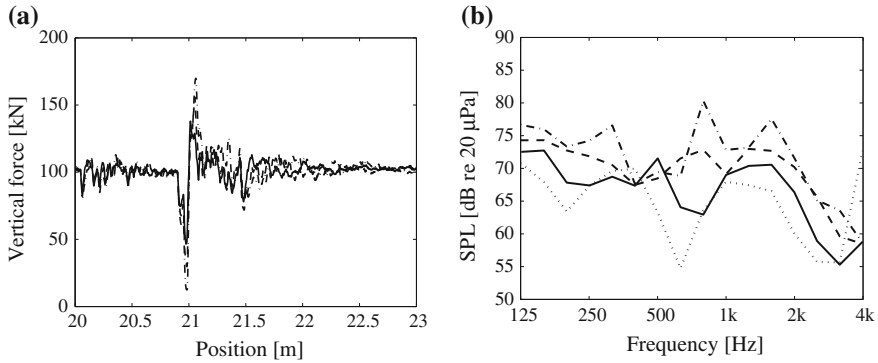


**Fig. 8** **a** Vertical wheel–rail contact force in the crossing panel and **b** associated prediction of sound pressure level. Axle load 20 tonnes, flexible wheel. ···: 80 km/h, —: 100 km/h, — —: 125 km/h and - · - ·: 150 km/h

In Fig. 10, the influence of the wheel profile is illustrated. In addition to the nominal S1002 wheel profile, two profiles with different depths of hollow wear are considered, see Fig. 10a. It is concluded that there is a significant influence of the wheel profile on the vertical wheel–rail impact force and the associated generation of noise. Changing from the nominal S1002 wheel profile to the hollow worn wheel profile labelled W2 results in an increase in equivalent noise level of 11 dB(A), see Fig. 9b. This can be attributed to the fact that the severely hollow worn wheel profile results in loss of contact when the contact is transferred from the wing rail to the crossing nose (not shown here).

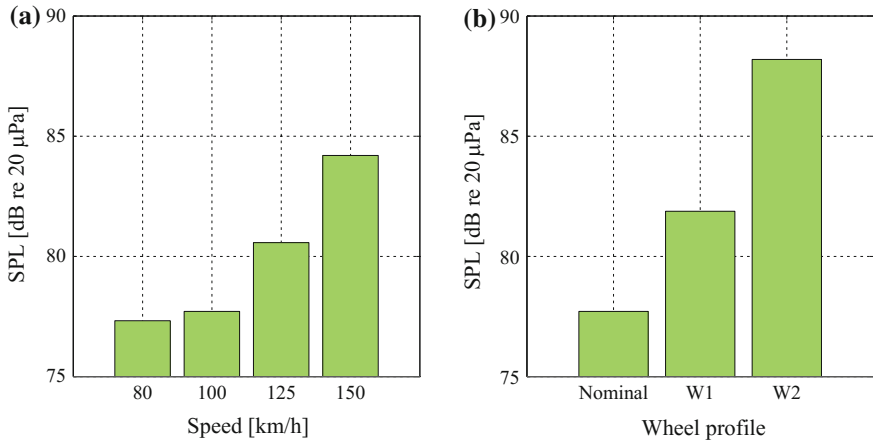


**Fig. 9** A-weighted equivalent sound pressure levels predicted for **a** different vehicle speeds and **b** different wheel profiles at 100 km/h

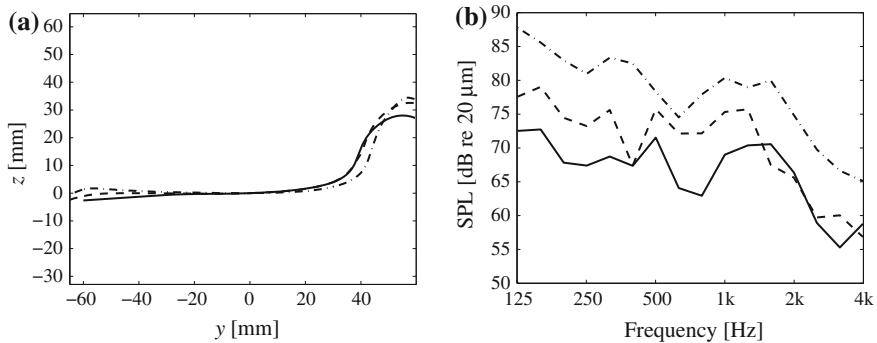


**Fig. 10** **a** Considered wheel profiles and **b** corresponding predictions of sound pressure level. Axle load 20 tonnes, flexible wheel. —: Nominal S1002 profile, - - : W1; ··· : W2

## 6 Conclusions

A model for the prediction of impact noise generation at railway crossings has been developed. The hybrid approach based on the concept of an equivalent roughness spectrum is used in order to combine two already existing and validated prediction models: RAVEN for numerical simulation of non-linear time-domain dynamic vehicle–track interaction, and the linear frequency-domain model TWINS for prediction of radiated sound pressure level. To describe the track, a simplified FE model of a discretely supported rail modelled by beam elements with spatially-varying properties is used. Properties of the simplified track model were collected from a more comprehensive FE model of the full turnout. To account for the structural flexibility of the wheel, axi-symmetric finite elements were used.

Based on simulations with three different axle loads in the interval 15–25 tonnes, it is concluded that the influence of axle load on impact noise level is small. On the other hand, a significant influence of vehicle speed and worn wheel profile on impact force magnitude and the associated radiation of noise was observed. An increase in vehicle speed from 80 to 150 km/h resulted in an increase in equivalent sound pressure level of 7 dB(A). The results obtained for a nominal S1002 wheel profile or a profile with hollow wear showed a difference of 11 dB(A). This suggests that, when comparing predictions with measurements, uncertainties in wheel and rail profiles will influence the outcome considerably.

In future work, a verification of the presented model will be made by comparing predicted results with field measurement data. For this reason, a measurement campaign at the studied crossing of the DB track network was conducted in November 2016. In order to calibrate the track model, track decay rates were measured. Acoustic roughness was measured to enable an estimation of the contribution of rolling noise in the pass-by noise measurements. The geometry of the crossing panel was measured using an equipment for three-dimensional scanning.

**Acknowledgements** This work is performed as part of the activities in the three-year project IN2RAIL, which started in 2015 and has received funding from the European Union's Horizon 2020 research and innovation programme under grant agreement no 635900.

## References

1. Thompson, D.J.: *Railway Noise and Vibration*. Elsevier, Oxford (2009)
2. Kaewunruen, S.: Effectiveness of using elastomeric pads to mitigate impact vibration at an urban turnout crossing. *Noise Vib. Mitig. Rail Transp. Syst.* **118**, 357–365 (2012)
3. Pålsson, B.A.: *Optimisation of railway switches and crossings*, PhD Dissertation, Department of Applied Mechanics, Chalmers University of Technology, 2014, Göteborg (Sweden)
4. Nordborg, A.: Wheel/rail noise generation due to nonlinear effects and parametric excitation. *J. Acoust. Soc. Am.* **111**(4), 1772–1781 (2002)
5. Kalker, J.J.: *Three-dimensional elastic bodies in rolling contact*. Kluwer Academic Publishers, Dordrecht (1990)
6. Pieringer, A.: A numerical investigation of curve squeal in the case of constant wheel/rail friction. *J. Sound Vib.* **333**(18), 4295–4313 (2014)
7. Andersson, R., Torstensson, P.T., Kabo, E., Larsson, F.: An efficient approach to the analysis of rail surface irregularities accounting for dynamic train–track interaction and inelastic deformations. *Veh. Syst. Dyn.* **53**(11), 1667–1685 (2015)
8. Wu, T.X., Thompson, D.J.: A hybrid model for the noise generation due to railway wheel flats. *J. Sound Vib.* **251**(1), 115–139 (2002)
9. Thompson, D.J., Hemsworth, B., Vincent, N.: Experimental validation of the TWINS prediction program for rolling noise, part I: description of the model and method. *J. Sound Vib.* **193**(1), 123–135 (1996)
10. <http://www.deutschebahn.com/laerm> (in German)
11. Li, X., Nielsen, J.C.O., Pålsson, B.: Simulation of track settlement in railway turnouts. *Veh. Syst. Dyn.* **52**(Suppl), 421–439 (2014)
12. European Standard EN 15610:2009. *Railway Applications—Noise Emission—Rail Roughness Measurements Related to Rolling Noise Generation*

# Classification of Impact Signals from Insulated Rail Joints Using Spectral Analysis



Andrew Yuen, Dingyang Zheng, Peter Mutton and Wenyi Yan

**Abstract** Insulated Rail Joints (IRJs) are a railway track component that generates impact noise and requires close maintenance. Instrumented Revenue Vehicles (IRVs) developed by the Institute of Railway Technology at Monash University measure the interaction between the vehicle and track. Impact signals were measured and post-processed from vibration sensors located on the side-frame at IRJ locations. Wavelet analysis was used to interrogate the non-stationary impact signals. Wavelet energy was used as the wavelet feature extraction techniques in the frequency domain. The wavelet energy impact signatures were clustered using multi-signal discrete wavelet transform clustering. These clusters classified the empty and loaded conditions of the wagon from the vibration response. Frequency identifications were created from the clustering and the severity of the impacts in the frequency domain could be determined from the cluster numbers.

## 1 Introduction

Instrumented Revenue Vehicles (IRVs) developed by the Institute of Railway Technology are an in-service wagon installed with instrumentation to measure vehicle-track interaction. The IRV consists of vibration sensors and linear displacement transducers to measure the dynamic behavior of the un-sprung and sprung masses, respectively. The accelerometers are mounted on the side-frame and the linear displacement transducers are located next to the spring nest. Also, lateral accelerations are measured from the bolster to give an indication of the hunting behavior. Longitudinal wagon dynamics are calculated from drawbar force measurements. Unattended Geometry Measurement Systems (UGMSs) and Track

---

A. Yuen (✉) · D. Zheng · P. Mutton  
Institute of Railway Technology, Monash University, Melbourne, Australia  
e-mail: andrew.yuen@monash.edu

A. Yuen · W. Yan  
Department of Mechanical and Aerospace Engineering, Monash University,  
Melbourne, Australia

Recording Vehicles (TRVs) are similar systems used by rail operators [1]. Delft University of Technology used a twin accelerometer configuration on an instrumented vehicle to detect squats [2]. The University of Virginia Polytechnic Institute and State University also used instrumented vehicles to detect various rail defects from accelerometer data [3].

Insulated Rail Joints (IRJs) are a bolted connection used for signaling purposes, where track circuits are used. Previous studies on IRJs can be categorised into mathematical modelling, Finite Element Analysis, in situ instrumentation or way-side monitoring and vehicle based monitoring. Queensland University of Technology conducted a complete in situ wayside experiment by directly strain-gauging IRJs. Data was obtained and analysed over several months using wavelet analysis [4]. Chalmers University of Technology used Finite Element Analysis to model the localised Rolling Contact Fatigue at the endpost of IRJs [5].

In this study, the vibration data was post-processed in the frequency domain in order to identify and classify impact signals from the traversing of the IRV over IRJs. The severity of the accelerometer response at IRJ locations gives an indication of the impact noise generated. Ensuring that IRJs are properly maintained will prevent the impact noise generated by a faulty joint from deteriorating.

Wavelet analysis was selected as the spectral method to be applied to this study due to its improved time-frequency resolution compared to short-time Fourier methods. Also, wavelets are suited for the analysis of non-stationary signals such as impacts. In [2], scale averaged wavelet power was the time-frequency feature extraction technique which was used to obtain the acoustic signatures of squats. In [3], the discrete wavelet transform and the Lipschitz exponent were the feature extraction techniques used to identify the vibration signatures of different track defects. The Lipschitz exponent was used to classify different track defects from a simulated acceleration signal. Thresholding was applied to both extracted features and the possible correlation to different defects was established.

## 2 Instrumented Revenue Vehicle Data Acquisition

Each IRV has four accelerometers located on each side-frame of the wagon. In this study, data was obtained from two side-frame accelerometers located on the same side of the wagon. This allowed for cross-correlation between the two accelerometers to be used as a measure of severity and consistency. Data was sampled at 1000 Hz and was collected over several months so that the data could be analysed longitudinally over time. It is stated in [6], that most of the frequency content of wheel impacts is generally below 1000 Hz. An anti-aliasing filter was applied using the data acquisition unit, on-board Butterworth and linear phase filtering was used. The IRVs that recorded the data were of the same wagon class and located on the same train. The data from different IRVs could be compared for repeatability at the same track locations.

Differential GPS is installed on the IRV giving high spatial resolution at the locations of IRJs. The GPS coordinates of the IRJs were matched with the time-series signal. At each IRJ location the speed was reasonably repeatable, although at some IRJ locations there was some variation in speed. A track kilometer lookup table was used which maps GPS coordinates to track kilometers and allowed different tracks to be identified.

The vibration signals from the accelerometers mounted on the side-frame provide a mechanically filtered response of the vehicle at the locations of IRJs. Figure 1 shows the vibration signal at an IRJ location, which is indicative of the impact noise that would be generated by the wagon.

### 3 Spectral Analysis of Impact Signals

Wavelet analysis has been widely used in vibration signal processing for frequency based analysis. Wavelet methods are suited for interrogating impact signals or transient signals which applies to this application. The continuous wavelet transform (CWT) is a time-frequency method which is defined as a convolution between an original signal  $x(t)$  and a wavelet function  $\psi$ . A two-dimensional coefficient matrix,  $W_f$  is created across time ( $u$ ) and scale ( $s$ ), where the wavelet scale being inversely proportional to frequency, as shown in the equation below [7]. In the current study, a Fourier implementation of the CWT was used so the wavelet scale could be easily mapped to its corresponding frequency. Figure 2 below shows the CWT contours of the coefficient matrix,  $W_f$  from vibration data from an accelerometer at the same IRJ as Fig. 1.

**Fig. 1** Vibration signal from the side-frame mounted accelerometer at an IRJ location

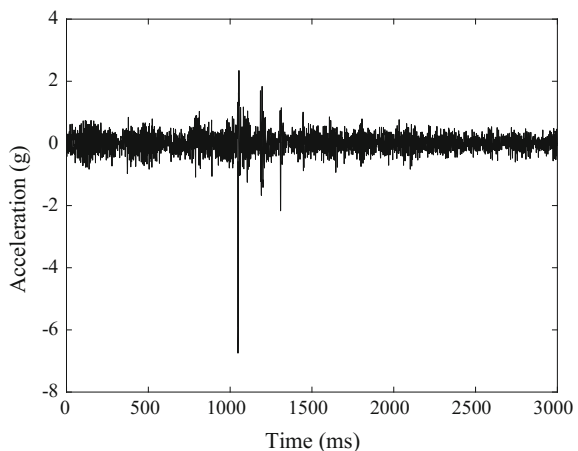
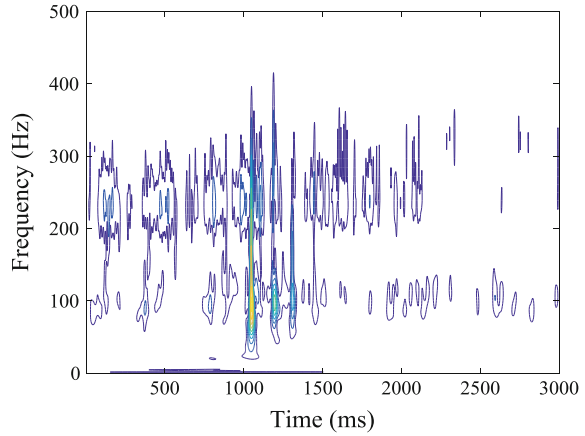




**Fig. 2** Continuous wavelet transform contours at an IRJ location



$$W_f(s, u) = \frac{1}{\sqrt{s}} \int_{-\infty}^{\infty} x(t) \psi \left( \frac{t-u}{s} \right) dt \quad (3.1)$$

### 3.1 Time-Frequency Based: The Discrete Wavelet Transform

The discrete wavelet transform (DWT) is analogous to the Fast Fourier Transform (FFT) and computational time for the DWT is much shorter than the CWT. The DWT is implemented via filter banks and it decomposes the signal until a maximum scale or minimum frequency is reached. The DWT uses these recursive filter banks to create a wavelet coefficient vector with the same number of points as the original signal. The DWT is incorporated into the clustering algorithm as discussed below, by decomposing signals into frequency bands. The DWT acts as a high and low pass filter interrogating these bands from the original signal [7]. The wavelet function or dyadic grid wavelet  $\psi_{j,k}$ , the DWT coefficients,  $T_{j,k}$ , the translation and dilation parameters  $j$  and  $k$  respectively are defined as follows [7]:

$$\psi_{j,k}(t) = 2^{j/2} \psi(2^j t - k) \quad (3.2)$$

$$T_{j,k} = \int_{-\infty}^{\infty} x(t) \psi_{j,k}(t) dt \quad (3.3)$$

The DWT was used in [3] to classify rail defects from a simulated vibration response signal. The DWT was used to split the data into frequency bands so that

thresholding could be applied for classification of track defects. In the current study the multi-signal clustering methodology utilises the DWT in its implementation to decompose the signals. The implementation of this method in the current study and the clustering algorithm will be discussed below.

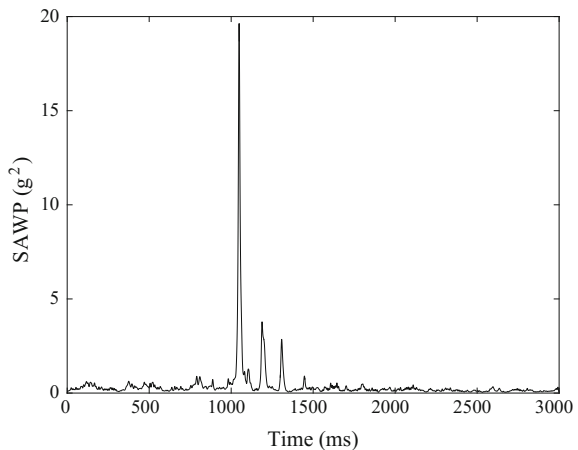
### 3.2 Time-Frequency Based: Scale Averaged Wavelet Power

As mentioned above, scale averaged wavelet power (SAWP) was the time-frequency wavelet technique used in [2] to identify squats in axle-box accelerometer data. In the equation below the terms before the summation are normalisation coefficients for the wavelet function selected, with the power of the wavelet coefficients,  $W_f$  and averaged across scales,  $s_j$ . SAWP reduces the two-dimensional wavelet coefficient matrix into a one-dimensional time-based vector. The calculation of SAWP is shown in the equation below:

$$SAWP(u) = \frac{\delta j \delta t}{C_\delta} \sum_{j=j_1}^{j_2} \frac{|W_f(s_j, u)|^2}{s_j} \tag{3.4}$$

This technique allows impact signals to be identified and detected in accelerometer measurements. Also, SAWP can be used to quantify the severity of impact signals in the frequency domain. In the current study this method was utilised and incorporated with other time-frequency and frequency based vibration signal analysis techniques to give a broad spectral view of the impact signals. Figure 3 shows the calculated SAWP at the same IRJ location as Fig. 2.

**Fig. 3** Scale averaged wavelet power at the same IRJ location as Figs. 1 and 2



### 3.3 Frequency Based: Wavelet Energy

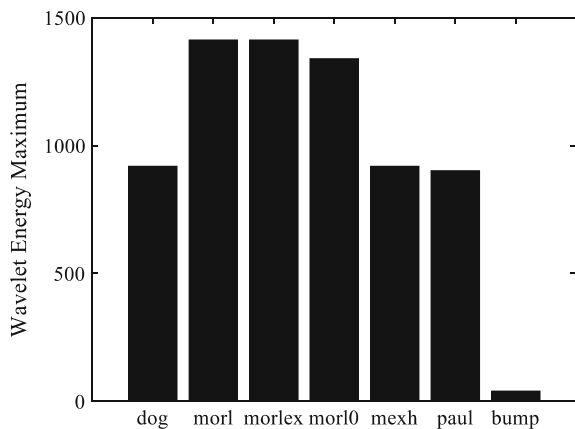
Wavelet energy is a frequency or scale only feature extracted from the wavelet coefficient matrix. The calculation of wavelet energy provides a vibration signature for the impacts at IRJs. Wavelet energy is analogous to power spectral density (PSD) in the Fourier domain but provides much better time–frequency resolution [8]. This can be seen in the wavelet energy plots shown in Figs. 5, 6 and 7. In the equation below the wavelet coefficient matrix,  $W_f$  is summated at each wavelet scale,  $s$ :

$$\text{Wavelet Energy}(s) = \sum_{j=1}^m |W_f(s,j)|^2 \tag{3.5}$$

### 3.4 Wavelet Selection

The selection of the wavelet function is an important aspect of wavelet analysis. Wavelet energy and wavelet Shannon entropy are the techniques that have been used to select the wavelet function [8]. According to [7], the wavelet function selected should closely match the signal being interrogated. To quantify this statement, if the resultant wavelet coefficient matrix is strongly correlated with the signal, the magnitude of the wavelet coefficients will be larger. This can be shown in the resultant wavelet energy, if the correct wavelet has been selected for the signal, the wavelet energy would be larger. The quantification for wavelet selection is shown in the figure below for seven wavelet function choices, where the Morlet wavelet was finally selected for this application to rail vehicle vibration signals. Figure 4 below shows the maximum energy for each type of wavelet showing that the Morlet wavelet is the most suitable wavelet function for this application.

**Fig. 4** Quantification of wavelet function selection using maximum wavelet energy for wavelet functions available for the Fourier implementation of the continuous wavelet transform



### 4 Clustering of Impact Signals

Multi-signal discrete wavelet transform clustering was used to classify the impact signals. The DWT component of this algorithm splits the wavelet energy features into frequency bands and constructs clusters from a hierarchical cluster tree. Six distinct groups of impacts were classified based on the wavelet energy at each IRJ location. It was found that each cluster corresponds to the frequency content of the wavelet energy and its magnitude. Most of the impact signatures from the IRJs were in Clusters 3 and 4. It can be inferred from the cluster signatures that Cluster 3 is wide band which implies a general rolling state. On the other hand, Cluster 4 showed a progression into higher magnitudes of energy whilst still remaining relatively wideband. This method gave an indication of the severity and energy of the impact signals obtained from the vibration sensors in the frequency domain. Individual examples of the six clusters are shown in Fig. 5.

Table 1 shows the effectiveness of clustering by identifying the empty and loaded conditions of the IRV and the corresponding frequency signatures. This clustering method essentially creates system identifications for IRJs and the loading state of the IRV. For Clusters 2, 5 and 6 the separation between empty and loaded is reasonably distinct. This is expected as the frequency content of the vibration signal is related to the dynamic characteristics of the loading state of the wagon. The correlation between the state of the wagon and the classification in each of these

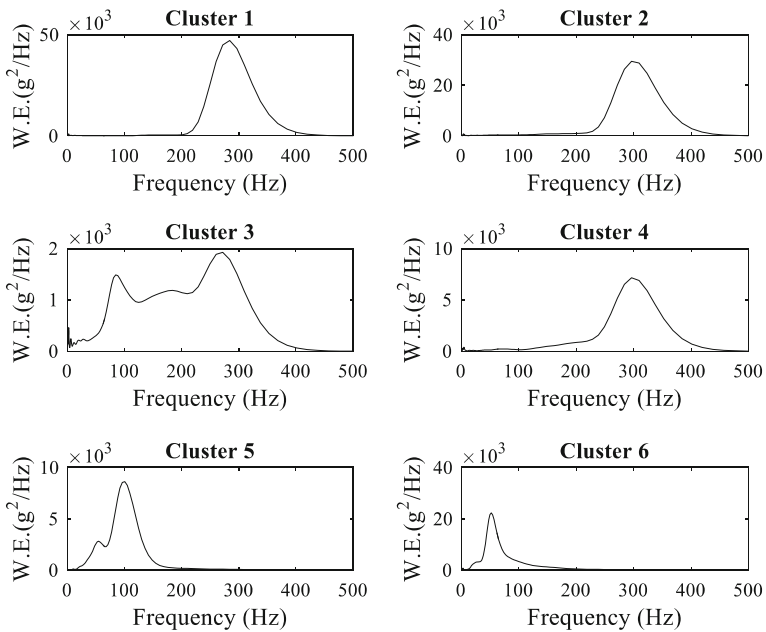


Fig. 5 Individual examples of the six clusters obtained for wavelet energy (W.E)

**Table 1** Categories of discrete wavelet transform clusters and their relationship to the loading condition of the IRV

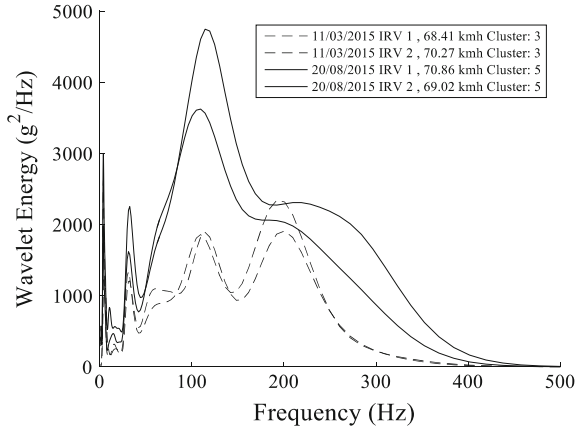
Cluster number	Frequency content of cluster	Percentage of empty/loaded data points
1	Peak at 300 Hz	Empty-100% Loaded-0%
2	Peak at 300 Hz	Empty-97.06% Loaded-2.94%
3	Wideband	Empty-53.06% Loaded-46.94%
4	Peak at 200–300 Hz	Empty-65.81% Loaded-34.19%
5	Peak at 100 Hz	Empty-3.19% Loaded-96.81%
6	Peak at 50–100 Hz	Empty-7.50% Loaded-92.5%

clusters is over ninety percent. It is noted that the peak frequency varies between empty and loaded. The empty condition has a peak in the range of 300 Hz and the loaded has a peak in the range of 100 Hz. This is consistent with the fact that the mass of loaded wagon is much larger than an empty wagon. Generally, it was found that a high wavelet energy peak in the frequency domain does not necessarily correspond to a high peak in the raw vibration signal. By using wavelet energy a clearer perspective of the IRJs spectral content can be seen.

## 5 Correlation of Clustering Analysis with Maintenance Records

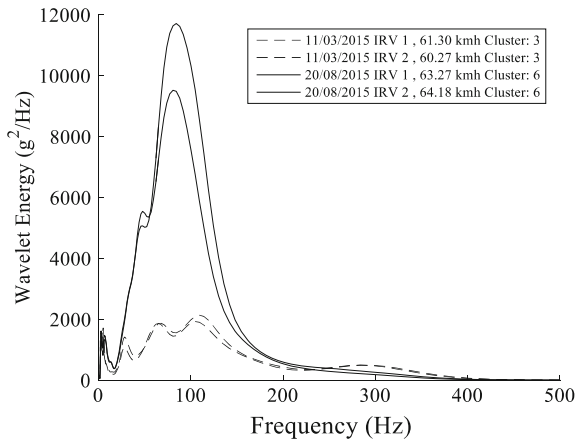
Maintenance records were obtained to determine if there is any correlation with the frequency based feature extraction methods. The maintenance records are a log of manual inspections conducted by track maintenance personnel which indicate the physical condition of the IRJ and the priority for action. The maintenance records provided information about the state of the IRJs and were used to validate the clustering analysis. Figures 6 and 7 show twin IRVs located on the same train travelling over an IRJ on two separate days. The lower magnitude wavelet energy curves are from one run in March of the twin IRVs travelling over an IRJ. The higher magnitude wavelet energy curves are from another run in August. There is a good agreement between the two IRV signals on the same day shown by similar peaks in the frequency content between each IRV. For this particular IRJ in Fig. 6, it was flagged for maintenance but not closed between the two data points. This case shows a change in the cluster number after the maintenance was flagged and in this case the IRJ was categorised as dipped. At this particular location the speed of the IRVs was reasonably consistent across runs. In this case the raw acceleration

**Fig. 6** Wavelet energy at an IRJ location showing deterioration by the change in cluster number. Open for maintenance but not closed on 17/05/2015 as a dipped IRJ with a priority of one month



value was consistent across runs. The low frequency component in the wavelet energy vector in Fig. 6 below may indicate that some track deflection is occurring, corresponding to the maintenance record category. This component is due to the vehicle body and bogie motions being registered by the accelerometers located on the side frame of the wagon. The magnitude of the lower frequency component captured by the wavelet energy could be used to classify the deterioration of the track condition indicating higher levels of track deflection. Figure 7 below shows a similar example where a particular IRJ has be flagged for maintenance but has not been maintained or closed. The progression to Cluster 6 from Cluster 3 demonstrates that this particular IRJ requires urgent maintenance. Both of the examples below show that the cluster numbers are independent to speed. This highlights the benefit of using frequency based methods to extract more information from the raw data.

**Fig. 7** Wavelet energy at an IRJ location showing deterioration by the change in cluster number. Open for maintenance but not closed on 02/12/2014 as an IRJ with surface flow and a high priority



## 6 Conclusions

The vibration impact noise signals of Insulated Rail Joints from bogie-frame accelerometers were obtained over several months. The continuous wavelet transform was used to transform the data into the frequency domain. The vibration signatures of IRJs were generated by post-processing the accelerometer signals using wavelet energy. The wavelet energy method was applied to the current study and provided improved time–frequency resolution over traditional Fourier based power spectral density methods. Multi-signal discrete wavelet transform clustering was used to classify the vibration signatures obtained from the wavelet energy. It was found that this method can successfully classify the IRJ vibration signatures into distinct groups of frequency identifications. By using clustering, the relationship between the vibration signal frequency content and the loading state of the wagon was found. The clusters gave an indication of the severity of the impact signals in the frequency domain and correlated with maintenance records. Maintenance records provided a reference point for the verification of the clustering methodology. The clustering methodology could potentially be used for predictive maintenance. Frequency based analysis of data from instrumented vehicles could be applied to other track defects such as, squats, welds, turnouts and corrugation.

## References

1. Weston, P., et al.: Perspectives on railway track geometry condition monitoring from in-service railway vehicles. *Veh. Syst. Dyn.* **53**(7), 1063–1091 (2015)
2. Molodova, M., Li, Z.L., Dollevoet, R.: Axle box acceleration: measurement and simulation for detection of short track defects. *Wear* **271**(1–2), 349–356 (2011)
3. Hopkins, B.M., Taheri, S.: Track health monitoring using wavelets. ASME 2010 Rail Transportation Division Fall Technical Conference, pp. 9–15 (2010)
4. Dhanasekar, M., Bayissa, W.: Performance of square and inclined insulated rail joints based on field strain measurements. *Proc. Inst. Mech. Eng. Part F: J. Rail Rapid Transit* **226**(F2), 140–154 (2012)
5. Kabo, E., Nielsen, J.C.O., Ekberg, A.: Prediction of dynamic train-track interaction and subsequent material deterioration in the presence of insulated rail joints. *Veh. Syst. Dyn.* **44** (sup1), 718–729 (2006)
6. Ver, I., Ventres, C., Myles, M.: Wheel/rail noise-part III: impact noise generation by wheel and rail discontinuities. *J. Sound Vib.* **46**(3), 395–417 (1976)
7. Addison, P.: *The illustrated wavelet transform handbook*. Institute of Physics Publishing, London (2002)
8. Bafroui, H.H., Ohadi, A.: Application of wavelet energy and Shannon entropy for feature extraction in gearbox fault detection under varying speed conditions. *Neurocomputing* **133**, 437–445 (2014)